

ICCC 2023 - Guidelines for citation and reuse



Please cite the conference proceedings as following:

Thailand Concrete Association, Ed. *Further Reduction of CO₂ -Emissions and Circularity in the Cement and Concrete Industry, 16th International Congress on the Chemistry of Cement 2023 - ICCC2023* (Bangkok 18.-22.09.2023). Bangkok, 2023. Available at: <https://www.iccc-online.org/archive/>

Please cite individual papers as following:

Author. Title. In: Thailand Concrete Association, Ed. *Further Reduction of CO₂ -Emissions and Circularity in the Cement and Concrete Industry, 16th International Congress on the Chemistry of Cement 2023 - ICCC2023* (Bangkok 18.-22.09.2023). Bangkok, 2023. Available at: <https://www.iccc-online.org/archive/>

All papers in the 2023 conference proceedings are published under the license CC-BY-ND 4.0.

(<https://creativecommons.org/licenses/by-nd/4.0/legalcode>)



Organized by



CONGRESS PROCEEDING **VOLUME III**

Further reduction of CO₂-emission
and circularity in the cement and concrete industry

SEPTEMBER 18-22, 2023

CENTARA GRAND & BANGKOK CONVENTION CENTRE @CENTRALWORLD

Co-Sponsor by



Contact information :

Email: iccc2023.tca@gmail.com

Website : <https://www.iccc2023.org/>

PREFACE

The International Congress on the Chemistry of Cement (ICCC) is the renowned global platform that summarizes the state of the art of cement chemistry as well as major trends in cement application. Since the first International Congress on the Chemistry of Cement started in London in 1918, it has provided a strong and fruitful link between the academic world and the cement industry. It has always stimulated scientific exchanges and discussions between researchers, students, and those who have already gained working experience in many fields of chemistry relevant to cement production and its use in concrete and mortar. The ICCC is the venue to present cement and environmental development together with meeting worldwide and renowned experts from all over the world who come to present their works at the congress.

This proceeding collects the papers submitted to the 16th International Congress on the Chemistry of Cement (ICCC 2023), which was held in Bangkok, Thailand between September 18-22, 2023, and organized by Thailand Concrete Association on the theme of “further reduction of CO₂-emission and circularity in the cement and concrete industry”. The ICCC 2023 attracted more than 565 papers and more than 800 delegates and students from 49 countries.

The scientific program covers the topics of the newest and the most important research and development describing the new dimensions in clinker production, advances in hydration chemistry, enhancing clinker substitution and supplementary cementitious materials, advances in characterization methods and modelling, new low carbon cement and carbonatable binders, new findings in admixture & rheology, new technology for quality concrete, durability & reactive transport, sustainability, circular economy, waste processing and recycling, and standardization of cement and concrete.

The Organizing Committee and the Scientific Committee believe that our participants will be most satisfied with the congress and will gain the knowledge to improve their professional works in the future.



Thanakorn Pheeraphan

Prof. Thanakorn Pheeraphan
Chairman of the Organizing Committee



Somnuk

Prof. Somnuk Tangtermsirikul
Chairman of the Scientific Committee

Steering Committee Members

The Steering Committee is comprised of 26 members.

1. Prof. Dr. Mark G. Alexander, University of Cape Town, South Africa
2. Prof. Dr. Alexandra Bertron, INSA Toulouse, France
3. Prof. Dr. Shashank Bishnoi; Indian Institute of Technology Delhi, India
4. Prof. Dr. Leon Black, University of Leeds, United Kingdom
5. Dr. Cesar Constantino; Titan America LLC, USA
6. Jesper Sand Damtoft, Aalborg Portland A/S, Denmark
7. Prof. Dr. Jan Deja; Stowarzyszenie Producentów Cementu – PCA, Poland
8. Dr. Wolfgang Dienemann, HeidelbergCement AG, Germany
9. Daniel Duque, Cementos Argos S.A., Columbia
10. Ing. Jan Gemrich, Czech Cement Association, Czech Republic
11. Prof. Dr. Frederik Paul Glasser, University of Aberdeen, Scotland
12. Prof. Dr. R. Doug Hooton, University of Toronto, Canada
13. Prof. Dr. Vanderley M. John, Escola Politécnica da USP, Brasil
14. Prof. Dr. Kimberly Kurtis, Georgia Institute of Technology, USA
15. Christophe Levy, Lafarge Holcim Innovation Center (Chairman), France
16. Prof. Dr. Ippei Maruyama, Nagoya University Furocho, Japan
17. Dr. Bibekananda Mohapatra, Director General of the National Council for Cement and Building Materials, India
18. Dr. Marta Palacios, Instituto Eduardo Torroja, Spain
19. Prof. Dr. Angel Palomo, Instituto Eduardo Torroja, Spain
20. Prof. Dr. Thanakorn Pheeraphan, Thailand Concrete Association (Deputy-Chairman), Thailand
21. Prof. Dr. Martin Schneider, VDZ e.V., Research Institute, Germany
22. Prof. Dr. Karen Scrivener, École Polytechnique Fédérale de Lausanne – EPFL, Switzerland
23. Prof. Dr. Caijun Shi, Hunan University, China
24. Prof. Dr. Sui Tongbo, Sinoma International Engineering Co., Ltd., China
25. Prof. Dr. Jannie S. J. Van Deventer, Zeobond Pty Ltd, Australia
26. Dr. Kazuo Yamada, National Institute for Environmental Studies, Japan

Dr. Joerg Rickert, VDZ (Permanent Secretariat of ICCC), Germany -
(Without the right to vote)

Organizing Committee Members

Advisory committee members

1. Dr. Wonchalerm Chalodhorn, Siam City Cement Co. Ltd.
2. Prof.Dr. Chai Jaturapitakkul, King Mongkut's University of Technology Thonburi
3. Prof.Dr. Parinya Jindaprasert, KhonKaen University
4. Mr. Ferdinand Leopolder, The South East Asia Drymix Mortar Association SEADMA,
5. Assoc.Prof.Dr. Pichai Nimityongskul , 1st President of Thailand Concrete Association
6. Mr. Chakporn Oonjitt, Construction Institute of Thailand
7. Mr. Wanchai Phanomchai, Thai Industrial Standards Institute
8. Mr. Chana Poomee, Thai Cement Manufacturers Association
9. Dr. Phirun Saiyasitpanich, Office of Natural Resources and Environmental Policy and Planning
- 10.Mr. Manasit Sarigaphuti, The Siam Cement Group Public Company Limited
- 11.Assoc.Prof. Anek Siripanichgorn, Engineering Institute of Thailand
- 12.Prof.Dr. Boonchai Stitmannathum, Chulalongkorn University
- 13.Prof.Dr. Piti Sukontasukkul, King Mongkut's University of Technology North Bangkok
- 14.Mr. Sumate Surabotsopon, Italian-Thai Development Public Company Limited
- 15.Prof.Dr. Somnuk Tantermsirikul, Sirindhorn International Institute of Technology
- 16.Dr. Saranyu Viriyavejakul, Neighboring Countries Economic Development Cooperation Agencies
- 17.Prof.Dr. Pennung Warnitchai, Asian Institute of Technology
- 18.Mr. Boonyanit Wongrukmit, Electricity Generating Authority of Thailand

Organizing Committee members

1. Prof.Dr. Thanakorn Pheeraphan, Thailand Concrete Association and NavamindaKasatriyadhiraj Royal Air Force Academy (Chairman)
2. Asst.Prof. Dr. Chuchai Sujivorakul, King Mongkut's University of Technology Thonburi (Deputy Chairman)
3. Mr. Boonrawd Kuptitanhi, The Concrete Products and Aggregate Co., Ltd. (Treasurer)
4. Asst.Prof.Dr. Nattapong Magaratat , King Mongkut's University of Technology North Bangkok (Secretariat)
5. Dr. Praveen Chompreda, K.C.S. & ASSOCIATES. Co., Ltd.
6. Assoc.Prof.Dr. Phongthorn Julphunthong, Naresuan University
7. Miss Sunkamol Khongsawatvorakul, Saint-Gobain Thailand.
8. Mr. Sumet Kiatmetha, Hilti (Thailand) Ltd.
9. Gp.Capt. Nuth Limsuwan, Office of Civil Engineering Royal Thai Armed Forces.
- 10.Dr. Nontapat Nimityongskul, Asia Cement Public Company Limited.
- 11.Assoc.Prof. Panuwat Joykad, Srinakharinwirote University
- 12.Dr. Yut Panitanwong, Concrete Product and Aggregate Co.,Ltd.
- 13.Mr. Suwatchai Puwapattanachai, Sika (Thailand) Ltd.
- 14.Mr. Narin Sayanwisuttikam, KAO Industrial (Thailand) Co., Ltd.
- 15.Dr. Kritsada Sisomphon, The Siam Cement Group Public Company Limited.
- 16.Mr. Chalermwut Snguanyat, The Siam Cement Group Public Company Limited.
- 17.Mr. Pakorn Sutthiwaree, Siam City Cement Public Company Limited.
- 18.Assoc.Prof.Dr. Weerachart Tangchirapat, King Mongkut's University of Technology Thonburi
- 19.Asst. Prof. Dr. WarangkanaSaengsoy, Construction and Maintenance Technology Research Center, SIIT
- 20.Prof.Dr. Wanchai Yodsudjai, Kasetsart University

Scientific Committee Members

1. Prof.Mark Alexander, South Africa
2. Prof.Carmen Andrade, Spain
3. Prof.Sergio Angulo, Brazil
4. Dr.Mohsen Ben Haha, Germany
5. Prof.Susan Bernal Lopez, UK
6. Prof.Alexandra Bertron, France
7. Prof.Shashank Bishnoi, India
8. Prof.Maria Blanco, Spain
9. Prof.Jeff Bullard, USA
- 10.Prof.Maria Alba Cincotto, Brazil
- 11.Prof.Jan Deja, Poland
- 12.Prof.Donguk Choi, South Korea
- 13.Prof.Josee Duchesne, Canada
- 14.Mr.Wilmar Echeverri, Colombia
- 15.Prof.Ivan Escalante, Mexico
- 16.Dr.Duncan Herfort, Denmark
- 17.Prof.Bruno Huet, France
- 18.Prof.Jason Ideker, USA
- 19.Prof.Edgardo Irassar, Argentina
- 20.Prof.Zhengwu Jiang, China
- 21.Prof.Maria Juenger, USA
- 22.Dr.Marios Katsiotis, Greece
- 23.Prof.Shiho Kawashima, USA
- 24.Prof.Paula Kirchheim, Brazil
- 25.Prof.Jiaping Liu, China
- 26.Mr.Federico Lopez, Mexico
- 27.Prof.Barbara Lothenbach, Switzerland
- 28.Prof.Horst Ludwig, Germany
- 29.Prof.Ippe Maruyama, Japan
- 30.Prof.Thomas Matschei, Germany
- 31.Mr.Mike McDonald, South Africa
- 32.Dr.Sea Monkman, Canada
- 33.Prof.Paulo Monteiro, USA
- 34.Mr.Carlos Orozco, Colombia
- 35.Dr.Marta Palacios, Spain
- 36.Prof.Martin Palou, Slovakia
- 37.Dr.César Pedrajas, Spain
- 38.Prof.Rafael Pileggi, Brazil
- 39.Prof.Kedsarin Pimraksa, Thailand
- 40.Prof.John Provis, UK
- 41.Prof.Francisca Puertas, Spain

Scientific Committee Members

42. Prof. Jueshi Qian, China
43. Prof. Aleksandra Radlinska, USA
44. Dr. Nailia Rakhimova, Russia
45. Prof. Matteo Romano, Italy
46. Prof. Nicolas Roussel, France
47. Dr. Kwesi Sagoe-Crentsil, Australia
48. Prof. Manu Sanathanam, India
49. Prof. Miguel Sanjuán, Spain
50. Prof. Caijun Shi, China
51. Dr. Denise Silva, USA
52. Prof. Somnuk Tangtermsirikul, Thailand (Chairman)
53. Dr. Theodor Staněk, CZ
54. Prof. Arezki Tagnit-Hamou, Canada
55. Mr. Antonio Telesca, Italy
56. Dr. Paul Tennis, USA
57. Prof. Michael Thomas, Canada
58. Prof. Jorge Tobon, Canada
59. Prof. Sandro Torres, Brazil
60. Prof. Matthieu Vandamme, France
61. Dr. Yury Villagrán Zaccardi, Argentina
62. Prof. Fazhou Wang, China
63. Prof. Zhang Wensheng, China
64. Prof. Claire White, USA
65. Dr. Frank Winnefeld, Switzerland
66. Dr. Hong Wong, UK
67. Dr. Kazuo Yamada, Japan
68. Prof. Cheng Yu, China
69. Prof. Doug Hooton, Canada
70. Peter Kruspan, Switzerland

Contents

| | Topics | Page |
|--------|--|------|
| | Preface | i |
| | Committees | |
| | - Steering Committee Members | ii |
| | - Organizing Committee Members | iii |
| | - Scientific Committee Members | v |
| | Papers | |
| PG0001 | Utilisation of Polycarboxylate Superplasticiser in Seawater Blended Cementitious Materials: Effect of Superplasticiser Molecular Structure and Seawater Salinity | 1 |
| PG0002 | Effect of alkanolamines in kaolinitic calcined clays pozzolanic reactivity | 6 |
| PG0003 | Study to improve vibration flowability of fresh concrete by controlling flocculation state of cement particles | 10 |
| PG0004 | How does the alternating current field affect the yield stress of fresh cement paste? | 14 |
| PG0005 | Functionalized transition metal doped silicate hydrate/PCE nanocomposites: an innovative hardening accelerator | 19 |
| PG0008 | The challenges of combining alkali activation and workability in low carbon binders: a molecular approach | 23 |
| PG0012 | Interpretation of rheological property of steel slag powder blended cement paste: from interparticle force to physico-chemical parameters | 27 |
| PG0014 | Influence And Strategies of Plug Flow on The Measured Rheological Properties of Cement-Based Materials | 31 |
| PG0016 | Effect of the microstructure of polycarboxylate ether (PCE) superplasticizers on the hydration kinetics of Ordinary Portland Cement (OPC) | 35 |
| PG0018 | C-S-H and pore structure on hardened cement mixed with volcanic glass fine powder | 39 |
| PG0022 | Early-age workability loss in LC3 systems | 43 |
| PG0027 | Impact of C-S-H Seeds on Cementitious Hydration Kinetics, Pore Structure, and Early Age Strength | 47 |
| PG0028 | Influences of Accelerators on the Compressive Strength of Clinker-Efficient Composite Cements with Slag and Limestone | 51 |
| PG0031 | On the CO ₂ Footprint of Polycarboxylate Superplasticizers (PCEs) and its Impact on the Eco Balance of Concrete | 55 |

Contents

| | Topics | Page |
|--------|--|------|
| PAPERS | | |
| PG0035 | A novel formulation concept for fast OPC based tile adhesives | 60 |
| PG0036 | Hydration and Viscoelastic Properties of Tricalcium Aluminate Pastes Influenced by Soluble Sodium Salts | 64 |
| PG0040 | Influence of pH value and temperature on the dispersion ability of PCEs containing ethyl acrylate and diethyl maleate segments and its mechanism study | 69 |
| PG0041 | The Purer the Better: How Monomer Purity Affects the Effectiveness of Phosphate Type Superplasticizers in Cement Paste | 73 |
| PG0042 | Paste rheology and surface charge of calcined kaolinite | 77 |
| PG0043 | Rheological properties of belite-calcium sulfoaluminate cement | 81 |
| PG0044 | Early-age elasticity in structuration of highly cohesive concrete with added pozzolanic diatomaceous earth | 85 |
| PG0045 | Cellulose ether behavior in slag cement-based tile adhesives | 89 |
| PG0046 | Influence of key synthetic factors on the molecular characteristics of polycarboxylate superplasticizers | 93 |
| PG0049 | Influence of retarders on the hydration and rheology of calcium sulfo aluminate cement | 97 |
| PG0053 | Pore structure of polymer-modified dry mix tile adhesive mortars | 101 |
| PG0055 | Microscopic tracking of superplasticizer adsorption in alkali activated materials | 105 |
| PG0058 | Influence of Kaolinite Content on the Fresh Properties of LC ³ Systems | 109 |
| PG0059 | Non-adsorbing polymers and depletion forces in cement pastes | 113 |
| PG0060 | Complexation Enthalpies of Organic Admixtures: Measurement Method Development and Application to Calcium Complexes | 117 |
| PG0063 | Rheology of ultra-high geopolymer concrete: Influences of activator types and silica fume | 121 |
| PG0065 | Effects of different types of shrinkage reducing agents on shrinkage properties of mortars incorporating slag or silica fume | 125 |

Contents

| | Topics | Page |
|--------|--|------|
| PAPERS | | |
| PG0067 | On the impact of sulphate source on admixtures in limestone calcined clay cements | 129 |
| PG0071 | A study on the adsorption and dispersion capability of PCEs with different structures on cement containing montmorillonite | 133 |
| PG0072 | Preparation and performance of EPEG-type PCE and its application in ultra-high performance concrete | 137 |
| PH0003 | Thermal Crack Resistance and DEF Suppression Effect of Concrete Using Fly Ash Cement | 141 |
| PH0004 | Gradient distribution of slender glass microfibers in 3D printed cementitious filaments | 145 |
| PH0005 | Effect of Hydrophobically Modified Hollow Glass microspheres on the flow behavior of lightweight high-performance concrete | 149 |
| PH0009 | Ohmic heating curing for cement-based materials: A promising new technology with enhanced fabrication efficiency | 153 |
| PH0011 | Preliminary Investigation of 0-3 Lead Zirconate Titanate – Lime Calcined Clay Cement Composites | 157 |
| PH0019 | New trend line of compressive strength and unit volume weight of cement composites: Lightweight and high-strength at the same time | 161 |
| PH0020 | Concrete Mix Design for Rigid Pavements Maintenance: Evaluating Compressive Strength Development and Curing Temperature Effect | 165 |
| PH0022 | Concrete performance with alkali-activated cement based on industrial side streams from Brazil | 170 |
| PH0023 | Strength Development Prediction and Mixture Optimization of Concrete Used in the Three Gorges Dam | 174 |
| PH0024 | Inorganic Capsule Based on MgO Expansive Agent for Self-healing Concrete | 178 |
| PH0025 | Design of High-Performance Concrete (HPC) using calcined clay as supplementary cementitious materials | 182 |
| PH0027 | The performance of 3D printing PCM concrete with novel hollow ceramsite composite | 186 |

Contents

| | Topics | Page |
|--------|---|------|
| PAPERS | | |
| PH0029 | Drying shrinkage and cracks in fresh cement-based materials for 3D printing: an X-Ray Tomograph investigation | 190 |
| PH0030 | Effect of self-healing on surface morphology in cracked reactive powder concrete | 194 |
| PH0034 | Sustainable Geopolymer Concrete for Thermoelectric Energy Harvesting | 198 |
| PI0002 | Various fundamental factors affecting the ion penetration in concrete | 202 |
| PI0004 | Durability of slag cement and sulfoaluminate cement exposed to acetic acid, ammonium nitrate and magnesium chloride | 207 |
| PI0005 | Anti-corrosion mechanism of LDHs-VB3- for rebar: insights from experiments and DFT simulations | 212 |
| PI0006 | Cement use under extreme marine environment–deep sea | 216 |
| PI0007 | Chloride Adsorption Does Not Retard Chloride Ingress in Concrete | 220 |
| PI0008 | Roles of slag on corrosion electrochemical measurement in carbonated mortar | 224 |
| PI0009 | Evaluation of transport properties in ITZ with coupled CT image analysis and simulation | 229 |
| PI0012 | Assessment of influence of cation type of sulphate ions on early age strength, and microstructure of geopolymer concrete | 233 |
| PI0015 | Antimicrobial performance of ZnO-modified geopolymer against microbial corrosion | 237 |
| PI0017 | Cold Water Extraction as a method to determine the free alkali content of cementitious binders | 241 |
| PI0020 | Understanding the behavior of magnesium potassium phosphate cements under leaching | 245 |
| PI0023 | Effect of Al on the structure and swelling behavior of synthetic ASR gels | 250 |
| PI0025 | Geochemical interactions between cementitious materials and water in the context of drinking water supply | 254 |
| PI0026 | Restraint effect of steel bar on cement-based materials at early age : A full cross section study | 258 |
| PI0029 | Effect of Sulfate Attack on the Cement Mortars and Pastes with Different Replacement Levels of Limestone at a Low Temperature | 262 |

Contents

| | Topics | Page |
|--------|--|------|
| PAPERS | | |
| PI0031 | Alkali-silica reaction resistance of alkali-activated calcined clays using accelerated mortar bar test | 266 |
| PI0032 | Investigation on the durability evolution of high belite cement subjected to thermal fatigue | 270 |
| PI0034 | Research on the leaching mechanism of C-S-H : experiments and molecular dynamics simulations study | 274 |
| PI0035 | The deterioration process of alkali activated slag exposed to sulfate attack and calcium leaching | 278 |
| PI0037 | Multiphysics discrete modeling for expansion and deterioration of concrete due to alkali-silica reaction | 282 |
| PI0039 | Kinetics of iron (hydr)oxide precipitation in cementitious materials | 287 |
| PI0040 | Preparation of (super)hydrophobic cement-based matrix with organosiloxanes and micromodification of the surface | 292 |
| PI0041 | Assessment of the ion diffusivity of cement-based materials using QXRD and micro-CT based random walk simulation | 296 |
| PI0043 | Effect of Mg-bearing water on the chemical and mechanical properties of a low C/S industrial cement paste | 300 |
| PI0044 | Corrosion kinetics of steel in artificial carbonated pore solutions under the effect of stirring and bicarbonate ions | 304 |
| PI0047 | Chloride ingress resistance of Ca(OH) ₂ activated GGBFS: Impact of curing temperature and additional activators | 308 |
| PI0048 | A new unidirectional testing approach for sulfate resistance on cement mortars | 312 |
| PI0049 | A comparative assessment of different additives to reduce carbonation degradations of alkali-activated slag using in-situ ftir technique | 316 |
| PI0050 | Appraisal of the microstructural properties of ASR affected concrete at different moisture conditions using the DRI | 320 |
| PI0052 | Property changes of calcium sodium aluminosilicate hydrates (C-NA-S-H) gels subjected to water immersion | 324 |
| PI0056 | Experimental investigation of expansion and damage due to alkali-silica reaction at low temperature | 328 |
| PI0057 | Physicochemical stability of calcium aluminate cement and hemihydrate-based material exposed to deep sea | 332 |

Contents

| | Topics | Page |
|---------------|--|------|
| PAPERS | | |
| PI0060 | Resistance against chloride and carbonation of binary and ternary binder with GGBS or/and limestone | 336 |
| PI0061 | The fate of ferrous ions in corroding steel reinforced concretes | 340 |
| PI0065 | Effect of waterproofing chemicals on carbonation in Low clinker cement with pore structure analysis | 344 |
| PI0066 | The square root law with an offset applied to chloride diffusion in slowly reacting blended cement pastes | 348 |
| PI0067 | Phase Evolution and Property Development of Alkali-Silica Reaction Gel in Carbonation | 352 |
| PI0068 | L-Ascorbic Acid used as green corrosion inhibitor in chloride-bearing steel reinforced cement mortars | 356 |
| PI0070 | Carbonation of Concrete with SCMs: a data analysis by RILEM TC 281-CCC | 360 |
| PI0073 | Towards the Development of Prescriptive-Based Specifications for Non-Traditional SCMs to Prevent Alkali-Silica Reaction | 364 |
| PI0074 | Elucidating the carbonation front in blended calcined kaolinite clays binders using analytical techniques | 368 |
| PI0078 | Cementitious materials for oil-well abandonment and numerical simulations of cement durability at oil well conditions | 372 |
| PI0081 | Alkali-silica reaction in calcium aluminate cement mortars | 377 |
| PI0084 | AAM – oil composite: a new highly durable material with a negative carbon footprint | 381 |
| PI0086 | Coefficient of thermal expansion of alkali-activated slag concrete | 386 |
| PI0090 | Study on the Deterioration Mechanism of Cementitious Waterproofing Membrane (Part I: Macroscopic Performance) | 390 |
| PI0091 | Impact of an evolving microstructure on the square-root law for chloride ingress | 395 |
| PI0092 | Formation Factor as a Non-Destructive Measure of Chloride Diffusion Coefficient | 399 |
| PI0098 | Surface effect on chloride diffusion in calcium silicate hydrate | 403 |
| PJ0001 | Preparation of reactive urchin-like recycled concrete aggregate by wet carbonation: towards improving the bonding capability | 407 |

Contents

| | Topics | Page |
|--------|---|------|
| PAPERS | | |
| PJ0002 | Physical and mechanical characterization of Alkali-Activated slag cement in presence of ion-exchange resins | 411 |
| PJ0005 | Evaluation of environmental technologies for cement production considering multiple environmental categories | 415 |
| PJ0011 | Structure and Reactivity of Aqueous Carbonated Blended Cement Pastes | 419 |
| PJ0013 | Statistical modelling and optimization of strength in hybrid binders based on volcanic pumice, environmental and cost analysis. | 423 |
| PJ0014 | CDW waste as retardants of ions harmful to cement | 428 |
| PJ0016 | Production of a hydraulic material from post treated steelmaking slags | 432 |
| PJ0020 | Influence of sisal fiber on mechanical, shrinkage and high temperature performance of UHPC | 437 |
| PJ0023 | Acid activation of phosphate by-products in geopolymerization technology | 442 |
| PJ0027 | Sulfate Resistance of Mortar Containing Low-Grade Calcined Clay | 447 |
| PJ0029 | The role of $C_{12}A_7$, α' H- C_2S and dehydrated amorphous nesosilicate in rehydration of recycled cement | 452 |
| PJ0031 | Carbonation and hydration kinetics of CO_2 injected ready-mixed concrete | 456 |
| PJ0033 | Assessment of the Microstructure and Mass Transfer in Strontium-Loaded Geopolymer Cement Wasteforms | 460 |
| PJ0034 | Pretreatments processes of alkaline recycled concrete aggregates to maximize CO_2 capture in accelerated carbonation processes. | 464 |
| PJ0041 | Effect of Manganese Sulfate Replacing Gypsum on Properties and Reducing Cr(VI) of Cement Paste | 468 |
| PJ0048 | Study on MSWI fly ash solidifiers based on product composition design | 472 |
| PJ0050 | An Experimental Study of Sulfur and Chlorine Stripping from Cement Hot Meal | 476 |
| PJ0052 | Effect of copper tailing powder on the hydration and mechanical properties of concrete under low atmospheric pressures | 480 |

Contents

| | Topics | Page |
|--------|---|------|
| PAPERS | | |
| PJ0056 | Mineralogical Characterization of Waste to Energy (WTE) Ashes - Insights from Raman Imaging | 484 |
| PJ0057 | Recycling of phosphate waste rocks to produce alkali-activated mortars | 488 |
| PJ0059 | Effect of strontium salts on the kinetics and mechanisms of geopolymer cement formation | 493 |
| PJ0062 | Developing Pickering emulsion routes towards oil immobilisation in geopolymers | 497 |
| PJ0064 | Developing circular concrete through acid leaching of waste fines | 501 |
| PJ0065 | Application of Recycled Cementitious Material from Concrete Waste for UK Nuclear Waste Encapsulation | 506 |
| PJ0067 | Investigation on the effect of recycled powders from demolished concrete on the rheological properties of cement paste | 510 |
| PJ0068 | Evaluating the potential of Steel slags as alternative raw materials for Portland cement clinker production | 515 |
| PJ0069 | Upcycling of bio-waste ashes into additive for concrete | 519 |
| PJ0071 | Decarbonizing UAE Cement Industry with Limestone Calcined Clay Cement (LC ³) | 523 |
| PJ0074 | Development of a CO ₂ mineralization technology for concrete wash water upcycling | 528 |
| PJ0075 | Properties of a Magnesium-Silicate-Hydrate Cement Paste Prepared Using Magnesium Hydroxide | 532 |
| PJ0078 | Influence of Rice Husk on the Thermal Activation and Pozzolanic Activity of Tropical Soils | 536 |
| PJ0080 | Effect of Mix Proportion as W/C and Amount of GGBS Contents on CO ₂ Adsorption | 541 |
| PJ0081 | Use of concrete slurry waste as an accelerator - Effect on early-age strength development and hydration of steam-cured specimen | 545 |
| PJ0082 | A Study on Mortar Properties Focusing on Water Absorption Ratio of Carbonated Recycled Fine Aggregate | 549 |
| PJ0083 | Effect of Conditions on Pore structure of silica gel in Wet Carbonated Recycled Cement Paste Powder | 553 |

Contents

| | Topics | Page |
|--------|---|------|
| PAPERS | | |
| PJ0084 | Aqueous Carbonation of Recycled Concrete Fines: Towards Higher Efficiency | 557 |
| PJ0085 | Study on the Use of Recycled Aggregates for the Production of Cementless Pervious Concrete | 561 |
| PJ0087 | Eco-toxicity assessment of cement. Bioassays on luminescent bacteria and sea urchin embryogenesis | 565 |
| PJ0090 | Influence of low carbon cement and recycled aggregates on mortar fresh state and early hydration | 569 |
| PJ0091 | Rehydration of ettringite: microstructure and mechanical properties | 573 |
| PJ0092 | Physical Properties of Biochar Enhance the Rheological Behavior of Cement-Based Materials | 578 |
| PJ0093 | The reactivity of hydrothermally activated basic oxygen furnace slag | 583 |
| PJ0095 | Optimization of low clinker limestone calcined clay cement (LC ³) concrete mixes as further carbon footprint reduction strategy | 588 |
| PJ0097 | Research on multi-solid waste co-excitation of lead smelting slag to prepare green filling materials for mines and its performance | 592 |
| PJ0105 | Effects of phosphate salts on the interfacial bonding between magnesium phosphate cement and steel fiber | 596 |
| PJ0114 | Formation of closed pore structure porous glass-ceramics for thermal insulation | 600 |
| PJ0116 | Carbonation effects on mechanical performance and microstructure of LWAs produced with hydrated cement paste powder | 604 |
| PK0001 | Study for New Japanese Industrial Standards; “Volcanic Glass Powder for Use in Concrete” | 609 |
| PK0002 | Cement types and seawater exposure in Europe – implications for infrastructure and its integration into marine habitats | 613 |
| PK0004 | Effect of water content on fluorescence intensities of cement-based materials | 617 |
| PK0005 | A micromechanical modelling approach to study the effect of shape of hydrates on creep properties of cement pastes | 621 |

Utilisation of Polycarboxylate Superplasticiser in Seawater Blended Cementitious Materials: Effect of Superplasticiser Molecular Structure and Seawater Salinity

Jun Ren¹, Shuo Yan¹, Shengye Xu², and Yunhui Fang^{3*}

¹ School of Architecture and Planning, Yunnan University, Kunming, 650500, P R. China
Email: renjun@ynu.edu.cn; yanshuo820@outlook.com

² Guangdong Power Grid Energy Development Co. Ltd, Guangzhou, 510000, P R. China
Email: Shixiao5561@163.com

³ KZJ New Materials Group Co., Ltd, Xiamen 361199, P R. China
Email:fangyunhui@126.com

ABSTRACT

The performance of polycarboxylate superplasticiser (PCE) in seawater blended cementitious materials depends on both molecular architecture of the polymer and salinity of seawater. The aim of this study is to investigate the effect of PCE molecular architecture and seawater salinity on the fresh properties of seawater blended cement paste. A series of six PCE with different molecular structure were synthesised and their performance in cement paste blended with different salinity seawater was determined by fluidity and rheological behaviour. Finally, the potential mechanism was proposed via the measurement of PCE adsorption amount and adsorption layer thickness. The results showed that the PCEs with long side length and high acrylic acid to Methylallyl polyoxyethylene ether ratio showed a significant improvement in fluidity and rheological properties of the cement paste blended with seawater, which was confirmed by the observed higher adsorption amount. However, the incorporation of sulfate and hydroxyethyl methacrylate showed limited ability in improving dispersion of cement. The increase of seawater salinity significantly hindered the performance of PCEs.

KEYWORDS: Polycarboxylate superplasticiser; Seawater; Molecular Structure; Salinity; Fresh Property

1. Introduction

The utilisation of seawater (SW) and seasand in manufacturing cement and concrete, which can partially solve the shortage of freshwater in construction industry, has been attempted in many countries (Zhao et al. 2021). However, the engineering application of seawater manufactured concrete has been debated for long time (Liu et al. 2021), because there are many substances, i.e., chloride (Cl⁻), sodium (Na⁺), sulfate (SO₄²⁻), magnesium (Mg²⁺) existed in seawater, which may introduce the intractable issues for the cementitious materials, and lead to the corrosion of reinforcement as well (Mahlknecht et al. 2017, Wang et al. 2018). Different from the concrete made with fresh tapwater (TW), the different properties of cement and concrete is observed in that with SW, which therefore, leads to the accelerated hydration process and the poor workability of the cement as well (Wang et al. 2020), which requires the employment of polycarboxylate superplasticisers (PCE) to compensate and ensure the sufficient fluidity (Ren et al. 2019).

Noticeably, the performance and working mechanism of PCEs highly depends the molecular structure of the polymers (Winnefeld et al. 2007, Pourchet et al. 2012), and the ions in seawater as well (Pang et al. 2021, Ren et al. 2021) studied the dispersion performance of PCE in cement paste with seawater, and found that the SO₄²⁻ and Mg²⁺ ions in SW reduced the dispersion efficiency of PCE. Therefore, although some pioneer work has been conducted to evaluate the performance of PCEs in

cementitious materials blended with seawater, the systematically investigation from PCE itself and environmental factors has not been conducted.

The aim of this study is, therefore, to systematically investigate the effect of molecular architecture of PCE and salinity in SW on the fresh properties and working mechanism of cementitious material blended with SW. A series of six PCEs with different structures were first synthesised and the performance of the six PCEs was determined by minislump, rheological behavior and adsorption amount of SW blended cementitious materials under three salinities.

2. Experimental

2.1 Materials

The standard cement in accordance to GB8076-2008 was supplied by Fushun Aosaier Co., Ltd. The tapwater (TW) was used for manufacturing cementitious materials. Natural seawater with medium ion concentration (MSW) was collected from Dapeng Bay in Shenzhen, China. The natural seawater was diluted with deionized water to simulate the seawater with lower salinity (LSW), while it was concentrated by heating to monitor the seawater with higher salinity (HSW). The ion concentrations of the tapwater and seawater are shown in **Table 1**.

Table 1. The ion concentrations of the tapwater and seawaters (mg/l)

| | Na ⁺ | K ⁺ | Ca ²⁺ | Mg ²⁺ | Cl ⁻ | SO ₄ ²⁻ |
|-----|----------------------|----------------|------------------|----------------------|----------------------|-------------------------------|
| TW | 4.37 | 14.04 | 19.64 | 1.76 | 17.29 | 13.63 |
| LSW | 4.28×10 ³ | 256.64 | 152.62 | 616.43 | 0.87×10 ⁴ | 1.47×10 ³ |
| MSW | 1.05×10 ⁴ | 393.27 | 383.02 | 1.28×10 ³ | 1.66×10 ⁴ | 2.15×10 ³ |
| HSW | 1.37×10 ⁴ | 839.27 | 452.90 | 1.88×10 ³ | 2.78×10 ⁴ | 4.20×10 ³ |

2.2 Synthesis and characterisation of PCE

A series consisting of six PCEs was synthesised; and the details are shown in **Table 2**.

The six PCEs used in this study with varied molecular structure were synthesized and determined by free radical polymerization reaction using KPS (Potassium persulfate) as initiator, which followed the procedure proposed by reported literature (Ren et al. 2019). After synthesised, a 30% solution of sodium hydroxide was used to neutralize the polymer solution.

Table 2. Molar ratio of the monomer and solid content of the PCEs

| Code | AA | MPEG | | HPEG | | Nanosilica | MAS | Solid Content(%) |
|---------|------|------|------|------|------|------------|------|------------------|
| | | 2400 | 3000 | 2400 | 3000 | | | |
| PCE-I | 4.00 | 1.00 | | | | | | 50.20 |
| PCE-II | 8.00 | | | | 1.00 | | | 50.21 |
| PCE-III | 4.00 | | | 1.00 | | | | 50.18 |
| PCE-IV | 8.00 | | 1.00 | | | | | 50.16 |
| PCE-V | 4.00 | | | | 1.00 | 5% | | 50.14 |
| PCE-VI | 4.00 | | | 1.00 | | | 1.00 | 49.07 |

2.3 Performance of PCEs in cementitious materials

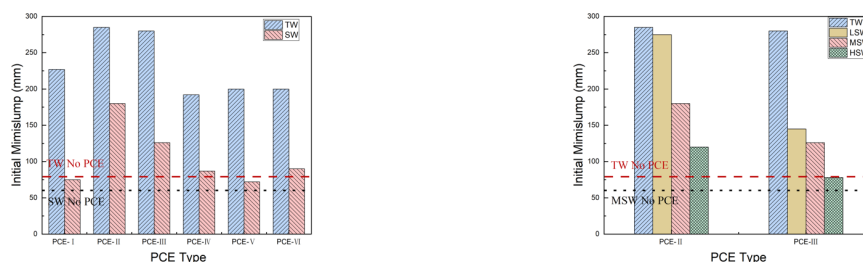
The cement paste was prepared according to the Chinese standard GB8077-2012, the water-to-cement (w/c) ratio for all mixtures was fixed at 0.29 and the concentration of PCE 0.15% of PCE. The workability of cement paste was conducted in accordance with the Chinese standard method GB/T 8077-2012 and the rheological properties of the cement pastes were obtained via a Lamy Viscometer RM100 and the shear rate increases from 2s⁻¹ to 200s⁻¹ in 9 steps and then gradually decreases to 10s⁻¹, maintaining a steady state for 5 min at each speed with six PCEs. Finally, the adsorption amount of the PCEs in cement particle surface was determined by analysis with a total organic carbon (TOC) unit.

3. Results

3.1 Workability

The workability of TW and SW blended cement pastes in the presence of PCEs was determined by minislump test and the results are presented in Fig. 1. It can be clearly seen from Fig. 1(a) that compared

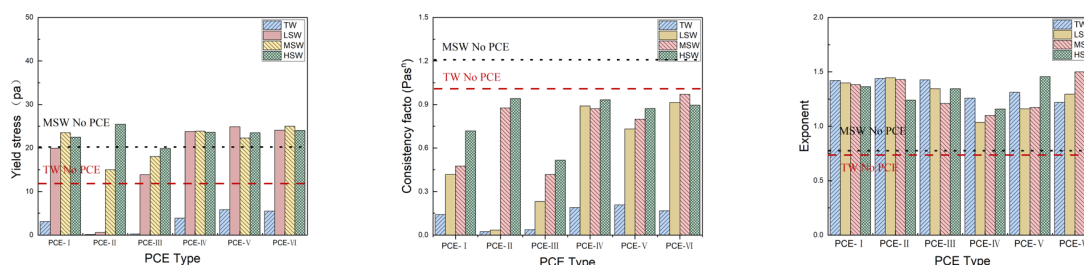
to the samples without PCE, the addition of PCE increased the initial minislump of cement paste. However, for the PCE with longer side chain (PCE-I and PCE-II), the increase of acid-ether ratio led to a higher initial minislump, while for the PCE with shorter side chain (PCE-III and PCE-IV), the lower minislump was observed with high acid-ether ratio. Moreover, the grafting of nanosilica and MAS did not significantly improve the dispersion performance of PCEs. It is worth noting that although the substitution of SW for TW significantly reduced the initial minislump of PCE superplasticised cement pastes, overall, PCE-II and PCE-III still showed the highest initial minislump. Moreover, as shown in Fig. 1(b), the increase salinity of the seawater further reduced the initial minislump of the cement paste, while the better performance was achieved by PCE-II.



(a) Effect of different PCEs in TW and MSW (b) Effect of different salinity
Fig. 1 Effect of PCE type and SW salinity on initial minislump of cement paste with PCEs

3.2 Rheological behaviour

The rheological properties based on the Herschel-Bulkley model are presented in Fig. 2. As shown in Fig. 2(a), compared to the reference (without PCE), the obvious reduction on the yield stress was found in the figure. Obviously, regardless the acid-ether ratio, the PCEs with longer side chain showed a better dispersion effect in the cementitious materials, which might due to the longer side chain provides a better steric repulsion. However, compared with the cement paste with other PCEs, incorporating of nanosilica (PCE-V) and MAS (PCE-VI, Sodium methallyl sulfonate) did not significantly reduce the yield stress of the cement paste. Similarly, when increasing the salinity (from LSW to HSW), the higher yield stress was observed. It should be noted that ability to resist salt various with different PCEs. This is well corroborated by the minislump results presented in Fig. 1 and will be further discussed in the discussion section below. Moreover, it can be seen from Fig 2(b) that, regardless of the rheological models, the addition of PCEs reduced the plastic viscosity of the cement paste. Compare with the six PCEs, the lower value was observed in PCE-I, PCE-II and PCE-III, indicating the PCEs with longer side chain or lower acid ether ratio could significantly affects the viscosity. However, when the SW was applied, the viscosity was significantly increased with higher viscosity at a high salinity. This could be due to the promoted hydration of the SW cement paste, in which the hydration product can bridge the particles and form the agglomerates. It should be noted that, the shear-thickening was also observed based on HB model according to the increased exponent to over 1 (Fig. 2(c)).



(a) Yield stress (b) Consistency factor (c) Exponent
Fig. 2 Effect of PCE type and SW salinity on rheological parameter of cement

3.3 Adsorption Amount

The adsorption amount of the PCEs in different solutions are shown in Fig. 3. It is evident from Fig. 3(a) that similar trend was observed in both TW and MSW, in which higher adsorption amount was observed in PCE-I, PCE-II and PCE-III. Although the general trend of the effect from different type of PCEs was

similar to that in TW, a significant lower adsorption was observed when the TW was replaced by MSW. Furthermore, as shown in Fig. 3(b), the increase of salinity, which mean the ions in the solution was increased, lead to a reduction of the adsorption. As presented in Table 2, regardless the salinity, the massive amount of Na^+ , Mg^{2+} , Cl^- and SO_4^{2-} were existed in SW. Moreover, the high AA:HPEG ratio generally indicated the higher charge density, therefore, the PCEs with higher AA: HPEG ratio should offer a higher adsorption. However, the lower adsorption was observed in PCE with short side chain, which could be due to the formation of the complex with the divalent ions and carboxylate.



(a) Effect of different PCEs in TW and MSW (b) Effect of different salinity
Fig. 3. Effect of PCE type and SW salinity on adsorption amount of the cement paste

4. Conclusions

1. The minislump of cement pastes mixed with the TW and the SW was increased by PCE-II with long side chain and high acid ether ratio, however grafting nanosilica or Sodium methallyl sulfonate showed no improvement on the function of PCEs, especially in the SW mixed cement paste. the increase salinity of the seawater further reduced the initial minislump of the cement paste.
2. The addition of PCEs altered the rheological behaviour of the cement paste and shear thickening occurred and reduced the yield stress and plastic viscosity of the cement paste.
3. The ions in seawater affected the adsorption behaviour of PCE by reducing absorption amount, but PCE-II with its long side chains and high acid ether structure improves the dispersion of the SW blended cement particles.

Acknowledgements

The financial supports from National Natural Science Foundation of China (NSFC) (Grant No: 52168038, 51908526), Yunnan Provincial Department of Science and Technology (202301AT070192), and the National Key R&D Program of China (2022YFE0109300) are greatly acknowledged.

References

- Liu, S. Y., Z. Y. Wang, M. Y. Han, G. D. Wang, T. Hayat and G. Q. Chen (2021). "Energy-water nexus in seawater desalination project: A typical water production system in China." *Journal of Cleaner Production* **279**: 123412.
- Mahlknecht, J., D. Merchán, M. Rosner, A. Meixner and R. Ledesma-Ruiz (2017). "Assessing seawater intrusion in an arid coastal aquifer under high anthropogenic influence using major constituents, Sr and B isotopes in groundwater." *Science of The Total Environment* **587-588**: 282-295.
- Pang, X., X. Kong, X. Liu and T. Hao (2021). "The dispersing performances of polycarboxylate superplasticizer in cement pastes prepared with deionized water and seawater." *Materials and Structures* **54**(2): 85.
- Pourchet, S., S. Liautaud, D. Rinaldi and I. Pochard (2012). "Effect of the repartition of the PEG side chains on the adsorption and dispersion behaviors of PCP in presence of sulfate." *Cement and Concrete Research* **42**(2): 431-439.
- Ren, J., Y. Fang, Q. Ma, H. Tan, S. Luo, M. Liu and X. Wang (2019). "Effect of storage condition on basic performance of polycarboxylate superplasticiser system incorporated sodium gluconate." *Construction and Building Materials* **223**: 852-862.
- Ren, J., X. Wang, S. Xu, Y. Fang, W. Liu, Q. Luo, N. Han and F. Xing (2021). "Effect of polycarboxylate superplasticisers on the fresh properties of cementitious materials mixed with seawater." *Construction and Building Materials* **289**: 123143.
- Wang, J., J. Xie, Y. Wang, Y. Liu and Y. Ding (2020). "Rheological properties, compressive strength, hydration products and microstructure of seawater-mixed cement pastes." *Cement and Concrete Composites* **114**: 103770.

Wang, Y. C., K. Yang, A. Long, Y. Bai, S. Nanukuttan, B. Magee, X. H. Zhu, Z. L. Zhang, C. H. Yang and M. Basheer (2018). "Effectiveness of preconditioning regimes for assessing water permeability of high performance concrete." *Cement Concr. Compos.* **94**: 126-135.

Winnefeld, F., S. Becker, J. Pakusch and T. Götz (2007). "Effects of the molecular architecture of comb-shaped superplasticizers on their performance in cementitious systems." *Cement and Concrete Composites* **29**(4): 251-262.

Zhao, Y., X. Hu, C. Shi, Z. Zhang and D. Zhu (2021). "A review on seawater sea-sand concrete: Mixture proportion, hydration, microstructure and properties." *Construction and Building Materials* **295**: 123602.

Effect of alkanolamines in kaolinitic calcined clays pozzolanic reactivity

I. Koufany¹, I. Santacruz¹, M.D. Rodríguez-Ruiz¹, E.P. Bescher², M.A.G. Aranda¹ and A.G. De la Torre^{1*}

¹ Dpt. Química Inorgánica, Cristalografía y Mineralogía. Universidad de Málaga, Málaga, Spain.

Email: imane.k@uma.es; isantacruz@uma.es; mdrodriguez@uma.es; g_aranda@uma.es; mgd@uma.es*

² CTS Cement Manufacturing Corp, 12442 Knott St, Garden Grove CA 92841, United States

Email: ebescher@CTSCEMENT.com

ABSTRACT

Five kaolinitic clays with different amounts of kaolinite, ranging between ~70 wt% and ~30 wt%, have been studied to unravel the possible activation effect of alkanolamines on the aluminate fraction of calcined clays. This is of interest for enhancing the reactivity of LC³ binders. These clays were calcinated at 860°C for 4 h and ground to particle sizes of $D_{V,50} \sim 10 \mu\text{m}$. Three alkanolamines were selected: triisopropanolamine (TIPA), triethanolamine (TEA) and methyldiethanolamine (MDEOA), added in two dosages, 0.025 and 0.050 wt% (by weight of calcined clay, *bwcc*). The role of alkanolamines as activators in calcined clays was assessed following the ASTM c1897 standard bases on R³-tests. Concretely, first by measuring the heat evolved due to the pozzolanic reaction of the calcined clay and Ca(OH)₂ (i.e. R³ mixture) by isothermal calorimetry at 40°C during 7 days, and second, the bounded water by measuring the weight loss of R³ mixture after heating them at 350°C. This study concludes that there is no significant activation of the pozzolanic activity of kaolinitic calcined clays just by adding alkanolamines. However, a mild activation was observed, i.e., higher heat evolved up to 7 days, by adding 0.05 wt% *bwcc* of TIPA, TEA and MDEOA to a high kaolinite content disordered metakaolin with high specific surface area calcined clay.

KEYWORDS: *Alkanolamine activator, kaolinitic calcined clay, isothermal calorimetry.*

1. Introduction

The reduction of the clinker factor is the best current way to decrease the CO₂ footprint of cement industry. Calcined clays (containing more than 40 wt% of kaolinite) are being used in limestone calcined clays cements, LC³, due to their inherent pozzolanic activity (Sharma et al., 2021). Moreover, due to the shortage of traditional supplementary cementitious materials (SCMs), calcined clays are promising alternatives (Yoon et al., 2022). These low clinker factor cements are considered as low CO₂ materials, with enhanced durability and long-term mechanical strengths. However, their main drawback is the poor early mechanical strengths, due to their slow hydration rate (Juenger et al., 2019). The use of chemical admixture to address this challenging is well spread, and recently, alkanolamines used as accelerators/activators of low CO₂ cements are attracting special attention (Dorn et al., 2022). Most of the studies agree that alkanolamines promotes the hydration of C₃A and C₄AF, also in LC³ (Huang et al., 2021; Zunino and Scrivener, 2021). However, there is a gap in the knowledge of the effect of alkanolamine in the pozzolanic activity of the aluminate fraction of calcined clays. Here, the study of the effect on the pozzolanic activity of five different kaolinite content clays with three different alkanolamines, in two dosages is presented. The final goal was to determine the possible admixture activation of the kaolinitic calcined clays as a first step before moving to early-age low-carbon cement activation by the admixture usage.

2. Materials

Five Spanish raw clays (rc) were selected: rc1 (CVPM3B-2021, by Arcimusa, S.A., Zaragoza); rc2 (SY(A)-1-2021, by Comercial Silices y Caolines de Aragón S.L., Teruel); rc3 (F-35-2021, by Caolines de Vimianzo, S.A.U., A Coruña); rc4 (Kaolin-CN-2021, by Caobar S.A., Guadalajara); and rc5 (Kaolin-C-

2021, by Caobar S.A., Guadalajara). The five raw clays were dried at 105°C for 2h in a furnace. The elemental compositions, determined by X-Ray Fluoresce (XRF), for all the raw clays are given in Table 1. The elemental composition of the calcined clays (see below) are also included in Table 1.

Table 1. Elemental compositions, determined by XRF, expressed as weight percentage of oxides (wt%) and loss on ignition (LOI) for the raw (rc#) and calcined at 800°C(cc#) clays. Numbers in brackets: standard deviation.

| | SiO ₂ | Al ₂ O ₃ | Fe ₂ O ₃ | CaO | MgO | SO ₃ | Na ₂ O | K ₂ O | TiO ₂ | P ₂ O ₅ | Other | LOI |
|------------|------------------|--------------------------------|--------------------------------|----------|----------|-----------------|-------------------|------------------|------------------|-------------------------------|-------|------|
| rc1 | 50.3(4) | 29.3(2) | 6.8(2) | 0.19(1) | 0.27(3) | 0.17(1) | - | 0.28(2) | 1.89(2) | 0.046(4) | 0.16 | 10.5 |
| cc1 | 54.7(4) | 33.5(2) | 7.1(2) | 0.54(4) | 0.13(3) | 0.20(1) | - | 0.33(3) | 2.16(2) | - | 0.25 | 1.1 |
| rc2 | 55.3(4) | 29.3(2) | 1.17(8) | 0.23(1) | 0.33(4) | 0.23(1) | 0.19(3) | 3.3(1) | 0.49(1) | 0.047(5) | 0.5 | 9.3 |
| cc2 | 60.4(4) | 32.0(2) | 1.34(8) | 0.26(2) | 0.35(4) | 0.25(1) | 0.18(3) | 3.6(2) | 0.56(1) | 0.044(5) | 0.04 | 1.0 |
| rc3 | 54.1(4) | 30.2(2) | 1.59(9) | 0.022(2) | 0.33(4) | - | 0.28(3) | 4.8(2) | 0.20(1) | 0.054(4) | 0.69 | 16 |
| cc3 | 58.9(4) | 32.4(2) | 1.79(9) | 0.037(3) | 0.35(4) | 0.020(4) | 0.30(3) | 5.3(2) | 0.231(4) | 0.049(5) | 0.03 | 0.7 |
| rc4 | 72.6(3) | 20.5(2) | 0.23(2) | 0.075(5) | 0.07(2) | - | - | 1.1(1) | 0.17(1) | 0.029(4) | 0.02 | 5.2 |
| cc4 | 76.5(3) | 20.5(2) | 0.27(2) | 0.104(8) | 0.080(2) | 0.030(5) | - | 1.4(1) | 0.175(3) | 0.019(5) | 0.00 | 1.0 |
| rc5 | 76.6(3) | 14.8(2) | 0.18(1) | 0.061(4) | 0.08(2) | - | - | 1.3(1) | 0.14(1) | 0.021(4) | 0.02 | 6.9 |
| cc5 | 81.4(3) | 16.4(2) | 0.21(2) | 0.077(6) | 0.05(2) | 0.013(5) | - | 1.33(9) | 0.157(3) | 0.019(5) | 0.01 | 0.3 |

The dried clays were mixed with ~20.0 wt% α -Al₂O₃, as internal standard, to determine the full phase contents, including the amorphous and not quantified crystalline content, ACn, by analysing the powder patterns by the Rietveld method (De la Torre et al., 2001). The raw clays were activated in an industrial brick kiln at 860°C for 4 hours and milled in a ball milling equipment up to particle sizes given in Table 2. Three alkanolamine from Sigma Aldrich were selected: triisopropanolamine (TIPA), triethanolamine (TEA) and methyldiethanolamine (MDEOA).

3. Methodologies: characterization techniques.

Table 2 gives the particle size distribution (PSD), BET specific surface area and density for the five calcined clays (cc), obtained as detailed elsewhere (Bernal et al., 2021). The PSD was computed using MIE-non-spherical methodology with a refractive index of 1.55 and an absorption index of 0.1 for cc1 and 0.01 for the remaining calcined clays.

Table 2. Textural properties and mass densities of the calcined clays.

| | cc1 | cc2 | cc3 | cc4 | cc5 |
|------------------------------|------------|-------------|-------------|-------------|-------------|
| D_{v,10} (μm) | 0.87 | 2.79 | 2.14 | 2.47 | 2.69 |
| D_{v,50} (μm) | 8.4 | 11.8 | 11.8 | 12.0 | 12.3 |
| D_{v,90} (μm) | 41.4 | 58.9 | 51.6 | 47.0 | 47.8 |
| BET (m²/g) | 27.3 | 10.0 | 7.6 | 4.0 | 3.2 |
| ρ (g/cm³) | 2.71 | 2.63 | 2.63 | 2.63 | 2.61 |

Laboratory X-Ray Powder Diffraction (LXRPD) data of rc2 and rc3 with internal standard were collected on a D8 ADVANCE (Bruker AXS) and the mixtures with rc1, rc4 and rc5 on a X'PertPro (PANalytical) diffractometers. D8 ADVANCE and X'PertPro are equipped with Johansson monochromators to have strictly monochromatic, Mo-K α_1 ($\lambda=0.7093$ Å) and Cu-K α_1 ($\lambda=1.54099$ Å) radiations respectively. Rietveld quantitative phases analyses (RQPA) were performed using the GSAS suite of programs and the EXPGUI graphic interface. Thermogravimetric analysis (TGA) measurements for all the dried raw clays were performed in a SDT-Q600 analyser from TA instruments (New Castle, DE). The temperature was raised to 1000°C at a heating rate of 10 °C/min. The assessment of the role as activators of alkanolamines directly in calcined clays was performed following the ASTM c1897 (based on R³-test). The R³ mixture (calcined clay and alkaline solution) consisted on Ca(OH)₂/calcined clay=3.0, CaCO₃/calcined clay=0.50 and water/solid=1.20, as detailed in the standard. The alkanolamines were added in two dosages, 0.025 and 0.050 wt% *bwcc*. The R³-mixtures were introduced in an eight channels Thermal Activity Monitor (TAM) isothermal calorimeter at 40°C during 7 days using glass ampoules and water as reference. The heat evolved was normalized to the mass of calcined clay and reported from 75 minutes to 7 days. Moreover, the chemically bounded water (BW) was carried out by measuring the weight loss of the R³ mixtures (30 g) at 7 days after thermal treatment from 40°C to 350°C in a furnace. The amount of bounded water is given by g/100g of calcined clay.

4. Results and discussion

4.1 Clays characterization.

The RQPA, including the ACn (amorphous and crystalline non-quantified) content, of the dried raw clays are given in Table 3. It is observed that all the clays contain kaolinite and quartz. Moreover, all, except rc1, contains microcline and muscovite. It is noted that the amorphous fraction may contains a fraction of kaolinite. Therefore, the reported values are minimum contents.

Table 3. RQPA, including the ACn, of the dried raw clays.

| | Kaolinite | Muscovite | Fe ₂ O ₃ | Quartz | Anatase | Rutile | Microcline | Calcite | ACn |
|-----|-----------|-----------|--------------------------------|--------|---------|--------|------------|---------|------|
| rc1 | 72.9 | - | 2.5 | 11.1 | 1.5 | 0.9 | - | 1.6 | 9.4 |
| rc2 | 54.9 | 3.4 | - | 12.8 | - | 0.6 | 8.1 | - | 20.2 |
| rc3 | 48.8 | 24.9 | - | 11.4 | - | 0.7 | 4.2 | - | 9.9 |
| rc4 | 20.3 | 5.7 | 0.3 | 47.5 | 0.6 | - | 4.4 | - | 21.3 |
| rc5 | 16.8 | 3.1 | 0.2 | 53.6 | 0.4 | - | 4.6 | - | 21.2 |

The content of kaolinite in the pristine clays have been assessed by four methodologies: i) RQPA including the ACn content, Table 3; ii) TGA of dried samples (Avet and Scrivener, 2018); iii) from the Al₂O₃ content by XRF, excluding the Al₂O₃ content within the other phases determined by RQPA; and iv) mineral intensity factor (MIF) (Schultz, 1964). The four values for each raw clay, and the final estimations are given in Table 4. The final contents are given as the average of the first three measurements. It seems that MIF approach consistently gives underestimated values.

Table 4. Kaolinite content (wt%) determined by different methodologies of the raw clays. Average of the four measurements and standard deviation are also included.

| Kaolinite content (wt%) | rc1 | rc2 | rc3 | rc4 | rc5 |
|-------------------------|------|------|------|------|------|
| TGA | 76.3 | 55.3 | 50.8 | 44.7 | 36.1 |
| RQPA | 72.9 | 54.9 | 48.8 | 20.3 | 16.8 |
| XRF | 74.2 | 67.2 | 48.8 | 44.5 | 32.4 |
| MIF | 61 | 53 | 27 | 24 | 17 |
| Final Kaolinite content | 74 | 59 | 49 | 37 | 29 |

4.2 Effect of alkanolamine on pozzolanic activity of calcined clays.

Figures 1a and 1b show the heat evolved by all the R³ mixtures up to 7 days.

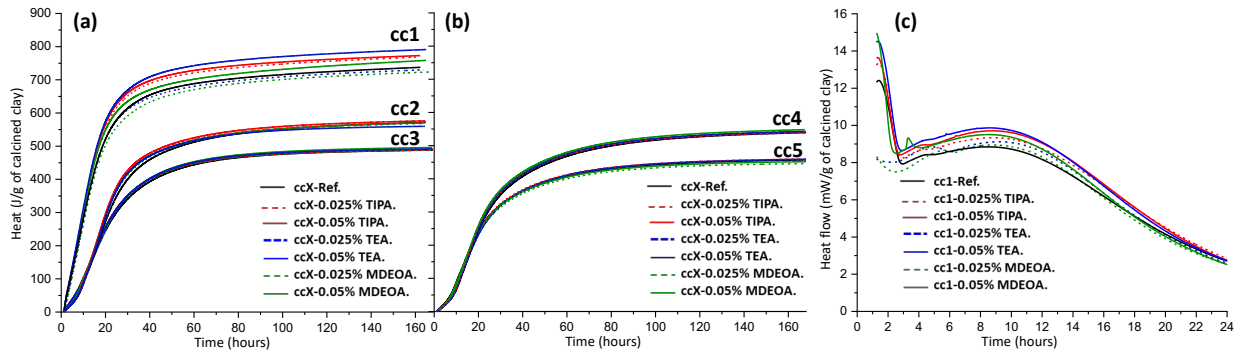


Figure 1. (a) and (b) Total heat curves for R³ mixtures without and with alkanolamines up to 7 days. (c) Heat flow of cc1 without and with alkanolamines up to 24 hours.

As expected, cc1 evolves higher heat at any time, due to the highest content of kaolinite in the pristine clay, the lowest PSD and the highest BET surface area of the calcined clay. In addition, it has been recently published that this calcined clay presents a highly disorder metakaolin, with higher amounts of Al(V) (Bernal et al., 2022). The most relevant result here is that the additions of 0.025% and 0.05% *bwcc* of any alkanolamine have almost negligible effects on the heat evolved by all calcined clays, except for cc1 (Fig. 1a and 1b). For cc1, the addition of TIPA increased the total heat released at 7 days, from 737 J/g_{cc} to ~780 J/g_{cc}, for the two studied dosages. For TEA and MDEOA, the low dosage, 0.025 wt% *bwcc* decreased the total heat when compared to the reference cc1, while the addition of 0.05 wt% *bwcc* enhanced it. Figure 1c shows the heat flow up to 24 hours of cc1 without and with the selected alkanolamines. The first signal observed before ~3 h, is likely due to the dissolution of cc1 on the alkaline solution. On the one hand, it is observed that the addition of 0.025 wt% *bwcc* of TEA and MDEOA

slightly decreased these signals while TIPA enhanced it. On the other hand, these signals are more intense in R³ mixtures with 0.05 wt% *bwcc* of the three alkanolamine, indicating an enhancement in the dissolution rate of the calcined clay components. The broad peak observed between 3 and 16 h is likely due to the reaction of cc1 components with the alkaline solution, to give C-A-S-H type products and possibly, calcium aluminate hydrates, AFm type (Avet et al., 2016). This signal is not significantly modified by the addition of alkanolamines. The bounded water obtained after 7 days for cc1-Ref, cc2-Ref, cc3-Ref, cc4-Ref and cc5-Ref are 12.1, 9.8, 9.4, 9.7 and 8.0 g/100 g dried R³ mixture. The addition of the studied alkanolamines, in the employed dosages, has had a negligible impact on these values, showing that the formed hydrated products have not been modified nor in amount neither in type. For TIPA addition to cc1, the BW increased to 12.1 and 12.3 wt% for 0.025 and 0.05% dosages. We consider this variation within the variability of the measurements, and hence, an increase of BW could not be firmly established.

5. Conclusions

Alkanolamines, TIPA, TEA and MDEOA, do not enhance the pozzolanic activity of typical calcined clays. It has been observed a mild increase in the dissolution rate by the addition of 0.05 wt% *bwcc* of the three alkanolamines for the calcined clay with higher kaolinite content, highly disordered metakaolin, lower particle size and higher specific surface area. We speculate that this dosage of alkanolamine has enhanced the dissolution rate of the aluminate fraction of the metakaolin which is richer in Al(V). However, the nature and amount of the pozzolanic hydrated products is not modified since the bounded water remains constant with the addition of alkanolamines.

Acknowledgements

Research grant PID2020-114650RB-I00 (Spanish Ministry and ERDF) is gratefully acknowledged.

References

- Avet, F., Scrivener, K.L. (2018). “Investigation of the calcined kaolinite content on the hydration of Limestone Calcined Clay Cement (LC³)”. *Cem. Concr. Res.* 107: 124–135.
- Avet, F., Snellings, R., Alujas Diaz, A., Ben Haha, M., Scrivener, K.L. (2016) “Development of a new rapid, relevant and reliable (R3) test method to evaluate the pozzolanic reactivity of calcined kaolinitic clays” *Cem. Concr. Res.* 85: 1–11.
- Bernal, I.M.R., Aranda, M.A.G., Santacruz, I., De la Torre, A.G., Cuesta, A. (2022) “Early-age reactivity of calcined kaolinitic clays in LC³ cements: A multi technique study including pair distribution function analysis” *J. Sustain. Cem. Mater.* <https://doi.org/10.1080/21650373.2022.2117248>
- Bernal, I.M.R., Shirani, S., Cuesta, A., Santacruz, I., Aranda, M.A.G. (2021) “Phase and microstructure evolutions in LC3 binders by multi-technique approach including synchrotron microtomography” *Constr. Build. Mater.* 300: 124054.
- De la Torre, A.G., Bruque, S., Aranda, M.A.G. (2001) “Rietveld quantitative amorphous content analysis” *J. Appl. Crystallogr.* 34, 196–202.
- Dorn, T., Blask, O., Stephan, D. (2022) “Acceleration of cement hydration – A review of the working mechanisms, effects on setting time, and compressive strength development of accelerating admixtures” *Constr. Build. Mater.* 323: 126554.
- Huang, H., Li, X., Avet, F., Hanpongpan, W., Scrivener, K. (2021) “Strength-promoting mechanism of alkanolamines on limestone-calcined clay cement and the role of sulfate” *Cem. Concr. Res.* 147: 106527.
- Juenger, M.C.G., Snellings, R., Bernal, S.A. (2019) “Supplementary cementitious materials: New sources, characterization, and performance insights” *Cem. Concr. Res.* 122: 257–273.
- Sharma, M., Bishnoi, S., Martirena, F., Scrivener, K. (2021) “Limestone calcined clay cement and concrete: A state-of-the-art review” *Cem. Concr. Res.* 149: 106564.
- Schultz, L.G. (1964) “Quantitative interpretation of mineralogical composition from X-ray and chemical data of the Pierre Shale”. United States. Geological Survey, Professional Paper, 391-C, 31 pp.
- Yoon, J., Jafari, K., Tokpatayeva, R., Peethamparan, S., Olek, J., Rajabipour, F. (2022) “Characterization and quantification of the pozzolanic reactivity of natural and non-conventional pozzolans” *Cem. Concr. Compos.* 133: 104708.
- Zunino, F., Scrivener, K.L. (2021) “Assessing the effect of alkanolamine grinding aids in limestone calcined clay cements hydration” *Constr. Build. Mater.* 266: 121293.

Study to improve vibration flowability of fresh concrete by controlling flocculation state of cement particles

K. Shimada^{1*}, H. Kawakami², Y. Nagoshi³, and K. Sagawa⁴

Performance Chemicals Research, Kao Corporation, Wakayama Prefecture, JAPAN

¹ *shimada.kouhei@kao.com*

² *kawakami.hiroyuki@kao.com*

³ *nagoshi.yuto@kao.com*

⁴ *sagawa.keiichirou@kao.com*

ABSTRACT

Flowability of fresh concrete is enhanced by vibration and filled into mold, however in some cases, gentle vibration leads to unfilled defect or noise issues occur by severe vibration. Fresh concrete shows shear thinning property, which derives from dispersed-flocculated state of cement particles. While concrete casting, shear stress generated by vibration decreases viscosity of concrete result in enhanced flowability, as we say, “vibration flowability”. So, we expected that if we can control flocculation state of cement particles, vibration flowability will be improved. In general, superplasticizer is used to disperse cement particles and flocculant is used to flocculate. In this report, we tried to improve vibration flowability of fresh concrete by controlling flocculation state of cement particles by combination use of cement dispersant and flocculants. We chose polycarboxylate ether (PCE) as superplasticizer and sodium poly(acrylate) (PAA), cellulose ether (CE), poly (ethylene oxide) (PEO), poly (vinyl alcohol) (PVA) and sodium poly (2-acrylamido-2-methyl-1-propanesulfonate) (PAMPS) as flocculants. We did concrete test with these flocculants and adjusted concrete slump by dosage of PCE. Vibration flowability was evaluated following JHS 733 (Japan Highway Public Corporation Standard). Surprisingly, we found that only PAA with specific molecular weight (Mw: 25,000 and 250,000) improve vibration flowability among these flocculants. Rheological studies of cement slurry with PCE and a series of PAAs indicated that these two PAAs increased flocculation of cement particles effectively.

KEYWORDS: *Vibration flowability, Unfilled defect, Flocculation, Superplasticizer, Flocculant*

1. Introduction

Fresh concrete is known as slurry with shear thinning property, this is why, we can improve flowability and/or workability of fresh concrete by vibration to fill it into mold (Sugamata et al. 2002). However, in some cases, gentle vibration leads to unfilled defect or noise issues occur by severe vibration (Kawabe et al. 2010). To prevent these issues, we utilize thickener with superplasticizer to make concrete self-compacted (Yonekura et al. 1995). This type of concrete is called as High-flow or Self-compacting concrete however, there are some issues such as equipment and cost. Fresh concrete has cement-water suspension as continuous phase, so, physical property of concrete is affected by that of cement slurry. Therefore, the shear thinning property of fresh concrete derives from dispersed-flocculated state of cement particles (Kazama et al. 1981). While concrete casting, shear stress generated by vibration decreases viscosity of concrete result in enhanced flowability, as we say, “vibration flowability”. So, we expected that if we can control flocculation state of cement particles, vibration flowability will be improved. On the other, some types of polymers are well known as flocculant against inorganic particles (Lee et al. 2014). In this report, we tried to improve vibration flowability of fresh concrete by controlling flocculation state of cement particles by combination use of cement dispersant and flocculants.

2. Experiments

We chose sodium poly (acrylate) (PAA), cellulose ether (CE), poly (ethylene oxide) (PEO), poly (vinyl alcohol) (PVA) and sodium poly (2-acrylamido-2-methyl-1-propanesulfonate) (PAMPS) as flocculants. And we used polycarboxylate ether (PCE) as superplasticizer with these flocculants to adjust concrete slump. Admixtures we used in this study are as shown in Table 1.

Table 1. Admixtures

| Admixture | Abbreviation | Remarks |
|--|--------------|--|
| sodium poly (acrylate) | PAA | Mw: 5,000 / 25,000 / 250,000 / 1,000,000 |
| cellulose ether | CE | Methyl cellulose, Mw: 140,000 |
| poly (ethylene oxide) | PEO | Mw: 20,000 / 300,000 / 1,000,000 |
| poly (vinyl alcohol) | PVA | 100% saponified, Dp: 1,500~1,800 |
| sodium poly (2-acrylamido-2-methyl-1-propanesulfonate) | PAMPS | Mw: 2,000,000 |
| polycarboxylate ether | PCE | Commercial, nonionic defoamer contained. |

Raw materials of concrete and mix design are as shown in Table 2, W/C=35% and s/a=46%. Procedure of preparation of fresh concrete is, firstly, aggregates and cement were mixed together by 45 rpm for 20 seconds in biaxial forced mixer, then, water, 0.8wt% (vs. cement) of PCE and 0.02wt% (vs. cement) of each flocculant were added and mixed by 45 rpm for 120 seconds at 20°C. As references, 0.5, 0.6, 0.7 and 0.8wt% (vs. cement) of PCE without flocculants also tested. Each admixture was dissolved into the water, all raw materials were stored at 20°C and aggregates adjusted as saturated and surface-dried condition beforehand.

Table 2. Raw materials of concrete and mix design

| Raw material | Abbreviation | Remarks | Unit (kg/m ³) |
|------------------|--------------|--|---------------------------|
| Water | W | Tap water, SG: 1.00 g/cm ³ | 144 |
| Cement | C | Japaneses OPC, SG: 3.16 g/cm ³ | 412 |
| Fine aggregate | S | Crushed sand, SG: 2.58 g/cm ³ , FM: 2.82 | 836 |
| Coarse aggregate | G | Crushed stone, SG: 2.63 g/cm ³ , Max. Dia.: 20 mm | 1028 |

Immediately after preparation of fresh concrete, vibration flowability was evaluated following JHS 733. Vibration testing machine is as shown in Figure 1. Test procedure of the vibration flowability is, firstly, measured concrete slump following JIS A 1101 (ISO 1920-2) on the top of the vibration testing machine, then, vibrated by 3.7 J/L for 10 seconds, finally, measured concrete slump flow following JIS A 1150 (ISO 1920-2).

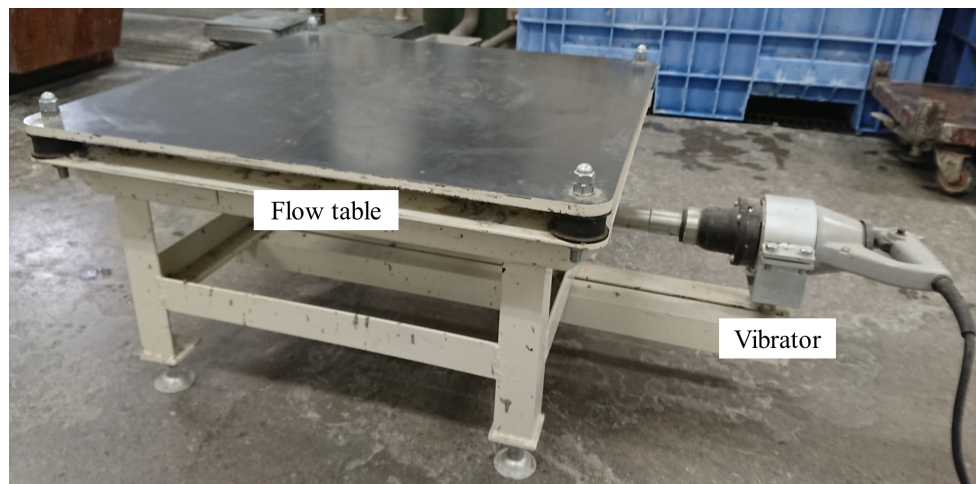


Figure 1. Vibration testing machine

Rheological study was done with W/C=35% cement slurry, the cement and the water were same as shown in Table 2. Procedure of preparation of cement slurry is, firstly, dissolved 0.8wt% (vs. cement) of PCE and 0.02wt% (vs. cement) of each PAA into water, then, added cement and mixed together by hand mixer, 620 rpm for 120 seconds at 20°C. Immediately after preparation of cement slurry, rheological measurements were taken place by rheometer with parallel plate. Flocculation energy among cement particles was calculated by below equation (Kajiura et al. 1974).

$$\Delta W = \dot{\gamma} \int_0^{t_s} (\tau(t) - \tau^s(t)) dt \quad (1)$$

Here represents, $\Delta W(\text{J/m}^3)$; flocculation energy, $\dot{\gamma}(\text{s}^{-1})$; shear rate, $t_s(t)$; the time $\tau(t)$ and $\tau^s(t)$ are crossed each other, $\tau(t)(\text{Pa})$; shear stress function (in this experiment, $\dot{\gamma}=1$), $\tau(t)(\text{Pa})$; shear stress function (in this experiment, $\dot{\gamma}=4$) (Figure 2).

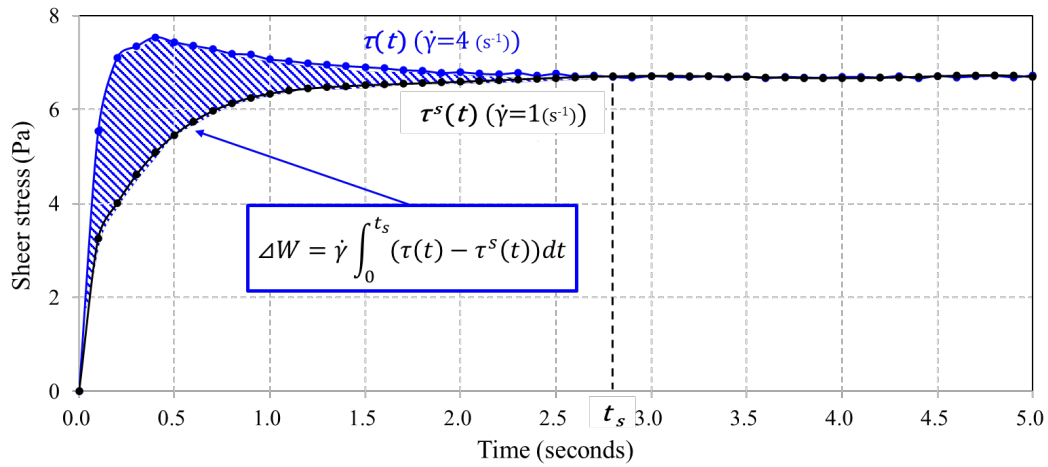


Figure 2. Schematic image of the way to calculate flocculation energy

3. Results and Discussions

Figure 3 shows results of concrete test with the concrete slump on horizontal line and the vibration flowability on vertical line.

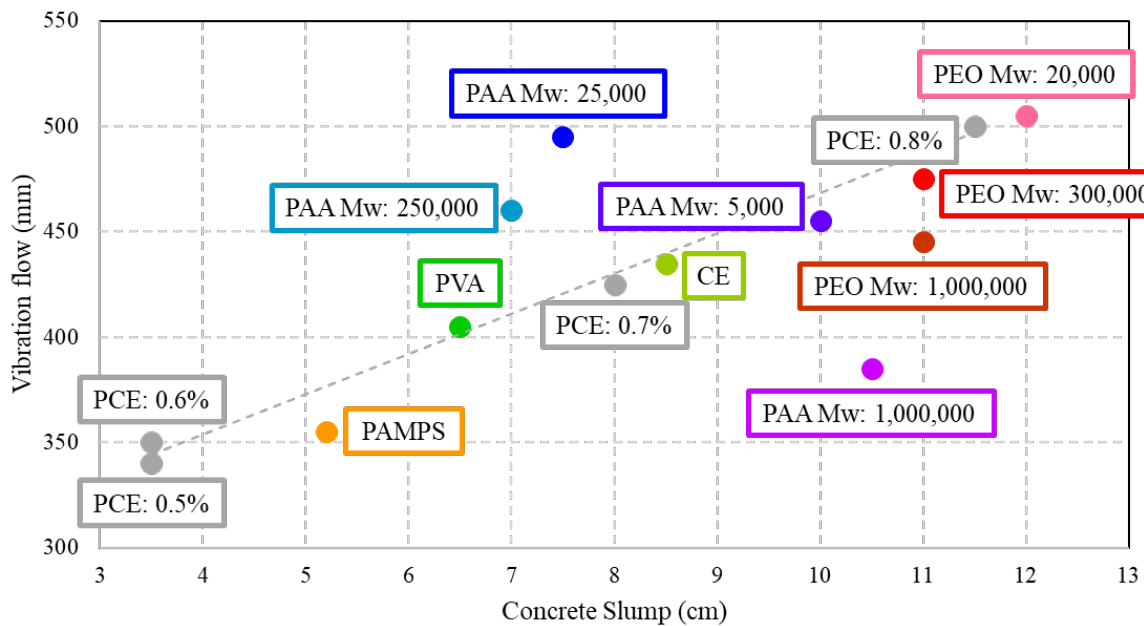


Figure 3. Relationship between concrete slump and vibration flowability with / without flocculants

Remember that all flocculants were tested with 0.8wt% (vs. cement) of PCE. Dashed line in grey shows test results with only PCE, we can see linear tendency as a reference. From the purpose of this study, we judged as “better” that if the fresh concrete shows high vibration flowability under the same concrete slump. In this point, we got better results by addition of PAAs with “Medium” molecular weight (Mw: 25,000 and 250,000) surprisingly. To understand this result more, we did the additional rheological study on cement slurry with PAAs and calculated flocculation energy (ΔW) by equation (1) (Figure 4).

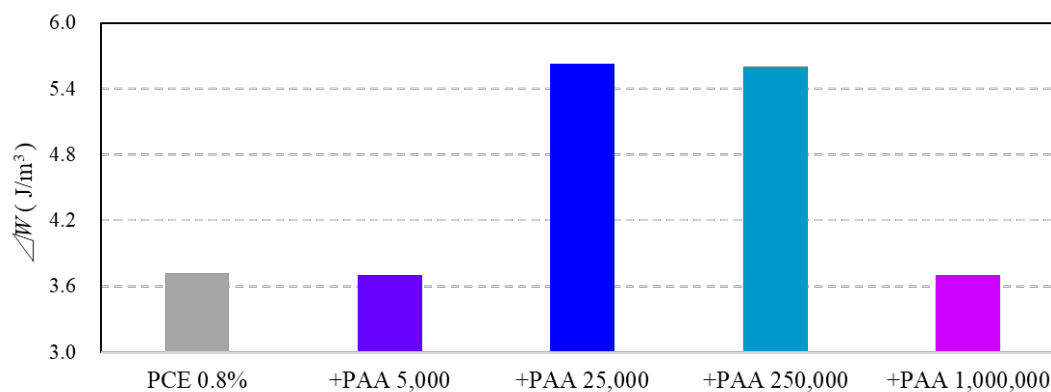


Figure 4. Flocculation energy among cement particles with / without PAAs

As results, we found that when we added PAAs with Mw: 25,000 and 250,000, the flocculation energy of the cement pastes also increased. We considered that these results come from two factors; one is molecular weight and the other is molar of the PAA macromolecules. Over adsorption of polymer onto solid surface, the larger macromolecule is, the more adsorption preferred (Kawaguchi et al. 1974). And flocculation starts from adsorption of flocculants onto surface of particles. So, we considered that this tendency, especially difference in the flocculation energies of PAA with Mw: 5,000 against that of Mw: 25,000 and 250,000 can be attribute to molecular weight of PAAs. Also in the following flocculation steps, collision of particles carrying an adsorbed flocculant with other particles results in growth of microflocs. Thus, in this point, the more flocculants on the surface of particles, the more effective in growth of flocs. So, we considered that this tendency, especially difference in the flocculation energies of PAA with Mw: 1,000,000 against that of Mw: 25,000 and 250,000 can be attribute to the molar effect of the PAA macromolecules because we did above tests with the same weight.

4. Conclusions

1. The combination use of flocculants with PCE effected vibration flowability of fresh concrete.
2. By addition of PAAs with “Medium” molecular weight (Mw: 25,000 and 250,000), vibration flowability was improved comparable with test results with only PCE.
3. Rheological study indicated that flocculation energy of cement pastes increased with these two PAAs.

References

- T. Sugamata, T. Sugiyama, K. Umezawa and S. Okazawa (2002) “Improvement Effect in Fresh Concrete Properties by Superplasticizer for Ultra-high Strength Concrete”, *Proceedings of the Japan Concrete Institute*, 24(1): 927-932
- S. Kawabe and K. Chin (2010) “Effect in Compactability of Reinforced Concrete by Horizontal Vibration Method”, *Proceedings of the Japan Concrete Institute*, 32(1): 515-520
- K. Yonekura (1995) “Introduction and Future Perspective of High-flow Concrete by Precast Concrete Plants”, *Cement and Concrete*, 585: 9-14
- Y. Kazama (1981) “Concrete and Rheology”, *Nihon Reoroji Gakkaishi*, 9: 99-110
- C. S. Lee, J. Robinson and M. F. Chong (2014) “A Review on Application of Flocculants in Wastewater Treatment”, *Process Safety and Environmental Protection*, 92: 489-508
- M. Nagasawa (1989) “Studies on Viscoelastic Properties of Macromolecules Using Some Model Polymers”, *Nihon Reoroji Gakkaishi*, 17: 171-182
- M. Kawaguchi, K. Maeda, T. Kato and A. Takahashi (1984) “Preferential Adsorption of Monodisperse Polystyrene on Silica Surface”, *Macromolecules*, 17: 1671-1678

How does the alternating current field affect the yield stress of fresh cement paste?

Q.Y. Xiao ¹, Y.X. Cai ², X.H. Zeng ³, and G.C. Long ^{4*}

1 Central South University, Changsha, China

Email: xqy_leo@qq.com

2 Central South University, Changsha, China

Email: 1138134934@qq.com

3 Central South University, Changsha, China

Email: zxhzlh@126.com

4 Central South University, Changsha, China

Email: longguangcheng@csu.edu.cn

ABSTRACT

Throughout the pumping and casting operations, there is always a conflict in the requirements for the rheological properties of fresh concrete. External alternating current (AC) field action has a significant contribution to the setting and hardening of concrete, therefore AC is expected to be used for real-time regulation of the rheological properties of fresh cementitious materials. In this paper, the effect of AC fields on the yield stress, hydration products, and pore solution of fresh cement paste was investigated. The results show that the yield stress of the paste grows exponentially with time in the presence of AC, which is significantly different from the linear rise of the paste without the action of AC. Moreover, this exponential growth trend increases with increasing voltage. The change in yield stress is mainly attributed to the fact that AC significantly reduces the concentrations of Ca^{2+} , SO_4^{2-} , and $\text{Al}(\text{OH})_4^-$ in the pore solution, thus promoting the formation of hydration products such as Aft.

KEYWORDS: *Alternating current field, Fresh cement paste, Yield stress, Pore solution*

1. Introduction

The advent of self-compacting concrete (SCC) has enabled the casting of fresh concrete to change from the traditional mechanically vibrated compacting to a vibration-free construction. Despite its many advantages (reduced labor, reduced energy consumption, reduced noise, and vibration, etc.), the performance of SCC is significantly time-dependent due to the physical and chemical effects between the components of the mix, admixtures, and water. In addition, human factors such as operational metering and non-human factors such as ambient temperature and humidity and raw material quality often lead to problems such as high formwork pressure, component segregation, and delayed demoulding after SCC has been cast into the mould. In many applications such as grouting, shotcrete, and 3D printed concrete, there are conflicting performance requirements between the transport, pumping, and manufacturing processes, as the fresh material should be easy to pump, and have a low hardening rate and high

flowability, while it must increase in strength quickly after placement. As a result, there are constantly conflicting requirements for the rheological properties of fresh concrete during pumping and placing. The pumping and placing process of fresh concrete would be more reliable and intelligent through external electromagnetic field methods as the rheology and stiffness of fresh concrete can be actively controlled by the electromagnetic method (De Schutter and Lesage, 2018; Xiao and Long et al., 2022).

Although some researchers have studied the effect of AC on the properties of cement-based materials, these studies mainly focused on mechanical properties and durability (Yang and Xie et al., 2021). There are few studies on how AC affects rheology. In this paper, the effects of various AC voltages on the yield stress of cement paste were studied, and X-ray diffraction (XRD) and inductively coupled plasma (ICP) spectra were utilized to explore the mechanism.

2. Experiment

2.1 Materials

The Portland cement P·I 42.5 (PC GB/T 175-2005) was used in part of this study. The specific chemical composition is shown in Table 1.

Table 1 Composition of Portland cement [%]

| Item | CaO | Al ₂ O ₃ | SiO ₂ | Fe ₂ O ₃ | MgO | SO ₃ | C ₃ S | C ₂ S | C ₃ A | C ₄ AF |
|------|-------|--------------------------------|------------------|--------------------------------|------|-----------------|------------------|------------------|------------------|-------------------|
| PC | 64.02 | 5.07 | 20.94 | 3.44 | 1.70 | 1.88 | 59.38 | 15.22 | 7.57 | 12.13 |

2.2 Experiment Method

The cement was poured into water and mixed at 140 r/min for 30 s, and then the mixer was stopped for 60 s to manually homogenize the paste sample. Afterward, the paste was stirred at 280 r/min for 90 s and 140 r/min for another 30 s. The water-to-cement ratio of the investigated paste was 0.38.

30V or 40 V AC field (50 Hz) was applied to the paste consisting of 60 min by graphite electrodes after mixing with water for 20 min, then samples were extracted at specific times for rheological test, XRD analysis, and pore solutions. The XRD samples were ground to less than 45 μ m and soaked in isopropanol for 15min, then the suspension was vacuum filtered and dried in a vacuum desiccator. The Rietveld method with an internal standard (20% Rutile by mass) strategy was used for the quantitative phase analysis of XRD. By centrifugation (for liquid) and press (for solid), pore solutions were obtained, then the produced solution was promptly filtered via 0.45 μ m nylon filters and acidified with HNO₃ (3.6% by volume) to avoid the solid phases from precip.

3. Results and Discussion

3.1 Development of yield stress with AC

The yield stress of paste is widely thought to progressively grow within 10 min of contact with water due to the nucleation and thixotropy of cement particles before the acceleration stage of hydration (Roussel and Ovarlez et al., 2012; Mostafa and Yahia, 2016). The development of the yield stress of cement paste

under various AC fields is shown in Fig. 1. In the absence of AC field, the yield stress of cement paste linearly increased (Lecompte and Perrot, 2017). The yield stress growth rate of the paste was dramatically increased under the action of AC. And the growth rate increases further as the voltage increases from 30V to 40V. And as the voltage raised from 30V to 40V, the growth rate accelerates even more. After 40 minutes, the yield stress of cement paste was dramatically raised by 12.7% and 86.3% by the 30V and 40V AC fields, respectively.

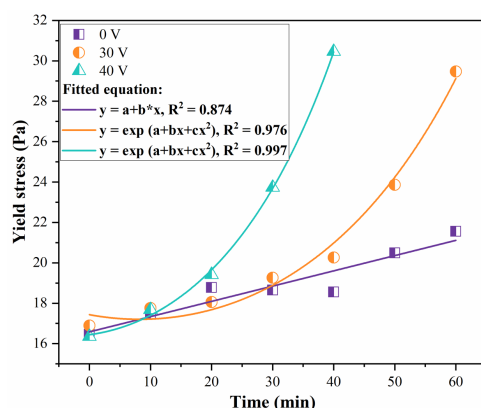


Fig. 1. Yield stress of pastes under different voltages.

3.2 Changes in cement clinker and main hydration products with time

According to XRD analysis, hydration of clinkers and formation of AFt up to 6 h based on Rietveld calculation is shown in Fig. 2. It is widely known that the early hydration of Portland cement is dominated by C_3S and C_3A , while the reaction of C_2S becomes significant after 10 days (Scrivener and Nonat, 2011). The hydration of C_3S and C_3A is the main reason for the formation of early hydration products (C-S-H and AFt). As shown in Fig. 2(a) and (b), the dissolution of C_3S and C_3A under the action of AC was much faster than that without AC. Moreover, Fig. 2(c) reveals that the action of AC accelerated the formation of AFt.

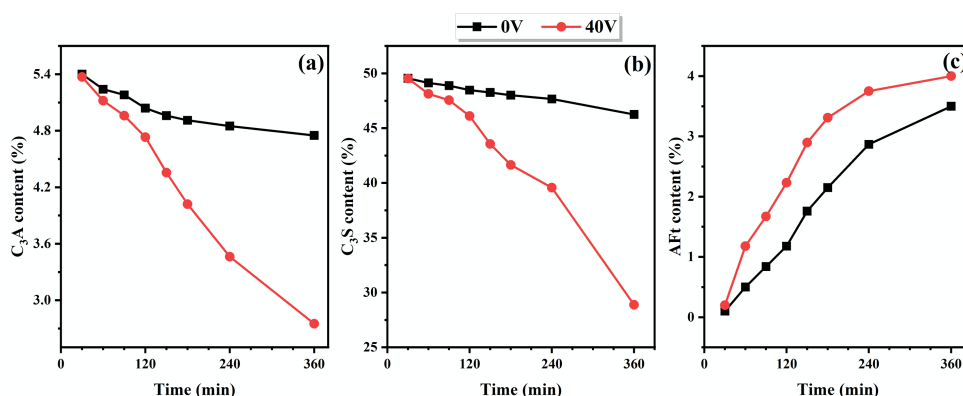


Fig. 2. (a) C_3S (b), C_3A , and (c) AFt content at various stages by Rietveld calculation.

3.3 The ionic composition variations of the pore solution

Fig. 3(a)–(d) shows the changes in ion concentrations of the pore solutions in pastes over time. $H_3SiO_4^{4-}$ in pore solution is derived from calcium silicate hydration, so the increase in $H_3SiO_4^{4-}$ concentration (Fig.

3(b)) could be attributed to AC promoting the dissolution of cement clinkers (Fig. 2). SO_4^{2-} concentration in pore solution maintained almost constant at a high level mainly due to the dissolution of gypsum during the first several hours of cement hydration (Fig. 3(d)), due to the continuous dissolution of gypsum (Zhou and Zheng et al., 2019). After the depletion of gypsum, SO_4^{2-} concentration rapidly decreased to a very low level in a short time. Once AC was applied, the concentration of SO_4^{2-} began to decline rapidly, which could also explain the increase in AFt content, as shown in Fig. 2(c). At the initial stage of hydration, $\text{Al}(\text{OH})_4^-$ derives from the rapid dissolution of C_3A , and the dissolution of C_3A is then slowed down due to the adsorption of SO_4^{2-} onto C_3A (Zhou and Zheng et al., 2019). The dissolutions of C_3A accelerate after the depletion of gypsum, and $\text{Al}(\text{OH})_4^-$ concentration increases with time (Zhou and Zheng et al., 2019). Under AC action, the substantially earlier rise in $\text{Al}(\text{OH})_4^-$ concentration can be attributed to the accelerated gypsum consumption by AC facilitating the production of AFt; the faster consumption of Ca is due to the more rapid production of CH and C-S-H (Huang and Yuan et al., 2022).

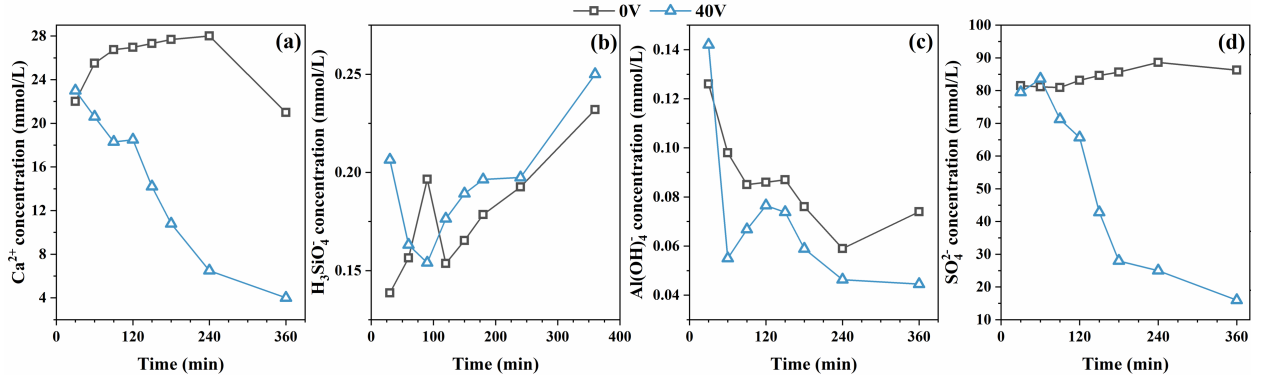


Fig. 3. Changes of ionic concentrations of (a) Ca^{2+} , (b) H_3SiO_4^- , (c) $\text{Al}(\text{OH})_4^-$, and (d) SO_4^{2-} ionic strengths of pore solutions.

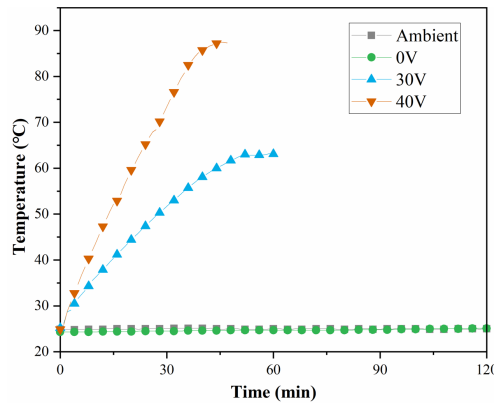


Fig. 4. Temperature evolution of pastes under the action of AC.

The influence of AC on rheological properties and hydration product evolution can be attributed to Joule heat caused by AC, as shown in Fig 4. A large number of conductive ions present in the fresh cement paste build up conductive pathways by the action of AC, which generates Joule heat to raise the hydration temperature (Xiao and Long et al., 2022). Therefore, AC action accelerates the clinker hydration and the

generation of hydration products, increasing particle contact points, cohesion, and static friction in the paste network structure.

4. Conclusions

The main scope of the thesis was to test the effect of AC on the yield stress of cement paste and to explore the changes in cement hydration products. It has been shown that the yield stress of cement paste exponentially rises when AC is present. And the increase happens more quickly the greater the voltage. Gypsum consumption is promoted by the AC action, which also promotes the hydration of C_3S and C_3A and accelerates the formation of hydration products such as Aft. Thus increasing the strength of the microstructural network in the paste and raising the yield stress.

The aforementioned results show that AC promises to be a creative way to improve the stability of concrete after pouring, hence enhancing the quality of concrete construction and helping to advance new construction technologies such as digital construction and 3D printed concrete.

Acknowledgments

This work is supported by the National Natural Science Foundation of China (Grant No. 52178261)

References

- De Schutter, G. and K. Lesage (2018). "Active control of properties of concrete: a (p)review." *Materials and Structures* 51(5).
- Huang, T. and Q. Yuan, et al. (2022). "Physio-chemical effects on the temperature-dependent elasticity of cement paste during setting." *Cement and Concrete Composites* 134: 104769.
- Lecompte, T. and A. Perrot (2017). "Non-linear modeling of yield stress increase due to SCC structural build-up at rest." *Cement and Concrete Research* 92: 92-97.
- Minard, H. and S. Garrault, et al. (2007). "Mechanisms and parameters controlling the tricalcium aluminate reactivity in the presence of gypsum." *Cement and concrete research* 37(10): 1418-1426.
- Mostafa, A. M. and A. Yahia (2016). "New approach to assess build-up of cement-based suspensions." *Cement and Concrete Research* 85: 174-182.
- Roussel, N. and G. Ovarlez, et al. (2012). "The origins of thixotropy of fresh cement pastes." *Cement and Concrete Research* 42(1): 148-157.
- Scrivener, K. L. and A. Nonat (2011). "Hydration of cementitious materials, present and future." *Cement and Concrete Research* 41(7): 651-665.
- Xiao, Q. and G. Long, et al. (2022). "Effect of alternating current field on rheology of fresh cement-based pastes." *Journal of Building Engineering* 48: 103771.
- Yang, Z. and Y. Xie, et al. (2021). "Experimental investigation on mechanical strength and microstructure of cement paste by electric curing with different voltage and frequency." *Construction and Building Materials* 299: 123615.
- Zhou, J. and K. Zheng, et al. (2019). "Chemical effect of nano-alumina on early-age hydration of Portland cement." *Cement and Concrete Research* 116: 159-167.

Functionalized transition metal doped silicate hydrate/PCE nanocomposites: an innovative hardening accelerator

Fabio Castiglioni^{1*}, Clelia Sarta¹, Anthony Biancardi¹, Anna Bravo¹, Gilberto Artioli², Maria Chiara Dalconi², Gregorio dal Sasso³ and Giorgio Ferrari¹

¹ Mapei S.p.A., Milan, Italy
Email: f.castiglioni@mapei.it

² University of Padua, Padova, Italy
Email: mariachiara.dalconi@unipd.it

³ Institute of Geosciences and Earth Resources, Padova, Italy
Email: gregorio.dalsasso@igg.cnr.it

ABSTRACT

Some inorganic and organic chemicals have been known for a long time for their ability to accelerate the hydration reaction of Portland cement. These species include chlorides, thiocyanates, nitrates, formates, alkanolamines and other chemicals and the mechanism through which the acceleration occurs vary according to the specific admixture. More recently, metal silicate hydrate MeSH/PCE nanocomposites aqueous suspensions were developed as hardening accelerator; they constitute the most powerful accelerator available today and they do not suffer from any shortcoming. In our previous works, we have demonstrated that copper is well suited for the preparation of MeSH/PCE nanocomposites. We then demonstrated that, in such nanocomposites, copper ions occupy surface silicate sites. Copper is known for its tendency to easily form complexes with a variety of chemical species, in particular N-donor ligands, such as alkanolamines. In this work we investigate the existence of interactions between different alkanolamines and the copper ions on the surface of a copper doped MeSH/PCE nanocomposite. The new surface functionalized MeSH/PCE nanocomposite is tested as hardening accelerator in mortars prepared with Portland cement where it is shown to be far superior compared to the amine-free copper-MeSH/PCE. In addition, we show how the accelerating performance of the surface functionalized MeSH/PCE nanocomposite is much higher than the sum of the effects of the copper-CSH/PCE nanocomposite and the alkanolamine, suggesting a synergetic effect of the functionalized product.

KEYWORDS: *MeSH/PCE nanocomposites, Hardening accelerators, Copper complexes; Innovative admixtures; Alkanolamines*

1. Introduction

Considering that water and concrete are, respectively, the first and the second most consumed material in the world each year (Gagg, 2014), one may affirm that cement hydration reaction is the most common and most performed anthropogenic chemical reaction. As thing stands, it is reasonable to believe that such reaction holds no more secrets to chemists, especially since we learned how to exploit it to literally build our world. The truth is, despite the enormous scientific advancements of the last 50 years, there is still much that we do not completely understand regarding Portland clinker hydration (Lavagna, 2023). As a consequence, there are still vast unexplored fields in the chemistry of cementitious materials open for the design of innovative advanced admixtures (Liu, 2019). One class of admixtures that underwent significant development in the last 15 years is that of hardening accelerators. As the name suggests, hardening accelerators are used to promote the early development of mechanical strength of cementitious materials and different chemicals, both inorganic and organic, are known for this property. Among them we find chloride, thiocyanate, nitrate salts and alkanolamines, such as diethanolamine (DEA), triethanolamine (TEA), diethanolisopropanolamine (DEIPA) and triisopropanolamine (TIPA) (Dorn, 2022). These materials influence the hydration mechanism of Portland cement leading to a faster dissolution of anhydrous phases and faster precipitation of hydration products, but this acceleration often comes with a price: for example, chlorides are incompatible with reinforced concrete as they induce rebar corrosion,

nitrates efficiency depends on cement composition (Chikh, 2008), while there is a thin threshold between accelerating and retarding effect for alkanolamines. The need for more efficient and reliable hardening accelerators pushed researchers towards the development of hybrid organic/inorganic nanocomposites consisting of polyether carboxylate/calcium-silicate-hydrate (PCE/CSH) nanoparticles. These nanoparticles enhance the secondary nucleation mechanism, acting as nucleation centres for the precipitation of additional CSH (Portland cement main hydration product), leading not only to a faster reaction but also to denser microstructure of the cement paste (Kanchanason, 2017). In our previous works we demonstrated that such nanocomposite particles could be doped with transition metal ions, in particular copper, to obtain metal-silicate-hydrate/PCE nanoparticles (MeSH/PCE) (Ferrari, 2013). Further studies allowed us to demonstrate that such copper ions are not randomly incorporated in the particle structure, but mostly reside on superficial sites, making them accessible from the outside environment (Dal Sasso, 2022). Knowing that copper can easily form complexes with a variety of donor ligands, in particular nitrogen-donor ligands, we were intrigued by the possibility to obtain surface-functionalized MeSH/PCE nanoparticles. In this work we describe the preparation of amine-functionalized MeSH/PCE (N-MeSH/PCE) nanocomposites and investigate the existence of interactions between copper atoms of MeSH/PCE nanocomposites and alkanolamines, particularly DEA, and we show the superior accelerating effect of such functionalized nanoparticles.

2. Materials and Methods

MeSH/PCE was obtained from Mapei S.p.A. (commercial name: MapeFast Ultra) and used as received. The copper doped CSH/PCE nanoparticle is obtained by double exchange precipitation from sodium silicate and a mixture of calcium and copper nitrate in the presence of a PCE superplasticizer.

DEA, TEA, ethanoldiisopropanolamine (EDIPA), DEIPA, TIPA and $\text{Cu}(\text{NO}_3)_2$ were purchased from Sigma Aldrich and used without further purification.

The cement used was a CEM I 52.5R (Cementerie Rossi, Piacenza, Italy), according to European nomenclature. Its oxide composition is as follows: $\text{SiO}_2 = 21.5\%$, $\text{Al}_2\text{O}_3 = 4.6\%$, $\text{Fe}_2\text{O}_3 = 2.3\%$, $\text{CaO} = 64.5\%$, $\text{Na}_2\text{O} = 0.3\%$, $\text{K}_2\text{O} = 0.7\%$, $\text{MgO} = 2.5\%$, $\text{SO}_3 = 3.4\%$. Its mineral composition is as follows: $\text{C}_3\text{S} = 60.0\%$, $\text{C}_2\text{S} = 13.3\%$, $\text{C}_3\text{A} = 10.1\%$, $\text{C}_4\text{AF} = 2.1\%$, $\text{CaCO}_3 = 3.4\%$, $\text{CaOH} = 1.7\%$, $\text{CaSO}_4 = 8.0\%$.

2.1 Preparation of amine-functionalized MeSH/PCE nanocomposites

Amine-functionalized MeSH/PCE were prepared by addition at room temperature of the amine to the MeSH/PCE suspension.

For all amines, we prepared 6 different mixtures by adding it at 0.5, 0.9, 1.3, 1.7, 2.5, 3.3 and 5% by weight of MeSH/PCE commercial admixture. Only the data that are relevant for the discussion are reported here.

As a reference sample, an aqueous solution of $\text{Cu}(\text{DEA})_2(\text{NO}_3)_2$ complex was prepared with a method derived from Maosoud *et al.* (2002): 50 ml of a 2M aqueous solution of DEA were added under vigorous stirring to 50 ml of a 1M aqueous solution of $\text{Cu}(\text{NO}_3)_2$. A pale blue precipitate initially formed upon the addition of DEA that eventually redissolved to give a clear deep blue solution which pH was adjusted to 11 with sodium hydroxide. The pH adjustment was done to simulate the basic environment of cement pore solution.

2.2 Mortar tests

The effect of N-MeSH/PCE on the development of mechanical strength of cementitious materials was tested on mortar mixtures. Mortars were prepared according to EN 196-1, employing CEM I 52.5R, with a W/C = 0.4. A PCE superplasticizer (Dynamon NRG 1030 from Mapei) was used to adjust the initial flow of the mortars in the same range (220-240 mm, measured on a dropping table, 15 drops). MeSH/PCE and N-MeSH/PCE were dosed at 3% by weight of cement (% bwc). A reference mortar (*i.e.* without hardening accelerator) was prepared as reference. Control mortars were prepared with 0.07% bwc of DEA, 0.06% of $\text{Cu}(\text{NO}_3)_2$ and 0.6% of $\text{Cu}(\text{DEA})_2(\text{NO}_3)_2$. Fresh mortars were cast in 4X4X16 cm polystyrene molds and cured at 22 ± 1 °C and $98 \pm 1\%$ RH until test. Compressive strengths were measured after 6, 7 and 8 hours of curing.

3. Results and Discussion

The accelerating properties of synthetic CSH nuclei on the strength development of Portland cement mixtures have been known for decades. For example, Duriez and Lezy (1956) observed that the addition of 2% bwc of seeds obtained from the hydration and milling of cement pastes could accelerate the strength development of cementitious materials. However, it was soon clear that these synthetic CSH particles must be small and well dispersed to be effective (John, 2018). In 2011, Nicoleau patented a method for the fast and scalable preparation of small and well dispersed CSH particles: the method consists in the precipitation of such nuclei from water soluble calcium and silicate precursors in presence of a PCE superplasticizer. The polymer acts as dispersant and prevents particle agglomeration, allowing the formation of a stable dispersion of nano sized CSH nuclei with high surface area. In 2013, Ferrari patented the synthesis of copper doped CSH/PCE (MeSH/PCE) nanoparticles and in 2022 Dal Sasso demonstrated that copper atoms in MeSH/PCE particles occupy superficial silicate sites. Knowing this and knowing that copper easily interacts with a variety of donor ligands, such as alkanolamines, we wondered whether it was possible to bind alkanolamine molecules on the surface of MeSH/PCE particles. If such interactions occurred, then the amines could potentially behave as a further bearing between individual particles, increasing the dispersion and, thus, their activity. In addition, alkanolamines themselves are hardening accelerators in proper conditions, and interesting synergetic effects might occur between the two chemical admixtures.

To verify such hypotheses, we prepared several mixtures between a commercially available MeSH/PCE nanocomposite (MapeFast Ultra from Mapei) and commercially available alkanolamines. Hereafter we will show the results obtained with N-MeSH/PCE containing 2.5% wt of amine. The effect of N-MeSH/PCE nanocomposite on the development of compressive strength was evaluated on mortar mixtures prepared with CEM I 52.5R. The results of the experiments are reported in Table 1.

It is evident that the addition of amines to MeSH/PCE results in an admixture with a stronger accelerating effect compared to the pure MeSH/PCE. This is true for all tested amines, with the sole exception of TEA. The enhanced acceleration can increase the compressive strength of the mortar up to 700% with EDIPA-MeSH/PCE at 6 hours of curing time, compared to a blank reference.

Table 1. Mortars flow and compressive strength development. For all mortars, cement = CEM I 52.5R, W/C = 0.4, PCE dosage (Dynamon NRG1030) = 0.7% bwc, accelerator dosage = 3% bwc.

| Admixture | Flow (mm) | Compressive strength (MPa) | | | Strength increase over Reference (%) | | |
|----------------|--------------|-------------------------------|-------|-------|---|-----|-----|
| | | 6 h | 7 h | 8 h | 6 h | 7 h | 8 h |
| Reference | 230 | 0.96 | 1.98 | 3.47 | \ | \ | \ |
| MeSH/PCE | 245 | 2.78 | 6.43 | 9.88 | 190 | 325 | 185 |
| DEA-MeSH/PCE | 215 | 6.03 | 10.24 | 12.5 | 528 | 518 | 260 |
| TEA-MeSH/PCE | 225 | 4.26 | 6.38 | 8.77 | 344 | 222 | 153 |
| EDIPA-MeSH/PCE | 215 | 7.79 | 9.68 | 14.31 | 711 | 389 | 312 |
| DEIPA-MeSH/PCE | 225 | 6.16 | 11.01 | 14.31 | 542 | 456 | 312 |
| TIPA-MeSH/PCE | 215 | 7.55 | 10.75 | 13.51 | 686 | 443 | 289 |

One might argue that alkanolamines themselves can behave as hardening accelerators, so what we observed might be a mere sum of effects.

To evaluate the separate effects of the individual components of the new admixture on the strength development of cementitious materials, we prepared another series of samples: one containing 3% bwc DEA-MeSH/PCE (2.5% DEA), one with 3% MeSH/PCE and one containing 0.07% bwc of DEA, *i.e.* the alkanolamine dosage added to a mortar admixed with 3% bwc DEA-MeSH/PCE. In addition, to further understand the specific activity of the Cu-DEA complex as hardening accelerator, we prepared a mortar with 0.06% bwc Cu(NO₃)₂ (equal copper dosage as 3% bwc DEA-MeSH/PCE) and one with 0.6% bwc of Cu(DEA)₂(NO₃)₂ (equal DEA dosage as 3% bwc DEA-MeSH/PCE) The results are shown in Figure 1.

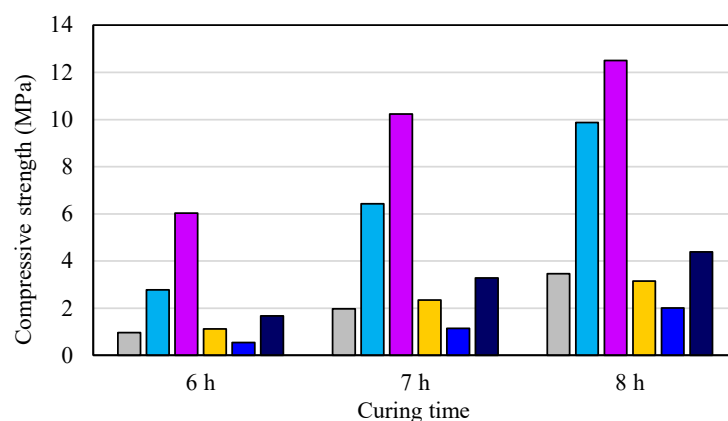


Figure 1. Compressive strength development for mortars prepared with CEM I 52.5R, W/C = 0.4, PCE (Dynamon NRG1030) = 0.7% bwc. Grey = reference; Cyan = 3% bwc MeSH/PCE; Purple = 3% bwc DEA-MeSH/PCE; Yellow = 0.07% bwc DEA; Blue = 0.06% bwc Cu(NO₃)₂; Deep Blue = 0.6% bwc Cu(DEA)₂(NO₃)₂

Notably, at such dosage, DEA by itself is neutral towards early age strength development. This means that the enhanced acceleration imparted by DEA-MeSH/PCE is the result of a synergetic effect between the two admixtures, possibly related with copper-alkanolamine interactions. This hypothesis is further supported by the data coming from the mortars containing copper nitrate and the copper-DEA complex: while copper by itself is even slightly retardant, a mild acceleration is obtained when the complex is observed. This prove that the complex has a specific interaction with cement.

4. Conclusions

An innovative hardening accelerator consisting in a mixture of a copper-doped MeSH/PCE nanocomposite and alkanolamines was prepared. The new hardening accelerator showed a superior performance compared to its individual components and was able to increase the compressive strength of a mortar sample after 6 hours of curing of more than 700% compared to the reference. Such synergetic effect between MeSH/PCE and alkanolamines is tentatively attributed to specific interactions between the amines and the Cu atoms occupying silicate superficial sites on MeSH/PCE nanoparticles. Further research is needed to understand the nature of the interactions and the mechanism through which the new N-MeSH/PCE hardening accelerator is able to accelerate cement hydration.

4. References

- Chikh, N., Cheikh-Zouaoui M., Aggoun S., Duval R. (2008) "Effects of calcium nitrate and triisopropanolamine on the setting and strength evolution of Portland cement pastes", *Materials and Structures*, 41, 31-36
- Dorn, T., Blask, O., Stephan D. (2022) "Acceleration of cement hydration – A review of the working mechanisms, effects on setting time, and compressive strength development of accelerating admixtures", *Construction and Building Materials*, 323, 126554
- Duriez M., Lezy R. (1956) "Possibilités nouvelles dans le durcissement rapide des ciments, mortiers et bétons", *Annales de l'Institut technique du bâtiment et des travaux publics. Liants hydrauliques*, 14, 137-158
- Ferrari G., Russo V., Squinzi M. (2013) "Accelerating Admixture for Cementitious Compositions", EP3080052B1
- Gagg, C. R. (2014) "Cement and concrete as an engineering material: An historic appraisal and case study analysis", *Engineering Failure Analysis*, 40, 114-140
- Liu, J., Yu C., Shub, X., Rana, Q., Yang, Y. (2019) "Recent advance of chemical admixtures in concrete", *Cement and Concrete Research*, 124, 105834
- Lavagna, L. (2023) "An Insight into the Chemistry of Cement—A Review", *Applied Sciences*, 13, 203
- John E., Matschei T., Stephan D. (2018) "Nucleation seeding with calcium silicate hydrate – A review", *Cement and concrete Research*, 113, 74-85
- Kanchanason V., Plank J. (2017) "Role of pH on the structure, composition and morphology of C-S-H/PCE nanocomposites and their effect on early strength development of Portland cement", *Cement and Concrete Research*, 102, 90-98
- Masoud M. S., Abou El-Enein S. A., Abed I. M., Ali A. E. (2002) "Synthesis and Characterization of Amino Alcohol Complexes", *Journal of Coordination Chemistry*, 55, 2, 153-178
- Nicoleau L., Leitner H. (2012), "Hardening accelerator composition for cementitious compositions", US9650298B2

The challenges of combining alkali activation and workability in low carbon binders: a molecular approach

C. Paillard^{1,2†}, N. Sanson¹, J.-B. d’Espinose de Lacaillerie^{1,*}, M. Palacios³, P. Boustingorry², M. Jachiet², C. Giraudeau² and V. Kocaba²

¹ Soft Matter Science and Engineering Laboratory (SIMM), UMR CNRS 7615, ESPCI Paris, Université PSL, Sorbonne Université, Paris, France
Email: jean-baptiste.despinose@espci.fr

² Saint-Gobain Construction Chemicals, Sermaises-du-Loiret, France
Email: vanessa.kocaba@chryso.com

³ Eduardo Torroja Institute for Construction Science (IETcc-CSIC), Madrid, Spain
Email: marta.palacios@ietcc.csic.es

ABSTRACT

Going toward carbon-neutral binders requires lowering the calcium content of the anhydrous phase of the cement paste. Since calcium chemistry is at the origin of the reactivity of ordinary silicate or aluminate based binders, lowering the calcium content necessarily implies externally activating the dissolution of the anhydrous phase by altering the composition of the liquid phase. The most common activators are alkali based.

This modification of the composition of the liquid phase, from, roughly speaking, a portlandite buffered solution, to a concentrated solution of sodium activators deeply affects our ability to control the workability of the paste. In this study, we discuss our recent results regarding the compared effect of NaOH and Na-silicate activators on a rheology controlling admixture and on the role of activator chemistry with respect to the yield stress and thixotropic behavior of the paste.

Taking the example of NaOH activated slag and a polycarboxylate ether, we show that the solvent quality depends on the sodium counter anion concentration. In consequence, the copolymer conformation in solution and on the surface of the anhydrous grains varies, thus explaining in part the efficiency losses observed in alkali-activated slag pastes. We also attempt to rationalize the time evolution of the rheological properties of the pastes using existing rheological models that reveals *a contrario* the importance of kinetics of the activation reactions.

KEYWORDS: *Rheology, polymer, admixtures, silicates, PCE*

[†] present address: Saint-Gobain Research Paris, Aubervilliers, France

1. Introduction

The availability of slag as a cement substitute is expected to be insufficient to meet the growing needs of the cement industry to decarbonate its production. However, slags constitute a well-studied archetype of low-calcium aluminosilicate glasses with latent hydraulicity. As such, numerous studies have been published concerning the efficiency of comb-copolymers superplasticizers in alkali-activated slag pastes (Douglas and Brandstettr, 1990; Palacios and Puertas, 2005; Habbaba and Plank, 2010; Conte and Plank, 2019). In particular, it was shown that traditional superplasticizers loose their dispersing ability due to a combination of factors including chemical degradation (Palacios and Puertas, 2005) and competitive adsorption (Plank and Hirsch, 2007; Marchon *et al.*, 2013). More recently, the issue of the dependence of the solubility of the organic admixture on the composition of the activating solution (Conte and Plank, 2019), and more precisely on the solvent quality of the activating solution with respect to the organic admixture has been explored either explicitly (Paillard *et al.*, 2023) or implicitly (Palacios *et al.*, 2022).

Here, we compare the respective impact of two alkali activators, NaOH and Na-silicate, on the rheological behavior of a fresh slag paste. First, going back in more detail on our previous study of the impact of NaOH on the solvent quality (Paillard *et al.*, 2023), we then explain using the Fox-Flory theory how the degradation of the solvent quality impacts the polymer conformation, which is known to be a determining factor for its dispersing ability (Giraudau *et al.*, 2009).

2. Materials and Methods

The slag, the NaOH activating solution and the polycarboxylate ether (PCE) superplasticizer used in this study were detailed in (Paillard *et al.*, 2023). The Na silicate activation was prepared from Betol 52T (Woellner, Germany) diluted in ultrapure water and a specific quantity of NaOH was dissolved to reach the $\text{Na}_2\text{Si}_{1.7}\text{O}_{4.4}$ molar ratio. Pastes were prepared by adding the slag to the solutions and mixing at 500 then 1500 rpm for a total of 2.5 min. The contents of Na_2O and water were kept respectively at 4 and 40 wt.% of mass of slag.

The PCE (Saint-Gobain Construction Chemicals, France) is a comb copolymer poly(methacrylic acid -g- ω -methoxypoly(ethylene glycol)). Its chemical structure may be described as $n=10$, $N=5$, $P=45$ according to (Gay and Raphaël, 2001). When used, it is mixed with the activating solutions before the paste preparation.

The rheological properties were investigated on a DHR3 rheometer (TA Instruments) fitted with a 4-blade vane geometry. Immediately after mixing, the paste was poured in the rheometer tank. The tests started 5 minutes after the beginning of the mixing with a pre-shear of 200 s^{-1} during 45 s. This was followed by a decreasing shear rate step flow curve from 200 to 0.01 s^{-1} . The evolution of the storage modulus during the aging of the paste is subsequently followed by oscillatory (1 Hz) imposed strain (0.01%).

Capillary viscometry was performed at 25°C with an Ubbelohde viscometer using a 0.53 mm diameter capillary tube.

3. Results and discussion

3.1. Rheological behaviour of slag pastes

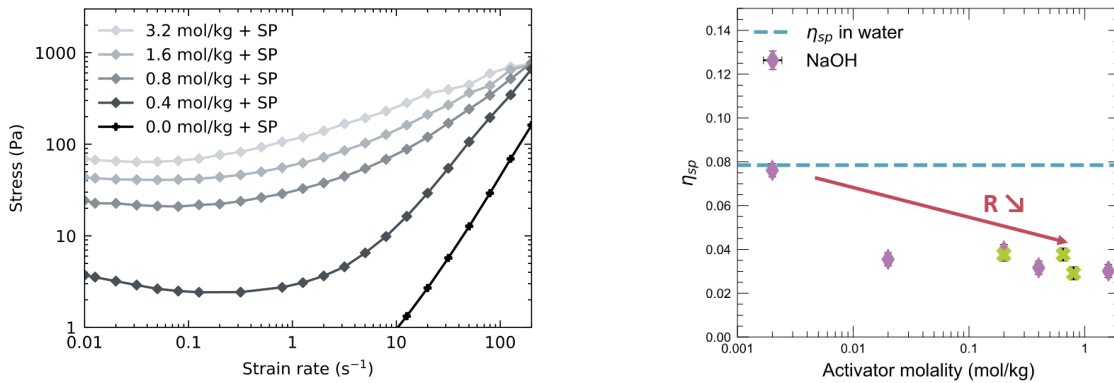


Figure 1. Left: Flow curves obtained in NaOH-activated systems with increasing NaOH molality at 13.4 g.L^{-1} of superplasticizer. Right: Evolution of the specific viscosity of the PCE solution with the NaOH molality.

The effect of NaOH molality on the dispersing ability of the PCE was studied by flow measurements and compared to the dependence of the specific viscosity of the superplasticizer with the NaOH molality (Fig. 1). Yield stress and apparent viscosity of the paste vary with the NaOH molality. Hence, a lower quantity of activator leads to a better efficiency of the superplasticizer. Due to the experimental limitations of the capillary viscometer, it was not possible to appreciate the specific viscosity in the full concentration range used in the rheology measurement, but the specific viscosity decreased with an increase in the NaOH concentration.

Since according to Fedors model, the specific viscosity η varies according to the polymer radius in solution R as

$$\eta \sim R^3 \quad (1)$$

and the comb copolymer radius in the dilute regime depends on the solvent quality through the Flory parameter χ (Gay and Raphaël, 2001)

$$R \sim (1-2\chi)^{1/5} \quad (2)$$

everything else being equal, the change in specific viscosity reflects the impact of the NaOH on the solvent quality for the PCE.

Since the adsorbed PCE extension from the surface R_{AC} is directly proportional to the radius in solution (Giraudeau *et al.*, 2009), it follows that the steric repulsion between the grains due to polymer adsorption scales in the same manner with the Flory parameter. This often overlooked phenomenon probably explains at least in part the loss of fluidity with the decrease of the solvent quality upon addition of NaOH, as discussed in (Paillard *et al.*, 2023).

3.2. Comparing the aging of slag pastes activated with NaOH or Na-silicate

When NaOH is substituted by Na silicate, the workability issue is fundamentally different. As shown in Fig. 2, sodium silicate reduces the yield stress and the storage modulus of the slag paste. The issue is then not to reduce the yield stress with a superplasticizer but to maintain the workability of the paste over time. The results reported below were consequently obtained without superplasticizer.

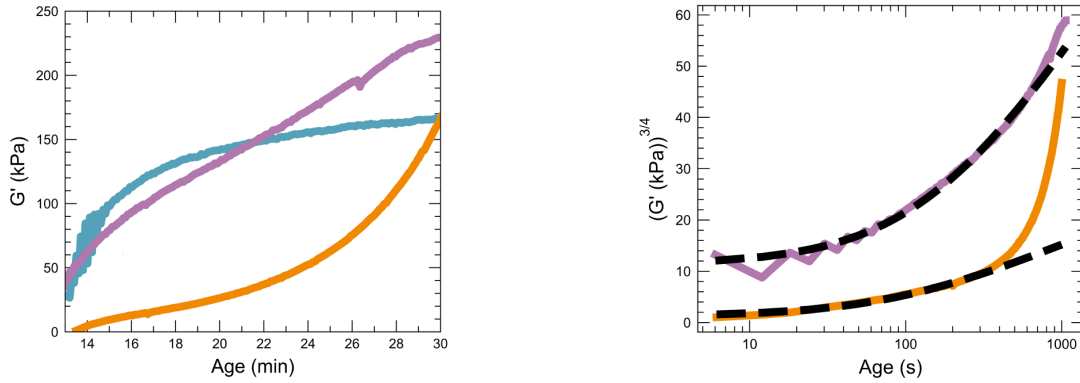


Figure 2. Left: Evolution of the storage modulus with aging of the slag pastes in water (blue), NaOH (purple) and a $\text{Na}_2\text{Si}_{1.7}\text{O}_{4.4}$ sodium silicate solution (orange). Right: Same measurements scaled to allow comparison with the predictions of Bonacci's model (dashed black lines).

In Fig. 2, two successive regimes can be distinguished in the aging of the paste. At early ages, the modulus increase could be explained by the stiffening of the solid contacts between the slag particles, as recently studied in model colloidal suspensions (Bonacci *et al.*, 2020). At early age, the effect of the bulk precipitation of hydrates on the rheology can be neglected, the volume solid fraction remains constant and the storage modulus G' scales with time t according to Bonacci's prediction:

$$G'(t) \sim \ln(t-t_0)^{4/3} \quad (3)$$

where t_0 is an adjustable delay time to account for the preparation of the paste. At longer times, the system significantly deviates from Bonacci's predictions, probably because the solid volume fraction increases in relation to the reactivity of the paste as evidenced by calorimetry and spectroscopy (Palacios *et al.*, 2021)(not shown, paper in preparation).

4. Conclusions

Taking slag as an example of a low calcium binder with latent hydraulicity, this study underlined that maintaining workability in alkali activated systems raises contrasted challenges depending on the activating solutions. With NaOH, the loss of efficiency of the superplasticizer is due in part to the salting-out of the superplasticizer PCE.

By contrast, Na silicate provides a higher fluidity and no superplasticizer is needed. However, Na silicate activation leads to a loss of workability in time due to rapid hydrate precipitation. In that case, the issue is thus essentially to regulate the kinetics of the activation reaction.

Acknowledgements

The authors wish to express their gratitude and sincere appreciation to the R&D Department of Saint-Gobain Construction Chemicals, for their technical and financial support to this research work.

C.P. gratefully acknowledges very helpful discussions with Prof. R. J. Flatt (ETH Zürich), Prof. S. Gauffinet (Université de Bourgogne) and Dr. N. Roussel (Université Gustave Eiffel) during her PhD examination.

References

- Bonacci, F. *et al.* (2020) ‘Contact and macroscopic ageing in colloidal suspensions’, *Nature Materials*, 19(7), pp. 775–780. <https://doi.org/10.1038/s41563-020-0624-9>.
- Conte, T. and Plank, J. (2019) ‘Impact of molecular structure and composition of polycarboxylate comb polymers on the flow properties of alkali-activated slag’, *Cement and Concrete Research*, 116, pp. 95–101. <https://doi.org/10.1016/j.cemconres.2018.11.014>.
- Douglas, E. and Brandstetr, J. (1990) ‘A preliminary study on the alkali activation of ground granulated blast-furnace slag’, *Cement and Concrete Research*, 20(5), pp. 746–756. [https://doi.org/10.1016/0008-8846\(90\)90008-L](https://doi.org/10.1016/0008-8846(90)90008-L).
- Gay, C. and Raphaël, E. (2001) ‘Comb-like polymers inside nanoscale pores’, *Advances in Colloid and Interface Science*, 94(1–3), pp. 229–236. [https://doi.org/10.1016/S0001-8686\(01\)00062-8](https://doi.org/10.1016/S0001-8686(01)00062-8).
- Giraudeau, C. *et al.* (2009) ‘Surface and Intercalation Chemistry of Polycarboxylate Copolymers in Cementitious Systems’, *Journal of the American Ceramic Society*, 92(11), pp. 2471–2488. <https://doi.org/10.1111/j.1551-2916.2009.03413.x>.
- Habbaba, A. and Plank, J. (2010) ‘Interaction Between Polycarboxylate Superplasticizers and Amorphous Ground Granulated Blast Furnace Slag: Interaction Between Superplasticizers and Blast Furnace Slag’, *Journal of the American Ceramic Society*, 93(9), pp. 2857–2863. <https://doi.org/10.1111/j.1551-2916.2010.03755.x>.
- Marchon, D. *et al.* (2013) ‘Molecular design of comb-shaped polycarboxylate dispersants for environmentally friendly concrete’, *Soft Matter*, 9(45), p. 10719. <https://doi.org/10.1039/c3sm51030a>.
- Paillard, C. *et al.* (2023) ‘The role of solvent quality and of competitive adsorption on the efficiency of superplasticizers in alkali-activated slag pastes’, *Cement and Concrete Research*, 163, p. 107020. <https://doi.org/10.1016/j.cemconres.2022.107020>.
- Palacios, M. *et al.* (2021) ‘Early reactivity of sodium silicate-activated slag pastes and its impact on rheological properties’, *Cement and Concrete Research*, 140, p. 106302. <https://doi.org/10.1016/j.cemconres.2020.106302>.
- Palacios, M. *et al.* (2022) ‘Heating cement to slow down its hydration: The unexpected role of PCE interpolymers bridge formation’, *Cement and Concrete Research*, 156, p. 106765. <https://doi.org/10.1016/j.cemconres.2022.106765>.
- Palacios, M. and Puertas, F. (2005) ‘Effect of superplasticizer and shrinkage-reducing admixtures on alkali-activated slag pastes and mortars’, *Cement and Concrete Research*, 35(7), pp. 1358–1367. <https://doi.org/10.1016/j.cemconres.2004.10.014>.
- Plank, J. and Hirsch, C. (2007) ‘Impact of zeta potential of early cement hydration phases on superplasticizer adsorption’, *Cement and Concrete Research*, 37(4), pp. 537–542. <https://doi.org/10.1016/j.cemconres.2007.01.007>.

Interpretation of rheological property of steel slag powder blended cement paste: from interparticle force to physico-chemical parameters

Zedi Zhang¹, Yamei Zhang^{1,2*}

¹ School of Materials Science and Engineering, Jiangsu Key Laboratory of Construction Materials, Southeast University, Nanjing 211189, China
 Email: 230228631@seu.edu.cn.

² Nanjing Institute for Intelligent Additive Manufacturing Co., Ltd, Nanjing 210000, China
 Email: ymzhang@seu.edu.cn

ABSTRACT

The blending of steel slag powder with cement can mitigate the carbon footprint of traditional cementitious composites. In this paper, the effects of steel slag powder on the rheological properties of cement paste were investigated, and the interparticle force was quantified and analyzed to provide a fundamental explanation. Results found that F_{EDLVO}^h can be used to interpretate the rheological properties within 1 h, which was found to greatly related to its ratio of apolar component to polar component of surface energy. A simple formula calculating normalized F_{EDLVO}^h conveniently from basic parameters, e.g., particle size, surface energy, etc. was proposed, which is believed can effectively and practically regulate the interparticle force. The results allow the manipulation of interparticle forces and rheological properties by changing fundamental parameters.

KEYWORDS: Cement, Steel slag powder, Rheological properties, Interparticle force, Surface energy

1. Introduction

Steel slag (SS), an industrial by-product produced in steel-making process, has a small utilization rate of only 30% (Huo et al. 2021). Using steel slag as solid waste in 3D printed concrete can not only improve the utilization rate of steel slag, but also reduce the use of cement. The critical reasons hindering the large-scale application of SS are its low activity and poor soundness. Considering this, dry chemistry modification approach were used in this study to improve the reactivity of SS (Huo et al. 2021). The modification process can change the surface characteristics and chemical composition of SS, which will inevitably affect the rheological properties. The studies on the rheological properties of cement paste containing SS are also still limited. To better understand the the effects of original SS and modified SS on the rheological properties of cement paste, the interparticle force was carefully quantified to clarify their influence mechanism.

2. Materials and Methods

P·I 42.5 Portland cement (C) was used in this study, and SS with a density of 3.22 g/cm³ was utilized as mineral admixture. The chemical composition and mineralogical composition of PC, SS were presented in Table 1 and Table 2, respectively. Modified SS, including MS2, MS4, etched by 2 wt.% phosphoric acid and 4 wt.% phosphoric acid, respectively, were also used as mineral admixtures, where the phosphoric acid concentration is 85 wt.%.

Table 1 The chemical composition of PC, SS, wt. %.

| Materials | CaO | SiO ₂ | Al ₂ O ₃ | MgO | Fe ₂ O ₃ | SO ₃ | MnO | K ₂ O | Na ₂ O | TiO ₂ | P ₂ O ₅ | Others |
|-----------|-------|------------------|--------------------------------|------|--------------------------------|-----------------|------|------------------|-------------------|------------------|-------------------------------|--------|
| PC | 63.08 | 17.02 | 3.96 | 2.47 | 2.90 | 3.58 | 0.15 | 0.66 | 0.23 | 0.27 | 0.08 | 5.60 |
| SS | 38.38 | 17.62 | 7.44 | 5.47 | 19.12 | 2.79 | 2.17 | 0.15 | 0.30 | 0.84 | 1.77 | 3.95 |

Table 2 The main phase composition of steel slag powder, wt.%.

| Mineral | C ₃ S | β-C ₂ S | C ₃ A | C ₄ AF | CaCO ₃ | gypsum | | | | | |
|---------|------------------|--------------------|-------------------|--------------------------------|-------------------|----------|------------------|---|--------|--|--|
| PC | 61.22 | 16.19 | 5.88 | 9.41 | 5.19 | 2.11 | | | | | |
| Mineral | C ₃ S | β-C ₂ S | C ₄ AF | C ₁₂ A ₇ | CaCO ₃ | Wuestite | SiO ₂ | Ca ₃ (PO ₄) ₂ | Others | | |

Cement pastes with the w/b of 0.4 were prepared for test. The replacement level of SS was 10 wt%, 20 wt% and 30 wt% of the cement, and the replacement level of the cement by MS2, MS4 was 10 wt%.

RST-SST rotational rheometer was used for rheological test. The rheological parameters of cement paste were tested at 7 min, 17 min, 27 min, 37 min, and 47 min after the initial contact of cement with water. Shear procedure was adopted as follows: the pastes were sheared at 100 s^{-1} , 80 s^{-1} , 60 s^{-1} , 40 s^{-1} , 20 s^{-1} , and 10 s^{-1} for 1 min each to obtain the equilibrium stress at each rate. Then the equilibrium stress vs. shear rate curves was fitted using the rheological model to get rheological parameters.

At the specified time (7 min, 17 min, etc.), the hydration process of cement paste was terminated by using isopropyl alcohol. After that, the obtained dry powders were used for particle size distribution test, contact angle test, and zeta potential test, etc. The particle size distribution of particles is determined by a laser particle size distribution analyzer. The contact angle of the particles is tested by thin layer wicking method (Tasci et al. 2014). The zeta potential of the particle is tested by the ZetaProbe equipment, where the liquid-solid ratio is consistent with the designed w/b. The determined particle size D , surface potential (Ψ), apolar (γ^{LW}) and polar (γ^{AB}) components of interfacial tension, non-retarded Hamaker constant (A) are partially presented in Table 3. Then the interparticle force can be calculated based on EDLVO theory, which describe the competition of van der Waals forces (F_{LW}), electrical double layer forces (F_{EL}) and acid-base interaction force (F_{AB}) (Han et al. 2020). Compared with DLVO theory, the EDLVO theory considers the F_{AB} , which has been shown to have an important effect on interparticle interactions (Han et al. 2020).

Table 3 Particle size, surface potential, surface energy and Hamaker constant of particles in cement paste.

| Sample | D (μm) | Ψ (mv) | γ^{LW} (mJ/m ²) | γ^{AB} (mJ/m ²) | $A \times 10^{-21}$ (J) |
|---------|-----------------------|-------------|------------------------------------|------------------------------------|-------------------------|
| PC-7 | 15.704 | -3.07 | 37.638 | 7.822 | -4.04 |
| PC-27 | 17.105 | -3.01 | 37.774 | 7.290 | -4.11 |
| PC-47 | 16.802 | -3.21 | 37.440 | 6.912 | -3.96 |
| PS30-7 | 17.850 | -3.04 | 37.180 | 8.891 | -3.84 |
| PS30-27 | 16.917 | -3.30 | 36.396 | 6.859 | -3.50 |
| PS30-47 | 15.804 | -3.21 | 35.952 | 6.735 | -3.31 |

3 Results and discussion

3.1 Rheological properties of steel slag powder blended cement pastes

Fig. 1 shows the effects of SS content on the rheological properties of cement paste. It can be seen both the dynamic yield stress and plastic viscosity increase first and then decrease with the rise of SS content. The pastes have the lowest dynamic yield stress and plastic viscosity when the SS content is 30%. Compared with the paste containing SS, the yield stress and plastic viscosity of the paste blended with MS2 increases, while they decrease when the modifier content of SS increases to 4%.

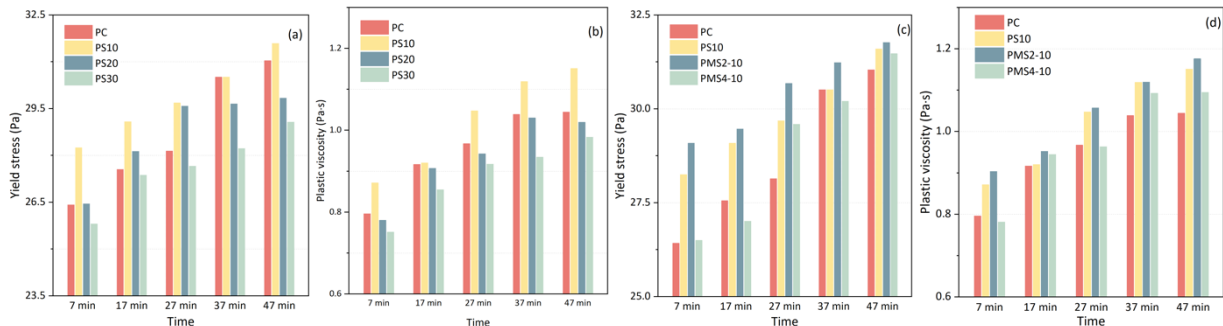


Fig. 1 Effects of (a)-(b) SS content, and (c)-(d) SS type on the rheological properties of cement paste

3.2 Interparticle force and its relationship with rheological property

The variations of attractive force (F_{AT}), repulsive force (F_{RP}) and total interparticle force (F_{EDLVO}^h) with the SS content and SS type are shown in Fig. 2. The detailed calculations about interparticle forces based on EDLVO theory can be seen in Han et al. 2020. F_{AT} and F_{EDLVO}^h have the same law of change, indicating

F_{AT} dominates the variations of F_{EDLVO}^h . Specifically, cement pastes blended with 10% SS have the largest F_{AT} and their F_{RP} is not the greatest, which leads to a maximum value of F_{EDLVO}^h when only considering the effects of SS content. On the contrary, the pastes mixed with 30% SS have smaller F_{AT} and higher F_{RP} , resulting in lower F_{EDLVO}^h . Compared with the interparticle force of pastes blended with SS, the incorporation of MS2 in pastes increases the F_{AT} and reduces the F_{RP} , thus promoting the F_{EDLVO}^h .

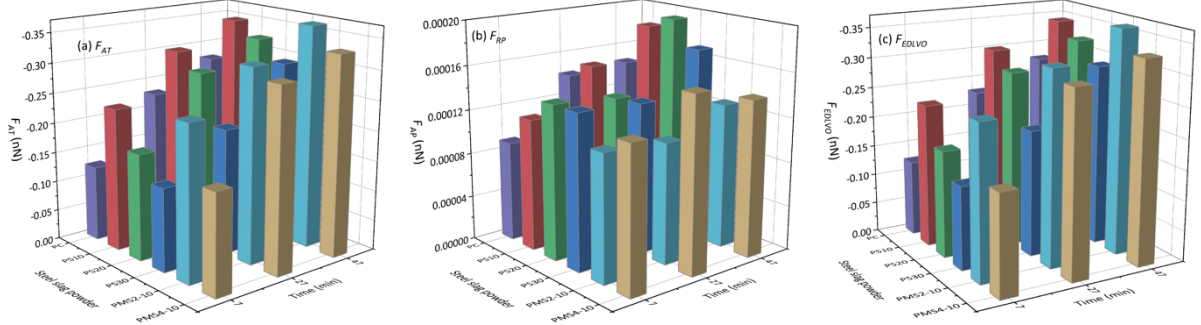


Fig. 2 The variations of interparticle force with SS at different time

The linear relationships between F_{EDLVO}^h and rheological properties, including dynamic yield stress and plastic viscosity, can be seen in Fig. 3, with the correlation coefficient R^2 of 0.90 and 0.88, which proves that interparticle force can characterize the variation of rheological properties of fresh SS blended cement paste within 1 h.

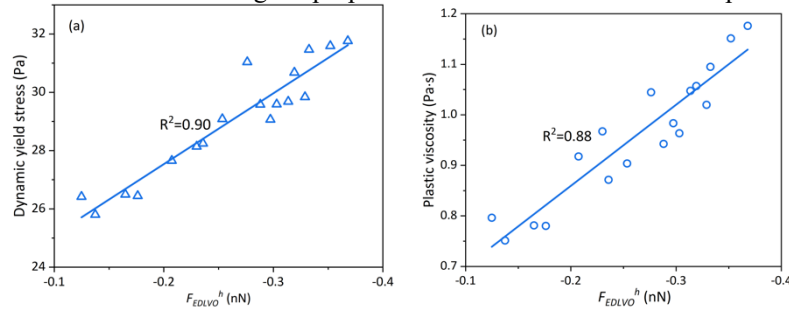


Fig. 3 The relationship between rheological properties and F_{EDLVO}^h of SS blended cement paste

4. Discussion

4.1 How physico-chemical parameters affect the interparticle force and then rheological property

As we know, the interparticle forces depend on the physico-chemical parameters in the system. Fig. 4 explore the relationships between normalized interparticle forces including van der Waals forces (F_{LW}), electrical double layer forces (F_{EL}) and acid-base interaction force (F_{AB}) and physico-chemical parameters $((D/h) \cdot \gamma^{LW}, (D/h) \cdot (\psi^2/\kappa), (D/h) \cdot (1/\gamma^{AB}))$. Then the relationship between total interparticle force F_{EDLVO}^h and physico-chemical parameters was explored. Good relationships between them were found and the corresponding fitting curves are obtained. According to Fig. 3 and Fig. 4, the rheological properties can be effectively regulated based on the physico-chemical parameters.

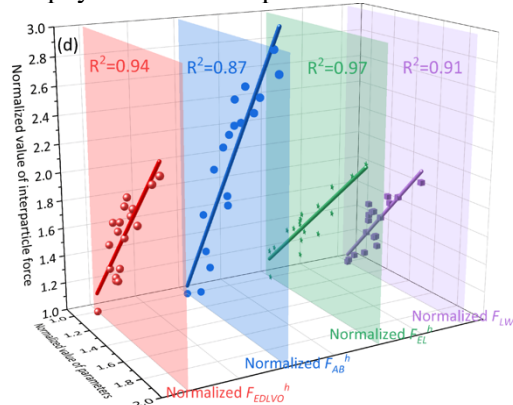


Fig. 4 Relationships between normalized parameters and interparticle force

More importantly, normalized interparticle forces can be calculated as follows from the fitting curve in Fig. 4:

$$\overline{F_{EDLVO}^h} = a \cdot \left(\overline{(D/h) \cdot \gamma^{LW}} + \overline{(D/h) \cdot (\psi^2/\kappa)} + \overline{(D/h) \cdot (1/\gamma^{AB})} \right) + b \quad (1)$$

Where, $\overline{F_{EDLVO}^h}$, $\overline{(D/h) \cdot \gamma^{LW}}$, $\overline{(D/h) \cdot (\psi^2/\kappa)}$, $\overline{(D/h) \cdot (1/\gamma^{AB})}$ represent the normalized value of F_{EDLVO}^h , $(D/h) \cdot \gamma^{LW}$, $(D/h) \cdot (\psi^2/\kappa)$, $(D/h) \cdot (1/\gamma^{AB})$, respectively; a , b represent the fitting coefficient of fitting curve; h is the particle separation distance, m; κ^{-1} is the Debye screening length, m.

Eq. (1) may have less physical meaning, but it gives a clear guidance on how various factors affect the interparticle force and a simple method to calculate the normalized interparticle force to compare their sizes, which is efficient and practical for regulating the interparticle force of cement pastes and then rheological properties.

Fig. 5 gives the variations of F_{EDLVO}^h and γ^{LW}/γ^{AB} with SS of cement paste, which shows that F_{EDLVO}^h and γ^{LW}/γ^{AB} have basically the same law of change with the variations of SS, indicating that γ^{LW}/γ^{AB} plays a leading role in F_{EDLVO}^h . Overall, the greater F_{EDLVO}^h of steel slag powder blended cement paste is largely related to its higher γ^{LW}/γ^{AB} .

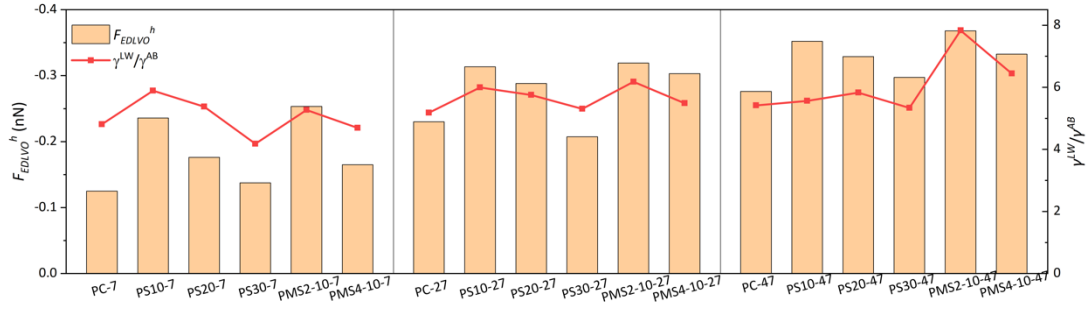


Fig. 5 Variations of F_{EDLVO}^h and γ^{LW}/γ^{AB} with SS of cement paste

5. Conclusions

This study provides a basic understanding of the effect of steel slag powder on the rheological properties of cement paste by quantifying interparticle force. It was found that the cement paste mixed with 30% SS has a low dynamic yield stress and plastic viscosity. F_{EDLVO}^h of steel slag powder blended cement paste was found to be able to interpretate the rheological properties of paste within 1 h. A simple formula calculating normalized F_{EDLVO}^h from basic parameters was proposed, which is believed can effectively and practically regulate the interparticle force and then rheological properties. The γ^{LW}/γ^{AB} is found to play a leading role in the variation of F_{EDLVO}^h .

Acknowledgements

The authors would like to acknowledge the financial support from National Natural Science Foundation of China (No.52130210).

References

- B. Huo, B. Li, C. Chen and Y. Zhang, Surface etching and early age hydration mechanisms of steel slag powder with formic acid, *Construction and Building Materials*. 280(2021) 122500.
- E. Tasci and B. Yilmaz, Charge and surface energy interface among particles in cement and pozzolan suspensions, *Advances in Cement Research*. 26 (2014) 213-221.
- K. Han, J. Xiao, Z. Zhang, J. Wang and X. Hu, Effect of particle size distribution on flocculation and its growth in cement-ground limestone suspensions, *Construction and Building Materials*. 262(2020) 120047.

Influence And Strategies of Plug Flow on The Measured Rheological Properties of Cement-Based Materials

Z. Xu^{1*}, W. Sun², J. Liu³

¹ Southeast University, Nanjing, China
Email: xuzs@seu.edu.cn

² China University of Mining and Technology, Xuzhou, China
Email: ts22030094a31@cumt.edu.cn

³ Southeast University, Nanjing, China
Email: liujiaping@cnjsjk.cn

ABSTRACT

This paper aims to discuss the influence of plug flow on the test results of rheological properties of cement-based materials (CBM), and to propose strategies to improve the test accuracy. Fresh cement pastes with different fluidities were prepared. A coaxial rotational rheometer was used to conduct the rheological tests. An image method was used to measure the actual shear radius of the sample in the container. Using the radius of the sample container and the actual shear radius, the rheological parameters were calculated. The results show that the plug flow dramatically influences the test results of the rheological properties of CBM. Based on the Herschel-Bulkley model, ignoring plug flow will lead to higher yield stress. The higher the fluidity of the paste, the smaller the influence of the plug flow on the measurement results. In addition, a numerical iterative algorithm was proposed in this paper to calculate the rheological parameters of CBM with incomplete shear state conditions. The iterative results were consistent with the experimental results, which verify the reliability of the iterative algorithm.

KEYWORDS: *Cement-based material, Rheological property, Plug flow, Image method, Iterative algorithm*

1. Introduction

The rheological properties are important properties of fresh cement-based materials (CBM). How to accurately measure the rheological parameters of CBM is an important matter. A coaxial cylindrical rotational rheometer is widely used to measure the rheological properties of fresh CBM (González-Taboada et al. 2017; Khayat et al. 2019). It is normally assumed that the sample in the container is completely sheared and no slip occurs on the boundary, the shear stress and shear strain rate can be calculated according to existing equations (Han et al. 2021). However, due to the existence of the yield stress, there will be a plug zone (Khayat et al. 2019) in the sample where the shear stress is lower than the yield stress, and the fluid remains static. Ignoring the plug zone's influence on the shear flow behaviour would result in the fitting error of the rheological parameters (Hafid et al. 2015). Therefore, it is an urgent issue to eliminate the influence of plug flow on the measurement of CBM's rheological properties.

In this study, the rheological properties of two kinds of cement paste with different fluidities were measured. An image method is used to analyze the plug flow during the test. A numerical iterative algorithm for calculating the rheological parameters was proposed considering the plug flow in samples. The rheological parameters were calculated three times using existing equations, image method, and numerical iterative algorithm. The influence of plug flow on the calculation results was investigated. The numerical iterative algorithm for the rheological properties test is verified and expected to improve the measurement accuracy of CBM's rheological properties.

2. Experiment

2.1 Materials and mixtures

Ordinary Portland cement and fly ash were used as binding materials. The cement used has a density of 3150 kg/m³ and a specific surface area of 320 m²/kg. The density of fly ash used is 2800 kg/m³, and the specific surface area is 350 m²/kg. Tap water and polycarboxylic acid high-performance superplasticizer were used to mix the paste. Two kinds of cement paste with low and high fluidities were prepared separately for the rheological test, and the mix dosage is shown in Table 1. The fluidity of the mixture was measured according to the fluidity testing statute (GB/T8077-2012 2012).

Table 1 Mix proportions of cement paste mixtures

| Series | Water/binder (%) | Fly ash/binder (%) | Water (kg/m ³) | Cement (kg/m ³) | Fly ash (kg/m ³) | Superplasticizer (kg/m ³) | Flow distance (mm) |
|--------|------------------|--------------------|----------------------------|-----------------------------|------------------------------|---------------------------------------|--------------------|
| No. 1 | 25 | 20 | 385.6 | 1234.0 | 308.4 | 15.42 | 161 |
| No. 2 | 25 | 40 | 379.2 | 910.0 | 606.8 | 15.16 | 247 |

2.2 Rheological measurement procedure and rheological model

The Herschel-Bulkley model $\tau = \tau_0 + K\dot{\gamma}^n$ was employed as the rheological model, where, τ is shear stress, τ_0 is yield stress, K is viscosity coefficient, $\dot{\gamma}$ is shear strain rate, and n is flow index. The rheological properties of paste mixtures were measured by a BROOKFIELD-made RST-SST type coaxial rotational rheometer. A four-blade vane rotor with a diameter of 30mm and a height of 60mm was used. The sample container had a diameter of 100mm and a depth of 110mm. The measurement procedure of each rotate speed is shown in Fig. 1. After the test of each speed, the paste was stirred again. Each paste mixture was measured at six rotate speeds of 5 rpm, 10 rpm, 15 rpm, 20 rpm, 30 rpm, and 40 rpm. A straight line was drawn along the radius direction on the surface of the mixture using red pigment. This line gradually formed a circle with the shearing flow of the mixture, as shown in Fig. 2. The image method was used to measure the actual shear radius of the paste according to the size of the circle.

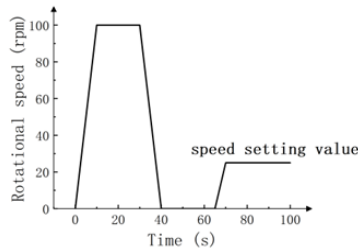


Fig. 1 Shear procedure of cement paste



Fig. 2 Distinguish of shear zone and plug zone by pigment
(Series No.2, 15 r/min)

3. Iterative algorithm for calculating rheological parameters

3.1 Shear behaviours of paste in rheometer

The 2D model of the coaxial rotational rheometer is shown in Fig. 3. The radius of the rotor is R_1 , and the height is h . The inner radius of the sample container is R_2 . The sample container keeps stationary and the rotor rotates at a set speed ω to drive the shear flow. Assuming that the sample is completely sheared, the shear strain rate $\dot{\gamma}$ at the rotor surface can be calculated by Eq (1). According to torque balance, the shear stress τ at the position r can be calculated as Eq. (2).

$$\dot{\gamma} = 2\omega \frac{R_2^2}{R_2^2 - R_1^2} \quad (1)$$

$$\tau = \frac{M}{2\pi r^2 h} \quad (2)$$

It is shown that the shear stress is inversely proportional to r , i.e. the farther away from the center, the smaller the shear stress in the paste. Exceeding a certain distance, the shear stress is lower than the yield stress of the paste, and a plug zone is formed beside the fixed boundary, as shown in Fig. 3.

3.2 Numerical iterative algorithm

Since the paste is not sheared completely, to accurately calculate the rheological properties of the paste, the actual shear radius R_s is needed. At the critical position, the shear stress in the paste is equal to τ_0 , and the shear radius R_s can be obtained by inverse deduction from Eq. (2), as shown in Eq. (3). The actual shear strain rate at the rotor surface can be obtained by substituting R_s into Eq. (1), as shown in Eq. (4).

$$R_s = \sqrt{\frac{M}{2\pi h \tau_0}} \quad (3)$$

$$\dot{\gamma} = 2\omega \frac{R_s^2}{R_s^2 - R_1^2} \quad (4)$$

We developed a numerical iterative algorithm to calculate the real shear radius and the rheological parameters of the paste. The paste is assumed to be completely sheared, the initial yield stress is fitted first. Using Eq.s (3) and (4), the shear radius is modified and the yield stress value is refitted after each loop. The iteration is repeated until the change of modified yield stress is less than 0.001 Pa.

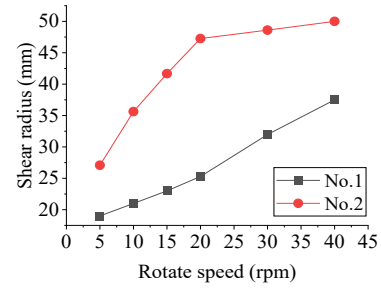
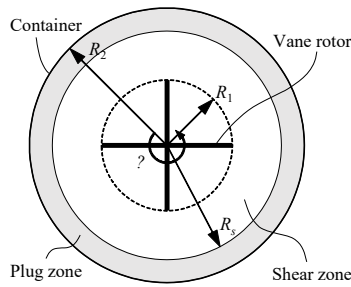


Fig. 3 2D diagram of shear flow of paste in rheometer Fig. 4 Measured shear radius at different rotate speeds

4. Results and discussions

4.1 Variation of shear flow radius with different shear rate

The shear radius of the two paste mixtures at each speed measured by the image method was shown in Fig. 4. The shear radius increases with the increase of rotate speed. This is because the energy input at high rotate speed can drive more fluid to undergo shear flow. The shear range also increases with the increase of pastes fluidity at the same rotate speed, since less energy would be dissipated by the internal resistance in the paste with high fluidity, and more paste can be driven by the rotor.

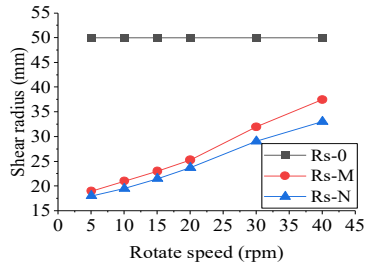
4.2 Influence of plug flow on rheological results

Regardless of the influence of plug flow on shear behaviour, the shear radius R_{s-0} is always equal to R_2 . Name the obtained shear radius by the image method and numerical iteration algorithm as R_{s-M} and R_{s-N} , respectively. The three kinds of shear radius are compared in Fig 5. According to shear radius R_{s-0} , R_{s-M} and R_{s-N} , the corresponding shear strain rates were calculated, the rheological curves of the two paste mixtures are plotted and shown in Fig. 6. The plug flow has great influence on the shear radius, especially in the case of low rotate speed. Therefore, larger errors between rheological curves can be found at a low shear strain rate. In addition, the three rheological curves of paste No.2 are close to each other, that is, the impact of plug flow is small in case of high fluidity.

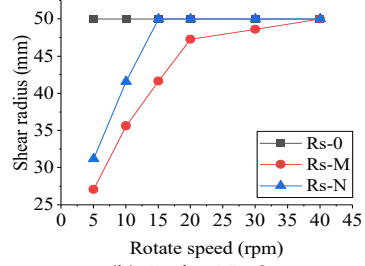
The fitted rheological parameters according to the rheological curves are compared in Fig. 7. It is found that neglecting the effect of plug flow on the shear range would lead to a large yield stress

4.3 Validation of numerical iterative algorithm

As shown in Fig. 5, the shear flow radius obtained by the numerical iterative algorithm is close to the shear radius measured by the image method. In Fig. 6, the rheological curves obtained using the

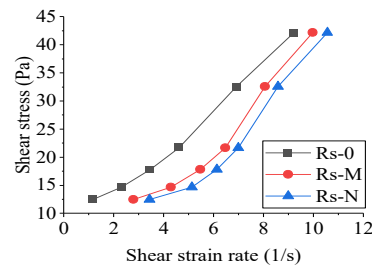


(a) Series No.1

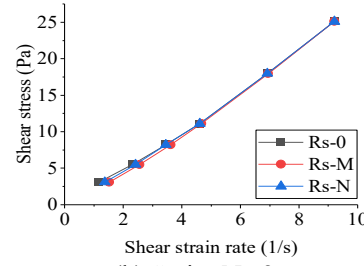


(b) Series No.2

Fig. 5 Shear radius obtained by different methods

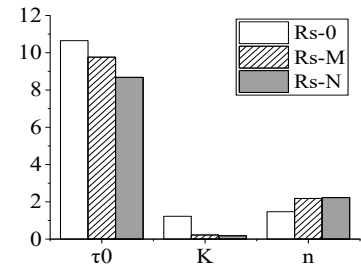


(a) Series No.1

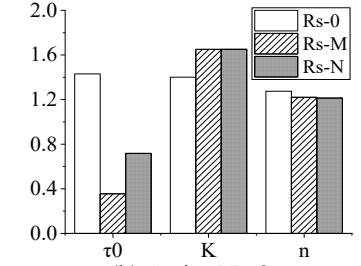


(b) Series No.2

Fig. 6 Rheological curves of paste mixtures



(a) Series No.1



(b) Series No.2

Fig. 7 Fitted rheological parameters of paste mixtures

numerical iterative algorithm almost match those obtained by the image method. As shown in Fig. 7, the fitted rheological parameters using the numerical iterative algorithm and those fitted by the image method are in good agreement. The above results verify the reliability of this numerical iterative algorithm.

5. Conclusions

This study discussed the plug flow in rheological test of CBM. An image method and a numerical iterative algorithm were proposed to eliminate the influence of plug flow. The main conclusions are as follows:

- (1) The plug flow of CBM during the rheological test has a significant adverse impact on the measured results. The range of plug flow is large in the situation of low shear rate and low fluidity.
- (2) Ignoring the effect of plug flow on the shear flow of the sample, the fitted yield stress is greater than the actual value.
- (3) The image method and numerical iterative algorithm can accurately calculate the rheological parameters of CBM. The numerical iterative algorithm can not only improve the fitting accuracy of rheological parameters but also make the calculation more convenient.

Acknowledgments

The authors would like to acknowledge the financial support of the National Key Research and Development Program of China (2021FY0500800), the National Natural Science Foundation of China (No. 52208231), and the Jiangsu Funding Program for Excellent Postdoctoral Talent.

References

- GB/T8077-2012. (2012). *Methods for Testing Uniformity of Concrete Admixture*. China: Chinese Standard Press.
- González-Taboada, Iris, Belén González-Fontebao, Javier Eiras-López, and Gemma Rojo-López. (2017). "Tools for the Study of Self-Compacting Recycled Concrete Fresh Behaviour: Workability and Rheology." *Journal of Cleaner Production* 156: 1–18.
- Hafid, H. et al. (2015). "Assessment of Potential Concrete and Mortar Rheometry Artifacts Using Magnetic Resonance Imaging." *Cement and Concrete Research* 71: 29–35.
- Han, Jianguo et al. (2021). "The Rheological Parameters of Bingham Fluid Were Obtained Using a Coaxial Double-Cylinder Rheometer." *Journal of Chinese Ceramic Society* 49(02): 323–30.
- Khayat, Kamal Henri, W. Meng, K. Vallurupalli, and Le Teng. (2019). "Rheological Properties of Ultra-High-Performance Concrete — An Overview." *Cement and Concrete Research* 124: 105828.

Effect of the microstructure of polycarboxylate ether (PCE) superplasticizers on the hydration kinetics of Ordinary Portland Cement (OPC)

A. Barquero^{1*}, S. Beldarrain¹, G. Goracci², J.S. Dolado² and J.R. Leiza¹

¹ POLYMAT, Kimika Aplikatua saila, Kimika Fakultatea, University of the Basque Country UPV/EHU, Joxe Mari Korta zentroa, 20018 Donostia-San Sebastián (Spain).

Email: aitor.barquero@ehu.eus, sara.beldarrain@ehu.eus, jrleiza@ehu.eus

² Centro de Física de Materiales (CSIC, UPV/EHU) Materials Physics Center (MPC) Paseo Manuel de Lardizabal 5, 20018 Donostia-San Sebastián (Spain).

Email: guido.goracci@ehu.eus, j.dolado@ehu.eus

ABSTRACT

Among the most important additives used in cement industry, we can find PCE (polycarboxylate ether) superplasticizers, which improve the workability of the cement paste by lowering the viscosity of the cement. Although they have been used for many years, their structure-property relationship is still not fully understood. In this work, we use methacrylic acid-co-polyethylene glycol methacrylate (MAA-PEGMA) copolymers, which are characterized by their comb-like structure. These copolymers were synthesized by free-radical copolymerization to obtain PCEs with homogeneous composition varying the charge density (N) or side-chain length (P). The main objective of this work was to analyze the effect of the microstructure of the synthesized PCEs on the hydration kinetics of an Ordinary Portland Cement (OPC). Both direct and delayed addition were studied. It was observed that as the PCE concentration increases, the hydration of the cement is delayed. This delay becomes even more pronounced when the MAA/PEGMA ratio of PCEs increases or when the side chain length decreases. Furthermore, since the delay in hydration is proportional to the carboxylate dose, all PCEs fit a master curve. In this way, it has been possible to demonstrate that the microstructure of the copolymers synthesized by free-radical copolymerization can be related to the retardation that affects the hydration of commercial OPC.

KEYWORDS: *Polycarboxylate ether superplasticizers, OPC, hydration of cement*

1. Introduction

Nowadays, concrete technology progresses in parallel to the development of modern polycarboxylate ether/ester (PCE) polymers. PCEs are comb-like structures with a backbone formed by anionic carboxylic groups and non-ionic polyethylene oxide (PEO) units as pendant groups (side chain, Figure 1 left). In spite of their wide use, our understanding on the PCE's performance has largely relied on a trial and error approach until very recently. Fortunately, a set of pioneering works has enabled to rationalize the performance of PCEs based on their structural topology.

In this regard, and with the aim of understanding the microstructure-property relationship of comb-like PCEs, Flatt et al.(2009) characterized the microstructure of comb-like PCE's by defining a model repeating unit (see Figure 1 right), which can be fully described by three characteristic structural parameters, which are the number of monomer units in the repeating unit of the backbone chain, N, the number of ethylene glycol units in the side chains, P, and the number of repeating units in the chain, n.

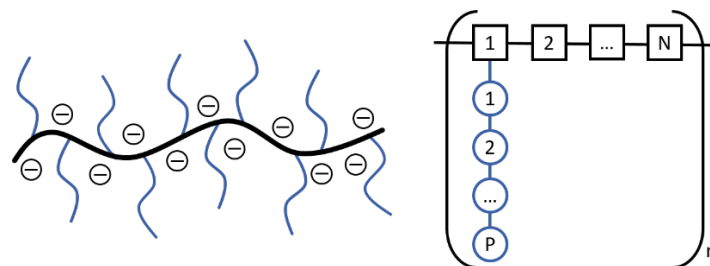


Figure 1. Schematic representation of a PCE polymer chain (left) and structural parameter of PCEs (right) as defined by Flatt et al. (2009)

Interestingly, an unprecedented insight on the interaction between the cement surfaces and PCEs was possible from this novel approach (Flatt et al., 2009). In particular, their work deeply analyzed the impact of a PCE on a specially designed model cement and proposed master curves capable of linking the cement hydration delay with dosages and molecular structure parameters. In this context, this work aims to extend our understanding on the influence of PCEs on cement hydration delay. To this end, PCEs with controlled topology have been synthesized by free-radical polymerization and their impact on the hydration of a commercial OPC has been carefully analyzed. Although these copolymers have been added by direct addition to a commercial OPC through a direct addition method, the experiments reveal that the hydration delay is proportional to the carboxylate dosage and can be effectively displayed in master curves, as proposed by Marchon et al. (2017). On the contrary, the delayed addition experiments show a more complex behaviour that requires further study.

2. Materials and methods

2.1 Materials and Synthesis of the PCEs

Methacrylic acid (MAA) was purchased from Acros Organics, polyethylene glycol methyl ether methacrylates (PEGMA) with 22.5 and 45 ethylene oxide (EO) units were kindly supplied by Evonik Industries. 3-Mercaptopropionic acid (3-MPA), potassium persulfate (KPS), sodium bicarbonate (NaHCO_3), sodium nitrate (NaNO_3) and sodium hydroxide (NaOH) were purchased from Sigma-Aldrich and used as received. Deionized water was used as solvent. The cement used was CEM type I 52.2R Ordinary Portland Cement (OPC), which was kindly supplied by Lemona Cements S.A (Spain).

The copolymerization reactions were carried out in aqueous solution in semibatch in a 250 mL glass jacketed reactor with a thermostatic water bath and a mechanical turbine stirrer at 200 rpm. To carry out the reactions, deionized water (100 g) was loaded to the reactor and heated to 80 °C. When the reaction temperature was achieved, the feeding started. The monomers (PEGMA and MAA), initiator (KPS), chain transfer agent (CTA, 3-MPA) and sodium bicarbonate dissolved in the rest of the water were fed in the same stream for three hours at $0.56 \text{ g} \cdot \text{min}^{-1}$. After, post polymerization was carried out for an hour, with the aim of reaching full conversion of the monomer. Table 1 summarizes the PEGMA type, MAA/PEGMA ratio, final solids content and CTA amount for each PCE that was synthesized.

Table 1. Summary of the PCEs synthesized for this work.

| PCE | PEGMA | MAA/PEGMA ratio (mol) | SC* (%) | CTA (% wbm**) |
|----------|-----------|-----------------------|---------|---------------|
| 0.67/1 M | PEGMA22.5 | 0.67/1 | 20 | 0 |
| 1/1 M | | 1/1 | 20 | 0 |
| 3/1 M | | 3/1 | 20 | 0 |
| 6/1 M | | 6/1 | 10 | 0 |
| 0.67/1 L | PEGMA45 | 0.67/1 | 10 | 0.5 |
| 1/1 L | | 1/1 | 10 | 0.5 |
| 3/1 L | | 3/1 | 5 | 0.5 |
| 6/1 L | | 6/1 | 5 | 0.5 |

*Solids Content; **Weight Based on monomer

2.2 Hydration kinetics of the OPC

The hydration kinetics were carried out using a TAM Air conduction calorimeter at room temperature for 48 hours with water as reference material. Cement pastes with a total mass of 5 g were prepared with a 0.4 water to cement ratio. The mixing of the components was made by a vortex mixer with the following procedure: For direct addition (with the PCE dissolved in the initial water), 90 seconds at 800 rpm, 60 seconds of pause and 90 seconds at 800 rpm. For delayed addition: 90 seconds at 800 rpm, 60 seconds of pause and 90 seconds at 800 rpm, 5 minutes wait, addition of the PCE in aqueous solution, and 60 seconds at 800 rpm

3. Results and discussion

Figure 2 shows representative plots of hydration calorimetry of OPC showing the effect of the PCE concentration (left), PCE composition or MAA/PEGMA ratio (center) and PEGMA side chain length (right) when the superplasticizer was added by direct addition.

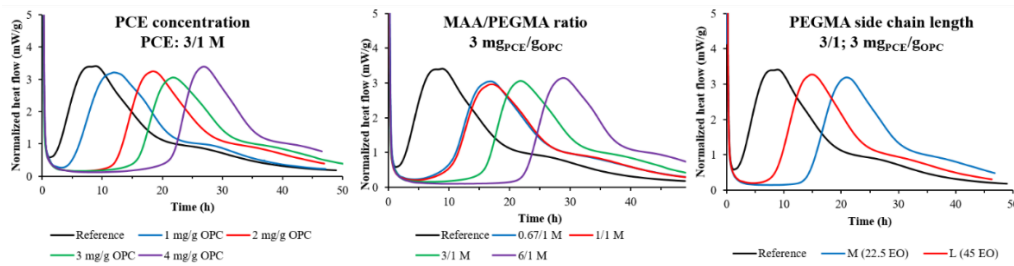


Figure 2. Effect of the PCE dosage (left), MAA/PEGMA ratio on the PCE (center) and number of EO units (right) on the hydration of a commercial OPC by direct addition.

Figure 2 (left) shows the effect of PCE concentration on OPC hydration kinetics for the case of PCE 3/1-M. As expected, as the PCE dose increases, the hydration of the PCE is retarded. It is noteworthy that all the synthesized PCEs showed the same trend. The center image in Figure 2 shows the effect of the PCE composition (that can also be defined as the MAA/PEGMA ratio), for PCEs of series M. Here, the hydration delay is increased as the MAA fraction increases in the copolymer. This is attributed to a higher carboxylate dose (for the same PCE dose), and in great agreement with Marchon et al. Last, Figure 2 right shows the impact of the side chain (or P) for PCEs with the same MAA/PEGMA ratio. As observed, increasing the length of the side chain the delay in the hydration is reduced. This is once again correlated with the carboxylate dose, as a PCE with a longer PEO side chain contains less carboxylic groups for the same dose. The retardation of the hydration (Δt) was plotted over the number of repeat units and a parameter that described the polymer structure, calculated with equation 1, to obtain the master curve proposed by Marchon et al. (2017). As presented in Figure 3, the master curve is obtained, despite using a commercial OPC and a direct addition method.

$$\Delta t \propto n_{RU}^{tot} \left(\frac{C/E}{C/E+1} \right)^{3/2} \quad (1)$$

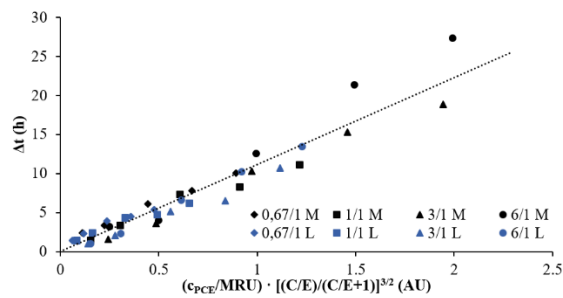


Figure 3. Retardation of the hydration of the OPC as a function of the number of repeat units and polymer structure.

The results of the hydration calorimetry with delayed addition of the PCE are presented in Figure 4. Once again, examples for the effect of the PCE concentration (left), PCE composition (center) and PEGMA side chain length (right) are presented.

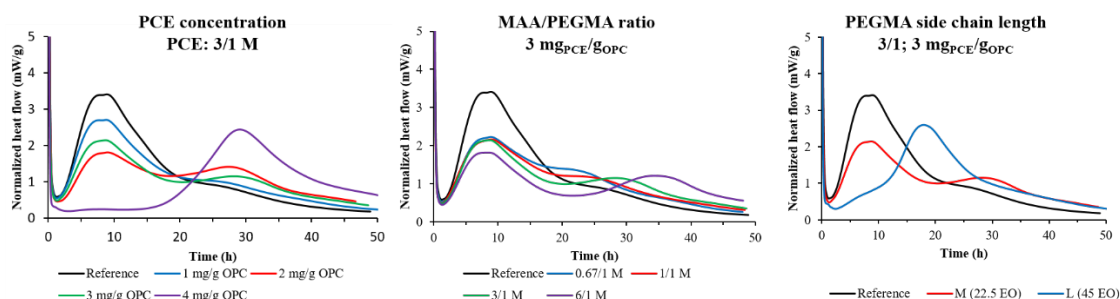


Figure 4. Effect of the PCE dosage (left), MAA/PEGMA ratio on the PCE (center) and number of EO units (right) on the hydration of a commercial OPC by delayed addition.

As observed in Figure 4, the behavior of the hydration kinetics was significantly different when delayed addition was used. In this case, it seems that the hydration mechanism is altered. Apparently, at low PCE dosages, there is no delay of the first peak, only a reduction, and the heat release occurs in the second peak (that appears as a shoulder in the reference). At high dosages, on the other hand, the hydration peak is completely shifted, and the results resemble those of direct addition. Similar behaviors are observed with PCEs of different compositions, or PEO chain lengths.

4. Conclusions

In this work, PCEs with uniform composition and different molecular architectures were synthesized by free-radical copolymerization varying the MAA/PEGMA ratios and ethylene oxide units in the PEGMA macromonomers. The effect of direct and delayed addition in the mixing water of these copolymers on the hydration kinetics of a commercial Ordinary Portland Cement (OPC) was analysed by isothermal calorimetry. In direct addition it was observed that by increasing the PCE concentration the hydration was delayed. Moreover, for any given PCE concentration the delay was longer as the MAA/PEGMA ratio increased or the side chain length of the PEGMA decreased. Interestingly, the hydration delays of all the PCEs were found to be proportional to the carboxylate dosage and fitted well the master curve proposed in the state of the art for delayed additions. On the contrary, in delayed addition a more complex behavior was observed, making the analysis challenging.

Acknowledgements

The financial support from Eusko Jaurlaritza (GV-IT-1512-22), Ministerio de Ciencia e Innovación (PID2021-123146OB-I00) and LTC Green Concrete is gratefully acknowledged. Sara Beldarrain thanks the scholarship for master grants of POLYMAT.

References

- Flatt, R. J., Schober, I., Raphael, E., Plassard, C., & Lesniewska, E. (2009). Conformation of adsorbed comb copolymer dispersants. *Langmuir*, 25(2), 845–855. <https://doi.org/10.1021/la801410e>
- Marchon, D., Juilland, P., Gallucci, E., Frunz, L., & Flatt, R. J. (2017). Molecular and submolecular scale effects of comb-copolymers on tri-calcium silicate reactivity: Toward molecular design. *Journal of the American Ceramic Society*, 100(3), 817–841. <https://doi.org/10.1111/jace.14695>

C-S-H AND PORE STRUCTURE ON HARDENED CEMENT MIXED WITH VOLCANIC GLASS FINE POWDER

Masashi TOJO^{1*}, Masaki SATO², Koshiro KOIZUMI³ and Yasuhiro UMEMURA⁴

¹ *Nihon university, Chiyoda-Ku, Tokyo, Japan*

Email: csms22001@g.nihon-u.ac.jp

² *Nihon university, Chiyoda-Ku, Tokyo, Japan*

Email: satou.masaki@nihon-u.ac.jp

³ *Nihon university, Funabashi-shi, Chiba, Japan*

Email: koizumi.koushirou@nihon-u.ac.jp

⁴ *Nihon university, Chiyoda-Ku, Tokyo, Japan*

Email: umemura.yasuhiro@nihon-u.ac.jp

ABSTRACT

In this study, the hydration reaction between cement and volcanic glass fine powder and its hydrates were clarified, assuming the use of volcanic glass powder (VG) as a substitute for silica fume (SF), which is often used in ultra-high-strength concrete. Furthermore, the relationship between the pore structure formed by the hydrates and the compressive strength development was also examined. As a result, the following findings were obtained. The total pore volume of the cement hardened body mixed with VG reached a minimum and the compressive strength peaked when the admixture ratio was 25%. On the other hand, in the case of SF, the total pore volume was at its minimum and the compressive strength peaked when the admixture ratio was 20%. As the mixing ratio of VG and SF increased, the amount of C-S-H produced increased by pozzolanic reaction, and the volume of pores decreased. The maximum mixing ratio of pozzolanic reaction was 25% and 20%, respectively. The volume of C-S-H generated at a mixing ratio of 30% VG increased more than the volume of C-S-H at a mixing ratio of less than 25%. As a result, the pore volume increased in the pore size range of 50 nm to 2 nm. The proportion of high-density C-S-H of VG was higher than that of SF under 30% mixture ratio, and the proportion of low-density C-S-H of VG rapidly increased over 30% mixture ratio.

KEYWORDS: *Ultra high strength, Volcanic glass, Silica fume, Pore structure, C-S-H*

1. Introduction

Ultra-high strength concrete (UHSC) typically contains silica fume (SF). SF is an admixture with particles smaller than cement particles, and can strengthen concrete by reducing the water-binder ratio (W/B) to 20% or lower. However, SF needs to be imported into Japan. Recently, as a substitute for SF, in 2020, JIS A 6209 specified a fine powder made of volcanic glass (VG) for concrete. Tomoyose A et al. (2019) developed a method for producing VG as an admixture and Kusumoto H. et al. (2019) showed that VG improves the compression strength by filling the space between capillaries, like SF. However, only a few studies have focused on the pozzolanic reaction and formation of calcium silicate hydrate (C-S-H). In this study, the effect of C-S-H on the compressive strength and pore structure of hardened cement mixed with VG was investigated.

2. Experiment

The samples had a W/B of 15% to mimic the properties of UHSC; they were heat-cured at 20 °C for 48 h, and again heat-cured at a maximum temperature of 90 °C for 48 h. The SF used for comparison had a specific surface area equivalent to that of the VG. In this study, the VG and SF are collectively termed as “PZ fine powder”. Five samples were prepared based on a previous study by Tojo M. et al. (2021), with a mixing ratio of 25% (corresponding to the maximum strength). The SF employed for comparison was used in a mixing ratio ranging from 15 to 30%. Mortar was used as the sample to test the compressive strength and pore size distribution, while a mixture of mortar without aggregates was used for the hydration reaction analysis. In addition, to measure the density of C-S-H derived from cement, PZ0 without SF and VG was prepared. The C-S-H derived from VG and SF, volcanic glass paste (VGP), and silica fume paste (SFP) was analyzed.

Table 1 Property of Material

| Material | Sign | Specifications |
|------------------|----------------------------|---|
| Cement | C | JIS R5210 Low Heat Portland Cement |
| PZ fine powder | Volcanic Glass Fine Powder | VG |
| | Silica fume | SF |
| Calcium Hydrate | CH | Guaranteed Reafent $\rho=2.21$ (g/cm ³) |
| Water | W | Distilled Water |
| Superplasticizer | SP | Polycarboxylic acid-based Superplasticizer for High strength concrete |
| Deformer | DEF | Polyether based Defoamer |
| Sand | S | ISO standard sand $\rho=2.64$ (g/cm ³) |

Table 2 Mix proportion of mortar

| Name | W/B (%) | Unit content (kg/m ³) | | | | | SP (B×%) | DEF (B×%) | |
|------|---------|-----------------------------------|------|-----|----------|------|----------|-----------|------|
| | | W | B | | | S | | | |
| | | | C | CH | VG or SF | | | | |
| PZ0 | 15 | 124 | 828 | - | 0 | - | 4.00 | 0.25 | |
| SF15 | | 138 | 1002 | - | 150 | 1066 | | | |
| SF20 | | 136 | 952 | - | 190 | | | | |
| SF25 | | 135 | 906 | - | 227 | | | | |
| SF30 | | 134 | 865 | - | 260 | | | | |
| SFP | | 232 | - | 774 | 774 | - | | | 1066 |
| VG15 | | 138 | 1002 | - | 150 | | | | |
| VG20 | | 136 | 952 | - | 190 | | | | |
| VG25 | | 135 | 906 | - | 227 | | | | |
| VG30 | | 134 | 865 | - | 260 | | | | |
| VG35 | | 134 | 828 | - | 290 | | | | |
| VGP | | 236 | - | 788 | 788 | - | | | |

The compressive strength was measured using mortar specimens of dimensions $\phi 5 \times 10$ according to JIS A 1108. The pore size distribution was measured using a mercury intrusion porosimeter with 2.5 mm cubes of mortar. Hydration analysis was performed based on a study by Sato M. et al. (2010). According to Nozawa S. et al. (2016), ettringite becomes amorphous when heated at 80 °C for 12 h or more. The conventional calculation method considerably overestimates the amount of C-S-H as it also includes the amount of amorphized ettringite. Therefore, the amount of amorphized ettringite was calculated from the quantitative amounts of gypsum, ettringite, and monosulfate by balancing calculations, and the amounts of the amorphized admixture, pore water content, and amorphized ettringite were subtracted from the amorphous amount to obtain the amount of C-S-H. The density of C-S-H was determined by Tanaka Y. et al. (2009), and the amount of C-S-H formed (vol.%) was determined using the calculated C-S-H density. Furthermore, according to a previous study (Tojo M. et al. 2021), the density of C-S-H from VG and SF was lower than those of C-S-H from cement and C-S-H from SF and VG mixed in the hardened cement as PZ fine powder. In this study, the density of C-S-H derived from VGP and SFP is denoted as $\rho_{PZ\text{ C-S-H}}$, and the density of C-S-H derived from PZ0 is expressed as $\rho_{C\text{ C-S-H}}$, because the density of C-S-H derived from cement is high while that of C-S-H derived from pozzolanic acid is low.

The ratio of ρ_{C-S-H} present in the sample was calculated using equation (1).

$$\beta = \frac{\rho_{C-S-H} - \rho_{PZ-C-S-H}}{\rho_{C-S-H} - \rho_{PZ-C-S-H}} \times 100 (\%) \quad (1)$$

Here, β is the ratio of C C-S-H (%), ρ_{C-S-H} is the density of C C-S-H (g/cm^3), ρ_{C-S-H} is the density of C-S-H in the sample (g/cm^3), and $\rho_{PZ-C-S-H}$ is the density of PZ C-S-H (g/cm^3)

3. Result and Discussion

3.1 Compressive Strength and Pore Structure

The relation between the mixing rate and compressive strength is shown in Figure 1. For VG, the maximum strength was 220 MPa at 25%, and for SF, it was 230 MPa at 20%. The pore volumes (Figure 2) of VG25 and SF20 were the smallest, but that of SF was larger than that of VG, which did not agree with the trends observed for the strength. This was considered to be caused by the large area of gel voids (0.007-0.003 μm , 0.007-0.02 μm) in SF. The pore volume for the same pore size increased in VG30 and VG35 than VG25.

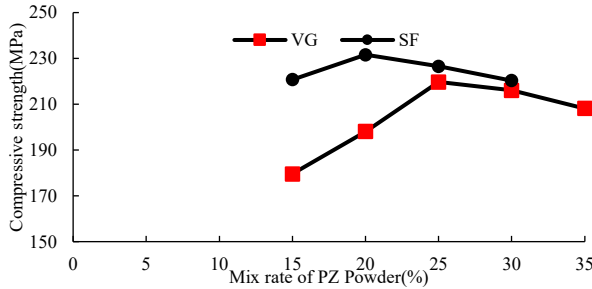


Figure 1 Compressive strength of mortar

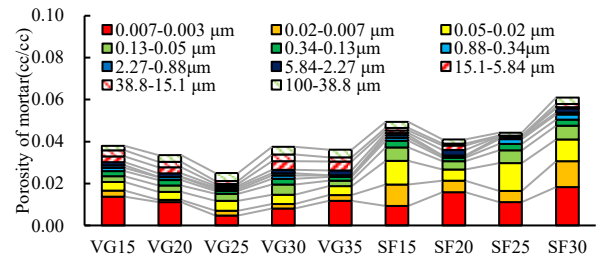


Figure 2 Porosity of mortar

3.3 Hydration Reaction of Cement and PZ Fine Powder

The PZ reaction rate (Figure 3) was decreased at VG35 and SF25 than more, possibly due to an insufficient amount of CH, which is required for the pozzolanic reaction (Figure 4). The density of C-S-H (Figure 5) decreased with increasing amounts of VG and SF. The maximum amount of C-S-H (Figure 6) was obtained using VG30 and SF20. This is because of a lack of CH. The relationship between the volume of C-S-H and the strength is shown in Figure 7. The strength and amount of C-S-H are proportional.

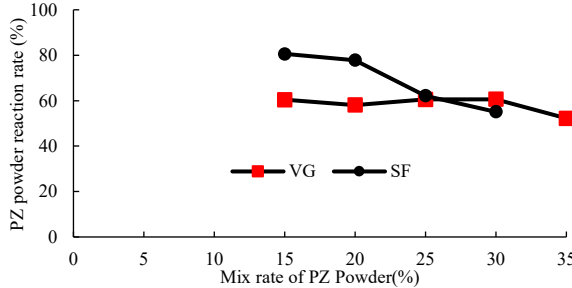


Figure 3 PZ powder reaction rate

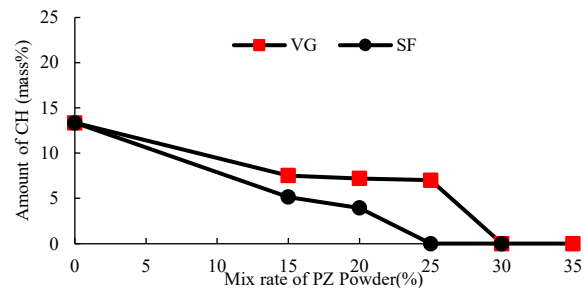


Figure 4 Amount of CH

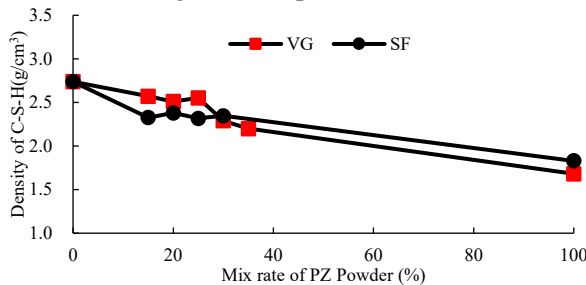


Figure 5 Density of C-S-H

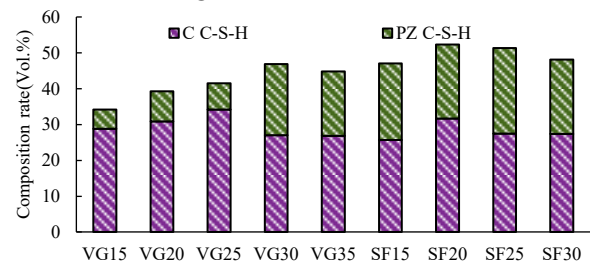


Figure 6 Amount of C/PZ C-S-H

Accordingly, the amount of C-S-H formed showed an increasing trend up to VG30. From VG25 to VG30, the amount of C-S-H increased but the strength decreased. To analyze this phenomenon, we focused on the composition ratio of C-S-H. VG30 and VG35 have more PZ C-S-H than VG25. The density of PZ C-S-H is lower than that of C C-S-H. According to Jennings H M. et al. (2007), the density of C-S-H is proportional

to Young's modulus. This indicates that the amount of C-S-H formed in VG30 is higher than that in VG25, but the strength of VG30 is lower because the amount of C-S-H, which is considered to be low Young's modulus because of low density, is larger. In addition, the amount of C C-S-H formed in VG35 is equivalent to that in VG30, and the strength of VG35 is lower because the amount of PZ C-S-H formed in VG35 is lower than that in VG30.

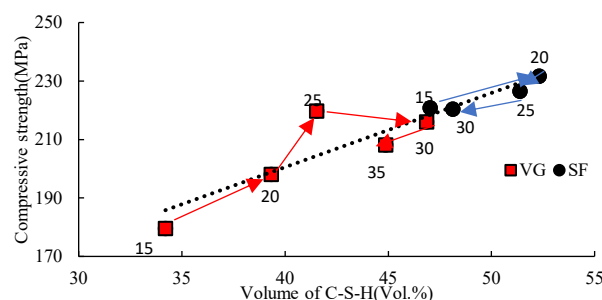


Figure 7 Relation between Volume of C-S-H and Compressive strength

3. Conclusions

In this study, hydration reaction between cement and VG fine powder and its hydrate was investigated, assuming the use of VG fine powder type I as a substitute for SF, which is often used in UHSC. Furthermore, the relationship between the pore structure formed by the cement-hardened and the compressive strength was examined. The following findings were obtained. 1. The compressive strength of the cement-hardened using PZ fine powder increased with increasing C-S-H formation. 2. When the mixing ratio of VG was 30% or more, the amount of VG was excessive and the pozzolanic reaction did not proceed. 3. The compressive strength of hardened cement mixed with PZ fine powder was considerably affected by the composition ratio of C-S-H derived from the hydration reaction of cement with different densities and C-S-H derived from PZ fine powder, the amount of C-S-H formed, and the amount of pores formed by C-S-H.

Acknowledgments

This research was supported by JSPS KAKENHI Grant Number JP 22K12477 and the "Committee for Advanced Utilization of Volcanic Deposits as Concrete Admixtures" of the Japan Concrete institute. The used volcanic glass fine powder was provided by Kenichi Sodeyama of Kagoshima Prefectural Institute of Industrial Technology.

References

- Tomoyose A, Nozawa T, Sodeyama K and Higashi K. (2019) "Effect of BET Surface Area and Replacement Ratio of Volcanic Glass Powder on Compressive Strength", *Cement Science and Concrete Technology*, 73(1): 467-470
- Kusumoto H, Nozawa T, Tomoyose A, Omori H, Sodeyama K, Higashi K. (2019) "Basic characteristics of volcanic glass fine powder for concrete Part 3 Relationship between strength development and pore size distribution of concrete using volcanic glass fine powder", *Academic lecture summaries of Architectural Institute of Japan*: 89-90.
- Tojo M, Umemura Y and Sato M. (2021) "The effect of pozzolan-reactive fine powder on compressive strength and C-S-H formation of hardened cement", *Japan Society of Civil Engineers 2021 Annual Meeting*, V-27
- Sato M, Umemura Y and Koizumi K. (2010) "Hydration of Hardened Ultra High Strength cement Using Silica Fume and Water-reducing Agent", *Cement Science and Concrete Technology*, 64(1): 442-449.
- Nozawa S, Saito G, Sato K and Saeki T. (2016) "Effect of Drying Condition and Temperature History on Water Content of Ettringite Structure", *Cement Science and Concrete Technology*, 70(1): 2-8.
- Tanaka Y, Saeki T, Sasaki K and Suda Y. (2009) "Fundamental Study of Density of C-S-H", *Cement Science and Concrete Technology*, 63(1): 70-76.
- Hamlin M, Jennings, Jeffrey J, Thomas, Julia S, Gevrenov, Georgios Constantinides, Franz-Joef Ulm. (2007) A multi-technique investigation of the nanoporosity of cement paste, *Cement and Concrete Research*, 37(3), pp.329-336

EARLY-AGE WORKABILITY LOSS IN LC3 SYSTEMS

L. Michel^{*1}, F. Zunino², R.J. Flatt³, D.S. Kammer⁴

¹ *Institute for Building Materials, ETH Zurich, Zurich, Switzerland*
Email: micheluc@ethz.ch

² *Institute for Building Materials, ETH Zurich, Zurich, Switzerland*
Email: franco.zunino@ifb.baug.ethz.ch

³ *Institute for Building Materials, ETH Zurich, Zurich, Switzerland*
Email: flatr@ethz.ch

⁴ *Institute for Building Materials, ETH Zurich, Zurich, Switzerland*
Email: dkammer@ethz.ch

The production of cement represents nearly 8% of yearly CO₂ emissions worldwide. Climate change being the most important challenge modern society has to face in the coming decades, alternative formulations of cementitious materials must be brought to the market. Limestone Calcined Clay Cements (LC3) are one viable option, presenting a high potential of reduction of CO₂ emissions while being easily transferable to existing technologies on the production scale. However, the main disadvantage of these systems from an implementation viewpoint is their loss of workability at early age. The origin of this workability loss is usually linked to water absorption by the clay particles, resulting in an effective decrease of w/c ratio. Here we show that the structuration at rest of such pastes cannot be brought back to absorption of water by clay particles. Rheometer measurements are performed on LC3 samples at different w/c ratios. One additional sample is prepared with metakaolin presaturated in water to assess the effect of water absorption on workability. The trends obtained show that no significant reduction of w/c ratio takes place in LC3 systems, thus challenging the proposed mechanism of water absorption by clay particles.

KEYWORDS: *Rheology, LC3, workability, early-age*

1. Introduction

The workability at early-age of Limestone Calcined Clay Cement (LC3) systems has been reported to be worse than that of Ordinary Portland Cement (OPC) systems (Favier et al., 2018; Hay and Celik, 2022; Hou et al., 2021; Nair et al., 2020). It was observed that a higher dosage of superplasticizers is required in LC3 systems to achieve a given slump as compared to OPC systems. One mechanism proposed to explain this difference is that water gets absorbed by the clay particles, resulting in an effective reduction of w/c ratio, and hence causing workability issues (Favier et al., 2018; Nair et al., 2020).

Oscillatory rheometry has proved to be a reliable way of measuring structural build-up in cement pastes at rest (Roussel et al., 2012; Schultz and Struble, 1993; Yuan et al., 2017a). Rheometer tests can be destructive or non-destructive, depending on the property investigated (Yuan et al., 2017b). Non-destructive small amplitude oscillatory shear (SAOS) measurements allow a continuous monitoring of storage modulus of pastes at rest. On the other hand, yield stress measurements require the paste structure to be destroyed, resulting in non-continuous measurements. Both storage modulus and yield stress are signatures of structural build-up in cement pastes, whereby the material is probed in different regimes. Destructive structural build-up measurements are closely related to flow onset, and thus allow to study workability. This does not translate directly to non-destructive build-up measurements, where the material is probed in its elastic regime. However, scaling between storage modulus and yield stress has been reported (Bonacci et al., 2022). Furthermore, both properties are strongly related to the colloidal network

formed by the cement particles in suspension (Roussel et al., 2012). Thus, given factors can be expected to influence both properties in analogous ways. However, conclusions made on workability of pastes based on storage modulus measurements are to be confirmed by destructive build-up measurements.

In the present work, we use SAOS rheometer measurements to investigate the early-age structuration at rest of LC3 at different w/b ratios. To challenge the hypothesis of water absorption by clay particles, one sample is prepared with metakaolin presaturated in water. It appears that presaturating the metakaolin does not result in drastic changes of workability as compared to a change in initial w/b ratio.

2. Materials and Methods

2.1 Materials

The LC3 pastes are composed of 53.25% of OPC (CEM I 52.5R - Holcim Normo 5R), 1.6% gypsum (ACROS Organics Calcium sulfate dihydrate ($\text{CaSO}_4 \cdot 2\text{H}_2\text{O}$ 98+% purity), 30% metakaolin (BURGESS OPTIPOZZ from Burgess pigment company) and 15% calcium carbonate (Sigma-Aldrich Calcium Carbonate ACS reagent Chelometric standard 99.95-100.05% dry basis).

The different pastes are prepared with a total mass of 15g of dry powder. All mixes are prepared with distilled water. The w/b ratios investigated are 0.7, 0.85, 1.0 and 1.1.

2.2 Methods

The mixer used is an IKA Eurostar EURO-ST P CV mixer with a 4-bladed propeller stirrer. The dry powder is first added to a fraction of the total mixing water corresponding to the lowest w/b ratio (0.7 for LC3 systems) and mixed for 1 minute at 500 RPM. The remaining mixing water needed to reach the targeted w/b ratio is then added and the paste is mixed for another 2 minutes at 500 RPM. This is done to reduce self-mixing energy effects, as done in (Mantellato et al., 2019).

The LC3 sample containing presaturated metakaolin is prepared by first immersing the target amount of metakaolin in water in a sealed container for 24 hours. Afterwards, the rest of powders is added to this paste and mixed for 3 minutes at 500 RPM.

The heat released by the hydration is monitored with a TAM AIR isothermal calorimeter at 23°C. The calorimeter measurement is started directly after the mixing.

Rotational rheometry measurements are performed with an Anton Paar MCR 501 rheometer in parallel plate geometry using serrated plates. Drying of the sample over the measurement period is hindered by using a plastic hood. The gap between the upper and lower plates is 1 mm and their diameters are 25 mm and 50 mm respectively. The measurement is strain controlled. The test starts right after sample insertion in the calorimeter and is divided in three phases. First, a large amplitude oscillatory shear at an amplitude of 10% is performed over 30 seconds, followed by a rest period (stress controlled, $\tau=0$) of 30 seconds. Finally, a small amplitude oscillatory shear measurement is performed at a frequency of 1Hz and an amplitude of 0.0003% over 4 hours, whereby the storage modulus G' of the system is recorded.

3. Results and discussion

Figure 1 shows the temporal evolution of rheometer and calorimeter measurements for the LC3 system at the different w/b ratios investigated. The purple curve corresponds to the presaturated metakaolin sample. From the rheometer curves (figure 1 left), a sorting of storage modulus with w/b ratio appears, showing that a lower initial w/b ratio results in a higher and faster storage modulus evolution. The presaturated metakaolin sample shows a similar but slower evolution than its LC3 counterpart. This contrasts with the

hypothesis of slow water absorption by clay particles causing rheological changes than can be understood as resulting from a reduced w/b ratio. Indeed, in this case the metakaolin of the presaturated sample was immersed for 24h in water before mixing the paste. If it were to absorb water and reduce the w/b ratio, the purple curve in figure 1 would be expected to be above the curve for w/c 0.7, given that lower w/b curves have faster storage modulus evolutions.

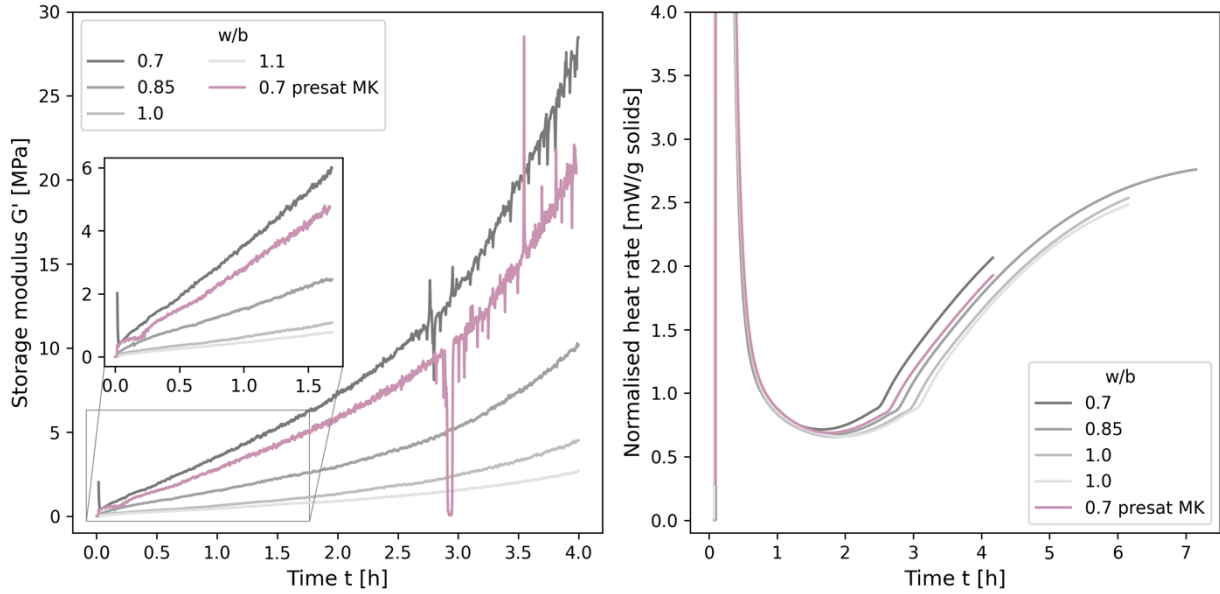


Figure 1: Time evolutions of storage modulus and heat rate for the LC3 systems.

The discrepancies between the presaturated sample and the LC3 at w/c 0.7 are likely to arise from different kinetics taking place in both systems. This can be observed in the plot on the right in figure 1, where the calorimetry curves of the different systems investigated are shown. The purple curve appears shifted in time with respect to the LC3 w/c 0.7 curve. This likely arises from the different mixing protocols used in both systems resulting in different mixing energies input in the systems, which cannot be avoided.

The clay particles may have a high or low water affinity to explain the same results in our experiments. In any case, their behavior does not result in effective w/b reductions having a sensible impact on the storage modulus evolution of LC3 systems. We infer, but this still remains to be demonstrated, that the same ought to hold for their workability, whereby in that case we would focus on irreversible structural build-up only. Our results nevertheless suggest that workability issues observed in LC3 systems are more likely linked to the fineness of calcined clays, as well as the strong interactions existing between clay particles in suspension, rather than by an effective reduction in w/c ratio due to water absorption by clay particles.

5. Conclusion

This work investigated the early-age structural build-up at rest of LC3 systems. Rheometer measurements were performed at different w/b ratios. It appeared that lower w/b ratios result in faster evolutions of storage modulus. One sample was prepared with metakaolin presaturated in water for 24h to assess whether water absorption by the clay particles has an influence on the storage modulus evolution. If the clay particles were to effectively reduce the w/b ratio, the evolution of the presaturated system would be faster than its non-presaturated counterpart. However, the evolution observed is slower than in the non-presaturated sample, allowing to exclude an effective reduction of w/b ratio from water absorption by the clay particles. The discrepancies between the curves are proposed to be arising from different kinetics taking place in the two systems, due to different mixing protocols. While these results may be expected to

apply also to irreversible structural build-up and workability loss, further work is needed to examine this question.

Acknowledgements

The authors would like to acknowledge support by the Swiss National Science Foundation under grant 200021_200343. The authors thank Dr. Lex Reiter and Dr. Arnesh Das for their support and useful discussions, especially in the method development.

References

- Bonacci, F., Chateau, X., Furst, E.M., Goyon, J., Lemaître, A., 2022. Yield Stress Aging in Attractive Colloidal Suspensions. *Phys. Rev. Lett.* 128, 018003. <https://doi.org/10.1103/PhysRevLett.128.018003>
- Favier, A., Zunino, F., Katrantzis, I., Scrivener, K., 2018. The Effect of Limestone on the Performance of Ternary Blended Cement LC3: Limestone, Calcined Clays and Cement, in: Martirena, F., Favier, A., Scrivener, K. (Eds.), *Calcined Clays for Sustainable Concrete*, RILEM Bookseries. Springer Netherlands, Dordrecht, pp. 170–175. https://doi.org/10.1007/978-94-024-1207-9_27
- Hay, R., Celik, K., 2022. Effects of Water-to-Binder Ratios (W/B) and Superplasticizer on Physicochemical, Microstructural, and Mechanical Evolution of Limestone Calcined Clay Cement (LC3). *SSRN Electron. J.* <https://doi.org/10.2139/ssrn.4024186>
- Hou, P., Muzenda, T.R., Li, Q., Chen, H., Kawashima, S., Sui, T., Yong, H., Xie, N., Cheng, X., 2021. Mechanisms dominating thixotropy in limestone calcined clay cement (LC3). *Cem. Concr. Res.* 140, 106316. <https://doi.org/10.1016/j.cemconres.2020.106316>
- Mantellato, S., Palacios, M., Flatt, R.J., 2019. Relating early hydration, specific surface and flow loss of cement pastes. *Mater. Struct.* 52, 5. <https://doi.org/10.1617/s11527-018-1304-y>
- Nair, N., Mohammed Haneefa, K., Santhanam, M., Gettu, R., 2020. A study on fresh properties of limestone calcined clay blended cementitious systems. *Constr. Build. Mater.* 254, 119326. <https://doi.org/10.1016/j.conbuildmat.2020.119326>
- Roussel, N., Ovarlez, G., Garraut, S., Brumaud, C., 2012. The origins of thixotropy of fresh cement pastes. *Cem. Concr. Res.* 42, 148–157. <https://doi.org/10.1016/j.cemconres.2011.09.004>
- Schultz, M.A., Struble, L.J., 1993. Use of oscillatory shear to study flow behavior of fresh cement paste. *Cem. Concr. Res.* 23, 273–282. [https://doi.org/10.1016/0008-8846\(93\)90092-N](https://doi.org/10.1016/0008-8846(93)90092-N)
- Yuan, Q., Lu, X., Khayat, K.H., Feys, D., Shi, C., 2017a. Small amplitude oscillatory shear technique to evaluate structural build-up of cement paste. *Mater. Struct.* 50, 112. <https://doi.org/10.1617/s11527-016-0978-2>
- Yuan, Q., Zhou, D., Khayat, K.H., Feys, D., Shi, C., 2017b. On the measurement of evolution of structural build-up of cement paste with time by static yield stress test vs. small amplitude oscillatory shear test. *Cem. Concr. Res.* 99, 183–189. <https://doi.org/10.1016/j.cemconres.2017.05.014>

Impact of C-S-H Seeds on Cementitious Hydration Kinetics, Pore Structure, and Early Age Strength

F. Qadri and N. Garg *

Department of Civil and Environmental Engineering, University of Illinois Urbana-Champaign, Urbana, United States

Email: fqadri2@illinois.edu, nishantg@illinois.edu

ABSTRACT

Some ordinary accelerators can have negative consequences on concrete properties. For instance, calcium chloride can cause steel corrosion for concrete reinforcement. C-S-H-based seeds have emerged as a new technology for accelerating concrete hydration and obtaining high early strength. However, there have been limited studies on the impact of C-S-H seeds on the pore-structure refinement and durability of cementitious systems. In this study, we investigate the role of C-S-H seeds in refining the microstructure of hydrated cement paste. Ordinary Portland cement pastes mixed with 8 different contents (0% to 3.5%) of the C-S-H seeds are evaluated. The increasing of seeds dosage from 0% to 3.5% affected the cement hydration, open porosity, and compressive strength of the cement paste. Specifically, after 3 days of curing, the dosage of 3.5% C-S-H seeds reduced the time corresponding to the main peak of the heat flow measured through isothermal calorimetry from 7.12 to 5.54 hours. Additionally, the open porosity decreased from 15.5% to 10.9%, indicating pore structure refinement. Finally, the compressive strength increased from 20.7 MPa to 31.3 MPa when doped at 3%. In summary, C-S-H seeds are able to improve early strength via accelerated hydration and refine the microstructure, thus enhancing early age durability.

KEYWORDS: *C-S-H seeds, accelerator, cement, cement hydration*

1. Introduction

Accelerating setting time and strength development without compromising durability aspects such as permeability is required in cases such as casting in cold weather (Liu et al. (2017)), increasing the production rate of precast concrete plants (Dorn, Hirsch, & Stephan (2022)), or concrete pavement patching (Qadri & Jones (2020)). Accelerators of the rapid set, rapid hardening, or both are used to enhance cement hydration and to obtain high strength at an early age (Shanahan, Sedaghat, & Zayed (2016)).

Chloride and non-chloride-based accelerators are available on the market. However, these accelerators are limited to certain applications. For example, calcium chloride is used to increase strength development at an early age, but it promotes corrosion in concrete reinforcement (Galan & Glasser (2015)). A nanoparticles C-S-H seeds-based accelerator is an alternative to ordinary accelerators. These C-S-H seeds provide nucleation sites that promote the growth of cement hydration products on their surfaces instead of growing on cement surfaces (Alizadeh, Raki, Makar, Beaudoin, & Moudrakovski (2009)). Several studies have found that the seeding effect is effective in accelerating hydration kinetics and improving early strength development. In this study, the effect of C-S-H seeds on microstructure refinement was studied, as there were limited studies focused on this aspect of C-S-H seeds. Several cement paste mixtures were evaluated using isothermal calorimetry, helium pycnometry to measure porosity, and compressive strength.

2. Materials and Methods

2.1 Sample Preparation

In this study, Type I cement and C-S-H seeds commercially available from X-seed 44, BASF as an accelerator admixture were used. Cement paste specimens mixed with a w/c ratio = 0.4 and the required dosage of C-S-H seeds were prepared. Eight specimens were prepared for each experiment with 0% to 3.5% C-S-H seeds dosages.

2.2 Methods

2.2.1 Isothermal Calorimetry

TAM Air Isothermal Calorimeter manufactured by TA instruments was used to measure heat flow and degree of hydration for a series of 8 cement paste specimens for 72 hours.

2.2.2 Helium Pycnometry

Open porosity was measured using AccuPyc 1330 Pycnometer. Eight cement paste specimens of size 10 mm × 10 mm × 40 mm (0.39" × 0.39" × 1.57") mold (cuvette) were molded and sealed-cured for 1 day. Then, the specimens were kept in water for curing until the day of testing. While the specimens were in the wet state, weight was taken before taking the volume using the helium pycnometer, and this supplied the bulk density. Then, the specimens were moved to an oven heated to 105 °C (221 °F) for 24 hours for drying (Krus, Hansen, & Künzel (1997)). Finally, the weight and volume were measured following the previous procedures, allowing for true density measurement. Equation (1) below was used to obtain open porosity volume using the bulk and true densities.

$$\eta = (1 - \rho_{\text{bulk}}/\rho_{\text{true}}) * 100\% \quad (1)$$

2.2.3 Compressive Strength

The compressive strength for cubic mortars was measured using Forney machine. Four mortar mixtures with 0, 1, 2, and 3% dosages of C-S-H seeds were cast and kept in the wet-curing room for 3 days. For each mixture, 3 cubes of size 50.8 mm × 50.8 mm × 50.8 mm (2" × 2" × 2") were cast following ASTM C109. Each mixture was prepared by mixing 250 grams of cement with 6887.5 grams of sand and water at a w/c ratio = 0.4, in addition to the required dosage of C-S-H seeds. The sand was obtained by sieving natural sand under sieve #8 (2.36 mm opening size).

On the day of testing, each cube was wiped with a dry cloth, then placed between the machine's cap ends. The load was applied at a rate of 200 – 300 lb/second.

3. Results and Discussion

3.1 Isothermal Calorimetry

Figure 1 (a) shows that adding C-S-H seeds into cement paste accelerates hydration, and the acceleration effect correlates linearly with the added dosage. Moreover, Figure 1 (b) shows that the degree of hydration increased with increasing the dosage of the C-S-H seeds. For example, the time corresponding to the main peak decreased from 7.12 to 5.54 hours and the degree of hydration increased from 290 J/g to 324 J/g, while the dosage of C-S-H increased from 0% to 3.5%. These results confirmed that C-S-H seeds enhance the cement hydration in addition to the acceleration effect.

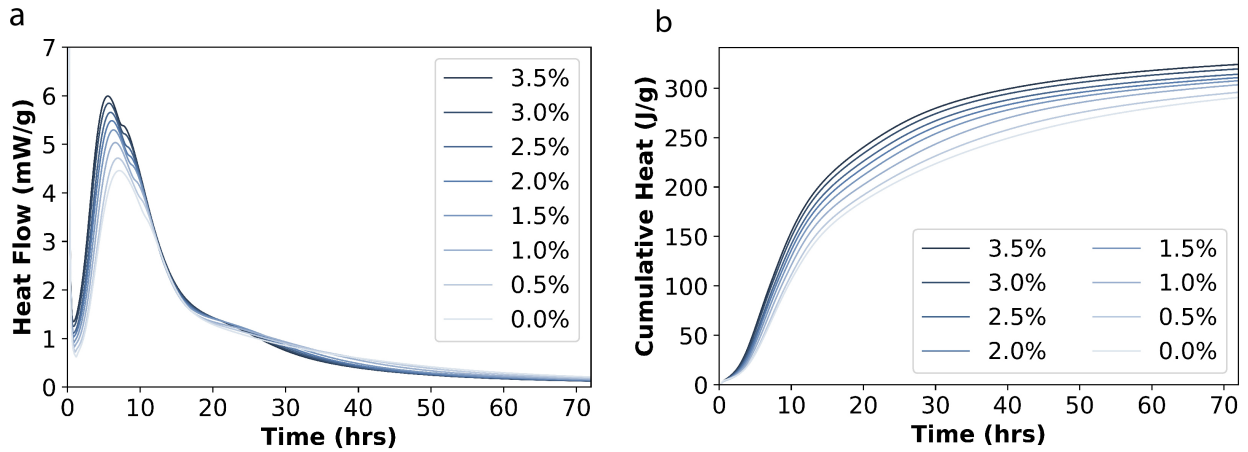


Figure 1. 8 cement paste specimens a) heat flow development, and b) cumulative heat development.

3.2 Open Porosity Measured Using Helium Pycnometry

After 3 days of hydration, porosity was measured to identify the effect of adding C-S-H seeds into cement paste. Figure 2 shows that adding these seeds reduced the open porosity, which consequently refined the microstructure. The open porosity decreased from 15.5% to 10.9%, while the dosage of C-S-H seeds increased from 0% to 3.5%. It was observed that the reduction in porosity was steep until the dosage of 1.5% (by cement weight), then the slope became less steep. This behavior indicates that a 1.5% dosage might be optimal in terms of cost and performance.

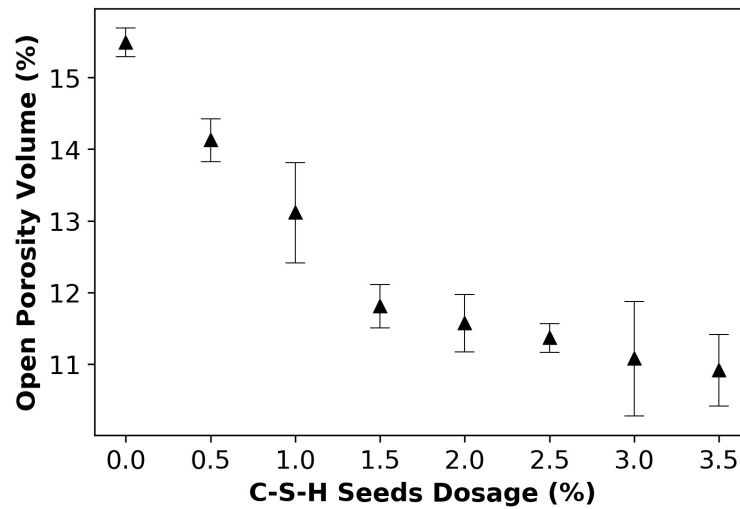


Figure 2. Open porosity as a function of % C-S-H seeds dosage for all cement paste mixtures mixed with C-S-H seeds 0 to 3.5% by cement weight at the age of 3 days. Each measurement had 3 replicates and the error bars represent the standard deviation.

3.3 Compressive Strength and Porosity

Only 4 mixtures were chosen for this experiment to validate that adding the C-S-H seeds increase compressive strength, in addition to enhancing the hydration and refining the microstructure. Figure 3 (a) shows that as the dosage of C-S-H seeds increases, the compressive strength of the mixture also increased. For example, the strength increased from 20.7 MPa to 31.3 MPa when the dosage of C-S-H seeds was increased from 0% to 3%.

Figure 3 (b) shows the inverse relationship between compressive strength and open porosity where compressive strength increases while porosity decreases. This is an expected trend that proves the addition of C-S-H seeds does not change the ordinary behavior of cement paste.

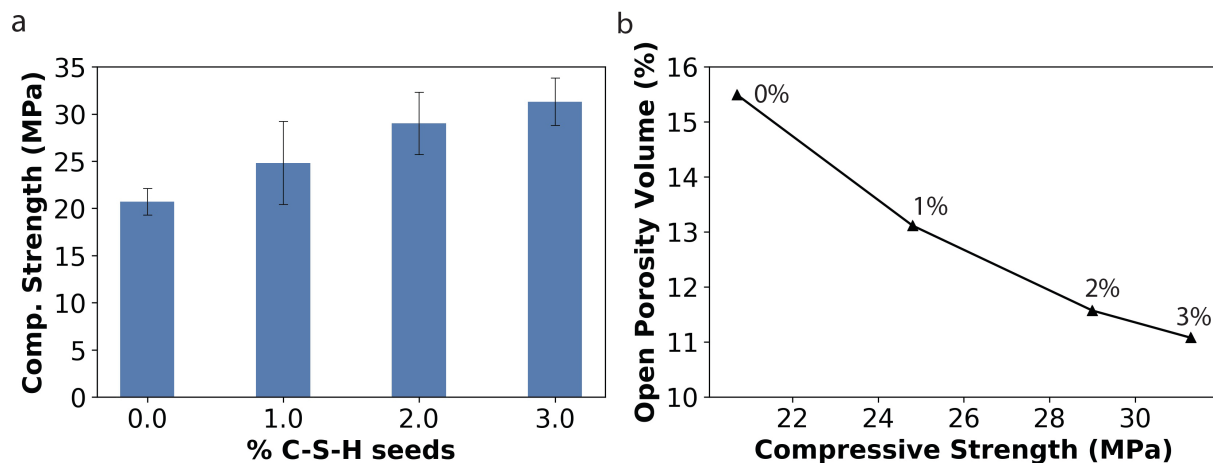


Figure 3. Data were obtained at the age of 3 days. a) shows the compressive strength of mortar mixtures mixed with C-S-H seeds (0 to 3.5% by cement weight), and b) shows the correlation between compressive strength and open porosity volume

4. Conclusions

Adding C-S-H seed into the cement paste affected the performance of the cement paste at an early age. Several conclusions can be drawn on kinetics, microstructure refinement, and strength of cement paste specimens after 3 days of curing. First, C-S-H seeds accelerated the cement paste hydration, in addition to enhancing the degree of. At dosage of 3.5% of C-S-H seeds, the time corresponding to the main peak of the heat flow decreased from 7.12 to 5.54 hours, and the degree of hydration increased by 12% due to the increase of the cumulative heat from 290 J/g to 324 J/g. Second, the open porosity decreased from 15.5% to 10.9% at the C-S-H seeds dosage of 3.5%. Third, the compressive strength increased by 51% (from 20.7 MPa to 31.3 MPa) when 3.5% of the C-S-H was used. Finally, the strong correlation between compressive strength and open porosity showed that C-S-H seeds have no negative consequences on the ordinary behavior of cement paste.

Based on these results, it was found that adding C-S-H seeds has no negative consequences on microstructure refinement. The open porosity measurements showed a slope change after 1.5% C-S-H seeds dosage, which suggests that the 1.5% dosage of C-S-H could be an optimum dosage.

Acknowledgments

This research was partly carried out in the Materials Research Laboratory Central Research Facilities. In addition, the authors acknowledge support from the Illinois Department of Transportation (IDOT).

References

- Alizadeh, R., Raki, L., Makar, J. M., Beaudoin, J. J., and Moudrakovski, I. (2009) "Hydration of tricalcium silicate in the presence of synthetic calcium-silicate-hydrate", *Journal of Materials Chemistry*, 19(42): 7937–7946
- ASTM International, West Conshohocken, P. (2021). ASTM C109 / C109M Standard Test Method for Compressive Strength of Hydraulic Cement Mortars. *ASTM International, West Conshohocken, PA*.
- Dorn, T., Hirsch, T., and Stephan, D. (2022) "Working mechanism of calcium nitrate as an accelerator for Portland cement hydration", *Journal of the American Ceramic Society*, 106(1): 752–766
- Galan, I. and Glasser, F. P. (2015) "Chloride in cement. *Advances in Cement Research*", 27(2): 63–97
- Krus, M., Hansen, K. K., and Künzel, H. M. (1997) "Porosity and liquid absorption of cement paste", *Materials and Structures*, 30(7): 394–398
- Liu, Z., Sha, A., Hu, L., Lu, Y., Jiao, W., Tong, Z., and Gao, J. (2017) "Kinetic and thermodynamic modeling of Portland cement hydration at low temperatures", *Chemical Papers*, 71(4): 741–751
- Qadri, F. and Jones, C. (2020) "Durable high early strength concrete via internal curing approach using saturated lightweight and recycled concrete aggregates", *Transportation Research Record*, 2674(7): 67–76
- Shanahan, N., Sedaghat, A., and Zayed, A. (2016) "Effect of cement mineralogy on the effectiveness of chloride-based accelerator", *Cement and Concrete Composites*, 73: 226–234

Influences of Accelerators on the Compressive Strength of Clinker-Efficient Composite Cements with Slag and Limestone

J. Herrmann^{1*} and J. Rickert²

¹ VDZ Technology gGmbH, Duesseldorf, Germany
Email: jens.herrmann@vdz-online.de

* corresponding author

² VDZ Technology gGmbH, Duesseldorf, Germany
Email: joerg.rickert@vdz-online.de

ABSTRACT

Clinker- and resource-efficient composite cements with their multiple concrete technology advantages can have an early strength that is too low for some applications. Hardening accelerators can increase the early compressive strength of Portland cement at the expense of decreased late strength.

To which extent two commercial admixtures influence the compressive strength development of ternary composite cements with granulated blast furnace slag and limestone was systematically investigated using compressive strength tests, ultrasound transmission experiments and heat flow calorimetry.

The accelerator must always be adjusted to the particular composite cement to be able to increase the early compressive strength. Cement constituents besides clinker can contribute to compensating for the reduced late strength of accelerated systems.

KEYWORDS: *Composite cement, hardening accelerating admixture, compressive strength, retardation*

1. Introduction

To achieve climate neutrality and conserve natural resources there is no alternative to the use of cements with several main constituents (so-called composite cements or blended cements) with their significantly reduced clinker content. However, with reducing the clinker content the early strength of concrete decreases, which is often considered as a disadvantage. It is generally known that admixtures which accelerate the initial hardening, i.e. hardening accelerating admixtures, can increase the early compressive strength of concrete with Portland cement, which mostly results in a decreased late compressive strength.

The aim was therefore to increase the early compressive strength of ternary cements with granulated blast furnace slag and limestone to a level comparable with Portland cement, using commercially available hardening accelerators recommended for composite cements. How the latent hydraulic reaction of blast furnace slag and synergies with limestone can counteract the decrease in late strength was also investigated.

According to John (2018), nanoparticles significantly increase the interface for heterogeneous nucleation due to their very large specific surface areas. This promotes nucleation during the hydration of Portland cement and shortens the induction period. The acceleration period therefore starts earlier and proceeds faster due to the higher number of nuclei. Pozzolan reacting nanoparticles are also nuclei at first. As a result of the pozzolan reaction, they form additional C-S-H phases and consume calcium hydroxide (John 2019) already after the first day of hydration (Land 2012). In contrast, as to John (2019) and Land (2012), the addition of synthetic crystallisation nuclei, i.e. C-S-H seeding, largely replaces the nucleation process and C-S-H phases already grow in the “pre-induction period”. Thus, the strength after the first day of Portland cement hydration is significantly higher than with nanosilica addition, and due to the lack of pozzolan reaction, post-hardening is slower from the third day (Land 2012). According to Ferrari (2019), Land (2015)

and Marazzani (2012), seeding can also accelerate the initial reaction of composite cements and can compensate for the early strength loss due to the reduced clinker content.

2. Materials and methods

A commercial Portland cement CEM I 52,5 R (“PZ”) served as reference. A CEM II/B-M (S-LL) 52,5 N (“PZ-20S-10LL”) and a CEM II/C-M (S-LL) 42,5 R (“PZ-30S-20LL”) were used as clinker-efficient composite cements. The PZ-20S-10LL was produced in the laboratory from ≈ 70 mass % PZ, ≈ 20 mass % blast furnace slag (“S”), ≈ 10 mass % limestone (“LL”) and some anhydrite dotation to optimise setting and hardening. The PZ-30S-20LL contained ≈ 50 mass % PZ, ≈ 30 mass % S, ≈ 20 mass % LL and the anhydrite dotation. Properties of the cements are given in Table 1.

Table 1. Cement properties.

| | Blaine ¹⁾ cm ² /g | $x^{(2)}$ μm | $n^{(3)}$ - | IST ⁴⁾ min | compressive strength ⁵⁾ , MPa | |
|-------------|--|-----------------|----------------|--------------------------|--|------------|
| | | | | | 2 days | 28 days |
| PZ | 4530 | 13.0 | 0.93 | 110 | 47.5 ± 0.7 | 69.4 ± 0.7 |
| PZ-20S-10LL | 4540 | 13.6 | 0.89 | 115 | 32.8 ± 0.4 | 63.7 ± 0.6 |
| PZ-30S-20LL | 4190 | 15.0 | 0.88 | 135 | 25.2 ± 0.2 | 56.1 ± 0.5 |

¹⁾ Blaine fineness acc. EN 196-6; ²⁾ position parameter and ³⁾ slope of RRSB particle size distribution; ⁴⁾ initial setting time acc. EN 196-3;

⁵⁾ compressive strength acc. EN 196-1

The cements’ clinker consisted of ≈ 75 mass % alite, ≈ 8 mass % belite, ≈ 10 mass % aluminate and ≈ 5 mass % ferrite. The glass content of S was ≈ 98 % and its fineness 3580 cm²/g acc. EN 196-6. The calcite content of LL was ≈ 89 mass %. The remains consisted mainly of quartz with some feldspars and mica. The LL fineness was 4390 cm²/g acc. EN 196-6.

Table 2 shows properties of the two commercial hardening accelerating admixtures (“BE”) used.

Table 2. Accelerator properties.

| | colour | MEC ¹⁾ | density ²⁾ g/cm ³ | content ³⁾ mass % | pH ⁴⁾ - | dosage ⁵⁾ mass % of c | max. dosage ⁶⁾ mass % of c |
|-----|------------|--------------------------|--|---------------------------------|-----------------------|-------------------------------------|--|
| BE1 | colourless | C-S-H seeds | 1.16 | 27 | 11.2 | 0.1 – 5.0 | – |
| BE4 | colourless | min. salts ⁷⁾ | 1.33 | 54 | 4.9 | 0.1 – 5.0 | 3.0 |

¹⁾ main effective component acc. product sheet; ²⁾ absol. density acc. ISO 758; ³⁾ convent. dry material content acc. EN 480-8; ⁴⁾ pH value acc.

ISO 4316; ⁵⁾ dosage range acc. product sheet; ⁶⁾ max. recommended dosage acc. product sheet; ⁷⁾ nitrates and thiocyanates; –: not stated

To classify the effect of the accelerators, the compressive strength development of accelerator-free mortar was first determined. For this purpose, mortar with 1350 g CEN standard sand, 500 g cement (c) and 175 g deionised water (w), i.e. w/c ratio = 0.35, was produced in a mortar mixer according to EN 196-1. The mortar consistency was adjusted to a spread of (150 ± 20) mm according to EN 1015-3 by adding a commercially available PCE-based superplasticiser. The water contained in the superplasticizer was deducted from the water added. The mixing regimes for mortar without and with accelerator are given in Table 3.

Table 3. Mixing regimes for mortar without and with accelerator.

| without accelerator | | | with accelerator | | |
|---------------------------|---------------------|----------|---------------------------|---------------------|----------|
| action | speed ¹⁾ | duration | action | speed ¹⁾ | duration |
| mixing of c and w | low | 60 | mixing of c and w | low | 60 |
| adding PCE and mixing | low | 30 | adding PCE and mixing | low | 30 |
| adding sand during mixing | low | 30 | adding sand during mixing | low | 30 |
| mixing | high | 60 | adding BE and mixing | high | 60 |

¹⁾ low: (140 ± 5) rpm rotation and (62 ± 5) rpm planetary movement; high: (285 ± 10) rpm rotation and (125 ± 10) rpm planetary movement

Preliminary tests showed that adding BE together with PCE or BE first and then PCE does not have a measurable effect on the early compressive strength. The dose of BE4 was 3 mass % of c (“3.0%”). BE1 was dosed at 3.0 as well as 1.0 and 0.3 mass % of c (“1.0%” and “0.3%”). Mortar compaction, storage and testing complied with EN 196-1.

The microstructure formation of cement paste (w/c = 0.35, PCE addition and mixing acc. Table 3 without sand addition) was determined using an ultrasound testing device IP8 from UltraTest. With an isothermal conduction calorimeter TAM Air from TA Instruments, the hydration kinetics of the cement paste was measured. Here, the deionised water (w/c = 0.35) was added volumetrically to the cement using the AD-MIX-AMPULLE with two syringes. One syringe contained half of the water and the other a solution of the second half of the water, the PCE and the accelerator if added. After the substances had been tempered in

the device to 20 °C, the internal stirrer was started. The water was added first and then the admixture-water-solution. The subsequent stirring time was 60 s.

3 Results

The compressive strength development of mortar with PZ, PZ-20S-10LL or PZ-30S-20LL without the addition of an accelerator (“0BE”) is shown in Figure 1.

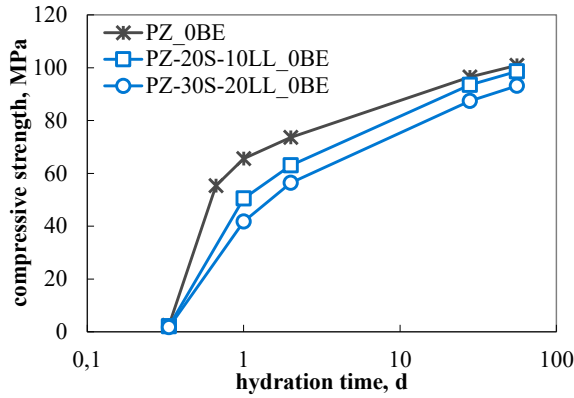


Figure 1. Compressive strength of accelerator-free mortar with Portland cement PZ or composite cement PZ-20S-10LL or PZ-30S-20LL as a function of hydration time.

As expected, the compressive strength of the accelerator-free mortars up to two days of hydration decreased with decreasing clinker content in the respective cement (Figure 1). In the further course of hydration, the compressive strengths of the mortars with clinker-efficient composite cement approached the compressive strength of the Portland cement mortar mainly due to the latent hydraulic reaction of the slag.

Figure 2 A and Figure 2 B shows the ratio of the compressive strength of mortar with PZ-20S-10LL or PZ-30S-20LL without and with up to 3 mass % accelerator BE4 or BE1 to the compressive strength of the accelerator-free PZ mortar shown in Figure 1.

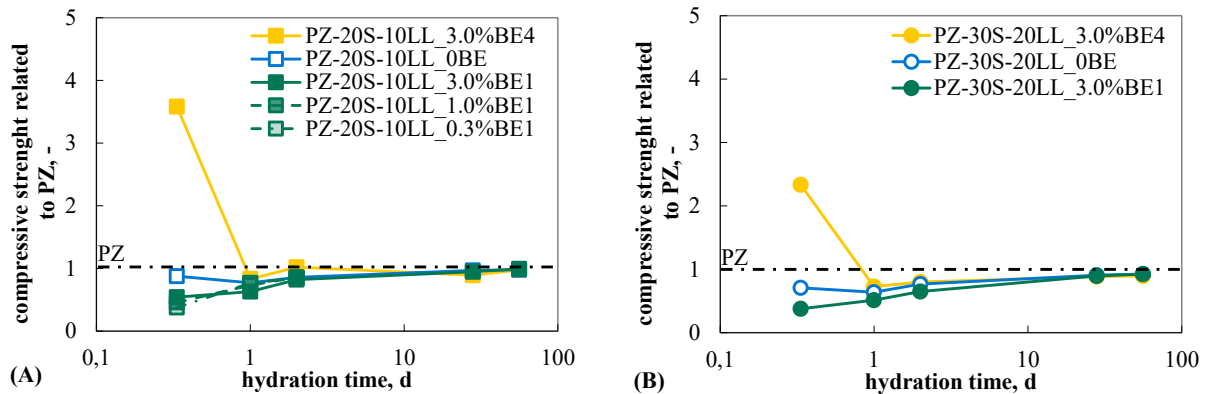


Figure 2. Ratio of the compressive strength of mortar with PZ-20S-10LL (A) or PZ-30S-20LL (B) without and with up to 3 mass % BE4 or BE1 to the compressive strength of accelerator-free PZ mortar shown in Figure 1 as a function of hydration time.

At 6 h of hydration, the early compressive strength of the mortar with PZ-20S-10LL and 3 mass % BE4 was about 3.6 times higher than that of the accelerator-free PZ mortar (Figure 2 A). With the same dose of BE4 and the decrease of the clinker content to 50 mass % in PZ-30S-20LL, the increase of the early mortar compressive strength was still about 2.3 times higher (Figure 2 B). At one day and two days of hydration, the compressive strengths of the mortars with 3 mass % BE4 tended to be lower than those of the accelerator-free PZ mortars. This confirms general knowledge on the slower post-hardening of accelerated cements. With increasing hydration time, the slower post-hardening was compensated mainly by the latent hydraulic reaction of the blast furnace slag.

Figure 2 A and Figure 2 B also show that 3 mass % BE1 could not increase the early compressive strength of the mortars with PZ-20S-10LL or PZ-30S-20LL to the early strength level of the accelerator-free PZ mortar. The early compressive strength of the mortars with 3 mass % BE1 and PZ-20S-10LL or PZ-30S-20LL was even lower than that of the respective composite cement mortar without accelerator, i.e. retardation.

In order to check if the retardation was due to an BE1 overdose, 1.0 and 0.3 mass % BE1 were added to the PZ-20S-10LL. Figure 2 A shows that the lower BE1 doses also led to the retarding effect. It has to be checked whether or not this retarding effect also occurs in combination with other clinkers.

The retarding effect of BE1 on the early reaction of e.g. PZ-20S-10LL is additionally shown by the delay in the microstructure formation (Figure 3 A) and hydration heat release (Figure 3 B).

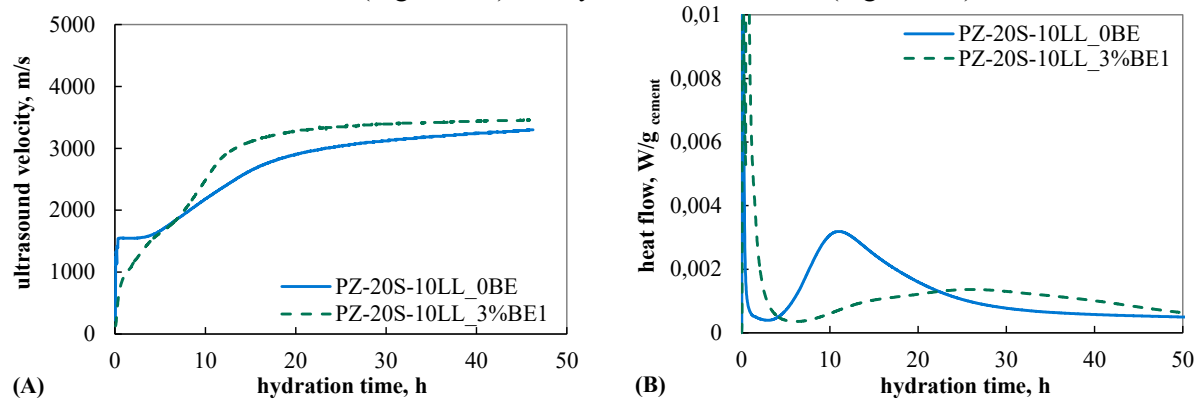


Figure 3. Ultrasound velocity (A) and heat flow (B) of cement paste with PZ-20S-10LL without and with 3 mass % BE1 as a function of hydration time.

3. Conclusions

Based on the above-mentioned results on the influences of commercially available hardening accelerators on the compressive strength of low-clinker composite cements containing blast furnace slag and limestone the following conclusions can be drawn:

- accelerators can increase the early compressive strength of composite cements with 50 mass % clinker to the level of Portland cement or beyond
- the accelerating effect decreased with decreasing clinker content in the cement
- synergetic effects from the other cement constituents besides clinker can partly compensate for the reduced late compressive strength caused by the accelerator addition
- as accelerator BE1 retarded the hydration of the composite cements, accelerators must always be adjusted to the cement and its constituents

Acknowledgements

The IGF project 21385 N of the research association VDZ Technology gGmbH is funded by the Federal Ministry of Economics and Climate Protection via the AiF in the programme for the promotion of joint industrial research (IGF) on the basis of a resolution of the German Bundestag.

References

- Ferrari, G. et al. (2018) “*New multifunctional composite inorganic/organic additive for sustainable cement compositions*” In: Research Institute of Binding Materials Prague (ed) 15th International Congress on the Chemistry of Cement (Prague 16.-20.09.2019)
- John, E., Matschei, Th. and Stephan, D. (2018) “*Nucleation seeding with calcium silicate hydrate – A review*” Cement and Concrete Research, 113: 74-85
- John, E. and Stephan, D. (2019) “*Revealing the impact of synthetic C-S-H onto cement hydration*” In: Research Institute of Binding Materials Prague (ed) 15th International Congress on the Chemistry of Cement (Prague 16.-20.09.2019)
- Land, G. and Stephan, D. (2012) “*The influence of nano-silica on the hydration of ordinary Portland cement*” Journal of Materials Science, 47(2): 1011-1017
- Land, G. and Stephan, D. (2015) “*Controlling cement hydration with nanoparticles*” Cement and Concrete Composites, 57: 64-67
- Marazzani, B., Kurz, Ch., Bürge, Chr. and Wombacher, F. (2012) “*Hardening accelerators for blended cements: New approaches to improve strength development*” In: Malhotra, V.M. (ed) Tenth international conference on superplasticizers and other chemical admixtures (Prague 28.-31.10.2012)

On the CO₂ Footprint of Polycarboxylate Superplasticizers (PCEs) and its Impact on the Eco Balance of Concrete

C. Schiefer¹, J. Chen², S. C. Wang³, and J. Plank^{4*}

¹ Technical University of Munich, Munich, Germany
E-mail: chris.schiefer@tum.de

² Technical University of Munich, Munich, Germany
E-mail: chen.jiaxin@tum.de

³ Technical University of Munich, Munich, Germany
E-mail: wsc.938445@tum-asia.edu.sg

⁴ Technical University of Munich, Munich, Germany
E-mail: johann.plank@tum.de

ABSTRACT

In this paper, the global warming potential (GWP) of structurally different MPEG PCEs (precast and slump retaining polymers) is presented based on the CO₂ emissions from their major raw materials EO, methacrylic acid and NaOH. An average value of 2310 ± 148 kg CO₂-eq/t was found based on a 100 % dry mass basis, with precast type PCEs exhibiting slightly higher GWPs than ready-mix type products. Furthermore, the CO₂ emission for a common 40 % liquid PCE admixture was determined at ~ 925 kg/t. In concrete mixes based on OPC, PCE contributes only negligibly to its GWP due to the very low dosages applied. Whereas in novel low carbon “green” binders such as LC³, the contribution of PCE becomes slightly higher, because of increased PCE dosages required there. It is concluded that overall PCE admixtures do not impair the environmental attractiveness of such low carbon binders since the GWP of a concrete mix is mainly determined by the binder.

KEYWORDS: *Global warming potential; Polycarboxylate (PCE) Superplasticizers; Concrete; CO₂ Footprint; Low Carbon Cements*

1. Introduction

Global warming represents a major challenge for modern civilization and mainly results from massive anthropogenic greenhouse gas (GHG) emissions [1], e.g. from the cement industry. Worldwide production of cement was recorded at 4.37 billion metric tons in 2021 which make up around 8 % of total global CO₂ emission which were 40.0 ± 2.9 Gt CO₂ in 2021 [2]. Consequently, the cement industry is undertaking massive steps to reduce its CO₂ footprint, e.g. by replacing clinker with supplementary cementitious materials (SCMs) including fly or rice husk ash, slag or calcined clays (such as in LC³).

At the same time, the use of concrete admixtures such as polycarboxylate based superplasticizers (PCEs) increases steadily. This causes the question about the global warming potential (GWP) of PCE superplasticizers and their share on the GWP of a concrete mix. In our study, structurally different MPEG-based PCEs (precast and ready-mix types) and a representative model concrete mix design were looked at and their GWPs were calculated for concrete mixes containing either Ordinary Portland Cement (OPC) or Limestone Calcined Clay Cement (LC³). There, contribution of the PCEs to the CO₂ emission of the concrete mixes was determined.

2. Materials and methods

2.1 Carbon footprint calculation for PCEs

The chemical structure of the investigated MPEG-type (poly-[(ω -methoxy poly(ethylene glycol) methacrylate ester)-co-methacrylic acid]) PCEs is presented in **Figure 1**. Their characteristic structural parameters, side chain strength (n) and acid-to-macromonomer ratio ($a:b$) were varied ($n = 20; 40; 60$ and $a:b = 2; 6; 10$).

The GWP of the PCEs (GWP_{PCE}) was calculated according to equation (1)

$$GWP_{PCE} = GWP_{manufacture} + \sum GWP_{educt} \cdot w_{educt} \quad (1)$$

whereby $GWP_{manufacture}$ denotes the GWP of the PCE manufacturing process (especially macromonomer synthesis), and GWP_{educt} the GWP of the particular raw material, with w_{educt} being the weight proportion of the raw material in the polymer.

For the manufacturing process, a value of 200 kg CO₂-eq/t which mainly represents the GHG emissions attributed to the energy input needed in the macromonomer production (EO polyaddition and esterification of MAA) was applied for the high temperature synthesis of MPEG PCE conducted at ~ 80 °C. For the raw materials, only the three main polymer components ethylene oxide (EO), methacrylic acid (MAA) and sodium hydroxide (NaOH) were considered since they account for most of the GWP of the PCE.

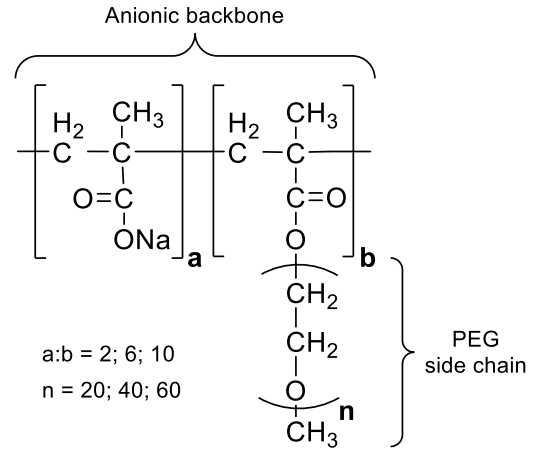


Figure 1 Structure of the MPEG PCEs looked at in this study; structural parameters: n = number of EO units and $a:b$ = ratio of

2.2 Carbon footprint calculation for model concrete

A representative model concrete mix was investigated. Its composition is shown in **Table 1**.

Table 1 Mix design of model concrete.

| Component | Portion [%, w/w] |
|--------------------|------------------|
| Cement | 15.0 |
| Sand (0 - 4 mm) | 25.0 |
| Gravel (4 - 32 mm) | 50.0 |
| PCE admixture | 0.1 |
| Water | 9.9 |
| Total | 100.0 |

The GWP of the concrete mix ($GWP_{concrete}$) was calculated according to equation (2).

$$GWP_{concrete} = \sum GWP_{component} \cdot w_{component} \quad (2)$$

Whereby $GWP_{component}$ expresses the GWP of the constituents and $w_{component}$ denotes the portion (w/w) of the respective component. The GWPs of mixing and transportation of the concrete mix were excluded from the study since both vary from production to production and generally do not significantly impact the total GWP of concrete manufactured at local plants.

2.3 Data inventory

2.3.1 PCE constituents

For the three main raw materials present in the PCE, namely EO, MAA and NaOH, values from literature were taken to account for the GWP of each chemical.

According to literature, a significant GWP of 2.0 kg CO₂-eq/kg needs to be attributed to ethylene oxide [3]. For methacrylic acid, an even higher value of 3.47 kg CO₂-eq/kg is found [4]. NaOH is needed to neutralize the initially acidic PCE solution resulting from the polymerization process and introduces a GWP of 0.633 kg CO₂-eq/kg [5].

2.3.2 Concrete constituents

The values for the GWP of the binders and aggregates shown in **Table 2** were utilized in the study.

Table 2 Literature values for the GWPs of OPC, LC³ and aggregates used in concrete.

| Binder/aggregate | Literature data | GWP [kg CO ₂ -eq/t] |
|---------------------|-------------------------------------|--------------------------------|
| OPC (42.5 R) | 0.833 kg CO ₂ -eq/kg [6] | 833 |
| LC ³ (F) | 550 kg CO ₂ -eq/t [7] | 550 |
| Gravel | 6.18 kg CO ₂ -eq/t [8] | 6.18 |
| Sand | 5.51 kg CO ₂ -eq/t [8] | 5.51 |

3. Results and discussion

3.1 Carbon footprint of PCE

Depending on its composition, the GWP of MPEG-type PCE can vary between 2108 kg CO₂-eq/t for the PCE exhibiting the longest side chain and lowest acid content ($n = 60$, $a:b = 2$) and 2573 kg CO₂-eq/t for the PCE with short side chain and high acid content ($n = 20$, $a:b = 10$). Details of the calculation of GWPs of various PCEs are disclosed in **Table 3**.

Generally, the GWP of PCEs lies at $\sim 2100 - 2600$ kg CO₂-eq/t. However, these values are valid for PCEs on a dry mass basis and do not refer to liquid admixtures which are commonly used. Furthermore, the GWPs of the PCEs significantly depend on their specific composition and structure. Accordingly, all precast type PCEs which are characterized by high acid content exhibit a slightly ($\sim 10 - 20$ %) higher GWP than slump retaining MPEG PCEs which contain higher portions of macromonomer.

Table 3 GWP of MPEG PCEs in dependence of their structural parameters n and $a:b$.

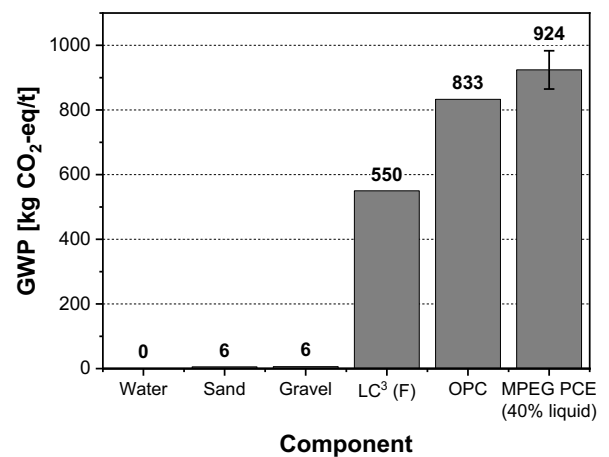
| Structural parameter | | Weight portion [kg/kg PCE] of | | | GWP of PCE [kg CO ₂ -eq/t] |
|----------------------|-------|-------------------------------|-------|-------|--|
| n | $a:b$ | EO | MAA | NaOH | |
| 20 | 2 | 735.8 | 215.7 | 66.8 | 2264 |
| 40 | 2 | 847.8 | 124.3 | 38.5 | 2153 |
| 60 | 2 | 893.1 | 87.3 | 27.0 | 2108 |
| 20 | 6 | 540.6 | 369.8 | 147.3 | 2460 |
| 40 | 6 | 701.8 | 240.0 | 95.6 | 2299 |
| 60 | 6 | 779.3 | 177.7 | 70.8 | 2222 |
| 20 | 10 | 427.3 | 459.2 | 194.1 | 2573 |
| 40 | 10 | 598.7 | 321.8 | 136.0 | 2402 |
| 60 | 10 | 691.2 | 247.6 | 104.6 | 2310 |

Based on this model, an average GWP of 2310 ± 148 kg CO₂-eq/t can be derived for MPEG PCEs. As mentioned before, in concrete not PCE powder, but a liquid SP admixture is applied. Hence, a 40 wt.% liquid MPEG PCE admixture exhibits an average GWP of ~ 925 kg CO₂-eq per metric ton.

3.2 PCE impact on carbon footprint of concrete mixes

In **Figure 2** the GWPs of individual concrete components are displayed. Interestingly, the GWP of the 40 % liquid MPEG PCE admixture lies slightly above that of OPC, hence it presents the component with the highest GWP per weight unit in a concrete mix. However, the very low dosage of PCE admixtures in concrete (~ 0.1 % by weight of concrete) needs to be taken into consideration.

In **Table 4**, the GWP of concrete mixes based on OPC and LC³ binder admixed with MPEG PCEs are displayed. Interestingly, the contribution of the SP admixture always remains below 2 % of the entire GWP, thus indicating that PCEs do not noticeable impact the environmental balance of concrete.

**Figure 2** GWP of concrete components.

It is worth noting that the contribution of PCE increases when OPC is replaced by an eco-friendlier alternative such as LC³. This increase is owed to the lower GWP contribution from the binder which in turn causes the GWP of PCE and aggregates to become more noticeable. In most cases, higher PCE dosage are required in those binders because of their higher water demand. As a consequence, the contribution of PCE to the GWP of such concrete mix is slightly higher. However, the main environmental benefit of PCEs is that they enable to significantly reduce the water demand and hence the amount of binder while still achieving high strength. As is apparent from **Table 4**, such reduction of the cement/binder content in a mix design results in a significant decrease of the CO₂ footprint of the concrete formulation which constitutes a key benefit of PCE superplasticizer technology.

Table 4 GWP of different concrete mixes admixed with MPEG PCE.

| Cement/ binder | Contribution of component to GWP | | | | | GWP of concrete | |
|---------------------|----------------------------------|--------|------|-------|----------|----------------------------|--|
| | Cement | Gravel | Sand | Water | PCE SP * | [kg CO ₂ -eq/t] | [kg CO ₂ -eq/m ³] |
| OPC | 95.9% | 2.4% | 1.1% | 0% | 0.7% | 130 | 310 |
| LC ³ (F) | 93.9% | 3.5% | 1.6% | 0% | 1.1% | 88 | 209 |

* a constant PCE dosage of 0.1 % was used in mixes; note that at comparable PCE dosage the workability of the LC³ mix is notably less than that of the OPC-based concrete.

According to **Table 4**, the GWP of the concrete mix based on OPC (310 kg CO₂-eq/m³) is reduced by 33 % to 209 kg CO₂-eq/m³ when LC³ (F) binder is used.

4. Conclusion

Our study clarifies the GWP of MPEG PCE superplasticizers and for the first time provides an in-depth analysis of materials and factors contributing to the CO₂ emissions related to PCEs in dependence of their individual structure. Accordingly, the average GWPs of common MPEG PCEs lie at 2310 ± 148 kg CO₂-eq/t and slightly vary with individual structure (with precast type PCEs being slightly higher than slump retaining PCE). This value corresponds to 924 ± 59 kg CO₂-eq/t for a 40 % liquid SP admixture which is commonly used.

A comparison between the GWPs of OPC and LC³ binder systems reveals that the impact of PCE on the overall GWP of many concrete mixes is rather insignificant, because of the low dosages applied. However, in most cases eco-friendlier low carbon binders require elevated PCE dosages. In such cases, the contribution of PCE to the total GWP of the entire mix at least should not be ignored completely, although it is still minor.

The data presented here refer to MPEG-type PCEs. They contain MAA which comes with a relatively high global warming potential. It can be expected that acrylic acid based PCEs (HPEG, IPEG types) exhibit a slightly lower carbon footprint than MPEG PCEs.

References

- [1] IPCC (2022) "Climate Change 2022: Impacts, Adaptation and Vulnerability - Contribution of Working Group II to the Sixth Assessment Report of the Intergovernmental Panel on Climate Change" [H.-O. Pörtner, D.C. Roberts, M. Tignor, E.S. Poloczanska, K. Mintenbeck, A. Alegría, M. Craig, S. Langsdorf, S. Löschke, V. Möller, A. Okem, B. Rama (eds.)], Cambridge, UK and New York, NY, USA.
- [2] Friedlingstein, P., O'Sullivan, M., Jones, M. W., Andrew, R. M., Gregor, L., Hauck, J., Le Quéré, C., Luijkx, I. T., Olsen, A., Peters, G. P. et al. (2022) "Global Carbon Budget 2022", *Earth System Science Data*, 14 (11): 4811–4900.
- [3] PlasticsEurope (2012) "Ethylene, propylene, butadiene, pyrolysis gasoline, ethylene oxide (EO), ethylene glycols (MEG, DEG, EG)", *Eco-profiles and Environmental Product Declarations of the European Plastics Manufacturers*, Belgium.
- [4] PlasticsEurope (2014) "Methyl methacrylate (MMA)", *Eco-profiles and Environmental Product Declarations of the European Plastics Manufacturers*, Belgium.
- [5] Thannimalay, L., Yusoff, S., Zin Zawawi, N. (2013) "Life Cycle Assessment of Sodium Hydroxide", *Australian Journal of Basic and Applied Sciences*, 7 (2): 421–431.
- [6] Stengel, T., Schießl, P. (2014) "Life cycle assessment (LCA) of ultra high performance concrete (UHPC) structures", in: *Eco-efficient Construction and Building Materials*, Elsevier, 528–564.

- [7] Cancio Díaz, Y., Sánchez Berriel, S., Heierli, U., Favier, A. R., Sánchez Machado, I. R., Scrivener, K. L., Martirena Hernández, J. F., Habert, G. (2017) "Limestone calcined clay cement as a low-carbon solution to meet expanding cement demand in emerging economies", *Development Engineering*, 2: 82–91.
- [8] National Stone Sand & Gravel Association (April 26, 2021) "The aggregates industry greenhouse gases: low emissions, high resiliency", Alexandria (VA), US.

A novel formulation concept for fast OPC based tile adhesives

J. Dengler^{*1}, J. Nehring, X. Li and F. Niedermair

¹ BASF Construction Additives, Trostberg, Germany
Email: joachim.dengler@basf.com

ABSTRACT

In this work, we investigated the impact of a novel hydration control additive (R+D HyCon) package on the hydration kinetics of Portland cement used for fast cementitious tile adhesives (CTA). This new hydration control additive controls the hydration kinetics of the aluminate phases in Portland cement. This allows an adjustable and fast setting with high strength increase via Ettringite formation. Further strength increase is obtained from the subsequent silicate reaction.

Due to the enhanced and adjustable smart setting profile, there is more freedom to optimize the binder mix design. This is presented here for a fast tile adhesive mortar exemplarily. This additive allows the formulation of a more efficient fast tile adhesive based on an ordinary Portland cement considering aspects such as rheology, durability, and costs without the negative impact of conventional accelerating additives.

KEYWORDS: *Hydration, dry mortars, cement reduction, admixtures, smart setting*

1. Introduction

Fast cementitious tile adhesive (CTA) mortars are used to enhance productivity on the construction site. These mortars contain ordinary Portland cement (OPC) which are accelerated using conventional accelerators (e.g. calcium formiate or C-S-H seeding) or ternary formulations containing OPC, calcium aluminate cement (CAC) and a calcium sulfate source (anhydrite or hemihydrate). These formulation concepts offer high early strength but come with some disadvantages. The high early strength profile of the accelerated Portland cement systems relates to a shortened workable time and a fast rheology increase.

Ternary systems made from OPC and CAC are rather cost-intensive due to the high cost of aluminate cements. In many countries, high aluminate cements are rarely available. For the formulation of these formulations, Lithium carbonate is to be used as an accelerator (Rodger and Double 1984). Also, durability issues like expansion or destruction due to freezing can be potentially increased (Lamberet 2005). The most abundant clinker phases of OPC are C3S, C2S, C3A, and C4AF. While C3A is reacting quite fast with calcium sulfate forming ettringite when mixed with water, the C3S reaction starts after several hours. This C3S reaction is usually responsible for setting and initial strength of the cementitious system. The initial formation of Ettringite does not result in a significant strength formation in the classic Portland cement hydration. Shifting the aluminate reaction allows to benefit from Ettringite forming strength (Jakob, Jansen et al. 2023).

2. Materials and Methods

Table 1: Mineral composition and Blaine (upper part) and CTA mortar formulation (lower part).

| | OPC 1 | OPC 2 |
|---|----------------------------------|-------------------------|
| CEM I | Phase amount [wt. %] | Phase amount [wt. %] |
| C3S Alite | 54,5 | 62,2 |
| b-C2S Belite | 13,4 | 19,0 |
| C3A total | 7,5 | 8,0 |
| C4(A,F) Ferrite | 9,0 | 1,9 |
| CaSO ₄ Anhydrite | 2,2 | 3,4 |
| CaSO ₄ * 0.5 H ₂ O | 2,8 | 1,5 |
| CaSO ₄ * 2 H ₂ O | 0,6 | 0,3 |
| CaCO ₃ Calcite | 3,1 | 1,3 |
| Minor phases | 6,9 | 2,4 |
| Specific surface Blaine [cm ² /g] | 3950 | 5177 |
| Composition [%] of CTA formulation | Raw material | |
| 40.0 | OPC | |
| 2.0 | Anhydrite (Cab 30) | |
| 6.0 | Limestone powder (0 – 180 µm) | |
| 40 / 38 | Sand (0 - 0.5 mm) | |
| 3.5 | Vinnapas 5010 N | |
| 0.35 | CE Culminal C 4053 | |
| 1.0 | R+D HyCon | |
| Mixing water: 25 % | | |

Mineral composition and Blaine fineness of the used cements are shown in Table 1, where the mineral composition of the samples is determined from XRD Rietveld analysis. Using these cements, tile adhesive mortars were formulated using the recipe in Table 2. The tile adhesive was tested according to DIN EN 1348, measuring 6 h adhesion strength.

Viscosity was determined with a Brookfield DV-II+Pro with a T-bar spindle (No. 96 – shear rate 2.5 rpm) For setting, a vicat robot was used. 300 g of weight was applied. Description open time. Open time was measured by applying the mortar with a 6x6 mm notched trowel on a non-absorbing background. Afterwards tiles (5x5 cm) were placed after 5, 10, 15, 20, 25 and 30 min and immediately after placing loaded with a 1 kg weight for 30s. The absolute content of mortar sticking to the tile determines the open time. The single weights are related to the initial content after 0 min. If less than 20% of the initial value is measured the open time is over.

The isothermal heat flow calorimetry measurements were conducted at 20°C in a TAM Air calorimeter. After external mixing of the mortars, 5 g of sample were weighed into the glass ampoule. XRD measurements were carried out using Bruker D8 Advance diffractometers. In-situ XRD experiments were carried out on freshly mixed paste (as described in the previous section) covered with a Kapton® film. Data were collected for ~24 hours continuously with ~14 min per scan. The temperature of the XRD chamber was 28 ± 2°C during the measuring process.

The formulated dry mortar products were compared with three commercially available fast tile adhesive mortars. The water amount proposed from the producer was applied.

The new hydration control additive R+D HyCon (available from BASF Construction Additives GmbH, Germany) was

used as a retarder. This hydration control additive is a formulation similar to the mix used in literature (Jakob, Jansen et al. 2023).

3. Results

Figure 1 shows the heat evolution of two mortars formulated with OPC 1. The mortar without R+ D HyCon shows the typical signal known from OPC. It consists of a strong exothermic peak directly after the mixing which is attributed to the reaction of C3A to Ettringite. After the dormant period, the heat evolution increases again after 6 h when the silicate reaction forming C-S-H starts. In presence of R+D HyCon, the initial aluminate reaction is blocked, starting after 1 h with a high exothermicity. The silicate reaction of this reaction is shifted by 12 h to later times. Such behaviour is like the reaction profile of a ternary CTA, formulated from a mix of Calcium Sulfoaluminate cement (CSA) or High Alumina Cement (HAC), a calcium

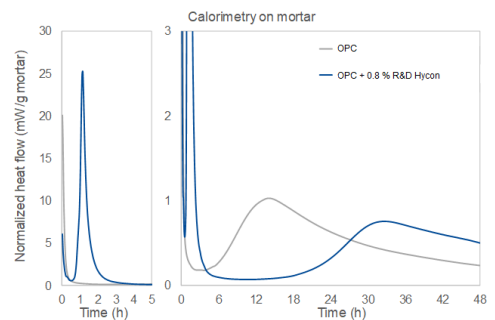


Figure 1: Calorimetry of tile adhesive mortar with and without R+D HyCon

sulfate source and OPC. The heat of hydration, which should be the determining factor for the strength of the mortar is comparable for all products at 6 h. Likely as they were designed to fit the norms requesting a 6 h pull-off strength of 0.5 MPa. The mortar containing R+D HyCon results in an even higher heat of hydration and a silicate reaction starting at similar times to the fastest commercial CTA product. Application tests and test results are summarized in Table 2. The cumulative heat at 6 h is increasing from CTA A < CTA B < CTA C < OPC1 + R+D HyCon, correlating well with the increase in pull-off strength. A higher heat increases strength.

The initial setting time fit to the start of the aluminate peak. This is due to the formation of ettringite in HAC/Gypsum formulations

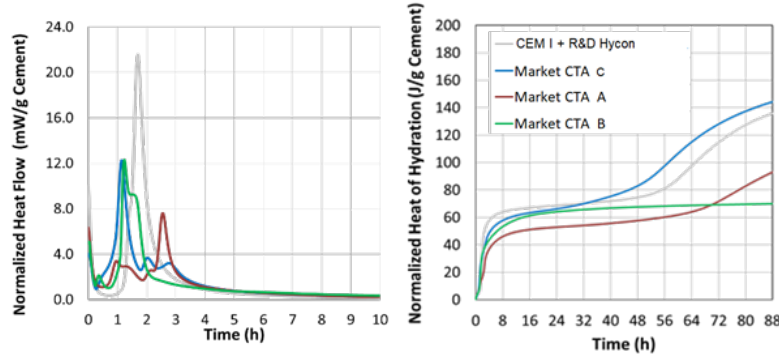


Figure 2: (a) heat flow and (b) cumulative heat of hydration of CTA formulation 1 and the comparison to ternary market products

than the heat with OPC + R+D HyCon, which is close to zero. This is well in line with the open time. Lowke describes that thixotropy and heat flow correlating as the formation of fine particles are increasing the colloidal surface interactions and result in particle bridging (Lowke 2018). Hydration and the development of rheology are part of the complex dynamic evolution of the wettability of the tile, which is called open time (Oberste-Padtberg and Sieksmeier 2007, Zurbriggen 2021). Therefore, it is reasonable that the difference in reactivity might be the influencing factor increasing the open time at standard conditions in the application. The narrow hydration peak shows therefor advantage also for the applicability, robustness and durability of the system (Greminger, Wetzel et al. 2010).

Table 2: Performance data of fast tile adhesives

| Sample | Mixing water [g/kg] | Viscosity [Pas] | Open time [min] | Initial/final setting [min] | 6h adhesion strength [MPa] |
|-------------------|------------------------|--------------------|--------------------|--------------------------------|-------------------------------|
| OPC 1 + R+D HyCon | 250 | 850 | 25 | 83/96 | 0.67 |
| OPC 2 + R+D HyCon | 250 | | | | 0.47 |
| Market CTA A | 370 | 1,600 | 10 | 59/72 | 0.47 |
| Market CTA B | 290 | 1,300 | 10 | 83/108 | 0.45 |
| Market CTA C | 300 | 900 | 25 | 71/87 | 0.43 |

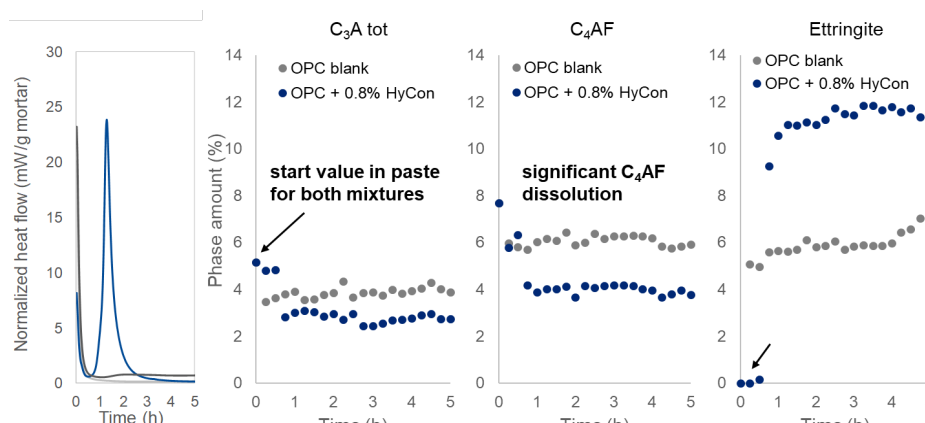


Figure 3: Aluminate phase development over time

Despite that no additional aluminate source has been added to the OPC based formulation, the heat release and strength development were comparable to the ternary CTA with CAC. Not all the C3A can be used to form ettringite in OPC even though the reactivity of C3A is

higher than that of CA. Figure 3 shows the phase development of the aluminate phases in OPC with and without R&D HyCon for the first 5 hours. At the beginning, the C3A content for the OPC blank sample drops from 6% to 4%, forming ~5% Ettringite. A small part of the C4AF reacts contributing to the amount of 6% of Ettringite. After this initial reaction, the conversion of C3A and C4AF to Ettringite stops until the Ettringite content starts to slowly increase again after 4 h. With R&D Hycon, the initial C3A and C4AF stays constant for nearly 1 h and then drops significantly. This reaction takes place at the same time when the exothermic peak in the calorimetry curve starts. The amount of dissolved C3A and C4AF is higher than those in the OPC blank sample, resulting in a higher amount of Ettringite (12 %) after 1h. The enhanced Ettringite formation is responsible for the high pull-off strength in the OPC based CTA. Another key parameter when using R+D HyCon is the available amount of calcium sulfate. Ettringite is formed by the reaction of C3A and C\$ in the classic OPC hydration routine. Using this new hydration control additive package, the turnover of the aluminate phases in OPC is increased. The sulfate added during clinker grinding is no longer sufficient to provide enough sulfate for a complete formation of ettringite. More sulfates must be added to the cement to guarantee the optimal formation of ettringite as can be seen in Figure 4. The heat of hydration without sulfate is lower, resulting in a decrease of the initial heat evolution. The consequence of the decrease in ettringite formation is a lower pull-off strength of 0.35 MPa instead of 0.56 MPa after 6 h. Also the silicate reaction is shifted to later times without the addition of aluminate, indicating an undersaturation in sulfate (Andrade Neto, De la Torre et al. 2021).

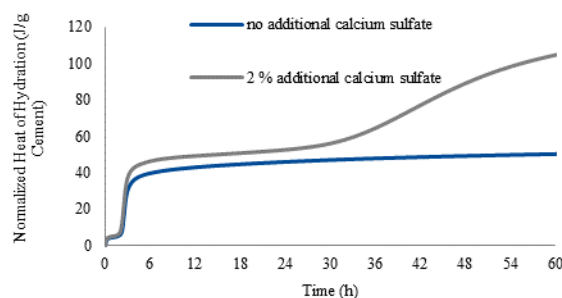


Figure 4: Calorimetry of a mortar containing OPC 1 + R&D Hycon with and without additional sulfate

3. Conclusions

In this work we have presented that C3A and C4AF present in OPC can be used instead of CA to form Ettringite at the right time when using using the right retarder. To enhance the selectivity for ettringite, extra amounts of sulfates must be added. This technology then mimics a ternary system only from OPC at comparable performance if sufficient aluminate phases are present in the OPC.

References

- Andrade Neto, J. d. S., et al. (2021). (2021) "Effects of sulfates on the hydration of Portland cement – A review", *Construction and Building Materials* **279**: 122428.
- Greminger, A., et al. (2010). (2010) "Mapping of failure structures of exterior tilings", *Poster presentation at the GDCh Bau fachtagung in Dortmund/Germany* **42**: 290-296.
- Jakob, C., et al. (2023). (2023) "Controlling ettringite precipitation and rheological behavior in ordinary Portland cement paste by hydration control agent, temperature and mixing", *Cement and Concrete Research* **166**: 107095.
- Lamberet, S. (2005). Durability of ternary binders based on Portland cement, calcium aluminate cement and calcium sulfate. Institut des matériaux, École Polytechnique Fédérale de Lausanne. PhD thesis.
- Lowke, D. (2018). (2018) "Thixotropy of SCC—A model describing the effect of particle packing and superplasticizer adsorption on thixotropic structural build-up of the mortar phase based on interparticle interactions", *Cement and Concrete Research* **104**: 94-104.
- Nehring, J., et al. (2018). (2018) "Acceleration of OPC by CAC in binary and ternary systems: The role of pore solution chemistry", *Cement and Concrete Research* **107**: 264-274.
- Oberste-Padtberg, R. and J. Sieksmeier (2007). (2007) "Factors influencing the open time of building mortars", *Drymix Mortar Yearbook 2007*: 44-49.
- Rodger, S. A. and D. D. Double (1984). (1984) "The chemistry of hydration of high alumina cement in the presence of accelerating and retarding admixtures", *Cement and Concrete Research* **14**(1): 73-82.
- Zurbruggen, R. (2021). (2021) "Extended Open Time – the need for standardization of an important characteristic of tile adhesives", *ZKG(7)*.

Hydration and Viscoelastic Properties of Tricalcium Aluminate Pastes Influenced by Soluble Sodium Salts

D. Axthammer¹, T. Lange¹, J. Dengler² and T. Gädt^{1*}

¹ Chair Chemistry of Construction Materials, School of Natural Sciences, Technical University of Munich,
Garching, Germany

* torben.gaedt@tum.de

² BASF Construction Additives GmbH, Trostberg, Germany
joachim.dengler@basf.com

ABSTRACT

The hydration of Portland cement is a complex process and interactions between ions in pore solution and reacting clinker phases play a major role. Tricalcium aluminate (C₃A) is of great importance in the early stages of hydration, as it exhibits the highest initial reactivity among the four main clinker phases. Consequently, understanding of the interactions of C₃A with the pore solution is relevant to elucidate the underlying hydration mechanism and the effect on viscoelastic properties of cement pastes.

In this study, we investigate the hydration behavior of C₃A in the presence of three sodium salts (NaCl, NaNO₃, Na₂SO₄). The heat flow of C₃A model suspensions (10 wt.% C₃A, 90 wt.% quartz, w/s 0.8) in the presence of the sodium salts was obtained by in-situ isothermal calorimetry and phase development was followed by in-situ XRD. Furthermore, we report on the structural build-up of the C₃A model suspensions in the first 3 hours of hydration, measured by small amplitude oscillatory shear tests (SAOS).

We found that the sodium salts influence the reaction of C₃A to different degrees. Addition of Na₂SO₄ results in the highest reduction of heat and the slowest consumption of C₃A. Furthermore, Na₂SO₄ decreases the initial storage modulus of the paste by three orders of magnitude. In contrast, the effect of both NaNO₃ and NaCl on the early storage modulus is much lower. After approximately 3 hours, the deviations in storage moduli of all suspensions are reduced. Using in-situ XRD, we determined the decrease in C₃A and assigned the reactivity differences to the formation of ettringite in the presence of Na₂SO₄ and the formation of AFm phases in the presence of nitrate and chloride. In summary, this study complements recently published work by other groups by demonstrating ion specific effects on C₃A hydration together with phase evolution and rheology data.

KEYWORDS: *Tricalcium aluminate, Hydration, Calorimetry, Rheometry, in-situ XRD*

1. Introduction

The hydration of tricalcium aluminate (C₃A) greatly affects the early properties of ordinary Portland cement (OPC) based system due to its instantaneous reaction after mixing with water. C₃A typically accounts for 5 to 10 wt.% in OPC. During the clinkering process, C₃A together with C₄AF facilitates the formation of tricalcium silicate by decreasing the necessary temperatures to 1450 °C (Aïtcin, 2016). Due to its high reactivity with water, C₃A can negatively influence cement properties such as setting time or workability. In the absence of calcium sulfates, the rapid precipitation of calcium-aluminate-hydrates (C-A-H) in the form of hexagonal plates (AFm) is responsible for this loss of workability known as flash set. These metastable C-A-H phases convert to the thermodynamically stable C₃AH₆ afterward (Andrade Neto et al., 2021; Black et al., 2006; Kirchheim et al., 2018). In order to avoid flash setting and extend the period of workability, calcium sulfate is interground with the cement clinker to act as a setting retarder and control the reactivity of C₃A. Calcium sulfate suppresses the initial reaction of C₃A presumably by the adsorption of sulfate on defect sites (Bullard et al., 2011; Minard et al., 2007) or calcium sulfate ion pair complexes on an Al-rich layer of partially dissolved C₃A (Geng et al., 2018; Liu et al., 2020; Myers et al., 2017). The addition of CaSO₄ results in an alternative reaction pathway that leads to the precipitation of ettringite

($C_6A_3H_{32}$). Recently, a study on the dissolution kinetics of C_3A in the presence of several ions (e.g., alkali sulfates) used digital holographic microscopy to demonstrate that alkali sulfates retard the dissolution of pure cubic C_3A (Brand et al., 2020). Additionally, Justnes and coworkers found that further soluble calcium salts (e.g., nitrate, formate, acetate, nitrite and propionate) can serve as suitable setting retarders for OPC (Justnes, 2014). The recent advances in understanding the hydration reactivity of C_3A in the presence of (inorganic) salts underline the importance of interactions of the pore solution with the C_3A surface during the early hydration period.

To further broaden the experimental evidence, this study aims to investigate the effect of three sodium salts ($NaCl$, $NaNO_3$ and Na_2SO_4) on the hydration behavior of C_3A . We focus on the influence of the salts on the heat of hydration of C_3A model suspensions and their effect on the structural build-up of the systems. All salts suppress the early reaction of C_3A . Na_2SO_4 reduces the initial heat flow most effectively, followed by $NaCl$ and $NaNO_3$. As demonstrated by in-situ XRD, the three sodium salts decelerate the dissolution of C_3A to different degrees. Additionally, Na_2SO_4 decreases the storage modulus by three orders of magnitude in the first minutes (as determined by SAOS). The comparison of heat of hydration and measured storage moduli showed significant differences due to ettringite formation compared to the formation of AFm phases. Our study suggests that sulfate ions in pore solution as well as ettringite precipitation have a significant impact on C_3A hydration.

2. Materials and Methods

All chemicals in this study were obtained from commercial sources and were used without further purification. Cubic C_3A was prepared by sintering stable green cylinders prepared from stoichiometric amounts of $CaCO_3$, Al_2O_3 , calcium aluminate cement and water (Axthammer et al., 2023). The purity of the reaction product was confirmed by XRD. All investigations were carried out on a C_3A model suspensions composed of a C_3A /quartz mixture. Therefore, 10 wt.% cubic C_3A were weighed in a plastic bottle with 90 wt.% fine quartz powder ($D_{95} = 34 \mu m$) and the anhydrous powder mix was homogenized in an overhead shaker (Heidolph REAX 20) for 4 h. This powder mixture was stored in a desiccator over silica gel until further usage. The reaction heats during the hydration of the C_3A model suspensions in the presence of sodium salts ($NaCl$, $NaNO_3$ and Na_2SO_4 ; Dosages 400, 1000 and 2000 $\mu mol/g$ C_3A ; Reference mix with MilliQ water) were measured using an eight-channel isothermal heat flow calorimeter (TAM Air, TA instruments, USA) at 20 °C. We used commercial in-situ mixing devices (Bohr-O-Mir 4000, Technisch Zeichnen Grassl, Germany). $3.0000g \pm 0.0005g$ of the C_3A /quartz mixture was weighed into the reaction vials and the aqueous sodium salt solutions were weighed into three syringes according to a w/s 0.8. After thermal equilibration overnight inside the calorimeter, the solutions were added, and the pastes were stirred for 1 min by an electrical motor. Measured data were normalized to the C_3A content. SAOS measurements at 20 °C were conducted on a rotational rheometer (MCR 302e, Anton Paar, Austria) to investigate the structural build-up during the hydration of the C_3A suspensions. We evaluated the temporal development of the storage modulus G' , as it describes the elastic response of the material to an applied periodic deformation. For the SAOS measurements, we conducted time sweeps at constant shear strains $\gamma = 10^{-4}$ and at constant frequencies $f = 0.16$ Hz. 10.00 g of the C_3A /quartz mixture were mixed with the salt solutions (w/s 0.8) by a mechanical stirrer at 600 rpm for 1 min. The pastes were filled on the serrated plate (diameter = 25 mm) and the gap was set to 1.00 mm. SAOS experiments started 2.5 min after solution addition and were performed for 3 h. Additionally, in-situ XRD measurements (using a Bruker D8 Advance diffractometer) were conducted to follow the temporal phase development. After mixing the paste analogous to the SAOS measurements, pastes were filled in the sample holder and covered with a polyimide film to avoid evaporation of the pore solution. Diffractograms were collected between 7 and 50° 2 θ and measurements started 10 min after addition of the solutions. One diffractogram was monitored every 15 min for 12 h. The phase contents were evaluated by using the Topas-Academic V7 software with utilizing the inert quartz filler as internal standard material (Coelho, 2018). Following structure files (ICSD code) were used: C_3A cubic (1841), Quartz (174), Ettringite (155395), Friedel's salt (62363), Katoite (94630).

3. Results and Discussion

The reactivity of C_3A in the presence of Na_2SO_4 , $NaCl$ and $NaNO_3$ is determined calorimetrically, and results are shown in Figure 1 (left). All salts suppressed the initial heat flow maximum, with Na_2SO_4

resulting in the highest reduction of the initial peak. Additionally, the cumulative heat after 1 hour is plotted against the salt concentration (see Figure 1, right). In all cases, an increased dosage (up to 1000 $\mu\text{mol/g}$) leads to a decreased reaction rate in the first hour. Na_2SO_4 (1000 $\mu\text{mol/g}$) significantly reduced the 1-hour heat by more than 60 %. Further, we found that heats after 1 h of hydration only marginally decrease for dosages exceeding 1000 $\mu\text{mol/g}$ C_3A for all salts.

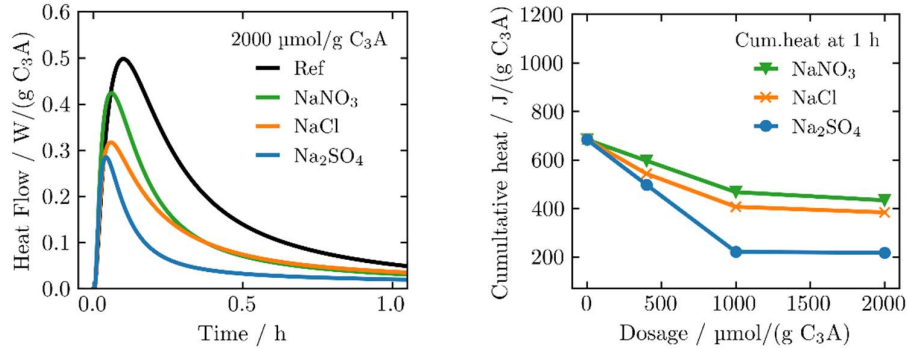


Figure 1: Left: Heat flow curves of the C_3A /quartz suspensions in the absence (black) and presence of the respective sodium salts. Right: Cumulative heat of the suspensions after 1 h at respective salt's dosages.

We conducted in-situ XRD measurements to study the temporal phase evolution during hydration. The C_3A content in the presence of the salts is obtained by Rietveld refinement (see **Error! Reference source not found.**). The first data points correspond to a hydration time of 25 min. A strong reduction of C_3A content is detected already after 25 min for all systems. Jupe and coworkers also found an extremely rapid decrease for pure C_3A in the first minutes by conducting synchrotron radiation X-ray powder diffraction (Jupe et al., 1996). The sodium salts reduced the consumption of C_3A compared to the reference, most prominently in the presence of Na_2SO_4 . Again, NaCl and NaNO_3 have less effect on the consumption of C_3A . We hypothesize that the reduced dissolution rate for NaCl and NaNO_3 is connected to the increased ion activity product in pore solution. Nicoleau and coworkers also reported the ion activity-related reduction in dissolution rate for C_3S and C_2S (Nicoleau et al., 2013). The increased reduction of C_3A consumption in the presence of Na_2SO_4 can likely be attributed to two factors: 1) the increased ion activity product and 2) blocking of

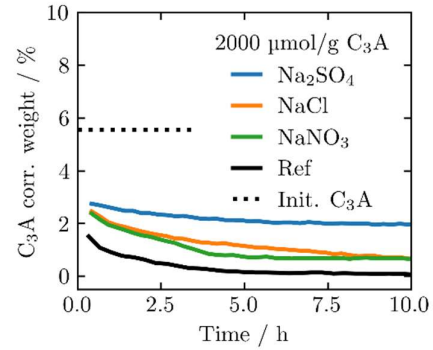


Figure 2: C_3A consumption measured by in-situ XRD in the absence (black) and presence of the sodium salts. Dotted line marks the initial C_3A content (5.6 wt.%) of all systems.

dissolution sites analogous to the retardation of C₃A hydration by CaSO₄ (Liu et al., 2020; Myers et al., 2017).

The development of the storage moduli obtained by SAOS over 3 h is displayed in **Error! Reference source not found.** (left). For the first minutes, Na₂SO₄ reduced the initial storage modulus by three orders of magnitude compared to the reference mix. The effect of NaCl and NaNO₃ is significantly smaller.

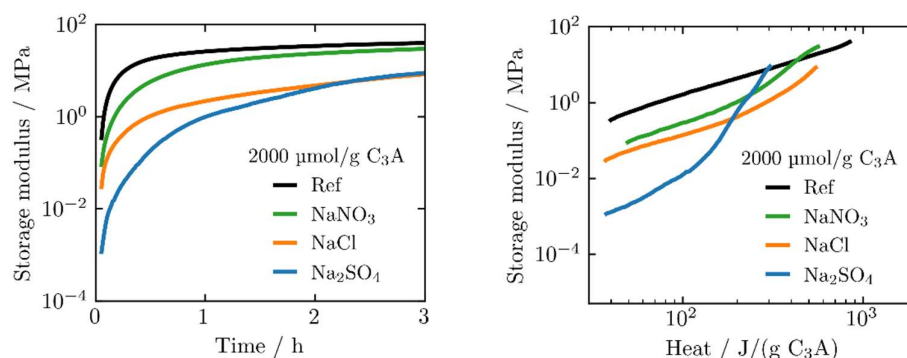


Figure 2: Left: Development of storage moduli over 3 h measured by SAOS in the absence (black) and presence of the sodium salts. Right: Comparison of heats and storage moduli for the respective C₃A/quartz suspensions.

Furthermore, the relative increase in the storage modulus over time is more distinct in the presence of Na₂SO₄ (as judged by the slope in Figure 3 (left)). We speculate that these differences in the structural development can be ascribed to the precipitation of ettringite (compared to the formation of AFm phases with chloride and nitrate). This different hydration mechanism is also evident if the storage modulus is plotted against the heat of hydration (see **Error! Reference source not found.**, (right)). Two regimes can be identified here, the early period where the structure is less dense and the second period showing a steep increase of the storage modulus. Again, this behavior appears to be a result of the precipitation of ettringite compared to AFm formation. Actually, ettringite formation was experimentally confirmed by XRD and SEM for the Na₂SO₄ system (details not shown here for brevity).

4. Conclusions

The interactions of reacting clinker phases with the pore solution are of major interest during the hydration of cement. With the present study, we demonstrated that soluble sodium salts have a significant impact on the hydration of C₃A. By combining calorimetry and in-situ XRD, we showed that Na₂SO₄ influences the hydration characteristics of C₃A most prominently, followed by NaCl and NaNO₃. The enlarged suppressing effect in the presence of Na₂SO₄ is assigned to an active blocking of dissolution sites of C₃A. SAOS measurements demonstrated that the salts also affect the structural build-up of the C₃A model suspensions to different degrees. We suggest that the different expected hydrate phases, ettringite in the case of Na₂SO₄ and AFm in the presence of NaCl and NaNO₃, may be responsible for the distinctions in structural development. Our findings contribute to a further understanding of C₃A hydration and shed light on the potential impact of precipitating hydrates on viscoelastic properties of cementitious pastes.

Acknowledgements T. G. and D. A. acknowledge financial support from BASF.

References

- Aïtcin, P.-C. (2016). 3—Portland cement. In P.-C. Aïtcin & R. J. Flatt (Eds.), *Science and Technology of Concrete Admixtures* (pp. 27–51). Woodhead Publishing.
- Andrade Neto, J. da S., De la Torre, A. G., & Kirchheim, A. P. (2021). Effects of sulfates on the hydration of Portland cement – A review. *Construction and Building Materials*, 279, 122428.
- Axthammer, D., Lange, T., Dengler, J., & Gädt, T. (2023). Kilogram Scale Synthesis of C₃A Polymorphs and Their Hydration Reactions. *CEMENT*, 100064.
- Black, L., Breen, C., Yarwood, J., Deng, C.-S., Phipps, J., & Maitland, G. (2006). Hydration of tricalcium aluminate (C₃A) in the presence and absence of gypsum—Studied by Raman spectroscopy and X-ray diffraction. *Journal of Materials Chemistry*, 16(13), 1263–1272.

- Brand, A. S., Feldman, S. B., Stutzman, P. E., Ievlev, A. V., Lorenz, M., Pagan, D. C., Nair, S., Gorham, J. M., & Bullard, J. W. (2020). Dissolution and initial hydration behavior of tricalcium aluminate in low activity sulfate solutions. *Cement and Concrete Research*, 130, 105989.
- Bullard, J. W., Jennings, H. M., Livingston, R. A., Nonat, A., Scherer, G. W., Schweitzer, J. S., Scrivener, K. L., & Thomas, J. J. (2011). Mechanisms of cement hydration. *Cement and Concrete Research*, 41(12), 1208–1223.
- Coelho, A. A. (2018). TOPAS and TOPAS-Academic: An optimization program integrating computer algebra and crystallographic objects written in C++. *Journal of Applied Crystallography*, 51(1), Article 1.
- Geng, G., Myers, R. J., Yu, Y.-S., Shapiro, D. A., Winarski, R., Levitz, P. E., Kilcoyne, D. A. L., & Monteiro, P. J. M. (2018). Synchrotron X-ray nanotomographic and spectromicroscopic study of the tricalcium aluminate hydration in the presence of gypsum. *Cement and Concrete Research*, 111, 130–137.
- Jupe, A. C., Turrillas, X., Barnes, P., Colston, S. L., Hall, C., Häusermann, D., & Hanfland, M. (1996). Fast in situ x-ray-diffraction studies of chemical reactions: A synchrotron view of the hydration of tricalcium aluminate. *Physical Review B*, 53(22), R14697–R14700.
- Justnes, H. (2014). Properties of gypsum-free Portland cement. *Journal of Sustainable Cement-Based Materials*, 3(2), 128–139.
- Kirchheim, A. P., Rodríguez, E. D., Myers, R. J., A. Gobbo, L., M. Monteiro, P. J., C. C. Dal Molin, D., De Souza, R. B., & Cincotto, M. A. (2018). Effect of Gypsum on the Early Hydration of Cubic and Na-Doped Orthorhombic Tricalcium Aluminate. *Materials*, 11(4), Article 4.
- Liu, X., Feng, P., Lyu, C., & Ye, S. (2020). The role of sulfate ions in tricalcium aluminate hydration: New insights. *Cement and Concrete Research*, 130, 105973.
- Minard, H., Garrault, S., Regnaud, L., & Nonat, A. (2007). Mechanisms and parameters controlling the tricalcium aluminate reactivity in the presence of gypsum. *Cement and Concrete Research*, 37(10), 1418–1426.
- Myers, R. J., Geng, G., Li, J., Rodríguez, E. D., Ha, J., Kidkhunthod, P., Sposito, G., Lammers, L. N., Kirchheim, A. P., & Monteiro, P. J. M. (2017). Role of Adsorption Phenomena in Cubic Tricalcium Aluminate Dissolution. *Langmuir*, 33(1), 45–55.
- Nicoleau, L., Nonat, A., & Perrey, D. (2013). The di- and tricalcium silicate dissolutions. *Cement and Concrete Research*, 47, 14–30.

Influence of pH value and temperature on the dispersion ability of PCEs containing ethyl acrylate and diethyl maleate segments and its mechanism study

Shuang Zou^{1,2}, Zhenping Sun^{1,2,3,*}, Haijing Yang^{1,2}, Weigang Zhu⁴, Qiong Luo⁴, Shu Xuejun⁵, Shu Doudou⁵

¹ Key Laboratory of Advanced Civil Engineering Materials of Ministry of Education, Tongji University, Shanghai 201804, China

² School of Materials Science and Engineering, Tongji University, Shanghai 201804, China

³ Research Center of Intelligent Evaluation and Restoration Engineering Technology of Urban Pipe Network of Shanghai Water Bureau, Shanghai 201900, China

⁴ Satellite Chemical Co., Ltd., Zhejiang Jiaxing 85000, China

⁵ Shanghai San Songguo New Materials Co., Ltd., Shanghai 201615, China

E-mail: 2111093@tongji.edu.cn, szhp@tongji.edu.cn, yanghaijings@tongji.edu.cn; zwg@weixing.com.cn; luoqiong@weixing.com.cn; 2391737928@qq.com; 453632681@qq.com

ABSTRACT

The dispersion performance of polycarboxylate superplasticizers (PCEs), especially slump retention ability, can be effectively improved by introducing monomers containing ester groups during the synthesis process. In this paper, ethyl acrylate (EA) and diethyl maleate (DEM) were applied to prepare PCEs, respectively. And the synthesized products were marked as PCE-EA and PCE-DEM accordingly. Furthermore, the influence of pH value and temperature on the dispersion performance of PCEs was investigated. And its mechanism was studied by the measurement of the adsorption amount of PCEs and hydrolysis amount of the ester groups within PCEs. The results showed that the pretreatment of PCEs at a pH value of 13.5 and a temperature of 60 °C, can effectively increase the initial dispersion ability of PCE-EA and PCE-DEM, meanwhile, the slump retention ability was decreased. Specifically, the effect was more obvious in PCE-EA. The adsorption amount measurement revealed that there was more PCE-EA adsorbed on cement particles, as more ester groups within PCE-EA was hydrolyzed after being pretreated under such high pH value and temperature condition.

KEYWORDS: *ester group, hydrolysis, adsorption amount, pretreatment, dispersion ability.*

1. Introduction

Polycarboxylate superplasticizers (PCEs) have become one of the indispensable components of modern concrete. However, PCEs are limited by poor slump retention ability (Winnefeld et al, 2007), and modifying PCEs by ester group is the most widely used method for improving it (Zhang et al, 2015). The ester group can reduce the carboxyl group density, which decreases the adsorption of PCEs. Besides, the hydrolysis of

the ester group in the alkaline condition of cement hydration can release the carboxyl group slowly and enhance the adsorbing ability of PCEs. It has been reported that the molecular structure of monomer with ester group, pH value as well as temperature affected the hydrolysis rate of the ester group (Zhang et al, 2015). Especially the amounts of ester groups in the monomer (Li et al, 2020). However, few studies focus on the interaction among these influence factors, which is crucial to improve the slump retention ability. To obtain the PCEs with suitable hydrolysis rates in different complex applications, two typical PCEs were modified by ethyl acrylate (one ester group) and diethyl maleate (two ester groups) monomers, respectively. After the pretreatment of PCEs, the slump retention ability of cement pastes mixed with the pretreated PCEs was measured.

2. Materials and methods

2.1 Materials

Portland cement 42.5R compliant with the Chinese standard GB 175–2007 was used. Analytical grade of chemicals including 3-mercaptopropionic acid (MPA), rongalite, acrylic acid (AA), ethyl acrylate (EA) and diethyl maleate (DEM) were purchased from Macklin. Besides, ethylene glycol monovinyl polyethylene glycol ether (EPEG) with M_w of 3000 were provided by Satellite Chemical, Jiaxing, China.

2.2 Preparation of PCEs

PCEs were prepared via free radical polymerization by co-polymerizing AA and EPEG with a molar ratio of 4:1, marked as PC and used as the reference sample. The preparation procedure of PCE-EA and PCE-DEM was basically the same as PC, with the difference of EA and DEM replacing 40% of AA, respectively. Then, for pretreatment, synthesized PCEs were added into the NaOH solution with a pH value of 12.5, 13 and 13.5, respectively, for 2 h. And the treatment temperatures were 25 °C and 60 °C, respectively. Then the treated solution was neutralized by dilute hydrochloric acid and then used to prepare cement pastes.

2.3 Fluidity of fresh cement pastes

The fluidity of cement pastes with a water to cement ratio (w/c) of 0.29 was determined by the mini-cone test according to the Chinese standard GB/T 8077-2012. The dosage of synthesized PCEs added to the cement pastes was 1.0‰, calculated as the ratio of the solid mass of PCEs to the mass of cement.

2.4 Adsorption amount

The adsorption amount of PCEs on cement grains was measured by total organic carbon (TOC) analyzer (TOC-VCPH, Shimadzu, Kyoto, Japan). The preparation procedure of cement paste was the same as the cement paste in the fluidity test. After mixing, cement paste was put into a centrifuge tube immediately and centrifuged for 10 min at 10000 rpm. The transparent supernatant liquid was carefully collected by using a syringe filter and diluted with deionized water to a suitable concentration for TOC test.

2.5 Hydrolysis rate analysis

The hydrolysis rate of ester groups within synthesized PCEs was measured by a simulated hydrolysis test. The PCEs polymers were subjected to alkaline treatment by adjusting the pH value of the PCEs solution (20 wt.%) to close to 13 using a NaOH solution. The PCE-EA and PCE-DEM solutions were treated at 25 °C and 60 °C, and PC solution was treated at 25 °C as control sample, then tested pH value of solutions after every 15 min. The pH value evolution of solutions was used to evaluate the hydrolysis rate of EA and DEM units.

3. Result and discussion

3.1 Dispersion performance

In Fig.1(a), the cement paste with the addition of pretreated PCE-EA at pH 13.5 exhibits the highest spread diameter in comparison to the other three cement pastes. Besides, the initial fluidity of the cement paste with alkaline pretreated PCE-EA is enhanced by increasing pretreatment temperature, especially for PCE-EA pretreated at pH value more than 13.0(Fig.1(b)). However, except pretreated at a pH 13.5, the initial dispersion ability of PCE-DEM pretreated at 60 °C is similar to that at 25 °C.

All the synthesized PCEs have similar slump retention ability, except PCE-EA pretreated at 60 °C (Fig.1(b)). The fluidity over time of cement paste with the addition of PCE-EA pretreated at 60 °C is increased with the increase of pH value. However, the fluidity increasing of cement paste with PCE-EA pretreated at pH 13.5 is little in 30 min, which means the pretreatment may lead to hydrolysis and failure of EA.

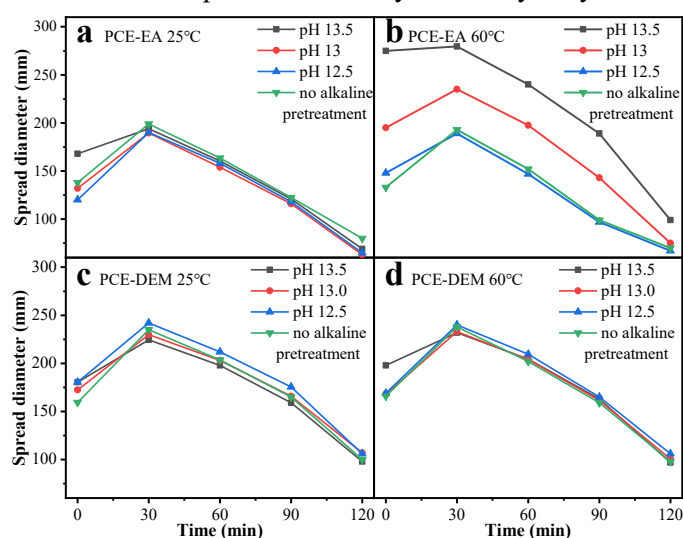


Fig. 1 Fluidity evolution of cement paste containing PCEs, the PCEs pretreated at 25°C(a. PCE-EA, c. PCE-DEM) and 60°C(b. PCE-EA, d. PCE-DEM), in PH value degree of 12.5, 13.0, 13.5 and no alkaline pretreatment

3.2 Adsorption behaviors

As shown in Fig.2, the adsorption amount of PC is not influenced by alkaline and high-temperature pretreatment, while the adsorption amount of PCE-EA and PCE-DEM increases notably after pretreatment. This result indicates that the high temperature and pH value of pretreatment increases the hydrolysis amount of the ester group, hence leading to an increased initial fluidity, as observed in Fig.1(b) and (d). Meanwhile, the adsorption amount of PCE-EA is evidently more than PCE-DEM after pretreatment of high temperature and pH value, which means more ester group of PCE-EA were hydrolyzed than that of PCE-DEM.

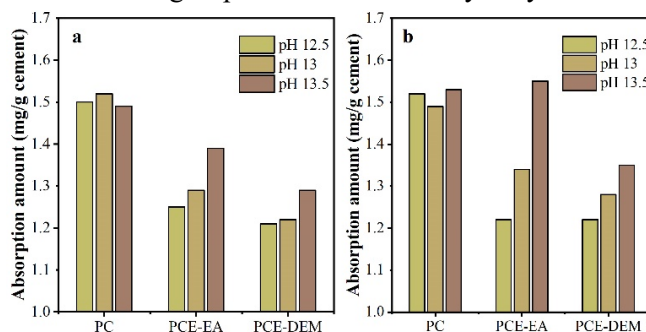


Fig. 2 Adsorption amount of synthesized PCEs after pretreatment (a)25 °C(b) 60 °C

3.3 Hydrolysis of synthesized PCEs

Fig.3(a) shows a slight decrease in pH value for the PC sample, which may be caused by CO₂ in the air dissolved in the treated solution used as the baseline. The pH value of PCE-EA solutions is lower than that of PCE-DEM solutions at the same time and decreases more obviously at 60 °C than at 25 °C. This indicates that EA pretreated at 60 °C tends to hydrolyze, resulting in a higher charge density of PCE-EA and an increase in adsorption, as shown in Fig.2. The effect of dissolved CO₂ on the pH value was eliminated by subtracting the baseline. The hydrolysis rate of the ester group in PCE-EA is higher than that in PCE-DEM, leading to a higher initial fluidity and slump retention ability loss of cement paste, as shown in Fig.1(b). The higher hydrolysis of PCE-EA can be attributed to the lower steric hindrance compared to PCE-DEM. The carboxylic acid esters form negatively charged four-sided intermediates during alkaline hydrolysis, which are more crowded in the case of PCE-DEM due to its higher ester group density, leading to greater steric hindrance and resistance to hydrolysis.

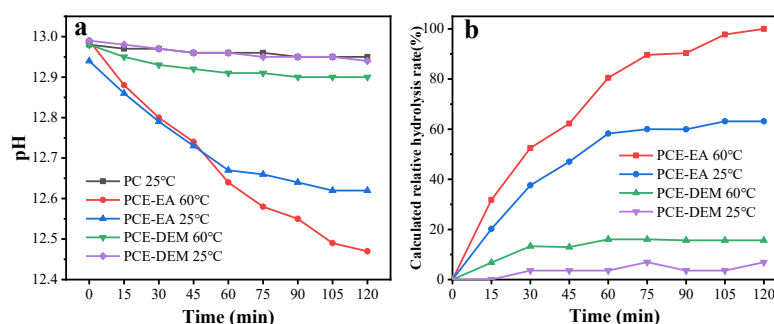


Fig. 3 The evolution of ester group within synthesized PCEs (a) pH evolution (b)hydrolysis rate evolution

4. Conclusions

The aim of this study was to identify the factors affecting the dispersion retention ability of PCEs and develop a suitable strategy for introducing monomer with ester groups into PCEs for various applications. Thus, a comparative study of PCEs with EA and DEM segments was carried out. And the following conclusions can be drawn.

With the increasing of pretreatment pH values and temperatures, the initial fluidity of cement paste with PCE-EA addition increased notably, but the slump retention ability of PCE-EA decreased. Conversely, PCE-DEM kept the slump retention ability in different pretreatment conditions.

In alkaline conditions, additional carboxyl groups were continuously produced in the PCE-EA and PCE-DEM, hence, the adsorption of the PCE-EA and PCE-DEM increased after alkaline pretreatment, especially the adsorption amount of PCE-EA.

The hydrolysis rate of ester group in EA was faster than that of DEM in the PCEs, which leading to a faster fluidity drop of fresh concrete. On the contrary, PCE-DEM was able to work at high temperatures and pH values for slump retention purposes in fresh concrete.

References

- Li, H., Yao, Y. and Wang, Z. et al. (2020) "Influence of Hydrolysis Rate of Carboxylates on Dispersion Performance of Slow-release Polycarboxylate Superplasticizer", *Journal of the Chinese Ceramic Society*, 48(02): 246-252
- Winnefeld, F., Becker, S. and Pakusch, J. et al. (2007) "Effects of the molecular architecture of comb-shaped superplasticizers on their performance in cementitious systems", *Cement and Concrete Composites*, 29(4): 251-62.
- Zhang, L., Kong, X. and Xing, F. et al. (2018) "Working mechanism of post-acting polycarboxylate superplasticizers containing acrylate segments", *Journal of Applied Polymer Science*, 135(5)

The Purer the Better: How Monomer Purity Affects the Effectiveness of Phosphate Type Superplasticizers in Cement Paste

O. Rindle¹ and T. Gädt^{2*}

¹ Technical University of Munich, Garching, Germany
Email: olivia.rindle@tum.de

² Technical University of Munich, Garching, Germany
Email: torben.gaedt@tum.de

ABSTRACT

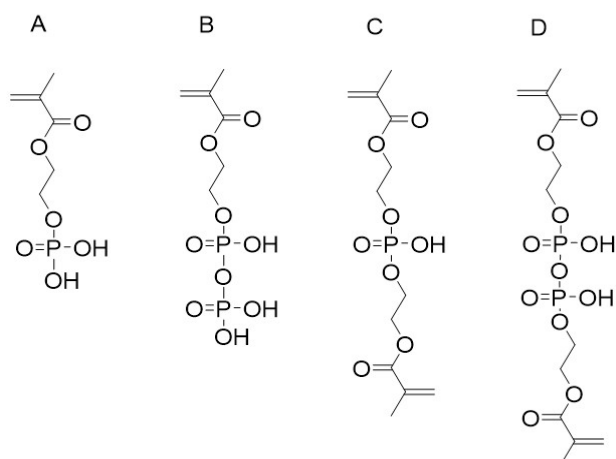
Polycarboxylate ethers (PCEs) are the most widely used superplasticizer class for concrete. Several aspects of the structure-activity relationship of PCEs have been elucidated, including scaling relationships for several properties such as adsorbed layer thickness. Phosphate type superplasticizers have received increasing attention recently. In theory, they differ from PCEs only with regard to the charged monomer. Due to their structural similarity, it should be possible to transfer the structure related properties of PCEs to phosphate type superplasticizers. This assumption rests on the availability of well-defined monomers and polymers. In this contribution, we show that a commercially available phosphate bearing monomer 2-(methacryloyl oxy) ethyl phosphate (MHP) is a mixture of different chemical species which also contains di-olefinic species. These by-products can act as crosslinker during polymerization. In this study, we synthesized a higher quality MHP compared to commercial sources. Subsequently, we copolymerized different MHP monomer qualities with polyethylene glycol (PEG) bearing methacrylic macromonomers to obtain comb copolymers. These polymers were evaluated as cement dispersants using a rotational rheometer. It is demonstrated that the presence of crosslinker strongly narrows the available structural copolymer space due to gel formation and degrades the dispersant properties.

KEYWORDS: *Superplasticizer, Phosphate Dispersant, Rheology, Cement Paste*

1. Introduction

Concrete is an important building material and its demand is increasing. By using polymeric dispersants, not only the rheology of concrete can be changed in terms of workability, but also its properties like durability or strength can be improved (Flatt *et al.* (2009), Yamada and Hanehara (2008)). These polymeric dispersants, so-called superplasticizers, consist of a backbone which comprises anionic functionalities which facilitate adsorption on the cement surface. Usually polyethylene glycol side chains are grafted onto this backbone and provide repulsive steric forces between the cement particles (Dalas *et al.* (2015), Flatt *et al.* (2019)). Together with the small negative charge due to the anionic functionality, this mode of stabilization is called “electro-steric” stabilization. It improves the dispersion of cement particles and avoids their agglomeration (Traumax *et al.* (2018)). By far the most common anionic functionality is the carboxylate group and the corresponding copolymers are known as PCEs. However, some studies have shown that the use of PCEs under certain conditions, such as high sulfate concentrations, can lead to problems that negatively affect their effectiveness (Pourchet *et al.* (2012)). Recently, phosphate groups as an alternative anionic functionality have become the subject of academic studies. The resulting copolymers differ from PCEs in terms of their higher ability to bind calcium ions or their lower sensitivity to adsorption competition with sulfate ions (Dalas *et al.* (2015)). A commonly used monomer for phosphate containing comb copolymers is MHP. This monomer is commercially available, but in contrast to the carboxylate containing monomers (such as acrylic or methacrylic acid) by-products form during synthesis. The most common by-products are shown in Figure 1 and in Table 1. The amount of these by-

Figure 1 Structure of polymerization active products of the commercially used synthesis.



products can vary due to the synthesis process. As a consequence, the composition of MHP differs depending on the supplier. Next to these by-products, phosphoric acid (PA) and pyrophosphoric acid (PyPA) are also formed. Since these acids have no double bonds, they cannot take part in the polymerization reaction to form comb copolymers.

Superplasticizers can be formed by different polymerization methods. One of the most common method is free radical polymerization. To start the polymerization, initial radicals are formed using an initiator. These radicals can attack the methacrylic C=C double bond. Subsequently, the double bond is reactive and attacks the double bond of another monomer. In this so-called propagation step, a bond between the activated double bond and the added monomer is formed.

Table 1 Polymerization active products of the commercially used synthesis.

| Compound | IUPAC Name | Abbreviation |
|----------|---|------------------------------|
| A | 2-(methacryloyl oxy) ethyl phosphate | monohema phosphate, MHP |
| B | 2-((hydroxy(phosphonooxy)phosphoryl)oxy) ethylmethacrylate | monohema pyrophosphate, MHPP |
| C | Bis[2-(methacryloyl oxy) ethyl] phosphate | dihema phosphate, DHP |
| D | 2-((hydroxy(phosphonooxy)phosphoryl)oxy) bis[ethylmethacrylate] | dihema pyrophosphate, DHPP |

Polymer chains are growing, while this propagation step is repeated. Finally, a termination reaction stops propagation and determines the ultimate chain length of the polymer. If a monomer contains more than one double bond, like DHP, both double bonds can be polymerized. This turns the monomer into a so-called crosslinker due to its ability to link two polymer chains. The consequence of crosslinking depends on the amount of crosslinker and the polymerization conditions. In general, a crosslinker leads to a higher molecular weight of the polymer and often forms a crosslinked polymer. Above a critical crosslinker density, crosslinked polymers become insoluble hydrogels and cannot be used as superplasticizers.

In this study, we investigated a synthesis route which yields MHP with less crosslinker as by-product in contrast to commercially available MHP. Polymerization of the lab based and the commercial MHP quality shows that the amount of crosslinker strongly narrows the available structural copolymer space due to gel formation. Furthermore, we report on the dispersing efficiency of the polymers made of both qualities in cement paste using a rotational rheometer.

2. Materials and methods

2.1 Materials

Quality of cement: CEM I 42.5 R, Blaine: 2995 cm²/g, d₅₀: 1.3 μm, C₃S: 48.7%, C₂S: 20.3%, C₃A_{cubic}: 4.6 %, C₃A_{orthorhombic}: 5.3 %, C₄AF: 9.0 %

Chemicals: MHP and both macromonomers were generously donated by a commercial supplier. Sodium persulfate was purchased by Thermo Fisher Scientific. The other chemicals were purchased by Merck. If necessary, any residual methacrylic acid was removed from the macromonomers by ion exchange.

Phosphate based monomer: 48.65 mL (52.05 g) HEMA were placed in a three-neck flask at 0 °C. 20.29 mL (41.79 g) polyphosphoric acid were placed in a dropping funnel and heated to 100 °C with a heat gun until they were fluid enough to be added dropwise. After the addition, the reaction mixture was stirred at 0 °C for 2 h. Subsequently, the sample was stored at 4 °C. Example copolymer synthesis: 0.84 g MHP and 2.72 mL MPEG 1005 were placed in a screw top vial. 4.5 mL water were added and the mix-

ture was preheated to 80 °C. Afterwards, 0.03 mL 3-mercaptopropionic acid and 0.01 g sodiumperoxodisulfate were added. The reaction mixture was stirred for 1.5 h at 80 °C. Subsequently, the pH value was adjusted to pH 7 with sodium hydroxide.

2.2 Methods

Monomer characterization: Quantification of the by-products was performed using ^{31}P -Nuclear magnetic resonance (NMR) spectra (Bruker 400 Mhz).

Polymer characterization: The molecular properties of the polymers were characterized by a water-based size exclusion chromatography (SEC) system.

Dispersing efficiency: The rheological properties of the polymer containing cement pastes were measured with an Anton Paar rheometer type MCR 302e using a serrated plate geometry. The mixing and measuring protocols will be published elsewhere.

3. Results and discussion

3.1 Influence of the monomer quality on the structural polymerization space

It is necessary for a superplasticizer to be soluble in water, otherwise it cannot be used to disperse cement particles. Insolubility in water can occur due to gel formation, which is caused by molecules containing two double bonds, such as DHP and DHPP. To investigate the influence of these crosslinkers on gel formation during polymerization, a synthesis route was developed that reduces the amount of DHP and DHPP. The difference in the amount of by-products was calculated using ^{31}P -NMR spectra and can be seen in Table 2.

Subsequently, both qualities were polymerized under the same polymerization conditions. As shown in Table 3, the commercially available MHP can only be polymerized using specific polymerization parameters. In contrast, no gel formation was observed using the lab based monomer quality. The influence of the crosslinker can also be seen in the SEC chromatogram (Figure 2). The higher amount of crosslinker in the commercially available MHP leads to a region of very high polymer mass and a by-modal distribution. This high polymer mass region cannot be observed by using the lab based MHP quality.

Table 2 Amount of the different compounds in the monomers quantified by ^{31}P -NMR spectroscopy.

| Monomer quality | PA | MHP | DHP | PyPA | MHPP, DHPP |
|-----------------|------|------|------|------|------------|
| Lab | 33 % | 45 % | 7 % | 6 % | 9 % |
| Commercial | 14 % | 30 % | 22 % | 11 % | 23 % |

Table 3 Influence of the monomer quality to the structural copolymer space. A successful polymerization is marked with a checkmark, gel formation is marked

| Ratio | Initiator [mol %] | CTA [mol %] | Commercial MHP | Lab MHP |
|-------|-------------------|-------------|----------------|---------|
| 3:1 | 1 | 4 | g | ✓ |
| 3:1 | 3 | 6 | ✓ | ✓ |
| 3:1 | 3 | 4 | g | ✓ |
| 3:1 | 1 | 6 | ✓ | ✓ |
| 5:1 | 1 | 4 | g | ✓ |
| 5:1 | 3 | 6 | g | ✓ |
| 5:1 | 3 | 4 | g | ✓ |
| 5:1 | 1 | 6 | g | ✓ |

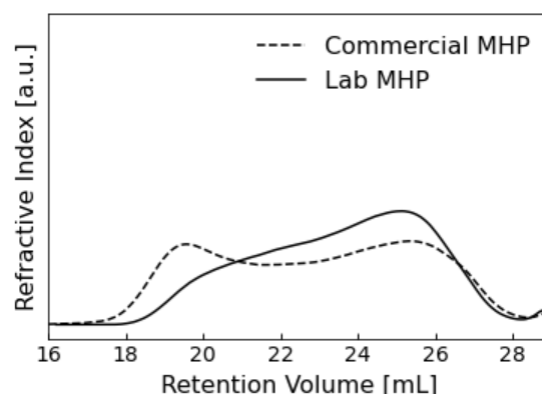


Figure 2 SEC chromatogram of polymers synthesized with commercial and lab based MHP.

3.2 Influence of the monomer quality on the dispersing efficiency

As shown above, the commercial monomer quality can lead to a partly crosslinked and thereby water-soluble polymer. Accordingly, only a reduced amount of these polymers can adsorb on the cement grain surface and work as a dispersing agent.

To examine the differences with regard to the dispersing efficiency, two polymers were synthesized with identical polymerization parameters from the different monomer qualities. Afterwards, the polymers were tested in cement paste as a model system for concrete or mortar by using a rotational rheometer. To evaluate the dispersing efficiency, the changes in yield stress and plastic viscosity compared to a reference cement paste without polymer were evaluated. The Bingham model was used to calculate the rheological parameters of the measured cement pastes. The changes of the yield stress by using the polymers compared to the yield stress of the reference are shown in Figure 3, the calculated rheological values are shown in Table 4. It can be seen, that both polymers lower the yield stress and plastic viscosity of the cement paste compared to the reference. However, the polymer with the Lab based MHP quality shows a higher influence on these rheological properties. Due to that, it has a higher dispersion effectiveness.

4. Conclusions

Phosphate based superplasticizers are an alternative to common used PCEs, but they are not as intensively studied as PCEs as of yet. As the monomer synthesis of MHP can lead to by-products which can act as crosslinkers, it is important to analyse the monomers. In this study, we developed a MHP synthesis route which led to less by-products. We analysed the purer MHP and a commercially available MHP with ^{31}P -NMR spectroscopy. Subsequently, we polymerized with these two different monomer qualities. We have shown with SEC that a higher amount of crosslinker leads to high molecular weight regions in the polymer up to gel formation, which makes the polymer unusable as a superplasticizer. This strongly narrows the polymerization space for phosphate based copolymers and thus limits the study of their mode of action. Additionally, we used cement paste as a model system to show the influence of the monomer quality on the dispersing effectiveness of the polymers. Using a rotational rheometer to analyse the rheological properties of the cement pastes, it can be seen that the purer MHP quality results in better performance of the polymers as superplasticizers. Ultra ecoefficient concrete formulations rely on further improvements in chemical admixture technology. To fully leverage the potential of phosphate based polymers, high purity monomers enable access to a broader range of comb polymer structures.

References

- Flatt, R. J., Schober, I., Raphael, E., Plassard, C. and Lesniewska, E. (2009) "Conformation of Adsorbed Comb Copolymer Dispersants", *Langmuir*, 25, 845–855
- Flatt, R. J., Marchon, D. and Boscaro, F. (2019) "First Step to the Molecular Structure Optimization of Polycarboxylate Ether Superplasticizers: Mastering Fluidity and Retardation", *Cement and Concrete Research*, 115, 116–123
- Dalas, F., Pourchet, S., Nonat, A., Rinaldi, D., Sabio, S., and Mosquet, M. (2015) "Fluidizing Efficiency of Comb-like Superplasticizers: The Effect of the Anionic Function, the Side Chain Length and the Grafting Degree", *Cement and Concrete Research*, 71, 115–123
- Pourchet, S., Liautaud, S., Rinaldi, D. and Pochard, I. (2012) "Effect of the Repartition of the PEG Side Chains on Adsorption and Dispersion of PCP in the Presence of Sulfate", *Cement and Concrete Research*, 42, 431–439
- Tramaux, A., Azema, N., David, G., Negrell, C., Poulesquen, A., Haas, J. and Remond S. (2018) "Synthesis of Phosphonate Comb-like Copolymers and Evaluation of Their Dispersion Efficiency on CaCO_3 Suspensions. Part I: Effect of an increasing Phosphonic Acid Content", *Powder Technology*, 333, 19–29
- Yamada, K. and Hanehara, S. (2008) "Rheology and early age properties of cement systems", *Cement and Concrete Research*, Vol. 38, 175–195

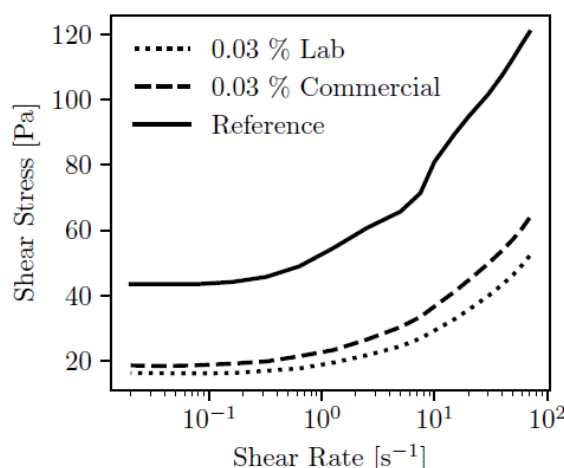


Figure 3 Measured shear stress of the cement pastes plotted against the shear rate.

Table 4 Yield stress and plastic viscosity of the measured cement pastes calculated using the Bingham model

| Cement paste | Yield stress [Pa] | Plastic viscosity [Pas] |
|----------------|-------------------|-------------------------|
| Reference | 82 | 0.64 |
| Commercial MHP | 35 | 0.45 |
| Lab MHP | 28 | 0.39 |

Paste rheology and surface charge of calcined kaolinite

Y. Demeusy*, S. Gauffinet, and C. Labbez

ICB UMR 6303 CNRS, Université de Bourgogne, FR-21000 Dijon, France

Email: yannick.demeusy@u-bourgogne.fr

ABSTRACT

Partial substitution of the clinker in the cement by a supplementary cementitious material (SCM) is one of the main solutions to reduce the carbon footprint. Calcined kaolinite is a good candidate due to its availability and relatively high reactivity compared to other SCMs. The main issue with these calcined clay types of cements is the high-water demand at low clinker factors, a problem which remains not well understood. In this proceeding, we will show the role played by electrostatic interactions in the paste stiffening using as a model system pure calcined kaolinite paste prepared at various pH as well as salt types and concentrations. The study combines dynamic rheometry measurements in strain-sweep modes, surface charge characterization using potentiometric titration and electrophoretic measurements as well as calculations of inter-particle interactions using Monte-Carlo (MC) simulations in the framework of the primitive model. The calcined kaolinite is found to possess a negative permanent charge, presumably due to the Si(IV)/Al(III) substitution, and a titratable charge (as due to ionization of silanol and aluminol surface groups) with a point of zero proton charge at pH 4.65. In conditions relevant for cement paste, the calcined clay bear a strong negative charge ~ 300 mC/m². The rheological measurements reveal that the paste stiffening is highly dependent on the pH, salt concentration and type as expected for systems controlled by electrostatic interactions. The stiffness increases with the salt concentration at natural pH and is the largest in solutions buffered with Ca(OH)₂, that is at high Ca²⁺ concentrations and pH where the negative charge of the calcined clay is the strongest. The MC simulations of the inter-particle interactions are found to qualitatively explain the observed variation in the paste stiffness.

KEYWORDS: *calcined clay, kaolinite, surface charge, rheology*

1. Introduction

The major source of CO₂ during cement manufacture is the decomposition of limestone into calcium oxide, $\text{CaCO}_3 \rightarrow \text{CaO} + \text{CO}_2$ (Flower et al 2007). This means that the emission of nearly 0.8 ton of CO₂ per ton of produced cement clinker are intrinsic to the material and cannot be reduced by the modernization of the plants, i.e., change of energy source. This can be achieved instead by substituting part of the cement clinker by supplementary cementitious materials (SCM) and, among those, one of the most promising is calcined clay (Scrivener et al (2018)). Calcined clay cements are already produced and in use in a few major European and world countries. However, above 30% of clinker substitution serious implementation problems are encountered mainly due to the high water demand of calcined clays. Numerous hypotheses have been formulated to explain this high water demand but none of them gives full satisfaction or has been clearly demonstrated. In this study we propose to investigate the link between the interfacial properties of calcined clays and in particular their surface electric charge with their rheological properties in paste. To do this we combined dynamic rheometry measurements in strain-sweep modes, surface charge characterization using potentiometric titration and electrophoretic measurements as well as calculations of inter-particle interactions using Monte-Carlo (MC) simulations. All these measurements and simulations were conducted with pure calcined kaolinite in various aqueous solutions where the pH, salt type and concentration were varied systematically.

2. Methodology

2.1 Clay and preparation

The material used in this study is a commercial kaolinite with a purity of 96% (Sigma-Aldrich 03584), calcined at 700°C for 2h and air quenched. The full dehydroxylation of the clay was controlled by TGA (not shown). The clay was cleaned by dispersing and mixing it in a solution of 10 mM HCl for 10 min. The clay sample was then vacuum filtered and rinsed with a solution of 1M NaCl. This procedure was repeated three times. Finally, the washed clay sample was purified by dialysis for 3 weeks in deionized water renewed every day. The composition of the clay as obtained by X-Ray fluorescence (XRF) is given in Table 1.

Table 1 Composition of kaolinite obtained by XRF

| Oxide | SiO ₂ | Al ₂ O ₃ | K ₂ O | Fe ₂ O ₃ | P ₂ O ₅ | TiO ₂ | PbO | BaO | MgO | CaO |
|--------------------|------------------|--------------------------------|------------------|--------------------------------|-------------------------------|------------------|-------|-------|-------|-------|
| Mass Concentration | 53.56% | 41.64% | 2.05% | 0.66% | 0.57% | 0.52% | 0.37% | 0.22% | 0.15% | 0.12% |

2.2 Rheometry

Dynamic rheometry in the strain sweep mode was used to measure the young modulus of the calcined kaolinite pastes using a parallel plate geometry. A sample consists of a disk of paste with a diameter of 25 mm and a 2 mm gap. Given these dimensions and the characteristics of the rheometer, the lowest measurable strain was 0.01% (10^{-4}). The liquid to solid ratio of the clay paste was set to $L/S = 1.33$. The rheological measurements were made with a controlled strain rheometer (ARES-G2 TA instrument) whereby the sample is submitted to a sinusoidal strain with an oscillatory frequency of $\omega = 10 \text{ rad.s}^{-1}$, and the stress response is recorded. The presented results are an average of at least 3 independent measurements.

2.3 Potentiometric titration

The titratable surface charge density was measured by potentiometric titration of 1g calcined kaolinite dispersed in 50mL aqueous solution containing NaCl as a background salt. Titration was performed using as titrant, 10 mM NaOH and 10 mM HCl solutions containing the same NaCl background salt concentration as the calcined kaolinite dispersion contained in the reactor. The titration was measured at background salt concentration of 1, 10 and 100 mM.

2.4 Electrophoretic mobility

The electrophoretic mobility was measured by dynamic light scattering using a Malvern zetasizer (nano zs) on diluted suspensions of well dispersed calcined clay particles. The latter was obtained by dispersing 2g of clay in 250mL of deionized water which was then decanted for 1h. The 3 upper centimeters were used for the zeta potential analysis.

2.5 Inter-particle forces simulations

The simulations within the so-called slit model which consists in two infinite parallel surfaces (the clay surfaces) separated with an electrolyte solution in equilibrium with a reservoir of set concentration. The model was solved with Monte-Carlo simulations in the grand canonical ensemble (Valleau et al 1980) with use of the Metropolis algorithm (Metropolis et al 1953). The calculated double layer osmotic pressure is converted to a double layer force by applying the Dejarguin approximation (Russel 1989). The total interparticle force is obtained by summing the latter and the van der Waals force. Further details on the model and simulations can be found elsewhere (Jönsson et al 2005). In the simulation an Hamaker constant equal to that of silica was used, $H = 2.4 \times 10^{-21} \text{ J}$.

3. Results & Discussion

Fig. 1-a shows the typical nonlinear oscillatory response (strain sweep measurements) of the calcined clay pastes in Ca(OH)_2 buffered solution. The clay paste has a viscoelastic behavior similar to that found with C-S-H gels. At low strain, the Young modulus (G') and the loss (viscous) modulus (G''), show a typical plateau characteristic of the linear viscoelastic region (LVR). G' is further found larger than G'' ($G' > G''$). In this region the paste thus behaves as an elastic solid where deformations are reversible, i.e., the microstructure of the paste remains unchanged. As the strain increases outside the LVR, above the critical

strain, the microstructure of the paste is changed and a drop in G' is observed but G' remains larger than G'' . In this region the paste behaves as a plastic solid where deformations are irreversible. As the strain is increased further, G'' crosses G' and becomes larger than G' . At this crossing point the paste starts to flow/yield and the yield stress can be estimated, see Fig. 2-b. The measured young modulus as a function of the strain in strain sweep mode of calcined clay pastes prepared in various electrolyte solutions are shown in Fig. 1-b in comparison to the clay paste in pure water at $\omega = 10$ rad/s. The lowest values of G' are obtained for pure water and are observed, for the same pH (pH~4.5), to increase with the ionic strength, i.e. $G'(100 \text{ mM Na}_2\text{SO}_4) < G'(1 \text{ M NaNO}_3)$. The highest G' values are observed for the paste buffered with $\text{Ca}(\text{OH})_2$, that is for high pH and calcium concentration (pH = 12.7 and $\text{Ca}^{2+} = 22 \text{ mM}$). In these conditions G' is 2 orders of magnitude higher than in pure water and 1 order of magnitude higher than in concentrated salt solution at pH ~ 4.5. These G' variations with the salt concentration and pH indicate that the electrostatic interactions play an important contribution to the change in the microstructure and bound strength between the clay particles in the paste.

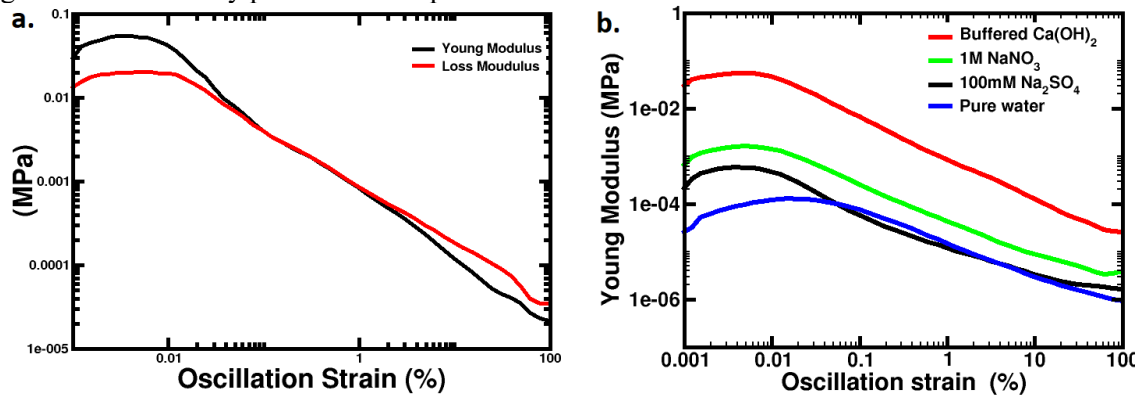


Figure 1 a- Strain-sweep measurements of the young modulus (G') and loss modulus (G'') of a calcined kaolinite paste in the presence of $\text{Ca}(\text{OH})_2$ solution. b- Young modulus versus strain of calcined kaolinite pastes in the presence of various electrolytes and in pure water with a liquid/solid ratio of 1.33. The pH of the paste in pure water, 100 mM Na_2SO_4 and 1M NaNO_3 is the same, pH ~4.5 while it is pH = 12.7 in buffered $\text{Ca}(\text{OH})_2$ conditions.

The charging behavior of the calcined clay at various pH and background salt concentration was thus studied by combining potentiometric titration and electrophoretic mobility. The potentiometric titration data shown in Fig. 2-a confirms that the calcined clay bear a pH dependent surface charge. The titratable surface charge (σ_{tit}) is further found to be amphoteric with a neutral titratable charge, the point of zero net proton consumption (PZNPC), between pH 4.5 and 5. At pH values below the PZNPC σ_{tit} is positive and negative above the PZNPC. and becomes strongly negative at high pH values, that is in the cement pore solution conditions. The PZNPC is further found to decrease with the ionic strength but the variation of the electric charge with the same remains weak. The shift of the PZNPC and the small change of σ_{tit} with the ionic strength indicate that in addition to a titratable surface charge the calcined clay particles bear a permanent structural charge (σ_{st}). The decrease of the PZNPC with the ionic strength further indicates that σ_{st} is of negative, presumably due to the substitution of silicon by aluminum. The value of isoelectric point (IEP), where the diffuse potential (zeta potential) and the total charge of the clay particles are null ($\sigma_{\text{tit}} + \sigma_{\text{st}} = 0$), obtained by electrophoretic mobility confirms the existence and sign of σ_{tit} . As shown in Fig. 2-a, the IEP is found at a pH value, pH ~ 2.8, much below that of the PZNPC. Indeed, the negative sign of the zeta potential at the pH value of the PZNPC can only be explained by $\sigma_{\text{st}} < 0$.

The interparticle forces between the clay particles were calculated, not shown. In pure water, the mean force is found to be purely repulsive and long range due to the long range electrostatic repulsion. When the ionic strength I is increased, $I(0.1 \text{ M Na}_2\text{SO}_4) < I(1 \text{ M NaNO}_3)$, the electrostatic interactions are screened and the force becomes attractive due to the short range van der Waals interactions. In buffered $\text{Ca}(\text{OH})_2$ solution (pH = 12.7 and $\text{Ca}^{2+} = 22 \text{ mM}$) the force becomes strongly attractive due to the appearance of attractive ion-ion correlation forces. The yield stress and young modulus can be correlated to, respectively, the contact mean force and curvature of the interaction-free-energy well between the particles. A rather good correlation between the measured yield stresses and simulated contact forces is obtained, see Fig. 2-

a. The same correlation is found for G' (not shown). The rheological behavior of the calcined clay pastes can thus be explained with the simple electrostatic model used. In pure water the interactions between the calcined clay particles are purely repulsive due to strong electrostatic repulsions which “lubricate” the contacts between the particles. The yield stress and G' are then the lowest. At neutral pH, when a salt is added to the solution the electrostatic repulsions are screened and a percolated network of clay particles is formed due to the prevalence of the attractive van der Waals forces over the repulsive electrostatic forces. The bounds between the particles strengthen and thus the yield stress and G' increase with increasing the ionic strength, e.g., $G'(100 \text{ mM Na}_2\text{SO}_4) < G'(1 \text{ M NaNO}_3)$. When the pH is increased the surface charge density of the calcined clay increases in absolute value. In these conditions when a calcium salt is added, strong bounds between the particles are formed due to strong attractive ion-ion correlation forces. This explains the highest values of yield stress and G' observed in the solution buffered with $\text{Ca}(\text{OH})_2$.

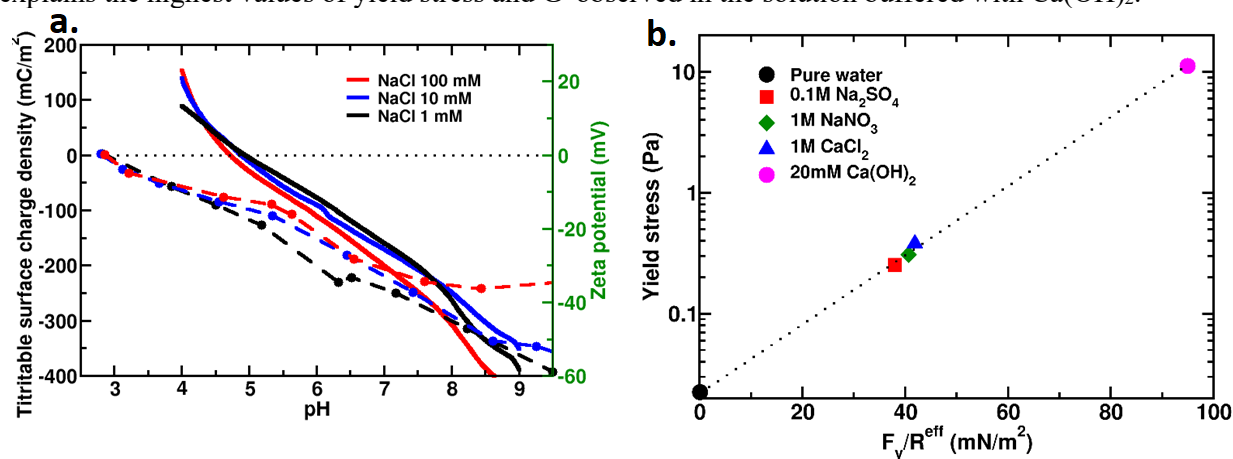


Figure 2 (a.) Titratable surface charge density and zeta potential of the calcined kaolinite in a 1/10/100mM NaCl background salt solutions as obtained by potentiometric titration and electrophoretic mobility. Plain curves: titratable surface charge density; Dashed curves: zeta potential. (b.) Measured yield stress versus simulated contact force. In the case of pure water, where the interactions are purely repulsive, the difference of the forces at separations of 1 micron and 500 nm is taken. These positions correspond to the equilibrium position of a particle surrounded by 8 neighbors and the minimal distance for the same to escape such a “cage”.

5. Conclusions

Calcined kaolinites are found to bear a titratable surface charge, which is positive at low pH and strongly negative at high pH, as well as a permanent structural surface charge of negative sign. The titratable charge comes from the ionization of silanol ($\text{Si-OH} = \text{Si-O}^- + \text{H}^+$) and aluminol ($\text{Al-OH}^{1/2+} = \text{Al-O}^{1/2-} + \text{H}^+$) surface groups. The structural charge comes presumably from the substitution of silicon by aluminum. One can expect that the latter varies with the origin of the clay mineral. The high water demand of the calcined clay paste can be rationalized by the formation of a percolated network. In particular, the increase of the yield stress and stiffness of the paste with ionic strength, pH and calcium concentration, is well captured with a simple model involving the superposition of electrostatic and van der Waals interactions between two clay particles. The yield stress and young modulus of the paste are observed to be the highest in solutions buffered with $\text{Ca}(\text{OH})_2$ where the charge of the particles and the attractive ion-ion correlation forces are found to be the strongest.

References

- Flower, D.J.M., and Sanjayan, J.G. (2007) "Green house gas emissions due to concrete manufacture." *The international Journal of life cycle assessment*, 12: 282-288
- Jönsson, B., Nonat, A., Labbez, C., Cabane, B. and Wennerström, H. (2005) Controlling the Cohesion of Cement Paste. *Langmuir*, 21: 9211–9221.
- Metropolis, N.; Rosenbluth, A. W.; Rosenbluth, M. N.; Teller, A. H.; Teller, E. (1953) “Equation of State Calculations by Fast Computing Machines”, *The Journal of Chemical Physics*, 21(6): 1087–1092.
- Russel, W.B., Saville, D.A. and Schowalter WR (1989) Colloidal dispersions. Cambridge: Cambridge University Press.
- Scrivener, K., Avet, F., Bishnoi, S., Maraghechi, H., Zunino, H., Ston, J., Hanpongpan, W. and Favier, A. (2018) “Impacting factors and properties of limestone calcined clay cements (LC3)”, *Green Materials*, 7: 3–14.

Rheological properties of belite-calcium sulfoaluminate cement

M. Mrak^{1*}, A. Brunčič², and S. Dolenec³

¹ Slovenian National Building and Civil Engineering Institute, Dimičeva ulica 12, 1000 Ljubljana, Slovenia
Jožef Stefan International Postgraduate School, Jamova cesta 39, 1000 Ljubljana, Slovenia

Email: marusa.mrak@zag.si

² Slovenian National Building and Civil Engineering Institute, Dimičeva ulica 12, 1000 Ljubljana, Slovenia
Email: ana.bruncic@zag.si

³ Slovenian National Building and Civil Engineering Institute, Dimičeva ulica 12, 1000 Ljubljana, Slovenia
Email: sabina.dolenec@zag.si

ABSTRACT

In this study, the rheological properties of fresh belite-calcium sulfoaluminate (BCSA) cement pastes were investigated. Two clinkers having different targeted phase compositions were synthesized: i) 65 wt. % C₂S, 20 wt. % C₄A₃ \bar{S} , 10 wt. % C₄AF and ii) 50 wt. % C₂S, 35 wt. % C₄A₃ \bar{S} , 10 wt. % C₄AF. Cements were prepared by adding gypsum to the cement clinker, which was based on a calcium sulfate to calcium sulfoaluminate molar ratio of 1.5. Water to cement ratio of 0.5 was used for cement pastes. Rotational as well as oscillatory tests were performed at 20 °C to assess rheological properties. Apart from the flow curve and viscosity, as well as storage and loss modulus were monitored during hydration time, and compared to data from isothermal calorimetry. Small amplitude oscillatory shear (SAOS) tests were conducted and linear viscoelastic range (LVR) was determined. The results showed changes in the development of the rheological properties of fresh cement pastes over time due to hydration processes (mainly the hydration of calcium sulfoaluminate) and development of hydration products, where also the composition of cement clinker plays an important role.

KEYWORDS: *belite-calcium sulfoaluminate cement, rheology, hydration, cement paste*

1. Introduction

Belite-calcium sulfoaluminate cements are presenting as a potential low-carbon alternative to Portland cement (Cuberos et al. 2010; Gartner and Sui 2018). During the production of belite-calcium sulfoaluminate clinkers, the CO₂ emissions can be reduced by about 30 % compared to Portland cement clinker (Gartner 2004; Juenger et al. 2011). In addition, the consumption of energy is lower and different industrial wastes can be used instead of natural raw materials. They are mainly consisting of belite (C₂S) and calcium sulfoaluminate (C₄A₃ \bar{S}) together with ferrite (C₄AF) and minor phases (Álvarez-Pinazo et al. 2016; Winnefeld and Lothenbach 2016). Depending on the amount of calcium sulfate addition these cements can exhibit expansive or non-expansive behaviour. The latter leads to high early mechanical strength and rapid setting due to the fast hydration of calcium sulfoaluminate producing ettringite (Telesca et al. 2014; García-Maté et al. 2015; Winnefeld and Barlag 2010). Despite being more widely investigated lately, relatively little is known about their early age mechanical characteristics such as rheological properties. This is thus important, to gain more knowledge on the properties of fresh cement pastes and the impact of early hydration products on the rheological behaviour of belite-calcium sulfoaluminate cement pastes. The aim of this study is therefore to investigate the rheological properties of belite-calcium sulfoaluminate cements with two different phase compositions by rotational and oscillatory tests using a rheometer.

2. Materials and methods

For the study two belite calcium sulfoaluminate cement clinkers were synthesized, CBCSA-B and CBCSA-Y. First having nominal targeted phase compositions of 65 wt.% belite (C_2S), 20 wt.% ye'elimite ($C_4A_3\bar{S}$) and 10 wt.% ferrite (C_4AF), and second of 50 wt.% belite (C_2S), 35 wt.% ye'elimite ($C_4A_3\bar{S}$) and 10 wt.% ferrite (C_4AF). The synthesis of the clinkers is described in detail in Borštnar, Daneu and Dolenc (2020), while their phase composition is shown in Mrak et al. (2021). The cement clinkers were ground using a vibratory disc mill (SIEBTECHNIK Labor Scheibenschwingmuhle TS. 250) and a ball mill (CAPCO Test Equipment Ball Mill Model 9VS), after Blaine specific surface areas were measured. Blaine fineness of cement clinker CBCSA-B was $4740 \text{ cm}^2/\text{g}$ and $4250 \text{ cm}^2/\text{g}$ for CBCSA-Y (Mrak et al. 2021). The cement mixtures BCSA-B and BCSA-Y were prepared by blending the ground clinkers with gypsum in order to achieve an M-value (calcium sulfate to ye'elimite molar ratio) of 1.5 in both cements (Mrak et al. 2021).

The pastes were mixed with an Ultra Turrax tube dispenser for 1 min using 10 g of the cement and the appropriate quantity of water to achieve a water-to-cement ratio of 0.5. Cement pastes were then immediately transferred to the lower plate of the rheometer. All rheological tests were performed using a rheometer Anton Paar MCR 302 with serrated parallel plates at 20°C . The samples were first presheared at 100 s^{-1} for 30 s in order to put the sample in a well-defined initial dispersed state and ensure reproducibility (Mostafa and Yahia 2016; Nicolas Roussel 2012). After preshearing, 60 s of recovery followed, before each of the measurements was performed. Flow curve was obtained, starting by increasing the shear rate from 0.1 s^{-1} to 100 s^{-1} within 60 s. Prior to small amplitude oscillatory shear (SAOS) tests, the linear viscoelastic range (LVR) was determined, where the critical value of shear strain was identified for each cement paste. Shear strain from 0.0001 % to 1000 % was applied at a constant frequency of 1 Hz. Using an identified LVR (by applying a constant shear strain), an evolution of storage G' and loss G'' modulus with rest time at a constant frequency of 1 Hz was measured for a duration of 4h, to determine the time-dependent structural changes in the material. Next, the evolution of the viscosity of cement pastes was tested. A measurement lasted for 4h at a constant shear rate of 100 s^{-1} .

3. Results and discussion

The typical rheological flow curves - shear stress versus shear rate and viscosity versus shear rate of BCSA-B and BCSA-Y are plotted in Figure 1. Shear stress increase with a higher shear rate and as the pastes stiffened. Both cement pastes show a decrease in viscosity with increasing shear rate, indicating shear thinning behaviour (Nicolas Roussel 2012). The viscosity is slightly higher in BCSA-Y compared to BCSA-B.

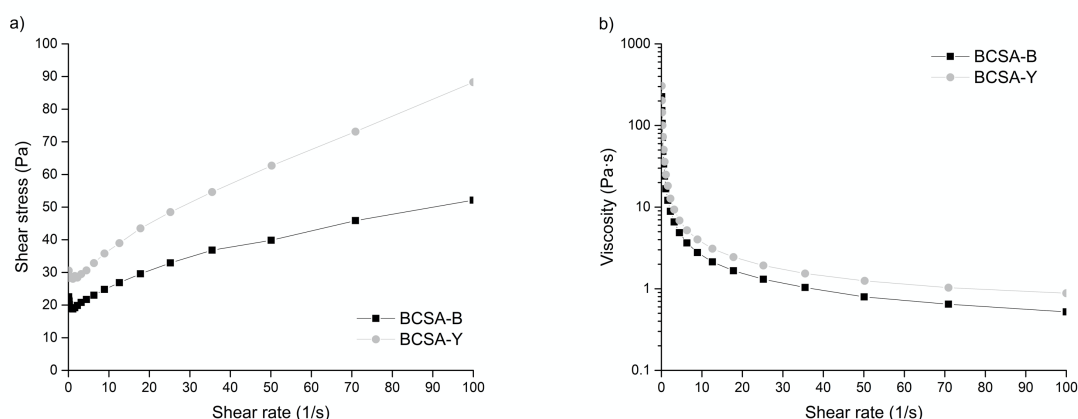


Figure 1. Typical rheological flow curves of cement pastes BCSA-B and BCSA-Y: a) shear stress vs. shear rate and b) viscosity vs. shear rate.

A critical strain of cement paste determined by the amplitude sweep test is shown in Figure 2a and it was found to be at 0.003 % for BCSA-B and BCSA-Y. This is the value of the limit of the linear viscoelastic regime (LVR) when the storage modulus starts to decrease. It is assigned to strain when the initial structure is modified as the particle network of interactions is ruptured (Palacios et al. 2021; Nicolas Roussel et al. 2010). The development of storage modulus G' with time of cement paste BCSA-B and

BCSA-Y is presented in Figure 2b. The increase of storage modulus G' is related non-directly to the structural build-up of the cement paste (Yuan et al. 2017). Two mechanisms that contribute to the storage modulus are described in the literature (Yuan et al. 2017; N. Roussel et al. 2012). At an early age, mainly colloidal interaction between cement particles takes place and at a later age, the formation of C–S–H bridges prevails. Storage modulus in the first 15 minutes did not change significantly, then it shows a slight increase. After 120 and 130 min, for BCSA-B and BCSA-Y, a sharp increase is observed. In addition, the timing is also in accordance with the timing of the calorimetry results (Figure 2c and d), which have already been reported by Mrak et al. (2021); that is the end of the induction period which is related to the slow dissolution of clinker phases and the slow formation of ettringite and just the beginning of the main hydration peak, which is attributed to the dissolution of ye'elite and gypsum and the precipitation of ettringite and aluminium hydroxide. The sharp increase of storage modulus could be therefore related to a small amount of hydrates that formed at an early ages.

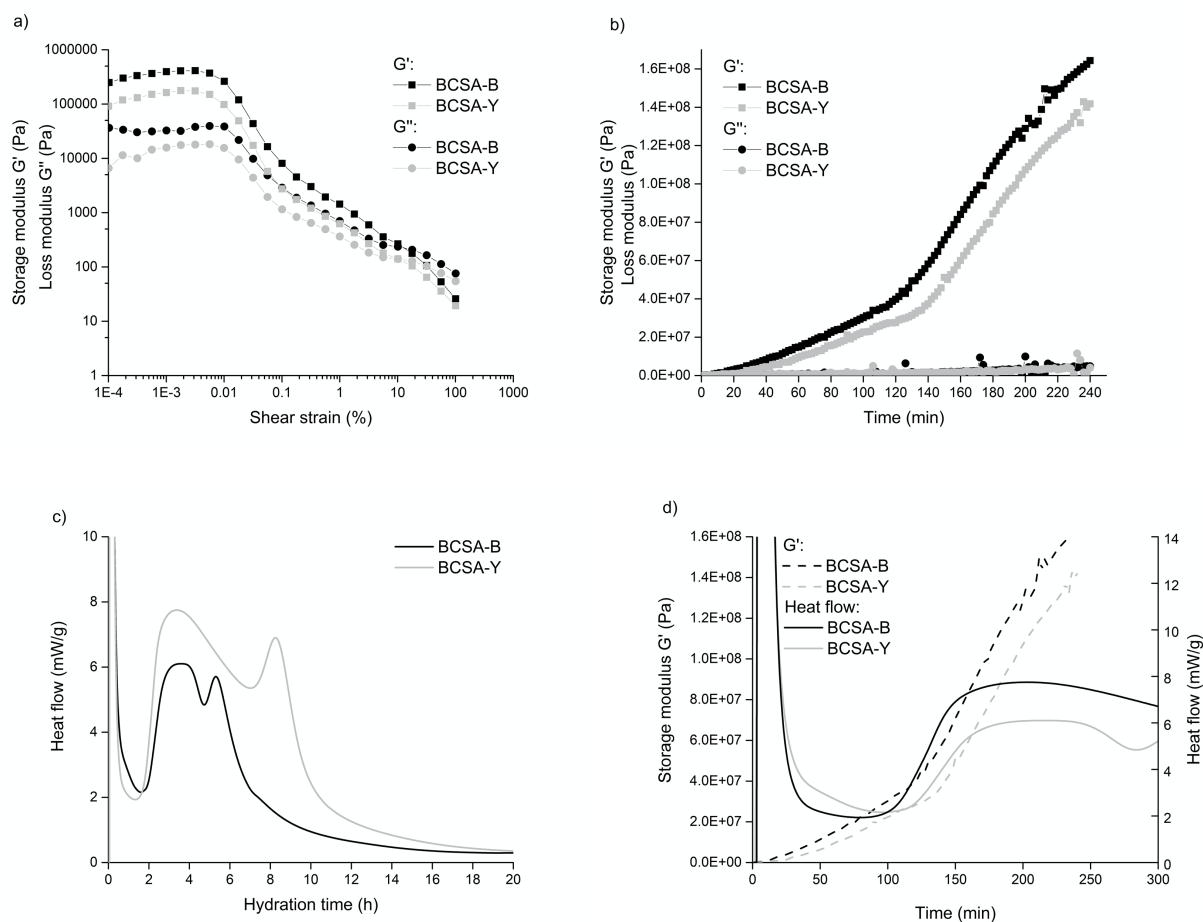


Figure 2. a) Critical strain of cement paste defined with SAOS. b) Development of storage G' and loss modulus G'' with time of cement paste BCSA-B and BCSA-Y. c) Hydration heat flow of BCSA-B and BCSA-Y. Data are taken from Mrak et al. (2021). d) Comparison of hydration heat flow and storage modulus G' with time.

3. Conclusions

In this study, the rheological properties of two belite-calcium sulfoaluminate cements were investigated. Both cement pastes, BCSA-B and BCSA-Y showed shear thinning behaviour. A critical strain was determined and the investigated storage modulus showed changes in the evolution of the rheological behaviour of cement pastes due to hydration processes and formation of hydrates, which was also in accordance with calorimetry results. The sharp increase of storage modulus could be mainly related to the hydration of calcium sulfoaluminate and formation of ettringite. In addition, various compositions of cement clinker also showed differences in the rheological properties of fresh cement pastes.

Acknowledgements

The research is performed within the Young Researcher Programme and is financially supported by the Slovenian Research Agency, contract number 1000 18 1502.

References

- Álvarez-Pinazo, Gema, Isabel Santacruz, Miguel A. G. Aranda, and Ángeles G. De la Torre. 2016. 'Hydration of Belite–Ye'elimite–Ferrite Cements with Different Calcium Sulfate Sources'. *Advances in Cement Research* 28 (8): 529–43. <https://doi.org/10.1680/jadcr.16.00030>.
- Borštnar, Maruša, Nina Daneu, and Sabina Dolenec. 2020. 'Phase Development and Hydration Kinetics of Belite–Calcium Sulfoaluminate Cements at Different Curing Temperatures'. *Ceramics International* 46 (18): 29421–28. <https://doi.org/10.1016/j.ceramint.2020.05.029>.
- Cuberos, Antonio J. M., Ángeles G. De la Torre, G. Álvarez-Pinazo, M. Carmen Martín-Sedeño, Katrin Schollbach, Herbert Pöllmann, and Miguel A. G. Aranda. 2010. 'Active Iron-Rich Belite Sulfoaluminate Cements: Clinkering and Hydration'. *Environmental Science & Technology* 44 (17): 6855–62. <https://doi.org/10.1021/es101785n>.
- García-Maté, Marta, Angeles G. De la Torre, Laura León-Reina, Enrique R. Losilla, Miguel A.G. Aranda, and Isabel Santacruz. 2015. 'Effect of Calcium Sulfate Source on the Hydration of Calcium Sulfoaluminate Eco-Cement'. *Cement and Concrete Composites* 55 (January): 53–61. <https://doi.org/10.1016/j.cemconcomp.2014.08.003>.
- Gartner, Ellis. 2004. 'Industrially Interesting Approaches to “Low-CO2” Cements'. *Cement and Concrete Research* 34 (9): 1489–98. <https://doi.org/10.1016/j.cemconres.2004.01.021>.
- Gartner, Ellis, and Tongbo Sui. 2018. 'Alternative Cement Clinkers'. *Cement and Concrete Research* 114 (December): 27–39. <https://doi.org/10.1016/j.cemconres.2017.02.002>.
- Juenger, M.C.G., F. Winnefeld, J.L. Provis, and J.H. Ideker. 2011. 'Advances in Alternative Cementitious Binders'. *Cement and Concrete Research* 41 (12): 1232–43. <https://doi.org/10.1016/j.cemconres.2010.11.012>.
- Mostafa, Ahmed M., and Ammar Yahia. 2016. 'New Approach to Assess Build-up of Cement-Based Suspensions'. *Cement and Concrete Research* 85 (July): 174–82. <https://doi.org/10.1016/j.cemconres.2016.03.005>.
- Mrak, Maruša, Frank Winnefeld, Barbara Lothenbach, and Sabina Dolenec. 2021. 'The Influence of Calcium Sulfate Content on the Hydration of Belite–Calcium Sulfoaluminate Cements with Different Clinker Phase Compositions'. *Materials and Structures* 54 (6): 212. <https://doi.org/10.1617/s11527-021-01811-w>.
- Palacios, M., S. Gismera, M.M. Alonso, J.B. d'Espinose de Lacaillerie, B. Lothenbach, A. Favier, C. Brumaud, and F. Puertas. 2021. 'Early Reactivity of Sodium Silicate-Activated Slag Pastes and Its Impact on Rheological Properties'. *Cement and Concrete Research* 140 (February): 106302. <https://doi.org/10.1016/j.cemconres.2020.106302>.
- Roussel, N., G. Ovarlez, S. Garrault, and C. Brumaud. 2012. 'The Origins of Thixotropy of Fresh Cement Pastes'. *Cement and Concrete Research* 42 (1): 148–57. <https://doi.org/10.1016/j.cemconres.2011.09.004>.
- Roussel, Nicolas, ed. 2012. *Understanding the Rheology of Concrete*. Woodhead Publishing Series in Civil and Structural Engineering. Woodhead Publishing. <https://doi.org/10.1533/9780857095282.frontmatter>.
- Roussel, Nicolas, Aneel Lemaître, Robert J. Flatt, and Philippe Coussot. 2010. 'Steady State Flow of Cement Suspensions: A Micromechanical State of the Art'. *Cement and Concrete Research* 40 (1): 77–84. <https://doi.org/10.1016/j.cemconres.2009.08.026>.
- Telesca, A., M. Marroccoli, M.L. Pace, M. Tomasulo, G.L. Valenti, and P.J.M. Monteiro. 2014. 'A Hydration Study of Various Calcium Sulfoaluminate Cements'. *Cement and Concrete Composites* 53 (October): 224–32. <https://doi.org/10.1016/j.cemconcomp.2014.07.002>.
- Winnefeld, Frank, and Stefan Barlag. 2010. 'Calorimetric and Thermogravimetric Study on the Influence of Calcium Sulfate on the Hydration of Ye'elimite'. *Journal of Thermal Analysis and Calorimetry* 101 (3): 949–57. <https://doi.org/10.1007/s10973-009-0582-6>.
- Winnefeld, Frank, and Barbara Lothenbach. 2016. 'Phase Equilibria in the System Ca₄Al₆O₁₂SO₄ – Ca₂SiO₄ – CaSO₄ – H₂O Referring to the Hydration of Calcium Sulfoaluminate Cements'. *RILEM Technical Letters* 1 (1): 10–16. <https://doi.org/10.21809/rilemtechlett.v1.5>.
- Yuan, Qiang, Dajun Zhou, Kamal H. Khayat, Dimitri Feys, and Caijun Shi. 2017. 'On the Measurement of Evolution of Structural Build-up of Cement Paste with Time by Static Yield Stress Test vs. Small Amplitude Oscillatory Shear Test'. *Cement and Concrete Research* 99 (September): 183–89. <https://doi.org/10.1016/j.cemconres.2017.05.014>.

Early-age elasticity in structuration of highly cohesive concrete with added pozzolanic diatomaceous earth

Ana Brunčič^{1*}, Katarina Šter², and Sabina Dolenec³

¹ Slovenian National Building and Civil Engineering Institute (ZAG), Laboratory for concrete, Ljubljana, Slovenia
Email: ana.bruncic@zag.si

² Slovenian National Building and Civil Engineering Institute (ZAG), Laboratory for concrete, Ljubljana, Slovenia
Email: katarina.ster@zag.si

³ Slovenian National Building and Civil Engineering Institute (ZAG), Laboratory for cements, mortar, and ceramics, Ljubljana, Slovenia
Email: sabina.dolenec@zag.si

ABSTRACT

The paper presents part of the results of the wider context research on effect of diatomaceous earth (DE) of various origins as a cement thixotropy and elasticity enhancer in concretes with pronounced cohesion. DE has long been recognized and used as an amorphous silica-based pozzolanic supplementary cementitious material (SCM), which, like silica fume, improves concrete performance, foremost cohesion and thixotropy in fresh state and strength in hardened state. Research was performed on cement paste. Calcined diatomaceous earth was used along with cement CEM I 52.5. Five different mixtures were prepared with DE used at a replacement rate ranging from 0 to 12 wt.% of ordinary Portland cement (OPC) and 0.5 water-to-binder ratio. Reactivity of cementitious systems and hydration kinetics were investigated with isothermal calorimetry, and rheological characterisation performed with rotational shear for flowability and thixotropy evaluation, and small amplitude oscillatory shear (SAOS) for elasticity evaluation. Flow curve and SAOS showed the greatest effect of diatomaceous earth used as SCM in terms of suspensions elasticity and adequate flowability at 6 wt.%, both test methods indicated instable mechanical performance of mixture with higher shares of added DE, probably caused by uneven leaching of water from pores of DE.

KEYWORDS: *diatomaceous earth, fresh state, elasticity, storage modulus, SAOS*

1. Introduction

Workability properties of highly cohesive concretes are difficult to evaluate since they exhibit low or no slump at all. Not only that flowability of low-slump concretes is hard to assess with standardized methods, but also other properties, necessary for non-conventional casting techniques, are poorly defined and described in terms of mechanics. Foremost but not solely printed concretes are mostly descriptively characterized through buildability and shape retention, the desired properties in minutes after extrusion of concrete through nozzle onwards [1]–[4]. Lately several approaches on how to measure, mathematically describe and evaluate those properties were proposed, mostly through thixotropy and structural build-up [5]–[12]. Small amplitude oscillatory shear (SAOS) and creep-recovery tests were lately employed for micro-scale assessment of thixotropy and viscoelasticity of cement pastes giving insight into mechanical transition of two states: liquid and solid-like [13]–[15]. The aim of this study is based on extended rheological characterization of cement paste as the adhesion provider within cement, foremost flow curve with shear strength τ and thixotropy evaluation as well as G' as indicator of elasticity in highly cohesive mixtures were studied. The latter is achieved through addition of DE as pozzolanic SiO₂-based supplementary cementitious material (SCM).

2. Materials and methods

Study and test methods were covering two scales: cement paste and concrete. CEM I 52.5 R was used and DE from Czech brewery Plzeňský Prazdroj, a. s., as input material for beer filtration. Elemental composition determined by X-ray fluorescence spectroscopy (WDXRF, Thermo Scientific ARL PERFORM'X, Thermo Fisher Scientific, MA, USA; fused beads, UniQuant program) and particle size distribution, determined by laser granulometry (Microtrac SYNC Model 5001, Microtrac Retsch GmbH, Haan, Germany; Isopropanol) are shown in Table 1 and on Fig. 1.

Table 1 – Chemical composition of CEM I and DE

| Composition | CEM I 52.5 R | DE |
|------------------------------------|--------------|-------|
| Na ₂ O (%) | 0.69 | 0.64 |
| MgO (%) | 1.78 | 0.44 |
| Al ₂ O ₃ (%) | 6.66 | 5.45 |
| SiO ₂ (%) | 20.64 | 88.84 |
| SO ₃ (%) | 2.16 | / |
| K ₂ O (%) | 0.70 | 0.46 |
| CaO (%) | 60.76 | 0.95 |
| Fe ₂ O ₃ (%) | 2.57 | 1.85 |
| Sum (%) | 96.83 | 99.99 |
| LOI (950 °C) | 3.15 | 0.83 |

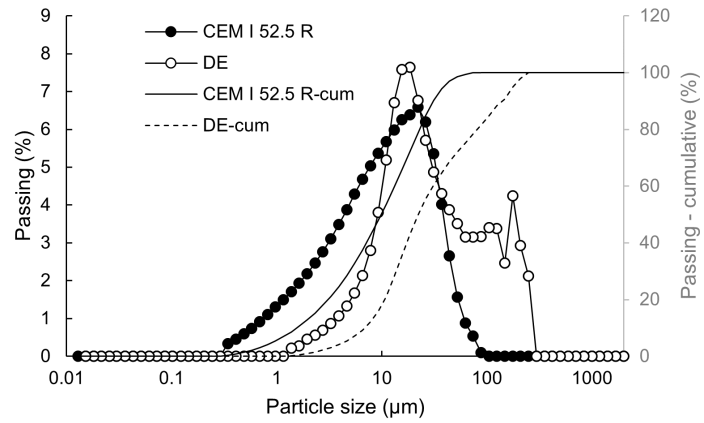


Figure 1 – Particle size distribution of CEM I 52.5 R and DE

Five mixtures were investigated at the cement paste scale with water-to-binder ratio of 0.5, differing in amount of added DE as cement replacement. High-rates rotational and small-amplitude oscillatory shear tests were performed using Vane probe with AntonPaar MCR 302 rheometer. 150 g of paste was prepared, and two sets of measurements performed, for DE shares 6 and 9 wt.% four sets of measurements were performed. After 3 minutes of dry hand mixing followed by 3 minutes of mixing after addition of water, cement paste was poured into the cup, pre-sheared at logarithmically increasing shear rate from 0 to 50 s⁻¹ for 60 s and left to recover and form the structure for three minutes. Two consecutive tests were then performed: 1) flow curve with three-branch protocol (ramp linear ascending shear rate 0-100 s⁻¹, constant shear rate 100 s⁻¹, and ramp linear descending shear rate 100-0 s⁻¹, 2) SAOS with shear strain ranging from 0.0001 % to 1 %. Shear strain was applied at a constant frequency of 1 Hz and one data point was captured per second. Kinematics of tests is shown on Fig.1. Four replacement rates of DE were tested: 3, 6, 9, and 12 wt.% respectively. Pure CEM I 52.5 R was taken as a reference. Based on the results of rheological characterization characteristic mixtures for isothermal calorimetry were selected, namely shares with 0, 6, and 12 wt.% replacement rate were selected. The reactivity of the systems was studied with TAM Air 8 (TA Instruments). 4 g of each system was used at a w/c ratio of 0.5. Measurements were performed using external mixing for 3 minutes. Heat evolution was measured at 20 °C for 2 days.

3. Results and discussion

From isothermal calorimetry (Fig. 2) can be seen that pozzolanic DE has impact on reactivity of blended system even in initial phase and accelerating period. Both shares of DE accelerated setting and decreased the reactivity of the system. Shear stress obtained from flow curve is shown on Fig. 3. DE has significant impact on flowability of cement paste. Beside reduction of flowability, mixtures with shares higher than 6 wt.% exhibit instable behaviour with varying shear thinning and shear thickening, causing bigger scatter of results. This can be attributed to water uptake of DE due to its porosity and leaching of water at higher shear rates.

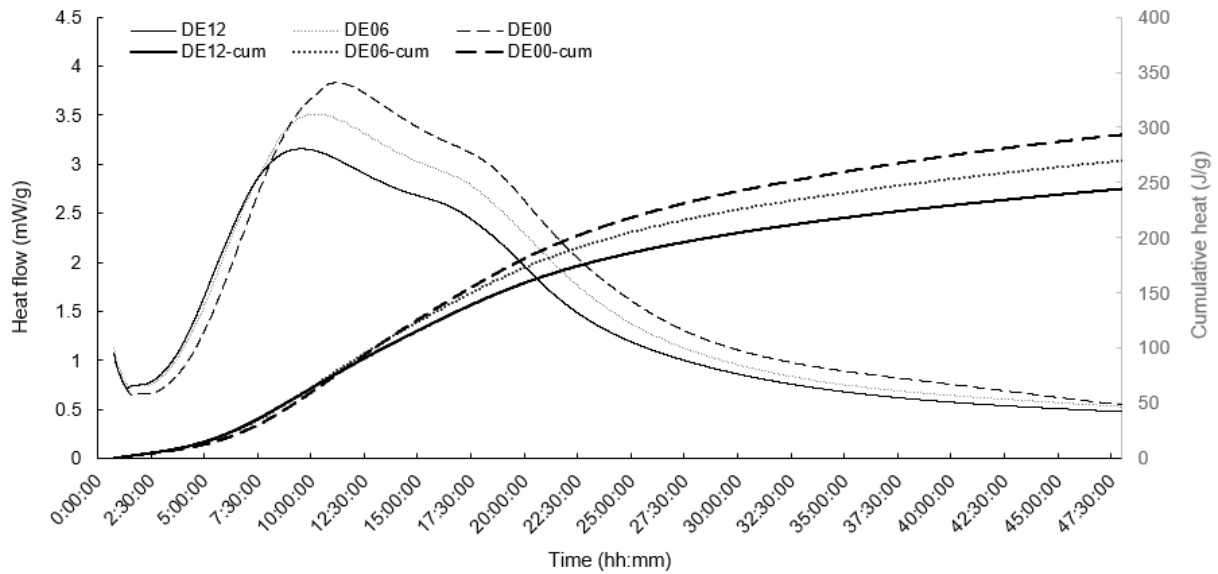


Figure 2 – Heat flow of studied mixtures (reference without DE addition, 6 wt.% DE and 12 wt.% DE)

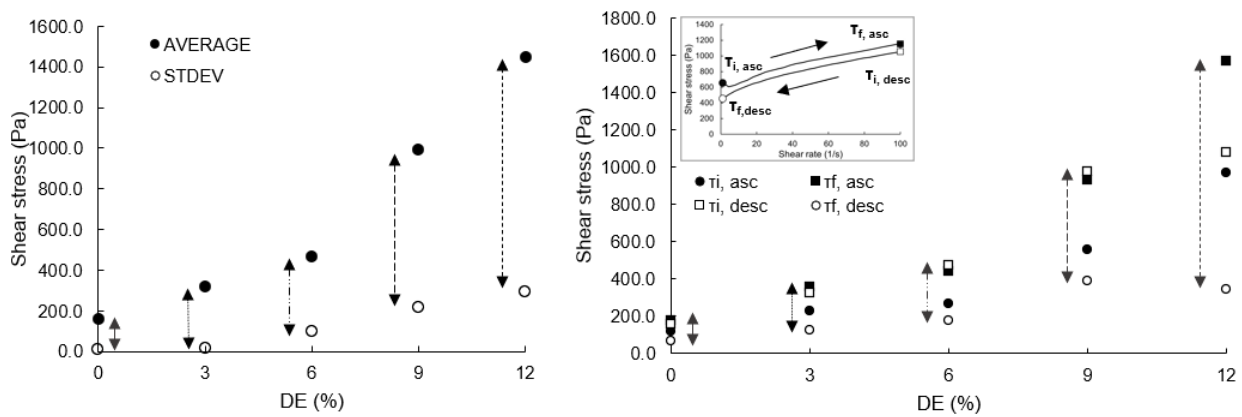


Figure 3 – Average value of shear stress at constant shear rate (100 s^{-1}) with standard deviation (left), and average values of significant shear stresses in 3-phase shearing protocol (right)

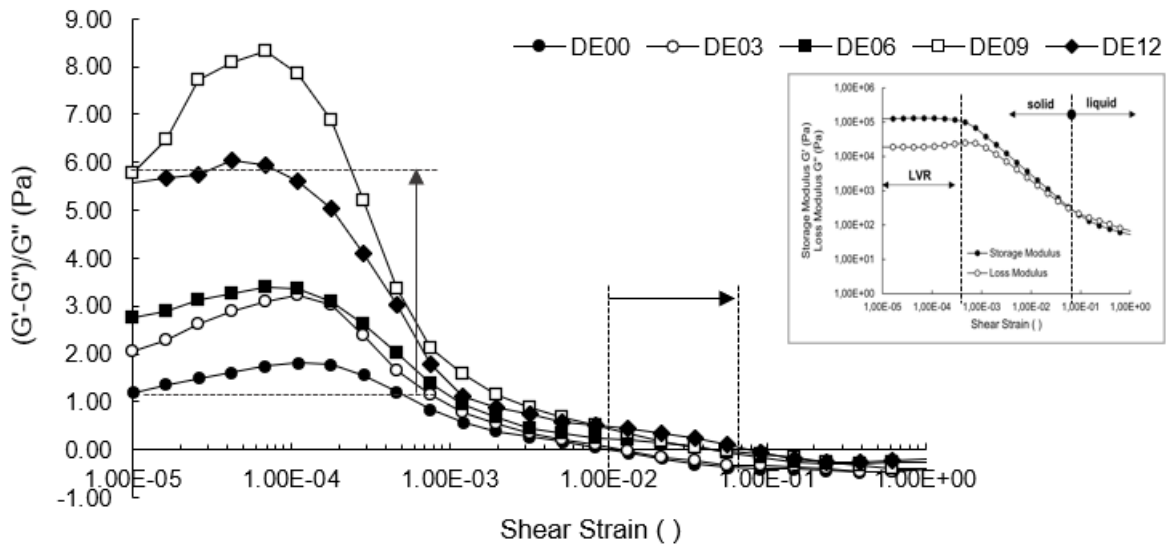


Figure 4 – Relative G' and G'' ratio for all studied wt.% of DE

DE also increases thixotropy of mixture. As seen from Fig. 3 (right) the increase is correlated to the wt.% of DE. Relative ratio of both moduli (G' and G'' ; Fig. 4) shows that addition of DE increases elasticity of

the system, still limit is reached at share of 9 wt.%. DE also stabilizes mixture, what can be seen from prolonged linear visco-elasticity range (LVR) and increases cohesion of system leading to delayed transformation from solid-like to liquid-like behaviour.

4. Conclusions

Paper presents a step in the direction of quantitative mechanical characterisation of highly cohesive no-slump cementitious materials. Rheological characterization of cement paste as the adhesive of the concrete was used to quantify the viscoelasticity of the cement system with added DE. As seen from the results SAOS can be used for quantitative evaluation of material's elasticity and prediction of its solid-state behaviour in fresh state. Coupled with flow curve, providing assessment of viscosity as well as thixotropy, characterization of mechanical properties and performance of the paste can be done. Addition of DE reduces intensity of hydration reactions and delays their acceleration. At the same time addition of DE reduces flowability of the paste and increases its thixotropy. It also causes inconsistent behavior of the paste, observed as either shear thinning or thickening, which can be attributed to leaching of water from pores of DE. DE like silica fume stabilizes the mixture and increases its cohesiveness since it increases G' as well as relative ratio between G' and G'' . Coupled flow curve and SAOS can serve for optimization of SCM amount.

Acknowledgements

The authors acknowledge the financial support from the Slovenian Research Agency (research core funding No. P2-0273).

References

- [1] D. T. Yi Wei, Q. Ye, and J. T. Ming, 'Printability region for 3D concrete printing using slump and slump flow test', *Compos. Part B*, no. 174, p. 106968, 2019.
- [2] S. Ghourchian, M. Butler, M. Krüger, and V. Mechtcherine, 'Modelling the development of capillary pressure in freshly 3D-printed concrete elements', *Cem. Concr. Res.*, vol. 145, p. 106457, Jul. 2021, doi: 10.1016/j.cemconres.2021.106457.
- [3] S. Chaves Figueiredo *et al.*, 'An approach to develop printable strain hardening cementitious composites', *Mater. Des.*, vol. 169, May 2019, doi: 10.1016/j.matdes.2019.107651.
- [4] J. Kruger, S. Zeranka, and G. Van Zijl, '3D concrete printing: A lower bound analytical model for buildability performance quantification', 2019, doi: 10.1016/j.autcon.2019.102904.
- [5] Q. Yuan, D. Zhou, K. H. Khayat, D. Feys, and C. Shi, 'On the measurement of evolution of structural build-up of cement paste with time by static yield stress test vs. small amplitude oscillatory shear test', *Cem. Concr. Res.*, vol. 99, pp. 183–189, Sep. 2017, doi: 10.1016/j.cemconres.2017.05.014.
- [6] Y. Zhang, Y. Zhang, G. Liu, Y. Y., M. Wu, and B. Pang, 'Fresh properties of a novel 3D printing concrete ink', *Constr. Build. Mater.*, no. 174, pp. 263–271, 2018.
- [7] P. F. G. Banfill, 'Rheology of fresh cement and concrete', *Br. Soc. Rheol.*, no. January 2003, pp. 61–130, 2006, [Online]. Available: <http://www.bsr.org.uk>.
- [8] A. M. Mostafa and A. Yahia, 'New approach to assess build-up of cement-based suspensions', *Cem. Concr. Res.*, vol. 85, pp. 174–182, Jul. 2016, doi: 10.1016/j.cemconres.2016.03.005.
- [9] J. T. Kolawole, R. Combrinck, and W. P. Boshoff, 'Rheo-viscoelastic behaviour of fresh cement-based materials: Cement paste, mortar and concrete', *Constr. Build. Mater.*, vol. 248, p. 118667, 2020, doi: 10.1016/j.conbuildmat.2020.118667.
- [10] N. Roussel, G. Ovarlez, S. Garrault, and C. Brumaud, 'The origins of thixotropy of fresh cement pastes', *Cem. Concr. Res.*, vol. 42, no. 1, pp. 148–157, 2012, doi: 10.1016/j.cemconres.2011.09.004.
- [11] N. Roussel, 'Rheology of fresh concrete: From measurements to predictions of casting processes', *Mater. Struct. Constr.*, vol. 40, no. 10, pp. 1001–1012, Dec. 2007, doi: 10.1617/s11527-007-9313-2.
- [12] N. Roussel, 'A thixotropy model for fresh fluid concretes: Theory, validation and applications', *Cem. Concr. Res.*, vol. 36, no. 10, pp. 1797–1806, 2006, doi: 10.1016/j.cemconres.2006.05.025.
- [13] T. Liberto, M. Bellotto, and A. Robisson, 'Small oscillatory rheology and cementitious particle interactions', *Cem. Concr. Res.*, vol. 157, no. April, p. 106790, 2022, doi: 10.1016/j.cemconres.2022.106790.
- [14] T. Liberto *et al.*, 'Detecting Early-Stage Cohesion Due to Calcium Silicate Hydration with Rheology and Surface Force Apparatus', *Langmuir*, 2022, doi: 10.1021/acs.langmuir.2c02783.
- [15] Q. Yuan, X. Lu, K. H. Khayat, D. Feys, and C. Shi, 'Small amplitude oscillatory shear technique to evaluate structural build-up of cement paste', *Mater. Struct. Constr.*, vol. 50, no. 2, Apr. 2017, doi: 10.1617/s11527-016-0978-2.

Cellulose ether behavior in slag cement-based tile adhesives

Y. Kaci ¹, M. Chaouche ², R. Alfani ¹

¹ ECOCEM Materials, 4 place Louis Armand, 75012 Paris, France
ykaci@ecocem.ie

² ENS Paris-Saclay, CNRS, Laboratoire de Mécanique Paris-Saclay, 91190, Gif-sur-Yvette, France
mohend.chaouche@ens-paris-saclay.fr

¹ ECOCEM Materials, 4 place Louis Armand, 75012 Paris, France
ralfani@ecocem.ie

ABSTRACT

Addition of cellulose ethers (CEs) in tile adhesives formulations is mandatory to insure water retention and therefore appropriate adhesion. In order to reduce the carbon footprint of such products, Ordinary Portland Cement (OPC) is often partially replaced by Supplementary Cementitious Materials (SCMs) as Ground Granulated Blast Furnace Slag (GGBS). To improve the reactivity of such blended cements, accelerators as alkaline salts (based on sulphate, carbonate, thiocyanate, formate, etc.) can be used. This may have a disruptive effect on CE solubility and filmification, preventing them from insuring their intended functions. In the present investigation, CE filmification/gelification behavior induced by heating or increase of concentration was characterized under different ionic environments via oscillatory rheology and negative staining transmission electron microscopy. The filmification of CEs was shown to be highly sensitive to the polarizing properties of the ions present according to the Hofmeister series. This highlighted the interaction of CEs with salt additives used in cementitious materials and the impact on water retention.

Originality: This study highlights the impact of salt additives used as accelerators in blended cementitious materials on the working mechanisms of CEs regarding water retention.

KEYWORDS: *Cellulose ethers, sol-gel transition, water retention, activated GGBS, ionic strength,*

1. Introduction

CEs are often used in industrial mortars as tile adhesives to ensure water retention and incidentally, to improve the rheological properties. The water retention mechanisms of CEs are largely debated in the literature. In particular, Bülichen and Plank (2013) attributed the exceptional ability of CEs for water retention against capillary suction to the formation microgels that plug the porosity of the substrate. Such microgel formation is typical for thermo-responsive polymers as CEs, and this is well studied in the literature (see for example Hussain et al (2002), Silva et al (2008)). Thermo-gelation of CEs is highly impacted by the presence of order-making (kosmotropic) or order-breaking (chaotropic) ions in solution. In cementitious materials, such ions (as sulfates, carbonates, thiocyanates, formates, etc.) are often present in high concentrations, in particular in the case of activated OPC-SCMs blends. This is expected to impact not only the solubility of CEs, but also their water retention ability since this depends on their gelation properties.

In the present investigation thermo-gelation of CEs is considered using linear oscillatory rheology. The impact of sulfate ions (kosmotropic) and thiocyanate ions (chaotropic) on the temperature of micro-phase separation (cloud point) is considered. The impact of those ions on the microgel structure, as induced by dewatering, was observed using TEM imaging.

2. Material and methods

The CE considered in this study is a Methyl Hydroxy Ethyl Cellulose (MHEC) and was graciously provided by the company Ashland. CE solution has been prepared by adding ultrapure water at 60 °C to

MHEC (for a final concentration of 1%) and stirred for approximately 24h to obtain a well-dispersed mixture, and then stored at 5°C. Prior to testing, the cold solutions were degassed with brief exposure to a vacuum while being stirred and then stored in a refrigerator for at least 24 h to allow for hydration and the removal of bubbles.

Small-amplitude oscillatory shear (SAOS) experiments were conducted using a TA Instruments AR2000ex rheometer equipped with a cone-plate geometry (angle: 2°) and a Peltier temperature control system. The SAOS tests were performed in a strain-controlled mode (1% strain), at 1 Hz frequency, and at 1 °C/min heating. A thin layer of silicone oil was disposed around the sample surface exposed to the ambient air to avoid water evaporation.

Imaging via negative staining transition electron microscopy was carried out to characterize CE filmification under dewatering. This technique allows imaging with molecular resolution in wet environments by using reactive dye contrast with a maximum resolution of 18-20 Å. The negative dye electron microscopy is useful for monitoring the organization of the CE macromolecules in different aqueous media (Fabre et al. (2017)). The sample is adsorbed onto a substrate, then a stain is applied, blotted and dried to produce a thin layer of electron dense stain, into which the particles are embedded Scarff et al. (2018). The improvement of image contrast is linked to the use of heavy metals. The heavy atom salt (or dye) preferentially binds to the surface of the adsorbed particles, creating a "fingerprint" of the particles in the dye. In this case, 400 Mesh copper grids covered with a carbon film are rendered hydrophilic by a glow discharge system. The CE solution deposited on the grid is then soaked in a dye allowing negative staining.

3. Results and Discussion

3.1 Thermal CE gelation using SAOS

Figure 1 shows the evolution of the linear visco-elastic modulus of a MHEC solution at a concentration of 1%, when the temperature is increased from 5 to 90 °C. At relatively low temperatures both the storage modulus (G') and loss modulus (G'') decrease with temperature, according to visco-elastic behavior correlated to the Arrhenius effect. At given high temperature a minimum of G'/G'' can be observed indicating that a demixing phenomenon may take place with the formation of polymer-rich clusters and solvent-rich zones Lodge et al. (2018) (clouding point). After reaching a minimum at around 70 °C, G' and G'' increase abruptly indicating the formation of a gel network. Beyond the transition, the modulus G' tends towards a second stabilization level, at which G' becomes greater than G'' again, indicating the formation of a new gel state. The transition from a homogeneous polymer solution to the formation polymer-rich micro domains is well studied in the literature and attributed to the temperature-induced breakdown of the hydrogen bonded water molecules domains around the polymer chains leading to strong hydrophobic-hydrophobic associations. Silva *et al* (2008), Fairclough *et al* (2012).

In a cement pore solution, the polymer concentration is expected to increase upon both hydration and water uptake by porous substrates. The clouding may then take place even at pore solution temperature. The impact of this parameter is then considered. Figure 2 shows the evolution of G' as a function of temperature at different CE concentrations. The cloud point temperature decreases with increasing concentration. Based on these results, it is possible to anticipate that the phenomenon of demixing followed by the formation of a high modulus gel can take place at room temperature if the CE concentration is increased sufficiently. Ex-situ observations on cement paste in the hardened state have also revealed the presence of CE films Graessley, and al (1979). At lower concentration, the probability of overlapping CE chains is lower, which makes it more difficult to form a microgel. Experimentally, at 0.5% CE, gelation occurs at 110°C. Other phenomena including evaporation may interfere with gelation at these temperatures. Therefore, the gel plateau cannot be reached experimentally at such low polymer concentrations Lyytikäinen, and al (2019).

Na_2SO_4 is commonly used to activate slag-based binders. This is then relevant to consider the effect of this salt on the behavior of CEs solutions. Figure 3 shows that the presence of Na_2SO_4 leads to a significant impact on the thermos-gelation properties of the CE solution. In particular the cloud point is significantly reduced. The addition of Na_2SO_4 tends to decrease the G' of the solution, even for small concentrations, and the plateau after the sol-gel transition is well defined. These results are general for kosmotropic ions as sulphates (Joshi (2011)).

Figure 4 shows the thermo-viscoelastic behavior of MHEC solutions in the presence of NaSCN at different concentrations. It can be observed that cloud point increases in the presence of this chaotropic ion. The G' plateau obtained after the sol-gel transition in the case of the reference solution no longer appears in the presence of NaSCN for the tested temperature range. It is likely that the plateau can appear at much higher temperatures, which is not accessible without evaporation interference.

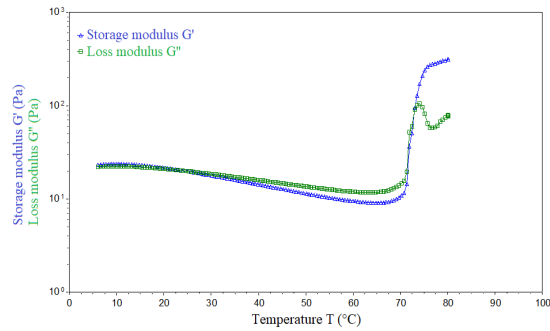


Figure 1: Linear viscoelastic properties of a 1% CE aqueous solution versus temperature

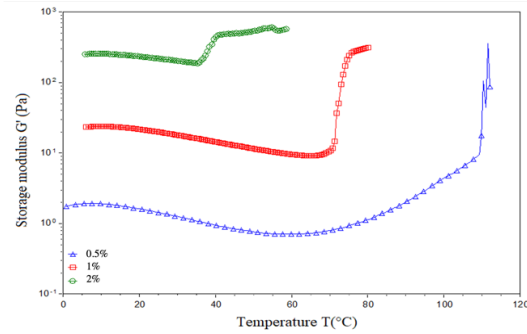


Figure 2 : Evolution of G' versus temperature for different CE concentrations.

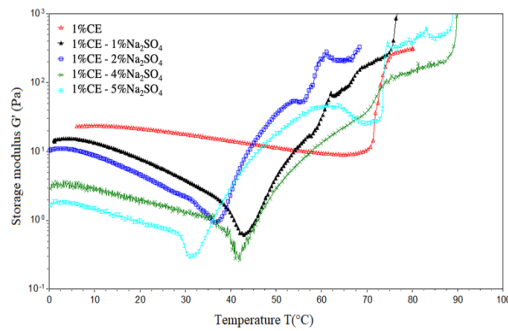


Figure 3: G' versus temperature of a 1% CE solution in the presence of sodium sulfate.

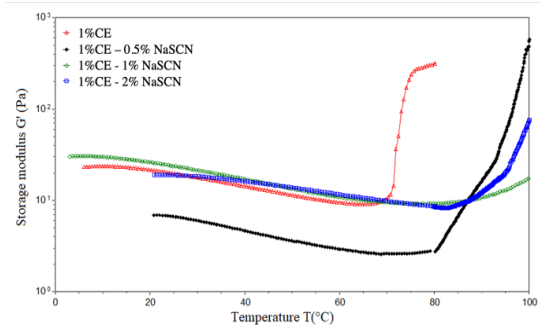


Figure 4: G' versus temperature of 1% CE solution in the presence of sodium thiocyanate

3.2 CE network by transmission electron microscopy: Effect of salts addition

Figures 5-7 present samples of CE gels (1%wt) in pure water (Figure 5), with sodium sulphate (Figure 6) and with sodium thiocyanate (Figure 7) observed by negative staining transmission electron microscopy, obtained after drying by capillary suction. CE chain aggregates appear white due to the negative staining. Figure 5 shows that the CE gel in pure water, after a transition induced here by capillary suction (that increases the concentration) forms a continuous and homogenous network. A significant proportion of voids can be observed. This is attributed to the air entrainment properties of CE. The minimum diameter of the filaments distinguished here is less than 3 nm, which corresponds to the size of only few molecular chains. The introduction of sulphate ions (Figure 6) leads to the destruction of the CE network, with the presence of heterogeneous agglomerates. It is expected that the network formed here as a result of capillary suction is quite permeable to water. This result would explain the abrupt transition loss as well as the loss of the water retention capacity of the CEs in the presence of a high sulphate concentration, Bülichen et Plank (2013). Figure 7 shows that in the presence of NaSCN, the network formed by the cellulose ether presents some heterogeneities. A dense polymer network is observed compared to the reference, with thicker polymer fibers. The porosity of this network seems to be low, which should not negatively impact the water retention. A stiffening of the system is observed in the presence of sodium thiocyanate, which would explain the constant rise in G' and the absence of a gelation plateau in the rheological measurements discussed before.

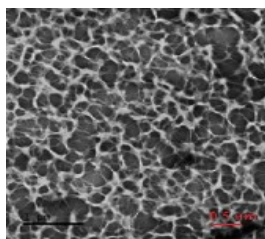


Figure 5 : TEM image of MHEC gel in water

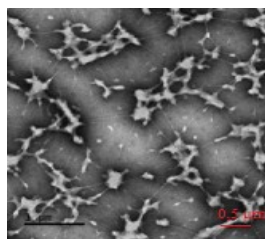


Figure 6 : TEM image of MHEC gel in the presence of Na_2SO_4 .

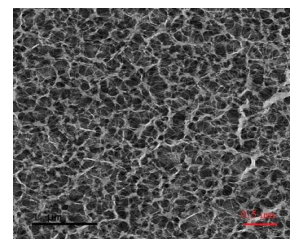


Figure 7 : TEM image of MHEC gel in the presence of NaSCN .

4. Conclusion

Two complementary techniques were used to consider the water retention mechanisms of CEs. Indeed, oscillatory rheology measurements showed that the sol-gel transition of cellulose ether is impacted by temperature, concentration of CE, type and concentration of ions in the solution. The TEM images taken under wet conditions showed that the water retention action of CEs could be attributed to stable film formation induced by an increase of the CE concentration in the pore solution with time, sol-gel transition and then the formation of a strong gel. This could be the main reason for the high-water retention capacity of CEs in cementitious systems. The formed network also showed a sensitivity to the type of ions in solution. It is therefore important to control the onset of the sol-gel transition and the quality of the polymer network formed afterwards in the new low carbon binders based on activated blast furnace slag.

References

- Bülichen, D., et J. Plank. 2013. « Water Retention Capacity and Working Mechanism of Methyl Hydroxypropyl Cellulose (MHPC) in Gypsum Plaster — Which Impact Has Sulfate? » *Cement and Concrete Research* 46 (avril): 66-72.
- Fabre, Lucien, Huan Bao, James Innes, Franck Duong, et Isabelle Rouiller. 2017. « Negative Stain Single-Particle EM of the Maltose Transporter in Nanodiscs Reveals Asymmetric Closure of MalK2 and Catalytic Roles of ATP, MalE, and Maltose ». *Journal of Biological Chemistry* 292 (13): 5457-64.
- Fairelough, J Patrick A, Hao Yu, Oscar Kelly, Anthony J Ryan, Robert L Sammler, et Michael Radler. 2012. « Interplay between Gelation and Phase Separation in Aqueous Solutions of Methylcellulose and Hydroxypropylmethylcellulose », 7.
- Hussain, S, C Keary, et D Q M Craig. 2002. « A Thermorheological Investigation into the Gelation and Phase Separation of Hydroxypropyl Methylcellulose Aqueous Systems », 6.
- Joshi, Sunil C. 2011. « Sol-Gel Behavior of Hydroxypropyl Methylcellulose (HPMC) in Ionic Media Including Drug Release », 45.
- Lodge, Timothy P., Amanda L. Maxwell, Joseph R. Lott, Peter W. Schmidt, John W. McAllister, Svetlana Morozova, Frank S. Bates, Yongfu Li, et Robert L. Sammler. 2018. « Gelation, Phase Separation, and Fibril Formation in Aqueous Hydroxypropylmethylcellulose Solutions ». *Biomacromolecules* 19 (3): 816-24.
- Lyytikäinen, Johanna, Teija Laukala, et Kaj Backfolk. 2019. « Temperature-Dependent Interactions between Hydrophobically Modified Ethyl (Hydroxyethyl)Cellulose and Methyl Nanocellulose ». *Cellulose* 26 (12): 7079-87.
- Mitchell, K., J.L. Ford, D.J. Armstrong, P.N.C. Elliott, C. Rostron, et J.E. Hogan. 1993. « The Influence of Concentration on the Release of Drugs from Gels and Matrices Containing Methocel® ». *International Journal of Pharmaceutics* 100 (1-3): 155-63.
- Sarkar, N. 1979. « Thermal Gelation Properties of Methyl and Hydroxypropyl Methylcellulose ». *Journal of Applied Polymer Science* 24 (4): 1073-87.
- Scarff, Charlotte A., Martin J. G. Fuller, Rebecca F. Thompson, et Matthew G. Iadaza. 2018. « Variations on Negative Stain Electron Microscopy Methods: Tools for Tackling Challenging Systems ». *Journal of Visualized Experiments*, n° 132 (février): 57199.
- Silva, Sérgio M.C., Fátima V. Pinto, Filipe E. Antunes, Maria G. Miguel, João J.S. Sousa, et Alberto A.C.C. Pais. 2008. « Aggregation and Gelation in Hydroxypropylmethyl Cellulose Aqueous Solutions ». *Journal of Colloid and Interface Science* 327 (2): 333-40.

Influence of key synthetic factors on the molecular characteristics of polycarboxylate superplasticizers

Jin Yuan^{1,2}, Qing Shen^{1,2}, Zhenping Sun^{1,2,3,*}, Haijing Yang^{1,2}, Weigang Zhu⁴, Qiong Luo⁴, Xuejun Shu⁵, Doudou Shu⁵

1 Key Laboratory of Advanced Civil Engineering Materials of Ministry of Education, Tongji University, Shanghai 201804, China

2 School of Materials Science and Engineering, Tongji University, Shanghai 201804, China

3 Research Center of Intelligent Evaluation and Restoration Engineering Technology of Urban Pipe Network of Shanghai Water Bureau, Shanghai 201900, China

4 Satellite Chemical Co., Ltd., Zhejiang Jiaying 85000, China

5 Shanghai San Songguo New Materials Co., Ltd., Shanghai 201615, China

E-mail: 2130625@tongji.edu.cn, shenqing@tongji.edu.cn, szhp@tongji.edu.cn, yanghaijings@tongji.edu.cn; zwg@weixing.com.cn; luoqiong@weixing.com.cn; 2391737928@qq.com; 453632681@qq.com

ABSTRACT

The performance of common polycarboxylate ester/ether-based superplasticizers (PCEs) can be influenced by their molecular characteristics significantly. In this paper, PCEs were synthesized using methyl allyl polyethenoxy ether (HPEG) and isoprenyl oxy polyoxyethylene ether (IPEG) as macromonomers, respectively. The effect of key synthetic factors including initiator and chain transfer agent on the molecular characteristics of PCEs was investigated via gel permeation chromatography (GPC) measurement. The results showed that, compared to the hydrogen peroxide-vitamin C (H₂O₂-VC) system, using ammonium persulfate-vitamin C (APS-VC) as an initiator in an adequate amount can increase the conversion rate of macromonomers as well as the homogeneity of molecular weight of the polymerized product, thus improve the dispersing ability. Furthermore, a shoulder peak was found in the GPC spectrum of polymerized product at a short flow time range if an inappropriate amount of chain transfer agent were adopted, which indicated a small number of polymers with large molecular weight was produced.

KEYWORDS: *polycarboxylate ester/ether-based superplasticizer, synthetic factors, initiators, molecular characteristics, dispersion performance*

1. Introduction

PCEs are one kind of polymer graft copolymer synthesized by the free radical copolymerization reaction of polyether monomer and small monomer containing carboxyl and sulfonic acid groups and other adsorption groups (Shui et al, 2020). Therefore, their copolymerization reaction process of the initiation system, reaction temperature and feeding time and other factors, have a significant impact on the structure and performance of the PCEs (Jiang et al, 2022). Researchers have been working on improving the dispersion properties of PCEs, developing functional PCEs, and investigating the adaptability of PCEs to various cementitious materials in recent years (Lei et al, 2021; Zhong et al, 2022). However, the influence of the various synthetic factors on the molecular properties of PCEs during the synthesis process has not been comprehensively investigated. In this work, a series of PCEs were synthesized with HPEG, IPEG and AA by varying the initiators, chain transfer agent, synthesis temperature as well as synthesis time to systematically investigate the effects of the synthesis factors on the molecular properties and dispersion performance of PCEs.

2. Experimental

2.1 Materials

2.1.1 Chemicals

Methyl allyl polyethenoxy ether (HPEG, $M=2400$ g/mol) and isoprene alcohol polyoxyethylene ether (IPEG, $M=2400$ g/mol) were provided by Aoke Chemical Co., Ltd., Liaoning, China. The ethylene oxide unit (EO) of HPEG and IPEG is 53. Acrylic acid (AA), hydrogen peroxide (H_2O_2 , solid content is 27.5%), vitamin C (VC, AR), sodium hydroxide (NaOH, AR) and mercaptopropionic acid (MPA, AR) were purchased from San Songguo New Materials Co., Ltd., Shanghai, China. Deionized water was used in the synthesis process.

2.1.2 Cement

The cement used in this paper was P I 42.5 reference cement purchased from Auxier Science and Technology Co., Ltd., Fushun, China. The chemical and mineralogical compositions of the reference cement were presented in Table 1.

Table 1 The chemical and mineral compositions of the reference cement (wt%)

| Chemical composition | | | | | | | Mineralogical composition | | | | | |
|----------------------|------------------|--------------------------------|--------------------------------|------|-------|-----------------|---------------------------------|------------------|------------------|------------------|-------------------|--|
| CaO | SiO ₂ | Al ₂ O ₃ | Fe ₂ O ₃ | MgO | f-CaO | SO ₃ | Na ₂ O _{eq} | C ₃ S | C ₂ S | C ₃ A | C ₄ AF | |
| 64.79 | 21.90 | 4.61 | 3.25 | 2.59 | 0.90 | 0.67 | 0.57 | 59.72 | 18.06 | 6.72 | 9.88 | |

2.2 Synthesis

HPEG (or IPEG) was mixed with deionized water in a four-neck round-bottom flask which was placed in a constant temperature bath with a stirrer, and then H_2O_2 or APS were added in sequence, followed by heating to 45 °C. Thereafter, AA solution was dropwise added to the flask within 3 h, VC and MPA solution was dropwise added to the flask within 3.5 h, and then retained stirring at 45 °C for 1 h. After the reaction was completed, the polymer solution was neutralized by NaOH aqueous solution at a concentration of 10 mol/L, thus yielding the final product (40%). The molar ratio of HPEG or IPEG to AA was 4.0.

2.3 Experiment methods

2.3.1 GPC

The number average molecular weight (M_n), weight average molecular weight (M_w) and polydispersity index (PDI) of PCEs specimens were determined by gel permeation chromatography (GPC) with an Agilent 1260 Infinity II GPC (Agilent Co., Ltd., Germany). The PCEs were prepared in deionized water to a concentration of 2.0%. Aqueous 1 mol/L sodium nitrate ($NaNO_3$) solution was used as a washout solution at a flow rate of 1.0 mL/min with 40 °C column temperature.

2.3.2 The fluidity of cement paste

The fluidity of the cement paste containing PCEs was measured according to Chinese national standards GB/T 8077-2012. The water-to-cement ratio (w/c) of the cement paste was 0.29. The dosage of PCEs was 0.1%, which was calculated as the ratio of the solid mass of PCEs to the mass of cement.

3. Results and discussion

3.1 Types and dosages of initiators

To compare the initiation effect of the H_2O_2 and APS on two different macromonomers, HPEG and IPEG, separate synthetic experiments were carried out in this study. The dosages of H_2O_2 were 0.8%, 1.0% and 1.2%, respectively. The dosages of APS were 0.6%, 0.8% and 1.0%, respectively. Further, the dosage of chain transfer agent, MPA is 0.35%. The characteristics of PCEs measured by GPC are displayed in Table 2. The GPC results show that when the initiator is H_2O_2 , the conversion rates of IPEG-PCE are over 88%, which is higher than that of HPEG-PCE. The initiation effect of H_2O_2 on IPEG is significantly better than

that on HPEG. When APS is the initiator, the conversion rates of both monomers reach 90%. The results demonstrated that APS is suitable to initiate IPEG and HPEG.

Table 2 The GPC results of PCEs

| PCE | Types and dosages of initiators | Dosages of initiators (%) | PDI | Conversion rate (%) |
|-----------|---------------------------------|---------------------------|------|---------------------|
| HPEG-PCEs | H_2O_2 -VC | 0.8 | 1.61 | 82.38 |
| | | 1.0 | 1.61 | 82.38 |
| | | 1.2 | 1.60 | 84.15 |
| | APS-VC | 0.6 | 1.79 | 89.31 |
| | | 0.8 | 1.80 | 91.79 |
| | | 1.2 | 1.82 | 93.20 |
| IPEG-PCEs | H_2O_2 -VC | 0.8 | 1.77 | 90.06 |
| | | 1.0 | 1.78 | 91.19 |
| | | 1.2 | 1.71 | 88.84 |
| | APS-VC | 0.6 | 1.80 | 90.42 |
| | | 0.8 | 1.77 | 90.49 |
| | | 1.0 | 1.87 | 89.90 |

Fig.1 shows the fluidity loss of cement pastes with PCEs as a function of time. The fluidity of all pastes increases first and then decreases with time prolonged. The cement pastes with HPEG-PCEs synthesized by H_2O_2 show considerably lower fluidity than that synthesized by APS. Whereas, the initial fluidity and fluidity retention of IPEG-PCEs synthesized with H_2O_2 are better than that synthesized with APS. In terms of fluidity, the optimum dosage of H_2O_2 is 1.0% and the optimum dosage of APS is 0.6%, which were used in the subsequent tests.

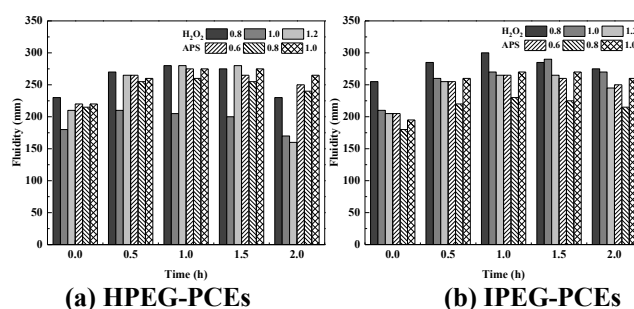


Fig.1 Fluidity of cement pastes with HPEG/IPEG PCEs synthesized by different initiators

3.2 Dosages of MPA

Table 3 The GPC results of PCEs

| PCE | Types and dosages of initiators | Dosages of MPA (%) | PDI | Conversion rate (%) |
|-----------|---------------------------------|--------------------|------|---------------------|
| HPEG-PCEs | H_2O_2 -VC | 0.30 | 1.65 | 84.05 |
| | | 0.35 | 1.61 | 82.38 |
| | | 0.40 | 1.82 | 62.55 |
| | APS-VC | 0.30 | 1.83 | 90.21 |
| | | 0.35 | 1.79 | 89.31 |
| | | 0.40 | 1.78 | 90.01 |
| IPEG-PCEs | H_2O_2 -VC | 0.30 | 2.28 | 70.00 |
| | | 0.35 | 1.78 | 91.19 |
| | | 0.40 | 2.37 | 73.94 |
| | APS-VC | 0.30 | 1.91 | 90.28 |
| | | 0.35 | 1.87 | 89.80 |
| | | 0.40 | 1.75 | 89.71 |

The amount of MPA was 0.30%, 0.35% and 0.40% respectively for the synthesis of PCEs with other factors constant. The GPC results of PCEs synthesized with different amounts of MPA and the paste fluidity are shown in Table 3 and Fig.2, respectively. When H_2O_2 -VC is used as the initiator, variations in MPA dosage for both HPEG-PCEs and IPEG-PCEs resulted in a significant decrease in the conversion rate. One of the GPC spectrums of IPEG-PCEs initiated by H_2O_2 -VC was shown in Fig.3. When the MPA dosage increases from 0.3% to 0.35%, a shoulder peak appears just before the main peak (at 6 min) with a relative molecular

mass of 330,000 g/mol. Adding the shoulder area to the main peak area leads to a conversion rate of about 90%. However, compared to TPEG-PCEs with MPA = 0.35%, the fluidity of cement pastes blended with TPEG-PCEs with MPA dosages of 0.30% or 0.40% (Fig.2) was significantly lower, with a fluidity of only 170 mm at 0 h and about 150 mm at 2 h. When MPA overdoses, the side chain density of PCE generated at the beginning of the reaction is high, giving the PCE an inhomogeneous structural sequence (Li et al, 2019). This large molecular weight of IPEG-PCE with an inhomogeneous side chain density didn't have a dispersion function. Thus, the optimum MPA dosage is 0.35% of the total mass of the monomer.

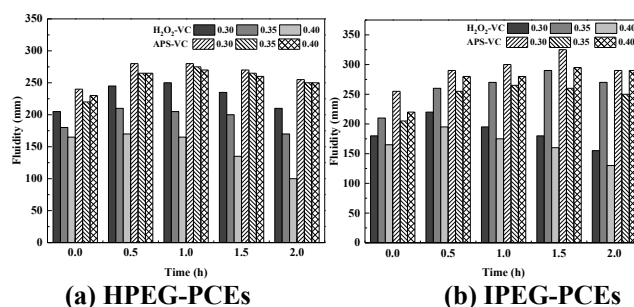


Fig.2 Fluidity of cement pastes with HPEG/IPEG PCEs synthesized by different amounts of MPA

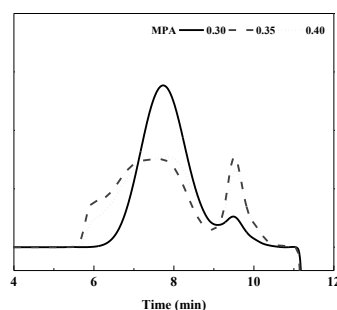


Fig.3 GPC spectra of IPEG-PCEs at different MPA dosages (the initiator is H₂O₂-VC)

4. Conclusion

The main conclusions of the present research were summarized as follows: The initiation effect of the APS was better than H₂O₂, and the performance of PCE synthesized by APS was stable and excellent. Increasing the amount of initiator is conducive to increasing the conversion rate of macromonomer while increasing the PDI of the product. As APS is more adaptable to temperature changes when APS is used as an initiator, the synthesis temperature can be appropriately lowered to reduce energy consumption. The mismatch of the initiator-reduction system and chain transfer agent has a great influence on the synthesis effect and is the primary reason for the appearance of shoulder peaks.

References

- Jiang, Z., You, R., Fang, Y., Guo, Y., & Lin, T. (2022). Effect of reaction time on properties of TPEG type polycarboxylate superplasticizer. *Journal of Physics: Conference Series*, 2194(1), 012017. <https://doi.org/10.1088/1742-6596/2194/1/012017>
- Lei, L., Zhang, Y., & Li, R. (2021). Specific molecular design of polycarboxylate polymers exhibiting optimal compatibility with clay contaminants in concrete. *Cement and Concrete Research*, 147, 106504. <https://doi.org/10.1016/j.cemconres.2021.106504>
- Li, H., Yao, Y., & Wang, Z. (2019). Influence of molecular mass of isoprenyloxy polyethylene glycol on monomer sequence in polycarboxylate superplasticizers. *Journal of The Chinese Ceramic Society*, 47(2), 201–206. <https://doi.org/10.14062/j.issn.0454-5648.2019.02.07>. (in Chinese)
- Shui, L., Yang, H., Sun, Z., He, Y., & Zeng, W. (2020). Research progress on working mechanism of polycarboxylate superplasticizer. *Journal of Building Materials*, 23(1), 64-69+76. (in Chinese)
- Zhong, D., Liu, Q., & Zheng, D. (2022). Synthesis of lignin-grafted polycarboxylate superplasticizer and the dispersion performance in the cement paste. *Colloids and Surfaces A: Physicochemical and Engineering Aspects*, 642, 128689. <https://doi.org/10.1016/j.colsurfa.2022.128689>

Influence of retarders on the hydration and rheology of calcium sulfo aluminate cement

M.K. Mohan^{1*}, A.V. Rahul², K. Van Tittelboom³, and G. De Schutter⁴

¹ Magnel-Vandepitte Laboratory, Department of Structural Engineering and Building Materials, Ghent University, Ghent, Belgium

Email: Manu.KurungodMohan@ugent.be

² Department of Civil and Environmental Engineering, Indian Institute of Technology Tirupati, Tirupati, India

Email: rahulav@iittp.ac.in

³ Magnel-Vandepitte Laboratory, Department of Structural Engineering and Building Materials, Ghent University, Ghent, Belgium

Email: Kim.VanTittelboom@UGent.be

⁴ Magnel-Vandepitte Laboratory, Department of Structural Engineering and Building Materials, Ghent University, Ghent, Belgium

Email: Geert.DeSchutter@ugent.be

ABSTRACT

Calcium sulfoaluminate (CSA) cement is a low-CO₂ footprint alternative for Portland cement (PC). The hydration of CSA cement is significantly faster than the hydration of PC; therefore, for practical applications, retarders are necessary. In the present study, the hydration characteristics of CSA cement were studied with three different retarders, i.e., borax, citric acid, and tartrate, using setting time measurements. The influence of these retarders on the structural build-up was assessed based on the evolution of storage modulus using small angle oscillatory shear tests with respect to time. Also, the effect of the retarders on the yield stress and viscosity of the cement pastes was investigated by fitting the flow curve to the Bingham model. In the presence of borax, the hydration of CSA gets delayed, and there exists a period of very low thermal activity (induction period), after which the hydration reinitiates. On the other hand, in the presence of citric acid and tartrate, the hydration is delayed without having a distinct induction period but with a constant lowered thermal activity. The growth of the storage modulus gives an indication of the stiffness evolution and the trends were similar to those observed from setting time measurements. The cement paste with borax has shown the highest yield stress and plastic viscosity, which can be due to the formation of the poorly crystalline calcium borate.

KEYWORDS: *Calcium sulfoaluminate cement, retarder, rheology, storage modulus, yield stress.*

1. Introduction

CSA cement can reduce the environmental impact as its production emits almost 50% less CO₂ due to the lower kiln temperature and lower energy demand for the grinding process (Gartner (2004)). CSA cement hydrates much more rapidly compared to PC due to the major phase present in CSA cement called ye'elimite. Also, it is difficult to control the hydration of CSA cement with gypsum addition as the hydration of ye'elimite gets accelerated in the presence of gypsum or other sulfate sources. One of the most promising ways to control the hydration of CSA cement is to use a suitable retarder and thereby achieving a workability window for the mixtures with CSA cement (Mohan et al. (2021a, 2022)).

The rheological behaviour of CSA cement pastes is different from PC pastes. It was reported that CSA cement paste has a higher viscosity compared to PC paste with the same water-to-cement ratio (Chen et al. (2020); Mohan et al. (2021a)). In this paper, the hydration and rheological behaviour of CSA cement pastes in the presence of different types of retarders are studied.

2. Materials and methods

Commercial calcium sulfoaluminate (CSA) cement (i.tech ALI CEM GREEN® by Italcementi) was used. The Blaine area of CSA cement was 408 m²/kg and the specific gravity amounted to 3.15. Three different types of retarders, di-sodium tetraborate decahydrate (labeled as B, Na₂B₄O₇·10H₂O), citric acid (labeled as C), tartrate (labeled as T, KNaC₄H₄O₆·4H₂O) in powder form were used to control the hydration reaction. CSA cement pastes were prepared with a water-to-cement ratio of 0.4 and with a constant retarder dosage of 0.1% by weight of the cement. The pastes were prepared by using a high-shear mixer and mixed for about 2 minutes. All the experiments were started 5 minutes after the CSA cement came in contact with water.

The initial and the final setting times of the CSA pastes were measured by an automatic Vicat apparatus according to EN 196-3:2007 (EN 196-3 2007). The penetration depth of the Vicat needle was measured every 30 seconds under the controlled temperature of 20 °C at 65% RH. The initial setting time was determined by the elapsed time from the first contact of CSA cement with water to the time at which the distance between the needle and the base plate is (6 ± 3 mm). The final setting time was determined by the time at which the needle first penetrated only 0.5 mm into the sample.

Rheological measurements were carried out using an MCR 52 rheometer attached with a six-blade vane (radius = 11 mm and height = 16 mm) and a cylindrical cup (radius = 13.8 mm and depth = 75 mm). The temperature was kept constant at 20 ± 0.5 °C during the rheological measurements and each mixture was tested three times to check the reproducibility of the results obtained. A plastic lid was used during the rheological measurements to minimize the influence of evaporation on the test results. The presented curves are representative curves for each mixture. The experimental protocol consisted of pre-shearing at 100 rpm for 30 s, followed by a resting period of 30 s. Then, the rotational speed of the vane was increased to 100 rpm from 0 rpm in steps of 20 rpm. At each step, the shearing was continued for 20 seconds, which was enough to achieve the steady state of the tested cement pastes. The strain rates corresponding to each rotational speed were computed after applying a suitable plug flow correction as outlined in (Mohan et al. (2021b)). Small angle oscillatory shear (SAOS) tests were carried out to measure the structural build-up of the CSA cement pastes. Initially, strain-sweep tests were carried out with strain amplitudes varying from 0.0001% to 10% and a constant frequency of 1 Hz. This was done to determine the linear visco-elastic (LVE) region of the cement pastes. Then, time sweep experiments were carried out at a constant frequency of 1 Hz and constant strain amplitude of 0.005% (within LVE) (Yuan et al. (2017)).

3. Results and discussions

3.1 Hydration characteristics

Table 1 shows the initial and final setting times of the different mixtures. It can be seen that the addition of retarders increases both the initial and final setting times of the CSA cement pastes. Borax increases the setting time to the maximum extent out of all the retarders tested. In the presence of borax, once the initial dissolution of ye'elimite starts, dissolved boron and sodium ions from the borax seize the release of calcium ions from the ye'elimite. This results in the formation of the crystallized phase called ulexite that grows on the surface of ye'elimite. This foil-like ulexite phase further inhibits the hydration of ye'elimite and results in retardation (Champenois et al. (2015); Mohan et al. (2021a, 2022)). When citric acid is added to the CSA cement paste, it adsorbs onto the surface of the cement grains and then delays the dissolution of cement grains. Later, the sequestration of Ca²⁺ from the solution due to the complexation between ions and citric acid inhibits the generation of ettringite (Burris and Kurtis (2018); Zou et al. (2020)). Tartrate directly adsorbs onto the surface of hydrating C₃A and blocks its reaction with water. Dissolution of calcium by extraction with tartaric acid (exposing the residual aluminium) was followed by precipitation of a layered calcium tartrate that binds to the surface of the C₃A grains, inhibiting further hydration. Also, it was reported that tartrate inhibits ettringite nucleation and growth (Bishop and Barron (2006); Cody et al. (2004); Zajac et al. (2016)).

Table 1: Initial and final setting time of the CSA pastes with retarders

| Mixture | Initial setting time (min) | Final setting time (min) |
|---------|----------------------------|--------------------------|
| CSA | 10 | 21 |
| CSA-1%B | 41 | 93 |
| CSA-1%C | 24 | 62 |
| CSA-1%T | 30 | 76 |

3.2 Rheological behaviour

Figure 1 (a) shows the flow curve and the Bingham model fit. The dynamic yield stress and plastic viscosity were determined from the Bingham model fit and are shown in columns 2 and 3 of Table 2. It can be noticed that with the addition of retarders, the yield stress and viscosity of the pastes reduce significantly. CSA cement paste with citric acid exhibited the lowest yield stress and plastic viscosity. CSA pastes with borax and tartrate show similar yield stress values; however, the CSA-1%T had lower viscosity. At the same time, CSA paste with borax exhibited the highest yield stress and plastic viscosity among all other retarders tested. The high yield stress could be attributed to the precipitation of poorly crystalline calcium borate phases in borated CSA paste (Champenois et al. 2013).

Figure 1(b) shows the evolution of the storage modulus of the CSA cement pastes at a very early age. It can be noticed that the pure CSA paste had a very rapid evolution of the storage modulus compared to the pastes with retarders. On the other hand, the growth of the storage modulus of the CSA pastes with retarders was found to be rather slow and followed a linear trend; which was also observed by other researchers for calcium aluminate cement (Das et al. (2022)). The initial storage modulus values of the pastes are given in column 4 of Table 2. Pure CSA cement paste had the highest storage modulus and paste with citric acid had the lowest initial storage modulus.

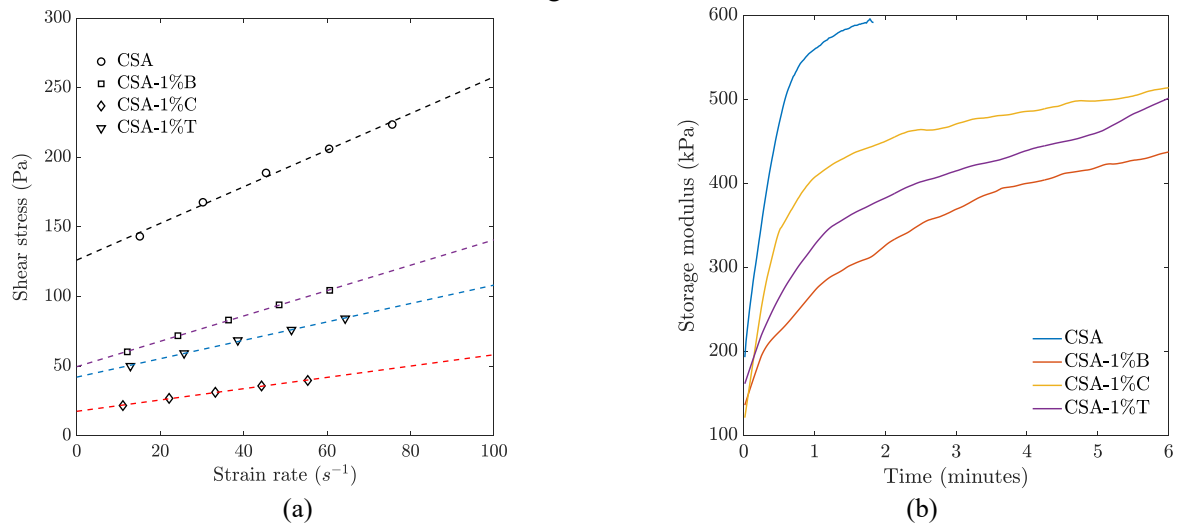


Figure 1: (a) Flow curve and the Bingham model fit (b) evolution of storage modulus

Table 2: Rheological parameters of the CSA cement pastes with retarders

| Mixture | Dynamic yield stress (Pa) | Viscosity (Pa.s) | Storage modulus (kPa) |
|---------|---------------------------|------------------|-----------------------|
| CSA | 126.14 | 1.32 | 193.0 |
| CSA-1%B | 49.58 | 0.91 | 135.9 |
| CSA-1%C | 17.53 | 0.41 | 121.0 |
| CSA-1%T | 42.09 | 0.66 | 161.0 |

3. Conclusions

The present study focuses on the early age hydration and rheological behaviour of CSA cement pastes in the presence of three different retarding admixtures (borax, citric acid, and tartrate). The summary and main conclusions obtained from the study are as follows:

- From the setting time measurements, it was observed that the extent of retardation caused by the retarding admixtures is different at the same dosage and water-to-cement ratio. This is due to the strikingly different retardation mechanisms of these admixtures.
- From the rheological measurements, it can be noticed that the rheological behaviour of the CSA pastes containing retarders is different. The addition of all the retarders reduced the dynamic yield stress and plastic viscosity significantly. The lowest yield stress and viscosity were observed for CSA paste with citric acid. At the same time, borated CSA cement paste exhibited relatively higher yield stress and viscosity; which could be due to the presence of a poorly crystalline calcium borate phase.
- In the presence of the retarders, the evolution of the storage modulus is slower and follows a linear trend compared to the pure CSA paste.

References

- Bishop, M., and A. R. Barron. 2006. "Cement hydration inhibition with sucrose, tartaric acid, and lignosulfonate: Analytical and spectroscopic study." *Ind. Eng. Chem. Res.*, 45 (21): 7042–7049. American Chemical Society . <https://doi.org/10.1021/IE060806T/ASSET/IMAGES/MEDIUM/IE060806TE00004.GIF>.
- Burris, L. E., and K. E. Kurtis. 2018. "Influence of set retarding admixtures on calcium sulfoaluminate cement hydration and property development." *Cem. Concr. Res.*, 104: 105–113. Elsevier Ltd. <https://doi.org/10.1016/j.cemconres.2017.11.005>.
- Champernois, J. B., C. Cau Dit Coumes, A. Poulesquen, P. Le Bescop, and D. Damidot. 2013. "Beneficial use of a cell coupling rheometry, conductimetry, and calorimetry to investigate the early age hydration of calcium sulfoaluminate cement." *Rheol. Acta*, 52 (2): 177–187. <https://doi.org/10.1007/s00397-013-0675-9>.
- Champernois, J. B., M. Dhoury, C. Cau Dit Coumes, C. Mercier, B. Revel, P. Le Bescop, and D. Damidot. 2015. "Influence of sodium borate on the early age hydration of calcium sulfoaluminate cement." *Cem. Concr. Res.*, 70: 83–93. Elsevier Ltd. <https://doi.org/10.1016/j.cemconres.2014.12.010>.
- Chen, M., L. Li, J. Wang, Y. Huang, S. Wang, P. Zhao, L. Lu, and X. Cheng. 2020. "Rheological parameters and building time of 3D printing sulphoaluminate cement paste modified by retarder and diatomite." *Constr. Build. Mater.*, 234: 117391. Elsevier Ltd. <https://doi.org/10.1016/j.conbuildmat.2019.117391>.
- Cody, A. M., H. Lee, R. D. Cody, and P. G. Spry. 2004. "The effects of chemical environment on the nucleation, growth, and stability of ettringite $[\text{Ca}_3\text{Al}(\text{OH})_6]_2(\text{SO}_4)_3 \cdot 26\text{H}_2\text{O}$." *Cem. Concr. Res.*, 34 (5): 869–881. Pergamon. <https://doi.org/10.1016/j.cemconres.2003.10.023>.
- Das, A., L. Reiter, S. Mantellato, and R. J. Flatt. 2022. "Early-age rheology and hydration control of ternary binders for 3D printing applications." *Cem. Concr. Res.*, 162: 107004. Pergamon. <https://doi.org/10.1016/J.CEMCONRES.2022.107004>.
- EN 196-3. 2007. *Methods of testing cement - Part 3: Determination of setting times and soundness*. BSI Stand. Publ.
- Gartner, E. 2004. "Industrially interesting approaches to 'low-CO₂' cements." *Cem. Concr. Res.*, 34 (9): 1489–1498. Elsevier Ltd. <https://doi.org/10.1016/j.cemconres.2004.01.021>.
- Mohan, M. K., A. V. Rahul, G. De Schutter, and K. Van Tittelboom. 2021a. "Early age hydration, rheology and pumping characteristics of CSA cement-based 3D printable concrete." *Constr. Build. Mater.*, 275: 122136. Elsevier. <https://doi.org/10.1016/j.conbuildmat.2020.122136>.
- Mohan, M. K., A. V. Rahul, Y. Tao, G. De Schutter, and K. Van Tittelboom. 2022. "Hydration re-initiation of borated CSA systems with a two-stage mixing process: An application in extrusion-based concrete 3D printing." *Cem. Concr. Res.*, 159: 106870. Pergamon. <https://doi.org/10.1016/j.cemconres.2022.106870>.
- Mohan, M. K., A. V. Rahul, K. Van Tittelboom, and G. De Schutter. 2021b. "Rheological and pumping behaviour of 3D printable cementitious materials with varying aggregate content." *Cem. Concr. Res.*, 139. <https://doi.org/10.1016/j.cemconres.2020.106258>.
- Yuan, Q., X. Lu, K. H. Khayat, D. Feys, and C. Shi. 2017. "Small amplitude oscillatory shear technique to evaluate structural build-up of cement paste." *Mater. Struct. Constr.*, 50 (2): 1–12. Kluwer Academic Publishers. <https://doi.org/10.1617/s11527-016-0978-2>.
- Zajac, M., J. Skocek, F. Bullerjahn, and M. Ben Haha. 2016. "Effect of retarders on the early hydration of calcium-sulphoaluminate (CSA) type cements." *Cem. Concr. Res.*, 84: 62–75. Elsevier Ltd. <https://doi.org/10.1016/j.cemconres.2016.02.014>.
- Zou, D., Z. Zhang, and D. Wang. 2020. "Influence of citric acid and sodium gluconate on hydration of calcium sulfoaluminate cement at various temperatures." *Constr. Build. Mater.*, 263: 120247. Elsevier. <https://doi.org/10.1016/J.CONBUILDMAT.2020.120247>.

Pore structure of polymer-modified dry mix tile adhesive mortars

M. Kupiński^{1*}, Ł. Kotwica²

¹ Henkel Polska Sp. z o.o., Stąporków, Poland

Email: marcin.kupinski@henkel.com

² AGH University of Science and Technology, Kraków, Poland

Email: lkotwica@agh.edu.pl

ABSTRACT

Organic admixtures are used to alter the properties of cementitious mortars' properties. As they usually are or contain surfactants, a large number of air bubbles can be introduced, having a major impact on the mix performance in the fresh as well as in the hardened state. The air entraining and stabilization process can be influenced by a variety of factors, such as the pH of the pore solution, the presence of certain ions in the solution, surface charges on the grains of cement, or interference of different additives present in the mix. Thus, designing the pore structure and resulting properties of the mortar creates a significant technological challenge.

In this paper, we are focusing on the combined air-entraining action of methylcellulose and redispersible polymer powder (copolymer of vinyl acetate and ethylene) on the mortars based on Portland Cement (PC), and binary blend of Calcium Sulfoaluminate Cement (CSA) and Calcium Sulfate (CS). An attempt to determine the pore structure of fresh mix was made, using the Air Void Analyzer (AVA), yet it failed due to the gelation of cellulose ether in contact with the air-release liquid (glycerin) necessary in this technique. Instead, the porosity of the hardened mortars was quantified by image analysis of the high-resolution scans of the samples.

Significant differences in the introduced air pore size distribution were found, depending on the binder system used. The porosity of CSA-based mortars is finer than those of OPC-based mortars. Such materials also show a higher content of pores below 300 µm of equivalent diameter. The reasons behind such behavior remain unclear, which proves the high complexity of the topic.

KEYWORDS: *Cellulose ether, redispersable polymer powder, mortar, aeration, pore structure*

1. Introduction

The polymer modification of cementitious mortars is widely used in the dry mix industry. The most common additives are cellulose ethers (CE), providing beneficial rheological properties, the cohesion of the mortar, and water retention, resulting in a prolonged open time after application. These are often combined with redispersible polymer powders (RDP), increasing the adhesion strength to difficult substrates and the flexibility of the products. It is nearly impossible to formulate modern dry mix mortar without such additives, yet the presence of both dramatically alters the microstructure of the hardened product and has a pronounced effect on the mechanical parameters and durability.

As organic additives contain or are surfactants, a large amount of air is introduced during mortar mixing and is further stabilised into a hardened material. Details of the porosity formation over time of setting and hardening of Ordinary Portland Cement (OPC) pastes were investigated by Pourchez et al (2010). It was stated that the resulting aeration structure depends on the CE chemistry, acting mainly on the capillary pores range (around 500 nm) and air voids range (50 – 250 µm). The hypothesis was presented that both ranges impact the transport of water and permeability, hence the durability of hardened mortar is affected. The claim was supported by the earlier work of Malatrait (1992), which showed that CE stabilises the pore network consisting of large air voids connected by large capillaries (<1 µm). In contrast, Wyrzykowski et

al. (2014) found that the effect of CE on the Portland cement mortar matrix is negligible and only air voids $> 10 \mu\text{m}$ can be varied with CE additions. The study referred to tile adhesive mortars and was limited to ethers of a specific degree of substitution of hydroxyl groups substitution degree ($\text{DS}=1,87$) without the presence of any redispersible polymer powder. Silva et al (2001) found the resulting pore structure of such mortars is a function of the interaction between cellulose ether and RDP. The especially strong impact of EVA (copolymer of vinyl acetate and ethylene) was noted at high dosages (up to 20%).

2. The aim of the study

Interestingly, little research has been found on the pore structure of polymer-modified mortars in binder systems other than OPC. However, the practice shows, that i.e. tile adhesive mortars formulated on: (OPC) solely, binary blend of Calcium Sulfoaluminate cement (CSA) and Calcium Sulfate (CS) or a ternary blend of PC, CS and Calcium Aluminate Cement (CAC) vary in durability, especially in case of resistance against water immersion as well as following freezing and thawing cycles. The exemplary results are shown in Table 1.

Table 1. The adhesion strength of tile adhesive mortars after various storage conditions acc, to EN 12004.

| Storage conditions | OPC - based | CSA - based |
|---|-------------|-------------|
| Adhesion after 28 days of ambient storage [N/mm^2] | 2,1 | 2,3 |
| Adhesion after water storage [N/mm^2] | 1,4 | 0,6 |
| Adhesion after freeze/thaw cycles [N/mm^2] | 1,7 | 1,1 |

The presented study aims to verify whether differences in water and freeze/thaw resistance of tile adhesives based on various binders can be explained by differences in their pore structure.

3. Materials and methods

Two simple tile adhesive mortars were prepared. Organic additives amount and type: copolymer of vinyl acetate and ethylene (EVA) re-dispersible polymer powder (in the form of free flowing powder of MFFT = 1°C , bulk density = 520 kg/m^3 and ash content after heating up to 1000°C = 13%, protective colloid: polyvinyl alcohol (PVA)) and pure methylcellulose (Brookfield viscosity of 2% solution, RVT 20rpm = 40 000 mPas) – were kept the same for each mortar. The mineral binder content was always scaled to 40% - while its composition has been varied from pure portland cement (OPC) CEM I 52,5 R to a binary blend of Calcium Sulfoaluminate Clinker (CSA) and Calcium Sulfate (CS) in a proportion of 80:20. The mix proportions and basic physical properties are given in Table 2.

All samples were prepared by blending 5 kg of material for 5 minutes in a powder mixer with a mixing speed of 340 rpm. The mortars were then mixed with water with a steel mixing paddle with a drill in 3 steps: 1 min of mixing, 3 min break, and 30 seconds of mixing to ensure sufficient maturation time for the dissolution of organic additives is provided.

The air content and density of the fresh mix were measured according to the PN-EN 1015-7:2000 (air pressure method). Then $40 \times 40 \times 160 \text{ mm}$ mortar prisms were prepared according to PN-EN 196-1:2016-07. After 14 days of curing, the prisms were cut into slices with the precise low-speed diamond saw. Further preparatory work corresponds to the procedure described in PN-EN 480-11:2008. Polishing with fine sandpaper of two different gradations: #800 and #1000 was carefully performed with the use of a Struers LaboPol-20 polisher. Difficulties to do so were noted – due to the high porosity of the the samples and the weakening of mineral microstructure by the presence of polymer additives.

Table 2. Compositions of the mortars tested.

| | TA 1 (OPC) | TA 2 (CSA) |
|------------------------------|--------------|--------------|
| OPC CEM I 52.5 R [%] | 40,0 | |
| CSA clinker [%] | | 24,0 |
| Calcium Aluminate Cement [%] | | |
| Natural Anhydrite [%] | | 16,0 |
| EVA polymer powder [%] | 2,0 | 2,0 |
| Methylcellulose [%] | 0,5 | 0,5 |
| Washed sand 0,1-0,5 mm [%] | 55,5 | 57,5 |
| | | |
| Total [%] | 100,0 | 100,0 |
| | | |
| Water [% of dry powder] | 25,0 | 25,0 |
| W/C [-] | 0,625 | 0,625 |
| | | |
| Air content [%] | 26% | 27% |
| Density [kg/m^3] | 1540 | 1490 |

The cross sections obtained (6 samples of TA1 and 7 samples of TA2) were coloured with black marker and the air voids were filled with zinc paste. Such prepared samples were scanned with the office scanner (Epson Perfection V19) in the 9600 dpi resolution, given the smallest analysed pores (equivalent diameter of 15 μm) are covered by at least 25 pixels. The images were then analysed with ImageJ software and air void area distribution was collected. The surface area analysed was always between 900 and 1000 mm^2 (56-63% of the sample cross-sectional area).

An attempt to measure the size distribution of air voids in fresh mortar was made with the AVA 3000 apparatus (Germann Instruments).

4. Results

An attempt has been made to investigate the pore size distribution in mortars with the air-void analysis method. It was found that the mortar increases its consistency dramatically immediately after contact with the air-release liquid: glycerol. As this led to further miscibility problems and air entrapment in the sample, it was not possible to obtain reliable results. It is assumed that the gelation of methylcellulose occurred since glycerol decreases the gelation temperature. In the example, for the binary mixture of 0.5 glycerol volume ratio, the gelation point of methylcellulose decreases from 57°C to 37°C - Kuang et al. (2006). Given the 20 cm^3 of mortar was dissolved in 180 cm^3 of release liquid, the obtained glycerol volume ratio was >1000. In this conditions, further decrease of the gelation point of cellulose ether below room temperature is suspected.

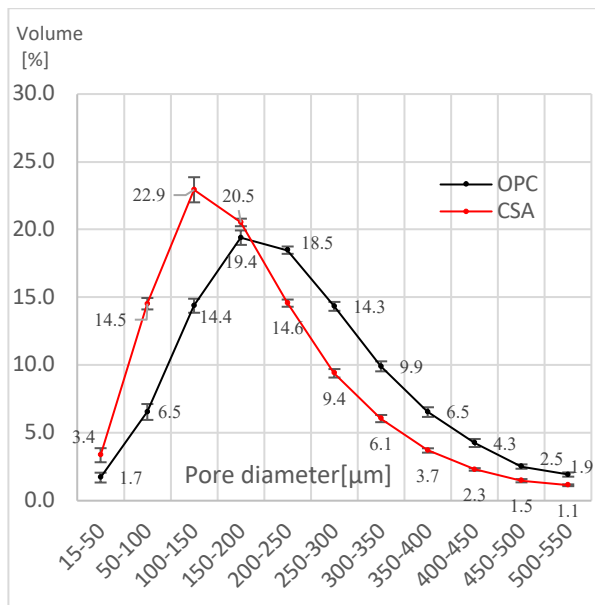


Figure 1. Pore size distributions as a function of pore size diameters. Error bars represent confidence intervals ($\alpha=0.05$).

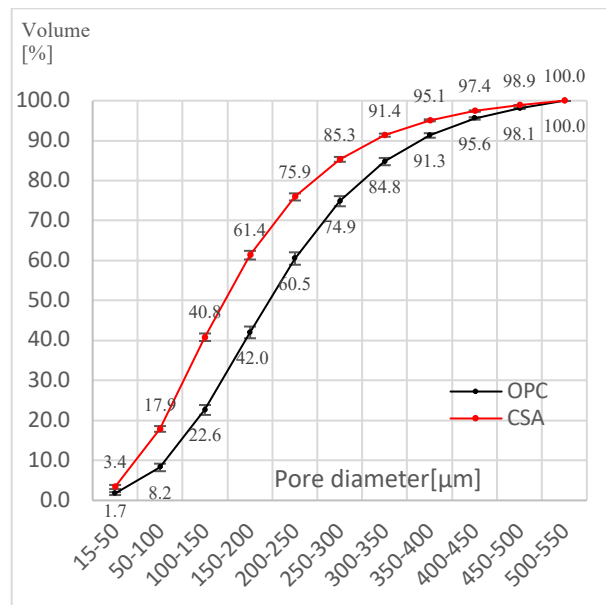


Figure 2. Cumulative distribution of pore volume. The error bars represent confidence intervals ($\alpha=0.05$).

Figure 1. presents the results of the air void size distribution measured by polished cross-section image analysis. Significant differences were found depending on the binder system used. The porosity of mortars based on the CSA-CS mixture is characterized by finer pores than the one based on OPC. The highest differences between samples are observed in the ranges of 50-100 μm (123% higher volume in TA2) and 100-150 μm (59% higher volume in TA2). The range of 100-150 μm of equivalent diameter also creates the largest volume of porosity in TA2: 22,9% whereas such a maximum in TA1: 19,4% places in the range of 150-200 μm of equivalent diameter. The observation finds its reflection in cumulative pore volume distribution (figure 2.). It is generally shifted towards smaller pores in TA2, where 85,2% of porosity has an equivalent diameter below 300 μm . For the sample TA1, the volume share of such pores is significantly smaller: 74,9%.

5. Discussion

As the results of the pore structure measurements by image analysis strongly depend on sample preparation, it is crucial to ensure the reproducibility of obtained results, especially given the difficulties encountered during the polishing of the mortar slices. Therefore, values of the confidence interval assuming the t-student distribution were calculated. For all data points, satisfactory accuracy was achieved proving the significance of the the measurements. The values of confidence intervals ($\alpha=0.05$) are graphically represented in figures 1. and 2. as error bars.

The porosity of CSA-based mortar seems to favour a higher freeze/thaw resistance than OPC-based mortars due to the higher volume of smaller pores. This remains in contradiction with empirically obtained results, showing the decrease of adhesion strength after water immersion of 74% and 52% after freeze/thaw cycles compared to the storage under lab conditions, while for OPC-based mortars these are 33% and 19% respectively. Therefore, the reasons for these differences in the mechanism of adhesion strength drops remain unclear.

Jenni et al. (2006) investigated the decrease of the adhesion strength after water storage of OPC systems. The authors concluded that the polymer matrix coexisting with a mineral one is prone to water attack because of its water solubility. It was also proven that organic admixtures can migrate, segregate, and accumulate in certain parts of the microstructure - (De Gasparo et al. (2009) – which may lead to the presence of weak spots in the mortar body. Therefore, it is likely that the water transport mechanism plays an important role in shaping the durability of such systems, and it is advisable to follow up the presented study with the comparison of the capillary porosity of the investigated samples.

6. Conclusions

The aim of the study was to find whether differences in the distributions of pore sizes are responsible for differences in the resistance to water and freeze/thaw cycles of tile adhesive mortars based on different binders. Air void distributions were successfully measured by image analysis of polished mortars' cross sections. When CSA is used as a binder, significantly finer porosity is achieved and a higher volume (85,3%) of a pore diameter below 300 μm is observed compared to OPC-based mortar (74,9%). This suggests superior freeze/thaw resistance of CSA-based adhesive, which is in contradiction with empirical data. Thus, durability differences cannot be explained by the pore size distributions in the tested area (15-550 μm). New light could be shed on the topic if pores below 15 μm were analyzed.

Acknowledgements

The research presented in the paper was financed by Henkel's International Innovation Centre for Building Materials in Słupsk.

References

- De Gasparo, A., Herwegh, M., Zurbruggen, R., Scrivener, K. (2009) "Quantitative distribution patterns of additives in self-leveling flooring compounds (underlayments) as function of application, formulation and climatic conditions", *Cement and Concrete Research*, 39(4): 313-323.
- Jenni, A., Zurbruggen, R., Holzer, B. and Herwegh, M. (2006) "Changes in microstructures and physical properties of polymer-modified mortars during wet storage", *Cement and Concrete Research*, 36(1): 79-90
- Kuang, Q., Cheng, G., Zhao, J. and Li, Y. (2006) "Thermogelation Hydrogels of Methylcellulose and Glycerol-Methylcellulose Systems", *Journal of Applied Polymer Science*, 100(5): 4120-4126
- Malatrait, M. (1992) "Propriétés hydriques du mortier pour enduits de façades en relation avec sa structure poreuse, mise en oeuvre, durabilité" PhD thesis, *INP Toulouse University*
- Pourchez, J. Ruot, B., Debayle, J., Pourchez, E. and Grosseau, P. (2010) "Some aspects of cellulose ethers influence on water transport and porous structure of cement-based materials", *Cement and Concrete Research* 40: 242-252
- Silva, D.A., John, V.M., Ribeiro, J.L.D and Roman, H.R. (2001) "Pore size distribution of hydrated cement pastes modified with polymers", *Cement and Concrete Research*, 31(8): 1177-1184
- Wyrzykowski, M., Kieseewetter, R., Kaufmann, J., Baumann R. and Lura, P. (2014) „Pore structure of mortars with cellulose ether additions – Mercury intrusion porosimetry study”, *Cement & Concrete Composites*, 53: 25-34

Microscopic tracking of superplasticizer adsorption in alkali activated materials

D. Kosenko^{1*}, A. Wetzel¹, and B. Middendorf¹

¹ *Department of Structural Materials and Construction Chemistry, University of Kassel, Kassel, Germany*
Email: denis.kosenko@uni-kassel.de

ABSTRACT

The threat of the man-made climate change requires a significant reduction of the anthropogenic emission of greenhouse gases. Alkali activated materials (AAM) offer an alternative for the CO₂-intensive ordinary Portland cement (OPC) concrete but some chemical admixtures for high performance applications of AAM are still not effective. Important chemical admixtures are superplasticizers (SP) which increase the workability at low water to binder ratios. Their effectivity depends on the presence of cations and on the adsorption on binder particles. The SP have been linked to a fluorochrome to enable the tracking of the SPs by fluorescence microscopy *in situ*. The data has been correlated with indirect adsorption measurements. It has been shown that the used SP have an optimum point regarding their effectiveness and an increasing effectiveness relative to the adsorption at higher activator (e.g. KOH) concentrations. Moreover, it is clarified which raw material parameters have to be taken into account and which chemical structure of SP is beneficial for application in AAM.

KEYWORDS: *superplasticizers, alkali activated materials, confocal laser scanning microscopy*

1. Introduction

In alkali activated materials (AAM), the traditional Portland cement can be fully replaced by supplementary cementing materials (SCM). The AAM binder is also inorganic, like in ordinary Portland cement (OPC), but has lower hydraulicity compared to OPC. The precursors for AAM contain metastable aluminosilicate phases that react with an alkaline solution (called activator) to initiate hydration. AAMs have high mechanical resistance and durability due to their chemical composition. However, there is a lack of numerous admixtures for high-performance applications. Superplasticizers (SP) are an important type of admixture, particularly polycarboxylate ethers (PCE), which have proven to be highly effective in cementitious systems. The adsorption of superplasticizers on AAM binder particles has only been indirectly determined, for example, by measuring the total organic carbon (TOC) like shown for IPEG by Lei and Zhang (2021). A new method using fluorescence microscopy is being developed to visualize the adsorption of superplasticizers in a spatially resolved manner. A similar method has been used for cementitious systems by Arend et al. (2020), but the method has been further developed for AAM to be able to visualize even the smallest particle sizes.

2. Materials

2.1 Binders

The surfaces of the binders, represented by S_m , were determined using Blaine or BET, while particle size was measured using laser granulometry. Density was measured using helium pycnometry. The ground-granulated blast furnace slag (GGBFS, Holcim Germany), which has a S_m value of 3920 cm²/g, a density of $\rho = 2.9$ g/cm³ and a d_{50} value of 10.95 μ m. The fly ash used was obtained from BauMineral, Germany, and has a Blaine value of 2770 cm²/g, a density of $\rho = 2.3$ g/cm³ and a d_{50} value of 10.97 μ m. The used metakaolin (MK) Metastar 501 from Imerys, Germany, has a specific surface of 13.8 m²/g and a d_{50} value of 3.49 μ m. The used as silica fume (SF) 971 U from Elkem, Germany, has a specific surface of 20 m²/g, a density of $\rho = 2.2$ g/cm³, and a d_{50} value of 3.85 μ m.

2.2 Superplasticizer

The superplasticizer used in this study was acquired from Prof. Dr. Plank's group at the Department of Chemistry at TU Munich. It is an isoprenol ether-based PCE (IPEG) with an average chain length of 52 units of (-CH₂-CH₂-O-) and a ratio of 4.5 -COOH per side chain.

2.3 Staining reaction

To visualize the PCE in the fluorescence microscope, a coupling reaction was carried out. After the reaction, a fluorochrome, for example aminofluorescein (AmF), is covalently bound to a PCE molecule (1). The coupling reaction is shown in Figure 1. It can be seen how a reactive intermediate (3) is formed from the PCE with the carbodiimide (2), to which a primary aromatic amine can couple to obtain a fluorescent PCE-marker molecule (4). A urea species (5) occurs as a byproduct which can be separated from the desired product by dialysis due to the high molar mass difference to the PCE.

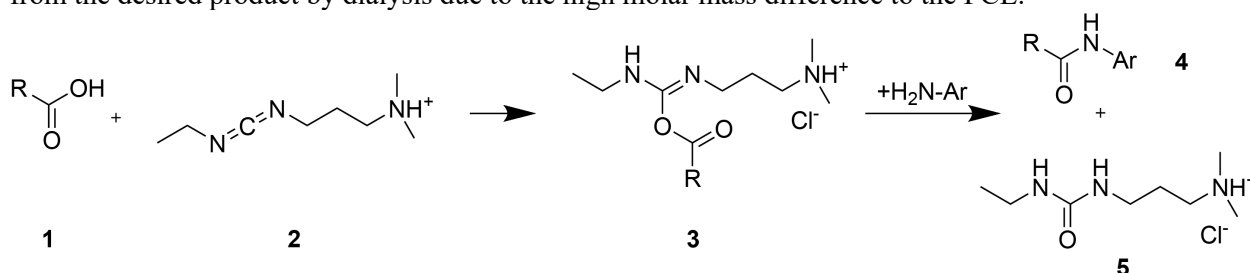


Figure 1: Coupling reaction of a fluorescent label to a PCE molecule.

2.3.1 Yield determination

With the aid of a detection reaction for primary aromatic compounds (Riqin et al., 2019), unreacted AmF could be detected in order to estimate the yield of the reaction. For this purpose, it is first diazotized (6) with NaNO₂ and reacted with *N*-(1-naphthyl)ethylenediamine (7) to obtain a strongly colored azo dye (8) as shown in Figure 2.

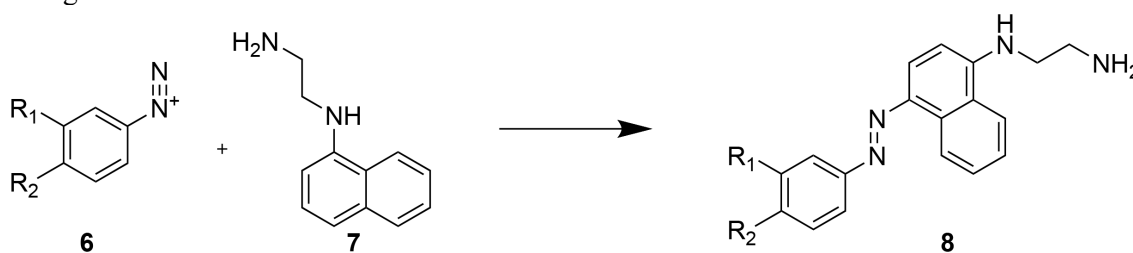


Figure 2: Azo-coupling of unreacted aminofluorescein.

2.4 Measurement setup

To be able to observe even the smallest range of the particles they were fixed in a solid layer. For this purpose, a thin fixation layer was applied to a glass substrate by spin coating and particles of the respective binder were deposited on it in an air stream. With the aid of a flow cell, the particles were brought into contact with the respective liquid, which contained the activator and PCE. A sketch of this setup is shown in Figure 3.

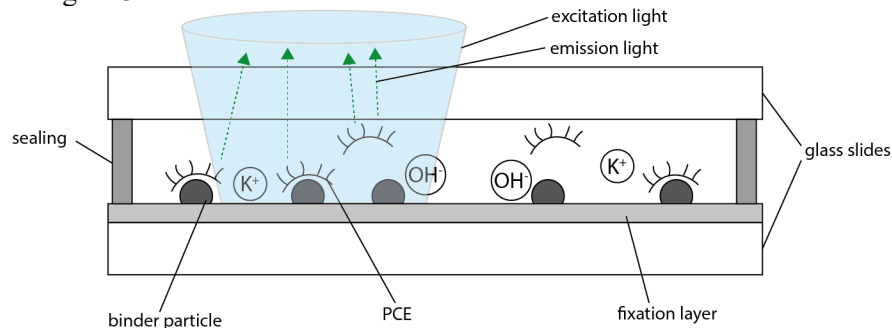


Figure 3: Cross section of fixed particles in activator solution with PCE.

Since the superplasticizer has been stained, its distribution can be viewed with spatial resolution using a fluorescence microscope or a confocal laser scanning microscope (CLSM). A stronger signal indicates a high adsorption of the superplasticizer.

Permanent preparations were made by mixing a paste of GGBFS at a w/b ratio of 1 with the respective proportion of superplasticizer for 20 min and centrifuging. The supernatant was discarded and the sediment was washed 3x with isopropanol and centrifuged again and decanted.

3. Results

As already shown by Arend et al (2020), coupling to a fluorochrome results in a shift of the absorption and emission spectra compared to an uncoupled blank sample. The spectra are shown in Figure 4.

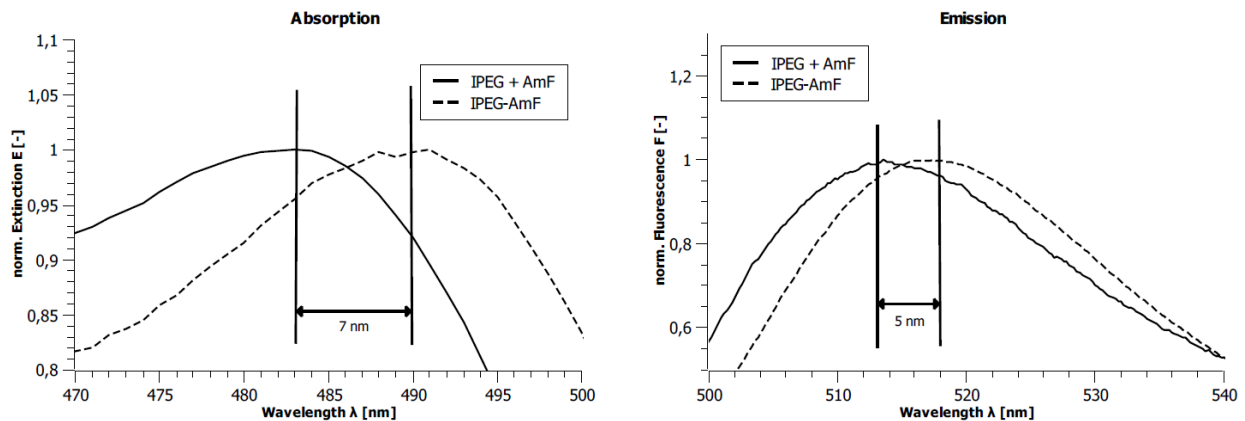


Figure 4: UV/Vis and photoluminescence spectra of stained IPEG PCE and its blind sample.

Shifts of 7 or 5 nm can be observed, as the pi-electron system of the aminofluorescein is slightly changed by coupling to a carboxy group. With the aid of absorption spectroscopy, the azo compound (section 2.3.1) could be detected at a wavelength of 550 nm. It was found that the yield of the staining reaction can have a maximum of up to 30 %.

The adsorption on inert quartz particles is very strong while other particles seem to be hardly occupied (Figure 5). The fluorescence image shown in false colors was recorded after an exposure time of 30 minutes while activator PCE solution was in the flow cell. The background fluorescence of the solution is clearly visible. After abundant rinsing of the solution and waiting for further 30 minutes, a relatively large amount of PCE is still detectable.

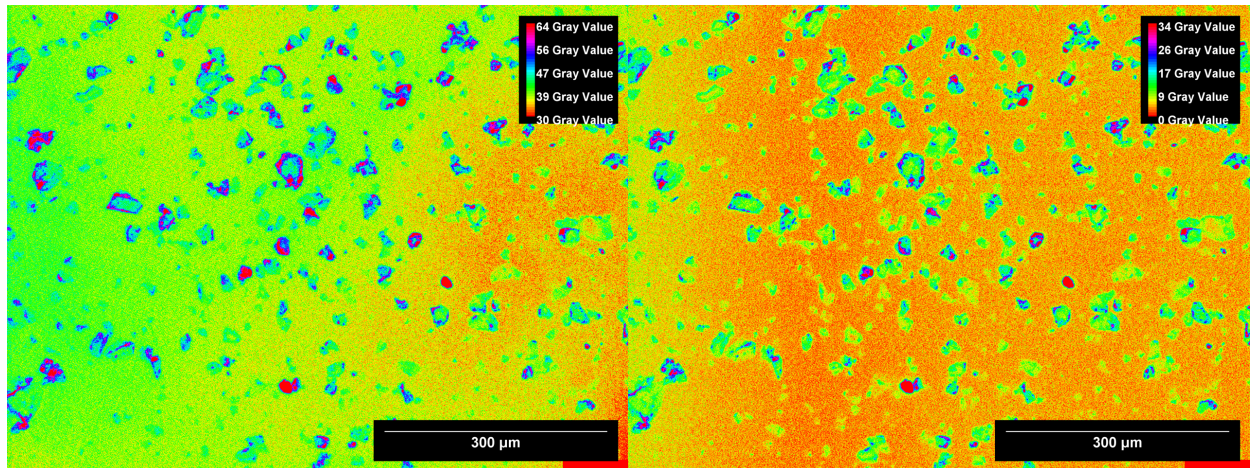


Figure 5: Fluorescence signal after 30 min exposure to solution (left) and after exposure to water for 30 min.

Inert particles were chosen to exclude the possibility of PCE molecules being incorporated into the material as a result of a hydration reaction. Thus, it can be shown that the desorption of PCE on a substrate after 30 minutes is very low. It was concluded that permanent preparations can be made by centrifugation that reflect *in situ* the distribution of superplasticizer within a GGBFS paste at a given time. Figure 6 shows the fluorescence image of a permanent specimen, the signal is clearly visible. By averaging the signal, a sorption isotherm corresponding to the langmuir type can be recorded. The signal can be calibrated using a second method (TOC) like shown in Figure 6.

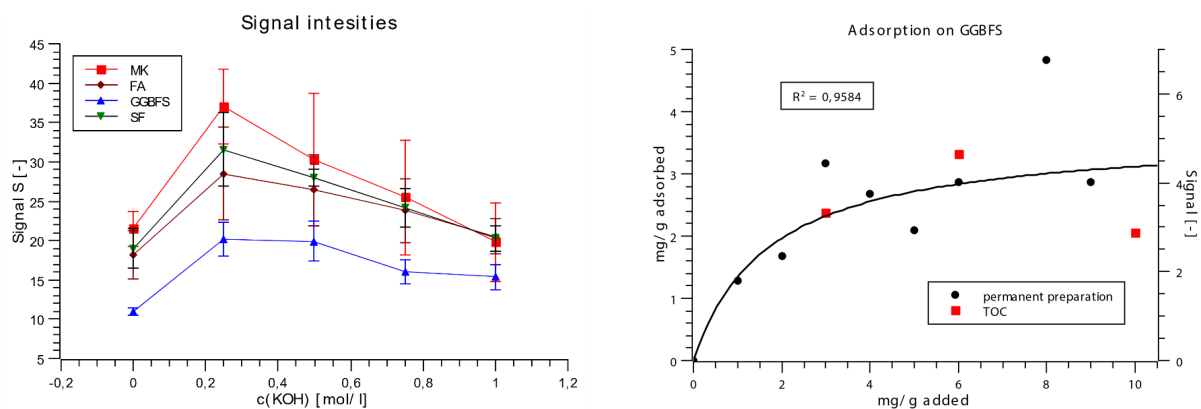


Figure 6: Adsorption on different binders (left) and sorption isotherm on slag (right).

Figure 6 also shows that the activator concentration has an optimum at which the adsorption is highest.

3. Conclusions

The investigations have shown adsorption dependency of PCE superplasticizers on the activator concentration. At low activator concentrations, adsorption can be increased. The desorption appears to be very slow, which can be used for the preparation of permanent preparations. A second method (TOC) allows a calibration of the fluorescence signal to quantify the adsorbed amount of PCE molecules.

References

- Arend, J., Wetzel, A. and Middendorf, B. (2020) "Fluorescence Microscopy of Superplasticizers in Cementitious Systems: Applications and Challenges", *Materials*, 13(17): 3733
- Lei, L. and Zhang, Y. (2021) "Preparation of isoprenol ether-based polycarboxylate superplasticizers with exceptional dispersing power in alkali-activated slag: Comparison with ordinary Portland cement", *Composites Part B: Engineering*, 223: 109077
- Riquin, L., Xingyi, H., Chunxia, D., Weitao, Y. and Xiaoyu, T. (2019) "A rapid colorimetric sensing unit for histamine content of mackerel using azo reagent", *Journal of Food Process Engineering*, 42(5): e13099

Influence of Kaolinite Content on the Fresh Properties of LC³ Systems

A. Satapathy^{1*}, and S. Bishnoi²

¹ Department of Civil Engineering, IIT Delhi, New Delhi, India
Email: satapathy.shrbd@gmail.com

² Department of Civil Engineering, IIT Delhi, New Delhi, India
Email: bishnoi@iitd.ac.in

ABSTRACT

In recent times, Limestone Calcined Clay Cement (LC³) has gained popularity worldwide due to its ability to achieve desirable mechanical and durability characteristics even at very low clinker factors. However, it has been observed that the workability of LC³ systems is severely affected due to the presence of calcined clay. This study intends to evaluate the effect of the kaolinite content of clays on the rheological behavior of LC³ concrete. For the purpose of the study, two calcined kaolinitic clays were procured – one of low grade (K1 – around 60% amorphous content) and the other one was a high-grade calcined clay (K2 – around 75% amorphous content). The clays were ground to comparable fineness and specific surface area values in order to isolate the effect of the calcined kaolinite content of the clays. The ground calcined clays were interblended with ground limestone, gypsum, and Ordinary Portland Cement (OPC) in a laboratory ball mill. The fresh concrete formulations were subjected to flow curve tests at a resting interval of every 30 minutes using a concrete rheometer. Additionally, the slump retention properties of all three concrete mixes were compared till a zero slump was obtained in any of them.

KEYWORDS: *Limestone Calcined Clay Cement (LC³), Rheology, Kaolinite Content, Slump retention, Concrete Rheometer*

1. Introduction

The recent advancement in the field of concrete technology includes the utilization of supplementary cementitious materials (SCMs) to enhance the strength and durability characteristics of concrete as well as reduce the construction cost and the carbon footprint. While fly ash and slag are the most common SCMs that have been used to produce blended cements and concrete mixes, the volume of generation of these industrial by-products is not adequate to meet the demands of cement production (Antoni et al. (2012)). Additionally, the availability of fly ash and slag is geographically constrained around the thermal power plants and steel industry, respectively. To this end, the Limestone Calcined Clay Cement (LC³) has emerged as a sustainable alternative to traditional Portland cement and other blended cements. The constituents of LC³ include, low-grade kaolinitic clay, which is abundantly available in the earth's crust and low-grade limestone rejected by cement industries. The clay with 40 - 60% kaolinite content is calcined at 750 - 800°C to convert the kaolinite into amorphous metakaolin while the limestone is simply ground and interblended with other constituents. A typical LC³ blend consists of 50% of clinker, 30% of calcined clay, 15% of limestone, and 5% of gypsum. It is the synergistic reactions between the metakaolin, the limestone and the cement hydration products as well as the reduced clinker content that give LC³ an edge over the other commercially available modern cements in terms of strength, refined pore structure, durability, lower cost, and lower carbon footprint. However, the use of LC³ also raises concerns of reduced workability and faster slump loss.

It has been reported that the calcined clay particles are known to have angular and flaky morphology which offers resistance to mixing (Cassagnabère et al. (2013)). The presence of a sheet-like

microstructure, high fineness, and a narrow range of particle size distribution further raises the water and the superplasticizer demand (Batis et al. (2005), Paiva et al. (2012), and Perlot et al. (2013)). This study intends to compare the slump loss and the rheological characteristics of LC³ systems produced using calcined clays with two different kaolinite contents with that of OPC concrete.

2. Materials and Methods

Ordinary Portland Cement (OPC) of grade 43, conforming to the requirements of Indian Standard IS 269:2015, was procured from a commercial cement company. Two different calcined clay types, K1 and K2, with an amorphous content of around 60% and 75%, respectively were used in the study. Out of the total content of amorphous phases, the amorphous silica and amorphous alumina phases were found to be around 34% and 30% in K1 and around 37% and 33% in K2, respectively, based on the XRD Rietveld analysis and the XRF oxide composition data. Limestone and gypsum were procured from local companies. All the constituents were ground separately and interblended in a rotary drum ball mill to produce LC³. Based on the characterization of the raw materials, the amount of each of the constituents were adjusted to obtain the proportion of clinker:calcined clay:limestone:gypsum as 50:30:15:5. The LC³ blends produced from K1 and K2 clays were named as W1 and W2, respectively. The concrete mix proportions for OPC, W1 and W2 blends were designed as listed out in Table-1.

Table 1: Concrete mix proportions for the OPC, W1 and W2

| Materials | O-04WC-S-0.55 | W1-04WC-S-0.80 | W2-04WC-S-0.80 |
|---|----------------------|-----------------------|-----------------------|
| Cement (kg/m ³) | 462.50 | 462.50 | 462.50 |
| Water (kg/m ³) | 185.00 | 185.00 | 185.00 |
| Fine Aggregate (Sand) (kg/m ³) | 912.21 | 896.03 | 899.62 |
| Coarse Aggregate (10 mm) (kg/m ³) | 861.32 | 846.05 | 849.43 |
| Superplasticizer (% bwoc) | 0.55 | 0.80 | 0.80 |
| Coarse aggregate-to-total aggregate (c/a) ratio | 0.48 | 0.48 | 0.48 |

A modified Polycarboxylate Ether (PCE) based chemical admixture was used for the purpose of the study. The solid content of the chemical admixture was obtained as per the provisions laid out in Indian Standard IS 9103:1999 and was found to be 46.5%. The concrete mixes were produced in a laboratory pan mixer and the mixing time was maintained at 3 minutes for all the mixes. The water-to-cement (w/c ratio) of the concrete mixes was 0.40 and the coarse aggregate-to-total aggregate (c/a) ratio was 0.48. The OPC, W1 and W2 concretes were named as O-04WC-S-0.55, W1-04WC-S-0.80, and W2-04WC-S-0.80, respectively. All the tests were carried out on the same batch of concrete for consistency and good correlation between the results.

2.1 Slump Retention Tests

The initial slump was taken using an Abram's cone after the mixing the concrete constituents for 3 minutes in a concrete pan mixer. The concrete was placed in three layers inside the cone and each layer was tamped for 25 times using a steel tamping rod. The placement of concrete took around 1 minute and therefore, the first slump measurement was taken at 4 minutes from the time of adding mixing water. Subsequently, after a resting period of every 30 minutes, the concrete was mixed for another 1 minute to homogenize, and the slump measurement was taken. The loss of slump with time was plotted to assess the slump retention in all the mixes.

2.2 Flow Curve Tests

Flow curve tests were performed in a concrete rheometer (Pheso, Calmetrix). After the concrete was mixed, it was poured in the rheometer bowl till the top of the vane impeller. The vane impeller used to carry out the shearing had four blades with a height of 0.10 m and the internal and external radii of the coaxial cylinder geometry were 0.06 m and 0.19 m, respectively. The time taken for placement of the concrete and the first flow curve measurement was 10 minutes (T0) from the time of addition of the mixing water. Subsequently, the flow curve tests were carried out at a resting interval of 30 minutes. Before each test, the material was pre-sheared at 110 rpm for 30 seconds after which it was allowed to rest for 30 seconds. The shearing phase involved the increasing rotating speed sweep from 10 rpm with 30 seconds at each step to 100 rpm with a step size of 10 rpm. At 100 rpm, the material was sheared for 60 seconds following the rotational speed was decreased back in the same manner. The torque variation with rotational speed was obtained and the Reiner-Riwlin equation was used to obtain the dynamic yield stress (DYS) values (Wallevik et al. (2015)). The DYS values obtained from all the three cement types at different resting periods were normalized to the initial DYS value of the reference concrete (OPC).

3. Results and Discussion

As seen from Table-1, the paste content and the c/a ratio were identical for all the three concrete mixes. However, to obtain similar initial slump as that of OPC concrete, the LC³ mixes were dosed with a higher superplasticizer content. Nevertheless, irrespective of the type of clay (K1 or K2) used in the LC³, both the LC³ mixes had the same superplasticizer content, i.e., 0.80% by weight of the cement.

The slump retention results are known to indicate the progressive loss of slump with time for any concrete mix. Fig. 1 shows a comparative analysis of the slump retention with time of the three concrete mixes.

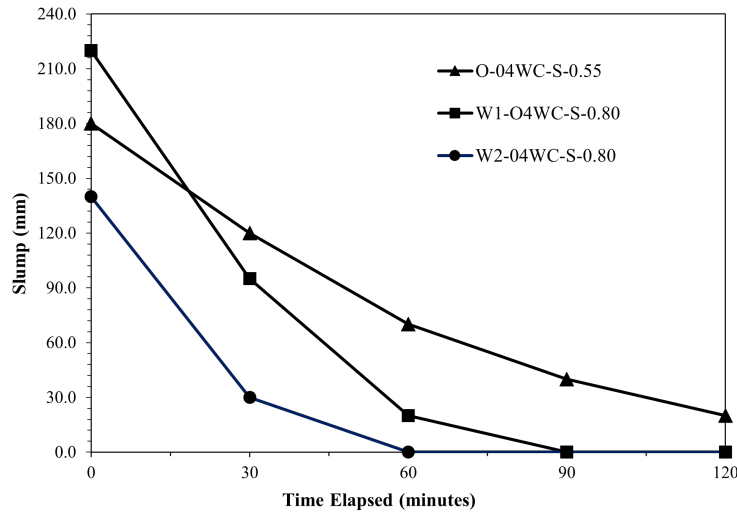


Fig. 1: Slump retention in OPC and LC³ concretes at 0.4 w/c ratio

It can be observed that the W2 and W1 concrete mixes exhibited a retention time of 30 minutes and 60 minutes, respectively beyond which a zero slump was obtained. On the other hand, the OPC concrete provided a retention time of 120 minutes, beyond which a zero slump was expected. Interestingly, the W1 concrete mix which had an initial slump of 220 mm as compared to the initial slump of 180 mm in OPC concrete, lost the slump to a lower value than that of the OPC concrete within the initial 30 minutes.

Fig. 2 depicts the variation of DYS values of each of the concrete types with time normalized to the initial DYS value obtained for OPC concrete. The bars marked with a red outline exhibit a decrease in the normalized DYS from the previous value indicate a localized shearing and hence, an underestimation of the yield stress. These red marked bars are not considered during the analysis.

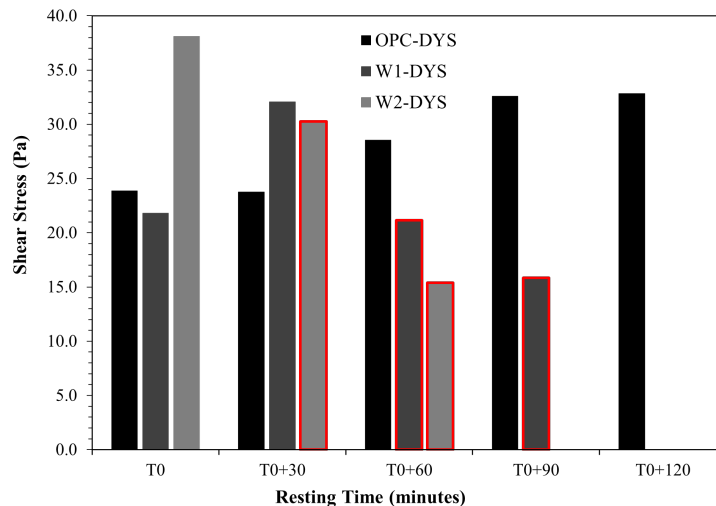


Fig. 2: : Variation of normalized DYS values with time for OPC & LC³ concrete a 0.4 w/c ratio

As seen from Fig. 2, the W2 concrete had the highest normalized DYS value at T0 time. Interestingly, the normalized DYS value of W1 was found to be slightly lower than OPC concrete at T0, as the initial slump of W1 was higher than that of the OPC mix (Fig. 1). This correlation validates the flow curve test results.

4. Conclusions

It was understood that a higher kaolinite content affected the slump retention, as well as the rheological properties in a similar manner. The inclusion of clay with a higher kaolinite content increases the total external and internal surface area of fine clay particles, thereby increasing the water adsorption and superplasticizer intercalation. The slump loss was found to be faster in the LC³ with higher kaolinite content. A good correlation was obtained between the slump retention and rheological measurements. It should be noted that a decrease in yield stress with time indicates probably inaccuracy in the rheological measurement and hence, such data should not be considered for analysis.

Acknowledgements

The support of Chryso is acknowledged by the authors. Aalborg cement is also acknowledged for making the Futurecem® technology available to us.

References

- Antoni, M., Rossen, J., Martirena, F., & Scrivener, K. (2012) "Cement substitution by a combination of metakaolin and limestone", *Cement and Concrete Research*, 42(12), 1579-1589.
- Batis, G., Pantazopoulou, P., Tsivilis, S., & Badogiannis, E. (2005) "The effect of metakaolin on the corrosion behavior of cement mortars", *Cement and Concrete Composites*, 27(1), 125-130.
- Cassagnabère, F., Diederich, P., Mouret, M., Escadeillas, G., & Lachemi, M. (2013) "Impact of metakaolin characteristics on the rheological properties of mortar in the fresh state", *Cement and Concrete Composites*, 37, 95-107.
- IS 269 : 2015 Indian Standard Ordinary Portland Cement – Specification, *Bureau of Indian Standards*, New Delhi
- IS 9103 : 1999 (Reaffirmed 2004) Indian Standard Concrete Admixtures – Specification, *Bureau of Indian Standards*, New Delhi
- Paiva, H., Velosa, A., Cachim, P., & Ferreira, V. M. (2012) "Effect of metakaolin dispersion on the fresh and hardened state properties of concrete", *Cement and Concrete Research*, 42(4), 607-612.
- Perlot, C., Rougeau, P., & Dehaut, S. (2013) "Slurry of metakaolin combined with limestone addition for self-compacted concrete. Application for precast industry", *Cement and Concrete Composites*, 44, 50-57.
- Wallevik, O. H., Feys, D., Wallevik, J. E., & Khayat, K. H. (2015) "Avoiding inaccurate interpretations of rheological measurements for cement-based materials", *Cement and Concrete Research*, 78, 100-109.

Non-adsorbing polymers and depletion forces in cement pastes

X.H. Yu¹, H. Bessaies-Bey², X. Liu¹, X. Shu³, J.P. Liu¹, N. Roussel^{2*}

¹ Southeast University, Nanjing, China

X. Y.: xhyu_smse@seu.edu.cn, X. L.: xinliu@seu.edu.cn, J. L.: liujiaping@cnjsjk.cn

² Gustave Eiffel University, Champs sur Marne, France

H. B. B.: hela.bessaies-bey@univ-eiffel.fr, N. R.: nicolas.roussel@ifsttar.fr

³ Jiangsu Sobute New Materials Co., Ltd., Nanjing, China

X. S.: shuxin@cnjsjk.cn

ABSTRACT

Superplasticizers, a fundamental component of modern concrete, have an extremely high dispersing ability through the adsorption on the cement surface producing electrostatic repulsion or steric hindrance. However, the adsorption of superplasticizers severely retards the early hydration of cement. This is one key issue in modern cement industry since more and more supplementary cementitious materials (SCMs) with lower reactivities are used. Non-adsorbing polymers were reported to modify the fluidity of cementitious suspensions in recent researches. Within this frame, a deeper understanding of the contribution of non-adsorbing polymers to cement dispersion and hydration as well as the underlying mechanism is required. In this work, a commercial polycarboxylate superplasticizer (PCE) and a polyethylene glycol (PEG) are used. We first measure the adsorption isotherm for PCE to set its dosage at full surface saturation. We then investigate the evolution of yield stress with PEG concentration at constant PCE dosage. Our results showed an oscillating decrease in the yield stress of the paste with PEG dosage. It illustrates the possibility of dispersing cement grains without having to rely on adsorbing polymers.

KEYWORDS: *non-adsorbing polymers, superplasticizers, rheology, depletion force*

1. Introduction

The use of superplasticizers is common practice in modern concretes. Among the options available in the market, PCEs are often the preferred choice, due to their high dispersing efficiency. The mechanism behind this dispersion has been deeply studied, resulting from the generation of steric hindrance after PCE adsorbs on the surface of cement. Nevertheless, PCEs are known for their negative effect on the rate of hydration of cement (Marchon et al (2017)). This currently represents a major drawback for this type of admixture, especially considering that the cement industry is prioritizing the development of greener cement based on the use of low-reactivity supplementary cementitious materials. In this context, new types of admixtures must be explored. Non-adsorbing polymers, like PEG, might constitute a viable alternative for PCE superplasticizers. However, even if some recent studies (Bessaies-Bey et al (2018); Ilg and Plank (2020); Lange and Plank (2016)) involve these polymers, their effects on cement dispersion and the underlying mechanism are still not well understood.

In this study, for the sake of simplicity, we chose deflocculated cement pastes without SCMs as the studied system and then varied the PEG dosage to have a deeper understanding of the dispersion mechanism of non-adsorbing polymers. Our results suggest that non-adsorbing polymers are at the origin of oscillating depletion forces. These polymers have the ability to reduce yield stress, which highlights the possibility of non-adsorbing dispersants for cementitious materials.

2. Materials and protocols

2.1 Cement

A commercial ordinary Portland cement, CEMI according to European standards, is employed in this study. Its chemical composition is measured by Inductively Coupled Plasma and Atomic Emission Spectrometry (ICP-AES Horiba Ultima 2000) as well as Thermogravimetric and Differential thermal analysis (ATD-ATG NETZSCH STA 409E), listed along with its mineralogical composition in Table 1. Its specific density and Blaine specific surface are 3.1 g/cm³ and 3650 cm²/g, respectively.

Table 1. Chemical and mineralogical composition of the studied Portland cement.

| Chemical composition (wt.%) | | Mineralogical composition (wt.%) | |
|--------------------------------|-------|----------------------------------|-------|
| CaO | 61.89 | C ₃ S | 65.47 |
| SiO ₂ | 19.08 | C ₂ S | 5.31 |
| Al ₂ O ₃ | 3.63 | C ₃ A | 2.56 |
| MgO | 0.72 | C ₄ AF | 12.70 |
| MnO | 0.05 | Gypsum | 5.25 |
| SO ₃ | 2.44 | CaO free | 0.78 |
| Fe ₂ O ₃ | 4.18 | Calcite | 0.48 |
| Na ₂ O | 0.27 | | |
| K ₂ O | 2.73 | | |
| TiO ₂ | 0.22 | | |
| Cl ⁻ | 0.07 | | |

2.2 Polymers

Two types of polymers, PCE and PEG, are used in this work, the first polymer for tuning the magnitude of Van der Waals attractive forces in the studied pastes and the second one for generating depletion forces. The PCE used here was synthesized by esterification and provided by Sika. It is a PCE with methacrylic acid backbone and polyethylene oxide side chains. For the average molecular structure, it contains 60 monomers in the backbone and 15 side chains of 23 monomers. Its molar mass is approximately 20,000 g/mol calculated based on its molecular structure. The PEG studied here was synthesized by ionic polymerization of ethylene oxide utilizing metal alkoxide compounds as catalysts (Bessaies-Bey et al (2018)) and provided by Sigma Aldrich. It is a linear polymer with a molar mass of 200 g/mol.

2.3 Mixing protocols

We, here, use a mixing and polymer addition protocol, which has been proven to eliminate almost all the consequences of early chemical processes (e.g. the nucleation of ettringite (Marchon et al (2017)), intercalation of PCEs (Hot et al (2014))). The cement powder and a constant amount of water (i.e. the water to cement mass ratio is 0.22) are first homogenized by hand and then mixed at 840 rpm for 2 min using a Turbo test Rayneri VMI mixer. PEG, PCE and the remaining water are added to the mixtures 17 min after the first contact between cement grain and water. The pastes are then mixed at 840 rpm for 1 min. After another 15 min of rest, the samples are mixed again at the same speed for 1 min.

For the rheological measurements, the cement pastes were prepared with a water to cement mass ratio (W/C) equal to 0.27, whereas, for the adsorption measurements, the W/C ratio was settled at 0.40 to facilitate the extraction of the interstitial solution by centrifugation. Only the dosage of PEG varied from one sample to another. Note that the polymer dosage in this paper is defined as a mass ratio between dry polymer and water. In addition, all the experiments are carried out immediately after the mixing protocol and performed at 20 ± 1 °C.

2.4 Adsorption measurements

A Total Organic Carbon (TOC) analyzer (Shimadzu TOC-V CSH) was used in this work. After the aforementioned mixing protocol, the cement pastes are centrifuged at 1000 g for 10 min to extract the interstitial solution, which thereafter is diluted with ultrapure water. The liquid samples are then analyzed by the TOC analyzer. Meanwhile, the organic carbon amounts in the polymer solutions and cement paste in the absence of polymer are measured as references. The specific adsorption amounts of polymer can

therefore be calculated based on the comparison between the organic carbon amounts of tested samples and the reference values.

In this study, we only measured the adsorption isotherm for PCE (see Fig. 1), since it has been well-proven that PEG has no affinity with cement surfaces (Bessaies-Bey et al (2018)). As shown in Fig. 1, the PCE adsorbed amount increases with dosage along with a saturated plateau at high dosages, corresponding to the full surface coverage. To maximize the effects of non-adsorbing polymers, we choose a constant PCE dosage of 2 % for the following rheological measurements, which can lead to full surface coverage.

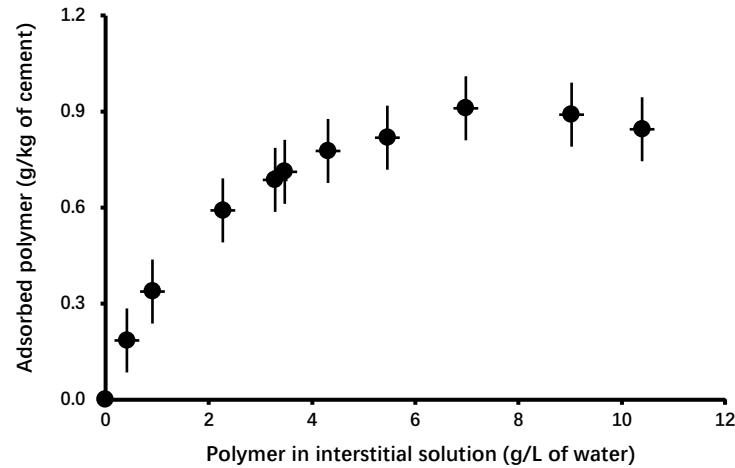


Fig. 1. Adsorption isotherm for PCE at W/C = 0.40. The error bar is the mean standard error calculated from randomly selected samples.

2.5 Rheological measurements

The shear rheological measurements were performed on a C-VOR Bohlin rheometer with a Vane geometry. The vane tool diameter is 25 mm and the outer cup dimensions are 50 mm in diameter and 60 mm in depth. For the measurement sequence, the test paste is first pre-sheared at 100 s^{-1} for 90 s. After a resting time of 3 s, an increasing shear rate ramp from 1 to 100 s^{-1} (with a logarithmic distribution of shear rates) is applied to the tested paste within 1000 s followed by a decreasing shear rate ramp for another 1000 s. Based on the flow curve obtained in the decreasing ramp, the yield stress of the paste is extrapolated from the measured apparent viscosity at low shear rates. Finally, we randomly chose several samples with different polymer dosages and repeated the related measurements for more than 20 times. We then computed the average relative error from the measured standard deviation and applied it to all measured yield stress values.

3. Experimental results

We plot in Fig. 2 the relative yield stress (i.e. the ratio between the yield stress of the paste with PEG and the yield stress of the reference paste without PEG) as a function of PEG dosage. We first note oscillations in the relative yield stress, which cannot be ignored when compared to the experimental error. In addition, we also observe an overall decrease in the measured relative yield stress, which decreases by more than 20% at a PEG dosage equal to 12.5%.

It has been well accepted that the yield stress of colloidal suspensions relates to the colloidal inter-particle force and the number of interacting particles, which itself relates to solid volume fraction (Hot et al (2014)). Therefore, the measured evolution in relative yield stress suggests a variation in the magnitude of inter-particle force. However, among all inter-particle forces (e.g. Van der Waals force, electrostatic force), only the depletion force is able to oscillate with increasing separation distance at high non-adsorbing polymer concentrations (Briscoe (2015); Piech and Walz (2004)). This feature is attributed to the mutual repulsion between polymers, leading to the formation of layered structures in the gap region (Piech and Walz (2004)). Hence, both the oscillatory depletion force and the increasing separation distance induced by the PEG structuring in the gap could be at the origin of the measured oscillatory decrease in yield stress of cement pastes. However, further studies are needed to confirm this hypothesis.

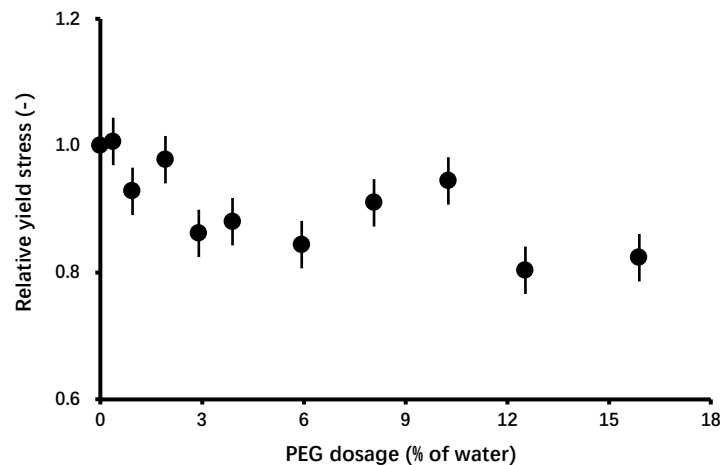


Fig.2 Relative yield stress as a function of PEG dosage. The relative yield stress is the ratio between the yield stress of the paste with PEG and the yield stress of the reference paste.

4. Conclusions

In this paper, we studied the effect of non-adsorbing polymers on the yield stress of cement paste. Our results suggested that non-adsorbing polymers can decrease yield stress in an oscillatory fashion, which may originate from the formation of layered structures in the gap between cement grains. However, further studies are needed to determine the underlying mechanism of this effect.

Acknowledgments

The authors wish to thank Sika and Sigma Aldrich for providing the polymers.

References

- Bessaies-Bey, H., Palacios, M., Pustovgar, E., Hanafi, M., Baumann, R., Flatt, R. J. and Roussel, N. (2018) "Non-adsorbing polymers and yield stress of cement paste: Effect of depletion forces", *Cement and Concrete Research*, 111:209-217.
- Briscoe, W. H. (2015) "Depletion forces between particles immersed in nanofluids", *Current Opinion in Colloid & Interface Science*, 20(1):46-53.
- Hot, J., Bessaies-Bey, H., Brumaud, C., Duc, M., Castella, C. and Roussel, N. (2014) "Adsorbing polymers and viscosity of cement pastes", *Cement and Concrete Research*, 63:12-19.
- Ilg, M. and Plank, J. (2020) "Non-adsorbing small molecules as auxiliary dispersants for polycarboxylate superplasticizers", *Colloids and Surfaces A: Physicochemical and Engineering Aspects*, 587.
- Lange, A. and Plank, J. (2016) "Contribution of non-adsorbing polymers to cement dispersion", *Cement and Concrete Research*, 79:131-136.
- Marchon, D., Juilland, P., Gallucci, E., Frunz, L. and Flatt, R. J. (2017) "Molecular and submolecular scale effects of comb-copolymers on tri-calcium silicate reactivity: Toward molecular design", *Journal of the American Ceramic Society*, 100(3):817-841.
- Piech, M. and Walz, J. Y. (2004) "The Structuring of Nonadsorbed Nanoparticles and Polyelectrolyte Chains in the Gap between a Colloidal Particle and Plate", *The Journal of Physical Chemistry B*, 108(26):9177-9188.

Complexation Enthalpies of Organic Admixtures: Measurement Method Development and Application to Calcium Complexes

R. Käser¹, C. Hartmann¹, P. Juilland², R.J. Flatt^{1*}

¹ *Institute for Building Materials, Department of Civil, Environmental and Geomatic Engineering, ETH Zürich, Zurich, Switzerland*

² *Sika Technology AG, Zurich, Switzerland*

* Corresponding author: flattr@ethz.ch

ABSTRACT

Sucrose is an extremely powerful retarder of which the working mechanisms remain under debate. To shed light onto the relative importance of various mechanisms, an understanding of its interaction with calcium ions in solution is desired, as for other admixtures impacting cement hydration. For this, enthalpies of complexation for sucrose with calcium ions were measured in solution by means of isothermal titration calorimetry. In order to reliably characterize the low heats involved, a protocol has been developed for precisely evaluating calorimetric data. For the complexation between calcium ions and sucrose, a significant influence of the matrix on the measured heat per mol of added sucrose was revealed.

The obtained heats were combined with a very simple calculation on sucrose deprotonation to obtain a stoichiometric ratio of about two calcium ions per deprotonated sucrose for the complexes and a molar heat of complexation for sucrose of around 20 kJ/mol.

The method is applicable to various combinations of organic admixtures and ions of interest and can be extended to adsorption processes. Knowledge about these molecular-scale processes in cementitious materials will improve the understanding of how admixtures impact the early stages of hydration.

KEYWORDS: *Isothermal calorimetry, Complexation, Organic admixtures, Thermodynamics, Sucrose*

1. Introduction

Organic admixtures are key components in cement and concrete as they can modify fresh state properties and hydration behaviour. Their mechanisms of action can proceed via adsorption on the surface of cement particles and hydration products,^[Thomas] or by modifying the behaviour of ions in the pore solution. This may go from simple complexation to more elaborate formation of nano-aggregates as evidenced by Caruso and coworkers, in synthetic pore solutions containing polycarboxylate ethers (PCEs).^[Caruso] Through such mechanisms admixtures can influence the pore solution,^[Bouzouaid,Nalet] thereby impacting the precipitation of hydration products and their morphology.^[Cody] This contrasts with the direct impact that admixtures can have by adsorption on cementitious phases and inhibiting their dissolution,^[Marchon] nucleation or growth. Which of these mechanisms dominates may vary depending on situations and in particular on the molecular structure of the chemical admixture considered.

The present paper contributes to clarifying this by presenting a systematic study of the complexation behaviour of organic admixtures in aqueous phases of mineral binders. More specifically, we introduce a protocol based on isothermal calorimetry to determine the heat resulting from those interactions.

2. Materials and Methods

Water was purified in a Milli-Q Reference A+ system. Sucrose ($\geq 99.5\%$), calcium chloride (anhydrous, $\geq 97.0\%$) and calcium hydroxide ($\geq 96\%$) were used from Sigma-Aldrich. For the samples with the $\text{Ca}(\text{OH})_2$ matrix, $\text{Ca}(\text{OH})_2$ was calcinated to CaO by heating it at 1000°C for 10 hours and the water was degassed while boiling, before mixing these two components. When untreated materials were used instead, there was CaCO_3 contamination, yet the results were very similar. All calorimetry measurements were performed in a TAM Air isothermal calorimeter at 25°C . Admix ampoules with two 1 mL syringes were utilized to inject admixture into the sample.

2.1 Approach

In order to keep unwanted dilution effects at a minimum, the use of a sample matrix was applied to each set of measurements. Thereby, the mixture initially in the syringes differed from the one in the vial only by additionally containing sucrose. 0.5 mL were drawn up into each syringe and injected one by one into 7 mL of the matrix. The whole sample preparation was done gravimetrically for highest possible precision.

2.2 Model

The heat transfer to the calorimeter's detector (heat flow) can be modelled by a PT1 function:^[Das]

$$\frac{dH}{dt} = \frac{H_0}{t_c} * e^{-t/t_c} \quad (1)$$

where H_0 is the heat released by the sample, t_c is the characteristic time of the instrument (a measure of how quickly heat flows decay), and t is the time. Integration yields an expression for the cumulative heat:

$$H(t) = H_0 * (1 - e^{-t/t_c}) = H_0 - H_0 * e^{-t/t_c} \quad (2)$$

These equations were adapted to a baseline correction. The measured data is corrected for the heat flow caused by sample insertion into the calorimeter due to the temperature difference between sample and calorimeter (Figure 1a). For the smallest heats and heat flows, a significant error may remain, caused by a baseline drift. The baseline correction can be improved by fitting a linear baseline drift to each heat flow signal in a second step (Figure 1b). This resulted in a very precise and robust procedure for extracting heat values from the raw data.

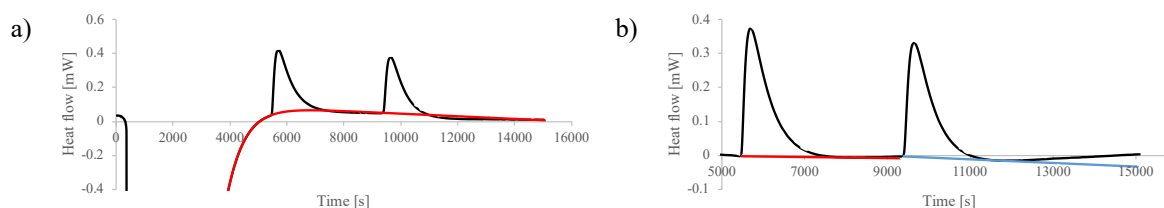


Figure 1. Baseline correction, presented for one of the experiments. a) Measured heat flow (black) vs. the PT1 (exponential) fit (red) and b) PT1-corrected heat flow (black) vs. linear baseline drift fits (red and blue).

The injections caused an additional heat which we concluded to be of mechanical origin. In each set of experiments a blank was measured, in which only the sample matrix was injected, and the resulting heat was used to correct the measured values.

3. Results and Discussion

Heats obtained both with 0.100 mol/L CaCl_2 and 5.55 mmol/L $\text{Ca}(\text{OH})_2$ matrices are reported in Figures 3a&b. A first observation is that values for CaCl_2 (diamonds) are very similar to the pure dilution experiments in which solutions of sucrose in pure water are injected into pure water (squares). Comparatively, the values obtained with $\text{Ca}(\text{OH})_2$ as a matrix (circles) are much more important at low dosages. It is worth noting that the pure dilution experiment, although spontaneous, should not involve a

change in enthalpy (no bonds are being broken or formed). In fact, at low dosages those heats are virtually zero. At higher dosages they increase, which probably results from the rather concentrated solutions used in those experiments most likely leading to non-negligible intermolecular bonds (modified by dilution). In some syringe solutions of the $\text{Ca}(\text{OH})_2$ matrix, visible white particles formed ($<0.3\text{mm}$) upon mixing in the sucrose (Figure 3c). Such particles have already been reported in the past.^[Pannetier]

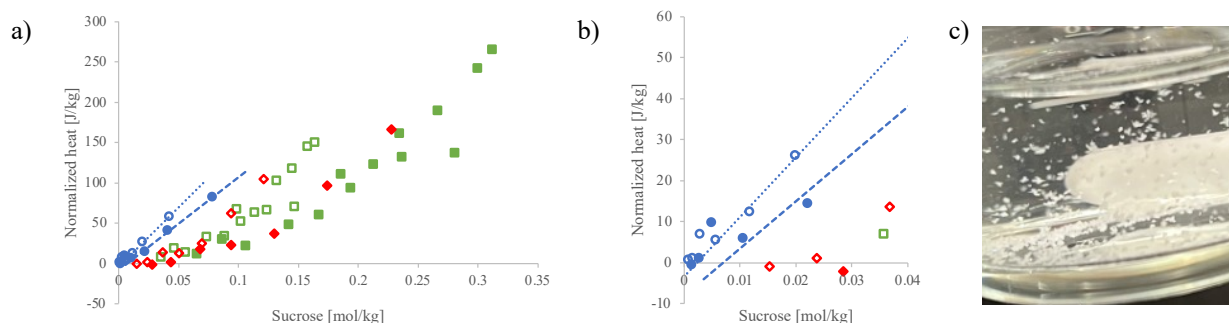


Figure 3. a) Comparison between the heat in a 0.100 mol/L CaCl_2 matrix (diamonds), the dilution heat (squares), and the heat in a 5.55 mmol/L $\text{Ca}(\text{OH})_2$ matrix (circles), normalized by mass of water and plotted vs sucrose concentration after injection. Heats are shown after the first injection (empty) and after both injections (filled). Linear regressions for the $\text{Ca}(\text{OH})_2$ matrix were obtained from the four higher dosage data points, excluding the lower three. **b)** Zoom of the low dosage range from a). **c)** Photograph of the particles which formed in some sucrose- $\text{Ca}(\text{OH})_2$ mixtures.

Most importantly at the lower dosages, while the CaCl_2 matrix shows similarly low heats to the dilution experiment, the $\text{Ca}(\text{OH})_2$ matrix shows much more substantial heats (above a threshold highlighted by the linear regressions in Figures 3a&b). This leads us to a first conclusion: The complexation of calcium by sucrose is negligible at neutral pH but not in at higher pH in the $\text{Ca}(\text{OH})_2$ matrix (pH = 11.94). Therefore, in what follows we only focus on that second matrix.

Figure 3b suggests the existence of a threshold dosage up to which the measured heat is zero (the intercepts on the horizontal axis). This would be expected for cases in which all the sucrose in the syringe solution is complexed and remains so when added into the vial. In turn, this implies high complexation free energies, making complexation essentially irreversible. Above this threshold concentration, sucrose would be in excess, allowing for additional complexation reactions to take place when the solution is introduced into the vial and additional calcium becomes available. This qualitatively also explains the roughly linear rise in heats above the threshold.

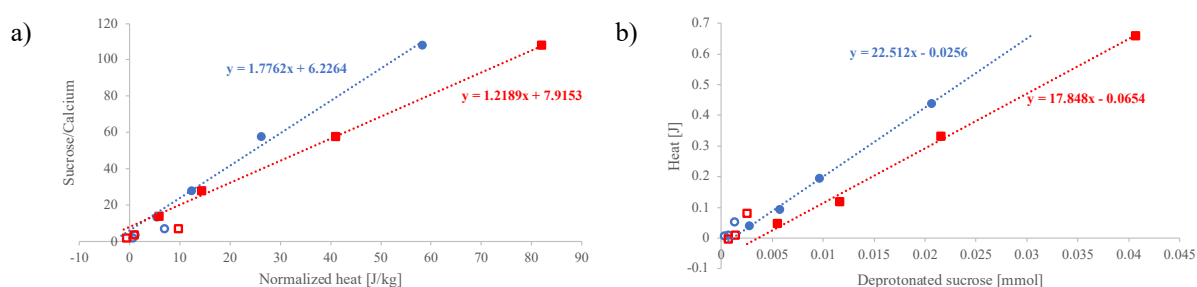


Figure 4. a) Relation between the sucrose/calcium ratio in the syringes and the corresponding normalized heats obtained for the $\text{Ca}(\text{OH})_2$ matrix, after the first injection (blue circles) and after both injections (red squares). The regressions are based on the filled points. **b)** Heat in a 5.55 mmol/L $\text{Ca}(\text{OH})_2$ matrix vs amount of deprotonated sucrose. Heats are shown after the first injection (blue circles) and after both injections (red squares). The regressions are based on the filled points. The slopes give the heat per mol of complexed sucrose.

While a full thermodynamic analysis of these data is beyond the scope of this paper, we may nevertheless extract additional basic information from these experiments with the following considerations. If a threshold dosage exists up to which all calcium is irreversibly bound by sucrose, then that threshold should also provide the stoichiometry of the complex. This can be obtained from the ordinate at the origin of a plot of sucrose to calcium ratio in the syringe (starting condition) versus the measured heat. Such a plot is shown

in Figure 4a, with both injections giving a similar intercept of 7.1 on average. It is however unrealistic to assume that so many sucrose molecules would share one calcium ion, which is why we propose to examine this ratio considering only the dissociated sucrose at the experimental pH of 11.94. using a pK_a of 13.1 for the deprotonation of sucrose,^[Popov] the fraction of deprotonated sucrose with respect to the dosed sucrose would be about 6.5%. This leads to a stoichiometric ratio of 1.9-2.5 calcium ions per deprotonated sucrose for the complexes, which is much more reasonable than before. However, there still is an issue as in principle there is only one hydroxyl group from the sucrose that would deprotonate. So, the number of calcium per sucrose is too high and this may be due to us neglecting the role of $CaOH^+$ ion pairs, an issue that we will examine in future work.

Let us now examine what happens above the threshold. This corresponds to cases where calcium does not mobilize all the sucrose in the syringe solutions prior to insertion in the vial. For these cases, we already noted a linear increase in the heat with the sucrose dosage. As previously mentioned, this suggests highly favourable complexation reaction from a free energy point of view (equilibrium fully shifted to the formation of complexes). For such conditions, the plot of heat versus sucrose provides a molar heat of complexation for sucrose. However as before, we should consider this for the deprotonated sucrose, which is the axis chosen in Figure 4b, and that gives us a complexation enthalpy of about 20 kJ/mol. Both injections do not give the same results as the two steps are not fully identical owing to a different final dilution. Those issues along with a more rigorous thermodynamical analysis of these experiments are the subject of ongoing work that will be reported elsewhere.

4. Conclusions

We have successfully developed a method for measuring very small heats, which allows us to investigate interactions between organic admixtures and ionic species present in cementitious systems. We showed that the heats in the presented calcium-sucrose systems show a significant dependence on pH. In addition, we found indications that deprotonated sucrose plays an important role in the complexation. Measurements at various pH values and a more sophisticated complexation model will allow us to obtain a better insight and to elucidate what the underlying process more precisely. Ultimately, this is just a start, and the method can be largely extended to various compounds and to adsorption measurements.

Acknowledgements

The work of Roland Käser and Céline Hartmann was partly supported by the Innovandi Research Network.

References

- Bouzouaid, L., Lothenbach, B., Fernandez-Martinez, A. and Labbez, C. (2021) "Portlandite solubility and Ca^{2+} activity in presence of gluconate and hexitols", *Cem. Con. Res.*, 149: 106563
- Caruso, F., Mantellato, S., Palacios, M. and Flatt, R.J. (2017) "ICP-OES method for the characterization of cement pore solutions and their modification by polycarboxylate-based superplasticizers", *Cem. Con. Res.*, 91: 52-60
- Cody, A.M., Lee, H., Cody, R.D. and Spry, P.G. (2004) "The effects of chemical environment on the nucleation, growth, and stability of ettringite $[Ca_3Al(OH)_6]_2(SO_4)_3 \cdot 26H_2O$ ", *Cem. Con. Res.*, 34: 869-881
- Das, A. (2022) "3D Concrete Printing: Early-age Strength Build-up and Long-term Durability", Doctoral Thesis, ETH Zurich, Zurich
- Marchon, D., Juilland, P., Gallucci, E., Frunz, L. and Flatt, R.J. (2016) "Molecular and submolecular scale effects of comb-copolymers on tri-calcium silicate reactivity: Toward molecular design", *J. Am. Ceram. Soc.*, 100: 817-841
- Nalet, C. and Nonat, A. (2016) "Retarding effectiveness of hexitols on the hydration of the silicate phases of cement: Interaction with the aluminate and sulfate phases", *Cem. Con. Res.*, 90: 137-143
- Pannetier, N., Khoukh, A. and François, J. (2001), "Physico-chemical study of sucrose and calcium ions interactions in alkaline aqueous solutions", *Macromol. Symp.*, 166: 203-208
- Popov, K.I., Sultanova, N., Römkkömäki, H., Hannu-Kuure, M., Jalonen, J., Lajunen, L.H.J., Bugaenko, I.F. and Tuzhilkin, V.I. (2006) " ^{13}C NMR and electrospray ionization mass spectrometric study of sucrose aqueous solutions at high pH: NMR measurement of sucrose dissociation constant", *Food Chemistry*, 96(2): 248-253
- Thomas, N.L. and Birchall, J.D. (1983) "The retarding action of sugars on cement hydration", *Cem. Con. Res.*, 13(6): 830-842

Rheology of ultra-high geopolymer concrete: Influences of activator types and silica fume

Y. Liu^{1,2} and C. Shi^{1,2,3}

¹ Key Laboratory for Green & Advanced Civil Engineering Materials and Application Technology of Hunan Province, College of Civil Engineering, Hunan University, Changsha, China

² Key Laboratory of Building Safety and Energy Efficiency of the Ministry of Education, Hunan University, Changsha, China

³Department of Civil Engineering, The University of British Columbia, Vancouver, Canada

Email: cshi@hnu.edu.cn

ABSTRACT

The slag-fly ash-silica fume based geopolymer was utilized as the binder phase of ultra-high geopolymer concrete (UHPGC). However, the research on the rheology of UHPGC is limited. This study has investigated the coupled influence of activator and silica fume on the rheological properties of UHPGC pastes. The results showed that with the uses of different activators, the effect of silica fume on the wetting packing density, flowability, thixotropy, yield stress and plastic viscosity of geopolymer pastes was totally different. For the geopolymer activated by sodium hydroxide (SH), the incorporation of silica fume caused the decrease of wetting packing density and rheological properties. On the other hand, for the geopolymer activated by sodium silicate (SS), the wetting packing density and rheological properties were improved by adding silica fume. The FTIR and LF-NMR analysis indicated that some silica fume dissolved and the formation of excessive water was found at the early stage, regardless of the activator types, which resulted in the increase of amount of polymeric silicate species in the liquid phase. However, it could be concluded that the formation of excessive silicate group by adding silica fume would play a different role in the geopolymer paste activated by SS and SH.

KEYWORDS: *Ultra-high performance geopolymer concrete, Rheology, Silica fume, Activator*

1. Introduction

Ultra-high performance geopolymer concrete (UHPGC) manufactured by using geopolymer binders, silica fume, fine aggregate and steel fibers, is one of examples of using geopolymer as binder to manufacture ultra-high performance concrete without affecting its properties. The proper silica fume dosage could effectively improve the workability of UHPGC. However, the effect of silica fume on the rheology of geopolymer-based materials, is not fully understood. The combined physical and chemical effects of silica fume make its contribution to further changes in the fresh properties of UHPGC more difficult to explain. The use of silica fume, such spherical ultra-fine powder, results in a higher water demand. On the other hand, the change in the liquid phase by the dissolution of silica fume should not be ignored, given the higher alkalinity in geopolymer systems (Lu et al., 2021, Vance et al., 2014). The formation of colloidal silica at very early stage as demonstrated would change the liquid phase chemistry. Therefore, it is very crucial to clarify the role of silica fume in the rheological properties of UHPGC.

This study aims therefore to investigate the influences of silica fume and activator types on the particle packing parameters, flowability, rheological properties including yield stress, plastic viscosity and thixotropy of slag-fly ash-based geopolymer paste. The influencing mechanism of silica fume on the rheological properties of geopolymer pastes containing different activators was discussed, in order to provide new insight into the role of silica fume in the rheology of UHPGC.

2. Experimental programs

2.1 Raw materials

Slag, fly ash and silica fume were used in this study. The average particle sizes of slag, fly ash and silica fume were 17.90, 36.94 and 0.15 μm , respectively. The densities of slag, fly ash and silica fume were 2.88, 2.30 and 2.21 g/cm^3 , respectively. These activators were prepared by using an analytical grade sodium hydroxide with a purity of 99%, waterglass containing 8.54 wt.% Na_2O , 27.45 wt.% SiO_2 and 64.01 wt.% HO and deionized water.

2.2 Mixture proportion

The liquid-to-binder and slag-to-fly ash mass ratio was 0.5 and 4:1, respectively. Silica fume was added in four different mass percentages (0%, 5%, 10% and 20%). The influence of silica fume content on the rheological properties of UHPGC was investigated by adopting two different activators and the constant liquid-to-binder mass ratio of 0.5 for all mixtures. In Group A, sodium hydroxide (SH) solution was used as an “inert” activator in Group A. In Group B, sodium hydroxide (SH) solution was used as an activator, and the Na_2O content of 7% was adopted in group A. The Group B were prepared by sodium hydroxide and silicate (SS) solution with a $\text{SiO}_2/\text{Na}_2\text{O}$ ratio of 1.5 and a Na_2O content of 7%.

2.3 Test methods

The maximum packing density (ϕ_{max}) was measured in triplicate following the method proposed by Fennis et al. Mini-slump tests were conducted in accordance with GB/T 8077-2012. Anton Paar MCR 302 rheometer was used to perform the rheological tests. LF-NMR analysis was carried out by using MAGMEDPM-1030 Cementitious Materials Analyzer to investigate the time-dependent variations of water content and distribution of the fresh geopolymer pastes. FTIR analysis on the interstitial fluid was conducted using Thermo Scientific Nicolet iS50 spectrometer workstation. All tests were conducted at a temperature of 20 $^{\circ}\text{C}$

3. Results and discussion

3.1 Packing parameters

Fig. 1 illustrates the influence of silica fume on the packing density and liquid film thickness (LFT) of UHPGC with different activators. With adding silica fume, the packing density of UHPGC with SH decreases, then increases, while that of UHPGC with SS increases. This could be attributed to that the superfine silica fume and different liquid medium could impact the interaction between solid particles caused by potential derived from van der Waals attraction and electrostatic repulsion forces, influencing thus the dispersion of solid particles in the suspensions. On the other hand, the incorporation of silica fume results in lower liquid film thickness as compared to the suspensions without silica fume. As the proportion of silica fume in the binders increases, the overall surface area of solid particles considerably increased due to a very-high specific surface area of silica fume, and thus the liquid film thickness decreases.

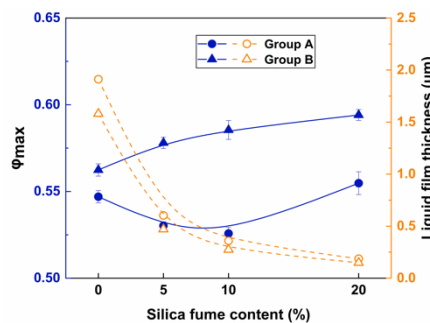


Fig. 1. Packing density and LFT of UHPGC with different silica fume contents and activators.

3.2 Rheological behaviour

Fig. 2 shows the flowability of UHPGC pastes with different silica fume contents and activators. The addition of silica fume decreases significantly in the flowability of the pastes containing water or SH solution, but increases the flowability when SS solution is used. Fig. 3 depicts the rheological parameters of UHPGC pastes. As the silica fume is added, the rheological parameters of geopolymer pastes with SS-based activators decrease, but they increase in the cases of geopolymer pastes with SH-based activator. The above results indicate that the influence of silica fume on the rheological properties of geopolymer is strongly dependent on the activator type.

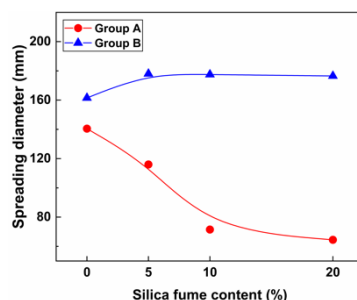


Fig. 2. Flowability of UHPGC pastes with different silica fume contents and activators.

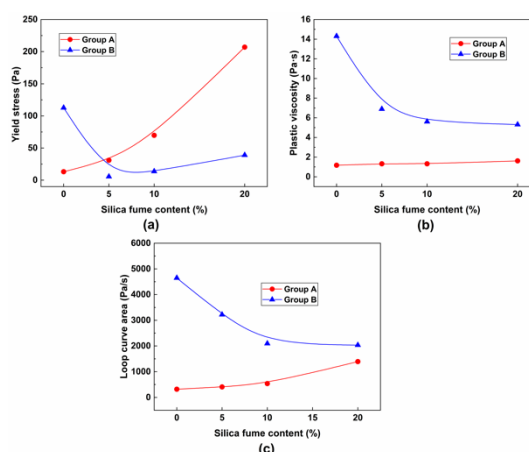


Fig. 3. Rheological parameters of UHPGC pastes with different silica fume contents and activators.

The very-high specific surface area of silica fume would cause the insufficiency of liquid for wetting and reacting, thus degrading in the rheological properties of geopolymer, and on the other hand, the lubricator and filler effect of silica fume induced by its spherical geometry and particle size, would improve the flowability. Also, the dissolution of silica fume that modifies the activator characteristics was considered as another reason. However, the results of this study, that adding silica fume into geopolymer with different activators brings about different consequences, cannot be explained well by the above inferences. This will be discussed later in this study.

3.3 Water content and FTIR

Figs. 4 and 5 are the water contents of the pastes detected by LF-NMR and FTIR spectra of their pore solutions, respectively. The increase of movable water content induced by adding silica fume is observed, regardless of the activator types. Combined with the spectra, this can be attributed the dissolution of silica fume, which leads to the generation of extra water. The excessive water should have contributed to improving the flowability. However, the different results in the SS and SH-based system demonstrate that the silica fume dissolution has a less influence on the rheology. The lubrication effect of silica fume exists only in the SS-based system. This indicates that the interaction between silica fume particles and silicate group from the activator may play a more crucial role in the rheology of UHPGC.

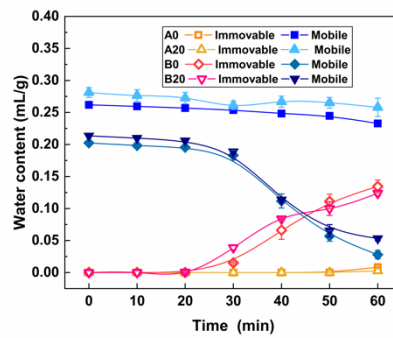


Fig.4. Water contents of UHPGC pastes

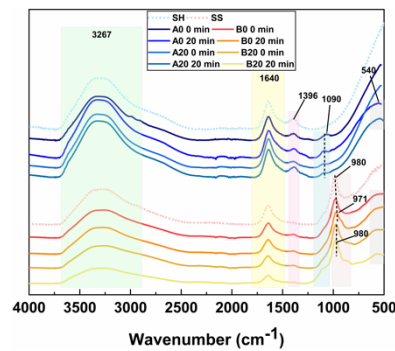


Fig. 5. FTIR spectra of the pore solution of UHPGC

4. Conclusions

The main conclusion of this study can be drawn as follows:

1. The packing density, spreading meters, yield stress, plastic viscosity and thixotropy of UHPGC pastes with SS-based activator decreased with the increase in the silica fume dosage.
2. The incorporation of silica fume resulted in the increase of the free water amount induced by silica fume dissolution.
3. There is a possibility that the interaction between silica fume particles and silicate group from the activator may play a more crucial role in the rheology of UHPGC.

References

- Lu, C., Zhang, Z., Shi, C., Li, N., Jiao, D. and Yuan, Q. (2021) "Rheology of alkali-activated materials: A review", *Composite Part B*, 121: 104061
- Vance, K., Dakhane, A., Sant, G. and Neithalath, N. (2014) "Observations on the rheological response of alkali activated fly ash suspensions: the role of activator type and concentration", *Rheologica Acta*, 53(10): 843-855

Effects of different types of shrinkage reducing agents on shrinkage properties of mortars incorporating slag or silica fume

B.B. Zhou¹, C.J. Shi^{1*}

¹Key Laboratory for Green & Advanced Civil Engineering Materials and Application Technology of Hunan Province, International Innovation Center for Green & Advanced Civil Engineering Materials of Hunan Province, Key Laboratory of Building Safety and Energy Efficiency of the Ministry of Education, College of Civil Engineering, Hunan University, Changsha, 410082, China
Email: beibeizhou@hnu.edu.cn
cshi@hnu.edu.cn

ABSTRACT

The effects of different types of shrinkage reducing agents (SRAs) on shrinkage of mortars containing slag or silica fume and their influence mechanisms on the shrinkage are not fully understood. This study aims to investigate the influences of small molecular-type and novel polymer-type SRAs on the shrinkage evolution of mortars incorporating ground granulated blast furnace slag (GGBFS) or silica fume (SF). The surface tension of pore solution and drying shrinkage of mortars containing GGBFS or SF were comprehensively investigated. The results indicated that the drying shrinkage of the GGBFS and SF cement mortars decreased with the increase of small molecular-type SRA dosage. Similarly, the addition of polymer-type SRA reduced the drying shrinkage of GGBFS and SF cement mortars, while the addition of 1% polymer-type SRA resulted in lower drying shrinkage than 2% polymer-type SRA. Compared to small molecular-type SRA, polymer-type SRA exhibited lower ability to decrease the drying shrinkage of the GGBFS and SF cement mortars.

KEYWORDS: *shrinkage reducing agent, drying shrinkage, mortar, slag, silica fume*

1. Introduction

Supplementary cementitious materials (SCMs) are widely used in concrete manufacturing by partially replacing cement to enhance the performance of cementitious materials and reduce carbon footprint (Juenger and Siddique (2015)). Some SCMs are industrial by-products such as ground granulated blast furnace slag (GGBFS) from pig iron industry and silica fume (SF) from ferrosilicon production (Lothenbach et al (2011)). The smaller grain size of GGBFS has been shown to increase autogenous and drying shrinkages compared to cement when used as a substitute for cement (Yalçinkaya and Yazıcı (2017)). SF exhibits higher pozzolanic activity and specific surface, compared to cement and GGBFS. It was found by Shen et al (2018) that SF increased the autogenous shrinkage due to the reduction of pore sizes and internal relative humidity (RH). Rao (2001) reported that the drying shrinkage of mortars containing higher SF content was observed to be 7-10 times higher than mortars without SF.

The shrinkage of mortar and concrete leads to deformation and cracking, which can affect the appearance of the building and even the safety of the structure. The application of shrinkage reducing agents (SRAs) is an effective technology for mitigating shrinkage cracking of cement-based materials. Zhang et al (2015) studied the effect of SRA (consisted of a hydrocarbon compound and a glycol ether system derivative) on the drying shrinkage of GGBFS mortar. The results showed that the addition of the SRA significantly reduced the drying shrinkage strains of ordinary Portland cement and low heat Portland cement mortars containing 45% GGBFS by total binder mass. However, the different dosages of SRA had an insignificant effect on the drying shrinkage of cement mortar with GGBFS. Folliard and Berke (1997) found that the drying shrinkages of normal concrete and SF concrete containing SRA at 28 d reduced by 28% and 52%, respectively, compared to the control concrete without SRA. Meanwhile, the drying shrinkage and cracks

of SF concrete with SRA reduced by 29% and 88% at 120 d, respectively. In spite of these efforts, the effect of different types of SRAs on the shrinkage of mortars containing GGBFS or SF and their influence mechanisms on the shrinkage are not fully understood. The complete understanding of these aspects is quite important for shrinkage control in concrete with GGBFS or SF.

The objective of this study is to clarify the influences of different types of SRAs with different dosage on the drying shrinkage evolutions of mortars incorporating different amount of GGBFS or SF. The surface tension and drying shrinkage measurements were performed.

2. Experimental

2.1 Raw materials

The cement used in this study was P-I 42.5 Portland cement conformed to Chinese Standard GB 8076-2008. The chemical compositions of cement, GGBFS and SF are presented in Table 1. The powder superplasticizer (SP) was used as an admixture. Diethylene-glycol monobutyl-ether (SRA-1) as a small molecule SRA was obtained from Shanghai Macklin Biochemical Co., Ltd (China). SRA-2 was a novel polymer-type shrinkage reducing agent and was obtained in laboratory.

Table 1 Chemical composition (%) of cement, GGBFS and SF.

| Sample | CaO | SiO ₂ | Fe ₂ O ₃ | Al ₂ O ₃ | MgO | SO ₃ | Na ₂ O _{eq} | f-CaO | Loss | Cl ⁻ |
|--------|-------|------------------|--------------------------------|--------------------------------|------|-----------------|---------------------------------|-------|------|-----------------|
| Cement | 62.05 | 20.53 | 3.17 | 4.45 | 2.81 | 2.10 | 0.55 | 0.80 | 1.74 | 0.032 |
| GGBFS | 42.73 | 29.61 | 1.64 | 15.67 | 4.35 | 2.14 | 0.39 | — | 0.73 | 3.60 |
| SF | 1.84 | 95.38 | 0.61 | — | 0.26 | — | 0.16 | — | 1.84 | 2.48 |

2.2 Mix proportions

Table 2 summarizes the mixture proportions of mortars.

Table 2 Mix proportions of mortars.

| Mix no. | Mix description | Binder (%)* | | | Water-to-binder ratio | Sand-to-binder ratio | SP (%)* | SRA-1 (%)* | SRA-2 (%)* |
|---------|-----------------|-------------|-------|----|-----------------------|----------------------|---------|------------|------------|
| | | Cement | GGBFS | SF | | | | | |
| M1 | C | 100 | 0 | 0 | 0.30 | 2 | 0.2 | 0 | 0 |
| M2 | 10GGBFS | 90 | 10 | 0 | 0.30 | 2 | 0.2 | 0 | 0 |
| M3 | 20GGBFS | 80 | 20 | 0 | 0.30 | 2 | 0.2 | 0 | 0 |
| M4 | 10SF | 90 | 0 | 10 | 0.30 | 2 | 0.3 | 0 | 0 |
| M5 | 20SF | 80 | 0 | 20 | 0.30 | 2 | 0.6 | 0 | 0 |
| M6 | C-1SRA-1 | 100 | 0 | 0 | 0.30 | 2 | 0.2 | 1 | 0 |
| M7 | C-2SRA-1 | 100 | 0 | 0 | 0.30 | 2 | 0.2 | 2 | 0 |
| M8 | 10GGBFS-1SRA1 | 90 | 10 | 0 | 0.30 | 2 | 0.2 | 1 | 0 |
| M9 | 10GGBFS-2SRA1 | 90 | 10 | 0 | 0.30 | 2 | 0.2 | 2 | 0 |
| M10 | 20GGBFS-1SRA-1 | 80 | 20 | 0 | 0.30 | 2 | 0.2 | 1 | 0 |
| M11 | 20GGBFS-2SRA-1 | 80 | 20 | 0 | 0.30 | 2 | 0.2 | 2 | 0 |
| M12 | 10SF-1SRA-1 | 90 | 0 | 10 | 0.30 | 2 | 0.3 | 1 | 0 |
| M13 | 10SF-2SRA-1 | 90 | 0 | 10 | 0.30 | 2 | 0.3 | 2 | 0 |
| M14 | 20SF-1SRA-1 | 80 | 0 | 20 | 0.30 | 2 | 0.6 | 1 | 0 |
| M15 | 20SF-2SRA-1 | 80 | 0 | 20 | 0.30 | 2 | 0.6 | 2 | 0 |
| M16 | C-1SRA-2 | 100 | 0 | 0 | 0.30 | 2 | 0.2 | 0 | 1 |
| M17 | C-2SRA-2 | 100 | 0 | 0 | 0.30 | 2 | 0.2 | 0 | 2 |
| M18 | 10GGBFS-1SRA-2 | 90 | 10 | 0 | 0.30 | 2 | 0.2 | 0 | 1 |
| M19 | 10GGBFS-2SRA-2 | 90 | 10 | 0 | 0.30 | 2 | 0.2 | 0 | 2 |
| M20 | 20GGBFS-1SRA-2 | 80 | 20 | 0 | 0.30 | 2 | 0.2 | 0 | 1 |
| M21 | 20GGBFS-2SRA-2 | 80 | 20 | 0 | 0.30 | 2 | 0.2 | 0 | 2 |
| M22 | 10SF-1SRA-2 | 90 | 0 | 10 | 0.30 | 2 | 0.3 | 0 | 1 |
| M23 | 10SF-2SRA-2 | 90 | 0 | 10 | 0.30 | 2 | 0.3 | 0 | 2 |
| M24 | 20SF-1SRA-2 | 80 | 0 | 20 | 0.30 | 2 | 0.6 | 0 | 1 |
| M25 | 20SF-2SRA-2 | 80 | 0 | 20 | 0.30 | 2 | 0.6 | 0 | 2 |

*by mass of total binder

2.3 Test methods

The surface tension was measured using a fully automatic surface tension meter (KINO A-601). Drying shrinkages of plain cement mortar and cement mortars containing GGBFS or SF in the absence and presence of SRAs were measured in accordance with JC/T603-2004.

3. Results and discussions

3.1 Surface tension

Effects of SRAs on surface tensions of supernatants of plain cement paste and GGBFS or SF cement pastes are illustrated in Fig. 1. In Fig. 1 (a), the surface tension decreased with the increase of SRA-1 content. The effects of SRA-1 on the surface tensions of supernatant solutions of plain cement paste and GGBFS or SF cement pastes were similar. The composition of SRA would lead to a difference in efficiency. As shown in Fig. 1 (b), the surface tensions of supernatant solutions of plain cement, 10% GGBFS, 20% GGBFS, 10% SF and 20% SF cement pastes significantly reduced by 31.47%, 31.96%, 32.26%, 29.92%, and 29.55%, respectively, due to the addition of 1% SRA-2. 2% SRA-2 exhibited a similar influence on the surface tension with 1% SRA-2. In presence of 2% SRA-2, the surface tensions of supernatant solutions of plain cement, 10% GGBFS, 20% GGBFS, 10% SF and 20% SF cement pastes were 48.783, 49.14, 49.3, 49.2, and 49.46 mN/m, respectively. The ability of decreasing surface tension of SRA-2 was higher than SRA-1.

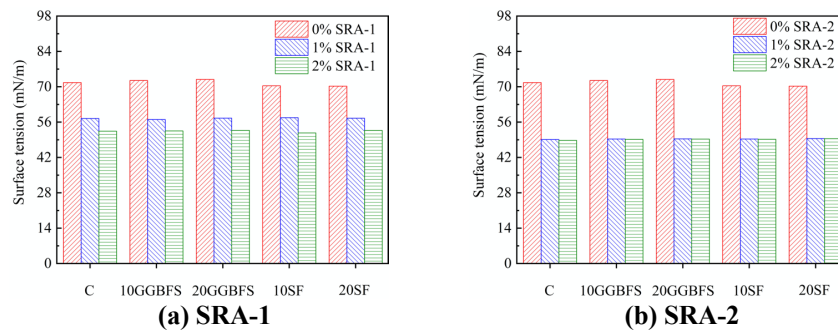


Fig. 1. Effects of SRAs on surface tensions of supernatants of cement pastes containing GGBFS or SF.

3.2 Drying shrinkage

The development of drying shrinkage of mortars containing GGBFS or SF in the absence and presence of different types of SRAs within 63 days is illustrated in Fig. 2. In Fig. 2 (a), 1% SRA-1 decreased the drying shrinkages of plain cement mortar, 10% GGBFS and 20% GGBFS cement mortars by 37.96%, 51.05%, and 59.95%, respectively, while 2% SRA-1 reduced their drying shrinkages by 57.74%, 64.34%, and 68.67%, respectively. In Fig. 2 (b), the addition of 1% SRA-1 decreased the drying shrinkages of 10% SF and 20% SF cement mortars by 61.65% and 54.03%, respectively, while 2% SRA-1 reduced their drying shrinkages by 68.45% and 61.41%, respectively. Fig. 2 (c) and (d) show the effects of SRA-2 on the drying shrinkage of all cement mortars. The drying shrinkages of all mortars in the addition of 1% SRA-2 were lower compared to 2% SRA-2. 1% SRA-2 decreased the drying shrinkages of plain cement mortar, 10% GGBFS and 20% GGBFS cement mortars by 48.90%, 41.86%, and 51.11%, respectively, while 2% SRA-2 reduced their drying shrinkages by 31.11%, 30.05%, and 29.44%, respectively. At the same time, the addition of 1% SRA-2 decreased the drying shrinkages of 10% SF and 20% SF cement mortars by 44.01% and 36.38%, respectively, while 2% SRA-2 reduced their drying shrinkages by 35.14% and 20.86%, respectively. The decreased drying shrinkage in the presence of SRA-1 and SRA-2 can be due to their reducing effect on the surface tension of pore solution, resulting in the reduction of capillary forces on the solid skeleton of the microstructure. Although the surface tension in the addition of SRA-2 was lower compared to SRA-1, the drying shrinkage of all cement mortars in the presence of SRA-2 was higher than SRA-1. This may be because that the drying shrinkage of cement-based materials is also related to their pore structure.

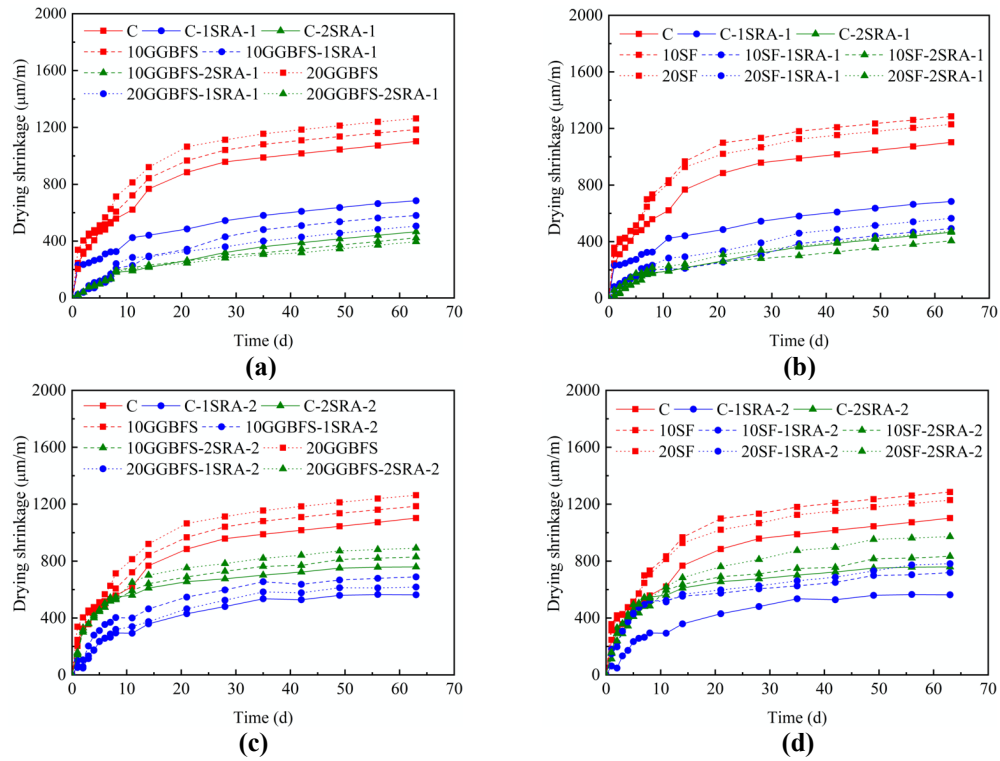


Fig. 2. Effects of SRAs on the drying shrinkages of mortars containing GGBFS or SF.

4. Conclusions

Based on results and discussions above, some conclusions can be obtained as follows:

- (1) The surface tensions of supernatant solutions of GGBFS and SF cement pastes reduced with the increase of SRA-1 dosage. The ability of SRA-2 in reducing surface tension was higher than SRA-1.
- (2) The drying shrinkage of GGBFS and SF cement mortars decreased with the increase of SRA-1 content. Similarly, it showed a reduction in the addition of SRA-2. However, it was lower in the addition of 1% SRA-2 compared to 2% SRA-2.

Acknowledgements

The authors gratefully acknowledge the financial supports from the Ministry of Science and Technology under Project No. 2018YFC0705400.

References

- Folliard, K.J. and Berke, N.S. (1997) "Properties of high-performance concrete containing shrinkage-reducing admixture", *Cement and Concrete Research*, 27 (9): 1357-1364.
- Juenger, M.C.G. and Siddique, R. (2015) "Recent advances in understanding the role of supplementary cementitious materials in concrete", *Cement and Concrete Research*, 78: 71-80.
- Lothenbach, B., Scrivener, K. and Hooton, R.D. (2011) "Supplementary cementitious materials", *Cement and Concrete Research*, 41 (12): 1244-1256.
- Rao, G.A. (2001) "Long-term drying shrinkage of mortar—Influence of silica fume and size of fine aggregate", *Cement and Concrete Research*, 31 (2): 171-175.
- Shen, P., Lu, L., He, Y., Rao, M., Fu, Z., Wang, F. and Hu, S. (2018) "Experimental investigation on the autogenous shrinkage of steam cured ultra-high performance concrete", *Construction and Building Materials*, 162: 512-522.
- Yalçinkaya, Ç. and Yazıcı, H. (2017) "Effects of ambient temperature and relative humidity on early-age shrinkage of UHPC with high-volume mineral admixtures", *Construction and Building Materials*, 144: 252-259.
- Zhang, W., Hama, Y. and Na, S.H. (2015) "Drying shrinkage and microstructure characteristics of mortar incorporating ground granulated blast furnace slag and shrinkage reducing admixture", *Construction and Building Materials*, 93: 267-277.

On the impact of sulphate source on admixtures in limestone calcined clay cements

S. Dhers^{1*}, B. Ecker¹, R. Guggenberger¹, B. Sachsenhauser¹, and P. Schwesig¹

¹ Master Builders Solutions Deutschland GmbH, Dr-Albert-Frank-Strasse 32, 83308 Trostberg, Germany

Email: sebastien.dhers@mbcc-group.com

ABSTRACT

Calcined clays appear to be one of the most promising supplementary cementitious materials (SCMs) to reduce the CO₂ footprint of cement, in particular Limestone Calcined Clay Cement (LC³). New and improved admixtures with tailored properties are necessary to ensure a broad implementation of LC³ in the concrete industry. The high specific surface requires increased sulphation for these cements, which poses a challenge for admixtures. In this work, different LC³ cements were prepared, by blending a CEM I (50 wt. %), two kaolinite based calcined clays (30 wt. %, specific surface area of 4.11 m²/g or 27.79 m²/g), limestone (15 wt. %) and two different sulphate sources (5 wt. %, gypsum or anhydrite). Two different superplasticizers, one conventional PCE-based slump retainer developed for ordinary concretes, and one new generation superplasticizer specifically suitable for LC³ (labelled as SP1 and SP2, respectively) were used for this investigation carried out in concrete (Figure 1). This study highlights the robustness of a new generation of superplasticizers towards different calcined clays and sulphate sources, in respect to workability retention.

KEYWORDS: *Admixture, calcined clay, workability, sulphate, concrete*

1. Introduction

One of the most promising avenues to decarbonize the cement industry is lowering the clinker content of cement and to do so Supplementary Cementitious Materials (SCMs) are key (Scrivener et al., 2019). SCMs have been used in cement worldwide for many years, however traditional SCMs such as fly-ash and ground granulated blast furnace slag are waste by-products from CO₂ generating industries, whereas calcined clays have the advantage of both worldwide availability and lower CO₂ footprint (Hache et al., 2020). Calcined clays generally have a more demanding workability; admixtures and in particular superplasticizers are therefore essential to allow the widespread utilization of these new cements (Lei et al., 2020). In this work, two superplasticizers and two calcined clays have been used to investigate the impact of sulphate source on the workability.

2. Materials and methods

2.1 Materials

The two calcined clays used in this study are kaolin based calcined clays from Europe, with a metakaolin content respectively of 40% and 30% (as given by the provider) and a BET value of around 4.11 and 27.79 m²/g, respectively, which are then abbreviated to reflect both these critical values: CC1-4 and CC2-28 (Table 1). The cement used in this study is an ordinary Portland cement CEM I 52.5 R, provided by

Schwenk GmbH. Particle size distribution and BET were measured for both calcined clay (Table 1), using Mastersizer 3000 (Malvern Panalytical) for PSD and a Nova 4000e (Quantachrom GmbH & Co. KG) for BET measurements done at 350°C. Two different superplasticizers provided by MBCC group were used in this study, SP1 and SP2, which are polymers with two different mechanisms for delayed action, based on acrylic acid and vinyl PEG monomers.

Table 1. Particle size and specific area of CEM I and calcined clays, and metakaolin content of calcined clays.

| | d10 | d50 | d90 | BET (m²/g) | MK (%) |
|---------------|------------|------------|------------|------------------------------|---------------|
| CEM I | 0.89 | 7.77 | 26.50 | 1.49 | - |
| CC1-4 | 1.12 | 9.84 | 34.33 | 4.11 | 40 |
| CC2-28 | 1.66 | 12.76 | 51.09 | 27.79 | 30 |

2.2 Methods

Concrete mix designs: 380 kg/m³ of total binder (including calcined clay and limestone) at w/b = 0,41 with a maximum aggregate size of 16 mm. As a descriptive example, LC³-50 2:1 (2: 1 being the ratio of calcined clay to limestone) mix design have 190 kg/m³ CEM I, 57 kg/m³ limestone, 114 kg/m³ calcined clay and 19 kg/m³ of gypsum. The mixing sequence/time was as follow: 80 % water added up-front, consequently after 2 minutes the admixture in 20% water remaining is added to the mix, for a total mixing time 4 minutes (mixer: Pemat ZK 30, shear rate 60 rpm). Slump measurements: the procedure is analogous to DIN EN 12350-2, the DIN flow was adjusted to 60 cm. Compressive strength: the concrete mixes were each filled into concrete steel cubes (15/15/15 cm), and after 24h the hardened concrete cubes were demolded and stored at a temperature of 20 °C and relative humidity of 65%. The hardened concrete cubes were demolded and stored for 7 days at 20 °C in a water bath and further 21 days at 20 °C and relative humidity of 65% in a climate chamber. Compressive strength was measured at 1 day and 28 days adapted from DIN EN 12390-3.

3. Results and discussion

DIN flow measurements were reported in concrete to compare the dispersing performances of the two superplasticizers, namely SP1 and SP2, with an initial value target between 50 and 60 cm (Figure 1). Both superplasticizers are pure PCE-based polymers, using two different release mechanisms. Four different LC³-50 systems have been tested, based on the combination of two calcined clays, low BET (CC1-4) and high BET (CC2-28) values, using two calcium sulphate sources, anhydrite and gypsum (Figure 1, shade of orange and red, respectively). To benchmark these LC³ concretes, three different references were selected (Figure 1, shades of blue): pure CEM I, a CEM I and limestone reference in a 2.8:1 ratio (same amount of limestone as in the LC³-50 mix design), and a CEM I and limestone reference in a 1:1 ratio (same amount of CEM I as in the LC³-50 mix design). A low w/b ratio of 0.41, rather than higher such as 0.5, was selected to test the admixtures in a more challenging mix design.

SP1 shows fresh properties performances dependent on both the calcined clay and the sulphate source. Using anhydrite as a sulphate source, it is possible to reach a 2h open time using a 0.26% solid content of polymer to binder dosage for CC1-4, whereas the LC³-50 mix containing CC2-28 reaches 1h30 open time with a higher dosage of 0.46%. When gypsum is used as the sulphate source, overall, a lower open time is obtained, whereas 1h30 is obtained using a dosage of 0.26% for CC1-4 and 1h with 0.52% dosage for CC2-28. When comparing the sulphate source, the workability of LC³-50 mixes with both calcined clays is superior when using anhydrite versus gypsum. A possible explanation would be that the difference in

dissolution rate and solubility between gypsum and anhydrite affecting the competitive adsorption between the sulphates and the superplasticizer, which has a particularly bigger impact when calcined clays with higher surfaces are involved in the mix design (CC1-4 vs CC2-28). The influence of the calcined clay is clear and can be explained by a higher specific surface at a similar kaolin content: the BET value of the calcined clay alone appears to be a major factor influencing the workability of the entire concrete mix.

SP2 exhibits an impressive robustness with similar performances in all systems, both references and LC³ mixes. The dependence on the sulphate source is not evidenced with this superplasticizer, as was the case for SP1, and 2 hours open time is reached with both calcined clays. Some refluidification is observed to different degrees for all systems, however it is important to note that this type of pure polymer is usually formulated to mitigate the observed refluidification – in this study both superplasticizers were used as pure polymer for direct comparison. The dosage needed is also higher compared to SP1, and when using CC2-28, two different dosages are needed depending on the sulphate source, 0.57% when anhydrite is used and 0.65% when gypsum is used, in line with the trends observed for SP1. This difference can likely be explained by the fact that a low BET calcined clay such as CC1-4 will have a smaller influence on the sulphate requirements than a higher BET calcined clay such as CC2-28 (Zunino et al., 2019).

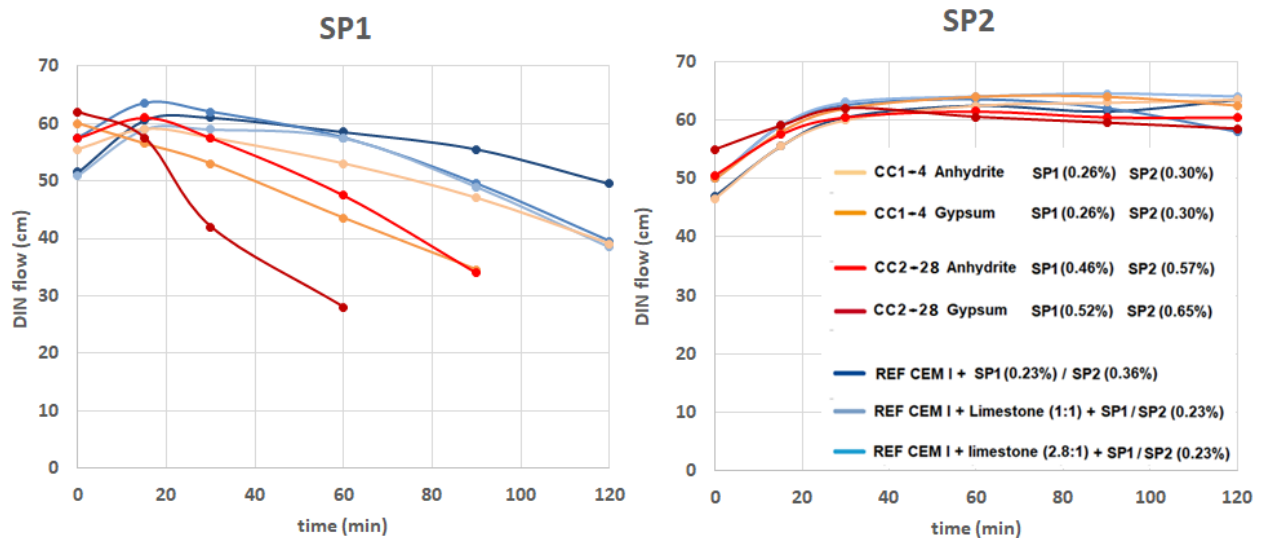


Figure 1. DIN flow values for concrete tests carried out at w/b = 0.41 in LC³-50 mixes, using two calcined clays and two sulphate sources. Dosage (M.%bwoc active) for each superplasticizer shown in brackets in the legend.

Compressive strength values were measured at 1 and 28 days were measured for all systems (Figure 2). Interestingly, the type of admixtures has little impact on early strength for LC³ mixes (Figure 2, 24h values) with SP2 showing slightly higher values than SP1. Overall, the compressive strength values at 1 day for LC³ mixes are, as expected, significantly lower than the CEM I reference, as well as the reference with a 2.8:1 CEM I to limestone ratio. However, the 1:1 CEM I to limestone reference shows similar values as the LC³-50 mixes, even slightly lower than the LC³-50 mixes using SP2, evidencing that SP2 can have a beneficial effect on early strength, on top of offering a superior workability.

When discussing the late strength, the impact of the superplasticizer is more important (Figure 2, left vs right for 28 days). Compressive strength values for LC³ mixes are roughly 10 MPa higher for SP2 than for SP1, which is quite a remarkable increase in late strength, around 15% for all 4 systems. References are also impacted by the superplasticizer but more importantly, using SP2 enables in these LC³ systems to

reach the same late strength as a CEM I / limestone (2.8 : 1) blend, i.e. a lower CO₂ concrete using 190 kg/m³ of CEM I instead of a concrete using 280 kg/m³ of CEM I for the blend (Figure 2, right).

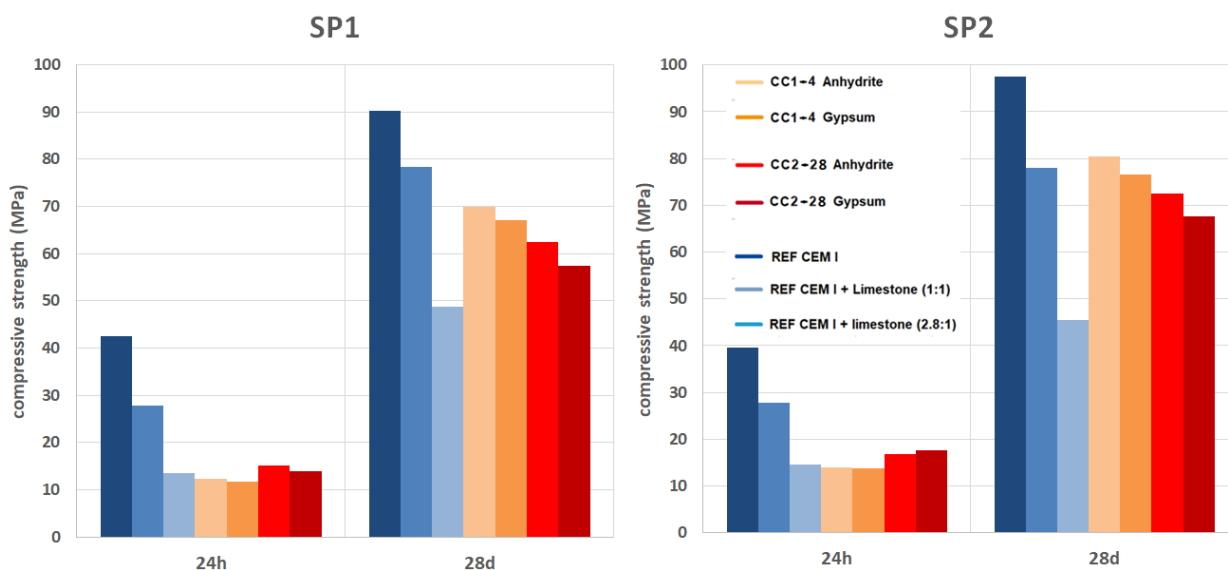


Figure 2. Compressive strength values at 24h and 28 days in concrete at w/b = 0.41 in LC³-50 mixes, using two calcined clays and two sulphate sources.

4. Conclusion

In this work several LC³-50 systems were tested for workability, as well as early and late strength, using low BET value (CC1-4) and high BET (CC2-28) calcined clays, and two sulphate sources, anhydrite and gypsum. SP1 showed good performances, with an interesting fresh properties performances dependence on both the calcined clay and the sulphate source. SP2 on the other hand exhibited an impressive robustness with similar performances in all LC³ systems and references, in addition to an enhanced early and late strength enabling a substantial reduction of CO₂ content of the final concrete (190 vs 380 kg/m³ CEM I).

Acknowledgements

This study was fully funded by MBCC Group.

References

- Scrivener, K.; Avet, F.; Maraghechi, H.; Zunino, F.; Ston, J.; Hanpongpan, W.; Favier, A. (2019) "Impacting factors and properties of limestone calcined clay cements (LC3)", *Green Materials*, 7: 3-14
- Hache, E.; Simoën, M.; Seck, G. S.; Bonnet, C.; Jabberi, A.; Carcanague, S. (2020) "The impact of future power generation on cement demand: An international and regional assessment based on climate scenarios" *International Economics*, 163: 114-133
- Lei, L.; Palacios, M.; Plank, J.; Jeknavorian, A. (2022) "Interaction between polycarboxylate superplasticizers and non-calcined clays and calcined clays: A review", *Cement and Concrete Research*, 154: 106717
- Zunino, F.; Scrivener, K. (2019) "The influence of the filler effect on the sulfate requirement of blended cements", *Cement and Concrete Research*, 126: 105918

A study on the adsorption and dispersion capability of PCEs with different structures on cement containing montmorillonite

Y. H. Ma¹ and C. J. Shi^{2*}

¹ College of Civil Engineering, Hunan University, Changsha, China

Email: yhma@hnu.edu.cn

² College of Civil Engineering, Hunan University, Changsha, China

Email: cshi@hnu.edu.cn

ABSTRACT

Two conventional comb-like PCEs and a cross-linked PCE were synthesized in this paper. The rheological properties of paste containing different montmorillonite (MMT) contents in the presence of these PCEs were measured and the adsorption behaviors of these PCEs on MMT were investigated. Results show that compared to conventional PCE with carboxylate groups, the introduction of $-\text{SO}_3^-$ anchoring groups enhances the dispersion of PCE, and the paste with it exhibits lower yield stress and plastic viscosity. This is due to the lower adsorption of the PCE with $-\text{SO}_3^-$ groups on MMT and stronger dispersion to aggregated cement particles. In terms of PCE molecular structure, the cross-linked PCE has more arms that increase the intercalation efficiency on MMT, and the corresponding paste with it shows better workability.

KEYWORDS: polycarboxylate ether superplasticizer, montmorillonite, adsorption, dispersion, intercalation

1. Introduction

Polycarboxylate ether (PCE) superplasticizer has the advantage of a higher water reduction rate even at a lower dosage. However, it exhibits high sensitivity to clay (Lei and Plank 2014). Montmorillonite (MMT) is considered the most adverse mineral for the dispersion performance of PCE. The root cause for such strong inhibition in the dispersion power of PCE polymer is that PCE polymer is preferably adsorbed on clay contaminants, and is consumed by surface adsorption and intercalation (Ait-Akbour et al. 2015). This greatly decreases the workability of concrete and limits the application of PCE.

Compared to conventional PCE with carboxylate groups, the introduction of $-\text{SO}_3^-$ and $-\text{PO}_4^{2-}$ groups is beneficial to the enhancement of the dispersion capability of PCE due to their stronger attractive force (Qiu et al. 2011, Ran et al. 2016). However, there is no research on the effect of anchoring groups on the adsorption and dispersion capability of PCEs, and the interactions between PCEs with different anchors and MMT are unclear. The use of sacrificial agents and modification of PCE molecular structure are considered as the two approaches to enhance the tolerance of conventional PCE to MMT. However, these PCEs with special structures are synthesized by multi-steps, which increases the complexity and difficulty of the synthesis. The cross-linked polymer with much stronger steric hindrance benefits to disperse aggregated cement particles (Liu et al. 2014). Moreover, it can be prepared by a much simpler synthesis process than polymers with those novel structures. Thus, cross-linked PCEs are expected to decrease the negative effects of MMT on the flow of cement paste containing MMT.

This study synthesized two comb-like PCEs and a cross-linked PCE, and investigated their effects on the rheological properties of cement pastes without and with MMT. The interactions between PCEs and MMT were revealed. This paper provides enlightenment for further design and synthesis of PCE with stronger tolerance to MMT.

2. Materials and Methods

2.1 Materials

IPEG monomer ($M_w = 2400$ g/mol) purchased from Hunan CJS Building Materials Technology Co., Ltd, was used. Analytical grade acrylic acid (AA), sodium vinyl sulfate (Vs), trimethylolpropane trimethacrylate (TMPTA), ammonium persulfate (APS), mercaptopropionic acid (MPA), and sodium hydroxide (NaOH) were provided by Shanghai McLean Biochemical Technology Co., Ltd.

PO 42.5R Portland cement with a specific gravity of 3150 kg/m^3 and a specific surface area (Blaine) of $341 \text{ m}^2/\text{kg}$ was supplied by China United Cement Group Co., Ltd. Clay was naturally Ca-MMT purchased from Xinyang penglai bentonite Co., Ltd (China).

2.2 Synthesis of PCEs

These PCEs were synthesized by free radical polymerization. Herein, comb-like PCEs with $-\text{COO}^-$ and $-\text{SO}_3^-$ groups, and the cross-linked PCE are named as CPCE, SPCE, and TPCE, respectively. The ratio of AA to IPEG is 3.5, and 0.5 mol AA was replaced by Vs to synthesize SPCE. The amount of the used cross-linker was 0.25% by the total mass of monomers.

2.3 Methods

Cement pastes with MMT replacements of 0%, 1%, 2%, and 3% by mass and PCE solutions were prepared, resulting in a water-to-powder ratio of 0.29. The mixed pastes were poured into the container immediately to measure the rheological properties on a rotational concentric rheometer (MCR 302, Anton Paar).

A mass of 1.5 g MMT was dissolved in 29 g synthetic pore solution with different concentrations of PCEs and then stirred using a magnetic stirrer. Then the suspension was centrifuged. The liquid was collected to measure the total organic carbon (TOC) content and the solid at the bottom of the centrifuge tube was collected and dried for X-ray diffraction (XRD) measurement.

3. Results and discussion

The H-B model was used to describe the rheological properties of pastes with the synthesized PCEs and the results are illustrated in Fig.1. Without MMT, the yield stress and plastic viscosity of cement pastes with these PCEs are in the same order of magnitude. However, they increase significantly with the incorporation of MMT, especially at high MMT contents, due to the adsorption of PCE on MMT. Compared to CPCE, the presence of SPCE decreases the rheological parameters of pastes, which indicates that SPCE shows better dispersion capability on the pastes containing MMT. The rheological properties of pastes are affected by PCE molecular structures. Paste with TPCE exhibits lower plastic viscosity than CPCE. This can be attributed to the stronger steric hinderance of TPCE with three arms and weaker interactions with MMT.

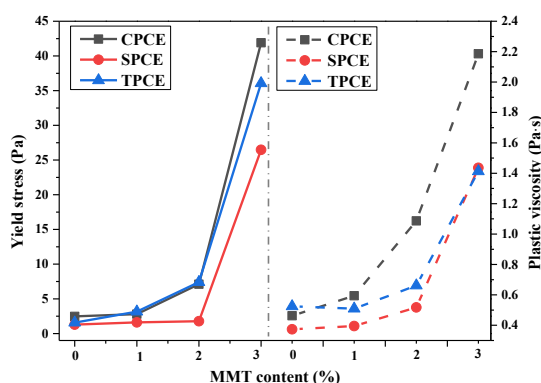


Fig.1 Rheological properties of pastes with these synthesized PCEs

The adsorption of the synthesized PCEs on MMT was measured and the result is shown in Fig.2. It can be seen that the adsorption amounts increase with the increased PCE concentrations. This is related to the physical and chemical adsorption of PCE molecules on MMT (Ma et al. 2020). It is well accepted that the lower adsorption of PCE on MMT results in its stronger tolerance to MMT (Lei et al. 2021). From Fig.2, SPCE shows lower adsorption on MMT than CPCE, which can explain the better rheological properties of paste with SPCE. However, TPCE has higher adsorption on MMT than that CPCE. This is related to their different molecular structures. Intercalation conformation of the side chains of PCE greatly depends on the molecular structure (Borralleras et al. 2020). Thus, it can be concluded that TPCE shows different intercalation modes than PCE with a comb-like structure.

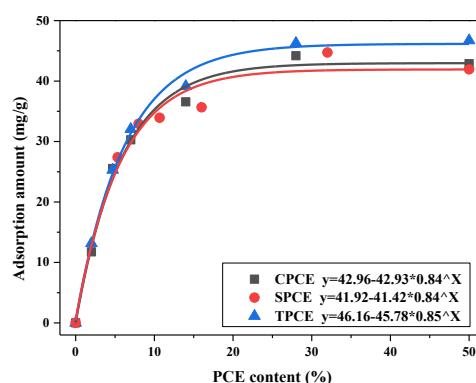


Fig.2 Adsorption of the synthesized PCEs on MMT

The XRD of MMT was conducted to investigate the intercalation behavior of CPCE and TPCE. According to the XRD pattern, the d-values of MMT are divided as 1.20 ± 0.05 , 1.40 ± 0.05 , and 1.70 ± 0.10 nm. The intercalation proportion of MMT was calculated and the result is shown in Fig.3. It can be seen that MMT has a lower intercalation proportion in the presence of TPCE, regardless of PCE concentrations. This indicates that the side chains of a single TPCE molecular can insert into multi-MMT particles, which enhances the intercalation efficiency and decreases the negative effects of MMT. Intercalation is the main hinderance to the dispersion of PCE (Ma et al. 2020, Lei et al. 2022). The less intercalation for TPCE contributes to its enhanced tolerance to MMT, which is in line with the results of the rheological properties of pastes.

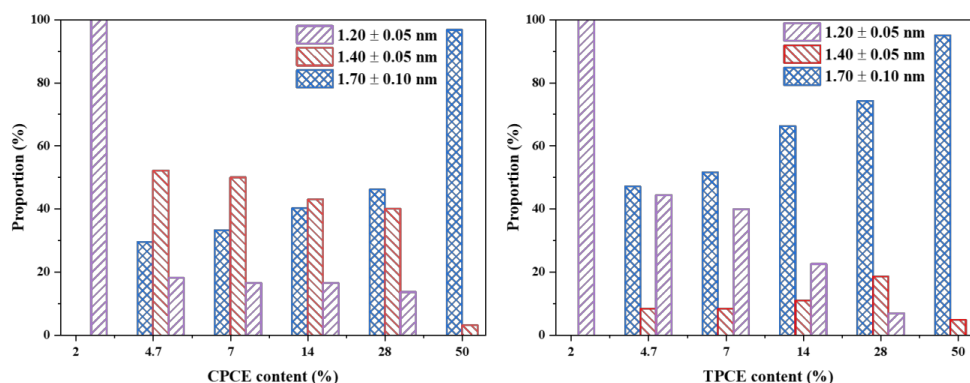


Fig.3 Intercalation proportion of MMT in the presence of CPCE and TPCE

4. Conclusions

This study synthesized two comb-like PCEs and a cross-linked PCE, and reported their effects on the rheological properties of cement pastes without and with MMT. Based on the analysis and discussion, the conclusions can be drawn.

- (1) Regardless of MMT content, SPCE and TPCE show better dispersion capability than CPCE, as evidenced by the lower yield stress and plastic viscosity of pastes. This can be explained by their different interactions with MMT.

- (2) SPCE has lower adsorption on MMT, which decreases the consumption of MMT to PCEs and enhances the dispersion capability of SPCE. Compared to comb-like PCEs, the less intercalation is attributed to the enhancement performance of TPCE on cement paste containing MMT.

Acknowledgements

The authors gratefully acknowledge the financial supports from the Ministry of Science and Technology under Project No. 2018YFC0705400.

References

- Ait-Akbour, R., Boustingorry P. and Leroux, F. (2015) "Adsorption of Polycarboxylate Poly (ethylene glycol) (PCP) Esters on Montmorillonite (mmt): Effect of Exchangeable Cations (Na^+ , Mg^{2+} and Ca^{2+}) and PCP Molecular Structure", *Journal of Colloid and Interface Science*, 437: 227-234
- Borralleras, P., Segura, I. and Aranda, M. A. G. (2020) "Absorption Conformations in the Intercalation Process of Polycarboxylate Ether-based Superplasticizers into Montmorillonite Clay", *Construction and Building Materials*, 236: 116657
- Lei, L., Palacios, M. and Plank, J. (2022) "Interaction Between Polycarboxylate Superplasticizers and Non-Calcined Clays and Calcined Clays: A Review", *Cement and Concrete Research*, 154: 106717
- Lei, L. and J. Plank. (2014) "A Study on the Impact of Different Clay Minerals on the Dispersing Force of Conventional and Modified Vinyl Ether Based Polycarboxylate Superplasticizers", *Cement and Concrete Research*, 60: 1-10
- Lei, L., Zhang, Y. and Li, R. (2021) "Specific Molecular Design of Polycarboxylate Polymers Exhibiting Optimal Compatibility with Clay Contaminants in Concrete", *Cement and Concrete Research*, 147:106504
- Liu, H., Pang, H. and Ou, J. (2014) "Effect of Cross-Linked Polycarboxylate Type Superplasticizers on the Properties in Cementitious System", *Journal of Applied Polymer Science*, 131(19): 40856(40851-40858)
- Ma, Y., Shi, C. and Lei, L. (2020) "Research Progress on Polycarboxylate Based Superplasticizers with Tolerance to Clays - A Review", *Construction and Building Materials*, 255: 119386
- Qiu, X., Peng, X. and Yi, C. (2011) "Effect of Side Chains and Sulfonic Groups on the Performance of Polycarboxylate-type Superplasticizers in Concentrated Cement Suspensions", *Journal of Dispersion Science and Technology*, 32(2): 203-212.
- Ran, Q., Ma, J. and Wang, T. (2016) "Synthesis, Characterization and Dispersion Properties of a series of Bis (phosphonic acid) amino-Terminated Polymers", *Colloid and Polymer Science*, 294(1): 189-198.

Preparation and performance of EPEG-type PCE and its application in ultra-high performance concrete

Tong Xue¹, Jie Bai^{1*}, Wenying Xu¹, Zuobao Song², Ting Li², Juan Li^{3*}, Ruijun Gao³

¹ China Building Materials Academy(CBMA), Beijing, China
Email: xuetongcbma@163.com

² CNBM Zhongyan Technology Co., Ltd., Beijing, China
Email: zhongyankeji@chinascem.com

³ Nonmetallic Excellence and Innovation Center for Building Materials, CBMA, Beijing, China
Email: lijuan@cbma.com.cn

ABSTRACT: To improve the workability and mechanical properties of ultra-high performance concrete (UHPC), a novel EPEG-type ultra-high dispersion polycarboxylate superplasticizer (EPEG-type PCE) was developed by radical copolymerization reaction, and the effect of EPEG-type PCE on the workability, mechanical properties and durability of UHPC was investigated in this paper. The results show that the EPEG-type PCE can improve the workability and mechanical properties of UHPC at an appropriate dosage. However, there is a critical dosage for the effect of EPEG-type PCE on the early compressive strength and fluidity of UHPC, which is 1.5% (by mass of cement). The fluidity of UHPC does not improve any more when the dosage of EPEG-type PCE increases continuously after exceeding the critical point. The compressive strength decreases with the increase of EPEG-type PCE dosage when exceeding the critical point. The long-term drying shrinkage and electric flux of UHPC increased significantly with the increase of EPEG-type PCE dosage. The higher the dosage of EPEG-type PCE, the faster the increase of electric flux value of UHPC, and the worse the chloride ion penetration resistance of UHPC.

KEYWORDS: UHPC, EPEG-type PCE, dosage, workability, compressive strength, shrinkage

1. Introduction

UHPC is a kind of cement-based composite material born in the 1990s, which is characterized by extremely low water-binder ratio, dense accumulation of multiple fine particles and toughening with steel fiber^[1]. It is widely used in strengthening and repairing bridges, building curtain walls, prefabricated buildings and other fields^[2-4]. However, the shortcomings of UHPC are also very prominent. The workability of UHPC has become very poor due to the ultra-low water-binder ratio and ultra-high amount of cementitious materials, it is usually necessary to add a large amount of polycarboxylate superplasticizer (PCE) to improve its fluidity^[5-6], and the role of superplasticizer becomes very critical. In this paper, a novel EPEG-type PCE with a high water reducing rate was synthesized, which successfully realized the ultra-high dispersion of cementitious particles under the condition of low water to binder ratio. The influence of EPEG-type PCE on the workability, mechanical properties and durability of UHPC was studied, and provide reference for the application of UHPC engineering.

2. Experiment

2.1 Materials

Ethylene glycol monovinyl polyethylene glycol ether (EPEG), self-developed; Acrylic acid (AA), hydrogen peroxide, ascorbic acid, and 3-mercaptopropanoic acid (3-MPA) purchased from Hongyan reagent factory of China.

Cement: PO 52.5, Tangshan Jidong Cement Co., LTD; Superfine mineral powder (SMP): 1250 mesh; Sand: quartz sand, 20~40 mesh and 40~80 mesh, Hebei; Silica fume (SF): amorphous SiO₂ content is 95.8% and specific surface area greater than 20 m²/g was purchased from Gansu Sanyuan Silicon Materials Co., Ltd; Steel fiber: copper-plated fiber with a diameter of 0.22 mm and a length of 13~15 mm. Polycarboxylate superplasticizer: EPEG-type PCE, solid content is 40%.

2.2 Synthesis of PCE

330 g EPEG, 3 g hydrogen peroxide and 210 g water were added to a four-necked flask with a stirring device. 60 g AA aqueous solution as A solution, and 103 g 3-MPA and ascorbic acid aqueous solution as B solution were dripped respectively into the flask at 20°C for 1h. and then continued reaction at a constant temperature for 1h to obtain EPEG-type PCE.

2.3 UHPC mix design

The mix design of UHPC is shown in Table 1.

Table 1 Mix ratio of UHPC

| Cement | SF | SMP | Sand 20~40 mesh | Sand 40~80 mesh | Steel fiber | Water |
|--------|-----|-----|--------------------|--------------------|-------------|-------|
| 800 | 150 | 150 | 630 | 420 | 150 | 198 |

2.4 Test Methods

2.4.1 Structure characterization of EPEG-type PCE

Fourier transform infrared (FT-IR) measurements were performed by FT-IR spectrometer (TENSOR 27, BRUKER, Germany) and relative molecular mass was characterized by Gel Permeation Chromatography (GPC, BI-Molecular weight Analyzer, USA).

2.4.2 UHPC performance test

UHPC fluidity test: The test was carried out according to Chinese standard of GB/T 2419-2005 'Cement mortar fluidity determination method' without vibration.

Drying shrinkage and electric flux test of UHPC: refer to Chinese standard of GB/T 50082-2009 'Test method for long-term performance and durability of ordinary concrete'.

3. Results and discussion

3.1 Characterization of EPEG-type PCE

Fig.1 is the infrared spectrum of EPEG-type PCE. There is an obvious peak at 3442 cm^{-1} , indicating the stretching vibration absorption of -OH. A strong peak at 2889 cm^{-1} and multiple peaks suggest the stretching vibration absorption of alkyl saturated carbon (-CH₃, -CH₂, etc.). 1469 cm^{-1} is the stretching vibration absorption peak of saturated carbon C-H. 1243 cm^{-1} should be the stretching vibration absorption peak of C-O in the alcohol or ether structure, a strong absorption peak at 1109 cm^{-1} should be the stretching vibration absorption peak of -O- in the ether structure. The strong peak at 842 cm^{-1} should be the trans vibration absorption peak of enyne, and the out-of-plane bending vibration absorption peak of olefin C-H at 962 cm^{-1} . The above analysis results show that the polyether molecule includes the characteristic functional groups C=C, C-O, and -OH. According to the GPC data (Fig.2), the average molecular weight of the EPEG-type PCE is 36856 $\text{g}\cdot\text{mol}^{-1}$, the molecular weight distribution value (PDI) is 1.72, and the conversion rate is 96.34%.

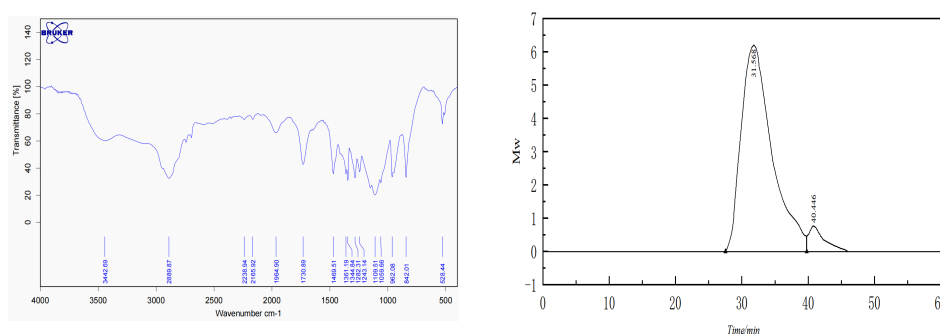


Fig.1 FT-IR of EPEG-type PCE

3.2 The effect of EPEG-type PCE dosage on the fluidity of UHPC

Table 2 shows the fluidity test results of UHPC with different EPEG-type PCE dosages. It can be seen from Table 2 that when the dosage of EPEG-type PCE is less than 1.5%, the amount of EPEG-type PCE

is positively correlated with the fluidity of UHPC. However, when the dosage of EPEG-type PCE is higher than 1.5%, this relationship is significantly changed. When the dosage of EPEG-type PCE is increased, the fluidity of the slurry remains stable and basically unchanged. Even when the dosage of EPEG-type PCE is very high, the fluidity tends to decrease slightly.

Table 2 Influence of dosage of EPEG-type PCE on fluidity of UHPC

| PEC dosage % | 0.5 | 1 | 1.5 | 2.0 | 2.5 |
|--------------|-----|-----|-----|-----|-----|
| Fluidity/mm | 115 | 225 | 267 | 266 | 262 |

The dispersion mechanism of EPEG-type PCE on cement is the dual mechanism of adsorption, electrostatic repulsion and steric hindrance, which is dominated by steric hindrance, thus ensuring the good dispersion of EPEG-type PCE on cement particles. When the amount of water reducing agent exceeds the saturation point (Fig.3), the adsorption vacancies on the surface of cement particles are gradually occupied and saturated. At this time, the adsorption amount of EPEG-type PCE is almost no longer increased with the dosage of EPEG-type PCE, and the fluidity of paste is no longer increased as well. When the amount of water reducing agent is too high, the free molecules of EPEG-type PCE in the pore solution will crosslink with the molecules adsorbed on the surface of the rubber particles, thus reducing the slump flow of UHPC.

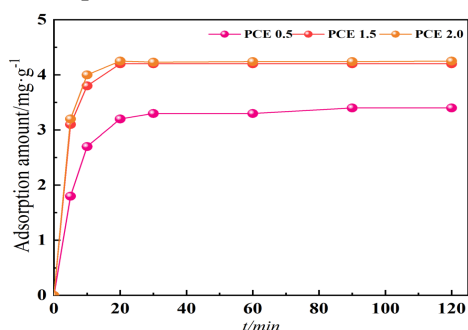


Fig.3 Adsorption capacity of EPEG-type PCE in binding material at different dosages

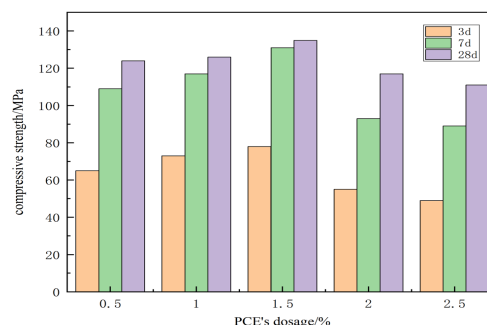


Fig.4 Compressive strength of UHPC with different dosage of EPEG-type PCE

3.3 Influence of dosage of EPEG-type PCE on compressive strength of UHPC

As shown in Fig.4. It can be seen that the dosage of EPEG-type PCE has a significant effect on the early strength of UHPC. Within a certain range, the early strength of concrete increases with EPEG-type PCE dosage, and the later strength develops steadily. When the dosage increased to 1.5%, the 3 d and 28 d compressive strength of UHPC increased to 78.6 MPa and 135.8 MPa respectively. While the water reduction dosage was 2.5%, the 3d and 28d compressive strength of UHPC decreased to 49.2 MPa and 111.9 MPa respectively. Before the saturated dosage point, the addition of EPEG-type PCE can release the flocculation water in the flocculation group of cement particles in the low water-binder ratio system and promote the hydration of cement particles. However, when the dosage of EPEG-type PCE exceeds the saturation point, EPEG-type PCE reacts with the free Ca^{2+} in the interstitial solution to form an unstable complex, which inhibits the hydration process and leads to the decrease of early strength. As the hydration process progresses, this unstable complex will decompose by itself, and hydration will continue normally.

3.4 Effect of EPEG-type PCE on durability of UHPC

3.4.1 Drying shrinkage

As shown in Table 3, The long-term drying shrinkage of UHPC increases significantly with higher PCE dosage. When the dosage of PCE increased from 1.0% to 1.5%, the drying shrinkage of UHPC increased by 9.4%. When the dosage of PCE increased to 2.0%, the drying shrinkage of UHPC reached 511×10^{-6} . The drying shrinkage of UHPC is due to the evaporation of water in the capillary pores and the gel. After the addition of PCE, the water in the system is relatively increased, and the size of the capillary pores is reduced. The greater the negative pressure generated due to the evaporation of water in the capillary pores, the more pronounced is the increase in negative pressure acting on the capillary pore wall, leading to enhanced drying shrinkage of UHPC^[7].

Table 3 Drying shrinkage of UHPC with different EPEG-type PCE dosage

| Age | | Drying shrinkage/ $\times 10^{-6}$ | | | | | | |
|-------------------------|-----|------------------------------------|-----|-----|-----|-----|-----|-----|
| | | 1d | 3d | 7d | 14d | 28d | 56d | 90d |
| EPEG-type PCE dosage | 1.0 | 93 | 154 | 276 | 331 | 402 | 431 | 443 |
| | 1.5 | 103 | 165 | 299 | 356 | 428 | 478 | 485 |
| | 2.0 | 132 | 209 | 324 | 376 | 444 | 501 | 511 |

3.4.2 Chloride penetration resistance

As Fig.5 shown, When EPEG-type PCE dosage is 1.0%, 1.5% and 2.0%, the electric flux values of UHPC are 100.3 C, 121.5 C and 145.7 C respectively. Compared to the electric flux at 1.0% dosage, it increases by 21.1% and 44.6% at dosage of 1.5% and 2% respectively, which indicates chloride ion penetration resistance decreases with the increase of dosage of EPEG-type PCE. This can be attributed to the low water to binder ratio, small porosity of hardened system, less internal interface defects and more active mineral admixtures in UHPC. The pozzolanic effect and secondary hydration reaction can effectively improve the pore structure of concrete.

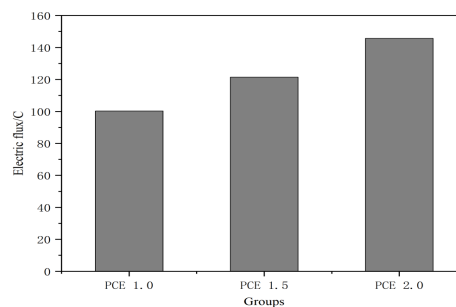


Fig.5 EPEG-type PCE on the electric flux of UHPC

4. Conclusions

A novel EPEG-type PCE was developed which can improve the workability and mechanical properties of UHPC at an appropriate dosage. When the dosage exceeds 1.5%, The slump of UHPC no longer increases with the increase of dosage of EPEG-type PCE and the compressive strength of UHPC gradually decreases. The drying shrinkage and electric flux of UHPC increase significantly with the increase of dosage of EPEG-type PCE, which indicates that the excessive addition of EPEG-type PCE will be detrimental to the durability of UHPC.

Acknowledgements

This study is sponsored by the program fund of NEXCEL, Non-Metallic Excellence and Innovation Center for Building Materials (Project No. 2022TDA3-1).

References

- [1] Shi, C.J., Wu, Z., M, Xiao., J.F, et al. (2015) "review on ultra-high-performance concrete: Part I. Raw materials and mixture design". *Construction and Building Materials*, (101): 741-751.
- [2] Hao L W. (2013) "Preparation of polycarboxylic acid water-reducing agent for ultra-high strength RPC", *New Building Materials*, (3): 27-28.
- [3] Shao, Z.C, Guo, K.Y, Liu, S.W, et al. (2020) "Study on synthesis of high performance polycarboxylic acid water-reducing agent". *Chemical Industry and Engineering*, 37(6): 30-37.
- [4] Li F, Kong W Y, Luo J, et al. (2019) "Preparation and application of ultra-high performance concrete (UHPC)", *Concrete and Cement Products*, (7): 26-29.
- [5] Huang Z, Yang Y, Ran Q, et al. (2018) "Preparing hyperbranched polycarboxylate superplasticizers possessing excellent viscosity-reducing performance through in situ redox initialized polymerization method". *Cement and Concrete Composites*, 93: 323-330.
- [6] Shu X, Ran Q, Liu J, et al., (2016) "Tailoring the solution conformation of polycarboxylate superplasticizer toward the improvement of dispersing performance in cement paste". *Construction and Building Materials*, 116: 289-298.
- [7] TAM, C.M., TAM, V.W.Y., NG, K.M. (2012) "Assessing drying shrinkage and water permeability of reactive powder concrete produced in Hong Kong". *Construction and Building Materials*, 26(1): 79-89.

Thermal Crack Resistance and DEF Suppression Effect of Concrete Using Fly Ash Cement

Yuji Mitani^{1*}, Akira Yoneyama¹, Masao Ishida¹, Takuya Ohno², Joseph S.H. Lim³,

Logendran Doraipandian³ and Somnuk Tangtermsirikul⁴

¹ Central Research Laboratory, Taiheiyo Cement Corporation, Japan

¹ Email: Yuuji_mitani@taiheiyo-cement.co.jp

² Taiheiyo Singapore Pte. Ltd., Singapore

³ Island Concrete Pte. Ltd., Singapore

⁴ Thammasat University, Thailand

ABSTRACT

This study aims to verify the effect of concrete using fly ash cement on controlling the thermal cracking and DEF expansion deterioration in mass concrete structures. Thermal cracking resistance of concrete containing 30% fly ash (FA30) was experimentally evaluated by TSTM (Thermal-Stress Testing Machine). TSTM is a thermal stress simulation apparatus with uniaxial restraint type, which can subject a concrete specimen to any temperature and restraint conditions. As a result of TSTM test, FA30 showed no cracks under the conditions with temperature history assuming inside of a mass concrete and complete restraint. Compared to the concrete containing 65% ground granulated blast furnace slag (BS65), thermal cracking resistance of FA30 was clearly higher than that of BS65 at the same water to binder ratio. Moreover, creep property was indirectly predicted by effective Young's modulus obtained from the relationship between the restrained strain and stress in the TSTM. Based on these results, the causes of the higher crack resistant of FA30 than BS65 could be presumed to be not only smaller autogenous shrinkage but also larger stress relaxation by creep. DEF (Delayed Ettringite Formation) risk of the concrete was assessed by accelerated test. The test result shows that expansion strain of FA30 was not abnormal at soaking time up to approximately 4-years. It was confirmed that DEF expansion risk of FA30 is very low, and that fly ash clearly has DEF suppression effect.

KEYWORDS: *Fly ash cement, Mass concrete, Thermal cracking, TSTM, DEF*

1. Introduction

Fly ash is one of the supplementary cementitious materials widely used all over the world not only to reduce environmental impact of concrete but also to improve concrete performance such as workability, long-term strength development, low-heat generation and durability. Fly ash is well known to cause problems in ensuring low early-term strength and proper air content. However, we can use fly ash more effectively in countries with warm climates, because of increasing early-term strength with the warm ambient temperature and unnecessary to control air content as a counter measure against freeze-thaw deterioration.

The objective of this paper is to verify the effect of fly ash cement to controlling thermal cracks and DEF cracks in mass concrete subjected to high temperature history at early age. Thermal cracking resistance was evaluated by using TSTM. DEF risk was evaluated by original accelerated test.

2. Experimental Program

2.1 Concrete Materials and Mix Proportions

Table 1 shows the concrete materials, and Table 2 shows the mix proportions. The concrete with OPC containing 30% of FA (FA30) was evaluated in this study. BS65 in which GGBS was replaced by 65% was prepared for comparative purpose. Water to binder ratio was 40%, and the unit water contents was 165 kg/m³. Dose of chemical admixture was adjusted to achieve a slump of 120±25 mm and an air content of 2.0% or below. Assuming warm climate, concrete mixing was carried out at 27°C

2.2 Thermal-Stress Testing Machine (TSTM)

Figure 1 shows outline of TSTM which was a uniaxial restraint-type thermal stress simulator capable of creating temperature and restraint conditions of real mass concrete structures (Springerschmid, R., *et al.* 1985; Mizobuchi, T. *et al.* 2010). TSTM specimen were applied with the temperature history obtained by thermal analysis for the central point of a 1.0m-thick wall member using 3D-FEM. Input data of heat generation property for thermal analysis was test results of adiabatic temperature rise measured by using air circulation type measurement apparatus (Figure 2). Water temperature flowing through the water conduction pipe was controlled to make concrete specimens keep the designed temperature history. The restrained specimen was controlled to complete restraint degree such that deformation of the gauge length was zero. In the unrestrained specimen, free strain including thermal strain and autogenous shrinkage was measured under the same temperature history as the restrained specimen.

2.3 DEF Accelerated Test

No standardized methods are available for DEF evaluation at present. In this study, an accelerated test was conducted in accordance with the method proposed by Duggan (Duggan, C.R., *et al.* 1986), which is taken up in the Research and Development Bulletin published by Portland Cement Association in USA (Robert L. DAY 1992). Cyclic treatment of oven dry curing and room-temperature water curing (Figure 3) was performed to accelerate occurrence of DEF after applying a temperature history with the maximum temperature of around 85°C assumed for the inside of mass concrete (Figure 4). Cylindrical specimens (diameter:100mm, length:200mm) were prepared for the test, and the change in length was measured on the side of each specimen using the contact gauge.

Table 1 Materials used

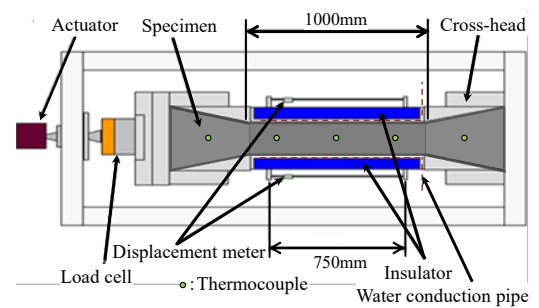
| Materials | Symbols | Types and properties |
|--------------------------------------|---------|---|
| Cement | OPC | Ordinary Portland cement, made in Japan /density: 3.15 g/cm ³ , SSA: 3320 cm ² /g |
| Fly ash | FA | Made in Japan /density: 2.23 g/cm ³ , specific surface area: 3330 cm ² /g |
| Ground granulated blast-furnace slag | GGBS | Gypsum added type (SO ₃ : 2.03%), made in Japan /density: 2.89 g/cm ³ , SSA: 4310 cm ² /g. |
| Fine aggregate | S1 | Manufactured sand, made in Malaysia / density: 2.57 g/cm ³ , absorption: 1.18% |
| | S2 | Natural sand, made in Malaysia / density: 2.55 g/cm ³ , absorption: 1.17% |
| Coarse aggregate | G | Crushed granite, made in Indonesia / density: 2.62 g/cm ³ , absorption: 0.71% |

SSA: Specific Surface Area

Table 2 Mix proportions

| Symbols | W/B (%) | Unit Contents (kg/m ³) | | | | | | |
|---------|---------|------------------------------------|-----|-----|------|-----|-----|------|
| | | W | OPC | FA | GGBS | S1 | S2 | G |
| FA30 | 40 | 165 | 289 | 124 | 0 | 398 | 286 | 1050 |
| BS65 | | 165 | 144 | 0 | 268 | 403 | 290 | 1063 |

[Restrained specimen]



[Unrestrained specimen]

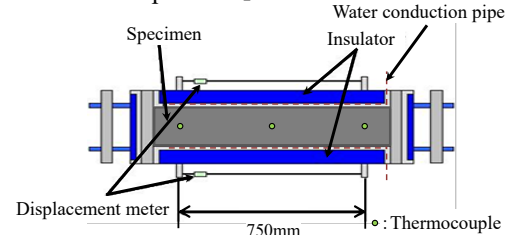


Figure 1 Outline of TSTM

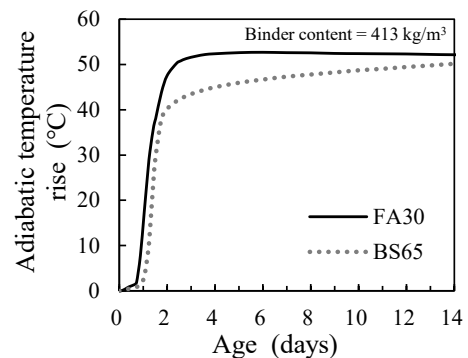


Figure 2 Adiabatic temperature rise

3. Results and Discussions

3.1 Thermal Cracking Risk

Figure 5 shows free strain in unrestrained specimen, and Figure 6 shows autogenous shrinkage. Autogenous shrinkage was calculated by subtracting thermal strain from the free strain. Thermal expansion coefficient of FA30 for calculating thermal strain was assumed to be $10 \times 10^{-6}/^{\circ}\text{C}$. On the other hand, thermal expansion coefficient of BS65 was $12 \times 10^{-6}/^{\circ}\text{C}$ based on the previous studies that thermal expansion coefficient of concrete containing GGBS is approximately 20% larger than that of normal concrete with OPC (Japan Concrete Institute 2008). Autogenous shrinkage of FA30 was clearly smaller than that of BS65.

Thermal stress measured in TSTM restrained specimen is shown in Figure 7. Measured concrete tensile strength was also shown in the figure. Regarding thermal stress of FA30, compressive stress of 1.0 N/mm^2 occurred in temperature rising period, after the compressive stress was decreasing and tensile stress of 2.1 N/mm^2 occurred at 14-day age after the temperature fall, which is about 1/2 of the tensile strength. FA30 had no cracks caused by the thermal change. In contrast, BS65 was cracked at 5-day age during temperature falling period. The tensile stress was about 2.0 N/mm^2 , which is 40% of the tensile strength. The results can indicate that FA30 has higher resistance to thermal cracking than BS65, and one of the causes seems to be small autogenous shrinkage.

Figure 8 shows the relationship between stress and restraint strain. The restraint strain was obtained by subtracting the strain of restrained specimen from the strain of unrestrained specimen. The relationship was basically linear in the four sections (i); the period until final setting time, (ii); the compressive stress increases greatly in temperature rising period, (iii); the compressive stress decreases in temperature falling period, (iv); the tensile stress is occurring. The gradient of the regression lines could be assumed to be the effective Young's modulus (E_{ce}) considering the influence of both elastic strain and creep strain under the restrained conditions. Table 3 summarizes E_{ce} and the Young's modulus ratio (E_{ce}/E_c) in each section. E_c is the static Young's modulus measured on cylindrical specimens. Compared with E_{ce}/E_c of FA30 and that of BS65, the values are the almost same in temperature rising period (i) and (ii). On the other hand, E_{ce}/E_c of FA30 is smaller than that of BS65 in temperature falling period, especially in section (iii). In general, the smaller E_{ce}/E_c , the larger the influence of concrete creep is assumed to be, because E_{ce} is lower than E_c measured under static loading condition due to effect of creep. From this result, one of the causes for higher cracking resistance of FA30 is presumed to be that the stress relaxation effect of FA30 due to creep is

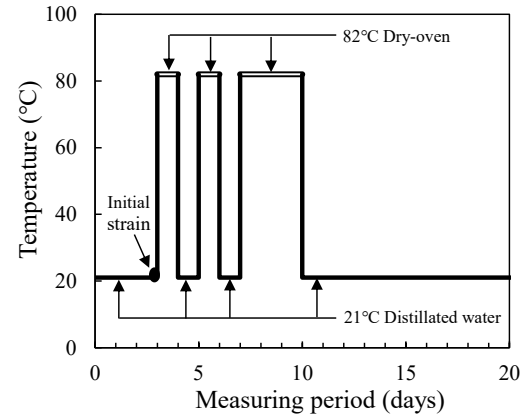


Figure 3 Curing conditions

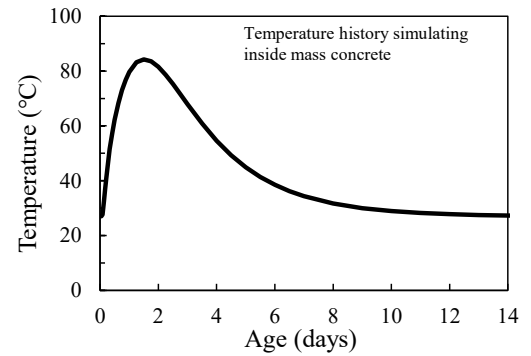


Figure 4 Temperature history

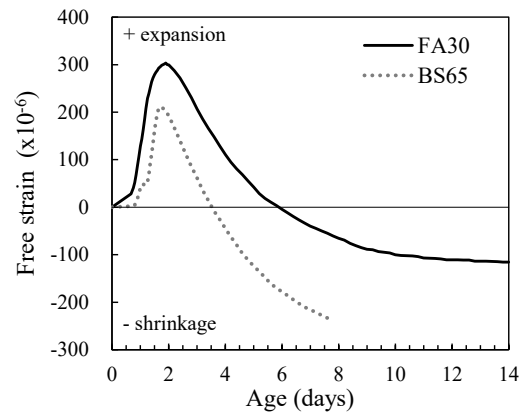


Figure 5 Free strain(unrestrained specimens)

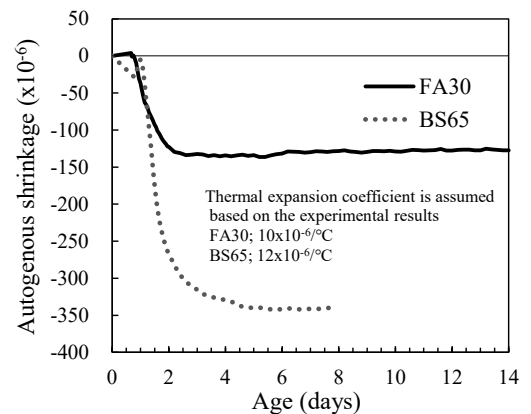


Figure 6 Autogenous shrinkage

greater than that of BS65.

3.2 DEF Risk

Figure 9 shows the measured change in length. FA30 and BS65 showed no abnormal expansion strain at more than 4 years, suggesting their high resistance to DEF. The figure also shows a case of higher DEF risk which used OPC containing potassium sulphate (K_2SO_4) at ratio equivalent to 1.0% and 2.0%. With the increase in alkali content, expansion strain of over 20000×10^{-6} occurred at 2 years. The specimen had significant cracks, and needle crystals of ettringite was observed in the interfaces between aggregates and cement pastes by scanning electron microscope (Figure 10).

4. Conclusions

The thermal crack resistance and DEF risk of fly ash cement on mass concrete in a warm environment were experimentally evaluated. It was clarified that concrete with fly ash cement has high cracking resistance due to its low autogenous shrinkage and large stress relaxation by creep, and also has the effect of reducing the occurrence of DEF in the long term.

Acknowledgements

The authors would like to acknowledge Prof. Toshiaki Mizobuchi of Hosei University for great support in TSTM experiment.

References

- Duggan, C.R. and Scott, J.F. (1986) "Potential New Test for Alkali aggregate Reactivity", *Roe. 7th Intl. Conf. on alkali Aggregate Reactions*: 319-323
- Japan Concrete Institute (2008) *The Guidelines for Control of Cracking of Mass Concrete 2008*: 93-114
- Mizobuchi, T. et al. (2010) "Experimental Study to Estimate Thermal Stress Caused by Heat of Cement Hydration in Massive Concrete Structures", *Proceedings of the 2nd International Symposium on Service Life Design for Infrastructures*: 733-740
- Robert L. DAY (1992) "The Effect of Secondary Ettringite Formation on the Durability of Concrete: A Literature Analysis, *Research and Development Bulletin RD108T*
- Springerschmid, R., et al. (1985) "Thermal Stresses in Mass Concrete: A New Testing Method and The Influence of Different Cements", *Quinzieme Congres des Grands Barrages, Lausanne, Commission Internationale Des Grands Barrages*: 57-72

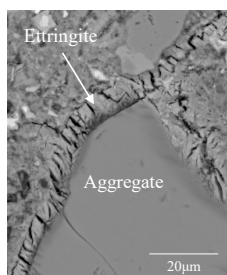


Figure 10 Ettringite in the interfaces between aggregate and cement paste (SEM)

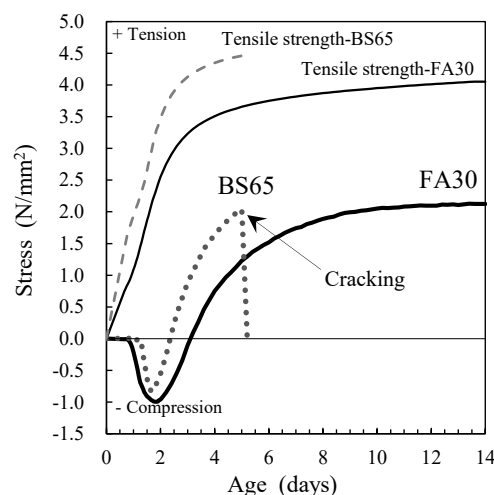


Figure 7 Thermal stress (TSTM)

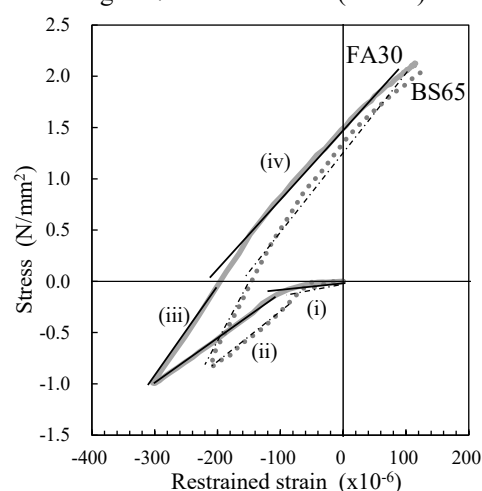


Figure 8 Relationship between restrained strain and stress

Table 3 Young's modulus ratio

| section | FA30 | | BS65 | |
|---------|-----------------------------------|--------------|-----------------------------------|--------------|
| | E_{ce} (kN/mm ²) | E_{ce}/E_c | E_{ce} (kN/mm ²) | E_{ce}/E_c |
| (i) | 0.9 | 0.07 | 1.3 | 0.08 |
| (ii) | 4.5 | 0.23 | 5.2 | 0.19 |
| (iii) | 9.1 | 0.33 | 12.7 | 0.42 |
| (iv) | 6.4 | 0.18 | 7.5 | 0.22 |

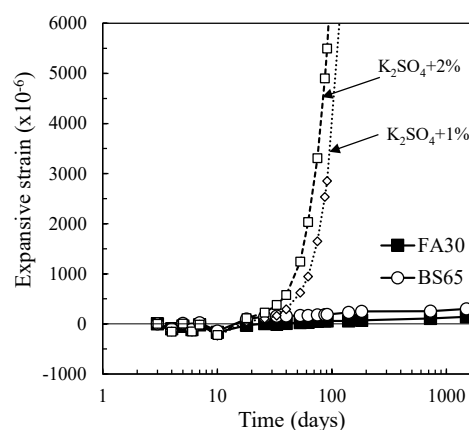


Figure 9 Expansion strain

Gradient distribution of slender glass microfibers in 3D printed cementitious filaments

Rijiao Yang ¹, Qiang Zeng ¹, and Zhendi Wang ²

¹ College of Civil Engineering and Architecture, Zhejiang University, Hangzhou, 310058, China.

Email: 12212088@zju.edu.cn (YR), cengq14@zju.edu.cn (ZQ)

² State Key Laboratory of Green Building Materials, China Building Materials Academy, Beijing 100024, P.R. China

Email: wzhendi@163.com

ABSTRACT

Extrusion is a widely used automatic construction technique that builds a structure through the pattern of material addition. The unique extrusion molding would greatly impact the microstructure of the printed cementitious filaments containing different particles in size, volume, and shape. Most studies reported the aligned distribution of fibers with small slenderness in extrusion molded cementitious filaments (EMCFs). However, the content and direction of highly slender microfibers in EMCFs have not been fully understood due to the gradient shearing forces acting on the cementitious slurries during printing. Here, we focus on the distribution of glass microfibers with the slenderness (length-to-diameter ratio) of 429 in EMCFs. X-ray computed tomography (XCT) was employed to track the glass microfibers in the EMCFs and provide the information of content and orientation of the fibers in different positions of EMCFs. To resolve the specific fibers' information, 25 layers of sheet (thickness of each layer = 0.2 mm) from the interface to the center of each EMCF were segmented during XCT analysis. The results show that the slender microfibers possessed the gradient distributions of orientation and content from the interface to the inner matrix of the EMCFs. Mechanisms of those behaviors are discussed in terms of particle collisions and distribution of shearing forces in the printing pipe during extrusion modeling. The findings would deepen the understandings in slender microfibers redistribution in non-Newtonian liquid during extrusion molding.

KEYWORDS: *3D printing, Microfibers, Spatial distribution, Orientation, Efficiency*

1. Introduction

Three-dimensional (3D) printing is one of the widely used automatic construction techniques showing great advantages in terms of economy and environmental benefits. There are different ways to 3D-printing concrete constructions, among which extrusion is easily accepted for low cost and simple equipment (Shakor et al 2020; Xiao et al 2021). During extrusion molding, the spatial distribution of particles in the printed cementitious filaments would be influenced by uneven shearing actions for different size, volume and shape of the particles, which would impact the mechanical properties of the materials (Fataei et al (2021) and Auernhammer et al (2020)).

Fibers that were often used as a reinforcement in cementitious materials could be regarded as a type of particle with large slenderness, so the spatial distribution of fibers would also be affected by the extrusion process. Moreover, fiber orientation also plays an important role on the overall performance of the materials. It is worth noting that the spatial and directional distribution of fibers should be further concerned in extrusion molded cementitious filaments (EMCFs). The studies (Hambach et al (2019), Liu et al (2022) and Dong et al (2022)) reported that fibers with small slenderness presented the aligned distribution during printing, which greatly improved the flexure strength of EMCFs. Different from macro fibers with relatively small slenderness, high slender microfibers cannot easily keep straight under shearing forces, which makes the fiber directional distribution more complex. To fully understand the effect of the gradient shearing forces on fibers, it is meaningful to characterize the spatial and directional distribution of high slender microfibers in EMCFs.

This paper mainly focuses on the mechanism of fiber migration and distribution under gradient shearing actions. EMCFs with two dosages of glass microfibers were prepared and non-destructive XCT test was obtained to characterize the spatial and directional distribution of the fibers. A layer-by-layer imaging analysis was specifically used to measure the content and orientation of the microfibers. The particle collisions and distribution of shearing forces on the cementitious slurries during extrusion molding may account for the observed gradient content and direction distributions of the microfibers.

2. Sample and Methods

Glass microfiber reinforced cementitious materials were prepared by extrusion 3D printing using the mix proportions as shown in Table 1. Glass microfibers with the diameter of 14 μm and length of 6 mm ($L/D = 429$) were used with the contents of 0.3 wt% and 0.6 wt% (EMCF3 and EMCF6). Filaments with the diameter of 10 mm were printed in the speed of 20 mm/s to construct a unit with 8 layers of filaments. After printing, the samples were cured for 28 days and small cuboids (around 6 mm \times 6 mm \times 6 mm) containing the interlayer zone (IZ) were cut.

Table 1 Mix proportions of the 3D-printed extrusion molded cementitious filaments (EMCFs)

| Sample ID | Water /wt% | Cement /wt% | Accelerator /wt% | HPMC /wt% | PCE-SP /wt% | Glass fiber /wt% |
|-----------|------------|-------------|------------------|-----------|-------------|------------------|
| EMCF3 | 30 | 100 | 2.25 | 0.15 | 0.44 | 0.3 |
| EMCF6 | 30 | 100 | 2.25 | 0.15 | 0.44 | 0.6 |

The specimens were put into XTH255/320 LC (Nikon, Japan) device for non-destructive XCT scans (Figure 1a). All X-ray projections were qualified and reconstructed by "CT 3D Pro" software, and the region of interest (ROI) of 5 mm cube was extracted by "VG Studio Max" software (Figure 1b). After fibers had been extracted using the threshold and filter tools in the visualizing software, fiber direction and content were analyzed by "fiber module". Small ROI of 0.2 mm thickness was segmented for further orientation analysis (Figure 1c). Fiber orientation was evaluated by orientation index, $OI = \cos^2\theta$, where θ is the angle between the fiber and the printing direction (Yang et al (2022b)).

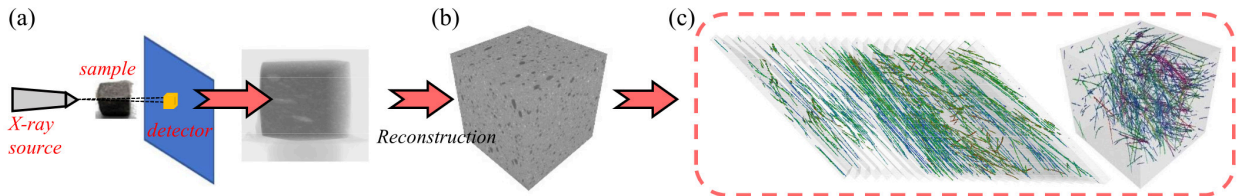


Figure 1 Test and data processing by μ -XCT: (a) XCT scans of a 3D-printed EMCF sample; (b) image stacking and reconstruction; and (c) fiber orientation analysis.

3. Results and discussion

The fiber content and directional distribution (i.e. OI) perpendicular to the interlayer plane are shown in Figure 2. The position at 0 mm denoted the center of IZ and the blue regions represented the range of IZ for both EMCF3 and EMCF6, respectively. In EMCF3, the fiber content slightly decreased from 0.3% to 0.02% and then sharply increased to 1.1% from -3 mm or 2 mm to the center of IZ (at 0 mm). The large fiber content in IZ means that the fibers migrated to IZ during extrusion, see Figure 2(a). Obviously, the fiber content changed acutely from -2 mm to 2 mm, indicating that the impact region of the uneven shearing forces on fiber spatial distribution was 4 mm in EMCF3. For EMCF6, the fiber content also increased from the matrix at -3 mm or 2 mm to the center of IZ (at 0 mm), and the impact region exceeded 5 mm. Note that the highest fiber content for EMCF6 was 0.96% (Figure 2b), less than that in EMCF3 (Figure 2a). It seems that increasing fiber dosage could enlarge the shearing impact region but lessen (limit) the fiber migration extent.

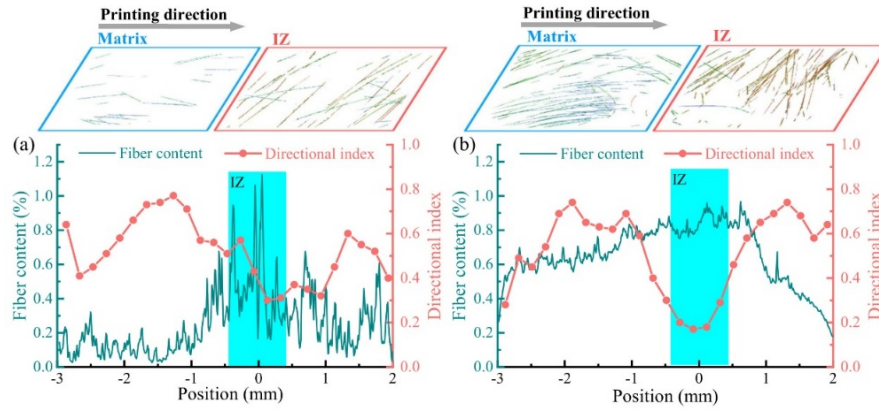


Figure 2 Fiber content and directional distributions in EMCF3 (a) and EMCF6 (b) and selective demonstrations.

The values of OI in EMCF3 increased to nearly 0.8 at 1.3 mm and then decreased to below 0.3 around the center of IZ at 0 mm (Figure 2a). The highest OI values were recorded at 0.77 and 0.74 for ECMF3 and EMCF6, respectively, and the lowest values at the interface were found at 0.3 for EMCF3 and at 0.17 for EMCF6. Roughly, the microfibers followed the printing direction in the matrices, but were perpendicular to the printing direction in the IZ.

To evaluate the efficiency of fiber content and OI distribution, a parameter of fiber efficiency (FE) was employed (Abrishambaf et al (2017)): $f_u = C_f \cos \theta \tau_f l_f \div d_f$, where C_f is fiber content; τ_f is the bonding strength between fiber and matrix; l_f is the length of fibers and d_f is the diameter of fibers. Because other parameters were constant in this work, the relationship can be simplified as $FE = C_f \times \cos \theta$. Figure 3a displays the distribution of FE. The trend of FE in EMCF3 and EMCF6 varied greatly. In EMCF3, the trend of FE was similar with that of fiber content. But in EMCF6, the variation of FE was similar with that of OI. The FE of EMCF6 was always higher than that of EMCF3 except in the IZ. The findings in Figure 3a meant that increasing fiber dosage could strengthen the matrix but weaken the IZ. Figure 3b shows the results of FC, OI and FE. In EMCF3, the values of FC and FE in the IZ were higher than those in the matrix by 114.3% and 78.6%, respectively, while the values of OI in the IZ was less than that in the matrix by 25.9%. EMCF6 showed quite different trend, where OI and FE in the IZ were less than those in the matrix by 63.8% and 27.3%, respectively, and FC in the IZ was higher than that in the matrix by 35.5%.

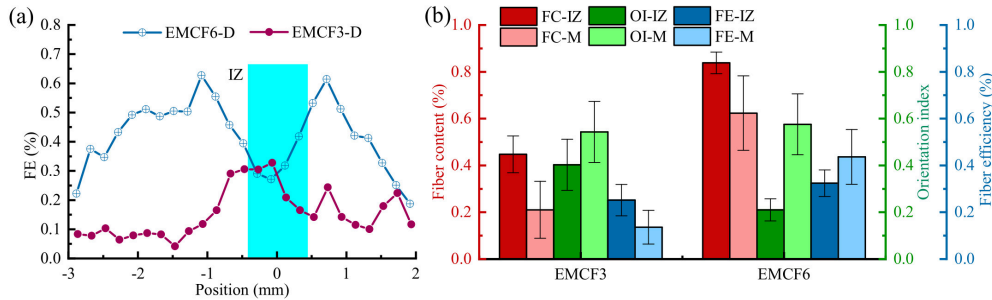


Figure 3 (a) FE distribution at different position and (b) statistical results of FC, OI and FE for both samples.

In a word, the spatial and orientation distribution of microfibers were uneven after extrusion molding. Figure 4 schematically shows the effect of non-uniform shearing actions on the gradient distribution of fibers. Our results demonstrated that the value of OI became smaller but the fiber content increased at IZ (Figure 2), indicating that microfibers were migrating to IZ with the aligned direction (Figure 4). During printing, the flowing speed of the EMCF slurries slowed down near the IZ, so the largely slender glass microfibers gradually became bent. Later, the microfibers were perpendicular to the printing direction to counterbalance the particle collisions and uneven shearing forces. The effect of gradient shearing force on the migration and orientation changes of microfibers in EMCFs has been documented in the literature (Yang et al (2022b)). It should be noted that excessively increasing fiber content would not strengthen materials, because a higher fiber dosage in cement slurries would considerably raise the gradient shearing forces, and consequently more microfibers would be perpendicular to the printing direction in IZ. However, the increased viscosity due to the increased fiber content would mitigate the migration of fibers

to IZ (Yang et al 2022a). This behavior was verified in this work as shown in Figure 2(b), where the OI values in the IZ of EMCF6 was reasonably smaller than that of EMCF3.

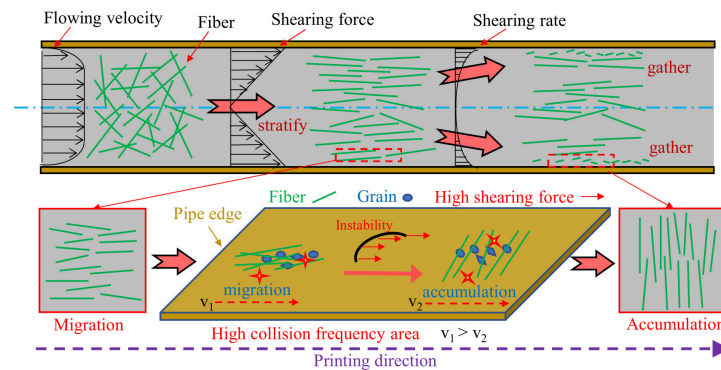


Figure 4 Schematic diagram of the effect of non-uniform shearing on the uneven distributions of fiber.

4. Conclusion

During extrusion printing, microfibers gradually migrated to IZ under gradient shearing forces leaving a matrix devoid of fibers. The large shearing forces with high fiber content and slow flowing speed resulted in bent microfibers perpendicular to the printing direction.

Acknowledgements

This work was supported by the Program Fund of Non-Metallic Excellence and Innovation Center for Building Materials (2022SFP1-1).

Reference

- Abrishambaf A., Pimentel M. and Nunes S. (2017) "Influence of fibre orientation on the tensile behaviour of ultra-high performance fibre reinforced cementitious composites", *Cement and Concrete Research* 97: 28-40.
- Auernhammer G. K., Fataei S., Hausteind M. A., Patela H. P., Schwarze R., Secrieru E. and Mechtcherine V. (2020) "Transparent model concrete with tunable rheology for investigating flow and particle-migration during transport in pipes", *Materials & Design* 193: 108673.
- Dong L., Yang Y., Liu Z., Ren Q., Li J., Zhang Y. and Wu C. (2022) "Microstructure and mechanical behaviour of 3D printed ultra-high performance concrete after elevated temperatures", *Additive Manufacturing* 58: 103032.
- Fataei S., Secrieru E., Mechtcherine V. and Roussel N. (2021) "A first-order physical model for the prediction of shear-induced particle migration and lubricating layer formation during concrete pumping", *Cement and Concrete Research* 147: 106530.
- Hambach M., Rutzen M. and D. Volkmer (2019) "Properties of 3D-Printed Fiber-Reinforced Portland Cement Paste", *3D Concrete Printing Technology* 73-113.
- Liu J., Li S., Fox K. and Tran P. (2022) "3D concrete printing of bioinspired Bouligand structure: A study on impact resistance", *Additive Manufacturing* 50: 102544.
- Shakor P., Nejadi S., Sutjipto S., Paul G. and Gowripalan N.(2020) "Effects of deposition velocity in the presence/absence of E6-glass fibre on extrusion-based 3D printed mortar", *Additive Manufacturing*. 32: 101069.
- Yang R., Zeng Q., Peng Y., Wang H. and Wang Z. (2022a) "Anomalous matrix and interlayer pore structure of 3D-printed fiber-reinforced cementitious composites", *Cement and Concrete Research* 157: 106829.
- Yang R., Zhu Y., Lan Y., Zeng Q., Peng Y. and Wang Z. (2022b) "Differences in micro grain/fiber distributions between matrix and interlayer of cementitious filaments affected by extrusion molding", *Additive Manufacturing* 60: 103236.
- Xiao J., Liu H. and Ding T. (2021)" Finite element analysis on the anisotropic behavior of 3D printed concrete under compression and flexure", *Additive Manufacturing* 39: 101712.

Effect of Hydrophobically Modified Hollow Glass microspheres on the flow behavior of lightweight high-performance concrete

J. Yang¹, D. Jeon², H. Kang³, and J. Moon^{4*}

¹ Department of Civil and Environmental Engineering, Seoul National University, Seoul, Republic of Korea
Email: snuyangjw@snu.ac.kr

² Department of Civil Engineering, Dong-A University, Busan, Republic of Korea
Email: donghojeon@dau.ac.kr

³ Department of Civil and Environmental Engineering, Seoul National University, Seoul, Republic of Korea
Email: kanghu93@snu.ac.kr

⁴ Department of Civil and Environmental Engineering, Seoul National University, Seoul, Republic of Korea
Email: juhyukmoon@snu.ac.kr

ABSTRACT

The use of hollow glass microspheres (HGMs) for developing lightweight high-performance concrete (L-HPC) generally reduces the workability of the mixture due to high water absorption capacity of HGMs. This study tried to improve the flow behavior of L-HPC by promoting the formation of a hydrophobic layer on the surface of microspheres. The hydrophobic HGMs were prepared by surface-modification using ball milling in the presence of stearic acid functional groups. The experimental results show that the production, including grinding for 2 hours or more with a 4 wt% addition of stearic acid, could convert hydrophilic HGMs into hydrophobicity. As a result, the water contact angle surpassed 102°. The composition results further proved that the surface of HGMs was successfully coated with a hydrophobic layer. The crystal peaks of stearic acid were detected by X-ray diffraction. Furthermore, the hydrophobic HGMs had a phase transition latent heat peak. However, microscopic results indicated that the ball milling method had a destructive effect on HGMs and decreased the particle size. Such damage also inevitably increased the density and thermal conductivity of L-HPC. Under steric repulsion, the fluidity of L-HPC added with hydrophobic HGMs was significantly improved compared to L-HPC added with original HGMs. The compressive strength of L-HPC also increased greatly under the combined effect of the small particle size of hydrophobic HGMs and less water absorption. Promoting the surface modification of particle can provide a new solution for increasing the flow behavior of UHPC.

KEYWORDS: *Lightweight HPC, Hollow glass microspheres, Surface, Hydrophobic, Workability.*

1. Introduction

Developing lightweight high-performance concrete (L-HPC) can effectively assist in constructing large-scale, complex, and high-level projects. According to our previous studies (Lee et al (2022) and Mahato et al (2022)), adding hollow microspheres to the high-performance concrete (HPC) matrix for L-HPC preparation would reduce the viscosity of the fresh concrete mixture and affect pumping, which is not conducive to the widespread promotion of hollow microspheres in the field of lightweight concrete structures. To improve the workability of concrete, superplasticizers (SP) are usually added, but they are expensive, and the design of HPC already has a higher SP dosage than ordinary concrete (Shi et al (2015) and Huang et al (2017)). Considering the economic benefits, it is not the optimal solution to continue to increase the SP to solve the impact of fluidity brought by hollow microspheres, so a lower-cost method is needed to deal with this problem.

Stearic acid (SA, C₁₈H₃₆O₂) is an environmental-friendly and practical material, often used as a surface modifier in various fields. Moreover, SA is cheap and abundant in nature. Combined applications of stearic acid in concrete materials are also extensive, and a very meaningful application is for

waterproofing concrete. The SA can be directly added to the concrete after being simply processed into an aqueous emulsion. This direct addition approach was used to prepare superhydrophobic concrete with integral waterproof properties (Lei et al (2020)). Similarly, the entire hydrophobic concrete can also be achieved by adding the hydrophobic supplementary cementitious materials. For example, SA hydrophobically modified waste paper sludge ash (PSA) and ground granulated blast furnace slag (GGBFS) could increase the water resistance of concrete structures (Wong et al (2015) and Qu et al (2018)).

The aim of this study was to modify hollow glass microspheres (HGMs) hydrophobic in a low-cost way to increase the fluidity of L-HPC. Based on knowledge of numerous applications of SA, this study used stearic acid to hydrophobically treat HGMs and examined the effects of hydrophobic HGMs on L-HPC workability. This research can enhance the application of HGMs in lightweight concrete.

2. Materials and methods

2.1 Surface modification of HGMs

Hollow glass microspheres (HGMs) provided by 3M Company were used in this study. The particle size distribution of most of the HGMs was between 0.66 and 39.3 μm . The water contact angle (WCA) test confirmed that the HGMs were surface hydrophilic micron-sized particles, and the WCA was 0°. The surface modify agent SA is a high-grade pure grade, and the purity can reach more than 95%.

The preparation of hydrophobic PSA by ball milling method was studied in Spathi's work (Spathi et al (2015)). Therefore, the hydrophobic surface modification of HGMs was carried out with reference to hydrophobic PSA processing conditions. A laboratory-type roller ball mill was used, and a 1L roller stainless steel ball mill tank was used to hold samples and grinding media. The outer diameter, inner diameter, and height of the tank were 106mm, 100mm, and 172mm, respectively. The mass ratio of the grinding sample, hydrophobic agent, and grinding medium was 25:1:125.

2.2 Evaluation of hydrophobic HGMs properties

A water drop experiment was initially used to determine the suitable parameter ranges of a ball mill, such as its speed, time, and grinding media size. After determining the appropriate range of milling parameters, the water contact angle test was used to quantitatively characterize the hydrophobic grade of the modified HGMs.

The surface hydrophobicity by the ball milling method was a modification at the physical level, so XRD was used to further detect the composition of the hydrophobic HGM components to confirm that no structural changes had occurred. Considering that SA is a phase change material, the phase transition temperature of hydrophobic HGMs could be measured by differential scanning calorimetry, and the amount of SA attached to the surface of hydrophobic HGMs after the coating process can be calculated.

2.3 L-HPC preparation and its performance evaluation

The sample preparation is slightly different from that of conventional HPC, mainly in the addition time of HGMs. HGMs did not participate in the dry mixing process in this sample preparation strategy. HGMs were added after the mixture formed a slurry, and the post-incorporation was to reduce the dust waste of HGMs during the dry mixing period. The mass ratio between the materials for developing L_HPC is shown in Table 1.

The flow of fresh L-HPC slurry was tested according to ASTM C230. After hardening, the mechanical properties and thermal properties of L-HPC were tested according to ASTM C109 and ISO 22007-2 respectively.

Table 1 Mix propotion of HPC and L-HPC (wt%)

| ID | Water | Cement | Silica fume | Quartz powder | Superplasticizer | HGMs |
|-------|-------|--------|-------------|---------------|------------------|------|
| HPC | 23 | 100 | 25 | 35 | 6 | 0 |
| L-HPC | 23 | 100 | 25 | 35 | 6 | 10 |

3. Results and discussions

3.1 Hydrophobic HGMs properties

Fig. 1 compares the water drop test results, water contact angle, phase, particle size, and phase change heat of HGMs before and after 8h modification. Drops of water were placed directly on the paved HGMs via a dropper. Water droplets were rapidly immersed into unmodified HGMs. On the surface of the modified HGMs, the water droplets remained spherical and were not absorbed. When accurately characterizing the hydrophobicity of HGMs with a water contact measuring instrument, first drop 20 μ l of water from the probe on the surface of the material, then take pictures after the droplet standing still for 10 seconds, and finally measure the angle formed between the water and the surface of the material. Obviously, the water contact angle of unmodified HGMs was 0°, and the droplet contact angle of modified HGMs could exceed 150°. Moreover, the HGMs modified for 2, 4, and 6h could all reach above 102°.

It was verified that the grinding was only a physical modification by XRD results that only the characteristic peak of SA appears in the XRD pattern of hydrophobized HGMs. In addition, traces of SA was also found in the heating and cooling process of hydrophobized HGMs by DSC test. Specifically, in the range of about 60-80°C (when heated) and 55-66°C (when cooled), the characteristics of SA melting and solidification appeared on the DSC curves. After modification, the size of HGMs decreased, and HGMs below 1 μ m disappeared.

When it is unknown whether the modification of HGMs is successful, the water drop test can be applied to quickly identify whether the material has a hydrophobic effect and save testing costs. Once the hydrophobic modification of HGMs has been achieved, the water contact angle test can accurately reflect the change in hydrophobicity of the HGMs with various parameters of ball milling.

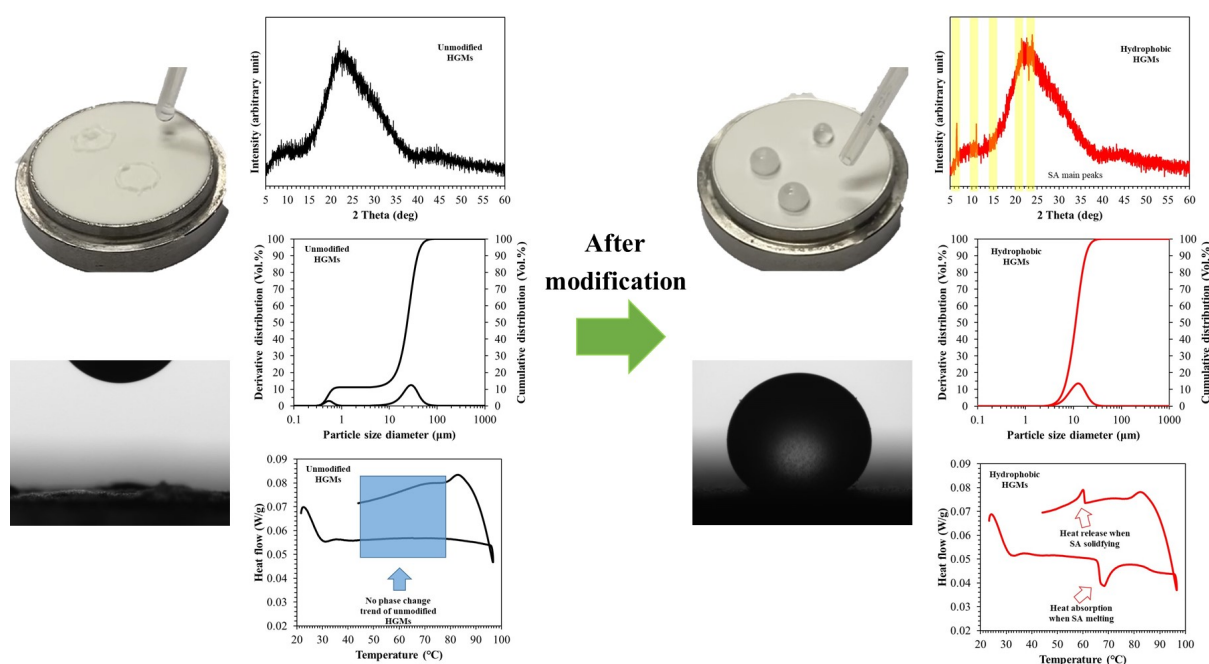


Fig.1. Comparison of properties of HGMs before and after modification

3.2 L-HPC performance

To study the fluidity, according to the flow table test procedure, after completing 25 jumps, the arithmetic mean of the diameters in two vertical directions was taken as the result of the concrete mixture fluidity test. The flow value of the HPC matrix without HGMs was 268mm, and the fluidity of L-HPC produced by adding unmodified HGMs was 17mm lower than that of HPC. After modification, the fluidity of L-

HPC added with hydrophobic HGMs could be increased by about 10mm compared with the original L-HPC. The application of modified HGMs in HPC could reduce the early hydration heat release of concrete and significantly improve the strength of concrete. However, there is a slight adverse effect on density and thermal conductivity, mainly attributed to the fragmentation of a small number of HGMs during the milling process.

4. Conclusions

In this study, low-cost stearic acid was used as a surfactant, which was mixed with HGMs for ball milling to prepare hydrophobic HGMs, and the modified HGMs were used to improve the rheological properties of L-HPC. The main conclusions are as follows: 1. Using stearic acid as the hydrophobic modifier, the hydrophobic hollow microspheres were successfully prepared after blending stearic acid and HGMs. All modified HGMs groups could have a water contact angle higher than 102°, with the best group reaching 154°. The hydrophobic modification method has the characteristics of low cost and simple operation. 2. Compared with the L-HPC mixture added with unmodified HGMs, hydrophobic HGMs were easily dispersed in the cement-based paste. The fresh mixture added with hydrophobic HGMs had lower viscosity during mixing and showed better mixability. It was measured that the fluidity of the fresh mixture had increased by a maximum of 10mm.

Acknowledgements

This work is supported by the Korea Agency for Infrastructure Technology Advancement (KAIA) grant funded by the Ministry of Land, Infrastructure and Transport (Grant RS-2020-KA156177). The Institute of Engineering Research at Seoul National University provided research facilities for this work.

References

- Lee, N., Pae, J., Kang, S. H., Kim, H. K., and Moon, J. (2022) “Development of High Strength & Lightweight Cementitious Composites using Hollow Glass Microsphere in a Low Water-to-Cement Matrix”, *Cement and Concrete Composites*, 130: 104541
- Mahato, J., Yang, J., Lee, N., Kang, H., & Moon, J. (2022) “Incorporation of a High Volume of Cenosphere Particles in Low Water-to-Cement Matrix for Developing High Strength and Lightweight Cementitious Composites”, *Journal of Sustainable Cement-Based Materials*, 1-12
- Shi, C., Wu, Z., Xiao, J., Wang, D., Huang, Z., and Fang, Z. (2015) “A Review on Ultra High Performance Concrete: Part I. Raw Materials and Mixture Design”, *Construction and Building Materials*, 101: 741-751
- Huang, W., Kazemi-Kamyab, H., Sun, W., and Scrivener, K. (2017) “Effect of Cement Substitution by Limestone on the Hydration and Microstructural Development of Ultra-High Performance Concrete (UHPC)”, *Cement and Concrete Composites*, 77: 86-101
- Lei, L., Wang, Q., Xu, S., Wang, N., & Zheng, X. (2020) “Fabrication of Superhydrophobic Concrete used in Marine Environment with Anti-Corrosion and Stable Mechanical Properties”, *Construction and Building Materials*, 251: 118946
- Wong, H. S., Barakat, R., Alhilali, A., Saleh, M., & Cheeseman, C. R. (2015) “Hydrophobic concrete using waste paper sludge ash”, *Cement and Concrete Research*, 70: 9-20
- Qu, Z. Y., & Yu, Q. L. (2018) “Synthesizing super-hydrophobic ground granulated blast furnace slag to enhance the transport property of lightweight aggregate concrete”, *Construction and Building Materials*, 191: 176-186
- Spathi, C., Young, N., Heng, J. Y., Vandeperre, L. J., and Cheeseman, C. R. (2015) “A Simple Method for Preparing Super-Hydrophobic Powder from Paper Sludge Ash”, *Materials Letters*, 142: 80-83

Ohmic heating curing for cement-based materials: A promising new technology with enhanced fabrication efficiency

Weichen Tian¹, Yushi Liu^{1*}, Wei Wang¹

¹*School of Civil Engineering, Harbin Institute of Technology, Harbin 150090, China*

Email: tianweichen@hit.edu.cn, liuyushi@hit.edu.cn, wwang@hit.edu.cn

**Corresponding author.*

ABSTRACT

The development of concrete construction is towards high-quality, low energy consuming and rapid fabrication direction. However, traditional concrete curing methods such as standard curing, high-temperature steam curing inevitably meet the problems of uncontrollable quality, high energy consuming and low efficiency. Under this circumstance, this work presents a novel concrete curing technology named ohmic heating (OH) curing, to realize the high-quality concrete construction for different cement-based materials system at severely-cold environment. To be specific, OH curing utilizes the heating and stimulation effect generated from alternative electric field to induce the hydration improvement and structure formation. Results showed that OH curing could effectively stimulate the strength formation of carbon fibers (CFs) strengthening conductive cement mortar (CFs-CCM) to 27.9 MPa at -20°C for 1 day, and possessed great long-term performance development regularity. Moreover, to prepare reactive powder concrete with higher compressive strength, Ni coated CFs and carbon nanofibers (CNFs) were further utilized to construct multi-scale conductive network inside the sample, and OH curing exhibited the ability to prepare NiCFs/CNFs synergistically strengthening reactive powder concrete (NiCFs/CNFs-RPC) at -20 °C with the compressive strength of 110 MPa. Microstructural result also revealed the microstructure improvement phenomenon of OH cured sample. This work deeply investigates the effect of OH curing on the performance improvement of cement-based materials, and lays a solid foundation for the promotion of this economical and efficient curing method.

KEYWORDS: *Ohmic heating curing, negative temperature, reactive powder concrete, conductive fibers*

1. Introduction

Cement-based materials have been widely utilized in the world for such a long time, with the increasing urbanization process, the utilization of this material will be further increasing. Under this circumstance, the high-quality fabrication of concrete material has become a research focus in the field. Existing research shows that the on-site fabrication of concrete mainly focuses on the traditional curing method and relies on the ambient temperature to realize the strength formation. However, this method can not promise the rapid strength formation of the structure and the construction period is long. To solve this problem, some novel curing methods have been presented to prepare cement-based materials, including high temperature steam curing method, microwave curing method, carbonization curing method, etc., aiming to realize the rapid fabrication of cement-based materials (Chen et al. 2019; Pan et al. 2021; Wang et al. 2015). As reported, these methods showed the ability to effectively improve the performance of cement-based materials. However, these methods are hard to operate in the actual engineering project, due to the complicated equipment and the complex requirement. In this case, our research group proposed a new method named ohmic heating (OH) curing to achieve the rapid and high-quality on-site fabrication of cement-based materials. The principle of this method is to use the ohmic heating generated by the alternating electric current inside the cement-based material to provide a high temperature curing environment for the sample. This method is easy to operate and is expected to be conducted in large-scale engineering.

Based on the above discussion, this work aims to verify the feasibility of the novel OH curing, and this curing method was utilized to prepare cement-based materials at -20°C as the harsh environment condition. Under this circumstance, the successful fabrication of cement-based materials can be strong evidence for the actual feasibility of OH curing method. Firstly, carbon fibers (CFs) were used as the

conductive medium to prepare CFs reinforced conductive cement mortar (CFs-CCM), and the development of compressive strength of OH prepared samples was investigated to clarify the feasibility of OH curing for on-site preparation of cement-based materials. Moreover, Ni coated CFs with better conductive performance and carbon nanofibers (CNFs) were used as conductive filler to synergistically prepare NiCFs/CNFs strengthening RPC (NiCFs/CNFs-RPC) at -20°C to further verify the feasibility of this method, aiming to realize the on-site fabrication of high performance concrete in various complex environments. This work provides a new solution and experimental basis for the rapid and high-quality on-site fabrication of concrete structure.

2. Experimental program

2.1 Materials and mix proportion

For CFs-CCM and NiCFs/CNFs-RPC samples, the mix proportion and the utilized materials were different. Detailed mix proportions for the samples were listed as below. Moreover, resistance measurement experiments were conducted to determine the optimal CFs, NiCFs and CNFs contents.

Table 1 Mix proportions of OH cured CFs-CCM samples

| Water to cement ration | Cement to sand ratio |
|------------------------|----------------------|
| 0.35 | 1:1.5 |

Table 2 Mix proportions of OH cured NiCFs/CNFs-RPC samples

| Water to binder ratio | Silica fume to cement ratio | Sand to binder ratio |
|-----------------------|-----------------------------|----------------------|
| 0.2 | 0.25 | 1.1 |

2.2 Curing regime

In this work, the curing regime of OH curing towards different curing conditions was different as shown in Fig. 1, the obtained curing temperatures were recorded during the curing process of the samples. To be specific, for CFs-CCM sample, a constant electric power OH curing regime was utilized to promise the constant temperature for the sample for 1 day, during the curing process, the curing temperature of the sample was kept at around 60 °C. For NiCFs/CNFs-RPC samples, the OH curing regime was modified, and a multi-step OH curing regime was designed to prepare samples under severely cold environment for 4 day, at the first 10 hours, the curing temperature of OH cured sample was set at around 35 °C, and the curing temperature was increased to the range 55 ~ 60°C for the next 10 hours, at the final curing stage, the curing temperature was kept around 75°C.

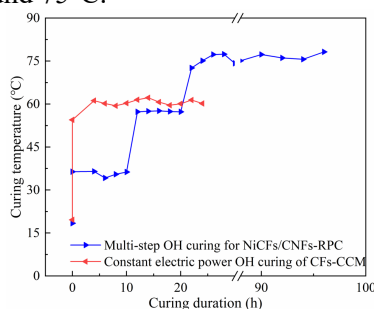


Fig. 1 Design of OH curing regimes of cement-based materials with different curing conditions

2.3 Performance measurement

In this work, the electric resistances of the samples were measured by two-electrode method with the frequency of 10 kHz, which has been proved to effectively eliminate the interface resistance between the electrode and the matrix, and the electrode size was 40 mm × 60 mm, due to the size of the samples was determined to be 40 mm × 40 mm × 160 mm, and the thermocouple was embedded at the center of the sample to measure and record the curing temperature during the whole process. The strengths of the samples subjected to different curing conditions were measured as the comparison.

3. Results and discussion

3.1 Performance development of OH cured CFs-CCM

3.1.1 Determination of CFs contents

The resistivities of the newly prepared samples was measured as the indicator for the determination of CFs. It can be seen from Fig. 2 that the electrical conductivity of CFs-CCM sample could be effectively enhanced with the increasing addition content of CFs. To be specific, with no CFs incorporation, the sample showed a low electrical conductivity with the resistivity of $208.7 \Omega \cdot \text{cm}$, while with the addition of CFs, the resistivity of the sample exhibited a sharp decreasing trend. The resistivity of the sample decreased to $47.2 \Omega \cdot \text{cm}$ with the CFs addition content of 0.6 vol. %. Therefore, the optimal addition content of CFs was determined to be 0.6 vol. % by experiments.

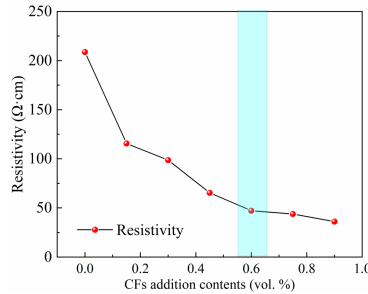


Fig. 2 Determination of CFs addition contents

3.1.2 Compressive strength

In this section, OH curing was utilized to prepare CFs-CCM samples for 1 day at -20°C , and the sample was cured at room temperature for another 150 d to clarify the strength development regularity of OH cured sample, as the evidence to prove the feasibility of OH curing as the novel curing method for concrete structure, and the strengths of OH cured samples were compared with the samples subjected to standard curing (SC). It can be seen from Fig. 3 that OH curing exhibited the advantage on improving the strength formation of CFs-CCM samples at -20°C , with the compressive strength of 27.9 MPa, and this is at the same level with the strength of the sample subjected to 2 days SC. Moreover, OH cured sample exhibited great strength development regularity with the 150-day strength of 43.9 MPa, and this is also comparable with the SC prepared sample, indicating the advantage of OH curing on the fabrication of cement-based materials under severely cold environment without sacrificing the long-term strength. This result verifies the feasibility of OH curing for concrete construction.

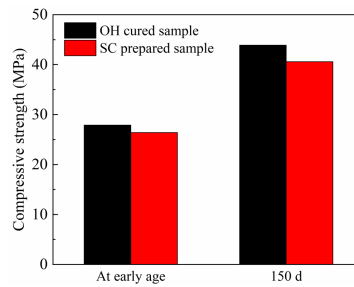


Fig. 3 Compressive strengths of CFs-CCM samples with different curing methods

3.2 Fabrication of NiCFs/CNFs-RPC under severely cold environment

The feasibility of OH curing has been verified in section 3.1, in this section, the multi-step OH curing strategy was further utilized to prepare the NiCFs/CNFs-RPC samples at -20°C , to disclose the ability of OH curing on preparing high performance concrete under severely cold environment. Moreover, 4 days SC and 4 days high temperature steam curing method were also conducted for comparison.

3.2.1 Determination of NiCFs and CNFs contents

The optimal of NiCFs and CNFs contents of NiCFs/CNFs-RPC samples were determined based on the resistivity measurement results. It can be seen from Fig. 4(a) that the resistivity of the samples exhibited the obvious decreasing trend with the increasing NiCFs addition contents, and the optimal NiCFs content was determined to be 1.5 vol. %. Further, during the OH curing process, with the increasing CNFs addition contents, the resistivity showed a much stable development situation. To be specific, with 0.5 vol. % CNFs addition amount, the increasing situation of resistivity for the sample during OH curing

process was subtle. Therefore, the optimal addition content of CNFs was determined to be 0.5 vol. %. During the whole curing process, the electric voltage was lower than 180 V.

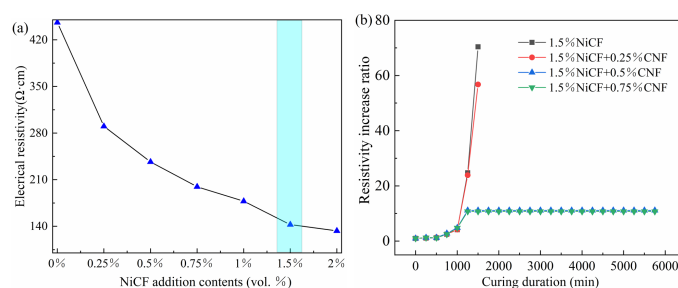


Fig. 4 Determination of NiCFs and CNFs contents

3.2.2 Strength of NiCFs/CNFs-RPC samples

The compressive strengths of NiCFs/CNFs-RPC samples with different curing methods were shown in Fig. 5, it can be seen that the conduction of multi-step OH curing could obviously enhance the compressive strength of the samples. To be specific, the samples subjected to 4-day OH curing endowed the compressive strength of 110 MPa, which is comparable with that of 4-day high temperature steam cured sample (108.2 MPa), and this is 66.9% higher than that of the sample subjected to 4-day SC. The strength measurement results further highlight the advantage of OH curing as the novel curing method to realize the rapid, high-quality fabrication of cement-based materials.

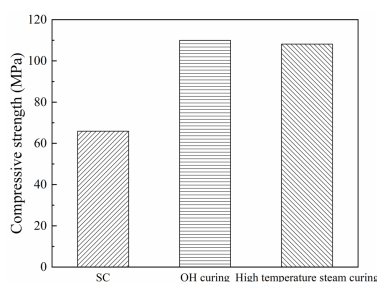


Fig. 5 Compressive strengths of NiCFs/CNFs-RPC samples subjected to different curing methods

4. Conclusions

In this work, OH curing was presented as the novel curing method for cement-based materials to respectively prepare CFs-CCM samples and NiCFs/CNFs-RPC samples at harsh environment with the temperature of -20°C , it was found that the compressive strength of CFs-CCM sample could be effectively improved to 27.9 MPa at 1 day, which is comparable with that of 2-day SC prepared sample. The compressive strength of OH cured sample was also at the same level with that of the sample prepared by SC for another 150 day SC curing, indicating the feasibility of OH curing for the fabrication of cement-based materials at harsh environment. Further, a multi-step OH curing strategy was conducted to prepare NiCFs/CNFs-RPC samples, the compressive strength of OH cured sample reached up to 110 MPa, highlighting the advantage of OH curing on the fabrication of high performance concrete at -20°C . This work presents a novel strategy for rapid and high-quality on-site concrete construction.

References

- Chen, T., X. Gao, and L. Qin. (2019) "Mathematical modeling of accelerated carbonation curing of Portland cement paste at early age." *Cement and Concrete Research*, 120: 187–197
- Pan, Y., Y. Zhang, and S. Li. (2021) "Effects of isothermal microwave curing on steel fibre-reinforced reactive powder concrete: Strength, microstructure and hydration products." *Construction and Building Materials*, 302: 124435
- Wang, D., C. Shi, Z. Wu, J. Xiao, Z. Huang, and Z. Fang. (2015) "A review on ultra high performance concrete: Part II. Hydration, microstructure and properties." *Construction and Building Materials*, 96: 368–377.

Preliminary Investigation of 0-3 Lead Zirconate Titanate – Lime Calcined Clay Cement Composites

A. Alchaar¹ and K. Celik^{2,*}

¹ New York University Abu Dhabi, Abu Dhabi, United Arab Emirates
asa7916@nyu.edu

² New York University Abu Dhabi, Abu Dhabi, United Arab Emirates
kemal.celik@nyu.edu

ABSTRACT

The development of cement-based piezoelectric composites (CPCs) was found to have great potential in sensor applications for concrete structural health monitoring. Popular CPCs are made of lead zirconate titanate (PZT) and ordinary Portland cement (OPC). Efforts continue to densify such composites to lower the energy-intensive polarization requirements or make them more efficient in composite response. Recently, adding alumino-silicate-based materials (kaolin) was found to cause refined microstructure, hence improving the dielectric and piezoelectric properties of CPCs. In this study, CPC was fabricated using limestone calcined clay cement (LC³) with 50% PZT as a functional phase to observe the composite's densification and assess its viability in the CPCs field. Results show that the microstructure is less porous with LC³ compared to conventional composites. In addition, the dielectric loss was found to be 0.54, similar to conventional CPCs. However, relative permittivity was found to be far lower than those of conventional CPCs. This was owed to the quick moisture loss after curing, the relatively lower relative humidity of curing, and irregularities at the electrode surfaces. The presented preliminary results can indicate a potential in this composite to have improved dielectric properties and lower polarization needs.

KEYWORDS: *Smart materials, piezoelectric, PZT, LC³, smart cement*

1. Introduction

Over the last 2 decades, cement-based piezoelectric composites (CPCs) have been investigated as smart sensors for structural health monitoring (SHM) applications. They comprise ordinary Portland cement (OPC) and a piezoelectric material such as lead zirconate titanate (PZT). Research has shown that such composites have better compatibility with concrete and are superior to normal piezoelectric composites like polymer-based ones. The enhanced compatibility of CPCs results from better volume stability and a lower acoustic impedance mismatch with the host concrete (Dong & Li, 2005). CPCs can be fabricated with ten different connectivity patterns, including 0-3, 1-3, and 2-2 (Chen et al., 2019). 0-3 configuration is the most popular due to the relatively easier fabrication (since ceramic is added as a powder) and overall better performance (Ding et al., 2021). However, the piezoelectricity of such composites requires activation through polarization. This is because ceramic particles have different dipole directions, which cannot be controlled during fabrication. It is important to note that dipoles of a smart material shall be in the same direction to exhibit a piezoelectric behavior (Chen et al., 2019). Polarization is an energy-intensive process that is performed by applying an external electric field using a high-voltage direct current (DC) power supply for a specific duration and at a certain temperature. Ever since it was developed, CPCs have been characterized by the evaluation of piezoelectric strain factor (d_{33}), electromechanical coupling coefficient (K_t), and dielectric constant (ϵ_r) (Li et al., 2002). Research efforts continue to enhance the piezoelectric performance (especially the d_{33} parameter) of CPCs by optimizing the poling process, fabrication techniques, and microstructure. The latter is specifically important due to the complexity of hydration products and the microstructure heterogeneity. The densification of CPCs can improve the connectivity

between piezoelectric particles and the host cement matrix and lower the porosity at interfacial regions. This is key to pushing the levels of d_{33} higher because porosity leads to discontinuities in stress transfer and dramatically increases polarization requirements (Ding et al., 2021). **Figure 1** shows Scanning Electron Microscopy (SEM) micrographs for OPC-PZT composites at different magnifications. It can be observed that despite the relatively good bond between cement hydration products and PZT particles (Chaipanich et al., 2013), pores take up a considerable part of the interface.

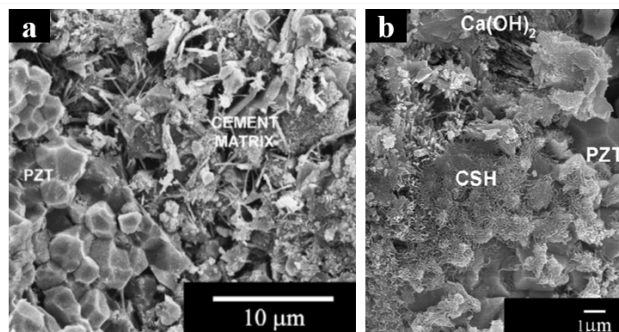


Figure 1. SEM micrographs of (a) CPC with 50% PZT (Chaipanich et al., 2007) and (b) CPC with PZT at large magnification (Chaipanich et al., 2013)

Several attempts to densify CPCs were recently made by incorporating supplementary cementitious materials (fly ash, silica fume, slag, and kaolin) and conductive fillers (carbon black and carbon nanotubes). Furthermore, the use of kaolin (alumino-silicate-based additive) has shown promising results in enhancing CPCs by lowering porosity to 1.86%, according to Pan et al (2015). While kaolin performs well as an additive, limestone calcined clay cement (LC³) can perform similarly as a cementitious matrix. LC³ is a recently developed sustainable binder with 20% less thermal energy requirement. It allows ~45% clinker replacement, larger binder density, and finer microstructure. Thereby, it significantly improves the mechanical and durability properties of cement. This is because alumina from calcined clay undergoes normal pozzolanic reactions and reacts with limestone carbonates (Sharma et al., 2021). This work is a preliminary investigation of the versatility of LC³ as a matrix in CPCs with PZT as a functional phase. It is believed that CPCs made with LC³ instead of OPC will be denser, especially at interfacial zones, which can lead to reducing polarization requirements and improving piezoelectric properties. In that context, this study sheds light on the dielectric properties and microstructure of 0-3 PZT-LC³ composites.

2. Methodology

2.1 Materials

The composite was fabricated with 50% PZT by volume. Water and polycarboxylate-based superplasticizers were used to fluidize the mixture before casting. The matrix phase comprises (by weight) 50% OPC type I, 30% high reactivity calcined clay (acquired from TARA, India), 15% Limestone, and 5% Gypsum. PZT was acquired as hollow spherical agglomerates 50-150 μm from APC International Ltd, United States.

2.2 Fabrication

Normal mixing and distribution method was employed in fabricating the composite. Samples were cast with size 15 x 15 x 3 mm and left to dry at ambient temperature for 2d. After drying, samples were cured at 60° C and relative humidity (RH) of ~90% for 4d. Part of the samples was coated with conductive silver paint on both surfaces to form electrodes for dielectric measurements.

2.3 Experiments

Capacitance and dielectric loss were measured using an impedance phase analyzer (Keysight E4980A/AL Precision LCR Meter) at the age of 10 days, ambient temperature, and unpoled status. Measured capacitance was used to calculate the relative dielectric permittivity (ϵ_r) as a parallel plate condenser using the formula

$Ct/\epsilon_0 A$, where C is the capacitance, t is the thickness of the sample, ϵ_0 is the permittivity of free space (8.854 pF/m), and A is the electrode area. In addition, the impedance spectrum of the composite was recorded to observe electromechanical coupling. Finally, the microstructure of the composite was characterized through a scanning electron microscope (SEM, Quanta 450 FEG) with an operating voltage of 10 kV.

3. Results and Discussion

SEM micrographs of the composite are shown at different magnifications in **Figure 2**. Compared to OPC-based composites, the microstructure is observed to be denser, as expected. In addition, there were hardly any indications of calcium aluminosilicate hydrates (C-A-S-H, which is the main hydration product of LC3). Getting high-resolution images at large magnification was challenging because of the charging effect. Besides, PZT particles can be seen surrounded by the matrix products with some porosity at the interface.

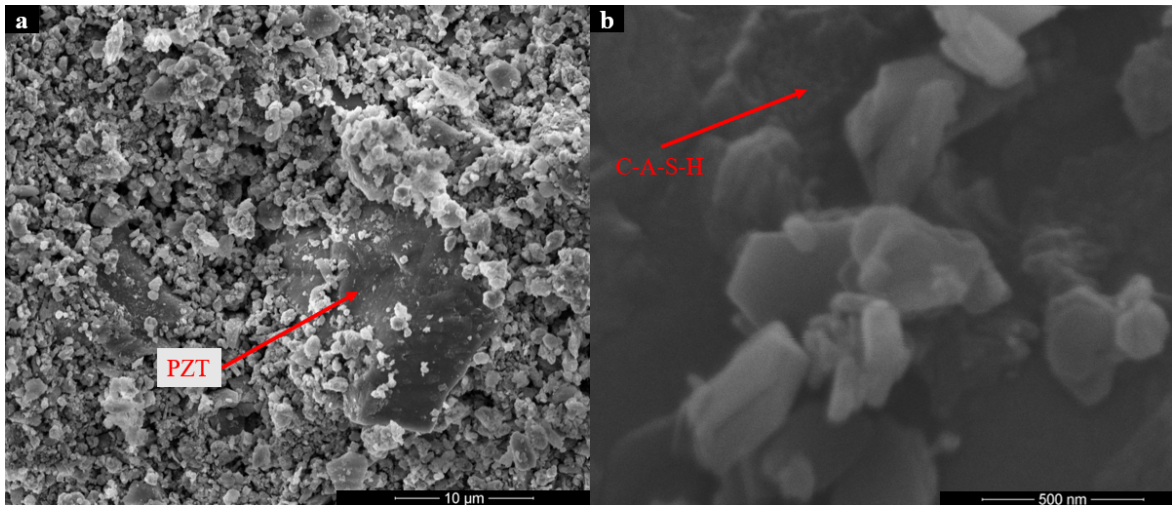


Figure 2. SEM micrographs of LC³-PZT Composite at (a) medium and (b) high magnifications

The impedance spectrum of the composite can be seen in **Figure 3**. A spike in the phase curve was observed at ~17 kHz, which can indicate coupling. However, coupling was not captured by the analyzer in the impedance spectrum.

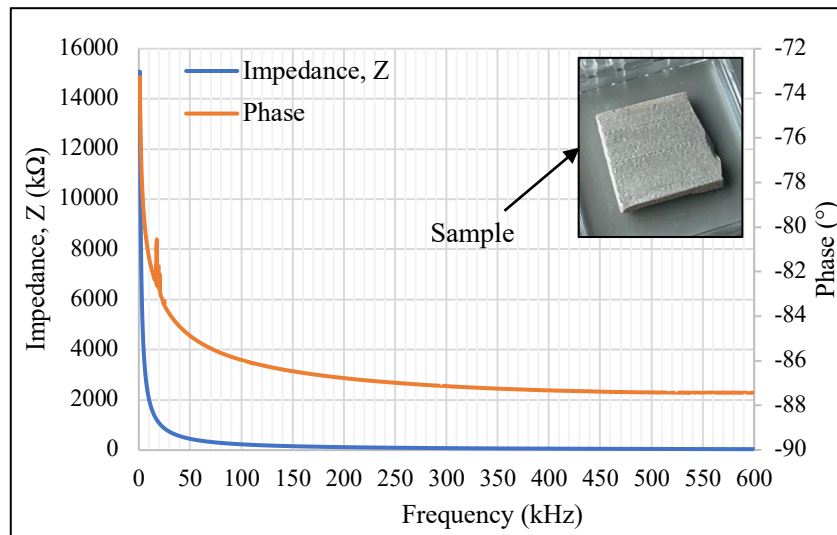


Figure 3. (a) Impedance spectrum of the LC³-PZT composite with the sample shown

The composite exhibited a dielectric constant ϵ_r of 22 and a dielectric loss (D) of 0.54. Conventional PZT-OPC 0-3 composites have ϵ_r that can reach up to 167 and D down to ~0.79 (Ding et al., 2021). In addition, Pan et al (2015) reported an ϵ_r up to 252 and D of 0.58 when kaolin was added as a cement replacement by 10%. It is important to note that for CPCs, higher relative permittivity is desired as it indicates charge generation in the application of an external electric field and therefore tells about the polarizability of the

material. On the other hand, lower dielectric loss (D) is desired for polarization efficiency. In this study, the measured dielectric loss is comparable to previous research, but the dielectric constant is 10-25% of the values reported for similar composites. There are some probable causes for a low ϵ_r . First, LC³ formulation has a higher fineness level than OPC, meaning a higher surface area and water requirement. In addition, samples were cured at RH of ~90% only, rather than 100%, due to the chamber's capability. As a result, composites have low moisture levels and fewer free water particles. Furthermore, silver-painted surfaces were observed to have non-uniformity. Such issues can significantly reduce permittivity and add up resistance to the composite.

4. Conclusions

This study presents a preliminary investigation of cement-based piezoelectric composites (CPCs) using limestone calcined clay cement (LC³) as a matrix with 50% PZT as a functional phase. The use of LC³ densified the composite and improved its dielectric properties. This will favor developing cement-based smart materials as polarization requirements can be reduced while maintaining good piezoelectric behavior. Previous research has shown several improvements in the dielectric, piezoelectric, and morphological properties of CPCs when kaolin was incorporated as an alumino-silicate cement replacement additive. Interestingly, LC³ has a nature similar to kaolin but is considered a matrix rather than an additive. The dielectric loss was demonstrated to be 0.54, which is reasonable. However, the spectral analysis of impedance showed a spike in the phase, which can resemble coupling, but resonant frequencies of impedance and admittance were not captured. In addition, dielectric permittivity was 10-25% of those achieved in previous works with similar composites. This was due to the low post-curing internal moisture and the presence of irregularities at the electrode surfaces of samples. Nonetheless, the refined microstructure, observed through SEM micrographs, confirmed the densification of the composite. Future work will attempt to fabricate composites with different mixing parameters, maximizing relative humidity in curing, monitoring moisture levels, and achieving better surface quality of electrodes. In that way, improved dielectric properties are expected to be exhibited by the composite.

Acknowledgments

The authors are grateful to Juan Esteban Villegas and staff members at the Core Technology Platforms at New York University Abu Dhabi (NYUAD) for helping in the experimental work of this study. This material is based upon works supported by the NYUAD Center for Smart Engineering Materials (NYUAD-CSEM), funded by Tamkeen under NYUAD RRC Grant No. CG011.

References

- Chaipanich, A., Jaitanong, N., & Tunkasiri, T. (2007). Fabrication and properties of PZT–ordinary Portland cement composites. *Materials Letters*, 61(30), 5206–5208. <https://doi.org/10.1016/j.matlet.2007.04.031>
- Chaipanich, A., Rianyai, R., Potong, R., Jaitanong, N., & Chindaprasit, P. (2013). Compressive Strength and Microstructure of 0–3 Lead Zirconate Titanate Ceramic-Portland Cement Composites. *Ferroelectrics*, 457(1), 53–61. <https://doi.org/10.1080/00150193.2013.847333>
- Chen, J., Qiu, Q., Han, Y., & Lau, D. (2019). Piezoelectric materials for sustainable building structures: Fundamentals and applications. *Renewable and Sustainable Energy Reviews*, 101, 14–25. <https://doi.org/10.1016/j.rser.2018.09.038>
- Ding, W., Liu, Y., Shiotani, T., Wang, Q., Han, N., & Xing, F. (2021). Cement-Based Piezoelectric Ceramic Composites for Sensing Elements: A Comprehensive State-of-the-Art Review. *Sensors*, 21(9), 3230. <https://doi.org/10.3390/s21093230>
- Dong, B., & Li, Z. (2005). Cement-based piezoelectric ceramic smart composites. *Composites Science and Technology*, 65(9), 1363–1371. <https://doi.org/10.1016/j.compscitech.2004.12.006>
- Li, Z., Zhang, D., & Wu, K. (2002). Cement-Based 0-3 Piezoelectric Composites. *Journal of the American Ceramic Society*, 85(2), 305–313. <https://doi.org/10.1111/j.1151-2916.2002.tb00089.x>
- Pan, H. H., Yang, R.-H., & Cheng, Y.-C. (2015). *High piezoelectric properties of cement piezoelectric composites containing kaolin* (P. J. Shull, Ed.; p. 94370R). <https://doi.org/10.1117/12.2085452>
- Sharma, M., Bishnoi, S., Martirena, F., & Scrivener, K. (2021). Limestone calcined clay cement and concrete: A state-of-the-art review. *Cement and Concrete Research*, 149, 106564. <https://doi.org/10.1016/j.cemconres.2021.106564>

New trend line of compressive strength and unit volume weight of cement composites: Lightweight and high-strength at the same time

Y. Jeong^{1*}, J.-I. Suh², J. H. Kim³, Y. Cho⁴, and S. Jung⁵, C.-W. Chung⁶

¹ Construction Technology Research Center, Korea Conformity Laboratories (KCL), Seoul, Republic of Korea

Email: yeonungjeong@kcl.re.kr

² Construction Technology Research Center, Korea Conformity Laboratories (KCL), Seoul, Republic of Korea

Email: rgtonesuh@kcl.re.kr

³ Construction Technology Research Center, Korea Conformity Laboratories (KCL), Seoul, Republic of Korea

Email: kjhmole@kcl.re.kr

⁴ Construction Technology Research Center, Korea Conformity Laboratories (KCL), Seoul, Republic of Korea

Email: young@kcl.re.kr

⁵ Construction Division, Korea Conformity Laboratories (KCL), Cheongju, Chungcheongbuk-do, Republic of Korea

Email: jsh2593@kcl.re.kr

⁶ Department of Architectural Engineering, Pukyong National University, Busan, Republic of Korea

Email: cwchung@pknu.ac.kr

ABSTRACT

The relationship between compressive strength and unit volume weight of cement composites is an inverse relationship, indicating that, in general, high-strength composites have high unit volume weight and lightweight composites possess low compressive strength. This study aims to develop high-strength cement composites simultaneously with low-level unit volume weight and suggests mix designs for the composites with over 80 MPa of compressive strength and less than 1.6 g/cm³ of unit volume weight at 28 days of curing age. The core constituents of the composites are ordinary Portland cement (OPC), silica fume, silica powder, artificial hollow microsphere, and lightweight fine aggregates, carbon nanotube suspension can be added for enhancing the compressive strength of the composites. The results indicate that compressive strength reaches 103 MPa with 1.53 g/cm³ of hardened density at 28 days of curing age. The use of carbon nanotubes enhances early-age strength development without an increase in the hardened density of the composites.

KEYWORDS: *high-strength, lightweight, cement composite, hollow microsphere*

1. Introduction

The development of admixture technology has enabled the production of concrete with a water-to-cement ratio (w/c) of 0.2 or less, and concrete with a compressive strength of 150 MPa or more is known as ultra-high performance concrete (UHPC) (Zhu 2020). Cement, silica fume, quartz powder, quartz sand, superplasticizer, and steel fiber are typically used as the raw materials for UHPC (Shi 2015). A design method was proposed to maximize the internal packing of the particle size of the raw material used and reduce air gaps, which resulted in a high performance of 150 MPa or more (de Larrard 1994). To further enhance the mechanical performance of UHPC, high-temperature curing of up to 60 °C or 90 °C is

usually performed following curing, and rice husk ash, calcium carbonate powder, and nanomaterials are sometimes used as additional raw materials (Kang 2019a, Kang 2019b, Ghagari 2015).

On the other hand, the development of lightweight concrete by utilizing various lightweight materials is actively carried out. Concrete with a unit volume weight of $2,000 \text{ kg/m}^3$ or less is generally regarded as lightweight concrete (Yang 2013). A range of lightweight aggregates have been proposed for the production of lightweight concrete. Choi and Kim (2018) proposed using bottom ash and calcined artificial lightweight aggregate for lightweight concrete, while Kim et al., (2009) suggested the use of artificial lightweight aggregate derived from waste glass. Additionally, studies are being conducted to utilize materials such as palm oil shells as lightweight aggregates (Shafigh 2011).

It is commonly known that the strength and density of cement composites are inversely proportional. Lightweight concrete typically has a compressive strength of between 15 MPa and 40 MPa, and developing high strength is difficult. UHPC's density is known to be around 2.3 g/cm^3 . Kılıç et al., (2003) reported that it was possible to produce a compressive strength of 43 MPa at 3 months of age at a unit volume weight of $1,944 \text{ kg/m}^3$ by using lightweight aggregate and admixture, but the strength level is still not enough to qualify as high-strength concrete. Furthermore, no substantial advances have been made in the development of lightweight high-strength concrete since then.

The objective of this study is to develop cement composites that are both lightweight and high-strength, by incorporating artificial microspheres and lightweight fine aggregate. The research presents the mixing conditions required to produce cement composites with specific properties, including a unit volume weight of $2,000 \text{ kg/m}^3$ at a compressive strength of 120 MPa, a unit volume weight of $1,800 \text{ kg/m}^3$ at a compressive strength of 100 MPa, and a unit volume weight of $1,600 \text{ kg/m}^3$ at a compressive strength of 80 MPa.

2. Materials and Methodology

2.1 Materials

This study investigated the use of several materials in mix design of cement composites, including type I ordinary Portland cement (OPC), silica fume (SF), silica sand (SS), silica powder (SP), hollow microsphere (HMS), lightweight fine aggregate (LFA), and polycarboxylate superplasticizer (PCE). The LFA used in this study was a kind of expanded clay aggregate that was produced by Liapor GmbH & Co. KG in Deutschland. The SF and SP used in the study had smaller particle sizes than OPC, while HMS had a larger particle size. The unit weight of each material was $3,150 \text{ kg/m}^3$ for OPC, $2,200 \text{ kg/m}^3$ for SF, $2,650 \text{ kg/m}^3$ for SP, $2,648 \text{ kg/m}^3$ for SS, 600 kg/m^3 for HMS, and $1,770 \text{ kg/m}^3$ for LFA. The absorption rate of LFA was found to be 10 % at 3 days. These materials were mixed in various ratios to determine the optimal combination for lightweight and high-strength cement composites.

The mineral phase compositions of the raw materials were investigated using X-ray diffraction (XRD). The OPC used in this study was found to contain 51.0% C_3S , 32.7% $\beta\text{-C}_2\text{S}$, 9.0% C_4AF , 2.6% C_3A , 3.1% gypsum, and 1.7% anhydrite. The C_3A content of the OPC was slightly lower than that of typical Portland cement, but its light-weight consistency was consistent with the low Al_2O_3 content of the OPC. The SP was found to be composed of quartz (SiO_2) and a small amount of cristobalite (SiO_2), and SF was found to be amorphous containing a small amount of moissanite (SiC). The HMS was found to be composed of an amorphous phase containing no crystalline phase.

The solid content of the PCE used in this study was found to be 38.5%.

2.2 Mix Design and Curing Scheme

Three types of lightweight and high-strength cement composites were formulated according to the target compressive strength and unit weight, as outlined in Table 1. The target compressive strength for the first composite is 80 MPa with a unit weight of 1.6 g/cm^3 , while for the second composite, it is 100 MPa with a unit weight of 1.8 g/cm^3 . Finally, the third composite aims for a target compressive strength of 120 MPa at a unit weight of 2.0 g/cm^3 .

The cement composite mixture described in Table 1 was cast into cylindrical specimens with dimensions of 10 cm in diameter and 20 cm in height. The specimens were then cured for 24 hours at a temperature

of 21°C and a relative humidity of 99%. After this initial curing period, the specimens were removed from their molds and placed in a chamber at a temperature of 90°C and a relative humidity of 99% for an additional 48 hours. Following this, the specimens were cured in a controlled environment at a constant temperature of 21°C and a relative humidity of 65% until the compressive strength measurements were taken.

Table 1. Mix design for lightweight and high-strength cement composites (unit: kg/m³)

| Label | Water | OPC | SF | SP | SS | HMS | LFA |
|------------|-------|--------|--------|-------|-------|-------|-------|
| 1.6 // 80 | 212.5 | 739.1 | 110.9 | 208.0 | 0 | 211.0 | 111.0 |
| 1.8 // 100 | 212.5 | 739.1 | 110.9 | 208.0 | 255.0 | 152.0 | 115.0 |
| 2.0 // 120 | 195.5 | 739.13 | 110.87 | 208 | 513 | 101 | 125 |

3. Results

Figure 1 illustrates the compressive strength and unit weight results of the lightweight and high-strength cement composites developed in this study, in comparison to previous results of lightweight and high-strength concrete. The blue dots in Figure 1 indicate the results of this study. The results demonstrate a noticeable deviation to the left from the established trends of lightweight or high-strength concrete, suggesting that a cement composite can achieve both high strength and lightweight properties through appropriate mixing of HMS and LFA.

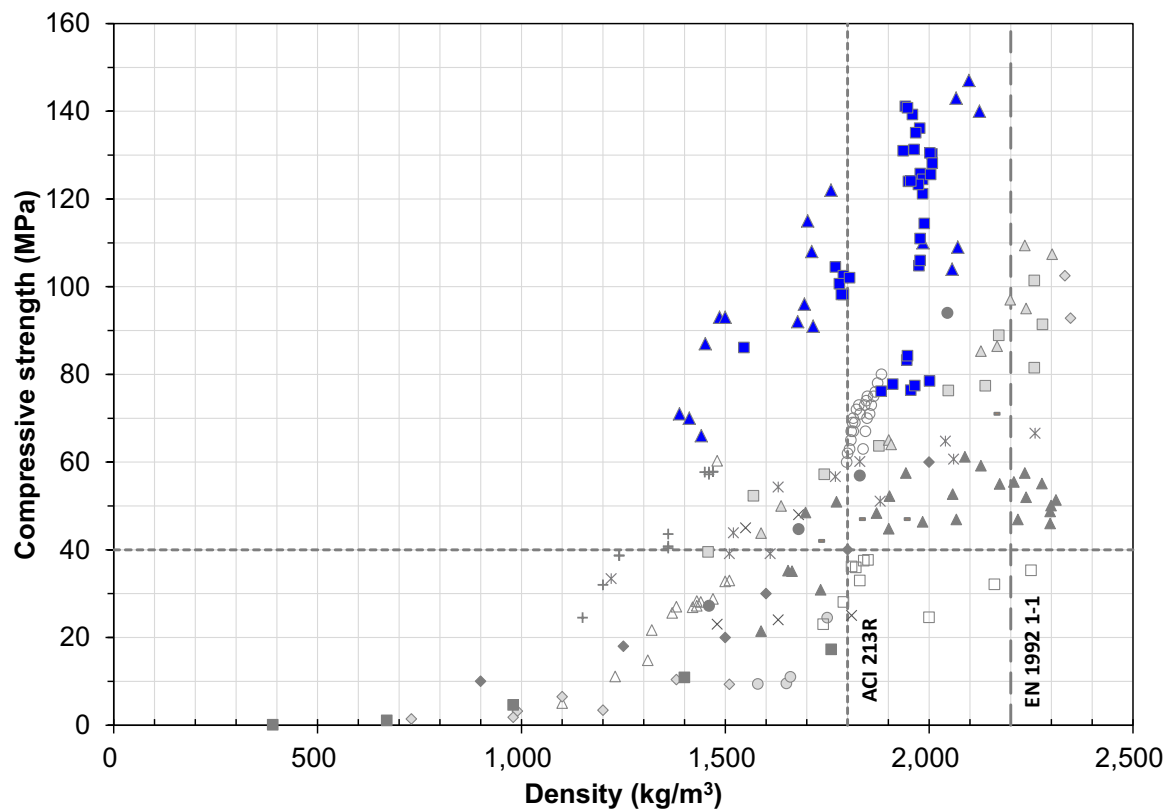


Figure 1. Results of compressive strength and density of hardened cement composites.

3. Conclusions

In this study, lightweight and high-strength cement composites were manufactured using hollow microspheres (HMS) and lightweight fine aggregate (LFA), and their compressive strength and density were investigated. The objective was to produce a lightweight and high-strength cement composite with compressive strengths of 80 MPa at a hardened density of 1.6 g/cm³, 100 MPa at a hardened density of 1.8 g/cm³, and 120 MPa at a hardened density of 2.0 g/cm³. As a result of the study, it was found that the proposed mixing conditions led to the target compressive strength being exceeded, even at a weight lower than the target density. The trend of compressive strength-density of the hardened body was clearly shifted to the left compared to previous research results, indicating that it is possible to manufacture a cement composite that is lighter and has excellent strength than previous results.

Overall, the results of this study suggest that incorporating HMS and LFA can effectively enhance the compressive strength of lightweight cement composites while also reducing their density. These findings have important implications for the development of sustainable construction materials that are both strong and lightweight.

Acknowledgements

This work is supported by the Korea Agency for Infrastructure Technology Advancement (KAIA) grant funded by the Ministry of Land, Infrastructure and Transport (RS-2020-KA156177).

References

- Choi, H.-B. Kim, J.-M. (2018) "Fundamental properties of lightweight concrete with dry bottom ash as fine aggregate and burned artificial lightweight aggregate as coarse aggregate", *Journal of Korean Recycled Construction Resources Institute*, 6(4): 267-274
- de Larrard, F. Sedran, T. (1994) "Optimization of ultra-high-performance concrete by the use of a packing model", *Cement and Concrete Research*, 24(6): 997-1009
- Ghagari, E. Costa, H. Júlio, E. (2015) "Critical review on eco-efficient ultra high performance concrete enhanced with nano-materials", *Construction and Building Materials*, 101: 201-208
- Kang, S.-H. Hong, S.-G. Moon, J. (2019a) "The use of rice husk ash as reactive filler in ultra-high performance concrete", *Cement and Concrete Research*, 115: 389-400.
- Kang, S.-H. Jeong, Y. Tan, K.-H. Moon, J. (2019b) "High-volume use of limestone in ultra-high performance fiber-reinforced concrete for reducing cement content and autogenous shrinkage", *Construction and Building Materials*, 213: 292-305
- Kılıç, A. CAtiş, C. D. Yaşar, E. Özcan, F. (2003) "High-strength lightweight concrete made with scoria aggregate containing mineral admixtures", *Cement and Concrete Research*, 33(10): 1595-1599
- Kim, S.-S. Lee, J.-B. Nam, B.-R. Park, K.-P. (2009) "Performance evaluation of artificial lightweight aggregate mortar manufactured with waste glass", *Journal of the Korea Concrete Institute*, 21(2): 147-152
- Shafigh, P. Jumaat, M. Z. Mahmud, H. (2011) "Oil palm shell as a lightweight aggregate for production high strength lightweight concrete", *Construction and Building Materials*, 25(4): 1848-1853
- Shi, C. Wu, Z. Xiao, J. Wang, D. Huang, Z. Fang, Z. (2015) "A review on ultra high performance concrete: Part I. Raw materials and mixture design", *Construction and Building Materials*, 101: 741-751
- Yang, K.-H. (2013) "Mix design of lightweight aggregate concrete and determination of targeted dry density of concrete", *Journal of the Korea Institute of Building Construction*, 13(5): 491-497
- Zhu, Y. Zhang, Y. Hussein, H. H. Chen, G. (2020) "Flexural strengthening of reinforced concrete beams or slabs using ultra-high performance concrete (UHPC): A state of the art review", *Engineering Structures*, 205: 110035

Concrete Mix Design for Rigid Pavements Maintenance: Evaluating Compressive Strength Development and Curing Temperature Effect

Wei-Chien Wang¹, Hoang Trung Hieu Duong^{2*}, Yu-Yang Li³, and Chia-Yun Huang⁴

¹ National Central University, Taoyuan City, 320, TAIWAN

Email: a654.joy@gmail.com

^{2*} National Central University, Taoyuan City, 320, TAIWAN

Email: trhieu.ncu@g.ncu.edu.tw

² National Central University, Taoyuan City, 320, TAIWAN

Email: sheu111422@outlook.com

² National Central University, Taoyuan City, 320, TAIWAN

Email: jacqueline1018qq999054@gmail.com

ABSTRACT

Currently, rigid pavement is widely utilized in highways and airports to improve transportation infrastructure. In order to decrease traffic congestion, maintenance of the rigid pavement is frequently scheduled for overnight construction. The rigid pavement's capacity to withstand traffic is evaluated based on its compressive strength value. The International Building Codes (IBC) mandates a minimum compressive strength of 21 MPa for opening roads, while airport rigid pavements should meet a minimum design compressive strength of 27 MPa (Wilson et al. 2000). To fulfil the need for rapid repair of roads, bridges, and high-rise building slabs, a new standardized process known as High Early Strength Concrete (HSC) has been introduced to produce early-strength concrete, which must achieve a compressive strength of about 21 MPa within 4 to 6 hours of curing (Mitchell et al. 2007). To fulfil this requirement, this research developed concrete mix designs that can achieve high early-age compressive strength, and evaluate their compressive strength development, slump, and slump loss in different curing temperatures. The results showed that using our concrete mix design can achieve over than 21 MPa within 4 to 6 hours of curing when the curing temperature is above 23°C. In the context of winter conditions where the air temperature could drop below 23°C, an appropriate heat-curing method should be applied to achieve more than 21 MPa after 4 to 6 hours of curing. Besides, this research finding also indicates that an increase in ambient temperature during the concrete curing period has a beneficial effect on early-age compressive strength development. However, when the external environment temperature is low and there is heat loss, the heat generated by the hydration of the cement is insufficient to promote the early-age hydration of the concrete. As a result, additional heat energy must be provided and steps are taken to ensure that the heat energy is retained during the concrete curing period, in order to facilitate the stable development of early-age compressive strength.

KEYWORDS: *High early strength concrete, rigid pavement maintenance, curing temperatures, ready-mix concrete design.*

1. Introduction

Recently, rigid pavement, which is constructed from cement concrete or reinforced concrete slabs, has been widely employed in highways and airports. However, this type of pavement frequently experiences long-term damage, such as corner breaks, transverse cracking, and scaling. Once the damage to the pavement becomes severe, there are a variety of methods to restore it, including using concrete pavement for partial or full-depth patching (Ansari and Luke 1996). Maintenance of rigid pavement on-site usually takes place at night to avoid traffic disruption, with the pavement typically being opened to traffic the following morning. The compressive strength of rigid pavement is usually evaluated to assess its suitability for open traffic use. The International Building Codes (IBC) establish minimum design compressive strength requirements for roads, bridges, buildings, and airport rigid pavement, which are 21 MPa and 27 MPa, respectively (Wilson et al. 2000). To address the need for rapid repair of roads, bridges, and high-rise building slabs, a new standard procedure for early strength concrete, called High Early Strength Concrete (HSC), has been developed. The FHWA, which stands for compressive strength of approximately 21 MPa after 4 to 6 hours of curing, is the compressive strength requirement for HSC (Mitchell et al. 2007). Numerous studies indicate that the properties of concrete used in the repair of rigid pavement are significantly influenced by environmental factors, such as air temperature and moisture conditions, due to the short duration of curing required. For instance, low temperatures during winter have been found to reduce the early strength of concrete. Thus, this research developed concrete mix designs that can achieve high early-age compressive strength that can adapt the FHWA requirement, and evaluate their compressive strength development, slump, and slump loss in different curing temperatures.

2. Materials and experimental method

2.1 Materials

The cement used in this experiment is Portland cement type I, which was popular in the ready-mixed concrete and pre-cast concrete. The physical and chemical properties of the cement were shown in Table 1.

Table 1 Cement chemical compositions

| Chemical composition | SiO ₂ | CaO | Al ₂ O ₃ | Fe ₂ O ₃ | MgO | SO ₃ | LL.* | f-CaO | Ca/Si |
|----------------------|------------------|-------|--------------------------------|--------------------------------|-----|-----------------|------|-------|-------|
| wt/% | 20.37 | 64.47 | 4.52 | 3.54 | 2.0 | 2.2 | 1.43 | 1.06 | 2.12 |

The admixtures used in this experiment are Sika-1250, and Sika-C100. The using dosages were conducted according to the manufacturer's guidelines.

2.2 Experimental method

The mix design was developed based on the Freeway Bureau (MOTC) (Chen and Fang 2018), and investigated the effect of curing temperatures and W/C ratio of the early-age compressive strength development. As per the guidelines outlined in ASTM C39, fresh concrete was introduced into cylinders (15cmx30cm), and a vibrating table was employed to compact it. The compressive strength examination was carried out in accordance with ASTM C109. For each test interval, three separate specimens from a batch of cement paste were employed. The fine and coarse aggregates were designed in accordance with CSN 1240. The coarse aggregate possessed a particle size of 8 to 16mm, 2.58 Relative density, 1.96% is the water absorption ratio, and a dry density of 1550 kg/m³. Meanwhile, the fine aggregate had a 2.9 fineness modulus, 2.64 Relative density, and 2.04% is the water absorption ratio. The details of the concrete mixture design can be found in Table 2.

Table 2. Concrete mix design

| Sample ID | Ratio | | | | Early Strength Admixtures | |
|-----------|--------|-----------|-------------|-------|---------------------------|------------|
| | Cement | Fine Agg. | Coarse Agg. | Water | Sika-1250* | Sika-C100* |
| M500-WC31 | 1 | 1.62 | 2.0 | 0.31 | 0.4 | 2.8 |
| M500-WC29 | 1 | 1.62 | 2.0 | 0.29 | 0.4 | 2.8 |
| M500-WC27 | 1 | 1.62 | 2.0 | 0.27 | 0.4 | 2.8 |

* The ratio of admixtures is the percentage of cement weight.

* Sika-1250 is high range water reducers which contents Superplasticizers. Sika-C100 is chloride-free set accelerator which contents $\text{Ca}(\text{NO}_3)_2 \cdot 4\text{H}_2\text{O}$.

3. Result and discussion

3.1 Concrete Compressive Strength

According to Figure 1, most of the test specimens achieved the required strength within 4 to 6 hours of curing when the curing temperature was between 23°C and 50°C. The compressive strength of the concrete increased as the amount of water decreased. Nevertheless, at a curing temperature of 50°C, the compressive strength of M500-WC27, M500-WC29, and M500-WC31 did not significantly differ. Therefore, when developing high early strength concrete, an appropriate curing temperature plays a crucial role in the early strength development of the concrete.

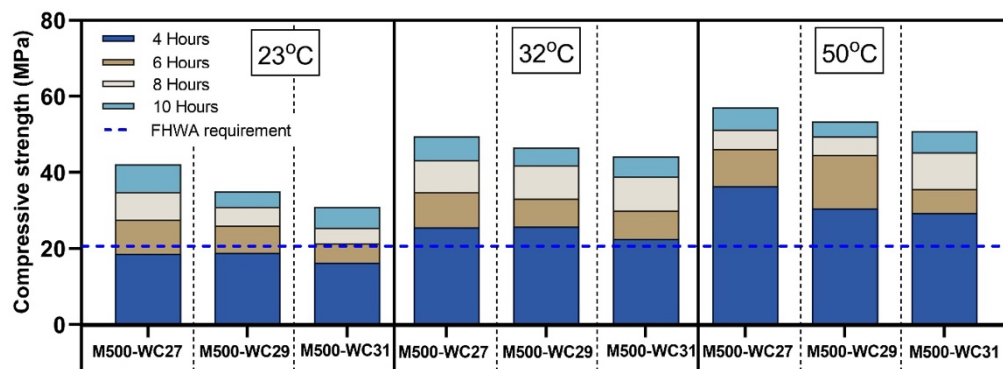


Figure 2. Test results compressive strength at different curing temperatures (MPa)

3.2 Concrete maintenance method

Figure 3 shows the results of the experiment, which evaluated the 4 hours and 6 hours compressive strength of M500-WC31 under different curing methods.

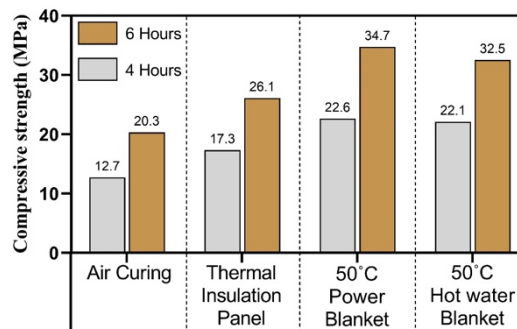


Figure 3. Test results of compressive strength of M500-WC31 using different curing methods (MPa)

The compressive strength of concrete during the curing process is observed to increase with the availability of more heat energy. At 4 hours of curing, air curing and thermal insulation cover curing were not able to meet the target compressive strength requirement, whereas electric blanket and hot water blanket curing achieved approximately 5% to 10% higher compressive strength than the target. This indicates that an increase in temperature during the curing period positively affects the early strength development of concrete. The hydration heat generated by the cement alone is insufficient to raise the concrete temperature,

necessitating the provision of additional heat energy and ensuring an adequate supply during the curing period.

3.3 Concrete slump loss

In Figure 4, the slump loss of M500-WC29 is presented. The study evaluates the slump loss of concrete after mixing and transportation to the construction site with an estimated travel time of 50 minutes at different ambient temperatures ranging from 25°C to 32°C. It is observed that the slump flow of each batch of tests ranged within 70±6 cm after 10 minutes of stirring. After 50 minutes of intermittent stirring, the slump fluidity decreased to 45±6 cm. However, it still satisfies the field workability standards, and there is minimal variation in slump flow among those samples.

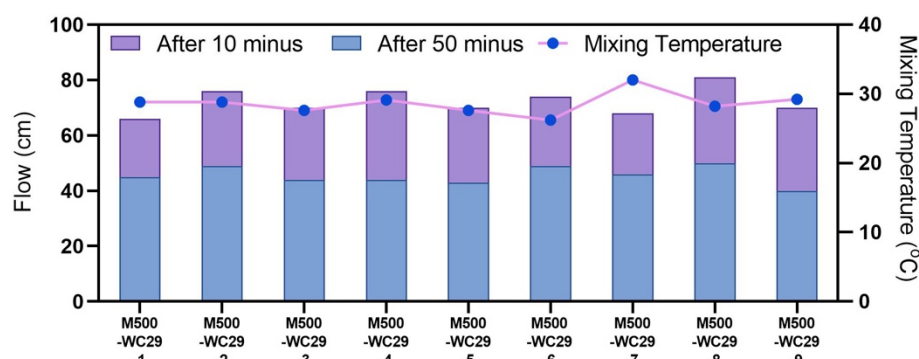


Figure 4. The slump loss of M500-WC29 at different curing temperatures.

4. Conclusion

This study aimed to create a high early strength concrete mix design suitable for maintaining rigid pavements. The study also investigated the impact of different curing methods and ambient temperatures on the slump flow of the concrete. Based on the findings, the following conclusions were drawn:

1. This research concrete mix design can be achieved in 4 to 6 hours of curing when the curing temperature is between 23°C and 50°C in laboratory conditions. However, when the air temperature could fall below 23°C, appropriate heat-curing methods should be applied.

2. The results suggest that the application of higher heat energy during the curing process leads to an increase in early-age compressive strength. Therefore, providing supplementary heat energy is necessary during the concrete curing period, which can be accomplished through methods such as using hot water blankets or electric blankets to ensure that the concrete receives adequate energy.

Acknowledgment

This work was supported by the [Ministry of Science and Technology] under Grant [number MOST-110-2221-E-008-035-MY3].

References

- Ansari, F. and Luke, A. (1996) "High Early Strength Concrete for Fast-Track Construction and Repair," Report to NJDOT.
- Chen, T. And Fang, S. (2018) , "Rigid pavement repair mixing design in 4 hour-concrete", *Freeway Bureau*, MOTC, ICSII 2018.
- Mitchell, M., Link, R., Punurai Sun, Punurai, Wonsiri Hsu, Cheng-Tzu. (2007), "A Very Early Strength Concrete for Highway Construction. *Journal of Testing and Evaluation*", *J TEST EVAL*, vol.35, pp152.

Wilson, T. P., Romine, A. R., & Smith, K. L. (2000) "Materials and Procedures for Rapid Repair of Partial-Depth Spalls in Concrete Pavements: Manual of Practice (No. FHWA-RD-99-152)" United States. Department of Transportation. Federal Highway Administration.

Concrete performance with alkali-activated cement based on industrial side streams from Brazil

F.S. Faria^{1*}, N. Tokudome², T.F. Oliveira³ and N.B. Justen⁴

¹ Federal University of Rio de Janeiro, Rio de Janeiro, Brazil
Email: filipe.soares.faria@gmail.com

² Circlua, São Paulo, Brazil

Email: naguisa.tokudome@circlua.com.br

³ Federal University of Ouro Preto, Belo Horizonte, Brazil
Email: thainafariaoliv@gmail.com

⁴ Circlua, Belo Horizonte, Brazil

Email: nicolejusten@gmail.com

ABSTRACT

To achieve the decarbonization targets proposed in the Paris Agreement, alkali-activated cements (AAC) emerge as an alternative to Portland cement. In Brazil, one of the pioneers on an industrial scale manufacturer, is starting the production of alkali-activated cements based on steel and mining industrial side streams. The formulation design allows to produce AAC with different properties, in this case, considering different mechanical strengths classes. One for general use – cement class 40 MPa, and other for precast applications – cement class 60 MPa. Considering the novelty of AAC in Brazilian market, the objective of this study is to evaluate the properties in fresh and hardened state of concretes made with two alkali-activated cements. The properties evaluated are workability, heat of reaction, compressive strength, modulus of elasticity and flexural strength. The results indicate that it is possible to make general use concrete with AAC class 40 and, the AAC 60 presents high early strength, which makes its suitable for special applications or precast. Thus, classes 40 and 60 cements incorporate tailings from steel and mining industry and prove to be a viable option to replace Portland cement and reduce CO₂ emissions.

KEYWORDS: *Alkali-activated cement, concrete, mechanical performance, tailing*

1. Introduction

The construction industry is crucial to the economy of any country, but it also contributes to 36% of global energy consumption and 39% of CO₂ emissions (IEA, 2019). In 2021, the production of Portland cement (OPC) was responsible for approximately 8% of global anthropogenic CO₂ emissions (GCP, 2020; IEA, 2021). To address this issue, the cement industry is aiming to reduce CO₂ emissions by 32% to 38% until 2050 through various alternatives, including different cements such as alkali-activated cements (AAC) (IEA and CSI, 2018). When well designed, AAC can have a lower carbon footprint than OPC, with emissions reductions of up to 80%, and can be made from industrial waste or byproducts without high-temperature calcination (Provis and van Deventer, 2009; Habert, D’Espinose De Lacaillerie and Roussel, 2011; McLellan *et al.*, 2011; Sambucci, Sibai and Valente, 2021). Despite all the technical development already made for this type of cement, its use in the construction industry is still limited, and this is also due to the reduced number of manufacturers of this material. This work aims to analyze the alkali-activated cements available in the Brazilian market when applied in concrete.

2. Materials and experimental program

Two types of alkali-activated cement were used in this study, and both were produced in Brazil by Circlua company. To compare, the Brazilian Portland Cement CP V-ARI (CPV) was used as a reference cement.

The CPV is a cement with a high clinker content and high initial strength that is similar to the American Portland Cement Type III and to the European Cement CEM I. The chemical composition and the properties of alkali-activated cements are summarized in Table 1 and Table 2.

Table 1: Chemical composition of the alkali activated cements.

| Composition (%) | SiO ₂ | Al ₂ O ₃ | Fe ₂ O ₃ | MgO | CaO | Na ₂ O | TiO | K ₂ O | P ₂ O ₅ | MnO | LOI |
|-----------------|------------------|--------------------------------|--------------------------------|------|------|-------------------|------|------------------|-------------------------------|------|------|
| AAC 40 | 34.30 | 9.49 | 0.94 | 4.47 | 39.2 | 4.00 | 0.41 | 0.50 | 0.02 | 0.34 | 5.70 |
| AAC 60 | 34.10 | 9.01 | 1.08 | 4.24 | 37.4 | 5.21 | 0.40 | 0.45 | 0.02 | 0.32 | 7.05 |

Table 2: Properties of cementitious materials.

| Cement | Real Density (g/cm ³) | Bulk Density (g/cm ³) | Superficial Area (m ² /g) | Strength (MPa) of 5x10 cm cylinders** | | | | |
|-----------|-----------------------------------|-----------------------------------|--------------------------------------|---------------------------------------|---------|---------|---------|---------|
| | | | | 1 day | 3 days | 7 days | 28 days | 63 days |
| AAC 40 | 2.83 | 1.29 | 0.84 | 20.20 | 32.67 | 39.60 | 45.43 | 52.87 |
| AAC 60 | 2.80 | 1.18 | 0.84 | 24.90 | 39.85 | 54.37 | 60.20 | 67.40 |
| CP V-ARI* | - | - | - | ≥ 14.00 | ≥ 24.00 | ≥ 34.00 | - | - |

* Requirements of ABNT NBR 16697 (2018), the Brazilian standard for Portland Cements.

** According to the procedure established by ABNT NBR 7125 (ABNT NBR 7215, 2019).

The materials used for concrete making, mixing method and the curing regime (temperature of 23 ± 2 °C and humidity of 95%) were in accordance with Brazilian standard ANBT NBR 12821 (2009). Admixture dosage and workability range were fixed (18 ± 3 cm) and slump was adjusted with water, resulting in w/b with slightly difference between binders (Table 3).

Table 3: Summary of concrete mixture proportions for AAC (kg/m³)

| Material ID | 40-a | 40-b | 40-c | 40-d | 40-e | 60-a | 60-b | 60-c | 60-d | 60-e |
|---|------|------|------|------|------|------|------|------|------|------|
| Cement | 422 | 346 | 292 | 253 | 224 | 422 | 346 | 292 | 253 | 224 |
| Fine Aggregate | 769 | 843 | 894 | 931 | 960 | 769 | 843 | 894 | 931 | 960 |
| Coarse Aggregate | 975 | 973 | 970 | 969 | 968 | 975 | 972 | 971 | 969 | 968 |
| w/b | 0.41 | 0.51 | 0.60 | 0.71 | 0.79 | 0.47 | 0.54 | 0.62 | 0.76 | 0.85 |
| Admixture – Powerflow 4104 (over cement weight) | 1.3% | | | | | | | | | |
| Slump (cm) | 17.0 | 17.0 | 18.0 | 17.0 | 17.0 | 18.0 | 17.5 | 17.0 | 18.0 | 18.0 |

Following Brazilian Standards, the concrete 40-c and 60-c were tested with more details for loss of workability (ABNT NBR 10342, 2012), indirect tensile strength (ABNT NBR 7222, 2011), tangent modulus of elasticity (ABNT NBR 8522-1, 2021) and absorption (ABNT NBR 9778, 2005). In parallel, using similar water-binder ratio (w/b), same tests were executed for CPV. The admixture used in the AAC concrete was not used with Portland cement because it is not the best compatible product. For the OPC concrete was used the admixture Powerflow 6308 with the dosage as 0.6% over the cement weight. Heat of reaction was tested in semi adiabatic calorimetry using w/b 0.38 for all samples and without admixture.

3. Results and discussions

In the comparison between the early strength of CPV and AAC60 (Figure 1 (a)), it shows that for smaller w/b ratios, the performance is between the two types of cement as similar. For the 28-days compressive strength (Figure 1(b)) we have the opposite, and the curves get closer with higher w/b ratio. The CPV is usually used in applications where its crucial to achieve high early strength, so, for lowers w/b ratio, AAC60 can be used as an alternative to CPV. The comparison between the AAC40 and CPV (Figure 1(b)) shows that the AAC40 achieves lower resistance than CP V-ARI and AAC60, but it is important to emphasize that those cements are designed for different applications.

Loss of workability was tested on w/b 0.6, until reach slump 6 ± 1 cm and both AAC60 and ACC40 maintained longer workability than Portland Cement used in this study. This demonstrates the efficiency

of the admixture; however, this can be a disadvantage for AAC60 on early strength. Usually, precast applications require a low maintenance compared to general applications. This indicates the admixture used for the test is more suitable for AAC40 needs, rather than AAC60. This effect is also due to the high level of admixture dosage.

The result of heat of reaction was measured on cements without admixtures and as expected, AAC60 presents a higher and faster reaction, compared to AAC40. Regarding to Portland cement, AAC presented faster reaction, nevertheless this is solved with proper admixture, as demonstrated with loss of workability. Figure 1 (e) and (f) shows the result of compressive strength on specimens molded within 15 minutes apart and indicates that the concrete with proper admixture, can be manipulated without any damaging.

For similar w/b ratio, all cements achieved the same range of Tangent Modulus of Elasticity and Indirect Tensile Strength on concrete with 28 days. The absorption of both AAC is slightly higher, despite the considerable difference in compressive strength. This might indicate the pores are not internally connected.

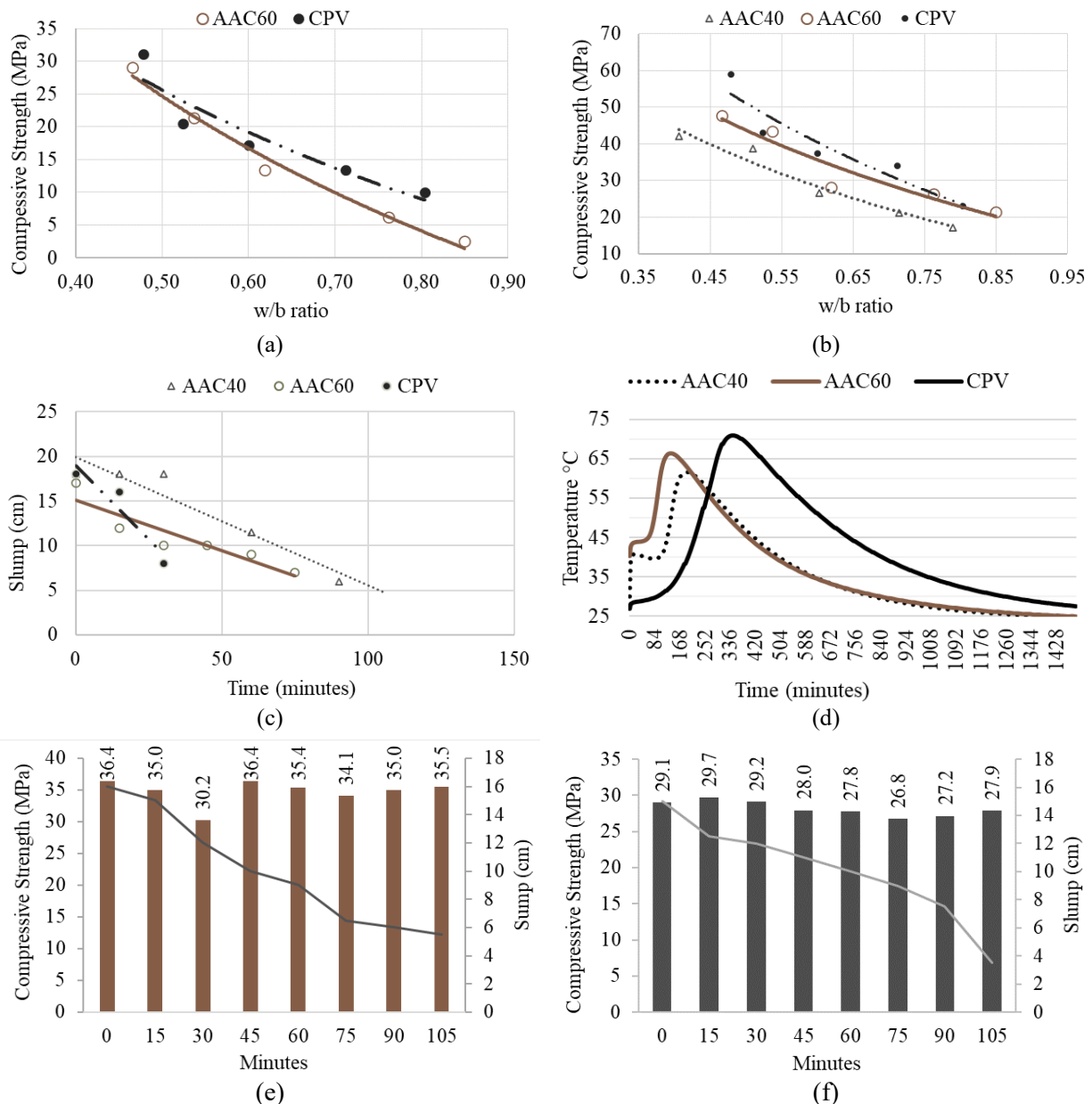


Figure 1: (a) Abrams' Law 1-day AAC60 vs CP V-ARI; (b) Abrams' Law 28 days AAC40 / AAC60 / CP II-E-40 / CP V-ARI; (c) Loss of workability for w/b 0.6; (d) Heat of reaction; (e) AAC60 loss of workability w/b 0.6; (f) AAC40 loss of workability w/b 0.6

Table 4: Modulus of Elasticity, Indirect Tensile Strength, and Absorption

| ID | w/b | Tangent Modulus of Elasticity (GPa) | Indirect Tensile Strength (MPa) | Absorption (%) |
|------|------|-------------------------------------|---------------------------------|----------------|
| 40-c | 0.60 | 30.60 ± 0.28 | 3.20 ± 0.14 | 7.10 |
| 60-c | 0.62 | 31.80 ± 1.18 | 3.40 ± 0.07 | 6.90 |
| CPV | 0.60 | 28.16 ± 0.2 | 3.40 ± 0.14 | 6.32 |

4. Conclusions

Based on the mechanical properties presented in this study, AAC60 can be an alternative to CPV for water/binder ratio lower than 0.6 without many adjustments on cement consumption. For certain applications, further investigations are necessary.

The results from AAC40 shows that this cement can be used for general application, however, it is not recommended for applications with early strength needs and so, cannot be compared directly with CPV. Further studies are recommended to compared with a general use application Portland cement.

Although the AAC60 presented a great mechanical performance, the results presented are from a product that still under development, and improvements in the formulation are possible. The main goal of the improvement can be to approximate the Abbrams Curve to the curve from CPV. Another important point is related to the content of admixture, that can be solved by improvements of cement formulations and improvement in the compatibility between AAC and admixtures. The formulation improvements stated for AAC60 also can be applied to AAC40.

Acknowledgements

We would like to express our gratitude to MC Bauchemie Brazil for the providence of the admixture and the execution of the heat of reaction test.

References

- ABNT NBR 7215 (2019) ‘Portland cement - Determination of compressive strength of cylindrical test specimens’. Rio de Janeiro: Associação Brasileira de Normas Técnicas.
- ABNT NBR 7222 (2011) ‘Concrete and mortar - Determination of the tension strength by diametrical compression of cylindrical test specimens’. Rio de Janeiro: Associação Brasileira de Normas Técnicas.
- ABNT NBR 8522-1 (2021) ‘Hardened concrete - Determination of elasticity and deformation modulus’. Rio de Janeiro: Associação Brasileira de Normas Técnicas.
- ABNT NBR 9778 (2005) ‘Hardened mortar and concrete - Determination of absorption, voids and specific gravity’. Rio de Janeiro: Associação Brasileira de Normas Técnicas.
- ABNT NBR 10342 (2012) ‘Concrete - Method for determination of slump loss with time - Test method’. Rio de Janeiro: Associação Brasileira de Normas Técnicas.
- ABNT NBR 12821 (2009) ‘Concrete - Preparation in laboratory - Procedure’, *Associação Brasileira de Normas Técnicas* [Preprint]. Rio de Janeiro: Associação Brasileira de Normas Técnicas.
- ABNT NBR 16697 (2018) ‘Portland cement - Requirements’, *Associação Brasileira de Normas Técnicas* [Preprint]. Rio de Janeiro: Associação Brasileira de Normas Técnicas.
- GCP (2020) *Global Carbon Project, Carbon Atlas*.
- IEA (2019) *2019 global status report for buildings and construction*. Paris: International Energy Agency.
- IEA (2021) *Cement - Tracking Report - November 2021*. Paris. Available at: <https://www.iea.org/reports/cement> (Accessed: 22 August 2022).
- IEA and CSI (2018) *Technology Roadmap - Low-Carbon Transition in the Cement Industry*. Paris, France. Available at: www.wbcsdcement.org.

Strength Development Prediction and Mixture Optimization of Concrete Used in the Three Gorges Dam

X.H. Xu¹, Z.L. Hu², J.P. Liu^{3*}, W.W. Li⁴

¹ School of Materials Science and Engineering, Southeast University, Nanjing, China
Email: seumaturity@163.com

² School of Materials Science and Engineering, Southeast University, Nanjing, China
Email: zhanglihu@seu.edu.cn

³ School of Materials Science and Engineering, Southeast University, Nanjing, China
Email: liujiaping@cnjsjk.cn

⁴ China Three Gorges Corporation, Beijing, China
Email: li_wenwei@ctg.com.cn

ABSTRACT

Machine learning (ML) based strength development prediction and mixture optimization of the massive concrete used in the Three Gorges Dam have benefits on efficiency and accuracy, providing guidance for mixture design employed in dam maintenance and other concrete constructions. This study established a relationship between material properties and strength development based on the compressive strength (CS) development data of concrete used in the main project of Three Gorges Dam with a time span of more than 20 years. A comprehensive determination method of the weight of strength influencing factors is proposed by combining models based on decision tree (DT) and statistical analysis. The water-to-cement ratio (W/C) and cement content are found to be the key feature parameters dominating the CS of the Three Gorges Dam concrete. For strength development prediction, the prediction efficiency of the commonly used ML regression model on concrete strength development are discussed. Meanwhile, this study presents a concrete mixture optimization method based on ML and multi-objective evolutionary algorithm (MOEA). NSGA-II and MOEA/D are used as the optimization model. By simultaneously optimizing multiple objectives (different development strength) with multiple variables (features), the Pareto fronts of the Three Gorges Dam concrete mixture optimization problem for strength development is successfully obtained.

KEYWORDS: *Strength development, Three Gorges Project, Machine learning, Multi-objective evolutionary algorithms, Mixture optimization*

1. Introduction

China is currently the country with the most high-arch dams under construction and in operation in the world, with the majority of dams using medium-heat and low-heat cement concrete (Fan et al (2017)). In previous mixture designs, low-heat cement concrete generally exhibited low early strength and high later strength growth, while medium-heat cement concrete exhibited high early strength but low later strength (Ji et al (2012)). To meet the requirements for high early strength during dam construction and high later strength for long-term loading, as well as to support the construction of the world's largest "clean energy corridor" in China, it is urgent to explore the laws of strength development and develop a mixture design that couples excellent early and later strength. However, traditional mixture design based on empirical methods suffer from problems such as large-scale experimentation, high economic costs, and significant environmental impact, leading to high carbon dioxide emissions and waste of precious resources. However, ML methods represent a new low-carbon path that can overcome the limitations of traditional empirical methods and predict the strength development of dam concrete and optimize mixture.

ML methods have been employed to identify crack behavior (Dai et al (2018)), predict deformation and monitor structural health (Kang et al (2020)), perform reliability analysis (Hariri-Ardebili and Pourkamali-

Anaraki (2018)) for concrete used in dams. In the field of using ML methods to predict concrete CS and optimize mixture, domestic and foreign scholars have conducted extensive research. ML methods for predicting CS include artificial neural network (ANN), support vector machine (SVM), DT, and others. These methods have achieved excellent prediction results for concrete materials such as ordinary concrete (Young et al (2019)) and high-performance concrete (Chou et al (2014)), etc. Research have been conducted using ML to evaluate the effects of industrial waste and curing methods on the strength development in geopolymer concrete (Ghosh and Ransinchung (2022)). Zhang et al. (Zhang et al (2020)) proposed a concrete mixture optimization method based on ML and metaheuristic algorithms, and successfully solved the bi-objective mix design optimization problem for high-performance concrete.

In this paper, for the strength development data of Three Gorges Dam concrete with a time span of more than 20 years, we analyzed the key features that affect the CS and predicted the strength development by using common ML. Furthermore, we employed a mixture optimization method based on ML and MOEA to obtain the Pareto front of mixture optimization for strength development.

2. Data and Methodology

2.1 Structured Data Sets

The structural data sets for predicting 7-day CS, 90-day CS and strength development were constructed. The data set for predicting strength development extracted the days of CS from the output targets with "day strength factor" as the input feature. The total sample size is 11,251, including 14 input features of mixtures and raw materials properties and one output target of CS without days label. The data sets of 7-day CS and 90-day CS retained 7 input features of optimizable continuous data, with total sample sizes of 1385 and 2814. 7-day CS and 90-day CS are used as output targets. For models based on ANN and SVM, the datasets should be normalized and (0,1) normalization was adopted in this study (Bishop and Nasrabadi (2006)).

2.2 ML Methods

2.2.1 Methods Used in Predicting Strength Development and CS

The Multilayer Perceptron Regression (MLPR), Random Forest Regression (RFR), and Epsilon-Support Vector Regression (SVR) were used to predict strength development and CS. For ML regression problems, R^2 and MSE are commonly used as evaluation criteria for model performance.

2.2.2 Methods Used in Feature Engineering (FE)

The regression method of eXtreme Gradient Boosting (XGBR) was used to evaluate the feature importance of influence strength development, and the influence of different normalization methods was considered.

2.3 MOEA Methods

In this study, MOEA adopted NSGA-II and MOEA/D. NSGA-II is a MOEA based on genetic algorithms and its main idea is to maintain population diversity and convergence by dividing the population into multiple different ranks and calculating the crowding distance of each individual, thereby effectively solving the Pareto front. MOEA/D is a popular MOEA, which determines the score of each solution on different objective functions by using the weight vectors, uses Tchebycheff decomposition formula to combine multiple objective functions into one function to optimize each subproblem, and finds the Pareto front by iteratively optimizing the subproblems and adjusting the weight vectors.

3. Results and Discussion

3.1 FE for Influence Strength Development

The three radar charts in Fig 1 show the feature importance of XGBR in the concrete strength development under different normalization methods. Combining all charts, it can be found that the weight values and ranking trends of each feature are basically consistent regardless of whether the dataset is normalized and which normalization method is used. From each chart, it can be seen that the W/C, cement content, and day strength factor have prominent feature weights. According to Pearson correlation analysis based on statistics, W/C, cement content, and day strength factor all have high correlation with CS in the data set for predicting strength development, which are -0.52122, 0.42381, and 0.34117.

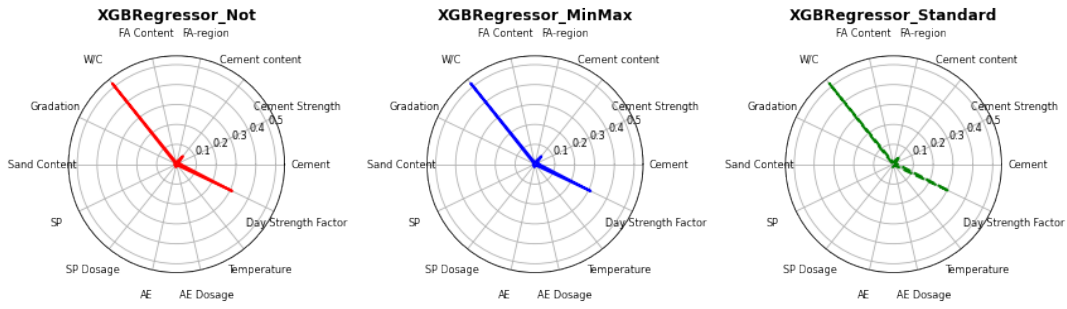


Fig 1. Feature importance of concrete strength development based on XGBR: Not normalized; (0,1) normalization; Z-score standardization

3.2 Strength Development Prediction

MLPR, SVR, and RFR were used to construct models for predicting the strength development. The performance of models was studied with default hyperparameters and hyperparameters optimized using GridSearchCV. Performance evaluation was based on 5-fold cross-validation. Fig 2 shows the comparison of the performance of various models on the training set. It can be found that the optimized RFR has the highest R^2 and the lowest MSE, which has relatively excellent fitting and bias. The hyperparameter is max_depth=13 and n_estimators=140. Fig 2 also shows the residual distribution of the optimized RFR on the training and testing sets. It can be observed that, except for a few outliers, the residual distributions are generally consistent, indicating the optimized RFR has a preferable predictive performance and robustness.

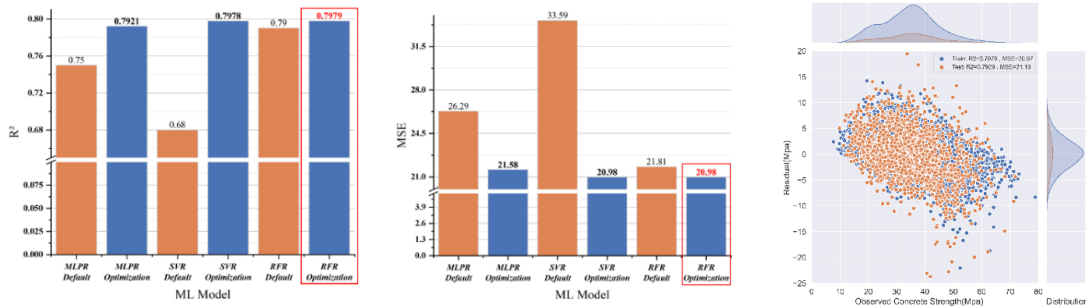


Fig 2. Comparison of performance on the training set among ML models and residual distribution of the optimized RFR model on the training and testing sets (For strength development prediction)

For the prediction of early and late CS, the optimized RFR also had the best performance on the training set compared to MLPR and SVR before and after optimization. The optimized RFR hyperparameters for 7-day CS and 90-day CS are max_depth=9 and 8, n_estimators=50 and 140, respectively. The predictive performance in the test set is also excellent. For 7-day CS and 90-day CS, $R^2=0.7059$ and 0.6361 , $MSE=15.47$ and 28.19 . The optimized RFR can be used as the objective functions of multi-objective optimization.

3.3 Mixture Optimization for Strength Development

Based on the objective of maximizing both 7-day CS and 90-day CS as the goal, multi-objective optimization was performed using NSGA-II and MOEA/D. In this study, the population size of NSGA-II was 50, and other parameters were default values. MOEA/D was set to 50 reference directions, 15 neighbors, and a 70% probability of mating. The total iterations were 500 for both. The constraint conditions were set based on the datasets of 7-day and 90-day CS, and Table 1 shows the range constraints and ratio constraints.

Table 1. Range constraints and ratio constraints in multi-objective optimization

| | Contents | Unit | Constraint value |
|-------------------|------------------------------|-------------------|------------------|
| Range constraints | Cement content | Kg/m ³ | [70,450] |
| | Temperature | °C | [0,32] |
| | 7-day CS | Mpa | [9.2,54] |
| | 90-day CS | Mpa | [16.3,70.8] |
| | W/C | / | [30,68] % |
| Ratio constraints | Fly ash content | / | [0,98] % |
| | Sand content | / | [18,63] % |
| | Superplasticizer dosage | / | [0.3,2] % |
| | Air entrain admixture dosage | / | [0,7] % |

Fig 3 shows the Pareto front of the optimized mixture for the Three Gorges Dam concrete and the actual engineering data. It can be seen that the two MOEA methods successfully and stably solved the Pareto front, and the Pareto solution set achieved preferable optimization of maximizing both the 7-day and 90-day CS.

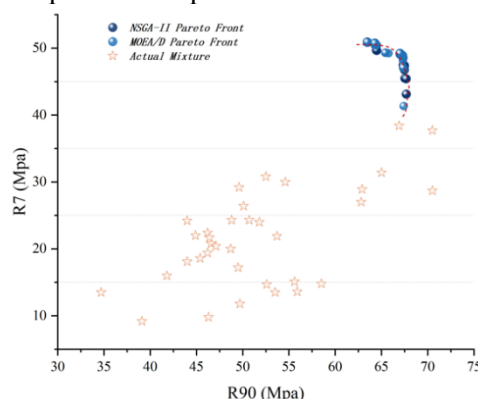


Fig 3. The Pareto front of optimized mixture based on 7-day CS and 90-day CS

4. Conclusions

This study mainly focused on FE, strength prediction, and mixture optimization for strength development. In terms of FE, based on the comprehensive evaluation method of influence factor weights, it was determined that normalization has little effect on the ranking of feature weights, and W/C and cement content are key factors affecting the CS. In terms of strength development prediction, the RFR with 13 max_depth and 140 n_estimators was found to have preferable predictive performance. In terms of mixture optimization, the Pareto front of the Three Gorges Dam concrete strength development optimization problem was successfully solved using NSGA-II and MOEA/D.

Acknowledgements

This work was financially supported by the Joint Program of National Natural Science Foundation of China (U2040222).

References

- Fan, Q.X., Li, W.W. and Li, X.Y. (2017) "Key construction technologies of low heat Portland cement dam concrete", *Journal of Hydroelectric Engineering*, 36(4): 11-7
- Ji, T., Ji, G. and Chen, G. (2012) "Influence of low-heat Portland cement on properties of dam concrete", *Journal of Hydroelectric Engineering*, 31(4): 207-10
- Dai, B., Gu, C., Zhao, E., et al. (2018) "Improved online sequential extreme learning machine for identifying crack behavior in concrete dam", *Advances in Structural Engineering*, 22(2): 402-12
- Kang, F., Liu, X. and Li, J. (2020) "Temperature effect modeling in structural health monitoring of concrete dams using kernel extreme learning machines", *Structural Health Monitoring*, 19(4): 987-1002
- Hariri-Ardebili, M.A. and Pourkamali-Anaraki, F. (2018) "Support vector machine based reliability analysis of concrete dams", *Soil Dynamics and Earthquake Engineering*, 104: 276-95
- Young, B.A., Hall, A., Pilon, L., et al. (2019) "Can the compressive strength of concrete be estimated from knowledge of the mixture proportions?: New insights from statistical analysis and machine learning methods", *Cement and Concrete Research*, 115: 379-88
- Chou, J.S., Tsai, C.F., Pham, A.D., et al. (2014) "Machine learning in concrete strength simulations: Multi-nation data analytics", *Construction and Building materials*, 73: 771-80
- Ghosh, A. and Ransinchung, G.D. (2022) "Application of machine learning algorithm to assess the efficacy of varying industrial wastes and curing methods on strength development of geopolymer concrete", *Construction and Building Materials*, 341
- Zhang, J., Huang, Y., Wang, Y., et al. (2020) "Multi-objective optimization of concrete mixture proportions using machine learning and metaheuristic algorithms", *Construction and Building Materials*, 253
- Bishop, C.M. and Nasrabadi, N.M. (2006) *Pattern recognition and machine learning*, Springer.

Inorganic Capsule Based on MgO Expansive Agent for Self-healing Concrete

J.L. Li¹, X.C. Guan^{2*}

¹ School of Civil Engineering, Harbin Institute of Technology, Harbin, China
Email: lijinglu_ljl@163.com

² School of Civil Engineering, Harbin Institute of Technology, Harbin, China
Email: guanxch@hit.edu.cn

ABSTRACT

Expansive minerals are commonly used to promote the self-healing efficiency of cracked concrete. Nonetheless, the expansive minerals added into concrete will react with water instantly, causing a decrease in later self-healing efficiency. In this study, an inorganic capsule based on MgO expansive agent was developed by granulation and encapsulation. The self-healing performance of cracked mortar was evaluated by the tests of crack observation, water permeability and microanalysis. Results showed that the mortar mixed with 25 vol.% inorganic capsules exhibited dominant self-healing efficiency. After curing in wet-dry cycles for 30 days, the crack closure effect was significantly better than that of the control group. For the mortar with an initial crack width of < 400 μm , the reduction rate of permeability coefficient increased from 38%-77% to 56%-84%. SEM and EDS analysis indicated that inorganic capsules promoted the generation of brucite, nesquehonite, hydromagnesite and calcite, thereby improving the self-healing capacity of cracked mortar.

KEYWORDS: *Self-healing, Inorganic capsule, MgO expansive agent, Permeability coefficient, Microanalysis*

1. Introduction

Concrete is prone to cracking due to the effect of external loads, temperature stresses and exposure environment. Cracks provide channels for aggressive ions, causing the durability deterioration of concrete. However, the traditional repair is expensive and inefficient. Therefore, self-healing concrete has been researched to meet the development needs of intelligent building.

Among the self-healing techniques, incorporating expansive mineral is a simple and effective method. Xue et al. (2021) studied the self-healing behavior of cement-based composites incorporating MgO expansive agent and crystalline admixture under chloride ingress. The products consisting of brucite and calcite were detected in cracks. Wu et al. (2020) investigated the effect of reactive magnesia on the self-healing capacity of ECC specimens. The formation of new products including hydromagnesite, brucite and hydrotalcite-like phase made cracks self-healing. Sherir et al. (2016) studied the expansion characteristics of cementitious composites with fly ash and MgO-type expansive agent, and confirmed the self-healing capability and potential of the ECC-MgO system.

However, the study by Qureshi et al. (2019) showed that the self-healing ability of the early age cement paste mixed with magnesium oxide, bentonite clay and quicklime was better than that of the cement paste at 28 days. The main reason was that the expansive minerals would be consumed due to participation in early hydration of cement. Therefore, Alghamri and Al-Tabbaa (2020) prepared mineral capsules with PVA-coated different expansive agents. The samples containing mineral capsules showed superior improvement in self-healing capacity. Moreover, Wu et al. (2020) developed artificial capsules encapsulated with cement and PMMA and investigated the self-healing efficiency and chemical binding of aggressive ions of cement paste.

To prevent the premature hydration of expansive minerals and further improve the long-term self-healing efficiency of the concrete containing expansive minerals, an inorganic capsule based on MgO expansive agent was prepared. The self-healing performance of the mortar mixed with inorganic capsules was characterized by the tests of crack observation, water permeability and microanalysis.

2. Materials and methods

2.1 Materials

In the preparation process of inorganic capsule, the core materials were MgO expansive agent, fly ash, $\text{Na}_2\text{O} \cdot 2\text{SiO}_2$, and the shell materials were epoxy resin and fine sand. The materials for the mortar preparation were ordinary Portland cement (P·O 42.5), water, river sand and inorganic capsule.

2.2 Preparation of inorganic capsule

The core materials were firstly put into the disc granulator with a diameter of 500 mm. The angle and speed of disk granulator were set to 40° and 50 rpm, respectively. After the powder was mixed evenly, water was sprayed slowly to make the powder into pellets. Then the pellets were oven-dried at 60°C for 24 hours to obtain strength. Subsequently, the pellets were coated with epoxy resin and fine sand. Finally, the granules were sieved and dried for later use.

2.3 Mortar preparation

Mortar was chosen as a representative material for concrete in this study. The mixture design of mortar is shown in Table 1. The content of inorganic capsule was 25 vol.% of the total volume of aggregates. After 28 days of standard curing, the mortars were pre-cracked and exposed to wet-dry cycles for 30 days.

Table 1. Mixture design of mortar (kg/m^3)

| Mixture code | Cement | Sand | Capsule | Water | SP |
|--------------|--------|------|---------|-------|----|
| M0 | 876 | 1752 | 0 | 307 | 5 |
| M1 | 876 | 1314 | 252 | 307 | 6 |

2.4 Evaluation of self-healing efficiency

The effect of cracks closure was observed by a 3D microscope with super depth of field. After curing for 30 days, the typical images of healed cracks with an initial width of $< 400 \mu\text{m}$ were taken.

The water permeability test was conducted before and after healing. Then the permeability coefficient was obtained. Self-healing efficiency was evaluated by the reduction rate of permeability coefficient.

Self-healing products were analyzed through SEM and EDS. The sample containing the healed cracks was oven-dried at 60°C for 3 days. Then microscopic analysis was carried out.

3. Results and discussion

3.1 Morphology of inorganic capsule

Morphology of inorganic capsule is shown in Fig. 1. Results showed that the particle size of capsule was about 3-4 mm, and the thickness of the shell consisting of epoxy resin and sand was around $400\text{-}500 \mu\text{m}$. The core-shell structure ensured the stability and healing potential of the inorganic capsules in matrix.

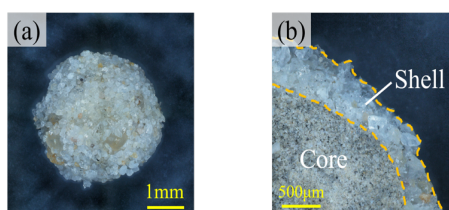


Fig. 1. (a) Exterior morphology and (b) cross-sectional morphology of inorganic capsule.

3.2 Cracks closure

Typical images of healed cracks with an initial width of $< 400 \mu\text{m}$ are shown in Fig. 2. It could be easily found that the crack of the M1 (mortar mixed with 25 vol.% inorganic capsules) was filled with products after healing, and the crack closure was significantly better than that of the M0 (control mortar without inorganic capsules). The study of Alghamri and Al-Tabbaa (2020) also showed that the products of the specimens containing MgO pellets remarkably improved compared to the control specimens.

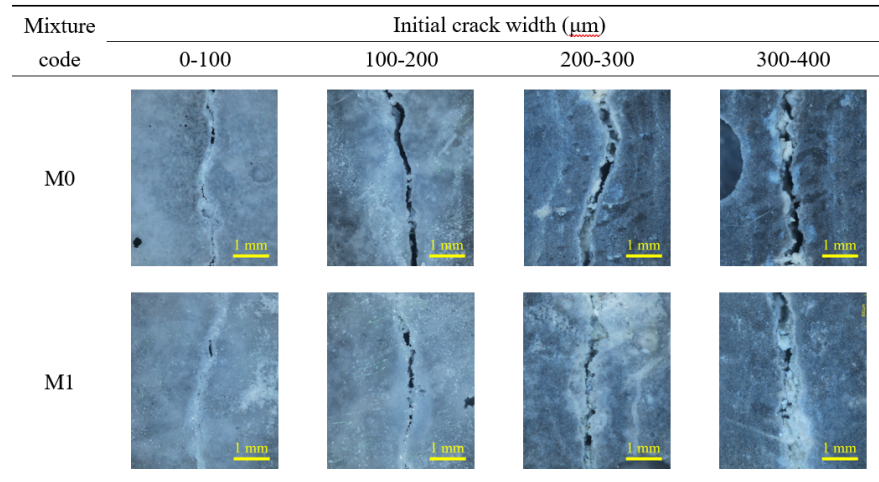


Fig. 2. Typical images of healed cracks with different widths.

3.3 Permeability coefficient

The permeability coefficient and the reduction rate of permeability coefficient of the M0 and M1 mortar are shown in Fig. 3. Results showed that the permeability coefficient increased with the increase of crack width. After healing for 30 days, the permeability coefficient decreased to varying degrees. Fig. 3(c) shows that the reduction rate of permeability coefficient of the M0 mortar was only approximately 38%-77%, while the reduction rate raised to about 56%-84% owing to the incorporation of inorganic capsules. It indicated that the cracks closed due to the self-healing effect of inorganic capsules, resulting in the reduction of the transmission performance of matrix.

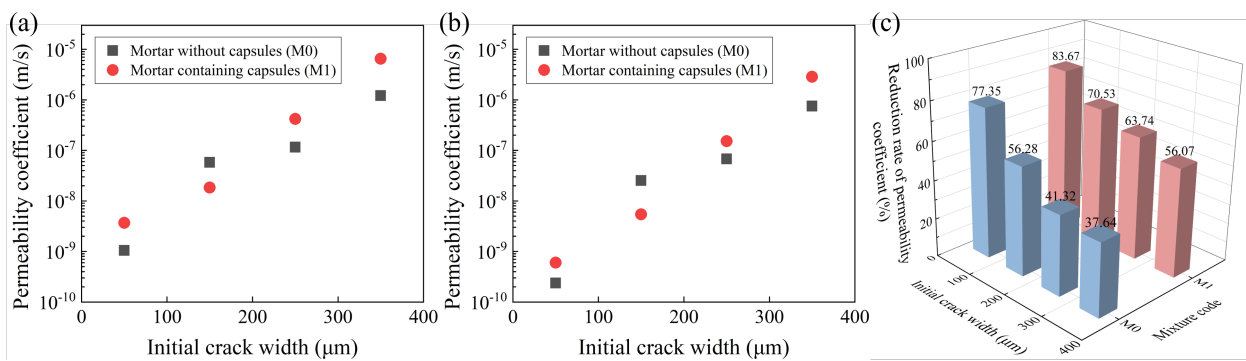


Fig. 3. Permeability coefficient of (a) before and (b) after healing, and (c) reduction rate of permeability coefficient.

3.4 Self-healing products

The SEM images and EDS patterns of self-healing products are shown in Fig. 4. It could be found that the products spread across the crack. According to the microanalysis and the studies of Qureshi et al. (2016) and Unluer et al. (2014), it could be determined that the self-healing products were mainly brucite, nesquehonite, hydromagnesite and calcite.

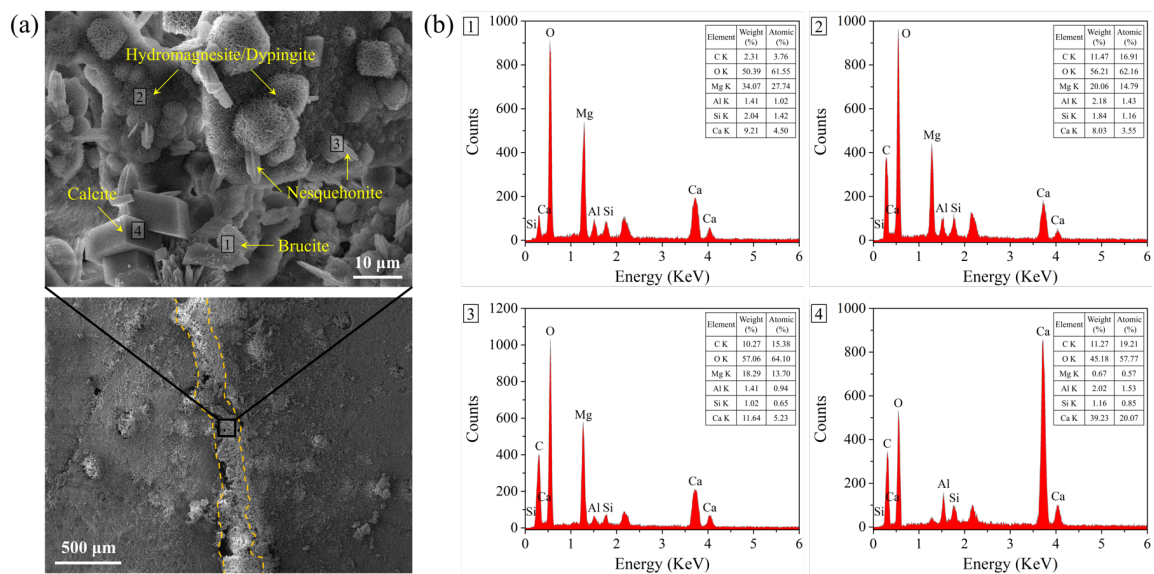


Fig. 4. (a) SEM images and (b) EDS patterns of self-healing products.

4. Conclusions

In this study, an inorganic capsule based on MgO expansive agent was prepared, and the self-healing capacity of the mortar was investigated. The main conclusions are as follows:

After curing in wet-dry cycles for 30 days, the crack closure effect of the mortar mixed with 25 vol.% inorganic capsules was significantly better than that of the control group. For the mortar with the cracks of < 400 μm in initial width, the reduction rate of permeability coefficient increased from 38%-77% to 56%-84%, due to the addition of inorganic capsules. SEM and EDS indicated that the products were mainly brucite, nesquehonite, hydromagnesite and calcite.

Acknowledgements

This study was supported by the National Key Research and Development Program of China (2022YFB2602605), the National Natural Science Foundation of China (51778189) and Heilongjiang Touyan Innovation Team Program.

References

- Alghamri, R. and Al-Tabbaa, A. (2020) "Self-healing of cracks in mortars using novel PVA-coated pellets of different expansive agents", *Construction and Building Materials*, 254: 119254
- Qureshi, T. and Al-Tabbaa, A. (2016) "Self-healing of drying shrinkage cracks in cement-based materials incorporating reactive MgO", *Smart materials and structures*, 25(8): 084004
- Qureshi, T., Kanellopoulos, A. and Al-Tabbaa, A. (2019) "Autogenous self-healing of cement with expansive minerals-II: Impact of age and the role of optimised expansive minerals in healing performance", *Construction and Building Materials*, 194: 266-275
- Sherir, M.A.A., Hossain, K.M.A. and Lachemi, M. (2016) "Self-healing and expansion characteristics of cementitious composites with high volume fly ash and MgO-type expansive agent", *Construction and Building Materials*, 127: 80-92
- Unluer, C. and Al-Tabbaa, A. (2014) "Enhancing the carbonation of MgO cement porous blocks through improved curing conditions", *Cement and Concrete Research*, 59: 55-65
- Wu, H.L., Zhang, D., Du, Y.J. et al. (2020) "Durability of engineered cementitious composite exposed to acid mine drainage", *Cement and Concrete Composites*, 108: 103550
- Wu, X.T., Huang, H.L., Liu, H. et al. (2020) "Artificial aggregates for self-healing of cement paste and chemical binding of aggressive ions from sea water", *Composites Part B: Engineering*, 182: 107605
- Xue, C., Li, W., Luo, Z. et al. (2021) "Effect of chloride ingress on self-healing recovery of smart cementitious composite incorporating crystalline admixture and MgO expansive agent", *Cement and Concrete Research*, 139: 106252

Design of High-Performance Concrete (HPC) using calcined clay as supplementary cementitious materials

J. K. Das^{1*}, N. Manhas², S. Bishnoi³, S. Bansal⁴ and A. Shukla⁵

¹Department of Civil Engineering, Indian Institute of Technology Delhi, New Delhi, India
Email: jk.das@iitg.ac.in

²Department of Civil Engineering, Indian Institute of Technology Delhi, New Delhi, India
Email: numairmanhas@yahoo.com

³Department of Civil Engineering, Indian Institute of Technology Delhi, New Delhi, India
Email: bishnoi@civil.iitd.ac.in

⁴Department of Civil Engineering, Indian Institute of Technology Delhi, New Delhi, India
Email: sahil.bansal@civil.iitd.ac.in

⁵Department of Civil Engineering, Madhav Institute of Technology & Science, Gwalior, Madhya Pradesh, India
Email: abhilash.shukla29@mitsgwalior.in

ABSTRACT

Ultra-High Performance Concrete (UHPC), incorporated with supplementary cementitious materials (SCMs), is a relatively new construction material with excellent mechanical and durability properties. The good pozzolanic characteristics and abundant availability of calcined clay make it an excellent SCM for UHPC. The present experimental work investigates the effect of different percentages of calcined clay replacement on the fresh properties and compressive strength of UHPC. In addition, the chloride penetration resistance of UHPC mixes in the presence of calcined clay were also determined. For this purpose, concrete mixes were prepared by replacing cement with calcined clay (metakaolin) at different replacement levels (i.e., 10%, 20%, and 30% by mass of cement). Control mixes were also prepared using silica fume as a partial replacement for cement. The obtained results indicated that in concrete substitution of silica fume by calcined clay led to a slight decrease in flow and compressive strength. Although the performance of calcined clay is slightly inferior compared to silica fume in the cement trials, it can be a promising SCM for the manufacture of High-Performance Concrete (HPC).

KEYWORDS: UHPC, Silica fume, Metakaolin, Compressive strength, RCPT.

1. Introduction

Ultra-High Performance Concrete (UHPC), is one of the most innovative concretes known for its exceptional strength, durability, and toughness, making it stand out among other concrete varieties. Typically, the amount of cement utilized in UHPC ranges from 800 to 1100 kg/m³, which is approximately three times higher than that required in the manufacturing of conventional concrete (Wang et al., 2022). The higher use of cement in UHPC results in high carbon emissions and depletion of natural resources, thus limiting the widespread adoption of UHPC in the construction industry. Thus, there is a necessity to create an environmentally friendly UHPC to minimize the adverse environmental consequences.

In recent years numerous studies have been conducted to incorporate different types of SCMs into UHPC to reduce the consumption of cement, thereby reducing its cost and carbon footprint. Among the commonly used SCMs, silica fume is the most effective and widely used pozzolanic material in the production of UHPC due to its extreme fineness (high specific surface area) and high silica content, which results in a positive effect on concrete rheology and mechanical performance (Ahmad, 2017). However, the entire UHPC production industry cannot depend on silica fume as they are not available in abundant quantity. Therefore, it is imperative to explore the possibilities of alternative SCMs which can fulfil the increasing construction demand while being sustainable. In calcined clay, metakaolin which is prepared by heating kaolin clay under 800 °C, holds high pozzolanic activity and can be a good alternative to silica fume in the production of UHPC (Mo et al., 2022). Taфраoui et al. (2009) found that under normal curing, the UHPC containing metakaolin showed equivalent or slightly lower compressive strength than those with silica fume, while in heat curing condition, metakaolin showed higher

compressive strength than silica fume. Further, the durability performance of UHPC containing metakaolin was equivalent to those UHPC containing silica fume (Taфраoui et al., 2009). Jiang et al. (2015) found that 10% metakaolin content in UHPC showed the best results in terms of compressive and flexural strengths of UHPC. Although numerous studies have been conducted on UHPC that incorporate metakaolin, but most of these investigations utilize metakaolin ranging from 5% to 25% of the cement mass (Jiang et al., 2015, Mo et al., 2022, Taфраoui et al., 2009). Only a few studies use higher percentage of metakaolin to produce UHPC (Amin et al., 2020). Therefore, there is a need to study the mechanical and durability performance of UHPC containing higher replacement levels of metakaolin. Keeping this in view, in the present experimental work, three different replacement levels of metakaolin i.e., 10%, 20%, and 30% by mass of cement were used in the production of UHPC. In addition, three UHPC mixes were also prepared using silica fume instead of metakaolin at the same replacement level. Flow and compressive strength tests were carried out to determine the fresh and mechanical properties of UHPC. In addition, Rapid Chloride Penetration Test (RCPT) was also carried out to evaluate the durability performance of UHPC.

2. Experimental work

2.1 Materials and mix proportion

The raw materials used to produce UHPC included 53-grade ordinary Portland cement, silica fume, metakaolin, quartz powder and quartz sand. The physical and chemical properties of Portland cement, silica fume and clays are presented in Table 1.

Table 1: Oxide composition and physical properties of binders

| Oxide in weight % | SiO ₂ | Fe ₂ O ₃ | Al ₂ O ₃ | CaO | MgO | SO ₃ | Na ₂ O | K ₂ O | Loss on ignition | Median particle size (d50) | Specific gravity |
|-------------------|------------------|--------------------------------|--------------------------------|-------|------|-----------------|-------------------|------------------|------------------|----------------------------|------------------|
| OPC | 19.18 | 6.37 | 4.49 | 62.34 | 1.33 | 2.53 | 0.15 | 0.51 | 1.32 | 16.9 µm | 3.21 |
| Silica fume | 88.83 | 2.86 | 1.85 | 0.60 | 1.90 | 0.49 | 0.23 | 0.58 | 0.60 | 9.59 µm | 2.22 |
| Metakaolin | 42.49 | 1.48 | 46.18 | 0.09 | 1.37 | 0.10 | 1.28 | 0.01 | 4.48 | 8.03 µm | 2.53 |

Quartz powder (specific gravity 2.64) having median particle size (d50) of 35.4 µm and quartz sand (specific gravity 2.64) having size in the range of 1180 - 300 µm were used in the production of UHPC. A polycarboxylate base superplasticizer with a high solid content percentage was used to enhance the workability of UHPC. In total six UHPC mixes were prepared using three replacement levels (i.e., 10%, 20% and 30% by mass of cement) of silica fume and metakaolin. The details of mix design are presented in Table 2. It may be noted that the dosage of superplasticizer used for UHPC mixes containing silica fume was 1.5% by mass of binder and for UHPC mixes containing metakaolin was 2% by mass of binder.

Table 2: Details of UHPC mixes

| Sl. No. | Abbreviation | w/b ratio | Cement (kg/m ³) | Silica fume (kg/m ³) | Metakaolin kg/m ³ | Quartz sand (kg/m ³) | Quartz powder (kg/m ³) | Superplasticizer (kg/m ³) |
|---------|--------------|-----------|-----------------------------|----------------------------------|------------------------------|----------------------------------|------------------------------------|---------------------------------------|
| 1 | UHPC10SF | 0.22 | 931.52 | 93.15 | 0 | 996.97 | 175.94 | 15.37 |
| 2 | UHPC20SF | 0.22 | 839.94 | 167.99 | 0 | 996.97 | 175.94 | 15.12 |
| 3 | UHPC30SF | 0.22 | 764.76 | 229.43 | 0 | 996.97 | 175.94 | 14.91 |
| 4 | UHPC10MK | 0.22 | 940.22 | 0 | 94.02 | 996.97 | 175.94 | 20.68 |
| 5 | UHPC20MK | 0.22 | 854.19 | 0 | 170.84 | 996.97 | 175.94 | 20.50 |
| 6 | UHPC30MK | 0.22 | 782.59 | 0 | 234.78 | 996.97 | 175.94 | 20.35 |

2.2 Specimens fabrication and curing procedure

For each UHPC mix, cubes of size 100 mm for 7- and 28-days compressive strength and cylinders of size Ø100 × 200 mm for RCPT test were prepared. The cube and cylindrical moulds were filled with fresh UHPC in single layer without compaction and subsequently covered with plastic sheets to avoid water evaporation. The specimens were demoulded after 24 h and then subjected to hot water curing conditions for 3 days at a constant temperature of 60 ± 3° C (ASTM C1856/C1856M-17, 2017). Thereafter the specimens were moist cured at ambient temperature till the day of testing.

2.3 Test methods

2.3.1 Flow test

The workability of UHPC prepared in the present investigation was determined through flow test following the guidelines mentioned in ASTM C1856/C1856M (ASTM C1856/C1856M-17, 2017).

2.3.2 Compressive strength test

The compressive strength of each mix was determined by testing three cube specimens at two different ages, i.e., 7 and 28 days.

2.3.3 Rapid chloride penetration test

For RCPT test, \varnothing 100 mm \times 50 mm concrete disks obtained from concrete cylinders (size \varnothing 100 mm \times 200 mm) were used. The test setup for RCPT consisted of two cells where one cell was filled with 0.3 N NaOH solution and the other cell was filled with 3% NaCl solution. The disk was placed in between the cells and the cells were connected to a power supply of 60 V. The current was measured and recorded during a time period of 6 hrs, and the total charge passed through the specimen was calculated from the current and time.

3. Results and discussion

3.1 Flow test and Compressive strength

The results obtained from flow test for different UHPC mixes are shown in Fig. 1. The 7-and 28-day compressive strength of UHPC mixes prepared from different replacement level of silica fume and metakaolin are shown in Fig. 2.

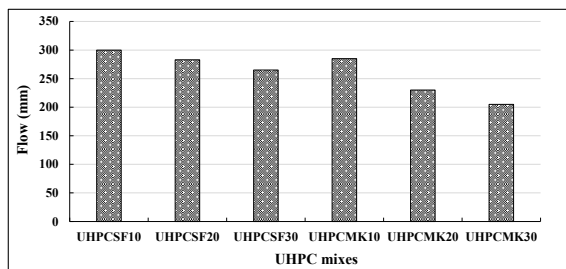


Fig. 1: Flow value for all UHPC mixes

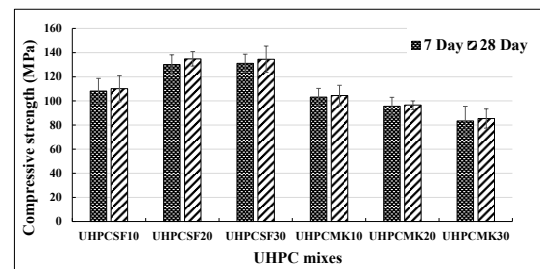


Fig. 2: 7- and 28-day compressive strength value for all UHPC mixes

From the flow value in Fig. 1, it is evident that the workability of UHPC mixes reduces with an increase in the replacement level of silica fume or metakaolin in UHPC mixes. This may be attributed to the very fine particle size of silica fume and metakaolin that adsorbed more water on its surface thereby increasing the water demand. Further, the UHPC mixes containing metakaolin showed slightly lower flow values as compared to those containing silica fume even though the UHPC mixes containing metakaolin were prepared with higher dosages of superplasticizer. The smaller particle size of metakaolin than silica fume may be the reason behind the lower workability of UHPC mixes containing metakaolin.

From Fig. 2, it is observed that the concrete mixes containing 10% silica fume and all those containing metakaolin showed compressive strength lower than 120 MPa. According to ASTM C1856/C1856M-17 (2017), concrete having a compressive strength of at least 120 MPa can be classified as UHPC. Therefore, in the current research, it is more appropriate to refer to the concrete containing 10% silica fume and all those containing metakaolin as High-Performance Concrete (HPC), rather than Ultra High Performance Concrete (UHPC). The results of 7-and 28-day compressive strength showed that, in case of the mixes with silica fume the compressive strength increases with an increase in the silica fume content from 10% to 20% by mass of cement. Further increase in the silica fume content does not have significant influence on the compressive strength value as evident from Fig. 2. The increase in compressive strength with an increase in silica fume content (from 10% to 20% by mass of cement) may be attributed to the greater extent of pozzolanic reactions that results in the formation of more amount of C-S-H gel. The results in Fig. 2 suggested that by replacing 20% of the cement with silica fume in UHPC mixes, the maximum particle packing can be achieved. Further with an increase in the metakaolin replacement level, the

compressive strength decreases at both testing ages. This may be attributed to the fact that the hydration reaction has a greater influence at higher cement content in comparison to the packing effect and pozzolanic reaction in mixes containing a higher proportion of metakaolin. While comparing the effect of silica fume and metakaolin on compressive strength, it is observed that the mixes with silica fume showed higher compressive strength at both 7- and 28-day as compared to those containing metakaolin. The reason behind this may be the high reactivity of silica fume that causes the amorphous silica to react with hydration products, resulting in the formation of a denser microstructure (Ashraf et al., 2022). In addition, the larger surface area of metakaolin leads to more water absorption, which creates voids and gaps in the cementitious matrix (Ashraf et al., 2022). Further with increase in testing age the compressive strength of all UHPC mixes slightly increases.

3.2 Rapid Chloride Penetration test

The RCPT values in terms of total charge passed in coulombs for UHPC mixes containing 10%, 20% and 30% silica fume are 41.70, 11.04, and 6.38 coulombs respectively. Similarly, the RCPT values for UHPC mixes containing 10%, 20% and 30% metakaolin are 77.68, 39.74, and 19.7 coulombs respectively. The total charge passing through a concrete specimen can provide an indication of its ability to resist the penetration of chloride ions. The lower value of total charge passed indicated higher chloride penetration resistance of concrete. All the UHPC mixes showed total charge passed value lower than 100 coulomb indicating negligible chloride ion permeability in the UHPC mixes (ASTM C1202, 2012). This may be due to the denser microstructure of UHPC mixes that resist the ingress of chloride ions into the concrete.

4. Conclusions

Based on the results obtained from the present study the following conclusions were drawn.

- The concrete made with metakaolin can be classified as HPC rather than UHPC as the obtained compressive strength results are less than 120 MPa.
- The use of metakaolin as a partial substitute for silica fume in UHPC tends to decrease the workability and strength. This impact was more prominent when higher levels of metakaolin are used as a replacement.
- The compressive strength results indicated that the optimum proportion of silica fume for achieving maximum particle packing was 20%.
- The RCPT results showed negligible chloride ion permeability in all the UHPC mixes indicating the formation of denser microstructure in the presence of SCMs.

Acknowledgements

The authors wish to express their gratitude to the Border Roads Organisation, Government of India for funding the research work.

References

- Ahmad, O. A. (2017) "Production of High-Performance Silica Fume Concrete", *American Journal of Applied Sciences*, 14 (11): 1031-1038.
- Amin, M., Tayeh, B. A., and Agwa, I. S. (2020) "Effect of using mineral admixtures and ceramic wastes as coarse aggregates on properties of ultrahigh-performance concrete", *Journal of Cleaner Production*, 273:123073.
- Ashraf, M., Iqbal, M. F., Rauf, M., Ashraf, M. U., Ulhaq, A., Muhammad, H., and Liu, Q. (2022) "Developing a sustainable concrete incorporating bentonite clay and silica fume: Mechanical and durability performance", *Journal of Cleaner Production*, 337: 130315.
- ASTM C1202 (2012) "Standard Test Method for Electrical Indication of Concrete's Ability to Resist Chloride Ion Penetration" *ASTM International*, Pennsylvania, United States.
- ASTM C1856/C1856M-17 (2017) "Standard Practice for Fabricating and Testing Specimens of UHPC", *ASTM International*, Pennsylvania, United States.
- Jiang, G., Rong, Z., and Sun, W. (2015), "Effects of metakaolin on mechanical properties, pore structure and hydration heat of mortars at 0.17 w/b ratio" *Construction and Building Materials*, 93: 564–572.
- Mo, Z., Bai, L., and Fu, X. (2022), "Strength properties and hydration of ultra-high performance concrete incorporating calcined clay and limestone with steam curing regimes", *Case Studies in Construction Materials*, 17: e011658.
- Tafraoui, A., Escadeillas, G., Lebailli, S., and Vidal, T. (2009) "Metakaolin in the formulation of UHPC", *Construction and Building Materials*, 23: 669–674.
- Wang, F., Sun, X., Tao, Z., and Pan, Z. (2022) "Effect of silica fume on compressive strength of ultra-high-performance concrete made of calcium aluminate cement/fly ash based geopolymer" *Journal of Building Engineering*, 62:105398.

The performance of 3D printing PCM concrete with novel hollow ceramsite composite

Z. Qiao, W. Zheng, F. Wang, Y. Qi, Y. Gou, and H. Li*

College of materials science and engineering, Xi'an University of Architecture and Technology, Xi'an 710055, China

Email: sunshine_lihui@126.com

ABSTRACT

This paper studied a new type of 3D printing phase change material (PCM)concrete, which uses hollow structure ceramsite composite with PCM(HCCP) as aggregate. HCCP was introduced into 3D printing concrete(3DPC) by equal volume replacement method, and the effects of HCCP with different volume contents on the fluidity, printing properties, and mechanical properties of 3DPC were studied. The changes of thermal conductivity and equivalent specific heat capacity were also discussed. A typical daytime temperature change was simulated using a cold-hot circulation box to monitor the change of the 3D printing inside sample to the ambient temperature. The results indicate that HCCP improves the construction performance of 3DPC, but reduces its flow performance. When the volume of HCCP is less than 40%, the 28d compressive strength is higher than 45.0 MPa, making it suitable for structural applications. The thermal conductivity is 0.853 ~ 1.938 W / (m ·K), and the maximum equivalent specific heat capacity is 2.028 J/ (g ·°C) (in the test range of 18 ~ 38 °C). Additionally, the addition of HCCP improves the thermal storage performance of 3D printing concrete, and the prepared model is found to weaken the internal peak temperature.

KEYWORDS: *3D printing concrete, novel hollow ceramsite, PCM, energy storage*

1. Introduction

Three-dimensional printing of concrete (3DPC) is a rapid manufacturing technology that uses building digital models to design and automatically print high-strength cementitious materials layer by layer. Compared with traditional construction methods, this technology has high mechanization, high efficiency, low labor consumption, and high safety performance. In addition, it does not use templates during the construction process, which has higher degree of freedom, saves raw materials, and can reduce costs (Ji, G., et al. (2022)). Researches in different areas have been studied on the printing performance, mechanical properties, structural design, and equipment development of 3DPC. However, less work has been done in the area of improving the thermal performance of 3DPC.

PCM offers a significant advantage due to its high heat storage density in a small temperature range. Several studies have investigated the addition of PCM to concrete as a means of enhancing its thermal performance. However, the incorporation of PCM and concrete may have a negative impact on both the fresh and hardened properties, depending on the specific approach used. Typically, encapsulated PCM and lightweight aggregate composite PCM are prepared using encapsulation and vacuum impregnation methods, and then these components are "indirectly" added to concrete during mixing to avoid the adverse effects caused by direct addition of PCM (Berardi, U. and A.A. Gallardo (2019)). Introducing PCM into 3DPC through encapsulation effectively improves the thermal properties of 3DPC, which has the potential to reduce the hot /cold load of 3DPC buildings and reduce energy consumption (Brooks, A.L., et al. (2022)). However, it cannot be ignored that the introduction of PCM of encapsulation into 3DPC usually has higher cement content, lower PCM introduction, and is more prone to shrinkage cracks, resulting in low quality, high raw material cost and heavy environmental burden. From the perspective of sustainable development and improving the thermal performance of concrete, the development of environmentally friendly phase change coarse aggregate for printable concrete materials is worthy of consideration.

In this study, HCCP were introduced into 3DPC using the volume replacement method, and the flowability, buildability, and mechanical properties of 3DPC with different amount of HCCP were tested and discussed. The thermal conductivity and equivalent specific heat capacity of 3DPC were tested, at different temperatures. Finally, the internal temperature of 3DPC test model under daily typical environmental temperature changes were evaluated and compared by using a cold-hot circulation box.

2. Materials and Method

The main materials used in the experiment are P.O. 42.5 cement, sulphoaluminate cement, silica fume and fly ash. P.O. 42.5 cement is produced by Liquean Conch cement Co., Ltd. (China), sulphoaluminate cement comes from Zibo Yunhe Color cement Co., Ltd., silica fume is provided by Sichuan Langtian Resources Comprehensive Utilization Co., Ltd., fly ash comes from first-class fly ash from a thermal power plant in Shaanxi, China, Na_2SO_4 is from National Pharmaceutical Group, and water-reducer is polycarboxylic water-reducer. When the temperature is 20 °C and the concentration is 2.0%(wt), the viscosity of HPMC is 20000 mpa·s. the specification of PP fibre is 9 mm, the diameter of the fibre is 18 ~ 48 μm , the fine aggregate is local river sand. The HCCP is a kind of self-made (Li, H., F. Wang and W. Zheng (2021)) coarse aggregate which is shown in figure 1 (a) and has a good sphericity, the HCCP with a particle size of 5.0~8.0 mm, a bulk density of 694 kg/m^3 , a surface density of 1240 kg/m^3 , a cylinder compressive strength of 6.2 MPa and a PCM adsorption capacity of 36.1% (wt) in this experiment. The state of HCCP after physical fragmentation is shown in figure 1 (b). The PCM is adsorbed in the cavity of HCCP. In addition, the adsorbed PCM is paraffin, the phase transition temperature is 28.0 °C and the phase transition enthalpy is 228.3 J/g.

Table 1 lists the composition ratio of all mixtures except HCCP. The proportion design of adding HCCP adopts by replacing the same volume of mortar, and the replacement rate is 0%, 10%, 20%, 30% and 40%. First dry and mix the powder for 5 minutes to ensure fully dispersion, and add the water reducer solution, PP fibre, early strength agent and HCCP in turn and stir for 10 minutes. Then transfer the evenly mixed concrete to the 3D printing equipment to complete the printing. Finally, the preparation of the 3D printed model specimen was completed and shown in Figure 1 (c).

Table 1 Mix design without HCCP (kg/m^3)

| P.O. 42.5 | SAC | Silica fume | FA I | Na_2SO_4 | Water reducer | HPMC | PP Fibre | H_2O | Sand |
|-----------|-----|-------------|------|--------------------------|---------------|------|----------|----------------------|------|
| 700 | 100 | 50 | 150 | 5 | 1.5 | 1 | 2 | 300 | 1000 |

3. Results and discussion

3.1 Flowability evaluation

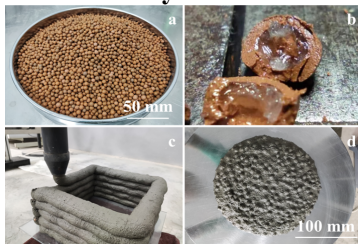


Figure 1 Physical drawing.

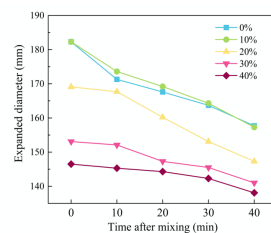


Figure 2 Flowability test data.

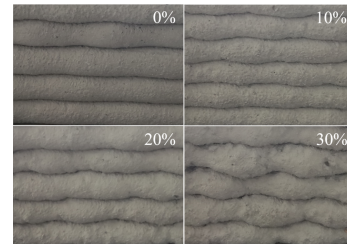


Figure 3 3DPC surface state.

The expanded state and test results of 3DPC with different volume content of HCCP after jumping platform vibration in fresh state as shown in Figure 1 (d) and Figure 2. The flowability of HCCP with different content varies between 183~146 mm and decreases with the passage of time. As a whole, the cementitious material is hydrated with time, resulting in hydration gel, and the HCCP is consolidated, so that its fluidity decreases. The difference is that when the HCCP is mixed with 10% volume, its fluidity increases in a local time period, which may be due to the high sphericity of the HCCP, resulting in the ball effect. Therefore, the addition of a small amount of spherical HCCP is beneficial to the increase of its fluidity, and then with the continuous increase of HCCP volume, the HCCP is overlapped with each other, and there is not enough slurry as lubricant, so that the expansion is small in the jump process.

3.2 Extrudability and constructability

In this study, when no HCCP was added, the 3DPC had good flowability but could not maintain its shape. As the HCCP content increased, the flowability decreased, making it difficult to extrude during printing,

and requiring a higher extrusion rate to ensure continuous printing. HCCP plays the role of a framework in the concrete system, forming bridges between the coarse aggregate and providing frictional forces between surfaces, resulting in difficulties in extrusion but also providing good constructability. As shown in Figure 3, the partial surface state of the specimens printed by 3DPC with different HCCP volume fractions is presented. As the HCCP volume fraction increases, the surface smoothness of the printed specimens decreases, accompanied by the appearance of defects such as air bubbles and cracks. When the HCCP content exceeds 20%, a small amount of HCCP leakage exposes, which affects the aesthetics.

3.3 Mechanical properties

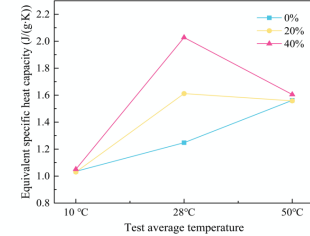
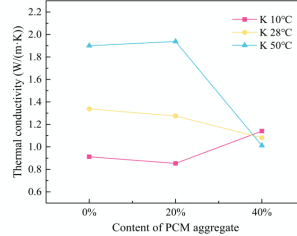
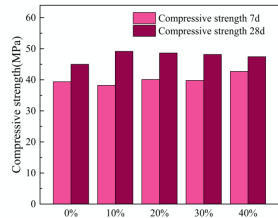


Figure 4 compressive strength test. Figure 5 Thermal conductivity test. Figure 6 Specific heat capacity test. Figure 4 shows the compressive strength of concrete specimens with different volume fractions of HCCP added after 7 and 28 days. The strength of 3DPC with varying HCCP volume fractions, ranging from 0% to 40%, were as follows: 45.0, 49.15, 48.63, 48.17 and 47.43 MPa. The results indicate that the compressive strength did not change significantly with the addition of different volume fractions of HCCP. The overall strength of concrete increased slightly with the addition of HCCP. Compare with the other studies the strength of concrete decreases after adding lightweight aggregate, it can be seen that the introduced ceramic particles have good mechanical properties. Another interesting phenomenon is that the compressive strength of 28 days compared to 7 days, with volume ratios ranging from 0% to 40%, increased by 5.6, 10.95, 8.53, 8.37, and 4.73 MPa, respectively. This is consistent with the pattern of compressive strength changes at 28 days, where the strength increases slightly with a small amount of aggregate added, but then the strength increases decreases as the content of aggregate increases. This is because the aggregate provides early support strength, which leads to a lower rate of strength increase in the later stages.

3.4 Thermal performance

The thermal conductivity of HCCPs with different volume fractions at an average temperature of 10°C, 28°C, and 50°C. The result (Figure 5) of thermal conductivity is 0.853 ~ 1.938 W / (m · K). The test was conducted using the plate heat transfer method. As the volume fraction increased at 10°C, the thermal conductivity increased, possibly due to the ceramic material of the aggregate, which has a higher thermal conductivity than the mortar component, resulting in an overall improvement in thermal conductivity. However, at higher temperatures, the measured thermal conductivity decreased. This could be due to the phase change of paraffin wax, which exhibits endothermic behavior, thus affecting the measurement of thermal conductivity using steady-state heat transfer methods.

Figure 6 shows the equivalent specific heat capacity of 3DPC with different volume fractions of HCCP at average temperatures of 10°C, 28°C, and 50°C. The temperature range for the specific heat capacity test was 20°C, as the start and end times of the experiment were far from 10°C at both ends of the temperature range. At 10°C and 50°C, there was no significant change in the specific heat capacity of different amounts of HCCP, as both temperatures were in stable solid and liquid states without phase transitions. However, at 28°C, the specific heat capacities of samples with volume fractions of 0%, 20%, and 40% were 1.248, 1.612 and 2.028 J/(g·K). The addition of 20% and 40% volume fractions of HCCP increased the specific heat capacity by 29.17% and 62.5%, respectively, compared to the sample with 0% volume fraction. This was because the start and end temperatures were on both sides of the phase transition temperature, resulting in the specific heat capacity being affected by both sensible and latent heat. The results indicate that the addition of HCCP has little effect on the specific heat capacity when there is no phase change. However, when a phase change occurs, the specific heat capacity of samples with 20% and 40% volume fractions significantly increases compared to samples without PCM.

3.5 Simulation analysis of temperature regulation performance

Using a cold-hot circulation box to simulate typical daily temperature fluctuations, the upper and lower surfaces of the model were insulated with 100mm thick XPS insulation board, and real-time data collection was carried out using thermocouples. Figure 7 shows the temperature simulation detection system.

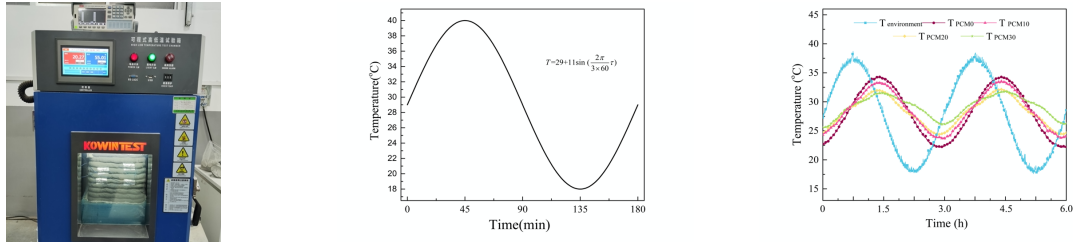


Figure 7 Daytime cold-hot circulation test. Figure 8 Temperature system. Figure 9 Internal temperature of the model. Figure 8 shows the temperature fluctuation curve used. The temperature changes inside the model with different HCCP mixing ratios measured inside the cold-hot circulation box as show in Figure 9. The results indicate that with an increase in the HCCP mixing ratio, the temperature fluctuation is significantly reduced. When 30% of HCCP is mixed, compared with the control sample, the peak temperature under daily fluctuation decreased by 2.8 °C, and the valley temperature increased by 3.8 °C. This is because the introduced PCM in the model can absorb and release heat when the external temperature rises or falls. The results show that introducing HCCP into 3DPC can improve building thermal comfort and demonstrate enormous energy-saving potential.

4. Conclusions

This article aims to evaluate the feasibility of introducing HCCP into 3DPC and preparing 3D printed phase-change energy storage concrete. Flowability, printability, mechanical properties, thermal performance, and simulation tests were conducted to assess the impact of HCCP on the performance of 3DPC. The following conclusions were drawn from this study:

1. HCCP can improve the fluidity of concrete when added in small amounts. However, excessive addition of HCCP reduce its fluidity, but it can enhance its ability to maintain fluidity.
2. The addition of HCCP can improve its constructability, but makes printing more challenging and requires an increase in extrusion speed to achieve printing.
3. The inclusion of HCCP has a positive effect on the strength of the concrete.
4. The impact of HCCP on thermal conductivity needs further exploration, but it is evident that its thermal storage density is significantly increased.
5. Experimental results from simulating temperature fluctuations suggest that the addition of HCCP can effectively reduce temperature fluctuations, providing a bright prospect for its application in the field of 3D concrete printing.

References

- Ji, G., et al. (2022), “Effects of extrusion parameters on properties of 3D printing concrete with HCCPs”, *Construction and Building Materials*, 325: p. 126740.
- Berardi, U. and A.A. Gallardo (2019), “Properties of concretes enhanced with phase change materials for building applications”, *Energy and Buildings*, 199: p. 402-414.
- Brooks, A.L., et al. (2022), “Incorporating PCM-enabled thermal energy storage into 3D printable cementitious composites”, *Cement and Concrete Composites*, 129: p. 104492.
- Li, H., F. Wang and W. Zheng (2021) “Study of a novel hollow ceramsite compounded with paraffin phase change materials for energy storage”, *Construction and Building Materials*, 309: p. 125042.

Drying shrinkage and cracks in fresh cement-based materials for 3D printing: an X-Ray Tomograph investigation

E. Keita^{1*}, W. Zuo¹, L. Caneda-Martinez¹, P. Aïmedieu¹, M. Bornert¹ and N. Roussel¹

¹ Laboratoire Navier (UMR 8205), CNRS, ENPC, Université Gustave Eiffel, Marne-la-Vallée F-77455, France

Email: emmanuel.keita@univ-eiffel.fr

Email: wengqiangzuo@seu.edu.cn

Email: laura.cmartinez@univ-eiffel.fr

Email: patrick.aimedieu@enpc.fr

Email: michel.bornert@enpc.fr

Email: nicolas.roussel@univ-eiffel.fr

ABSTRACT

During extrusion-based additive manufacturing (3D printing) for cement-based materials, formworks do not protect printed filaments from drying. The competition between various shrinkage origins should be revisited in the context of 3D printing. The chemical and autogenous shrinkages are limited in the first hours after casting. Still, due to high surface-to-volume ratio and increase in temperature induced by accelerators, drying should play a significant role in the shrinkage and the crack pattern initiation. This study focuses on drying kinetics, drying-induced shrinkage, and drying-induced cracks at the length scale of inclusions (microcracks) and samples (structural cracks). Mass loss of samples during drying was recorded. In the meantime, X-ray computed tomography was performed to track the microstructural development during drying. Digital image correlation was applied to the obtained images to quantify the local shrinkage and microcracks inside the fresh samples. Our results suggest that, in the case of printed filaments (slender elements with no protection from a formwork), drying-induced shrinkage and drying-induced cracking dominate all other sources of shrinkage and cracking. After drying for 2.5 hours, the final crack patterns have emerged and will not evolve significantly during the hydration peak. Our results showcase several drying regimes, shrinkage regimes, and cracking regimes that depend on the printable material mix-design: many cracklets emerge or long structural cracks can be observed. We finally showcase the practical consequences of the final hardened sample flexural behavior. The results indicate that the early-age drying-induced microcracks provide a propagating path for fracture cracks, thereby weakening the mechanical strength of the hardened filament.

KEYWORDS: 3D printing; Drying; Shrinkage; Microcracking; X-ray computed tomography

1. Introduction

3D concrete printing technology offers significant advantages in construction manufacturing by reducing the need for manual labor during the production of structural components (Wangler et al. 2019). This technology, which relies on extrusion-based additive manufacturing, allows for the construction of structures without using formwork. The process involves the layer-by-layer extrusion of concrete filaments, which can be digitally controlled to achieve the desired shape. While the technology has promising potential, its implementation requires carefully assessing the fresh and hardened properties of the printed concrete elements (Keita et al. 2019; Nerella, Hempel, and Mechtcherine 2019).

It is quite accepted that concrete materials have microscopic damage. Several studies indicate that shrinkage and micro-cracking can be triggered by chemical reactions and self-desiccation phenomena at the early hydration stage (Slowik et al. 2014).

However, for 3D printing, the extruded concrete filaments are exposed to drying condition upon deposit. The water inside printed filaments evaporates toward the external environment with low relative humidity.

Plastic shrinkage and cracking are expected to occur due to the development of the capillary pressure-induced contraction in the material under drying [14–16].

This study aims at characterizing the impact of drying on the microstructural damage of fresh samples with the length scale of printed filaments. In order to analyze drying-induced damages, a one-dimensional model configuration with one face of the fresh sample exposed to drying is used. Static X-ray tomography and dynamic X-ray radiography are performed to in situ observe the evolution of shrinkage and the initiation of cracks of the length scale of inclusions (cracklets).

The results suggest that, in the case of printed filaments (slender elements with no protection from a formwork), drying-induced shrinkage and drying-induced cracking dominate all other sources of shrinkage and cracking.

2. Materials and Methods

2.1 Materials

A CEM I Cement with a specific density of 3.15 was used, with a median particle diameter of 11.5 micrometers. For mortar, glass beads with a diameter of 0.85 and 1.5 mm were used. Two commercial polycarboxylate-based superplasticizers (SP), Sika Viscocrete Tempo 12 (T12) and Sika Viscocrete Krono 947 (K947) were used. In this study, a commercially available cement hydration accelerator known as MasterX-Seed 100 (S100) was utilized. S100 is a suspension of crystal seeds that contain nanoparticles, which promote the development of calcium silicate hydrate crystals in the cement paste during the early stages of the hydration process.

Table 1: Mix proportions and basic parameters of samples.

| Sample Name | W/C | Bead_1.5 mm | Bead_0.85 mm | SP | Accelerator |
|---------------|------|----------------|-----------------|-------|-------------|
| Monocomponent | 0.35 | 50% | - | 0.65% | - |
| Intermediate | 0.20 | 50% | - | 2.0% | - |
| Bicomponent | 0.20 | 42% | 18% | 2.0% | 2.5% |

Three mortar samples with two different Water-to-Cement (W/C) ratios (i.e., 0.35 and 0.20) were designed. The mix proportions are shown in Table 1. Glass beads were used to represent the aggregates to facilitate the distinction between matrix and inclusions. The mix proportion of the samples is within the scope of the typical range of 3D printing cement-based materials [21].

The mortars were mold 3D printed acrylonitrile butadiene styrene (ABS) materials with an internal dimension of 50 mm in length, 20 mm in height, and 15 mm in width. When samples were placed in the mold, the drying surface was the exposed surface. However, for samples that were not placed in a mold, they were deposited freely onto a smooth plastic plate, and all surfaces, except for the bottom surface, were exposed to the drying process.

2.2 X-Ray Tomography

XRCT images were obtained on the XRCT laboratory scanner available at Laboratoire Navier (Ultratom from RX-Solution). The study employed two different curing conditions: ambient air drying and sealing by covering the free surface of the samples with a paraffin film. Samples subjected to the drying condition were simultaneously monitored using an analytical balance with a measurement accuracy of 1 mg during XRCT measurements to record the in-situ mass loss of fresh samples.

Each fresh sample underwent four XRCT measurements, taken at the time of casting, 2.5 hours, 7 hours, and 24 hours after casting. To account for the evolving nature of fresh samples, the total scanning time for each sample was limited to 20 minutes. Additionally, radiograph projections were recorded every 10 seconds between the first two scans of each sample to monitor the evolution of fresh samples.

3. Results

3.1 Drying kinetics

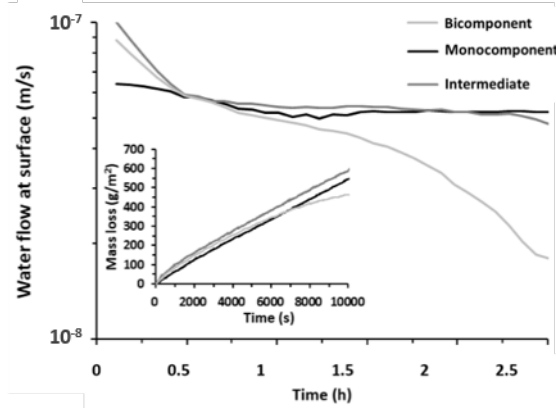


Figure 1: Evaporative water flow at the free surface of fresh samples as a function of time before setting (inset plot: mass loss of fresh samples per unit).

The drying rate of the samples was primarily influenced by environmental conditions, resulting in similar magnitudes of mass loss. To compare the drying kinetics of the fresh samples, the liquid water flow at the free surface J_e , expressed as the drying rate $\frac{dm}{dt}$ per unit area of the fresh sample, was computed using Equation (1) and plotted in Figure 1:

$$J_e = \frac{-1}{\rho_0 S} \frac{dm}{dt} \quad (1)$$

where S is the drying surface area, and ρ_0 is the water density. The results showed that the liquid water flow for all samples during the initial drying stage (i.e., first tens of minutes) was approximately 10^{-7} m/s. Additionally, while both the Monocomponent and Intermediate samples exhibited a constant flow of liquid water throughout the test, the Bicomponent sample's flow was reduced by a factor of three. It is worth noting that the initial flow of liquid water for the Bicomponent and Intermediate samples was higher than that of the Monocomponent sample due to the heat generated by aluminates dissolution in the first few minutes [36], resulting in a higher initial liquid water flow in these two samples [37]. The inset plot in Figure 1 displays the mass loss of the sample per unit area as a function of time. We also observed that microcracks or long structural cracks appeared at around 95% saturation level for all samples. Furthermore, at the end of the test, the saturation level remained above 80%, which was adequate for hydration.

3.2 Microstructural observations

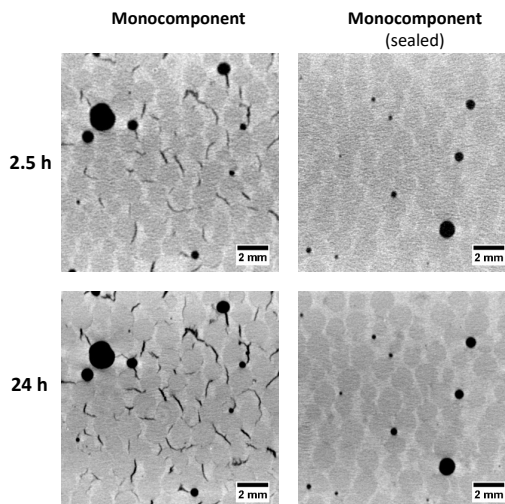


Figure 2: Microtomographic images of samples subjected to drying or sealing conditions.

For all the samples, three phases are observed (see Figure 2): air bubbles (in black color), glass beads (in dark grey color), and cement paste (in light grey color). It can be noted that, after 2.5 h of drying, dispersed cracklets with a typical length of the size of glass beads can be widely found in the matrix. We finally remind that, by comparing the scans at 2.5 h and after 24 h, cracklets do not close after the setting of samples. This suggests that drying fresh small-scale concrete elements before setting might damage the printed objects at hardened state. Besides, it is known that as drying-induced shrinkage is prevented, only plastic shrinkage and chemical shrinkage can occur [7,35]. This is the case for the sealed sample. We observed no change in the sealed sample during and after the setting. This suggests that, for the drying sample, which is the typical size of printed filaments, the drying effect dominates the evolution of the sample.

4. Conclusion

Typical formulations for 3D printing can display three harmful responses during the drying process. Firstly, there is the anticipated shrinkage, which may cause long, conventional cracks to develop. This behavior was observed in the Intermediate and Bicomponent formulations. Secondly, there is the formation of patterns of micro defects, also known as "cracklets," which can further weaken the structural integrity of the printed element. The formation of cracklets was predominant in the Monocomponent sample, characterized by its lower rigidity and higher permeability. These two responses can significantly affect the properties of the final product and reduce its overall strength. Therefore, it is crucial to understand and mitigate these responses during the manufacturing process of 3D-printed concrete.

Acknowledgments

The authors would like to acknowledge the financial support of the DiXite project and Alluvium project, which is supported by a public grant overseen by the French National Research Agency (ANR) as part of the « Investissements d'avenir » program (reference: ANR-16-IDEX-0003) in addition to the contributions of the institutions and partners involved. In addition, L. Caneda-Martinez would like to thank Xunta de Galicia (Spain) for the financial support through its post-doctoral contracts program (ED481B-2021-001). The authors would also like to thank P. Belin for his help in fabricating the experimental tools and conducting the mechanical tests.

References

- Keita, Emmanuel et al. 2019. "Weak Bond Strength between Successive Layers in Extrusion-Based Additive Manufacturing: Measurement and Physical Origin." *Cement and Concrete Research* 123(November 2018): 105787. <https://doi.org/10.1016/j.cemconres.2019.105787>.
- Nerella, Venkatesh Naidu, Simone Hempel, and Viktor Mechtcherine. 2019. "Effects of Layer-Interface Properties on Mechanical Performance of Concrete Elements Produced by Extrusion-Based 3D-Printing." *Construction and Building Materials* 205: 586–601. <https://doi.org/10.1016/j.conbuildmat.2019.01.235>.
- Slowik, Volker, Markus Schmidt, Daniel Kassler, and Michael Eiserbeck. 2014. "Capillary Pressure Monitoring in Plastic Concrete for Controlling Early-Age Shrinkage Cracking." *Transportation Research Record* 2441(2441): 1–5.
- Wangler, Timothy et al. 2019. "Digital Concrete: A Review." *Cement and Concrete Research* 123(May): 105780. <https://linkinghub.elsevier.com/retrieve/pii/S0008884619303680>.

Effect of self-healing on surface morphology in cracked reactive powder concrete

S. Hou^{1,2,3,a}, C. Shi^{1,2,3,b*}, K. Li^{1,2,3,c} and X. Hu^{1,2,3,d}

¹ College of Civil Engineering, Hunan University, Changsha, PR China

² Key Laboratory for Green & Advanced Civil Engineering Materials and Application Technologies of Hunan Province, Changsha, PR China

³ International Innovation Center for Green & Advanced Civil Engineering Materials of Hunan Province, Changsha, PR China

Email: ^acivilhsl@hnu.edu.cn

Email: ^bcshi@hnu.edu.cn

Email: ^clikai@hnu.edu.cn

Email: ^dxianghu@hnu.edu.cn

ABSTRACT

This study investigated the surface morphology of four types of reactive powder concrete (RPC) containing artificial cracks of varying widths (123.45 μm , 312.47 μm , 355.67 μm , and 412.36 μm). The crack surfaces were scanned before and after undergoing 45-day wet/dry cycles in tap water using a laser scanner. The point cloud data were re-meshed using the point Kriging method, and the researchers quantified surface roughness using a surface roughness coefficient (the ratio of true surface area to projective area). The findings reveal that the surface roughness of post-conditioned crack surfaces initially decreases and then increases with increasing crack width. This suggests that the self-healing reactions of healing products that accumulate within the crack space have a significant impact on the surface roughness of the crack surfaces. The study further reveals that the roughness of surface morphology in cracks with small roughness and sufficient width will increase following the healing process. Ultimately, these results suggest that the self-healing effect of RPCs on surface morphology may be influenced by both crack width and roughness.

KEYWORDS: *Self-healing; Surface roughness; Reactive powder concrete; Laser scanner; Morphology*

1. Introduction

Surface morphology plays a crucial role in concrete performance and is therefore an area of great interest. Roughness is widely used as a means of quantifying surface morphology, as it provides valuable information about surface texture and its impact on bonding, friction, and durability (Courard et al (2015), Sadowski and Mathia (2016)). Roughness can be closely related to the healing effects, for example, a rough surface morphology contributes to healing products formation in crack sealing by using bio-cementation (Cardoso et al (2021)). Self-healing effects in concrete have gained significant attention in recent decades due to their eco-friendly and sustainable properties. This research area has become increasingly popular as researchers explore innovative ways to enhance the durability and longevity of concrete structures (Zhang et al (2020)). (Hou et al (2022)) reviewed the mechanisms of autogenous healing in concrete, with a focus on the healing products that accumulate in the crack topography and seal the crack width. They suggested that these processes could also alter surface roughness. However, the study did not provide a clear understanding of the relationship between crack width and surface roughness variation. Autogenous healing of concrete can involve further hydration and subsequent carbonation, as previously reported by (Huang and Ye (2012), Huang et al (2013)). However, the distribution of self-healing products in crack topography is often uneven (Suleiman and Nehdi (2018)). (Fan and Li (2022)) attempted to explain

this phenomenon by investigating the mechanisms of the healing process along the crack depth, using modeling and experiments to analyze the physicochemical actions involved. The uneven stacking of self-healing products in crack topography is a factor that may influence surface roughness variation. As the healing products accumulate and redistribute within the crack, they can alter the morphology of the surface, resulting in changes to the surface roughness. This aspect should be considered when exploring the impact of self-healing on concrete surface morphology.

In this study, four RPCs were firstly splitted into two pairs for subsequent artificial crack manufacturing. Then, the surface morphology after cracking was scanned by a laser scanner for the digital data. The specimens with crack width of 123.45 μm , 312.47 μm , 355.67 μm , and 412.36 μm were made, respectively, which were put into wet/dry cycles curing with top water for 45 days. Finally, the surface morphology after healing processing was conducted the scanning again. The healing effect on surface roughness in cracks with different widths is discussed.

2. Experimental program

2.1 Raw material and specimen preparation

The specimens were prepared using Portland cement Type I 42.5 (PI 42.5), silica fume (SF), and ground granulated blast-furnace slag (GGBS) listed in Table 1. Aggregates such as silica sand (SS), fine river sand (FS), and coarse river sand (CS) were used, with particle sizes listed. The s/c ratio was 1 and the w/c ratio was 0.2, with the addition of tap water and high range water reducer. The mixture proportion used is outlined in Table 2.

Table 1. Properties of PI 42.5, SF and GGBS

| Components/Properties | PI 42.5 | SF | GGBS |
|---|---------|-------|--------|
| SiO ₂ | 22.87% | 95.4% | 35.02% |
| Al ₂ O ₃ | 4.47% | - | 14.84% |
| Fe ₂ O ₃ | 3.48% | 0.54% | 1.2% |
| CaO | 64.05% | 1.65% | 37.01% |
| MgO | 2.46% | 0.26% | 0.2% |
| SO ₃ | 2.44% | - | 1.21% |
| Na ₂ O(eq) | 0.52% | - | - |
| f-CaO | 0.9% | - | - |
| NaO | - | 0.16% | - |
| K ₂ O | - | 0.87% | - |
| C | - | 1.12% | - |
| Loss on ignition | 1.21% | 2.25% | - |
| Specific surface area(m ² /kg) | 341 | 18650 | 422 |

Table 2. Mixture design

| Mixtures | Aggregates | | | Cementitious materials | | | Relative weight ratio to cementitious materials | | |
|----------|------------|-----|-----|------------------------|------|------|---|-----|------|
| | CS | FS | SS | PI 42.5 | SF | GGBS | w/c | s/c | HRWR |
| SF0 | 0.2 | 0.3 | 0.5 | 0.45 | 0.25 | 0.3 | 0.2 | 1 | 0.02 |

2.2 Artificial crack generation and surface morphology digitalization

Fig. 1 shows the process of creating artificial cracks of specific widths on RPC specimens and digitizing their surface morphology. A novel splitting device was used to achieve a single macro crack fracture, resulting in two perfectly matched halves (A and B) of plain concrete. A tinfoil block was folded to attain a width of 0.5 mm to separate the two surface morphologies with a specific in-between width. The specimens were scanned by a laser scanner and cured with wet/dry cycles for 45 days.

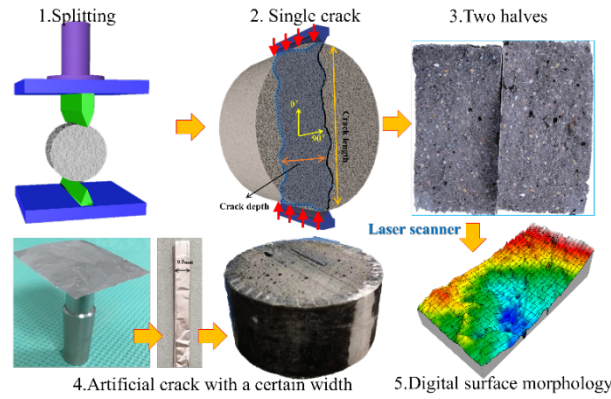


Fig. 1 Manufacturing artificial crack with a certain width and digitizing surface morphology (Hou et al (2023))

2.3 Determination of surface roughness coefficient

The surface morphology was reconstructed using triangular patches from laser scanner point cloud data. Surface area (S_f) was calculated from the sum of all triangular patch areas, while the projected area on the mean plane (S_0) was obtained from the sum of all triangular patch projected areas. The surface roughness coefficient (R_s) was then calculated as $R_s = S_f/S_0$ (Hou et al (2023)). Roughness variation was determined by comparing the roughness values before and after healing, with an increase or decrease indicated by a positive or negative value, respectively.

3 Results and discussion

Prior to any healing treatment, the roughness of four specimens, labeled as A and B, was found to be different. This discrepancy can be attributed to the presence of damages and original pores in the RPC material, as reported by (Hou et al (2023)). When the healing products are applied to the surface, they accumulate in the crack space, leading to a reduction in surface roughness in specimens 123.45 μm , 312.47 μm , and B (355.67 μm) as shown in Fig. 2(a-c). This decrease in roughness could be due to the healing products collecting in the hollows of the surface in shallow cracks (as depicted in Fig. 3(a)). However, when the crack width increases, such as in the case of surface morphology in A (355.67 μm) and A (412.36 μm), the healing products can easily form on the swelling of asperity, resulting in an increase in roughness of the crack surface, as shown in Fig. 3(b). Therefore, the accumulation of healing products in the 3D crack topography could be closely related to crack width and surface roughness, which can result in their uneven stacking. Previous investigations (Suleiman and Nehdi (2018), Huang et al (2016), Hou et al (2022)) have reported that the distribution of healing products is uneven due to non-uniform solubility in autogenous healing, which often results in the open mouth of a fully closed crack but less sealing in the internal crack. (Hou et al (2022)) proposed a feedback model, predicting that the surface roughness of specimens with a crack width of 300 μm under wet/dry cycles would decrease. The surface roughness of 123.45 μm indeed decreased, further confirming the validity of the feedback model (see Fig. 2(a-e)). Fig. 2(f) suggests that γ will first increase but then decrease as the crack width increases. Moreover, as depicted in Fig. 3(c), the effect of crack width and roughness on roughness variation can be observed. Specifically, when the crack width are large enough but roughness is small enough, roughness will increase due to $\gamma < 0$. On the other hand, when the crack width smaller than a certain value, the roughness will decrease. However, decreasing to a minimal value does not necessarily mean the smallest crack width.

3. Conclusions

This study supports the deduction made by (Hou et al (2022)) that surface roughness in cracks with a width smaller than 300 μm decreases under wet/dry cycles. The findings also demonstrate that the variation in surface roughness is closely related to both crack width and roughness. Specifically, for cracks with small roughness and a width not less than 355.67 μm , the surface roughness actually increases following wet/dry cycles.

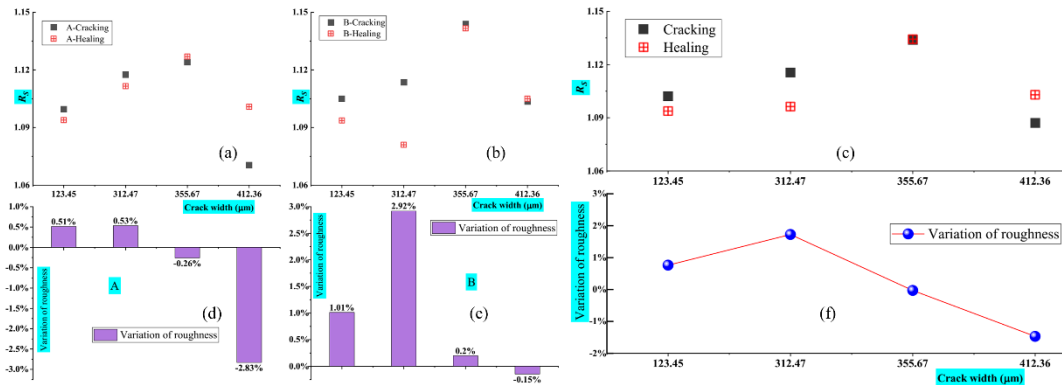


Fig. 2 R_s vs. crack width in (a) A (b) B (c) Total crack; variation of roughness in (d) A (e) B (f) Total crack.

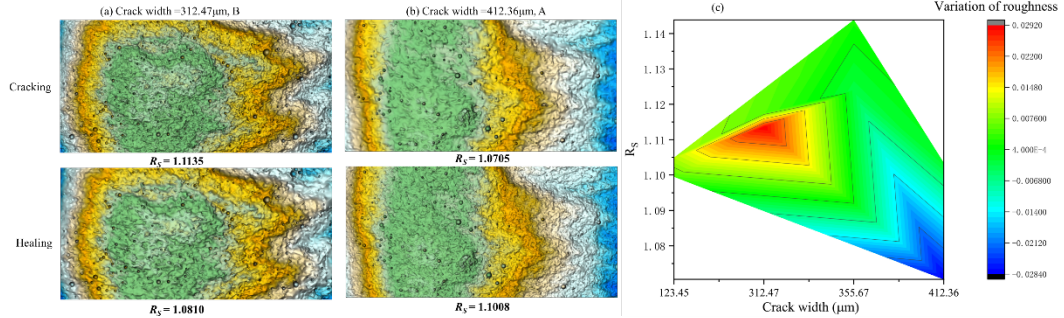


Fig. 3 (a) Decreased roughness in A of 312.47 μm (b) Increased roughness in B of 412.35 μm , (c) The effect of crack width and roughness on roughness variation.

Acknowledgements

The authors gratefully acknowledge the financial supports from the Ministry of Science and Technology under Project No. 2018YFC0705400 and the National Natural Science Foundation of China (No. 51908207).

References

- Cardoso, R., E. Arbabzadeh, J. T. de Lima, I. Flores-Colen, M. F. C. Pereira, M. Costa e Silva, S. O. D. Duarte and G. A. Monteiro (2021) "The influence of stone joints width and roughness on the efficiency of biocementation sealing ". *Construction and Building Materials*, 283
- Courard, L., B. Bissonnette and A. Garbacz. 2015. *Concrete Surface Engineering*. Boca Raton: CRC Press.
- Fan, S. and M. Li (2022) "Understanding intrinsic healing process in cementitious cracks through modeling and experiments ". *Cement and Concrete Research*, 162
- Hou, S., K. Li, X. Hu and C. Shi (2023) "Exploring the nonlinear behavior of the flow through cracked concrete by water permeability test ". *Cement and Concrete Research*: Under review
- Hou, S., K. Li, Z. Wu, F. Li and C. Shi (2022) "Quantitative evaluation on self-healing capacity of cracked concrete by water permeability test – A review ". *Cement and Concrete Composites*, 127: 104404
- Huang, H. and G. Ye (2012) "Simulation of self-healing by further hydration in cementitious materials ". *Cement and Concrete Composites*, 34(4): 460-467
- Huang, H., G. Ye and D. Damidot (2013) "Characterization and quantification of self-healing behaviors of microcracks due to further hydration in cement paste ". *Cement and Concrete Research*, 52: 71-81
- Huang, H., G. Ye, C. Qian and E. Schlangen (2016) "Self-healing in cementitious materials: Materials, methods and service conditions ". *Materials & Design*, 92: 499-511
- Sadowski, Ł. and T. G. Mathia (2016) "Multi-scale metrology of concrete surface morphology: Fundamentals and specificity ". *Construction and Building Materials*, 113: 613-621
- Suleiman, A. R. and M. L. Nehdi (2018) "Effect of environmental exposure on autogenous self-healing of cracked cement-based materials ". *Cement and Concrete Research*, 111: 197-208
- Zhang, W., Q. Zheng, A. Ashour and B. Han (2020) "Self-healing cement concrete composites for resilient infrastructures: A review ". *Composites Part B: Engineering*, 189: 107892

Sustainable Geopolymer Concrete for Thermoelectric Energy Harvesting

Mohamad Barzegar¹, Guido Goracci², Pavel Martauz³, Jorge S. Dolado⁴

1 Centro de Física de Materiales, CSIC-UPV/EHU, Paseo Manuel de Lardizábal 5, 20018 Donostia-San Sebastián, Spain. Mohamad.barzegar@ehu.eus

2 Centro de Física de Materiales, CSIC-UPV/EHU, Paseo Manuel de Lardizábal 5, 20018 Donostia-San Sebastián, Spain. guido.goracci@ehu.eus

3 Považská Cementáreň Cement Plant (PCLA), Ulica Janka Kráľa, 01863 Ladce, Slovakia. martauz.p@pcla.sk

4Donostia International Physics Center (DIPC), Paseo Manuel de Lardizabal 4, 20018 Donostia-San Sebastián, Spain. j.dolado@ehu.eus

ABSTRACT

Concrete is the most widely used material in the world and has the potential to play a significant role in energy harvesting technologies. In this context, thermoelectric concretes permit fascinating prospects for future applications in harvesting urban and industrial waste heat. While Ordinary Portland Cement is the most commonly used cementitious material in thermoelectric applications, it has low electrical conductivity and Seebeck coefficient. Geopolymer-based cement composites have gained attention as a sustainable alternative to traditional Portland cement due to their lower carbon dioxide emissions during production and potential for using industrial by-products as raw materials. The present study evaluates the performance of scalable geopolymer-based concrete, which incorporates recycled aggregates as a potential low-cost and environmentally friendly additive for thermoelectric energy harvesting applications. The geopolymer concrete exhibits a significantly high Seebeck coefficient of 570 $\mu\text{V/k}$, about 300 times greater than the typically reported Seebeck coefficient of OPC paste. Overall, this research demonstrates the potential for geopolymer-based cement to play a crucial role in sustainable energy harvesting and shows its great potential for helping to reach the 2050 climate goals.

KEYWORDS: *Geopolymer, Energy harvesting, Thermoelectric cement concrete, Seebeck coefficient*

1. Introduction

The growing energy demand underscores the urgent need for clean and renewable energy sources. On account of the heat gradient generated by the sun and high energy loss in industries, thermoelectric (TE) sources can be a key component of the transition to a more sustainable energy future. In particular, cement-based TE materials offer exciting prospects for ambient energy harvesting. The TE process converts heat into electricity based on the Seebeck effect, which states that a voltage is generated when there is a temperature difference between two ends of a material. TE voltage results from the thermo diffusion of electronic or ionic charge carriers under heat gradient (Singh et al. (2021), Wei et al. (2023)). The discovery by Sun et al. (1998) that carbon fiber-reinforced cement-based composites exhibit thermoelectric effects has led to numerous attempts by other scholars to enhance the TE efficiency of cementitious materials. However, the TE properties of typical plain Ordinary Portland Cement (OPC) are inferior, with the Seebeck coefficient around 2 $\mu\text{V/k}$ (Wen et al. (1999)). Geopolymer is a sustainable substitute binder for Portland cement. However, despite the potential of geopolymer as a smart material, its TE properties have not been extensively studied. Concerning the plain geopolymer matrix, previous research conducted by Cai et al. (2019) reported Seebeck coefficients of -15.12 $\mu\text{V/k}$ and -6.31 $\mu\text{V/k}$ for geopolymers made of fly ash and metakaolin, respectively. Additionally, some limited studies have examined the impact of additives on the thermoelectric properties of geopolymers. Therefore, further research is necessary to fully understand the TE mechanism of geopolymer materials.

While many studies evaluate the properties of lab-scale geopolymers, this paper investigates the TE properties of industrially prepared geopolymer-based hybrid cement (GHC), which is ready for scaling up energy harvesting applications. Additionally, copper slag (CS) is added to the GHC to develop

sustainable concrete with TE properties for construction applications. The energy conversion efficiency of the cement paste and concrete is determined by measuring thermal and electrical conductivity as well as the Seebeck coefficient. The Seebeck coefficient of 570 $\mu\text{V/K}$ is recorded for concrete with 75 %wt CS. The study findings suggest that the geopolymer has a high potential for ambient energy harvesting.

2. Experimental

Materials and sample preparation: Industrial geopolymer-based hybrid cement (GHC), provided by Považská cementáreň a.s., consists of 90% geopolymer and 10% OPC and the particle size of less than 40 μm is used to prepare pure cement paste and concrete. For concrete preparation, 75%wt copper slag (CS) was added to the cement powder. A vibrating sieve with an aperture size of 120 μm was employed to reach a uniform aggregate particle size. Table 1 shows the chemical composition of the GHC and CS aggregates. For sample preparation, firstly one-minute dry mixing at 300rpm is done. Then distilled water with the w/c ratio of 0.6 is added and the solution was mixed for 90s at 700rpm. Later, samples were molded and sealed for 24h and then cured in distilled water for 7 days. The following measurements were conducted on the prepared samples in order to determine the thermoelectric figure of merit. The reported results are the average of tested parameters for three samples.

Table 1. Chemical composition of the Geopolymer-based hybrid cement GHC and CS aggregates.

| | SiO ₂ | Al ₂ O ₃ | Fe ₂ O ₃ | MnO | MgO | CaO | Na ₂ O | K ₂ O | TiO ₂ | P ₂ O ₅ | SO ₃ | LOI (%) |
|-----|------------------|--------------------------------|--------------------------------|------|------|-------|-------------------|------------------|------------------|-------------------------------|-----------------|---------|
| GHC | 35.86 | 13.51 | 4.63 | 0.06 | 1.79 | 23.93 | 3.36 | 1.97 | 0.61 | 0.21 | 5.02 | 5.51 |
| CS | 22,01 | 8,86 | 50,87 | 0,80 | 1,48 | 7,90 | 0,43 | 0,24 | 0,18 | 0,54 | 0,25 | 2.63 |

Thermal conductivity: Thermal conductivity was measured utilizing the modulated differential scanning calorimeter Q2000 TMDSC-TA. This method consists in measuring a thin and a thick disc of the same specimen. The thin sample (<0.5 mm) is measured to obtain the specific heat capacity (CP), as the specimen thickness is less than the temperature penetration length the sample reaches the temperature equilibrium in a shorter time. On the other hand, by measuring the thick sample (1.5 mm) at the same time, the apparent specific heat (C) is obtained. The measured value is lower than that of the thin sample due to non-uniform temperature distribution. The specific heat capacity and the apparent heat capacity are related to the thermal conductivity by Eq. 1 as below (Marcus & Blaine, 1994):

$$\lambda = (8LC^2)/(CPMd^2P) \quad (1)$$

Where λ is the thermal conductivity in W/(K m), C is the thick sample apparent heat capacity in mJ/K, Cp is the specific heat capacity of the thin sample in J/(g K), L is the thick sample height in mm, M is the thick sample mass in mg, d is the thick sample diameter in mm, and P is the modulation period in s.

Electrical conductivity measurement: Two probs AC Impedance Spectroscopy was carried out using the Novocontrol Alpha-A broadband dielectric spectrometer to analyze the electrical behavior of the samples. The DC conductivity of the samples was calculated and reported from Impedance data. The samples for ACIS measurement were cast in a disc mold from the same batch of TE measurement samples. Gold-coated disc electrodes with a diameter of 10 mm were used for data acquisition. Electrical conductivity measurement was carried out under the heat ramp of 1 °C/min from room temperature to 160 °C to evaluate the effect of temperature on conductivity.

Seebeck behavior: The open circuit Voltage (V_{OC}) of the samples as a function of time is measured using a homemade experimental setup to evaluate Seebeck behavior. Both sides of cylinder samples with a diameter of 40 mm and a height of 20 mm are polished and covered by copper adhesive. Silver paste and a thin copper adhesive were used with the 4mm distance with each hot and cold side. Different temperatures were applied using a small ceramic heating plate on the top end of the samples. The temperature of each side of the wire connection was measured by a P-type thermocouple connected to the Picolog datalogger. KEITHLEY 2100 6 ½ DIGIT Multimeter connected to Labview software was used to monitor the voltage difference between the two copper connections.

3. Results

Thermal conductivity: The thermal conductivity of cement pastes with and without additives is measured as a function of temperature and is presented in Fig.1. It can be seen that adding CS to

geopolymer increased the stability of thermal conductivity at different temperatures. The average thermal conductivity of GHC and GHC-75CS were 0.49 W/mK and 0.58 W/mK, respectively. The results indicate that at 50 °C, the thermal conductivity of the GHC-75CS is 16% lower than that of pure cement paste. This suggests that incorporating CS aggregates into cement-based materials can enhance the efficiency of TE cement for low to medium-temperature, which is in line with the operating temperature range of cement-based materials for energy harvesting.

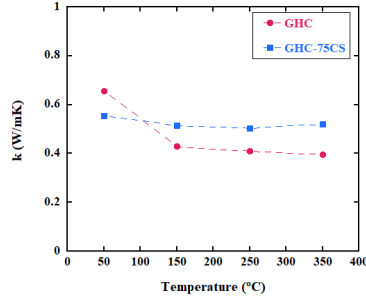


Fig.1. thermal conductivity of pure of GHC and GHC-75CS.

Electric conductivity: Fig.2. displays the DC conductivity of the cement concretes under a heating rate of 1 °C/min. The conductivity of GHC and GHC-75CS at 30 °C are 2.3×10^{-3} and 3.0×10^{-4} , respectively. The results demonstrate two distinct stages in the behavior of the samples. In the first stage, at lower temperatures, the σ_{DC} slightly increases with temperature. In the following stage, at higher temperatures, the conductivity falls with a further temperature increase. The decrease in conductivity around 100 °C is correlated with the loss of bulk water, indicating that ionic charge carriers dominate conduction in the samples. Similarly, the addition of the aggregate resulted in lower conductivity of the concrete at room temperature by reducing the amount of bulk water. However, adding CS made the first stage more stable leading to an increase in the working temperature of the cement paste from 70 °C to 90 °C.

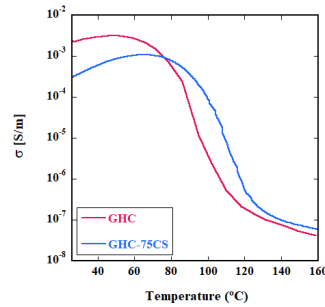


Fig.2. The heating ramp's effect on the electrical conductivity of the samples.

Seebeck's behavior: The Seebeck coefficient is determined by conducting a time-dependent open-circuit voltage (V_{OC}) measurement. To evaluate the Seebeck behavior, three temperatures of 90 °C, 120 °C, and 150 °C are applied on the top surface of the samples. Fig.3. shows the V_{OC} measurement for the first applied temperature for GHC and GHC-75CS. The voltage profile of both samples reveals three distinct stages during heating.

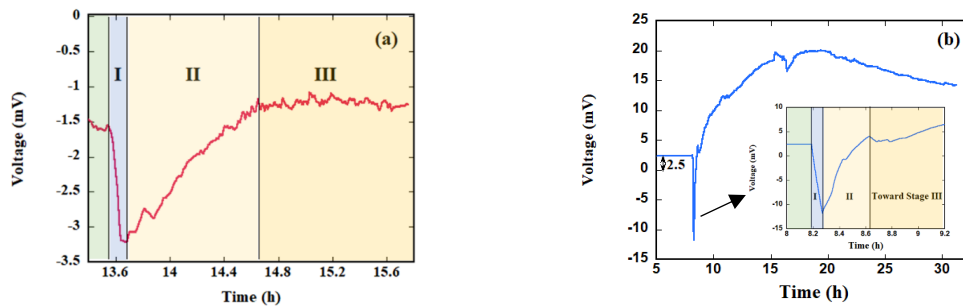


Fig.3. (a) the voltage profile of GHC and (b) GHC-75CS at the applied temperature of 90 °C

In stage I, the ceramic heater is turned on, and the temperature difference builds up immediately. It can be seen that as temperature increases, the TE voltage moves towards more negative values. Subsequently, in stage II, the voltage moves to more positive values after reaching the highest negative value of V_{oc} . Finally, in stage III, V_{oc} reaches a stable value.

Fig.4. presents a comparison of the Seebeck coefficient and the figure of merit of GHC and GHC-75CS. The Seebeck coefficient is determined using the voltage value of the stable part at each temperature. For both samples, the Seebeck coefficient decreased with an increase in temperature. This behavior might be attributed to the loss of water at higher temperatures. Furthermore, the higher Seebeck coefficient of the cement concrete resulted in a significant increase in the figure of merit of the concrete.

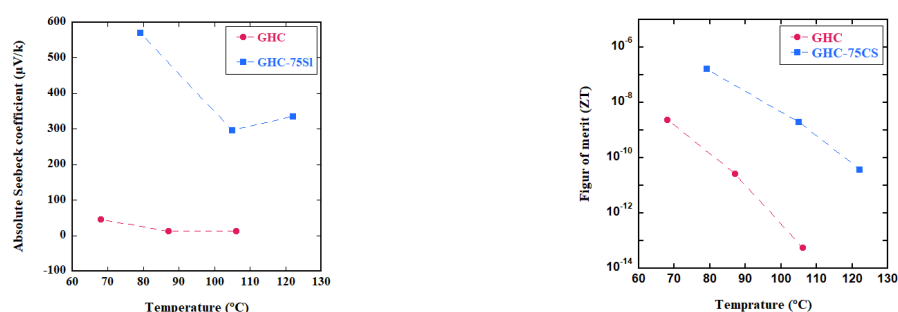


Fig.4. (a) Seebeck coefficient and (b) figure of merit of the samples

4. Conclusion:

This study evaluated the potential of using geopolymer hybrid cement with commercially recycled copper slag aggregates as a sustainable and cost-effective material for thermoelectric energy harvesting. Our results demonstrate that the addition of copper slag aggregates to the cement matrix enhances the stability of thermal conductivity at various temperatures, resulting in a 16% reduction in the thermal conductivity of cement at 50°C. Additionally, the presence of copper slag aggregate increases the temperature range where electrical conductivity remains stable, thus demonstrating the potential for using this material in ambient energy harvesting applications. Furthermore, we found that the addition of copper slag aggregate to the cement matrix improves the Seebeck voltage, resulting in a significantly high Seebeck coefficient of 570 $\mu\text{V/K}$ for the geopolymer concrete.

Our study contributes to the development of sustainable and cost-effective materials for thermoelectric energy harvesting. This research has practical implications for the construction industry, where the use of geopolymer hybrid cement with recycled copper slag aggregates can significantly reduce the environmental impact of building materials while also contributing to the production of clean energy. Overall, our study highlights the promising potential of geopolymer materials for energy harvesting and encourages further research in this area.

5. References

- Cai, J., Tan, J., & Li, X. (2020). Thermoelectric behaviors of fly ash and metakaolin based geopolymer. *Construction and Building Materials*, 237. <https://doi.org/10.1016/j.conbuildmat.2019.117757>
- Marcus, S. M., & Blaine, R. L. (1994). Thermal conductivity of polymers, glasses and ceramics by modulated DSC. *Thermochimica Acta*, 243(2), 231–239.
- Singh, V. P., Kumar, M., Srivastava, R. S., & Vaish, R. (2021). Thermoelectric energy harvesting using cement-based composites: a review. In *Materials Today Energy* (Vol. 21). Elsevier Ltd.
- Sun, M., Li, Z., Mao, Q., & Shen, D. (1998). STUDY ON THE HOLE CONDUCTION PHENOMENON IN CARBON FIBER-REINFORCED CONCRETE.
- Wei, Y., Cui, Y., & Wang, Y. (2023). Ionic thermoelectric effect of pure cement paste and its temperature sensing performance. *Construction and Building Materials*, 364.
- Wen, S., & Chung, D. D. L. (1999). Seebeck effect in carbon fiber-reinforced cement. In *Cement and Concrete Research* (Vol. 29).

Various fundamental factors affecting the ion penetration in concrete

K. Yamada^{1*}, I. Maruyama², T. Ichikawa³, H. Hokora⁴, S. Tomita⁴, Y. Tojo⁵, K. Shibuya⁴, K. Haga⁴, Y. Hosokawa⁶, and G. Igarashi⁷

¹ National Institute for Environmental Studies/Taiheiyo Cement, Miharu, Japan
yamada.kazuo@nies.go.jp

² The University of Tokyo, Tokyo, Japan
i.maruyama@bme.arch.t.u-tokyo.ac.jp

³ Hokkaido University/National Institute for Environmental Studies, Sapporo, Japan
tsuneki@eng.hokudai.ac.jp

⁴ Taiheiyo Consultant, Co., Ltd, Sakura, Japan
⁵ Hokkaido University

⁶ Taiheiyo Cement Corp., Sakura, Japan

⁷ Nagoya University, Nagoya, Japan

ABSTRACT

The penetration of ions into concrete is considered to be a diffusion phenomenon within the pores of concrete involving the interaction of ions in solution with the solid phases. The main dominant factors affecting the penetration depth have been considered to be the adsorption of ions and pore connectivity. Therefore, we compared various experimental results on the penetration of Cs⁺ and Cl⁻, which interact differently with the solid phases, into various cement materials to clarify the role of these factors. In the experiments, the concentration of CsCl was changed in a wide range from 0.5 M to 3.5 μM, and the adsorption capacities of Cs⁺ and Cl⁻ were changed by varying the type of aggregate and the carbonation of the cement paste, and the factors affecting adsorption. The results showed that in rapid ion-exchange adsorption, for example, ionic binding of Cl⁻ by AFm phase and ionic binding of Cs⁺ by carbonated cement paste did not affect permeation retardation, but irreversible fixation of Cs⁺ by aggregates significantly affected permeation retardation. The addition of supplemental cementitious material (SCM, fly ash was examined here) reduces pore connectivity, but this effect appears to be lost with carbonation.

KEYWORDS: *Ion penetration, adsorption, ion exchange, connectivity, carbonation*

1. Introduction

Ion penetration into concrete has been studied for many years because of its importance for various functions of concrete, such as durability and containment of various toxic components. The penetration of chloride ions (Cl⁻) into concrete has been considered to be a diffusion phenomenon involving so-called "binding" by Ca-aluminate hydrates (AFm) (Yuan et al 2009). This paper reviews the factors affecting ion penetration into concrete and re-examines the effects of binding and pore structure on ion penetration of Cs⁺ and Cl⁻. The pore structure was changed by carbonation. Cs⁺ was used to study the effect of adsorption because of the strong interaction of Cs with aggregates containing clays because of its high Cs⁺ ion selectivity (unfortunately, there is no space to explain the mechanism), although Cl⁻ interacts with AFm by reversible ion exchange with existing anions. The adsorption of Cs⁺ onto clay is also an ion exchange, but once Cs⁺ is adsorbed onto the clay, the ion exchange kinetics is significantly reduced and appears irreversible. Therefore, by using two ions with completely different adsorption properties, it is expected that the effect of adsorption on ion penetration can be investigated. In this paper, the interaction between Cl⁻ and AFm will be referred to as "binding", and the interaction between Cs⁺ and the solid phase will be referred to as "adsorption," which is ion exchange but simplified.

2. Reorganizing factors affecting prediction of ion penetration into concrete

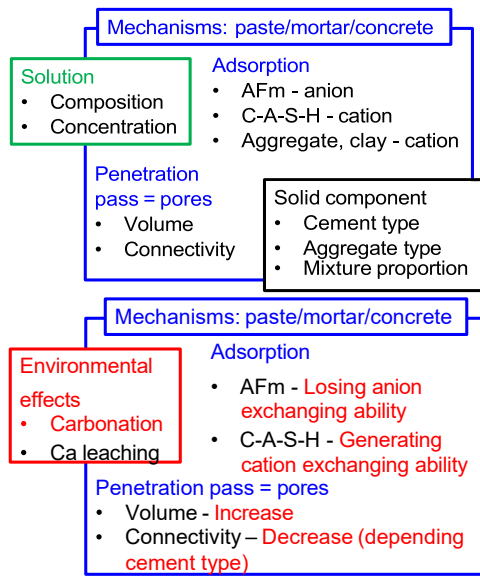


Fig. 1 Effects of carbonation on affecting mechanisms for ion penetraions in cementitious materials

In order to discuss the factors affecting the penetration of ions interacting with cementitious materials, the model shown in Fig. 1 is considered. Reflecting the characteristics of the solid and solution, two important mechanisms affecting ion penetration are determined: adsorption and the penetration pathway, the pore. The environment influences here, and carbonation changes the adsorption properties and pore structure. First, consider the non-carbonated condition. Under high $\text{Ca}/(\text{Al}+\text{Si})$ conditions of ordinary Portland cement (OPC), anions such as Cl^- interact mainly with AFm and alkali metal ions (cations) such as Cs^+ interact little with cement hydrates, but when supplemental cementitious material (SCM) is added and the $\text{Ca}/(\text{Al}+\text{Si})$ molar ratio becomes low, alkali metals interact electrostatically with C-A-S-H. Since these are ion adsorption, adsorption of one ion always releases another ion due to charge conservation. This principle is different from the adsorption of neutral molecules, such as the adsorption of odour molecules by activated carbon or nitrogen gas molecules at low temperatures. In other words, the interaction between ions and cementitious hydrates or aggregates is ion exchange.

Both cations and anions move through the complex pores formed by the cement paste. It is important to note that the depth of penetration of ions is not related to the amount of pores, but is affected by its connectivity. It is possible to determine the tortuosity, or connectivity of pores by the comparison between the Cs^+ penetration in OPC paste, having no interaction with hydrated OPC, and its self-diffusion coefficient. Then, assuming that Cl^- moves through the same pore with Cs^+ moves, we can evaluate the effect of binding of Cl^- by AFm. Since this binding is considered to be a reaction that removes Cl^- ions from the liquid phase, Cl^- penetration is said to be delayed. If so, because the phenomenon is expected more significant at lower concentration, it will be possible to evaluate the effect of binding by penetration experiments with different ion concentration. Since Cs^+ is irreversibly adsorbed on certain aggregates the effect of adsorption on penetration can be evaluated similarly by experiments with different concentration.

Ion interaction with cement paste is also affected by its carbonation. Carbonation eliminates Cl^- binding by the decomposition of AFm, and it results in Cs^+ adsorption by the generation of aluminosilicate hydrate, a cation exchanger (Haga et al 2019). Therefore, by measuring how carbonation changes the penetration of Cl^- and Cs^+ , the effect of adsorption on ion penetration can be investigated from a different angle. By comparing OPC with fly ash cement (FAC) as examined by Ngala and Page 1997, we can simultaneously evaluate how the connectivity of the pores formed by C-A-S-H is affected by carbonation.

Table 1 Materials and immersion conditions

| | Material | Immersion condition | Factors |
|----|-------------------------------|---|--------------------------|
| 1) | OPC paste | CsCl -0.5 M | Carbonation |
| 2) | Limestone OPC mortar | CsCl -0.5 M, 3 mM | Concentration |
| 3) | Limestone OPC/FAC mortar | Cl^- = 6.6 M, Cs^+ = 3 mM | Cement type, carbonation |
| 4) | Hornfels OPC concrete | CsCl -0.1 M, 56 days | Aggregate, carbonation |
| 5) | Crushed river sand OPC mortar | CsCl -3.5 μM , 435 days | Aggregate, concentration |
| 6) | Crushed river sand OPC mortar | CsCl -0.1 M, 56 days | Aggregate, carbonation |

3. Experimental data for comparative study

In this study, the results of immersion tests of cementitious materials in CsCl solutions for different purposes are compared: limestone crushed sand without Cs adsorption and hornfels crushed stone and river gravel with Cs^+ adsorption, as shown in Table 1 (Yamada et al 2021, 2023). Specimens were cured

for at least 56 days. Fly ash cement (FAC, 15 mass% FA replacement) was used to study pore connectivity and carbonation effects. Table 1 summarizes the materials used, the presence or absence of carbonation, the soaking conditions, and the factors examined. Analytical methods used included: for the 0.5 M and 0.1 M immersion conditions, Cs^+ and Cl^- permeation were quantified by electron probe microanalysis; for the 3 mM immersion condition, samples were taken from the surface by grinding and quantified by wet analysis; for the 3.5 μM condition, a solution labeled with Cs-137 was used for quantitative analysis by autoradiography using an imaging plate.

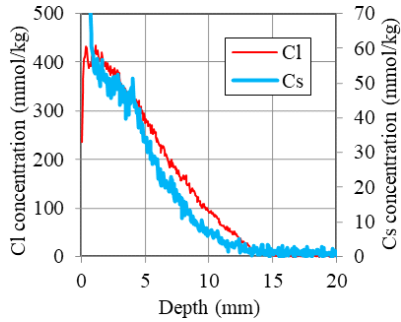


Fig. 2 Cs and Cl penetrations in limestone OPC mortar (0.5 M CsCl, 28 days)

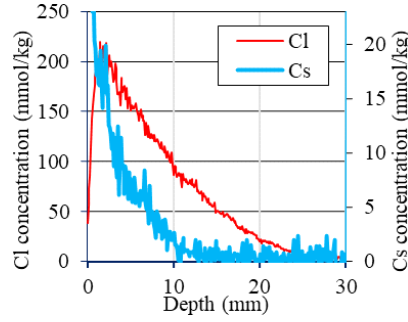


Fig. 3 Cs and Cl penetrations in concrete made of OPC, hornfels and land sand (0.1 M CsCl, 56 days)

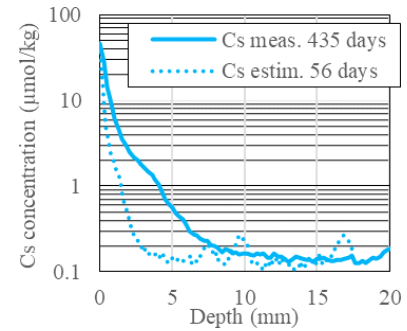


Fig. 4 Cs penetration in river sand mortar (3.5 μM CsCl, 435 days)

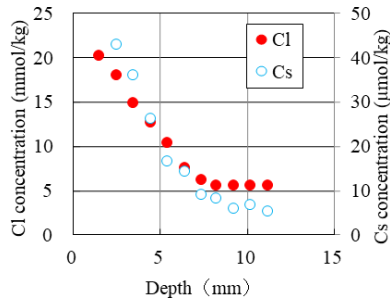


Fig. 5 Cs and Cl penetrations in limestone OPC mortar (3 mM CsCl, 28 days)

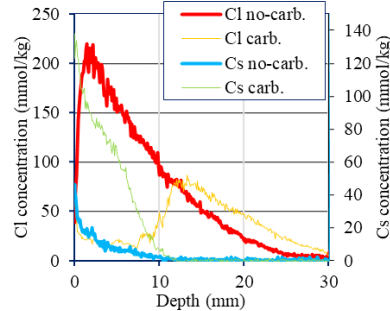


Fig. 6 Effects of carbonation on Cs and Cl penetrations in concrete made of OPC, hornfels and land sand (0.1 M CsCl, 56 days, Carbonation depth = 10mm.)

4. Discussions

Fig. 2 shows the penetration profiles of Cs^+ and Cl^- when the OPC mortar of limestone sand with low Cs^+ adsorption capacity was immersed in a 0.5M CsCl solution; Cl^- is bound to AFm and thus has a higher concentration than Cs^+ , which does not interact with the cement paste. However, the penetration depths were similar as 13 mm.

Fig. 3 shows the penetration profiles of Cs^+ and Cl^- when hornfels, which irreversibly adsorbs Cs^+ , and land sand concrete

were immersed in a 0.1M CsCl solution. The penetration depth of Cs^+ is reduced by half compared to that of Cl^- . Fig. 4 shows the Cs^+ penetration profiles of OPC mortar made of crushed river gravel, which also irreversibly adsorbs Cs^+ , immersed in a 3.5 μM CsCl solution. Assuming the Cs^+ penetration is governed by the simple diffusion law, Cs^+ concentration profile is estimated from the measured one at 435 days and plotted in the same figure. Compared to the penetration depth of 12 mm in Figs. 3 and 4, that is decreased to 3 mm, confirming that Cs^+ adsorption by the aggregate suppressed Cs^+ penetration.

Fig. 5 shows the penetration profiles of Cs^+ and Cl^- when OPC mortar made of limestone with low Cs adsorption capacity was immersed in 3 mM CsCl solution. Similar to the results shown in

Fig. 2 with 0.5 M of CsCl concentration, also in Fig. 4 with that of 3 mM, the penetration depths of Cs^+ and Cl^- comparable. As Cs^+ does not interact with OPC paste, the apparent diffusion coefficient is constant over a wide concentration range (Yamada et al 2021), but Cl^- bound to AFm has a similar penetration depth as Cs^+ , indicating that binding does not affect penetration for Cl^- .

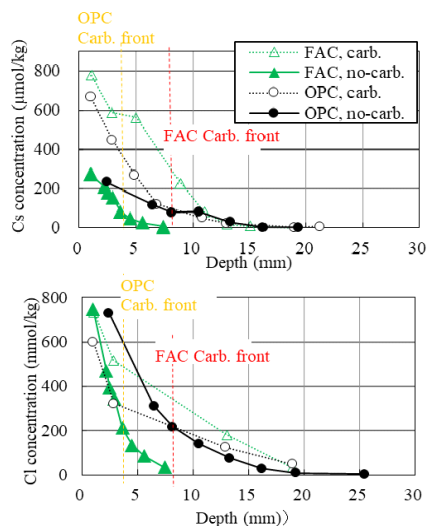


Fig. 7 Effects of carbonation on Cs (upper) and Cl (lower) penetrations in limestone OPC/FAC mortar (0.1 M CsCl, 56 days)

permeation. In other words, Cl^- "binding" by AFm does not affect Cl^- diffusion. Based on this understanding, the interaction between Cs^+ and carbonate cement paste is also presumed to be a reversible ion exchange by the 4-coordinated alumina that replaced silica in the aluminosilicate hydrates.

Figure 7 shows the effect of carbonation on the penetration of Cs^+ and Cl^- into the limestone mortar of OPC and FAC. Under non-carbonation conditions, both ions penetrate about 17 mm in OPC and 8 mm in FAC, and although FA addition suppresses the penetration of both ions, the penetration depth is similar to that of Cl^- even though the Cs^+ adsorption capacity is increased by FA addition, indicating that alkali metal adsorption on C-A-S-H with low $\text{Ca}/(\text{Al}+\text{Si})$ is also considered to be a reversible ion exchange. Carbonation reduced the pore volume of the OPC and FAC mortars, but did not affect the penetration depth of Cs^+ and Cl^- in the case of OPC, and increased the penetration depth of both ions in the case of FAC to the same extent as OPC. Pore connectivity, rather than pore volume, is the dominant factor in ion penetration, and carbonation is expected to cause FAC to lose its low pore connectivity and increase it to the same level as OPC.

5. Conclusions

The effects of adsorption and pore structure on ion penetration were experimentally verified by immersing cementitious materials in various concentrations of CsCl solution. The results showed that ion binding/adsorption by ion exchange does not affect ion penetration, but irreversible adsorption suppresses ion penetration. It was also shown that the effect of FA addition on the increase in the tortuosity or the decrease in the connectivity of C-A-S-H with low $\text{Ca}/(\text{Al}+\text{Si})$ disappears upon carbonation.

Acknowledgements

This research was supported by the JAEA Nuclear Energy S&T and Human Resource Development Project through Concentrating Wisdom Grant Number JPJA20P20333545.

References

- Ichikawa, T. (2022) "Theory of Ionic Diffusion in Water-saturated Porous Solid with Surface Charge", *J. Adv. Concr. Tech.*, 20: 430-443
- Haga, K., Watanabe, S., Yamada, K. (2019) "Quantification of interaction between alkali metal ions and C-(A-)S-H/cement paste for a wide range of ion concentrations", 15th Int. Cong. on the Chemistry of Cement, Prague, 339
- Ngala, V.T. and Page, C.L (1997) "Effects of carbonation on pore structure and diffusional properties of hydrated cement pastes", *Cement and Concrete Research*, 27: 995-1007

- Yamada, K., et al. (2021) “Experimental study investigating the effects of concrete conditions on the penetration behaviors of Cs and Sr at low concentration ranges”, *J. Adv. Concr. Tech.*, 19: 756-770
- Yamada, K., Himori K., Tomita, S., Ichikawa, T. (2023) “Relationship between ion absorption on concrete constituents and ion penetration”, *Proc. of JCI* (in print, in Japanese)
- Yuan, Q., Shi, C., Schutter, G. De, Audenaert, K. and Deng, D. (2009) “Chloride binding of cement-based materials subjected to external chloride environment – A review“, *Const. and Building Mat.*, 23: 1-13

Durability of slag cement and sulfoaluminate cement exposed to acetic acid, ammonium nitrate and magnesium chloride

M. Giroudon^{1*}, A. Duchemin¹, C. Ferry¹, X. Hardy¹, C. Llobet¹, A. Lopez¹, M. Mille¹, E. Ourliac¹, L. Pages¹, M. Poey¹, E. Taillade¹, F. Tressières¹, E. Tucoulet¹, V. Sonois¹, C. Roosz¹, A. Bertron¹

¹ LMDC, Université de Toulouse, UPS, INSA Toulouse, France
marie.giroudon@insa-toulouse.fr

ABSTRACT

In order to ensure the durability and the sustainability of concrete structures in chemically aggressive environments, this study intends to provide some insights in the alteration mechanisms of low-carbon cements in different aggressive solutions. Reference ordinary Portland cement pastes and low-carbon cement pastes (slag cement and sulfoaluminate cement) were immersed in synthetic solutions made of acetic acid, ammonium nitrate and magnesium chloride for 12 weeks. Rates of alteration were assessed by measuring mass changes and thickness of degraded layers throughout the experiment. Deterioration mechanisms were evaluated by mineralogical, chemical, and microstructural analyses by X-Ray diffraction, scanning electron microscopy and energy dispersive X-ray spectroscopy. The performances and alteration mechanisms of the three binders were assessed in these media and the low-carbon cements show interesting behaviour in the less aggressive solutions (ammonium nitrate and magnesium chloride).

KEYWORDS: *Low-CO₂ cement, sulfoaluminate cement, acid, ammonium nitrate, magnesium attack*

1. Introduction

Concrete is the most widely used construction material throughout the world, and is therefore subject to a wide variety of chemically aggressive liquid environments. However, the use of Portland cement-based concrete is known to be responsible for large greenhouse gas emissions. In this context, the latest IPCC report recommends the use of low-emission construction materials as well as the optimization of the use of buildings (IPCC, 2022). Thus, there is a need to assess the durability properties of more energy-efficient binders under chemically aggressive conditions. For this purpose, three materials were immersed in different aggressive solutions: an ordinary Portland cement (CEM I) as a reference, a blast-furnace slag cement (CEM III) as a low-carbon cement (Juenger et al., 2019) showing increased durability to acid attack compared with CEM I (Bertron et al., 2005a; Gruyaert et al., 2012; Oueslati and Duchesne, 2012) and a sulfoaluminate cement (CSA) due to its significative low CO₂ emission compared to that of OPC (Sherman et al., 1995), associated with interesting durability properties in certain situations (sulphate attack, chloride penetration, e.g.) (Afroughsabet et al., 2021; Quillin, 2001). They were immersed in three aggressive solutions made of: (i) acetic acid to represent an attack by organic acids encountered in many natural environments, including agricultural ones, (ii) ammonium nitrate since ammonium is found in many biological environments (sewage treatment plants, anaerobic digestion, agricultural buildings, etc.), and is used in laboratory tests to simulate concrete leaching by pure water and (iii) magnesium chloride to represent the magnesium attack occurring during the exposure of concrete to soft water, groundwater and seawater, e.g. (Bertron et al., 2005b, 2005a; Dauzères et al., 2016; Dewitte et al., 2022; Giroudon et al., 2021a; Jakobsen et al., 2016; Rosenqvist et al., 2017).

2. Materials and methods

Cement pastes were manufactured from CEM I 52,5 N SR3 (CEM I), CEM III/B 42.5 LH/SR PM (CEM III) and CSA with a water/binder ratio of 0.35. They were mixed according to a protocol adapted from of the French standard NF EN 196-1 (AFNOR, 2016) and cast in 4*4*16 cm³ molds. After a 28-day

endothermic cure, the 4*16 cm² sides of the prismatic samples were coated with epoxy resin (RESOLTECH 3030 with hardener 3034). After hardening of the resin 1*4*4 cm³ slices were sawn from the samples. They were then immersed in three different aggressive solutions: a 300 mmol.L⁻¹ acetic acid solution (pH = 2.6) (glacial acetic acid 99.8–100.5%, AnalaR® NORMAPUR – VWR); a 444 mmol.L⁻¹ NH₄NO₃ solution (industrial ammonium nitrates, 99.0% minimum of NH₄NO₃, Orange Label Ammonium Nitrate, MAXAM Tan) and a 5 mmol.L⁻¹ MgCl₂ solution (magnesium chloride, anhydrous, 99%, Crystalline, Alfa Aesar). For each type of solution, 3 samples (1*4*4 cm³) of each cement paste type were added in 2 L of solution in closed plastic boxes, i.e. an exposed surface/volume of solution ratio of 48 cm².L⁻¹. The exposure lasted 12 weeks (84 days), the aggressive solutions being renewed every two weeks. Regularly throughout the experiment, the solutions' pH was measured, and mass changes were assessed. Degraded depths were measured according to the protocol of Giroudon et al. (2023) (phenolphthalein spray). After 3 weeks (for acetic acid and ammonium nitrate solutions) and 7 weeks (magnesium chloride solution), one sample per solution type and per cement paste type was cut with a diamond saw. One of the resulting pieces was used to conduct X-ray diffraction analyses (XRD) (Bruker D8 Advance, Cu AntiCathode, 40 kV, 40 mA) from the outer degraded surface to the inner core of the sample. To do so, the sample surfaces were successively analysed, gently abraded and then submitted to the further analysis. Another piece was embedded in epoxy resin (Mecaprex Ma2+, Presi) and polished using silicon carbide polishing disks (Presi). The flat polished section was then coated with carbon and analysed with scanning electronic microscopy (SEM) (JEOL JSM6380LV, 15 kV) in back scattered electrons (BSE) mode combined with energy dispersive X-ray spectroscopy (EDS) (Bruker XFlash 6/30 SD).

3. Results

3.1 pH variations

In the presence of cementitious materials, due to the release of hydronium ions, the pH of the solutions increased over time. Between each renewal, the pH of the acetic acid solution varied from its initial value of 2.6 to about 4.0; the pH of the ammonium nitrate solution varied between 5.75 and about 9.0; and the pH of the magnesium chloride solution varied between 7.6 and about 10. For a given period of time, the pH of the solutions varied little with respect to the nature of the cementitious binder they contained.

3.2 Mass changes

Figure 1 shows the mass variations ($\Delta m = m_{\text{initial}} - m_t$) of the different cement pastes in the three aggressive solutions according to the time as well as their degraded depths after 7 weeks of immersion.

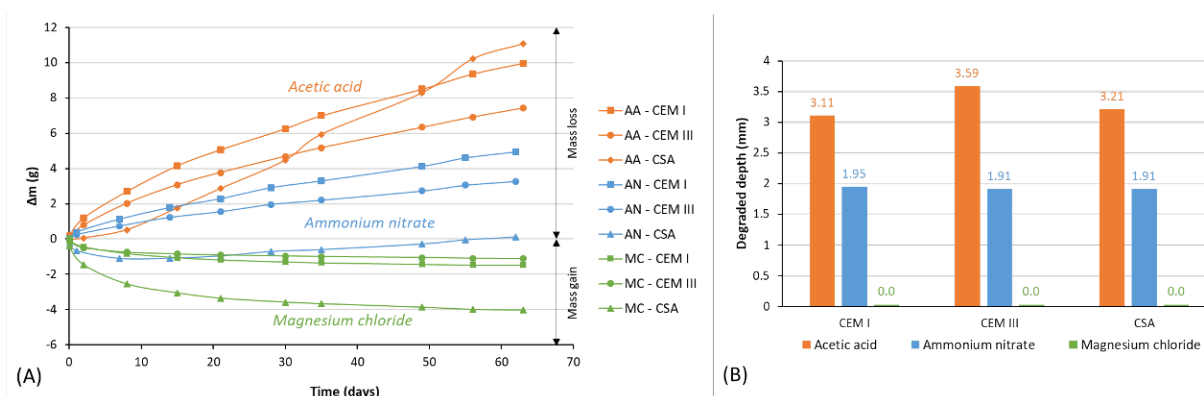


Figure 1. (A) Mass losses of the cement pastes according to the time of immersion in the aggressive solutions (AA: acetic acid, AN: ammonium nitrate, MC: magnesium chloride) and (B) degraded depths of the paste after 7 weeks in the aggressive solutions

After 63 days, the cement pastes immersed in the acetic acid solution have undergone the highest mass losses, followed by the samples immersed in ammonium nitrate. Mass gains were observed for the cement pastes immersed in the magnesium chloride solution. In the two most aggressive solutions, mass changes

of CEM I and CEM III pastes followed the same trend, i.e. a progressive decrease of the mass, the CEM I having higher mass losses than CEM III pastes. In these two solutions, the mass monitoring of the CSA pastes shows a singular behaviour since they started to gain in mass during the first days. Subsequently, the CSA paste immersed in acetic acid showed a much faster mass loss than the other two samples, while the CSA paste immersed in ammonium nitrate followed the same trend as CEM III. In the magnesium chloride solution, all three pastes gained mass continuously throughout the experiment. The CEM I and CEM III pastes showed similar behaviours while the CSA paste gained much more mass than the other two. The results of the degraded depths were different from what the mass losses suggested, in particular for CSA paste which showed degraded depths close to those of the other two binders for a significantly lower mass loss. Thus, mass losses alone should not be relied upon to assess the durability of a binder, as these depend in particular on the calcium content, which leaves the matrix massively in the case of leaching, whereas the initial calcium contents vary according to the type of binder.

3.3 Deterioration mechanisms

In the acetic acid solution, the three samples showed clear zonation visible to the naked eye. SEM/EDS analyses showed that the degradation was characterised by the sharp decrease of the calcium content of the paste between the sound core and the degraded layer, associated with a decreased density (darker zone on the SEM-BSE image), the dissolution of the initial phases and an amorphous outer degraded area (XRD). The boundary between the sound core and the degraded external layer was found to be at about 2250 μm depth for the CEM I cement paste, 2900 μm for the CEM III paste and 2000 μm for the CSA cement paste. As an example, CEM I paste analyses are shown on Figure 2.

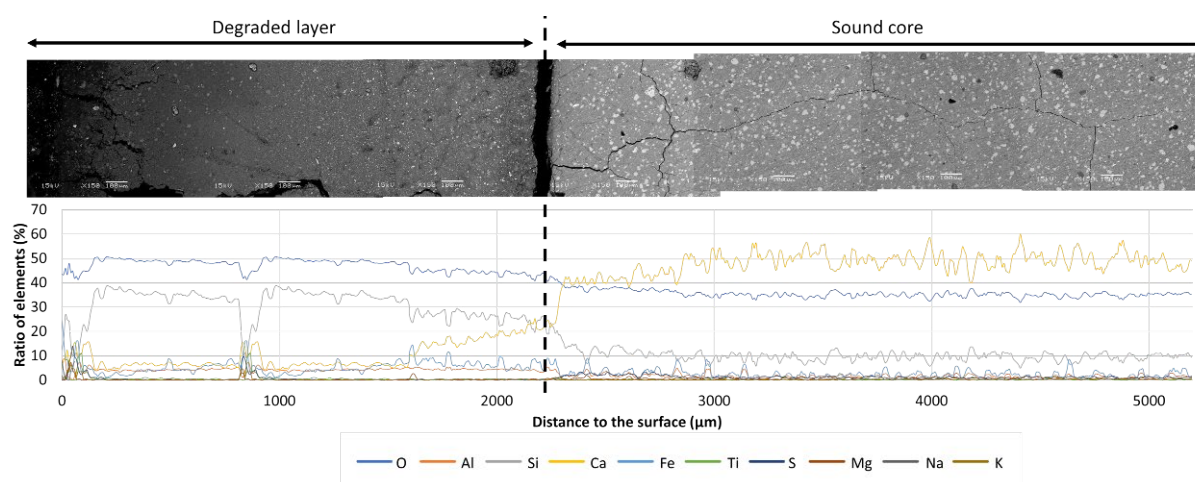


Figure 2. SEM observations in BSE mode and EDS analyses of the CEM I paste after being immersed in the acetic acid solution

In the ammonium nitrate solution, in contrast with the acetic acid attack, the cement pastes showed a progressive partial decalcification with a calcium content comprised between about 20 and 50% in the degraded layer, with the dissolution of the initial phases (XRD) and a decrease in density although much less marked than for the acetic acid attack, as shown in Figure 3. The sound core was found at about 3400 μm deep for CEM I and 3000 μm for the CEM III and CSA pastes. A calcium-rich precipitate was observed on the CSA paste surface (SEM-EDS).

The cement pastes immersed in the magnesium chloride solution did not show significant structural and chemical variations along the cross section. However, the SEM observations on the CEM I and CSA pastes showed an external magnesium-rich precipitate, covering the surface of the samples (Figure 4). It is likely that the same type of precipitate covered the CEM III paste and came off during the preparation of the samples. This precipitate was identified as brucite with XRD analyses.

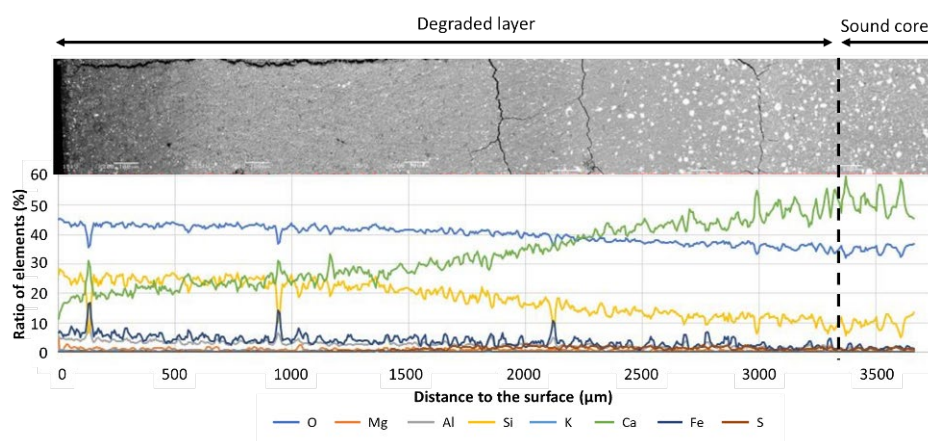


Figure 3. SEM observations in BSE mode and EDS analyses of the CEM I paste after being immersed in the ammonium nitrate solution

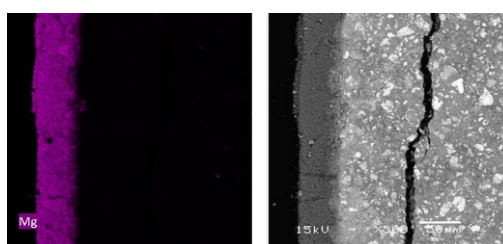


Figure 4. SEM observations in BSE mode and EDS mapping of the CSA paste after being immersed in the magnesium chloride solution

4. Discussion

The results highlight a particular behaviour of CSA since it is the only material to systematically gain mass in the aggressive solutions. Since this does not correspond to the precipitation of secondary phases on the surface (except in the case of MgCl_2), it could be due to a large open porosity allowing the sample to soak up the solution once immersed or to the continuity of its hydration. The penetration of the aggressive solution into the core of the material does not seem to have had a negative effect on its durability as CSA shows similar degraded depths to the other two materials. However, the evolution of its mass loss in the acetic acid solution is very rapid and this could suggest that CSA would have a less favourable long-term behaviour. CEM I and CEM III pastes showed similar behaviours during the experiment, with slightly lower mass losses of the CEM III likely due to lower Ca content of the binder. Attacks by acetic acid, ammonium nitrate and magnesium chloride induced very different degradation phenomena. On the one hand, the acetic acid and ammonium nitrate solutions caused significant mass losses, associated with a decalcification of the materials with dissolution of the phases initially present. Two behaviours can be distinguished (Giroudon et al., 2021b): the attack by acetic acid led to intense degradation reflected by the presence of alteration fronts and a sharp decalcification at depth, revealing an amorphous outer zone; the attack by ammonium nitrate led to the progressive and partial decalcification of the materials along the depth. On the other hand, the immersion in the low concentrated MgCl_2 solution led to the precipitation of brucite on the surface of the material, which seemed to protect the matrix from further penetration of aggressive species.

5. Conclusion

In this innovative study, the still poorly known magnesian attack and the durability of CSA in aggressive chemical environments were assessed through the immersion of CEM I, CEM III and CSA pastes in acetic acid, ammonium nitrate and magnesium chloride aggressive solutions. In the studied experimental

conditions, the magnesian attack resulted in the precipitation of a protective brucite layer in surface for all three pastes. CSA pastes showed interesting performances in ammonium nitrate and magnesium chloride solutions but a very rapid evolution of its mass loss in the acetic acid solution suggests a poor long-terms behaviour in acidic environments.

References

- AFNOR, 2016. NF EN 196-1. Methods of testing cement - Part 1: Determination of strength. Paris, France.
- Afroughsabet, V., Biolzi, L., Monteiro, P.J.M., Gastaldi, M.M., 2021. Investigation of the mechanical and durability properties of sustainable high performance concrete based on calcium sulfoaluminate cement. *Journal of Building Engineering* 43, 102656. <https://doi.org/10.1016/j.jobbe.2021.102656>
- Berthomier, M., 2019. Etude de la lixiviation de l'aluminium de matériaux cimentaires à base de CEM III utilisés dans les canalisations d'eau potable : approche expérimentale et numérique (Thèse). INSA Toulouse.
- Bertron, A., Duchesne, J., Escadeillas, G., 2005a. Accelerated tests of hardened cement pastes alteration by organic acids: analysis of the pH effect. *Cement and Concrete Research* 35, 155–166. <https://doi.org/10.1016/j.cemconres.2004.09.009>
- Bertron, A., Duchesne, J., Escadeillas, G., 2005b. Attack of cement pastes exposed to organic acids in manure. *Cement and Concrete Composites* 27, 898–909. <https://doi.org/10.1016/j.cemconcomp.2005.06.003>
- Dauzères, A., Achiedo, G., Nied, D., Bernard, E., Alahrache, S., Lothenbach, B., 2016. Magnesium perturbation in low-pH concretes placed in clayey environment—solid characterizations and modeling. *Cement and Concrete Research* 79, 137–150. <https://doi.org/10.1016/j.cemconres.2015.09.002>
- Dewitte, C., Bertron, A., Neji, M., Lacarrière, L., Dauzères, A., 2022. Chemical and Microstructural Properties of Designed Cohesive M-S-H Pastes. *Materials* 15, 547. <https://doi.org/10.3390/ma15020547>
- Giroudon, M., Patapy, C., Peyre Lavigne, M., Andriamiandroso, M., Cartier, R., Dubos, S., Bacquié, C., André, L., Pommier, S., Lefevbre, X., Cyr, M., Bertron, A., 2023. Potential of low carbon materials facing biodeterioration in concrete biogas structures. *Mater Struct* 56, 80. <https://doi.org/10.1617/s11527-023-02174-0>
- Giroudon, M., Peyre Lavigne, M., Patapy, C., Bertron, A., 2021a. Blast-furnace slag cement and metakaolin based geopolymer as construction materials for liquid anaerobic digestion structures: Interactions and biodeterioration mechanisms. *Science of The Total Environment* 750, 141518. <https://doi.org/10.1016/j.scitotenv.2020.141518>
- Giroudon, M., Peyre Lavigne, M., Patapy, C., Bertron, A., 2021b. Laboratory assessment of the contribution of aggressive to concrete chemical compounds to the degradation of Portland cement-based materials during anaerobic digestion. *Mater Struct* 54, 218. <https://doi.org/10.1617/s11527-021-01810-x>
- Gruyaert, E., Van den Heede, P., Maes, M., De Belie, N., 2012. Investigation of the influence of blast-furnace slag on the resistance of concrete against organic acid or sulphate attack by means of accelerated degradation tests. *Cement and Concrete Research* 42, 173–185. <https://doi.org/10.1016/j.cemconres.2011.09.009>
- IPCC, 2022. Summary for Policymakers, in: Shukla, P.R., Skea, J., Slade, R., Al Kouradje, A., van Diemen, R., McCollum, D., Pathac, M., Some, S., Vyas, P., Fradera, R., Belkacemi, M., Hasija, A., Lisboa, G., Luz, S., Malley, J. (Eds.), *Climate Change 2022: Mitigation of Climate Change. Contribution of Working Group III to the Sixth Assessment Report of the Intergovernmental Panel on Climate Change*. Cambridge, UK and New York, NY, USA. <https://doi.org/10.1017/9781009157926.001>
- Jakobsen, U.H., De Weerd, K., Geiker, M.R., 2016. Elemental zonation in marine concrete. *Cement and Concrete Research* 85, 12–27. <https://doi.org/10.1016/j.cemconres.2016.02.006>
- Juenger, M.C.G., Snellings, R., Bernal, S.A., 2019. Supplementary cementitious materials: New sources, characterization, and performance insights. *Cement and Concrete Research* 122, 257–273. <https://doi.org/10.1016/j.cemconres.2019.05.008>
- Oueslati, O., Duchesne, J., 2012. The effect of SCMs and curing time on resistance of mortars subjected to organic acids. *Cement and Concrete Research* 42, 205–214. <https://doi.org/10.1016/j.cemconres.2011.09.017>
- Quillin, K., 2001. Performance of belite–sulfoaluminate cements. *Cement and Concrete Research* 31, 1341–1349. [https://doi.org/10.1016/S0008-8846\(01\)00543-9](https://doi.org/10.1016/S0008-8846(01)00543-9)
- Rosenqvist, M., Bertron, A., Fridh, K., Hassanzadeh, M., 2017. Concrete alteration due to 55years of exposure to river water: Chemical and mineralogical characterisation. *Cement and Concrete Research* 92, 110–120. <https://doi.org/10.1016/j.cemconres.2016.11.012>
- Sherman, N., Beretka, J., Santoro, L., Valenti, G.L., 1995. Long-term behaviour of hydraulic binders based on calcium sulfoaluminate and calcium sulfosilicate. *Cement and Concrete Research* 25, 113–126. [https://doi.org/10.1016/0008-8846\(94\)00119-J](https://doi.org/10.1016/0008-8846(94)00119-J)

Anti-corrosion mechanism of LDHs-VB3⁻ for rebar: insights from experiments and DFT simulations

Ende Zhuang¹, Yumei Nong¹, Mosong Luo¹, Zheng Chen¹, Bo Yu¹, and Jing Li^{1*}

¹ Key Laboratory of Disaster Prevention and Structural Safety of China Ministry of Education, School of Civil Engineering and Architecture, Guangxi University, Nanning, 530004, China
Email: jingli@gxu.edu.cn

ABSTRACT

The anti-corrosion mechanism of LDHs-VB3⁻ inhibitor for rebar was studied by experiments and density functional theory (DFT) simulations. Chloride ion adsorption test shows that 60 mg/g chloride could be adsorbed by LDHs-VB3⁻ in 0.14 M NaCl solution, indicating that the LDHs-VB3⁻ inhibitor could capture the environmental chloride ion. The critical chloride concentration of rebar in simulated concrete solution containing LDHs-VB3⁻ was 0.26 M, which was much higher than that in the solution without LDHs-VB3⁻ (0.14 M) according to the electrochemical tests. The DFT simulations suggest that VB3⁻ could be replaced by Cl⁻ and released to environment easily, since LDHs-VB3⁻ has a more positive binding energy and uneven binding forces than LDHs-Cl⁻. Moreover, the released VB3⁻ could adsorb on Fe (100) surface via the interaction of surface Fe atoms with C, N, and O atoms of VB3⁻. The preadsorbed VB3⁻ could weaken the interaction of Cl⁻ with Fe (100) surface by reducing the bonding between Fe and Cl atoms.

KEYWORDS: LDHs, Anti-corrosion, DFT; Ion exchange, Chloride ion

1. Introduction

In the marine environment, chloride can accelerate the corrosion of steel, which shorten the service life of coastal concrete structures and bring a great economic loss (Cao et al (2019)). Hence, it is of significant importance to seek effective ways to protect steel from corrosion induced by chloride. Recently, researchers have focused on the LDHs (layered double hydroxides) inhibitors (Xu et al (2018)), which can adsorb the chloride ions and release the interlayer anions with inhibition effect to steel bars.

Liu et al. (2018) reported that the inhibition efficiency of LDHs-MTT⁻ (94.7%) was much higher than that of LDHs-NO₃⁻ (52.8%), since the coordination bonds could be formed between the 5-Methyl-1,3,4-thiadiazole-2-thiol (MTT) and the surface of steel bar, which isolated the aggressive Cl⁻, O₂ etc. Kanojia et al. (2013) found that nicotinic acid (VB3) had a good anti-corrosion effect on steel in 0.5 M H₂SO₄ solution. Moreover, VB3⁻ also presented violent chemisorption on the γ -FeOOH surface (Zhang et al (2021)), suggesting that VB3⁻ has potential protection to steel bars in concrete. Therefore, it is inferred that LDHs intercalated with VB3⁻ (LDHs-VB3⁻) may have the dual anti-corrosion effects, which could release the VB3⁻ to protect the steel from corrosion and capture Cl⁻ to prevent steel from chloride attacking.

In this study, the chloride adsorption capacity of LDHs-VB3⁻ inhibitor was evaluated by means of chloride adsorption test. Electrochemical impedance spectroscopy (EIS) was conducted to study the electrochemical behavior of rebar in the simulated concrete solution with/without LDHs inhibitor. The configurations of LDHs loaded with Cl⁻ and VB3⁻ were built by DFT method to analyze the mechanism of capturing chloride. Moreover, the interactions between Cl⁻ and Fe (100) surface with/without VB3⁻ were simulated to explore the mechanism of VB3⁻ retarding the chloride attack to the iron surface.

2. Experimental and computational methods

2.1 Chloride ion adsorption test

0.5 g LDHs-VB3⁻ was dispersed in the 50 mL 0.14 M NaCl solution for 48 hours to assess the adsorption ability of LDHs-VB3⁻ to chloride. The chloride adsorption capacity (q_e) of LDHs-VB3⁻ could be calculated according to the following equation (1):

$$q_e = (C_0 - C_e)V/m \quad (1)$$

where, q_e is the chloride adsorption capacity of MgAl-LDHs (mg/g); C_0 and C_e are the initial and equilibrium chloride concentration (mg/L); V and m are the volume of solution and mass of LDHs-VB3⁻.

2.2 Electrochemical measurements

The size of steel specimens were $\Phi 10 \text{ mm} \times 10 \text{ mm}$, and the test surfaces of steels were polished with sandpaper of 240#~1500# grade. Two types of simulated concrete pore solutions with a fixed volume of 150ml were prepared, which were saturated calcium hydroxide solutions with and without 0.75g LDHs-VB3⁻. The steel electrodes were immersed in two simulated concrete pore solutions for 7 days, then adding sodium chloride into the two simulated concrete pore solutions to increase the chloride concentration by 0.02 M per day. The saturated calomel electrode (SCE), platinum electrode (PE), and steel were each applied as the reference electrode, counter electrode, and working electrode. Electrochemical impedance spectroscopy (EIS) was carried out on a CS3004 electrochemical workstation.

2.3. DFT simulation details

The density functional theory (DFT) calculations in this paper were performed based on the CASTEP code in the Materials Studio. For the calculations of MgAl-LDHs, the GGA-PBE functional with plane-wave basis set was adopted. The ultrasoft pseudopotentials were used to describe the ionic cores. Moreover, Monkhorst-Pack meshes of $3 \times 3 \times 1$ k-point sampling in the Brillouin zone were applied for LDHs, and the cut-off energy was set to 340 eV. The energy and the SCF tolerances were set to be 2×10^{-5} eV/atom and 2×10^{-6} eV/atom, respectively. In addition, the maximum force and displacement tolerance converged to 0.03 eV/Å and 0.001 Å, respectively. For the electron calculations of the iron surface and released VB3⁻, the GGA-PW91 was chosen as exchange-correlation functional. The $4 \times 4 \times 1$ Monkhorst and Pack k-points were used in the Brillouin zone, and the cut off energy was set to 340 eV. The energy and SCF tolerances converged to 2×10^{-5} eV/atom and 2×10^{-6} eV/atom, respectively. The maximum force and displacement converged separately to 0.03 eV/Å and 0.001 Å.

3. Results and discussion

3.1. Chloride adsorption capacity of LDHs-VB3⁻

The chloride ions adsorption capacity (q_e) of LDHs-VB3⁻ was 60.7 mg/g, indicating that LDHs-VB3⁻ can capture chloride ions and decrease the chloride concentration of the environment, thereby declining the corrosion risk of steel bars.

3.2. Electrochemical impedance spectroscopy (EIS)

Fig. 1 illustrates the OCP curves of steel electrodes in the simulated concrete pore solutions with and without LDHs-VB3⁻ as a function of chloride concentration. The OCP values of Blank and E-B dropped below -250 mV sharply at chloride concentrations of 0.14 M and 0.26 M, respectively. The higher critical chloride concentrations of the steels in E-B group implies that the synthetic LDHs-VB3⁻ had a fine corrosion inhibition effect on the steel bars. Through calculation, the maximum chloride adsorption capacity of 0.75 g LDHs-VB3⁻ is 45.5 mg, and the reduction of chloride concentration derived from the adsorption of LDHs in 150 ml simulated concrete pore solution will be no more than 0.013 M, which is much less than the difference value of critical chloride concentration between E-B and blank groups (0.12 M). Thus, the reduction of chloride concentration induced by LDHs adsorption is difficult to raise the

critical chloride concentration of steels in E-B group to 0.26 M, suggesting that the VB_3^- was indeed released from LDHs and played a crucial role in protecting the steel bars from corrosion.

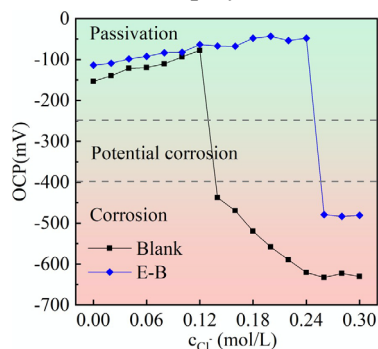


Fig. 1. Open circuit potential plots of steels in simulated concrete pore solutions with/without LDHs- VB_3^- .

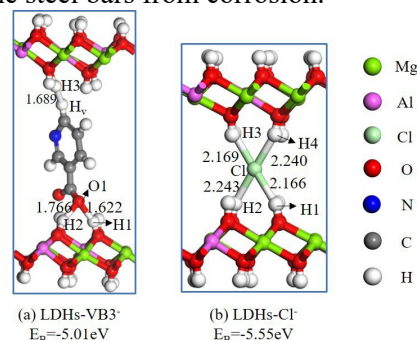


Fig. 2. The optimized configuration of LDHs- VB_3^- and LDHs- Cl^- .

3.3. Anti-corrosion mechanisms of LDHs inhibitors

The optimized configurations of LDHs and the corresponding binding energies (E_B) between anions and laminates of LDHs are shown in Fig. 2. The E_B values of LDHs laminates with VB_3^- is -5.012 eV, which is more positive than that with Cl^- (-5.552 eV), implying that LDHs- Cl^- was more stable than LDHs- VB_3^- . In Fig. 9 (a), O1 atom of the carboxyl group and H_v atom of the pyridine ring in VB_3^- only connect with H atoms in the laminate. In Fig. 9 (b), the Cl atom also connects with H atoms in the laminate. Fig. 3 shows the partial density of states (PDOS) of H1-O1, H2-O1, and H3- H_v bonds of LDHs- VB_3^- . The overlaps of H 1s and O 2p orbitals in H1-O1 and H2-O1 bonds were similar, which is much more than that of H 1s and H_v orbitals in H3- H_v bond, indicating that the bonding of H1-O1 and H2-O1 are stronger than that of H3- H_v , suggesting that there exists a difference in the bonding force of VB_3^- with the upper and lower LDHs laminates. The PDOS results of H1-Cl, H2-Cl, H3-Cl, and H4-Cl bonds of LDHs- Cl^- are plotted in Fig. 4. The overlaps of Cl 3p and H 1s orbitals indicate that H-Cl bonds are composed of Cl 3p and H 2p orbitals. The bonding and the anti-bonding states of H1-Cl ~ H4-Cl bonds are similar, illustrating that the bonding force of Cl with the upper and lower LDHs laminates are uniform. This may be why the bonding of LDHs laminate with Cl is more stable than that with VB_3^- .

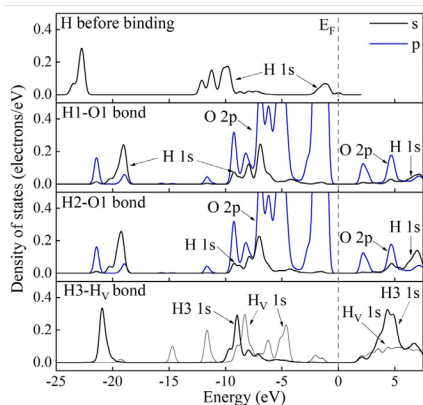


Fig. 3. PDOS of H1-O1, H2-O1 and H3- H_v bonds of LDHs- VB_3^- .

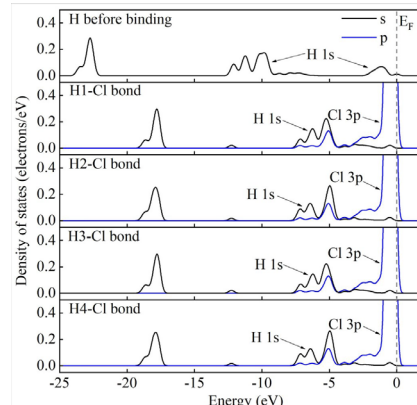


Fig. 4. PDOS of Cl-H1, Cl-H2, Cl-H3 and Cl-H4 bonds of LDHs- Cl^- .

Fig. 5 shows the optimized configurations of (a) chloride ions adsorbed on the clean Fe (100) surface and (b) VB_3^- -preadsorbed Fe (100) surface, with adsorption energies of -4.624 eV and -4.457 eV, respectively. The more positive adsorption energy of Cl on the VB_3^- -preadsorbed Fe (100) surface indicates that the pre-adsorption of VB_3^- weakens the adsorption of chloride on the iron surface. The length of Fe1-Cl and Fe2-Cl bonds in Fig. 5 (a) are much shorter than that of in Fig. 5 (b), implying that the presence of VB_3^- could elongate the bond length of Fe-Cl bonds. Fig. 6 shows the PDOS of Fe1-Cl and Fe2-Cl bonds on the clean Fe (100) surface and VB_3^- -preadsorbed Fe (100) surface. The states of Cl 3p and Fe 3d orbitals on VB_3^- -preadsorbed Fe (100) surface are more localized than that on the clean Fe (100) surface, implying that the interaction between Cl^- and VB_3^- -preadsorbed Fe (100) surface is weaker than that

between Cl^- and clean Fe (100) surface, and the pre-adsorption of VB_3^- could inhibit the adsorption of chloride on the iron surface.

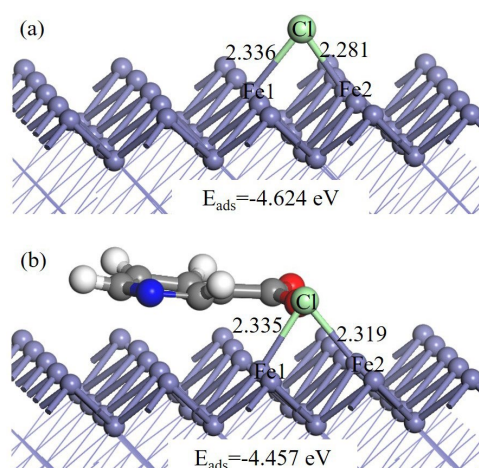


Fig. 5. The configurations of Cl^- adsorbed on (a) clean and (b) VB_3^- -preadsorbed Fe (100) surface.

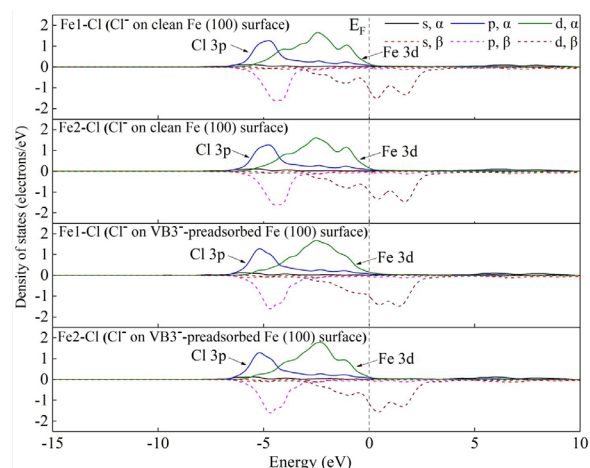


Fig. 6. PDOS of Fe1-Cl and Fe2-Cl bonds on clean Fe (100) surface and VB_3^- -preadsorbed Fe (100) surface.

4. Conclusions

The anti-corrosion mechanism of LDHs- VB_3^- for steel bars was analyzed via the chloride ion adsorption test, electrochemical experiments and DFT method. The Cl^- adsorption capacity of LDHs- VB_3^- is 60.7 mg/g, suggesting that the LDHs- VB_3^- has the ability to capture the environmental Cl^- . Moreover, OCP result indicates that the critical chloride concentration of rebar is 0.26 M and 0.14 M in concrete pore solution contained with/without LDHs- VB_3^- , indicating that LDHs- VB_3^- has a superior inhibition for rebar in the concrete subjected to the chloride attack. The binding energy of LDHs laminates with VB_3^- is -5.012 eV, which is more positive than that with Cl^- (-5.552 eV), suggesting that the bonding of LDHs- Cl^- is more stable than that of LDHs- VB_3^- . Moreover, the Cl^- and VB_3^- both mainly interact with the H atoms of LDHs laminate, while there exists a difference in the bonding force of VB_3^- with the upper and lower layer of LDHs laminates. The more positive binding energy and uneven binding force between VB_3^- and LDHs laminates would result in that the VB_3^- is easily replaced by Cl^- in LDHs laminate. In addition the adsorption of Cl^- on VB_3^- -preadsorbed Fe (100) surface shows that the preadsorbed VB_3^- weakens the interaction of Cl^- with the Fe (100) surface, thereby retarding the chloride-induced rebar corrosion.

Acknowledgements

This Work Supported by the Interdisciplinary Scientific Research Foundation of GuangXi University (Grant No. 2022JCC016), and the National Key Research and Development Program of China (Grant No. 2021YFB2600903).

Reference

- Cao, Gehlen, Angst, Wang, Wang and Yao. (2019) "Critical chloride content in reinforced concrete — An updated review considering Chinese experience", *Cement and Concrete Research*, 117: 58-68.
- Xu, Song, Zhao, Jiang, Mei and Chen. (2018) "Chloride removal and corrosion inhibitions of nitrate, nitrite-intercalated MgAl layered double hydroxides on steel in saturated calcium hydroxide solution", *Applied Clay Science*, 163:129-136.
- Liu, Tian, Li, Wang, Gao, Han and Ding. (2018) "Delamination and self-assembly of layered double hydroxides for enhanced loading capacity and corrosion protection performance", *Applied Surface Science*, 462:175-186.
- Kanojia and Singh. (2013) "An interesting and efficient organic corrosion inhibitor for mild steel in acidic medium", *Surface Engineering*, 21(3): 180-186.
- Zhang, Xu, Sun, Xiong, Wang, Chen, Sun, Guan, Ding, Li and Hou. (2021). "Insights into vitamin B3, B6 and C as inhibitor of steel reinforcement: A DFT + U study", *Construction and Building Materials*, 294.

Cement use under extreme marine environment—deep sea

K. Takahashi^{1*}, Y. Kawabata², M. Iwanami³, and M. Kobayashi⁴

¹ Mitsubishi UBE Cement Corporation, Ube, Japan / Kagawa University, Takamatsu, Japan
Email: keisuke.takahashi@mu-cc.com / takahashi.keisuke@kagawa-u.ac.jp

² Port and Airport Research Institute, Yokosuka, Japan
Email: kawabata-y@p.mpat.go.jp

³ Tokyo Institute of Technology, Tokyo, Japan
Email: iwanami@cv.titech.ac.jp

⁴ Mitsubishi UBE Cement Corporation, Ube, Japan
Email: mari.kobayashi@mu-cc.com

ABSTRACT

Achieving breakthroughs in marine technologies requires the development of infrastructure in deep sea environments. Physicochemical impacts on a base construction material—cement considerably differ from those in shallow seas due to extreme low temperature and high hydraulic pressure in deep seas. However, very few studies focused on cement mortars and concretes subjected to deep sea conditions. We have launched a project targeted at creating a technology platform for the cement use at deep ocean bottom sites from the aspects of seawater attack, pressure impact observation, in situ monitoring of mechanical properties and construction methods. Our test results show that both high hydraulic pressure and extreme low temperature accelerated the disintegration of cement hydrates, which occurred owing to the interaction of microstructural damage, seawater penetration, ion ingress and the resultant reaction. This paper also shows the first ever in situ mortar connection on the deep seafloor using a specific mortar kit.

KEYWORDS: *Deep sea, Low temperature, High pressure, Seawater attack, In situ connection*

1. Introduction

Japan is surrounded by the ocean and the world's 6th largest maritime nation as its exclusive economic zone (EEZ) is about 12 times larger than land area. More than 95 % of the ocean is occupied by the deep sea, which is not well developed from a viewpoint of economics as well as an understanding of nature. Although the deep sea has attracted much attention within the fields of natural science and resource mining, achieving breakthroughs in marine technologies, such as offshore floating wind power, carbon capture and storage (CCS) and deep-sea cities, require the development of infrastructure in deep-sea environments. Cement-based materials can be an excellent choice as base materials because of their economic merits and design flexibility. However, very few studies focused on cement mortars and concretes subjected to deep-sea conditions. In this paper, recent studies, mainly reported by the authors, on the changes in physicochemical properties of cementitious materials in deep seas are summarized. This paper is the first to show the successful in situ connection using a specific mortar kit on deep seafloor.

2. Durability of cement-based materials in deep seas

In deep seas, physicochemical effects on cement mortars and concretes considerably differ from those in shallow seas owing to extreme low temperature and high hydraulic pressure. At the surface layer of the ocean, seawater temperature is maintained at ca. 15–25 °C near the most areas of Japanese archipelago. But the temperature at depths greater than 1,000 m rapidly drops to below 2–3 °C. Hydraulic pressure increases at a rate of 1 MPa with every 100 m of depth. The authors have investigated the durability of cement-based materials under such extreme conditions as follows.

2.1 Seawater attack

Many studies on the durability of cement-based materials in shallow seas have been conducted during the last 50 years in Refs. e.g., Gjorv (1971), De Weerd and Justnes (2015), and Jakobsen (2016). Chloride, sulfate, magnesium, and carbonate etc. ions derived from seawater penetrate hardened cement concretes and change phase assemblage such as the dissolution of portlandite, decalcification of calcium silicate hydrate (C-S-H), and precipitation of magnesium silicate hydrate (M-S-H), brucite, and thaumasite. Each ion strongly influences the ingress of other ions and their binding/incorporating capacities; thus, mineralogical zonation in the marine-exposed specimens can be observed from their surface to core. The deterioration of concrete specimens was detected after several and more than ten years in shallow seas.

The authors have investigated seawater attack on mortars with several types of binder under deep seas at depths of 1,680 m and 3,515 m and have reported that the degradation of the mortar is significantly accelerated in deep sea environments. With only approximately one year of exposure to the deep seas, Portland cement (PC) mortar specimens exhibited severe visible damages including softened mashy structures and significant dissolution/decalcification (Kobayashi et al. 2021), and calcium aluminate cement (CAC) based specimens showed large expansion (Kobayashi et al. 2022, Takahashi et al. under review). The impact of seawater on the PC hydrates was calculated with GEMS3 in Fig. 1. Temperature and pressure were set at 20 °C and 0.1 MPa, predicting the changes in shallow seas, and at 2 °C and 35 MPa, predicting the changes in deep seas. The seawater compositions of general shallow seas pre-installed in GEMS3 were used for modelling, as the compositions influencing seawater attack do not differ significantly between shallow and deep seas. The hydrated PC was computationally titrated with 0–30 kg of seawater per 100 g of PC to predict progressive phase assemblage variations provoked by the penetration of Cl and other ions in seawater. Figure 1 indicated that there was little change in phase assemblages for small amounts of seawater addition between shallow-sea and deep-sea conditions, but a difference appeared with more than 1 kg of seawater addition to 100 g of binder. Compared to shallow sea conditions, the dissolution of portlandite, decalcification of C-S-H and formation of M-S-H and thaumasite became more pronounced owing to extreme low temperature (noted that pressure between 0.1 MPa and 35 MPa did not affect the calculation results). Furthermore, liquid water penetration is enhanced under high hydraulic pressure conditions (Kawabata et al. 2022 and Takahashi et al. 2021), and the increased water saturation of pores in specimens also enhances the diffusion of chloride ions, where hydroxide ions migrate from the specimens to the seawater to facilitate the dissolution and decalcification. The deterioration in deep seas could have a size effect. Although portlandite was completely dissolved in the surface of a small size specimen (Kobayashi et al. 2021), it was remained at the surface area (5 mm below the specimen surface) of a larger size specimen as shown in Fig. 2, since the inner specimen acts as a reservoir of alkali. Moreover, several popouts were observed at the surface of the large-size specimen. In the popouts, white substances such as brucite and calcite were precipitated spherically.

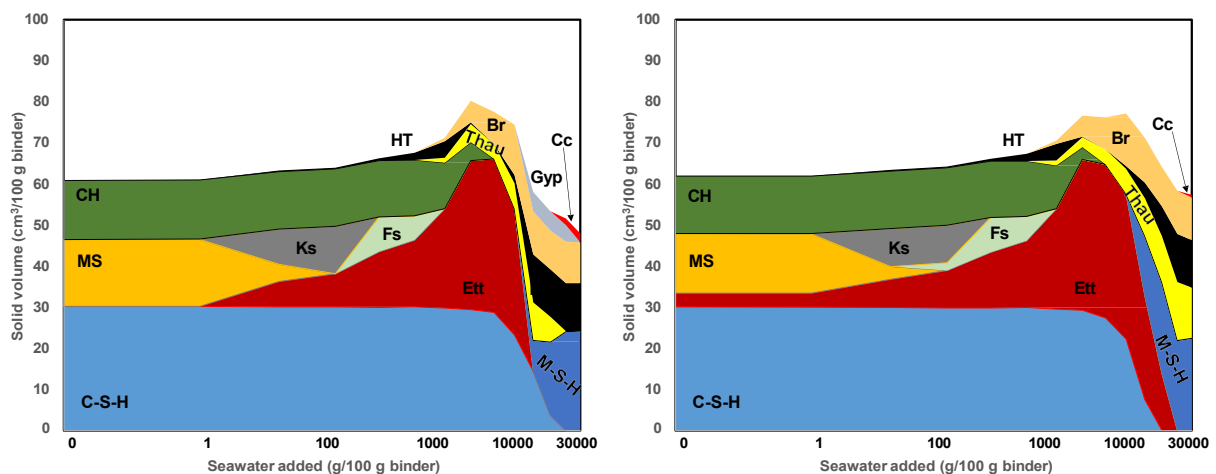


Fig. 1 Predicted changes in the phases and volumes of PC paste at 20°C and 0.1 MPa (*left*) and 2 °C and 35 MPa (*right*) calculated with GEMS3 and the Cemdata 18. Ett: ettringite, Fs: Friedel's salt, Ks: Kuzel's salt, Br: Brucite, MS: monosulfate, CH: portlandite, HT: hydrotalcite, Thau: thaumasite, Gyp: Gypsum, Cc: calcite.

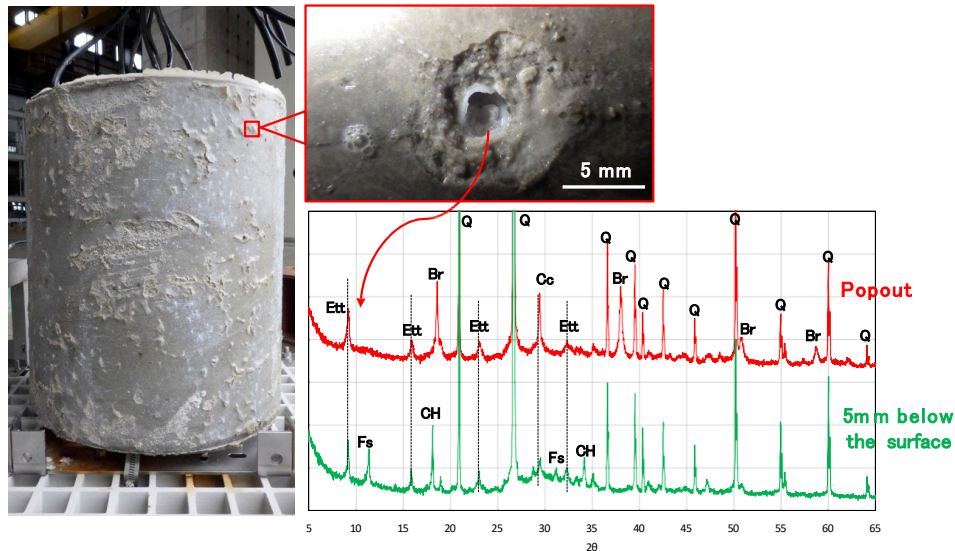


Fig. 2 Portland cement mortar ($\Phi 350 \text{ mm} \times 400 \text{ mm}$, water/cement = 0.60) retrieved from deep seafloor with a depth of 3,515 m after 309 days exposure. Several popouts with the size of a few mm in diameter were observed in a horizontal mortar surface. White substance was precipitated in the popouts. The white substance and the sample cut from 5 mm below the specimen surface were measured by XRD. Ett: ettringite, Br: Brucite, CH: portlandite, Fs: Friedel's salt, Q: Quartz, Cc: calcite.

2.2 Mechanical property of specimens

Both hydraulic pressure as a confinement mechanism and water infiltration as a stress-relaxation mechanism strongly affect the increase of strains and the resultant internal damage on porous medium. Kawabata et al. (2022) observed in situ the initial damage of a cement mortar under up to 20 MPa of hydraulic pressure using X-ray micro-computed tomography. The volumetric strain development due to the hydraulic pressure varied greatly with location, owing to heterogeneous water infiltration in the mortar specimen. Therefore, the balance of the above two mechanisms must be considered to assess the risk of internal damage of cementitious materials under high hydraulic pressure conditions. Takahashi et al. (2022) reported that the changes of strain and hydraulic pressure in a mortar specimen was successfully monitored in situ during a long-term exposure to the deep seafloor with a depth of 3,515 m. The internal damage due to high hydraulic pressure affects the mechanical properties. Clayton (1998) reported that compressive strength and bending strength of concrete while under hydraulic pressure decreased about 30–50 %. When the applied hydraulic pressure was high enough, hydraulic confinement was dominant as the result and permanent damages occurred during the rise and/or sustainment of the high hydraulic pressure. The internal damage also decreased substantially Young's modulus (Kawabata et al. 2022) and could increase the size of microscopic pore entry (Tanaka et al. 2020).

3. In-situ connection on deep seafloor

The authors firstly applied a PC-based mortar to fix measuring instruments 20 m below the seafloor at a depth of 1,890 m for monitoring the real-time crustal deformation at the ocean bottom, enabling the discussion of rupture regions of future mega-thrust earthquakes (Kimura et al. 2021). In this trial, ready-mixed mortar was pumped and placed into frameworks on the seafloor, and they found that transporting only several tens of litres of fresh mortar to the seafloor and placing there were hard. Thus, an easier method, such as connecting precast members in situ, is necessary to construct deep-sea infrastructures. Figure 3 depicts in situ connection using a cement mortar kit specifically designed for deep sea applications. This mortar mix containing CAC can be stored as a suspension for more than one year and activated only when it is mixed with activators. After jointing the precast mortar members on deep seafloor with a depth of 980 m, the cement mortar was discharged by using manipulators and filled in a hole between two precast members. The injected mortar was hardened after 1 day and retrieved afterwards. The retrieved specimens revealed that the mortar was filled properly without any gaps.



Fig. 3 Connecting of precast mortar members on the seafloor with a depth of 980 m by using the deep-submergence research vehicle Shinkai 6500 (left) and discharging of the mortar and activator conducted by manipulators (right). These photos were provided by Japan Agency for Marine-Earth Science and Technology (JAMSTEC).

4. Conclusions

Recent investigations and trials focused on seawater attack and hydraulic pressure under deep sea conditions were summarized in this paper. Considerable research and development that will target at material designs, structure designs and construction methods will be necessary to build and maintain underwater deep-sea infrastructures.

Acknowledgements

We would like to thank Dr. Takafumi Kasaya from JAMSTEC, and Prof. Toshiro Yamanaka, Assoc. Profs. Shun Nomura and Hiroko Makita from Tokyo University of Marine Science and Technology for their assistance in conducting the deep-sea field tests.

References

- Clayton, N. (1998) "Effect of water pressure on concrete strength" *Proceedings of the 2nd International Conference on Concrete under Severe Conditions*, Tromsø: 978-987
- De Weerd, K. and Justnes, H. (2015) "The effect of sea water on the phase assemblage of hydrated cement paste", *Cement and Concrete Composites*, 55: 215-222
- Gjorv, O.E. (1971) "Long-time durability of concrete in seawater", *ACI Journal*, 68, 10: 60-67
- Jakobsen, U.H., De Weerd, K., and Geiker, M.R. (2016) "Elemental zonation in marine concrete", *Cement and Concrete Research*, 85: 12-27
- Kawabata, Y., Takano, D., Takahashi, K. and Iwanami, M. (2022) "In situ observation for the influence of hydraulic pressure on internal damage of cement-based materials", *Materials & Design*, 216: 110556
- Kimura, T., Araki, E., Yokobiki, T., Nishida, S., Cook, M., Zumberge, M., Takahashi, K., Hori, T. and Kodaira, S. (2021) "Real-time SSE monitoring by optical borehole tiltmeter in the Nankai Trough, Japan" *Proceedings of Japan Geoscience Union Meeting 2021*: C002173
- Kobayashi, M., Takahashi, K., and Kawabata, Y. (2021) "Physicochemical properties of the Portland cement-based mortar exposed to deep seafloor conditions at a depth of 1680 m", *Cement and Concrete Research*, 142: 106335
- Kobayashi, M., Takahashi, K., Kawabata, Y., and Bier, T.A. (2022) "Physicochemical properties of Portland cement/calcium aluminate cement/calcium sulfate ternary binder exposed to long-term deep-sea conditions", *Materials and Structures*, 55: 182
- Takahashi, K., Kawabata, Y., Kobayashi, M., Gotoh, S., Nomura, S., Kasaya, T., and Iwanami, M. (2021) "Action of hydraulic pressure on Portland cement mortars – current understanding and related progress of the first-ever in-situ deep sea tests at a 3515 m depth", *Journal of Advanced Concrete Technology*, 19: 226-239
- Takahashi, K., Kawabata, Y., Iwanami, M., Kobayashi, M., Kasaya, T., Yamanaka, T., Nomura, S., Makita, H. (2022) "In-situ deep-sea monitoring of cement mortar specimen at a depth of 3515 m and changes in mechanical properties after exposure to deep sea condition", *Journal of Advanced Concrete Technology*, 20: 254-266
- Takahashi, K., Akitou, T., and Kobayashi, M. "Changes in the physicochemical properties of calcium aluminate cement paste with high alumina content under deep seas", under review
- Tanaka, K., Nakayama, K. and Iwanami, M. (2020) "Fundamental study on mechanical behavior of concrete subjected to high water pressure" *Proceedings of the Japan Concrete Institute Annual Convention*, 42: 233-238

Chloride Adsorption Does Not Retard Chloride Ingress in Concrete

T. Ichikawa^{1*,2}, K. Yamada², and K. Haga³

¹ Hokkaido University, Sapporo, Japan

Email: tsuneki@eng.hokudai.ac.jp

² National Institute for Environmental Studies, Miharuru, Japan

Email: yamada.kazuo@nies.go.jp

³ Taiheiyo Consultant Co. Ltd, Tokyo, Japan

Email: Kazuko_Haga@taiheiyo-c.co.jp

ABSTRACT

It has generally been believed that chloride adsorbents in concrete such as AFm and C-S-H suppress the ingress of chloride ions by immobilizing them in the adsorbents. However, the EPMA and electrical conductivity measurements of chloride ions revealed that the adsorbed chloride ions are highly mobile. The EPMA maps of chloride and cesium ions in concrete measured after immersing in a 0.5 mol/dm³ cesium chloride solution showed that the amount of diffused chloride ions was much larger than that of cesium ions and the diffusion of chloride ions was faster than that of cesium ions, which indicates that adsorbed chloride ions are as mobile as free chloride ions in the pore solution. The steady-state electrical conductivity measurement of concrete immersed in a potassium chloride solution with different concentrations showed that the concentration of mobile chloride ions in concrete was given as a sum of the concentrations of the adsorbed ions and of the external solution, which also indicates that the adsorbed chloride ions are as mobile as free chloride ions.

KEYWORDS: Chloride, Diffusion, Adsorption, Mobility, Osmosis

1. Introduction

Since the penetration of chloride ions (Cl⁻) into concrete damages concrete structures by inducing the corrosion of reinforced bars (for example, Zhu *et al.* 2021), to suppress the penetration of Cl⁻ is important for prolonging the service lives of concrete structures. Portland cement paste, one of the main constituents of regular concrete, is a porous anion exchanger which absorbs about 0.5 eq of exchangeable anions (1 eq of ions with valence z is equivalent to $1/|z|$ mol of the ions) per 1 kg of dry cement (Sasaki and Saeki 2005). The effect of the ionic adsorption on the penetration rate of Cl⁻ depends on the mobility of adsorbed Cl⁻. Provided that the adsorbed ions are immobile, the adsorption prevents further penetration of the ions by the diffusion. On the other hand, if the adsorbed ions are mobile, the adsorption does not suppress the penetration but merely increases the concentration of penetrated Cl⁻. To know the mobility of adsorbed Cl⁻ is therefore crucial for estimating the penetration rate of Cl⁻. Although most of previous works assumed with no firm reason that adsorbed Cl⁻ are immobile in concrete, the present study shows that adsorbed Cl⁻ are as mobile as free Cl⁻ in the pore solution of concrete.

2. Evidences on Mobile Adsorbed Anion

The assumption of immobile adsorbed Cl⁻ may arise by considering that the adsorption structures of neutral molecules and ions are the same. However, the adsorption structure of ions is essentially different from that of neutral molecules. The neutral molecule is adsorbed on the adsorption site by orbital interactions between the molecule and the adsorption site. Since the orbital interactions are short-range interactions, the molecule is desorbed as soon as the molecule is detached from the site. The adsorbed molecule is therefore immobile as long as the molecule is adsorbed. The fundamental force acting between the adsorbed ion and the adsorption site is the long-range Coulomb attractive force, so that the

adsorbed ion is still adsorbed, or under the influence of the attractive force, even if the ion is detached into the pore solution of concrete. Since the adsorption of ions takes place under the condition of electrical neutrality, which is one of the fundamental conditions constituting the universe, ionic adsorption is essentially ion-exchange reactions between mobile adsorbed ions and mobile free ions. Several examples indicating that adsorbed Cl^- are mobile will be shown in the following section.

2.1 Diffusion Profiles of Cl^- and Counter Cation

Figure 1 shows the diffusion profiles of Cl^- and cesium ions (Cs^+) in hardened cement paste with water to cement ratio of 0.6 after immersing in a 0.5 mol/dm³ (M) of CsCl solution for one week. The diffusion profile of Cs^+ accords with that of Cl^- by multiplying the concentration and the distance by factors of 4.5 and 1.35, respectively. The multiplication factor of 4.5 arises from adsorbed Cl^- . Since the concentration of free Cl^- is the same as that of Cs^+ , the difference of the concentrations between Cs^+ and Cl^- , 3.5, corresponds to that of adsorbed Cl^- . The multiplication factor of 1.35 implies that Cl^- diffuse faster than Cs^+ , which indicates that adsorbed Cl^- are mobile. The similarity of the diffusion profiles between Cl^- and free Cs^+ suggests that adsorbed Cl^- are as mobile as free Cl^- .

Figure 2 compares the observed diffusion profiles with those obtained by solving the Nernst-Planck diffusion equations under the conditions of mobile and immobile adsorbed Cl^- . Assuming that adsorbents in the paste initially adsorb OH^- , the diffusion equations under the condition of mobile and immobile adsorbed Cl^- are given by

$$\frac{\partial c_{\text{Cl}}}{\partial t} = D_{\text{Cl}} \frac{\partial}{\partial x} \left(\frac{\partial c_{\text{Cl}}}{\partial x} - \frac{c_{\text{Cl}} F}{RT} \frac{\partial U}{\partial x} \right), \quad \frac{\partial c_{\text{Cs}}}{\partial t} = \frac{D_{\text{Cl}}}{1 + \frac{a_{\text{Cl}}}{c_{\text{Cl}}}} \frac{\partial}{\partial x} \left(\frac{\partial c_{\text{Cs}}}{\partial x} - \frac{c_{\text{Cs}} F}{RT} \frac{\partial U}{\partial x} \right) \quad (1)$$

respectively, where D_{Cl} and c_{Cl} are the diffusion coefficient and the concentration of mobile Cl^- , a_{Cl} is the concentration of adsorbed immobile Cl^- , and U is the electrostatic diffusion potential determined by the conditions of null electric current and null net charge. The observed profiles compare well with the theoretical ones obtained under the assumption of mobile adsorbed Cl^- . Adsorbed Cl^- are therefore mobile.

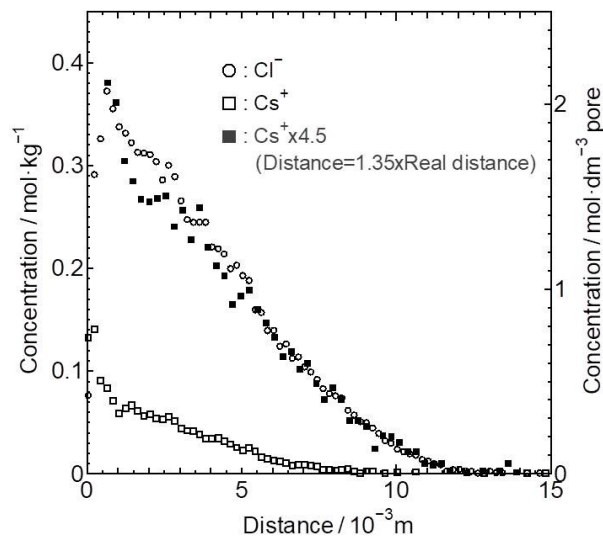


Fig. 1. Diffusion profiles of Cl^- and Cs^+ ions in hardened cement paste obtained by EPMA measurement after immersing in 0.5 M CsCl solution for one week.

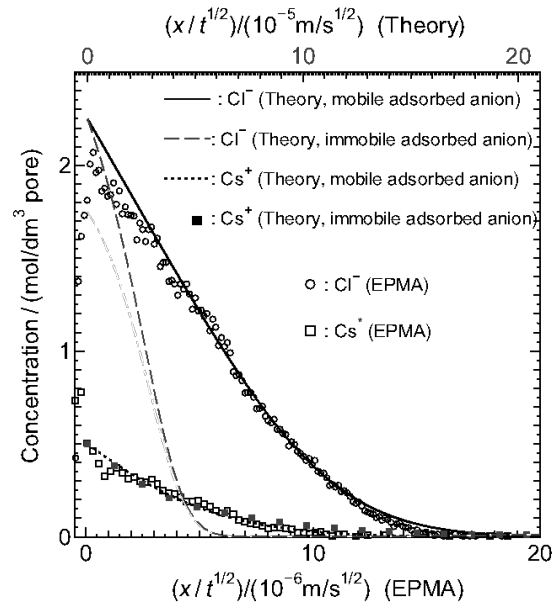


Fig. 2. Comparison of the observed diffusion profiles of Cl^- and Cs^+ ions with theoretical ones calculated under the assumption of mobile or immobile adsorbed anions.

2.2 Electrical Conductivity

Figure 3 shows the AC electrical conductivities of a porous ceramic plate with porosity of 0.32 in KCl solutions. The plate was immersed in the solutions until the conductivity became constant. The ratio of the conductivities between the plate and a KCl solution does not depend on the conductivity of the solution, which implies that the concentration of KCl in the pore solution is the same as that in the external KCl solution. Modeling the conduction path of the plate with an assembly of tortuous paths, the conductivity σ_s of the plate is given as a function of the conductivity σ_L of the external solution by

$$\chi \rho_s = \chi \rho_L N(s/A) = \chi \rho_L (NsA)/A^2 = \chi \rho \phi / A^2 \quad (2)$$

where N and λ are the number and the length of diffusion paths per unit volume of the plate, respectively, s is the average cross-sectional area of the paths, and $\phi = Ns\lambda$ is the porosity of the plate. The value of $\sigma_s/\sigma_L = 0.0827$ gives the tortuosity of $\lambda = 1.967$.

Figure 4 shows the AC conductivity of a mortar specimen immersed in Ca(OH)_2 -saturated KCl solutions until the conductivity became constant. The conductivity ratio of the mortar to the external solution is not constant but linearly depends on the resistivity $1/\sigma_L$ of the external solution. The linear dependency is due to the migration of adsorbed Cl^- . The conductivity of the mortar containing adsorbed Cl^- is given by the sum of the conductivities of free and adsorbed ions as

$$\chi \rho_s = (\chi \rho_L + \chi \rho_{ads}) \phi / A^2 = (\chi \rho_L \phi / A^2) (1 + \chi \rho_{ads} / \chi \rho_L) \quad (3)$$

where σ_{ads} is the conductivity of adsorbed Cl^- . The observed conductivity of $\sigma_s/\sigma_L = 0.00215(1+0.0732/\sigma_L)$ indicates that the conductivity of adsorbed Cl^- is 0.0732. Assuming that the mobility of adsorbed Cl^- is the same as those of free Cl^- and K^+ , the conductivity of 0.0732 corresponds to $\sigma_L = 2 \times 0.0732$ for the external solution. The concentration of the KCl solution at $1/\sigma_L = 1/(2 \times 0.0732)$ is 1.37 M. The average concentration of adsorbed Cl^- in the mortar with the porosity of 0.15 is therefore $1.37 \times 0.15 = 0.21 \text{ mmol/cm}^3$. The average concentration of adsorbed Cl^- calculated from the anion exchange capacity of cement is 0.24 mmol/cm^3 , which is close to the concentration derived from the conductivity measurement. The mobility of adsorbed Cl^- is therefore very close to that of free Cl^- .

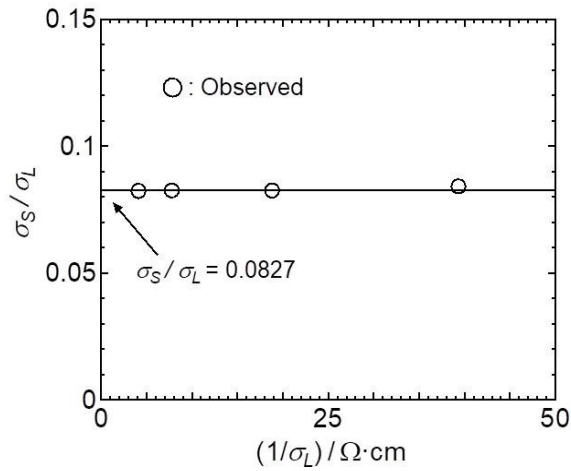


Fig. 3. Conductivity σ_s of porous ceramic plate with porosity of 0.32 and thickness of 10.7 mm against resistivity $1/\sigma_L$ of external KCl solution.

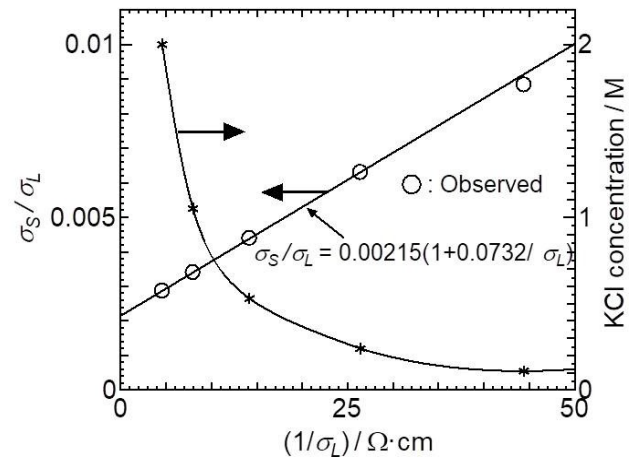


Fig. 4. Conductivity σ_s of mortar with porosity of 0.15 and thickness of 5.7 mm against the resistivity $1/\sigma_L$ of external KCl solution.

3. Mobilization Mechanism of Adsorbed Cl^-

One of the reasons why adsorbed Cl^- in concrete have been assumed to be immobile may arise from an assumption that structures of ionic adsorbents in aqueous solutions are the same as those determined by X-ray diffraction (XRD) analysis. XRD is usually measured after eliminating free water in a sample, so that XRD reflects the structure of a partially dried sample. Baquerizo *et al.* (2015) determined the XRD

structure of AFm under different relative humidity. Although the interlayer space was slightly expanded by increasing the humidity, the space was too narrow for the migration of adsorbed anions locating in the interlayer space. However, as will be mentioned, the interlayer space is significantly expanded by the intrusion of an external solution due to osmotic pressure arising from the difference of ionic concentrations between external and interlayer solutions, and allows the migration of both the adsorbed and intruded ions.

Figure 5 shows the apparent specific volume of AFm in liquids under centrifugal forces. The liquids used were distilled water, 0.3 M and 0.5 M NaCl aqueous solutions, and 1 : 1 mixture of acetonitrile and propylene carbonate with the specific density of 1.0. One gram of AFm was packed in a 10 mL centrifugal tube with 10 mL of a liquid. After pre-swelling the AFm overnight, the sample was centrifuged under the lowest centrifugal force for 15 min until the apparent volume of AFm became constant. The sample was repeatedly centrifuged for 15 min under higher centrifugal forces. A sample without pre-swelling was also centrifuged.

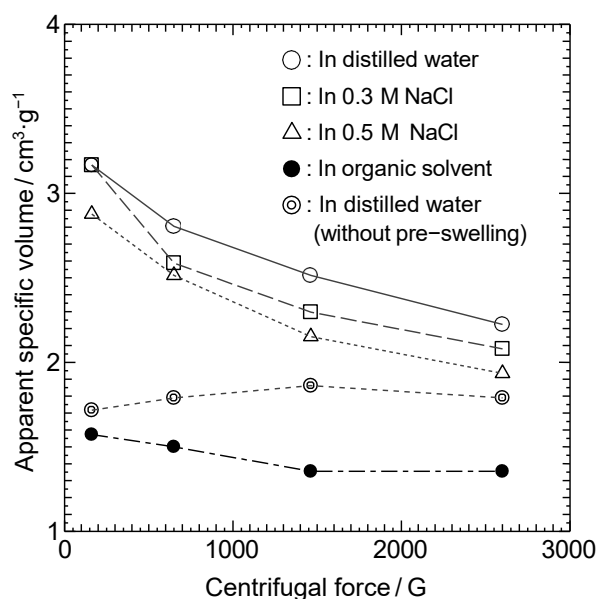


Fig. 5. Apparent specific volume of AFm in liquids under centrifugal force. Organic solvent used is the mixture of acetonitrile and propylene carbonate with 1:1 volume ratio and the density of 1 g/cm³.

AFm in the organic solvent shows the lowest apparent specific volume, which indicates that AFm maintains the structure of $3\text{CaO} \cdot \text{Al}_2\text{O}_3 \cdot \text{CaSO}_4 \cdot 12\text{H}_2\text{O}$ in the solvent. The volumes of pre-swollen AFm in aqueous solutions are much larger than that in the organic solvent, which indicates that the aqueous solutions are intruded into the interlayer space of AFm to expand the interlayer space. The intrusion is due to the osmotic pressure arising from the difference of ionic concentrations between the external solutions and the interlayer solution dissolving adsorbed SO_4^{2-} and Cl^- , so that the volume expansion decreases with increasing the concentration of NaCl in the external solution. Since the intruded Cl^- diffuse in the interlayer solution while exchanging with SO_4^{2-} , AFm does not prevent the diffusion of Cl^- . The rigorous theoretical calculation of the diffusion rate of ions in charged parallel plates like AFm showed that the diffusion parallel to the plates is scarcely suppressed (Ichikawa, 2022).

4. Conclusion

The experimental and theoretical evidences showed that adsorbed Cl^- in water-saturated concrete are as mobile as free Cl^- in the pore solution, so that the addition of Cl^- adsorbent such as AFm does not retard the penetration of Cl^- into concrete. If the addition of a Cl^- adsorbent suppresses the penetration, it is not due to the immobilization of Cl^- but mainly due to the increase of the tortuosity of concrete. Increase of the tortuosity suppresses the penetration of both Cl^- and counter cations.

References

- Baquerizo L.G., Matschei T, Scrivener K.L., Saeidpour M and Wadsö L. (2015). "Hydration states of AFm cement phases." *Cement and Concrete Research*, 73, 143-157.
- Ichikawa T., (2022). "Theory of Ionic Diffusion in Water-saturated Porous Solid with Surface Charge." *Journal of Advanced Concrete Technology*, 20, 430-443.
- Sasaki, K. and Saeki, T., (2005). "Konwazai wo mochiita semento kookatai ni okeru enkabutsu ion koteiseijou." *Proceedings of the Japan Concrete Institute*, 27 (1), 691-696 (in Japanese).
- Zhu, Y., Macdonald, D.D., Qui, J. and Engerhardt G.R., (2021). "Corrosion of rebar in concrete. Part II: Literature survey and statistical analysis of existing data on chloride threshold" *Corrosion Science*, 285, 109439.

Roles of slag on corrosion electrochemical measurement in carbonated mortar

L. Cheng^{1*}, I. Maruyama^{1,2}

¹ *The University of Tokyo, Graduate School of Engineering, Department of Architecture, Tokyo, Japan
Email: chengluge@g.ecc.u-tokyo.ac.jp*

² *Nagoya University, Graduate School of Environmental Studies, Department of environmental engineering and architecture, Nagoya, Japan
Email: i.maruyama@bme.arch.t.u-tokyo.ac.jp*

ABSTRACT

The application of supplementary cementitious materials (SCMs), including blast furnace slag (BFS), has been identified as a viable replacement for ordinary Portland cement (OPC) with the advantage of carbon emission reduction. However, the reduced capacity to buffer the pH in the alkaline range makes the protection provided by the alkaline environment against steel corrosion in concrete no longer feasible. In this study, the corrosion rate of steel rebar in the carbonated blast furnace slag (BFS)-based mortar with replacement ratios of 0%, 30%, and 70% under three controlled relative humidity (RH) conditions was investigated through electrochemical impedance spectroscopy (EIS) technique and gravimetric weight loss method. The results detected by the EIS technique showed that the corrosion rate increases with the increase of the replacement ratio of BFS. In contrast, the corrosion states of the surfaces of steel rebars showed contradictory results that the most serious corrosion occurred in the carbonated mortar without the BFS. Such overestimation of the corrosion state for carbonated slag-based mortar in electrochemical results can be attributed to sulfide in BFS. The oxidation of sulfide ions in pore solution and the formation of the FeS lead to misleading results from the EIS technique and prevention of the corrosion process in carbonated slag-based materials. The overestimation of electrochemical measurement on the corrosion state in carbonated slag-based mortar gets more obvious with the higher slag replacement ratio by comparing the actual weight loss of steel rebars and the corrosion amount calculated from the monitored corrosion rate.

KEYWORDS: *carbonation, slag-based mortar, steel corrosion, electrochemical method*

1. Introduction

There is a strong trend of using an alternative to Portland cement clinker, substituting a part of the cement with supplementary cementitious materials (SCMs). It is desirable that ordinary Portland cement (OPC) can be replaced by alternative materials, including blast furnace slag (BFS) and fly ash (FA), with the advantage of carbon emission reduction to ensure sustainable concrete production (Duxson et al. (2007)). Some research indicated that SCM exhibited a dense microstructure and chemical reaction products within it can reduce chloride mobility, thus having a high corrosion resistance (Kayali, Khan, and Sharfuddin Ahmed (2012)). However, a reduced capacity to buffer the pH in the alkaline range on exposure to carbon dioxide was reported (Papadakis (2000))(Vu et al. (2019)). And because the lower pH destroys the passive layer on the steel rebar surface and promotes active corrosion, the protection by the alkaline environment in concrete against corrosion during the service life of a reinforced concrete structure is no longer feasible. However, there is limited research focusing on carbonation-induced steel corrosion in SCM mortar. On the other hand, relative humidity (RH) has also been found to have a considerable effect on the corrosion process of steel rebar. Therefore, this study aims to investigate the influence of RH on the corrosion behavior of steel rebar in carbonated slag-based mortar with two different replacement ratios of BFS (30% and 70%).

2. Experiment methods

2.1 Material mix proportions and sample preparation

OPC was used throughout the experiment. SCM that BFS was used as replacements with the weight ratios of 0%, 30%, and 70%, denoted by OPC, 30SL, and 70SL, respectively. Two sizes of silica sand (UBE INDUSTRIES 5A and 7) with a density of 2.6 g/cm³ were used as fine aggregates for all mortar mixes. The fine sand size (<0.2 mm) was utilized to ensure the homogeneity of materials. Polypropylene fibers (length of 6 mm, diameter of 0.028 mm) were used to prevent cracking in the mortar cover caused by carbonation and corrosion products. The water-to-binder ratio (W/B) of 0.60 and sand-to-binder ratio (S/B) of 2 were constant throughout the experiment. The mortar mix proportions are shown in Table 1.

Table 1 Mortar mix proportion (W/B=0.6, S/C=2)

| Mortar | OPC cement (kg/m ³) | BFS (kg/m ³) | Water (kg/m ³) | Sand (kg/m ³) | | Fiber (kg/m ³) |
|--------|------------------------------------|-----------------------------|-------------------------------|---------------------------|---------|-------------------------------|
| | | | | 1.7-0.2 mm | <0.2 mm | |
| OPC | 593 | - | 356 | 593 | 593 | 0.91 |
| 30SL | 413 | 177 | 354 | 590 | 590 | 0.91 |
| 70SL | 176 | 411 | 352 | 587 | 587 | 0.91 |

A miniaturized mortar sample satisfying the measurement demand with dimensions of 20×20×40 mm³ was conducted to shorten the experiment duration, and the details can be found in our previous study (Cheng, Maruyama, and Ren (2021)). A 30 mm long steel rebar (SGD-400D) with a diameter of 10 mm was embedded in the central position of the mortar with an exposed surface area of 9.42 cm². The cover depth of the mortar sample is 5 mm. The mortar samples were demolded twenty-four hours after casting and then seal-cured for sixty days at a temperature of 20±1°C.

Accelerated carbonation was achieved using a chamber under the condition of 5% CO₂, 60% RH, and 20°C. Since carbon dioxide can penetrate more easily when liquid water is evaporated, prior to the carbonation process, the specimens were kept in an oven at 105°C until they reached a constant weight. Meanwhile, reference specimens under the same conditions were prepared to verify the carbonation depth by a phenolphthalein test during the accelerated carbonation.

As carbonation depth reached the cover depth of 5 mm, the mortar specimens were subject to the three different RH conditions controlled by saturated KCl (84% RH), BaCl₂ (91%RH) , and K₂SO₄ (97% RH) solutions in desiccators at a temperature of 20±2°C until the mass equilibrium of mortars. The water content by mass ω (%) was calculated after the samples of reference mortar fragments in different RH conditions reached relative humidity equilibrium given as follows:

$$\omega = \frac{m_{sample} - m_{dry}}{m_{dry}} \quad (1)$$

where m_{sample} is the mass of the mortar sample, m_{dry} is the mass after drying at 105°C under vacuum conditions for twenty-four hours.

2.3 Electrochemical measurements

Corrosion rate (corrosion current density, i_{corr}) measurement of rebar embedded in mortar sample was performed using an electrochemical potentiostat (HOKUTO HZ-7000) with a three-electrode cell setup: Ag/AgCl is the reference electrode, stainless plate acts as a counter electrode while the steel rebar acts as a working electrode. The electrochemical impedance spectroscopy (EIS) method was conducted using a 10-mV amplitude sine wave signal in the 0.1 Hz - 100 kHz frequency range with twenty points per decade. Fitted charge transfer resistance (R_{ct}) from measured Nyquist plots can be used to calculate corrosion current according to the Stern-Geary equation (Mansfeld and Oldham (1971)):

$$i_{corr} = \frac{B}{R_{ct} \cdot A} \quad (1)$$

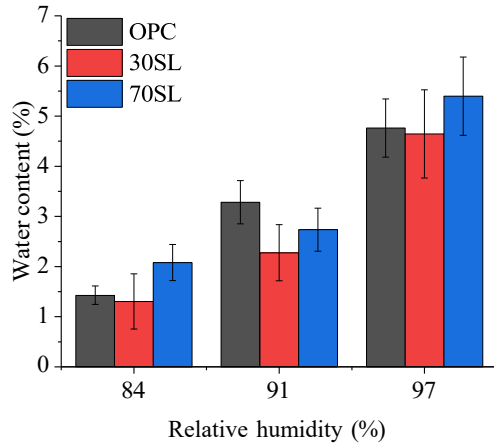


Fig.1 Water content of carbonated OPC, 30SL and 70SL at different RH conditions

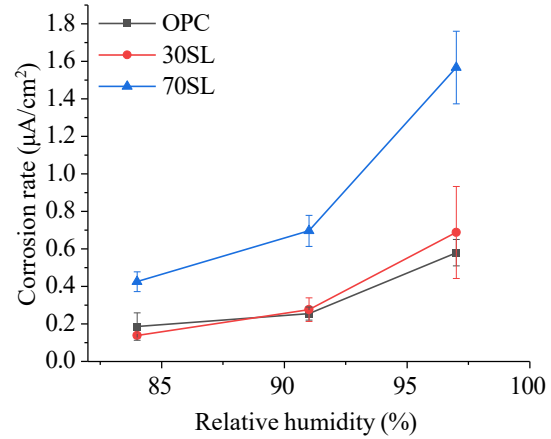


Fig.2 Corrosion rate of carbonated mortar with slag replacement ratios of 0 (OPC), 30, 70% at different RH conditions

Table 2. Comparison between measured weight loss and corrosion amount from i_{corr} at 97%RH condition

| mortar | OPC | 30SL | 70SL |
|---|-------|-------|--------|
| Measured weight loss (mg) | 47.99 | 40.05 | 31.62 |
| Calculated corrosion amount from monitored i_{corr} | 54.42 | 64.58 | 147.07 |
| Ratio | 0.88 | 0.62 | 0.22 |

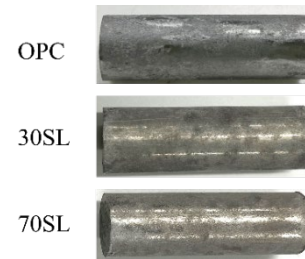


Fig.3 Steel rebar removed from the carbonated OPC, 30SL and 70SL at 97%RH condition.

where B is a constant, which can be assumed to be 26 mV (Alonso and Andrade (1988)), and A is the exposed area of the rebar (9.42cm²).

3. Results and discussion

Figure. 1 shows the results of water content change in carbonated OPC, 30SL, and 70SL under different RH conditions. As expected, the water content increases with RH due to more liquid water condensed in the pores, and shows a significant increase when RH increases from 91% to 97%, which is attributed to the significantly increased capillary pore volume due to carbonation (Thiéry et al. (2011)).

The corrosion rates of steel rebar embedded in carbonated OPC, 30SL, and 70SL under three different RH conditions are shown in Fig. 2. When RH changes from 84% to 91%, the corrosion rate in carbonated OPC, 30SL, and 70SL increases gradually (from 0.186 to 0.255 $\mu\text{A}/\text{cm}^2$ for carbonated OPC, from 0.138 to 0.277 $\mu\text{A}/\text{cm}^2$ for carbonated 30SL, and from 0.43 to 0.697 $\mu\text{A}/\text{cm}^2$ for carbonated 70SL), while the corrosion rate shows a significant increase when RH increases from 91% to 97%. Values of corrosion rate of steel rebar when RH reaches 97% increase to 0.580 $\mu\text{A}/\text{cm}^2$ for carbonated OPC, 0.688 $\mu\text{A}/\text{cm}^2$ for carbonated 30SL, and 1.568 $\mu\text{A}/\text{cm}^2$ for carbonated 70SL. Such a change trend of corrosion rate corresponds to the change of electrolyte. As Fig. 1 shows, increased RH leads to more electrolytes in mortar, which can be used to transfer hydroxyl ions from the cathode to anode sites on the steel surface, thus promoting the corrosion reaction process and increasing the corrosion rate of steel rebar. A significant increase in corrosion rate from 84% to 97% RH condition corresponds to a significant increase in water content.

In addition, it is obvious that the corrosion rate of steel rebar in carbonated 70SL mortars is almost seven times higher than that in carbonated OPC mortars under all RH conditions. However, Figure 3 shows the actual corrosion state of steel rebar surface in OPC, 30SL, and 70SL under 97%RH after the chemical cleaning of the corrosion products followed the steps in (ASTM G1-03 (2002)), it can be seen that the corrosion state of steel rebar in OPC is more serious than in 30SL and 70SL, which means that the corrosion result based on the electrochemical method is not consistent with the corrosion state observed in the steel rebar. Therefore, the electrochemical measurement misinterprets the corrosion behavior and overestimates

the corrosion rate. This phenomenon can be explained by the existence of sulfide species (S^{2-} , $S_2O_3^{2-}$, HS^-) in the pore solution of slag-based mortar. The dissolution and reaction of slag release sulfide ions into the pore solution, which can be oxidized into sulfur and sulfur oxides, consuming local oxygen on the steel rebar surface. The measured charge transfer resistance (R_{ct}) detected in electrochemical measurement will combine the anodic reaction of steel oxidation and sulfide species oxidation. Since the oxidation of reduced sulfide species at the steel rebar surface is not distinguishable from the actual corrosion of steel rebar, the corrosion rate is overestimated in slag-based materials. Similar misleading results from electrochemical measurement were reported that a significant increase in corrosion current density and a decrease in corrosion potential were shown in slag-containing material even though no corrosion initiation occurred (Criado and Provis (2018)) (Yeau and Kim(2005)).

The weight loss of the corroded steel rebar after corrosion rust cleaning can be seen as the actual corrosion state of the steel rebar. Table 2 shows the measured corrosion weight loss and the corrosion amount calculated from the monitored corrosion rate by electrochemical measurement under 97%RH condition. It can be seen that the ratio of actual corrosion to the electrochemically determined corrosion decreases with the slag replacement ratio, which indicates that the overestimation effect of electrochemical measurement on the corrosion state is more obvious when the slag replacement ratio in mortar is higher. It is expected to obtain the actual corrosion rate of reinforced slag-based mortar by applying these ratios to improve the results obtained from electrochemical methods.

4. Conclusions

A higher corrosion rate was detected in 70SL because the higher amount of electrolyte provides more channels for ions' transformation and higher connectivity between the pore system. The higher existence of sulfide causes FeS to form on the steel surface, inhibiting the passive layer formation, and resulting in a further corrosion process. In addition, the reaction of sulfite and oxygen causes an overestimation of the detected corrosion rate of the steel rebar.

The replacement ratio of slag determines the overestimation degree of electrochemical results on real corrosion state: when the slag replacement ratio is higher, the ratio of real corrosion amount to calculated corrosion amount is lower. The appropriate electrochemical measurement of corrosion behavior considering the sulfide oxidation reaction for reinforced sulfide-containing mortar should be studied in the future.

References

- Alonso, C., and C. Andrade. 1988. "Corrosion of Steel Reinforcement in Carbonated Mortar Containing Chlorides." *Advances in Cement Research* 1(3): 155–63.
- ASTM G1-03. 2002. *Standard Test Practice for Preparing, Cleaning, and Evaluating Corrosion Test Specimens*.
- Cheng, Luge, Ipppei Maruyama, and Yuqi Ren. 2021. "Novel Accelerated Test Method for RH Dependency of Steel Corrosion in Carbonated Mortar." *Journal of Advanced Concrete Technology* 19(3): 207–15.
- Criado, Maria, and John L. Provis. 2018. "Alkali Activated Slag Mortars Provide High Resistance to Chloride-Induced Corrosion of Steel." *Frontiers in Materials* 5: 34.
- Duxson, Peter, John L. Provis, Grant C. Lukey, and Jannie S.J. van Deventer. 2007. "The Role of Inorganic Polymer Technology in the Development of 'Green Concrete.'" *Cement and Concrete Research* 37(12): 1590–97.
- Kayali, Obada, M. S.H. Khan, and M. Sharfuddin Ahmed. 2012. "The Role of Hydrotalcite in Chloride Binding and Corrosion Protection in Concretes with Ground Granulated Blast Furnace Slag." *Cement and Concrete Composites* 34(8): 936–45.
- Mansfeld, Florian, and Keith B. Oldham. 1971. "A Modification of the Stern-Geary Linear Polarization Equation." *Corrosion Science* 11(10): 787–96.
- Papadakis, Vagelis G. 2000. "Effect of Supplementary Cementing Materials on Concrete Resistance against Carbonation and Chloride Ingress." *Cement and Concrete Research* 30(2): 291–99.
- Thiéry, Mickaël et al. 2011. "Effect of Carbonation on the Microstructure and the Moisture Properties of Cement-Based Materials." *International Conference on Durability of Building Materials and Components* 55(1): 1–8.
- Vu, Tran Huyen et al. 2019. "Carbonation and Chloride Induced Steel Corrosion Related Aspects in Fly Ash/Slag Based Geopolymers - A Critical Review." *FIB 2018 - Proceedings for the 2018 fib Congress: Better, Smarter, Stronger* (October): 3061–76.
- Yeau, Kyong Yun, and Eun Kyum Kim. 2005. "An Experimental Study on Corrosion Resistance of Concrete with Ground Granulate Blast-Furnace Slag." *Cement and Concrete Research* 35(7): 1391–99.

Evaluation of transport properties in ITZ with coupled CT image analysis and simulation

Y. Tan^{1*}, T. Sugiyama², and K. Hashimoto³

¹ *Environmental Material Engineering Laboratory, Graduate School of Engineering, Hokkaido University, Sapporo Japan*

Email: yingyao.tan.x0@elms.hokudai.ac.jp

² *Environmental Material Engineering Laboratory, Faculty of Engineering, Hokkaido University, Sapporo Japan*

Email: takaf@eng.hokudai.ac.jp

³ *Environmental Material Engineering Laboratory, Faculty of Engineering, Hokkaido University, Sapporo Japan*

Email: hashimoto.k@eng.hokudai.ac.jp

ABSTRACT

Decommissioning project is in progress after the disaster of Fukushima Daiichi Nuclear Power plant. Because real deteriorated concrete used in the facilities is not directly investigated due to possible contamination with radioactive substances, a numerical simulation needs to conduct to predict the deterioration. One of deterioration is calcium leaching in concrete in contact with water and then it is necessary to simulate the current condition of leaching-deteriorated concrete. Relatively more porous interfacial transition zone (ITZ) in concrete has an important impact on the leaching process, which makes it crucial to estimate the transport properties of ITZ. In this study the dissolution front of cement hydrates inside concrete specimen was evaluated by synchrotron X-ray microtomography at SPring-8, Japan. A tiny cylindrical specimen with 3mm in diameter and 6mm in height was prepared and a piece of limestone was placed inside the specimen as an aggregate. At a resolution of 2.46 μ m/voxel, CT image analysis was applied with random walk simulation to obtain the diffusion parameters in the cement paste as well as in potential ITZ. Using diffusion coefficients and porosities, a numerical simulation for predicting the dissolution of cement hydrates was conducted. Results of the simulation were verified by CT image in which the validity of the input parameters was indicated. Based on the parameters, a two-dimension multiple aggregate model imitating concrete section was established to predict the leaching behavior of real concrete under immersion. The dissolution front of portlandite after 10 years was calculated to be 6.8 mm. In addition, it was found that the dissolution front penetrates deeper into the concrete along the ITZ region.

KEYWORDS: *Calcium leaching, synchrotron X-ray CT, Interfacial transition zone (ITZ), simulation*

1. Introduction

A number of research on calcium leaching from concrete has been conducted in the past [1][2]. However, little studies have focus on the effect of the ITZ in leaching deterioration. This is because at present, quantitatively obtaining transport parameters of ITZ through experimental method is still difficult. Recently, the effect of ITZ on the dissolution front of the Portlandite in leaching deterioration for hardened cement paste in contact with water was visualized by X-ray computed tomography and X-ray diffraction technique (CT-XRD) [4]. It is expected to further analyse the impact of interfacial transition zone (ITZ) on the alteration process of the concrete. In this study, diffusion properties of ITZ and sound hardened cement paste were identified by coupling CT image and random walk algorithm for lab-cured specimen. Obtained relevant diffusion parameters of the region of interests were verified by numerical calculation based on a modified simultaneous ion transport model (SiTraM) [5]. Two-dimension multiple aggregate model was then established and the dissolution of the Portlandite after 10 years was predicted.

2. Experiment

2.1 Materials and non-accelerated leaching test

Tiny cylindrical cement paste specimens with 3mm in diameter and 6mm in height was prepared for the non-accelerated leaching test. The water to cement ratio of specimens is 0.6, and ordinary Portland cement (OPC) was used. By mass, the oxide composition was 65.01%-CaO, 21.41%-SiO₂, 4.84%-Al₂O₃, 3.20%-Fe₂O₃, 1.08%-MgO, and 2.02%-SO₃. Cement paste was mixed and placed into plastic mold and insert one piece of limestone as aggregate. Specimen was demolded after 24h and then cured by being wrapped in wet towel at 20±2°C for four weeks. Following curing, specimen was submerged in 1cm³ purified water filled in a plastic bottle as solvent for a period of 60 days. Solvent was replaced irregularly according to the amount of leaching calcium ions.

2.2 CT imaging and in-situ XRD measurement

Micro tomographic images of specimen were acquired at a resolution of 2.46µm/voxel using an X-ray computed tomography (CT) system at SPring-8, Japan. Raw images with different angles were obtained by rotating the specimen at 0.12° in each step until a 180° rotation was completed. The details of CT imaging and the integrated non-destructive CT-XRD method in SPring-8 have been described in elsewhere[3].

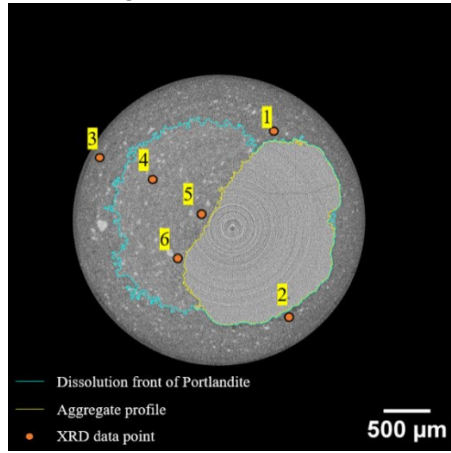


Fig.1 CT image after 60 days leaching

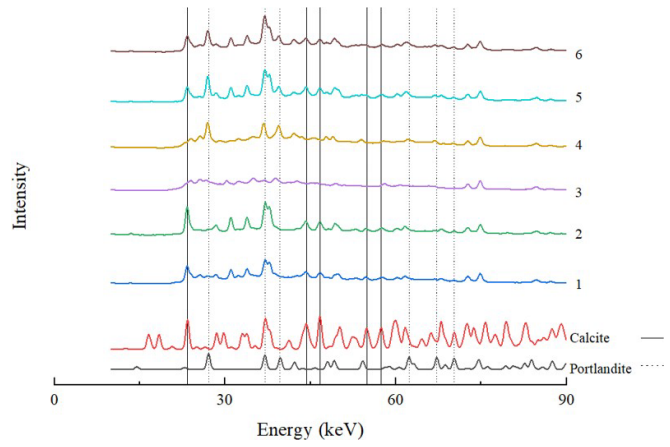


Fig.2 XRD result

Blue and yellow lines in Fig.1 outline regions with different grayscale value (GSV), in which the yellow line region can be easily identified as aggregate according to its shape. Fig.2 shows XRD result of point 1-6 given in the CT image respectively, and reference pattern of portlandite and calcite are also attached. XRD result of point 4,5 and 6 shows distinct signal of portlandite while point 1, 2 and 3 doesn't, which suggests that the blue line marks dissolution front of portlandite. Point 1, 2, 5 and 6 also show distinct signal of calcite, which is due to interference from adjacent aggregate. It should be noted that the dissolution front in the direction away from aggregate (upper left) basically maintains circular shape consistent with the edge of specimen, and where dissolution front contacts with aggregate, the front obviously invades into inner, which is due to presence of ITZ.

3. Numerical Simulation

3.1 Transport parameters

Volume of interest (VOI) was selected from the stack of CT slice images to analyse diffusion properties in ITZ and sound cement paste. Corresponding pore space of VOI can be obtained by thresholding them based on their gray-level histogram. Nakashima[6] has proposed random walk algorithm to quantify the diffusion tortuosity and further calculate diffusion coefficient, as shown in Eq (1):

$$\tau_{\#} = \frac{\#_{\%}}{\#_{\&}} = \frac{\langle (r^2)^{\&} \rangle_{\%}}{\langle (r^2)^{\&} \rangle_{12/0}}; D_4 = \frac{\#_{50}}{67} \quad (1)$$

In which, $\langle r^2 \rangle$ is mean-square displacement (MSD) of walkers, which is a function of lattice time t . Ratio of $\langle r^2 \rangle$ in free space and pore space describes the tortuosity ($\tau_{\#}$) of the pore space. Effective diffusion coefficient D_4 is subsequently calculated by introducing effective porosity (ρ_4) and diffusion coefficient in free water ($D_{<}$). Fig.3 shows the process of extracting pore structure from CT images stack. To analyse diffusion properties of ITZ and sound cement paste regions, VOI A and B were selected. Previous study[4]

shows the diffusion coefficient of region within 50 μ m adjacent to the aggregate is significantly higher than that of sound cement paste region. On basis of this, region within 50 μ m was selected as ITZ.

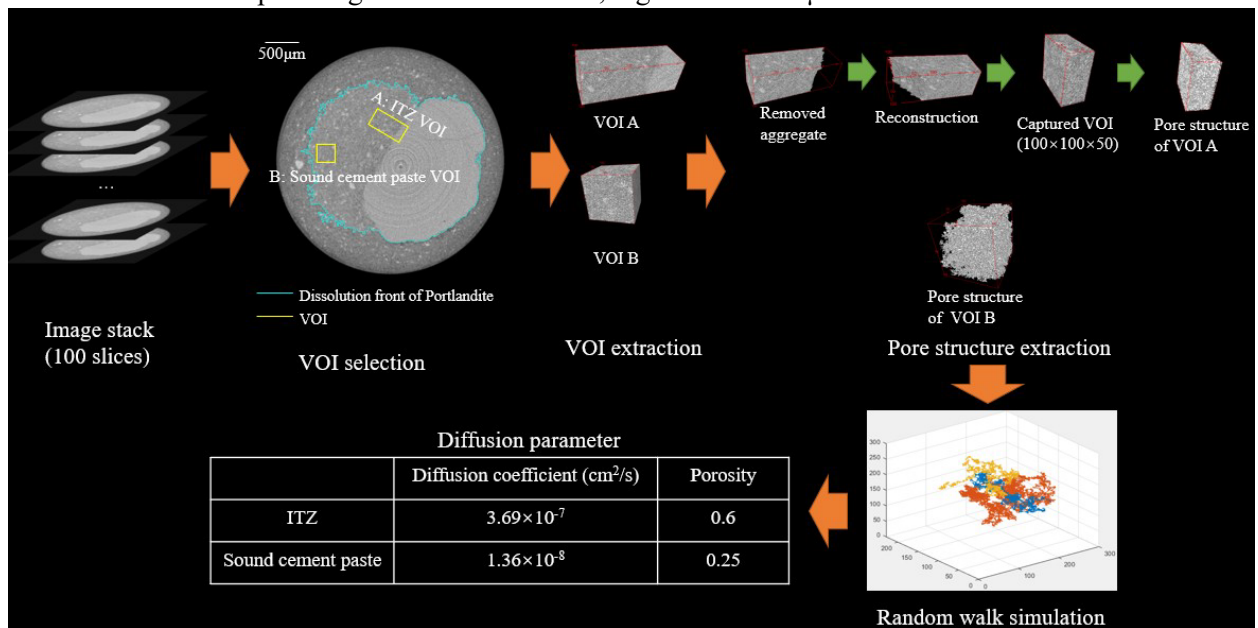


Fig.3 Determination of modelling parameters

3.2 Modelling and result

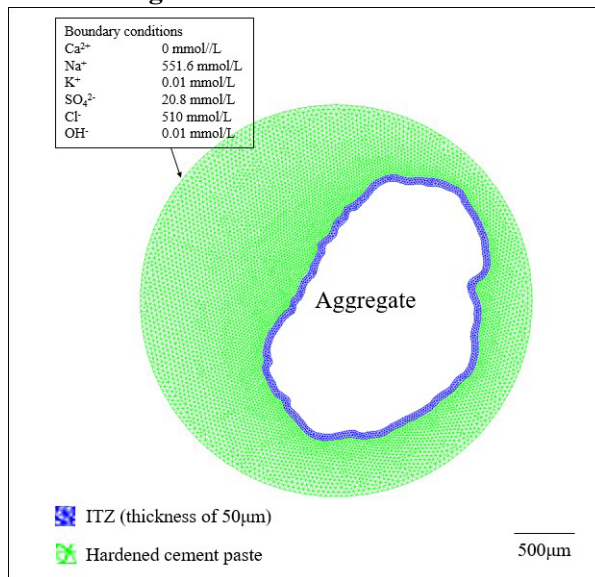


Fig.4 Modelling

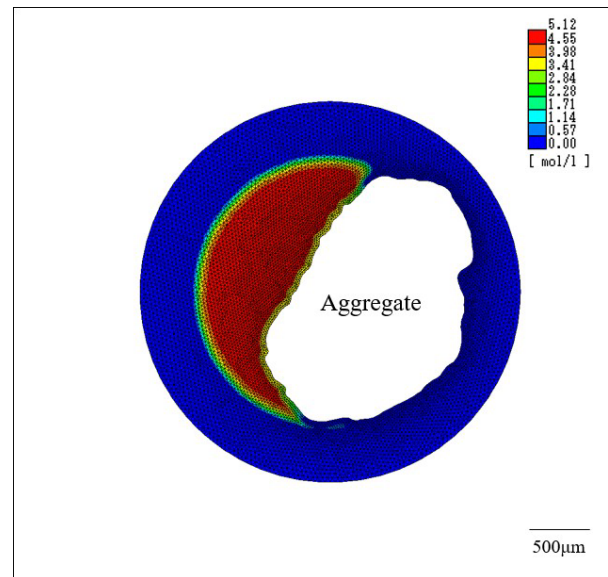


Fig.5 Portlandite in solid phase after 60 days

Numerical simulation allows the calculation of calcium remaining in the hydrated cement paste and update the diffusion coefficient of elements after each calculation step. It is composed of three models, namely Mutual ion diffusion coefficient model, Characterizing pore structure model and ion-solid interaction model. Fig.4 shows modelling mesh, ITZ was set and the ion environment of external solution was set referring to seawater. Leaching in simulation period was set as 60 days, which was consistent with the period in actual leaching experiment. Fig.5 shows portlandite content in solid phase after 60 days leaching. Taking position with half of the maximum portlandite solid phase content as the dissolution front of portlandite, the front in simulation matches well with CT image. Same diffusion parameters were also applied in multiple aggregate model in order to simulate the leaching behaviour of a real concrete material and coordinating result was shown in Fig.6.

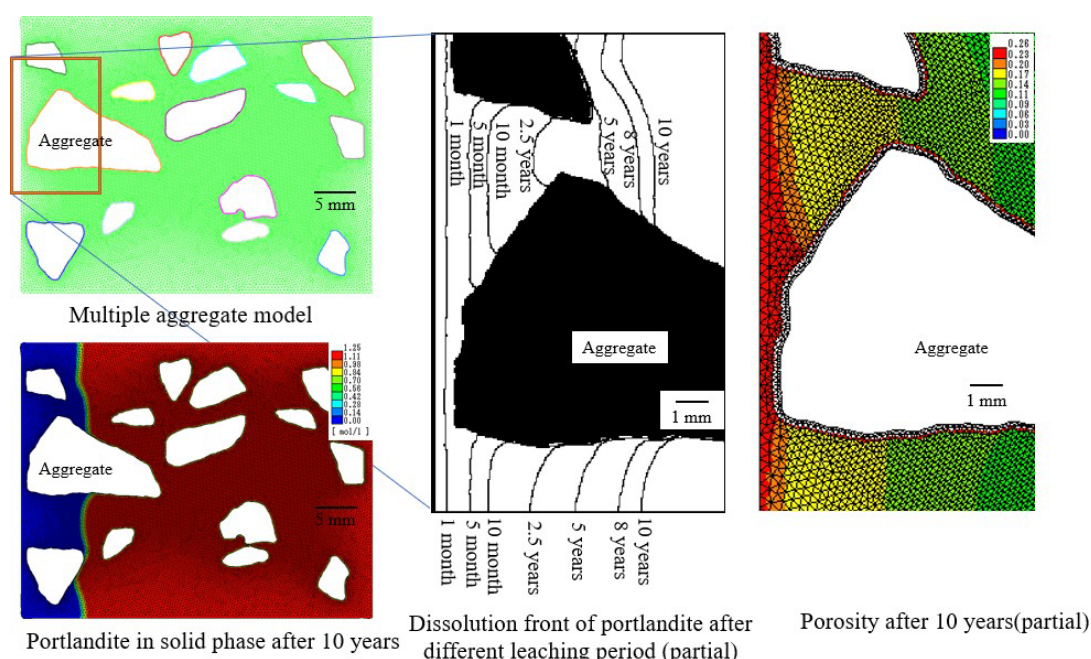


Fig.6 Simulation of multiple aggregate model

4. Conclusion

Using a tiny specimen subjected to 60 days leaching test, the integrated CT-XRD method coupling random walk simulation has successfully quantified the diffusion properties for ITZ and sound cement paste region. Obtained parameters were verified in the numerical simulation that exhibited the similar Portlandite dissolution front to the leaching experiment. Dissolution front in a multiple aggregate model was predicted around 6.8mm after a leaching period of 10 years and to invade into inner region along the ITZ.

Acknowledgements

Part of this research was funded by the Japan Society for Promotion of the Science (JSPS KAKENHI Grant Number 21H01402) and the Nuclear Safety Research Association. The synchrotron radiation experiments were performed at the BL28B2 in SPring-8 with the approval of Japan Synchrotron Radiation Research Institute (Proposal No. 2021B1025, 2022A1662).

References

- [1] Kazuko Haga, Shunkichi Sutou, Michihiko Hironaga, Satoru Tanaka, Shinya Nagasaki. "Effects of porosity on leaching of Ca from hardened ordinary Portland cement paste." *Cement and concrete research* 35.9 (2005): 1764-1775.
- [2] Buil,M., et al.: A Model of the attack of pure water or undersaturated lime solutions on cement, *Stabilization of Hazardous, Radioactive and Mixed Wastes*, Vol.2, pp.227-241, 1992
- [3] Kentaro Uesugi, Yoshio Suzuki, Naoto Yagi, Akira Tsuchiyama, and Tsukasa Nakano. (2001) "Development of high spatial resolution X-ray CT system at BL47XU in SPring-8." *Nuclear Instruments and Methods in Physics Research Section A: Accelerators, Spectrometers, Detectors and Associated Equipment* 467: 853-856.
- [4] Yingyao Tan, Takafumi Sugiyama, Katsufumi Hashimoto. (2023) "Evaluation of transport properties of deteriorated concrete due to calcium leaching with coupled CT image analysis and random walk simulation." *Construction and Building Materials*, 369: 130526.
- [5] Takafumi Sugiyama, Worapatt Ritthichauy, Tsuji Yukikazu. (2008) "Experimental investigation and numerical modeling of chloride penetration and calcium dissolution in saturated concrete." *Cement and Concrete Research* 38(1): 49-67.
- [6] Yoshito Nakashima, and Susumu Kamiya. (2007) "Mathematica programs for the analysis of three-dimensional pore connectivity and anisotropic tortuosity of porous rocks using X-ray computed tomography image data." *Journal of Nuclear Science and Technology* 44.9: 1233-1247.

Assessment of influence of cation type of sulphate ions on early age strength, and microstructure of geopolymer concrete

M. Leela Sai Rangarao^{1*}, and Bulu Pradhan²

¹ Research scholar, Department of Civil Engineering, Indian Institute of Technology Guwahati, Guwahati, India
Email: maradanileela@iitg.ac.in

² Professor, Department of Civil Engineering, Indian Institute of Technology Guwahati, Guwahati, India
Email: bulu@iitg.ac.in

ABSTRACT

The major objective of this investigation is to study the influence of chloride-sulphate salts on workability, compressive strength, and microstructure of geopolymer concrete (GpC). GpC was prepared with fly ash and ground granulated blast furnace slag as precursor materials (at proportions of 100%/0% and 65%/35%). The GpC was activated with an alkaline solution comprising of sodium hydroxide solution (12 M concentration) and sodium silicate solution. The GpC mixes were admixed with blended salts i.e., 3.5% sodium chloride with 5% sodium sulphate, and 3.5% sodium chloride with 5% magnesium sulphate. The compressive strength test was done at the early age of 7 days. The microstructural investigations were conducted on GpC powder samples through X-ray diffraction (XRD), and Field emission scanning electron microscope (FESEM) analyses. The sulphate ion concentration of GpC was also determined to assess the effect of associated cation type on sulphate concentration. The results showed, sulphate ions associated with Mg²⁺ cation resulted in lower strength as compared to that associated with Na⁺ cation. The concentration of sulphate ions in GpC was lower in case of Mg²⁺ cation than Na⁺ cation. The microstructure analysis indicated the formation of halite and gypsum in salt admixed GpC. The formation of less dense microstructure in GpC in the presence of admixed salts was observed from FESEM, this is consistent with the variations in strength of GpC.

KEYWORDS: *Geopolymer concrete, Fly ash, Ground granulated blast furnace slag, Sulphate, Microstructure.*

1. Introduction

After water, Portland cement is the second most consumed product throughout the world. Recent studies have found that approximately 5% of global CO₂ emissions are due to production of OPC (Deb et al. 2014). To overcome this problem either Portland cement has to be partially or completely replaced. The complete replacement of Portland cement can be achieved by using geopolymer binder. Geopolymers are produced by combination of alumino-silicate materials such as granulated blast furnace slag, and fly ash with alkali solutions. The subsequent aluminium and silica oxides further continue polymeric reactions to form 3-dimensional aluminosilicate network (Mehta and Siddique 2017). Geopolymer binders exhibit high compressive strength, fire resistance, and optimum acid resistance. Before implementation of GpC in field applications, it is necessary to investigate the behaviour of concrete toward aggressive environment. Most of the literature discussed about chloride (Cl⁻) ion concentration in fly ash and fly ash-ground granulated blast furnace slag GpC mixes (Gunasekara et al. 2019, Chindaprasirt and Chalee 2014). There are very few studies available in literature that discussed about the variation in sulphate ion concentration in GpC. The study on variation in sulphate (SO₄²⁻) ion concentration is also essential because sulphate attack, a serious durability problem, causes concrete deterioration. The objective of present research investigation is to study the influence of admixed salt on workability, compressive strength, SO₄²⁻ ion concentration, and microstructural properties of fly ash (FA), FA and ground granulated blast furnace slag (GBFS) GpC.

2. Materials and test methods

2.1 Materials used in production of GpC mixes

FA, and GBFS (used at 0% and 35% by mass of precursor material) were used as precursor materials, and mixture of sodium hydroxide solution (12 M concentration) along with sodium silicate solution (Na_2O : 8%, and SiO_2 : 26.5%) was used as alkaline solution. In addition, fine aggregate (river sand) and coarse aggregate (blend of 10 mm and 20 mm maximum size aggregate) were used in the preparation of GpC. To study the influence of cation type of sulphate ions in GpC, the mixes were admixed with blend of salts i.e., 3.5% sodium chloride (NaCl, NC) with 5% sodium sulphate (Na_2SO_4 , NS), and 3.5% NC with 5% magnesium sulphate (MgSO_4 , MS), by the mass of geopolymer solids i.e., total mass of precursor materials and solids content present in the alkaline solution. The liquid content and mass ratio of sodium silicate to sodium hydroxide solutions were kept constant in the preparation of GpC i.e., 210 kg/m^3 , and 1.5 respectively.

2.2 Test methods

2.2.1 Workability, compressive strength test, and preparation of pore solution

Workability of freshly prepared GpC was determined by performing a slump test. Subsequently, 150 mm cubes were prepared from fresh GpC mixes. After 24 h, GpC cubes made with fly ash and GBFS were demoulded and left to ambient room condition till the age of testing, whereas the fly ash GpC cubes were left to ambient room condition for 48 h from casting and then placed in oven at 80° C for another 48 h, followed by demoulding and storing in ambient room condition till the age of testing. GpC cubes were tested for compressive strength at 7 days age. After compressive strength test, fragments of GpC cube were collected and grounded. The grounded powder was passed through 75 μm sieve and sieved powder was used to prepare GpC pore solution. The GpC powder was mixed in a 1:1 mass proportion with distilled water and stirred with a magnetic stirrer with simultaneous heating on a hot plate. The powder solution was allowed to settle and cool to room temperature, and filtrated through Whatman no. 1 filter paper. The filtered GpC powder pore solution was used to determine SO_4^{2-} ion concentration by using turbidimetric method as per American Public Health Association (APHA 2005).

2.2.2 Microstructure studies on GpC

The XRD and FESEM analyses were conducted as part of microstructure studies on GpC powder. The XRD was conducted in 9 kW model Rigaku SmartLab, with a scan range of 5° to 60° (2 θ) and step size was taken as 0.03° 2 θ . Morphology of GpC was conducted by using FESEM: ZEISS Gemini model.

3. Results and discussion

3.1 Workability, compressive strength, and sulphate ion concentration in GpC

The slump values of GpC mixes are depicted in Figure.1(a). The slump values of FA/GBFS GpC mixes were lower than fly ash GpC mixes. This was due to angular shaped particles of GBFS than spherical particles of fly ash that led to decrease in workability of FA/GBFS GpC mixes. GpC admixed with salt had greater slump values than control mixes, which was due to higher mobility of particles in salt admixed GpC. The variation in slump values is as follows, control < 3.5% NC with 5% NS < 3.5% NC with 5% MS. Figure 1(b) shows 7-day compressive strength of GpC mixes. It was noted that the strength of FA/GBFS GpC mixes was greater than FA GpC mixes. This was due to the influence of higher calcium (Ca) content of GBFS that led to development of greater amount of calcium (Ca) based binding gels in FA/GBFS GpC. GpC admixed with salt had lower strength than control GpC mixes. The variation in strength of GpC mixes is as follows, 3.5% NC with 5% MS < 3.5% NC with 5% NS < control GpC mix. The decrease in strength of salt admixed GpC could be ascribed to the effect of salt crystallization in geopolymer system, which led to hindering of the geopolymerization process. It was found that the mixes admixed with 3.5% NC and 5% MS exhibited strength loss (%) of 45.66% in FA GpC mixes and 48.26% in FA/GBFS GpC mixes as compared to control mix.

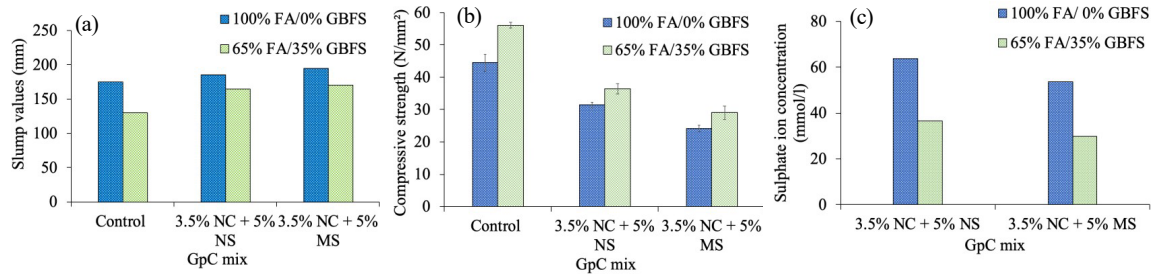


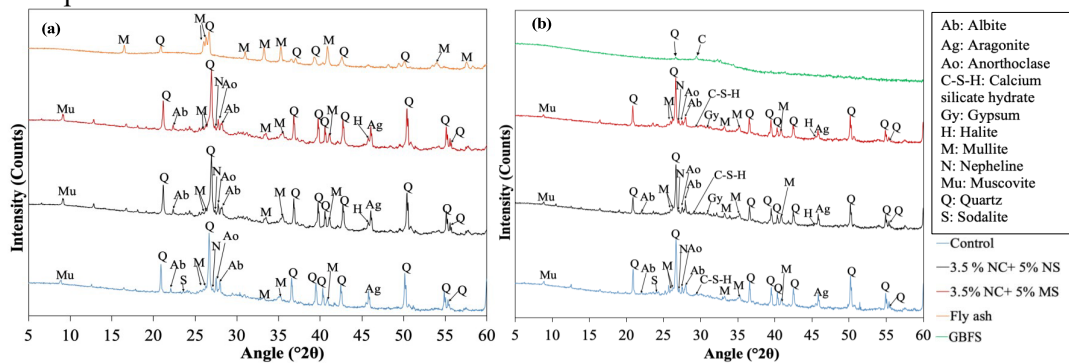
Figure 1. Workability, compressive strength, and SO_4^{2-} ion concentration in pore solution of GpC mixes: (a) slump value, (b) compressive strength, (c) SO_4^{2-} ion concentration.

The SO_4^{2-} ion concentration of concrete powder pore solution made from salt admixed GpC mixes are shown in Figure. 1(c). The SO_4^{2-} ion concentration was more in pore solution made of FA GpC than FA/GBFS GpC. This could be attributed to the reaction of SO_4^{2-} ion with calcium oxide (CaO) present in GBFS that resulted in formation of gypsum thereby reducing SO_4^{2-} ion concentration in pore solution made from FA/GBFS GpC. It was observed that the concentration of SO_4^{2-} ions was lower in the mixes with 3.5% NC with 5% MS than that GpC admixed with 3.5% NC with 5% NS. This is due to the effect of cation type related with SO_4^{2-} ions, which could have altered the concentration of SO_4^{2-} ion in the pore solution.

3.3 Microstructural analysis of GpC

3.3.1 X-ray diffraction analysis of GpC

The XRD plots of precursor materials i.e., FA and GBFS, and different GpC mixes are depicted in Figure 2. The crystalline phases of quartz and mullite were observed in XRD plots of FA, GBFS, and as well as in all the GpC mixes. In addition, semi-crystalline phases of muscovite, sodalite, albite, anorthoclase, and nepheline were found in all the XRD plots of GpC mixes, which indicates the formation of geopolymeric compounds in the GpC mixes as compared with the XRD plots of precursor materials. Further, the C-S-H gel peak was identified in FA/GBFS GpC. From Figure 2, the peaks corresponding to nepheline, albite and anorthoclase were mostly greater in FA/GBFS GpC than FA GpC mixes irrespective of addition of salts. The presence of GBFS enhanced the extent of geopolymerization and led to development of more amount of nepheline, anorthoclase, and albite leading to higher strength of FA/GBFS GpC (Figure 1(b)). Mehta et al. (2020), also stated that the geopolymeric compounds improves the microstructure, and the strength of FA/GBFS GpC.



From Figure 2, in case of salt admixed GpC, albite and anorthoclase peak intensities were decreased in FA GpC, and in FA/GBFS GpC, the peak intensities of nepheline, anorthoclase, and C-S-H gel were reduced than respective control GpC. It was found that the GpC admixed with 3.5% NC with 5% MS had lower peak intensity of geopolymeric compounds when compared with that admixed with 3.5% NC with 5% NS. The same pattern was found in both FA, and FA/GBFS GpC mixes. Gypsum peak was identified in XRD plots of salt admixed FA/GBFS GpC, which was ascribed to the reaction between CaO in GBFS with SO_4^{2-} ion from admixed salts. Further, FA/GBFS GpC admixed with 3.5% NC with 5% MS had higher gypsum peak intensity than GpC admixed with 3.5% NC with 5% NS. The halite peak was observed in all XRD plots of GpC admixed with salt. It was found, GpC admixed with 3.5% NC with 5% MS had higher halite peak intensity than the mixes admixed with 3.5% NC with 5% NS. Halite formation was attributed to the

crystallization of added NaCl in the mix, which might have hindered the geopolymerization reaction. As a result, the peak intensity of geopolymer compounds were decreased and reduced the strength (Figure 1(b)).

3.3.2 FESEM analysis

Typical FESEM micrographs of FA and FA/GBFS GpC mixes are illustrated in Figure 3. FESEM micrographs showed the existence of unreacted and partly reacted FA particles in both FA and FA/GBFS GpC. In addition, partially reacted GBFS particles were also found in FA/GBFS GpC mixes. Further, it was observed that the geopolymer gel formation was more in FA/GBFS GpC mixes than FA GpC mixes. This corroborates the results obtained from compressive strength test and XRD analysis of GpC. Mehta et al. (2020), also found that the addition of GBFS led to the formation of dense microstructure in FA/GBFS GpC mix than FA based GpC mix. From Figure 3(c), halite and gypsum crystals were identified in FESEM micrographs of FA/GBFS GpC admixed with salt. The existence of gypsum crystals in FA/GBFS GpC mixes admixed with salt indicates that the calcium oxide present in GBFS reacted with SO_4^{2-} ions from admixed salt and formed gypsum. The micrograph of salt admixed GpC mix (Figure 3(c)) showed voids and less dense microstructure as compared to control GpC mix (Figure 3(b)), which is in line with the results of XRD analysis and strength.

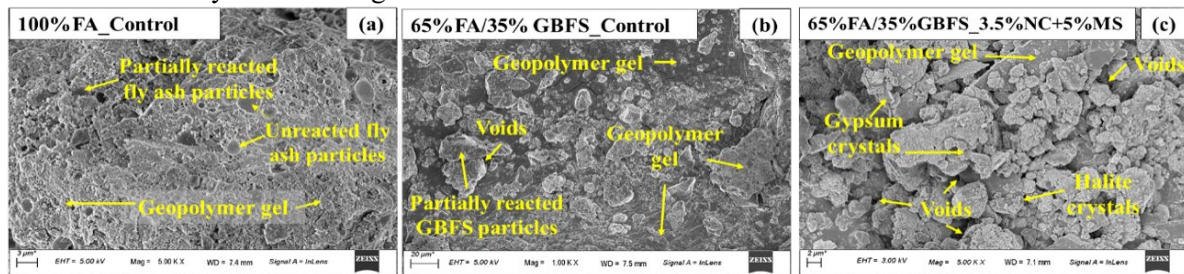


Figure 3. FESEM micrographs: (a) Control FA GpC mix, (b) Control FA/GBFS GpC mix, and (c) FA/GBFS GpC admixed with 3.5% NC with 5% MS.

4. Conclusions

The significant conclusions that are derived from the present research investigation are as follows:

- FA GpC mixes had attained lower compressive strength than FA/GBFS GpC. Further, compressive strength was reduced in GpC admixed with salt as compared to control GpC mix.
- The SO_4^{2-} ion concentration of pore solution was greater in FA GpC mix. The mix admixed with 3.5% NC with 5% NS had higher SO_4^{2-} ion concentration than that admixed with 3.5% NC with 5% MS.
- From XRD analysis, nepheline, anorthoclase, and albite peak intensities were increased due to presence of GBFS in GpC mixes. FA GpC mixes showed lower peak intensities related to anorthoclase and albite, and FA/GBFS GpC mixes indicated lower peak intensities corresponding to nepheline, anorthoclase, and C-S-H gel in the presence of salts.
- The FESEM micrograph indicated less dense microstructure in salt admixed GpC mix than control mix.

References

- A. Mehta and R. Siddique, "Strength, permeability and micro-structural characteristics of low-calcium fly ash based geopolymers," *Constr Build Mater*, vol. 141, pp. 325–334, Mar. 2017.
- A. Mehta, R. Siddique, T. Ozbakkaloglu, F. U. A. Shaikh, and R. Belarbi, "Fly ash and ground granulated blast furnace slag-based alkali-activated concrete: Mechanical, transport and microstructural properties," *Constr Build Mater*, vol. 257, pp. 119548, May. 2020.
- C. Gunasekara, D. Law, S. Bhuiyan, S. Setunge, and L. Ward, "Chloride induced corrosion in different fly ash based geopolymer concretes," *Constr Build Mater*, vol. 200, pp. 502–513, Dec. 2019.
- P. S. Deb, P. Nath, and P. K. Sarker, "The effects of ground granulated blast-furnace slag blending with fly ash and activator content on the workability and strength properties of geopolymer concrete cured at ambient temperature," *Mater Des*, vol. 62, pp. 32–39, May. 2014.
- P. Chindaprasirt and W. Chalee, "Effect of sodium hydroxide concentration on chloride penetration and steel corrosion of fly ash- geopolymer concrete under marine site," *Constr Build Mater*, vol. 63, pp. 303–310, Jul. 2014.
- Standard Methods for the Examination of Water and Wastewater, 21st edition, APHA, Washington, 2005.

Antimicrobial performance of ZnO-modified geopolymer against microbial corrosion

Xiaojuan Kang¹, and Hailong Ye^{2*}

¹ University of Hong Kong, Hong Kong, China

Email: kangxiaojuan@connect.hku.hk

² University of Hong Kong, Hong Kong, China

Email: hlye@hku.hk

ABSTRACT

The ZnO-modified geopolymer is a new generation of biologically resistant construction materials that show great promise in wastewater infrastructure threatened by microbially induced concrete corrosion. The ZnO nanoparticles serve as the antibacterial agents in alkali-activated metakaolin geopolymer, with the aims of structuring and incorporating Zn into the framework of sodium-aluminosilicate-hydrates (N-A-S-H) gel during geopolymerisation. This study reveals the nanostructure of Zn-doped N-A-S-H gel in metakaolin-based geopolymers, as well as its antibacterial performance. The results demonstrate a nearly doubled reaction degree in ZnO-modified geopolymer than neat geopolymer sample, owing to the seeding effect of nanoparticles that facilitates the nucleation and precipitation of (N, Zn)-A-S-H gel. Higher proportion of Q⁴(4Al) and Q⁴(3Al) leads to higher Al/Si ratio of N-A-S-H in ZnO-modified geopolymer. The assessments of bacterial activity and the reduction in corrosion depth prove that ZnO-modified geopolymer has a significant bactericidal effect and is effective in inhibiting the production of biogenic sulfuric acid by sulphur oxidising bacteria *A.thiooxidans*. The results of this research could contribute to the development of eco-friendly and more durable civil engineering material for next-generation wastewater infrastructure.

KEYWORDS: *N-A-S-H gel, antibacterial geopolymer, A. thiooxidans, MICC, microbial corrosion.*

1. Introduction

The microbial induced concrete corrosion (MICC) is commonly encountered in sewers, where the activity of microorganisms produces biogenic acids that deteriorate the concrete structure of the sewer (Grengg et al 2020). Ordinary Portland cement (OPC) is the most widely used and heavily used construction material in sewerage facilities at present. Biogenic sulphuric acid attack dominated by sulphur oxidising bacteria causes decalcification of the concrete and produces gypsum which reacts with residual C₃A to form expanded ettringite (Ding et al 2017). Eroded and damaged concrete structures in sewers can lead to sewage leaks which can be a public health hazard and require significant annual maintenance and repair costs, for example over HK\$7.5 billion per year in Hong Kong (Kang and Ye 2022). The choice of durable, cost-effective, and environmentally friendly construction materials for sewerage facilities is a trend for the future of construction. Geopolymers are green, innovative alkali-activated inorganic materials with relatively low carbon emissions and are recognised as having better chemical stability than OPC (Walkley et al 2016). However, current research on geopolymers with antimicrobial functionality is limited. In this work, a newly developed ZnO-modified geopolymer is proposed and aims to structure and incorporate Zn into the framework of N-A-S-H gel during geopolymerisation process to serve as an antimicrobial geopolymer. The geopolymers have a stronger biocidal effect and may become a new binder system for durable and green concrete infrastructure resistant to MICC.

2. Materials and methods

2.1 Raw materials

Metakaolin was used for the preparation of antibacterial geopolymer. The XRD diffractogram of unreacted metakaolin was provided in Fig. 1a. There is a hump centered at $23^\circ 2\theta$, which is attributed to the amorphous metakaolin. Trace amounts of anatase and quartz can be found in the unreacted metakaolin. The oxide composition of metakaolin was 52.57% SiO_2 , 44.38% Al_2O_3 , and 3.05% other oxides. ZnO nanoparticles (Alfa Aesar) was used as the antibacterial agent in this experiment.

2.2 Sample preparation

Metakaolin-based geopolymer was prepared by mixing metakaolin powder and alkali solution, which was obtained by dissolving sodium silicate with a modulus of 2.58 and sodium hydroxide (Uni-chem). The geopolymers were prepared in the following molar ratios of oxides: $\text{Na}_2\text{O}/\text{Al}_2\text{O}_3=1$, $\text{SiO}_2/\text{Al}_2\text{O}_3=4$, $\text{H}_2\text{O}/\text{Al}_2\text{O}_3=14.7$. The addition of ZnO nanoparticle was 1.0 wt.% of metakaolin, which was added after the pre-mixing of neat geopolymer paste. The obtained geopolymers were cured in sealed specimen tubes for 24 h under 60°C and then stored for six months under 25°C .

2.3 Microbial corrosion setup

A.thiooxidans (DSM 504) was used as the sulphur oxidising bacteria in the simulated microbial corrosion, which was cultivated with a liquid medium (Medium 35) and S^0 as the energy source. *A.thiooxidans* converted S^0 to biogenic sulfuric acid (H_2SO_4). Epoxy was used to wrap the cylindrical samples except for one side which was left as the exposed surface. The samples were suspended in a bacterial solution with an initial pH of 2.0 and placed in a shaker (25°C , 100 rpm) for one month for biogenic sulfuric acid attack as shown in Fig. 1b.

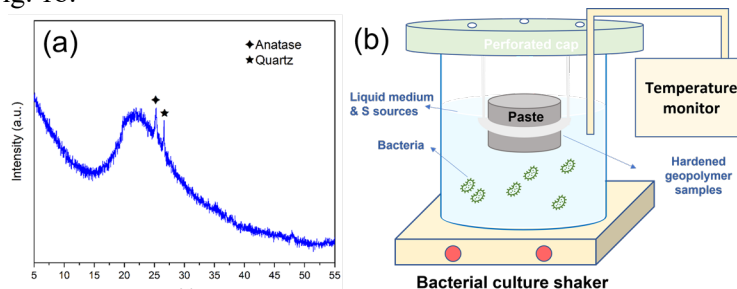


Figure 1 (a) XRD pattern of unreacted metakaolin. (b) Microbial corrosion setup.

3. Results and discussion

3.1 Nanostructure of ZnO-modified geopolymer

The XRD results and deconvolution results of ^{29}Si NMR spectra of geopolymers are shown in Fig.2. The hump at $\sim 26^\circ 2\theta$ (Fig. 2a) is attributed to amorphous N-A-S-H gel, which is the predominant reaction phase in geopolymers. A small amount of zeolite X can be found in geopolymers. Fig. 2b gives the chemical environment information of ^{29}Si NMR spectra. It is obvious that the unreacted MK is dominant by $\text{Q}^4(0\text{Al})$ resonance. After geopolymerisation process, $\text{Q}^4(4\text{Al})$, $\text{Q}^4(3\text{Al})$, $\text{Q}^4(2\text{Al})$, and $\text{Q}^4(1\text{Al})$ resonances appear. The remaining $\text{Q}^4(0\text{Al})$ of ZnO-modified geopolymer is much smaller than R, indicating a nearly double reaction degree than R, which is attributed to the seeding effect of ZnO nanoparticles. Higher proportion of $\text{Q}^4(4\text{Al})$ and $\text{Q}^4(3\text{Al})$ signals can be detected in ZnO-modified geopolymer compared with R, leading to a higher Al/Si molar ratio of N-A-S-H gel.

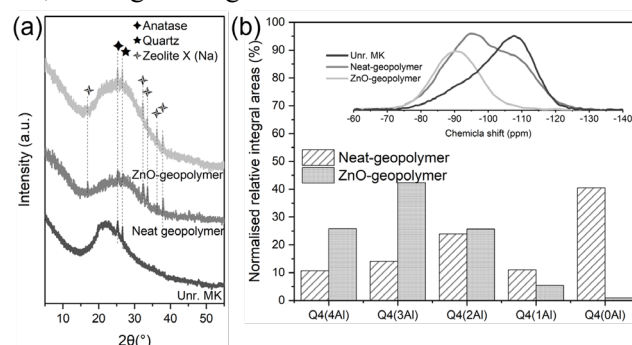


Figure 2 (a) XRD results of geopolymers. (b) ^{29}Si NMR spectra and corresponding deconvolution results.

3.2 Antimicrobial performance of ZnO-modified geopolymer under microbial corrosion

The fluorescent staining image of surrounding bacterial solutions are present in Fig. 3. The spatial distribution of microorganisms in neat geopolymer (Fig. 3a) is dominant by live bacteria with a small amount of dead bacteria. However, fluorescence staining image of ZnO (Fig. 3b) shows that most of the bacteria are dead, demonstrating that the addition of ZnO nanoparticles is effective in killing the sulphur-oxidising bacteria. The decreasing live/dead ratio of bacteria confirms the antibacterial property of ZnO-modified geopolymer when subjected to biogenic attack. In Fig. 3c, the corrosion depth of ZnO-modified geopolymer is reduced by a factor of 4 compared to R, demonstrating the excellent antibacterial properties of ZnO nanoparticles.

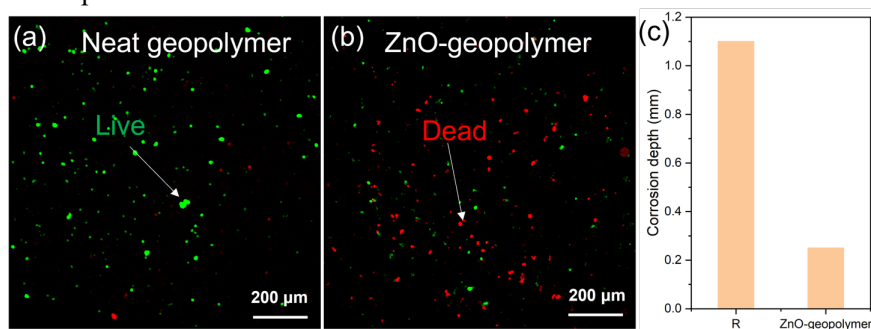


Figure 3 Spatial distribution of live and dead bacteria of the surrounding bacterial solutions of (a) neat geopolymer and (b) ZnO-modified geopolymer. (c) Corrosion depth of geopolymers.

A slight decrease in the pH value of surrounding bacterial solutions in neat geopolymer can be found in Fig. 4a. Because sulphur oxidising bacteria *A.thiooxidans* converts S^0 to biogenic sulfuric acid (H_2SO_4) and acidifies the solution. An upward trend in pH value can be detected in ZnO-modified geopolymer, indicating that the sulphur oxidising bacteria have stopped or reduced their bacterial activity to produce biogenic sulphuric acid, consequently the alkaline samples continue to leach alkali ions and the pH of the bacterial solution increases. In Fig. 4b, the concentration of sulphate in the bacterial solution is directly related to the activity of the bacteria because *A.thiooxidans* produce sulphate. Sulphate concentrations in the R group increase with microbial corrosion, indicating a continuous accumulation of sulphate due to ongoing bacterial activity. However, the tendency for the sulphate of ZnO-modified geopolymer to remain constant after 6 d demonstrates the effectiveness of the antibacterial effect of ZnO nanoparticles in inhibiting the production of sulphate by bacterial activity. The optical density measured at 60 nm wavelength (OD_{600}) by ultraviolet-visible spectroscopy (UV-VIS) is an important indicator for the bacterial activity in Fig. 4c. In reference group, the OD_{600} increases with increasing biogenic corrosion time, which indicates an increasing bacterial concentration and active bacterial activity. However, the ZnO-modified geopolymer shows the opposite trend, with OD_{600} values decreasing with biogenic attack. This indicates a decreasing bacterial concentration, which is also consistent with the fluorescent staining results, where the addition of ZnO nanoparticles reduces the concentration of live bacteria.

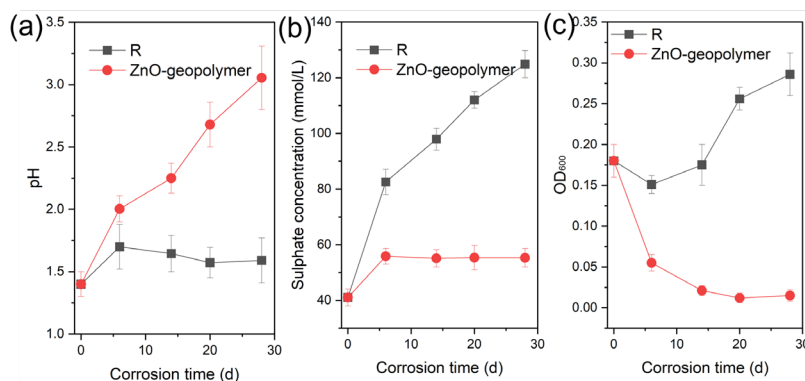


Figure 4 (a) pH, (b) OD_{600} , and (c) sulphate concentration evaluations of surrounding bacterial solutions.

3.3 Phase evaluations of ZnO-modified geopolymer under microbial corrosion

The phase evaluations of antibacterial geopolymers under microbial corrosion are shown in Fig. 5. N-A-S-H is the main reaction product of geopolymer as shown in Fig. 5a. Comparison of the non-MICC samples of R and ZnO-modified geopolymer shows that the DTG peak of N-A-S-H of ZnO-modified geopolymer is much higher than that of R, which is consistent with the NMR findings. After one month of simulated MICC corrosion, the DTG peaks of the N-A-S-H of the antimicrobial geopolymers are reduced and shifted towards higher temperatures due to the breakage of the Si-O-Al and Si-O-Zn network bonds under bio-sulphuric acid corrosion, resulting in the formation of siliceous structures. The chemical bond information of geopolymers is provided in Fig. 5b. Comparison of the R and ZnO-modified geopolymer samples after MICC reveals a shift towards the higher wavenumbers of the Si-O-T bond (T for Si or Al) of ZnO-modified geopolymer, confirming that the loss of Al under biogenic sulphuric acid attack allows for a structural change in N-A-S-H gel.

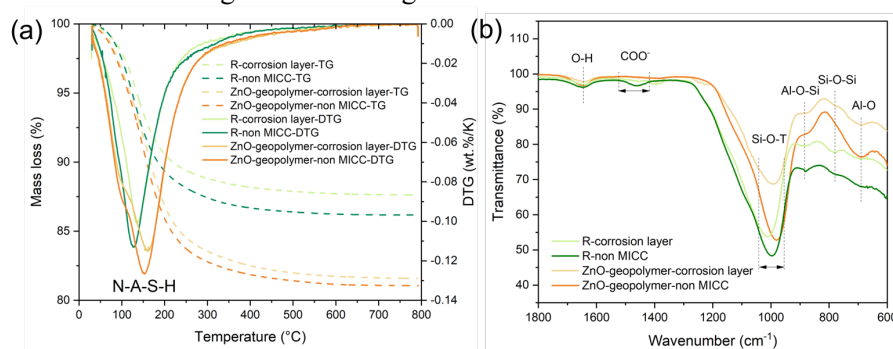


Figure 5 TGA and FTIR results of corrosion layer and non-MICC samples.

4. Conclusions

A newly designed antimicrobial metakaolin-based geopolymer is proposed and its nanostructure and antimicrobial properties are investigated in this work. The main findings can be drawn as follows.

(1) The ZnO nanoparticles dramatically increase the reaction degree (up to 99.1%) of metakaolin and increase the $Q^4(4Al)$, $Q^4(3Al)$ and Al/Si ratio of N-A-S-H gel owing to the seeding effect to facilitate nucleation.

(2) The ZnO-modified geopolymer shows excellent antimicrobial efficacy in inhibiting the bacterial activity of *A.thiooxidans*, which is evidenced by increasing pH value, decreasing sulphate concentration, OD₆₀₀ value and corrosion depth compared to neat geopolymer.

(3) The shifts of DTG peak of N-A-S-H and the Si-O-T bond in FTIR demonstrate a structural alteration of N-A-S-H under biogenic sulfuric acid attack.

References

- Ding, L., W. J. Weiss and E. R. Blatchley. (2017) "Effects of concrete composition on resistance to microbially induced corrosion", *Journal of Environmental Engineering*, 143(6): 04017014.
- Grengg, C., N. Ukrainczyk, G. Koraimann, B. Mueller, M. Dietzel and F. Mittermayr. (2020) "Long-term in situ performance of geopolymer, calcium aluminate and Portland cement-based materials exposed to microbially induced acid corrosion", *Cement and Concrete Research*, 131: 106034.
- Kang, X. and H. Ye. (2022) "Antimicrobial performance and biodeterioration mechanisms of alkali-activated slag", *Cement and Concrete Research*, 158: 106844.
- Walkley, B., R. San Nicolas, M.A. Sani, J. D. Gehman, J. S. van Deventer and J. L. Provis. (2016) "Phase evolution of Na₂O-Al₂O₃-SiO₂-H₂O gels in synthetic aluminosilicate binders", *Dalton Transactions*, 45(13): 5521-5535.

Cold Water Extraction as a method to determine the free alkali content of cementitious binders

M. Ranger^{1,2*}, M.T. Hasholt², and R.A. Barbosa³

¹ *Department of Environmental and Resource Engineering, Technical University of Denmark, Kgs. Lyngby, Denmark*

Email: maug@dtu.dk

² *Danish Road Directorate, Copenhagen, Denmark*

Email: math@vd.dk

³ *Danish Technological Institute, Taastrup, Denmark*

Email: riba@teknologisk.dk

ABSTRACT

The alkali content (Na₂O and K₂O) of cement is of major importance when evaluating the risk of developing Alkali-Silica Reaction (ASR) in concrete. During hydration, alkali metals (Na and K) can either be bound to unreacted particles, bound to hydrates, or free in the pore solution. The latter category is the most critical one with respect to ASR, but its quantification remains more complex than the total content.

Blended cements containing e.g. fly ash or calcined clay are known to have less free alkalis than ordinary Portland cement, despite a larger total amount. Thus, using the total content to classify cements or calculate the alkali loading of a concrete mix may result in irrelevant figures regarding ASR. A procedure enabling to quantify free alkalis, which can be performed in most cement laboratories, would therefore be a useful tool.

This paper introduces the possibility to use Cold Water Extraction (CWE) as a method to determine the free alkali content of a cementitious binder. CWE is a technique aiming at extracting the pore solution of hardened samples, which can be performed with standard laboratory equipment. Three different cement types were investigated: a CEM I, a CEM II/B-M (35 % clinker replacement) and a prototype CEM II/C-M (50 % clinker replacement), all manufactured with the same clinker. The more traditional Pore Water Extraction method was also performed to benchmark CWE results. The free alkali content was determined after performing extraction on paste samples cured for 28 days at 20°C. Both methods indicated the same trends, namely lower relative and absolute free contents for blended cements compared to CEM I. The results were also in agreement with expansions obtained with the Danish accelerated mortar bar test (TI-B 51), which is currently prescribed in the Danish standards when total alkalis requirements cannot be met.

KEYWORDS: *Alkalies, Alkali-Silica Reaction, Blended Cement, Cold Water Extraction*

1. Introduction

Alkali-Silica Reaction (ASR) is a well-known concrete deterioration mechanism which can severely affect structures. ASR requires the presence of a reactive aggregate, a high alkali content (Na₂O and K₂O) and a high relative humidity. If the use of reactive aggregates cannot be avoided, a typical prevention measure consists in keeping the pH low by limiting the alkali content of the binder, see Fournier and Bérubé (2000). Even though the pH (or [OH⁻]) is often mentioned as the key driving factor of ASR, it is known that the chemistry of the pore solution can often be described by $[Na^+] + [K^+] \approx [OH^-]$, see for instance Kasaniya and Thomas (2022). Thus, it seems reasonable to use the sum of alkali metals ions (referred to as “free”) as an estimate of the hydroxide ion concentration. However, one must be careful with such assumption, in particular when other ions are present in significant amounts (e.g. Cl⁻ or SO₄²⁻). While the total alkali content is routinely determined when manufacturing cementitious materials (e.g. by X-Ray Fluorescence, XRF),

the free alkali content requires to extract the pore solution and determine its alkali metal content. Plusquellec et al. (2017) published a review on the different methods related to this topic. The so-called “Pore Water Extraction” method (PWE) is the most common procedure in the literature, but it requires a specific and expensive equipment able to squeeze out the pore solution from a hardened sample. The complexity of the setup therefore limits its use outside research laboratories. An alternative to PWE is the “Cold Water Extraction” method (CWE), which consists in leaching a crushed sample into an extraction liquid with basic laboratory equipment. Both methods allow to calculate either the concentration in the pore solution or the free content of alkali metals, however the amount of pore solution may greatly affect the results, see Tuinukuafe et al. (2022) and Ranger et al. (2023).

As long as Portland cement is used, the ratio between free and total alkalis is rather constant, previous studies reporting values between 60 to 80%, see Ranger et al. (2023). However, the ratio changes significantly when blended cement is used, as supplementary cementitious materials (SCMs) are known to have a larger total alkali content than Portland cement but a lower free content due to alkali metal binding on hydration products. Using the total alkali content across all types of cements may therefore result in serious inconsistencies between the declared value and the ASR performance of the binder.

In Denmark, the standard DS/INF 135 is used to classify cements into four categories depending on the total alkali content of the clinker: extra low (≤ 0.4 wt.% $\text{Na}_2\text{O}_{\text{eq}}$), low (≤ 0.6), moderate (≤ 0.8) and high (> 0.8). This rule applies to CEM I, CEM II/A-V and B-V, and CEM II/A-M and B-M. For other binders, ASR documentation is required via the Danish accelerated mortar bar test (TI-B 51, immersion in a saturated NaCl solution for 8 or 20 weeks).

2. Research significance

Because of the complexity to determine the free alkali content, the total content is generally the default parameter in ASR regulations. However, the total alkali content does not correlate with ASR expansion when blended cements are used. Thus, this work investigates the possibility of using CWE to determine the free alkali content of a cementitious binder, to allow a more fair comparison between Portland cements and blended cements. The study also focuses on using a method that can be applied at an industrial scale.

3. Materials and methods

Three binders were investigated: a CEM I, a CEM II/B-M and a prototype CEM II/C-M (respectively 35 and 50 % clinker replacement with calcined clay and limestone), all produced with the same clinker. The chemical composition of the cements measured by XRF is given in Table 1.

Table 1: Chemical composition of the cements (determined by XRF).

| Oxide | CEM I | CEM II/B-M | CEM II/C-M |
|---|-------|------------|------------|
| SiO_2 | 19.2 | 22.1 | 26.6 |
| Al_2O_3 | 5.2 | 6.4 | 8.5 |
| Fe_2O_3 | 3.67 | 3.95 | 4.94 |
| MgO | 1.0 | 1.1 | 1.4 |
| CaO | 63.4 | 54.2 | 45.7 |
| Na_2O | 0.33 | 0.38 | 0.45 |
| K_2O | 0.38 | 0.69 | 1.09 |
| SO_3 | 3.14 | 2.73 | 2.47 |
| Loss on ignition | 3.21 | 7.86 | 7.88 |
| $\text{Na}_2\text{O}_{\text{eq}}$ (total) | 0.58 | 0.83 | 1.17 |
| Fineness [m^2/kg] | 430 | 700 | - |
| Density [kg/m^3] | 3140 | 3020 | - |

Paste samples were cast with $w/b = 0.50$ and sealed-cured before performing CWE (28 and 140 days) and PWE (28 days). CWE was carried out following the procedure described in Ranger et al. (2023): crushing paste to obtain 20.0 g between 0.5 and 1 mm, leaching for 5 min in 20 g of deionised water and filtering.

PWE was done by squeezing a sample at a pressure of 1000 MPa for 15 min. The content of Na and K in the solutions were determined by ICP-OES. The amount of pore solution was determined by drying a piece of paste in a desiccator containing silica gel and stored at 40°C until reaching constant mass. The detailed formulas to derive the free alkali content are shown in Ranger et al. (2023).

In parallel, the TI-B 51 method was conducted using a typical Danish reactive sand containing porous opaline flint (Øde Hastrup). Mortars bars (40 x 40 x 160 mm) were cast with w/b = 0.50 and a sand-to-cement ratio of 3. The bars were cured in deionised water for 28 days at 20°C before being immersed in a saturated NaCl solution kept at 50°C. The expansion of the bars was measured up to 20 weeks.

4. Results and discussion

Figure 1 presents the free alkali content determined for the three cements with two parameters varying: the extraction method (left) and the curing time (right).

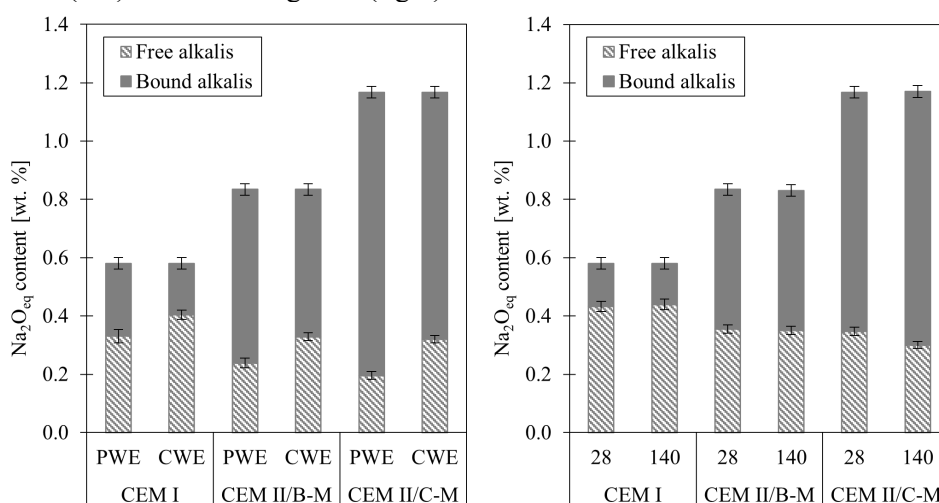


Figure 1: Free and bound alkali content: comparison between CWE and PWE at 28 days (left), comparison between CWE at 28 and 140 days (right).

Independently of the method used (CWE or PWE), the free alkali content in pastes produced with blended cements is lower than in pastes with CEM I, despite the rise in total alkalis induced by SCMs (Figure 1, left). These results were expected, as other authors reported a decrease of the concentrations of alkali metal ions in the pore solution for limestone calcined clay cements, see Nguyen et al. (2018). Although CWE and PWE show the same trend, CWE systematically results in higher values than PWE. In CWE, leaching in water induces the dissolution of portlandite, so that the leaching solution has more Ca than the initial pore solution. Consequently, the thermodynamic equilibrium between the C-S-H and the leaching solution is shifted toward a higher Ca/Si of the C-S-H, thereby reducing its alkali metal binding capacity. More data and a detailed discussion can be found in Ranger et al. (2023). The practical implication is that CWE probably tends to overestimate free alkalis, which is however on the safe side. Moreover, it can also be seen that the curing time has a limited influence on the results (Figure 1, right). Only CEM II/C-M presents a slight drop from 28 to 140 days, probably due to the pozzolanic reaction binding more alkali metals over time.

Blended cements also perform better than CEM I in the TI-B 51 test (Figure 2). However, a clear difference can be seen between CEM II/B-M and CEM II/C-M, the latter showing no expansion after 20 weeks of exposure. This behaviour can hardly be explained by the free alkali content, which is almost equal for the two cements. Since the TI-B 51 is an immersion test, a possible explanation is that the two cements influence transport properties in different ways, so that the resistance to ion and/or water ingress is a major factor influencing the test outcome. This point is currently under investigation. According to the Danish standards (national annex of EN 206), the TI-B 51 test must be used to document the ASR performance of a cement that is not already included in the Danish standards. In practise, the test outcome is also used to decide on the alkali classification of the cement. For instance, it may be chosen to exclude the alkalis from the SCM in the calculations if a blended cement causes less than a Portland cement.

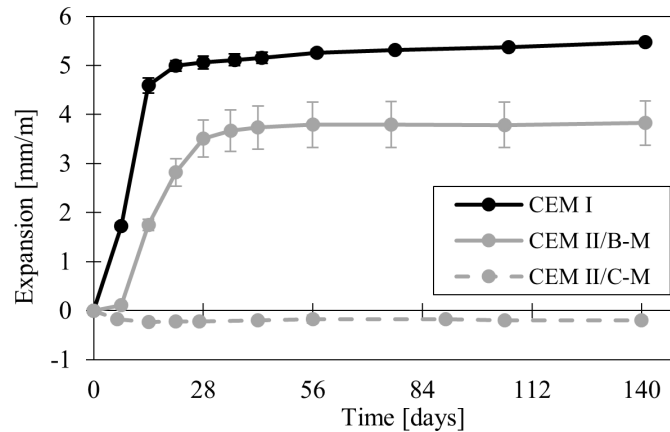


Figure 2: Expansions measured in the TI-B 51 test.

When making an alkali classification of cements, the free alkali content seems to be a parameter that is more chemically meaningful than the TI-B 51 expansion. In this respect, CWE is a relatively simple method to measure the free alkali content directly. It should be emphasised that the free alkali content is only one parameter affecting ASR. Thus, for mitigation purposes, more testing is required.

5. Conclusions

With the increasing use of blended cements, it is important to compare all types of cements on a relevant basis, i.e. with suitable parameters for a given purpose. While blended cements often perform better than Portland cements against ASR, they usually have a larger total alkali content because of the presence of SCMs. The present work investigated a method, namely Cold Water Extraction, to determine the free alkali content of cementitious binders, which seems more appropriate than the total content in an ASR context. CWE can be performed on paste samples with standard laboratory equipment, and the results suggest that 28 days of curing at 20°C are sufficient to obtain a value of appropriate accuracy. Additional binders are currently under investigation to further explore the potential of the method.

Acknowledgements

This work is part of an industrial PhD project financed by the Danish Road Directorate and a joint grant from Innovation Fund Denmark (Innovationsfonden) and Realdania under the program Circular Built Environment. This financial support is gratefully acknowledged. The Research and Quality Centre of Aalborg Portland is warmly thanked for supplying CEM I and CEM II/B-M, hosting Pore Water Extraction tests, and performing XRF analyses. Finally, we would like to acknowledge the support of the CALLISTE project for developing and supplying the prototype CEM II/C-M.

References

- Fournier, B. and Bérubé, M.-A. (2000) “Alkali-aggregate reaction in concrete: a review of basic concepts and engineering applications”, *Canadian Journal of Civil Engineering*, 27(2): 167–191
- Kasaniya M. and Thomas, M.D.A. (2022) “Role of the alkalis of supplementary cementing materials in controlling pore solution chemistry and alkali-silica reaction”, *Cement and Concrete Research*, 162: pp. 107007
- Nguyen, Q. D., Khan, M. S. H. and Castel, A. (2018) “Engineering properties of limestone calcined clay concrete”, *Journal of Advanced Concrete Technology*, 16(8): 343–357
- Plusquellec, G., Geiker, M. R., Lindgård, J., Duchesne, J., Fournier, B. and De Weerd, K. (2017) “Determination of the pH and the free alkali metal content in the pore solution of concrete: Review and experimental comparison”, *Cement and Concrete Research*, 96: 13–26.
- Ranger, M., Hasholt, M. T. and Barbosa, R. A. (2023) “Pore solution alkalinity of cement paste as determined by Cold Water Extraction”, *Cement*, 11: pp. 100055.
- Tuinukuafe, A., Chopperla, K.S.T., Weiss, W.J., Ideker, J.H. and Isgor, O.B. (2022) Estimating Na⁺ and K⁺ concentrations of the pore solution based on ex-situ leaching tests and thermodynamic modeling, *RILEM Technical Letters*, 7: 88–97.

Understanding the behavior of magnesium potassium phosphate cements under leaching

L. Diaz Caselles^{1*}, C. Cau Dit Coumes¹, P. Antonucci¹, A. Rousselet², A. Mesbah³ and V. Montouillout⁴

¹ CEA, DES, ISEC, DPME, SEME, Univ Montpellier, Marcoule, France

Email: laura.diazcaselles@cea.fr, celine.cau-dit-coumes@cea.fr, pascal.antonucci@cea.fr

² Université Paris-Saclay, CEA, Service de recherche en Corrosion et Comportement des Matériaux, 91191, Gif-sur-Yvette, France. Email: angelique.rousselet@cea.fr

³ Univ Lyon, Université Lyon 1, Institut de Recherches sur la Catalyse et l'Environnement de Lyon, IRCELYON, UMR5256, CNRS, Villeurbanne, France. Email: adel.mesbah@ircelyon.univ-lyon1.fr

⁴ CNRS, CEMHTI UPR3079, Univ. Orléans, F-45071 Orléans, France
Email: valerie.montouillout@cnrs-orleans.fr

ABSTRACT

Magnesium potassium phosphate cements (MKPCs), sometimes referred as acid-base binders, are prepared by mixing magnesium oxide (MgO) with potassium dihydrogen phosphate (KH₂PO₄), a water-soluble acidic phosphate salt. Their main hydration product, formed by a dissolution / precipitation process, is K-struvite (MgKPO₄·6H₂O). This study aims at understanding the degradation mechanisms of MKPC pastes under leaching. Semi-dynamic leaching tests were carried out on monolith samples (having a Mg/P molar ratio of 1) by using two different solutions (at pH 7 and pH 13). Experimental results showed that leaching was mainly controlled by diffusion since the cumulative quantities of analyzed ions in the leachates tended, in most cases, to increase linearly versus the square root of time. Examination of the solids revealed a zonation process. At pH 7, a poorly cohesive residual layer (K-struvite depletion) formed at the exposed surface of the sample. This layer was followed by an intermediate zone, in which K-struvite coexisted with cattite Mg₃(PO₄)₂·22H₂O. Finally, the sound core was detected. At pH 13, the main differences were the precipitation of hydroxyapatite Ca₅(PO₄)₃(OH) on the exposed surface, the absence of cattite, but the transient precipitation of brucite Mg(OH)₂.

KEYWORDS: *magnesium phosphate cement, durability, leaching*

1. Introduction

Magnesium phosphate cements (MPCs) are suitable for structural applications and have been used as rapid-repair cements for roads, runways, pavements and highways because of their fast-setting properties (Arora et al., 2019; Li et al., 2014; Seehra et al., 1993). MPCs are also of interest for the immobilization of toxic wastes containing heavy metals, or certain types of radioactive wastes (especially those containing Al metal) (Buj et al., 2010; Cau Dit Coumes et al., 2014; Delpech et al., 2017; Lahalle, 2016; Pyo et al., 2021; Torras et al., 2011). Magnesium potassium phosphate cements (MKPCs) are thus alternative binders to Portland Cement (PC) for niche applications and their main constituents are MgO and potassium dihydrogen phosphate (KH₂PO₄). Their hydration mainly yields K-struvite (MgKPO₄·6H₂O) and a nearly neutral pH pore solution when MgO and KH₂PO₄ are introduced in equimolar amounts (Wagh, 2013; Wagh et al., 1997; Weill & Bradik, 1988; Xu et al., 2018). Information about the long-term durability of these binders is still limited (Lahalle et al., 2019; Yang et al., 2000). Therefore, this study aims at understanding the degradation mechanisms of MKPC pastes under leaching. To this end, semi-dynamic leaching tests were carried out on monolith samples by using demineralized water (pH maintained at 7) and an alkaline solution (pH 13). Leaching solutions were periodically renewed and composition of the leachates was analyzed by ICP-AES. After leaching, the mineralogy and microstructure of the solid samples were characterized from the external surface to the sound core by using XRD and SEM/EDS analyses.

2. Materials and Methods

MKPC pastes were prepared with a $\text{MgO}/\text{KH}_2\text{PO}_4$ molar ratio and a water-to-cement ($\text{MgO} + \text{KH}_2\text{PO}_4$) weight ratio equal to 1 and 0.51, respectively. The Mg/P molar ratio was set to 1 to keep the pore solution pH below 10 (mitigation of Al metal corrosion). Fly ash and boric acid were added at constant fly ash/cement and boric acid/cement weight ratios of 1 and 0.02, respectively. Paste samples were prepared in a normalized mixer in accordance with European Standard NF EN 196-3 and cast into hermetic and cylindrical plastic containers. Curing was carried out for six months in a controlled chamber at 20 °C and 95% RH. Table 1 presents the composition design of the MKPC paste.

Table 1 - Composition design of 1 L MKPC paste.

| | MgO (g) | KH_2PO_4 (g) | Fly ash (g) | Boric acid (g) | Water ^a (g) | w/c ^b |
|------|---------|------------------------------|-------------|----------------|------------------------|------------------|
| MKPC | 131.39 | 443.58 | 574.97 | 11.50 | 293.24 | 0.51 |

^aDemineralized water; ^bWater-to-cement weight ratio (cement: $\text{MgO} + \text{KH}_2\text{PO}_4$).

Two semi-dynamic leaching tests were performed on monolith samples by using (i) demineralized water (pH maintained at 7 by adding nitric acid), and (ii) an alkaline solution (pH 13) mimicking the pore solution of a conventional concrete (composite cement containing blast-furnace slag and fly ash). The alkaline solution was prepared using demineralized water with 0.05 mol/L NaOH, 0.15 mol/L KOH and 0.001 mol/L CaO. Leaching tests were performed under nitrogen atmosphere for 28 days and 14 days at pH 7 and pH 13, respectively. To generate unidirectional diffusion through the samples, the lateral surface of the MKPC cylinders were covered with an epoxy resin. The samples (one per type of solution) were suspended in double-walled reactors maintained at 25 °C and previously filled with 1.7 L of the leaching solution (liquid volume-to- solid surface area ratio of 43.29 cm). Magnetic stirring was applied during the whole tests and solutions were periodically renewed to limit accumulation of dissolved species. Leachates were analyzed over time by ICP-AES. Before and after leaching, MKPC pastes were characterized by XRD and SEM/EDS analyses. SEM/EDS observations were carried out on carbon-coated polished sections, previously soaked into isopropanol and mounted in resin. For XRD analyses, pastes were manually ground (<63 μm). Analyses were performed with a PANalytical X'Pert Pro diffractometer in transmission configuration with a copper radiation source ($\text{Cu K}\alpha$, $\lambda = 1.54 \text{ \AA}$, PIXcel detector). The anode voltage and the electric current intensity were 40 kV and 40 mA, respectively.

2. Results and discussion

2.1 Investigation of MKPC paste samples before leaching

Figure 1 presents the XRD pattern and the EDS point analyses of the MKPC paste samples after six months of curing (before leaching).

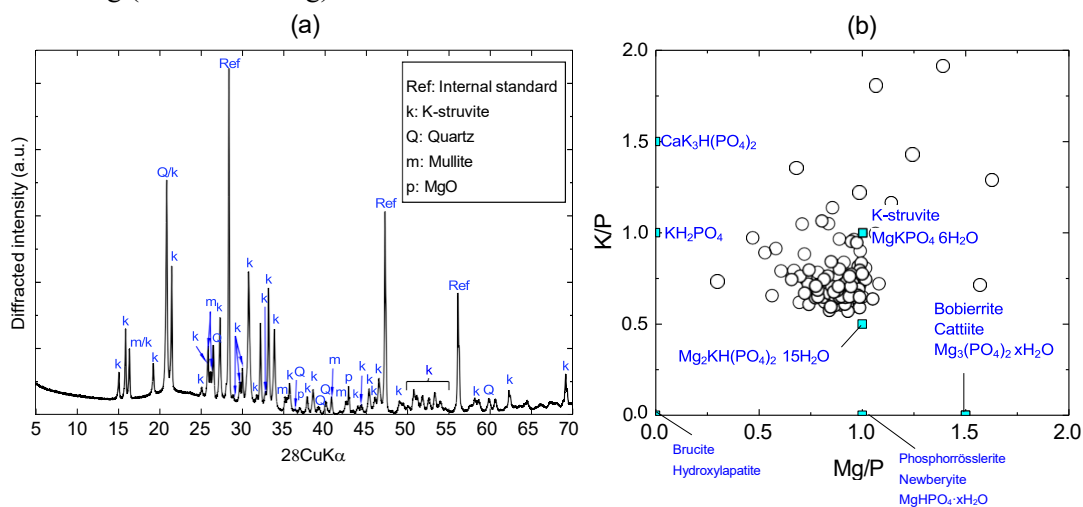


Figure 1 – MKPC after 6 months of curing (a) XRD pattern, and (b) EDS mixing diagram of K/P versus Mg/P atomic ratios.

XRD analyses (cf. Figure 1-b) indicated that MKPC samples were characterized by the presence of K-struvite ($\text{MgKPO}_4 \cdot 6\text{H}_2\text{O}$), residual MgO , quartz, mullite (silicate mineral) and an amorphous content, mainly coming from fly ash, but which could also include transient magnesium phosphate phases or poorly crystallized K-struvite (Ding et al., 2012; Lahalle et al., 2019). EDS analyses suggested that at least one intermediate hydrate, possibly $\text{Mg}_2\text{KH}(\text{PO}_4)_2 \cdot 15\text{H}_2\text{O}$, coexisted with K-struvite in the MKPC matrix (cf. Figure 1-a). Total water porosity was $15.5 \% \pm 0.2 \%$.

2.2 Behavior of MKPC paste samples under leaching

Figure 2 presents the evolution of K, P, Mg and Ca concentrations in the leachates for MKPC samples leached at pH 7 and pH 13.

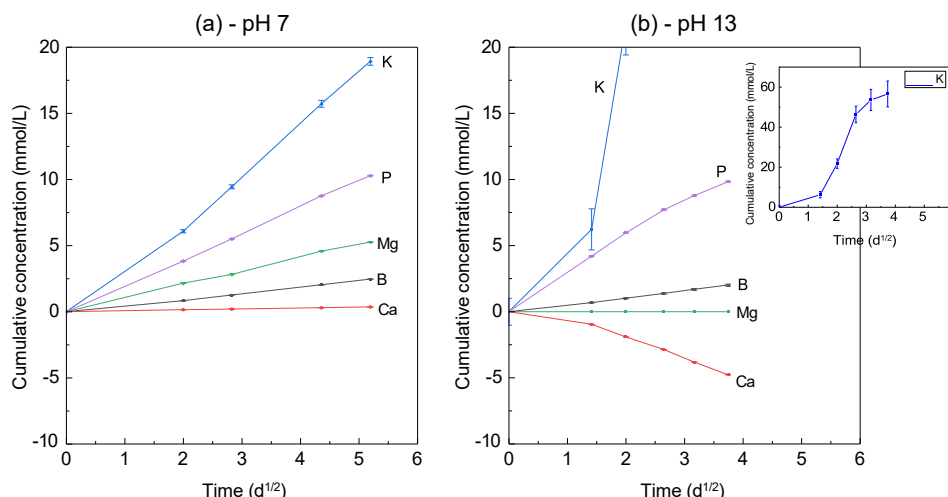


Figure 2 – Evolution of the K, P, Mg, B and Ca concentrations in the leachates (in mmol/L) versus the square root of time in days **(a)** pH 7, and **(b)** pH 13.

Immersion of MKPC samples into demineralized water and the alkaline solution induced a continuous release of ions into solution. At pH 7, leaching was mainly controlled by diffusion since cumulative concentrations showed a linear tendency when plotted against the square root of time (cf. Figure 2-a). The flux of dissolved K exceeded that of Mg and P by factors of 3.4 and 1.8, respectively, and thus did not check the stoichiometry expected assuming congruent dissolution of K-struvite ($\text{MgKPO}_4 \cdot 6\text{H}_2\text{O}$). This result suggested additional processes such as release of K from fly ash and/or precipitation of secondary phases poor in K. At pH 13, the release of K was much higher than that of P, and Mg (which was below the detection limit). In this case, the release of K did not present a linear tendency probably due to the precipitation/dissolution of secondary phases. On the other hand, Ca was consumed from the alkaline leaching solution.

2.3 Solid characterization of MKPC samples after leaching

Figure 3 shows a SEM image and the XRD pattern of the MKPC paste leached at pH 7.

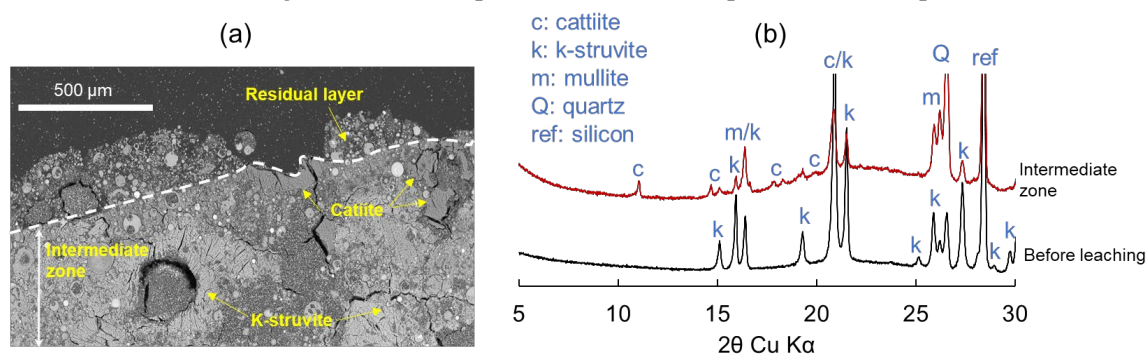


Figure 3 – MKPC paste after 28 days leaching at pH 7 **(a)** SEM image of a polished section, and **(b)** XRD patterns.

At pH 7, difference in thickness before and after leaching was $0.55 \text{ mm} \pm 0.15 \text{ mm}$. The MKPC sample presented a poorly cohesive residual layer (200 -300 μm thick) at the exposed surface, where K-struvite was completely depleted (cf. Figure 3). Then, an intermediate zone was observed, where K-struvite coexisted with cattite $\text{Mg}_3(\text{PO}_4)_2 \cdot 22\text{H}_2\text{O}$ which formed due to the deficit in K (cf. Figure 3-b). This zone presented a higher thickness and XRD analyses indicated that cattite was present in the sample up to 2 mm depth.

On the other hand, at pH 13, the exposed surface of the sample was coated by a thin layer (of about 10-13 μm thick) composed of hydroxyapatite $\text{Ca}_5(\text{PO}_4)_3(\text{OH})$. This layer formed from the reaction between Ca ions (from the alkaline leaching solution, as shown in Figure 2-b by its Ca concentration decreasing with time) and P ions (released by the sample). The formation of hydroxyapatite was followed by a zone of about 842 μm thick, where K and P concentrations decreased; meanwhile, the Mg concentration increased due to precipitation of brucite $\text{Mg}(\text{OH})_2$. Formation of this low-solubility mineral explains why Mg ions remained below the detection limit in the leachates.

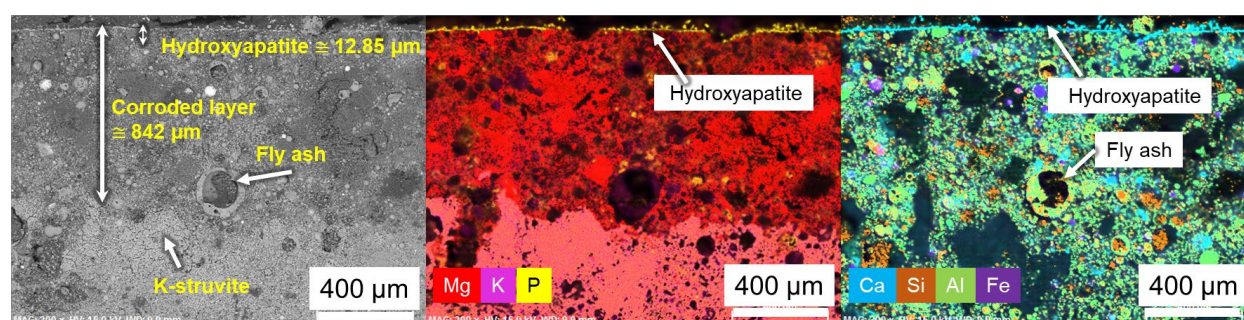


Figure 4 – EDS mapping of MKPC sample after alkaline leaching (pH 13).

3. Conclusions and perspectives

The present paper investigated the leaching behavior of MKPC pastes by using semi-dynamic leaching tests and two different leaching solutions: demineralized water (keeping the pH at 7) and an alkaline solution (pH 13). Leaching solutions were periodically renewed and analyzed by ICP-AES. Solid samples were investigated by XRD and SEM/EDS. The main data obtained from this study are summarized in Table 2.

Table 2 – Summary of experimental results obtained from MKPC leaching tests.

| | pH 7 (28 days of leaching) | pH 13 (14 days of leaching) |
|--|---|--|
| Rate-limiting degradation process | Diffusion of dissolved species K: 3.69 ± 0.15 | Diffusion except for K K: Non-linear |
| Rate of release ($\text{mmol.L}^{-1}.\text{d}^{-1/2}$) | P: 1.99 ± 0.02 Mg: 1.02 ± 0.03 B: 0.47 ± 0.01 | P: 2.66 ± 0.12 Mg: 0 (non-detected) B: 0.54 ± 0.01 |
| Altered front (mm) | 2.12 ± 0.1 | 0.842 ± 0.02 |

Degradation of MKPC samples under leaching results from a combination of diffusive transport and chemical reactions (dissolution/precipitation fronts), the rate limiting process being diffusion at pH 7. A mineralogical zonation effect is evidenced, as reported for Portland cement (Faucon et al., 1998). Nevertheless, the degradation rate of MKPC seems much higher. For instance, Adenot and Buil 1992 report a degradation depth of only 500 μm for a PC paste sample (water-to-cement ratio of 0.4) leached at pH 7 for 3 months under similar conditions.

Precipitation of a coating layer of hydroxyapatite is evidenced when leaching of MKPC paste is performed at pH 13. Longer studies should be carried out to verify whether hydroxyapatite might clog the porosity and slow down the paste degradation. Finally, this work, carried out under well-controlled conditions, provides input data for reactive transport modeling of the degradation of MKPC pastes under leaching.

Acknowledgements

This project has received funding from the European Union's Horizon 2020 research and innovation programme for Nuclear Fission and Radiation Protection Research (Call NFRP-2019-2020) under grant agreement No. 945098 (PREDIS).

References

- Adenot, F., & Buil, M. (1992). Modelling of the corrosion of the cement paste by deionized water. *Cement and Concrete Research*, 22(2–3), 489–496.
- Arora, A., Singh, B., & Kaur, P. (2019). Novel material i.e. Magnesium phosphate cement (MPC) as repairing material in roads and buildings. *Materials Today: Proceedings*, 17, 70–76. <https://doi.org/10.1016/j.matpr.2019.06.402>
- Buj, I., Torras, J., Rovira, M., & de Pablo, J. (2010). Leaching behaviour of magnesium phosphate cements containing high quantities of heavy metals. *Journal of Hazardous Materials*, 175(1–3), 789–794. <https://doi.org/10.1016/j.jhazmat.2009.10.077>
- Cau Dit Coumes, C., Lambertin, D., Lahalle, H., Antonucci, P., Cannes, C., & Delpech, S. (2014). Selection of a mineral binder with potentialities for the stabilization/solidification of aluminum metal. *Journal of Nuclear Materials*, 453(1–3), 31–40. <https://doi.org/10.1016/j.jnucmat.2014.06.032>
- Delpech, S., Cannes, C., Barré, N., Tran, Q. T., Sanchez, C., Lahalle, H., Lambertin, D., Gauffinet, S., & Coumes, C. C. D. (2017). Kinetic Model of Aluminum Behavior in Cement-Based Matrices Analyzed by Impedance Spectroscopy. *Journal of The Electrochemical Society*, 164(13), C717–C727. <https://doi.org/10.1149/2.0211713jes>
- Ding, Z., Dong, B., Xing, F., Han, N., & Li, Z. (2012). Cementing mechanism of potassium phosphate based magnesium phosphate cement. *Ceramics International*, 38(8), 6281–6288. <https://doi.org/10.1016/j.ceramint.2012.04.083>
- Faucon, P., Adenot, F., Jacquinet, J. ., Petit, J. ., Cabrilac, R., & Jorda, M. (1998). Long-term behaviour of cement pastes used for nuclear waste disposal: review of physico-chemical mechanisms of water degradation. *Cement and Concrete Research*, 28(6), 847–857. [https://doi.org/10.1016/S0008-8846\(98\)00053-2](https://doi.org/10.1016/S0008-8846(98)00053-2)
- Lahalle, H. (2016). *Conditionnement de l'aluminium métallique dans les ciments phospho-magnésiens*. Université de Bourgogne.
- Lahalle, H., Patapy, C., Glid, M., Renaudin, G., & Cyr, M. (2019). Microstructural evolution/durability of magnesium phosphate cement paste over time in neutral and basic environments. *Cement and Concrete Research*, 122(April), 42–58. <https://doi.org/10.1016/j.cemconres.2019.04.011>
- Li, J., Zhang, W., & Cao, Y. (2014). Laboratory evaluation of magnesium phosphate cement paste and mortar for rapid repair of cement concrete pavement. *Construction and Building Materials*, 58, 122–128. <https://doi.org/10.1016/j.conbuildmat.2014.02.015>
- Pyo, J. Y., Um, W., & Heo, J. (2021). Magnesium potassium phosphate cements to immobilize radioactive concrete wastes generated by decommissioning of nuclear power plants. *Nuclear Engineering and Technology*, 53(7), 2261–2267. <https://doi.org/10.1016/j.net.2021.01.005>
- Seehra, S. S., Gupta, S., & Kumar, S. (1993). Rapid setting magnesium phosphate cement for quick repair of concrete pavements - characterisation and durability aspects. *Cement and Concrete Research*, 23(2), 254–266. [https://doi.org/10.1016/0008-8846\(93\)90090-V](https://doi.org/10.1016/0008-8846(93)90090-V)
- Torras, J., Buj, I., Rovira, M., & de Pablo, J. (2011). Semi-dynamic leaching tests of nickel containing wastes stabilized/solidified with magnesium potassium phosphate cements. *Journal of Hazardous Materials*, 186(2–3), 1954–1960. <https://doi.org/10.1016/j.jhazmat.2010.12.093>
- Wagh, A. S. (2013). Recent Progress in Chemically Bonded Phosphate Ceramics. *ISRN Ceramics*, 2013, 1–20. <https://doi.org/10.1155/2013/983731>
- Wagh, A. S., Jeong, S.-Y., & Singh, D. (1997). High Strength Phosphate Cement Using. *Proceedings of the 1st International Conference on High Strength Concrete*, 542–553.
- Weill, B., & Bradik, J. (1988). *US Patent n°4,756,762 - Magnesium phosphate cement systems*. 19.
- Xu, B., Lothenbach, B., Leemann, A., & Winnefeld, F. (2018). Reaction mechanism of magnesium potassium phosphate cement with high magnesium-to-phosphate ratio. *Cement and Concrete Research*, 108(April), 140–151. <https://doi.org/10.1016/j.cemconres.2018.03.013>
- Yang, Q., Zhu, B., & Wu, X. (2000). Characteristics and durability test of magnesium phosphate cement-based material for rapid repair of concrete. *Materials and Structures/Materiaux et Constructions*, 33(4), 229–234. <https://doi.org/10.1007/bf02479332>

Effect of Al on the structure and swelling behavior of synthetic ASR gels

M. E. Krüger^{1*}, L. Stelzner², A. Heisig¹, H. Hilbig¹, A. Machner¹

¹ *Technical University of Munich, TUM School of Engineering and Design, Department of Materials Engineering, Professorship for Mineral Construction Materials, Franz-Langinger-Str. 10, 81245 Munich, Germany*
**Email: miriam.krueger@tum.de*

² *Bundesanstalt für Materialforschung und –prüfung (BAM), Division 7.3 Fire Engineering, Unter den Eichen 87, 12205 Berlin, Germany*

ABSTRACT

During the alkali-silica reaction (ASR) in concrete, alkali hydroxides present in the pore solution react with silica originating from reactive aggregates to form an ASR gel. This gel can absorb considerable amounts of water, which leads to expansion in volume and consequently to the deterioration of concrete structures. An efficient way to enhance the resistance of concrete against ASR is the addition of Al-rich supplementary cementitious materials (SCMs). To further understand the beneficial mechanisms of the Al-rich SCMs regarding the mitigation of ASR, we investigated the effect of Al on the structure and the swelling behavior of ASR gels. For this, we synthesized ASR gels with a Ca/Si ratio of 0.2, a (K + Na)/Si ratio of 0.5 and various Al contents. Directly after mixing, the synthesized ASR gels were placed in swelling cells filled with CO₂-free water and the vertical swelling strain was measured with a dial gauge over the period of 72 hours. Afterwards, the ASR gels were structurally characterized by solid-state NMR. Before and after the swelling experiment FTIR spectroscopic and ¹H NMR relaxometry measurements were performed to link the effect of the swelling to the structure of the ASR gels. The results show that the addition of Al(OH)₃ changes the structure of the synthetic ASR gels. This structural change leads to an increased connectivity of the ASR gel structure and therefore to a reduced swelling potential. The results of this study provide new insights for the beneficial effect of Al on the mitigation of ASR related to the alteration of the ASR gel structure.

KEYWORDS: *Concrete, Alkali-silica reaction (ASR), Durability, FTIR, NMR relaxometry and spectroscopy*

1. Introduction

ASR gels are the reaction products of the alkali-silica reaction (ASR), a deterioration mechanism in concrete. During the ASR, the alkalis (K, Na) in the pore solution of concrete react with the silica in the aggregates to form a swellable ASR gel, which can lead to cracks in concrete while absorbing water (Hasan (2020)). The swelling and damage potential of ASR gels is dependent on their chemical composition and their nanostructure. The swelling pressure evolves due to the adsorption of water and electrostatically repulsion of dissociated negatively charged silicate layers (Wieker et al. (2000)). Dependent on the degree of crosslinking of the silicate framework, the incorporation of the water amount is limited, therefore swelling is expected to change (Dent Glasser (1979)). It is already known that the use of SCMs reduces the ASR potential in concrete because they reduce alkalinity and thus the pH of the pore solution (Ramlochan et al. (2004)). Beside this, SCMs like fly ash or calcined clays can provide larger amounts of Al to the pore solution, which can mitigate the ASR induced expansion in concrete (Leemann et al. (2015); Schmidt et al. (2007)). However, little is known on how Al-rich SCMs affect the chemical composition, structure and swelling behavior of ASR gels (Krüger et al. (2023)). To determine the mitigation potential of Al-rich SCMs, it is important to understand the role of Al on the ASR. For this, we investigated ASR gels regarding their structural change, water bonding and swelling behavior by adding different amounts of Al(OH)₃ to the synthesis.

2. Methods

The ASR gels were synthesized by mixing precipitated silica, CaO, Al(OH)₃, NaOH, KOH and water in an argon atmosphere, as described in (Krüger et al. 2023). The molar ratios of the gels targeted were (Na + K)/Si = 0.5, Ca/Si = 0.2 and Al/Si = 0.0 – 0.1. These ratios are within a range of reported compositions of ASR gels formed in concrete (Krüger et al. 2022). The labels of the investigated gels correspond to the rounded molar ratios of the synthesized gels determined by ICP-OES. Prior to each swelling experiment, the synthetic ASR gels were structurally characterized by solid-state NMR (²⁹Si NMR, ²⁷Al NMR). To link the effect of the ASR gel structure to the swelling behavior, FTIR spectroscopic and ¹H NMR relaxometry measurements were performed on the gels before and after the swelling tests.

The ²⁹Si and ²⁷Al NMR investigations were performed using a *Bruker Avance 300* spectrometer (magnetic field strength 7.0455 T, resonance frequency for ²⁹Si: 59.63 MHz and ²⁷Al: 78.12 MHz) using single pulse technique in MAS mode (magic angle spinning) in 7 mm (5 kHz) respectively 4 mm (15 kHz) zirconia rotors (spinning speeds in brackets). The measurement setup and deconvolution performance is described in detail in (Krüger et al. 2023). The FTIR spectra were recorded on a Perkin Elmer FT-IR spectrometer Spectrum 100, equipped with a Golden Gate Diamond ATR unit. Transmittance was measured between 600 and 4000 cm⁻¹ with a resolution of 4 cm⁻¹.

The determination of the transverse relaxation time distribution (T₂ -RTD) as well as the detectable moisture content by means of ¹H NMR were carried out using an NMR Tomograph from Pure Devices GmbH (magnetic field strength 0.21 T, resonance frequency 8,97 MHz). The 0D-measurements were performed with a 22 mm coil and an echo time of 50 µs using a standard CPMG pulse sequence (Meiboom and Gill (1958)). Each measurement consisted of 64 excitations (including phase cycling) with an echo train length of 1000 ms and an inter-experimental time of 5000 ms. The gained decay curves were subsequently inverted into T₂ -RTD using the Matlab based software tool NUCLEUS from (Thomas Hiller (2022)). For all inversions, a multi-exponential least square fit was utilized in the time range of 0.1 ms and 1000 ms with 30 grid points per decade. Additionally, a reference measurement of H₂O was used to calculate the detectable moisture content of the ASR gels.

In order to investigate the vertical swelling strain of the ASR gels, a powder swelling cell according to Thuro adapted for the purpose of ASR gels was used (Thuro (1993)) and the gels were placed in the swelling cells on a filter paper and filter plate directly after synthesis. The swelling experiment started after adding deionized CO₂-free water to the water basin and stopped after 72 h. The vertical swelling strain is the quotient of the axial swelling deformation, measured by a precision dial gauge and calculated against the specimen initial height (13.0 ± 1.0 mm).

3. Results & Discussion

The results are described and discussed in the following by showing results of selected samples of Al-containing and Al-free ASR gels. The ²⁹Si NMR results of all investigated ASR gels show resonances at, -80 ppm, -88 ppm -92 ppm and -97 ppm, corresponding to Q¹, Q² and Q³ units respectively (Hou et al. (2005); Krüger et al. (2023)). The Al-ASR gel show additional peaks at -86 ppm, -103 ppm and -107 ppm, which can be attributed to Q²(I)/Q²(1Al), Q⁴(1Al) and Q⁴ sites indicating an increased connectivity (Hou et al. (2005); Krüger et al. (2023)) (Figure 1, a). The comparison of the ²⁹Si NMR spectra moreover shows that the peaks become broader after adding Al to the synthesis. This can be explained by an increasing structural disorder with increasing Al/Si ratio (Krüger et al. (2023)) and most likely also by differences in their sample age. These differences limit quantitative evaluation, but do not prohibit a qualitative comparison of the results. The ²⁷Al NMR spectrum of the Al-ASR gel (Figure 1, b) exhibit two main peak positions for Al: Al^{IV} at 55 ppm (Gutberlet et al. (2015)) and Al^{VI} at 9 ppm (He et al. (2020)). The Al^{IV} q⁴(4Si) at 55 ppm can be attributed to an alumino-silicate structure (Gutberlet et al. (2015)). About 93 % of the Al is four-fold coordinated and 7 % six-fold coordinated. The FTIR results (Figure 2 a)) of the Al-free ASR gel show two main peaks at 1040 cm⁻¹ and 960 cm⁻¹, which indicate the presence of two different ASR types of gel: a Ca-poor ASR gel and a Ca-rich/C-S-H-like phase (Krüger et al. (2023)). By adding Al to the synthesis, the maximum peak position for Si-O stretching vibration shifts to lower wavenumbers from 1040 cm⁻¹ (Q³) to 980 cm⁻¹ (Q²) indicating the substitution of Si by Al, and the formation of an alumino-silicate structure (He et al. (2020)).

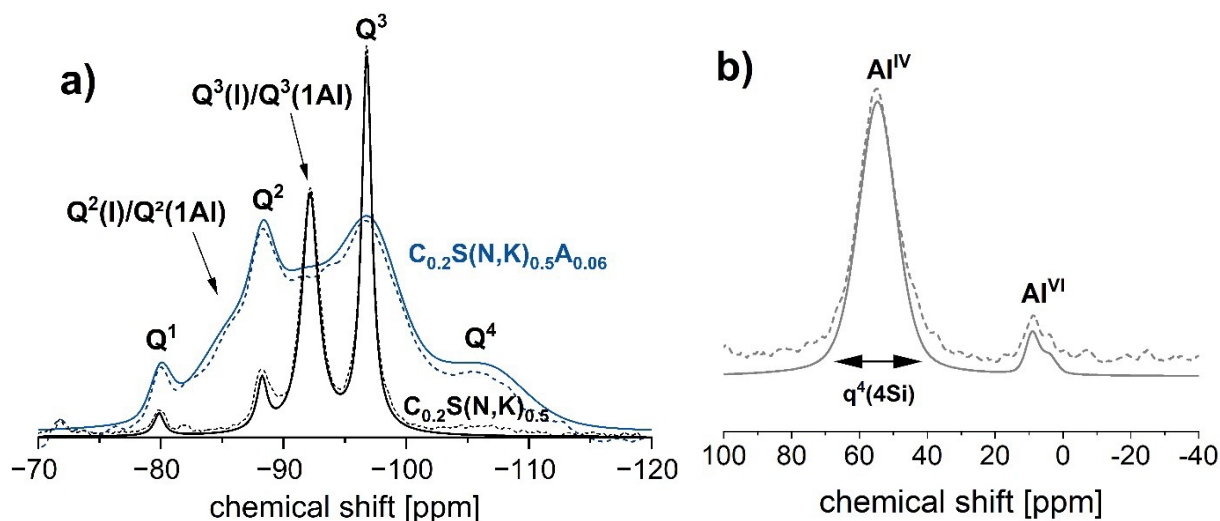


Figure 1: ^{29}Si NMR spectra a) of the ASR gels $\text{C}_{0.2}\text{S}(\text{N},\text{K})_{0.5}$ (black) and $\text{C}_{0.2}\text{S}(\text{N},\text{K})_{0.5}\text{A}_{0.06}$ (blue), ($\text{Ca}/\text{Si} = 0.2$, $(\text{Na} + \text{K})/\text{Si} = 0.5$, $\text{Al}/\text{Si} = 0.06$) and ^{27}Al NMR spectrum b) of the Al-ASR gel $\text{C}_{0.2}\text{S}(\text{N},\text{K})_{0.5}\text{A}_{0.06}$, solid line = measured spectrum, dashed line = cumulative fit.

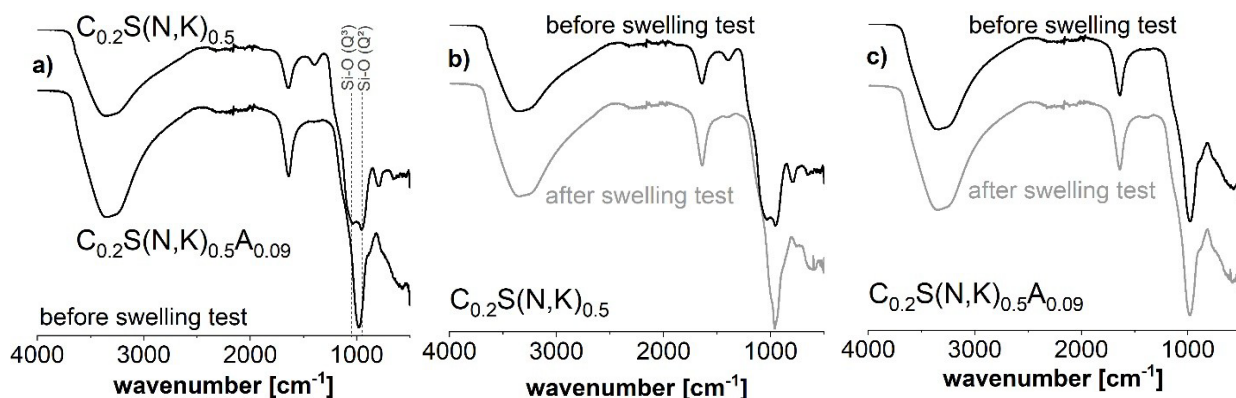


Figure 2: FTIR spectra of the ASR gels $\text{C}_{0.2}\text{S}(\text{N},\text{K})_{0.5}$ and $\text{C}_{0.2}\text{S}(\text{N},\text{K})_{0.5}\text{A}_{0.09}$, a) in direct comparison before, and for each gel before and after the swelling experiment b) and c).

In order to correlate the structural observations on the gels to their swelling behavior, swelling tests were carried out (Figure 3, left). The results show a vertical swelling strain of 5% for the ASR gel without Al. For the Al-ASR gels the vertical swelling was approx. zero. This indicates that Al-ASR gels are non swellable.

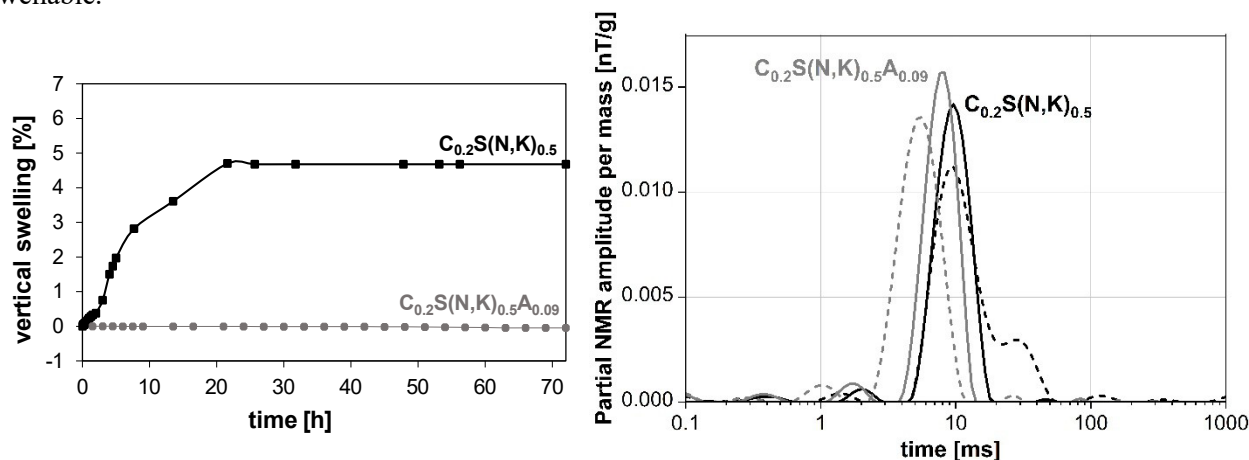


Figure 3: Swelling experiment (left) and transverse relaxation time distribution (right) results for the ASR gels $\text{C}_{0.2}\text{S}(\text{N},\text{K})_{0.5}$ (black) and $\text{C}_{0.2}\text{S}(\text{N},\text{K})_{0.5}\text{A}_{0.09}$ (grey) ($\text{Ca}/\text{Si} = 0.2$, $(\text{Na} + \text{K})/\text{Si} = 0.5$ and $\text{Al}/\text{Si} = 0.09$), solid line = before the swelling experiment, dotted line = after the swelling experiment.

The FTIR results show no structural change for the Al-ASR gel (Figure 2 c)) after the swelling experiment, whereas the Al-free ASR gel indicate a structural change (Figure 2 b)), seen by the change of the main peak from 1040 cm^{-1} to 960 cm^{-1} . This indicates that the swelling experiment does not affect the structure of the Al-ASR gels. The ^1H NMR relaxometry results (Figure 3, right) show that the main portion of the detectable water of both ASR gels is bound in pores with a peak transverse relaxation time (T_2 time) of 8-9 ms before the swelling experiment. The conversion of the ^1H NMR results into the moisture content, showed that during the swelling test, the water content of originally 65 wt% increases for both ASR gels. Thereby, the Al-free-ASR gel incorporated almost double as much water than the Al-ASR gel after the swelling test (11 wt% to 6 wt%). Additionally, the T_2 -RTD in Figure 3, right, reveals a signal increase at longer T_2 times for the Al-free ASR gel, which can be attributed to water present in larger cavities or loosely bound in this gel. Whereas for the Al-ASR gel, the T_2 -RTD slightly shifts to shorter T_2 times, which indicates water present in smaller cavities or tightly bound.

4. Conclusions

We investigated the effect of Al on the structure and vertical swelling strain of ASR gels with molar ratios of $(\text{Na} + \text{K})/\text{Si} = 0.5$, $\text{Ca}/\text{Si} = 0.2$ and $\text{Al}/\text{Si} = 0.0 - 0.1$. The following conclusion can be drawn: (i) Al is incorporated into the ASR structure. (ii) Al is incorporated in four- and six-fold coordination leading to an increased connectivity (Q^4 sites) of the ASR gel structure. (iii) The incorporation of Al into the ASR gel suppresses the vertical swelling of the gel, and correlates with a stronger binding of water in the gel structure. These results serve as a proof of concept for the effect of Al on the structure and swelling behavior of ASR gels and help elucidating another mechanism responsible for the ASR mitigation potential of Al-rich SCMs. Currently, additional ASR gels with various compositions (different Ca/Si , $(\text{Na}+\text{K})/\text{Si}$ ratios) are under investigation, with the aim to validate this effect.

Acknowledgements

The authors would like to thank the German Research Foundation (project number: 438217913) for their financial support.

References

- Dent Glasser, L.S. (1979) Osmotic pressure and the swelling of gels. *Cem. Concr. Res.*, 9(4): 515–517.
- Hasan, N. (2020) *Durability and Sustainability of Concrete*, Springer International Publishing, Cham.
- He, P., Zhang, B., Lu, J.-X., and Poon, C.S. (2020) ASR expansion of alkali-activated cement glass aggregate mortars. *Constr. Build. Mater.*, 261: 119925.
- Hou, X., Kirkpatrick, R.J., Struble, L.J., and Monteiro, P.J.M. (2005) Structural Investigations of Alkali Silicate Gels. *J. Am. Ceram. Soc.*, 88(4): 943–949.
- Krüger, M.E., Heisig, A., Hilbig, H., Eickhoff, H., Heinz, D., and Machner, A. (2023) Effect of Aluminum on the Structure of Synthetic Alkali-Silica Gels. *Cem. Concr. Res.*, 166: 107088.
- Leemann, A., Bernard, L., Alahrache, S., and Winnefeld, F. (2015) ASR prevention — Effect of aluminum and lithium ions on the reaction products. *Cem. Concr. Res.*, 76: 192–201.
- Ramlochan, T., Thomas, M., and Hooton, R. (2004) The effect of pozzolans and slag on the expansion of mortars cured at elevated temperature. *Cem. Concr. Res.*, 34(8):1341–1356.
- Krüger, M. E.; Woydich, E.; Weerdt, K. de; Heisig, A.; Machner, A. Can the R^3 -test be used as a rapid screening test for the ASR mitigation potential of calcined clays? *Calcined Clays for Sustainable Concrete 2022*, Lausanne, Switzerland.
- Meiboom, S. and Gill, D. (1958) Modified spin-echo method for measuring nuclear relaxation times. *Rev. Sci. Instrum.*, 29: 688–691.
- Schmidt, K., Hilbig, H., and Heinz, D., Eds. (2007) ASR in Concrete with Supplementary Cementitious Materials Effect of Pore Solution Composition on Damage, *12th International Congress on the Chemistry of Cement*, Montreal.
- Thomas Hiller (2022, Aug 11) ThoHiller/nmr-nucleus: v0.1.13: DOI: 10.5281/zenodo.4022195 Zenodo.
- Thuro, K. (1993) Der Pulver-Quellversuch - ein neuer Quellhebungsversuch (in German). *Geotechnik*, 16(3): 101–106.
- Wieker, W., Hübert, C., Heidemann, D., and Ebert, R., Eds. (2000) Zur Reaktion von Alkaliverbindungen mit Kieselsäure und Silicaten im Hinblick auf betonschädigende Dehnungsreaktionen: *14. Internationale Baustofftagung - Ibausil*, Weimar.

Geochemical interactions between cementitious materials and water in the context of drinking water supply

M. Desoteux^{1*}, A. Bertron¹, L. Lacarriere¹, C. Roosz¹ and A. Robin²

¹ LMDC, Université de Toulouse, UPS, INSA Toulouse, France
Email: desoteux@insa-toulouse.fr

² LMDC, Université de Toulouse, UPS, INSA Toulouse, France
Email: bertron@insa-toulouse.fr

³ LMDC, Université de Toulouse, UPS, INSA Toulouse, France
Email: lacarri@insa-toulouse.fr

⁴ LMDC, Université de Toulouse, UPS, INSA Toulouse, France
Email: roosz@insa-toulouse.fr

⁵ Saint-Gobain PAM Canalisation, Technocentre, Pont-à-Mousson, France
Email: adrien.robin@saint-gobain.fr

ABSTRACT

Ductile iron water supply pipes are protected by a cement coating that can induce a transient increase in the pH of the water. This phenomenon depends on different parameters, including the calcocarbonic balance of the water in contact with the coating. This study aims to identify and understand the geochemical interactions between a CEM III cement matrix and drinking water of different hardnesses. The aim is to evaluate, as a function of the initial chemical composition of the water, (i) the amplitudes and kinetics of pH evolution and cement ion release into the water, and (ii) the mechanisms of cement paste alteration. CEM III pastes (containing blast furnace slag) were subjected to leaching tests with ultra-pure water and mineralized water. These tests were carried out in successive batches with regular renewal of the solution during 1 month. The pH of the leaching solutions is continuously monitored and the concentrations of ions in solution are analyzed at each renewal. The mineralogical, microstructural and chemical modifications of the leached materials are analyzed at the end of the experiment by XRD and SEM+EDS.

KEYWORDS: *cementitious material, Slag, Calco-carbonated water, Leaching*

1. Introduction

Drinking water is one of the most controlled resources in the world with regulations at the European and national levels. The pH of drinking water should be between 6.5 and 9. The World Health Organization (2017) also notes that high pH levels negatively impact certain decontamination processes, which can lead to insufficient treatment of drinking water, thus harming consumers. Drinking water compositions reflect the wide disparity in the geology of a territory. The geographical areas corresponding to particularly aggressive waters correspond to regions whose soil is made up of magmatic and metamorphic rocks. Conversely, water passing through chalk or limestone massifs (sedimentary rocks) will be highly charged with ions.

The drinking water supply pipes manufactured by Saint-Gobain PAM Canalisation are protected by a CEM III/B cement coating. This mortar is applied by centrifugation, which results in the development of a particular gradient of microstructural properties, Berthomier (2020) notes that its characteristics are (i) similar to those of a CEM III mortar richer in sand in contact with cast iron, and (ii) similar to those of a CEM III cement paste directly in contact with water.

The flow of water over the liner can lead to the leaching of chemical elements contained in the cementitious matrix (Ca, Mg, Al, Si, Na, K ...) and consequently to a change in the pH and composition of the water. According to Gauthier (2021) These modifications depend mainly on the calcocarbonic balance of the water. In water chemistry, this balance is defined by the Langelier index characterizing the aggressiveness

of the water towards calcium carbonate. Müller-Steinhagen and Branch (1988) found that a water with a positive Langelier index will be likely to precipitate calcium carbonate while a water with a negative Langelier index will tend to dissolve it.

This work aims at studying the mechanisms and kinetics of interactions between a CEM III paste and pure and highly mineralized waters. This requires the understanding of two phenomena; on the one hand the influence of the coating on the water (modification of its quality with modification of the pH and possible releases) and on the other hand the effects of the water on the coating (chemical and mineralogical modifications due to the aqueous leaching or carbonation). The CEM III pastes were subjected to leaching tests with ultra-pure water (UPW) and mineralized water (MW). The amounts of chemical elements as a function of time were determined by ICP-OES analysis. The degraded materials were also studied by scanning electron microscopy coupled with energy dispersive spectroscopy (SEM-EDS) and by X-ray diffractometer (XRD) to highlight their microstructural, chemical and mineralogical evolution.

2. Materials and methods

2.1 Cementitious material

The cement used to make the lining is a slag cement similar to that of a CEM III. The cement paste samples were made with the same slag cement used by Saint-Gobain PAM Canalisation to manufacture its cementitious coatings. A water/cement ratio of 0.31 was used, corresponding to the average W/C ratio of several pipe lining surface layers at the factory.

The cementitious pastes were obtained with a standard mixer and by following the NF EN-196-1 norm. 4x4x16cm molds were then filled and vibrated on a vibrating table. The molded pastes are stored at 20 °C and protected by a plastic sheet. The pastes were then demolded after 24 h and stored at 20 °C in sealed plastic bags for 27 days. The resulting prisms are then resinated and sawed into 1 cm slices. The samples thus offer two facing surfaces that can be leached (exposed surface 2x16 cm²).

2.2 Leaching water

The choice of the waters is based on their Langelier indexes, this index was used to evaluate two poles of compositions met in France (aggressive waters on one side and scaling on the other). The compositions chosen reflect these two poles, the system was then simplified by choosing an ultra-pure water as aggressive water and a highly mineralized water of the brand Vittel as scaling water.

2.3 Leaching tests

Successive batch leaching tests were carried out on CEM III monolithic pastes. The waters pH were monitored for the duration of the experiment. The exposure solutions are renewed every day. The experimental device is composed of two reactors, each containing two liters of exposure solution and two monolithic CEM III paste samples (i.e. a ratio of liquid volume to solid surface of 32 cm). The exposure solution is continuously stirred with a magnetic stirrer. The leaching tests lasted 1 month at a temperature of 20 °C. During the first hours of the test, samples of the exposure solution were taken at regular intervals (1 h, 3 h, 6 h, 24 h, 48 h). Samples were then taken at each renewal.

3. Results and discussion

Figure 1 shows the leaching results obtained for the leaching test using ultra-pure water (measurements made at each renewals). Ion concentrations in the solution are presented in cumulative amounts and plotted as a function of the square root of time. In the case of mineralized water, the cumulative concentrations presented are corrected by deducting the elements already present in the mineralized water. A positive value indicates a possible release by the matrix and a negative value an absorption.

For ultra-pure water, the curves show kinetic phenomena controlled by diffusive transport. The release of Ca, Si, Al and Mg ions evolves linearly as a function of the square root of time. A break of slope is observed from the 4th day for the elements K and Na.

The mineralized water tests show different release/uptake behaviours than the ultra-pure water tests. Figure 1 shows a significant release of Ca at the beginning of the experiment with a higher aggressiveness towards calcium on the first days compared to the ultrapure water test. The aluminium release is less important than for the ultra-pure water test and shows a break of slope from the 4th day. Capture phenomena are also observed (decreasing corrected cumulative concentrations), in particular for the elements Mg and Si with an acceleration of the fixation by the cement matrix from the 4th day.

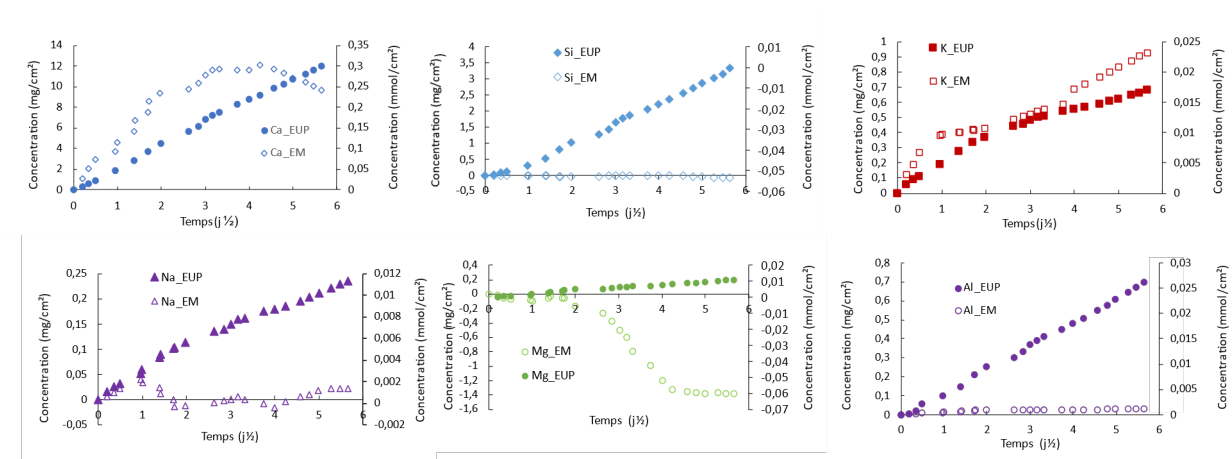


Figure 1 : Cumulative corrected concentrations of elements leached (positive values) or captured (negative values) during the Vittel Mineralized Water (EM) and Ultra-Pure Water (UPW) leaching test of a monolithic cement paste. The elements already present in the in the water were removed and the concentrations were cumulated to have the totality of the elements entering or leaving the matrix

Figure 2 shows SEM profiles, in backscattered electron mode, of the materials after 1 month of exposure to the tested waters. The images show a heterogeneous cement paste containing the lower density hydrated paste and residual anhydrous grains. For the pure water tests, the EDS scores reveal decalcification of the degraded cement paste compared to the sound cement paste. The average CaO content of the hydrated paste over the first 50 microns decreases from 54.2% to 36.9% after exposure to pure water. Since the number of chemical elements analysed is normalized to 100%, this results in a relative increase in the percentages of SiO_2 , Al_2O_3 and MgO . For the mineralized water tests, it is observed that the material shows a surface deposit. The analysis by EDS points out that this deposit is composed mainly of calcium (95 % CaO). The chemical composition of the hydrated paste under the calcium deposit is close to that of a healthy cement paste. The mineralogical analysis by XRD of the CEM III pastes leached with ultrapure water shows the dissolution of portlandite, ettringite, C_3S and C^*S initially present in the healthy material.

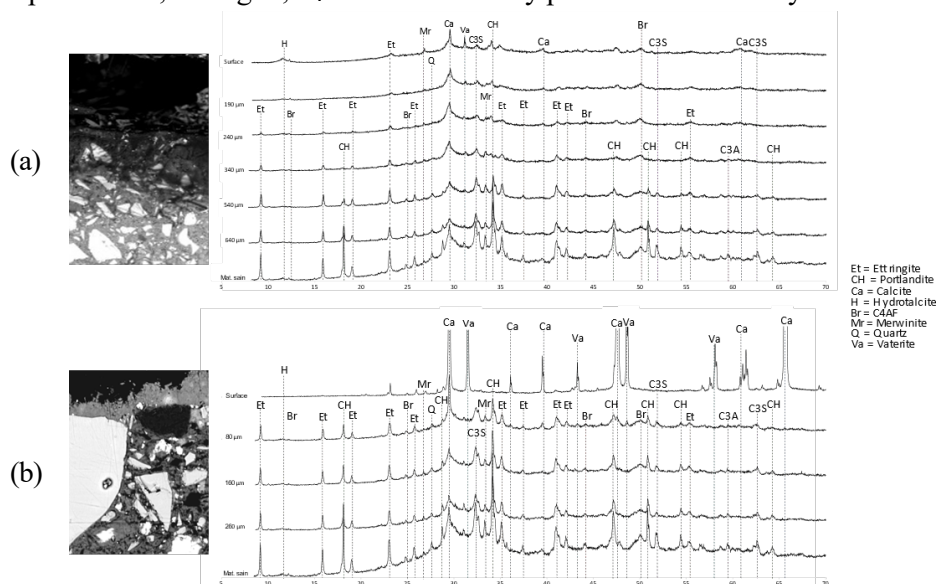


Figure 2 : Mineralogical analysis of monolithic cement pastes leached by ultrapure water (a) and by mineralized water (b)

Merwinite and hydrotalcite are also detected on the surface of the sample, as well as a low intensity peak corresponding to brownmillerite (C_4AF). The surface of the sample leached with mineralized water shows a highly crystallized calcite and vaterite deposit, under the deposit we observe a slight amorphization of the material with peak intensities increasing as we go along, notably for ettringite, portlandite, merwinite and C_1S/C_2S .

Analyses of the leaching solutions show very different leaching/captation phenomena between the tests. The leaching tests with ultrapure water show diffusion phenomena with linear cumulative concentrations as a function of the square root of time, whereas the leaching with mineralized water shows breaks in slope for several elements from the 4th day.

Our tests with mineralized water also show phenomena of capture by the cement matrix for magnesium as well as breaks in slope on the 4th day of the test for the elements Mg, Al, Ca, K. The quantities leached are lower than during the test with ultra-pure water. The sample leached with mineralized water reveals a calcic deposit corresponding to a mix of calcite and vaterite. The average composition of the hydrated paste under the deposit corresponds to that of a healthy paste. It is possible that this calcite precipitate played a protective role, it would be interesting to correlate the slope breaks to the mineralogical changes of the cementitious paste during the mineralized water leaching test. If calcite deposition appears on day 4, it could play a role in the kinetics of release and uptake by the cement matrix. The cementitious coating is therefore likely to change the chemical composition of the water via the release of elements (Ca, Mg, Si, Al) and to affect its composition by increasing its pH significantly. The composition of the water also has an effect on the cementitious lining, the changes in its mineralogical composition are strongly correlated to the composition of the water. A demineralized water tends to degrade the material while a highly mineralized water may result in a protective calcium deposit. Future leaching tests on the same cement pastes will include various water composition in order to determine concentrations for which the rise in pH and the leaching are limited.

3. Conclusions

The purpose of this study was to determine the interactions between a CEM III cementitious lining and potentially highly mineralized drinking water. The impact of the lining on the water quality and the effects of the water on the lining were investigated. Cement pastes were therefore subjected to leaching tests with aggressive water and highly mineralized water. The results of the leaching tests with ultrapure water show a degradation of the cementitious material as well as an amorphization of the cementitious phases present on the surface of the leached sample. Indeed, the peaks observed during the mineralogical analysis by XRD are less important for the leached material, indicating less crystallized phases. The cement matrix leachings lead to significant pH changes. Leaching tests with mineralized water show the appearance of a potentially protective calcite layer and no impact on pH. The release of elements is more limited and capture phenomena by the cement matrix have been highlighted. Water with little or no mineralization will tend to increase the pH of the water significantly, influencing its quality but also any downstream treatments with a rise in pH up to 11 in our tests. Further studies with a more complete panel of mineralized water may reveal a tipping point on the indicators used (calcium concentration, Langelier index) for which pH rises are limited, strongly reducing the impact of the cementitious lining on drinking water quality. Variations of the test protocol would also be interesting to account for the various hydrodynamic conditions of the drinking water in the pipes (stagnation, weak flows, important renewal, pressurized pipe...).

References

- Berthomier, M., 2020. Etude de la lixiviation de l'aluminium de matériaux cimentaires à base de CEM III utilisés dans les canalisations d'eau potable : approche expérimentale et numérique. *Institut National des Sciences Appliquées de Toulouse*.
- Gauthier, A., 2021. Approche expérimentale et modélisation de la lixiviation des ouvrages de traitement d'eau potable en béton exposés à des eaux agressives.
- Müller-Steinhagen, H.M., Branch, C.A., 1988. Comparison of indices for the scaling and corrosion tendency of water. *Can. J. Chem. Eng.* 66, 1005–1007.
- World Health Organization. Regional Office for South-East Asia, 2017. WHO South-East Asia Journal of Public Health, Volume 6, Issue 2, September 2017. *World Health Organization. Regional Office for South-East Asia, New Delhi*.

Restraint effect of steel bar on cement-based materials at early age : A full cross section study

H. Wang¹, Z.L. Hu², and J.P. Liu^{3*}

¹ School of Materials Science and Engineering, Southeast University, Nanjing, 210098, China
Email: 230218274@seu.edu.cn

² School of Materials Science and Engineering, Southeast University, Nanjing, 210098, China
Email: 10102698@seu.edu.cn

³ School of Materials Science and Engineering, Southeast University, Nanjing, 210098, China
Email: liujiaping@cnjsjk.cn

ABSTRACT

In view of the importance of restraint in the cracking of cement-based materials, this paper focuses on the restraint effect of a single steel bar on the early-age cement-based materials. In this study, the distribution characteristics of steel bar restraint on the section were obtained by mapping the dry strain field in the whole section of steel reinforced mortar specimens at different ages using Digital Image Correlation (DIC). A variation law with time was explored. The restraint effect and distribution at different ages are different, which is related to the evolution of elastic modulus of mortar and the bond property between mortar and steel bar. Furthermore, according to the gradient characteristics of the restraint effect, the concept of the restraint zone is given and the time-varying law of it is described qualitatively. The findings of this research provide a basis for establishing the restraint field model of a single steel bar and further exploring the restraint field model under the superposition of multiple steel bars.

KEYWORDS: *restraint, steel bar, shrinkage, cement-based materials, crack*

1. Introduction

This study focuses on the continuous restraints imposed on cement-based materials by steel bars. This form of restraint effect is often uneven on the cross section, resulting in a gradient shrinkage strain and stress field. (Yoo et al. 2014) believed that the overall restraint effect of steel bar is related to reinforcement ratio and steel modulus, and higher reinforcement ratio and modulus mean stronger restraint effect. (Gao, Qu, and Zhang 2012) believed that the restraint effect decreased with the increase of the distance from the steel bar, and the restraint phenomenon could not be observed after a certain distance. In previous studies, the influence of steel bar on the gradient strain of the sectional surface is relatively little involved. Only studies, such as (Gao, Qu, and Zhang 2012), mostly adopted the method of placing an appropriate amount of measuring points at a certain distance from the steel bar to achieve the observation. Digital Image Correlation is an advanced non-contact image measurement method that uses computer vision technology and is considered to be an effective means for full-field strain analysis of materials. DIC provides a new idea of integrated monitoring for shrinkage and cracking. DIC has two main applications in the research of cement-based materials. One is to detect tiny strains in cement-based materials (Wang et al. 2021; Dzaye et al. 2019). The second is to detect the development form of cracks in cement-based materials, which mainly focuses on the exploration of the development mode of load cracks (Guo et al. 2020; He, Lei, and Xu 2020; Liu et al. 2020). One of the motivations of this study is to explore the feasibility and robustness of using DIC to conduct full-section strain field of steel reinforced cement-based composites under the influence of shrinkage.

2. Experimental program

2.1 Test set-up

The objective of this test is the cross section strain distribution of cuboid specimen with intermediate steel bar reinforcement with size of 150mm×150mm×450mm. A quadriprisal window with trapezoidal bottom surface is reserved when pouring, similar to the practice of (Okeil, Matsumoto, and Nagai 2020). The specific geometry and size of the sample are shown in Fig.1. In order to meet the basic observation requirements and minimize the effect of the window on mechanical properties, the size of the window was determined to be 100mm long, accounting for about 22% of the length of the specimen.

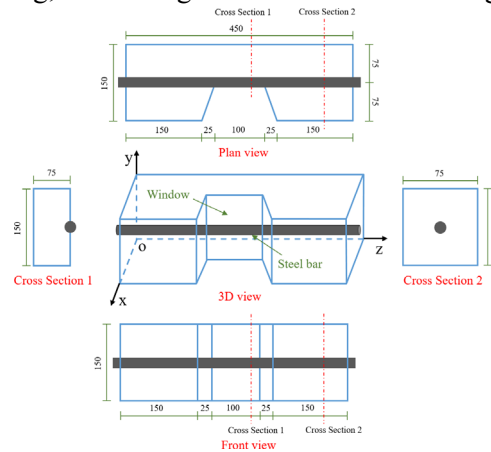


Fig.1 The geometric shape and size of the specimen used for the observation of the section strain field

2.2 Materials

Commercial ordinary Portland cement (OPC) is used, whose main oxide components and proportions are given in Table.1. The mix ratio information is given in Table.2.

Table 1

Chemical components of cement used in the study.

| Chemical constituent %w.t. | SiO ₂ | Al ₂ O ₃ | CaO | Fe ₂ O ₃ | K ₂ O | MgO | Na ₂ O | TiO ₂ |
|----------------------------|------------------|--------------------------------|-------|--------------------------------|------------------|------|-------------------|------------------|
| Cement | 21.48 | 6.77 | 57.94 | 3.11 | 0.87 | 1.77 | 0.14 | 0.35 |

Table 2

Mix proportion of the mortar used in the study.

| Component | Cement | Water | Sand | Superplasticizer |
|------------|--------|-------|------|------------------|
| Mass ratio | 1 | 0.3 | 2 | 0.0045 |

The steel bar selected is the optical round steel bar with diameter of 16mm, whose yield strength f_y is 300MPa and elastic modulus 2.1×10^5 MPa. Compared to ribbed steel bars, the interface between circular steel bars and cement-based materials is clearer and easier to identify in digital photographs.

2.3 Technical background

The core link of this test is to calculate the deformation and strain value of the region of interest, which is realized through Matlab2021 combined with an open-source DIC code 'ncorr_2D'. The compute intensive algorithms are optimized through the use of C++/ mex, while the GUI is written mostly in m-code(Blaber, Adair, and Antoniou 2015).

2.4 Test procedure

The sample was placed horizontally on a smooth surface after mold removal and spray speckle treatment. A high resolution single lens reflex camera was placed 300mm away from the observed surface of the specimen where the speckle was sprayed to capture the window section image of the specimen during shrinkage. The true resolution of the obtained image is about 31.5μm. The environmental conditions were

(20±2)°C and (60±5)%RH. The image acquisition of the camera began at 12h after the mold removal, and was conducted every 1h for a total of 14d.

3 Results and discussion

Fig.2(a) shows the strain distribution obtained from DIC test. The region with higher strain is indicated as dark blue while the region with lower strain as red. It can be observed that a relatively small shrinkage strain appears in the area near the steel bar and a relatively large shrinkage strain appears in the area far away from steel bar. The boundary between the two areas is clear. This indicates that the restraint effect of steel bar on nearby mortar is significantly stronger than that of mortar far away from steel bar. Subsequently, the strain data were calculated according to the distance from the steel bar, see Fig.2(b). The shrinkage of mortar under steel bar restraints is shown in Fig.2(b). With 24h shrinkage as the zero state, the un-uniform strain after 48h can be observed, but the gap between shrinkage at a distance (70mm) and shrinkage near the interface of steel bar is not very large. From the result of 48-168h, it can be seen that with the increase of shrinkage, the gradient characteristics of the strain field also increase.

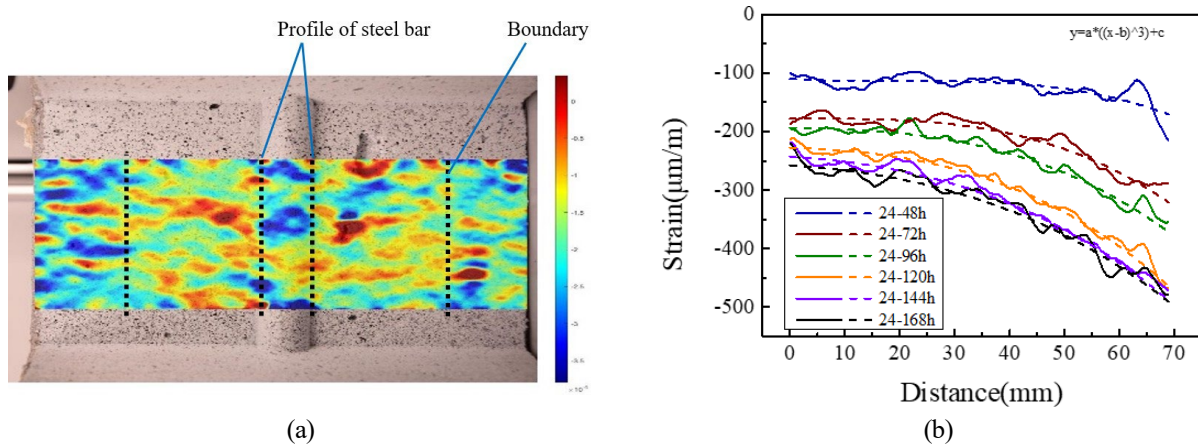


Fig.2 DIC test results (a) strain cloud image (b) relationship between distance and strain

In order to quantitatively describe the relationship between restrained strain and distance, cubic function $y=a*((x-b)^3)+c$ was used in this study to fit strain curve in Fig.2(b), and the fitting curve was also expressed in Fig.2(b). The fitting parameters and fitting effects are shown in Table 3. For cubic functions, when fitting parameter a is roughly the same, fitting parameter b moves in the negative direction of the coordinate axis, which reflects that the gradient deformation trend of the section becomes more and more obvious with the increase of time. The size of parameter c roughly reflects that the overall strain of the specimen increases with time, and the change rate of c value increasing first increases and then decreases, which is also consistent with the general law of shrinkage development.

Table 3

Fitting parameters and fitting effect

| Time | a | b | c | rsquare |
|---------|----------|----------|----------|----------|
| 24-48h | -0.00048 | 20.82399 | -113.564 | 0.562367 |
| 24-72h | -0.0005 | 3.946409 | -178.073 | 0.925945 |
| 24-96h | -0.00038 | -7.96158 | -193.418 | 0.96515 |
| 24-120h | -0.00038 | -15.5259 | -225.59 | 0.98392 |
| 24-144h | -0.00028 | -26.6918 | -236.695 | 0.983863 |
| 24-169h | -0.00026 | -27.5579 | -251.668 | 0.96681 |

Fig.3 shows the relationship of strain at different distances with time, and it is more intuitive to describe the development trend of strain at different distances. In addition, Fig.3 also shows the range of strain with a shrinkage gap of 10%-80% near the steel-mortar interface. By observing the relative relationship between these gap ranges and the strain curves at various distances, the degree of un-uniform strain at the section can be compared. It can be seen that the strain curve has a tendency to cross the strain difference curves, which indicates that the strain gap between the mortar far away from and near the steel bar increases with time.

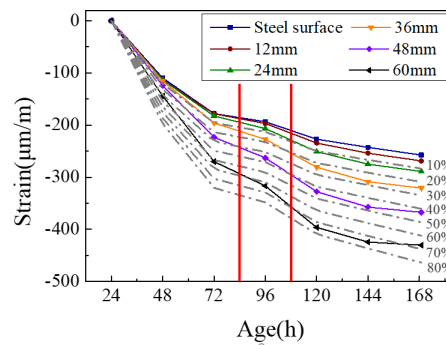


Fig.3 The relationship of strain at different distances with time and the curve of strain difference

4 Conclusions

- DIC can be used as a tool to study the strain gradient of cement-based materials. It performs well in verifying the the gradient of shrinkage strain, stress and restraint field due to steel bar restraints
- The restraint of steel bar on cement-based materials is distributed in a gradient on the cross section. The mortar near the steel bar has larger restraint degree, larger restraint stress and smaller shrinkage
- The shrinkage of cement-based materials in the restrained state has no regular difference with the free shrinkage over time, but the quantity is less than that of free shrinkage. The gradient restraint field of the steel bar on the section is time-varying, and the difference of the restraint degree increases with time

Acknowledgements

The financial support from the National Key R&D Program of China (Project No. 2021YFF0500802) to this work is gratefully acknowledged.

References

- Blaber, J., B. Adair, and A. Antoniou. 2015. "Ncorr: open-source 2d digital image correlation MATLAB software." Review of. *Experimental Mechanics* 55 (6):1105-22. doi: 10.1007/s11340-015-0009-1.
- Dzaye, Evin Dildar, Eleni Tsangouri, Karel Spiessens, Geert De Schutter, and Dimitrios G. Aggelis. 2019. "Digital image correlation (DIC) on fresh cement mortar to quantify settlement and shrinkage." Review of. *Archives of Civil and Mechanical Engineering* 19 (1):205-14. doi: 10.1016/j.acme.2018.10.003.
- Gao, Xiaojian, Guangbin Qu, and Ailian Zhang. 2012. "Influences of reinforcement on differential drying shrinkage of concrete." Review of. *Journal of Wuhan University of Technology-Mater. Sci. Ed.* 27 (3):576-80. doi: 10.1007/s11595-012-0508-1.
- Guo, Qinglin, Hongyu Wang, Ying Gao, Yubo Jiao, Fuchun Liu, and Zizhen Dong. 2020. "Investigation of the low-temperature properties and cracking resistance of fiber-reinforced asphalt concrete using the DIC technique." Review of. *Engineering Fracture Mechanics* 229. doi: 10.1016/j.engfracmech.2020.106951.
- He, Jintao, Dong Lei, and Wenxiang Xu. 2020. "In-situ measurement of nominal compressive elastic modulus of interfacial transition zone in concrete by SEM-DIC coupled method." Review of. *Cement and Concrete Composites* 114. doi: 10.1016/j.cemconcomp.2020.103779.
- Liu, Yanhua, Lei Zeng, Sheng Xiang, Jinxu Mo, Jicheng Zhang, Juan Chen, and Guoyuan Cheng. 2020. "Compressive performance evaluation of concrete confined by stirrups at elevated temperature using DIC technology." Review of. *Construction and Building Materials* 260. doi: 10.1016/j.conbuildmat.2020.119883.
- Okeil, Ahmed, Koji Matsumoto, and Kohei Nagai. 2020. "Investigation on local bond behavior in concrete and cement paste around a deformed bar by using DIC technique." Review of. *Cement and Concrete Composites* 109. doi: 10.1016/j.cemconcomp.2020.103540.
- Wang, Xiaoxian, Zuquan Jin, Jiaping Liu, Fanxiu Chen, Pan Feng, and Jinhui Tang. 2021. "Research on internal monitoring of reinforced concrete under accelerated corrosion, using XCT and DIC technology." Review of. *Construction and Building Materials* 266. doi: 10.1016/j.conbuildmat.2020.121018.
- Yoo, Doo-Yeol, Jung-Jun Park, Sung-Wook Kim, and Young-Soo Yoon. 2014. "Influence of reinforcing bar type on autogenous shrinkage stress and bond behavior of ultra high performance fiber reinforced concrete." Review of. *Cement and Concrete Composites* 48:150-61. doi: 10.1016/j.cemconcomp.2013.11.014.

Effect of Sulfate Attack on the Cement Mortars and Pastes with Different Replacement Levels of Limestone at a Low Temperature

S.T. Lee^{1*}, J.P. Kim², D.G. Kim³, and S.W. Ha⁴

¹ Kunsan National University, Kunsan, South Korea
Email: stlee@kunsan.ac.kr

² Bucheon University, Bucheon, South Korea
Email: jpkim0307@nate.com

³ KICT., Goyang, South Korea
Email: dgkim@kict.re.kr

⁴ Buildchem Ltd., Gongju, South Korea
Email: swha@buildchem.co.kr

ABSTRACT

The purpose of this paper is to establish sulfate resistance of cement mortars and pastes incorporating limestone exposed to severe sulfate attack at 20 and 4 °C. Specimens with 0, 10, 20 and 30% replacement levels of cement by limestone were continually exposed to sodium sulfate solution with 33,800 ppm of SO₄²⁻ concentration. Sulfate exposure tests include compressive strength and expansion measurements of mortar specimens. Additionally, in order to identify products formed by sulfate attack, XRD observations were performed on the paste samples. Results revealed that the mortar specimens incorporating limestone were much more susceptible to sodium sulfate attack, compared to those without limestone, especially when exposed at 4 °C sulfate solution. It was found that the main deterioration product of the damaged samples with higher limestone content was identified as thaumasite, but neither ettringite nor gypsum, by means of XRD analysis. Furthermore, data on mechanical characteristics confirmed that the sulfate deterioration of mortar specimens was greatly dependent on the replacement levels of limestone.

KEYWORDS: *Sulfate attack, Limestone, Solution temperature, Thaumasite*

1. Introduction

It has been generally accepted that conventional sulfate attack in concrete involves the formation of ettringite (3CaO·Al₂O₃·3CaSO₄·32H₂O) and gypsum (CaSO₄·2H₂O). However, recent studies revealed that the thaumasite (CaSiO₃·CaCO₃·CaSO₄·15H₂O) formation is recognized as a cause of deterioration of cement based products [Skaropoulou et al., 2013]. The effect of solution temperature on the sulfate resistance of cement based materials was studied by several authors and it is considered a critical factor in the aggressiveness of sulfate attack. Bensted [1999] also reported that the environmental temperature plays an important role in thaumasite sulfate attack (TSA), emphasizing that TSA might be minimized by employing a low water-binder ratio. Recently, limestone has been used in concrete as a filler or as a main cement constituent for many years. The material is generally considered to be non-hydraulic, and it has been widely assumed that it does not react with the cement, water or aggregate in the mortar or concrete. Regarding external sulfate attack, cement based materials incorporating limestone are more susceptible to thaumasite formation.

The purpose of this work is to establish reasonably performance of cement mortars and pastes incorporating limestone exposed continually to 4 °C sodium sulfate solution. Additionally, the effect of replacement levels (0, 10, 20, and 30% of cement by mass) of limestone on sodium sulfate attack was examined.

2. Experimental

ASTM C 150 Type I Portland cement was used in all the mortar and paste mixtures. The specific gravity and fineness of the cement were 3.13 and 324 m²/kg, respectively. Four replacement levels (0, 10, 20, and 30% by mass) of limestone as a partial replacement of the cement were chosen as the main variable. Ottawa standard grade sand was selected for making mortar specimens. A polycarbonic acid-based superplasticizer was added at the time of mixing to impart good workability to all the mortar mixtures.

The sand/cementitious material ratio and water/cementitious material ratio (w/cm) were fixed at 2.0 and 0.50, respectively, in all the mortar mixtures. Mortar specimens were demoulded 24 hr after casting, and cured in tap water at room temperature for an additional 6 days. Thereafter some of the specimens were transferred to the sodium sulfate solution. Paste samples were made using 100g of total cementitious materials (cement + limestone) and 50g of de-ionized water with no superplasticiser.

The solution temperatures chosen were 20 and 4 °C. Solution concentration was 5% sodium sulfate by mass, which equates to 33,800 ppm as SO₄²⁻ ions.

Compressive strength tests were carried out on 50 mm cube mortar specimens, and performed after 0, 20 and 44 weeks of sulfate exposure. Expansion tests on prismatic mortar specimens (25×25×285 mm), based on ASTM C 1012, were also carried out.

Paste samples exposed to sodium sulfate solutions were used for XRD analysis. XRD was conducted using the RINT D/max 2500 (Rigaku, Japan) X-ray diffractometer. For the XRD tests, CuK α radiation with a wavelength of 1.5405Å at a voltage of 30kV, scanning speed of 2°/min. and current of 30 mA were used.

3. Results and discussion

3.1 Compressive Strength

Fig. 1(a) shows the compressive strength values of mortar specimens after exposure for 20 and 44 weeks as well as prior to exposure in 20 °C sodium sulfate solution. For control specimens (LS0), after 20 weeks of exposure, the compressive strength was 48.7 MPa, while the initial compressive strength of the specimens was 36.2 MPa. This is probably why the loss of compressive strength due to sodium sulfate attack is much lower to a certain extent than the gain of compressive strength by cement hydration in the sulfate solution. However, after 44 weeks, a significant reduction in compressive strength due to continued sulfate attack was observed. The compressive strengths for both LS10 and LS20 mortar specimens after 20 weeks of sodium sulfate exposure were almost similar to those prior to exposure to sodium sulfate solution. The replacement of 30% limestone led to the considerable decrease of compressive strength due to severe sulfate deterioration as well as the lower initial compressive strength of mortar specimens.

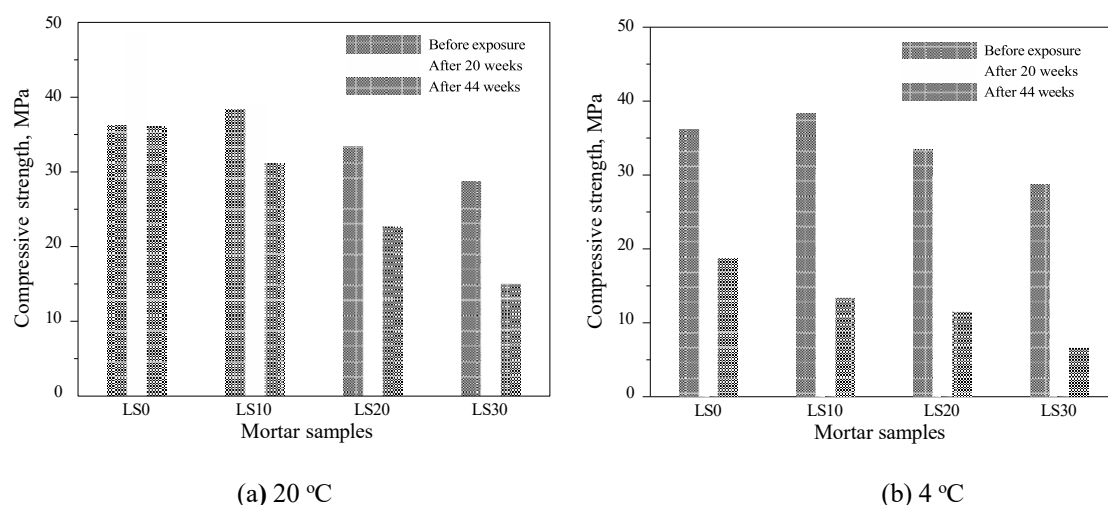


Fig. 1 Compressive strength of mortar specimens exposed to sodium sulfate solution at (a) 20 °C, and (b) 4 °C

The effect of low temperature exposure on the compressive strength of mortar specimens incorporating limestone is shown in Fig. 1(b). For the LS0 mortar specimens, compared to the general trend of compressive strength of mortar specimens exposed to 20 °C sodium sulfate solution, the effect of low solution temperature was notable, with a clear decrease of compressive strength after 20 weeks of exposure. Under 4 °C sodium sulfate attack, the extent to which compressive strength of mortar specimens decreased was proportional to the replacement levels of limestone.

3.2 Expansion

Fig. 2 show the expansion results of the prismatic mortar specimens exposed to 5% sodium sulfate solution at 20 and 4 °C, respectively. The expansion results shown in Fig. 2(a) relates to mortar specimens with 20 °C sulfate exposure. The results show a sudden expansion in the LS30 mortar mixture after 20 weeks of exposure. Moreover, it is evident that the higher the replacement levels of the limestone, the greater was the expansion; and this was true over the entire exposure duration of 44 weeks. After 44 weeks of exposure, the mortar specimens with 10, 20 and 30% replacement levels of cement with limestone recorded expansion values of about 0.378, 0.542 and 0.765 %, respectively, whereas no limestone mortar specimens (LS0) showed about 0.289 % of expansion at the same exposure duration.

The data on expansion of mortar specimens incorporating limestone exposed to sodium sulfate solution at 4 °C are shown in Fig. 2(b). It was observed that the sudden expansion of LS30 mortar specimens had occurred as early as 12 weeks of exposure. Furthermore, after 28 weeks of exposure, the mortar specimens with 30% limestone content began to disintegrate due to excessive sulfate expansion. The expansion values for LS0, LS10 and LS20 mortar specimens were about 0.445, 0.625 and 0.885 % after 44 weeks of exposure, respectively. These results imply that deterioration mode by sulfate attack is greatly dependent on the exposure temperature.

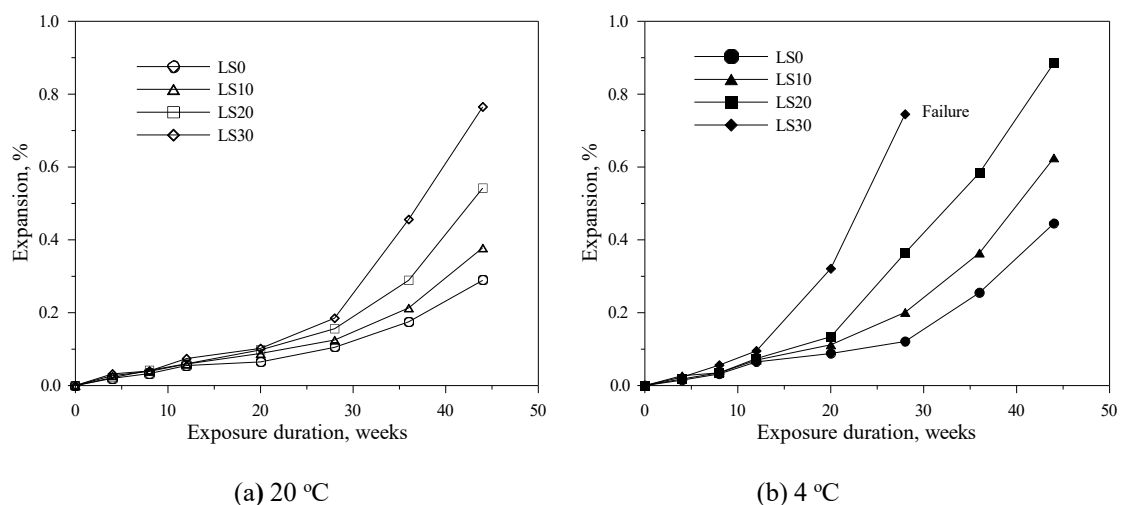


Fig. 2 Expansion of mortar specimens exposed to sodium sulfate solution at (a) 20 °C, and (b) 4 °C

3.3 XRD

XRD patterns of the paste samples with 0 and 30% limestone content exposed to sodium sulfate solution at 20 and 4 °C are shown in Fig. 3. The XRD trace for LS0 paste sample at 20 °C (Fig. 3(a)) is typical of normal cement paste exposed to sodium sulfate solution, indicating formation of gypsum, ettringite and/or thaumasite as sulfate reaction products. At low temperature, it appeared that some peaks for thaumasite were detected at around 26.0 and 28.0° 2θ, which are absent from the ettringite pattern (Fig. 3(b)). The strongest thaumasite peak at around 9.15° 2θ was obtained from the LS30 sample at 4 °C (Fig. 3(d)). Comparatively, LS30 paste sample exposed to sodium sulfate solution at 20 °C shows the coexistence of thaumasite and ettringite at around 9.1 and 16.0° 2θ.

With 20 °C sulfate exposure, formation of ettringite was also obvious in the paste sample incorporating 30% limestone. However, at low temperature, there was no evidence for ettringite formation in the limestone blended paste sample. It must be noted that low temperature can initiate the thaumasite formation by decreasing the stability of ettringite in the condition of sufficient pH. With continued exposure at low temperature, the amount of thaumasite increases as ettringite decreases.

Another important observation was the absence of gypsum in the samples containing 30% limestone, as shown in Fig. 3 (c) and (d). This indicates that in case of cement systems incorporating limestone, one of primary causes for sulfate deterioration may be thaumasite formation, but not gypsum formation.

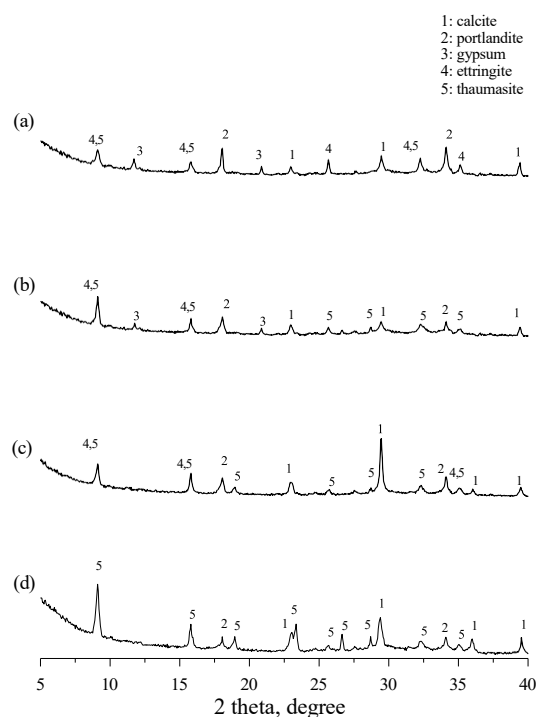


Fig. 3 XRD patterns of paste samples exposed to sodium sulfate solutions for 44 weeks; (a) LS0-20 °C, (b) LS0-4 °C, (c) LS30-20 °C, and (d) LS30-4 °C.

4. Conclusions

The present study emphasized the negative effect of low temperature of the test solution on the resistance of mortar specimens against sodium sulfate attack. The 44-week data on compressive strength and expansion make it clear that the incorporation of limestone in the cement system leads to a poor resistance against sodium sulfate attack. In particular, mortar specimens with higher limestone content were severely deteriorated due to sodium sulfate attack at both normal and low temperature. Based on XRD analysis, it appeared that thaumasite formation is primarily responsible for the severe degradation caused in the limestone blended cement system, especially at low temperature.

Acknowledgements

This research was funded by the National Research Foundation of Korea (No. 2020R1I1A3064980134 0182064070103).

References

- Bensted, J. (1999) "Thaumasite-background and nature in deterioration of cement, mortars and concretes", *Cement and Concrete Composites*, 21(3): 117-121.
- Skaropoulou, A., Sotiriadis, K., Kakali, G. and Tsivilis, S. (2013) "Use of mineral admixtures to improve the resistance of limestone cement concrete against thaumasite form of sulfate attack", *Cement and Concrete Composites*, 37: 267-275.

Alkali-silica reaction resistance of alkali-activated calcined clays using accelerated mortar bar test

S. Mishra^{1*}, S. Peethamparan²

¹ Clarkson University, Potsdam, USA
Email: shumish@clarkson.edu

² Clarkson University, Potsdam, USA
Email: speetham@clarkson.edu

ABSTRACT

Ground granulated blast furnace slag and fly ash are the typical precursors for alkali-activated binder concrete. Recent shortages of these materials prompted us to find alternative nontraditional aluminosilicate materials such as calcined clays, volcanic ashes, and ground bottom ashes. The mechanical and durability performances of such non-traditional precursors containing alkali-activated material remain unexplored. In this study, we investigated the performances of different calcined clay-based alkali-activated mortars (AAM) to one of the most critical durability issues, alkali-silica reactivity resistance. Three calcined clays with different oxide compositions and amorphous contents are considered. The activator solution used had a silica modulus of 1.25 and a Na₂O content of either 9.25 or 13% by mass of the precursors. The binder-to-sand ratio of 1:2.25 and the solution-to-binder ratio varying from 0.6-0.9 depending upon the type of clay are considered. These mixture proportion parameters yielded the optimum compressive strengths for each calcined clay. Three different classes of aggregates with varying degrees of reactivity, as established by ASTM C 1260, are used. To examine the performance, mortar bar prisms are prepared, cured and exposed to 1N NaOH solution as per ASTM C 1567. The changes in the lengths of these specimens are monitored for 14 days, followed by microstructural investigations. The performances of AAM mixtures with and without reactive aggregates compared to portland cement mortars. The results of the accelerated test indicate that irrespective of curing regime, precursor composition, and aggregate combination, alkali-activated calcined clays showed better ASR resistance than the OPC counterparts.

KEYWORDS: *Alkali-activated, Precursors, Alkali-silica reaction, Activator solution*

1. Introduction

The rapid infrastructural growth in the last few decades has increased the global demand for cement by multifold. Developing eco-efficient cementitious materials can significantly cut off cement consumption and contribute to sustainable development goals. Alkali-activated materials have emerged as a sustainable alternative to conventional concrete specifically due to their low carbon footprint (Scrivener et al (2018)). Alkali activation involves the reaction of aluminosilicate powder commonly known as precursors with highly alkaline activator solutions to form a well-compacted cementitious matrix. Fly ash and blast furnace slag are the most popularly used precursors for alkali-activated materials (Provis (2018)). The global supply of both of these materials is declining owing to the rapid decommissioning of coal thermal power plants, which generate Pulverized Fuel Ash (PFA) as a by-product, and widespread use of GGBS as Supplementary Cementitious Material (SCM) for Portland cement (Heath (2014)).

Calcined clays have tremendous potential to be used as an alternative to the existing of available SCMs (Scrivener et al. (2018)). The composition of calcined clays is less variable than fly ash and slag thereby rendering the properties of such clays more predictable and controllable (Zunino and Scrivener (2020)). Calcined clays are currently recognized as a more sustainable supply option and an economically feasible substitute for high-purity metakaolin clay. This is because clay deposits are widespread around the world and a lot of clay waste is created by the ceramics industry and construction projects. Calcined clay-based

alkali-activated concrete can completely substitute clinker and offers several advantages in terms of mechanical properties, such as compressive strength and durability.

Alkali silica reaction (ASR) is one of the key degradation mechanisms responsible for the disintegration of concrete. The alkaline activator solutions and high pH of pore solution in AAMs make them more susceptible to ASR-induced deterioration. The literature mainly reports ASR-induced expansion behavior of fly ash and slag-based AAMs. Williamson and Juenger (2016) and Li et al. (2019) reported that the alkali-activated systems based on fly ash and slag demonstrated better resistance to ASR than OPC concrete, particularly in the presence of highly reactive aggregates. However, the realm of investigating ASR in the calcined clay-based alkali-activated binder remains mostly unexplored. The study presented here examines the ASR resistance of alkali-activated calcined clay mortar AAM, using the accelerated mortar bar test (AMBT) as established by ASTM C1567. The paper also aimed to detect the presence of ASR gels if any in such unconventional geopolymers through scanning electron microscopic analysis.

2. Materials and Methods

Three distinct types of calcined clays obtained from different regions in the United States with varying oxide compositions, as described by Tokpatayeva et al. (2022) have been studied and presented in table 1. These heat-treated clays are activated using caustic solutions of sodium hydroxide pellets mixed in the reagent-grade sodium silicate solution. The solution parameters and the precursor mix described in table 2 for each clay are designed to achieve high strength. Type I Ordinary Portland Cement is used to prepare control specimens to compare relative to the performance exhibited by AAMs.

Table 1: Oxide composition of calcined clays

| Element | Na ₂ O | MgO | Al ₂ O ₃ | SiO ₂ | P ₂ O ₅ | SO ₃ | K ₂ O | CaO | TiO ₂ | Fe ₂ O ₃ |
|---------|-------------------|------|--------------------------------|------------------|-------------------------------|-----------------|------------------|------|------------------|--------------------------------|
| CC1 | 0.17 | 0.41 | 25.02 | 56 | 0.19 | 0.04 | 1.28 | 0.06 | 1.1 | 14.55 |
| CC2 | 0 | 0.34 | 34.89 | 56.33 | 0.21 | 0.05 | 1.19 | 0.32 | 2.06 | 2.68 |
| CC3 | 0 | 0 | 36.83 | 54.44 | 0.05 | 0.09 | 0.3 | 0.08 | 3.1 | 0.74 |

Table 2: Mortar mix composition and Activator solution parameters (*CH - calcium hydroxide, #Ms - silica modulus)

| Mortar Id | Precursor Composition | Solution Parameters | | |
|-----------|-----------------------|---------------------|--|------|
| | | Ms [#] | Na ₂ O (% by mass of precursor) | s/b |
| AAM1 | 93% CC1 + 7% CH* | 1.25 | 13 | 0.85 |
| AAM2 | 97% CC2+3% CH* | 1.25 | 9.25 | 0.6 |
| AAM3 | 97% CC3+3% CH* | 1.25 | 13 | 0.9 |

Three types of aggregates - river sand, roaring spring, and Spratt limestone - were assessed for their reactivity using ASTM C1260, and categorized as R0 (non-reactive), R1 (moderately reactive), and R2 (highly reactive) according to the ASTM C 1778 standard. All the mentioned fine aggregates satisfied the gradation specifications of ASTM C1567. In this experimental investigation, performance of all the binders was examined in combination with two types of aggregates: non-reactive sand and highly reactive Spratt. AAM3 mix and OPC binders were also specifically evaluated when paired with moderately reactive roaring spring sand.

The original version of ASTM C 1567 was adopted for OPC control specimens, while the standard was modified to meet the specific requirements of Alkali-Activated Materials (AAMs) for the experimental specimens. The modifications involved the use of 1 part of calcined clay mix to 2.25 parts of fine aggregate activated with the solution-to-binder ratio as mentioned in table 2. Three replicates for each

composition were studied. Two curing methods were used for AAMs: (1) Ambient curing (-A): mortar bar specimens cured at laboratory temperature of $25 \pm 2^\circ\text{C}$. and (2) elevated temperature curing (-H): mortar bar specimens seal cured at $50 \pm 2^\circ\text{C}$ after casting for 24 hours.

Field emission scanning electron microscopy (SEM) was used to conduct backscattered electron imaging observations, deploying an acceleration voltage of 15-kV, 12- μA probe current, and a chamber pressure of 5×10^{-4} Pa. Microscopy specimens were extracted from AAM specimens that had undergone the former discussed ASR test for 14 days.

3. Results and discussion

The expansion expressed in microstrains of the AAM bars exposed to 1N NaOH solution and stored at 80 degrees Celsius at definite intervals of AMBT is presented in figure 1. Figure 1(a) demonstrates the innate expansion of the AAMs even in the absence of any reactive aggregates. None of the examined mortars

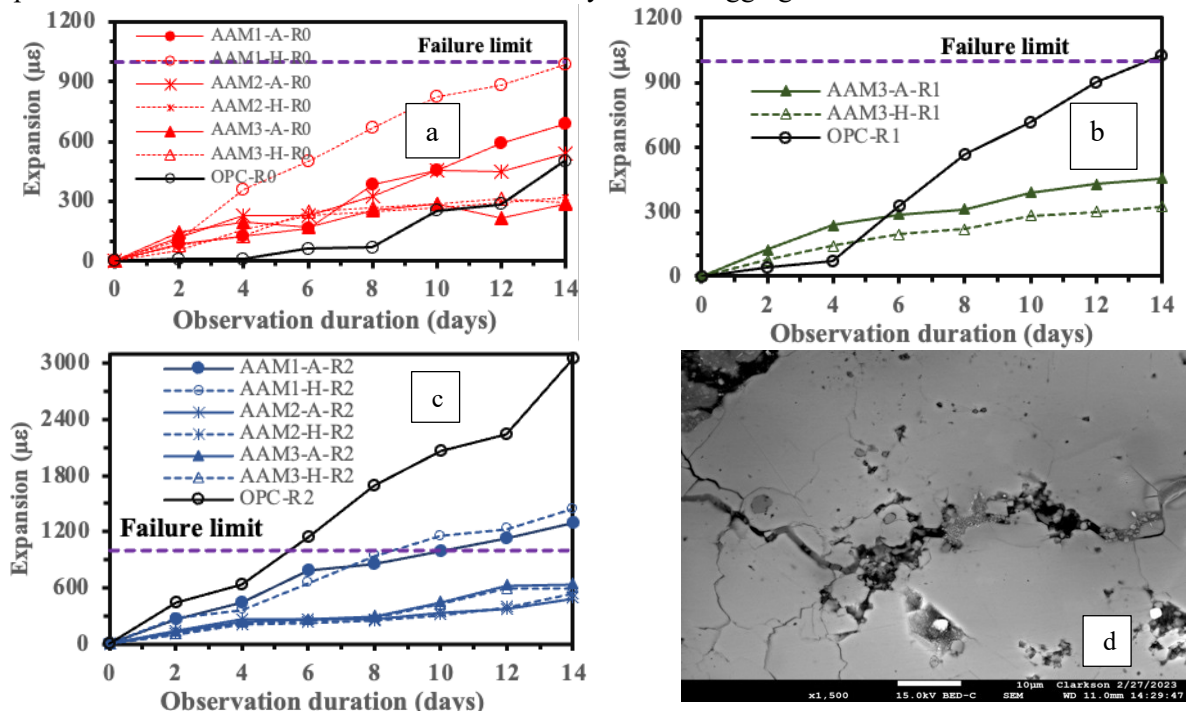


Figure 1:AMBT Expansion of AAM and OPC mortar with (a)control aggregates (b)moderately reactive sand (c)highly reactive sand (d) Backscattered SEM image of AAM1-H- Spratt sample after 14 days testing

surpassed the failure limit. However, AAM1-H exhibited a considerably higher level of expansion. Figure 1(b) shows the expansion of AAM3 and conventional mortar in the presence of moderately reactive (R1 type) fine aggregates. The finding demonstrated a substantial difference of 600 microstrains in the levels of ASR-induced expansion of AAM3 relative to OPC. This supports the notion of using alkali-activated clays with the given composition in an ASR active environment. The expansions of the AAMs and traditional mortar in combination with highly reactive Spratt limestone are displayed in Figure 1(c). OPC mortar expands significantly between 4 to 6 days breaching the failure threshold limit. This observation suggests OPC underwent deleterious ASR. Fine map cracks on the external faces were observed on visual inspection. AAM2 and AAM3, irrespective of the curing method, perform exceptionally well in terms of mitigating ASR when used in the presence of highly reactive aggregates. This can be related to improved alkali binding mechanism, refined pore structure, dense microstructure, and low levels of calcium in the raw material. AAM1 expanded beyond the failure criterion regardless of curing regimes that could be potentially attributed to ASR. The sample was studied under SEM in the backscattered mode. The resulting SEM micrograph revealed that the cracks in the aggregates were filled with Na rich ASR gel.

4. Conclusion

The alkali-silica resistance of three different types of alkali-activated calcined clay mortars was investigated in the presence of moderately and highly reactive aggregates. The following conclusions can be drawn from the study: (1). AAM2 and AAM3 can potentially mitigate the deleterious ASR irrespective of the curing technique which is evident in the presence of highly reactive Spratt limestone. The potential reason for such high resistance can be the dense microstructure and low availability of free alkalis and calcium. (2). Despite such high solution-to-binder ratios as compared to the water/cement ratio of 0.45 for conventional OPC mortar, the performance of AAMs was comparatively superior.

Acknowledgements

This work has been funded by Federal Highway Administration (FHWA), USA. Clarkson University is acknowledged for the facilities provided for the experiments. We also thank and acknowledge Purdue and Penn State Universities for collaborating on this project.

References

- Heath, A., Paine, K., and McManus, M. (2014) "Minimising the global warming potential of clay-based geopolymers" *Journal of Cleaner Production*, 78, 75-83,
- Li, Z., Thomas, R. and Peethamparan, S. (2019) "Alkali-silica reactivity of alkali-activated concrete subjected to ASTM C 1293 and 1567 alkali-silica reactivity tests", *Cement and Concrete Research*, 123. 10.1016/j.cemconres.105796.
- Provis, J.L. (2018) "Alkali-activated materials", *Cement and Concrete Research*, 114, 40-48
- Tokpatayeva, R., Castillo, A., Yoon, J., Kaladharan, G., Jafari, K., & Arachchige, R., Rajabipour, F., Peethamparan, S. and Olek, J. (2022) "Comparative Study of the Reactivity and Performance of Different Nontraditional and Natural Pozzolans in Cementitious System", *Advances in Civil Engineering Materials*. 11. 10.1520/ACEM20220021.
- Williamson, T. and Juenger, M.C.G. (2016) "The role of activating solution concentration on alkali-silica reaction in alkali-activated fly ash concrete", *Cement and Concrete Research*, 83, 124-130
- Zunino, F. and Scrivener, K.L., (2020) "Processing of calcined clays for applications in cementitious materials: the use of grinding aids and particle classification after grinding", *Proceedings of the international conference of sustainable production and use of cement and concrete*, Springer (2020)

Investigation on the durability evolution of high belite cement subjected to thermal fatigue

H.Y. Zeng¹, M. Jin², and J.P. Liu^{3*}

¹ School of Material Science and Engineering, Southeast University, Nanjing, China
Email: 220202234@seu.edu.cn

² School of Material Science and Engineering, Southeast University, Nanjing, China
Email: jinming@seu.edu.cn

³ School of Material Science and Engineering, Southeast University, Nanjing, China
Email: liujiaping@cnjsjk.cn

ABSTRACT

Due to the further promotion of CO₂ reduction strategies, high-belite cement (HBC) has been gradually utilized in civil engineering for its low emissions and good performance in production and service processes. Those concrete facilities in the atmosphere, especially hydraulic engineering concrete made from HBC, are continuously subjected to the thermal fatigue (TF) induced by varying environmental temperatures. This study conducted a temperature-accelerated experiment to understand the possible effect of TF. Results show that TF undermined the macro- and micromechanical performance of HBC and OPC pastes and coarsened the pore structure, especially the pore size below 200 nm. This work explained that TF negatively affected the performance of both HBC and OPC pastes. However, HBC pastes with more C-S-H, a denser matrix, performed better than OPC pastes.

KEYWORDS: *High belite cement, thermal cycle, performance evolution*

1. Introduction

Due to the further promotion of CO₂ reduction strategies, high-belite cement (HBC) has been gradually utilized in civil engineering for its low emissions and good performance in production and service processes (Xin et al. 2020). Those concrete facilities in the atmosphere, especially hydraulic engineering concrete, made from HBC are continuously subjected to varying environmental elements such as sunlight and winds with the temperature of the atmosphere fluctuating continuously (Zeng et al. 2022b). The fluctuating environmental temperature creates the temperature difference between the inside and outside of a cement-based material, and the corresponding contraction and expansion, which in turn causes the fluctuating thermal stress (Arabzadeh and Guler 2019). The long-term and repeated temperature alternation causes macroscopic deformation and cracking of concrete (Gil and Golewski 2018), the deterioration of microscopic pore structure (Zeng et al. 2022a), and the degradation of mechanical properties and durability of cement-based materials (An et al. 2020). Thereby, it is crucial to investigate the effect of environmental heat cycle on the evolution of material performance and to anticipate the service life of building materials.

In this study, the temperature alternating humidity-heat test chamber was utilized to strictly control the temperature and humidity in tests. We examined the influence of thermal fatigue on the mechanical properties and microstructure of high belite cement and ordinary Portland cement paste by testing the compressive strength, ultrasonic pulse velocity, Vickers hardness, and pore structure changes of cement paste.

2. Experimental program

2.1 Materials

In this investigation, normal P-II 42.5 cement and high belite cement was adopted. **Table 1** displays theirs Chemical, mineral compositions.

Table 1 Chemical, mineral compositions of OPC and HBC.

| Chemicals | Oxide constituents (wt.%) | | Minerals | wt.% | |
|--------------------------------|---------------------------|------|-------------------|------|------|
| | OPC | HBC | | OPC | HBC |
| CaO | 63.2 | 61.4 | C ₃ S | 59.8 | 31.5 |
| SiO ₂ | 20.3 | 23.4 | C ₂ S | 14.1 | 42.5 |
| Al ₂ O ₃ | 4.5 | 4.1 | C ₃ A | 4.2 | 3.6 |
| Fe ₂ O ₃ | 4.6 | 4.2 | C ₄ AF | 13.7 | 12.8 |
| SO ₃ | 2.3 | 2.2 | Gypsum | 4.1 | 3.9 |
| MgO | 3.1 | 3.5 | | | |
| LOI | 0.9 | 1.1 | | | |

2.2 Experiment regime

This research examines cement paste with water-to-cement ratios (w/c) of 0.4, denoted OPC as PC4, HBC as BC4. The cement was mixed with water and the mixture was poured into 40mm × 40mm × 160mm mold following the demolding and curing (RH=95%, Temperature=20 °C, 300d) process.

After curing, all samples were separated into the control group and tested group. The temperature of the temperature control box changes between 5-45°C, and each cycle lasts 3 hours. The samples of the tested group were placed in a temperature control machine under 200, 500, and 1200 temperature cycles.

2.3 Characterizations of cement paste specimens

The mechanical property test of cement paste is carried out according to the method of GB/T 50107-2010 standard. Vickers hardness (VH) is conducted using a FUTURE-TECH FM-700 on thin sheet (20 mm × 20 mm × 4 mm). Mercury intrusion porosimetry was conducted using a Micromeritics AutoPore IV9500 (grain size of 5 mm, total weight of 2 g).

3. Results

3.1 Compressive strengths

there appears to be an apparent reduction in both HBC and OPC. The compressive strength first declines sharply and then the change degree becomes gentle. The compressive strength of PC4 and BC4 decreases by 39% and 32%, respectively, after 1200 cycles. It can be deduced that TF has a negative effect on the strength of cement-based materials, and HBC exhibits a better resistance to TF.

Table 2 indicates the evolution of compressive strength with the increasing cycles. Before TF, the compressive strength of HBC is roughly larger than that of OPC, which is attributed to the higher content of C₂S promoting the gain of long-term strength (Wang et al. 2018). However, after TF, there appears to be an apparent reduction in both HBC and OPC. The compressive strength first declines sharply and then the change degree becomes gentle. The compressive strength of PC4 and BC4 decreases by 39% and 32%, respectively, after 1200 cycles. It can be deduced that TF has a negative effect on the strength of cement-based materials, and HBC exhibits a better resistance to TF.

Table 2 The evolution of Compressive strength with the increasing cycles

| Samples | Compressive strength (MPa) | | | |
|---------|----------------------------|------------|------------|------------|
| | 0 | 200 | 500 | 1200 |
| PC4 | 70.67±2.65 | 59.69±5.87 | 48.88±4.21 | 43.11±3.45 |
| BC4 | 72.03±4.34 | 62.47±5.23 | 54.82±5.77 | 48.69±4.06 |

3.2 UPV

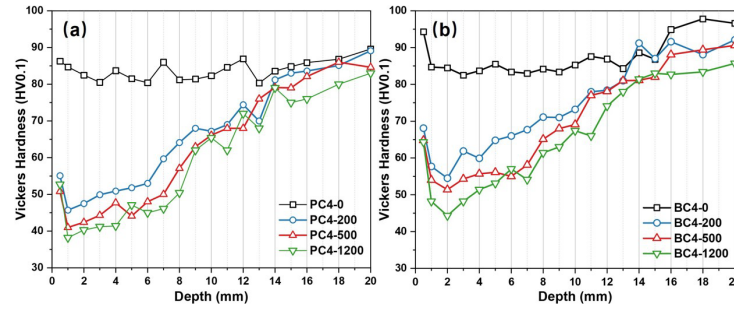
The results of UPV shows the overall thermal damage of cement-based materials under TF (Ramaniraka et al. 2022). As shown in **Table 3**, before TF, the UPV of BC4 is slightly higher than that of PC4, indicating that there is a denser matrix in HBC than OPC due to the sufficient hydration. When exposed to TF, UPV declines with the growing cycles, consistent with the results of the compressive strength. The reduction in UPV for PC4 and BC4 is 12.3 %, and 11.60%, respectively, after 1200 cycles, which hints HBC has a stronger performance and durability subjected to TF.

The UPV measurements indicates that TF has evident adverse effects on the properties of cement pastes. HBC, with robust matrix, shows a greater durability under TF.

Table 3 The evolution of UPV with the increasing cycles

| Samples | UPV (m/s) | | | |
|---------|-----------|---------|---------|---------|
| | 0 | 200 | 500 | 1200 |
| PC4 | 3921.56 | 3629.44 | 3568.53 | 3439.21 |
| BC4 | 4088.96 | 3957.65 | 3766.48 | 3614.37 |

3.3 Vickers hardness

**Fig. 1** The effect of TF on Vickers hardness with depths and cycles

As shown in **Fig. 1(a)** and **(b)**, Vickers hardness is conducted on PC4 and BC4. Consistent with the aforementioned results, the hardness values of HBC in different depths are slightly higher than that of OPC in the initial time, due to the denser internal structure. After TF, it can be clearly seen that the hardness values decrease from the outside to the inside, and the adverse effect dies down with the depth. In OPC, results show that the negative effect mainly happens in the period from 0 to 200 cycles, and the same phenomena also can be found in HBC. Compared to OPC, the curves shows that the reduction degree of HBC is relatively less, hinting a better performance under TF. Interestingly, when the depth reaches about 14 mm, the reduction of Vickers hardness becomes relatively small. Thereby, it can be predicted that there might be a certain depth where the negative effect of TF disappears.

3.4 Pore structure

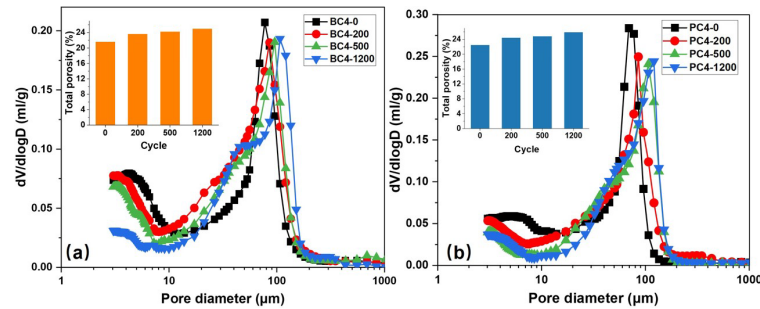
**Fig. 2** The effect of TF on the total porosity and pore size distribution.

Fig. 2(a) and **(b)** depict the evolution of total porosity and pore size distribution of OPC and HBC under TF. PC4 has an initial total porosity of 22.45%, which is greater to that of BC4 at 20.76%. This furtherly confirms the denser structure in HBC than OPC, consistent with the above results. After TF, the total porosity rises with the increasing cycles, indicating the coarsening effect happens. The porosity of HB4 increases from 20.76% to 24.93% and that of PC4 increases from 22.45% to 25.91%, which means HBC has a better resistance to the coarsening of pore structure.

Pore size distribution of PC4 and BC4, plotted as pore diameter versus $dV/d\log D$ are shown as well. As for every sample, the curves move upper right after TF, which directly means that evident coarsening of pore happens in the range of 1nm-1000nm. This also verified a previous study on the evolution of pore structure (Huang et al. 2019). For HBC and OPC pastes, the coarsening of pores most happens in the gel pores (<10nm) and capillary pores (10-200 nm). (Li et al. 2023).

4. Conclusions

The purpose of this study is to examine the influence of thermal fatigue on the performance of high belite cement. After different cycles, the evolution of mechanical characteristics and pore structure of two types of cement pastes are examined. The following conclusions could be drawn:

- (1) On the macroscale, UPV and compressive strength of cement pastes decrease considerably. With increasing cycles, a decreasing degradation rate trend was identified, indicating upper limit damage. After 1200 cycles of TF, the compressive strength of HBC and OPC decline by 32 %, 39 %, respectively. Similarly, TF is observed to systematically coarsen the pore structure of cement pastes, especially the pore size <200nm, which likewise considerably impacts the damage degree of cement pastes. On the mesoscale, TF has a diminishing destructive effect from the outside to the inside. At about 14 mm below the surface, the negative effect is largely mitigated.
- (2) High belite cement paste, with a higher C₂S content and enabling a low emission of CO₂, though has a slower hydration degree in the earlier stage, yet its long-term performance is reliable. Later hydration gives it a denser and more stable structure as measured by strength, hardness, and pore structure, which makes it better prepared for thermal cycling service performance

Acknowledgements

Authors appreciate the financial supports from the National Natural Science Foundation of China (U1706222, 52008097), the Key Project of Natural Science Foundation of China (51738004), Jiangsu Planned Projects for Postdoctoral Research Funds (2020Z029)

References

- An, M., H. Huang, Y. Wang, and G. Zhao. 2020. "Effect of thermal cycling on the properties of high-performance concrete: Microstructure and mechanism". *Construction and Building Materials* 243:118310.
- Arabzadeh, A., and M. Guler. 2019. "Thermal fatigue behavior of asphalt concrete: A laboratory-based investigation approach". *International Journal of Fatigue* 121:229-236.
- Gil, D. M., and G. L. Golewski. 2018. "Effect of Silica Fume and Siliceous Fly Ash Addition on the Fracture Toughness of Plain Concrete in Mode I". *IOP Conference Series: Materials Science and Engineering* 416:012065.
- Huang, H., M. An, Y. Wang, Z. Yu, and W. Ji. 2019. "Effect of environmental thermal fatigue on concrete performance based on mesostructural and microstructural analyses". *Construction and Building Materials* 207:450-462.
- Li, Z., H. Shang, S. Xiao, L. Yang, and Z. Li. 2023. "Effect of thermal fatigue on mechanical properties and microstructure of concrete in constant ambient humidity". *Construction and Building Materials* 368:130367.
- Ramaniraka, M., S. Rakotonarivo, C. Payan, and V. Garnier. 2022. "Effect of Interfacial Transition Zone on diffuse ultrasound in thermally damaged concrete". *Cement and Concrete Research* 152:106680.
- Wang, L., H. Yang, Y. Dong, E. Chen, and S. Tang. 2018. "Environmental evaluation, hydration, pore structure, volume deformation and abrasion resistance of low heat Portland (LHP) cement-based materials". *Journal of Cleaner Production* 203:540-558.
- Xin, J., G. Zhang, Y. Liu, Z. Wang, N. Yang, Y. Wang, R. Mou, Y. Qiao, J. Wang, and Z. Wu. 2020. "Environmental impact and thermal cracking resistance of low heat cement (LHC) and moderate heat cement (MHC) concrete at early ages". *Journal of Building Engineering* 32:101668.
- Zeng, H., W. Li, M. Jin, J. Zhang, Y. Ma, C. Lu, and J. Liu. 2022a. "Deterioration of performances and structures of cement pastes under the action of thermal cycling fatigue". *International Journal of Fatigue* 165:107181.
- Zeng, H., C. Lu, L. Zhang, T. Yang, M. Jin, Y. Ma, and J. Liu. 2022b. "Prediction of Temperature Distribution in Concrete under Variable Environmental Factors through a Three-Dimensional Heat Transfer Model". *Materials* 15 (4):1510.

Research on the leaching mechanism of C-S-H : experiments and molecular dynamics simulations study

Yuefeng Ma¹, Ming Jin², Jiale Huang², and Jiaping Liu^{1,2*}

¹ College of Materials Science and Engineering, Chongqing University, Chongqing, 400045, China

Email: myf@cqu.edu.cn; liujiaping@cnjsjk.cn;

² School of Material Science and Engineering, Southeast University, Nanjing, 211189, China

Email: jinming@seu.edu.cn; jialehuang@seu.edu.cn; liujiaping@cnjsjk.cn;

ABSTRACT

C-S-H is the key hydration product in cement-based materials, exploring the deterioration mechanism of C-S-H under leaching is a prerequisite to understanding the leaching mechanism of cement-based materials. In this study, C-S-H with different Ca/Si ratios is synthesized by the double-decomposition method and leached in NH₄Cl solution. The leaching action of C-S-H with different Ca/Si ratios and decalcification degrees is investigated by TG, ICP-OES and ²⁹Si NMR. The effects of leaching action on the composition, chemical structure, and atomic structure evolution of C-S-H were analyzed comprehensively. Furthermore, molecular dynamics simulations reveal the in-situ interfacial changes of C-S-H on the atomic scale during Ca leaching.

KEYWORDS: *Leaching; C-S-H; nanostructure; composition; molecular dynamics simulations*

1. Introduction

Almost all concrete buildings in contact with liquids face the problem of leaching. C-S-H is the most important hydration product in cement-based materials and plays a key role in leaching cement-based materials [1]. Understanding the deterioration mechanism of C-S-H under leaching is a prerequisite to exploring the leaching mechanism of cement-based materials.

This study focused on the leaching mechanism of C-S-H. C-S-H with different Ca/Si ratios were synthesized by the double-decomposition method and leached in 1 mol/L NH₄Cl solutions. The composition and nanostructure of C-S-H before and after leaching were determined by Inductively coupled plasma optical emission spectroscopy (ICP-OES), Thermogravimetric analysis (TGA), ²⁹Si nuclear and magnetic resonance (²⁹Si NMR). In addition, the in-situ interfacial changes of C-S-H are studied by molecular dynamics simulations (MDS).

The experimental results show that leaching breaks the chemical structure of C-S-H. After leaching, a large amount Q¹ into Q² and Q³. In addition, the silica gel is generated after leaching. Although the initial Ca/Si ratio of C-S-H differs, it becomes similar after leaching. The MDS results showed that NH₄Cl solution could accelerate the destruction of Ca_{C-S-H}-O_{C-S-H} bond in C-S-H, making Ca more easily leach from the C-S-H surface.

2. Method

2.1 Synthesis and leaching of C-S-H

The C-S-H was prepared according to ref.[2]. C-S-H with initial Ca/Si ratios of 0.8, 1.2 and 2.0 were prepared, denoted as Ca/Si0.8, Ca/Si1.2 and Ca/Si2.0. All the synthesis and filtration processes are carried out in a glove box filled with N₂. After the preparation, the 3g C-S-H with every Ca/Si ratio was immersed into 100 ml 1mol/L NH₄Cl solution for 24 h, denoted as Ca/Si0.8L, Ca/Si1.2L and Ca/Si2.0L.

2.2 Characterization techniques

ICP-OES was used for the elemental analysis (Perkin Elmer optima 8000, USA). Before the test, C-S-H powder was mixed with LiBO₂ in a ratio of one to three and heated in a 1000°C muffle furnace for 3h, then dissolved with 5 wt.% HNO₃ solution. Ca and Si concentrations in the lysate were measured. TGA (SDT Q600, USA) was used to analyse the compositions in C-S-H. The heating temperature was 10 °C/min from room temperature to 1000 °C under the N₂ atmosphere. The chemical structure of C-S-H was analyzed by ²⁹Si NMR (Burker AvanceIII 400M, USA). In addition, TEM instrument (FEI Talos-F200S, USA) was used to observe the morphology of C-S-H.

2.3 Molecular dynamics simulations (MDS)

Molecular dynamics simulations were used to analyze the in-situ changes of C-S-H leaching in water and NH₄Cl solution. Molecular model of C-S-H was based on the realistic model reported in ref. [3]. LAMMPS was employed to carry out the MDS. In addition, the leaching behavior of C-S-H was investigated using the ClayFF Force Field [4, 5].

3. Results and discussion

3.1 The change of composition and nanostructure of C-S-H

Fig. 1 (a) shows the TG result of C-S-H before and after leaching. The calculation results of the different compositions are shown in Fig. 2(a). Before leaching, Ca(OH)₂ existed in high Ca/Si ratio samples (Ca/Si1.2 and Ca/Si2.0). However, it has dissolved after leaching. In addition, the bound water content is reduced in all the samples after leaching. The ²⁹Si NMR spectra of C-S-H before and after leaching are demonstrated in Fig. 1(b) and 1(c). Meanwhile, the deconvolutions results of ²⁹Si NMR spectra are shown in Fig. 2(c). Q¹, Q² and Q³ represent the terminal silicate tetrahedra, middle silicate tetrahedra and the chain branching silicate tetrahedra in silicate chain, respectively. Q³(gel) and Q⁴ represent the silica gel, respectively. In the un-leached samples, the Q¹ increases with the increasing Ca/Si ratio, while Q² decreases. After leaching, the Q¹ in all the samples decreases, and Q² becomes the main silicate tetrahedra. In addition, the silica gel is generated in the leaching samples. The content of silica gel is decreased with the increasing Ca/Si ratios.

The stoichiometric formula of C-S-H can be expressed as (CaO)_{C/S}·(SiO₂)·(H₂O)_x [6]. The parameter C/S is the actual Ca/Si ratio of C-S-H, which can be calculated by Eqs. (1) and (2) for the un-leached and leached samples. According to Eqs. (1) and (2), the Ca/Si of C-S-H are calculated and listed in Table 1. Before leaching, the Ca/Si ratios of C-S-H are increased with the initial Ca/Si ratios. However, the Ca/Si ratios of C-S-H are close after leaching.

$$C/S = \frac{\%Si(100 - \%ml_1 - 4.113\%ml_2 - 2.274\%ml_3) - 3.336\%ml_2}{100 - \%ml_1 - \%ml_2 - 2.274\%ml_3} \quad (1)$$

where $\frac{Si}{Ca}$ is the initial Ca/Si in C-S-H (determined by ICP-OES in Fig. 2(a)); %ml₁, %ml₂ and %ml₃ are the weight loss of bound water, Ca(OH)₂ and CaCO₃,

$$C/S = \frac{\%Si(100 - \%ml_1 - 4.113\%ml_2 - 2.274\%ml_3) - 3.336\%ml_2}{\%C-S-H(100 - \%ml_1 - \%ml_2 - 2.274\%ml_3)} \quad (2)$$

where $\frac{Si}{Ca}$ is the Ca/Si ratio in leached samples (determined by ICP-OES results in Fig. 2(a)); %C-S-H is the percentage of silica gels, which can be calculated by %100 - %Q³(OH) - %Q⁴.

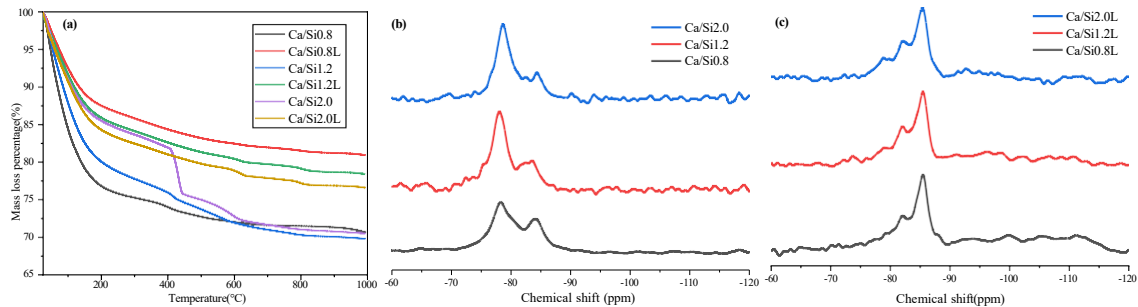


Fig. 1. (a) The TG curves of C-S-H before and after leaching; (b) The ²⁹Si NMR spectra of C-S-H before leaching. (c) The ²⁹Si NMR spectra of C-S-H after leaching.

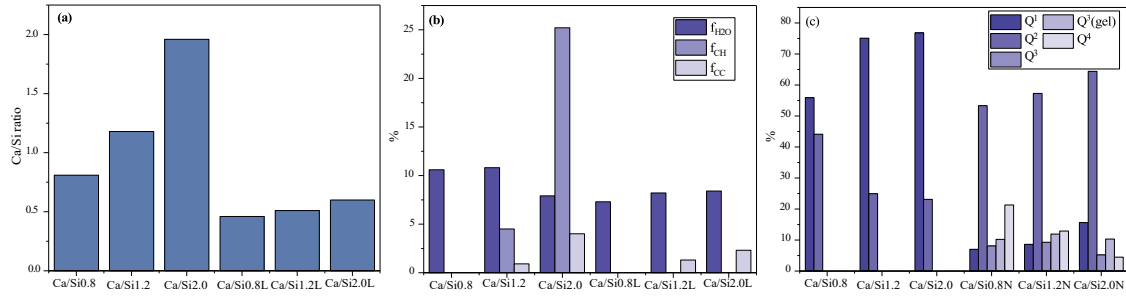


Fig. 2. (a) The total Ca/Si ratio in C-S-H solid powders. (b) The fraction of different compositions in C-S-H was calculated based on TG results. (c) The deconvolutions results of ^{29}Si NMR spectra

Table 1 The actual Ca/Si ratio in C-S-H samples before and after leaching

| | Ca/Si0.8 | Ca/Si1.2 | Ca/Si2.0 | Ca/Si0.8L | Ca/Si1.2L | Ca/Si2.0L |
|-------------|----------|----------|----------|-----------|-----------|-----------|
| Ca/Si ratio | 0.82 | 1.11 | 1.39 | 0.67 | 0.68 | 0.70 |

3.3 Molecular dynamics simulations analysis

In molecular dynamics simulations, the radial distribution function (RDF) is used to gain insight into the interaction of atoms at the interface during the leaching process. **Moreover, the changes and stability of chemical bonds at the C-S-H interface are investigated using the time correlation function (TCF), by which the atomic-scale leaching driving force of solution at the interface can be analyzed.** Additionally, the difference between Ca^{2+} leaching behavior in water and NH_4Cl solution is described by comparing the mean square function (MSD) of Ca^{2+} .

Fig. 3 shows the RDF results of C-S-H in water and NH_4Cl solution. **In all cases, $\text{Ca}_{\text{C-S-H}}\text{-O}_{\text{C-S-H}}$ bond is the main source of the valence bond binding network at the C-S-H interface, and its bond stability is the driving force of the resistance to leaching.** In water, Ca in C-S-H is likely to bond with O in C-S-H and O in water. However, in the case of NH_4Cl solution, Ca in C-S-H bonds with O in C-S-H, O in water and Cl in NH_4Cl solution. Especially, the O in C-S-H can bond with H in NH_4Cl solution. Specially, the O in C-S-H can bond with H in NH_4Cl solution.

Fig. 4 shows the TCF evolution of $\text{Ca}_{\text{C-S-H}}\text{-O}_{\text{C-S-H}}$ bond in water and NH_4Cl solution. **Generally, the connectivity stability in $\text{Ca}_{\text{C-S-H}}\text{-O}_{\text{C-S-H}}$ bond will decrease when TCF values are less than 1.** On the initiation of leaching, the TCF values are less than 1 in both water and NH_4Cl solution, indicating the reduction in the connectivity stability of $\text{Ca}_{\text{C-S-H}}\text{-O}_{\text{C-S-H}}$ bond and the increase of the breakage in $\text{Ca}_{\text{C-S-H}}\text{-O}_{\text{C-S-H}}$ bond. The TCF values of $\text{Ca}_{\text{C-S-H}}\text{-O}_{\text{C-S-H}}$ bond in NH_4Cl solution are lower than that in water, which suggests that $\text{Ca}_{\text{C-S-H}}\text{-O}_{\text{C-S-H}}$ bond is more unstable in NH_4Cl solution. When the TCF values drop to about 0.92 in two solutions, they tend to be steady. Altogether, there is a possibility of rupture of $\text{Ca}_{\text{C-S-H}}\text{-O}_{\text{C-S-H}}$ bond during leaching, which is more rapid and violent in NH_4Cl solution than in water. As mentioned in the RDF results, H and Cl in NH_4Cl solution can bond with O and Ca in $\text{Ca}_{\text{C-S-H}}\text{-O}_{\text{C-S-H}}$ bond, respectively. Both interactions will affect the bonding strength of $\text{Ca}_{\text{C-S-H}}\text{-O}_{\text{C-S-H}}$ bond in C-S-H, as confirmed in the TCF results. Consequently, the C-S-H interface is more accessible to decalcify in NH_4Cl solution than in water.

Fig. 5 shows the MSD results of Ca in water and NH_4Cl solution. Comparing Fig. 5(a) with Fig. 5(b), the MSD of Ca in NH_4Cl solution is significantly higher than that in water, illustrating the more vigorous movement of Ca in NH_4Cl solution than in water. The MSD results corroborate the RDF and TCF results.

In conclusion, MDS is an effective tool for studying the in-situ leaching mechanism of C-S-H in water and NH_4Cl solution. The main mechanism is that NH_4Cl solution can accelerate the destruction of $\text{Ca}_{\text{C-S-H}}\text{-O}_{\text{C-S-H}}$ bond, making Ca more easily leached from the surface of C-S-H.

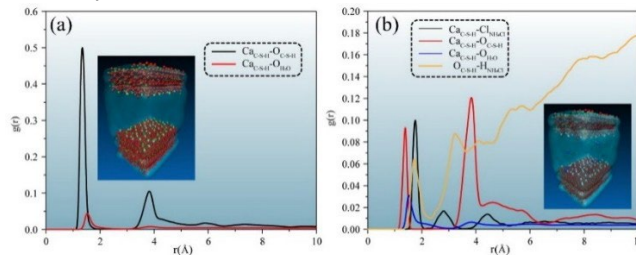


Fig. 3. RDF of the coordination environment of Ca in C-S-H exposed to water (a) and NH_4Cl solution (b).

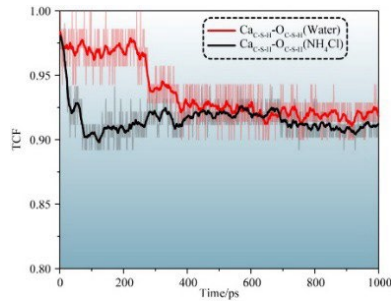


Fig. 4. Mean square function of Ca in C-S-H exposed to water (a) and NH_4Cl solution (b).

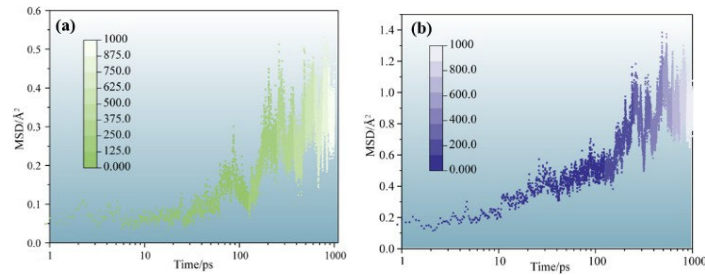


Fig. 5. Mean square function of Ca in C-S-H exposed to water (a) and NH_4Cl solution (b).

4. Conclusions

$\text{Ca}(\text{OH})_2$ existed in high Ca/Si ratio sample before leaching. However, it has dissolved after leaching. In addition, the bound water content is reduced in all the samples after leaching. Although the initial Ca/Si ratio of C-S-H differs, it becomes similar after leaching. The leaching converts a large amount of Q^1 into Q^2 and Q^3 . In addition, the silica gel is generated after leaching.

The MDS results showed that the main mechanism of accelerated C-S-H decalcification by NH_4Cl solution was that NH_4Cl solution could accelerate the destruction of $\text{Ca}_{\text{C-S-H}}\text{-O}_{\text{C-S-H}}$ bond in C-S-H, making Ca more easily leach from the C-S-H surface.

Acknowledgments

Authors appreciate the Graduate Scientific Research and Innovation Foundation of Chongqing, China (CYB22001), the financial supports from the National Natural Science Foundation of China (U2040222, 52008097).

References

- [1] Y. Ma, W. Li, M. Jin, J. Liu, J. Zhang, J. Huang, C. Lu, H. Zeng, J. Wang, H. Zhao, Influences of leaching on the composition, structure and morphology of calcium silicate hydrate (C-S-H) with different Ca/Si ratios, *Journal of Building Engineering* 58 (2022) 105017.
- [2] Z. Hu, M. Wyrzykowski, M. Griffo, K. Scrivener, P. Lura, Young's modulus and creep of calcium-silicate-hydrate compacts measured by microindentation, *Cem. Concr. Res.* 134 (2020).
- [3] R.J.-M. Pellenq, A. Kushima, R. Shahsavari, K.J. Van Vliet, M.J. Buehler, S. Yip, F.-J. Ulm, A realistic molecular model of cement hydrates, *Proceedings of the National Academy of Sciences* 106(38) (2009) 16102-16107.
- [4] A.G. Kalinichev, R.J. Kirkpatrick, Molecular dynamics modeling of chloride binding to the surfaces of calcium hydroxide, hydrated calcium aluminate, and calcium silicate phases, *Chem. Mater.* 14(8) (2002) 3539-3549.
- [5] A.G. Kalinichev, J. Wang, R.J. Kirkpatrick, Molecular dynamics modeling of the structure, dynamics and energetics of mineral-water interfaces: Application to cement materials, *Cem. Concr. Res.* 37(3) (2007) 337-347.
- [6] J.J. Kim, E.M. Foley, M.M. Reda Taha, Nano-mechanical characterization of synthetic calcium-silicate-hydrate (C-S-H) with varying CaO/SiO_2 mixture ratios, *Cem. Concr. Compos.* 36 (2013) 65-70.

The deterioration process of alkali activated slag exposed to sulfate attack and calcium leaching

Zijian Jia¹, Yamei Zhang^{2*}

¹ Jiangsu Key Laboratory of Construction Materials, School of Materials Science and Engineering, Southeast University, Nanjing, 211189, China

Email: jzjjzj18@163.com

² Jiangsu Key Laboratory of Construction Materials, School of Materials Science and Engineering, Southeast University, Nanjing, 211189, China

Email: ymzhang@seu.edu.com

ABSTRACT

The coupling corrosion of sulfate attack and calcium leaching can lead to the deterioration of the microstructure of cementitious materials, which has great challenge to its durability and service life. Alkali-activated slag is a kind of low CO₂ emission cementitious material which has been considered to be an alternative material for Portland cement. To better understand the deterioration process of alkali-activated slag exposed to sulfate attack and calcium leaching, an in-situ observation method was applied to investigate the change of different hydration products in deionized water, Na₂SO₄ solution and MgSO₄ solution. The change of hydration products in different degradation area was also analyzed by the combination of BSE and EDS. The results indicate that the deterioration process of alkali-activated slag is quite different from that of Portland cement, which is closely related to characteristic of hydration products.

KEYWORDS: Sulfate attack, calcium leaching, alkali-activated slag, deterioration, hydration products

1. Introduction

The leaching of calcium from cementitious materials has long been recognized as an important problem in hydraulic structures (Segura et al. 2013). The sulfate attack is also a serious problem for cementitious materials used for marine structures. Alkali-activated slag (AAS) is a kind of low carbon footprint material made with industrial by-product. Previous investigations found that the properties of AAS are better than that of Portland cement after immersion in Na₂SO₄ solution and MgSO₄ solution, which is mainly related to the lower calcium content in the hydration products of AAS (Bakharev, Sanjayan, and Cheng 2002). To better understand the deterioration of the hydration products of AAS in different solutions, a kind of in-situ leaching observation method was applied to investigate the change of hydration products of AAS after immersion in different solutions in this paper.

2. Experimental

Ground granulated blast-furnace slag (here after called slag) is used as the raw material to prepare alkali-activated slag paste (AAS). The chemical composition of slag is shown in Table 1. The specific surface area and density of slag are 436 m²/kg, 2.90 g/cm³, respectively.

Table 1. Chemical composition of slag

| Material | CaO | SiO ₂ | Al ₂ O ₃ | MgO | Na ₂ O | SO ₃ | K ₂ O | Fe ₂ O ₃ | TiO ₂ | LOI |
|--------------|-------|------------------|--------------------------------|------|-------------------|-----------------|------------------|--------------------------------|------------------|-----|
| slag (wt. %) | 41.79 | 32.06 | 15.4 | 7.45 | 0.39 | 1.2 | 0.27 | 0.26 | 0.69 | – |

The water to binder ratio of AAS is 0.35. The alkali-activator is a mixture of liquid water glass and solid NaOH. The molar ratio of SiO₂/Na₂O for the alkali-activator is 1.2 and the content of Na₂O is 4.0%. After

mixing, the samples were casted into a steel mold with the size of $40 \times 40 \times 160$ mm and demolded after 24 h. The samples were then stored in the curing room with a temperature of 20 ± 2 °C and RH of 95% until the age of 210 d. After curing, small pieces with a cross section of $10 \text{ mm} \times 10 \text{ mm}$ and a thickness of 5 mm were cut from the center of the samples with diamond saw. The small pieces were then immersed into ethanol to stop further hydration. The samples used for nanoindentation test were prepared following the regime in previous research (Jia et al. 2019) to meet the requirement for the BSE test.

The leaching behavior of AAS in deionized water (here after called DI water), Na_2SO_4 solution and MgSO_4 solution were studied. DI water was used to prepare the Na_2SO_4 solution and MgSO_4 solution. The concentration of Na_2SO_4 solution and MgSO_4 solution was 0.35 mol/L. The pH values of DI water, Na_2SO_4 solution and MgSO_4 solution were 6.41, 5.83 and 8.78, respectively.

The polished samples were immersed in different solutions for 3d. In this investigation, a kind of in-situ observation method was used to characterize the deterioration of hydration products in different solutions, which has been proposed in the previous research (Jia et al. 2019). The effect of different solutions on the hydration products on the surface layer of the sample can be obtained by using this method. In order to understand the deterioration of hydration products from the surface to the interior, the samples after immersion process were cut from the middle with a saw. The cross section of the sample was characterized with the combination of BSE and EDS-mapping to observe the elemental distribution from the surface to the interior. The illustration about the characterization is shown in Fig.1.

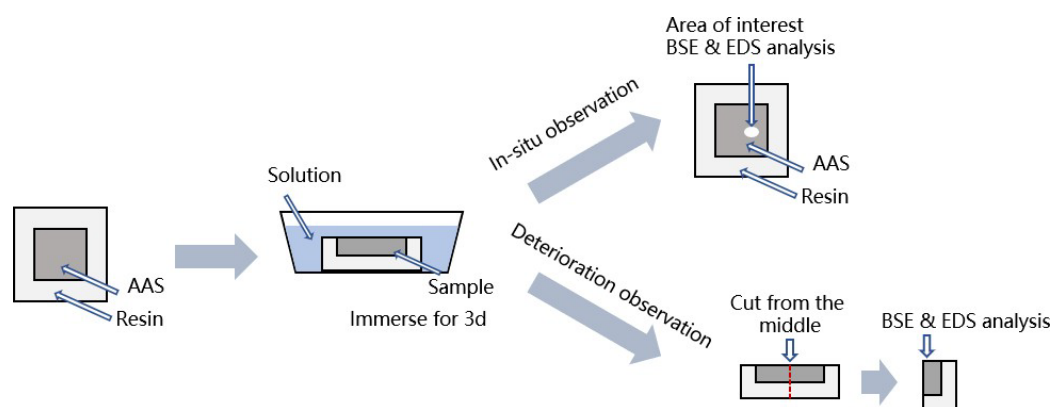


Fig.1 Illustration about the characterization of the sample after deterioration

3. Results and discussion

3.1 The deterioration of hydration products on surface layer

The BSE images of AAS before and after immersion in different solutions are shown in Fig.2. Before immersion in DI water, the grey level of the dark rim is significantly lower than that of the C-A-S-H, while the grey levels of the dark rim and C-A-S-H are quite close to each other after immersion in DI water. A hole appears at the location of the slag, indicating that the slag has been dissolved during the 3d of immersion. The dissolve of slag can also be found in the Na_2SO_4 solution. After immersion in MgSO_4 solution, the slag particle still maintain integrity.

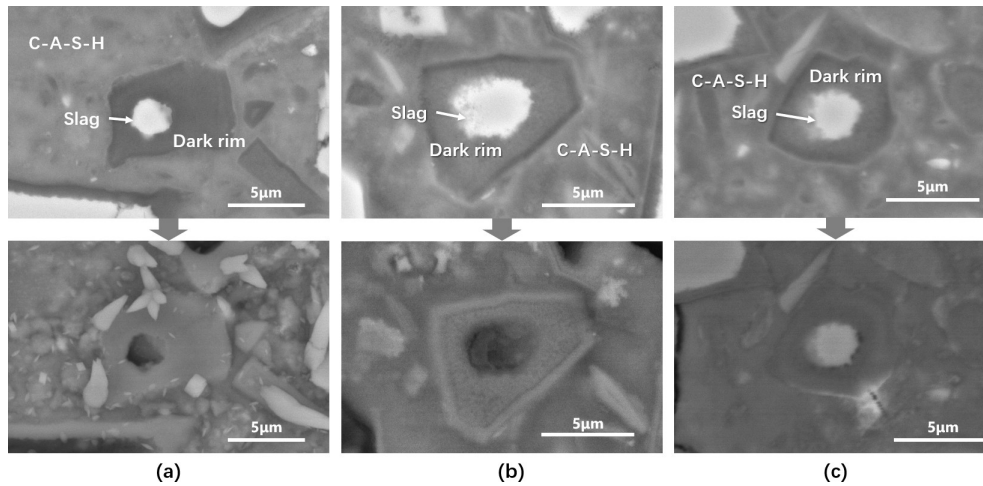


Fig.2 The BSE image of AAS before and after immersion in (a) DI water, (b) Na_2SO_4 solution and (c) MgSO_4 solution

The composition change of slag, C-A-S-H and dark rim are shown in Fig.3. According to the results, slightly decline of Ca/Si can be found in slag after immersion in DI water, Na_2SO_4 solution and MgSO_4 solution. However, significant decrease of Ca/Si can be found in C-A-S-H and dark rim after immersion in these solutions, indicating the hydration products are more vulnerable than that of slag. It is worth noting that the Mg/Si of C-A-S-H increases after immersion in MgSO_4 solution, which could be related to the substitution of Mg for Ca in the C-A-S-H gel.

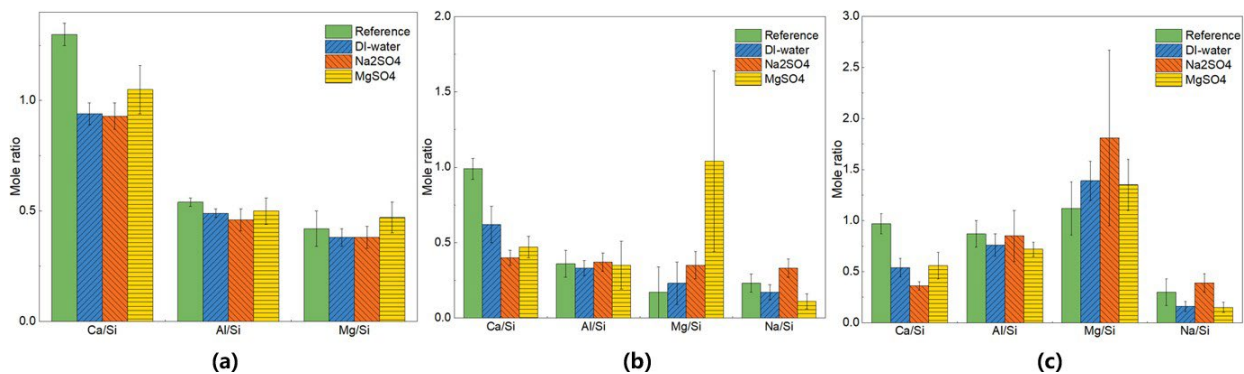


Fig.3 The composition change of (a) slag, (b) C-A-S-H and (c) dark rim after immersion in DI water, Na_2SO_4 solution and MgSO_4 solution

3.2 The deterioration of hydration products from the surface towards the interior

The BSE and EDS-mapping results of AAS from the surface towards the interior after immersion in different solution are shown in Fig.4. According to the BSE images, a noticeable area with grey level reduction can be found near the surface of the sample after immersion in DI water and Na_2SO_4 . The EDS-mapping also shows that a significant decline of Ca can be found in the area near the surface of the sample. The deterioration depth of AAS in Na_2SO_4 is deeper than that in DI water. Different from the sample immersed in DI water and Na_2SO_4 , no obvious grey level reduction area can be found in the sample immersed in MgSO_4 .

EDS-line scanning has also been used to observe the change of elements from the surface towards the interior, and the results are shown in Fig.5. According to the results, significant reduction of Ca can also be found in the sample immersed in DI water and Na_2SO_4 . Moreover, a Na rich area can be found in the sample immersed in DI water and MgSO_4 , indicating that the Na in AAS is not stable. The Na in AAS will move towards to the surface of the sample during the immersion process.

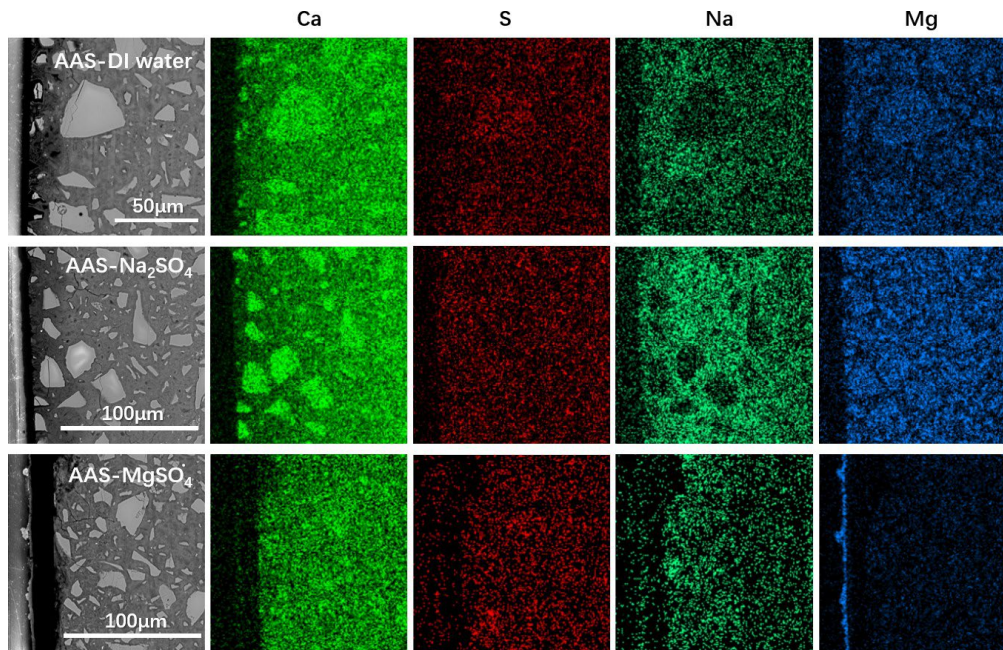


Fig.4 The BSE and EDS-mapping results of AAS from the surface to the interior after immersion in different solutions

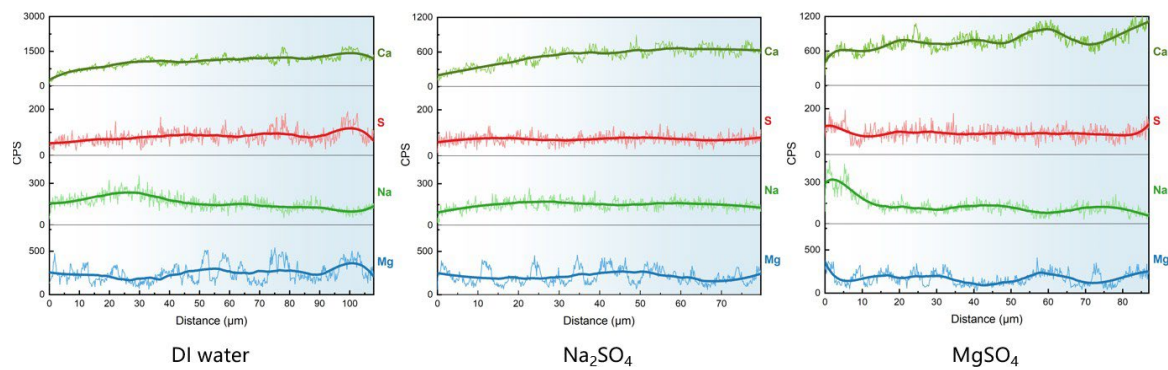


Fig.5 The EDS-line scanning results of AAS from the surface to the interior after immersion in different solutions

4. Conclusions

In this paper, the deterioration of AAS in different solutions was investigated by the application of BSE and EDS analysis. Based on the results above, several important conclusions can be drawn:

The in-situ observation facilitates the comparison between the leaching resistance of different phases in AAS. The deterioration of AAS in Na_2SO_4 solution is more significant than in DI water. No obvious grey level reduction area can be found in AAS after immersion in MgSO_4 solution.

Acknowledgements

This work is supported by the National Natural Science Foundation of China (project No. 52002062)

References

- Bakharev, Tanya, JG Sanjayan, and Y-B Cheng. (2002). "Sulfate attack on alkali-activated slag concrete", *Cement and Concrete Research*, 32: 211-16.
- Jia, Zijian, Ruilin Cao, Chun Chen, and Yamei Zhang. (2019). "Using in-situ observation to understand the leaching behavior of Portland cement and alkali-activated slag pastes", *Composites Part B: Engineering*, 177: 107366.
- Segura, I, M Molero, Sofia Aparicio, JJ Anaya, and A Moragues. (2013). "Decalcification of cement mortars: characterisation and modelling", *Cement and Concrete Composites*, 35: 136-50.

Multiphysics discrete modeling for expansion and deterioration of concrete due to alkali-silica reaction

L. Yang¹, K. Li², X. Hu³, G. Cusatis⁴ and C. Shi^{5*}

¹ College of Civil Engineering, Hunan University, Changsha, PR China
Email: lifuyang@hnu.edu.cn

² College of Civil Engineering, Hunan University, Changsha, PR China
Email: kaili@hnu.edu.cn

³ College of Civil Engineering, Hunan University, Changsha, PR China
Email: xianghu@hnu.edu.cn

⁴ Department of Civil and Environmental Engineering, McCormick School of Engineering and Applied Science,
Northwestern University, Evanston, IL, USA
Email: g-cusatis@northwestern.edu

⁵ College of Civil Engineering, Hunan University, Changsha, PR China
Email: cshi@hnu.edu.cn

ABSTRACT

The durability performance of concrete significantly influences the service life of concrete structures. Alkali-silica reaction (ASR) is a kind of severe deterioration in concrete, which causes concrete expansion and cracking. Extensive work on modeling and testing ASR-induced deterioration, manifesting itself in material expansion and cracking, has been performed over the years and it has been long known that both the aggregate **features** (size distribution, content, and size range of reactive aggregate) and environmental conditions (temperature and relative humidity) play a key role in the ASR process and affect significantly the evolution of ASR in real structures. Despite such importance, it is quite challenging to formulate a comprehensive ASR deterioration model that is able to account for all these effects and further validate the model against reliable experimental data.

This work presents a constitutive model for the simulation of temperature and relative humidity effects on concrete expansion due to ASR. The ASR model was formulated within the Multiphysics framework of the Lattice Discrete Particle Model (LDPM) in which the particle generation was extended in this study to include a general piecewise linear sieve curve that allows selecting aggregate pieces to be reactive or non-reactive according to content and size range of actual reactive aggregate. The effects of size range, distribution and content of reactive aggregate on concrete expansion and deterioration caused by ASR is investigated in this work. As such the Multiphysics framework accounts for the heterogeneous character of ASR expansion, cracking and damage, creep, hygrothermal deformation as well as moisture transport and heat transfer. The overall framework was calibrated and validated by comparing several numerical simulations with a large database of experimental data gathered from the literature.

KEYWORDS: *Alkali-silica reaction, LDPM, Multiphysics modeling, Heterogeneity, Deterioration*

1. Introduction

Concrete is a highly heterogeneous composite material. Its durability is of paramount importance in the service life of structures and infrastructures. Due to the limited amount of nonreactive aggregates with respect to alkali-silica reaction (ASR), more and more concrete structures incorporate reactive aggregate as

raw material. For these structures, ASR poses a threat to their structural health, especially for the ones operating in water or wet environments. ASR-induced damage causes deformation and cracks in the structure due to the long term formation and expansion of ASR gel. For concrete containing reactive aggregates, the aggregate itself was able to act as the inhibitor of the expansion and damage caused by ASR. The inhibition effect is relevant with the distribution, content and size range of reactive aggregate. Besides, it has been long known that temperature and relative humidity play a key role in the ASR process. Despite such importance, the existing literature lacks a comprehensive ASR deterioration model that accounts for these material and environmental effects and that is validated against accurate and reliable experimental data. The main purpose of this work is to fill this gap.

The proposed numerical framework was presented in two recent publications (Yang et al. (2021), Yang et al (2022)), and the main innovation and model validation are here reported.

2. The Multiphysics Lattice Discrete Particle Model

The Multiphysics Lattice Discrete Particle Model (M-LDPM) framework combines the Lattice Discrete Particle Model (LDPM) (Cusatis et al (2011)) with the dual Flow Lattice Element (FLE) framework. LDPM is a mesoscale model for simulating the mechanical response of concrete under a wide range of loading and environmental conditions. The FLE framework simulates the flow behavior in concrete and is inherently coupled with the LDPM system.

2.1 Particle generation

In the numerical model, each aggregate is approximated as a sphere. This section presents a novel formula of sieve curve, entitled Piecewise Linear (PL) sieve curve. The proposed PL sieve curve assumes that the passing percentage changes linearly with the sieve size between each two adjacent sieves. In this case, the particle size distribution function of the PL sieve curve can be represented as

$$f(d) = \frac{\phi_i}{d^3}; (\phi_i < d < \phi_{i+1}), i = 1, 2, 3, \dots, N-1 \quad (1)$$

where ϕ_i is a constant, and d represents a sieve diameter.

The sieve curve is divided into several linear segments characterized by different ϕ_i in different size ranges. Once the experimental sieve curve is known, $(\phi_i, W_i), i = 1, 2, 3, \dots, N$, the PL sieve curve can be written as

$$F(d) = W + \frac{1}{\phi_i} \int_{\phi_i}^d f(d) d^3 dd = W + \frac{\phi_i}{\phi_i} (d - \phi_i) \quad (2)$$

where $F(d)$ is the percentage of aggregate by weight passing through a sieve of diameter d , $\phi_i < d < \phi_{i+1}, i = 1, 2, 3, \dots, N-1$; $1/\phi_i$ is the volume-to-percentage conversion ratio which converts the cumulative volume of aggregate into the passing percentage.

Let $F(d)$ fit the experimental sieve curve in some discrete points $(\phi_i, W_i), i = 1, 2, 3, \dots, N$. One can then compute ϕ_i as

$$\phi_i = \phi_i \frac{W_{i+1} - W_i}{\phi_{i+1} - \phi_i}, i = 1, 2, 3, \dots, N-1 \quad (3)$$

By interpreting the particle size distribution function as the probability density function (pdf) of having a certain diameter d , the cumulative distribution function (cdf) can be computed and its value for $d = \phi_N$ set to be equal to 1.0. This leads to

$$\int_{\phi_1}^{\phi_N} f(d) dd = \int_{\phi_1}^{\phi_N} \frac{\phi_i}{d^3} dd = 1.0 \quad (4)$$

and by substituting Eq. 3 into Eq. 4, one obtains

$$= 2 \sum_{i=1}^{N-1} \frac{W_{i+1} - W_i}{\phi_{i+1} - \phi_i} \left(\frac{1}{\phi_i^2} - \frac{1}{\phi_{i+1}^2} \right) \quad (5)$$

2.2 Dual lattice numerical framework

Within the LDPM geometry (as shown in Fig. 1c for a 3D visualization), a dual lattice system for coupled simulation of chemical/transport processes is constructed from a FLE system. The FLE system is anchored to the LDPM system and is constructed in such a way that each FLE connects two tet-points belonging to two adjacent tetrahedra (as shown in Fig. 1a for a 2D visualization). The FLE, visualized by the solid thick line segment in Figs. 1b, d and e, connects the two points T_1 and T_2 , in which the field variables are defined, i.e. temperature, T , and relative humidity, h . A similar approach for heat transfer and moisture transport was also used by Bolander and collaborators (Bolander and Saito (1998)) and Grassl and collaborators (Grassl et al (2015)).

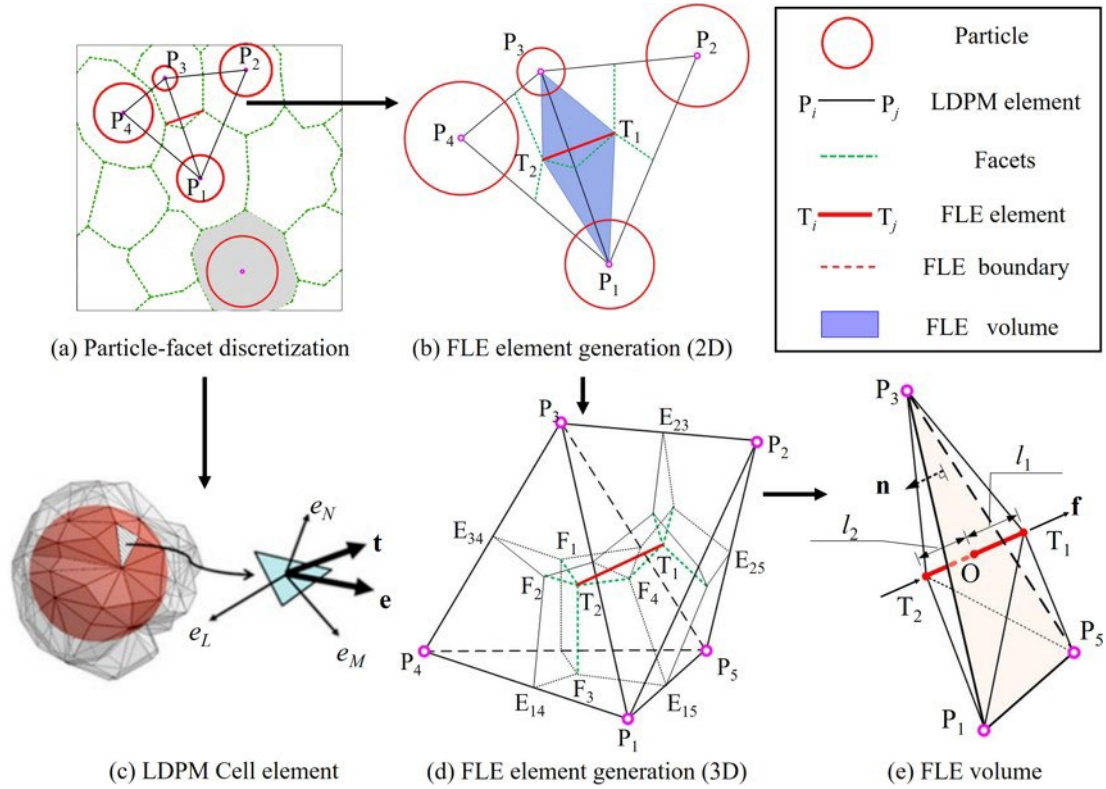


Figure 1 Visualization of basic element in dual lattice system

2.3 Alkali-silica reaction model

It should be mentioned that the M-LDPM framework concerns the effect of aging, creep, hygrothermal and ASR strains, as well as moisture transport and heat transfer and fracture behavior of concrete, while due to the limitation of page length, only the ASR model is reported here.

For the ASR gel to form, alkali-rich water needs to be available in the cement paste surrounding the aggregate and needs to reach pockets of silica inside the aggregates via diffusion (Alnaggar et al (2013)). For the sake of simplicity, the present simplified model is not specifically describe the individual behaviors of the sodium, potassium, and calcium ions (Bažant and Steffens (2000)). In this work, the evolution of ASR is modelled as reaction rim behavior based on diffusion theory. Hence, the average ASR reaction front z can be obtained from a radial diffusion process in the aggregate as

$$z = \frac{w_e C_z(h, T)}{\pi_w \rho_\Lambda z (1 - z/r)} \quad (6)$$

where w_e is the amount of the evaporable water in the cement paste surrounding the aggregate, π_w is the mass density of water, and r is the average radius of a generic aggregate piece approximated as a sphere.

The diffusion coefficient, C_z , of alkali-rich water into the aggregate at the current temperature, T , and relative humidity, h , can be formulated as

$$C_z(h, T) = C_z^0 \exp \left(\frac{E}{RT_0} - \frac{E}{RT} \right) \frac{\phi}{1 + \frac{\phi}{C_{z0}}} \frac{1}{1 + (1-h)^{n_z}} \lambda^{-1} \quad (7)$$

where C_z^0 represents the diffusion coefficient of alkali rich water into the aggregate at reference temperature T_0 and full saturation.

The current position of the reaction front z can be calculated from the time integration of Eq. 6. For a given value of z , one can further define the total mass of ASR gel at that moment, M_g , as

$$M_g = \frac{4\pi r_g^3 \nu}{3} (r^3 - z^3) \quad (8)$$

The process of gel expansion can be formulated as

$$M_w(h, T) = \frac{C_w(h, T)}{4r^2} \phi_3(h, T) M_g - M_w^0 \quad (9)$$

where C_w can be interpreted as bulk diffusion coefficient of water or ions into the ASR gel.

The ultimate gel expansion, governed by $\lambda_w^0(h, T) M_g$, is a nonlinear function of the relative humidity h and temperature T , and the effect of temperature and humidity can be formulated as

$$\lambda_w^0(h, T) = \frac{\exp \left(\frac{K_T(T - T_0)}{1 + K_h(1-h)} \right)}{1 + K_h(1-h)} \quad (10)$$

where λ_w^0 represents the equilibrium coefficient of gel expansion at reference temperature and full saturation. The coefficient K_T and K_h represents the temperature and relative humidity effects on the gel expansion capacity, respectively.

It should be noted that the cracking pattern and expansion of concrete induced by ASR is influenced by loading conditions, and the present work only considers free expansion behavior due to ASR.

3. Conclusions

In this work, a novel formulation of the sieve curve in the LDPM model and the selection rules of reactive aggregate particles for the ASR model to account properly for the effect of reactive aggregate size range, distribution and content on the ASR behavior is proposed. The Multiphysics Lattice Discrete Particle Model (M-LDPM) framework in present work reproduces the time-dependent features of concrete affected by ASR, including the effect of aging, creep, hygrothermal and ASR strains, as well as moisture transport and heat transfer. A discrete formulation for moisture mass conservation and enthalpy energy balance for the flow elements is presented to model the transport behavior in concrete by taking into account explicitly various chemical reactions. The LDPM framework is coupled with the FLE framework in a one-way coupling scheme. In addition, the ASR kinetics model is extended in this study to account properly for the effect of temperature and relative humidity. The proposed model is extensively validated against relevant experimental data from the literature.

References

- Alnaggar, M., Cusatis, G., Di Luzio, G. (2013) "Lattice discrete particle modeling (LDPM) of alkali silica reaction (ASR) deterioration of concrete structures", *Cement and Concrete Composites*, 41: 45-59.
- Bazant, Z.P. and Steffens, A. (2000) "Mathematical model for kinetics of alkali-silica reaction in concrete", *Cement and Concrete Research*, 30(3), 419-428.
- Cusatis, G., Pelessone, D., Mencarelli, A. (2011) "Lattice discrete particle model (LDPM) for failure behavior of concrete. I: Theory", *Cement and Concrete Composites*, 33(9): 881-890.
- Bolander, J.E., Saito, S. (1998) "Fracture analyses using spring networks with random geometry", *Engineering Fracture Mechanics*, 61(5-6): 569-591.
- Grassl, P., Fahy, C., Gallipoli, D., Wheeler, S. (2015) "On a 2D hydro-mechanical lattice approach for modelling hydraulic fracture", *Journal of the Mechanics and Physics of Solids*, 75: 104-118.
- Yang, L., Pathirage, M., Su, H., Alnaggar, M., Di Luzio, G., Cusatis, G. (2021) "Computational modeling of temperature and relative humidity effects on concrete expansion due to alkali-silica reaction", *Cement and Concrete Composites*, 124: 104237.

Yang, L., Pathirage, M., Su, H., Alnaggar, M., Di Luzio, G., Cusatis, G. (2022) “Computational modeling of expansion and deterioration due to alkali–silica reaction: Effects of size range, size distribution, and content of reactive aggregate”, *International Journal of Solids and Structures*, 234: 111220.

Kinetics of iron (hydr)oxide precipitation in cementitious materials

F.E. Furcas^{1*}, S. Mundra¹, B. Lothenbach², O.B. Isgor³ and U.M. Angst¹

¹ ETH Zürich, Zürich, Switzerland,

Email: ffurcas@ethz.ch, shishir.mundra@ifb.baug.ethz.ch, ueli.angst@ifb.baug.ethz.ch

² Empa, Concrete & Asphalt Laboratory, Dübendorf, Switzerland

Email: barbara.lothenbach@empa.ch

³ Oregon State University, Corvallis, OR, USA

Email: burkan.isgor@oregonstate.edu

ABSTRACT

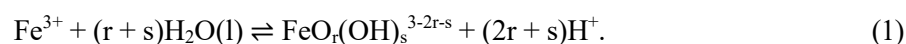
The accumulation of corrosion products throughout the concrete pore network may lead to the development of internal stresses and spalling of the concrete cover, thus facilitating further structural deterioration. To gain a more profound understanding of this self-sustaining sequence of events, both the type of corrosion product(s) as well as their rate of formation within the chemical environment characteristic to cementitious materials must be investigated. By employing a combination of time-resolved TGA, XRD, XAS and ICP studies, we show that the formation of the thermodynamically stable end member goethite (α -FeOOH(s)) is preceded by rapid precipitation of 2-line ferrihydrite (2l-Fe(OH)₃(s)) at alkaline pH. Over time, dissolution of the amorphous intermediate prompts re-crystallisation of goethite from solution. Here, precipitation rates scale with the H⁺ activity. Kinetic rate laws deduced from the progression of aqueously dissolved iron and the amount of solid phase(s) present at any time can lead to better reactive transport models that predict the service life of reinforced concrete structures more accurately.

KEYWORDS: *Precipitation, nucleation, kinetics, pH, thermodynamic modelling,*

1. Introduction

Cementitious pore solutions contain a variety of dissolved species adding up to an ionic strength of up to 1.5 (Albert, Isgor et al. 2022). Their high alkalinity as well as the presence of silica, sulphates and carbonates make up for a unique set of crystallisation conditions for iron (hydr)oxide corrosion products that may favour the formation of amorphous intermediate phases over those that are thermodynamically stable (Schwertmann and Cornell 2008). Whilst a variety of studies investigate the formation of iron oxides at acidic, circumneutral and mildly basic pH (Schwertmann, Friedl et al. 1999, Schwertmann, Stanjek et al. 2004, Zhu, Frandsen et al. 2016), no attempt has been made to characterise the type of corrosion products stabilised at a pH greater than 12. This study shows that the two main corrosion products formed at alkaline pH are 2-line ferrihydrite (2l-Fe(OH)₃(s)) and goethite (α -FeOOH(s)). Here, rapid precipitation of 2l-Fe(OH)₃(s) dictates the solubility limit of iron within the first minutes of equilibration. Over time, re-dissolution of the amorphous intermediate prompts the precipitation of α -FeOOH(s) from solution. As goethite features a comparatively low specific molar volume compared to any other iron (hydr)oxide phase initial stabilisation of 2-line ferrihydrite may severely impact the evolution of internal stresses and thus the structural degradation over time.

The precipitation of solid Fe(III) (hydr)oxides from solution can be formulated according to the general reaction



Whilst there are a range of analytical techniques at disposal to characterise the type and amount of solid corrosion product formed and monitor the coinciding drop in the aqueous Fe³⁺ concentration, a systematic investigation of the kinetic mechanism leading up to the formation of FeO_r(OH)_s^{3-2r-s} remains challenging. This is due to a number of reasons. Firstly, even though only a few iron (hydr)oxides are thermodynamically

stable within the Fe-H-O system, many others precede the formation of their energetically more favourable counterparts or are shown to be stable at nanoscale (Soltis, Feinberg et al. 2016, Furcas, Lothenbach et al. 2022). Secondly, the solubility limit, as dictated by the dissolution e.g. α -FeOOH(s) is low ($\sim 10^{-8}$ M at pH 13.0) and differs from that of the more soluble iron hydroxide phases by more than 4 orders of magnitude (Wieland, Miron et al. 2023). Moreover, Fe^{3+} concentration in equilibrium with α -FeOOH(s) is significantly lower than that of other elements (Si, Na, K) commonly present in cementitious pore solutions. As some of the latter elements are frequently taken up by 2-line ferrihydrite (Thomas Arrigo, Mikutta et al. 2014) or inhibit the growth of other high stability iron phases (Rzepa, Pieczara et al. 2016), the aqueous matrix can severely impact the relative amounts of corrosion products stabilised as well as the measurement of the dissolved iron itself. Lastly, in-situ XAS measurements estimate time for iron (hydr)oxide precipitation to be in the orders of microseconds at room temperature. Given the already low solubility limit of ferric iron at alkaline pH, the limit of detection (LOD) of many measurement devices at disposal to quantify the total amount of dissolved iron is surpassed rapidly after reaction initiation (Caruso, Mantellato et al. 2017). Any attempt to measure the progression of aqueously dissolved iron over time requires a precise, matrix-matched calibration across the entire concentration range observed.

2. Materials and methods

To investigate the type and amount of corrosion product(s) stabilised at alkaline pH, three supersaturated iron stock solutions at pH 13.0, 13.5 and 14.0 have been prepared by dissolving $\text{FeCl}_3 \cdot 6\text{H}_2\text{O}$ in HNO_3 . The acidic iron source was subsequently mixed with concentrated NaOH to achieve the desired final pH and a final Fe^{3+} concentration of 20 mM across all experiments conducted. The aqueous iron concentration was monitored over time by means of ICP-OES. Solids precipitated through the course of the reaction were centrifuged out and immediately freeze dried for two days and stored as dry powders to prevent further phase transition (Schwertmann, Friedl et al. 1999). Minerals were characterised using TGA and XRD within a time span of 30 days.

2.1. ICP-OES

Previous to ICP analysis, aliquots extracted from supersaturated iron stock solution were filtered and re-dissolved in 2 wt. % HNO_3 to prevent further precipitation. Measured signal intensities are related to the total amount of aqueously dissolved iron by an 8-point calibration at concentrations ranging from 50 to 0.01 ppm. To capture above mentioned matrix effects and avoid spectral interference due to other elements present, four spectral lines of iron, namely 234.340, 238.204, 239.563 and 259.940 nm are considered. The level of detection (LOD) and quantitation (LOQ) of the device utilised is determined by following the recommendations of Caruso, Mantellato et al. (2017).

2.2. TGA

Powders extracted from supersaturated iron stock solution were heated from 303 to 1273 K at a rate of 10 K min^{-1} . Obtained TGA and DTG curves were compared to those of pure iron (hydr)oxide reference components and the conversion of one phase to another determined by means of the tangential method (Scrivener, Snellings et al. 2016).

2.3. XRD

X-ray diffractograms were measured on the interval between 4° to 80° in steps of 0.02° using Co $\text{K}\alpha$ radiation using a Bruker D8 Advance diffractometer. Crystalline phases stabilised over the timespan investigated are identified by comparing the obtained diffractograms to those of 2- and 6-line ferrihydrite, lepidocrocite, goethite, hematite and magnetite.

3. Results

DTG curves of the iron phases extracted from aged stock solutions feature two distinct peaks at $\sim 100^\circ\text{C}$ and $\sim 250^\circ\text{C}$. Whilst the majority of water lost occurs within the first region of interest at early equilibration times, the second, high temperature peak is significantly more prominent in the long term samples. This is evident from Figure 1. Comparison to the derivative thermogravimetry signals of 2-line ferrihydrite (2l-

$\text{Fe}(\text{OH})_3(\text{s})$), lepidocrocite ($\gamma\text{-FeOOH}(\text{s})$) and goethite ($\alpha\text{-FeOOH}(\text{s})$) suggests that an FeOOH-type iron hydroxide is stabilised from 2-line ferrihydrite over time.

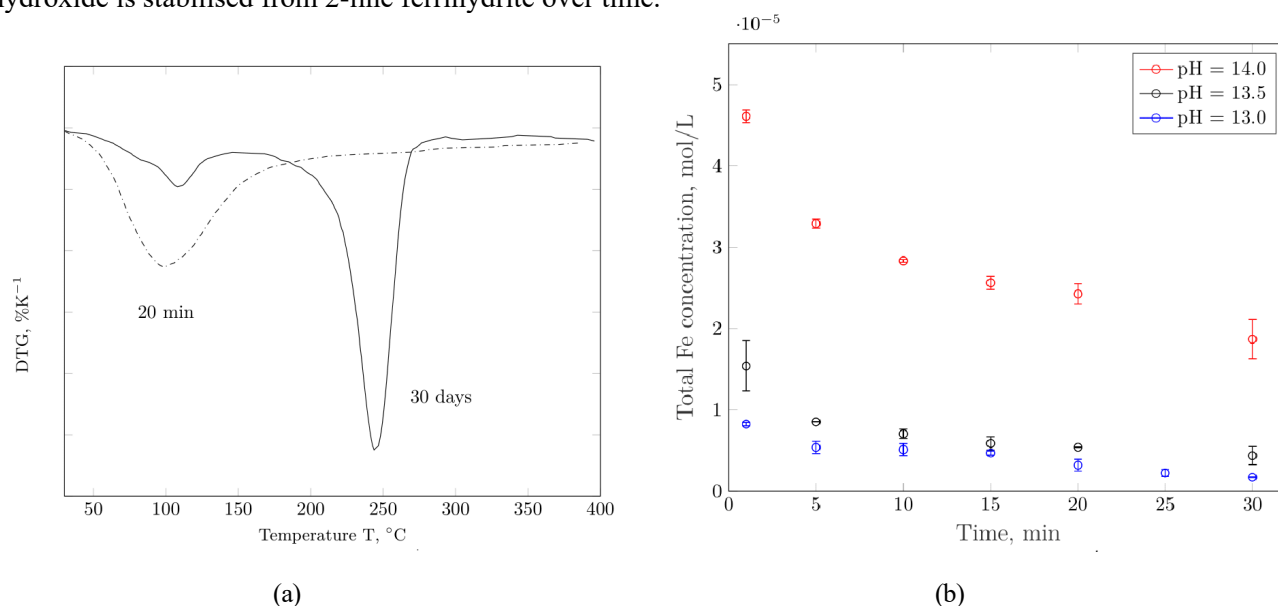


Figure 1: DTG curves of solid iron phases extracted from supersaturated iron stock solutions (Subfigure 1a) together with the total aqueous iron concentration, as measured by ICP-OES at the spectral line of 259.940 nm (Subfigure 1b).

X-ray diffractograms further support this hypothesis and identify the FeOOH-type phase formed to be goethite. Aqueous iron concentrations in equilibrium with the mixture of solid phases stabilised decrease surpass the solubility limit of 2-line ferrihydrite within the first minute of observation and subsequently approach the solubility limit of goethite over time. As illustrated in Figure 1b, initial precipitation rates scale inversely to the pH. This is to be expected, as the degree of supersaturation with respect to both iron hydroxides stabilised is significantly higher at low pH. It is furthermore found that concentration measurements agree well across all emission lines considered. As measured iron concentrations drop continuously but remain close to the solubility limit of 2-line ferrihydrite, the stabilisation of goethite can be considered a dissolution-controlled process. Overall first order kinetics in the rate of iron precipitation furthermore suggest that the precipitation of 2-line ferrihydrite and goethite are competing processes, but do not involve particle-mediated growth mechanisms. In line with existing investigations into the precipitation pathways of $\alpha\text{-FeOOH}(\text{s})$, transformation likely occurs via the dissolution of 2l- $\text{Fe}(\text{OH})_3(\text{s})$ and re-precipitation from solution (Schwertmann, Stanjek et al. 2004, Soltis, Feinberg et al. 2016).

4. Conclusions and future outlook

This study has demonstrated that the formation of thermodynamically stable goethite is controlled by the redissolution of amorphous 2-line ferrihydrite. Due to the slow dissolution kinetics, aqueous iron concentrations remain in the order of 10^{-5} M within the first 30 minutes of equilibration, irrespective of the pH investigated. Given this progression, thermodynamic Gibbs free energy minimisation routines would hence underestimate the amount of iron at disposal to be transported across the concrete pore network. As the specific molar volume of 2-line ferrihydrite is more than 50% larger than that of goethite, the magnitude of internal stresses generated would moreover be underestimated. Aiming to accurately predict degree of structural deterioration over time, the evolution of aqueously dissolved [Fe] as well as the respective fractions of 2l- $\text{Fe}(\text{OH})_3(\text{s})$ and $\alpha\text{-FeOOH}(\text{s})$ present must be fitted by a set of pH dependent kinetic rate expressions that complement the existing thermodynamic modelling approach.

Acknowledgements

All XAS measurements were performed at the PHOENIX beamline at the Swiss Light Source, Paul Scherrer Institut, Villigen, Switzerland. The authors would like to thank Dr. Michael Plötze, Annette Röthlisberger and Marion Rothaupt for provision of the facility, valuable discussions and assistance with the XRD measurements presented in this study. The authors are furthermore grateful to the European Research Council (ERC) for the financial support provided under the European Union's Horizon 2020 research and innovation program (grant agreement no. 848794). The support from ETH Zurich internal Funding and NSF CMMI 1728358 helped enable the collaboration between ETH Zurich and Oregon State University.

References

- Albert, C., O. B. Isgor and U. Angst (2022). "Literature-based data on pore solution compositions of cementitious systems."
- Caruso, F., S. Mantellato, M. Palacios and R. J. Flatt (2017). "ICP-OES method for the characterization of cement pore solutions and their modification by polycarboxylate-based superplasticizers." *Cement and Concrete Research* 91: 52-60.
- Furcas, F. E., B. Lothenbach, O. B. Isgor, S. Mundra, Z. Zhang and U. M. Angst (2022). "Solubility and speciation of iron in cementitious systems." *Cement and Concrete Research* 151: 106620.
- Rzepa, G., G. Pieczara, A. Gawel, A. Tomczyk and R. Zalecki (2016). "The influence of silicate on transformation pathways of synthetic 2-line ferrihydrite." *Journal of Thermal Analysis and Calorimetry* 125(1): 407-421.
- Schwertmann, U. and R. M. Cornell (2008). *Iron Oxides in the Laboratory: Preparation and Characterization*, John Wiley & Sons.
- Schwertmann, U., J. Friedl and H. Stanjek (1999). "From Fe (III) ions to ferrihydrite and then to hematite." *Journal of Colloid and Interface Science* 209(1): 215-223.
- Schwertmann, U., H. Stanjek and H.-H. Becher (2004). "Long-term in vitro transformation of 2-line ferrihydrite to goethite/hematite at 4, 10, 15 and 25 C." *Clay Minerals* 39(4): 433-438.
- Scrivener, K., R. Snellings and B. Lothenbach (2016). *A practical guide to microstructural analysis of cementitious materials*, Crc Press Boca Raton, FL, USA.
- Soltis, J. A., J. M. Feinberg, B. Gilbert and R. L. Penn (2016). "Phase transformation and particle-mediated growth in the formation of hematite from 2-line ferrihydrite." *Crystal Growth & Design* 16(2): 922-932.
- Thomas Arrigo, L. K., C. Mikutta, J. Byrne, K. Barmettler, A. Kappler and R. Kretzschmar (2014). "Iron and arsenic speciation and distribution in organic flocs from streambeds of an arsenic-enriched peatland." *Environmental Science & Technology* 48(22): 13218-13228.
- Wieland, E., G. D. Miron, B. Ma, G. Geng and B. Lothenbach (2023). "Speciation of iron (II/III) at the iron-cement interface: a review." *Materials and Structures* 56(2): 31.
- Zhu, M., C. Frandsen, A. F. Wallace, B. Legg, S. Khalid, H. Zhang, S. Mørup, J. F. Banfield and G. A. Waychunas (2016). "Precipitation pathways for ferrihydrite formation in acidic solutions." *Geochimica et Cosmochimica Acta* 172: 247-264.

Preparation of (super)hydrophobic cement-based matrix with organosiloxanes and micromodification of the surface

E. Erkizia^{1*}, J.J. Gaitero¹, I. Mendikoa¹

¹ *TECNALIA, Basque Research and Technology Alliance (BRTA)*
c/Astondo, Edificio 700, Parque Tecnológico de Bizkaia, Derio 48160, Spain
Email: edurne.erkizia@tecnalia.com
Email: juanjose.gaitero@tecnalia.com
Email: inigo.mendikoa@tecnalia.com

ABSTRACT

In order to reduce chloride ingress and improve concrete's durability in different environments such as marine, often hydrophobic sealants are used to cover the surface of the material. However, sealants and organic coatings tend to degrade mechanically by wear in relatively short time thus increasing again the permeability of the concrete element.

In this work, the authors have investigated the preparation of intrinsically hydrophobic cement-based matrix by chemically hybridizing it with siloxane compounds which contain organic chains (such as polydimethylsiloxane (PDMS) and hexadecyltrimethoxysilane (HDTMS)). Furthermore, with the aim of obtaining superhydrophobic properties, the surface texture was modified using a stainless steel and a copper mesh in the moulding process. The new materials have been characterized by isothermal calorimetry, mechanical properties and effect of the surface modification by contact angle measurements. Moreover, the hydrophobic characteristic was also evaluated by determining the water absorption coefficient of the samples by the Fagerlund test method (UNE 83982).

KEYWORDS: *(Super)hydrophobic cement matrix, organosiloxane, surface texture, concrete durability*

1. Introduction

Concrete is widely used in construction due to its good mechanical strength, availability, and durability. However, due to its hydrophilicity and pore network water can diffuse into the concrete and insert damaging chemical agents such as CO₂, SO₄²⁻ and Cl⁻. Chlorides, for example, can corrode the steel in the reinforced concrete and reduce the mechanical strength of the infrastructure (Angst et al. (2017)). In order to avoid the ingress of these ions often hydrophobic sealants are used on the concrete surface (Saravanan et al (2013); Zhu et al (2013)). However, these coatings chemically degrade and get removed from the surface by radiation and wear in a short period of time compared to the life service of the structure. In order to avoid this drawback Song et al (2017) investigated the fabrication of a mortar with superhydrophobic properties by adding a fluoroalkylsilane compound and changing the microstructure of the surface of the mortar by metal mesh covering. However fluorinated organic compounds are quite toxic (Fenton et al (2021)) and their implementation on market products can be impaired due to their toxicity. Taking this into account, in the current work, the addition of two different nontoxic organosiloxane compounds, polydimethylsiloxane and hexadecyltrimethoxysilane and their effect in the water absorption (hydrophobicity) of the pastes has been studied. Furthermore, two different metal mesh coverings with different pore sizes have been studied with the aim of developing superhydrophobic cement paste surfaces.

2. Experimental section

Cem I 52.5R provided by Lemona was used for the cement pastes. Polydimethylsiloxane (PDMS) and hexadecyltrimethoxysilane (HDTMS) were purchased from Sigma-Aldrich and they were used without further purification. Distilled water was used to mix the cement pastes. The stainless-steel mesh (SSM) is made by Fororeh (Fororeh 120 pcs) and it has a pore size of 125 µm and the diameter of the wire is 80 µm. The copper mesh (CM) (mesh number 200, pore size 75 µm and diameter of wire 50 µm) was made by Sourcing map. Cement pastes with different additions of PDMS (0.1 wt% and 0.5 wt% based on

cement weight (bocw)) and HDTMS (1wt% and 3wt% bocw) were prepared. Table 1 shows the mix dosage of the different pastes.

Table 1. The dosages of the different pastes prepared

| Paste reference | Material | | | |
|-----------------|------------|-----------|----------|-----------|
| | Cement (g) | water (g) | PDMS (g) | HDTMS (g) |
| REF | 100 | 40 | - | - |
| P-PDMS0.1% | 100 | 40 | 0.1 | - |
| P-PDMS0.5% | 100 | 40 | 0.5 | - |
| P-HDTMS1% | 100 | 40 | - | 1 |
| P-HDTMS3% | 100 | 40 | - | 3 |

In all cases, first, the organosiloxane compounds were added to the cement and they were mixed over 30 seconds at 300 rpm. Then, water was added (w/c=0.4) and all the components were mixed at 750 rpm for 1.5 minutes. The mixing was stop for 1 minute and then it was mixed again for 1.5 minutes at 750 rpm. Specimens of 1x1x6 cm³ (see figure 2a) were prepared to carry out mechanical properties at 7 and 28 days. In order to prepare the texturized specimens rectangular prisms moulds of 2x4x8 cm³ were used. At the bottom of the moulds the stainless-steel or copper mesh was placed, and then the cement paste was poured into the mould. In all cases the specimens once moulded were kept at 20°C and 100% RH for 24 hours, then they were demoulded and placed in distilled water until 28 days curing, after which the different tests were carried out. The reference of the texturized specimens is shown in table 2.

Table 2. Reference of the pastes with texturized surface by using a SSM or CM

| Paste reference | PDMS (wt%) | HDTMS (wt%) | Mesh type |
|-----------------|------------|-------------|----------------------|
| REF-SSM | - | - | Stainless steel mesh |
| REF-CM | - | - | Copper mesh |
| P-PDMS0.1%-SSM | 0.1 | - | Stainless steel mesh |
| P-PDMS0.1%-CM | 0.1 | - | Copper mesh |
| P-PDMS0.5%-SSM | 0.5 | - | Stainless steel mesh |
| P-PDMS0.5%-CM | 0.5 | - | Copper mesh |
| P-HDTMS1%-SSM | - | 1 | Stainless steel mesh |
| P-HDTMS1%-CM | - | 1 | Copper mesh |

The hydration heat of the different pastes was characterized by isothermal calorimetry. Six grams of the readily mixed pastes were introduced in the calorimetry and the reaction was followed by several days. The calorimetry experiments were carried out in a TAM air isothermal calorimeter. The equipment is at 25±0.02°C constant temperature. The sample is introduced into a 20 mL hermetic glass or plastic bottle, and the measurement is done using water as reference. The mechanical properties were carried out on an Ibertest universal machine. The contact angle of the texturized samples were characterized by adding a water drop on the surface of the specimens and measuring the height (h) and width (w) of the drop. With that data the contact angle was calculated using equations 1 and 2.

$$\text{Contact angle (rad)} = 2\text{wtg}(2h/w) \quad (1)$$

$$\text{Contact angle (°)} = (\text{contact angle (rad)} * 180) / \pi \quad (2)$$

The water absorption of the different samples was characterized based on the standard UNE 83982:2008. The surface texturized specimens of 2x4x8 cm³ were used in the test. The specimens were dried at 80°C until constant weight before placing them in a container with a water level of 2 mm. Only one face of the sample was in contact with the water and periodically the sample was weighed until constant weight. From this curve the water absorption coefficient (K (Kg/(m²*min^{0.5}))) was calculated.

3. Results and discussion

Figure 1a and 1b show the comparison of calorimetry curves obtained from the reference paste and the pastes with 0.1 wt% and 0.5 wt% of PDMS (a) and pastes with 1 wt% and 3 wt% of HDTMS (b). The pastes with PDMS show the same calorimetric curve as the reference paste indicating that the PDMS does not alter the cement hydration reaction. However, in the case of the HDTMS, the calorimetric curve changes in shape as well as intensity. Furthermore, the change is more drastic as the quantity of the HDTMS is increased. It has to be mentioned that more quantity of HDTMS is added per cement than PDMS therefore it is not an unexpected result.

The mechanical properties at 7 and 28 days of these pastes also show that with the addition the compressive strength of the pastes are reduced compared to the reference especially in the case of 3wt% addition (figure 2b).

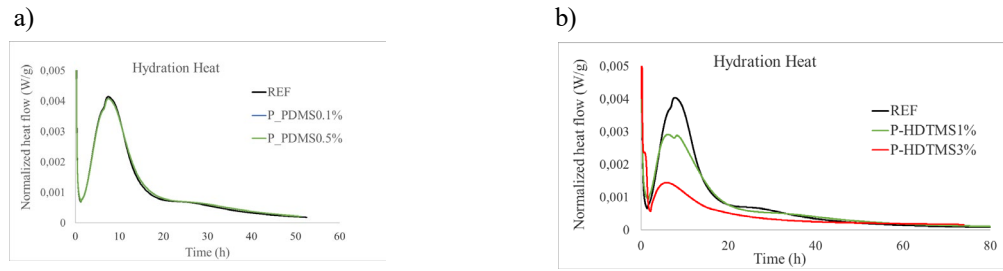


Figure 1. a) Comparison of the hydration heat flow of the reference paste, paste with 0.1wt% and 0.5wt% of PDMS. b) Comparison of the hydration heat flow of the reference paste and paste with 1wt% and 3wt% of HDTMS.

In fact, in the latter case there is a reduction of around 50% at 7 days curing and around 38% at 28 days curing. However, the pastes with PDMS show similar strength as the reference paste. These results indicate that the addition of HDTM is inhibiting somehow the hydration of the cement paste, especially at 3wt% addition.

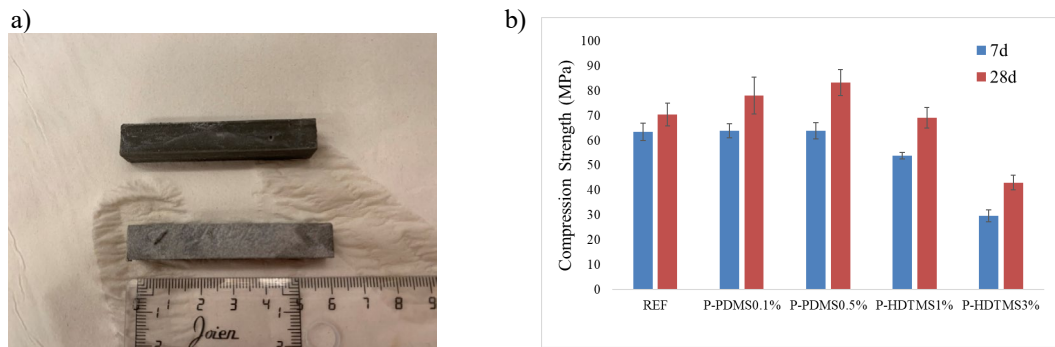


Figure 2. a) Specimens of 1cm x 1cm x 6cm used for mechanical properties characterization; b) Compressive strength at 7 and 28 days for pastes with PDMS (0.1wt% and 0.5wt%) and HDTMS (1% and 3%)

Considering the calorimetric curve and the reduction in the mechanical properties of the pastes the 3wt% HDTMS addition was discarded for the measurement of the water absorption coefficient. For the absorption coefficient test stainless-steel mesh (SSM) and copper mesh (CM) texturized surface specimens were used. Figure 3 shows the water absorption coefficients of the texturized specimens.

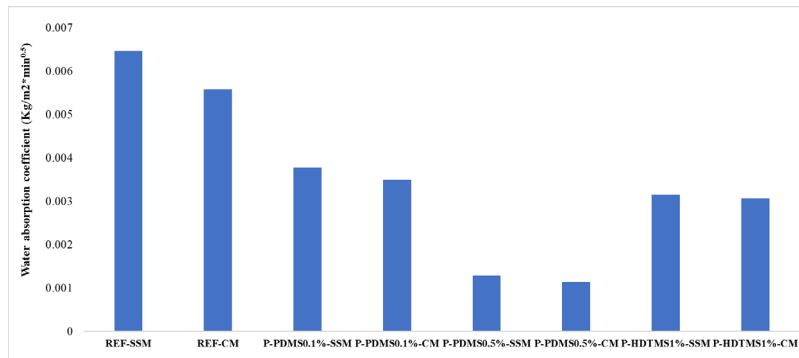


Figure 3. Water absorption coefficient of the SSM and CM surface texturized of the reference, PDMS and HDTMS specimens.

The graph shows that the addition of PDMS as well as HDTMS reduces the water absorption coefficient compared to the reference paste. Therefore, the addition of the siloxane compounds does help to do the matrix less hydrophilic. The highest reduction is obtained with the 0.5wt% addition of PDMS. Pastes with 0.1wt% PDMS and 1wt% HDTMS show similar absorption coefficients. Within the same type of paste the different meshes do not seem to have much effect since in both cases a similar absorption coefficient is obtained. The contact angle of water drops on the surface were also calculated to characterize the superhydrophobicity of the surface. In the literature (Law (2014)) a surface with contact angle (θ) lower than 90 is considered hydrophilic, θ higher than 90 is considered hydrophobic and θ higher than 150 then the surface is superhydrophobic. In the actual case, only surfaces of P-PDMS0.5%-CM, P-HDTMS1%-SSM and P-HDTMS1%-CM show certain hydrophobicity ($\theta > 90$) (see table 3 and figure 4) but none of the specimens show superhydrophobicity. In table 3 the contact angles of the same pastes without the surface texture are also shown. The θ of these latter pastes (P-PDMS0.5% and P-HDTMS1%) are lower

than 90 which indicates that in order to obtain a (super)hydrophobic surface its microstructure needs to be modified.

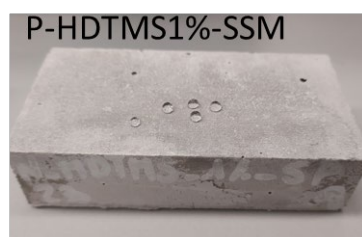


Figure 4. Paste mixed with 1% HDTMS and its surface texturized with SSM with water drops. The water drops maintain their shape which indicates the hydrophobicity of the surface.

Table 3. Contact angles (θ) of specimens P-PDMS0.5% and P-HDTMS1% without and with texturized surface

| SAMPLES | P- PDMS0.5% | P- HDTMS1% | P- PDMS0.5%- CM | P- HDTMS1%- SSM | P- HDTMS1%- CM |
|--|----------------|---------------|-----------------------|-----------------------|----------------------|
| CONTACT ANGLE ($\theta(^{\circ})$) | 43,0 | 55,1 | 60,2 | 107,0 | 84,0 |
| | 40,1 | 54,5 | 108,5 | 103,6 | 105,9 |
| | 39,1 | 63,1 | 106,3 | 105,9 | 119,4 |
| | 37,4 | 60,5 | 110,1 | 53,9 | 94,5 |
| | | | 108,9 | 41,1 | 76,9 |
| | | | 67,0 | 33,4 | 110,7 |

4. Conclusions

Hydrophobization of the cement paste by addition of two nontoxic siloxane compounds, PDMS and HDTMS have been carried out. The calorimetric curves showed that the PDMS addition (0.1wt% and 0.5wt%) did not inhibit the cement hydration whereas the addition of HDTM changed the morphology of the hydration curve and reduced its intensity. These results indicated that the HDTMS compound was inhibiting the cement hydration. Compression strength characterized at 7 and 28 days confirmed the results obtained with the calorimetry. The strength of the pastes with HDTMS, especially with 3wt%, were lower (50% at 7 days and around 38% at 28 days) than the reference paste whereas in the case of PDMS similar strengths were obtained. Regarding the hydrophobicity of the pastes, the addition of PDMS and HDTMS caused a reduction of the water absorption coefficient, in particular with 0.5wt% PDMS. This indicates that PDMS is a good compound to obtain a more hydrophobic cement matrix since good results were obtained with low addition quantities. According to this study the best amount of PDMS to add is 0.5 wt% since it shows the lowest water absorption coefficient without reducing the mechanical properties. However, the addition of these siloxane compounds is not enough for the surface of these pastes to repel water drops. For that the micro/nanostructure of the surface needs to be modified. In this study two meshes have been used, SSM and CM. With this texturization the surface of the samples (except for the case of P-PDMS0.1%) went from hydrophilic to being hydrophobic, although it did not occur homogeneously in all the surface. More work needs to be carried out to better understand the interaction of the siloxane compounds with the cement matrix and to improve its “superhydrophobicity”.

Acknowledgements

The authors would like to acknowledge the Laboratory for Trans-border Cooperation Green Concrete and the funding from the Basque Government through the NEOMAT project (project NEOMAT, KK-2021_00059 Elkartek programme).

References

- Angst, U.M. (2017) “The size effect in corrosion greatly influences the predicted life span of concrete infrastructures”, *Science Advances*, 3(8), el700751, DOI: [10.1126/sciadv.1700751](https://doi.org/10.1126/sciadv.1700751)
- Saravanan, K., Sathiyarayanan, S., Muralidharan, S., Azim, S.S. and Venkatachari, G. (2007) “Performance evaluation of polyaniline pigmented epoxy coating for corrosion protection of steel in concrete environment” *Progress in Organic Coatings*, 59, 160-167
- Zhu, Y., Kou, S., Poon, C., Dai, J. and Li, Q. (2013) “Influence of silane-based water repellent on the durability properties of recycled aggregate concrete”, *Cement and Concrete Composites*, 35, 32-38
- Song, J., Zhao, D., Han, Z., Xu, W., Lu, Y., Liu, X., Liu, B., Carmalt, C.J., Deng, X. and Parkin, I.P. (2017) “Super-robust superhydrophobic concrete”, *Journal of Materials Chemistry A*, 5, 14542-14550
- Fenton, S.E., Ducatman, A., Boobis, A., De Witt, J.C., Lau, C., Ng, C., Smith, J.S. and Roberts, S.M. (2021) “Per- and Polyfluoroalkyl substance toxicity and human health review: current state of knowledge and strategies for informing future research” *Environmental Toxicology and Chemistry*, 40(30), 606-630
- Law, K.-Y. (2014) “Definition for Hydrophilicity, Hydrophobicity, and Superhydrophobicity: Getting the Basics Right” *The Journal of Physical Chemistry Letters*, 5, 686-688

Assessment of the ion diffusivity of cement-based materials using QXRD and micro-CT based random walk simulation

J. Pae^{1*}, and J. Moon²

¹ Seoul National University, Seoul, Republic of Korea
Email: sdc03055@snu.ac.kr

² Seoul National University, Seoul, Republic of Korea
Email: juhyukmoon@snu.ac.kr

ABSTRACT

The ion diffusivity of the cement-based material having interconnected pore system could be evaluated based on the tortuosity calculated through random walk simulation. However, since common random walk simulation cannot be performed on the cement-based material having disconnected pore system, further studies are required to calculate tortuosity of that. This study aimed to quantitatively calculate the tortuosity parameter of cement-based materials having disconnected pore system using quantitative X-ray diffraction (QXRD) and micro-computed tomography (micro-CT) based modified random walk simulation. Cement paste samples were prepared to obtain 3D tomographic images composed of pore, hydrate, and anhydrous phases, which were reconstructed from the CT scanned data using theoretical linear attenuation coefficients of each phase. The modified random walk simulation which allows the migration on the hydrated product was proposed by fully understanding the small capillary and gel pores presented in the hydrated product. This method enabled the calculation of tortuosity of cement-based materials having disconnected pore system for the first time which led to the evaluation of the diffusivity.

KEYWORDS: *ion diffusivity, QXRD, micro-CT, random walk simulation*

1. Introduction

The ion diffusivity of the cement-based material having interconnected pore system could be evaluated based on the tortuosity calculated through random walk simulation (Liu, Sun et al. 2012). However, since common random walk simulation cannot be performed on the cement-based material having disconnected pore system, further studies are required to calculate tortuosity of that. This study aimed to quantitatively calculate the tortuosity parameter of cement-based materials having disconnected pore system using quantitative X-ray diffraction and micro-computed tomography (micro-CT) based modified random walk simulation. Cement paste samples were prepared to obtain 3D tomographic images composed of pore, hydrate, and anhydrous phases, which were reconstructed from the CT scanned data using theoretical linear attenuation coefficients of each phase (Promentilla, Sugiyama et al. 2008, Bossa, Chaurand et al. 2015). The modified random walk simulation which allows the migration on the hydrated product was proposed by fully understanding the small capillary and gel pores presented in the hydrated product. This method enabled the calculation of tortuosity of cement-based materials having disconnected pore system for the first time which led to the evaluation of the diffusivity. The ion diffusivity was successfully calculated by the modified random walk simulation compared to the numerical simulation and experimental data.

2. Materials and experiments

The cement paste samples were prepared by mixing ordinary Portland cement (OPC, Ssangyoung C&E, Korea) and water with a water-to-cement ratio of 0.3, 0.4, 0.5, 0.6, and 0.7. After mixing, all samples were cast into PVC moulds and cured for 28 days at 20°C and 60% RH conditions. The X-ray CT scanner

Skyscan1272 (Bruker, Belgium) was used for X-ray tomographic imaging. The X-ray was configured to have a voltage of 90 kV and a current of 111 μ A. The tomographic data were used to reconstruct an image that was 3,000 by 3,000 pixels with a 0.5 μ m pixel resolution. 2,000 layers of the X-ray projection picture were acquired with an exposure interval of 5,000 ms and an angle step of 0.1°. The X-ray diffractometer D2 Phaser (Bruker, Germany) with Cu-K α radiation ($\lambda = 1.5418$ Å) was used to measure the XRD patterns of the samples. TGA was carried out in a N₂ atmosphere using the TA Instrument Q600 (TA Instrument, USA) at a heating rate of 10 °C /min for up to 1,000 °C. To validate the ion diffusivity obtained by modified random walk simulation, rapid chloride migration test was performed to experimentally measure the ion diffusivity following NT Build 492.

3. Image Segmentation

2000 layers of the X-ray projection image were stacked to construct the 3D greyscale images with a width of 1,500 μ m, a length of 1,500 μ m, and a height of 1,000 μ m. In order to segment the greyscale images to ternary images containing pore, hydrate, and anhydrous phases, two thresholding values were carefully determined based on mean linear attenuation coefficient value (LAC) of each phase calculated by QXRD. The mass ratio of all chemical compositions included in the cement paste was accurately calculated through QXRD using XRD and TGA data. Theoretical LAC values of the chemical composition found to be included in the cement paste were calculated according to (Promentilla, Sugiyama et al. 2008). Mean LAC of each phases was calculated based on theoretical LAC value and mass ratio of all included chemical compositions. Considering calculated mean LAC value as a mean of gaussian distribution, greyscale histograms of 3D images were successfully decomposed to Gaussian distributions, which each representing pore, hydrate, and anhydrous phases. All voxels of the 3D grayscale images were classified into pore, hydrate, and anhydrous phases by using the intersection of the Gaussian distributions as the thresholding value.

4. Modified Random Walk Simulation

Random walk simulation is a computationally efficient method for determining transport parameters from binary porous media. The main purpose of random walk simulation is obtaining the mean square displacement of the walkers as a function of lattice time which leads to quantification of diffusion tortuosity. Subsequently, diffusion tortuosity was utilized to evaluate the ion diffusivity of cement paste regarding the effective porosity and self diffusion coefficient in pore fluid. However, the random walk simulation can only be performed in a connected pore system, which is a fatal disadvantage considering that most cementitious materials have a disconnected pore system at the microscale. In addition, in real cementitious materials, ions can be transported through small pores that cannot be observed in micro tomography (e.g. small capillary pores and gel pores in calcium silicate hydrate), but this is not reflected in conventional random walk simulations. Therefore, in this study, we proposed a modified random walk simulation that can solve these limitations. In this random walk simulation, walkers can move not only to pore voxels but also to hydrate voxels. However, by introducing the concept of “hydrate voxel retention time”, the algorithm was modified so that when a walker moves a hydrate voxel, it takes more time by the hydrate voxel retention time than when moving a pore voxel.

5. Results and Discussion

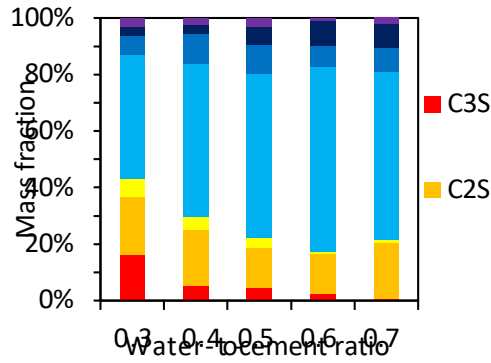


Figure 1. Mass fraction of chemical composition in OPC paste by QXRD.

Figure 1 shows mass fraction of chemical composition in OPC paste by QXRD. Volume fraction converted from mass fraction and LAC of chemical compositions was shown in Figure2.

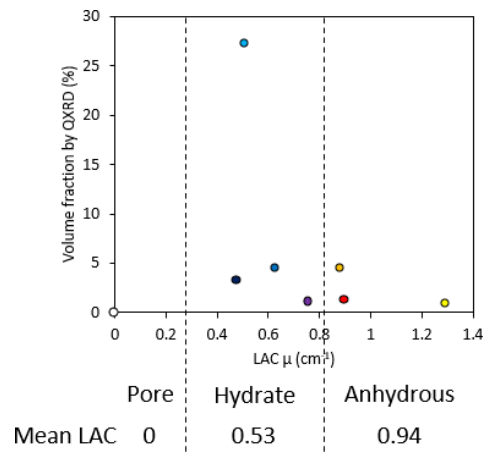


Figure 2. Volume fraction and LAC of chemical compositions in OPC paste.

Figure 3 shows the volume fraction of pore, hydrate, and anhydrous phase in OPC paste. It was confirmed that the most hydration reaction occurred when the water content was 0.6.

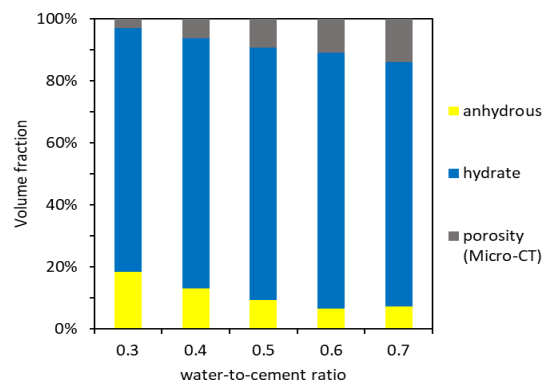


Figure 3. Volume fraction of pore, hydrate, and anhydrous phase in OPC paste.

By repeating the modified random walk simulation with different hydrate voxel delay times as shown in figure 4, the hydrate voxel delay time resulting the ion diffusivity closest to the experimental value was inversely estimated.

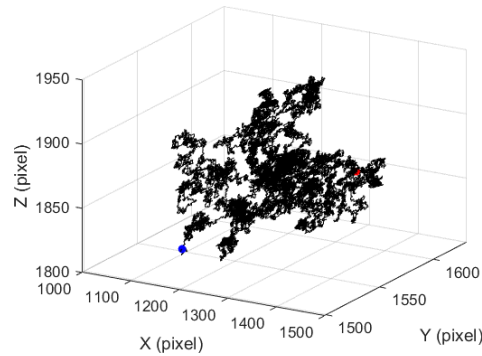


Figure 4. Trajectory of a walker randomly moving in the 3D microstructure of OPC paste with a water-to-cement of 0.5.

Figure 5 depicts hydrate voxel retention time as a function of water-to-cement ratio.

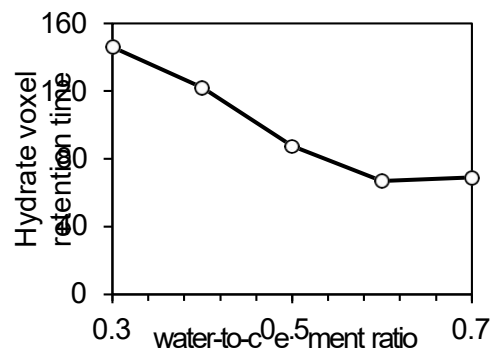


Figure 5. Hydrate voxel retention time as a function of water-to-cement ratio.

6. Conclusions

This study aimed to quantitatively calculate the tortuosity parameter of cement-based materials having disconnected pore system using QXRD and micro-CT based modified random walk simulation. 3D tomographic images composed of pore, hydrate, and anhydrous phases of OPC paste were successfully obtained using theoretical linear attenuation coefficients of each phase. The modified random walk simulation which allows the migration on the hydrated product was performed several times and successfully estimated the optimized hydrate voxel retention time. This method enabled the calculation of tortuosity of cement-based materials having disconnected pore system for the first time which led to the evaluation of the diffusivity. The ion diffusivity was successfully calculated by the modified random walk simulation compared to the numerical simulation and experimental data. It is expected that the ion diffusivity can be calculated quickly and accurately even with a small sample through the modified random walk simulation proposed in this study.

Acknowledgements

This work was supported by the Industrial Strategic technology development program-Development of manufacturing technology of hardened cement with carbonation curing (RS-2022-00155662, Development of manufacturing and application technology of 1,000 ton/year class hardened cement with carbonation curing) funded By the Ministry of Trade, industry & Energy (MOTIE, Korea).

References

- Bossa, N., et al. (2015). "Micro- and nano-X-ray computed-tomography: A step forward in the characterization of the pore network of a leached cement paste." *Cement and Concrete Research* 67: 138-147.
- Liu, L., et al. (2012). "Estimation of the ionic diffusivity of virtual cement paste by random walk algorithm." *Construction and Building Materials* 28(1): 405-413.
- Promentilla, M. A. B., et al. (2008). "Characterizing the 3D Pore Structure of Hardened Cement Paste with Synchrotron Microtomography." *Journal of advanced concrete technology* 6(2): 273-286.

Effect of Mg-bearing water on the chemical and mechanical properties of a low C/S industrial cement paste

C. Dewitte^{1,2*}, L. Lacarrière², A. Bertron², M. Neji¹, and A. Dauzères¹

¹ Institut de Radioprotection et de Sûreté Nucléaire (IRSN), PSE-ENV/SEDRE/LETIS, Fontenay-aux-Roses 92260, France

Email: mejdi.neji@irsn.fr, alexandre.dauzeres@irsn.fr

² LMDC (Laboratoire Matériaux et Durabilité des Constructions), Université de Toulouse, UPS, INSA, 135 Avenue de Rangueil, CEDEX 04, 31077 Toulouse, France

Email: cdewitte@insa-toulouse.fr, laurie.lacarrière@insa-toulouse.fr, bertron@insa-toulouse.fr

ABSTRACT

The use of Supplementary Cementitious Materials (SCMs) in civil engineering concrete structures is becoming increasingly common. The incorporation of additions such as silica fume, fly ash or slag changes the mineralogy of cementitious materials, questioning their durability in chemically aggressive environments, including soft water, and seawater. These environments contain magnesium, the reaction of which with cementitious materials leads to a magnesium enrichment of the matrix, corresponding to the formation of magnesium silicates hydrates (M-S-H) and/or brucite (MH). In the case of highly substituted binders (low C/S), the absence of portlandite is expected to favour the formation of M-S-H whose mechanical properties are poorly known. In order to characterise the behaviour and mechanical properties of such materials under magnesium attack, an industrial low-pH cement paste (C/S=0.7) was exposed to a 50 mmol/L MgCl₂ solution for 4 months. EDS coupled with XRD analyses showed Mg enrichment of the paste resulting in the formation of M-S-H, associated with Ca and S leaching corresponding to the dissolution of C-S-H and ettringite. The Mg-enriched zone had similar microstructural properties to those previously determined on pure M-S-H pastes and it showed a lower Young's modulus than the sound zone ($E_{deg}/E_{sound} = 45\%$).

KEYWORDS: SCM, M-S-H, EDS, XRD, microindentation

1. Introduction

In the last decades, a growing number of Supplementary Cementitious Materials (SCMs) have been developed and used in the construction of concrete civil engineering structures. This increasing use is justified by environmental considerations and efforts to improve physical, mechanical or setting properties for example (Buffo-Lacarrière et al. (2011); Juenger et al. (2012); Langan et al. (2002); Lauch et al. (2016); Sánchez de Rojas et al. (1993); Thomas et al. (2012)). However, the use of mineral additions substituting part of Portland cement changes the mineralogical and chemical composition of cementitious materials. Thus, with the use of silica fume, slag and/or fly ash, the pH of the pore solution and the C/S ratio of the hydrated material decrease. The amount of portlandite in hydrated binders decreases to zero when the C/S ratio of raw materials becomes very low (Codina et al. (2008); Sakai et al. (2005); Shehata et al. (1999)). A magnesium attack of the concrete of infrastructures (ports, bridges, dams, nuclear waste repository, etc.) can occur from contact with soft water (Rosenqvist et al. (2017)), seawater (Jakobsen et al. (2016)) or clay poral water in the context of Cigeo (Dauzères et al. (2014)). Cigeo is a French project to design and implement a possible deep geological repository for radioactive wastes in France. In the contact zones between the rock and the concrete, the use of low-pH (or low-C/S) concrete is envisaged in order to limit the disturbance of the concrete contact on the clay of the host rock and the swelling clay used to close the galleries (Dauzères et al. (2010); Gaucher & Blanc (2006); Savage et al. (2007)). Portlandite plays an important role in the magnesium attack. Its dissolution leads to the formation of a protective layer of brucite (Dauzères et al. (2014); Jakobsen (2013); Rosenqvist et al. (2017)). In the absence of portlandite, the

reaction mechanisms and the consequences of the chemical attack on the properties of the materials are expected to be different. For example, Dauzères et al. (2014) observed a much deeper magnesium enrichment of the cementitious paste in the case of a low C/S material compared to a Portland cement-based material (1.6mm versus 10 μ m). In order to better characterize and further predict the behaviour of low-C/S binders in these complex environments, understanding the mechanism of the different attacks is crucial. To estimate the durability of energy or safety related structures in these magnesium environments, the chemo-mechanical behaviour of low-pH (or low-C/S) materials subjected to magnesium attack needs to be characterized.

A previous study investigated the effect of magnesium attack on a low-pH model paste (Dewitte et al. (2022b)). The Ca and Si distribution of the hydrated material was homogeneous and its mineralogy very simple (C-S-H and ettringite). A deep and homogeneous Mg enrichment was observed, associated with the formation of M-S-H. In parallel, a decalcification and dissolution of the C-S-H was observed. The mechanical properties measured in the Mg-enriched zone were much weaker than those of the sound material. An industrial cement paste, i.e. a complex material (heterogeneous Ca and Si distribution and more complex mineralogy) closer to real-life cementitious materials, was then considered, and exposed to the same chemical conditions (immersion in 50 mmol/L MgCl₂ solution) for 4 months. This paper presents the multi-physical characterization of the altered T3 industrial paste.

2. Materials and method

An industrial low-pH cement paste (called T3) was produced by the mixing of a silica fume, CEM III A, milli-Q water and superplasticizer. The water/binder ratio was 0.43, the superplasticizer/binder ratio was 0.02 and the C/S ratio of the mixture was 0.71. The presence of ettringite and C-S-H was revealed by XRD analysis of the sound hydrated material, and no portlandite was detected.

After two years of curing, the T3 cement paste was immersed in a 50 mmol/L MgCl₂ solution (corresponding to seawater Mg concentration in Jakobsen et al. (2016)) at pH = 5.5.

After 4 months of degradation, the deteriorated samples were characterized by multi-physics techniques, including elemental chemical analysis (EDS and microprobe), mineralogical analysis (XRD), microstructure analysis (autoradiography, microtomography), and estimation of elastic mechanical properties (microindentation).

3. Results and discussion

Figure 1 (a) shows the EDS elemental Mg and Ca maps of the sample after 4 months of degradation. In parallel to a strong leaching of calcium, a magnesium enrichment took place in the solid. Combined with mineralogical analyses (XRD), it was shown that (i) the Mg-enriched zone (Z3) was composed of M-S-H, (ii) the transition zone (Z2) contained M-S-H and C-S-H, and (iii) the sound zone (Z1) exhibited the presence of ettringite and C-S-H. By plotting the averaged M/S and C/S intensity profiles (from the EDS data) along the sample, a zone of a few tens of microns, with a slightly more pronounced Mg enrichment appeared (average M/S of 0.6 versus 0.5). Outside this zone, the M/S ratio was stable in zone 3 (M/S=0.5). Zone 2 showed a linear decrease of M/S in conjunction with a linear growth of C/S. Finally, zone 1 showed a plateau of C/S at 0.7 and M/S at 0.1. The Mg enrichment was progressive and homogeneous. This pattern had already been observed on the model cement paste exposed to MgCl₂ solutions (Dewitte et al. (2022b)). As the degradation time increases, the Mg-enriched zone expands without changing its composition.

The microstructure and porosity of the exposed samples were studied by MIP, N₂ Physisorption, microtomography and autoradiography. The degraded zone showed an increased total open porosity (and decreased density) compared to the sound zone, despite the formation of M-S-H (autoradiography and microtomography). The capillary porosity of the sound and degraded zones was similar (MIP), while the porosity associated with micropores and thus hydrates was higher (N₂ physisorption). The microstructural properties of the Mg-enriched zone were similar to those of synthetic M-S-H pastes (Dewitte et al. (2022a)) but could not be assimilated to a purely M-S-H zone. Other phases were likely present, and would account for the difference in B.E.T specific surface and BJH pores size distribution. As the paste initially contained large amount of silica fume clusters, remaining silica could also be present and not detected by XRD because of its amorphous nature. Moreover, calcium clusters corresponding to slag were still observable on

EDS mapping in the degraded zone (Figure 1 (a)). As the microstructure, chemistry and initial mineralogy of T3 was more varied than for the model paste (see Dewitte et al. (2022b)), M-S-H coexisted with other phases and the influence of M-S-H formation on the microstructural properties was reduced.

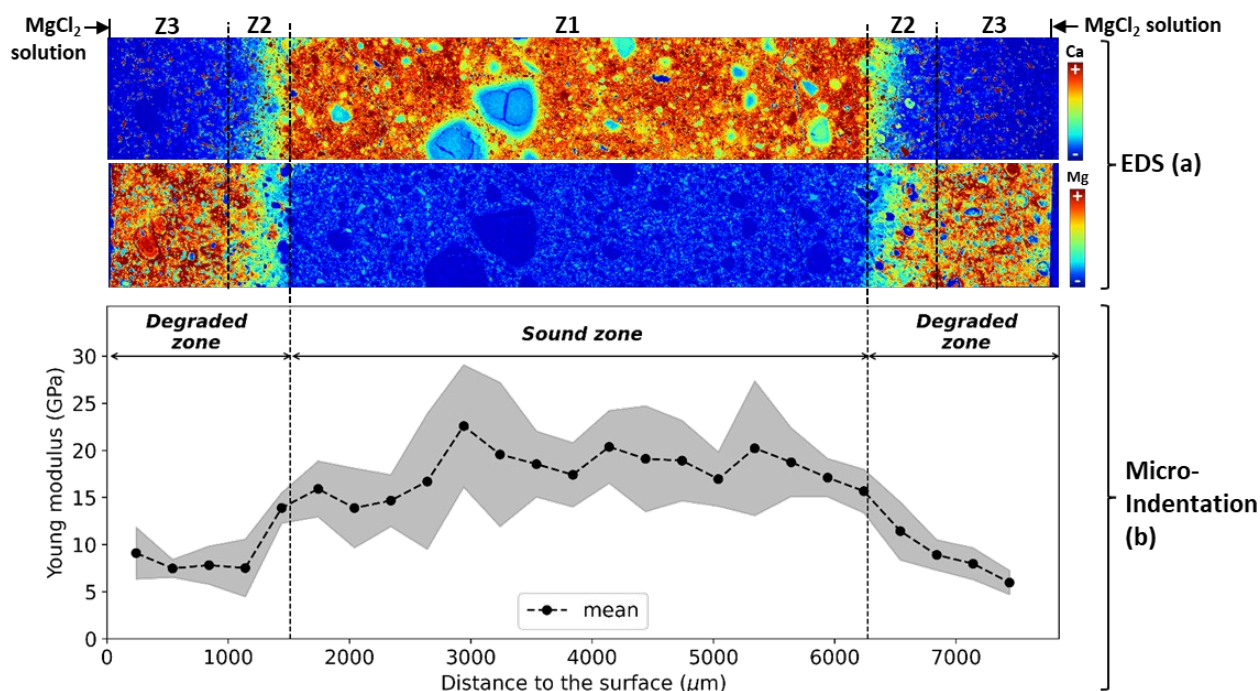


Figure 1: Elemental maps (EDS) of calcium and magnesium (a) and Young's modulus profile (b) after 4 months of degradation

Figure 1 (b) illustrates the results of microindentation (Load = 200 mN, penetration depth around 10 μm) after removal of outliers. The Young's modulus was evaluated from the microindentation results considering a constant Poisson's ratio of 0.24 and Oliver & Pharr (1992) scheme. A significant decrease of the elastic mechanical properties was observed in the magnesium enriched zone (Z3) and the Young's modulus decreased to about 8 GPa at the surface while the sound zone (Z1) exhibited a mean value of 18 GPa. The T3 industrial cementitious paste showed a lower loss of mechanical properties than the model paste ($E_{deg}/E_{sound} = 45\%$ for the T3 vs. 15% for the model paste, see Dewitte et al. (2022b)) and a lower mechanical loss than a similar low-pH paste, developed by Bes (with $w/b=0.5$), under accelerated nitrate leaching ($E_{deg}/E_{sound} = 10\%$, Bes (2019)). While the depth of the Ca-leached and Mg-enriched zones were comparable (at 4 months, the deterioration front for 50 mM $MgCl_2$ (EDS) was 1600 μm for the model paste versus 1500 μm for T3), the mechanical properties were better preserved for the T3. This difference may be due (i) to the non-homogeneous distribution of initial Si and Ca, (ii) to the presence of other phases such as slag, and/or (iii) to a lower porosity of the sound paste. The presence of these non-degraded residual phases could limit the impact of M-S-H formation and C-S-H dissolution on the mechanical properties of the degraded zone, as for the microstructural properties. The porosity increase associated with decalcification or the naturally low mechanical characteristics of M-S-H may be the cause of this drop in mechanical properties. A pure water leaching test of the industrial cement paste (T3) is in progress to discuss these hypotheses.

4. Conclusions

In order to understand the mechanisms and effects of degradation of cementitious materials in contact with Mg-bearing environments, an industrial low-pH cement paste was exposed to $MgCl_2$ solution (model environment) at 50 mmol/L during 4 months. The cement paste (T3) is a cementitious paste representative of the low-pH concrete planned for the Cigéo underground geological repository project. The use of slag and silica fume, which formed clusters, led to a heterogeneous distribution of calcium and silicon. The magnesium attack resulted in Mg enrichment of the paste in parallel with Ca and S leaching. It corresponded to the formation of M-S-H, the decalcification/dissolution of C-S-H and the dissolution of Aft phases. The

degradation front was deep (1700 μm in 4 months). The degraded zone showed higher porosity than the sound zone despite the formation of M-S-H. The capillary porosity was approximately the same in the degraded and sound zones while the microporosity was higher in the former. The mechanical properties measured by microindentation showed that the Young's modulus of the degraded zone was reduced by half compared to that of the sound zone. This reduction was lower than the one observed on the low-pH model cement pastes likely due to the heterogeneous distribution of Ca and Si and the more complex mineralogy of the industrial cement paste (T3).

Acknowledgements

The first author would like to thank the french University Civil Engineering Association (AUGC) for their support.

References

- Bes, T. (2019) Etude du comportement des bétons bas-PH sous sollicitations chimiques. These de doctorat. Toulouse 3
- Buffo-Lacarrière, L., A. Sellier, et al. (2011) Finite element modelling of hardening concrete: application to the prediction of early age cracking for massive reinforced structures. *Materials and Structures* (44) 10: 1821–1835.
- Codina, M., C. Cau-dit-Coumes, et al. (2008) Design and characterization of low-heat and low-alkalinity cements. *Cement and Concrete Research* (38) 4: 437–448.
- Dauzères, A., P. Le Bescop, et al. (2010) Physico-chemical investigation of clayey/cement-based materials interaction in the context of geological waste disposal: Experimental approach and results. *Cement and Concrete Research* (40) 8: 1327–1340.
- Dauzères, A., P. Le Bescop, et al. (2014) On the physico-chemical evolution of low-pH and CEM I cement pastes interacting with Callovo-Oxfordian pore water under its in situ CO₂ partial pressure. *Cement and Concrete Research* (58) : 76–88.
- Dewitte, C., A. Bertron, et al. (2022a) Chemical and Microstructural Properties of Designed Cohesive M-S-H Pastes. *Materials* (15) 2: 547.
- Dewitte, C., L. Lacarriere, et al. (2022b) Effet d'une eau contenant du magnésium sur les propriétés chimiques et mécaniques d'une pâte de ciment à faible rapport C/S.
- Gaucher, E.C. & P. Blanc (2006) Cement/clay interactions – A review: Experiments, natural analogues, and modeling. *Waste Management* (26) 7: 776–788.
- Jakobsen, U.H. (2013) Microstructural surface deterioration of concrete exposed to seawater; results after 2 years exposure. : 10–14.
- Jakobsen, U.H., K. De Weerd, et al. (2016) Elemental zonation in marine concrete. *Cement and Concrete Research* (85) : 12–27.
- Juenger, M., J.L. Provis, et al. (2012) Supplementary Cementitious Materials for Concrete: Characterization Needs. *MRS Online Proceedings Library (OPL)* (1488) .
- Langan, B.W., K. Weng, et al. (2002) Effect of silica fume and fly ash on heat of hydration of Portland cement. *Cement and Concrete Research* (32) 7: 1045–1051.
- Lauch, K.-S., V. Dieryck, et al. (2016) The use of ternary cements to reduce the environmental impact of concrete. *RILEM Technical Letters* (1) : 88–93.
- Oliver, W.C. & G.M. Pharr (1992) An improved technique for determining hardness and elastic modulus using load and displacement sensing indentation experiments. *Journal of Materials Research* (7) 6: 1564–1583.
- Rosenqvist, M., A. Bertron, et al. (2017) Concrete alteration due to 55years of exposure to river water: Chemical and mineralogical characterisation. *Cement and Concrete Research* (92) : 110–120.
- Sakai, E., S. Miyahara, et al. (2005) Hydration of fly ash cement. *Cement and Concrete Research* (35) 6: 1135–1140.
- Sánchez de Rojas, M.I., M.P. Luxán, et al. (1993) The influence of different additions on portland cement hydration heat. *Cement and Concrete Research* (23) 1: 46–54.
- Savage, D., C. Walker, et al. (2007) Alteration of bentonite by hyperalkaline fluids: A review of the role of secondary minerals. *Physics and Chemistry of the Earth, Parts A/B/C* (32) 1: 287–297.
- Shehata, M.H., M.D.A. Thomas, et al. (1999) The effects of fly ash composition on the chemistry of pore solution in hydrated cement pastes. *Cement and Concrete Research* (29) 12: 1915–1920.
- Thomas, M.D.A., R.D. Hooton, et al. (2012) The effect of supplementary cementitious materials on chloride binding in hardened cement paste. *Cement and Concrete Research* (42) 1: 1–7.

Corrosion kinetics of steel in artificial carbonated pore solutions under the effect of stirring and bicarbonate ions

C. C. Albert^{1*}, S. Mundra², O. B. Isgor³, and U. Angst⁴

¹*Institute for Building Materials, ETH Zurich, Zurich, Switzerland
cristhiana.albert@ifb.baug.ethz.ch*

²*Institute for Building Materials, ETH Zurich, Zurich, Switzerland
shishir.mundra@ifb.baug.ethz.ch*

³*School of Civil and Construction Engineering, Oregon State University, Oregon, USA
burkan.isgor@oregonstate.edu*

⁴*Institute for Building Materials, ETH Zurich, Zurich, Switzerland
ueli.angst@ifb.baug.ethz.ch*

ABSTRACT

Steel corrosion is the prime reason for the early deterioration of reinforced structures. The carbonation of concrete and subsequent decrease in the pH of the concrete cover can induce corrosion of the steel reinforcement, and potentially lead to safety and serviceability issues. Since low-clinker cements are known to carbonate faster, the propagation phase of rebar corrosion becomes a crucial aspect to consider for the service life of these environmentally friendly cements. Whilst it is well known that the corrosion rate can vary significantly in carbonated cementitious binders, depending on the microstructure and the moisture content of the steel-concrete interface (SCI), the role of the pore solution composition on the corrosion kinetics remains unclear. This study focuses on electrochemical experiments with steel in artificial carbonated pore solutions, more specifically, we assess the influence of bicarbonate species and stirring methods on the corrosion of carbon steel. Corrosion kinetics was investigated for steel immersed in typical carbonated pore solutions of pH 8, with 1 mM HCO₃⁻, under three stirring conditions (no stirring, air bubbling and mechanical stirring). Open circuit potential (OCP) and polarization resistance (Rp) were measured to monitor the corrosion kinetics, providing insights into the mechanisms taking place on steel in carbonated media. The influence of stirring on the reproducibility of the experiments was also assessed, considering its impact on the diffusion of species through the solution. This study will further support investigations on the influence of concrete microstructure and SCI moisture on the carbonation-induced reinforcement corrosion in concretes produced with low-clinker binders.

KEYWORDS: *Corrosion kinetics, Pore solution, Stirring, Bicarbonates, Low-carbon steel.*

1. Introduction

Carbonation-induced corrosion is one of the potential reasons for the early deterioration of reinforced concrete structures (Bertolini *et al.*, 2013). Reinforced concretes produced with blended (or low-clinker) cements are generally perceived as being particularly prone to this type of corrosion, which might reduce their service life compared to traditional plain Portland cement concretes (Angst *et al.*, 2020). Thus, avoiding carbonation-induced corrosion is an urgent need for the sustainable and safe application of low-clinker cements. If corrosion rates are high, besides the structural safety concerns possibly arising from loss of steel-concrete bond or steel sectional area, the corrosion products exert expansive stresses on the concrete microstructure, and might cause cracking and, in extreme cases, spalling of the concrete cover. Consequences are the repair and demolition of reinforced structures, associated with significant costs, social drawbacks, and the environmental burden of raw-material consumption and waste generation.

Upon the ingress of atmospheric CO₂ through the concrete cover, CO₂ dissolves into carbonate species (HCO₃⁻, CO₃²⁻), which react with Ca-bearing phases and form calcite (Ca²⁺ + CO₃²⁻ → CaCO₃) (von Greve-Dierfeld *et al.*, 2020). This process alters the microstructure and the pore solution of concrete.

According to De Weerd *et al.* (2019), the main changes in the pore solution are the pH decrease to values reported as low as 8, and the increase in concentration of HCO_3^- , CO_3^{2-} ions due to CO_2 dissolution. The final pH depends on the thermodynamic stability and concentration of carbonate species. Additionally, the content of aggressive species (Cl^- and SO_4^{2-}) increases due to the decomposition of AFm phases that were previously binding these ions. Proper investigation of these processes, particularly their effect on the kinetics of corrosion reactions, starts at the pore solution level; therefore, it is critical to conduct well-designed corrosion experiments in simulated pore solutions.

When exposed to carbonated pore solutions with such low pH~8, steel might no longer retain a thermodynamically stable passive film (Pourbaix, 1966). The presence and the chemical composition of the pore solution plays a relevant role for the corrosion current densities developed on steel. In this regard, the moisture content of the concrete has been identified as one of the most influential factors controlling whether or not active corrosion occurs after loss of passivity (Stefanoni, Angst and Elsener, 2018; Zhang *et al.*, 2022). Furthermore, the access of O_2 to the steel surface and the diffusion of species through the pores on the steel-concrete interface (SCI) will determine the kinetics of reactions. For experimental bench-top electrochemical studies, this means that the mass-transfer conditions in the setup need to be carefully considered in the experimental design. For example, it is well known that mass-transfer controlled reactions are enhanced upon increased rotation speeds of a rotating disk electrode, due to the decrease of the diffusion layer, thus enhancing the supply of species that affect electrochemical processes – such as O_2 and HCO_3^- – to the metal surface (Davies and Burstein, 1980). Bubbling air into solution further influences the concentration of O_2 available for the cathodic reactions, for instance to ensure that this does not become a limiting factor. Finally, the agitation of the solution favours homogeneous mixing of the species through the solution.

In this paper, we investigate the effect of bicarbonate species and three stirring methods - no stirring, air bubbling, and mechanical stirring - on the corrosion kinetics of low-carbon steel in simulated pore solutions of pH 8. While bicarbonates represent the chemical aspect of the pore solution, the stirring incorporates diffusion conditions into the experimental setting.

2. Materials and methods

The electrochemical experiments were conducted with low-carbon steel immersed in solutions simulating carbonated concrete. The pH of the solutions was 8, achieved with 5 mM Hepes buffer, adjusted with NaOH solution. HCO_3^- ions varied from 0 to 1 mM NaHCO_3 . The stirring methods were (a) no stirring, (b) air bubbling (compressed air) and (c) mechanical stirring (HDPE stirrer with rotation speed 50 rpm), and the setups are illustrated in Fig. 1. The electrochemical cell contained 300 mL of electrolyte.

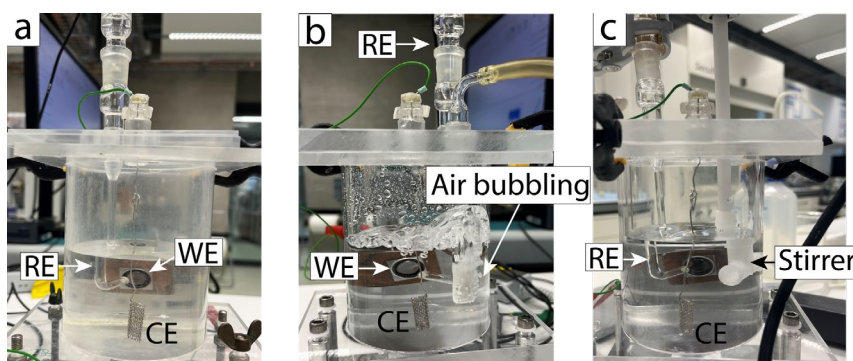


Fig. 1: Overview of the experimental setup.

A cold-rolled 1.0330 low-carbon steel plate (0.785 cm^2) was used as the working electrode (WE). It was ground at #240, #500, and #1000 SiC paper and polished with diamond paste (9, 3, and $1 \mu\text{m}$ particles). The WE was positioned in a small hole at the side of the cell, with a NBR O-ring to prevent crevice corrosion and leaking, and a copper plate for electrical connection. An Ag/AgCl sat. KCl electrode was the reference (RE), within an outer Luggin capillary containing the test solution and two inner Luggin capillaries with saturated KCl. A Pt mesh (1 cm^2) was used as the counter-electrode (CE). The relatively large distance from CE to WE (7 times the diameter of the WE) ensured a homogeneous polarization current distribution at the WE during electrochemical measurements. To investigate the corrosion

kinetics, open circuit potential (OCP) and polarization resistance (R_p) were measured over ~1-hour cycles during 6h, at room temperature (23°C). R_p was measured within the range OCP ± 15 mV, at a sweep rate of 0.17 mV/s, with negligible IR drop, according to EIS tests. The tests were repeated at least 2 times.

3. Results and discussion

The data for OCP and R_p is shown in Fig. 2. The main feature apparent from these data is the clear influence of experimental conditions (stagnant, stirring, bubbling) of the solution. Steel samples in stagnant solutions showed greater variability in OCP and R_p values compared to steel in stirred solutions, especially when HCO_3^- was introduced. To address this, two additional specimens (3 and 4) were tested in the stagnant solution with HCO_3^- .

The influence of 1 mM HCO_3^- on the corrosion kinetics of steel was not pronounced. In the absence of HCO_3^- the OCP of steel in the three stirring conditions was in a similar range (within approx. 80 mV). For agitated solutions, a tendency towards more negative OCPs for steel in HCO_3^- containing solutions was observed compared to solutions without HCO_3^- . The effect of HCO_3^- on R_p was minor. The R_p values in stirred solutions were in the same range to those measured in stagnant solutions without HCO_3^- .

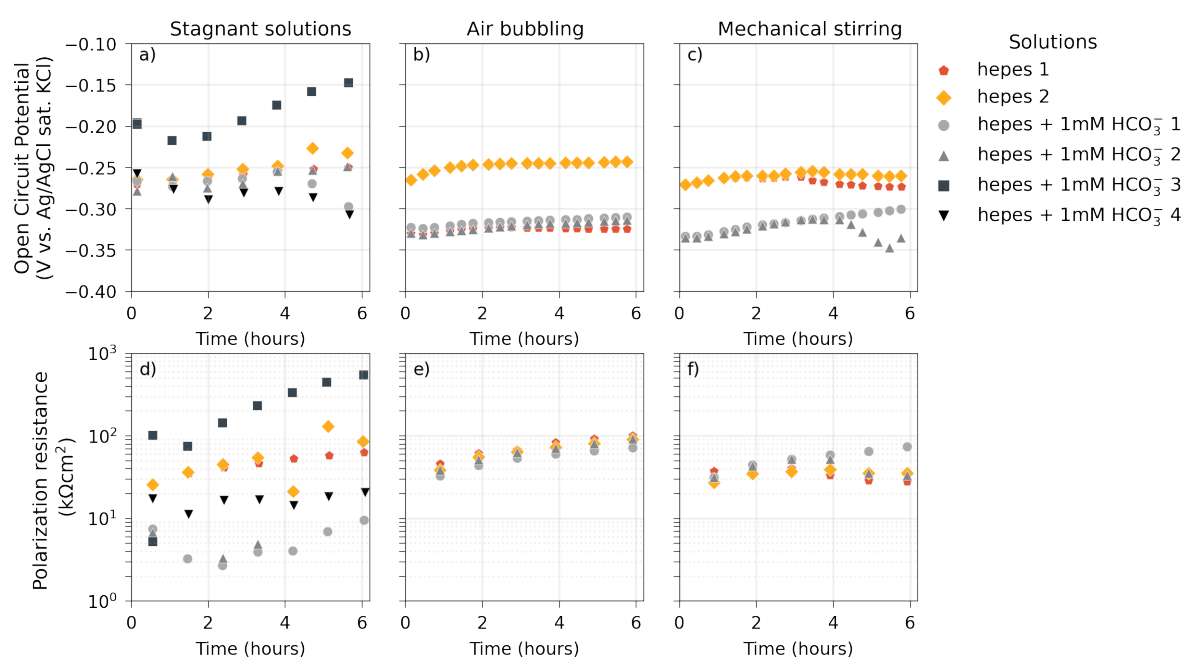


Fig. 2: Open circuit potential (OCP) and Polarization resistance (R_p) over time for low-carbon steel immersed in artificial pore solutions of pH 8 containing or not 1 mM HCO_3^- , in (a,d) stagnant conditions, or subjected to (b,e) air bubbling or (c,f) mechanical stirring. Numbers (1,2,3,4) in the label indicate the replicates.

The range of OCPs indicates that the cathodic reaction was the oxygen reduction (ORR), and thus the O_2 concentration in the solutions is a relevant parameter (Pourbaix, 1966). Stagnant solutions probably had less well-defined O_2 supply than the other two cases, whereas bubbling air and stirring the solutions favored the diffusion of O_2 from the bulk solution to the metal surface in a controlled manner. This may partially explain the higher variability in OCP and R_p observed in the stagnant solutions.

The solution agitation due to stirring also increased the diffusion of ionic species. Thus, Fe(II) species released at the metal surface could be transported more efficiently to the bulk solution, decreasing their concentration near the metal. Consequently, dissolution of steel would be thermodynamically favored and higher corrosion rates are theoretically expected (Stefanoni, Angst and Elsener, 2019; Martinelli-Orlando, Shi and Angst, 2020) and have been reported in the literature (Davies and Burstein, 1980; Hasan and Sadek, 2014). Although this effect was limited due to the low rotation speed of only 50 rpm applied here, it might have contributed to the slightly lower R_p s of steel in mechanically stirred solutions.

Regarding the possible sources of error, the compressed air pressure in our setup was subjected to occasional fluctuations and could not always generate a constant pressure. When immersed in solutions

under mechanical stirring, the steel samples consistently had a small zone of corrosion on the top edge, in a circular shape, suggesting the presence of an air bubble. This localized corrosion spot might have also contributed to some of the slightly lower R_p values for steel in the mechanically stirred solutions. Despite these uncertainties, stirring the solutions clearly provided more reproducible environments.

Translating these experiments to the context of corrosion in reinforced concrete, the higher diffusion and O_2 supply offered by stirring may represent steel in partially saturated concrete or concrete subjected to wet-dry cycles. In the experimental setup used (beaker) the diffusion length for O_2 was of the order of centimeters, while in partially saturated concrete, the diffusion length from air-filled pores to the steel surface is likely orders of magnitude lower. Thus, the stagnant solution may not represent the aeration conditions in concrete well, especially not exposure conditions relevant for carbonation-induced corrosion (wet-dry cycles). These factors should be considered when determining the effective corrosion current of steel in simulated solutions. Such corrosion currents can be complemented with data on the SCI microstructure and the active area of steel, finally allowing to calculate the apparent corrosion rates of steel in carbonated concrete (Stefanoni, Angst and Elsener, 2018, 2020).

4. Conclusions

We investigated the influence of HCO_3^- species and stirring methods on the corrosion kinetics of steel immersed in artificial pore solutions representative of carbonated concrete, at pH 8. The results confirmed the strong influence of the hydrodynamic conditions in the electrolyte (stagnant, stirring, bubbling) on the obtained results. The steel in stagnant solutions presented highly variable OCP and R_p values, while air-bubbled or mechanically stirred solutions provided more reproducible results. Stirring increased the diffusion of species in solution, creating a more controlled environment in terms of O_2 supply. Besides advantages in the reproducibility of agitated solutions, stirring may also introduce conditions more representative of the SCI than stagnant solutions. This is because the higher diffusion and exchange of species may resemble the wet-dry cycles relevant for carbonation-induced corrosion. More conclusive trends on the influence of HCO_3^- species on corrosion kinetics require additional tests.

Acknowledgements

This work is part of Innovandi's Core Project 14, supported by the Global Cement and Concrete Association (GCCA).

References

- Angst, U. *et al.* (2020) "Corrosion of steel in carbonated concrete: Mechanisms, practical experience, and research priorities – A critical review by RILEM TC 281-CCC", *RILEM Technical Letters*, 5, pp. 85–100.
- Bertolini, L. *et al.* (2013) *Corrosion of Steel in Concrete: Prevention, Diagnosis, Repair*. John Wiley & Sons.
- Davies, D.H. and Burstein, G.T. (1980) "Effects of Bicarbonate on the Corrosion and Passivation of Iron", *Corrosion*, pp. 416–422.
- von Greve-Dierfeld, S. *et al.* (2020) "Understanding the carbonation of concrete with supplementary cementitious materials: a critical review by RILEM TC 281-CCC", *Materials and Structures/Materiaux et Constructions*.
- Hasan, B.O. and Sadek, S.A. (2014) "The effect of temperature and hydrodynamics on carbon steel corrosion and its inhibition in oxygenated acid-salt solution", *Journal of Industrial and Engineering Chemistry*, 20(1), pp. 297–307.
- Martinelli-Orlando, F., Shi, W. and Angst, U. (2020) "Corrosion Behavior of Carbon Steel in Alkaline, Deaerated Solutions: Influence of Carbonate Ions", *Journal of The Electrochemical Society*, 167(6), p. 061503.
- Pourbaix, M. (1966) *Atlas of electrochemical equilibria in aqueous solutions*, NACE International Cebelcor.
- Stefanoni, M., Angst, U. and Elsener, B. (2020) "The mechanism controlling corrosion of steel in carbonated cementitious materials in wetting and drying exposure", *Cement and Concrete Composites*, 113(June), p. 103717.
- Stefanoni, M., Angst, U.M. and Elsener, B. (2018) "Electrochemistry and capillary condensation theory reveal the mechanism of corrosion in dense porous media", *Scientific Reports*, 8(1), pp. 1–10.
- Stefanoni, M., Angst, U.M. and Elsener, B. (2019) "Kinetics of electrochemical dissolution of metals in porous media", *Nature Materials*, 18(9), pp. 942–947.
- De Weerd, K. *et al.* (2019) "Effect of carbonation on the pore solution of mortar", *Cement and Concrete Research*, 118(July 2018), pp. 38–56.
- Zhang, Z. *et al.* (2022) "Dynamic effect of water penetration on steel corrosion in carbonated mortar: A neutron imaging, electrochemical, and modeling study", *Cement*, 9(July), p. 100043.

Chloride ingress resistance of Ca(OH)₂ activated GGBFS: Impact of curing temperature and additional activators

Qi Zhai^{1*} and Kiyofumi Kurumisawa^{2*}

¹ Graduate School of Engineering, Hokkaido University, Hokkaido, Japan
zhaiqi0703@gmail.com

² Faculty of Engineering, Hokkaido University, Hokkaido, Japan
kurumi@eng.hokudai.ac.jp

ABSTRACT

Calcium hydroxide (Ca(OH)₂) activated ground granulated blast furnace slag (GGBFS) shows advantages over alkali activated GGBFS in cost and durability. However, the strength development is slow at early age. To strengthen the application of Ca(OH)₂ activated GGBFS, several normal methods have been used such as additional activators and evaluating curing temperature, which could significantly change the hydration products and pore structure and in turn influence the long term performance such as durability, with chloride resistance as the well-known topic. However, the chloride binding capacity and chloride ingress resistance of Ca(OH)₂ activated GGBFS cured at variable conditions has not been focused.

To address the aforementioned issues, the influence of sodium sulfate (Na₂SO₄), sodium nitrite (NaNO₂) and calcium nitrite (Ca(NO₂)₂) on chloride binding and ingress resistance of Ca(OH)₂ activated ground granulated blast furnace slag cured at 20 and 35 °C was investigated. The experimental results present that the chloride binding capacity of samples cured at 20 and 35 °C show similar trends. Compare to the control group and samples added with nitrites, Na₂SO₄ shows lower chloride binding capacity. In addition, the carbonation and leaching seem influence the chloride binding capacity. The chloride ingress resistance has been demonstrated to have a significant link to leaching and carbonation, where denser calcite layer formed at the exposure layer shows positive effects in chloride ingress resistance.

Key words: *chloride binding; chemical durability; additional activators; diffusion*

1. Introduction

Alkali activated slag (AAS) is the most commonly utilized alkali activated material, which aims to alleviate the CO₂ emissions caused by cement production (Provis 2018). In addition, AAS has good chemical resistance. The commonly used activators of sodium hydroxide (NaOH) and water glass are associated with high cost and flash setting issues. Based on previous research, Ca(OH)₂ can also be used to activate slag reaction (Jeong et al., 2016). However, due to the lower pH value, the early reactivity, and mechanical properties of this system are lower. To improve the early performance drawbacks, it has become a common method to change the reaction environment by adding additional activators and changing the curing temperature (Snellings et al. 2022). However, previous studies have shown that the changes may have some impact on the chloride resistance. The most noticeable effect when incorporating additional activators is on the AFm phase. Due to ion exchange-induced phase transformation, chlorides can be chemically incorporated into the AFm phase as Friedel's salts and Kuzel's salts. The interlayer of the AFm-like phase can be structurally altered by added anions, such as CO₃²⁻, SO₄²⁻, and NO₂⁻, which affect the polymorphs of Friedel's salt produced by AAS (Ye et al., 2019). Raising the curing temperature is believed to enhance the reactivity of slag and reduce porosity, thereby increasing the adsorption of chloride ions. Osio-Norgaard et al., (2018) investigated the effects of curing temperature ranging from 20 to 38 °C on the chloride ingress resistance of a slag blended system and found that a higher curing temperature could increase the chloride

binding capacity. However, they also found that the pore structure became coarser at a high curing temperature and aggravated chloride ingress.

However, there is a paucity of information on how additional activators and curing temperature affect the durability performance of $\text{Ca}(\text{OH})_2$ -activated slag in chloride-rich environments. Hence, the objective of this study was to investigate the mineralogical changes induced by chloride ingress in slag activated by $\text{Ca}(\text{OH})_2$, in order to gain insights into the mechanisms behind the chloride binding capacity and resistance of $\text{Ca}(\text{OH})_2$ -activated slag exposed to sodium chloride.

2. Experimental

2.1. Materials and samples

The slag comply with the Japanese standard JIS A 6206 was used in this study. The specific surface area of slag are 3260 and 4000 cm^2/g , respectively. A $\text{Ca}(\text{OH})_2$ /slag ratio of 0.2/0.8 and a water/binder ratio of 0.55 were employed for the pastes and mortars, based on previous research (Zhai et al., 2022). Additional activators were prepared by dissolving Na_2SO_4 , $\text{Ca}(\text{NO}_2)_2$, and NaNO_2 in deionized water at a concentration of 0.1 mol/kg. The pastes and mortars were mixed using a Hobart mixer. After mixing, the samples were then sealed with polythene sheets and cured for 28 days at 20 or 35 °C, respectively.

2.2. Methodology

To conduct the chloride isotherm test, solutions of NaCl with concentrations of 0.025, 0.05, 0.1, 0.25, and 0.5 M were prepared. After 28 days of curing, the pastes were crushed and sieved with a sieve size of 2-5 mm. Next, 6.0 g of the paste particles were mixed with 60 mL chloride solutions in a 100 mL plastic cup and left at ambient temperature until adsorption equilibrium was reached. After 2 months, the supernatants were collected for chloride adsorption calculation. The chloride concentration was measured using ion chromatography. The total and free chloride content was determined using Equation (1):

$$Cl_b = (Cl_i - Cl_{\#} \cdot f) \times \frac{V}{m} \quad (1)$$

where Cl_b is the bound chloride in mol/g of dry paste, Cl_i is the initial chloride concentration in mol/L, $Cl_{\#}$ is the chloride concentration of the diluted solution in mol/L, f is the dilution times, V is the volume of the solution in mL, and m is the sample mass in grams. For chloride ingress test, the mortar specimens were demolded and cut into halves after being cured for 28 days. Epoxy resin was applied to all surfaces except for the sawn surface. To minimize capillary suction effect, the sealed samples were saturated in $\text{Ca}(\text{OH})_2$ solution for 1 day before being exposed to a 0.5 M NaCl solution for 28 days. After exposure, the samples were cut parallel to the direction of chloride ingress. The slice was then polished and carbon-coated before being analyzed using SEM-EDS at a 15 keV operating voltage and a working distance of 10 mm. Fick's second law was used to determine the surface concentration and apparent chloride diffusion coefficient. The data were collected by EPMA (JAX-8530F) with 15 kV accelerating voltage and 50 nA beam current. After chloride exposure test, the powder samples from 0-1, 2-3 mm, and center grinding layers were gathered for TG analysis. Approximately 10 mg of powder was used. The crucible was heated in a range of 30 to 1000 °C, with a heating rate of 10 °C/min with a nitrogen flow.

3. Results and Discussion

3.1. Chloride binding capacity

Figure 1 illustrates the chloride binding isotherms fit by Langmuir isotherms; the amount of bound chloride increases in all samples. The samples containing added nitrites exhibit a strong capacity for chloride binding, while those containing added Na_2SO_4 exhibit the lowest binding capacity among the samples. In comparison to specimens cured at 35 °C, samples cured at 20 °C demonstrated a higher capacity for chloride binding.

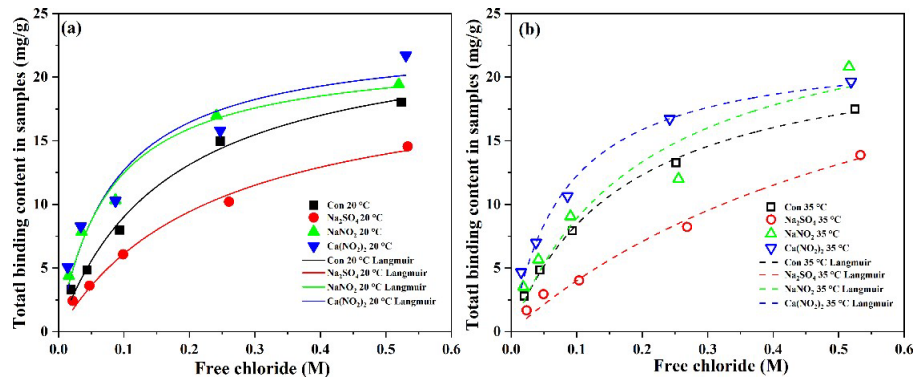


Figure 1. Chloride binding isotherms: (a) Samples cured at 20 °C and (b) Samples cured at 35 °C

3.2. Apparent chloride diffusion coefficient

Table 1 presents the apparent chloride diffusion coefficients. Samples with added nitrite, regardless of curing temperature, exhibited relatively lower apparent chloride diffusion coefficients, indicating enhanced resistance to chloride compared to the control group and samples with added Na_2SO_4 . However, the results indicate that the changes in the curing temperature have negligible effects on the apparent chloride diffusion coefficient, which will be further discussed in the next section.

Table 1. Apparent chloride diffusion coefficient

| Sample | Con 20 °C | Na_2SO_4 20 °C | NaNO_2 20 °C | $\text{Ca}(\text{NO}_2)_2$ 20 °C | Con 35 °C | Na_2SO_4 35 °C | NaNO_2 35 °C | $\text{Ca}(\text{NO}_2)_2$ 35 °C |
|---|--------------|-----------------------------------|--------------------------|-------------------------------------|--------------|-----------------------------------|--------------------------|-------------------------------------|
| Apparent chloride diffusion coefficient ($10^{-10} \text{ m}^2/\text{s}$) | 1.0 | 1.0 | 0.65 | 0.55 | 1.1 | 1.1 | 0.65 | 0.65 |

3.3. Element map after chloride diffusion

The results of the samples cured at 35 °C are presented in this paper. Figure 2 displays the elemental map of the samples after chloride exposure, revealing a calcium-rich layer on the exposed surface. The calcium-rich layer is believed to consist of carbonates, further evidence is provided in Section 3.4. These results suggest the potential of additives to influence the formation of calcium-rich layers in cementitious materials and the importance of understanding their composition and distribution for assessing durability.

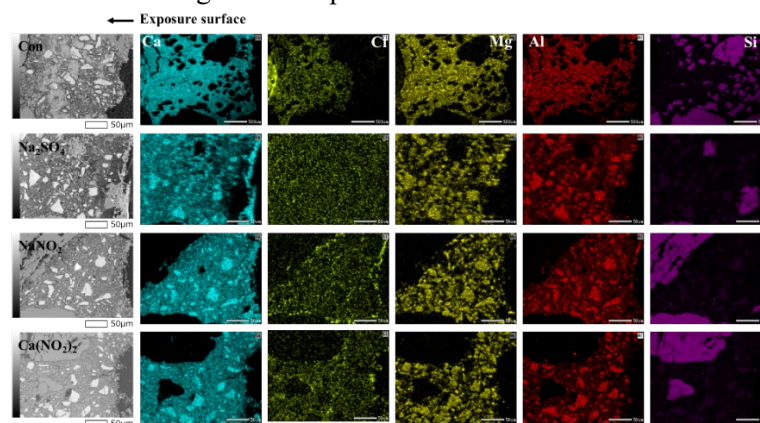


Figure 2. Element map of samples cured at 35 °C after chloride exposure

3.4. TG-DTG analysis of the samples after chloride exposure

The TG-DTG analysis results presented in Figure 3 confirmed the carbonations. The peak related to carbonates was observed at around 600 °C. Following NaCl exposure, the most notable observation was that the amount of portlandite decreased as the samples were taken closer to the contact surface, and the

corresponding carbonation became more prominent. Thus, the calcium-rich layer was more likely to precipitate on the exposed surfaces of the samples, which may have inhibited the chloride ingress to some extent.

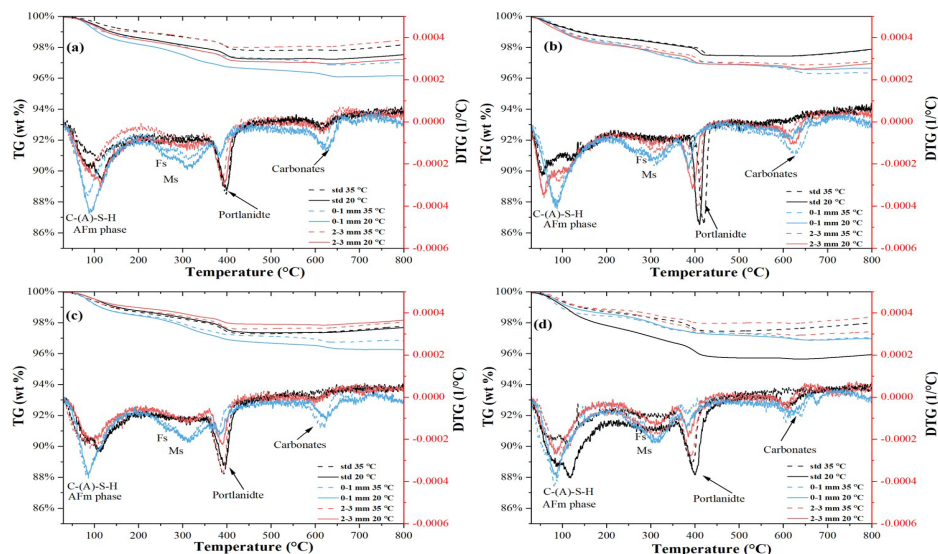


Figure 3. TG-DTG of samples cured at 35 °C after chloride exposure

4. Conclusions

This study utilized SEM-EDS and TGA to investigate the influence of curing temperature (20 and 35 °C) and additional activators (Na_2SO_4 , NaNO_2 , and $\text{Ca}(\text{NO}_2)_2$) on the chloride ingress resistance of $\text{Ca}(\text{OH})_2$ -activated GGBFS upon exposure to NaCl . The findings can be summarized as follows:

1. The samples added with Na_2SO_4 exhibited a lower chloride binding capacity compared to the control group and samples added, which was mainly influenced by the types of the AFm phase, which further influenced the alteration in the phase assemblage after NaCl exposure.
2. The samples containing nitrites exhibited superior resistance to chloride ingress compared to both the control group and samples containing Na_2SO_4 , with negligible influence from the curing temperature. The phenomena of carbonations appear to enhance chloride ingress resistance by promoting the formation of a denser layer on the exposed surface.
3. Calcium hydroxide ($\text{Ca}(\text{OH})_2$) activated ground granulated blast-furnace slag (GGBFS) shows advantages over alkali activated GGBFS in cost and durability

Acknowledgements

This work was supported by JSPS KAKENHI Grant Number 21K04349 and the Steel Foundation for Environmental Protection Technology.

References

- Provis, J.L. (2018) "Alkali-activated materials", *Cement & Concrete Research*. 114.
- Jeong, Y., Oh, J.E., Park, J., Ha, H. J and Sohn, S.G. (2016) "Influence of four additional activators on hydrated lime [$\text{Ca}(\text{OH})_2$] activated ground granulated blast-furnace slag", *Cement & Concrete Composites*, 65: 1-10.
- Snellings, R., Machner, A., Bolte, G., Kamyab, H., Durdzinski, P., Teck, P., Zajac, M., Muller, A., Weerde, K.de and Ben Haha, M. (2022) "Hydration kinetics of ternary slag-limestone cements: Impact of water to binder ratio and curing temperature", *Cement & Concrete Research*. 151: 106647.
- Ye, H., Huang, L and Chen, Z. (2019) "Influence of activator composition on the chloride binding capacity of alkali-activated slag", *Cement & Concrete Composites*, 104: 103368.
- Osio-Norgaard, J., Gevaudan, J.P and Srubar, W.V. (2018) "A review of chloride transport in alkali-activated cement paste, mortar, and concrete", *Construction and building materials*. 119: 191-2016.
- Zhai, Q and Kurumisawa, K. (2022) "Mechanisms of inorganic salts on $\text{Ca}(\text{OH})_2$ -activated ground granulated blast-furnace slag curing under different temperatures", *Construction and building materials*. 338: 127637.

A new unidirectional testing approach for sulfate resistance on cement mortars

Qiao Wang^{1*}, William Wilson², and Karen Scrivener³

¹ *École polytechnique fédérale de Lausanne (EPFL), Lausanne, Switzerland*

Email: qiao.wang@epfl.ch

² *Université de Sherbrooke, Sherbrooke, Canada*

Email: william.wilson@usherbrooke.ca

³ *École polytechnique fédérale de Lausanne (EPFL), Lausanne, Switzerland*

Email: karen.scrivener@epfl.ch

ABSTRACT

A new sulfate penetrating approach, used for unidirectional sulfate attack on Portland cement mortar, is introduced. This testing approach addresses the sulfate attack problem, which is often present in situations of capillary action, commonly found in field cases. This technique integrates the so-called “chemical sulfate attack” and salt crystallization attack (also the so-called physical sulfate attack) into one single sample, which can be done in a practical, reproducible way in a typical construction materials laboratory. Sodium sulfate penetrates cement paste microstructure from one solution-exposed surface and reacts with the cement hydrates, which results in ettringite/gypsum formation in this region (bottom zone). This is usually called a “chemical sulfate attack”, causing expansion and cracks. However, on the other air-exposed surfaces (top zone, 55 % RH), salt crystallization attacks may be more likely to take place due to the lower relative humidity. In this study, Portland cement mortars with water-to-cement ratios of 0.5 and 0.6 were used at a Na₂SO₄ concentration of 50 g/L. The results showed that expansion and cracking can occur in the region affected by ettringite crystallization pressure. In the sample, as the solution reached the top surface, sodium sulfate could be reprecipitated in the drying zone, which caused sufficient crystallization stress for spalling damage to occur at the surface. This new technique is quite promising for understanding the sulfate degradation process as a whole. The interaction between two aspects is understood: in particular, the spalling damage from salt crystallization attack can be more representatively and practically examined.

KEYWORDS: *Sulfate attack, sulfate uniaxial ingress, expansion, cracking, spalling.*

1. Introduction

Sulfate attack is an important durability issue for cementitious materials. It has been investigated for decades, since the first external sulfate attack field case was found in Paris in 1887 (Breyse 2010). Second only to water, concrete is the most heavily consumed material in the world, and cement – the binder of concrete – is produced in quantities of 4 billion tons per year (Miller et al. 2021). Due to this large rate of consumption the carbon footprint, produced during cement manufacture, is considered to contribute as much as 8 % to global anthropogenic CO₂ emission (Andrew 2017). In this context, therefore, the durability and sustainability of concrete are key to keeping CO₂ emissions as low as possible.

To use concrete more efficiently in field conditions, in this study, we aim to get a better understanding of the damaging process of sulfate attack, and guidelines for real applications, based on the obtained results. A field case representative uniaxial testing approach was established to combine “chemical” and “physical” sulfate attacks in the same sample (Q. Wang, Wilson, and Scrivener 2021; 2023). In this testing approach, sulfate ions penetrate the microstructure by capillary rise action unidirectionally, then react with aluminum-containing hydrates that potentially cause expansion/crack. On the other drying side of the sample, salt (in this case, Na₂SO₄) may crystallize due to the water evaporation underneath the sample’s surface, potentially causing spalling damage. A more practical characterization is recommended, and the possible damage mechanism of the commonly observed concrete surface spalling in the field is discussed.

2. Materials and methods

2.1 Materials

CEM I, Portland cement, was used as the reference cement. The chemical compositions of raw materials are shown in Table 1. The phase compositions of CEM I cement are shown in Table 2.

Table 1 Chemical composition of cement

| Material | SiO ₂ | Al ₂ O ₃ | Fe ₂ O ₃ | CaO | MgO | SO ₃ | Na ₂ O | K ₂ O | TiO ₂ | P ₂ O ₅ | LOI |
|----------|------------------|--------------------------------|--------------------------------|------|-----|-----------------|-------------------|------------------|------------------|-------------------------------|-----|
| CEM I | 20.4 | 5.1 | 1.9 | 64.2 | 1.0 | 2.9 | 0.4 | 0.7 | 0.2 | 0.2 | 1.7 |

Table 2 Phase composition of cement wt. %.

| Phase composition wt. % | CEM I |
|-------------------------|-------|
| C ₃ S | 63.8 |
| C ₂ S | 13.9 |
| C ₃ A | 10.6 |
| C ₄ AF | 1.9 |
| Anhydrite | 4 |
| Calcite | 5.2 |
| Gypsum | 0.6 |

2.2 Sample preparation

Mortar samples. Cement mortars were prepared according to EN 196-1 with w/c of 0.5 and 0.6. For each mix, 1 part of cement (450 g) to 3 parts of sand (1350 g) by mass was used. The samples were cast in the plastic cylindrical container with a diameter of 33 mm, a length of 50 mm.

The uniaxial setup. A new partial immersion configuration was designed as shown in (Q. Wang, Wilson, and Scrivener 2023). A plastic container was employed to contain the sulfate solution. In each container, 16 samples were fixed with red silicone moulds on a plastic support plate installed at the middle height of the container. On the other side, the top surface is exposed to an environment-controlled room with a constant relative humidity of 55 %, and a temperature of 20 ± 2 °C.

2.3 Methodology

Visual inspections. Photographs of the bottom and top surfaces were taken to monitor the degradation process as a function of time. The occurrence of cracking/spalling and efflorescence can be compared between different systems and different exposure conditions.

Expansion and mass measurements. The diameter was measured in the direction parallel to the degradation front (parallel to the exposed surface). The measurement was carried out using a digital slide calliper and stacked 1-mm thick hollowed steel rings. The measurements were done at the same points before and after expansion. In addition, the mass of the samples was measured.

Scanning electron microscopy. Sections were cut perpendicular to the exposed surface and polished progressively to 1 µm with diamond pastes. The samples were coated with carbon and then examined by scanning electron microscopy (FEI Quanta 200) with backscattered electron imaging (BSE) and elemental hyper mapping from energy dispersive spectroscopy (EDS). The accelerating voltage was 15.0 kV and a working distance of 12.5 mm. Each mapping area along the line for the pastes was about 860×645 µm (magnification 300 \times) with a resolution of 1000×750 pixels. After processing, the mappings were quantitatively analysed by using the *edxia* approach developed by Georget et al (Georget, Wilson, and Scrivener 2021). The 8-10 individual maps were stitched together by ImageJ (Preibisch, Saalfeld, and Tomancak 2009).

3. Results and discussion

3.1 Appearance

Fig. 1 shows the visual inspections of mortars after exposure to sulfate solution. At 91 days of exposure, samples are still in good shape and no visible cracks or efflorescence appear. With an exposure age of 290

days, mortars with two w/c ratios are cracked on the bottom surfaces but with a different magnitude (MPC06 shows more significant cracks). The observed efflorescence on the top side demonstrates that sulfate ions penetrate completely through the samples. As the exposure time reaches 440 days, the salt crystallizes accumulatively in the subsurface in MPC05 and causes dramatic damage. However, in MPC06, only an abundance of efflorescence occurs, which is not harmful to the structure. Overall, damage on bottom surfaces from the ettringite formation is more profound in MPC06. In contrast, the possible salt crystallization pressure causing spalling damage seems more problematic to MPC05.

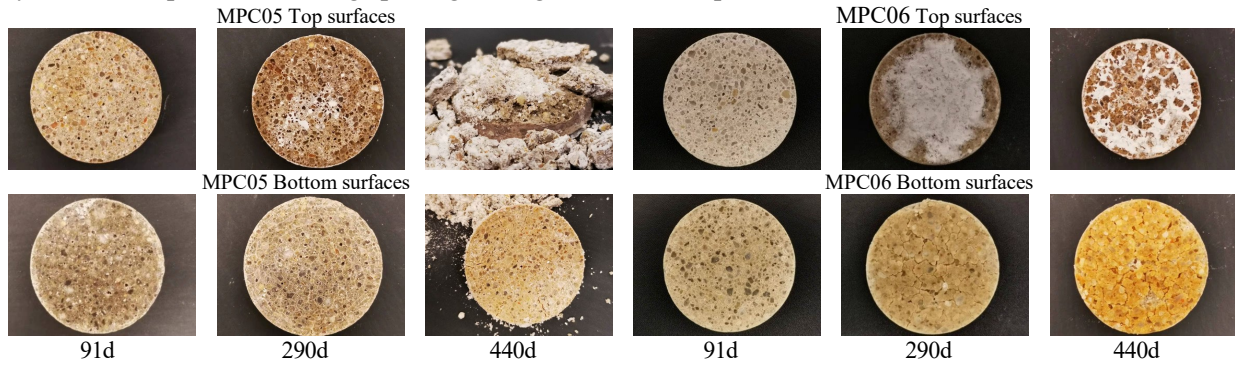


Fig. 1 Visual observations from the sulfate degradation on cement mortars with w/c ratios of 0.5 and 0.6.

3.2 Mass changes and expansion

Fig. 2 shows the expansion of the diameter and thickness dimensions of mortar samples, which demonstrates a similar tendency of the mass changes and is similar to what was observed by a conventional longitudinal expansion from the full immersion test. MPC06 shows larger ultimate expansion and mass changes than that MPC05. The expansion rate is faster in MPC06, which is consistent with the mass changes. This interesting phenomenon implies that the secondary phases (mainly ettringite) forming inside the pores initiate the expansion, and large expansion (10 mm/m for lateral expansion) occurs when the mass change is above 0. The negative mass change period shows there is a threshold time for the accumulation of the new phase formation, which corresponds to the low expansion period where the crystallization pressure is still low. Mass loss occurs in MPC05 when the surface spalls out. Mass changes may be a good assessment scenario, as it is simple and representative of microstructure changes discussed in the next section, which reflects both aspects of sulfate degradation.

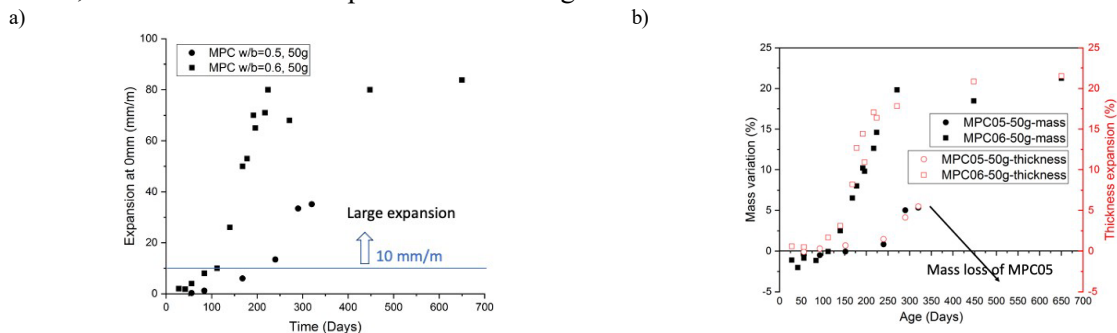


Fig. 2 Expansion of diameter and thickness dimensions and mass changes as a function of time, a) expansion vs. time, b) mass changes and thickness expansion vs. time.

3.3 Sulfur front maps

In this section the links between the sulfate ingress in the microstructure and the macroscopic damage are examined. Fig. 3 shows an example of the sulfur front evolution (marked as yellow) of MPC06. A relatively small layer from the solution-exposed surface is affected at 56 days after exposure (a sulfur concentration gradient is detected), where the negative mass gain and negligible expansion is found. Large expansion occurs when the sulfur penetrates completely from the bottom surface to the other side (if the sulphur is also detected in the region near the top surface, the salt is crystallizing due to drying), which corresponds to the exposure age of 140 days (mass gain and large expansion started from this point). A clear subflorescence showing an accumulation of sulfate is also observed in the subsurface at this stage, however,

it does not cause any visible damage (or not yet). After this point, the sulfur concentration gradient vanishes and the sulfur-rich zone around the aggregates, which is gypsum, moves further towards the other side until it reaches the carbonated layer. The phenomenon of a progressive degradation layer was already demonstrated in the study of Gollop and Wang in the 1990s by a full immersion test (Gollop and Taylor 1992; J. G. Wang 1994). From the sulfur maps, it shows that the presence of subflorescence stays only for a very short period and then efflorescence dominates the salt crystallization outside the sample. One can predict that the ingress of sulfur front in MPC05 is similarly taking place but with a relatively slower speed. Nevertheless, the subflorescence is predicted to be likely longer retained inside the sample which accumulates the crystallization pressure and spalling is more potentially happening.

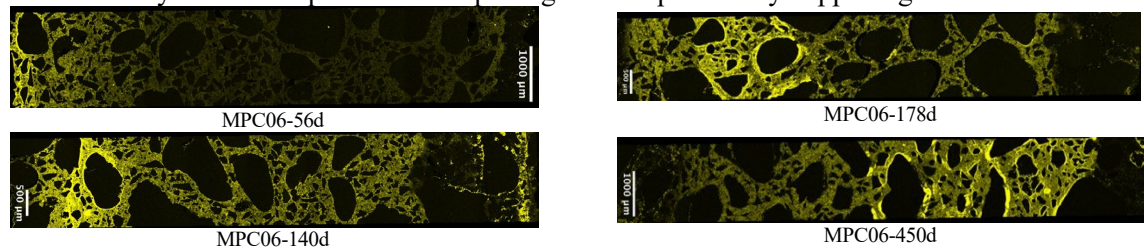


Fig. 3 Dynamic depth increase of sulfur front of MPC06 over exposure time. Left side of the image is the bottom surfaces exposed to the solution, right side of the image is the top surfaces exposed to the air.

4. Conclusions

This study investigates a potential setup that can be used to understand better sulfate attack in field cases, where the capillary rise is the process that dominates the sulfate ingress. Based on the results obtained, the following conclusions can be drawn:

- The newly established uniaxial testing approach is a promising setup, which enables us to look at both the ettringite-caused and salt crystallization-caused deterioration on cement mortars.
- w/c ratios can impact the extent of expansion/mass variations, consequently the levels from ettringite-induced damage. Lowering the w/c ratio is expected to be an efficient way to increase the sulfate resistance to ettringite, however, it might be problematic for spalling in drying zones.
- The mortars are eventually disintegrated once the sulfate penetrates the samples completely, either by expansion-induced cracking or subflorescence-induced surface spalling.

References

- Andrew, Robbie. 2017. "Global Co2 Emissions From Cement Production." Zenodo. <https://doi.org/10.5281/ZENODO.831455>.
- Breyse, D. 2010. "3 - Deterioration Processes in Reinforced Concrete: An Overview." In *Non-Destructive Evaluation of Reinforced Concrete Structures*, edited by Christiane Maierhofer, Hans-Wolf Reinhardt, and Gerd Dobmann, 1:28–56. Woodhead Publishing Series in Civil and Structural Engineering. Woodhead Publishing. <https://doi.org/10.1533/9781845699536.1.28>.
- Georget, Fabien, William Wilson, and Karen L. Scrivener. 2021. "Edxia: Microstructure Characterisation from Quantified SEM-EDS Hypermaps." *Cement and Concrete Research* 141 (March): 106327. <https://doi.org/10.1016/j.cemconres.2020.106327>.
- Gollop, R. S., and H. F. W. Taylor. 1992. "Microstructural and Microanalytical Studies of Sulfate Attack. I. Ordinary Portland Cement Paste." *Cement and Concrete Research* 22 (6): 1027–38. [https://doi.org/10.1016/0008-8846\(92\)90033-R](https://doi.org/10.1016/0008-8846(92)90033-R).
- Miller, Sabbie A., Guillaume Habert, Rupert J. Myers, and John T. Harvey. 2021. "Achieving Net Zero Greenhouse Gas Emissions in the Cement Industry via Value Chain Mitigation Strategies." *One Earth* 4 (10): 1398–1411. <https://doi.org/10.1016/j.oneear.2021.09.011>.
- Preibisch, Stephan, Stephan Saalfeld, and Pavel Tomancak. 2009. "Globally Optimal Stitching of Tiled 3D Microscopic Image Acquisitions." *Bioinformatics* 25 (11): 1463–65. <https://doi.org/10.1093/bioinformatics/btp184>.
- Wang, James G. 1994. "Sulfate Attack on Hardened Cement Paste." *Cement and Concrete Research* 24 (4): 735–42. [https://doi.org/10.1016/0008-8846\(94\)90199-6](https://doi.org/10.1016/0008-8846(94)90199-6).
- Wang, Qiao, William Wilson, and Karen Scrivener. 2021. "Investigating Dual Sulfate Attack Mechanisms Using Unidirectional Penetration Approach." *Special Publication* 349 (April): 623–28.
- Wang, Qiao, William Wilson, and Karen Scrivener. 2023. "Unidirectional Penetration Approach for Characterizing Sulfate Attack Mechanisms on Cement Mortars and Pastes." *Cement and Concrete Research* 169 (July): 107166. <https://doi.org/10.1016/j.cemconres.2023.107166>.

A COMPARATIVE ASSESSMENT OF DIFFERENT ADDITIVES TO REDUCE CARBONATION DEGRADATIONS OF ALKALI-ACTIVATED SLAG USING IN-SITU FTIR TECHNIQUE

N. Nair¹, M. I. Haque², and W. Ashraf^{3*}

¹ *Department of Civil Engineering, The University of Texas at Arlington, Texas, USA
Email: nnv2965@mavs.uta.edu*

² *Department of Civil Engineering, The University of Texas at Arlington, Texas, USA
Email: muhammad.haque@mavs.uta.edu*

^{3*} *Department of Civil Engineering, The University of Texas at Arlington, Texas, USA
Email: warda.ashraf@uta.edu*

ABSTRACT

This paper discusses the effectiveness of incorporating different additives into the matured alkali-activated slag-cement system to resist carbonation degradation. A total of four batches – control, 5% magnesia, 5% portlandite, and 5% biomimetic molecule dosage were taken into consideration. The 18-hour in-situ FTIR (Fourier transform infrared spectroscopy) showed the peak shifting of C-A-S-H to polymerized silica gel in the system. It confirmed the stabilization of the calcium carbonate polymorph, which eventually explains the reduction of carbonation degradation. X-ray diffraction (XRD) technique and thermogravimetric analysis (TGA) confirmed the crystallography of calcium carbonate polymorph formation. Based on the experimental findings, the biomimetic molecule was most effective in reducing the carbonation degradation of alkali-activated materials. Reduced carbonation degradation of alkali-activated materials will eventually enhance their sustainability and assist the global effort to achieve net zero emissions.

KEYWORDS: *Slag-carbonation, biomimetic molecule, microstructures, calcium carbonate polymorphs, CO₂ reduction*

1. Introduction

Slag is a widely accessible steel industry byproduct and has latent hydraulic properties. The superior durability of slag-based cement composites has also been demonstrated by their strong resistance to chemical attacks, including chloride penetration. However, due to the poor carbonation resistance, it is not accepted much in the cement-concrete industry. Here, we will assess the carbonation resistance in the alkali-activated slag (AAS)-based system by introducing bio-stimulated materials. Marine organisms such as algae, mussel shells, sea urchins, corals, etc., can convert CO₂ into biogenic materials. This biomimetic molecule has the ability to control the crystallization of inorganic calcium carbonate by producing the ‘organic-inorganic’ hybrid phases (Khan et al., 2022). This process was also found to be efficient in reducing the carbonation degradation of C-S-H (Haque et al., 2023). Recent studies show other additives such as Ca(OH)₂, Zn(OH)₂, air-entraining agents, shrinkage-reducing admixtures, etc., mixed with AAS mortar/concrete used to control the carbonation of AAS systems (Charitha et al., 2022; He et al., 2018). Another study by (Gardeh et al., 2022) found that reactive magnesium oxide-based cement can control the degree of carbonation and be a suitable binder for the partial replacement of OPC systems. The present study mainly focuses on reducing the carbonation rate in an alkali-activated slag (AAS) system. Therefore, the following additives (i) 5% L-Aspartic acid (biomimetic molecule, addressed as L-Asp) (ii) 5% Ca(OH)₂ (iii) 5% Mg(OH)₂ were added to a matured AAS paste sample (after 28 days of curing) and subjected to accelerated carbonation to understand the formation of carbonates due to decalcification of C-A-S-H gel.

2. Experimental Methodology

In this study, the NaOH-activated (5% Na₂O) AAS paste samples were sealed cured for 28 days. The paste samples were pulverized into a fine ground powder, and each additive of 5% by weight of the AAS sample was mixed separately into the AAS sample to form four batches: (i) control (no additives), (ii) 5% L-Asp (iii) 5% Mg(OH)₂ (iv) 5% Ca(OH)₂. The in-situ Fourier-Transformed Infrared (FTIR) spectra of the powder samples were collected using the Attenuated Total Reflection (ATR) mode with 4 cm⁻¹ resolution and 32 scans for each sample. A total of 280 spectra were collected, maintaining a time interval of 3.75 mins between the two spectra. 99% CO₂ gas purging was maintained. The signal-to-noise ratio was lower than 3:1. For XRD and TGA techniques, the powdered AAS samples with the respective additives were mixed with water (0.2 water-to-binder ratio) to ensure uniform mixing. The samples were then subjected to accelerated carbonation using a carbonation chamber at 20% CO₂ concentration and 65% relative humidity. The samples were collected after one-hour and six-hour durations. After six hours of accelerated carbonation, the samples were fully carbonated. As a result, the samples after one hour of carbonation were presented in the study for TGA and XRD analyses for comparison. XRD was conducted on a Bruker D-8 spectrometer, using Cu K α radiation (40 kV, 40 mA). The sample was scanned over a range of 5°- 60°(2 θ), using a step size of 0.01 per second. TGA was conducted on the TGA 550 TA instrument. The sample was kept in an isothermal condition at around 25°C for 5 minutes before being raised to 980 °C at a rate of 15 °C per minute. Nitrogen gas was purged into the chamber to ensure an inert environment.

3. Results and discussion

3.1 Carbonate formation

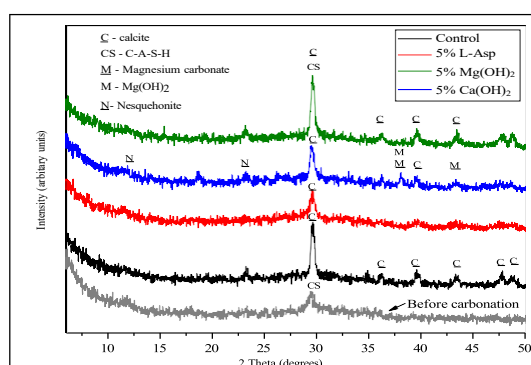


Figure 1: XRD pattern after one hour of accelerated carbonation

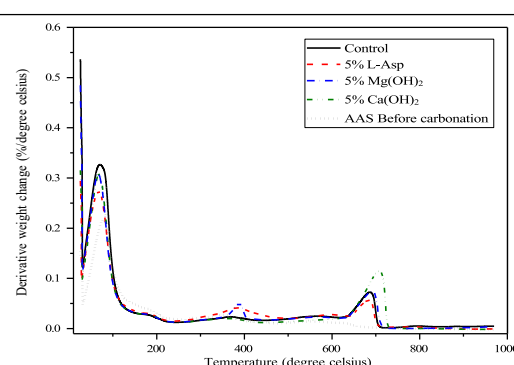


Figure 2: DTG curves after one hour of accelerated carbonation

Carbonate formation is prioritized in the XRD (**Figure 1**) and TGA (**Figure 2**) results to understand the microstructural changes caused by accelerated carbonation. The broad hump peak at 2 θ of 29° indicates the major hydration product, C-S-H/C-A-S-H gel, in the amorphous form (**Figure 1**) before carbonation (ben Haha et al., 2011). After accelerated carbonation, there was a sharp peak at 2 θ of 28°-29° for the control batch, indicating calcite formation (Nedeljković et al., 2018; Seo et al., 2021). The DTG curves (**Figure 2**), which have a sharp peak at 700°C, validate these carbonate formation findings. The intensity of the calcite peak was not dominant in the AAS sample with 5% L-Aspartic acid compared to the control batch (**Figure 1**). This indicates that incorporating L-Asp into the AAS system slowed the rate of calcite formation. From DTG curves (**Figure 2**), the comparatively broader peak at the 200°C - 650°C associated with the decomposition of amorphous CaCO₃ polymorphs was observed along with the crystalline calcite decomposition peak at 700°C (Khan et al., 2021). Therefore, L-Asp stabilizes the formation of the metastable CaCO₃ polymorphs and delays the transformation into crystalline calcite. From **Figure 1**, the intensity of the calcite peak in the AAS sample mixed with 5% Mg(OH)₂ was lower than in the control batch and almost identical to the batch containing 5% L-Asp. The XRD pattern showed other magnesium-based products, including nesquehonite (MgCO₃·3H₂O), and unreacted Mg(OH)₂ (Zhang & Panesar, 2017)). The calcite peak at 700°C is similar to the control batch in the DTG curve. Compared to all other batches, the 5% Ca(OH)₂ mixed AAS system displayed a higher intensity peak at 2 θ of 29° (**Figure 1**), indicating higher calcite formation. This is expected since the presence of additional Ca²⁺ ions reacts with the CO₃²⁻ ions to form additional calcite formation. The DTG curve (**Figure 2**) validates this with no visible

peak at 450°C, depicting that the Ca(OH)_2 was consumed almost fully into calcium carbonate formation (peak at 700°C). (He et al., 2018) showed that when Ca(OH)_2 was mixed with AAS concrete as an additive, it improved the carbonation resistance of the composite. Therefore, incorporating Ca(OH)_2 as an external agent to a matured AAS system serves as a buffer or sacrificial agent, which slows down the conversion of the C-A-S-H gel into calcium carbonate polymorphs.

3.2 Silica polymerization

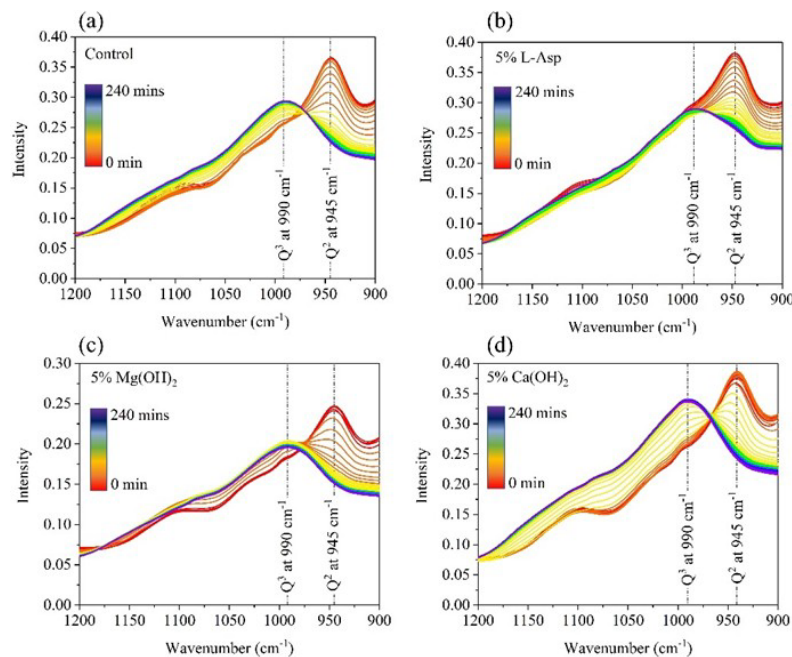


Figure 3: In-situ FTIR spectra showing Q^2 to Q^3 conversion due to the carbonation

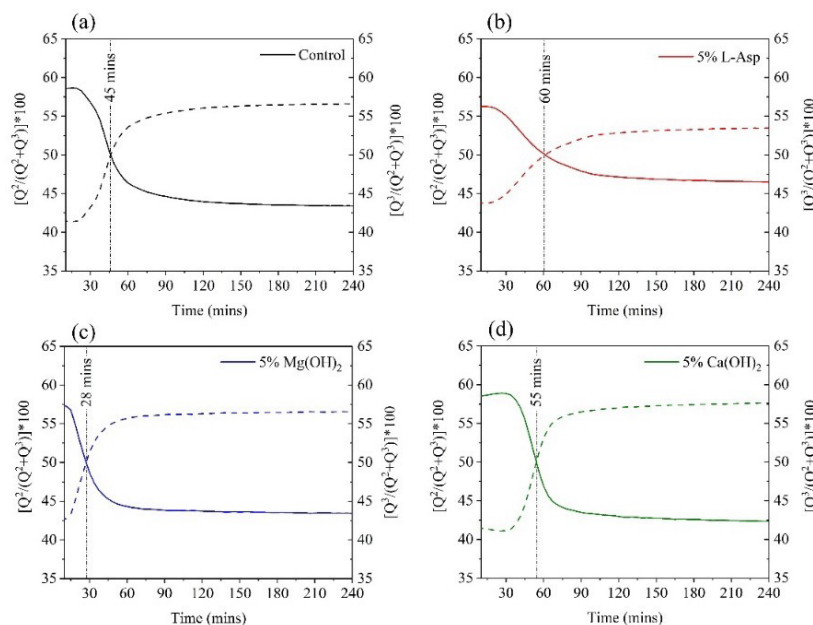


Figure 4: Q^2 to Q^3 convergence of different batches.

The conversion of C-A-S-H to silica gel due to the carbonation-induced decalcification in the AAS paste was investigated with the in-situ FTIR. The peaks in the range from 900 cm^{-1} to 1200 cm^{-1} are prominent, which were generated because of the asymmetric and stretching vibration (ϖ_3) of the Si-O bond (Ashraf & Olek, 2016; Haque et al., 2023; Ping et al., 1999). Here in this AAS paste, the C-A-S-H gel was identified at around 945 cm^{-1} (Figure 3) which matched previous literature (Khan et al., 2022,) and this band was due

to the Si-O stretching vibration (ν_3) of the Q^2 tetrahedron (Kupwade-Patil et al., 2018; Li et al., 2017)). With time and enhanced carbonation, a peak at around 990 cm^{-1} , corresponding to the Q^3 species, started forming (Figure 3). The conversion from Q^2 to Q^3 occurred within the first 240 mins of carbonation (Figure 4). Among the batches, 5% $Mg(OH)_2$ converged fastest within 30 mins, which is faster than the control batch. Therefore, the addition of 5% $Mg(OH)_2$ accelerated the C-A-S-H decalcification rate. The Q^2 to Q^3 conversion was the slowest (60 min) for the 5% L-Asp batch. This indicates that the 5% dosage of L-Asp delayed silica polymerization even in 99% CO_2 purging. After stabilization, the Q^3/Q^2 ratio was also lowest for the 5% L-Asp batch compared to others, indicating a lower degree of polymerization of the final gel product in this batch. The 5% $Ca(OH)_2$ containing batch also showed delayed silica polymerization convergence (55 mins) compared to the control batch (45 mins).

4. Conclusions

Based on the experimental observations, it was found that the addition of 5% $Ca(OH)_2$ batch resulted in increased calcite formation and delayed C-A-S-H decalcification. It also confirmed that if both $Ca(OH)_2$ and C-A-S-H are present in the system, first $Ca(OH)_2$ gets carbonated, and then C-A-S-H is decalcified. Therefore, $Ca(OH)_2$ can be an appropriate additive when higher CO_2 sequestration is preferred without damaging the C-A-S-H structure. On the other hand, the 5% $Mg(OH)_2$ batch exhibited enhanced decalcification of C-A-S-H with less calcite formation, and other types of Mg-carbonates were formed. The 5% L-Asp-containing batch delayed the extent of decalcification and prevented calcite formation by primarily producing amorphous calcium carbonates (ACC). The polymerization of the final gel product was also the lowest for the L-Asp containing batch compared to the other additives. Therefore, the usage of L-Asp can potentially reduce the carbonation-induced shrinkage of the AAS.

References

- Ashraf, W., & Olek, J. (2016). Carbonation behavior of hydraulic and non-hydraulic calcium silicates: potential of utilizing low-lime calcium silicates in cement-based materials. *Journal of Materials Science*, 51(13), 6173–6191.
- Charitha, V., Athira, G., Bahurudeen, A., & Shekhar, S. (2022). Carbonation of alkali activated binders and comparison with the performance of ordinary Portland cement and blended cement binders. In *Journal of Building Engineering* (Vol. 53). Elsevier Ltd.
- Gardeh, M. G., Kistanov, A. A., Nguyen, H., Manzano, H., Cao, W., & Kinnunen, P. (2022). Exploring Mechanisms of Hydration and Carbonation of MgO and $Mg(OH)_2$ in Reactive Magnesium Oxide-Based Cements. *Journal of Physical Chemistry C*, 126(14), 6196–6206.
- Haha, M. B., le Saout, G., Winnefeld, F., & Lothenbach, B. (2011). Influence of activator type on hydration kinetics, hydrate assemblage and microstructural development of alkali activated blast-furnace slags. *Cement and Concrete Research*, 41(3), 301–310.
- Haque, M. I., Borno, I. B., Khan, R. I., & Ashraf, W. (2023). Reducing carbonation degradation and enhancing elastic properties of calcium silicate hydrates using biomimetic molecules. *Cement and Concrete Composites*, 136.
- He, J., Gao, Q., Wu, Y., He, J., & Pu, X. (2018). Study on improvement of carbonation resistance of alkali-activated slag concrete. *Construction and Building Materials*, 176, 60–67.
- Khan, R. I., Ashraf, W., & Olek, J. (2021). Amino acids as performance-controlling additives in carbonation-activated cementitious materials. *Cement and Concrete Research*, 147.
- Khan, R. I., Haque, M. I., Ashraf, W., Shah, S., & Saleh, N. (2022a). Role of biopolymers in enhancing multiscale characteristics of carbonation-cured cementitious composites. *Cement and Concrete Composites*, 134.
- Kupwade-Patil, K., Palkovic, S. D., Bumajdad, A., Soriano, C., & Büyüköztürk, O. (2018). Use of silica fume and natural volcanic ash as a replacement to Portland cement: Micro and pore structural investigation using NMR, XRD, FTIR and X-ray microtomography. *Construction and Building Materials*, 158, 574–590.
- Li, N., Farzadnia, N., & Shi, C. (2017). Microstructural changes in alkali-activated slag mortars induced by accelerated carbonation. *Cement and Concrete Research*, 100, 214–226. <https://doi.org/10.1016/j.cemconres.2017.07.008>
- Nedeljković, M., Zuo, Y., Arbi, K., & Ye, G. (2018). Carbonation Resistance of Alkali-Activated Slag Under Natural and Accelerated Conditions. *Journal of Sustainable Metallurgy*, 4(1), 33–49.
- Ping, Y., Kirkpatrick, R. J., Brent, P., McMillan, P. F., & Cong, X. (1999). Structure of calcium silicate hydrate (C-S-H): Near-, mid-, and far-infrared spectroscopy. *Journal of the American Ceramic Society*, 82(3), 742–748.
- Seo, J., Kim, S., Park, S., Bae, S. J., & Lee, H. K. (2021). Microstructural evolution and carbonation behavior of lime-slag binary binders. *Cement and Concrete Composites*, 119.
- Zhang, R., & Panesar, D. K. (2017). Investigation on Mg content in calcite when magnesium calcite and nesquehonite co-precipitate in hardened cement paste. *Thermochimica Acta*, 654, 203–215.

Appraisal of the microstructural properties of ASR affected concrete at different moisture conditions using the DRI

O.D. Olajide^{1*}, M.R. Nokken², and L.F.M. Sanchez³

¹ Concordia University, Montreal, Canada

Email: olusola.olajide@concordia.ca

² Concordia University, Montreal, Canada

Email: m.nokken@concordia.ca

³ University of Ottawa, Ottawa, Canada

Email: Leandro.sanchez@uottawa.ca

ABSTRACT

Alkali silica reaction (ASR) is a widely known destructive mechanism in concrete caused by the reaction between poorly crystallized siliceous phases in aggregate particles and alkali from cement in the presence of favorable environmental conditions. Moisture is required in sufficient amount to trigger and sustain the reaction and a relative humidity threshold (RH) of 80% has been often stated in literature as a minimum requirement. However, there exists few research studies on the evaluation of the role of moisture conditions on the induced deterioration of concrete affected by ASR. This work presents the assessment of ASR damage resulting from a large range of exposure conditions using the damage rating index (DRI); a semi-quantitative microscopic tool that has been prominently used to appraise ASR affected concrete. The results show that the DRI is effective in assessing the role of moisture in ASR-induced internal damage.

KEYWORDS: *ASR expansion, Moisture, Relative humidity, Microstructure, Damage rating index*

1. Introduction

Alkali silica reaction (ASR) is a prominent deterioration mechanism that can lead to the loss of serviceability in affected concrete, resulting from the reaction between poorly crystallized siliceous phases in aggregate and alkali in the concrete pore solution (Poyet et al., 2006). This reaction results in the formation of an ASR gel that expands in the presence of moisture. Common symptoms of the reaction can include map-cracking, gel exudation on the surface of affected concrete. The described reaction can subsequently lead to reduction in the mechanical properties of affected concrete. After several decades of research about the reaction, our understanding of the mechanisms involved, and mitigation techniques has improved significantly. Although, there is no known way to stop the reaction in affected structures, the reduction in available moisture has been recommended as one of the techniques to slow down the reactivity. As a result, a relative humidity threshold (RH) of 80% has often been stated to mitigate the reaction.

Several researchers have evaluated the influence of different moisture levels on the reaction (Deschenes et al., 2018; Poyet et al., 2006), but all of these has been limited to expansion over time without an appraisal of the resulting induced deterioration. Several tools have been developed for such appraisal; one of these is the damage rating index (DRI). The DRI is a semi-quantitative microscopic analysis that can be used to assess the extent of ASR damage in affected concrete (Sanchez et al., 2016), adjudged through the assessment of internal damage (cracks). According to Sanchez et al. (2016), the level of ASR-induced expansion in concrete can be correlated to the initiation and propagation of cracks in concrete. A slightly induced expansion will have most of the cracks in the aggregates. Otherwise, a highly damaged concrete

presenting high expansion will have cracks propagating from the aggregate particles into the cement paste, with cracks linking and causing a significant reduction in mechanical properties.

This work investigated the development of ASR at numerous moisture conditions (RH). The internal damage attained at these moisture levels over time were evaluated using the DRI. In addition, the expansion results were used to discuss the influence of moisture on the kinetics of the reaction and their relationship to DRI.

2. Methods

A concrete mixture with a design strength of 45 MPa containing a reactive coarse (Spratt aggregate) and non-reactive fine (manufactured sand) aggregate was selected for this study. An ordinary Portland cement was used, and the alkali content of the mix was boosted to 1.25% Na_2O_{eq} by adding sodium hydroxide pellets as per ASTM C1293. Cylindrical concrete specimens (100 mm diameter and 200 mm height) were cast. After casting, the specimens were demolded and moist cured at room temperature for 48 hours; holes were drilled on both sides and studs were installed using a fast-setting cement slurry during the first 24 hours. The initial length readings were conducted after 48 hours, and specimens were ready for storage.

The specimens are placed in sealed buckets, each containing four concrete cylinders. The buckets were all stored at 38°C temperature but in different moisture conditions. Relative humidities of 100%, 90%, 82%, 75% and 62% were targeted and maintained for each moisture conditions using saturated salt solution as used by Poyet et al. (2006). Sensors were attached to the inside lid of the buckets and inserted internally in an additional specimen for each condition to monitor the external and internal RH (IRH and ERH) respectively. Each moisture condition (i.e. family) consists of twelve (12) identical concrete specimens.

Expansion and mass change measurements were conducted periodically on all the specimens from each family over a period of 1 year, results are presented in Figure 1. The damage rating index (DRI) is a petrographic-based semi-quantitative analysis that can provide the extent of ASR damage in concrete. The test is performed on a 100 x 200mm polished surface using a stereomicroscope with a magnification of 15-16x. The petrographic features are counted in 1 x 1cm square grids drawn on the surface of polished concrete; each distinct features are multiplied by weighting factors as proposed by Sanchez et al. (2015). The DRI number is obtained by taking the sum of the weighted count for all the petrographic features and normalizing to 100 cm².

The DRI analyses were conducted on specimens from each exposure conditions after 6 and 12 months. The specimens were cut longitudinally and polished using a mechanical polishing table with grits 30, 60, 120, 240, 600, 1200 and 3000. A grid of 1 x 1cm was drawn on the polished surface prior to the counting of the petrographic features.

3. Results and discussions

3.1 ASR kinetics and development

The results of the IRH shows that all specimens have similar internal moisture (85-90% RH) at the start of the test which will influence the reaction until the IRH either reduces or increases to equilibrate with the ERH. For the 62% and 75% RH conditions, the measured IRH dropped below 80% within 20 and 40 days, respectively. The average ASR expansion and mass change as a function of time in specimens incorporating reactive Spratt aggregate, stored at 38°C and numerous ERH conditions (i.e., 100%, 90%, 82%, 75% and 62%) are presented in Fig. 1. The kinetics of ASR differs depending on the availability of moisture; the specimens stored at 100% RH (humid condition) attained the highest ultimate expansion of 0.211% while a shrinkage of -0.002% was recorded in specimens stored at 62% RH (dry condition) after 365 days of exposure. Furthermore, the rate of the reaction was influenced by the available moisture. The reaction started slowly at low RH, resulting in the early age drying shrinkage and reduction in mass recorded at 82%, 75% and 62% RH. However, the expansion due to ASR increased significantly beyond the drying shrinkage in 82%RH specimens after a couple of weeks. For the specimens at 62% RH although the behaviour changed to expansion at approximately 90 days, these samples failed to attain a net positive induced expansion throughout the period of exposure. Specimens from each moisture condition were selected for the DRI after 6 and 12 months of expansion measurements.

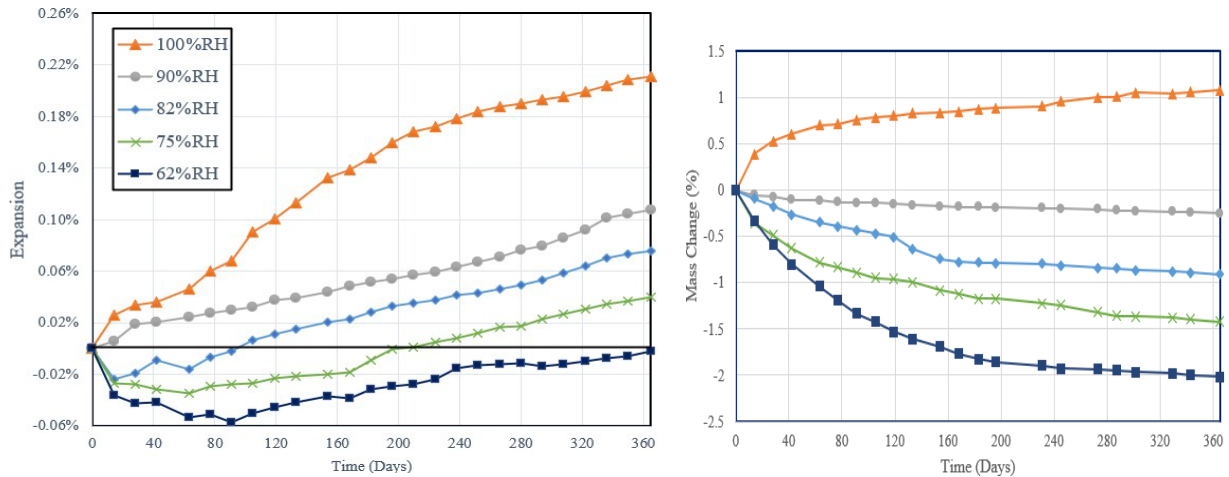


Figure 1: Expansion and mass change vs. Time of ASR affected concrete specimens at 38°C and different relative humidity (a) Expansion (b) Mass change

3.2 Damage rating index (DRI)

Fig. 2 shows the DRI for ASR affected concrete specimens stored at the studied relative humidity conditions (i.e., 100%, 90%, 82%, 75% and 62%) after 6 and 12 months. The DRI numbers show that concrete specimens at high moisture levels experienced higher amount of ASR induced deterioration after 6 and 12 months. At 6 months, high number of cracks in the cement paste (CCP) caused by drying shrinkage was recorded at low RH conditions (62%, 75% and 82% RH) and similar DRI number were reported. At this age, $\sim 0.02\%$ and $\sim 0.03\%$ shrinkage was recorded at 62% RH and 75% RH respectively, and $\sim 0.02\%$ expansion at 82% RH. Hence, similar level of distress (shrinkage/expansion) occurs at these moisture levels, thus, the similar DRI number obtained. Furthermore, the cause of this induced distress (shrinkage or expansion) can be evaluated using the petrographic features. Considering 62% RH versus 82% RH (both with $\sim 0.02\%$, but in a shrinkage versus expansion condition); as shown in Figure 3a, the main distress features observed at 62% RH is cracks in cement paste (CCP) with $\sim 80\%$ of the total microscopic features (cracks), which indicates shrinkage. Whereas for the specimens stored at 82% RH, $\sim 53\%$ of the total cracks are present in the aggregates (CCA + OCA + OCAG), indicating a slight ASR-induced expansion.

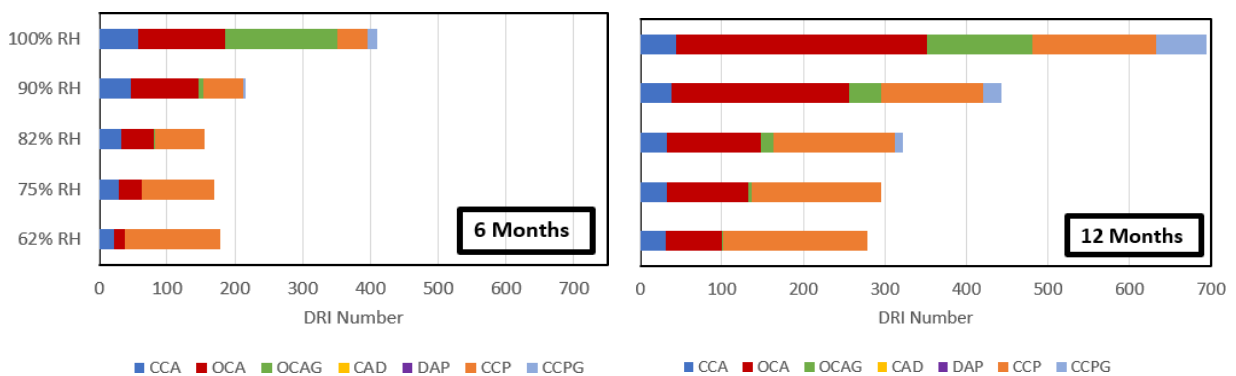


Figure 2: DRI for ASR affected concrete at different relative humidity after 6 and 12 months

At the glance of the evolution of the petrographic features, the RH conditions generates different damage pattern from ASR. Nonetheless, crack initiation and propagation follows the process described by Sanchez et al. (2016). As illustrated in Figure 3b, the open cracks in aggregates (OCA) increases with expansion and across all RH conditions. As shown in Fig. 3A and considering the 82% RH condition, one would see that 32% of the total microscopic features at 6 months is OCA which increases to 41% after 12 months. Even at a low RH of 62%, the OCA increased from 9.5% to 25.5% after 6 and 12 months

respectively which likely indicates the development of ASR despite the shrinkage of -0.032% and -0.002% recorded at 6 and 12 months respectively.

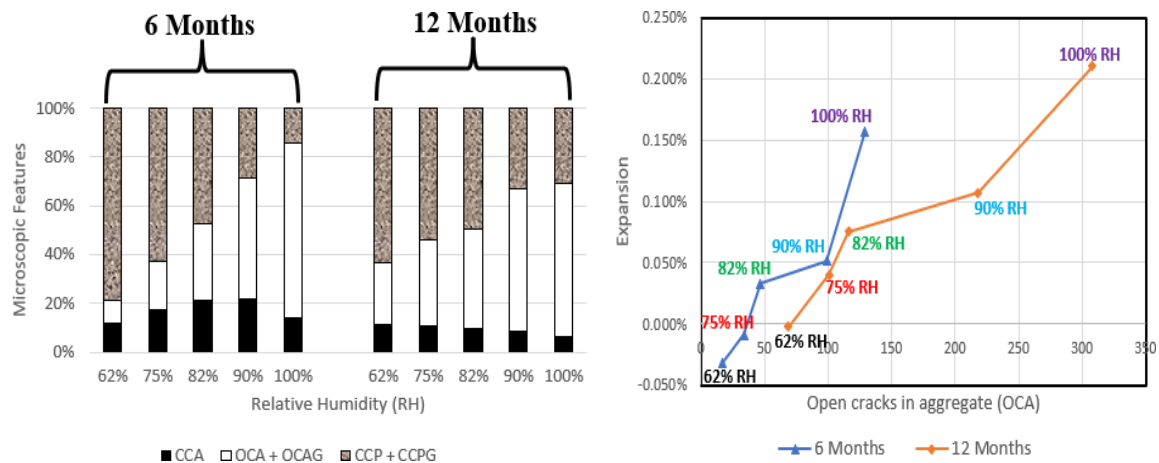


Figure 3: Comparison of deterioration features of ASR affected concrete at different RH after 6 and 12 months
(a) crack numbers in percentage (b) open cracks in aggregates (OCA) versus expansion

4. Conclusions

This study was focused on assessing the microstructural properties of ASR affected concrete stored at different relative humidity conditions using the damage rating index. Some conclusions can be drawn from the results. However, some recommendations are to be made for further studies on the gaps highlighted during the discussion of the results. Therefore, the conclusions and recommendations are:

- Moisture significantly affects the kinetics of ASR. The reaction can be maintained at RH lower than 80%. The reaction is coupled with drying shrinkage at low moisture conditions. Hence, decoupling of drying shrinkage will give a detailed information on the development of ASR at low moisture conditions. This factor is currently under investigation for this research.
- The damage rating index number at 82%, 75% and 62% RH is similar despite a notable difference in their expansion. However, the induced deterioration differs as shown by the petrographic features. DRI on specimens with non-reactive samples is currently underway to decouple the two effects.

References

- Deschenes, R. A., Giannini, E., Drimalas, T., Fournier, B., & Hale, W. M. (2018). Effects of Moisture, Temperature, and Freezing and Thawing on Alkali-Silica Reaction. *ACI Materials Journal*, 115(4), 575–584. <https://doi.org/10.14359/51702192>
- Poyet, S., Sellier, A., Capra, B., Thèvenin-Foray, G., Torrenti, J.-M., Tournier-Cognon, H., & Bourdarot, E. (2006). Influence of Water on Alkali-Silica Reaction: Experimental Study and Numerical Simulations. *Journal of Materials in Civil Engineering*, 18(4), 588–596. [https://doi.org/10.1061/\(ASCE\)0899-1561\(2006\)18:4\(588\)](https://doi.org/10.1061/(ASCE)0899-1561(2006)18:4(588))
- Sanchez, L., Fournier, B., Drimalas, T., Bastien, J., Mitchell, D., & Noël, M. (2016). Comprehensive Microscopic Assessment of Concrete Distress Through the Damage Rating Index. *15th International Conference on Alkali-Aggregate Reaction*.
- Sanchez, L., Fournier, B., Jolin, M., Bedoya, M., Bastien, J., & Duchesne, J. (2016). Use of Damage Rating Index to Quantify Alkali-Silica Reaction Damage in Concrete: Fine versus Coarse Aggregate. *ACI Materials Journal*, 113. <https://doi.org/10.14359/51688983>
- Sanchez, L., Fournier, B., Jolin, M., & Duchesne, J. (2015). Reliable quantification of AAR damage through assessment of the Damage Rating Index (DRI). *Cement and Concrete Research*, 67, 74–92. <https://doi.org/10.1016/j.cemconres.2014.08.002>

Property changes of calcium sodium aluminosilicate hydrates (C-N-A-S-H) gels subjected to water immersion

C. Liu^{1*}, S. Nie², Z. Li¹, and G. Ye¹

¹ Department of Materials and Environment (Microlab), Faculty of Civil Engineering and Geoscience, Delft University of Technology, Delft, the Netherlands

Email: C.Liu-12@tudelft.nl; Z.Li-2@tudelft.nl; G.Ye@tudelft.nl

² Department of Chemistry and Interdisciplinary Nanoscience Center (iNANO), Aarhus University, 8000 C Aarhus, Denmark

Email: shuainie@chem.au.dk

ABSTRACT

Alkali-activated materials (AAMs) are commonly considered to be susceptible to water-contacting conditions due to the possibility of the leaching of ions. So far, there is a lack of knowledge on the property change of the main reaction products (C-N-A-S-H gels) of AAMs subjected to underwater conditions. To avoid the interference with other phases involved in an AAM system, this study investigates this issue using synthesized C-N-A-S-H gels. Three stoichiometrically controlled C-N-A-S-H gels were synthesized using the double decomposition method considering different Ca/Si and Al/Si ratios. The gels were then immersed in deionized water with a gel/water mass ratio of 1:100 for 28 days. The leaching behavior, phase assemblage and structural evolution of the gels were investigated. The results show that Na readily leaches out of the gel structure in a short time. Water immersion does not result in a change in the phase assemblage of C-N-A-S-H gels, but is confirmed to slightly enhance the degree of polymerization of the gels. This paper provides new insight into the properties of C-N-A-S-H gels due to water immersion, which is essential for further understanding the properties of AAMs in engineering practice.

KEYWORDS: *C-N-A-S-H gels, alkali-activated materials, water immersion, leaching*

1. Introduction

Alkali-activated materials (AAMs) have gained considerable interest in the academic and engineering communities since this material can significantly reduce energy consumption and carbon emission [1]. Besides, AAMs have comparable mechanical properties to traditional cementitious materials and, in some conditions, even better durability [2]. Nonetheless, AAMs still face some hurdles. Leaching, a process that often occurs when a substance is exposed to a moist or aqueous environment, is a pervasive problem that merits consideration. Researchers found that water immersion can coarsen the pore structures and lower the mechanical properties of AAMs [3]. The degradation mechanisms of alkali-activated slag paste after long-term tap water immersion were preliminarily investigated in a previous work [4], but the change in the main reaction product (C-N-A-S-H gel) remains still unclear.

In this work, three C-N-A-S-H gels with Ca/Si and Al/Si ratios of 0.8 and 0.1, 0.8 and 0.3, and 1.2 and 0.3 were synthesized under alkali conditions. The gels were then immersed in deionized water for different durations. The ion concentration of the leachate of gels was determined by inductive coupled plasma-optical emission spectrometry (ICP-OES) spectrometer. X-ray diffraction (XRD) and Fourier-transform infrared spectroscopy (FTIR) were conducted to investigate the phase change of the gels with time.

2. Materials and methods

2.1 Materials

The C-N-A-S-H gels were prepared by the double decomposition method [5]. Three stoichiometrically tailored gels were tested, namely 0.8_0.1, 0.8_0.3, and 1.2_0.3, with 0.8 and 1.2 representing the target Ca/Si ratio and 0.1 and 0.3 representing the target Al/Si ratio, respectively. A 0.6 M Na₂SiO₃·5H₂O solution,

a 0.24 M $\text{Ca}(\text{NO}_3)_2 \cdot 4\text{H}_2\text{O}$ solution, a 0.12 M $\text{Al}(\text{NO}_3)_3 \cdot 9\text{H}_2\text{O}$ solution, and a 10 M NaOH (using for pH adjustment) solution were prepared using deionized water as the starters of gel synthesis. The proportions of chemical solutions for each gel are presented in **Table 1**. Three solutions were dripped with the sequence of NaOH, Na_2SiO_3 , $\text{Al}(\text{NO}_3)_3$ and $\text{Ca}(\text{NO}_3)_2$ in a N_2 atmosphere and then mixed with deionized water for 7 days. The centrifuged gel was ultrasonically washed and then freeze-dried for 3 days. After that, the gels were pulverized to powder and stored in a desiccator at 25 °C and RH \approx 30%. The realized elemental ratios of the synthesized gels are presented in **Table 2**.

Table 1. The proportion of chemical solutions for gel synthesis (unit/ml).

| | $\text{Na}_2\text{SiO}_3 \cdot 5\text{H}_2\text{O}$ | $\text{Ca}(\text{NO}_3)_2 \cdot 4\text{H}_2\text{O}$ | $\text{Al}(\text{NO}_3)_3 \cdot 9\text{H}_2\text{O}$ | NaOH | Deionized H_2O |
|---------|---|--|--|------|--------------------------------|
| 0.8_0.1 | 80 | 100 | 40 | 50 | 80 |
| 0.8_0.3 | 80 | 100 | 120 | 50 | - |
| 1.2_0.3 | 50 | 150 | 75 | 50 | 25 |

Table 2. Elemental ratio of synthesized C-N-A-S-H gels

| | Ca/Si | Al/Si | Na/Si |
|---------|-------|-------|-------|
| 0.8_0.1 | 0.89 | 0.09 | 0.18 |
| 0.8_0.3 | 0.87 | 0.24 | 0.32 |
| 1.2_0.3 | 1.23 | 0.21 | 0.07 |

1.5 g (± 0.001 g) gel and 150 grams (± 0.1 g) deionized water were added into a sealed polyethylene bottle, which was shaken twice a week. 8 h, 1 d, 7 d, and 28 d equilibrated gel were filtrated and washed as described above. The supernatant of the leachate of the gel was obtained for ion concentration measurements.

2.2 Methods

A PerkinElmer Optima 5300DV ICP-OES spectrometer was used to quantify the ionic concentrations of Na, Ca, Si and Al in the leachate. XRD analysis was performed on a Bruker D8 Advance diffractometer with $\text{CuK}\alpha$ radiation (1.54 Å). FTIR measurement was conducted by using a Nicolet™ iS50 FTIR Spectrometer, of which the wavenumber spans from 600 to 4000 cm^{-1} with a resolution of 4 cm^{-1} .

3. Results and discussion

3.1 ICP analysis

Fig. 1 shows the ionic concentration of Na and Ca in the leachate of the C-N-A-S-H gel over time. Compared with Ca, the equilibrium of Na is faster, which stabilizes within 1 d. This is consistent with the results of [6] that Na is more active than Ca and is weakly bounded in the interlayer of gels. In addition, the Na content in the leachate positively depends on the Na/Si ratio content in the unexposed C-N-A-S-H gel as shown in **Table 2**. Ca ions leach more slowly than Na, suggesting a stronger binding capacity of Ca in the silicate chain. The concentration of Ca increases with time for all three gels, with the group of 1.2_0.3 showing a higher value than the other two, which is consistent with the initial Ca content in the gels. Since Ca in CaO sheets is more stable than in the basal spacing, it is more likely that the Ca in the leachate comes from the charge-balanced Ca in the interlayer.

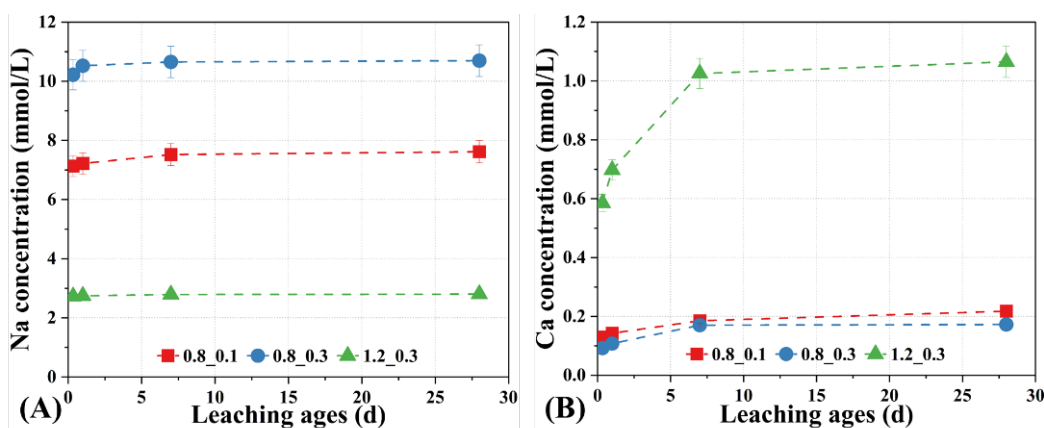


Fig. 1. Ion concentration of Na and Ca in the leachate of C-N-A-S-H gels during 28 days.

3.2 XRD

Fig. 2 shows the XRD results for gels with different leaching durations. It is observed that all three samples are dominated by the reflection of gels (PDF# 00-029-0331). The groups 0.8_0.1 and 0.8_0.3 show lower intensity than 1.2_0.3 around 29° and 32° , which indicates that the gel with a higher Ca/Si ratio has a higher crystallized degree. Unlike the 1.2_0.3 group, where traces of calcium carbonate were detected in the exposed samples, the other two groups did not form additional phases. This is due to the superficial carbonation of the gel during drying. In general, water immersion does not alter the phase assemblage of C-N-A-S-H gels, and gels with higher Ca/Si ratios appear to be easier to be carbonated.

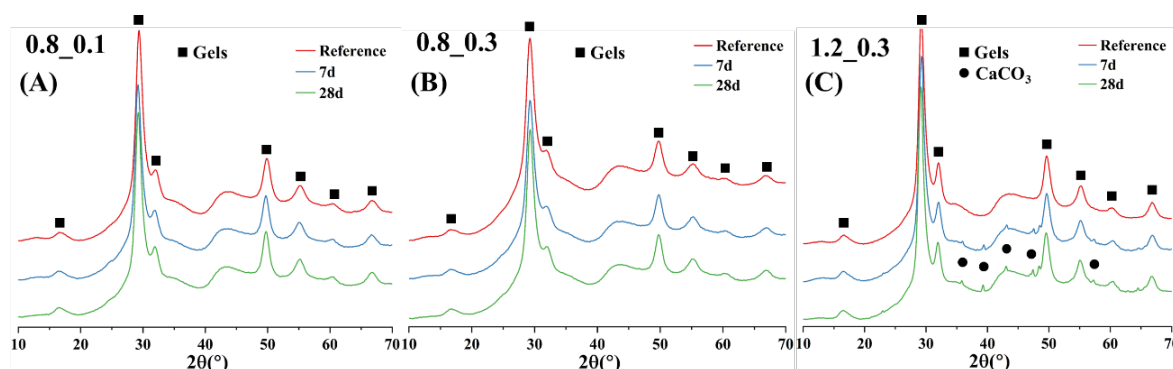


Fig. 2. XRD pattern of three gels with immersion time. “Reference” refers to the gel before leaching.

3.3 FTIR

Fig. 3 (A) shows the FTIR spectra of the three C-N-A-S-H gels without immersion. Overall, five main signals are detected from 600 to 1300 cm^{-1} . The band at $600\text{--}800$ is assigned to the bending vibration of Si-O-Si(Al) groups and the liberation of water molecules [7]. The band at 830 cm^{-1} is regarded as the symmetric stretching vibration of Si-O [7], indicating the presence of Q^1 site in the gel chain. The band at 883 cm^{-1} is attributed to the Si-O bending vibrations. It is observed that the gel with a higher Ca/Si ratio has higher Si-O strength, most likely because the structure of the 1.2_0.3 gel exhibits a lower silicate chain length. The dominant absorption peak is located at around 960 cm^{-1} , which is considered as the asymmetric stretching vibration of Si-O and the reflection of Q^2 [7]. The gel with a higher polymerization degree has a higher wavenumber of the Q^2 peak [8]. As shown in Fig. 3 (A), the 0.8_0.3 gel shows the highest value, which is because it has lower Ca and higher Al contents. Besides, the band at 1050 cm^{-1} is interpreted as the asymmetric stretching vibration of Si-O in Q^3 or Q^4 [8]. The results indicate that the gel with a higher Al/Si ratio has a higher crosslinked structure [9]. Fig. 3 (B) shows the change in the infrared spectra of the 0.8_0.3 gel with immersion time. In general, there is no significant difference among the five samples, but the wavenumber of Q^2 appears to increase after water immersion. This indicates that the gel after leaching exhibits a higher degree of polymerization.

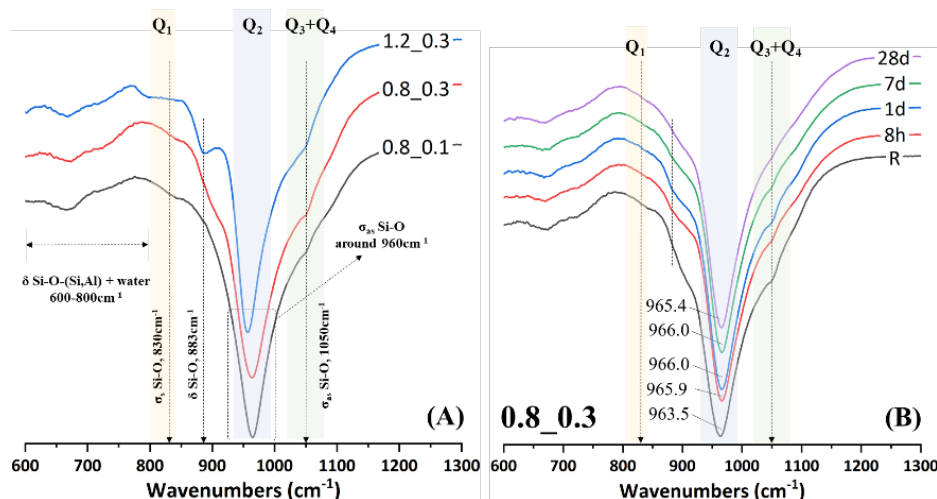


Fig. 3. FTIR spectra of three unexposed C-N-A-S-H gels (A) and the change of the 0.8_0.3 gel with immersion time.

4. Conclusion

In this study, we investigate the changes in properties of C-N-A-S-H gels as a function of the time of water immersion. The main conclusions can be drawn as follows.

- 1) Water immersion results in the leaching of Na and Ca in C-N-A-S-H gels, and the leaching of Na is quicker than that of Ca.
- 2) Water immersion does not significantly change the phase assemblage of gels, but the gel with a high Ca/Si ratio is vulnerable to carbonation.
- 3) The main structure of C-N-A-S-H gel is slightly changed with leaching time. Gels immersed in water show a higher polymerized structure than before.

Acknowledgments

Chen Liu would appreciate the funding supported by the China Scholarship Council (CSC) under grant No. 201906950102.

References

- [1] J.L. Provis, Geopolymers and other alkali activated materials: Why, how, and what?, *Mater. Struct. Constr.* 47 (2014) 11–25. <https://doi.org/10.1617/s11527-013-0211-5>.
- [2] J.L. Provis, Alkali-activated materials, *Cem. Concr. Res.* 114 (2018) 40–48. <https://doi.org/10.1016/j.cemconres.2017.02.009>.
- [3] G. Huang, Y. Ji, L. Zhang, J. Li, Z. Hou, The influence of curing methods on the strength of MSWI bottom ash-based alkali-activated mortars: The role of leaching of OH⁻ and free alkali, *Constr. Build. Mater.* 186 (2018) 978–985. <https://doi.org/10.1016/j.conbuildmat.2018.07.224>.
- [4] C. Liu, X. Liang, Y. Chen, Z. Li, G. Ye, Degradation of alkali-activated slag subjected to water immersion, (2023) (under review).
- [5] L. Gomez-Zamorano, M. Balonis, B. Erdemli, N. Neithalath, G. Sant, C-(N)-S-H and N-A-S-H gels: Compositions and solubility data at 25°C and 50°C, *J. Am. Ceram. Soc.* 100 (2017) 2700–2711. <https://doi.org/10.1111/jace.14715>.
- [6] F. Škvára, V. Šmilauer, P. Hlaváček, L. Kopecký, Z. Cílová, A weak alkali bond in (N, K)-A-S-H gels: Evidence from leaching and modeling, *Ceram. - Silikaty.* 56 (2012) 374–382.
- [7] F. Spectroscopy, Structure of Calcium Silicate Hydrate (C-S-H): Near-, Mid-, and Far-Infrared Spectroscopy, 48 (1999) 742–748.
- [8] A. Vidmer, G. Schlauser, A. Pasquarello, Infrared spectra of jennite and tobermorite from first-principles, *Cem. Concr. Res.* 60 (2014) 11–23. <https://doi.org/10.1016/j.cemconres.2014.03.004>.
- [9] R.J. Myers, S.A. Bernal, J.D. Gehman, J.S.J. Van Deventer, J.L. Provis, The role of al in cross-linking of alkali-Activated slag cements, *J. Am. Ceram. Soc.* 98 (2015) 996–1004. <https://doi.org/10.1111/jace.13360>.

Experimental investigation of expansion and damage due to alkali-silica reaction at low temperature

T. Kawakami^{1*}, Y. Sagawa², Y. Kawabata³, and K. Yamada⁴

¹ Kyushu University, Fukuoka, Japan
Email: t.kawakami@doc.kyushu-u.ac.jp

² Kyushu University, Fukuoka, Japan
Email: sagawa@doc.kyushu-u.ac.jp

³ Port and Airport Research Institute, Kanagawa, Japan
Email: kawabata-y@p.mpat.go.jp

⁴ National Institute for Environmental Studies, Fukushima, Japan
Email: yamada.kazuo@nies.go.jp

ABSTRACT

The rate of deterioration due to the alkali-silica reaction (ASR) is strongly influenced by temperature. Many studies to evaluate ASR reactivity or to elucidate its mechanisms are often conducted in high-temperature environments to rapidly obtain results; however, there is a gap with the actual environment acting on concrete structures. Therefore, it is important to ensure a consistency in deterioration characteristics in cold climates to quantitatively detect long-term degradation risks and apply reliable ASR control measures. In this study, an alkali-wrapped concrete prism test was performed at 10°C on concrete specimens with higher alkali contents and reactive aggregates. The expansion was measured over time, and the effect of temperature on the expansion behavior was discussed with reference to experimental data at different temperatures. Furthermore, the macroscopic damage was visualized using a fluorescence epoxy resin to characterize the cracks. In high-temperature environments, a higher alkali content tends to result in greater expansion. However, at low-temperatures environments, the lower alkali content showed greater expansion in the long term. It was pointed out that an experiment under excessive acceleration conditions does not capture such phenomena that can occur in actual environments. It is assumed that this is partly because of differences in the fluidity of the ASR product and the damage form process.

KEYWORDS: *alkali-silica reaction, concrete prism test, crack observation, temperature effect.*

1. Introduction

In alkali-silica reaction (ASR), reactive minerals which are present in the aggregates dissolve to form a swelling ASR product inside concrete at high pH, causing expansion cracks in the concrete. The rate of this reaction strongly depends on the temperature. It is generally recognized that higher-temperature conditions lead to earlier deterioration. Many factors influence the temperature dependence of ASR expansion: alkali leaching, pore solution composition, stiffness of ASR product, etc. In the EU PARTNER project (Lindgård et al. (2010)), which exposed the similar concrete blocks to different climatic conditions, there is no clear trend between temperature and the occurrence of ASR expansion.

Kawabata et al. (2019) stated that in early-stage expansion, the ASR product is confined so that expansion is controlled by the reaction kinetics. In the late expansion phase, the expansion rate is smaller because the damage reduces the confinement of the ASR product and it leaks out of the expansion site through cracks and voids. The observed decrease in expansion rate is more significant at higher temperatures. This change in the effect of expansion pressure development on the ASR product has been described in a numerical damage model (Kawabata et al. (2022)). These indicate that although the reaction is slow at low temperatures, the ASR product efficiently accumulates expansion pressure, which could be one of the reasons for long-term expansion in actual structures exposed to cold climates.

However, concrete prism tests (CPT) are conducted as aggregate tests or job mix tests which are often performed at high temperatures to obtain early test results. For advanced evaluation of the relationship between ASR in the natural environment and that in laboratory, It is essential to examine the effects of the mechanisms occurring at low temperatures.

In previous studies, few laboratory experiments have been conducted in low-temperature environments. In order to predict expansion at temperatures that are actually observed in natural environments, it is important to understand the characteristics of deterioration such as expansion and cracking patterns under low temperature conditions. In this study, ASR expansion tests were conducted at 10°C and compared with the expansion behavior in the conventional temperature range; 20, 40, and 60°C. In addition, a 10-40°C temperature cycle was also performed to understand the effect of temperature variation. For the tests, AW-CPT based on RILEM AAR-13 was conducted to suppress alkali leaching (Yamada et al. (2021)).

2. Experimental program

A reactive aggregate, andesite, which has a high ASR reactivity, was used as the coarse aggregate. This aggregate is identical to the aggregate used in the study by Yamada et al. (2016) and was found to have a pessimum mixing ratio of 30 vol% by the JIS mortar bar method. It contains a high amount of cristobalite as a reactive mineral and some very reactive opal. Ordinary Portland cement was used. As a non-ASR reactive aggregate, crushed limestone sand was used as the fine aggregate and crushed limestone was used as the coarse aggregate. The alkali content was increased by mixing a granular reagent, NaOH, dissolved in the mixing water. The concrete mixture was based on the work of Yamada et al. (2016) with a water-to-cement ratio of 50%, fine aggregate ratio of 45%, and water content of 160 kg/m³.

Table 1 lists the specimen types and experimental factors such as reactive aggregate ratio, alkali content, and temperature. The base material was 30% reactive aggregate (30 vol% of coarse aggregate as reactive aggregate and the remaining 70 vol% of limestone) with a total alkali content of 5.5 kg/m³ and constant storage at 10°C. As a comparison, another three types of specimens were prepared; one with 100% reactive coarse aggregate, one with a total alkali content of 3.0 kg/m³, and with a storage temperature cycle (TC) of 10 °C and 40 °C, respectively.

The dimensions of the specimens were 75 mm × 75 mm × 250 mm, and plugs were embedded at both end surfaces to measure the length changes in the longitudinal direction with a dial gauge. Four specimens per level were prepared: three samples were used for the length tests and last one was used for the cross-sectional observation. The prism specimens were prepared in a 20°C room and demolded after one day to measure the initial values. The specimens were then alkali-wrapped and stored in a temperature controlled container at 10°C. The concentrations of NaOH solution used for wrapping were 1.33 mol/L and 0.72 mol/L for the specimen with alkali content of 5.5 kg/m³ and 3.0 kg/m³, respectively. In subsequent measurements, the specimens kept in a cold container were taken out and measured within three minutes per specimen to ensure that the temperature did not change. The temperature of the measurement chamber was uniformly set at 20°C. When calculating the expansion, the coefficient of thermal expansion of concrete was assumed to be 10×10^{-6} .

Observations of cracks in the cross-section were made after six months from the start of the test. TC was also performed when cracks were observed on the surface of the specimen. A 20 mm thick slice of 75 mm by 75 mm cross-section was cut out of the specimen, vacuum impregnated with fluorescent resin, and the polished cross-section was observed under 365 nm UV light.

3. Results and discussion

Figure 1 shows the expansion behavior of concrete. The X mark in the figure indicates the point at which a 0.1 mm crack is observed on the specimen's surface. The blue and red plotlines represent periods corresponding to 10°C and 40°C, respectively. At 30-5.5TC, the specimen expanded at 40°C and

Table. 1 Experimental factors and concrete specimen types

| Name | Concrete mixture | | Condition |
|----------------|--------------------|-------------------------------------|------------------|
| | Reactive aggregate | Alkali content (kg/m ³) | Temperature (°C) |
| 100-5.5-10 | 100% | 5.5 | 10 |
| 30-5.5-10 | 30% | | |
| 30-3.0-10 | | 3.0 | |
| 30-5.5-TC10/40 | | 5.5 | 10 ↔ 40 |

remained constant at 10°C before cracking on the surface after 8 weeks. After crack initiation, however, the specimens swelled at 10°C, and at 40°C, the trends of stable state and expansion were reversed from the initial trend. The expansion of 100-5.5 was greater than that of 30-5.5. This seems to be because of the higher percentage of reactive aggregates under the higher total-alkali content condition, generated more ASR product. A slow progression of ASR during 10°C curing, as is the case in this study, would result in a slow decrease in the alkali consumed by ASR. It is considered that the ASR continues slowly for a long period of time, even with a high reactive aggregate content, resulting in a different pessimum ratio from that under 40°C. The lower alkali content of 30-3.0 exceeded that of 30-5.5 at approximately 40 weeks, reaching 0.1% expansion in 60 weeks. Yamada et al. (2016) found that, AW-CPT using this aggregate had little effect on the degree of expansion in the alkali content range of 3.0-5.5 kg/m³ in the long-term age of the material; similar results were obtained in this study.

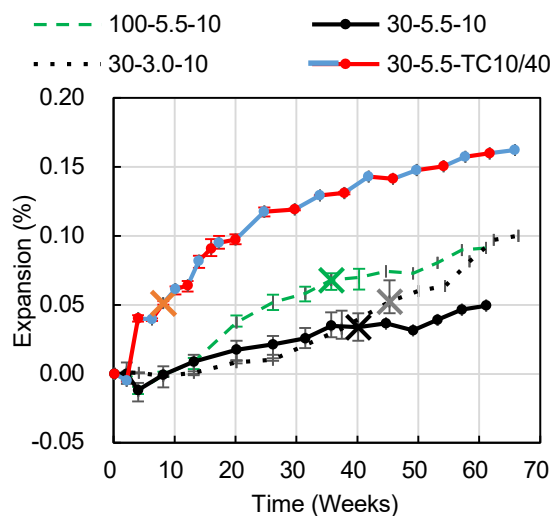


Fig. 1 Expansion versus time for AW-CPT

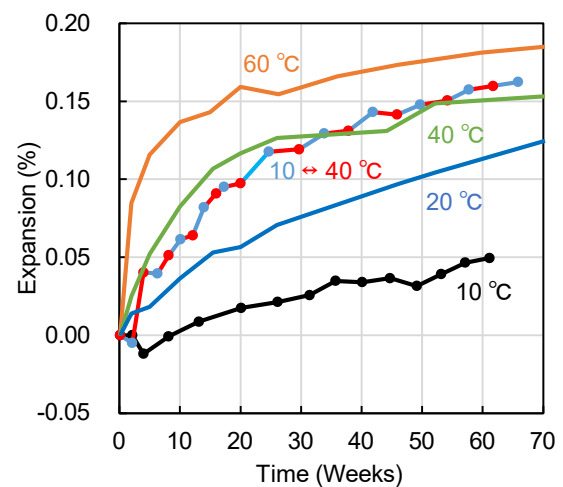


Fig. 2 Comparison of the same concrete at different temperatures (Yamada et al., 2015)

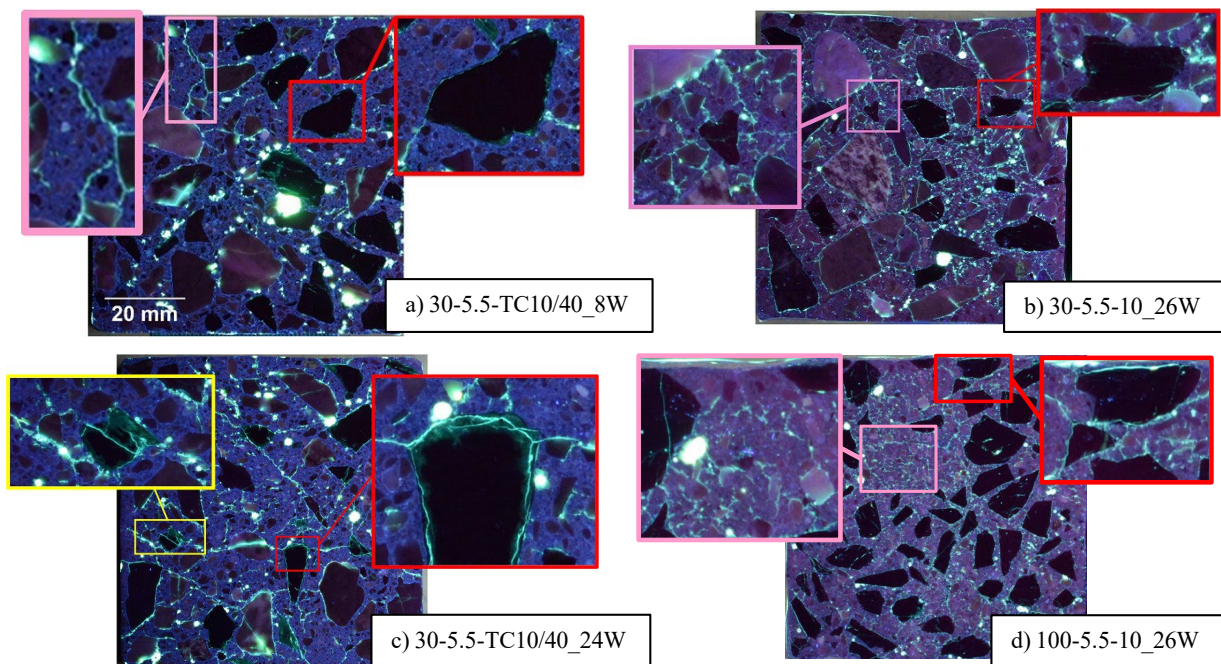


Fig. 3 Internal cracks visualized by fluorescent resin impregnation under UV.

The pink frames display areas of mortar with cracks.

The red frames show cracks propagating into the mortar along the aggregate.

The yellow frame shows cracks that penetrate through the aggregate into the mortar.

In addition to <30-5.5> and <30-5.5TC>, the expansion behavior of the same concrete mixture at different temperatures, as reported by Yamada et al. (2016), is indicated with solid lines in Figure 2. The slope of the expansion curve is strongly correlated with temperature, indicating that the temperature dependence of the initial expansion is consistent, even at temperatures as low as 10°C. Focusing on TC, the curve is almost similar to that of constant storage at 40°C, despite being in the 40°C environment for half the time. Since more ASR product is produced at higher temperatures, this indicates that expansion is not simply directly related to the amount of ASR product. Considering that the generated ASR product loses its mobility at lower temperatures and occludes cracks, leading to a higher expansion pressure, is consistent with the discussion of the difference in late-stage expansion rates expressed by Kawabata et al. (2019). The effect of this intermittent reconfiguration of the expansion site is considered to be more significant under conditions in which the ASR kinetics are slower. Without accounting for the above mechanisms, excessively accelerated conditions could lead to underestimation in the degree of expansion.

Figure 3 shows the internal cracks visualized by the fluorescent resin impregnation. The 30-5.5TC shown in a) and c) tend to have a larger crack width in the mortar section and fewer cracks than that continuously stored at 10°C shown in b) and d). Further, following Sanchez et al. (2015), crack classification of b) and d) at 10°C storage shows only “onion skin” cracks along the aggregate surface layer within the reactive aggregate. In contrast, two types of cracks were observed in the TC: onion skin cracks, as shown using the red frame in the image, and “sharp cracks”, which are cracks that cross the aggregate, as shown using the yellow frame. This result agrees with that of Kawabata et al. (2019).

4. Conclusions

This study experimentally examined expansion behavior and internal cracking caused by ASR at a low temperature of 10°C. The following conclusions were drawn:

- 1) The temperature-cycled CPT showed that after cracking, the specimen swelled more during storage at low temperatures. This indicates that the generated ASR product lost flexibility at low temperatures and occluded the cracks, thus promoting the development of expansive pressure.
- 2) At low temperatures, cracks developed inside the aggregates as the “onion skin crack” and radiated into the mortar. After the high temperature cycle, cracks penetrated the aggregate into the mortar.
- 3) This study suggests that excessive accelerated testing is inappropriate for considering long-term expansion due to ASR in cold climates, as it could lead to underestimation of the expansion ability.

Acknowledgments

Part of this research was supported by JSPS KAKENHI Grant Number JP22J12727. The authors thank Mr. S. Kitagawa of Kyushu University for his cooperation in the experiment.

References

- Kawabata, Y., Dunant, C., Yamada, K. and Scrivener, K., (2019) “Impact of temperature on expansive behavior of concrete with a highly reactive andesite due to the alkali–silica reaction”, *Cement and Concrete Research*, 125, 105888
- Kawabata, Y., Dunant, C., Nakamura, S., Yamada, K. and Kawakami, T. (2022) “Effects of temperature on expansion of concrete due to the alkali-silica reaction: A simplified numerical approach”, *Materiales de Construcción*, 72, e282
- Lindgård, J., Nixon, P.J., Borchers, I., Schouenborg, B., Wigum, B.J., Haugen, M. and Åkesson, U. (2010) “The EU “PARTNER” project—European standard tests to prevent alkali reaction in aggregates: final results and recommendations”, *Cement and Concrete Research*, 40: 611-635
- Sanchez, L.F.M., Fournier, B. and Duchesne, J. (2015) “Reliable quantification of AAR damage through assessment of the Damage Rating Index (DRI)”, *Cement and Concrete Research*, 65: 74-92
- Yamada, K., Tanaka, A., Sagawa, Y., Ogawa, S. and Ochiai, T. (2016) “Exact effects of temperature increase and alkali boosting in concrete prism tests with alkali wrapping”, *Proceedings of 15th International Conference on Alkali Aggregate reaction in concrete*.
- Yamada, K., Kawabata, Y., de Rooij, M.R., Brueckner, R. and Ideker, J.H. (2021) “Recommendation of RILEM TC 258-AAA: RILEM AAR-13: application of alkali-wrapping for concrete prism testing to assess the expansion potential of alkali-silica reaction”, *RILEM Materials and Structures*, 54, 201

Physicochemical stability of calcium aluminate cement and hemihydrate-based material exposed to deep sea

T. Akitou^{1*}, K. Takahashi²

¹ Mitsubishi UBE Cement Corporation, Ube, Japan
Email: Tetsu.akito@mu-cc.com

² Mitsubishi UBE Cement Corporation, Ube, Japan
Email: keisuke.takahashi@mu-cc.com

ABSTRACT

In recent years, ocean utilization such as construction of offshore wind power generation and tidal power generation and development of seabed mineral resource has attracted much attention. Cementitious materials can be used as one of the base materials for these applications. Previously the authors reported that deterioration behaviour of a Portland cement mortar under deep sea differed from shallow sea due to the low temperature and high hydraulic pressure. The focus of this study is to investigate the physicochemical stability of a hardened binary binder paste consisting of calcium aluminate cement and hemihydrate exposed to a depth of 1,882 meters. The specimen consisting mainly of ettringite were recovered after 295 days of exposure. The recovered specimen did not show any microstructural fracture as observed in the Portland system. However, compositional analysis of the cross section by EPMA showed that ettringite decomposed to form Mg-containing hydrates in the surface layer of the specimen. Interestingly, chlorine was only detected penetrating up to 9 mm from the surface layer. This binary binder system could be a new option for the use of cementitious materials in deep sea applications.

KEYWORDS: *Deep sea, calcium aluminate cement, hemihydrate, durability, sea water attack*

1. Introduction

In recent years, much attention has focused on the utilization of the ocean for the construction of floating wind and tidal power generation facilities and the development of offshore mineral resources. The authors are investigating the use of cementitious materials as base materials for the construction of these structures. The authors reported that long-term exposure of Portland cement (PC) materials to deep-sea floor, which is a special environment of low temperature and high pressure, resulted in significant deterioration compared to those exposed to shallow sea (Kobayashi et al. 2021). Furthermore, a ternary-binder system consisting of calcium aluminate cement (CAC), PC, and anhydrite prevented calcium leaching, but the penetration of chloride ions caused the formation of Friedel's salt from monosulfate, which also produced a lot of ettringite, resulting in extremely large expansion of the specimen (Kobayashi et al. 2022). In this paper, a binary cement paste specimen consisting of calcium aluminate cement and hemihydrate (HH), which was designed to mitigate chloride ion penetration and also decrease monosulfate formation owing to a sulfur-rich condition in the specimen, was exposed to a deep seafloor at a depth of 1,882 m. Specimens recovered after 295 days were analyzed to evaluate their physicochemical properties.

2. Experimental

2.1 Materials

A high alumina CAC consisting of $\text{CaO-Al}_2\text{O}_3$ and $2\text{CaO-Al}_2\text{O}_3$ was used. The paste contained CAC, HH (30 wt% of CAC), water, acrylic acid-based dispersant, gum-based viscosity modifying agent (VMA), and setting regulators (sodium tartrate and lithium sulfate). The main hydrates were ettringite, monosulfate and aluminium hydroxide (gibbsite). The water to cement ratio was 0.6. The size of the specimens was 40 mm × 40 mm × 160 mm. The specimens were cured for 91 d at 20 °C under sealed conditions before exposure.

2.2 Testing field and related conditions

Exposure tests on the deep seafloor were conducted at a depth of 1,882 m at Nankai Trough Kumano-nada, Japan for 295 days from January to November 2021. Three paste specimens were set on the seafloor using a remote operated vehicle KM-ROV. The temperature and salinity of seawater at the exposure site were 2.2 °C and 34.6 PSU, respectively. After 295 days of exposure, the specimens were salvaged by KM-ROV. The descension and ascension speed of the vehicle was approximately 50 m/min and 30 m/min, respectively. Three paste specimens were immersed in a laboratory-scale seawater tank (216 L) at ambient pressure to investigate the effect of hydraulic pressure on the property changes of the hardened paste. The seawater temperature in the tank was maintained to 2 °C using a heat exchanger. Seawater in the tank was supplied from a shallow sea area near the laboratory and replaced approximately every 24 h.

2.3 Analytical methods for specimens

The length and weight of the specimens were measured according to JIS A 1129. Changes in the length and weight of the specimens immersed in the laboratory were measured at 44, 98, 160, and 295 days. Expansion was considered a positive change in length and the gauge length was 100 mm. The specimens were cut near the center and its cross-section was mapped for elemental distribution by electron probe micro analyzer (EPMA). The specimens were cut from the surface to the center into three areas (0-5mm, 5-10mm and 10-20mm), which were referred to as areas A, B and C. The specimens from the three areas were subjected to mineral identification by X-ray diffraction (XRD). All specimens were dried and stopped hydration with isopropanol prior to measurement.

3. Results

3.1 Visible specimen and dimensional changes

The specimen after retrieval is shown in Fig. 1. Although the specimens recovered from deep seafloor (referred to as “deep-sea specimens”) showed fine cracks on the surface, there was no significant mudding as observed in the Portland cement system. The specimens immersed in a seawater tank inside the laboratory (referred to as “laboratory specimens”) had no visible fine cracks.

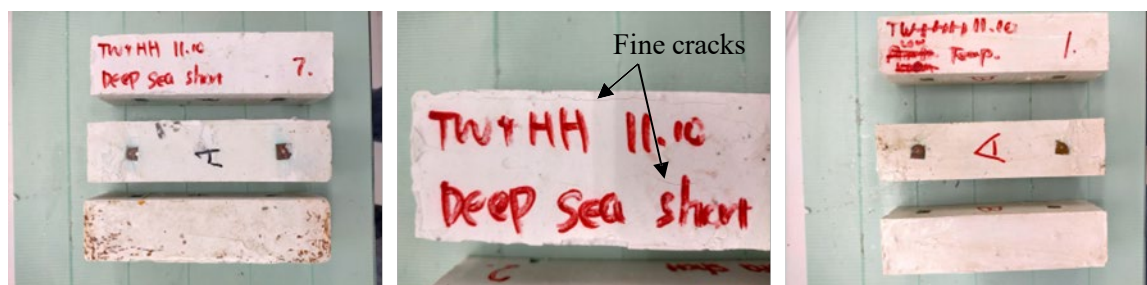


Fig. 1 View of the recovered specimens (left: deep-sea specimens, right: laboratory specimens). The specimen recovered from the deep sea had fine cracks on the surface (center).

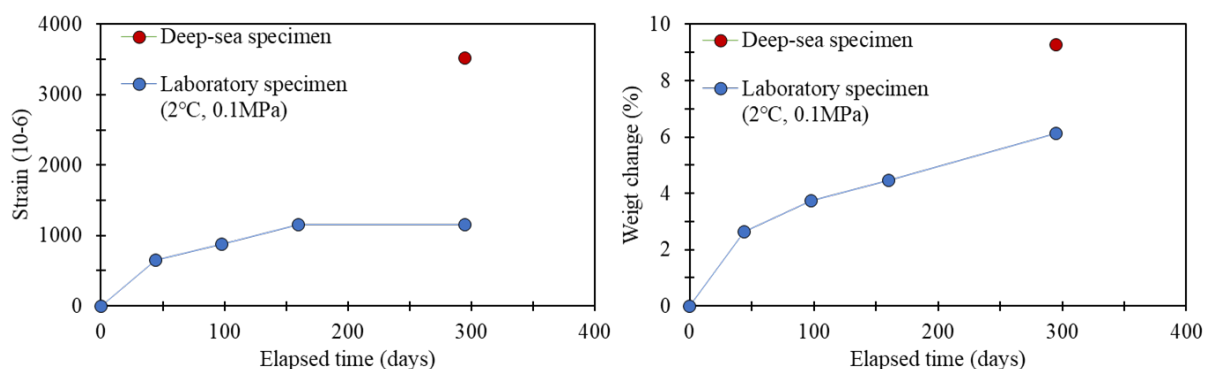


Fig. 2 The changes in the strain (*left*) and weight (*right*) of the specimens

Figure 2 shows the changes in the strain and weight of the specimens as a function of the exposure/immersion time. The deep-sea specimens showed a larger strain and higher weight gain than the laboratory specimens. The strain and weight gains of the laboratory specimen first increased quickly and then continued to increase slowly. These results indicate a good correlation between seawater uptake into the specimen and its expansion.

3.2 Chemical characterization

Figure 3 shows the EPMA results of the cross-section analysis for each element. Deep-sea specimens and laboratory specimens showed similar trends. Near the surface, the concentrations of calcium and sulfur decreased, while the concentrations of chlorine, sodium and magnesium increased. It is observed that the changes in elemental concentrations were more pronounced in the deep-sea specimens than in the laboratory specimens. Chlorine penetrated 9 mm from the surface in the deep-sea specimens and 5 mm from the surface in the laboratory specimens. Aluminum concentrations were constant regardless of depth. Figure 4 shows the XRD peak diagrams of the specimens. The deep-sea specimens showed a clear peak of Friedel's salt in area A (0-5mm), while the laboratory specimens showed a somewhat indistinct peak. This is consistent with the results of the EPMA elemental diagrams, and some of the monosulfate peaks around 10° may contain Kuzel's salt. No significant Friedel's salt peaks were identified in areas B (5-10 mm) and C (10-20 mm). At the superficial layers of both specimens, the calcium-containing hydrates that were originally present dissolved and decomposed, and products containing magnesium, sodium, aluminum, sulfur, and chlorine could be precipitated. Since gibbsite forming the binder phase was stable against the pH decrease (Gayer et al. 1958), the dissolution or decomposition of hydrates near the surface layer would not have affected the aluminum concentration. As a result of the gibbsite not being decomposed, there may have been no significant damage to the specimen's appearance.

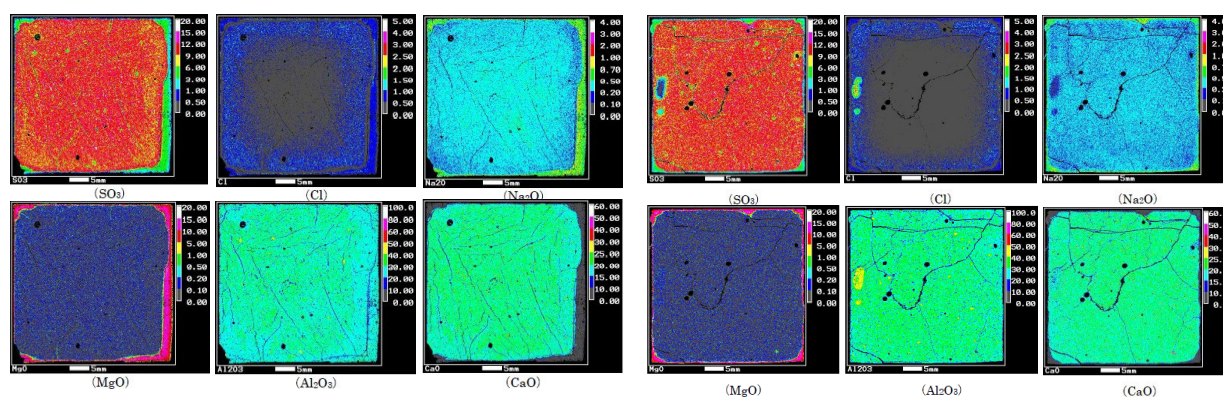


Fig. 3 The EPMA results of the cross-section analysis for each element (unit: mm). *left*: deep-sea specimen, *right*: laboratory specimen. SO₃, Cl, Na₂O, MgO, Al₂O₃ and CaO were analyzed for each specimen. The color bar presents the concentration range (unit: wt.%). Calcium was dissolved at 0.5-2.5 mm from the surface in the deep-sea specimens and at less than 1 mm in the corner of the laboratory specimens.

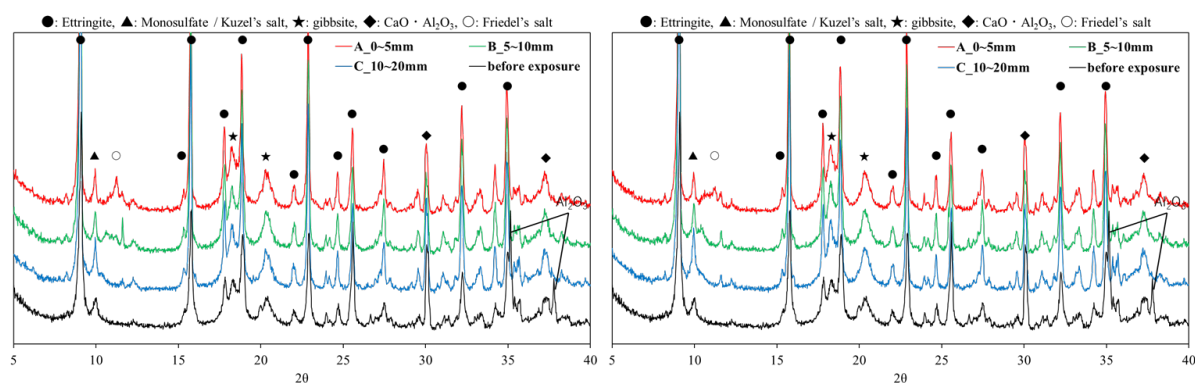


Fig. 4 The XRD patterns of the specimens. *left*: deep-sea specimen, *right*: laboratory specimen.

Further investigation of the relationship between changes in hydrate in the specimens and hardened physical properties is needed, taking into account the pore structure and other factors. At inner of the specimen, seawater penetration could decrease pH, and the unstable monosulfate and ettringite reacted with chloride ions in the seawater to form Friedel's salt and Kuzel's salt. Since liquid water penetration is enhanced under high hydraulic pressure conditions (Kawabata et al. 2022 and Takahashi et al. 2021), the deep-sea specimens were more strongly affected by seawater than the laboratory specimens. This may have resulted in the differences in element concentrations between the specimens shown in Figure 3. However, chlorine was fixed up to 9 mm from the surface layer, even in the deep-sea specimens, and the amount of chloride fixation was minimal. This suggests that the binary binder-based materials used in this study are more resistant to chloride ion penetration than the Portland and the ternary binder system.

3. Conclusions

Analysis of a binary binder paste specimens consisting of CAC and HH exposed to a deep seafloor at a depth of 1,882 m for 295 days showed that seawater penetration caused hydrate changes in the surface layer of the specimens. Chlorine was hardly fixed at depths deeper than 9 mm from the surface layer of the deep-sea specimens, and the appearance of the specimens showed no noticeable damage, although there were some fine surface cracks. This suggests that the binary-binder based material consisting of CAC and HH used in this study may be one candidate cementitious material for use on the deep seafloor. The effects of hydrate changes on the physicochemical properties of the hardened material should be studied continuously in the future.

Acknowledgements

We would like to thank Dr. Toshinori Kimura, Dr. Shuhei Nishida, Takashi Yokobiki and Dr. Eiichiro Araki from JAMSTEC for their assistance in conducting the deep-sea field tests and Dr. Yuichiro Kawabata from Port and Airport Research Institution for his assistance in conducting the laboratory tests.

References

- Kobayashi, M., Takahashi, K., and Kawabata, Y. (2021) "Physicochemical properties of the Portland cement-based mortar exposed to deep seafloor conditions at a depth of 1680 m", *Cement and Concrete Research*, 142: 106335
- Kobayashi, M., Takahashi, K., Kawabata, Y., and Bier, T.A. (2022) "Physicochemical properties of Portland cement/calcium aluminate cement/calcium sulfate ternary binder exposed to long-term deep-sea conditions", *Materials and Structures*, 55: 182
- Gayer, K.H., Thompson, L.C., Zajicek, O.T., (1958) "The solubility of aluminum hydroxide in acidic and basic media at 25 °C", *Canadian Journal of Chemistry*, 36, 9
- Kawabata, Y., Takano, D., Takahashi, K. and Iwanami, M. (2022) "In situ observation for the influence of hydraulic pressure on internal damage of cement-based materials", *Materials & Design*, 216: 110556
- Takahashi, K., Kawabata, Y., Kobayashi, M., Gotoh, S., Nomura, S., Kasaya, T., and Iwanami, M. (2021) "Action of hydraulic pressure on Portland cement mortars – current understanding and related progress of the first-ever in-situ deep sea tests at a 3515 m depth", *Journal of Advanced Concrete Technology*, 19: 226-239

Resistance against chloride and carbonation of binary and ternary binder with GGBS or/and limestone

M. Bertin^{1,2*}, C. Bacquie^{2,3}, Y. Jainin^{2,3}, E. Myrtja³, R. Alfani³, L. Frouin³ and M. Cyr^{1,2}

¹ LMDC-INSa/UPS-Université de Toulouse, Toulouse, France

² ORISON, LMDC-ECOCEM Common Laboratory, Toulouse, France

³ ECOCEM Materials, Paris, France

Email: matthieu.bertin@insa-toulouse.fr

Email: cbacquie@ecocem.ie

Email: yjainin@ecocem.ie

Email: emyrtja@ecocem.ie

Email: ralfani@ecocem.ie

Email: lau.frouin@gmail.com

Email: martin.cyr@insa-toulouse.fr

ABSTRACT

To reduce the environmental impact of cement production and to save energy, one solution is to replace clinker by supplementary cementitious materials (SCM) to design binary or ternary binders. However, these low clinker binders can have various phase assemblages and pore structures which may have an impact on the durability of concretes. In particular, as corrosion is the main cause of damage in reinforced concretes, whether due to chloride ingress or carbonation of concrete, specific attention should be given to this aspect of durability.

Two binary binders, CEM III/A and CEM I/ Limestone filler (50/50), and one ternary binder, CEM I / Limestone filler / GGBS (20/50/30), are studied. The microstructure is evaluated by means of TGA and XRD on sound, carbonated and chloride-contaminated cement pastes. Moreover, for the resistance against chloride, chloride binding isotherm are performed on cement paste and chloride diffusivity on concrete. Then, carbonation rates are evaluated in accelerated conditions (T=20°C, RH=57% & [CO₂]=3%) on concrete specimens. Despite the lower CO₂ binding capacity of ternary binder, the carbonation kinetics for CEM III/A and ternary binder are similar when decreasing the W/B ratio of the ternary concrete.

KEYWORDS: Carbonation, chloride, limestone, GGBS, microstructure

1. Introduction

In the current environmental context, it is important to reduce the environmental impact of the construction industry. One way to do this is to reduce the impact of cement by replacement of clinker with supplementary cementitious materials (SCM). However, these low clinker binders can have various phase assemblages and pore structures, which may impact the transport properties and binding capacity of aggressive species like CO₂ or Cl⁻. These changes have an effect on the durability of concretes. It is therefore important to study the different aspects of durability to ensure that these binders, when used in concrete, will be sustainable. As corrosion is the main cause of damage in reinforced concretes, the chloride ingress and the carbonation is studied. In this paper, the effect of Cl⁻ and CO₂ on the phase assemblage is studied by means of XRD and TGA on cement pastes. Moreover, the chloride ingress and carbonation kinetics is assessed on concrete for a ternary binder compared to reference concretes.

2. Materials & methods

Three paste systems with a W/B ratio of 0.335 and three concretes were investigated (Table 1). P-S60 and C-S60 were cast with a CEM III/A (60% GGBS) cement and C-S68 were cast with a CEM III/B (68% GGBS). Aggregates are crushed limestone.

Table 1: Mix proportions

| | Binder (kg/m ³) | CEM I 52.5 N (%) | GGBS (%) | Limestone Filler (%) | Aggregate 10/20 (kg/m ³) | Aggregate 4/10 (kg/m ³) | Aggregate 0/4 (kg/m ³) | Water (kg/m ³) | W _{eff} /B |
|----------|--------------------------------|---------------------|-------------|-------------------------|--|---|--|-------------------------------|---------------------|
| P-S30L50 | 1448 | 20 | 30 | 50 | - | - | - | 485 | 0.335 |
| P-L50 | 1448 | 50 | - | 50 | - | - | - | 485 | 0.335 |
| P-S60 | 1448 | 40 | 60 | - | - | - | - | 485 | 0.335 |
| C-S30L50 | 350 | 20 | 30 | 50 | 683 | 423 | 921 | 117 | 0.334 |
| C-S60 | 300 | 40 | 60 | - | 683 | 423 | 921 | 150 | 0.500 |
| C-S68 | 350 | 32 | 68 | - | 683 | 423 | 921 | 157 | 0.450 |

The chemical composition of binders and SCMs were determined by ICP (Table 2).

Table 2: Chemical composition of binders

| | LOI | K ₂ O | Na ₂ O | SiO ₂ | Al ₂ O ₃ | CaO | Fe ₂ O ₃ | MgO | TiO ₂ | SO ₃ | Specific gravity |
|------------|-------|------------------|-------------------|------------------|--------------------------------|-------|--------------------------------|------|------------------|-----------------|---------------------|
| CEM I | 2.39 | 0.54 | 0.20 | 19.60 | 5.16 | 65.50 | 2.94 | 2.43 | 0.39 | 3.37 | 3.14 |
| S30L50 (%) | 21.56 | 0.33 | 0.15 | 15.16 | 4.01 | 53.09 | 0.76 | 2.65 | 0.23 | 1.86 | 2.82 |
| L50 (%) | 22.07 | 0.3 | 0.12 | 9.79 | 2.55 | 60.72 | 1.46 | 1.33 | 0.19 | 2.69 | 2.87 |
| S60 (%) | 0.94 | 0.48 | 0.23 | 28.8 | 8.47 | 52.03 | 1.39 | 4.5 | 0.48 | 3.42 | 3.02 |

Cement paste samples were cast in PS moulds (40 mm x 40 mm x 160 mm) and concretes were cast in cylinder cardboard moulds (d=110 mm x h=220 mm). Specimens were demoulded after 24h. Then, they were kept under water during 90 days. After the curing time, the cement pastes were dried at 40°C during 3 days. Subsequently, specimens were crushed and sieved. The particles with a size smaller than 2.50 mm were kept, ensuring that more than 50% by mass were smaller than 1.25 mm. This particle size distribution was selected to optimize the measurement time. Then cement pastes were split in two batches: one for the carbonation study and the other for the chloride binding isotherm measurement. For the carbonation study, after crushing, cement pastes were exposed to natural carbonation in sheltered conditions. Then carbonation was monitored by thermogravimetric analyses (TGA). Chloride binding isotherms (CBIs) were obtained by the equilibrium method (Arliguie et Hornain 2007). Crushed specimens of cement pastes were put in contact with NaCl solution for two months. Moreover, the solid was recovered in order to perform TGA and XRD after a hydration stop by solvent exchange with isopropanol. Crystalline phases were characterized by XRD with a Bruker D8 ADVANCE. TGA was carried out with a Mettler Toledo TGA2 by heating from 30°C to 1050°C with 10°C/min step. After the curing time of concrete specimens, resistance against carbonation in accelerated condition was studied according to (XP P18-458 2022). However, the following deviation was made: carbonation performed at T=20°C, HR=57% and [CO₂]=3%. Migration tests were studied according to (XP P18-462 2022) and the diffusion test in natural condition were performed according to (NF EN 12390-11 2015).

3. Results and discussion

CBIs obtained by equilibrium method on cement pastes are presented in Figure 1a. The results show that P-S60 bound more chloride than P-S30L50, which bound more chloride than P-L50. As shown in Figure 1b, the chemically bound chloride is made by the yield of Friedel's salt for the three binders. Moreover, for the P-L50 and P-S30L50, the peaks for hemicarboaluminate (Hc) and monocarboaluminate (Mc) disappeared after the contact with the NaCl solution. For binders with limestone filler, it seems that the Mc and Hc are transformed in Friedel's salt due through anion exchange. The higher binding capacity of P-S60 can be explained by a higher alumina content of binder (%Al₂O₃:8.47%) and a higher content of C-S-H which is responsible of physical adsorption of chloride. The higher binding capacity of P-S30L50 than P-L50 can be explained by a higher alumina content (P-S30L50: 4.01% and P-L50: 2.55%). From the TGA data, it seems that the Friedel's salt content is higher for the P-S30L50 than P-L50. Figure 1c shows total and bound chloride profiles for concretes C-S30L50 and C-S68. The bound chloride profiles are similar for both concretes. The total chloride profile of C-S68 reached a higher chloride content. This can be due to the higher porosity ($\Phi=14.6\pm0.3\%$) than C-S30L50 ($\Phi=12.3\pm0.5\%$). From the chloride profiles, the apparent and effective chloride diffusion coefficient are determined (Figure 1d). Although the apparent and

effective chloride diffusion coefficients are higher for C-S30L50, the values are comparable. According to the French technical report on performance-based approach of durability of concrete (FD P18-480 2022), both concretes have an exposure class of XS3t. Therefore, although the P-S30L50 has a lower binding capacity, it is possible to make concrete with the most aggressive exposure class if using a low W/C ratio.

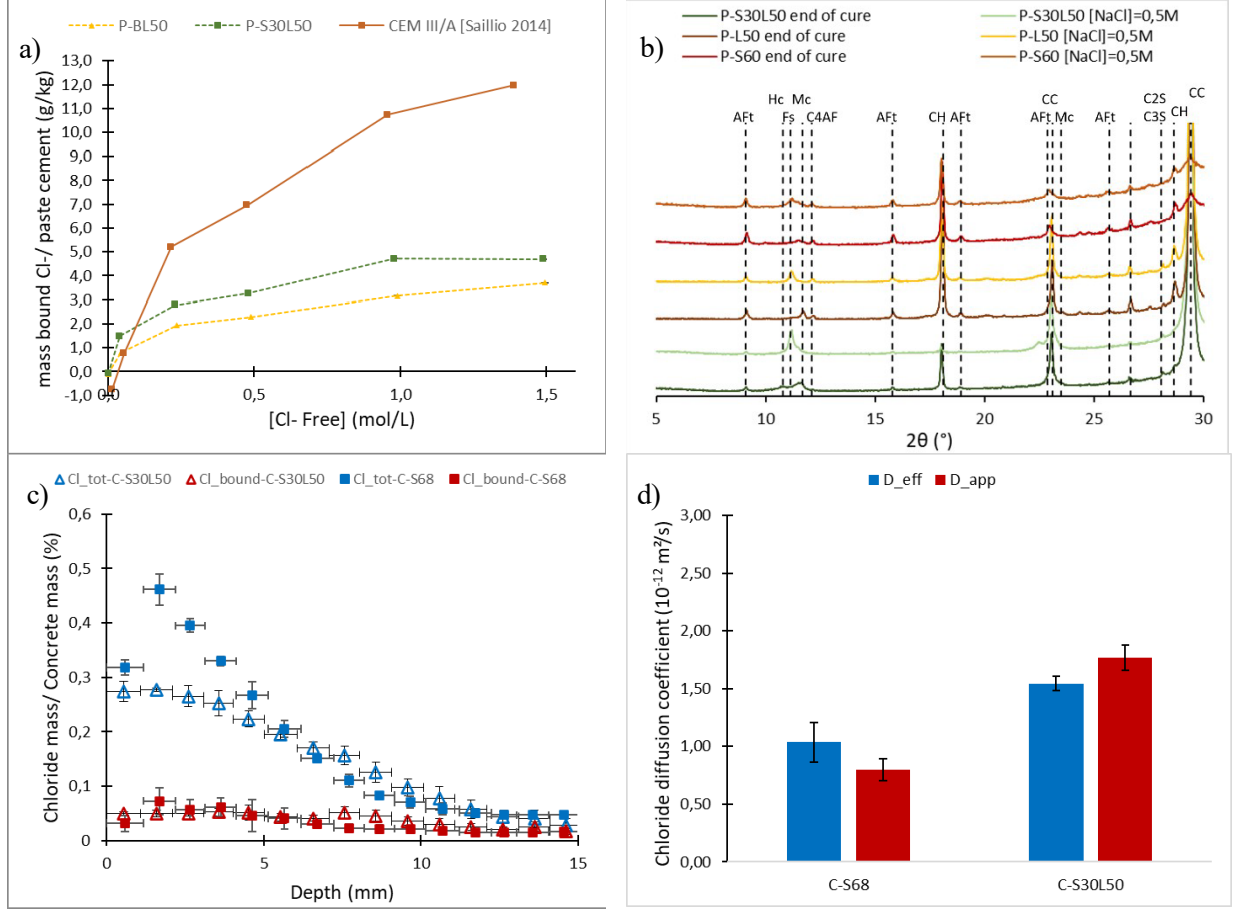


Figure 1: CBLs of cement pastes {CEM III/A paste data are from (Saillio 2014)} (a) and XRD diffractograms for cement pastes at the end of the cure and after 2 months of contact with a solution [NaOH]=0.1M and [NaCl]=0.5M (b), Total and bound chloride profiles for C-S30L50 and C-S68 after immersion in a NaCl solution of 6 months (c), chloride diffusion coefficient obtained for concrete (d). The TGA measurements for cement pastes are shown in Figure 2a. The portlandite content is calculated from Eq 1, the CaCO₃ content from the Eq2 and maximum CO₂ binding capacity (MBC) by Eq3.

$$x_{CH} = \frac{\Delta m_{T=450^{\circ}C \rightarrow T=500^{\circ}C}}{m_{s,T=1000^{\circ}C}} \cdot \frac{1}{1 - \alpha} \cdot \frac{MW_{CH}}{MW_w} \cdot 100 \quad (1)$$

where x_{CH} (%) is the Portlandite content per g of binder, $\Delta m_{T=450^{\circ}C \rightarrow T=500^{\circ}C}$ (g) is the mass loss between 450°C and 500°C, $m_{s,T=1000^{\circ}C}$ (g) is the sample mass at T=1000°C, MW_{CH} (g.mol⁻¹) is the Portlandite molecular weight and MW_w (g.mol⁻¹) is the water molecular weight.

$$x_{CC} = \frac{\Delta m_{T=560^{\circ}C \rightarrow T=1100^{\circ}C}}{m_{s,T=1100^{\circ}C}} \cdot \frac{1}{1 - \alpha} \cdot \frac{MW_{CC}}{MW_{CO_2}} \cdot 100 \quad (2)$$

where x_{CC} (%) is the calcium carbonate content per g of binder in percent, $\Delta m_{T=560^{\circ}C \rightarrow T=1100^{\circ}C}$ (g) mass loss between T=560°C and T=1100°C, $m_{s,T=1100^{\circ}C}$ (g) sample mass at T=1100°C, MW_{CC} (g.mol⁻¹) calcium carbonate molecular weight and MW_{CO_2} (g.mol⁻¹) CO₂ molecular weight.

$$MBC = \frac{CaO_{12345}}{2 \cdot MW_{130}} + \frac{MgO}{MW_{670}} \cdot 6 \cdot MW_{108} - \frac{SO_3}{9 \cdot MW_{109}} \cdot MW_{108} \quad (3)$$

where MBC (%) is the maximum CO₂ binding capacity, CaO_{react} (%) is the reactive CaO content of binder, MW_{CaO} (g.mol⁻¹) is the CaO molar weight, MgO (%) is the MgO content of binder, MW_{MgO} (g.mol⁻¹) is the MgO molar weight, SO_3 (%) is the SO₃ content of binder and MW_{SO_3} (g.mol⁻¹) is the SO₃ molar weight.

At the end of the curing time, the Portlandite content was higher for P-L50 (Table 3), due to the higher clinker content. Moreover, hydrotalcite was observed in the P-S30L50, but not in P-L50, as the ternary

binder contained GGBS in contrast to the L50 binder. Once the carbonation was completed for the cement pastes, the CO₂ binding capacity was determined (Table 3). P-L50 had a higher CO₂ binding capacity than P-S30L50, which could be explained by a higher content in reactive CaO + MgO. The carbonation kinetics of concretes in accelerated conditions are shown in Figure 2b. The carbonation rates were similar for both concretes, despite the lower maximum CO₂ binding capacity of the ternary binder (22.02%) than S60 (43.1% (Boumaaza et al. 2020)). C-S60 has an exposure class XC4 according to (NF EN 206+A2/CN 2014). Therefore, despite the lower CO₂ binding capacity of ternary binder, it is possible to design low-clinker concretes with an exposure class XC4.

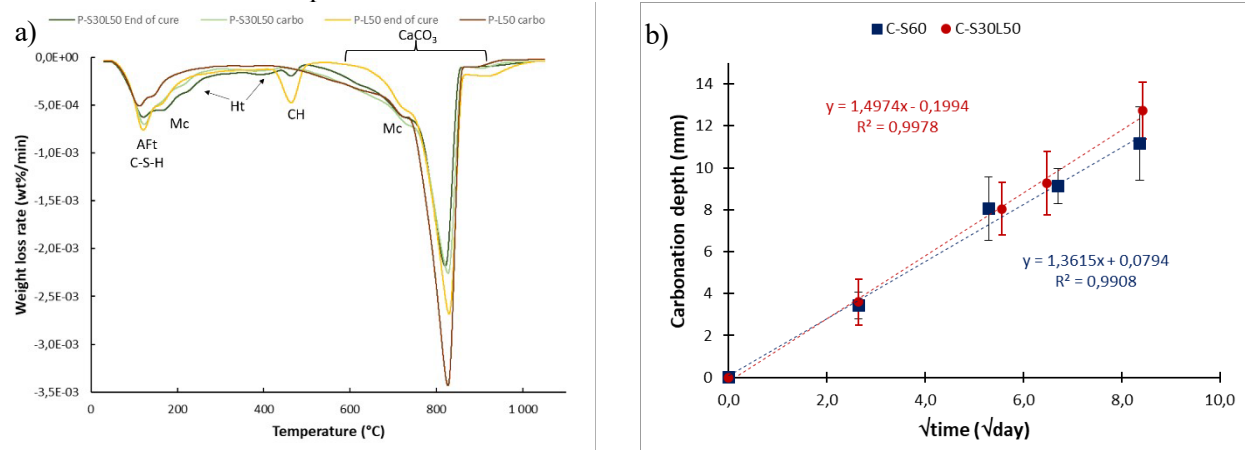


Figure 2: DTG curves of cement pastes at the end of the cure and carbonated (a) and carbonation kinetics in accelerated condition T=20°C, RH=57%& [CO₂]=3% (b).

Table 3: Effect of carbonation on the Portlandite and the CaCO₃ content and CO₂ binding capacity of binder

| Ref. | End of cure | | Carbonated | | CO ₂ binding capacity (%) | MBC (%) |
|------|---------------|-----------------------------|---------------|-----------------------------|--------------------------------------|---------|
| | CH/binder (%) | CO ₂ /binder (%) | CH/binder (%) | CO ₂ /binder (%) | | |
| Ter | 6.91 | 41.88 | - | 47.79 | 5.91 | 22.02 |
| BLL | 18.16 | 44.46 | - | 63.40 | 18.94 | 25.59 |

4. Conclusions

The ternary binder paste has a lower chloride binding capacity than a CEM III/A paste but a better one than binary binder (CEM I 50/50 Limestone filler) which can be explained by a lower alumina content of the binder. Moreover, the ternary binder has a lower CO₂ binding capacity than the two binary binders studied. Despite a lower binding capacity for the ternary binder, it is possible to make concrete resistant to the most aggressive exposure classes XC4 and XS3t by working at low W/C with a binder which has a low clinker content and a high limestone filler content. This reduction in the W/B ratio leads to a change in pore structure and thus an improvement in the transport properties.

References

- Arliguie, G, et H Hornain. 2007. « GranDuBé: measures associated to the durability of concrete ». French.
- Boumaaza, Mouna, Philippe Turcry, Bruno Huet, et Abdelkarim Aït-Mokhtar. 2020. « Influence of carbonation on the microstructure and the gas diffusivity of hardened cement pastes ». *Construction and Building Materials* 253: 119227.
- FD P18-480. 2022. « Concrete - Performance-based approach for justifying concrete structures durability ». AFNOR.
- NF EN 206+A2/CN. 2014. « Concrete - Specification, performance, production and conformity - National addition to the standard NF EN 206+A2 ». *AFNOR, La Plaine St-Denis*.
- NF EN 12390-11. 2015. « Testing hardened concrete - Part 11 : determination of the chloride resistance of concrete, unidirectional diffusion ». AFNOR.
- Saillio, Mickael, Véronique Baroghel-Bouny, et Fabien Barberon. 2014. « Chloride binding in sound and carbonated cementitious materials with various types of binder ». *Construction and Building Materials* 68: 82-91.
- XP P18-458. 2022. « Testing hardened concrete - Accelerated carbonation test ». AFNOR.
- XP P18-462. 2022. « Testing hardened concrete - Chloride ions migration accelerated test in non-steady-state conditions - Determining the apparent chloride ions diffusion coefficient ». AFNOR.

The fate of ferrous ions in corroding steel reinforced concretes

Shishir Mundra^{1*}, Jan Tits^{2,a}, Erich Wieland^{2,b} and Ueli M. Angst^{1,c}

¹ Institute for Building Materials (IfB), ETH Zürich, Zürich, Switzerland

*Email: smundra@ethz.ch

² Paul Scherrer Institut (PSI), Villigen, Switzerland

^aEmail: jan.tits@psi.ch

^bEmail: erich.wieland@psi.ch

^cEmail: uangst@ethz.ch

ABSTRACT

Corrosion of the steel reinforcement is the main reason for the premature degradation of concrete structures. Majority of the studies in the literature have been concentrated on understanding how corrosion initiates in concrete environments and the failure state. There remains a substantial gap in our knowledge about the processes occurring between these two abovementioned phenomena (or during the propagation phase), and this is particularly concerning when these processes can significantly influence both, the corrosion rate and the failure state. To address this, a conceptual model of the corrosion propagation phase exists, where steel corrosion proceeds by the dissolution of Fe(II) ions in solution, that either oxidise to Fe(III) or precipitate as Fe(II) oxides/hydroxides, or diffuse away from the steel-concrete interface. Fe(III) ions (formed due to the oxidation of Fe(II)) could also precipitate as Fe(III) oxides/hydroxides or diffuse. All processes of oxidation, diffusion, and precipitation occur simultaneously, are interdependent and in kinetic competition. One major factor that influences the corrosion rate and the precipitation of corrosion products is the kinetics of Fe(II) oxidation. Therefore, it is critical that we have experimental values of rate constants for Fe(II) oxidation under both aerobic and anaerobic environments that might prevail in reinforced concrete structures. This study experimentally assesses the oxidation behaviour of Fe(II) in solutions representative of conditions (aerobic and anaerobic) where the steel reinforcement is undergoing carbonation-induced corrosion. We use spectrophotometric techniques to quantify the kinetics of iron oxidation in solutions with pH ranging between 7 and 9. Additionally, a mechanism for the anaerobic oxidation of Fe(II) in concrete structures has been developed.

KEYWORDS: *Corrosion, Oxidation, Anaerobic, Carbonation, Durability*

1. Introduction

In the macroscopic sense, the service-life of reinforced concrete can be classified into three stages on the basis of Tuutti's service life model (Tuutti, 1982). The ingress of aggressive species such chlorides, or the carbonation of the concrete cover represent the initiation stage, which is followed by the onset of corrosion (Tuutti, 1982). Majority of the studies and standards assessing the long-term durability of reinforced concrete structures define the onset of corrosion as the limit state. However, it is well known that serviceability of reinforced concrete structures goes well beyond this limit state. The duration between the onset of corrosion and the end of serviceability for a reinforced concrete structure is defined as the propagation stage (Tuutti, 1982).

With regards to the propagation stage, a conceptual model has been developed only recently (Stefanoni et al., 2018). The corrosion of steel proceeds by the electrochemical dissolution of iron as Fe(II) ions in the pore solution at the steel-concrete interface (SCI). Fe(II) ions can oxidise to their Fe(III) counterparts, precipitate as Fe(II) oxides/hydroxides (depending on the solubility), or diffuse away from the SCI.

Additionally, Fe(III) ions can also precipitate as Fe(III) hydroxides and transform to the thermodynamically most stable oxide phase, as well as be sorbed on the surface of different cementitious hydrate phases and be transported away from the SCI. The precipitated Fe(II) and Fe(III) oxides/hydroxides may cause expansive stresses within the porous network of the concrete cover and result in cracking and spalling of the concrete cover, leading the end of the service-life. Here, it is important to highlight that the above-mentioned processes of oxidation, diffusion and precipitation occur simultaneously and are in competition with each other (Stefanoni et al., 2018). This competitive mechanism has direct implications on the [Fe(II)] and [Fe(III)] species at the SCI and a thorough understanding of the processes can help in answering a number of scientific questions and engineering challenges related to corrosion of steel in concrete. For example, the electrochemical dissolution of iron (or corrosion rate) from the steel depends on the reversible potential of the Fe/Fe(II) electrode, according to the Nernst equation, which in turn is influenced by the [Fe(II)] at the steel surface. However, the current unavailability of quantitative data in the literature, particularly pertaining to the different processes outlined above (oxidation kinetics, diffusion and precipitation kinetics), presents a huge gap in our understanding of the propagation phase. Whilst diffusion is extremely slow and precipitation of the most soluble corrosion product is instantaneous upon reaching the solubility (Furcas et al., 2022), the kinetics of Fe(II) oxidation (as a function of pH) becomes a highly important parameter and is hypothesised to be rate-limiting for all the processes occurring during the propagation stage of corrosion (Wieland et al., 2023).

This study, therefore, focusses on assessing the oxidation kinetics of Fe(II) in solutions that are representative of carbonated concretes (with regards to pH) where the steel is actively corroding. The oxidation of ferrous ions in anaerobic solutions in the near neutral pH (relevant to carbonated concretes), between ~5 and ~9, is experimentally measured by colorimetric means using a UV-Vis spectrometry. Additionally, thermodynamic and experimental observation from this study have been used to postulate a mechanism for the oxidation behaviour of Fe(II) in conditions relevant at the SCI, and may find significant use in reactive transport models to study corrosion of steel in the case of radioactive waste disposal facilities and reinforced concrete infrastructure.

2. Materials and Methods

All solutions were prepared using Fluka or Merck analytical grade chemicals. Ultrapure water (Milli-Q water, 18.2 MO.cm resistance) used for the preparation of solutions and for sample dilution was generated by a Milli-Q Gradient A10 purification system (Millipore, USA). Ultrapure water was boiled for 2 h under continuous N₂ purging in order to prepare degassed water. The O₂ concentration of the degassed water was measured and found to be below the detection limit (1 ppb) of a PreSens PST6 planar oxygen sensor (Regensburg, Germany). All experiments were conducted in glove boxes under an inert N₂ atmosphere (O₂, CO₂ < 0.1 ppm). A stock solution of 10⁻² M FeCl₂ was prepared using 0.01 M HCl at pH 2. To assess the oxidation of Fe(II) under varying pH conditions, solutions with pH 5, 7, 8 and 9 were prepared using 1 mM concentrations of different buffers to stabilise the pH. Table 1 shows the concentrations of different buffers used for different solutions. Known aliquots of the stock 10⁻² M FeCl₂ solution were pipetted into the buffer solutions to achieve an initial concentration (C₀) below the solubility limit w.r.t Fe(OH)₂ at the corresponding pH. Table 1 shows the initial Fe(II) concentration in solutions at pH 5, 7, 8 and 9. Depending on the pH, these solutions were labelled as FeII_{Ox}-5, 7, 8 and 9. Fe(II) concentrations were measured using the ferrozine method, as described by Viollier et al. [5]. An aliquot was drawn from FeII_{Ox}-5, 7, 8 and 9 at different times and mixed with a 0.01 M Ferrozine solution and then transferred into a 5 cm quartz cuvette. The absorbance of each of the solutions was measured with the Cary 6000i spectrophotometer (Agilent, USA) at 562 nm wavelength, over time to quantify the aqueous [Fe(II)].

Table 1: The initial concentration of various species in solutions to experimentally measure Fe(II) oxidation. The concentrations are prior to the addition of ferrozine, the Fe(II) complexing agent.

| pH | Fe(II) (M) | Cl (M) | CH ₃ COONa (M) | HEPES (M) | Na ₂ B ₄ O ₇ ×10H ₂ O (M) |
|----|----------------------|----------------------|---------------------------|-----------|---|
| 5 | 2 ± 10 ⁻⁵ | 4 ± 10 ⁻⁵ | 0.001 | -- | -- |
| 7 | 2 ± 10 ⁻⁵ | 4 ± 10 ⁻⁵ | -- | 0.001 | -- |
| 8 | 2 ± 10 ⁻⁵ | 4 ± 10 ⁻⁵ | -- | 0.001 | -- |
| 9 | 5 ± 10 ⁻⁶ | 1 ± 10 ⁻⁵ | -- | -- | 0.001 |

3. Results and Discussion

Figure 2 shows the influence of pH on the oxidation of Fe(II) in aqueous solutions in a glove-box atmosphere with a constant O₂ (g) concentration being < 0.1 ppm. The oxidation of ferrous ions in pH 5 and 7 was found to be extremely slow and the changes in concentration over 60 mins were found to be negligible (within the margin of error of the spectrophotometer). A dramatic increase in the oxidation kinetics was observed for solutions with pH 8 and 9. As seen in Figure 2, the kinetics of Fe(II) oxidation can be considered pseudo first-order w.r.t. [Fe(II)], and depends strongly on the pH of the solution under anaerobic conditions (Mundra et al., 2022). A change in the pH of the solution alters the thermodynamic stability of different aqueous Fe(II) species. For a given concentration of Fe(II), an increase in the pH results in an increased molar fraction of hydrolysed Fe(II) species (such as Fe(OH)⁺, Fe(OH)₂ (aq.) and Fe(OH)₃⁻), that have a higher affinity to donate electrons than their non-hydrolysed counterparts (Fe²⁺) (Luther, 1990). Therefore, in the absence of oxygen, the increase in the oxidation rate can be explained by the increased molar fractions of hydrolysed Fe(II) species, and all Fe(II) species oxidise simultaneously (possibly at different rates) to Fe(III) species.

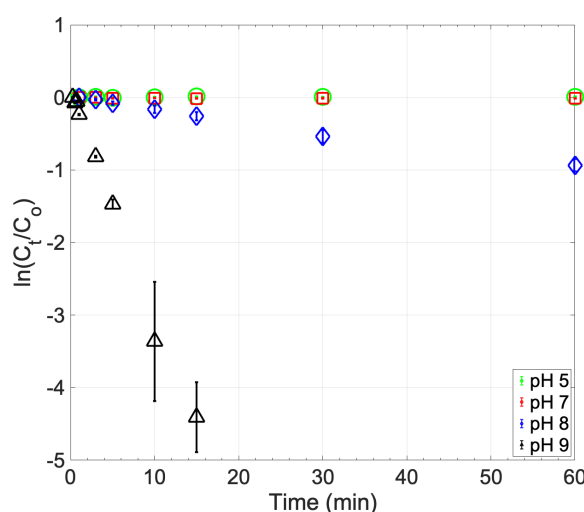


Figure 1: Influence of pH on the oxidation of ferrous ions. C_0 and C_t refer to the measured [Fe(II)] at time = 0 and time = t (x-axis), respectively.

Whilst there exists significant literature on the mechanism and kinetics of Fe(II) oxidation in the presence of oxygen, anaerobic oxidation of Fe(II) hasn't been studied thoroughly (Morgan & Lahav, 2007). In aerobic conditions, the dissolved oxygen in solution acts as the oxidant and is the electron acceptor. However, in anaerobic conditions, there must be a species acting as an electron acceptor forming the cathodic reaction of the system, that does not involve dissolved oxygen. To decipher the oxidant in anaerobic conditions, we must consider the products of Fe(II) oxidation, namely Fe(III) species. Like Fe(II), Fe(III) also speciates as a function of pH and can exist in its hydrolysed (Fe(OH)²⁺, Fe(OH)₂⁺, Fe(OH)₃ (aq.) and Fe(OH)₄⁻) or non-hydrolysed state (Fe³⁺). At pH 5, Fe(III) species predominantly exist as Fe(OH)₂⁺ along with minor quantities of FeOH²⁺, and Fe(OH)₃ (aq). Fe(OH)₃ (aq) is the predominant species at pH 7 and 8, followed by Fe(OH)₂⁺ and some minor quantities of Fe(OH)₄⁻. At pH 9 though, the Fe(III) aqueous species are constituted of mainly Fe(OH)₃ (aq) and Fe(OH)₄⁻. At a given pH, Fe(II) ions speciate and are present in solution in different hydrolysed or non-hydrolysed states. The molar fractions of each of the species are governed by the thermodynamics of the system and the anions present ([OH⁻] in this study) in the solution. Fe(II) species oxidise to form the most thermodynamically favoured Fe(III) species in solution. Based on the initial concentrations of each of the Fe(II) and Fe(III) aqueous species present at pH 5, 7, 8 and 9 (assuming initial oxygen concentration of dissolved oxygen as 10⁻¹⁰ M), we could decipher the initial reversible potential (E_{rev}), using the Nernst equation, of all possible Fe(II)/Fe(III) oxidation reactions. Within the anaerobic corrosion community, it is often assumed that the reduction of water (or hydrogen evolution) acts as the cathode, but without much evidence. For this to be true, the E_{rev} of different Fe(II)/Fe(III) oxidation reactions (coupled with thermodynamic stability of different species) must be below the E_{rev} of water reduction at a given pH. Based on all possible oxidation

reactions (involving different Fe(II) and Fe(III) species), we conclude that the mechanism of Fe(II) oxidation is different at different pH. In the case of pH 5, the anodic reaction proceeds by the oxidation of Fe^{2+} to $\text{Fe}(\text{OH})_3$ (aq), FeOH^{2+} and $\text{Fe}(\text{OH})_2^+$. Similarly at pH 7, the anodic reaction proceeds by the oxidation of Fe^{2+} to FeOH^{2+} , $\text{Fe}(\text{OH})_3$ (aq) and $\text{Fe}(\text{OH})_4^-$; as well as the oxidation of FeOH^+ to $\text{Fe}(\text{OH})_3$ (aq) and $\text{Fe}(\text{OH})_4^-$; and the oxidation of $\text{Fe}(\text{OH})_2$ (aq) to $\text{Fe}(\text{OH})_2^+$ and $\text{Fe}(\text{OH})_4^-$. At pH 8, Fe^{2+} and FeOH^+ oxidises to $\text{Fe}(\text{OH})_3$ (aq) and $\text{Fe}(\text{OH})_4^-$, whereas $\text{Fe}(\text{OH})_2$ (aq) oxidises to $\text{Fe}(\text{OH})_4^-$. In the case of pH 9, Fe^{2+} undergoes oxidation to form $\text{Fe}(\text{OH})_3$ (aq) and $\text{Fe}(\text{OH})_4^-$; whereas, both FeOH^+ and $\text{Fe}(\text{OH})_2$ (aq) oxidise to form $\text{Fe}(\text{OH})_4^-$. The E_{rev} of all these reactions lie below the E_{rev} of water reduction making it the perfect candidate for acting as the cathode, and confirming the possibility of oxidation of Fe(II) under anaerobic conditions.

The implications of this study in the context of steel reinforced concrete are far and wide. For example, the pH of a carbonated concrete cover (whether considered as 8 or 9) highly influences the kinetics of Fe(II) oxidation and consequently, alters other processes during the propagation stage of corrosion, such as transport or precipitation. Another parameter to be considered is the dissolved oxygen content at the SCI. When the pore solution at the SCI is in equilibrium with atmospheric oxygen, the oxidation rate of Fe(II) is roughly two-orders of magnitude faster than that observed under anaerobic conditions. Therefore, availability of dissolved oxygen significantly influences the rate of Fe(II) oxidation in corroding reinforced concrete structures, and consequently alters transport or precipitation of ferrous/ferric species.

3. Conclusions

An understanding of the mechanism and kinetics of Fe(II) oxidation in corroding steel reinforced concrete is critical in developing accurate service-life models. This study focussed on the experimentally quantifying the oxidation kinetics of Fe(II) in anaerobic near-neutral solutions, representative of carbonated structures. The findings indicate that the rate of Fe(II) oxidation is pseudo first-order w.r.t. $[\text{Fe}(\text{II})]$, and highly dependent on the pH of the solution and the speciation of Fe(II). Unlike oxygenated conditions, the cathodic reaction accompanying the anodic oxidation of Fe(II), is the reduction of H_2O (l) releasing H_2 (g). Additionally, Fe(II) oxidation proceeds by the oxidation of the thermodynamically most stable Fe(II) aq. species to the thermodynamically most stable Fe(III) aq. species.

Acknowledgements

The authors would like to thank the Swiss National Science Foundation for funding the project under the grant PP00P2_194812.

References

- Furcas, F. E., Lothenbach, B., Isgor, O. B., Mundra, S., Zhang, Z., & Angst, U. M. (2022). Solubility and speciation of iron in cementitious systems. *Cement and Concrete Research*, 151, 106620.
- Luther, G. W. (1990). The Frontier-Molecular-Orbital Theory approach in geochemical processes. In W. Stumm (Ed.), *Aquatic Chemical Kinetics - Reaction rate Processes in Natural Waters* (pp. 173–198). Wiley-Interscience, John Wiley and Sons.
- Morgan, B., & Lahav, O. (2007). The effect of pH on the kinetics of spontaneous Fe(II) oxidation by O_2 in aqueous solution - basic principles and a simple heuristic description. *Chemosphere*, 68(11), 2080–2084.
- Mundra, S., Kunz, D., Tits, J., Wieland, E., & Angst, U. (2022). Stability of Fe^{2+} in cementitious media. *6th International Conference on Concrete Repair, Rehabilitation and Retrofitting (ICCRRR 2022)*, Cape Town, South Africa, October 3-5, 2022.
- Stefanoni, M., Zhang, Z., Angst, U., & Elsener, B. (2018). The kinetic competition between transport and oxidation of ferrous ions governs precipitation of corrosion products in carbonated concrete. *RILEM Technical Letters*, 3, 8–16. <https://doi.org/10.21809/rilemtechlett.2018.57>
- Tuutti, K. (1982). Corrosion of steel in concrete. In *CBI Report 4:82, The Swedish Cement and Concrete Institute*. Swedish Cement and Concrete Research Institute.
- Wieland, E., Miron, G. D., Ma, B., Geng, G., & Lothenbach, B. (2023). Speciation of iron(II/III) at the iron-cement interface: a review. *Materials and Structures/Materiaux et Constructions*, 56(2), 1–24.

Effect of waterproofing chemicals on carbonation in Low clinker cement with pore structure analysis

Lav Singh¹ and Shashank Bishnoi^{2*}

¹ Research Scholar, Department of Civil Engineering, Indian Institute of Technology, Delhi, India
Email: singh.lav1987@gmail.com

² Professor, Department of Civil Engineering, Indian Institute of Technology, Delhi, India
Email: bishnoi@iitd.ac.in

ABSTRACT

Most of the SCMs used as a substitution in cement are industrial by-products and help in reducing the impact on the environment. However, it is also observed that blended cement with a higher percentage replacement with fly- ash, slag and metakaolin exhibit a higher carbonation rate. Since the carbonation process is difficult to limit, our idea is to use water-repellent chemicals to inhibit the corrosion process by altering or transforming the inherently permeable, porous and hydrophilic nature of the concrete microstructure and fluid transport properties. For this study, we considered two different applications of waterproofing chemicals- Integral admixtures and hydrophobic coatings. For each type of application, oligomeric-silane-based commercial compounds are considered added to standard mortar samples made with different SCMs including two ternary mixes composed of composite cement (FA - slag) and LC³ (calcined clay-limestone). The experiments were conducted to understand the two transport factors – sorption characteristics (capillarity), and porosity (permeable pore space) of the microstructure. The properties in the mortar were investigated before and after the carbonation process according to standard practices. Experimental results show hydrophobic treatment lowered capillary sorption in all the blends. The results indicate the potential of these chemicals to prevent water penetration, and thus their usefulness in areas where there is a risk of corrosion of reinforcement and penetration of aggressive substances by water transport. The results also demonstrate the influence of carbonation on the effectiveness of these WP techniques.

KEYWORDS: *Waterproofing technique, LC³, Hydrophobic Treatment, Carbonation, Sorptivity*

1. Introduction

Clinker manufacturing produces 2.4% of the world's CO₂ emissions, making it an energy-intensive process. Clinker substitution and blended cement can reduce emissions but may increase carbonation risk, which can cause concrete degradation [Sharma et al (2021)]. Waterproofing (WP) techniques like integral waterproofing admixture (IWA) and hydrophobic impregnation (HI) can help mitigate water ingress [Dia et al (2010), Frosch et al (2013)]. Our research aims to compare the efficacy and durability of these techniques on low-clinker cement mortars and to compare them with ordinary Portland cement. The study examines durability characteristics that affect fluid movement in the cement structure, focusing on capillarity by examining the sorption characteristics, and pore structure by obtaining the permeable pore space of the microstructure.

2. Experimental Work

The procedure tests the durability of mortar specimens made with two binary blends and two ternary mix combinations using different SCMs. The ratio of clinker to total cementitious binder is shown in Table 1. The mixes were prepared in the lab using a 3D Turbo mixer with a water-binder ratio of 0.4. Standard Indian sand was used in an equal weight ratio, and the mortar mix had a standard ratio of 1:3 (cement/binder: standard sand).

Table 1 Various types of cement with different types of SCMs

| Binder Name (CF) | SCMs replacement (%) | Remarks |
|-----------------------|--|---------------------|
| OPC (0.95) | Nil | 43 Grade OPC |
| PPC (0.65) | Fly ash (FA)– 30 | |
| PSC (0.5) | Slag (GGBS) – 50 | |
| CC (0.5) | Fly ash (FA)– 30 Slag (GGBS) – 15 | FA: Slag ratio 2: 1 |
| LC ³ (0.5) | Calcined Clay (CC) – 30 Limestone (LS) – 15 | CC: LS ratio 2: 1 |

Two different categories of waterproofing chemicals were used in the study - integral waterproofing admixtures, and hydrophobic surface coating [Gaur et al & Narula et al (2020)]. For both WP treatments, the same chemical was used with two different application techniques. The use of integral water-repellent had a minor decrease in compressive strength across all cement blends. The details of the type, chemical description, and dosage are shown in Table 2 below.

Table 2 Chemical description of waterproofing techniques

| Waterproofing Techniques | Chemical Description | Dosage | Remarks |
|------------------------------|---|-----------------------------|---|
| Integral admixture - IWA | IWA-5: Silane/siloxane-based Admixture (with 99% active content) | 0.2 % of the cement content | A mixture of octyl-tri-ethoxy-silanes isomers |
| Hydrophobic impregnation -HI | HI-4: Solvent Based Silane/siloxane-based liquid coat (with 99% active content) | 2-layer coats | A mixture of octyl-tri-ethoxy-silanes isomers |

Cement mortar specimens were cast in the lab, cured in lime-saturated water for 120 days, and pre-conditioned as per ASTM standards. Sorption characteristics and total porosity were obtained through ASTM 1585-2013 and ASTM C642-06, respectively, with each test result an average of 3 measurements. The samples were subjected to accelerated carbonation at 3% CO₂, 27°C, and 65% RH to evaluate transport property changes after the carbonation process. The specific waterproofing chemical used in the study does alter concrete structure properties from hydrophilic to hydrophobic. The integral admixture technique affects bulk properties, while hydrophobic impregnation alters only surface properties.

3 Experimental Results and Discussion

The data plot in Figure 1(a & b) indicates that blended cement has greater resistance to capillary absorption (S_i & S_s) than OPC. Lower sorption rates were found in non-carbonated systems with low clinker content. Both the waterproofing techniques – Integral IWA-5 and HI-4 with oligomeric-silane-based hydrophobic compound displayed extremely low water absorption characteristics for all blends. Both integral chemical treatment IWA-5 and impregnated HI-4 having common hydrophobic ingredients had almost equally significant impacts on initial and secondary absorption properties across all non-carbonated system blends.

Following carbonation, control specimens containing supplementary cementitious materials (SCMs) displayed higher sorption gradient values (S_i & S_s), with a marked increase in short-term absorption observed in the ternary blends of untreated and IWA-treated LC³ specimens. Moreover, the increased long-term sorption (S_s) was observed with other cement blends. The increased water absorption can be attributed to a higher degree of carbonation achieved in low clinker cement, especially in CC and LC³. Hydrophobic impregnation proved more effective in reducing short-term S_i values, particularly after carbonation. The sorptivity results suggest that surface properties mainly govern initial absorption characteristics, while secondary sorption is governed by bulk properties. However, its impact weakened under prolonged immersion conditions, as indicated by the long-term S_s values. Carbonation altered the

microstructure, with the secondary sorption S_s values increasing for all blends, particularly in untreated systems. The HI treatment modifies the surface properties, making it impervious to water penetration from the outside.

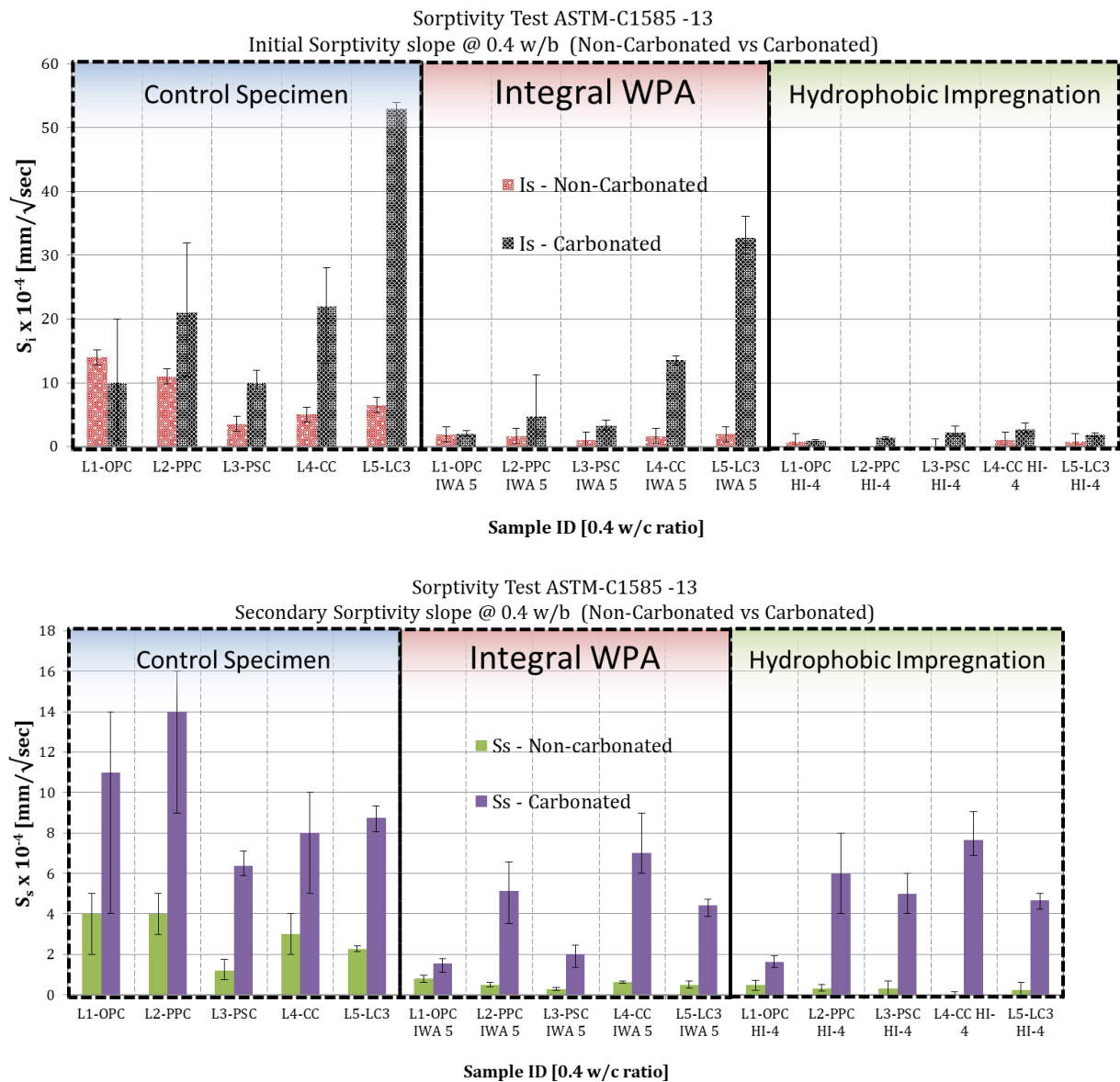


Fig.1 (a & b): Comparison of NC and C samples treated with Integral waterproofing chemicals – Initial (a) and Secondary (b) Absorption: Control (left), IWA -5 (Middle), and HI -4 (Right) sorption slope values as per ASTM 1585-13

Experimental results presented in Fig 2 suggest that reducing the clinker factor (CF) does not have a significant impact on the permeable pore volume. The integral waterproofing admixture was effective in reducing pore volume in all types of cement mortars. Although both Integral IWA and HI have been effective in reducing pore volume, it would be theoretically inappropriate to calculate the pore volume for hydrophobically treated mortar specimens because the nature of the test procedure is based on the amount of water ingress in the concrete microstructure. However, after the carbonation process, porosity increased, indicating that the integral admixture was not effective, especially which low clinker cement with CF 0.5. The results show that the carbonation process decreases the percentage of voids in hardened concrete at higher clinker content. But once the CF value is decreased to 0.5, the carbonation process increases the volume of permeable pores in blended systems and makes them less effective against external water penetration. The hydrophobic impregnation (HI) was much more effective against water

penetration. After the carbonation process, there was an increase in the volume of permeable pores, but overall, the porosity was much lower compared to the control samples.

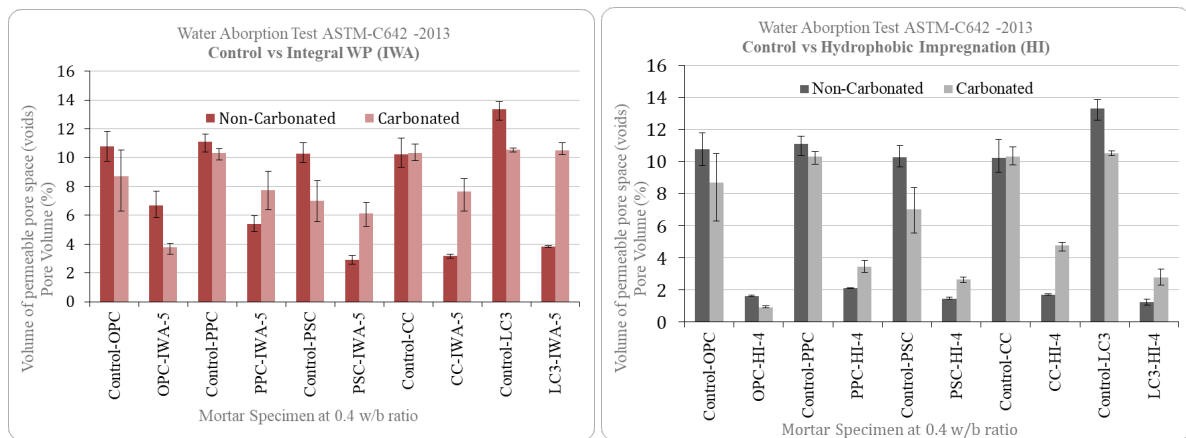


Fig. 2: Comparison of permeable pore space (NC vs C) for 5 cement blends with both waterproofing techniques at 0.4 w/b ratio

4 Conclusion

Based on the presented results and observations, the following conclusions can be made. The use of different SCM substitutions led to a decrease in absorption rates, but this trend was reversed for all blends when subjected to the carbonation process. Hydrophobization through integral and coating applications was found to limit water penetration and impact sorption properties. When comparing different water-repellent chemical applications, it was concluded that hydrophobic coating on the concrete surface was more effective in reducing absorption and pore volume and remained effective after the carbonation process. The hydrophobic treatment has the potential to significantly extend the life of structural elements, particularly vertical elements such as walls, columns, and beams that are vulnerable to carbonation and water permeability.

Acknowledgements

The authors acknowledge that this study which is part of Low carbon cement project is financially supported by Swiss Development Cooperation (SDC) and Aalborg for making FutureCem technology available to us.

References

- [1] Sharma, M., Bishnoi, S., Martirena, F., & Scrivener, K. (2021). Limestone calcined clay cement and concrete: A state-of-the-art review. *Cement and Concrete Research*, 149, 106564.
- [2] Dai, J. G., Akira, Y., Wittmann, F. H., Yokota, H., & Zhang, P. (2010). Water repellent surface impregnation for extension of service life of reinforced concrete structures in marine environments: The role of cracks. *Cement and Concrete Composites*, 32(2), 101-109.
- [3] Frosch, R. J., M. E. Kreger, and B. V. Strandquist. Implementation of Performance-Based Bridge Deck Protective Systems. Publication FHWA/IN/JTRP-2013/12. Joint Transportation Research Program, Indiana Department of Transportation and Purdue University, West Lafayette, Indiana, 2013.
- [4] Gaur, T., Singh, L., & Bishnoi, S. (2020). Influence of Carbonation on Mechanical and Transport Properties of Limestone Calcined Clay Blend Mortar Mix. In *Calcined Clays for Sustainable Concrete* (pp. 621-629). Springer, Singapore.
- [5] Narula, Nitin, Lav Singh, and Shashank Bishnoi. "Assessment of the Efficacy of Waterproofing Admixtures Using Calcined Clay and SCMs." *Calcined Clays for Sustainable Concrete*. Springer, Singapore, 2020. 641-645.

The square root law with an offset applied to chloride diffusion in slowly reacting blended cement pastes

W. Wilson^{1*}, F. Georget², and K.L. Scrivener³

¹ Université de Sherbrooke, Sherbrooke, QC, Canada
Email: william.wilson@usherbrooke.ca

² Institute of Building Materials Research, RWTH Aachen University, Aachen, Germany
Email: georget@ibac.rwth-aachen.de

³ Laboratory of Construction Materials, EPFL, 1015 Lausanne, Switzerland
Email: karen.scrivener@epfl.ch

ABSTRACT

The urgency to develop and deploy new low-CO₂ alternatives to Portland cement has led to a renewed interest in rapid methods for assessing and predicting chloride ingress in cementitious materials. As part of a comprehensive project on chlorides in blended cement pastes, this paper focusses on characterizing the evolution of chloride penetration in systems exposed before the end of their microstructure development (i.e., after 28 days of curing). Slag-Portland cement pastes were prepared with different water-to-binder ratios ($w/b = 0.3, 0.4$ & 0.5) and exposed to a $0.5M$ NaCl solution. After $0.5, 1$ and 4 years of bulk diffusion, chloride profiles were obtained by micro-X-ray fluorescence and analyzed in terms of penetration depths (X) for selected reference chloride contents (C_r). Results showed that the square root of time (\sqrt{t}) law of diffusion can be applied with an offset (b_{Cr}) for slowly reacting blended cement systems exposed before the end of their microstructure evolution. This was clearly demonstrated with the collapse into a master curve of chloride profiles at different ages when plotted as a function of $(X - b_{Cr=400})/\sqrt{t}$. This paper thus provides additional evidence to support the development of a simple and efficient use of the square root law to predict long-term chloride penetration based on ingress measurements over a relatively short period.

KEYWORDS: *Chloride bulk diffusion, chloride profile, chloride ingress prediction, square root law.*

1. Introduction

Climate change urges the adoption of new low-CO₂ cementitious systems, which in turns requires rapid and reliable methods to assess long-term durability (e.g., against chloride-induced corrosion). The prediction of chloride ingress (and service life) has been studied for decades, but new binders bring new challenges due to their diverse chemistry, hydration kinetics, microstructure and interactions with chlorides. If several accelerated tests can be used for classification of binders, the bulk diffusion test (e.g., ASTM C1556 or NT Build 443) best mimics real field exposure in submerged conditions. However, bulk diffusion is a complex non-steady-state reactive transport process combining diffusion and binding (i.e., chloride concentration and binding vary as a function of depth and time). The common engineering solution fits profiles with a solution of Fick's second law to obtain apparent chloride diffusion coefficients and uses ageing coefficients to account for changes of coefficients over time, both of which have been criticized from a theoretical point of view (e.g., in Georget et al. (2023)).

Recently, the square root law has brought attention as an alternative approach to analyze series of chloride profiles and predict long-term chloride ingress, see Poulsen & Sørensen (2014), Poulsen et al. (2018), Fjendbo et al. (2021). Good predictions were obtained using chlorides profiles from concrete exposed to seawater for decades. The square root law for chloride ingress was further investigated with reactive transport modelling and chloride profiles on cement pastes by Georget et al. (2023), clearly showing that diffusion was the dominant mechanism in saturated conditions. Furthermore, laboratory investigations at the scale of cement pastes (e.g., Jensen et al. (1999) or Maraghechi et al. (2018)) showed great interest as

the resolution of profiles could be improved by using electron probe micro-analyses (EPMA) or μ XRF measurements (compared to the conventional grinding and titration approach to obtain chloride profiles from concrete samples exposed to field conditions). Although cement pastes cured and exposed under ideal conditions differ from concrete structures exposed to field conditions, the cement paste scale can be used to develop new methods or to compare the behavior of binders, before upscaling to mortars and concrete. In this context, this paper aims to contribute to the understanding and use of the square root law for blended cement systems at the paste scale. More specifically, the square root law has been shown to describe the long-term behaviour of chloride bulk diffusion (starting at 1 year of exposure to avoid early-age effects, Georget et al. (2023)), but can it also be used for shorter exposure times considering that microstructure changes occur after the initial exposure to chlorides? This paper illustrates that using an offset with the square root law is a promising solution, based on results obtained with slag-Portland blended cement pastes at different water-to-binder ratios exposed after 1 month of curing to a 0.5M NaCl solution, up to 4 years.

2. Materials and methods

Blended cement pastes were produced with a slag-Portland blended cement (CEM III/A) at three different water-to-binder ratios, $w/b = 0.3, 0.4$ and 0.5 . The pastes were blended with a high-shear mixer (5-cm axial-flow impeller, 1600 rpm) for two minutes, before being vacuum mixed for one minute to remove entrapped air (450 rpm). To ensure sufficient workability for casting or avoid bleeding, either a superplasticiser was used ($w/b = 0.3$) or a waiting time was included between mixing steps ($w/b = 0.5$). Specimens were cast and sealed in cylindrical polypropylene moulds (33 mm diameter, 50 mm height). Specimens were demoulded after ~ 20 hours and cured up to 28 days in slightly larger containers with a few millilitres of water. Leaching of the specimen was limited by adding a finely ground specimen of the same batch in the curing container. More details can be found in Wilson et al. (2021, 2022).

Surfaces of the cured specimens were sealed with Araldite® epoxy (Huntsman Corporation). After about 24 hr of epoxy curing, a surface for exposure to chlorides was created by a cutting off a slice of ~ 3 mm from the specimen. Specimens were then exposed in sealed containers to a 0.5 M NaCl solution prepared with chemical grade sodium chloride salt. Specimens were completely covered with the solution which was added at a ratio of exposed surface area to solution volume of $50 \pm 30 \text{ cm}^2/\text{L}$ (as in ASTM C1556). To mimic continuous leaching and field conditions, the solution was regularly renewed. After 0.5, 1 and 4 years of exposure to the chloride solution, a specimen of each system was taken out for analysis. A cross section perpendicular to the exposed surface was dry cut from in the middle of each specimen (as in Maraghechi et al. (2018)). The cross section was polished perpendicular to the chloride ingress direction (to avoid contamination) with silicon carbide sandpapers P180 and P500, before being freeze-dried.

Polished surfaces were analyzed with an Orbis PC Micro EDXRF analyzer system (μ XRF) equipped with a Rh micro-focus X-ray tube focussed with $30 \mu\text{m}$ poly-capillary X-ray optics. The signal from the sample was filtered with a $25 \mu\text{m}$ aluminum filter (to remove overlapping rhodium spurious peaks and improve chlorine detection) and collected with an Apollo XRF-ML50 Silicon Drift Detector (Edax Ametek). Instrument parameters were optimized to obtain a distinct chlorine signal while allowing relatively rapid measurements. The chlorine intensity is reported in counts, as the quantification of elemental concentrations was not attempted in this study. Profiles were obtained by performing 15 spot analyses per depth with depth increments of 1 mm starting from the exposed surface. A few erroneous data points were identified and removed before averaging chlorine intensity for each depth. In the following, the measured profiles are called chloride profiles as it is assumed that chlorine is only present as chloride.

3. Results and discussion

Fig. 1 shows chloride profiles obtained after different exposure times for CEM III/A cement pastes at different w/b . As expected, a higher w/b is associated with a faster penetration of chloride. Interestingly, similar penetration depths were obtained at $w/b = 0.5$ after 6 months, $w/b = 0.4$ after 1 year and $w/b = 0.3$ after 4 years, i.e., reducing w/b is a valid means to reduce chloride ingress. As described in Wilson et al. (2023a), chloride ingress resistance could be compared in terms of penetration depths (X_{Cr}) using any reference chloride content (C_r) in the bottom half of profiles. Here, a value of $C_r = 400$ counts was selected to compare systems and perform square root law analyses, as illustrated **Fig. 1** and described below.

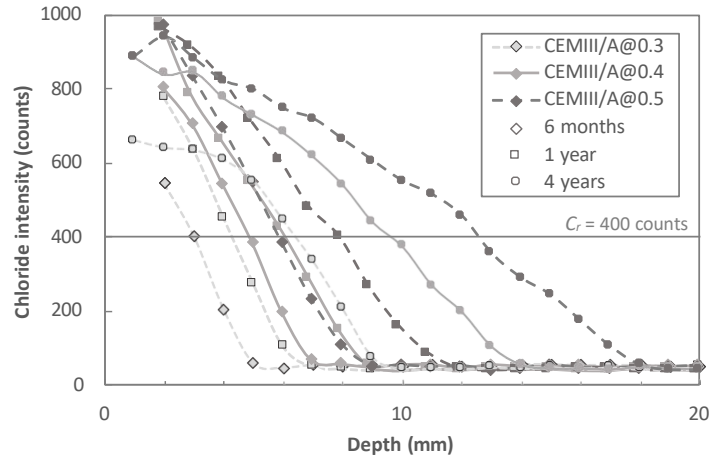


Fig. 1. Chloride intensity profiles measured by μ XRF on CEM III/A cement pastes at $w/b = 0.3, 0.4$ & 0.5 after exposure to a $0.5M$ NaCl solution for 6 months, 1 year and 4 years.

Fig. 2 illustrates for each system the relationship between the penetration depth and the square root of exposure time for a reference chloride content of $C_r = 400$ counts. The square root law with an offset is then defined as follows (as in Poulsen & Sørensen (2014), Poulsen et al. (2018), Fjendbo et al. (2021)):

$$X_{Cr}(t) = a_{Cr}\sqrt{t} + b_{Cr} \quad (1)$$

where X_{Cr} is the depth of chloride ingress, t is the exposure time, a_{Cr} is an ingress parameter and b_{Cr} is an offset. Linear correlations with very high coefficients of determination were obtained in **Fig. 2**. Although this is an expected consequence of Fick's second law, it shows that even with interactions between chlorides and cement hydrates (i.e., chemical and physical binding), the chloride ingress in these blended cement pastes was controlled by diffusion (see more in Wilson et al. (2023a & 2023b)).

The use of a non-zero b_{Cr} value generally allowed improvements of the fit (**Fig. 2b** compared to $b_{Cr} = 0$ in **Fig. 2a**), although the difference appears relatively minor in the representation of **Fig. 2** with the available data. Linear correlations are illustrated here for $C_r = 400$ counts, but similar coefficients of determination were also obtained for other C_r values in the bottom half of profiles.

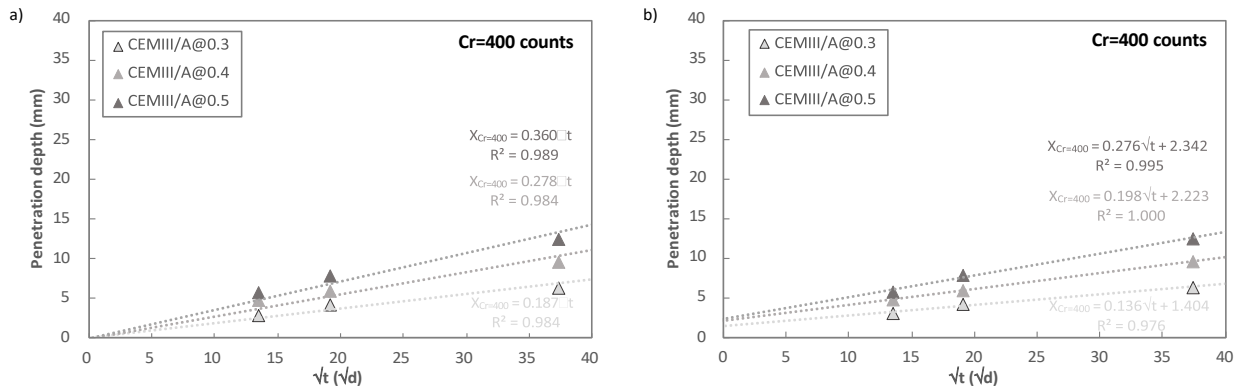


Fig. 2. Linear regressions of the penetration depth at $C_r = 400$ counts as a function of the square root of time, providing an ingress parameter $a_{Cr=400}$ (a) with a fit forced at the origin and (b) with a $b_{Cr=400}$ offset, for CEM III/A cement pastes at $w/b = 0.3, 0.4$ & 0.5 .

Fig. 3 provides a different representation of the same square root law, this time in terms of chloride intensity as a function of the penetration depth divided by the square root of time (X/\sqrt{t}). As described in Georget et al. (2023), chloride ingress is expected to respect the square root law (without offset) and profiles in the X/\sqrt{t} representation should collapse into a master curve, if no separate time dependent process was occurring. This is not the case here in **Fig. 3a**, because the slag-Portland cement hydration is incomplete at the beginning of exposure to chlorides after 1 month of curing. However, chloride profiles do collapse into a master curve for each system in **Fig. 3b**, when considering non-zero b_{Cr} values.

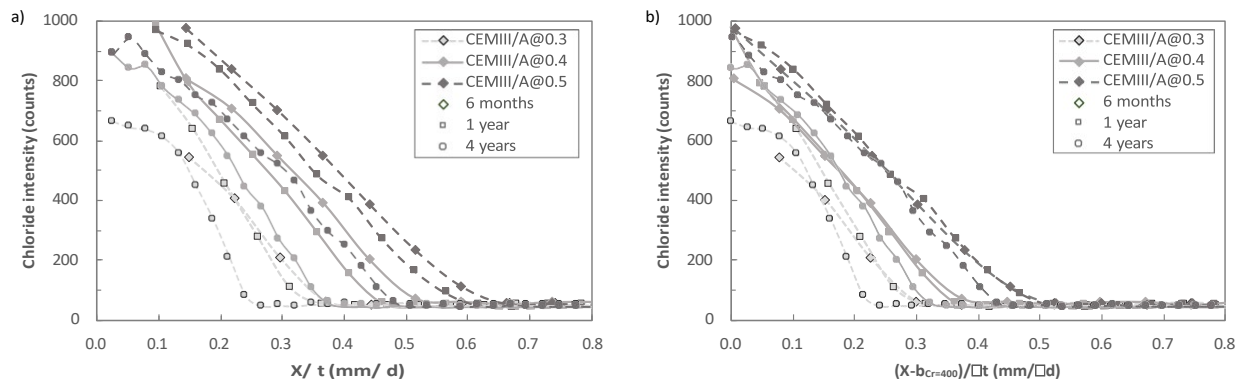


Fig. 3. Square-root-law master curves for CEM III/A systems represented in terms of chloride intensity as a function of (a) X/\sqrt{t} and (b) $[X-b_{Cr=500}]/\sqrt{t}$.

4. Conclusions

Results showed that the square root law of diffusion can be applied with a b_{Cr} offset for slowly reacting blended-cement systems exposed before the end of their microstructure evolution. Chloride bulk diffusion experiments on slag-Portland cement pastes (CEM III/A systems) led to the following conclusions:

- For each reference chloride content C_r , the penetration depth between 6 months and 4 years increased linearly as a function of \sqrt{t} (i.e., chloride ingress was controlled by diffusion).
- Stronger linear regressions were obtained for cement pastes when an offset b_{Cr} was used with the ingress parameter a_{Cr} , compared to the latter without offset.
- For each w/b ratio, chloride intensity as a function of $(X-b_{Cr=400})/\sqrt{t}$ obtained at different ages (0.5, 1 & 4 years) collapsed into a master curve representative of the system.

Overall, although diffusion properties may change during the early exposure to chloride for slowly reacting blended-cement systems, chloride ingress can still be described by the square root law if an offset is used to account for the initial microstructure evolution. Nevertheless, this paper relies on a single type of binder, which is insufficient to generalize the approach to all types of binders. The next step is thus to characterize square root law ingress parameters and offset values for a wide range of systems. A better understanding of the offset variation as a function of the selected reference chloride content is also needed, along with similar testing at the scale of mortars and concrete. This is currently being investigated in parent studies that include a wide range of systems and show great potential for the approach (e.g., Wilson et al. (2023b)).

References

- Fjendbo, S., Sørensen, H. E., De Weerd, K., & Geiker, M. R. (2021). The square root method for chloride ingress prediction—Applicability and limitations. *Materials and Structures/Materiaux et Constructions*, 54(2), 1–19.
- Georget, F., Wilson, W., & Matschei, T. (2023). Long-term extrapolation of chloride ingress: an illustration of the feasibility and pitfalls of the square root law. *Cement and Concrete Research*, Under Review.
- Maraghechi, H., Avet, F., Wong, H., Kamyab, H., & Scrivener, K. (2018). Performance of Limestone Calcined Clay Cement (LC3) with various kaolinite contents *Materials and Structures/Materiaux et Constructions*, 51(5).
- Mejlhede Jensen, O., Hansen, P. F., Coats, A. M., & Glasser, F. P. (1999). Chloride ingress in cement paste and mortar. In *Cement and Concrete Research* (Vol. 29).
- Poulsen, S. L., & Sørensen, H. E. (2014, December). Chloride ingress in old Danish bridges. *Proceedings of the 2nd International Congress on Durability of Concrete (2nd ICDC)*.
- Poulsen, S. L., Sørensen, H. E., & Jönsson, U. (2018). Chloride ingress in concrete blocks at the Rødbyhavn marine exposure site. *4th International Conference on Service Life Design for Infrastructures (SLD4)*, 192–203.
- Wilson, W., Georget, F., & Scrivener, K. (2021). Unravelling chloride transport/microstructure relationships for blended-cement pastes with the mini-migration method. *Cement and Concrete Research*, 140, 106264.
- Wilson, W., Gonthier, J. N., Georget, F., & Scrivener, K. L. (2022). Insights on chemical and physical chloride binding in blended cement pastes. *Cement and Concrete Research*, 156, 106747.
- Wilson, W., Georget, F., & Scrivener, K. L. (2023a). XCr/\sqrt{t} as an Indicator of the Resistance Against Bulk Chloride Diffusion. *Proceedings of SynerCrete 2023, RILEM Bookseries 43*.
- Wilson, W., Georget, F., & Scrivener, K. L. (2023b). Towards a two-step assessment of the chloride ingress behaviour of new cementitious binders. *Cement and Concrete Research*, Under Review.

Phase Evolution and Property Development of Alkali-Silica Reaction Gel in Carbonation

A. Sinha, and J. Wei*

Department of Civil and Environmental Engineering, University of Massachusetts Lowell, Lowell, United States
Email: arkabrata_sinha@student.uml.com, jianqiang_wei@uml.edu

ABSTRACT

The formation and swelling of alkali-silica reaction (ASR) gels, products of the reaction between amorphous silica from aggregates and alkalis from cement capable of absorbing moisture, are considered the primary mechanism of ASR-induced deteriorations in concrete. To date, the ASR mitigation approaches mainly focus on the incorporation of supplementary cementitious materials and the use of lithium-based admixtures. These traditional approaches possess limitations in the extent of ASR suppression and might compromise concrete performance. Effective ASR mitigation under carbonation has been recently documented but the underlying mechanisms still remain unclear. To fill this knowledge gap, phase evolution and property development of ASR gels under carbonation are investigated in this study. A synthetic ASR gel with a calcium-to-silica ratio of 0.3 and an alkali-to-silica ratio of 1.0 was synthesized and conditioned under 20% CO₂ concentration, 75% relative humidity, and 25°C. The extent of carbonation and phase evolutions were characterized and quantified through X-ray diffraction (XRD), Fourier transform infrared spectroscopy (FTIR), and thermogravimetric analysis (TGA). The modulus of elasticity and hardness of the carbonated ASR gels were measured using nanoindentation, and the moisture uptake capacity was evaluated using dynamic vapor sorption in stepwise relative humidity levels. The results indicate complete conversion of ASR gels into stable carbonates (nahcolite, vaterite, calcite and silica gel) with increased mechanical properties and suppressed hygroscopicity.

KEYWORDS: *Alkali-silica reaction, Mitigation, Carbonation, Phase conversion, Moisture absorption*

1. Introduction

Alkali-silica reaction (ASR) is one of the most deleterious reactions in concrete involving reactions of amorphous silica from reactive aggregates and alkalis from cement to form hygroscopic ASR gels that can absorb moisture, expand, and exert internal stresses to the surrounding concrete. Prior research showed ASR gel has a layered silicate structure with Q³ polymerization sites, which is responsible for the hygroscopic swelling behavior (Geng et al (2020)). The cracks caused by ASR render concrete more permeable by providing pathways for the ingress of external agents into concrete leading to a variety of secondary deteriorations. It was reported that the ASR-induced expansion in concrete can be decreased in the presence of CO₂ due to the carbonation of Ca(OH)₂ and densification of pore structure (Kihara (1997)), reduction of alkalinity in cement pore solution (Wang et al (2022) and Liu et al (2022)). A recent study on ASR gels showed the formation of calcite with enhanced modulus of elasticity (MOE) and hardness after 3 days under a CO₂ concentration of 3% (Narneni and Panesar (2021)). However, the interaction mechanisms between ASR gels and CO₂, and evolutions of phase, structure hygroscopic and mechanical properties of ASR gels under carbonation that can explain the ASR mitigation mechanism have not been explored.

The present study aims to fill this knowledge gap by elucidating the development of the phases, structure, and properties of a synthetic ASR gel during carbonation. The components, crystallization, and functional groups of the ASR gel before and after carbonation were characterized using thermogravimetric analysis (TGA), X-ray diffraction (XRD), and Fourier transform infrared spectroscopy (FTIR). The moisture

absorption and nano-mechanical properties of the raw and carbonated ASR gels were determined through the dynamic vapor sorption (DVS) and nanoindentation tests, respectively.

2. Materials and Methods

2.1 Materials and sample preparation

An ASR gel with a water-to-solid ratio of 0.5, and calcium-silica (Ca/Si) and alkali-silica ((Na+K)/Si) ratios of 0.3 and 1.0, respectively, based on hygroscopic and swelling behavior observed in the authors' previous work, was synthesized via a sol-gel method. The materials used for the synthesis of the ASR gel are reagent-grade calcium hydroxide (>95%), sodium hydroxide (>99%), potassium hydroxide (>97%), and colloidal nano-silica solution with a concentration of 50%, a particle size of 0.02 μm , and an average particle surface area of 180 m^2/g . The detailed synthesis procedure can be found in the authors' previous paper (Luo et al (2022)). The sample was sealed to allow the formation of ASR gel with eliminated interferences from external moisture, oxygen, and carbon dioxide. After 500 days, the ASR gel sample was crushed into powders and carbonated under a CO_2 concentration of 20%, relative humidity (RH) of 75% RH, and a temperature of 25°C for up to 3 days.

2.2 Experimental procedures

The phase evolution of the ASR gel during carbonation was evaluated through (i) XRD by scanning the powdered samples between 5° and 65° 2 θ at a 0.1° step size and step scanning time of 4 seconds using a benchtop XRD equipped with a Cu-K α X-ray source, and (ii) TGA by determining the mass loss of the samples from 30°C to 900°C at a heating rate of 15°C/min under an N_2 inert gas atmosphere. The development of functional groups in the raw and carbonated ASR gels was studied via FTIR spectroscopy by collecting 128 scans in an attenuated total reflection (ATR) mode at a resolution of 4 cm^{-1} .

The hygroscopicity of the raw and carbonated ASR gels was measured using DVS, where the mass changes of the samples were recorded under a constant temperature (25°C) and staged RH. A full desorption-absorption cycle consists of a drying process from 95% to 90% RH followed by a 10% RH decreasing step to 0 RH and a reversed wetting process with the same steps. The mass equilibrium at each RH step was reached when the rate of mass change decreased to 0.0015 mg/min for 10 minutes. The changes in hardness and MOE of ASR gels were evaluated via nanoindentation. The raw and carbonated ASR gels were first dried under a vacuum pressure of 500 mTorr for 24 hours followed by 2-minute compaction into pellets with a diameter of 16 mm under a compaction pressure of 95 MPa to achieve improved particle packing, low surface irregularities, and eliminated preferential orientation of crystals (Hay et al (2022)). The samples were loaded to 2000 μN in 10 seconds, held for 180 seconds, and unloaded at the same rate under a Berkovich diamond tip. The reduced MOE was determined based on the slope of the unloading curve according to the Oliver-Pharr non-linear curve fit method and the hardness was calculated as the ratio of peak load and the projected area of indentation.

3. Results and discussions

3.1 Solid phase evolution

The TGA and differential thermogravimetric (DTG) curves (Figure 1a) show a large weight loss due to the evaporation of free and bound water indicating the high moisture absorption capacity of the raw ASR gel. The decompositions of sodium silicate hydrate (Na-kanemite) at around 230°C and tobermorite at around 275°C indicate the primary products in the ASR gel, which is similar to the real ASR gels collected from the existing ASR-impacted concrete structures and simulated concrete with reactive aggregates (Hou et al (2005)). After 1 day of carbonation, the weight loss of free and bound water disappeared, which indicates the suppressed ASR gel's hygroscopicity. No tobermorite and kanemite were observed with the detections of nahcolite (sodium bicarbonate) between 115° and 225°C, vaterite between 350 and 600°C, and calcite between 600° and 800°C. A small weight loss between 425° and 460°C after 1-day carbonation, suggesting the formation of a transient $\text{Ca}(\text{OH})_2$, which became undetectable after 3 days of carbonation as it was carbonated into vaterite.

The XRD pattern of raw ASR gel shows a semi-crystalline structure with distinct peaks at 29.4° , 31.9° , and 49.9° 2θ indicating the presence of tobermorite, a C-S-H-like mineral with a layered silicate structure, while the broad peak between 25° and 35° 2θ signify the existence of amorphous Na- and K-kanemite (Figure 1b), which agrees with the results in Hou et al (2005) and our TGA results. After 1 day of carbonation, enhanced crystallinity of the ASR gel indicated by the replacement of semi-crystalline and broad peaks of tobermorite and kanemite with the sharp peaks of carbonates (nahcolite, vaterite, and calcite) was observed. In line with the findings from TGA, the enhanced nahcolite from 1 to 3 days indicate further carbonation in the sodium silicate phases whereas the contents of vaterite and calcite did not exhibit increases. The FTIR spectra of the raw ASR gel show the presence of Si-O-Si ($800\text{--}600\text{ cm}^{-1}$) and Si-O ($1100\text{--}900\text{ cm}^{-1}$) bonds (see Figure 1c). The Q^2 polymerization of tobermorite and kanemite is indicated by the bands at 900 cm^{-1} and 966 cm^{-1} . The Q^3 site in tobermorite and kanemite, a unique feature of ASR gels causing hygroscopic swelling, is signified by a peak at 1056 cm^{-1} . After 1 day of carbonation, Q^2 and Q^3 polymerization sites were replaced by Q^4 sites due to the formation of free silica triggered by the decalcification of ASR gel during carbonation. The bands at 876 cm^{-1} and 1425 cm^{-1} indicate the formation of C=O and CO_3^{2-} functional groups in calcite and vaterite, while the peaks at 695 cm^{-1} , 836 cm^{-1} , 1055 cm^{-1} , 1450 cm^{-1} , and 1680 cm^{-1} indicate the formation of C-O and OH⁻ in nahcolite. The decreased HOH band in water detected from the raw ASR gel (1650 cm^{-1}) and the absence of the broad band for free and bound water (between 2500 and 3700 cm^{-1}) indicate the mitigated hygroscopicity in the carbonated ASR gel. In line with the XRD results, no significant change was observed in vaterite and calcite bands from 1 to 3 days of carbonation but the bands in nahcolite showed a slight increase.

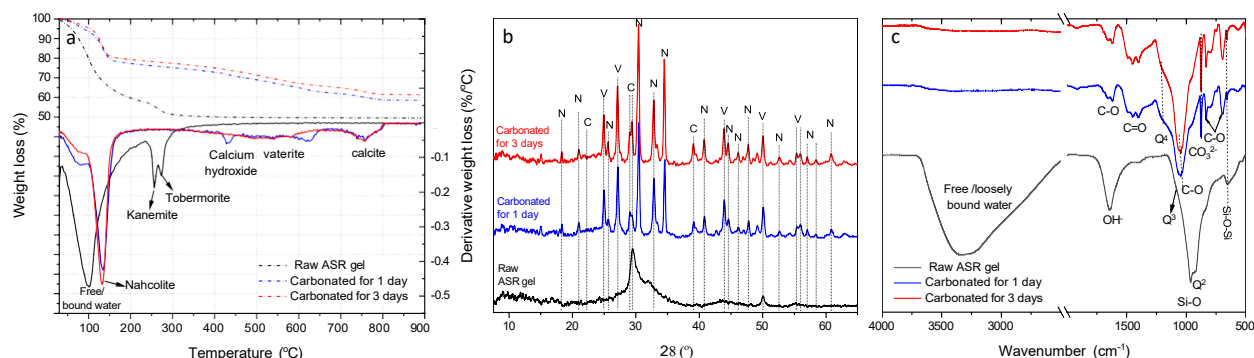


Figure 1. (a) TGA/DTG, (b) XRD, and (c) FTIR results of the raw and carbonated ASR gels (C-Calcite, N-Nahcolite and V-Vaterite).

3.2 Moisture sorption behavior

The raw ASR gel exhibited a total desorption of 146.2% and absorption of 145.9% in the drying and wetting cycles, respectively, between 95% and 0 RH (Figure 2a). A majority (83%) of total mass change was observed between 70% and 95% RH, indicating a high hygroscopicity of the ASR gel in a humid environment and the potential for deleterious swelling. After 3 days of carbonation, the ASR gel showed 26.7% and 9.5% reductions in the overall desorption and absorption, respectively. The non-swelling free silica gel formed during the decalcification of ASR gel, a known desiccant with abundant Q^4 silica polymerization and capable of imbibing moisture, might be the reason for the remarkable absorption of the carbonated ASR gel at the RH levels over 80%.

3.3 Mechanical properties

Based on nanoindentation, the raw ASR gel showed an average MOE and hardness of 1.16 GPa and 0.03 GPa (Figure 2b), respectively, which are lower than the previously reported values (Narneni and Panesar (2021)). This is most likely due to the lower Ca/Si ratio (0.409 vs. 0.3) adopted in this study, as well as the difference in sample synthesis and preparation (in-situ measurement vs. measurement on pellet samples). After carbonation, the MOE and hardness of the ASR gel increased by 79.3% and 267%, respectively, which indicates the conversion of ASR products into carbonates with enhanced crystallization is favorable to enhance the overall mechanical properties. It is worth noting that the uneven distribution of calcium-rich products (calcite and vaterite) during carbonation might be a reason for the increased standard error in the

MOE and hardness of the carbonated ASR gel. Further studies on the microstructure and molecular structure of carbonated ASR gels are necessary to get better into the evolution of mechanical properties.

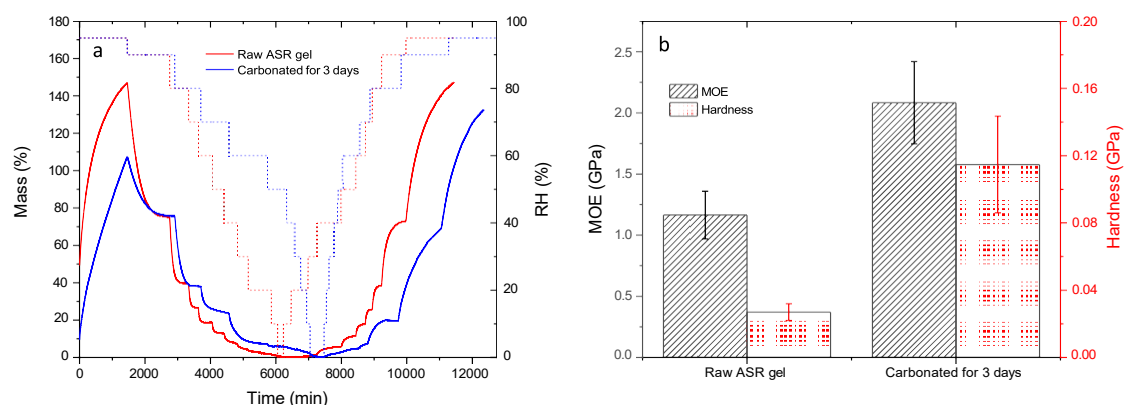


Figure 2. (a) DVS and (b) nanomechanical properties of the ASR gel before and after carbonation.

4. Conclusions

In this study, the carbonation behavior of a synthetic ASR gel under a CO₂ concentration of 20% for up to 3 days was investigated in terms of phase evolution and developments of hygroscopicity and mechanical properties. Before carbonation, the raw ASR gel consists of tobermorite and Na- and K-kanemite as the main components. During carbonation, conversions of tobermorite and kanemite into nahcolite, vaterite, and calcite were observed. As a result, the Q² and Q³ polymerization sites of ASR gel were converted into Q⁴ sites due to the formation of silica gel and C-O and C=O bonds in the formed carbonates. The overall reductions in moisture desorption and absorption of the ASR gel and increases in MOE and hardness indicate the suppressed hygroscopicity of ASR gels after carbonation along with improved stiffness and enhanced crystallinity.

Acknowledgments

The authors would like to thank the support from National Science Foundation (NSF) under award No. 1935799 and the U.S. Department of Transportation (DOT) for partially supporting this research through a University Transportation Center (UTC) Standard Federal Region 1 Transportation Infrastructure Durability (TIDC) Project 3.19.

References

- Geng, G., Shi, Z., Leemann, A., Borca, C., Huthwelker, T., Glazyrin, K., ... & Wieland, E. (2020) "Atomistic structure of alkali-silica reaction products refined from X-ray diffraction and micro X-ray absorption data", *Cement and Concrete Research*, 129, 105958.
- Hay, R., Li, J., & Celik, K. (2022). Phase evolution, micromechanical properties, and morphology of calcium (alumino) silicate hydrates C-(A-) SH under carbonation. *Cement and Concrete Research*, 152, 106683.
- Hou, X., Kirkpatrick, R. J., Struble, L. J., & Monteiro, P. J. (2005) "Structural investigations of alkali silicate gels", *Journal of the American Ceramic Society*, 88(4): 943-949.
- Liu, Z., Shi, C., Shi, Q., Tan, X., & Meng, W. (2022) "Recycling waste glass aggregate in concrete: Mitigation of alkali-silica reaction (ASR) by carbonation curing", *Journal of Cleaner Production*, 370, 133545.
- Luo, D., Sinha, A., Adhikari, M., & Wei, J. (2022) "Mitigating alkali-silica reaction through metakaolin-based internal conditioning: New insights into property evolution and mitigation mechanism", *Cement and Concrete Research*, 159, 106888.
- Narneni, S. R., & Panesar, D. K. (2021) "The Response of Synthetic Alkali-Silica Reaction Products to Carbonation", *Proceedings of the 3rd RILEM Spring Convention and Conference (RSCC 2020) Volume 2: New Materials and Structures for Ultra-durability*, 3:119-130
- Wang, Y., Mo, K. H., Du, H., & Ling, T. C. (2022) "Effects of CO₂ curing treatment on alkali-silica reaction of mortars containing glass aggregate", *Construction and Building Materials*, 323, 126637.

L-Ascorbic Acid used as green corrosion inhibitor in chloride-bearing steel reinforced cement mortars

C. Argiz^{1*}, C. Arroyo¹, A. Bravo¹, A. Moragues¹, C. Andrade² and F. Bolzoni³

¹ E.T.S.I. Caminos, Canales y Puertos, Universidad Politécnica de Madrid, Madrid, Spain
Email: celia.arroyo@alumnos.upm.es; av.bravo@alumnos.upm.es; amparo.moragues@upm.es

² International Center for Numerical Methods in Engineering (CIMNE), Madrid, Spain
Email: candrade@cimme.upc.edu

³ Politecnico di Milano, 20133 Milano, Italy
Email: fabio.bolzoni@polimi.it

*Correspondence: Email: cg.argiz@upm.es

ABSTRACT

Corrosion inhibitors in reinforced concrete structures can be considered as a quite efficient procedure to minimize or prevent corrosion of reinforced concrete structures because it can be applied in a rapid and easy way. The aim of this work is to study the effect of ascorbic acid (AA) as a green corrosion inhibitor in comparison with the performance offered by sodium nitrite. Efficacy of both inhibitors tested with 2% of chloride ions was about 97%. However, it should be noted that the molar ratio between the chloride ion and the nitrite or AA is quite different, i.e., $[Cl^-]/[NO_2^-] = 1$ y $[Cl^-]/[AA] = 1129$. Both, inhibitors and chloride ions, were added to the mortar mixing water to ensure their contact with the reinforcement at once. Electrochemical testing methods, i.e., corrosion potential measurements (E_{corr}) and linear polarization resistance (LPR) were used to evaluate the corrosion rate of the steel reinforcement embedded in mortars. The results showed that the ascorbic acid could be either a corrosion activator or an effective corrosion inhibitor depending on its concentration in a similar way to sodium nitrite. Concentrations of ascorbic acid below 10^{-2} mol/L promote a corrosion rate decrease. Furthermore, it was found that the optimum concentration of ascorbic acid is 10^{-3} mol/L.

KEYWORDS: *green corrosion inhibitor, ascorbic acid, nitrites, chloride-contaminated mortars*

1. Introduction

Sodium and calcium nitrites are well-known anodic corrosion inhibitors in concrete. These inhibitors have been in use for some time for corrosion protection (Bolzoni et al 2022; Rozenfel'd, 1981). Nevertheless, their utilization was not always supported due to their unfavourable toxicity profile. The requirements of sustainability and quality of products in the construction sector are the use of low-cost, non-hazardous, and environmentally friendly materials. Therefore, biocompatible inhibitors, which are named as “green” inhibitors, is currently booming. Accordingly, L-ascorbic acid (C₆H₈O₆) or vitamin C (AA), which is a hydro-soluble weak dibasic acid is a potential “green” inhibitor. In addition, it is a free-radical scavenger and a strong antioxidant. Only few papers on the performance of the ascorbic acid as a “green” corrosion inhibitor have been published.

Valek et al (2008) have reported that a concentration of 10^{-3} mol/L of ascorbic acid reaches the optimum inhibition in saturated Ca(OH)₂ solutions with 0.14 mol/L of chlorides. By contrast, the inhibition effect decreases at higher AA concentrations as consequence of the iron chelates formation.

The object of this paper is to assess the effectiveness of the ascorbic acid as a potential corrosion inhibitor in mortar samples in comparison to the sodium nitrite, which is a well-known corrosion inhibitor. For this purpose, corrosion potential and linear polarization resistance measurements were made on mortar specimens.

2. Materials and Methods

2.1 Materials

A common Portland cement CEM I 52.5 R-SR3 (EN 197-1:2011), which chemical composition is shown in Table 1, was employed to manufacture the mortar specimens. Two steel corrosion inhibitors were assessed, i.e., L(+)-ascorbic acid (AA) and NaNO₂.

Table 1. CEM I 52.5 R-SR3 chemical composition (%).

| SiO ₂ | Al ₂ O ₃ | Fe ₂ O ₃ | CaO | MgO | SO ₃ | K ₂ O | Na ₂ O | TiO ₂ | P ₂ O ₅ | Cl ⁻ | LOI |
|------------------|--------------------------------|--------------------------------|------|------|-----------------|------------------|-------------------|------------------|-------------------------------|-----------------|-----|
| 20.7 | 3.5 | 4.5 | 64.3 | 1.05 | 2.48 | 0.53 | 0.36 | 0.28 | 0.13 | 0.04 | 1.7 |

Mortar specimens of $8 \times 5.5 \times 2$ cm³ described by Alonso et al (2000), with cement:sand:water proportions of 1:3:0.5 were made. Two corrugated steel bars of 6 mm in diameter by 90 mm in length were embedded in the mortars. An insulating tape was utilized to limit an exposed area of 5.65 cm². Table 2 shows the concentrations of ascorbic acid added to the mixing water. In addition, a reference mortar made with 2.6% of NO₂⁻ ions by weight of cement (1.13 mol/L of NO₂⁻) was made.

Table 2. Ascorbic acid content in mortar specimens.

| Ascorbic acid concentration | | | | | | | |
|-----------------------------|---|-------|-------|-------|-------|-------|-------|
| mol/L | 0 | 0.5 | 0.1 | 0.05 | 0.01 | 0.005 | 0.001 |
| (% by weight of cement) | 0 | 4.403 | 0.881 | 0.440 | 0.088 | 0.044 | 0.009 |

All the mortar specimens were made with a concentration of 2% of Cl⁻ by weight of cement (1.13 mol/L of Cl⁻ ions), which were added to the mixing water.

2.2 Methods

Corrosion potential and linear polarization resistance measurements were performed in the mortar specimens by using an Autolab PGSTAT 204 potentiostat/galvanostat and through a 3 M KCl Ag/AgCl (Metrohm) reference electrode. The open circuit potential (OCP) and linear polarization resistance values were determined from the $\Delta E/\Delta I$ slope by applying a potential ± 20 mV at the corrosion potential at a rate of 0.1667 mV/s. The corrosion current density (I_{corr}) was calculated from the Stern and Geary equation: $I_{\text{corr}} = B/R_p$, Stern and Geary (1957), considering a constant value of $B = 26$ mV.

3. Results and discussion

3.1. Electrochemical Measurements

The open circuit potential (OCP) data were recorded periodically to a maximum of seventyfive days. Figure 1a shows the results of the chloride-contaminated mortars with 4.4, 0.88 and 0.44% of AA and 2.6% of NO₂⁻ by weight of cement. It can be appreciated that all the specimens exhibited potentials about -700 to -500 mV indicating active corrosion of the steel reinforcement. Such corrosion risk assessment is based on the ASTM C876-15 criteria.

The steel embedded in the mortar made with nitrites has a corrosion potential of -500 mV, which is the less negative (noble) corrosion potential. Figure 1b shows the corrosion current density (I_{corr}) vs. time. The corrosion current density values with regard to the reinforced concrete service life are given in the RILEM TC 154-EMC Recommendations. As the I_{corr} results of the mortars made with nitrite are below 0.1 $\mu\text{A}/\text{cm}^2$, it is conducted that non-significant corrosion is recorded. By contrast, higher I_{corr} results ranging from 1.5 to 25 $\mu\text{A}/\text{cm}^2$ were measured in mortars made with ascorbic acid inhibitor, stating steel bars active corrosion. Summing up, the greater the AA content, the greater corrosion current density is.

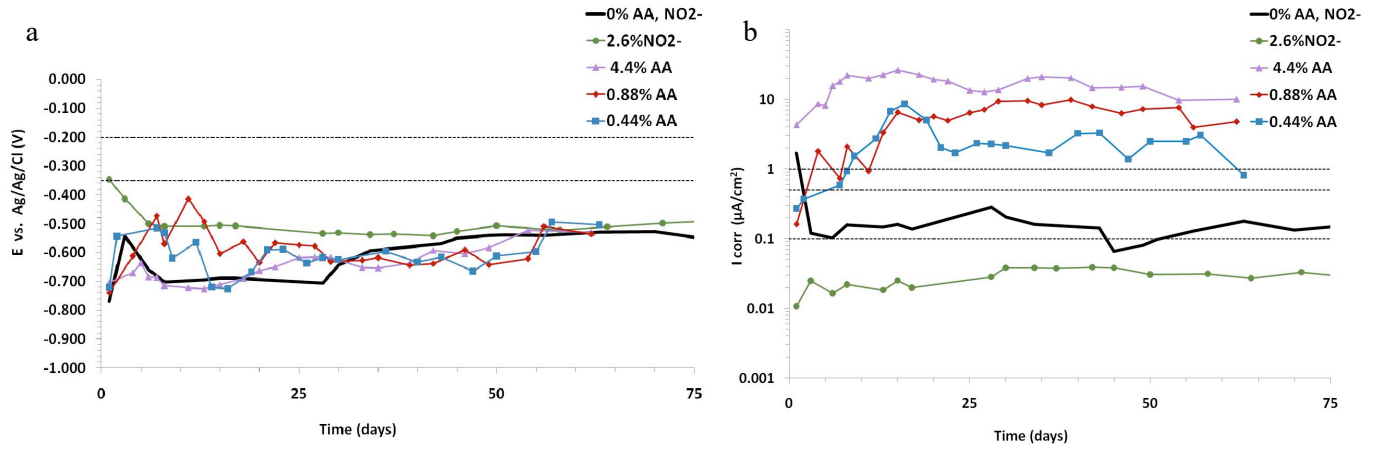


Figure 1. Reinforced mortars made with chlorides and 4.4; 0.88 and 0.44% of AA or 2.6% of NO_2^- (a) OCP, (b) I_{corr} .

The corrosion potential up to 240 days of chloride-bearing mortars with 0.088, 0.044 and 0.009% of ascorbic acid, a blank mortar with only chlorides and a reference mortar with 2.6% of NO_2^- with chlorides is shown in Figure 2a. From 100 days, nitrite mortars and those with 0.009% AA exhibited a shift towards more positive potential values (-200 mV) indicating passivation of the rebars. Mortars with 0.044 and 0.088% of AA would need longer exposition to achieve passive potentials.

Corrosion current density (Figure 2b) of the mortar made only with chlorides began above $0.1 \mu\text{A}/\text{cm}^2$, but later, it increases beyond $0.5 \mu\text{A}/\text{cm}^2$, showing a high corrosion risk. By contrast, a low content of ascorbic acid sharply reduces these values. Accordingly, the steel passive state, i.e., $I_{\text{corr}} < 0.1 \mu\text{A}/\text{cm}^2$ was achieved with at least 0.044% AA. Mortars made with 0.009% AA and nitrite ions lower the corrosion rate to levels between 0.05 and $0.005 \mu\text{A}/\text{cm}^2$. The lower the ascorbic acid content, the greater the inhibitory efficiency of ascorbic acid in chloride induced corrosion environments. Furthermore, low ascorbic acid contents show similar inhibitory results to nitrite ions.

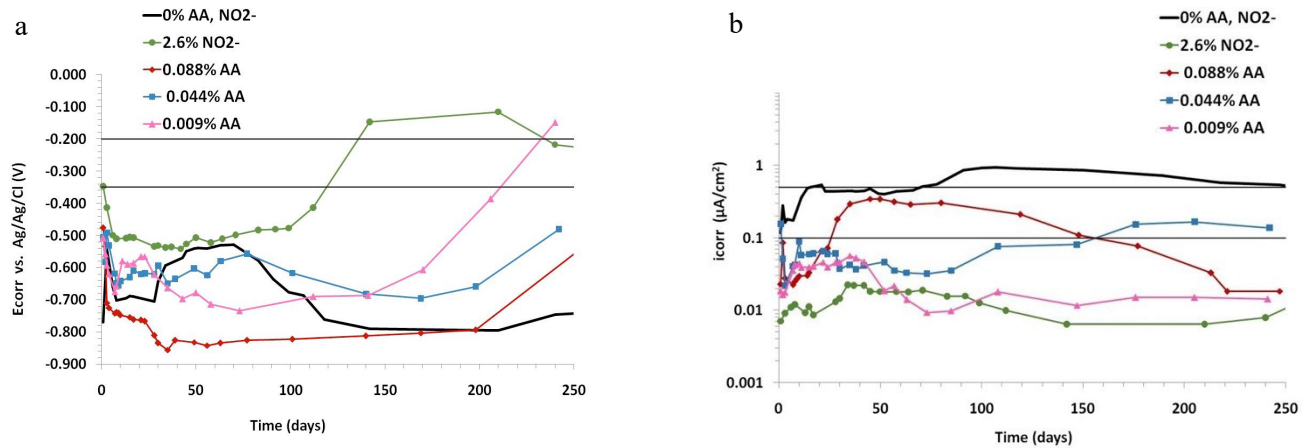


Figure 2. Effect of AA and NO_2^- in chloride-contaminated mortars (a) OCP; (b) I_{corr} .

Inhibitory efficiency η (%) determined following Equation (1) from the integral under the corrosion current density of mortars without (I_{corrRef}) and with (I_{corrInh}) inhibitor.

$$\eta(\%) = \frac{I_{\text{corrRef}} - I_{\text{corrInh}}}{I_{\text{corrRef}}} \times 100 \quad (1)$$

In chloride-bearing mortars the inhibitory efficiency increases with the lowering of ascorbic acid content. Thus, the inhibitory efficiency of 97.3% found in the 0.009% of AA was like the inhibitory effectiveness of the 2.6% nitrite (97.8%) as shown in Table 3.

Table 3. Inhibitory efficiency η (%) of 2% chloride-bearing mortars.

| Inhibitor Content | Inhibitory efficiency η (%) |
|----------------------|----------------------------------|
| 0.088% AA | 78.5 |
| 0.044% AA | 87.4 |
| 0.009% AA | 97.3 |
| 2.6% NO_2^- | 97.8 |

4. Conclusion

The following conclusions can be drawn:

1. Ascorbic acid is a reliable corrosion inhibitor for steel embedded in chloride-bearing mortars. The effectiveness depends on the inhibitor concentration in the mortar. Higher concentrations than 10^{-2} mol/L, i.e., 0.088% AA, could promote the opposite effect, i.e., an increase of the corrosion rate of the steel embedded in the mortar. By contrast, lower inhibitor concentrations reduce the corrosion rate induced by chloride ions.
2. The greatest efficiency (IE = 97.3%) of ascorbic acid as a corrosion inhibitor was found with 10^{-3} mol/L (0.009% AA), which is similar (IE = 97.8%) to that found with a concentration of 1.13 mol/L of NO_2^- (2.6% NO_2^-). Finally, it should be noted that the chloride ion/ascorbic acid molar ratio, i.e., $\text{Cl}^-/\text{AA} = 1,129$, for this concentration of ascorbic acid is 1000 times higher than the chloride-nitrite molar ratio ($\text{Cl}^-/(\text{NO}_2^-) = 1$).

5. References

- Bolzoni, F., Brenna, A. and Ormellese, M. (2022) “Recent Advances in the Use of Inhibitors to Prevent Chloride-Induced Corrosion in Reinforced Concrete”, *Cement and Concrete Research*, 154: 106719, doi:<https://doi.org/10.1016/j.cemconres.2022.106719>.
- Rozenfel'd, I.L. *Corrosion Inhibitors*; McGraw-Hill: New York, 1981; ISBN 978-0-07-054170-2.
- Valek, L., Martinez, S., Mikulić, D. and Brnardić, I. (2008) “The Inhibition Activity of Ascorbic Acid towards Corrosion of Steel in Alka-line Media Containing Chloride Ions”, *Corrosion Science*, 50:, 2705–2709, doi:[10.1016/j.corsci.2008.06.018](https://doi.org/10.1016/j.corsci.2008.06.018).
- Alonso, C., Andrade, C., Castellote, M. and Castro, P. (2000) “Chloride Threshold Values to Depassivate Reinforcing Bars Embedded in a Standardized OPC Mortar”, *Cement and Concrete Research*, 30: 1047–1055, doi:[10.1016/S0008-8846\(00\)00265-9](https://doi.org/10.1016/S0008-8846(00)00265-9).
- Stern, M. and Geary, A.L. (1957) “Electrochemical Polarization”, *Journal of the Electrochemical Society*, 104: 56–63.
- ASTM C876-15; Standard Test Method for Corrosion Potentials of Uncoated Reinforcing Steel in Concrete. ASTM International: West Conshohocken, PA, USA, 2016.
- Polder, R.B. (2001) “Test Methods for on Site Measurement of Resistivity of Concrete — a RILEM TC-154 Technical Recommendation”, *Construction and Building Materials*, 15: 125–131, doi:[10.1016/S0950-0618\(00\)00061-1](https://doi.org/10.1016/S0950-0618(00)00061-1).

Carbonation of Concrete with SCMs: a data analysis by RILEM TC 281-CCC

A. Vollpracht^{1*}, C. Thiel², Z. Zhao³, Y.A. Villagrán Zaccardi⁴, G.P. Cordoba⁵, G.J.G. Gluth⁶, H. Vanoutrive⁷, E. Gruyaert⁷, A. Kanellopoulos⁸, R. Mi⁹ and N. De Belie¹⁰

¹ Institute of Building Materials Research, RWTH Aachen University, Aachen, Germany
Email: vollpracht@ibac.rwth-aachen.de

² Laboratory for Construction Materials, OTH Regensburg University of Applied Sciences Regensburg, Germany
Email: charlotte.thiel@oth-regensburg.de

³ Research Group for Recycled Concrete Structures and Construction, College of Civil Engineering, Tongji University, Shanghai, China. Email: zengfengzhao@tongji.edu.cn

⁴ Flemish Institute for Technological Research (VITO), Mol, Belgium; Email: yury.villagranzaccardi@vito.be

⁵ Faculty of Engineering, Research Center in Physics and Engineering, National University of the Center of Buenos Aires Province, Olavarría, Argentina. Email: gcordova@fio.unicen.edu.ar

⁶ Division 7.4 Technology of Construction Materials, Bundesanstalt für Materialforschung und -prüfung (BAM), Berlin, Germany. Email: gregor.gluth@bam.de

⁷ Department of Civil Engineering, Materials and Constructions, KU Leuven, Ghent Campus, Ghent, Belgium
Email: hanne.vanoutrive@kuleuven.be and elke.gruyaert@kuleuven.be

⁸ Centre for Engineering Research, School of Physics, Engineering & Computer Science, University of Hertfordshire, Hertfordshire, UK. Email: a.kanellopoulos@herts.ac.uk

⁹ Department of Civil and Environmental Engineering, Hong Kong Polytechnic University, Hong Kong, China
Email: renjie.mi@polyu.edu.hk

¹⁰ Magnel-Vandepitte Laboratory, Department of Structural Engineering and Building Materials, Ghent University, Ghent, Belgium. Email: Nele.DeBelie@UGent.be

ABSTRACT

The RILEM TC 281–CCC “Carbonation of concrete with supplementary cementitious materials” is studying the effect of supplementary cementitious materials (SCMs) on natural and accelerated carbonation of blended cements. In this context a large database with carbonation depths over time has been set-up with currently 910 concrete and mortar mixes, which have been tested at different curing conditions. The collected data includes information on chemical composition and physical properties of the raw materials, on mix-design, compressive strength, curing and carbonation testing conditions. Data for a large variety of binders (with up to 94 % SCMs) and mix designs (with w/b ratios ranging from 0.26 to 0.75) were collected from the literature and unpublished material testing projects. Natural carbonation was recorded for several years in many cases, and indoor as well as outdoor results are included. However, in this contribution only lab conditions are considered. Carbonation kinetics are investigated considering the binder composition and mix design. Furthermore, the accuracy of accelerated carbonation testing is evaluated. As described in literature, the w/CaO_{reactive}-ratio is a decisive factor for carbonation resistance but curing and exposure conditions influence the results as well. Even with identical test conditions, the scatter is very large.

KEYWORDS: *natural carbonation, accelerated carbonation, SCMs, database*

1. Introduction

In order to study the effects of concrete composition, curing, pre-storage and exposure conditions on carbonation kinetics the RILEM TC 281–CCC “Carbonation of concrete with supplementary cementitious materials” has been setting up a database for carbonation experiments. In each case the phenolphthalein test was used to measure the carbonation depth at different carbonation times. Currently the database includes 910 concrete and mortar mixes, which contain the following binders / binder components:

- 90 Portland cements (CEM I)
- 97 Portland composite cements (CEM II)
- 63 blast furnace slag cements (CEM III)
- 62 silicious fly ashes, one calcareous fly ash
- 28 ground granulated blast furnace slags (GGBS)
- 16 calcined clays and 3 natural pozzolans
- 4 silica fumes

Due to the amount of available data, this conference paper focuses on mixes with silicious fly ashes and GGBSs as binary or ternary mixes and compares the carbonation kinetics to pure Portland cement recipes. In the first step the carbonation rate is fitted (s. paragraph 2), afterwards some of the influencing factors pointed out in the literature review of the TC (von Greve-Dierfeld et al. (2020)) are further investigated with the collected data. The references of the database cannot all be listed here; they will be published in conjunction with the database elsewhere.

2. Determination of Carbonation Rate

Based on the measured carbonation depths d_c within the first year, the carbonation rate k_c is calculated as the slope of a best fit line of d_c vs. \sqrt{t} as shown in Fig. 1 (a). Often the calculated initial carbonation depth is not zero (see Fig. 1 (b)). Since a negative intercept is not possible from a physical point of view, the intercept is fixed at zero in these cases (dashed line in Fig 1 (b)). For accelerated carbonation the testing times are shorter, nevertheless the carbonation rate was determined in the same way. Some authors only tested one point in time. In these cases, the intercept was assumed to be zero.

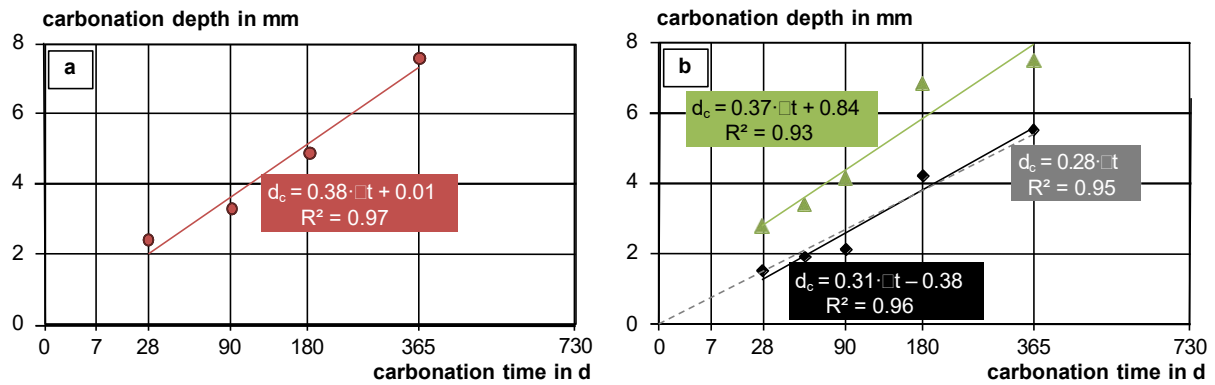


Fig. 1: Determination of carbonation rate; (a) ideal example of best fit; (b) best fit with intercept

3. Natural Carbonation

3.1 Impact of $w/\text{CaO}_{\text{reactive}}$

The amount of CaO available to react with CO_2 plays an important role for the carbonation resistance. For this evaluation, the reactive CaO was calculated according to equation (1), assuming that CaO in GGBS and FA glass is taking part in the hydration and carbonation reactions.

$$\text{CaO}_{\text{reactive}} = \text{CaO}_{\text{total}} - \text{CaO}_{\text{CaCO}_3 \text{ init}} - \text{CaO}_{\text{CaSO}_4} \quad (1)$$

The water/binder ratio is determining the porosity and thereby the diffusion coefficient of CO_2 in concrete. The ratio $w/\text{CaO}_{\text{reactive}}$ is an approach to combine both effects. Fig. 2 shows the results for the different binder types tested in laboratory conditions. For most binders the carbonation rates after 2 d of curing are higher than the average line for 7 d, indicating that the hydration degree at the beginning of the carbonation test was too low. Most results for 3 and 4 d of curing fall in the range of the 7 d curing results. All binder types show the expected trend towards increasing carbonation rates with increasing $w/\text{CaO}_{\text{reactive}}$, but the scatter is quite high. The difference between the binder types is relatively small, only the ternary blends seem to give slightly higher carbonation rates.

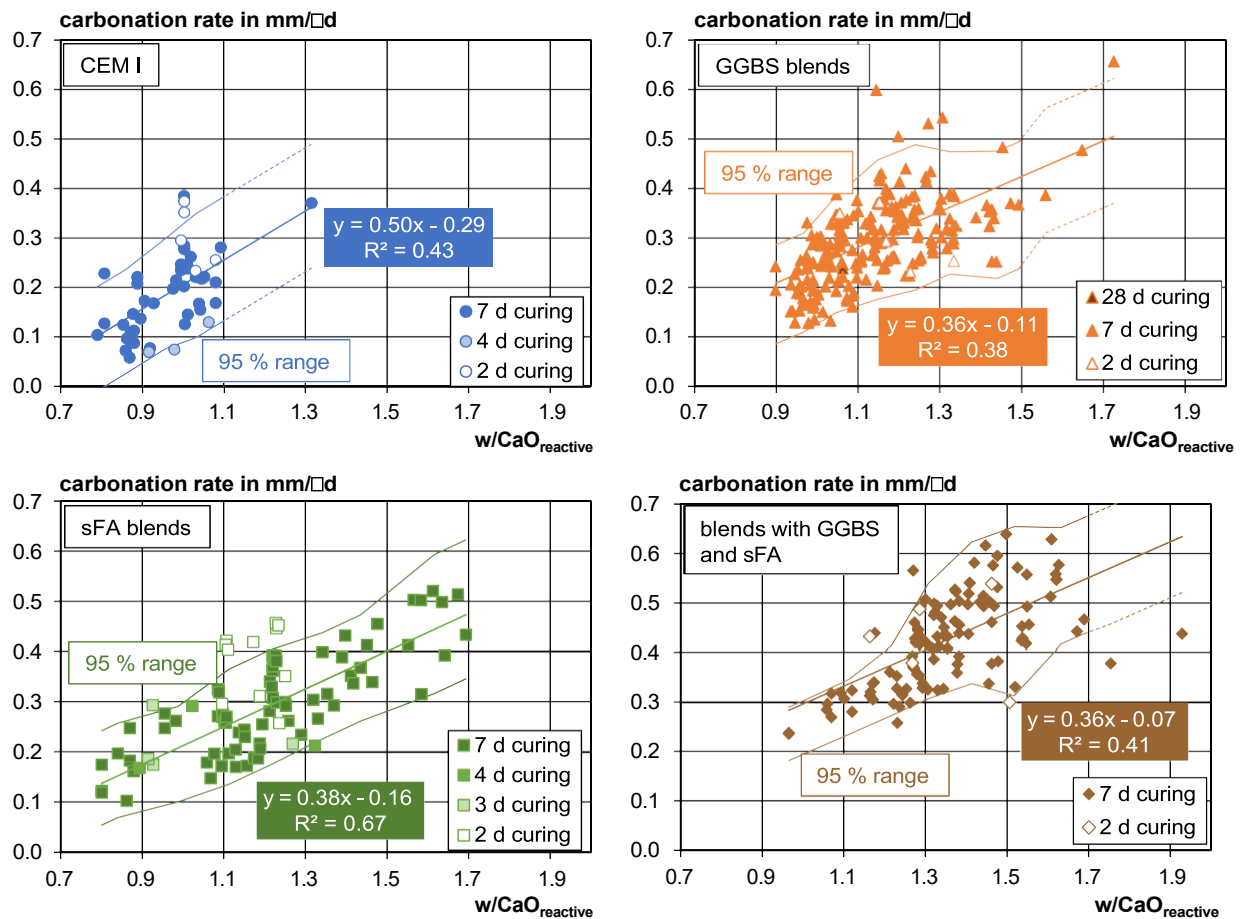


Fig. 2: Carbonation rate vs. $w/\text{CaO}_{\text{reactive}}$ for natural carbonation at 20 °C and 65 % RH for different binder types and curing conditions (comment: the best fit line and 95 % range apply for 7 d curing)

The correlation could possibly be improved by considering unreacted CaO in the SCMs and the cement clinker (hydration degree). However, this information is not available in most cases. It has to be considered that repeatability and reproducibility of the test itself contribute to the scatter (see Vanoutrive (2022)).

3.2 Binder Content

As a further influencing factor, the binder content was considered since mixes with higher binder contents may offer a higher CO_2 consumption. Fig. 3 shows the results at two exemplary $w/\text{CaO}_{\text{reactive}}$ -ratios.

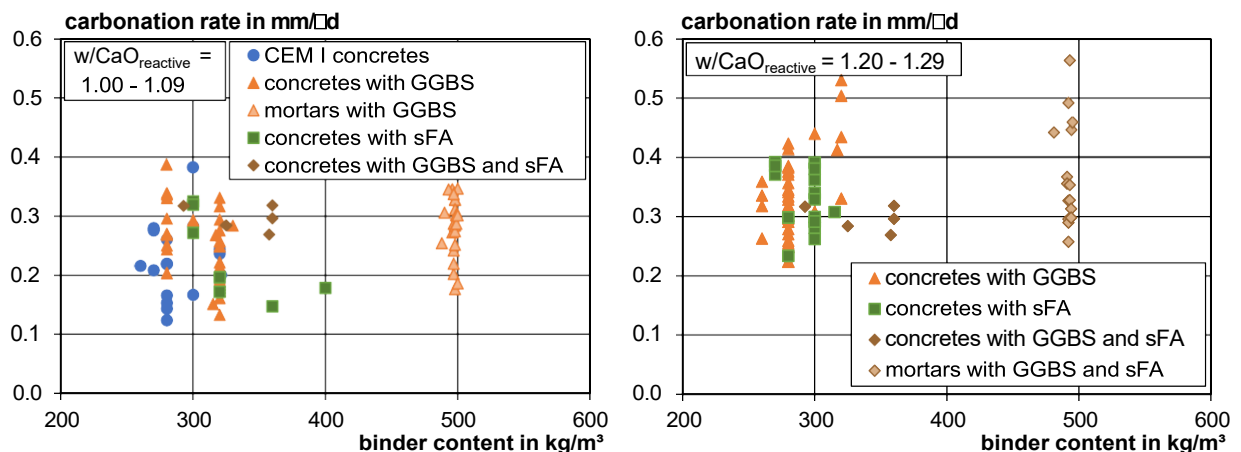


Fig. 3: Carbonation rate vs. binder content for natural carbonation at 20 °C and 65 % RH after 7 d of curing

It is obvious that the binder content is not relevant as long as $w/\text{CaO}_{\text{reactive}}$ stays constant. This also means that there is no systematic difference between mortar and concrete.

4. Accelerated Carbonation

At the current status, the database contains significantly fewer datasets on accelerated carbonation than on natural carbonation. The CO_2 concentration ($\text{CO}_{2\text{acc}}$) varies between 1 and 4 vol.-%. All samples were preconditioned at a relative humidity between 55 and 70 % for at least 14 days. Using the experimental carbonation rate in the accelerated tests, the carbonation rate under natural conditions was calculated using the theoretical factor of $\square(\text{CO}_{2\text{nat}}/\text{CO}_{2\text{acc}})$ with $\text{CO}_{2\text{nat}} = 0.04$ vol.-%. In Fig. 4 the predicted carbonation rate is plotted vs. the measured natural carbonation rate.

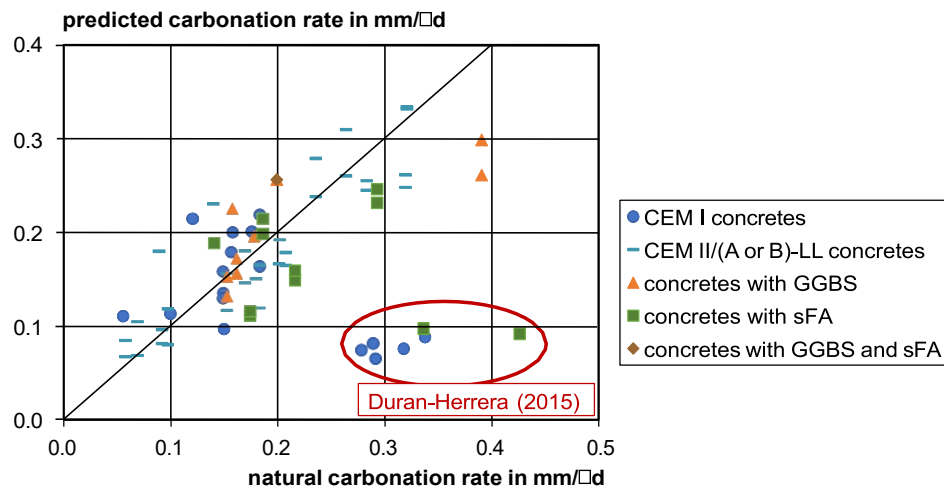


Fig. 4: Comparison between the predicted carbonation rate (based on accelerated carbonation tests) and the experimentally determined carbonation rate in natural conditions

Considering the scatter of carbonation testing, the compliance is relatively good, only the results of one reference are far of the line. Additional data shall be used to support these findings. Some results are currently being generated in a round robin test of TC 281-CCC.

5. Conclusions

The implemented carbonation database offers the possibility to determine the influence of mix-design, curing, pre-storage and exposure conditions on carbonation resistance of concrete. New raw materials can be evaluated based on the existing data and different test methods can be compared. In this contribution only a few aspects could be illuminated. The data collection is still ongoing, finally the database shall be published to offer the possibility for individual evaluations. This preliminary analysis of international data supports the idea of the $w/\text{CaO}_{\text{reactive}}$ as an efficient universal parameter to describe the combined effects of transport properties and buffer capacity in concrete with different types of binders.

References

- von Greve-Dierfeld, S. et al (2020) "Understanding the carbonation of concrete with supplementary cementitious materials: a critical review by RILEM TC 281-CCC", *Materials and Structures*, 53:136 (34 pages)
- Vanoutrive, H. et al. (2022) "Report of RILEM TC 281-CCC: outcomes of a round robin on the resistance to accelerated carbonation of Portland, Portland-fly ash and blast-furnace blended cements", *Materials and Structures*, 55:99 (29 pages)
- Duran-Herrera, A. et al (2015) "Accelerated and natural carbonation of concrete with internal curing and shrinkage/viscosity modifiers", *Materials and Structures*, 48:1207-1214

Towards the Development of Prescriptive-Based Specifications for Non-Traditional SCMs to Prevent Alkali-Silica Reaction

K.S.T. Chopperla^{1*} and J.H. Ideker²

¹ Oregon State University, Corvallis, OR, USA
Email: krishna.chopperla@oregonstate.edu

² Oregon State University, Corvallis, OR, USA
Email: Jason.Ideker@oregonstate.edu

ABSTRACT

Current specifications in standard guides for preventing alkali-silica reaction (ASR) such as ASTM C1778 are limited to traditional supplementary cementitious materials (SCMs). As the availability of traditional SCMs is reducing, the use of non-traditional SCMs has increased and there is a need to develop prescriptive-based specifications to prevent ASR for them. In addition, the current specifications are based on only the chemical composition of the SCMs and do not consider the reactivity of SCMs. This paper discusses potential ways to improve the current prescriptive-based specification by including the reactivity of SCMs in addition to the chemical composition. Another approach based on proposing alkali loading limits of concrete and minimum SCM amounts required to prevent ASR in concrete mixtures with reactive aggregates for different alkali threshold values is discussed. Additional research that is needed to improve prescriptive-based specifications to prevent ASR using non-traditional SCMs is discussed.

KEYWORDS: *Alkali-silica reaction, Supplementary cementitious materials, Specifications, Pozzolanic reactivity, Alkali sensitivity.*

1. Introduction

Alkali-silica reaction (ASR) is a chemical reaction between alkali hydroxides in the pore solution of concrete and reactive silica of aggregates to form expansive products that may crack the concrete. Above a certain pore solution alkalinity (alkali threshold), reactive aggregates will cause expansion in concrete due to ASR (Thomas et al. 1996). Using supplementary cementitious materials (SCMs) in concrete with reactive aggregates is the most used strategy to prevent ASR. Using appropriate amount of SCM(s) can prevent ASR as their usage reduces alkalinity of concrete pore solution from dilution effects and alkali binding by pozzolanic reaction products (Thomas 2011). In addition, alumina in SCMs can reduce silica dissolution from aggregates and usage of SCMs can reduce transport of external alkalis and moisture thus limiting the reaction (Chappex and Scrivener 2013, Thomas 2011).

Standard guides such as ASTM C1778, “Standard Guide for Reducing the Risk of Deleterious Alkali-Aggregate Reaction in Concrete”, includes specifications to prevent ASR using traditional SCMs such as coal ashes, slag, and silica fume. As there has been an increase in short supply of traditional SCMs such as coal ashes in the recent years, interest in the use of non-traditional SCMs such as natural pozzolans, harvested ashes, blended pozzolans, and ground glass has increased (Juenger et al. 2019). It is reported that non-traditional SCMs are reported to have a large variability in their composition and reactivity (Juenger et al. 2019). Therefore, it requires careful characterization of non-traditional SCMs for developing specifications for their use in concrete to prevent ASR.

The current prescriptive-based specifications recommend minimum amounts of SCMs to be used to prevent ASR are based on the chemical composition of the SCMs and not their reactivities. SCMs with similar oxide composition may have different reactivities as their amorphous contents may be different. SCMs with very low reactivity may not be able to form enough pozzolanic products (such as calcium-

silicate-hydrates) to bind alkalis and lower the pore solution alkalinity to prevent ASR. In addition, current guidelines specify prevention strategies based on the reactivity levels of aggregates (for example, R0, R1, R2, and R3 aggregate reactivity classes in ASTM C1778) and not on alkali threshold values.

The goal of this paper is to review recent research that showed that the reactivity of SCMs is related to their efficacy in preventing ASR and discuss potential ways to improve specifications by including the SCM reactivity measures. In addition, an approach to improve the specifications by recommending appropriate ASR prevention measures based on alkali sensitivity of reactive aggregates is discussed.

2. Potential approaches to improve the prescriptive-based specifications

Two measures of SCM reactivity - calcium hydroxide consumed by SCMs in a model system and electrical resistivity measurement of binder systems were used as tools to determine the SCMs efficiency to prevent ASR. These approaches are discussed in sections 2.1. An approach to improve specifications regarding alkali sensitivity of reactive aggregates and alkali loading is discussed in section 2.2.

2.1 Determining SCM amount for ASR prevention based on SCM reactivity

SCM pozzolanic reactivity can be measured by determining the amount of CH consumed by SCM in a model system, where SCM and calcium hydroxide (CH) were mixed at 1 to 3 mass ratio, and then the blend was mixed with 0.5 M KOH solution at a liquid to solid ratio of 0.9 (Suraneni and Weiss 2017). The mixture was seal cured at 50 °C for 10 days, and these conditions are expected to react the SCM entirely in most cases (Choudhary et al. 2022). CH consumed by SCM at the end of the test was determined by measuring the remaining CH in the system using thermogravimetric analysis (TGA). Recent research (Chopperla and Ideker 2022, Wang et al. 2022) showed that CH consumed as an SCM reactivity measure along with amount of SCM in the binder correlated well with the ASR expansion determined using the accelerated mortar bar test (AMBT; ASTM C1567) and the miniature concrete prism test (MCPT; AASHTO T 380). Figure 1a shows that higher the reactive SCM fractions in the binder, lower the expansion. The data shown in Figure 1a is for materials such as limestone (LS), slag (SL), pumice (PU), and glass powder (GP). Similar observations were made when SCMs such as fly ashes and silica fume are used; more details can be found in ref. (Chopperla and Ideker 2022). Figure 1b shows the correlation between the MCPT expansion and bulk electrical resistivity of concrete.

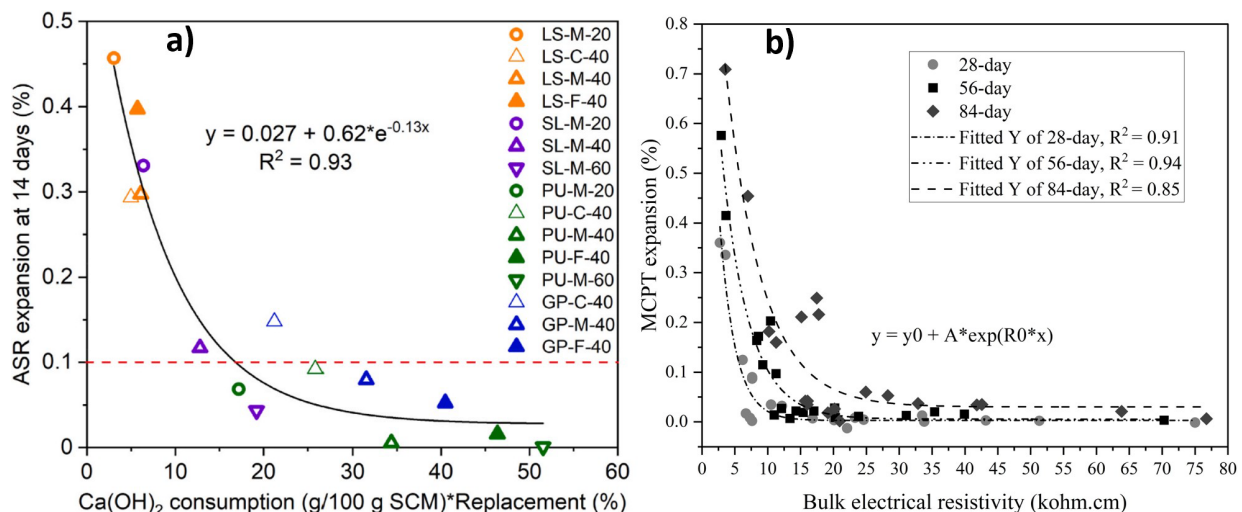


Figure 1. a) Correlation between AMBT expansion and the product of CH consumption and SCM amount (Wang et al. 2022); b) Correlation between MCPT expansion and bulk electrical resistivity (Chopperla and Ideker 2022)

It has been shown that electrical resistivity of cementitious binders can be used as an alternate method for evaluating SCMs with different reactivities (Wang et al. 2021), and it can also be used to evaluate SCMs efficiency to prevent ASR (Chopperla and Ideker 2022, Wang et al. 2022). This is because reaction of SCMs increase bulk resistivity by reducing pore connectivity and pore solution alkalinity. Therefore, cementitious systems with higher reactive SCM(s) will have higher electrical resistivity. As electrical

resistivity is a non-destructive and simple test, it could be used as an alternate test for SCM reactivity measurement (Wang et al. 2021), and specifications could be developed based on resistivity values. Using the discussed approaches, SCM amounts can be specified based on their composition and reactivity for different levels of aggregate reactivities and alkali loadings to prevent ASR.

2.2 Alkali sensitivity of aggregates

Another approach that is being investigated by the authors is to develop information on the alkali sensitivity of specific aggregates or aggregate classes. That information could then be combined that with the available alkali in the total cementitious blend (e.g. portland cement or portland limestone cement + supplementary cementitious materials) as well as any alkalis that are releasable by the aggregates themselves (Menendez et al. 2021). Externally available alkalis may also be included in this calculation. The idea of this approach is summarized as a schematic shown in Figure 2.

The alkali content in the pore solution governs the pH and in turn will dictate when deleterious ASR occurs. Our standard accelerated mortar bar testing methods rely on an external soak solution of 1N which is often criticized for being overly aggressive. **Figure 3a** shows the impact of varying the alkali normality in the soak solution in the accelerated mortar bar test. For a very highly reactive aggregate a 0.265 N soak solution showed that the aggregate related expansion was suppressed at, or near this level. More work is underway to determine the exact alkali threshold needed to induce expansion in this aggregate. But this demonstrates an important proof of concept that limiting the alkali content can prevent deleterious ASR. This was well known and is shown in a 1996 publication by Thomas and co-workers as shown in **Figure 3b**. However, this approach was long considered too arduous to establish these relationships for all aggregates. It is proposed to start by establishing this for aggregate reactivity classes and/or mineralogies. Though, not much additional testing would be needed to run a normality series on each aggregate for consideration in concrete construction. To determine the total alkali available to the system the cold water extraction technique (CWE) proposed by Plusquellec et al. (2018), and later refined by Tuinukuafe et. al. (2022) could be used. An alternative approach called the alkali leaching test (ALT) outlined by Ghanizadeh and Thomas (2023) in this conference may also be possible.

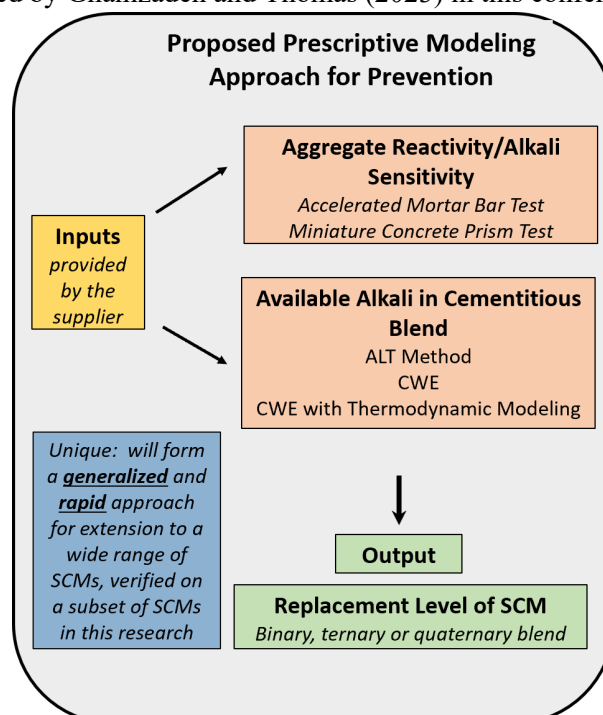


Figure 2: Proposed Approach For Assessing Alkali Sensitivity of Aggregates And Available Alkali Loading of the System For ASR Prevention

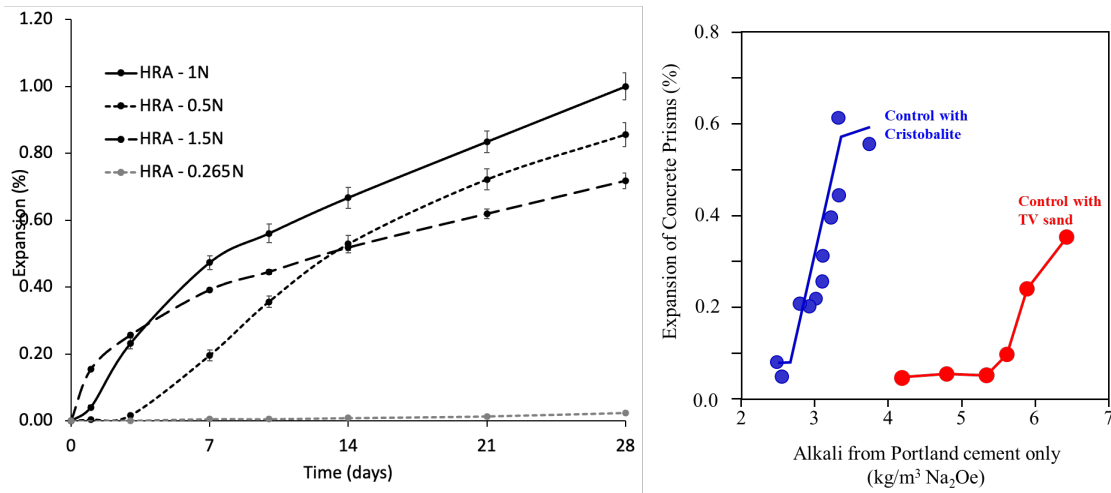


Figure 3: a) expansion of mortar bars (Parashar and Ideker unpublished data, 2023); b) expansion of concrete prisms (Thomas et al., 1996)

3. Conclusions

Two approaches to develop prescriptive specifications to prevent ASR using non-traditional SCMs are discussed in this paper. Both measures of SCM reactivity, calcium hydroxide consumed by SCM and electrical resistivity of binder, showed good correlation to the mortar and concrete expansions measured in mixtures with reactive aggregates. Considering SCM reactivity in addition to their composition could improve the specifications for ASR preventive measures. Also, a prescriptive approach of ASR prevention based on aggregative alkali sensitivity and alkali loading of concrete is discussed in this paper.

References

- Chappex, T. and Scrivener, K.L. (2013) "The effect of aluminum in solution on the dissolution of amorphous silica and its relation to cementitious systems", *Journal of the American Ceramic Society*, 96 (2)
- Chopperla, K.S.T. and Ideker, J.H. (2022) "Using electrical resistivity to determine the efficiency of supplementary cementitious materials to prevent alkali-silica reaction in concrete", *Cement and Concrete Composites*, 125: 104282
- Choudhary, A., Bharadwaj, K., Ghantous, R.M., Isgor, O.B. and Weiss, W.J. (2022) "Pozzolanic Reactivity Test of Supplementary Cementitious Materials", *ACI Materials Journal*, 119(2): 255-268
- Ghanizadeh, A. and Thomas, M.D.A. (2023) "Alternatives to pore solution extraction method to determine available alkalis of cement pastes", *The 16th International Congress on the Chemistry of Cement (ICCC)* (In Review)
- Juenger, M.C., Snellings, R. and Bernal, S.A. (2019) "Supplementary cementitious materials: New sources, characterization, and performance insights", *Cement and Concrete Research*, 122: 257-273
- Menendez, E., Silva, A.S. and Duchesne, J. (2021) "Recommendation of RILEM TC258-AAA: RILEM AAR-8: determination of potential releasable alkalis by aggregates in concrete", *Materials and Structures*, 54 (205)
- Plusquellec, G., Geiker, M.R., Lindgard, J. and de Weerd, K. (2018) "Determining the free alkali metal content in concrete - Case study of an ASR affected dam", *Cement and Concrete Research*, 105: 111-125
- Suraneni, P. and Weiss, W.J. (2017) "Examining the pozzolanicity of supplementary cementitious materials using iso-thermal calorimetry and thermogravimetric analysis", *Cement and Concrete Composites*, 83: 273-278
- Thomas, M.D.A., Blackwell, B.Q. and Nixon, P.J. (1996) "Estimating the Alkali Contribution from Fly Ash to Expansion due to Alkali-Aggregate Reaction in Concrete", *Magazine of Concrete Research*, 48 (177): 251-264
- Thomas, M.D.A. (2011) "The effect of supplementary cementitious materials on alkali-silica reaction: A review", *Cement and Concrete Research*, 41 (12): 1224-1231
- Tuinukuafe, A., K. S. T. Chopperla, J. Weiss, J. Ideker and B. Isgor (2022). "Estimating Na⁺ and K⁺ concentrations of the pore solution based on ex-situ leaching tests and thermodynamic modeling", *RILEM Technical Letters*, 7: 88-97
- Wang, Y., Burris, L., Shearer, C.R., Hooton, D. and Suraneni, P. (2021) "Strength activity index and bulk resistivity index modifications that differentiate inert and reactive materials", *Cement and Concrete Composites*, 124: 10420
- Wang, Y., Ramanathan, S., Chopperla, K.S.T., Ideker, J.H. and Suraneni, P. (2021) "Estimation of non-traditional supplementary cementitious materials potential to prevent alkali-silica reaction using pozzolanic reactivity and bulk resistivity", *Cement and Concrete Composites*, 133: 104723

Elucidating the carbonation front in blended calcined kaolinite clays binders using analytical techniques

Y. Dhandapani¹, L. Black², M. C. G. Junger³ and S. A. Bernal⁴

Email: Y.Dhandapani@leeds.ac.uk

¹School of Civil Engineering, University of Leeds, Leeds, United Kingdom

Email: L.Black@leeds.ac.uk

²School of Civil Engineering, University of Leeds, Leeds, United Kingdom

Email: mjuenger@mail.utexas.edu

³Architectural and Environmental Engineering, University of Texas at Austin, USA

Email: S.A.BernalLopez@leeds.ac.uk

⁴School of Civil Engineering, University of Leeds, Leeds, United Kingdom

ABSTRACT

Low-purity calcined clays are gaining traction as new sources of supplementary cementitious materials (SCMs) to produce sustainable low-clinker cements. Sustainable use of binders must also be linked with ensuring the durability of concrete structures. It is then crucial to develop a fundamental understanding of mechanisms governing long-term durability of new SCM cement formulations. Carbonation performance is commonly determined using a pH indicator, which gives a speculative indication of the affected region. However, numerous physicochemical changes occur in the microstructure that govern the progression of the carbonation front, which cannot be traced and explained using carbonation depth measurement per se. This study characterised the carbonation front of calcined clay-blended binders using conventional pH indicators, and scanning electron microscopy coupled with energy-dispersive X-ray spectroscopy (EDX). The microstructural variation at the carbonation front could be used to explain the reaction mechanism. While OPC showed densification along the carbonation front, calcined clay cements showed a visible increase in porosity during carbonation. The progression of the carbonation-affected depth shows densification along the reacted front, a layer enriched in sulfate ahead of the front (diffusing inwards due to the decomposition of ettringite in the carbonated region) and a higher concentration of alkalis within the carbonated region. While the conventional pH indicator did not show any signs of carbonation in reference Portland cement paste, the microstructural investigation does reveal the underlying carbonation process and presents a more rational approach to assess and benchmark the carbonation performance of low clinker cements. This combined approach gives unique insights to explain the carbonation performance of new sustainable cements.

KEYWORDS: *Carbonation; Calcined clays; sulfate front; alkalis; microstructure*

1. Introduction

Low-clinker cements containing calcined clays are a promising solution for reducing carbon emissions associated with Portland cement production (Scrivener, John and Gartner, 2018). Application of such low-carbon cements requires a sufficient understanding of their long-term durability performance, particularly when exposed to CO₂, a process known as carbonation. Carbonation is a major durability concern for reinforced concrete structures that could lead to reinforcement corrosion, especially when concrete is produced with cements containing high-volume replacement of Portland clinker (von Greve-Dierfeld *et al.*, 2020; Saillio *et al.*, 2021). Although using SCMs can lead to significant environmental benefits and advantageous performance enhancements for numerous durability-related conditions, the carbonation resistance of binders with high contents of SCMs is not well understood yet, and it has been

identified to be relatively low based on accelerated test methods. The testing conditions adopted when applying such methods do not resemble natural environmental conditions, and therefore it is unclear how accurately accelerated testing can help understand the performance of sustainable cements. This study focuses on characterising the carbonation process in cement paste exposed to atmospheric CO₂ conditions to develop insights into the underlying carbonation interaction with the hydrated cementitious matrix formed in calcined clay-containing cements.

2. Materials and Methods

A commercial ordinary Portland cement (OPC) (CEM I 52.5R, Heidelberg cements) was used. A flash calcined clay (CCF) supplied by Argeco (France) Ltd. with an estimated kaolinite content of ~50 wt.% was used as a calcined clay source at 30 wt.% cement replacement to produce blended cements (denoted as CCF30 hereafter). The chemical compositions of the materials used in the study are given in Table 1.

Table 1 Oxide composition in wt.% of the materials used determined by X-ray fluorescence.

| | CaO | Al ₂ O ₃ | SiO ₂ | MgO | SO ₃ | K ₂ O | MnO | Fe ₂ O ₃ | Na ₂ O | LOI* | Traces |
|-------------------|-------|--------------------------------|------------------|------|-----------------|------------------|------|--------------------------------|-------------------|------|--------|
| OPC | 64.80 | 3.90 | 21.80 | 0.76 | 3.57 | 0.67 | 0.05 | 1.33 | 0.30 | 2.20 | 0.73 |
| Calcined clay CCF | 0.81 | 22.60 | 69.30 | 0.27 | 0.08 | 0.28 | 0.06 | 2.89 | 0.37 | 1.90 | 1.50 |

*LOI stands for loss on ignition at 900°C determined using a muffle furnace

Cylindrical specimens of 33 mm diameter and 50 mm were prepared using cement paste mixed using a high shear mixer at 1600 rpm for 2 min. Specimens were sealed and cured for 28 days before exposure to atmospheric CO₂ in a standard conditioning chamber with a controlled temperature of 20 °C and RH of 57%, simulating sheltered carbonation conditions. Carbonation depth was monitored by spraying a fresh mist of 1% phenolphthalein indicator and thymolphthalein indicator (prepared in 100 ml isopropyl alcohol) on fresh slices (4-5 mm thickness) of cement paste cut using Struers Secotom Precision Cutting Machine. Discs were immersed in isopropyl alcohol for a period of about 20 min to remove free water from cutting before using pH indicator. Slices of cement paste containing carbonation edge were impregnated using low viscosity epoxy to characterise the physical and chemical changes along with the carbonation front using a Zeiss Evo 15 scanning electron microscope (SEM) at 20KV at a working distance of 8.50 mm with a backscattered electron (BSE) detector coupled with an Oxford Energy dispersive X-ray spectrometer.

3. Results and Discussion

2.1 Carbonation depth determined using a pH indicator

Fig 1 shows the carbonation depth of OPC and calcined clay binder revealed using different pH indicators – the most widely used and standardised method to determine carbonation depths in cementitious systems. The OPC paste did not show signs of carbonation after 240 days' exposure when evaluated using either indicator. CCF30 showed a visible carbonation depth, i.e., change to colourless, indicating that carbonation reaction had occurred, lowering pH in that region. About 8 points along the disc were measured using a digital calliper, and images obtained using handheld digital microscope. The average carbonation depth was 0.36 ± 0.14 mm after 240 days of carbonation.

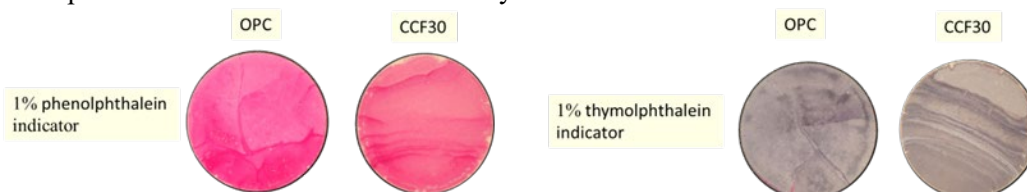


Figure 1 Photograph of cement paste slices after sprayed with two different pH indicator

2.2 SEM analysis of the carbonated regions

SEM micrographs were obtained at 250X to observe a large area near the carbonation front (Fig 2). A specimen sealed and cured for 240 days was used to compare and identify the microstructure changes due to carbonation. While the cement paste kept in sealed conditions showed a homogenous microstructure with no signs of physical alterations along the exposure surface for both OPC (Fig 2A) and CCF30 (Fig 2C), specimens subjected to carbonation showed variations in the microstructure along the carbonation surface. In the case of OPC (Fig 2B), a denser microstructure along the carbonation front, i.e., initial 100-200 micrometers was observed upon carbonation. This could be attributed to the precipitation of carbonation reaction products along the exposed front, consistent with observation of carbonation in OPC systems (Shah *et al.*, 2018). In the case of CCF30 (Fig 2D), there was a more prominent change in the microstructure upon carbonation showing an increased porosity in the carbonated region, similar to the observations by Shah *et al.* (Shah *et al.*, 2018). Additionally, the depth of the affected region, showing an increase in porosity, was higher in the case of the calcined clay binder.

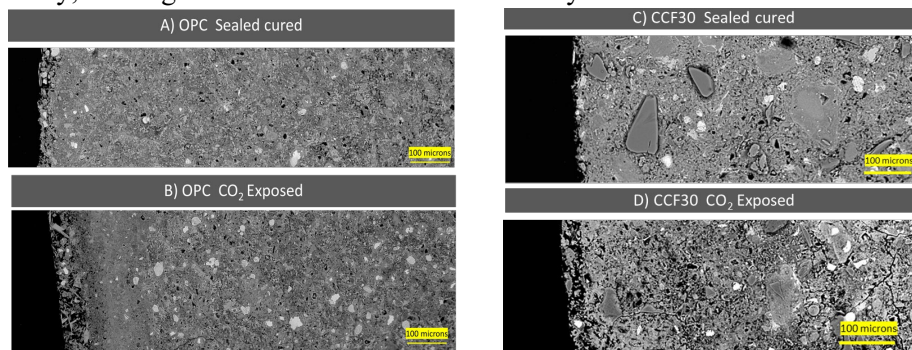


Figure 2 Micrographs showing carbonation front in OPC and CCF30

2.3 Chemical analysis of the carbonated regions

Figure 3 presents the EDX maps of OPC after 120 days (Fig. 3A) and 240 days (Fig. 3B) of carbonation. It can be seen that sulfate was depleted in the carbonated region, and the depth of this sulfate depletion increases as carbonation progresses, consistent with observations in previous studies (Collier *et al.*, 2019; Georget, Soja and Scrivener, 2020). The sulfate depletion is most likely associated with the decomposition of ettringite, leading to the formation of gypsum. Gypsum formation could lead to a concentration gradient of sulfate, enabling inwards movement of sulfate, as observed from the EDX maps. Additionally, ettringite carbonation is often reported to occur when pH reaches about 9.7 at high levels of reacted CO_2 (Shi *et al.*, 2016). This demonstrates that EDX maps could be used as an alternative method to measure the region affected by carbonation by tracing the carbonation of the ettringite phase formed in the low clinker cements. Alkalis were concentrated in the carbonated region (showed in Figures 3A and 3B by potassium) due to the leaching upon carbonation of both anhydrous clinker or reaction products, or potential binding of a higher amount of alkalis in the low Ca/Si calcium aluminium silicate hydrate (C-A-S-H). Further investigation to explain the increased concentration of alkalis in the carbonated region is required.

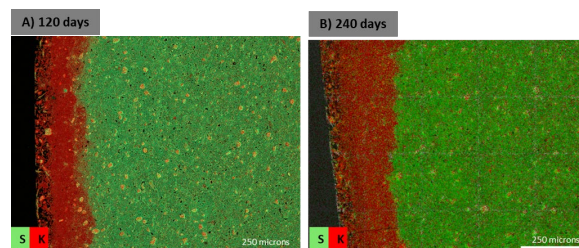


Figure 3 EDX maps of carbonated OPC for (A) 120 days and (B) 240 days

The carbonation-affected depth from EDX data was obtained using the built-in Aztec software tool, analysing maps obtained in two different locations. Four depth measurements were taken in each map. Figure 4 summarises the depth (average of 8 depth measurements) of sulfate depletion in the region considered to be carbonation-affected region. Although OPC specimens showed no signs of carbonation using the pH indicators, EDX maps show a possible carbonation affected region of 110 and 275 μm after 120 and 240 days of carbonation, respectively. CCF30 showed a carbonation affected depth of about 265

and 386 μm after 120 and 240 days, respectively. Additionally, the carbonation depth of CCF30 at 240 days compares well with the depth measurement obtained when using a pH indicator, i.e., 0.36 mm, indicating that there is likely underestimation of the carbonated region in OPC, when using standardised testing methods based on pH indicators, as those only capture depletion of portlandite rather than carbonation of other binding phases, which could lead to bias in the interpretation of the carbonation performance of low clinker cement.

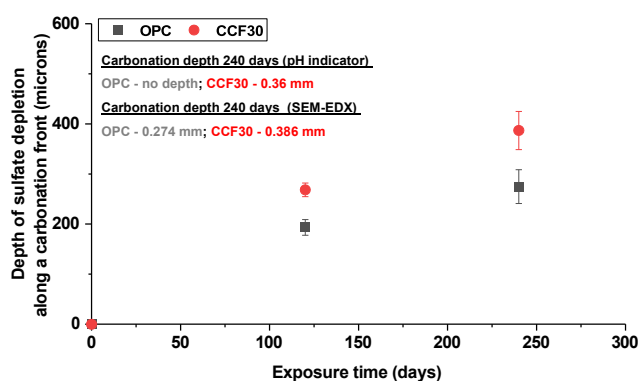


Figure 4 Carbonation depth obtained from EDX elemental maps for OPC and CCF30

4. Conclusions

Characterisation of carbonated specimens using electron microscopy reveals that pH indicators can underestimate the carbonation occurring in the OPC system. There is visible densification due to carbonation in OPC, while cements containing calcined clay may tend to show increased porosity. Estimation of the carbonation-affected zone, obtained using EDX maps, reveals a similar progression of carbonation front in OPC and calcined clay binders over time, unlike the phenolphthalein indicator measurement. The sulfate front formed along the carbonation exposure surface should be investigated further to explain the role of other reaction products during carbonation in low clinker cements.

Acknowledgements

This study was sponsored by the National Science Foundation (NSF) through award 1903457 and the UK Engineering and Physical Sciences Research Council (EPSRC) through grant EP/T008407/1.

References

- Collier, N. C. *et al.* (2019) 'Gaseous carbonation of cementitious backfill for geological disposal of radioactive waste: Nirex Reference Vault Backfill', *Applied Geochemistry*, 106, p. 120–133.
- Georget, F., Soja, W. and Scrivener, K. L. (2020) 'Characteristic lengths of the carbonation front in naturally carbonated cement pastes: Implications for reactive transport models', *Cement and Concrete Research*, 134, p. 106080.
- von Greve-Dierfeld, S. *et al.* (2020) 'Understanding the carbonation of concrete with supplementary cementitious materials: a critical review by RILEM TC 281-CCC', *Materials and Structures/Materiaux et Constructions*, 53(6).
- L'Hôpital, E. *et al.* (2016) 'Alkali uptake in calcium alumina silicate hydrate (C-A-S-H)', *Cement and Concrete Research*, 85, p. 122–136.
- Saillio, M. *et al.* (2021) 'Effect of supplementary cementitious materials on carbonation of cement pastes', *Cement and Concrete Research*, 142, p. 106358.
- Scrivener, K. L. *et al.* (2018) 'Eco-efficient cements: Potential economically viable solutions for a low- CO_2 cement-based materials industry', *Cement and Concrete Research*, 114, p.p. 2–26.
- Shah, V. *et al.* (2018) 'Changes in microstructure characteristics of cement paste on carbonation', *Cement and Concrete Research*, 109, pp. 184–197.
- Shi, Z. *et al.* (2016) 'Experimental studies and thermodynamic modeling of the carbonation of Portland cement, metakaolin and limestone mortars', *Cement and Concrete Research*, 88, pp. 60–72.

Cementitious materials for oil-well abandonment and numerical simulations of cement durability at oil well conditions

S.Y. Yang^{1*}, W. Kunther², A. Michel² and J. Skibsted¹

¹ Department of Chemistry, Aarhus University, 8000 Aarhus, Denmark
Email: syyang@chem.au.dk; jskib@chem.au.dk

² Department of Environmental and Resource Engineering, Materials & Durability, Technical University of Denmark, DK-2800 Kgs. Lyngby, Denmark
Email: wolku@dtu.dk; almic@dtu.dk

ABSTRACT

In this work, we investigate Portland cement hydration and durability at elevated temperatures of 60°C – 80°C and at pressures up to 300 bar in water and in artificial brine solutions that mimic the exposing environments of cement plugs used for abandonment of out-sourced off-shore oil wells. A principal aim is to follow the structural and compositional evolution of the C-S-H phase, and thus, solid-state ²⁷Al and ²⁹Si NMR are used as the main analytical tools. The NMR results indicate that hydration at high pressure (300 bar) has no significant impact on the C-S-H phases formed at 60 and 80 °C, however, it may retard the decomposition of ettringite and the AFm phases at 80 °C. Interestingly, the exposure of the hydrated cement paste to the laboratory-made brine solution significantly impacts the microstructure of the formed C-S-H product as a cross-linked C-S-H phase is formed at a high ratio of solution to solid. The samples are additionally cured in CO₂-injected brine, and the effect of particle size on the carbonation degree is studied. The experimental phase assemblages from the investigations will be used in thermodynamic reactive-transport modeling to estimate the durability and physical properties of the hardened cement on a prolonged time scale.

KEYWORDS: *Oil-well abandonment, cement hydration, C-S-H phase, brine solution, reactive-transport modeling*

1. Introduction

When an offshore oil well reaches the end of its lifetime, it must be permanently plugged and abandoned. These plugs and abandonment (P&A) operations are usually done by placing several cement plugs in the wellbore to isolate the reservoir and other fluid-bearing formations from entering the seabed. An essential part of P&A is to ensure the structural integrity of the wells after abandonment, which can be very challenging at offshore conditions, where temperatures of 60 - 80 °C and pressures up to 300 bar are present in the well along with brine solutions, hydrocarbon gasses, and CO₂. Furthermore, the durability and lifetime of the cement plugs are highly important parameters as future maintenance operations are hardly possible.

2. Sample Preparation

Cement pastes were prepared by mixing white Portland cement with Milli-Q water at a water-to-cement ratio of 0.5 for the high pressure and high temperature hydration experiments. For the cement bar experiments, the blends were initially hydrated at ambient pressure and a temperature of 40 °C (7 days) in plastic tubes with a 7.8 mm diameter and a length of 30 mm. The bars were then exposed to the brine solutions and CO₂ injection experiments. The curing was stopped by stirring the crushed paste in isopropanol for 1 hour. All samples were ground and dried in a desiccator over silica gel at room temperature for at least 24 h prior to the microstructural characterization.

3. Results and Discussions

3.1 High pressure and temperature experiments. The cement paste was poured as a slurry into a 1.5 mL snap ring vial and autoclaved at 300 bar and temperatures of 60 – 80 °C for 1, 7, and 28 days. After curing, the degree of hydration (DOH) and the mean chain length (MCL) of the formed C-(A)-S-H phase were determined by ^{29}Si MAS NMR whereas a distinction between different Al species was achieved by ^{27}Al MAS NMR. The ^{29}Si NMR spectra of the pastes cured for one day are shown in Figure 1a. The spectra reveal that no apparent changes are induced by the 300 bar pressure at the different temperatures, whereas a significant increase in DOH and MCL is observed at 80 °C at a given pressure. This suggests a further polymerization of the C-(A)-S-H phase at higher temperatures. However, an effect of the pressure change is seen in the ^{27}Al NMR spectra for the 80 °C samples (Figure 1b) since the ettringite resonance at 13.2 ppm is still present at 300 bar despite high-temperature curing above its degradation point (~60 – 70 °C). This may reflect that pressure can stabilize ettringite and thus a delayed decomposition of this phase at 80 °C. These observations indicate that pressures up to 300 bar have no impact on the C-(A)-S-H phase but a small effect on the Al distribution between different phases.

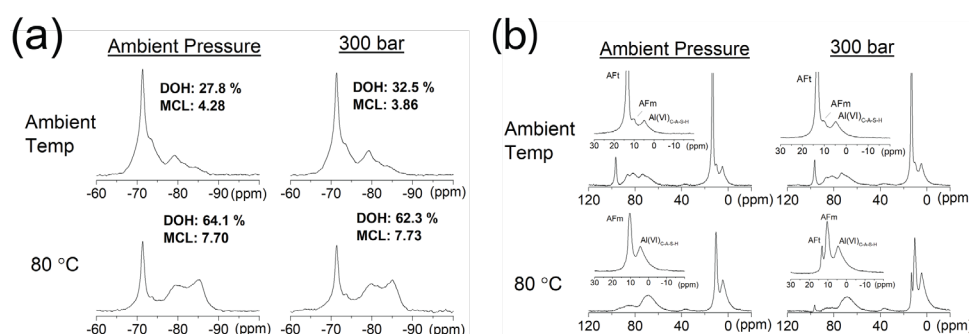


Figure 1. (a) ^{29}Si MAS NMR spectra recorded at 7.1 T ($\nu_R = 7.0$ kHz) and (b) ^{27}Al MAS NMR spectra (14.1 T, $\nu_R = 13.0$ kHz) for the cement paste cured for one day at ambient condition and at a pressure of 300 bar and an elevated temperature of 80 °C.

3.2 Exposure of the hardened cement paste to the brine solution. To mimic the exposure conditions of the cement plugs in the well, a brine solution is made by following the elemental analysis of the production water from an oil-well in the North Sea. The composition is given in Table 1 and is saturated with calcite at a pH of 6.6. After 7 days of hydration, the cement bars are demolded, ground, and submerged into the brine solution for another 7 days. Four ratios of the solution to solid (1500, 150, 100, and 50 mL brine/g cement) are used to represent the variability in conditions at different depths for the cement in the wellbore.

Table 1. Chemical Composition of Laboratory-Made Brine.

| Element | C | Na | K | Ca | Mg | Cl | S |
|----------------------|-----|-------|-----|-----|-----|-------|------|
| Concentration (mg/L) | 457 | 17989 | 308 | 897 | 600 | 30333 | 1050 |

TGA data for these samples are shown in Figure 2a. It is noted that indications of a CaCO_3 precipitate (600 to 850°C) is only seen for the 50 mL/g sample. Additionally, the 50 mL/g sample also contains a small quantity of portlandite. This indicates a near saturation of portlandite for the system, as manifested by the high pH of 12.5. Furthermore, a brucite peak (~380°C) is observed for all ratios, which increases as portlandite dissolves. The first broad peak below 200°C can be assigned to the C-(A)-S-H phase where the weight loss stems from the removal of water molecules from the interlayer or the C-(A)-S-H surface. Its presence may reflect limited carbonation for the cement exposed to the laboratory-made brine.

The ^{29}Si NMR of the samples (Figure 2b) reveals an increase in the degree of hydration (DOH) with increasing brine/cement ratio which may reflect that more water is available for the hydration process. A variation is also observed for the mean chain length (MCL) of the C-(A)-S-H phase which tends to increase with increasing brine/cement ratio as can be evaluated visually from the apparent Q^2/Q^1 ratios. This may reflect a decalcification of the C-(A)-S-H phase where calcium is removed from the interlayer (Sevelsted and Skibsted (2015)) and potentially leached to the solution. In the 1500 mL/g sample, a resonance from a Q^3 site at -91.9 ppm is additionally resolved, which indicates a cross-linking within the

silicate network. Furthermore, the 5 ppm resonance from octahedral Al associated with the C-(A)-S-H phase is absent in the ^{27}Al NMR spectrum (Figure 2c). These observations suggest significant changes in the structural properties of the C-S-H phase. However, further insight into the interaction between the cement paste and the brine solution requires experiments conducted at longer times than implemented in the present study (i.e. 7 days of curing). In addition to peaks from the C-(A)-S-H phase, the ^{27}Al NMR spectra also show the presence of ettringite (13.2 ppm) and hydroxy-AFm (10.5 ppm).

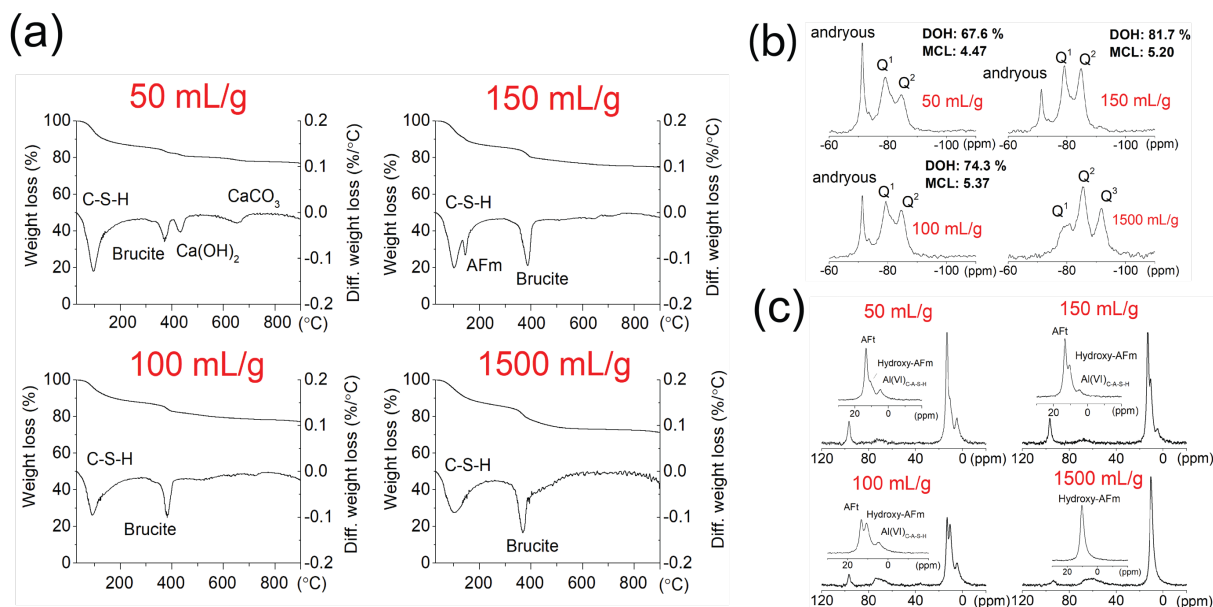


Figure 2. (a) Thermogravimetric mass-loss curves, (b) ^{29}Si MAS NMR spectra recorded at 7.1 T ($\nu_R = 7.0$ kHz), and (c) ^{27}Al MAS NMR spectra recorded at 14.1 T ($\nu_R = 13.0$ kHz) for the cement paste exposed for 7 days to the laboratory-made brine solution using the ratios of 50, 100, 150 and 1500 mL brine/g cement.

3.3 CO₂ injection treatment. Carbon sequestration in geologic reservoirs, utilizing decommissioned oil wells is considered a possible solution to reduce the atmospheric CO₂ level (Reichle et al. (1999)). The viability of this strategy strongly depends on the structural integrity of the cement plugs upon exposure to CO₂-saturated brine. To assess its potential impact on the cement, a continuous CO₂ injection into the brine with a flow of 1.2 L/hour has been applied during the curing of cement paste (100 mL/g) at an elevated temperature (80 °C) for 7 days. Two types of samples (cement bar and powder) are used to investigate the effect of particle size. The TGA data are shown in Figure 3a where a clear difference is apparent between the bar and powder samples. A dominating mass loss corresponding to CaCO₃ precipitates is observed in the powder samples, whereas the C-(A)-S-H phase is present as a major component in the bar samples. The remaining portion of portlandite in the bars may potentially originate from the core of the cement bar which has not been affected by the CO₂-saturated brine solution at 7 days. These results are supported by the observation of a broad ^{29}Si resonance in the range of -90 to -130 ppm (Figure 3b) and an Al(IV) resonance at 56 ppm (Figure 3c), indicating the formation of an amorphous alumina-silica gel and thus, the degradation of the C-(A)-S-H phase. A slightly slower decomposition is seen for the sample cured at 80 °C by the presence of small peaks of AFm and Friedel's salt in the ^{27}Al NMR spectra. This can be ascribed to a lower solubility of CO₂ at 80 °C as compared to ambient temperature. For the bulk samples, the structural integrity of the C-(A)-S-H phase has been highly retained, as evidenced by the presence of Q¹ and Q² silicate sites in the ^{29}Si NMR spectra and the absence of a 56 ppm peak in the ^{27}Al NMR spectra. The low permeability of the cement bars may account for a weak interaction between CO₂-saturated brine and the cement bar. This follows earlier studies of oil well samples where a penetration depth of 1 to 10 mm in 30 years (54 °C and 18 MPa) was observed for different field samples (Carey et al. (2007)). A simulated penetration depth of ~ 1.04 mm in 50 years (50 °C and 30.3 MPa) has also been predicted in a series of Monte Carlo simulations (Kutchko et al. (2008)).

By a continuous injection of CO₂ (1.2 L/hour), the system can reach saturation in carbonate species in a short time of 180 seconds for the samples at ambient conditions and 30 seconds for those stored at 80 °C. The concentrations of carbonate ions in water in equilibrium with CO₂ correspond to 0.029 M and 0.004

M at ambient conditions and 80 °C, respectively (Duan and Sun (2003)). A similar carbonation degree has been reached for the same particle size independent of the concentration of carbonate species. However, these reactions are significantly faster with CO₂ flow as compared to exposure to a static volume of brine solution (Figure 2). This reflects that the flow is an essential influencing factor for the carbonation process, whereas the actual concentration at a given temperature has a minor effect. These observations are consistent with a previous study (Duguid and Scherer (2010)) and our simulations (data not shown).

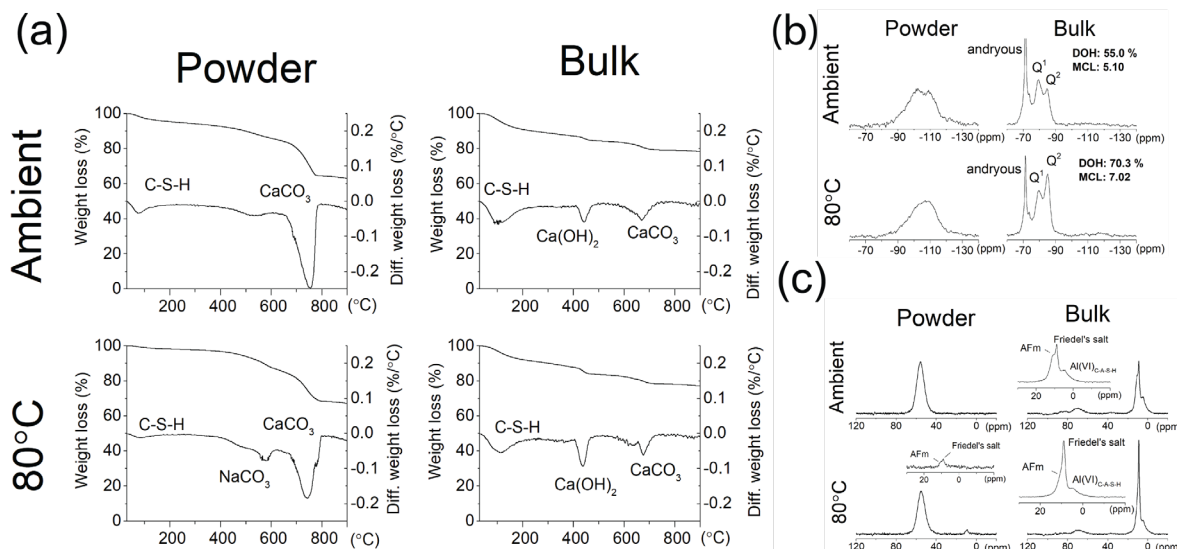


Figure 3. (a) Thermogravimetric mass-loss curves, (b) ²⁹Si MAS NMR spectra recorded at 7.1 T ($\nu_R = 7.0$ kHz), and (c) ²⁷Al MAS NMR spectra recorded at 14.1 T ($\nu_R = 13.0$ kHz) for the cement pastes (powder and bars) exposed to CO₂-saturated brine solution of 100 mL/g for 7 days.

4. Conclusions

Cement hydration at elevated pressure and temperature, cement deterioration in laboratory-made brine solution as well as in a CO₂-saturated brine solution has been examined by TGA, ²⁹Si NMR and ²⁷Al NMR. The curing pressure is found to be less critical relative to the curing temperature on the hydration mimicking oil-well conditions, where the degree of hydration and the polymerization degree for the formed C-(A)-S-H phase are higher at elevated temperatures. A high stability of the C-(A)-S-H phase is observed on exposure to static brine solutions, whereas full carbonation of the hydrated cement paste is achieved within 2 hours when exposed to a flowing CO₂-saturated brine solution. The particle size is also found to be decisive for the degree of carbonation.

Acknowledgments

The Danish Offshore Technology Centre (DOTC) is acknowledged for financial support to this project.

References

- Carey, J.W., Wigand, M., Chipera, S.J., WoldeGabriel, G., Pawar, R., Lichtner, P.C., Wehner, S.C., Raines, M.A., Guthrie, G.D. (2007) "Analysis and performance of oil well cement with 30 years of CO₂ exposure from the SACROC Unit, West Texas, USA", *International Journal of Greenhouse Gas Control*, 1(1): 75–85.
- Duan, Z. and Sun, R. (2003) "An improved model calculating CO₂ solubility in pure water and aqueous NaCl solutions from 273 to 533 K and from 0 to 2000 bar", *Chemical Geology*, 193(3): 257–271.
- Duguid, A. and Scherer, G.W. (2010) "Degradation of oilwell cement due to exposure to carbonated brine", *International Journal of Greenhouse Gas Control*, 4(3): 546–560.
- Kutchko, B.G., Strazisar, B.R., Lowry, G.V., Dzombak, D.A., Thaulow, N. (2008) "Rate of CO₂ Attack on Hydrated Class H Well Cement under Geologic Sequestration Conditions", *Environmental Science & Technology*, 42(16): 6237–6242.
- Reichle, D., Houghton, J., Kane, B., Ekmann, J., Benson, S., Clarke, J., et al. (1999) "Carbon sequestration research and development", *United States*.

Sevelsted, T.F. and Skibsted, J. (2015) “Carbonation of C–S–H and C–A–S–H samples studied by ^{13}C , ^{27}Al and ^{29}Si MAS NMR spectroscopy”, *Cement and Concrete Research*, 71: 56–65.

Alkali-silica reaction in calcium aluminate cement mortars

Ł. Kotwica^{1*}, J. Szydlowski²

¹ AGH University of Science and Technology, Kraków, Poland

szydlows@agh.edu.pl

² AGH University of Science and Technology, Kraków, Poland

lkotwica@agh.edu.pl

ABSTRACT

The alkali-silica reaction (ASR) in Portland cement-based composites is a serious problem that is responsible for the deterioration of numerous structures around the world. The reason for the alkali-silica reaction is the use of de-icing salt solutions, both organic and inorganic. This topic is well described in the literature, however, there are some knowledge gaps regarding this phenomenon. Calcium aluminate cement composites are sometimes used for pavements repairing in airfields and roads, and thus may be subjected to the action of de-icing solutions, especially those based on acetates and formates. The present work reports the results of investigations on the possibility of an alkali-silica reaction in calcium aluminate cement mortars. Fused silica was used as a model reactive aggregate and was introduced into mortars as a partial replacement for quartz sand. The influence of both inorganic salts (chlorides, nitrates) and organic salts (acetates, formates) of sodium and potassium was investigated. The results obtained showed that salt solutions may cause an alkali-silica reaction in calcium aluminate cement mortars. In general, organic salts cause much more severe deterioration of mortars than inorganic salts. In all cases, expansion was associated with the formation of an alkali-silica gel. It was shown that the alkali-silica reaction can proceed in the system without the presence of solid calcium hydroxide and without an external source of hydroxyl ions.

KEYWORDS: *alkali-silica reaction, calcium aluminate cement, fused silica, organic deicers, pH*

1. Introduction

The reaction of aggregates with alkalis was first described by Stanton in 1940 (Stanton, 1940). Since then, this issue has been one of the main topics in concrete chemistry and technology. This is because the reaction of siliceous aggregates with pore solution of cement paste is a phenomenon whose mechanism has not been fully elucidated to this day, hence the interest of researchers (Rajabipour et al., 2015). At the same time, because of the huge costs of repairing concrete structures affected by the reaction of aggregates with alkalis, it is an issue of great practical importance (Rangaraju and Olek, 2007).

Typical concrete corrosion by the alkali-silica reaction (ASR) involves the reaction of the active forms of silica present in the aggregate with the sodium and potassium hydroxides present in the pore solution of the cement paste (Glasser, 1992). Aggregates susceptible to the alkali-silica reaction are primarily those containing amorphous forms of silica, such as opal or volcanic glasses, as well as metastable forms, such as tridymite, cristobalite, or strained quartz, and microcrystalline, highly defective forms, such as chalcedonite. ASR results in formation of alkali-silica gel, which swells and expands (Gholizadeh Vayghan et al., 2016).

The silica-alkali reaction can also be triggered by externally-derived alkalis. These are usually salts in solid form or in concentrated solutions, used for de-icing and ice prevention on road and airport surfaces. Since the 1970s, research has been conducted on the effects of inorganic salts, primarily chlorides, on the aggregate corrosion process (Chatterji et al. 1986). The main explanation for their effect is to increase the concentration of alkaline cations in the system, on the one hand, and to increase the alkalinity of the pore solution, on the other. The first factor is self-explanatory and unquestionable. The second is more difficult to explain, especially in light of recent results from tests on the liquid phase of mortars treated with sodium

chloride. The alkalinity of the pore solution in the sodium chloride treated mortar was found not to increase, but decrease (Heisig et al., 2016). Nevertheless, an intensification of the corrosion process of the aggregate is observed.

The action of organic deicers was extensively investigated by Diamond et al. (2006) and Rangaraju et al. (Rangaraju et al., 2006, Rangaraju and Olek, 2007). Detailed investigation of the composition of soaking solutions, as well as pore solution in concretes subjected to the action of acetates and formates, showed that alkalinity measured as a concentration of hydroxyl ions is surprisingly low compared to the concentration of hydroxyl ions in sodium hydroxide soaked concrete (Rangaraju and Olek, 2007). Despite this, the deterioration of concrete soaked in acetates and formates was much more severe compared to that of sodium hydroxide soaked concrete. On the basis of these observations, a hypothesis was put that ASR is possible in a system with low alkalinity, measured by the concentration of hydroxyl ions. An example of such a system is calcium aluminate cement mortar. By its nature, it is an environment with much lower hydroxyl ion content compared to OPC systems (Gaztafiaga et al., 1993). It was experimentally proven that ASR is possible in calcium aluminate cement mortars (Kotwica and Malich, 2022). However, there are still some problems to complete the description of that phenomenon.

The present work describes the influence of concentrated organic and inorganic solutions on the course of ASR in high alumina cement mortars. Expansion and microstructure were investigated and some important conclusions were drawn.

2. Experimental

2.1. Materials

White high alumina cement (HAC) of grade 70 was used as a binder. Fused silica (pure silica glass) was used as a reactive aggregate. The fraction 0.1-1.0 mm was used, because it gives the largest expansions of mortars (Taylor, 1997). Fused silica was used as a 10% replacement for standard quartz sand (the sand used was in accordance with EN 196-1). Soak solutions were prepared using distilled water and reagent grade sodium acetate trihydrate, potassium acetate, sodium chloride, sodium nitrate delivered by Avantor Performance Materials Poland, and sodium formate and potassium formate delivered by ChemPur, Poland.

2.2. Methods

The expansion of mortars subjected to the action of salt solutions was determined according to a modified ASTM C 1260 method. Mortars were cast in 20 x 20 x 160 mm moulds with steel gauges at both ends. After 24 hours of curing in moulds at 20°C±2°C, samples were transferred to containers with water and placed in an oven at 80°C±1°C for 24 hours. The length of samples was measured and taken as a zero measurement. The samples (three per solution) were placed in a container with 900 cm³ of the investigated solution previously heated to 80°C±1°C. Containers were tightly sealed to prevent evaporation, and possible changes in solution concentrations. The length of the samples was measured using length comparator with an accuracy of 0.001 mm. The composition of the samples is presented in Table 1.

The microstructure of the mortars was investigated using SEM. Samples were first cut with a precision diamond saw with propylene glycol as lubricant. The samples were washed in isopropyl alcohol using an ultrasonic washer. After drying under vacuum, samples were vacuum impregnated with low viscosity epoxy resin. The samples were subjected to lapping and polishing using water-free diamond suspensions. Before testing, samples were covered with a thin carbon layer to avoid charging. The samples were observed using a FEI Nova NanoSEM 200 microscope in backscatter mode.

Table 1. Composition of mortars

| | reference mortar | test mortar |
|---------------------------|------------------|-------------|
| | g | |
| High alumina cement (HAC) | 648 | 717 |
| Quartz sand 0 - 2.0 mm | 1350 | 1350 |
| Fused silica 0.1-1.0 mm | 0 | 135 |
| Water | 259 | 287 |

3. Results and discussion

Figure 1 presents an expansion of mortar bars soaked in 3M solutions of organic and inorganic salts. It can be seen that the control mortar, without reactive aggregate (fused silica), did not expand, while the mortar bars containing 10% fused silica expanded significantly. It can be clearly seen that the type of anion plays a crucial role in the course of expansion caused by ASR. Organic salts, i.e. acetates and formates, cause much higher expansion compared to inorganic salts (chloride and nitrate). The type of anion also decides the kinetics of expansion at early ages, i.e. after 1 to 4 days.

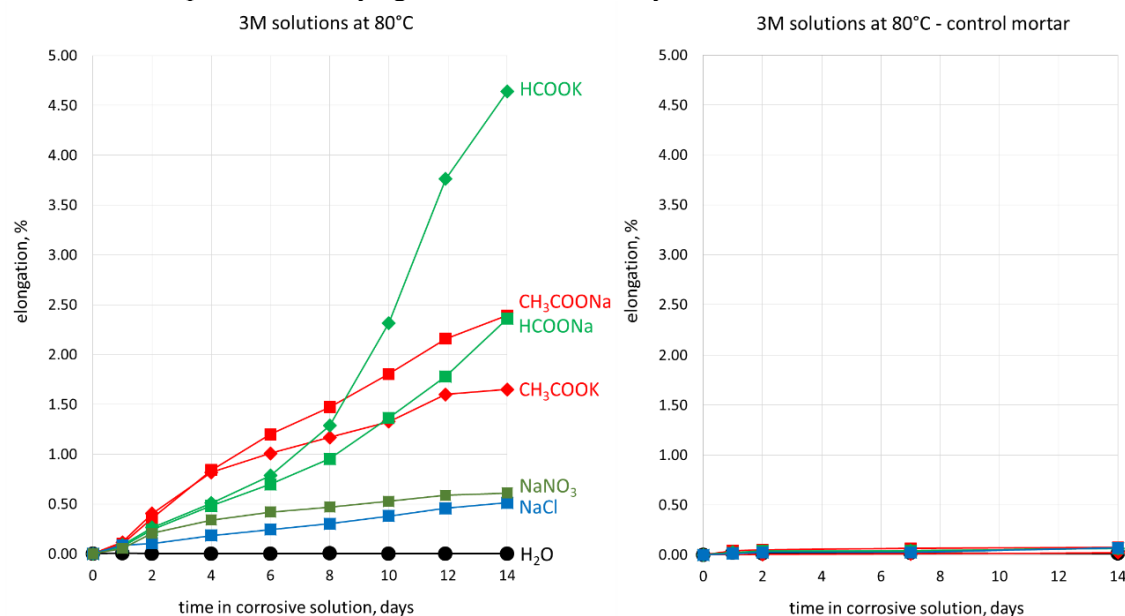


Figure 1. Expansion of mortars made of high alumina cement soaked in 3 mole/dm³ solutions of various salts at 80°C. On the left – test mortar with 10% of fused silica, on the right – control mortar without reactive aggregate.

Microstructural examination revealed that the reason for the expansion was the formation of an alkali-silica gel within the samples. Gel was found in all samples soaked in corrosive solutions. Figure 2 presents an example of a corrosion product that forms a rim around the glass grain. Gel is present within the aggregates, forms rims, and is also present within the hydrated cement paste. An example of such a situation is illustrated in Fig. 3. The gel flowed out of the aggregate forming a ‘stream’ within the crack in the paste.

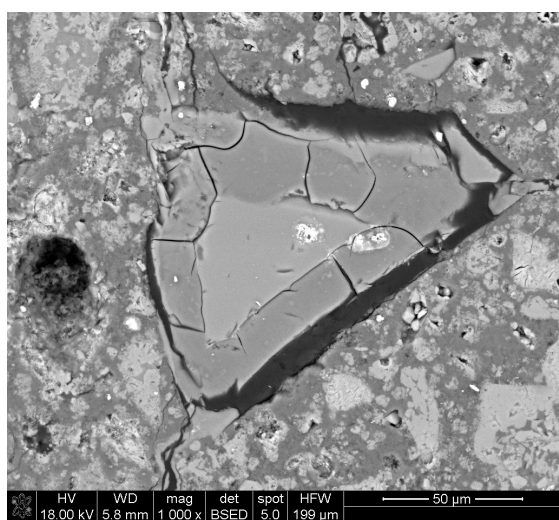


Figure 2. ASR in calcium aluminate cement mortar soaked in 3M sodium chloride solution. Grain of glass with an alkali-silica gel rim.

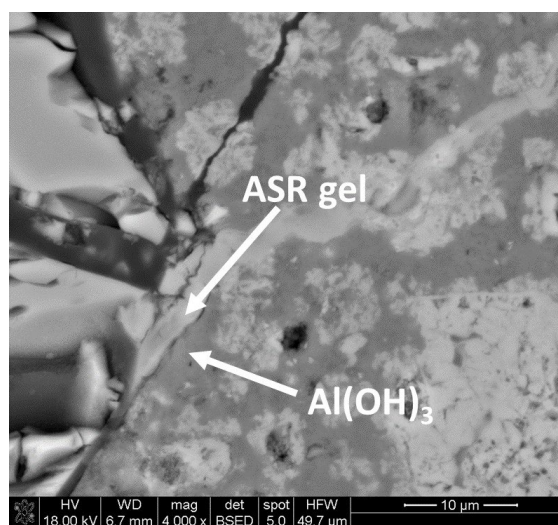


Figure 3. Details of the microstructure of HAC mortar subjected to the action of the 3M potassium acetate solution. Alkali-silica gel is in the direct contact with aluminium hydroxide.

The fact that the alkali-silica gel is in direct contact with aluminium hydroxide has profound implications. Aluminium is an amphoteric element, which means that, in a strongly alkaline environment, it forms soluble aluminate ions (Wefers and Misra, 1987). This is a fundamental difference from calcium hydroxide, which is a buffer for hydroxyl ions in Portland cement paste. This issue was discussed in detail by Kotwica and Malich (2022). The formation of an ASR gel without altering the stability of aluminium hydroxide suggests that ASR gel formation is possible in environments with relatively low concentrations of hydroxyl ions, less than the commonly accepted threshold level of 0.2 M (Rajabipour et al., 2015). Other important issue which should be raised is the fact that the severe expansion occurs in the system without external source of hydroxyl ions and without calcium hydroxide, which is often referred to as a source of hydroxyl ions in a specific hydroxyl ions cycle (Thomas, 2001).

3. Conclusions

The research presented in this article investigated the possibility of an ASR reaction in high-alumina cement mortars caused by the influence of organic and inorganic deicing agent solutions. The following conclusions were drawn:

- 3 mole/dm³ solutions of organic salts (acetates and sodium and potassium) and inorganic (sodium chloride and nitrate) caused severe deterioration of high alumina cement mortars containing fused silica (10%) as reactive aggregate. Samples without fused silica did not exhibit expansion.
- Organic anions (acetate and formate) caused much higher expansion compared to inorganic anions (chloride and nitrate).
- ASR gel was found within all expanding samples.
- The alkali-silica reaction occurred in the system with low concentration of hydroxyl ions, compared to Portland cement.
- The alkali-silica reaction occurred in the system without external supply of hydroxyl ions and without solid calcium hydroxide within the hydrated cement paste.
- The results show the necessity of further research on the influence of pH and pOH on the initiation and course of the alkali-silica reaction in cement-based composites.

Acknowledgements

The study was supported by the Polish National Science Centre, research project No. 2020/04/X/ST5/02090.

References

- Chatterji, S., Jensen, A.D., Thaulow, N., Christensen, S. (1986) "Studies of Alkali-Silica Reaction. Part 3. Mechanism by Which NaCl and Ca(OH)₂ Affect the Reaction" *Cement and Concrete Research*, 16: 246-254
- Diamond, S., Kotwica, L., Olek, J., Rangaraju, P.R., Lovell, J., Fournier, B., (2006) "Chemical aspects of severe ASR induced by potassium acetate airfield pavement de-icer solution", *Proc. M.A Berube Symp. on AAR in Concrete*, 261-279
- Gaztariaga, M.T., Gofii, S., Sagrera, J.L. (1993) "Reactivity of high-alumina cement in water: pore-solution and solid phase characterization" *Solid State Ionics*, 63-65:797-802
- Glasser, F.P. (1992) "Chemistry of the alkali – aggregate reaction" in Swamy, R.N. (ed.), *The Alkali – Silica Reaction In Concrete*, Blackie, Van Nostrand Reinhold, New York
- Gholizadeh Vayghan, A., Rajabipour, F., Rosenberger, J. L. (2016) "Composition–rheology relationships in alkali–silica reaction gels and the impact on the gel's deleterious behaviour" *Cement and Concrete Research* 94: 45-56.
- Heisig, A., Urbonas, L., Beddoe, R.E., Heinz, D. (2016) "Ingress of NaCl in concrete with alkali reactive aggregate: effect on silicon solubility" *Materials and Structures* 49: 4291-4303
- Kotwica, L., Malich, M. (2022) "Alkali-silica reaction in calcium aluminate cement mortars induced by deicing salts solutions" *Road Materials and Pavement Design*, 23: 1707-1730
- Rajabipour, F., Giannini, E., Dunant, C., Ideker, J.H., Thomas, M.D. (2015) "Alkali-silica reaction: current understanding of the reaction mechanisms and the knowledge gaps" *Cement and Concrete Research* 76: 130–146
- Rangaraju, P.R., Sompura, K.R., Olek, J. (2006) "Investigation into Potential of Alkali–Acetate–Based Deicers to Cause Alkali-Silica Reaction in Concrete" *Transportation Research Record*, 1979:69-78
- Rangaraju, P.R., Olek, J. (2007) "Potential for acceleration of ASR in presence of pavement deicing chemicals", IPRF (Innovative Pavement Research Foundation) Research Report, No. 01-G-002-03-92007
- Taylor, H.F.W. (1997) *Cement Chemistry* 2nd ed., Thomas Telford, London
- Thomas, M. (2001) "The role of calcium hydroxide in alkali recycling in concrete" in Skalny, J., Gebauer, J., Odler I. (ed.) *Materials Science of Concrete: Calcium Hydroxide in Concrete*, Wiley-Blackwell.

AAM – oil composite: a new highly durable material with a negative carbon footprint

F. Mittermayr^{1*}, O. Rudic¹, M.R.M. Saade², C. Grengg³

¹ *Institute of Technology and Testing of Building Materials, Graz University of Technology, Graz, Austria*

Email: f.mittermayr@tugraz.at; ognjen.rudic@tugraz.at

² *Institute of Structural Design, Graz University of Technology, Graz, Austria*

Email: m.ruschimendessaade@tugraz.at

³ *Institute of Applied Geosciences, Graz University of Technology, Graz, Austria*

Email: cyrill.grengg@tugraz.at

ABSTRACT

In this study the effects of very high (waste) vegetable oil additions (up to 12vol.%) on the mechanical and microstructural properties of metakaolin-slag-based alkali-activated materials (AAMs) were investigated. Oil addition resulted in the formation of metal soap phases which significantly modified the porous microstructure reducing the inner specific surface area by a factor up to 15 for mortars. Oil-induced microstructural modifications strongly increased the resistance of AAMs against sulfuric acid attack by shifting the diffusion- and crack-controlled processes, known for AAMs without oil, towards a framework dissolution process controlled by the intrinsic phase stabilities. These promising results will help solving well-known AAM weaknesses such high drying shrinkage, low carbonation and chloride resistance and therefore, increase the range of potential future applications. In addition to improvements of the material properties, the utilization of vegetable oils permanently binds carbon in the construction material. Life Cycle Assessment calculations revealed that in case new vegetable oil is used, near carbon neutrality can be achieved. When waste cooking oil is modelled, assuming a polluter-pays-principle, a negative GWP was reached. These new findings highlight the potential of AAM-vegetable oil composites as a future high-tech and negative-carbon construction material.

KEYWORDS: *Alkali activated materials, vegetable oil, porosity, durability, negative carbon emission*

1. Introduction

Worldwide, there is the unresolved problem that Portland cement based concrete structures cause very high gray CO₂ emissions - reported as global warming potential (GWP) (Moro et al., 2022). Geopolymer or alkali-activated building materials are “cement-free” and are known to have a lower GWP than Portland cement-based concretes thanks to lower firing temperatures during raw material production and/or the use of secondary raw materials (Valente et al., 2022). Furthermore, alkali-activated materials (AAMs) are also well known for their higher durability compared to OPC based concretes in aggressive environments (Gluth et al., 2022). According to the current state of the art, however, there is no mineral-based building material whose performance is durable on the long term under extremely aggressive environmental conditions frequently encountered in, for example, wastewater systems, sewage treatment plants, landfills, composting plants and biogas plants.

On the one hand this study deals with the development of a highly durable AAM for the application in strongly aggressive environmental conditions. For this purpose, a high-performance normal concrete and a well performing AAM, that have been tested previously, are taken as the references (Juhart et al., 2021). Oil additions and modifications to the mix of the latter, led to significant performance increase which will be briefly described here. On the other hand, vegetable oils contain large amounts of carbon from fast growing plants, thus when stabilized in the AAM, the carbon from the oil acts as a carbon sink. Currently, carbon storage in building materials via vegetable oils has not been elucidated, current solution to store

carbon in mineral-based building materials, such as concrete comprise e.g. bio chars, natural fibers, bio-based aggregates or algae (Chen et al., 2022; Danish et al., 2021; Kuittinen et al., 2023; Pittau et al., 2018). Even though vegetable oils have not been described in this context, they have been used in AAMs to produce a mineral foam by introducing distinct macro porosity. After the hardening phase, the oil and potential reaction products get removed by heat or solvents (Cilla et al., 2017).

For the first time this study describes the benefits of oil additions on the material properties combined with permanent storage of carbon (or CO₂) in the building material. Compared to all known mineral building materials, outstanding material properties and a negative CO₂ balance (positive contribution to climate neutrality in the construction industry) can be achieved through this innovation.

2. Materials and Methods

The reference normal concrete was a so-called B6 concrete (according to ÖN B-4710). This type of concrete is commonly used for aggressive conditions in wastewater systems (B6 concrete mix, see Table 1). The AAM mortars are based on a metakaolin-slag K-water glass-based system and a 0/4 siliceous sand. Sunflower oil from a local market was used for the AAM – oil composite production (AAMoil_mortar, see Table 1). Mixing, casting and curing was performed according to national cement and concrete standards (EN 196 and ÖN B-4710), or described further in detail in (Juhart et al., 2021; Rudic et al., 2023; Seyrek et al., 2023). Strength tests were performed in accordance to the national cement and concrete standards (EN 196 and ÖN B-4710/ONR 23303. The inner surface was determined by nitrogen absorption using a BELSORP-mini X. Acid immersion tests were carried out on 4x4x4 cm samples in accordance to the setup described by Grengg et al. (2021) using an automatic titration reactor and sulfuric acid at pH_{stat}=2 for 8 weeks. After the exposure, the samples were dried and further optically inspected.

Table 1. Mix design

| Sample | CEM I 42.5 N SR0 (kg/m ³) | precursor* (kg/m ³) | water glass (kg/m ³) | water (kg/m ³) | oil (kg/m ³) | aggregates (kg/m ³) | plasticizer (kg/m ³) |
|---------------|---|------------------------------------|--|-------------------------------|-----------------------------|------------------------------------|-------------------------------------|
| B6_concrete | 390 | 0 | 0 | 156 | 0 | 1830 | 1.05 |
| AAM_mortar | 0 | 392 | 272 | 122 | 0 | 1520 | 0 |
| AAMoil_mortar | 0 | 392 | 272 | 122 | 122 | 1520 | 0 |

*70% metakaolin and 30% GGBFS

The environmental impact of all three mixes was assessed by calculating their global warming potential (GWP). The following GWP values for the source materials (Table 2) were taken from the ecoinvent database, environmental product declarations (EPD) and literature. For the oil, the use of waste cooking oil was assumed, therefore having zero emissions and solely an uptake of CO₂. Due to lacking data in the literature, values for sodium silicate solutions as the activator were used as an approximation for the used potassium silicate solution. The GWP values were calculated using the characterization factors published in IPCC (2021).

Table 2. Global warming potential of the source materials

| Source material | [kg CO _{2eq} /kg] | Reference |
|------------------------------|----------------------------|---|
| CEM I | 0.7179 | ecoinvent v3.7 |
| Tab water | 0.0002 | ecoinvent v3.7 |
| Plasticizer | 1.8868 | EPD of the European federation for concrete admixtures (EFCA) |
| Gravel | 0.0067 | ecoinvent v3.7 |
| Sand | 0.0100 | ecoinvent v3.7 |
| Waterglass (sodium silicate) | 0.5040 | (Komkova and Habert, 2023) |
| Metakaolin | 0.0924 | (Habert et al., 2011) |

| | | |
|--|---------|---|
| Slag | 0.0200 | (Chen et al., 2010) |
| Vegetable oil | 1.4616 | ecoinvent v3.7 |
| Uptake of CO ₂ in (waste) oil | -2.7530 | Preliminary calculations with an assumed content of 75 % C in the waste oil |

3. Results and Discussion

The addition of vegetable oil to AAMs leads to a new material, an AAM – oil composite. This short paper only enables a brief overview on material properties, thus interested readers are referred to our future studies (Rudic et al., 2023; Seyrek et al., 2023). Compressive strength results, results from the inner surface (Sp) and the total GWP of each individual mix is shown in Table 3.

Table 3. Compressive strength, BET and GWP results

| Sample | Compressive strength | | | Sp (m ² /g) | Global warming potential (kg CO ₂ eq/m ³) |
|---------------|----------------------|----------|-----------|---------------------------|---|
| | 1d (MPa) | 7d (MPa) | 28d (MPa) | | |
| B6_concrete | n.d. | n.d. | 84 | n.d. | 348 |
| AAM_mortar | 47 | 60 | 63 | 46.7 | 218 |
| AAMoil_mortar | 32 | 41 | 46 | 3.2 | -117 |

It is obvious that the oil lowers the compressive strength for the here presented mix as it creates a well pronounced macroporosity (Rudic et al., 2023). In future studies this effect could be reduced by optimizing the mix design and also the mixing procedure (Seyrek et al., 2023). Due to the process of saponification, the addition of oil leads to greatly reduced internal surfaces and significantly reduced open porosity (data not shown). As a result, diffusion related processes and capillary moisture transport are significantly reduced. In other words, substances harmful to the AAM can only penetrate the building material to a small extent - in most cases not at all. This is well visible in Figure 1, where the high-performance concrete suffered the most damage after the 8 weeks in sulfuric acid immersion. The AAM without oil showed less but still very noticeable deterioration signs. The surface was covered with white crystalline efflorescence which is known to be K-alum and some cracks are visible. The detailed description on the damaging mechanisms of similar AAMs in sulfuric acid and in real sewers with microbial induced acid corrosion can be found in (Grenng et al., 2021a; Grenng et al., 2021b). The AAM with the oil addition displayed little to no signs of corrosion, emphasizing the low acid diffusion rates and the high stability of the metal soap phases.

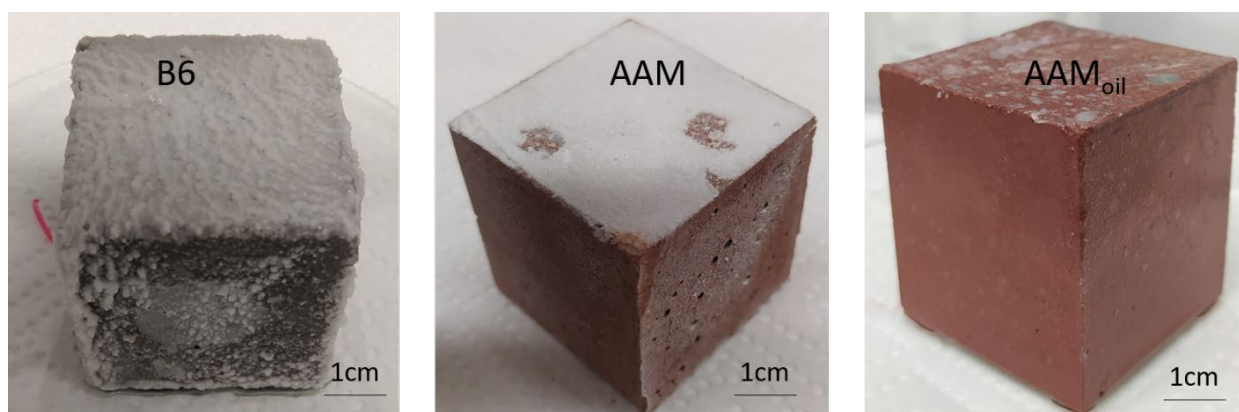


Figure 1. Specimen B6 (high-performance concrete for wastewater applications), AAM and AAMoil after exposure to sulfuric acid (pHstat = 2) for 8 weeks.

In addition to improvements in terms of material performance, the use of vegetable oils makes it possible to permanently bind carbon in the building material. Life cycle calculations showed that with the use of new vegetable oils (carbon content ~75%) almost CO₂-neutral AAMs can be produced. The use of, for example, ~100 kg of waste cooking oil per m³ of AAM results in a negative GWP, if adopting a cut-off approach for end-of-life modelling. For our laboratory tests, (waste) cooking oil quantities of 80 - 160 kg/m³ were successfully used (data not shown here). This results in a GWP of about 70 to -150 kg CO_{2eq}/m³ of AAM. Figure 2 shows the calculation of the formulation from this study where 122 kg/m³ oil and a corresponding GWP of -117 kg CO_{2eq}/m³ AAM was achieved.

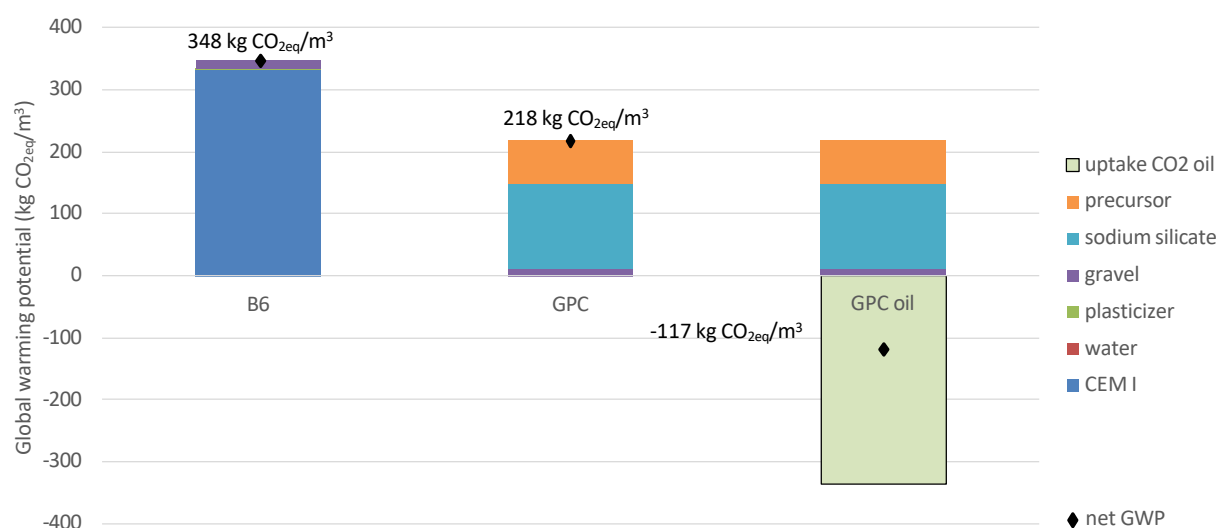


Figure 2. Global Warming Potential (GWP) of B6 concrete (high performance concrete for wastewater applications) compared to AAMs with and without oil addition. The addition of 122 kg of waste cooking oil to the AAM formulation results in a net GWP of -117 kg CO_{2eq} per m³.

4. Conclusions

When (waste) vegetable oil in high quantities (up to 12 vol.%) was added to the alkali-activated materials investigated in this study, numerous beneficial effects and material properties could be achieved and the following conclusions can be drawn:

- Oil addition resulted in the formation of metal soap phases which significantly modified the porous microstructure reducing the inner specific surface area by a factor up to 15.
- Oil-induced microstructural modifications strongly increased the resistance of AAMs against sulfuric acid attack mainly due to reduced diffusion of the aggressive species, thus changing the nature of degradation mechanism from diffusion- and crack-controlled processes, towards a framework dissolution process controlled by the intrinsic phase stabilities.
- The utilization of (waste) vegetable oils permanently binds carbon in the construction material. When waste cooking oil is modelled, a negative GWP was reached.

These new findings highlight the potential of AAM-vegetable oil composites as a future high-tech and negative-carbon construction material.

Acknowledgements

The authors gratefully acknowledge the funding by the Austrian Research Promotion Agency FFG (BioResComp Project-No. 871279) and the involved industry partners.

References

- Chen C, Habert G, Bouzidi Y, Jullien A, Ventura A. LCA allocation procedure used as an incitative method for waste recycling: An application to mineral additions in concrete. *Resour Conserv Recycl* 2010;54:1231–40. <https://doi.org/10.1016/J.RESCONREC.2010.04.001>.
- Chen L, Zhang Y, Wang L, Ruan S, Chen J, Li H, et al. Biochar-augmented carbon-negative concrete. *Chem Eng J* 2022;431:133946. <https://doi.org/10.1016/J.CEJ.2021.133946>.
- Cilla MS, de Mello Innocentini MD, Morelli MR, Colombo P. Geopolymer foams obtained by the saponification/peroxide/gelcasting combined route using different soap foam precursors. *J Am Ceram Soc* 2017;100:3440–50. <https://doi.org/https://doi.org/10.1111/jace.14902>.
- Danish A, Ali Mosaberpanah M, Usama Salim M, Ahmad N, Ahmad F, Ahmad A. Reusing biochar as a filler or cement replacement material in cementitious composites: A review. *Constr Build Mater* 2021;300:124295. <https://doi.org/10.1016/J.CONBUILDMAT.2021.124295>.
- Gluth G, Grengg C, Ukrainczyk N, Mittermayr F, Dietzel M. Acid resistance of alkali-activated materials: recent advances and research needs. *RILEM Tech Lett* 2022;7:58–67. <https://doi.org/10.21809/rilemtechlett.2022.157>.
- Grengg Cyrill, Gluth GJG, Mittermayr F, Ukrainczyk N, Bertmer M, Guilherme Buzanich A, et al. Deterioration mechanism of alkali-activated materials in sulfuric acid and the influence of Cu: A micro-to-nano structural, elemental and stable isotopic multi-proxy study. *Cem Concr Res* 2021;142:106373. <https://doi.org/10.1016/J.CEMCONRES.2021.106373>.
- Grengg C., Koraimann G, Ukrainczyk N, Rudic O, Luschnig S, Gluth GJG, et al. Cu- and Zn-doped alkali activated mortar – Properties and durability in (bio)chemically aggressive wastewater environments. *Cem Concr Res* 2021;149:106541. <https://doi.org/10.1016/J.CEMCONRES.2021.106541>.
- Habert G, D'Espinose De Lacaillerie JB, Roussel N. An environmental evaluation of geopolymer based concrete production: reviewing current research trends. *J Clean Prod* 2011;19:1229–38. <https://doi.org/10.1016/J.JCLEPRO.2011.03.012>.
- IPCC, 2021: Climate Change 2021: The Physical Science Basis. Contribution of Working Group I to the Sixth Assessment Report of the Intergovernmental Panel on Climate Change [Masson-Delmotte, V., P. Zhai, A. Pirani, S.L. Connors, C. Péan, S. Berger, N. Caud, Y. Chen, L. Goldfarb, M.I. Gomis, M. Huang, K. Leitzell, E. Lonnoy, J.B.R. Matthews, T.K. Maycock, T. Waterfield, O. Yelekçi, R. Yu, and B. Zhou (eds.)]. Cambridge University Press, Cambridge, United Kingdom and New York, NY, USA, In press, doi:10.1017/9781009157896.
- Juhart J, Gößler C, Grengg C, Mittermayr F, Rudic O, McIntosh A, et al. Material characterization of geopolymer mortar for its beneficial use in composite construction. *RILEM Tech Lett* 2021;5:174–85. <https://doi.org/10.21809/rilemtechlett.2020.125>.
- Komkova A, Habert G. Environmental impact assessment of alkali-activated materials: Examining impacts of variability in constituent production processes and transportation. *Constr Build Mater* 2023;363:129032. <https://doi.org/https://doi.org/10.1016/j.conbuildmat.2022.129032>.
- Kuittinen M, Zernicke C, Slabik S, Hafner A. How can carbon be stored in the built environment? A review of potential options. *Archit Sci Rev* 2023;66:91–107. <https://doi.org/10.1080/00038628.2021.1896471>.
- Moro C, Francioso V, Lopez-Arias M, Velay-Lizancos M. The impact of CO₂ uptake rate on the environmental performance of cementitious composites: A new dynamic Global Warming Potential analysis. *J Clean Prod* 2022;375:134155. <https://doi.org/10.1016/J.JCLEPRO.2022.134155>.
- Pittau F, Krause F, Lumia G, Habert G. Fast-growing bio-based materials as an opportunity for storing carbon in exterior walls. *Build Environ* 2018;129:117–29. <https://doi.org/10.1016/j.buildenv.2017.12.006>.
- Rudic O, Mittermayr F, Gluth GJG, Simon S, Ukrainczyk N, Seyrek Y, et al. On the benefits of vegetable oil addition for alkali activated systems. Submitted 2023.
- Seyrek Y, Mittermayr F, Grengg C, Freytag B, Juhart J. Impact of humidity and vegetable oil addition on mechanical properties and porosity of geopolymers. Submitted 2023.
- Valente M, Sambucci M, Chougan M, Ghaffar SH. Reducing the emission of climate-altering substances in cementitious materials: A comparison between alkali-activated materials and Portland cement-based composites incorporating recycled tire rubber. *J Clean Prod* 2022;333:130013. <https://doi.org/10.1016/J.JCLEPRO.2021.130013>.

Coefficient of thermal expansion of alkali-activated slag concrete

Z. Li^{1,2*}, X. Liang², C. Liu², and G. Ye²

¹ *Department of Materials Science and Engineering, The University of Sheffield, Sheffield, United Kingdom*
Email: Zhenming.li@sheffield.ac.uk

² *Department of Materials and Environment, Faculty of Civil Engineering and Geoscience, Delft University of Technology, Delft, the Netherlands*

ABSTRACT

Alkali-activated slag (AAS) is a new type of binder that has lower carbon footprint than ordinary Portland cement (OPC). AAS concrete can show high strength and good durability. However, its volume stability issues have not been fully understood. For example, the thermal deformability of AAS concrete has seldom been studied, although it is vital for the cracking control of the concrete under practical conditions. To estimate the thermal deformation of AAS concrete under a certain temperature history, coefficient of thermal expansion (CTE) of the concrete is needed. Currently, there is little information on this in the literature. In this study, two methods are proposed to determine the CTE of AAS concrete. One is by directly experimental measurement and the other is by calculation based on the total deformation and autogenous deformation. The CTE of AAS concrete is found to stabilize at around $18 \times 10^{-6}/^{\circ}\text{C}$, much higher than that of OPC concrete, which normally falls in the range of $5\text{--}13 \times 10^{-6}/^{\circ}\text{C}$. This information is worthy consideration for the design of AAS concrete in structural applications.

KEYWORDS: *Coefficient of thermal expansion, alkali-activated slag, thermal deformation, autogenous shrinkage, modelling*

1. Introduction

Alkali-activated materials have emerged as promising alternative binders to ordinary Portland cement in civil engineering in order to improve the sustainability of this sector. Ground granulated blast-furnace slag is the most widely used precursor for alkali-activated materials due to the high strength and satisfactory durability of alkali-activated slag (AAS) (Bernal & Provis (2014), Nedeljković et al. (2018)). However, the volume stability of AAS has not been clearly understood. Binder materials and concrete show various volume changes, such as autogenous shrinkage, drying shrinkage and thermal deformation. For concrete with a considerable thickness, thermal deformation is critical since the heat generated in the concrete cannot be readily transmitted to the environment. This will result in two thermal-related issues. First, the temperature within concrete will be spatially heterogenous, with the core part hotter than the edge. The gradient of thermal deformation will induce internal stress within the concrete, e.g., tensile stress in the concrete edge. The second issue is the temperature change with time and the corresponding thermal deformation. To reach equilibrium with the environment, the heat generated in concrete will eventually be released and the thermal shrinkage associated with cooling of concrete will induce tensile stress if the concrete is restrained by rebar, adjacent concrete, etc. Considering the relatively low tensile capacity of concrete, tensile stress should be limited in order to avoid the development of cracking. However, the thermal deformation of AAS concrete has rarely been investigated (Lacante et al. (2022), Li et al. (2022)). A key factor governing the thermal deformation of concrete is its coefficient of thermal expansion (CTE). In this paper, the CTE of AAS concrete is measured by a meticulously designed experimental approach. The measured data is then compared with the simulated one, which is obtained by extracting thermal deformation from the total deformation. This study is expected to provide some useful data for structural design of AAS concrete.

2. Methods

2.1 Materials and mixture design

Ground granulated blast-furnace slag was the precursor used in this study to make AAS concrete. Sodium hydroxide combined with sodium silicate was used as the activator. Per 100 g of activator contained 13.8 g of SiO₂, 9.4 g of Na₂O and 76.8 g of water (i.e., M_s = 1.5). Round gravel and river sand were used as aggregates. The volume fraction of aggregate in the concrete was 0.67. The detailed mixture design is shown in Table 1.

Table 1. Mixture proportion of AAS concrete.

| Components (kg/m ³) | Slag | Activator | Aggregate [0-4 mm] | Aggregate [4-8 mm] | Aggregate [8-16 mm] |
|------------------------------------|------|-----------|-----------------------|-----------------------|------------------------|
| AASC | 400 | 200 | 789 | 440 | 525 |

2.2 Experimental method

Two Autogenous Deformation Testing Machines (ADTM)s with foam plastics moulds were employed in this study to obtain CTE. One ADTM was used to measure the temperature evolution and the free deformation of the concrete under semi-adiabatic condition (results can be found in (Li et al. (2022))), while the other ADTM was used to impose small temperature changes (± 1 °C) for a short period at certain ages. In the rest of the time, the temperatures of the two ADTM)s were kept the same to minimize the difference in maturity of the two concrete samples. The CTE was obtained according to the measured deformation of the concrete in ADTM2 associated with each temperature fluctuation (Figure 1).

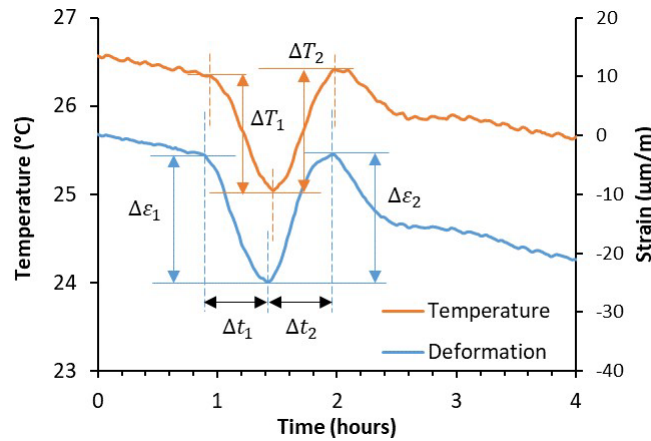


Figure 1. Deformation of the concrete associated with an imposed temperature fluctuation.

It needs to be noted that the measured $\Delta\epsilon_1$ and $\Delta\epsilon_2$ were not strictly thermal deformation. Autogenous shrinkage also contributed even though the time intervals (Δt_1 and Δt_2) were short. To obtain the CTE, autogenous shrinkage should be separated from the thermal deformation, as shown in Equation 1.

$$\alpha_{CTE} = \frac{\Delta\epsilon_{th}}{\Delta T} = \left(\frac{\Delta\epsilon_{th1}}{\Delta T_1} + \frac{\Delta\epsilon_{th2}}{\Delta T_2} \right) / 2 = \left(\frac{\Delta\epsilon_1 - \Delta\epsilon_{au1}}{\Delta T_1} + \frac{\Delta\epsilon_2 + \Delta\epsilon_{au2}}{\Delta T_2} \right) / 2 = \left(\frac{\Delta\epsilon_1}{\Delta T_1} + \frac{\Delta\epsilon_2}{\Delta T_2} \right) / 2 + \left(\frac{\Delta\epsilon_{au1}}{\Delta T_1} - \frac{\Delta\epsilon_{au2}}{\Delta T_2} \right) / 2 \quad (1)$$

where $\Delta\epsilon_{th}$ and $\Delta\epsilon_{au}$ is the thermal strain and autogenous shrinkage in a certain time interval, respectively. ΔT is the temperature difference. $\Delta\epsilon_1$ and $\Delta\epsilon_2$ are the successive deformations during the first temperature cycle, as shown in Figure 1.

Since the time intervals Δt_1 and Δt_2 were short (around 0.5 hour), the developing rate of autogenous shrinkage in this period can be assumed as constant. Moreover, the increasing and decreasing rates of the concrete temperature were rather similar. Therefore, the sum of the terms for autogenous shrinkage in Equation 1 is approximately equal to zero. In this case, the CTE of the concrete at a certain age t can be approximately calculated as Equation 2.

$$\alpha_{CTE}(t) = (\frac{\Delta\epsilon_1(t)}{\Delta T_1(t)} + \frac{\Delta\epsilon_2(t)}{\Delta T_2(t)})/2 \quad (2)$$

2.3 Simulation method

The other method to obtain CET was based on the temperature history and thermal deformation under semi-adiabatic condition measured by ADTM1. To obtain the thermal deformation, the autogenous deformation needed to be separated from the total deformation (Equation 3). The autogenous deformation under semi-adiabatic condition can be simulated by the autogenous deformation under isothermal condition using equivalent age. The autogenous shrinkage data under isothermal condition was taken from (Li et al. (2020)). Arrhenius law was used to obtain the equivalent age.

$$\alpha_{CTE}(t) = \frac{\Delta\epsilon_{th}(t)}{\Delta T(t)} = \frac{\Delta\epsilon_{tot}(t) - \Delta\epsilon_{au}(t)}{\Delta T(t)} = \frac{\Delta\epsilon_{tot}(t) - \Delta\epsilon_{au,iso}(t_{eq})}{\Delta T(t)} \quad (3)$$

3. Results and discussion

3.1 Experimentally measured CTE

The measured CTEs at different curing ages are shown in Figure 2. It can be seen that the CTE first decreases from more than $22 \times 10^{-6}/^{\circ}\text{C}$ to around $13 \times 10^{-6}/^{\circ}\text{C}$, indicating the hardening process of the concrete. Afterwards, the CTE of AAS concrete keeps increasing. The trend is like what has been observed for OPC concrete (Li et al. 2021). After 7 days, the change in CTE is minor. Comparing the results in literature (Carette et al. 2018), it can be seen that AAS concrete shows higher CTE than OPC concrete, the CTE of which normally falls in the range of $5\text{--}13 \times 10^{-6}/^{\circ}\text{C}$. This information is worthy consideration when designing AAS concrete for structural applications. It needs to be noted, nonetheless, that the CTE of AAS concrete should be dependent on the mixture design and curing conditions. Future studies are recommended to investigate the deviation resulting from these factors.

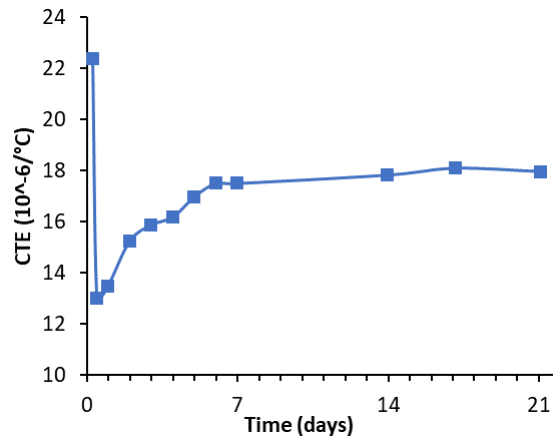


Figure 2. Measured CTE of AAS concrete.

3.2 Simulated CTE

The simulated CTE shows a large deviation from the experimentally measured one, as indicated from Figure 3. In the first days, the simulated CTE decreases first and then increases, showing a consistent trend with the measured one, and the magnitudes of the two sets of data are at in the same order. However, afterwards, the deviation becomes much larger and even negative CTE was obtained (not shown in Figure 3). This is because the temperature of the concrete was stabilized after the first five days. The temperature change became rather minor and could be disturbed by even small changes in environment temperature. Dividing the calculated thermal deformation by a very small and fluctuated temperature change results in a largely scattered CTE. In addition, the determination of autogenous shrinkage at equivalent ages based on Arrhenius law may also induce error since it has not been validated that Arrhenius law applies for alkali-activated materials. By comparison, it seems that experimental measurement is more reliable than the simulation method used to obtain CTE.

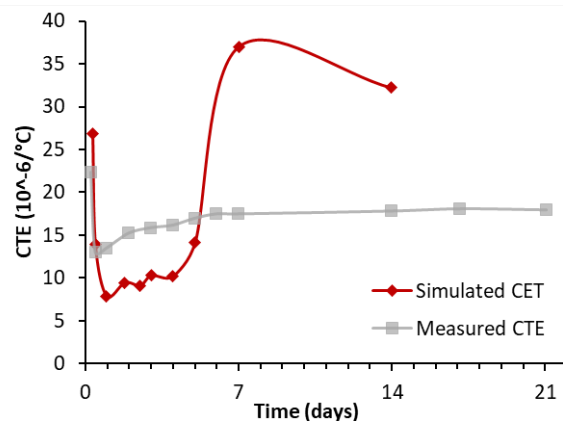


Figure 3. Simulated CET of AAS concrete.

4. Conclusions

Based on the experiment and simulation results of this study, the following conclusions can be drawn:

- The CTE of AAS concrete decreases during the hardening process and then increases with time, reaching a plateau after 7 days.
- The CTE of AAS concrete is generally higher than that of OPC concrete, which needs to be considered during design of AAS concrete structure.
- The CTE obtained from the simulated thermal deformation shows a big deviation from the experimentally measured one, especially in the late age, indicating a low accuracy of the simulation method used. Experimental measurement seems a more reliable way to determine CTE of AAS concrete.

Acknowledgements

WOOL2LOOP project (grant number 821000) funded by the European Union's Horizon 2020 research and innovation programme and MSCA project (grant number EP/X022587/1) funded by UK Research and Innovation are acknowledged for the support of Zhenming Li.

References

- Bernal, S. A., & Provis, J. L. (2014). Durability of alkali-activated materials: progress and perspectives. *Journal of the American Ceramic Society*, 97(4), 997–1008.
- Carette, J., Joseph, S., Cizer, Ö., & Staquet, S. (2018). Decoupling the autogenous swelling from the self-desiccation deformation in early age concrete with mineral additions: micro-macro observations and unified modelling. *Cement & Concrete Composites*, 85, 122–132.
- Lacante, M., Delsaute, B., Gambacorta, J., Königsberger, M., & Staquet, S. (2022). Development of early age autogenous and thermal strains of alkali-activated slag-fly ash pastes. *Frontiers in Built Environment*, 8, 286.
- Li, L., Dao, V., & Lura, P. (2021). Autogenous deformation and coefficient of thermal expansion of early-age concrete: Initial outcomes of a study using a newly-developed Temperature Stress Testing Machine. *Cement and Concrete Composites*, 119, 103997. <https://doi.org/10.1016/j.cemconcomp.2021.103997>
- Li, Z., Liang, X., Liu, C., Liang, M., van Breugel, K., & Ye, G. (2022). Thermal deformation and stress of alkali-activated slag concrete under semi-adiabatic condition: Experiments and simulations. *Cement and Concrete Research*, 159, 106887.
- Li, Z., Zhang, S., Liang, X., & Ye, G. (2020). Cracking potential of alkali-activated slag and fly ash concrete subjected to restrained autogenous shrinkage. *Cement and Concrete Composites*, 114, 103767. <https://doi.org/10.1016/j.cemconcomp.2020.103767>
- Nedeljković, M., Li, Z., & Ye, G. (2018). Setting, Strength, and Autogenous Shrinkage of Alkali-Activated Fly Ash and Slag Pastes: Effect of Slag Content. *Materials*, 11(11), 2121. <https://doi.org/10.3390/ma11112121>

Study on the Deterioration Mechanism of Cementitious Waterproofing Membrane (Part I: Macroscopic Performance)

J. Wang¹, W.Y. Li¹, B. Peng², J.X. Liao¹, S.X. Wang², Z. Zeng² and X. Kong^{1*}

¹ Department of Civil Engineering, Tsinghua University, Beijing, 100084, China

Email: kxm@mail.tsinghua.edu.cn

² BASF Advanced Chemicals Co., Ltd., Shanghai 200137, China

Email: bo.a.peng@basf.com

ABSTRACT

Understanding the deterioration mechanism is essential for improving the service life and durability as well as upgrading the formula of cementitious waterproofing membranes (CWPM). This study discloses the correlation between the deterioration process and evolution of microstructures, which is further divided into part I, the change of macroscopic performance; and part II, the evolution of microstructures and compositions including inorganic cementitious part, organic polymer film, and inorganic/organic (I/O) interface. The accelerated deterioration process of CWPM was investigated by the method of water immersion. It is found that the degree of cement hydration in the freshly prepared CWPM is only about 5%, suggesting that a large amount of cement is unreacted and still reactive during the long service period. In the early stage of water immersion, the plummet of mechanical strength of the CWPM is majorly related to the plasticizing effect of water on the polymer film. For long-term evaluation, it is shown that the organic polymer phase exhibits negligible variations indicated by Fourier transform infrared spectroscopy (FTIR). The key to durable CWPM is primarily the waterproofing property of the polymer film itself as water migration may occur through the channels between the fused polymer particles in the formed polymer films.

KEYWORDS: *waterproofing membrane, composite cementitious material, deterioration mechanism, mechanical strength.*

1. Introduction

Polymer emulsion is widely used in cement and concrete. The addition of emulsion can significantly improve the toughness and impermeability of cement products. (Benali, 2017; Wang et al, 2015; Waldvogel et al. 2021) Cementitious waterproofing membrane (CWPM) is a kind of water-based building waterproof coating, which is made of different types of polymer emulsion and inorganic fillers such as cement, quartz, and calcium carbonate in a reasonable proportion. (Fu et al, 2011) CWPM is widely used in the roof waterproofing of industrial and civil buildings, as well as the wall and ground waterproofing of bathrooms, kitchens, basements, swimming pools, etc. (Muhammad et al, 2015) Therefore, impermeability, mechanical properties, and durability are the main indicators to evaluate the quality of CWPM.

This paper mainly studies the mechanical properties of the CWPM and the changes of the emulsion and cement, which are the main components of the CWPM, in the deterioration process by the technology of mechanical test, moisture content test, thermogravimetric test (TG) and Fourier transform infrared spectroscopy (FTIR). The accelerated deterioration of the CWPM is realized by immersing the membrane in water, which can well simulate the real service conditions of the CWPM.

2. Experiments

2.1 Materials and Methods

Styrene-acrylic emulsion and Portland cement are used to prepare CWPM, and a small amount of defoamer is added to the paste to eliminate bubbles generated during high-speed mixing. The emulsion and defoamer are provided by BASF Auxiliary Chemicals Co. Ltd. (Shanghai). The cement is P.I 42.5 type standard cement conforming to Chinese national standards GB 8076-2008. Two kinds of quartz sand, 70-120 mesh, and 100-200 mesh are used after being mixed evenly according to the mass ratio of 1:1. The properties of styrene-acrylic emulsion and cement used in this study are shown in Table 1. The specific mix proportion of the waterproof membrane is shown in Table 2. The preparation of CWPM was referred to the Chinese industry standard JC/T1017-2006. The thickness of the CWPM prepared according to the standard method is about 2mm. Cut the CWPM to obtain a rectangular film sample with a length of 150 mm and a width of 20 mm for the immersing experiment.

Table 1 The properties of styrene-acrylic emulsion and cement

| Styrene-acrylic emulsion | | Cement | |
|--------------------------|-----------|---------------------------|-------|
| Properties | value | Mineralogical composition | wt. % |
| Polymer content | 57% | C ₃ S | 58.3 |
| Polymer size | 220 nm | C ₂ S | 19.3 |
| Charge density (pH=7) | 705 ueq/g | C ₃ A | 7.1 |
| Charge density (pH=12) | 312 ueq/g | C ₄ AF | 10.2 |
| | | Gypsum | 5.0 |

Table 2 The specific mix proportion of CWPM

| Component | cement | emulsion | water | sand | defoamer |
|-----------|--------|----------|-------|-------|----------|
| Mass (g) | 100.0 | 100.0 | 9.0 | 100.0 | 1.0 |

2.2 Deterioration process and properties test of CWPM

The service environment of CWPM is simulated by water immersion. The mass ratio of water to CWPM samples is 10:1. Place the samples in water until it is taken out at a specific age, and test the mechanical strength, moisture content, hydration degree of cement, and properties of the polymer. The moisture content test is to dry the surface water of the sample that has reached the soaking time and then put it in the drying oven to dry to constant weight, and then weigh the mass difference of the waterproof film before and after drying, which is the moisture content of the CWPM. The mechanical properties of the CWPM, including tensile strength and elongation, were tested using SHIMADZU EZ-LX-100N universal testing machine. Before the test, the water on the surface of the water-soaked CWPM should be absorbed by the absorbent paper. The samples used in the test are I-shaped membranes, and the sample size conforms to the China national standard GB/T16777-1997. The test adopts displacement control mode, and the loading rate is 50 mm/min. Setline STA synchronous thermal analyzer (SETARAM, France) was used for the TG-DSC test of CWPM. The heating temperature increased from 25 °C to 1000 °C at the rate of 10 °C/min and the whole heating procedure was in a nitrogen atmosphere. The sample carrier is made of alumina and the mass of the sample for each test was about 50 mg. The polymer of the CWPM was characterized on a VERTEX 70 infrared spectrometer (Bruker, Germany). The patterns were collected in the wavenumber range from 4000 cm⁻¹ to 600 cm⁻¹. The number of scans was 128 for each sample.

3. Results and discussion

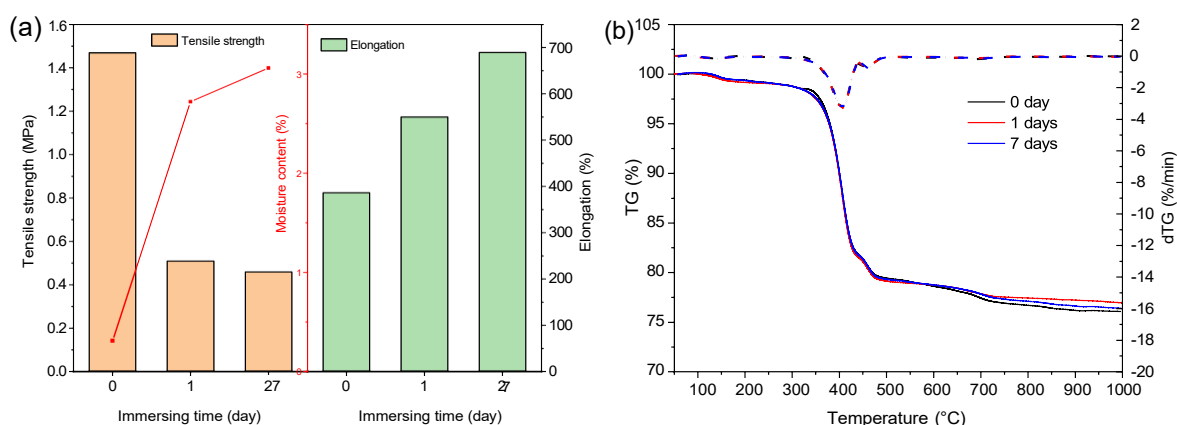


Fig. 1 (a) Changes in tensile strength, moisture content, and elongation of CWPM over immersing time; (b) TG-dTG results of CWPM after different immersing time

As shown in Fig. 1 (a), the moisture content of the CWPM increases with the increase of immersing time, while the tensile strength decreases rapidly. Corresponding to tensile strength, the elongation of CWPM increases with the increase of the moisture content of CWPM. After immersing for several days, the CWPM has an obvious tensile strength decline. This degradation of mechanical properties is not irreversible. After drying the CWPM after immersing, that is, the dry CWPM after the moisture content test, the mechanical properties of the CWPM are tested again, and its tensile strength and elongation are the same as that of the 0-day sample. This means that the degradation of the mechanical properties of the CWPM during the early immersing period is not caused by the deterioration of the CWPM but by the plasticizing effect of water on the polymer.

The TG-DSC results also showed that the components of the CWPM such as cement and polymer did not change significantly during the 7-day immersion as shown in Fig. 1(b). It can be seen from the thermogravimetric curve that there are three obvious weight-loss stages in the whole heating process of the CWPM. The weight loss at 100–200 °C mainly comes from the hydration products of cement, such as ettringite and calcium silicate hydrates (C-S-H) dehydration, and a small amount of free water left in the CWPM after the polymer film formation. The weight loss at 300–500 °C is the largest, which is mainly caused by the decomposition of polymer and calcium hydroxide (CH). The weight loss at 600–800 °C is the weight loss of calcium carbonate decomposition. The weight loss at 430–500 °C belongs to CH decomposition, which can be used to estimate the hydration degree of cement. The estimated result shows that cement in CWPM just had very weak hydration, only about 5% (the largest CH content in complete hydration cement paste is 27%). This shows that polymer has a strong inhibition on cement hydration. (Su et al, 1991; Kong et al, 2016)

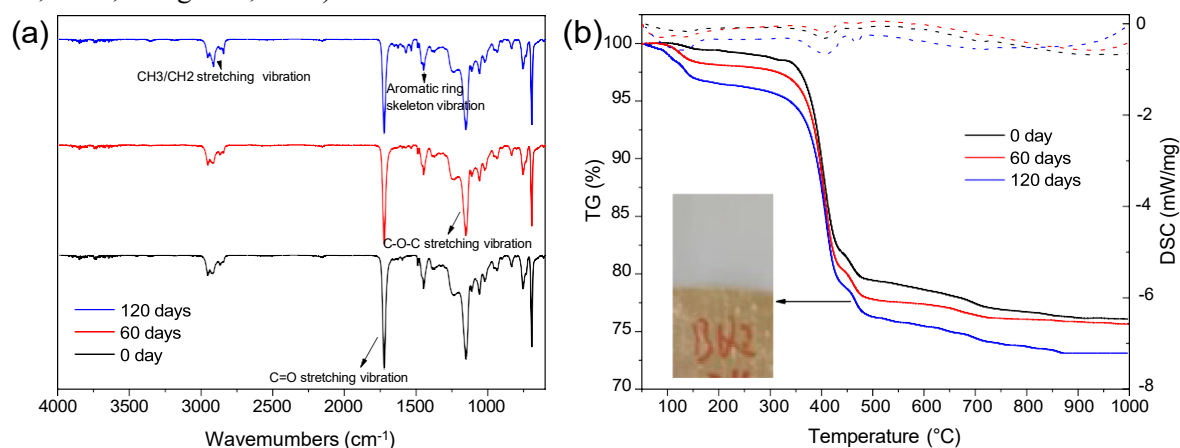


Fig. 2 The FTIR spectrum (a) and TG-dTG results (b) of CWPM after different immersing time

Combined with the data of mechanical strength and thermogravimetry, it can be seen that the CWPM had not to cause secondary hydration of the cement inside it after soaking in water for a short time, and its strength decline is mainly caused by the plasticizing effect of water on the polymer. The real deterioration

of the CWPM needs to wait until enough water enters the CWPM to wake up the cement hydration again or make the polymer undergo irreversible degradation and destruction. As shown in Fig. 2 (a), the structure of the polymer in the CWPM did not change significantly during the immersion period within 120 days, that is, the performance of the polymer was very stable during this period. However, the mechanical strength of the CWPM has been completely lost at 120 days and cannot be recovered. This means that the CWPM has completely deteriorated after 120 days of soaking, and the reason can be seen from the thermogravimetric results in Fig. 2 (b). With the increase in soaking time, the weight loss of CWPM gradually increases. This is mainly due to the secondary hydration of cement in the membrane. The secondary hydration of cement produced a large number of hydration products, which severely destroyed the inorganic-organic interface (I-O interface) in the CWPM, and in the macro view, there are a large number of cracks and bulges on the surface of the CWPM.

The mechanical test, FTIR and TG results showed that the deterioration of CWPM was mainly related to the secondary hydration of cement. Due to the high polymer content in the CWPM, which has a strong retardation effect on the cement hydration, the cement particles act as the inert filling phase rather than the active minerals, so the deterioration process of the CWPM is the process of water migrating from the outside to the I-O interface inside the CWPM and further hydration of the cement. Time-domain NMR can be very convenient to characterize the water migration process and polymer changes in the membrane. The characterization results and analysis of TD-NMR of waterproof membranes will be displayed in the second part of this study.

4. Conclusions

In this study, the mechanical properties of the cementitious waterproofing membrane (CWPM) and the changes of the emulsion and cement, which are the main components of the CWPM, in the deterioration process by the mechanical test, thermogravimetric (TG) and Fourier transform infrared spectroscopy (FTIR). The accelerated deterioration condition is realized by immersing the membrane in water. It is found that the degree of cement hydration in the freshly prepared CWPM is only about 5%, suggesting that a large amount of cement is unreacted and still reactive during the long service period. In the early stage of water immersion, the plummet of mechanical strength of the CWPM is majorly related to the plasticizing effect of moisture on the polymer film. For long-term evaluation, it is shown that the organic polymer phase exhibits negligible variations. The secondary hydration of the unreacted cement in films is the main reason for the deterioration of CWPM. The key to durable CWPM is primarily the waterproofing property of the polymer film itself as water migration may occur through the channels between the fused polymer particles in the formed polymer films.

Acknowledgments

This work is supported by the cooperation project “Durability of cementitious waterproofing membrane” between Tsinghua University and BASF Advanced Chemicals Co., Ltd.

References

- Benali, Y. and Ghomari F. (2017) “Latex influence on the mechanical behavior and durability of cementitious materials”, *Journal of adhesion science and Technology*, 31.3: 219-241.
- Fu, W., Wang L. and Huang J. (2011) “Polymer cement waterproof coating and its properties.”, *Advanced Materials Research*, 189: 252-255.
- Kong, X., et al. (2016) “Effect of polymer latexes with cleaned serum on the phase development of hydrating cement pastes”, *Cement and Concrete Research*, 84: 30-40.
- Muhammad, N Z, et al. (2015) “Waterproof performance of concrete: A critical review on implemented approaches”, *Construction and Building Materials*, 101: 80-90.
- Su, Z., J. M. J. M. Bijen, and J. A. Larbi. (1991) “Influence of polymer modification on the hydration of Portland cement”, *Cement and concrete research*, 21.2-3: 242-250.
- Waldvogel, M., et al. (2020) “The microstructural evolution of cementitious, flexible waterproofing membranes during deformation with special focus on the role of crazing”, *Cement and Concrete Composites*, 107: 103494.
- Wang, R., et al. (2015) “Study on waterproof mechanism of polymer-modified cement mortar”, *Magazine of Concrete Research*, 67.18: 972-979.

Impact of an evolving microstructure on the square-root law for chloride ingress

F. Georget^{1*}, W. Wilson², K. Scrivener³, and T. Matschei¹

¹ Institute of Building Materials Research, RWTH Aachen University, Aachen, Germany
Email: georget@ibac.rwth-aachen.de, matschei@ibac.rwth-aachen.de

² Université de Sherbrooke, Sherbrooke, QC, Canada
Email: william.wilson@usherbrooke.ca

³ Laboratory of Construction Material, EPFL, Lausanne, Switzerland
Email: karen.scrivener@epfl.ch

ABSTRACT

The square root law was proposed as an easy analytical tool to assess chloride ingress in cementitious materials, and validate the performance of novel binders with respect to durability issues. However, it was observed experimentally that an offset to the square root law is often required to fit the chloride penetration depth as function of the square root of time. This offset was found more pronounced in systems with slow hydration. Using a single-species reactive transport model, we investigate the link between a decreasing diffusion coefficient and the evolution of the penetration depth, to analyze how early-age effects influence our interpretation of the square root law.

KEYWORDS: Chloride ingress, Square-root law, Reactive Transport, Diffusion Coefficient

1. Introduction

The performance assessment of novel binders requires the development of experimental and analytical methods to quickly assess the properties of these binders, and extrapolate it to long-term conditions. In this study, we focus on chloride ingress as the main durability issue. In recent works, the square-root method was proposed as an analysis and extrapolation tool (Fjendbo et al., 2021; Georget et al., 2023). The square root law is a direct consequence of the control of the chloride ingress by the ionic diffusion in the cementitious material. It relates the penetration depth of chloride (x_l) to the square root of time:

$$x_l = a \sqrt{t} \quad (1)$$

Where a is an empirical parameter dependent on the diffusion coefficient of the material, the exposure conditions and the chloride threshold chosen. An equivalent view proposed in (Georget et al., 2023), was to use a master chloride profile curve, where the chloride content is plotted as function of x/\sqrt{t} rather than just x . The master curve was illustrated to be a very good tool to analyse a variety of in-situ chloride exposed concrete for long-term. However, in some systems, limitations of the square-root law were highlighted. In particular, it was proposed (Fjendbo et al., 2021; Wilson et al., 2023) to use a modified version of the square-root law including an offset:

$$x_l = a \sqrt{t} + b \quad (2)$$

However, the empirical evidences are not yet sufficient to understand the physical interpretation or meaning to attach to this parameter. It is hypothesized that it is related to slowly evolving microstructure, where hydration has a long-term (>1 month) impact on the diffusion coefficient. This is a similar interpretation to the more common aging-coefficient use in the apparent diffusion coefficient approach. In this presentation, we aim to investigate this hypothesis and analyse the impact of a decreasing diffusion coefficient on a single-species reactive transport of model ingress using preliminary simulations of cement pastes samples.

2. Methods

The model presented in (Georget et al., 2023) is used in this study. It is a single-species reactive transport implemented in the reactive transport framework ReactMiCP (Georget et al., 2017). Single species means here that only the chloride is considered, i.e. all the effects of ion-competitions are hidden in the macroscopic parameters. The governing equation is written as :

$$\frac{\partial \varphi c}{\partial t} = \frac{\partial y}{\partial x} \cdot D \cdot \frac{\partial c}{\partial x} - B \quad (3)$$

Where, B is the binding model, such that the total chloride content is $C = \varphi c + B$, and D^* is the diffusion coefficient. As this study aims to understand concepts, the models and values for these parameters are chosen to be representative rather than calibrated to particular experiments.

The chemical model (B) uses competitive Langmuir-based model for a pH-dependent binding isotherm as presented in (Georget et al., 2023), using the same parameters. This model was used as it leads to more representative chloride profile shapes.

Two different diffusion coefficient models were used. In the results section, the *fixed microstructure* simulations correspond to the model where a fixed diffusion coefficient is used ($2.5 \cdot 10^{-9} \text{ cm}^2/\text{s}$). It is the control case. The *hydrating sample* results correspond to the model where the diffusion coefficient is updated at every timestep according to the following formula:

$$D_{i,\$ \% \&} = \max(D_{i,\$} - k \Delta t \$ \% \&, D_{i,(\$)} \quad (4)$$

Where $D_{i,\$} = 2.0 \cdot 10^{-8} \text{ cm}^2/\text{s}$, $D_{i,(\$)} = 2.5 \cdot 10^{-9} \text{ cm}^2/\text{s}$, and $k = 1.0 \cdot 10^{-9} \text{ cm}^2/\text{s}^2$. This corresponds to a relatively fast initial diffusivity, and a slow “hydration”-like behaviour, where the diffusion coefficient reaches its minimum in around a month.

The mesh, solver and other parameters are kept identical to (Georget et al., 2023). A non-uniform mesh was used to accurately model the initial gradients. A sequential iterative splitting algorithm is used to solve separately the governing (diffusion, eq. 3) equations, the chemical reactions (binding) and the upscaling parameters (diffusion coefficient). The binding term and the diffusion coefficient are solved using a backward-Euler algorithm. The diffusion equation (eq. 3) is discretized using a finite volume scheme. It is solved using an implicit scheme using the predictor-multicorrector approach presented in (Georget et al., 2017). The residuals of eq. 3 is used to control the convergence of the sequential iterative algorithm.

3. Results

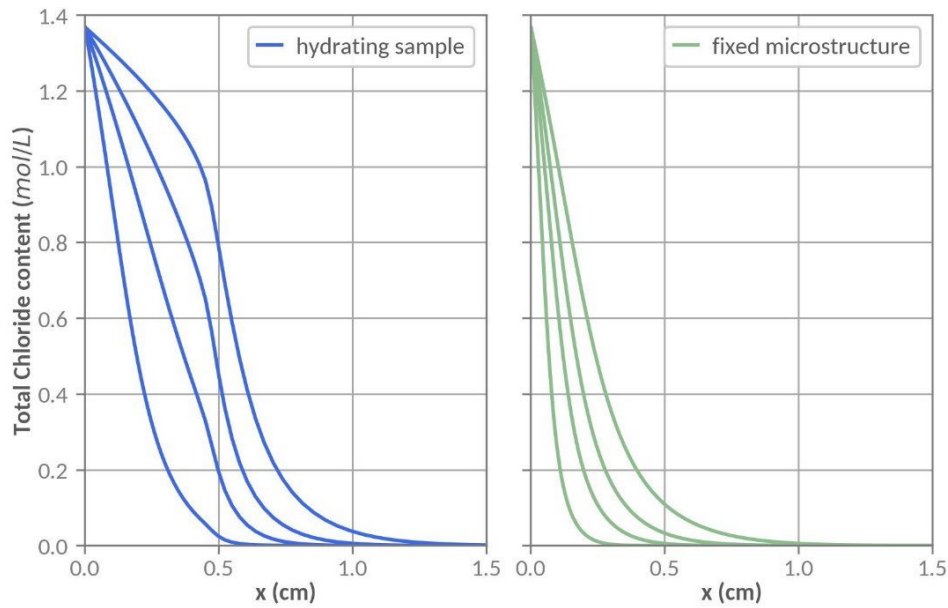


Figure 1: Simulated chlorides profiles at 28, 90, 180 and 365d for cement pastes exposed to a 0.5M NaCl solution

Figure 1 presents the simulated chloride profiles at 28d, 90d, 180d and 365d for a) the evolving microstructure and b) the fixed microstructure set of parameters. The fixed microstructure profiles are typical of diffusion profiles and could be fitted using the error function without problems. On the other hand, the evolving microstructure profiles are “deformed”. They show untypical undulations in the profiles, even at late age (>3 months). However, in practice, these bumps and indents could easily be attributed to experimental scatter, especially at the typical experimental resolution (~2-10 mm), and the error function would still be used in practice.

The penetration depths as function of the square root of time are presented in Figure 2. If the common square root fit ($x_i = a\sqrt{t}$) is valid anytime for the fixed diffusion coefficient simulation, it is clear that a modified version is needed for the evolving microstructure. In particular, if late age is of interest, a simple offset is sufficient to capture the trends: $x_i = a\sqrt{t} + b$. The linear regression is shown in Figure 2. We can observe that the sampling is crucial to obtain the correct slope in the regression. In particular, for a threshold of 0.5 mol/L, the 90 days data should not be included in the regression, although it is perfectly valid for the 0.1 mol/L threshold. Of course, this cannot be inferred only using bulk diffusion experiments, given the low number of experimental data points, due to the difficulty to obtain traditional chloride profiles. The effect of the experimental sampling and the threshold on the validity of the square-root law will be explored in-depth in a further publication.

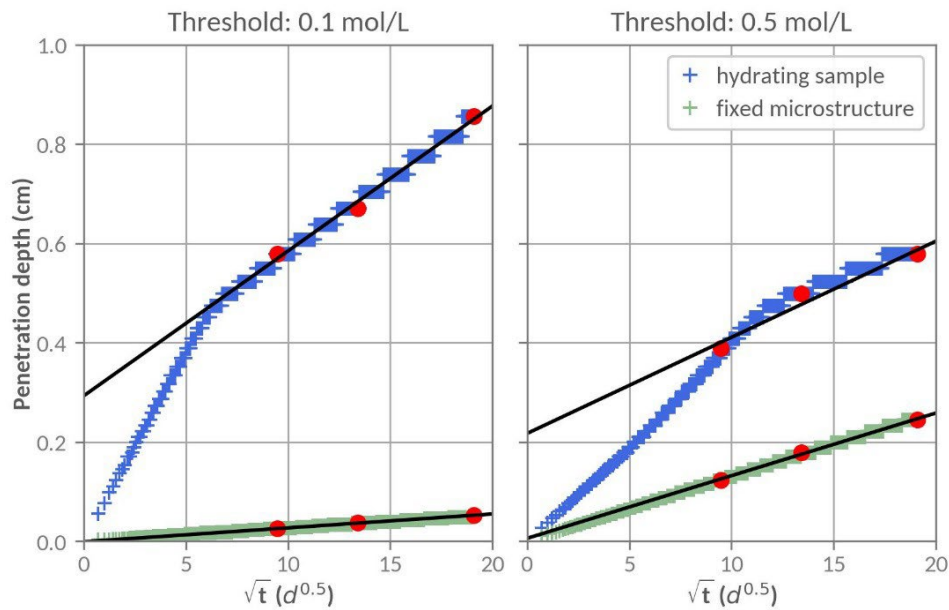


Figure 2: Chloride penetration depths as function of the square root of time for two chloride thresholds. Red points correspond to the sampling of the data at 90, 180 and 365d, and the black line is the linear regression corresponding to this sampling.

In (Georget et al., 2023), the master curve approach was utilized to assess the validity of the square root law approach. As expected, we can observe in Figure 3 the master curve is well adapted to describe the fixed microstructure samples. However, in the case of the hydrating samples, the curves do not overlap perfectly. This is related to the bumps and indents observed in Figure 1. It was proposed to correct the master curve using the offset. We can observe that applying the offset on the master curve ($(x - b)/\sqrt{t}$) is sufficient to recover the master curve, at least partially for 90, 180 and 365d. As a general observation, the master curve cannot be recovered at early-age or for high threshold, where the early-age effects can be observed for longer. Nevertheless, the master curve approach is still valid for the ingress in the material, if the surface effects are neglected.

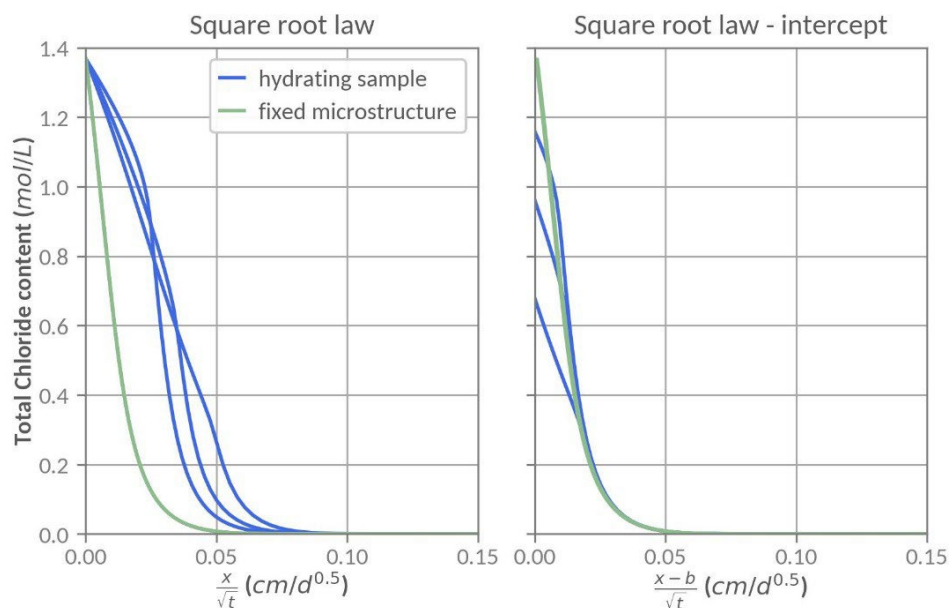


Figure 3: Master curve view using a) the square root law and b) the square root law with intercept for the 90d, 180d and 365d using a threshold of 0.25mol/L

4. Conclusions

In this set of simulations, we investigated the impact of a slow hydration on the chloride profiles and their analysis with the square root law. Although, a non-trivial binding model (e.g. including the effect of leaching) do not impact the validity of the square-root law, a slow change of the diffusion coefficient can lead to a significant to the square-root law.

As proposed in the literature, an offset to the square-root law can be sufficient to fit the experimental data point. In this study, we showed that the offset can be caused by a time-dependent diffusion coefficient. However, the definition of this offset is highly dependent on the chloride threshold used to obtain the penetration depth, and the *a-priori* definition of the early-age. To obtain a meaningful fitting it is important to clearly identify which points should be included in the fit to avoid artefacts. A difficulty identified in these simulations is that the chloride threshold has an effect on the definition of the early-age. A higher threshold means that the early-age effects have a longer influence.

An *a-posteriori* method to validate the choice of threshold and experimental data is the use of the master curve. When the offset is correctly defined, the master curve can be recovered, especially at the tail of the profile, the most representative of the late-age microstructure. However, the tail of the curve is also the most sensitive to the sample heterogeneities. Further investigation is needed to adapt these theoretical results into practical analysis methods.

References

- Fjendbo S, Sørensen HE, De Weerd K, Geiker MR. The square root method for chloride ingress prediction—Applicability and limitations. *Mater Struct* 2021;54:61. <https://doi.org/10.1617/s11527-021-01643-8>.
- Georget F, Prévost JH, Huet B. A reactive transport simulator for variable porosity problems. *Computational Geosciences* 2017;21:95–116. <https://doi.org/10.1007/s10596-016-9596-x>.
- Georget F, Wilson W, Matschei T. Long-term extrapolation of chloride ingress: An illustration of the feasibility and pitfalls of the square root law. *Cement and Concrete Research* 2023;170:107187. <https://doi.org/10.1016/j.cemconres.2023.107187>.
- Wilson W, Georget F, Scrivener KL. The square root law with an offset applied to chloride diffusion in slowly reacting blended cement pastes. *The 16th International Congress on the Chemistry of Cement 2023 (ICCC2023) "Further Reduction of CO₂ -Emissions and Circularity in the Cement and Concrete Industry," Bangkok, Thailand: 2023.*

Formation Factor as a Non-Destructive Measure of Chloride Diffusion Coefficient

S. Hasnat^{1*}, S. Rafiuzzaman², A. Chowdhury³, B. Baten⁴ and T. Manzur^{5*}

¹Dept. of Civil Eng., Bangladesh University of Engineering and Technology, Dhaka, Bangladesh

Email: 1704037@ce.buet.ac.bd

²Dept. of Civil Eng., Bangladesh University of Engineering and Technology, Dhaka, Bangladesh

Email: 1704049@ce.buet.ac.bd

³Dept. of Civil Eng., Bangladesh University of Engineering and Technology, Dhaka, Bangladesh

Email: 1704167@ce.buet.ac.bd

⁴Dept. of Civil and Env. Eng., University of Illinois Urbana-Champaign, Champaign, Illinois, United States

Email: bbaten2@illinois.edu

⁵Dept. of Civil Eng., Bangladesh University of Engineering and Technology, Dhaka, Bangladesh

Email: tanvirmanzur@ce.buet.ac.bd

ABSTRACT

Ensuring pozzolanic activity of supplementary binders (particularly with fly ash) is essential to enhance permeability characteristics and service life of reinforced concrete (RC) structures in environment susceptible to chloride induced corrosion. As a measure of chloride intrusion, chloride diffusion coefficient (D_{rcm}) comprises an essential tool which however relies on standard destructive migration test. Meanwhile, in recent years, the concept of Formation Factor (FF) has emerged as a viable non-destructive measure of concrete microstructure refinement. As a measure of the resistivity of the non-conductive solid phase (ρ_o) and resistivity of the conductive medium of the pores (ρ_w) within concrete matrix, FF possess an immense potential in assessing ion transfer characteristics within concrete matrix. Moreover, with the addition of supplementary cementitious materials (SCM) having active silica within cement mix, the resultant pozzolanic activity results in greater pore refinement and causes significant variation in pore solution resistivity. Hence, the impact of pore refinement in lowering the diffusion coefficients of concrete is expected to be substantially reflected by the FF. This study investigated the potential of using FF as a reliable indicator of D_{rcm} values and more importantly, as a non-destructive alternative of standard RMT test. In addition, some relevant issues affecting the reliability of FF as a non-destructive measure of concrete durability have been pointed out. The study involved a wide range of concrete mixes with different fly-ash replacement level (0-35%) to ensure a varied pozzolanic reactivity for a target design strength and slump. The ion-transport properties were evaluated through measurements of electrical resistivity and simulated pore solution conductivity. The results represent the correlation of the predicted D_{rcm} values to the RMT tests and signify potential of FF as a reliable indicator of concrete microstructure refinement.

KEYWORDS: Chloride diffusion coefficient, resistivity, pore solution conductivity, non-destructive alternative, formation factor

1. Introduction

Poor durability of concrete is one of the major setbacks of modern construction as it results in reduced service life of reinforced concrete (RC) structures. In recent times, regular durability assessment and structural health monitoring have become an essential component of sustainable construction (Baten and

Manzur, 2022). Such assessment is imperative in vulnerable conditions such as marine environments, where corrosion induced by chloride intrusion can significantly affect the structural capacity and service life of RC structures (Manzur et al., 2019). The service life assessment of RC structures involve determination of chloride diffusion coefficients (D_{rcm}), which can be obtained by standard methods such as NT BUILD 492 (1999). However, such methods are destructive and usually require core extraction from existing structures which can further reduce the capacity of structures under consideration. Hence, it is essential that non-destructive and convenient methods are applied for assessing the diffusion characteristics of concrete as an indicator of durability. It is well established that an understanding of the ion transport properties within concrete matrix can be determined using the electrical resistivity of concrete (Spragg et al., 2013a). Electrical resistivity is a measure of the ability of concrete to resist the movement of ions through its micro-structure and therefore, the movement of substances which attribute to its deterioration. Resistivity measurements are relatively low cost and quick to perform while having the most desirable feature of being non-destructive. In addition, electrical resistivity could provide a trustworthy indicator of D_{rcm} since both of the characteristics are controlled by the pore structure of the concrete (Sallehi et al., 2018). Therefore, electrical resistivity, when related to D_{rcm} , can be used to predict the service life of a RC structure (Baten and Manzur, 2022). A very potent tool in relating the electrical resistivity of concrete to D_{rcm} is the concept of Formation Factor (FF) (Spragg et al., 2013a; Baten and Manzur, 2022). As the ratio of bulk resistivity (ρ_o) of concrete to the resistivity of the liquid phase, also known as the pore solution resistivity (ρ_w), FF concept has the ability to assess the pore structure characteristics of a concrete mix. The electric resistivity (ρ_t) of porous composite material like concrete depends on three factors i.e., a) the resistivity of the pore solution (ρ_w) which depends on the composition and the chemical concentrations of the solution, b) the porosity of the system (ϕ), and c) the connectivity of the pores in the system (β). The ρ_t can be expressed as $\rho_t = \rho_w (1/\phi\beta)$ where, $1/\phi\beta$ constitutes the parameter, FF since, ϕ and β have similar effects and are inseparable. Comprehensive details of FF concept can be found in Spragg et al., 2013a; 2013b; Baten and Manzur, 2022 etc. However, not many significant studies are available that investigated the applicability of FF concept for evaluating the diffusion coefficient of concrete especially under chloride induced corrosion exposure. Hence, it is important to evaluate the validity of such method through conducting adequate experimental investigations in order to ensure practical application of FF concept as a simpler indicator of the micro-structural properties. With this end in view, a study has been attempted to utilize the concept of FF in estimating the D_{rcm} for a wide range of concrete mixes with normal to moderate compressive strengths and varying common design mix parameters (water/binder ratio, target slump etc.) along with different proportions of SCMs. In this article, the initial outcome of the study is presented that covers some common concrete mixes of Bangladesh having certain mix design parameters and fly ash (FA) as SCM with replacement level up to 35%. The results predicted from FF concept were validated against actual test data obtained through rapid migration test (RMT), the conventional destructive method. The correlation between the D_{rcm} predicted from FF and those obtained from RMT has been discussed and potential direction of future investigation has been identified.

2. Experimental Program

2.1 Materials and Concrete Mix Design

The cement used for this study was Type-I Ordinary Portland Cement (OPC) and Class-F fly ash was used to incorporate the effects of pozzolanic activity in the concrete pore system. Concrete mix design with w/c ratios ranging from 0.35 to 0.57 and design compressive strengths from 38 MPa to 18 MPa were chosen by varying the cement content from 586 kg/m³ to 360 kg/m³, following the ACI Mix Design Manual. The target slump of 75-100 mm was achieved without the addition of admixtures by increasing the water content while keeping the w/c ratio constant to investigate the impact of higher water content on durability performance.

2.2 Electrical Resistivity Measurements

Surface resistivity measurements using a commercially available Wennerfour-electrode (Wenner, 1916) system were conducted in this study following the provisions of AASHTO T 358-15 after 45 days of

casting. To ensure uniformity, the specimens were continuously submerged from the point of mold removal to measurement, and measurements were taken on four different surfaces at 90 degrees. However, surface resistivity measurements require correction factors such as specimen geometry, temperature, degree of saturation, storage conditions, and pore solution composition, which were all applied before computing the FF (Spragg et al., 2013a; 2013b; Weiss et al., 2013; Bu and Weiss, 2014). Pore solution resistivity was obtained by an online tool developed by Bentz (2007) which is available at the website (nist.gov/el/materials-and-structural-systems-division-73100/inorganic-materials-group-73103/estimation-pore).

2.3 Non-steady state rapid migration test

Migration tests were performed on the specimens following nordtest method NT BUILD 492 after 45 days of casting. After the completion of the migration tests on the 50 ± 2 mm concrete disks, they were split and sprayed with a solution of AgNO_3 until the precipitation of a white AgCl . The depth of the precipitate was measured resulting in the non-steady state migration coefficient D_{rcm} .

3. Results and Discussions

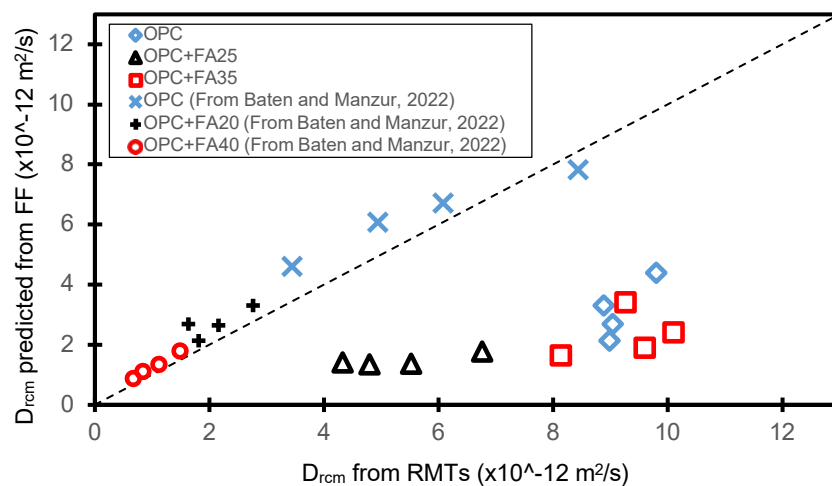


Fig 1: Variation of D_{rcm} predicted from FF with D_{rcm} determined experimentally

Fig. 1 shows the results obtained from this study. The dotted line refers to the 45° line. It can be observed that for the data obtained for this study, the D_{rcm} obtained from non-steady state migration tests ($D_{\text{rcm-RMT}}$) are higher than those predicted from the FF concept ($D_{\text{rcm-FF}}$). A similar study was done by the same research group (Baten and Manzur, 2022), which exhibited a particularly good relationship between $D_{\text{rcm-RMT}}$ and $D_{\text{rcm-FF}}$, with almost all of the scatter points falling relatively close to the 45° line. For the experiments done in this study, the leaching of alkalis was not controlled as the samples were saturated by submergence in water. Previous studies have shown (Weiss et al., 2013; Spragg et al., 2013a) that leaching of alkalis from the pore solution results in a higher resistivity than sealed curing. Such leaching also results in a pore solution gradient (Spragg et al., 2013a), thus causing the pore solution near the surface of the cylinder to have a higher resistivity, while the pore solution resistivity lessens towards the core. This causes uncertainties in surface resistivity measurements that are only limited to the surface proximity. The degree of hydration used for the estimation of pore water resistivity was assumed from studies done by Liu et al. (2017). As such, there may be inaccuracies in the assumptions of degree of hydration at 45 days. Another interesting observation obtained from this study is the reduced durability properties for the FA35 mixes compared to the FA25 ones. Increased alkalinity is believed to have an effect on this behavior. The study done by Bu and Weiss (2014) has observed the bulk resistivity in concrete to decrease with increasing alkali content up to a certain amount, after which it plateaus. Although it is a well established concept that increasing alkali content results in a faster pozzolanic reaction, thus a more rapid pore refinement (Song et al., 2000); the pore solution resistivity reduces with increasing alkali content. Shehata and Thomas (2010) showed the pore solution alkalinity to vary

proportionally with the oxide index that has been defined as $(\text{Na}_2\text{O}_e \times \text{CaO})/(\text{SiO}_2)$ of the cementing blend. The oxide index values for this study for the OPC, OPC+FA25 and OPC+FA35 mixes were 0.22, 0.078 and 0.056, respectively while those for the mixes by Baten and Manzur (2022) were 0.10, 0.045 and 0.038, respectively which are lower by a significant margin. This indicates that the pore solution alkalinity of the current study are definitely higher than the one done by Baten and Manzur (2022). There have not been many studies observing the effects of varying alkalinity on the electrical and transport properties of concrete with varying SCMs. Previous studies (Shehata and Thomas, 2010; Chopperla and Ideker, 2022) have suggested that SCMs with a higher alkalinity and lesser pozzolanic activity will result in a lower bulk resistivity and pore solution resistivity.

4. Conclusion

Based on the results, this study highlighted some key considerations required to establish FF as a reliable non-destructive measure of concrete durability. The effect of leaching of alkalis needs to be considered for using FF as a durability evaluation tool. Leaching initially affects the resistivity in the external surface zone resulting in a pore solution gradient which primarily impacts surface resistivity measurements. As a result, leaching of alkalis can considerably impact the concrete surface resistivity. However, such leaching of alkalis is not an influencing factor for determining D_{rcm} . This nonlinear relationship has not been accounted for in computations regarding D_{rcm} determination from the FF approach. It is also important to consider the effects of curing conditions and degree of saturation. Addressing these factors properly, FF can have undeniable applicability to assess the D_{rcm} rather economically and rapidly compared to conventional codes and practices. Therefore, this study provides valuable insights on potential of using FF as a measure of transport properties of concrete under various conditioning.

5. References

- Baten, B. and Manzur, T. (2022) "Formation Factor Concept for Non-Destructive Evaluation of Concrete's chloride diffusion coefficients", *Cement and Concrete Composites*. Elsevier Ltd, 128(December 2021): 104440.
- Bentz, D.P. (2007) "A virtual rapid chloride permeability test", *Cement and Concrete Composites*, 29(10): 723-731.
- Bu, Y. and Weiss, J. (2014) "The influence of alkali content on the electrical resistivity and transport properties of cementitious materials", *Cement and Concrete Composites*, 51: 49–58.
- Chopperla, K.S. and Ideker, J.H. (2022) "Using electrical resistivity to determine the efficiency of supplementary cementitious materials to prevent alkali-silica reaction in concrete", *Cement and Concrete Composites*, 125: 104282.
- Liu, Z., Xu, D. and Zhang, Y. (2017) "Experimental investigation and quantitative calculation of the degree of hydration and products in fly ash-cement mixtures", *Advances in Materials Science and Engineering*, vol. 2017, Article ID 2437270, 12 pages.
- Manzur, T. *et al.* (2019) "Significance of service life based concrete mix design in marine environment", Proceedings, Annual Conference - Canadian Society for Civil Engineering, 2019-June.
- NT BUILD 492, Concrete, Mortar and Cement Based Repair Materials: Chloride Migration Coefficient from Non steady-state Migration Experiments, Nordtest Method, 1999.
- Sallehi, H., Ghods, P. and Isgor, O.B. (2018) "Formation factor of fresh cementitious pastes", *Cement and Concrete Composites*, 91: 174–188.
- Shehata, M.H. and Thomas, M.D.A. (2010) 'The role of alkali content of Portland cement on the expansion of concrete prisms containing reactive aggregates and supplementary cementing materials', *Cement and Concrete Research*, 40(4), pp. 569–574. doi:10.1016/j.cemconres.2009.08.009.
- Song, S. *et al.* (2000) "Hydration of alkali-activated ground granulated blast furnace slag", *Journal of Materials Science*, 25: 249-257.
- Spragg, R. P. *et al.* (2013) "Electrical Testing of Cement-Based Materials: Role of Testing Techniques, Sample Conditioning, and Accelerated Curing", Joint Transportation Research Program, Indiana Department of Transportation, and Purdue University, West Lafayette, Indiana, 2013. Report No. FHWA/IN/JTRP-2013/28.
- Spragg, R. *et al.* (2013) "Factors that influence electrical resistivity measurements in cementitious systems", *Transportation Research Record: Journal of the Transportation Research Board*, 2342(1): 90–98.
- Weiss, J. *et al.* (2013) "Using a saturation function to interpret the electrical properties of partially saturated concrete", *Journal of Materials in Civil Engineering*, 25(8): 1097–1106.
- Wenner, F. (1916) "A method of measuring earth resistivity", *Bulletin of the Bureau of Standards*, 12(4): 469-478.

SURFACE EFFECT ON CHLORIDE DIFFUSION IN CALCIUM SILICATE HYDRATE

L. Xiong¹ and G. Geng^{1*}

1 Department of Civil and Environmental Engineering, National University of Singapore, 117576, Singapore

** ceegg@nus.edu.sg*

ABSTRACT

The diffusivity of chloride ion in calcium silicate hydrate (C-S-H) has been intensively discussed via modelling or theoretical methods due to experimental challenges caused by preparing a bulk volume of pure C-S-H with certain pore structure. The surface effect of C-S-H on chloride ion transport is lumped into a hypothetical parameter called constrictivity which again requires investigation from experimental aspects. In this study, C-S-H with nominal Ca/Si 1.3 was synthesized using hydrothermal method. The synthetic C-S-H powder was pressed into solid platelets with different compactness and chloride ingress tests in concentration-driven and voltage-driven migration setup were directly conducted on these pure porous C-S-H platelets. The effective diffusivities of C-S-H samples were calculated from the through-diffusion test results, based on which the surface effect on chloride transport were discussed. The effect of change of pH in pore solution during migration test on chloride diffusion was captured by two-segment behavior of downstream chloride content evolution. The difference in effective diffusivities obtained from diffusion and migration tests showed that the surface effect played an important role in determining Cl⁻ transport rate within C-S-H. This work provides a novel insight into the transport of Cl⁻ in C-S-H pore structure.

KEYWORDS: *Calcium silicate hydrate, Through-diffusion tests, Effective chloride diffusivity, pH, Surface effect*

1. Introduction

Chloride-related durability issues are widely discussed and studied since its' universal existence in the steel reinforced concrete infrastructure serving under chloride environment. The measurement of chloride ion penetration into concrete, commonly referred to as chloride diffusivity, holds significant importance as an essential factor in predicting the service life of steel-reinforced concrete structures described in Alexander et al (2015). The process of chloride diffusion within saturated concrete, characterized as the movement of ions driven by concentration, occurs through accessible pathways including pre-existing cracks, capillary pores, and the diffusive porous structure of the hydration product known as Calcium silicate hydrate (C-S-H). Cl⁻ transport within C-S-H phase, the main diffusive solid when porosity is smaller than certain threshold value demonstrated in Patel et al (2018), is thought to be subjected to the effect from C-S-H pore wall. The effect of electric double layer on ion diffusion in cement paste was modeled or analytical solution from simplified ideal Poisson-Boltzmann equation described in Yang et al (2019) and Zhang et al (2023). The surface effect is yet to be explored from the experiment aspect. This paper examines the transport behavior of Cl⁻ in C-S-H by quantifying the effective diffusivity from through-diffusion tests conducted on pure C-S-H solids for the first time. Samples with varying pore structures were tested to identify the role of pore size information on Cl⁻ transport rate and possible relation to the surface effect, as indicated by the obtained diffusivity values. Furthermore, the impact of

pH variations in the pore solution on transport was assessed by comparing the diffusivity values obtained from natural diffusion tests and migration experiment results.

2. Methodology

C-S-H sample with nominal Ca/Si of 1.3 was synthesized via hydrothermal method and the procedure was detailed in the previous study of Geng et al (2022). C-S-H solid pellets with a specific pore structure were obtained through the application of mechanical compression on synthetic C-S-H powders. To compare the impact of pore structure on chloride ion transport, stress levels of 200 MPa and 800 MPa were employed in this study. Afterwards, the solid pellets were submerged in epoxy and subsequently polished to achieve an approximate height of 10 mm, allowing both ends to be exposed once the epoxy had hardened. This preparation was done to facilitate the ingress of chloride ions. The polished samples underwent an additional step wherein they were individually immersed in an equilibrium solution of C-S-H within a desiccator that was slightly vacuumed to account for any water loss that occurred during the polishing process. Once their mass reached a stable state, the samples were mounted to diffusion cells specifically designed for accommodating such small sample sizes, as shown in Figure 1. The study aimed to examine the transport of chloride ions in C-S-H pellets, driven by the ion concentration gradient, using a natural diffusion setup as illustrated in Figure 1(a). The diffusion cell employed had a volume of approximately 113 mL in the upstream part (containing the chloride ion source) and 23 mL in the downstream part (without chloride addition). For each sampling interval, the solution in the downstream cell was completely replaced to maintain a relatively constant chloride concentration difference between the upstream and downstream regions. Moreover, the diffusion test employed a solution prepared from the filtered solution of C-S-H powder that had reached equilibrium. To account for the potential influence of different hydroxide ion (OH^-) concentrations on chloride ion transport rate, the pH of the filtered solution was adjusted by adding solid NaOH. To compare the steady-state diffusivity obtained from the natural diffusion test, another commonly employed method, namely the external electric field accelerated migration test, was conducted. In this test, the electrolyte cell volume was approximately 113 mL to facilitate frequent sampling, as depicted in Figure 1(b). To expedite the experiment, a constant voltage output of 5 V for the 200 MPa-compressed sample and 10 V for the 800 MPa-compressed sample was applied to the stainless-steel mesh, which functioned as the two electrodes in the setup. During the test, the voltage across the specimen was also recorded to account for any polarization effects of the electrodes. The catholyte consisted of a 0.5 M NaCl and 0.01 M NaOH (or 0.3 M NaOH) solution and a 0.3 M NaOH solution was chosen as the anolyte. The pore structure information was investigated from nitrogen sorption tests on samples after through-diffusion tests via density functional theory (DFT).

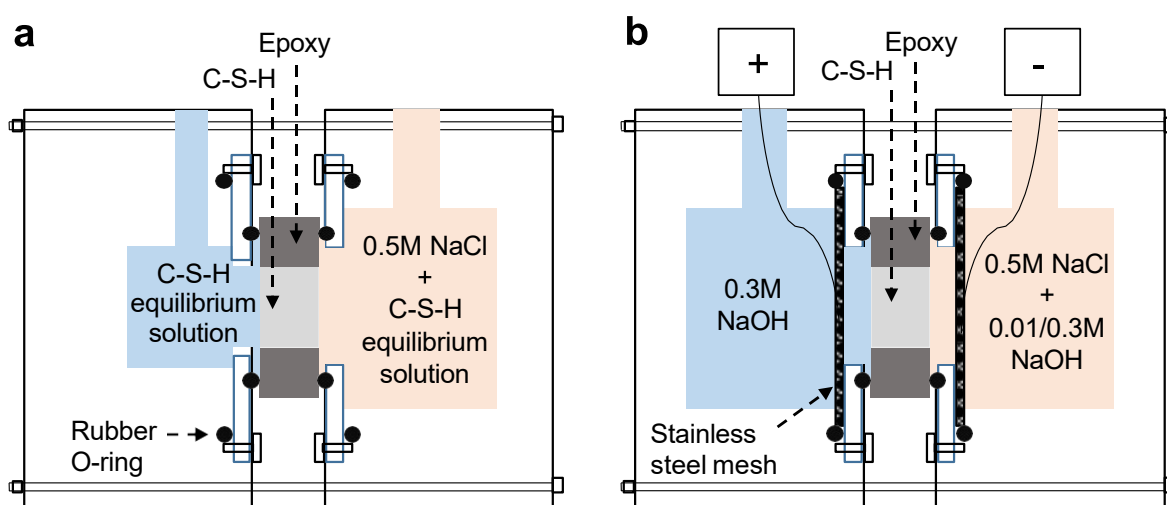


Figure 1 Schematics of through-diffusion experiment setup, (a) concentration-driven natural diffusion test, and (b) external electric field accelerated migration test.

3. Results and discussion

Pore structure of compacted platelets from 200 MPa and 800 MPa treatment by DFT analysis is shown in Figure 2 (a). Total porosity of samples prepared from 800 MPa (27.0%) is smaller than that of samples compressed under 200 MPa (41.3%) which is quite intuitive since the higher compaction load made sample denser. More fine pores can also be noticed in 800 MPa-compacted samples.

Typical chloride content evolution results in the downstream cell from diffusion and migration tests are shown in Figure 2 (b) and (c). Corresponding effective diffusivity was calculated based on Fick's 1st law and simplified Nernst-Planck equation, respectively. Obtained diffusion coefficients are listed in Table 1 and Table 2.

Based on diffusion test results, D_e was smaller for sample of same Ca/Si prepared from 800 MPa-compression compared with 200 MPa sample due to smaller total porosity which can also be noticed in migration tests. However, the diffusivity was not only influenced by the total porosity but the pore size distribution and different degree of interaction between C-S-H substrate and Cl^- . A clear shift towards smaller size regarding the most probable pores of 800 MPa compaction group compared with these of 200 MPa group can be noticed, indicating the higher chances that these diffusive pathways are interconnected via these critical pores. As a result, more pronounced constrictive effect in these small pores would also contribute to the reduction of Cl^- transport rate. When change pH of the equilibrium solution, the obtained effective diffusivities varied and is dependent on the concentration of source chloride. As shown in 800 MPa diffusion test with different upstream chloride concentration and equilibrium solution pH, When the upstream Cl^- concentration is 0.5 M, adjusting the equilibrium solution pH to 0.005 M would double the ion transport rate. However, the effective diffusivity decreased around 20% for the group with source chloride concentration of 0.01 M. And the diffusivity for 0.01 M group without pH adjust to equilibrium solution was relatively smaller than that of 0.5 M group. Thus, when the steady state diffusion was achieved, the ionic strength of the pore solution would affect the charged C-S-H pore wall's interaction with Cl^- and the role of OH^- would also change since the introduction of extra screening Na^+ to charged C-S-H surface would compete with the effect of C-S-H silanol group deprotonation caused by OH^- causing the different Cl^- transport rate.

Regarding the migration test results, two-segment linear evolution of chloride content in downstream cell can be observed. This behaviour was thought be related to the continue increase of OH^- concentration in the upstream due to the electrolysis of water during migration process. Effective diffusivity D_{e1} calculated from the first linear part was of the same magnitude to that from natural diffusion test D_e while this coefficient decreased sharply when using the second linear part to compute D_{e2} . Similar results were also obtained when change the upstream OH^- concentration from 0.01 M to 0.3 M. One of possible reasons could be the competition of current carrier for OH^- and Cl^- . However, it is not suitable to account for the reduction degree between 200 MPa and 800 MPa group since the concentration ratio of OH^- to Cl^- was similar when the chloride content began to slow down. As a result, the external electric should change the interaction between the charged C-S-H surface and Cl^- during migration and this interaction should be pore size dependant. In addition, the choice of OH^- in the chloride source part should also be careful based on the difference between diffusion and migration test results.

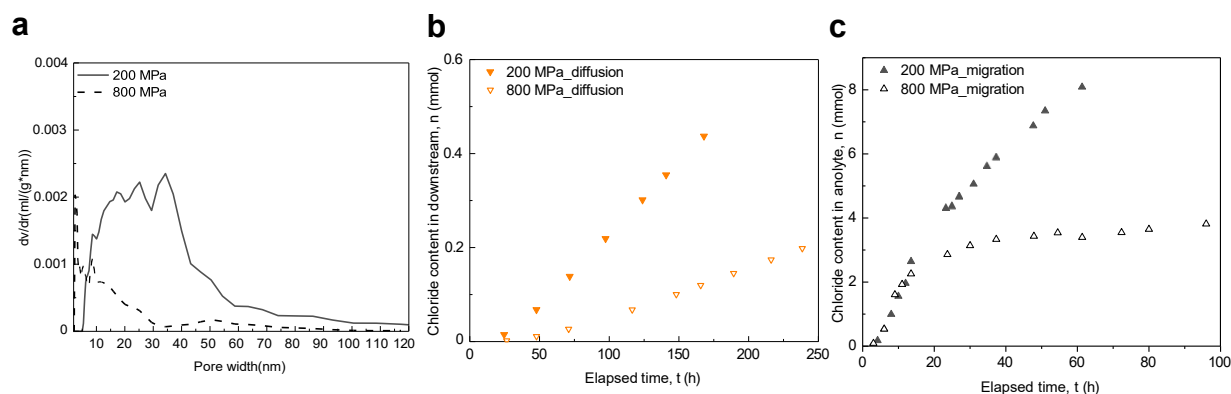


Figure 2 a) pore size distribution of 200 MPa and 800 MPa-compacted C-S-H platelets from nitrogen sorption test via DFT; typical chloride ion content evolution in downstream cell during b) diffusion test and c) migration test without pH adjustment showing two linear-segment behavior where D_{e1} and D_{e2} are calculated

Table 1 Effective diffusivity calculated from diffusion test with different pH and Cl⁻ concentration

| | Diffusion | | | | |
|---------------------------------------|----------------------|----------------------|---------------------------------------|----------------------|---------------------------------------|
| upstream chloride concentration (M) | 0.5 | 0.5 | 0.5 | 0.01 | |
| Compaction load (MPa) | 200 | 800 | 800 | 800 | 800 |
| pH adjustment | equilibrium solution | equilibrium solution | equilibrium solution with 0.005M NaOH | equilibrium solution | equilibrium solution with 0.005M NaOH |
| D_e (10^{-11} m ² /s) | 4.09 | 1.28 | 2.68 | 1.11 | 0.90 |

Table 2 Effective diffusivity calculated from migration test with different pH

| | Migration | | | |
|--|-------------|------------|-------------|------------|
| upstream chloride concentration (M) | 0.5 | | 0.5 | |
| Compaction load (MPa) | 200 | | 800 | |
| pH adjustment | 0.01 M NaOH | 0.3 M NaOH | 0.01 M NaOH | 0.3 M NaOH |
| D_{e1} (10^{-11} m ² /s) | 4.16 ± 0.14 | 1.58 | 1.64 | 0.056 |
| D_{e2} (10^{-12} m ² /s) | 14.5 ± 2.23 | | 0.57 | |

4. Conclusion

To sum up, the effect of charged C-S-H surface on chloride ion transport within C-S-H was investigated from the obtained macro diffusivities via diffusion and migration tests on pure C-S-H platelets. The OH⁻ played a different role in Cl⁻ ingress process considering the competition of effect from silanol group deprotonation caused by OH⁻ and the screening cations (Na⁺ in this study) to the charged pore wall in diffusion test setup. On the other hand, the increase of OH⁻ concentration in the upstream during migration test would hinder chloride transport and the reduction extent was related to C-S-H pore structure, providing information on the choice of OH⁻ in the migration test to make the accelerated test results comparable to that from diffusion test. And these results demonstrated the importance role of charged C-S-H surface on chloride ion transport.

References

- Alexander, M. and Thomas, M. (2015). "Service life prediction and performance testing—Current developments and practical applications", *Cement and Concrete Research*, 78, 155-164
- Liu, C. and Zhang, M. (2023). Microstructure-based modelling of chloride diffusivity in non-saturated cement paste accounting for capillary and gel pores. *Cement and Concrete Research*, 168, 107153
- Patel, R. A., Perko, J., Jacques, D., De Schutter, G., Ye, G. and Van Bruegel, K. (2018). Effective diffusivity of cement pastes from virtual microstructures: Role of gel porosity and capillary pore percolation. *Construction and Building Materials*, 165, 833-845
- Yang, Y., Patel, R. A., Churakov, S. V., Prasianakis, N. I., Kosakowski, G. and Wang, M. (2019). Multiscale modeling of ion diffusion in cement paste: electrical double layer effects. *Cement and Concrete Composites*, 96, 55-65
- Zhang, Z., Yan, Y., Qu, Z. and Geng, G. (2022). Endowing strength to calcium silicate hydrate (CSH) powder by high pressure mechanical compaction. *Cement and Concrete Research*, 159, 106858

Preparation of reactive urchin-like recycled concrete aggregate by wet carbonation: towards improving the bonding capability

Peiliang Shen^{1*}, Yi Jiang², Zihan Ma³, and Chi Sun Poon⁴

Department of Civil and Environmental Engineering, The Hong Kong Polytechnic University, Hung Hom, Kowloon, Hong Kong

¹Email: peiliang.shen@polyu.edu.hk, ²Email: yi289.jiang@connect.polyu.hk

³Email: zihan.ma@connect.polyu.hk, ⁴Email: cecspoon@polyu.edu.hk

ABSTRACT

To enhance the bonding capability between recycled concrete aggregate (RCA) and paste, an innovative carbonation method was developed to modify the surface characteristic of RCA by promoting the formation of needle-like aragonite using accelerated carbonation in Mg(NO₃)₂ solution under an elevated temperature (75 °C). The evolution of surface microstructure and phases was investigated using multiple testing methods including scanning electron microscopy, X-ray diffraction, etc. The results revealed that reactive urchin-like RCA could be prepared within less than an hour after exposing to CO₂ in 0.1 M Mg(NO₃)₂ solution and at an elevated temperature of 75 °C. The urchin-like wrapping was seen rapidly grown on the surface of RCA, consisting of an outermost layer of aragonite coating and a silica-rich layer. The mineral wrapping induced by carbonation significantly modified the roughness, topography and geochemistry of RCA's surface entirely, contributing to enhanced bonding strength between RCA and new mortar (33.54%).

KEYWORDS: *Carbonation, recycled concrete aggregate, urchin-like aragonite, bonding strength, kinetics*

1. Introduction

The incorporation of RCA in new concrete amplified the complexity of the paste matrix (Xuan, Zhan et al. 2016). This weak ITZ has been confirmed to be the main reason for the reduction in mechanical and durability properties of recycled aggregate concrete (RAC) (Gómez-Soberón 2002, Xuan, Zhan et al. 2016). Accelerated carbonation is a common method not only to improve the quality of RCA but also modify the microstructure and surface of RCA (Xiao, Li et al. 2002, Wu and Ye 2017, Zhan, Xuan et al. 2020). The increased bonding strength was mainly attributed to the calcite-aluminate reaction and the promotion of preferential growth of C-S-H due to the formation of calcite on the carbonated RCA surface (Zhan, Xuan et al. 2020). In fact, the bonding capacity of ITZ in concrete depends on many factors, which are the roughness, topography and geochemistry of aggregate, as well as the mixture proportion of the cement paste (Tasong, Lynsdale et al. 1998, Tasong, Lynsdale et al. 1999). However, the outer surface of RCA could be adversely smoothed by the precipitation of small calcite crystals, leading to a reduced bonding capacity. On another note, aragonite is another polymorph of calcium carbonate (CC) can be produced during carbonation (Zhan, Xuan et al. 2020), which has an orthorhombic system with crystal shapes such as needle-like, spindle-shape, and columnar. It was anticipated an urchin-like surface could be developed on RCA surface with the precipitation of aragonite crystals, consequently, increase the bonding interaction between RCA and paste matrix.

In this study, a rapid wet carbonation method was applied to prepare a reactive urchin-like RCA, with the control of roughness, topography and geochemistry of RCA's surface, aiming to strengthen the bonding interaction between RCA and the new cement paste. The urchin-like microstructure of the carbonated RCA was characterized by microstructural analysis. The bonding capability between urchin-like RCA and new mortar was evaluated by applying a push-out test.

2. Experimental program

2.1 Materials

The RCA was simulated by a six-month-aged pure cement paste produced using Type I Portland cement manufactured by Green Island Cement Company Limited (Hong Kong). It was prepared with a water to cement ratio of 0.45 and cured in water for 6 months before use. Table 1 shows the chemical compositions of cement that was used to prepare simulated RCA. Crushed RCA with size between 0.6-1.18 mm was used to characterize the phase and microstructure assemblage during carbonation. The crystal stabilizer ($\text{Mg}(\text{NO}_3)_2$) with a concentration of 0.1 M/L was used.

Table 1 Chemical compositions of cement (wt. %)

| Oxide | Na_2O | Al_2O_3 | SiO_2 | Fe_2O_3 | SO_3 | CaO | MgO | K_2O | LOI |
|--------|-----------------------|-------------------------|----------------|-------------------------|---------------|--------------|--------------|----------------------|------|
| Cement | 0.13 | 7.32 | 19.61 | 3.32 | 2.03 | 63.15 | 2.14 | 0.59 | 1.09 |

2.2 Preparation of urchin-like RCA and test methods

RCA was firstly added into the solution heated to 75 °C at a water to solid ratio of 10. A 5 min static immersion was performed before injecting CO_2 in order to achieve a stable environment and temperature. Subsequently, the CO_2 was injected and bubbled into the solution (0.1M/L $\text{Mg}(\text{NO}_3)_2$) at a constant rate of 0.1 L/min per 10 g RCA, while the solution was stirred rapidly with a speed of 300 rpm. The carbonated RCA particles were collected at different time intervals (5, 10, 20, 30, 60 and 180 min) and washed thoroughly by deionized water, following by a drying step in a freezer afterward.

The microstructure of the carbonated RCA was characterized by scanning electron microscopy (SEM). The phases evolution of urchin-like RCA was determined by powdered X-ray diffraction (XRD) and solid-state nuclear magnetic resonance (NMR). **The urchin-like RCA with a cylindrical shape and diameter of 20 mm were placed in the center of a cylindrical mortar specimen with a diameter of 75 mm. The bonding capability between urchin-like RCA and new mortar was evaluated by applying a push-out test with a loading speed of 0.5 mm/min.**

3. Results and analysis

3.1 Characterization of the urchin-like microstructure of carbonated RCA

The surface morphology of RCA was characterized by SEM, and the micrographs are shown in Figure 1. It can be observed from the image of non-carbonated RCA (Figure 1a) that hydration products including CH and C-S-H were present on the surface. However, under carbonation curing, the surface characteristic of RCA was completely changed. The amount of porous hydration products decreased rapidly, and they almost disappeared after carbonating for 10 min, replacing by needle-like clusters initiated started to form on the surface. Subsequently, with the prolonging of carbonation duration, the clusters gradually grow into needle-like fibers with clear edges, and eventually, after 180 min carbonation, fibers with a length ranging 5-20 μm and a diameter ranging 0.5-2 μm were formed and consolidated the surface morphology. These fibres contributed to the urchin-like microstructure of the RCA.

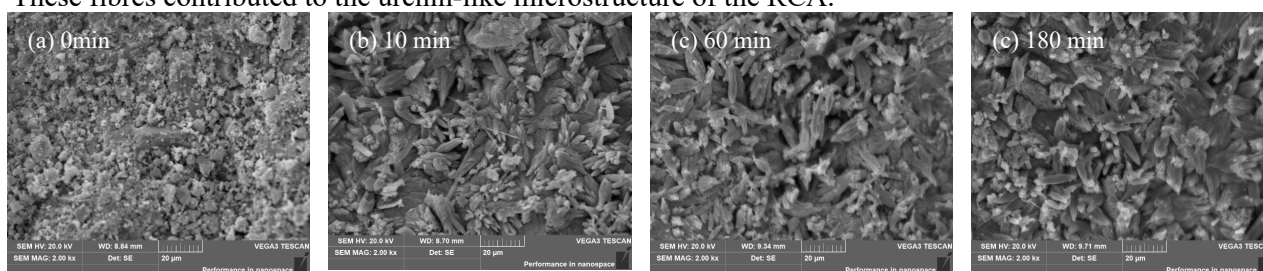


Figure 1 Morphologies of RCA carbonated for 0 min, 10 min, 60 min and 180 min

3.2 Phases evolution of the urchin-like RCA

The XRD spectra of RCA carbonated for different periods were tested. The Rietveld analysis based on XRD results was used to obtain the contents of crystalline carbonation products, and the calculated results are shown in Table 2. It can be observed from Table 2 that new products including aragonite and brucite were presented after injecting CO_2 , meanwhile, the intensity of peaks related to CH was significantly decreased. Table 2 also shows that the CH decreased rapidly within the first 5 min and then decreased very slowly for the rest carbonation period. Through parallel comparison of CC content, the consumption of CH didn't lead to the generation of the most common polymorph of CC-calcite, but a new carbonation product-aragonite was formed rapidly after injecting CO_2 and reached 5.10% at 5 min. Afterwards, the

formation of aragonite continued, but the formation rate was significantly slowed down. This retardance effect might be attributed to the continuously densified surface.

Table 2 Contents of carbonation products obtained by Rietveld analysis (wt.%)

| NO. | Calcite | Portlandite | aragonite | Brucite |
|------------|---------|-------------|-----------|---------|
| RCA-0min | 8.02 | 21.43 | 0 | 0 |
| RCA-5min | 8.14 | 9.11 | 5.10 | 1.49 |
| RCA-10min | 8.57 | 9.08 | 6.71 | 1.24 |
| RCA-20min | 8.54 | 9.24 | 6.96 | 1.30 |
| RCA-30min | 8.70 | 8.88 | 6.56 | 1.25 |
| RCA-60min | 9.09 | 8.70 | 6.37 | 1.33 |
| RCA-180min | 8.63 | 7.65 | 6.77 | 1.38 |

The ^{29}Si NMR and ^{27}Al NMR spectra of RCA carbonated for different periods are shown in Figure 2, respectively. For the ^{29}Si NMR spectra of un-carbonated RCA, Q^0 (-71 ppm) corresponding to the silicate in anhydrous cement and Q^1 (-80 ppm) and Q^2 (-85 ppm) corresponding to the silicate in C-S-H gel (Sevelsted and Skibsted 2015) could be observed. Upon carbonation, the intensity of Q^0 and Q^1 decreased slightly with the carbonation progress, while the intensity of Q^2 showed an increasing trend, indicating the transformation from Q^1 to Q^2 . Moreover, Q^{2b} (-93.4 ppm) and Q^3 (-101 ppm) could be observed when the carbonation duration reached 20 min, indicating the formation of decalcified of C-S-H (Q^{2b} , $(\text{SiO})_3\text{Si}^*-1/2 \text{ Ca}$) and alumina-silica gel or silica gel (Q^3 , $(\text{SiO})_3\text{-Si-OH}$) (Sevelsted and Skibsted 2015). Figure 2b shows the ^{27}Al NMR spectra of RCA subjected to different carbonation periods. For reference RCA without carbonation, resonance centered at 70 ppm corresponding to six-fold coordination (AlO_6) and resonance centered at 10 ppm corresponding to four-fold coordination (AlO_4) could be observed. The alumina bearing phase was dominated by the form of six-fold coordination due to the high intensity. Usually, these two resonances revealed aluminum substituting silicon in the C-S-H, the presence of AlO_6 in AFm and other calcium aluminate hydrates (Sevelsted and Skibsted 2015, Shen, Lu et al. 2017). The intensity of resonance centered at 70 ppm decreased gradually after injecting CO_2 , but the intensity decrease of the resonance was rather limited. Meanwhile, a resonance centered at about 60 ppm became visible at 60 min, which was usually attributed to the incorporated aluminum in alumina-silica gel (Stebbins 1995, Macedo, Osawa et al. 2004).

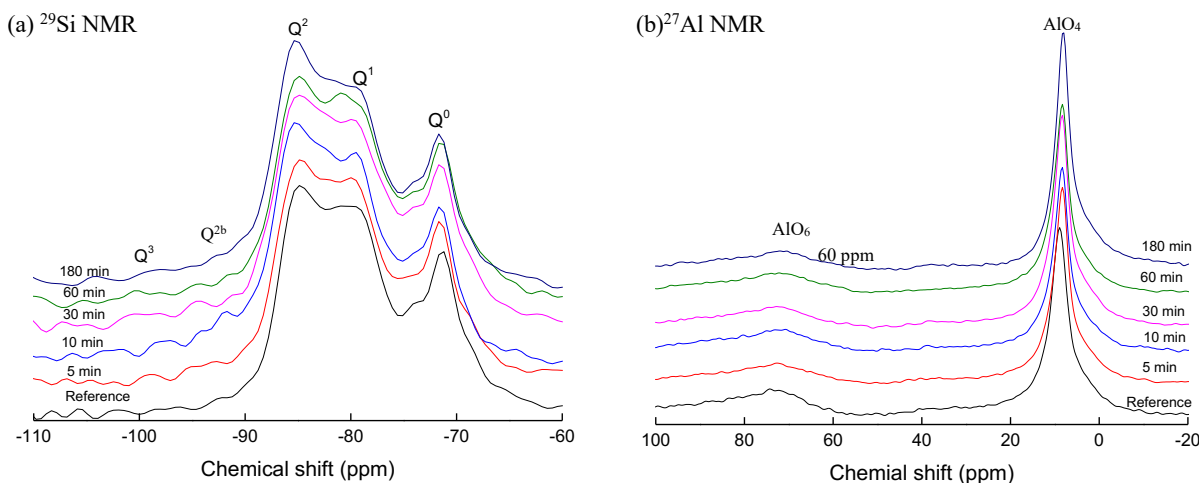


Figure 2 ^{29}Si NMR spectra and ^{27}Al NMR spectra of carbonated RCA

3.3 Bonding strength between urchin-like RCA and new mortar

The frictional bonding strength between RCA and the new mortar was determined. The test results are shown in Figure 3. The bonding strength tests of samples carbonated for 60 min and 180 min were chosen. The frictional bonding strength of RCA carbonated for 60 min and 180 min reached 8.33 MPa and 8.72 MPa, respectively, which was an increase of 27.57% and 33.54 % respectively compared to the non-carbonated RCA. Based on the preceding section, an urchin-like surface was formed on the surface of RCA that consisted of needle-like aragonite, brucite and amorphous phases. The newly formed surface modified the roughness, topography and geochemistry of RCA. The bonding strength further confirmed that the urchin-like RCA effectively enhanced its bonding capacity in new concrete.

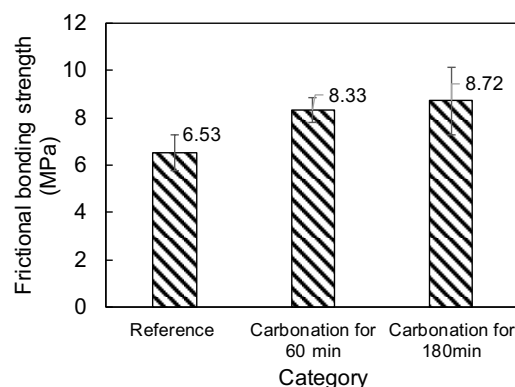


Figure 3 Frictional bonding strength between RCA and new mortar

4. Conclusions

In this study, a reactive urchin-like RCA was prepared by a wet carbonation method in 0.1 M $\text{Mg}(\text{NO}_3)_2$ solution and at an elevated temperature of 75°C. Based on the experimental results, the following conclusions can be drawn.

(1) The surface microstructure of RCA was rapidly modified after contacting with CO_2 in an aqueous environment, and a reactive urchin-like surface consisting of an aragonite coating layer, brucite and a silica-rich layer was developed.

(2) The portlandite in RCA was the main component that participated in the initial age (<5 min) of carbonation, following by the consumption of other cement hydrates. As a result, needle-like aragonite, alumina-silica gel, silica gel and decalcified C-S-H were the main carbonation products formed on the surface of RCA.

(3) The wet carbonation process entirely modified the roughness, topography and geochemistry of RCA surface, contributing to the enhanced bonding strength between RCA and the new mortar (up to 33.54%).

Acknowledgements

The authors wish to acknowledge the financial supports of the Research Grant Council (GRF) and the Construction Industry Council Funding Scheme for financial support.

References

- Gómez-Soberón, J. M. (2002). "Porosity of recycled concrete with substitution of recycled concrete aggregate: An experimental study." *Cement and concrete research* 32(8): 1301-1311.
- Macedo, M. I., C. C. Osawa and C. A. Bertran (2004). "Sol-gel synthesis of transparent alumina gel and pure gamma alumina by urea hydrolysis of aluminum nitrate." *Journal of sol-gel science and technology* 30(3): 135-140.
- Sevelsted, T. F. and J. Skibsted (2015). "Carbonation of C-S-H and C-A-S-H samples studied by ^{13}C , ^{27}Al and ^{29}Si MAS NMR spectroscopy." *Cement and Concrete Research* 71: 56-65.
- Sevelsted, T. F. and J. Skibsted (2015). "Carbonation of C-S-H and C-A-S-H samples studied by ^{13}C , ^{27}Al and ^{29}Si MAS NMR spectroscopy." *Cement and concrete Research* 71: 56-65.
- Shen, P., L. Lu, W. Chen, F. Wang and S. Hu (2017). "Efficiency of metakaolin in steam cured high strength concrete." *Construction and Building Materials* 152: 357-366.
- Stebbins, J. F. (1995). "Nuclear magnetic resonance spectroscopy of silicates and oxides in geochemistry and geophysics." *Handbook of physical constants* 2: 303-332.
- Tasong, W., C. Lynsdale and J. Cripps (1998). "Aggregate-cement paste interface. II: Influence of aggregate physical properties." *Cement and Concrete Research* 28(10): 1453-1465.
- Tasong, W. A., C. J. Lynsdale and J. C. Cripps (1999). "Aggregate-cement paste interface: Part I. Influence of aggregate geochemistry." *Cement and Concrete Research* 29(7): 1019-1025.
- Wu, B. and G. Ye (2017). "Development of porosity of cement paste blended with supplementary cementitious materials after carbonation." *Construction and Building Materials* 145: 52-61.
- Xiao, J., J. Li, B. Zhu and Z. Fan (2002). "Experimental study on strength and ductility of carbonated concrete elements." *Construction and Building Materials* 16(3): 187-192.
- Xuan, D., B. Zhan and C. S. Poon (2016). "Assessment of mechanical properties of concrete incorporating carbonated recycled concrete aggregates." *Cement and Concrete Composites* 65: 67-74.
- Zhan, B. J., D. X. Xuan, C. S. Poon and K. L. Scrivener (2020). "Characterization of interfacial transition zone in concrete prepared with carbonated modeled recycled concrete aggregates." *Cement and Concrete Research* 136: 106175.

Physical and mechanical characterization of Alkali-Activated slag cement in presence of ion-exchange resins

M. Criado^{1*} and M.J. de Hita²

¹ Eduardo Torroja Institute for Construction Sciences - CSIC, Madrid, Spain
Email: maria.criado@ietcc.csic.es

² Eduardo Torroja Institute for Construction Sciences - CSIC, Madrid, Spain
Email: mariajimena.dehita@ietcc.csic.es

ABSTRACT

Ion-exchange resins are a radioactive waste that is produced in the operation of nuclear power plants and is currently managed by its immobilisation in Portland cement-based matrixes. Alkali-activated materials are a potential alternative for their disposal that reduces the environmental impact of the material while achieving good cementitious properties. This study presents a physical and mechanical characterisation of two alkali-activated slag/fly ash-based formulations in presence of spent resin. The effect of two alkali activators, with high and low pH, sodium silicate and sodium carbonate, has been analysed. The physical and mechanical characterisation of the cementitious matrices is carried out through mercury intrusion porosimetry, capillary water absorption, drying shrinkage, and mechanical strengths in the presence and absence of resin. For comparative purposes, the formulation based on Portland cement currently used for the immobilisation of spent nuclear-grade resins in Spain is also evaluated. The results show that, although the drying shrinkage is increased in the case of alkaline cements with respect to the reference cement, the new formulations exhibit an improved mechanical development with a lower pore volume.

KEYWORDS: *Alkali-Activated Cement, Ion-exchange resins, Physical properties, Mechanical properties, Blast Furnace Slag*

1. Introduction

In the normal operation of nuclear power plants, it is necessary to decontaminate different effluents of chemical impurities and radioisotopes, for this purpose ion exchange resins are used. These resins, when they exceed the chemical concentrations established in the operating specifications, are replaced and categorised as low- and intermediate-level waste. The ionic resins are conditioned and immobilised in cement matrices to prevent the release of radioisotopes to the outside. However, the production of Portland cement entails significant energy and environmental costs; it is responsible for around 7% of annual CO₂ emissions worldwide, enormous energy consumption due to the decarbonation of limestone, and the destruction of quarries to extract the raw materials. For these reasons, in recent years better performing alternatives have been sought, such as alkali-activated cements.

The alkali-activated cements are the product of the reaction between an aluminosilicate source, for example, industrial by-products or wastes such as blast furnace slag (from steel manufacturing) and fly ash (generated in the combustion of coal in thermal power plants) and an aqueous "activator" that supplies alkaline constituents. The selection of the alkaline activator largely determines the properties and the ecological implications of the cement (Ishwarya et al. 2019). Sodium silicate is an activator that is widely used due to its good workability and high pH that favours the dissolution of precursors, but it contributes to carbon footprint due to its production process. Sodium carbonate is employed for its safer handling and lower energy cost, but it can delay the hardening and mechanical performance at early ages. In this study, the use of two alkali-activated formulations with different percentages of blast furnace slag and fly ash activated with sodium carbonate and sodium silicate is proposed in order to immobilise the spent ion exchange resins and their mechanical and physical properties such as pore volume, capillary water absorption, and drying shrinkage are determined. With comparative proposals, these properties are also evaluated for a reference based on Portland cement immobilising the resin.

2. Experimental

2.1 Raw materials characterisation and preparation of the mortar specimens

The simulated radioactive waste for immobilisation was a mixture of cationic in H^+ form and anionic in OH^- form exchange resins with a proportion of 1:1 with around 50% water content by mass. The resins were loaded using a simulated primary circuit solution from a pressurised water reactor (PWR) for 7 days. The solution, where the resins are loaded, was composed of boric acid, cobalt chloride, nickel nitrate, strontium chloride, cesium chloride and copper sulfate. To produce the alkali-activated materials, blast furnace slag and fly ash were used as starting materials, whose main components were CaO (46%), SiO_2 (32%), Al_2O_3 (10%), MgO (7%), and SiO_2 (42%), Al_2O_3 (27%) Fe_2O_3 (18%) and CaO (5%) and their specific surfaces were $1154 \text{ m}^2/\text{kg}$ and $2023 \text{ m}^2/\text{kg}$ respectively. The alkaline activators were sodium silicate (S) and sodium carbonate (C) powders, which were dissolved in deionised water. Moreover, a CEM I 42.5 R was employed to prepare the reference formulation used for the immobilisation of spent nuclear-grade resins in Spain. Deionised water was used to hydrate it. Initially, the slag and the fly ash (two different samples: A and B, being the percentage of fly ash higher in B) or the Portland cement and the fly ash (reference sample, R) were mixed with the loaded ion-exchange resins. The mortar specimens of the alkali-activated cements and reference cement were prepared using a liquid/solid ratio of 0.45 and an aggregate/solid ratio of 3. Mortars with different sizes, $4 \times 4 \times 16 \text{ cm}^3$ and $5 \times 5 \times 5 \text{ cm}^3$, were manufactured and cured at room temperature ($20 \pm 2 \text{ }^\circ\text{C}$).

2.2 Characterisation of the mortar specimens

The mechanical strength of the prismatic ($4 \times 4 \times 16 \text{ cm}^3$) mortars was determined using an Autotest-200/10-SW (Ibertest) testing frame according to UNE-EN 196-1 at 28 days of curing. The pore size distribution and pore volume of the specimens were analysed through the Micromeritics Autopore IV 9500. The capillary water sorption coefficient, k , was determined using the Fargelund method according to UNE 83982:2008. The cubic ($5 \times 5 \times 5 \text{ cm}^3$) specimens were dried at $50 \text{ }^\circ\text{C}$ for 4 days, then wrapped with a waterproof polyethylene sheet and kept in the oven at $50 \text{ }^\circ\text{C}$ for 3 more days. Finally, the polyethylene sheet was removed and specimens were placed in a room at $20 \text{ }^\circ\text{C}$ with 65% RH for 21 more days. After conditioning, the specimens were placed in a plastic container with a layer of water (5 mm in depth). The mass gain was measured over time until reaching a constant mass gain and k was determined. The drying shrinkage deformation was measured using a digital length comparator (Ibertest) on the prismatic ($4 \times 4 \times 16 \text{ cm}^3$) specimens with two edge-studs pre-inserted at the center of the $4 \times 4 \text{ cm}^2$ lateral surfaces after 48 hours of curing, based on UNE 80112:2016.

3. Results and discussion

Figure 1 shows the compressive strengths of the two formulations: A and B activated with sodium carbonate (C) and sodium silicate (S) and the Portland cement-based reference (R) in the absence and presence of the resin at 28 days. All alkali-activated samples presented higher compressive strength values than the reference one both in absence and in presence of resin, regardless of the activator used.

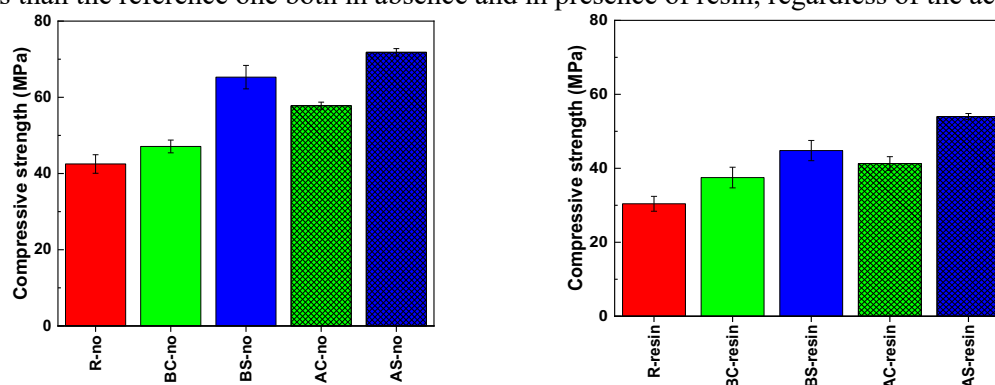


Figure 1. Compressive strength of the alkaline A and B formulations activated with sodium carbonate (C) and sodium silicate (S) and the reference (R) formulation in the absence and presence of ion-exchange resin.

Regarding the influence of the activator, the high pH of the sodium silicate solution favoured the dissolution of calcium and silicate ions in the slag and fly ash particles, accelerating the alkaline reaction and forming a greater amount of gel, which is responsible for the mechanical performance of the material. Moreover, a decrease in the slag percentage in the formulation, the B samples, implied a lower calcium content in the medium and a lower generation of gel. Finally, the interaction between the loaded resin which was enriched in boron with the pore solution could form borate compounds and disfavoured the formation of gel and the mechanical development (Lafond et al. 2013; Kryvenko et al. 2016).

The pore volume and pore size distribution of the three formulations, A and B activated with sodium carbonate (C) and sodium silicate (S) and R, in the absence and presence of the resin at 28 days of curing are reported in Figure 2. The total pore volume of the alkali-activated A and B samples with and without resin was similar to or lower than that obtained for the reference sample. When sodium silicate was employed as an alkaline activator decreased slightly the total pore volume in comparison to the sodium carbonate-activated samples, being more remarkable in the BS-no sample. In general, these sodium silicate-activated samples exhibited a higher volume of smaller pores ($<0.01 \mu\text{m}$). An increase in the amount of fly ash, induced a reduction in total porosity so that this could act as a filler due to the low reactivity at room temperature (Winnefeld et al. 2010), refining the pores structure. However, this effect was masked when the resin was presented and the behaviour was the opposite. Moreover, the presence of the resin led to an increase in the total pore volume of all the samples.

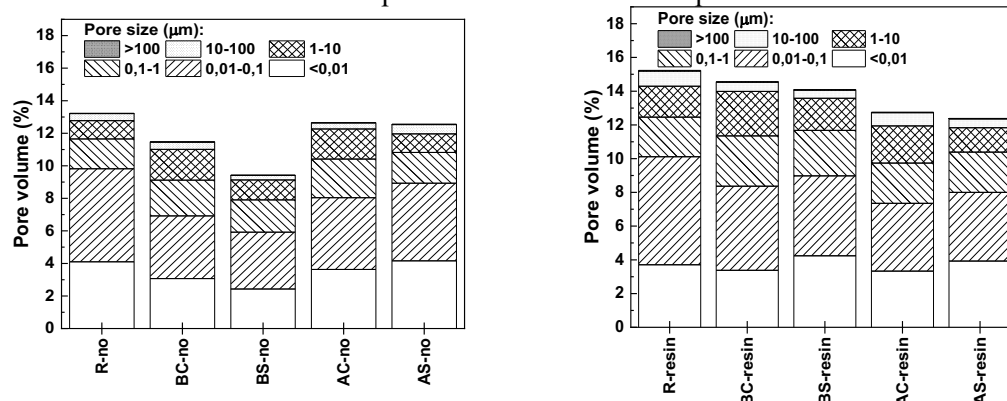


Figure 2. Pore volume and pore size distribution of the alkaline A and B formulations activated with sodium carbonate (C) and sodium silicate (S) and the reference (R) formulation in the absence and presence of resin.

The capillary suction coefficients of the three formulations, A and B activated with sodium carbonate (C) and sodium silicate (S) and R, in the absence and presence of the loaded resin at 28 days are shown in Figure 3. The k values of the reference samples were lower than those of the alkali-activated samples in the absence of waste. This effect was enhanced in the presence of more fly ash and for the sodium carbonate activator, the BC sample, indicating greater interconnected pores and less resistance to water penetration. On the other hand, the k parameter was raised with the addition of resin, equalling the values obtained between the reference system and the alkaline ones. The resins tended to water uptake but no volume changes were produced in the specimens.

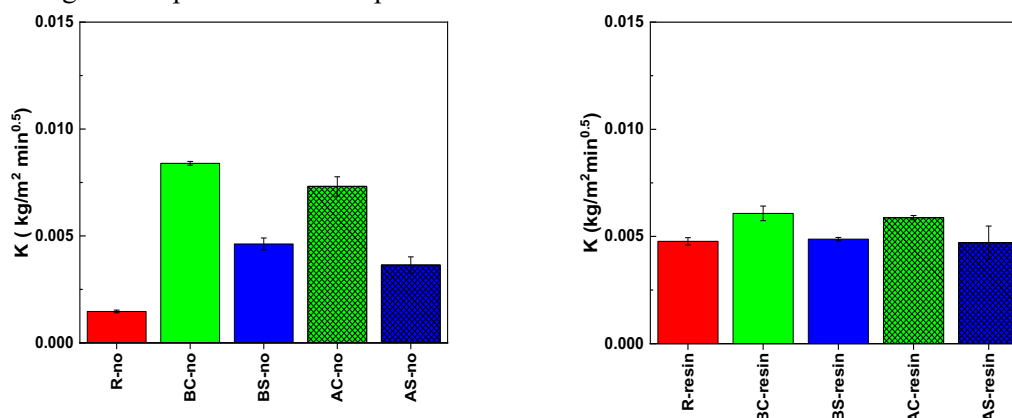


Figure 3. Water capillary sorption coefficient, k , of the alkaline A and B formulations activated with sodium carbonate (C) and sodium silicate (S) and the reference (R) formulation in the absence and presence of resin.

Figure 4 reports the evolution of the drying shrinkage of the three formulations, A and B activated with sodium carbonate (C) and sodium silicate (S) and R, in the absence and presence of the loaded ion-exchange resin over time, about 50 days. All alkali-activated matrices showed both in the absence and in the presence of resin a higher shrinkage than the reference matrix. The greatest dimensional changes took place in the first 15 days. The samples continued contracting, but it was more slowly until the values reached a horizontal asymptote. The percentage of fly ash added to the sample did not significantly change the shrinkage response of mortars. However, when sodium silicate is used, the drying shrinkage experienced was slightly higher. Finally, the incorporation of resin into the formulations induced a higher drying shrinkage in the alkali-activated formulations, regardless of the type of binder and nature of the activator. Nevertheless, none of the samples showed cracks, or delamination.

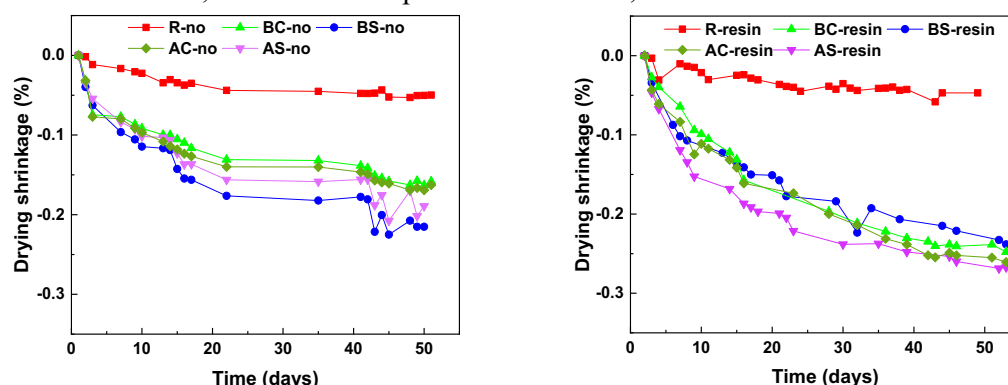


Figure 4. Drying shrinkage of the alkaline A and B formulations activated with sodium carbonate (C) and sodium silicate (S) and the reference (R) formulation in the absence and presence of ion-exchange resin.

4. Conclusions

- All the alkaline matrices showed an improvement in terms of compressive strength with respect to the reference matrix, both in the presence and absence of immobilised residue. Higher percentages of slag in the formulation and the use of sodium silicate improved the mechanical development of the matrices.
- Regardless of whether or not resin was incorporated into the different formulations, the alkaline-activated matrices showed an improvement in terms of total pore volume over the reference matrix.
- Although in the absence of the immobilised resin, the water absorption by capillarity was higher in the alkaline matrices, the results pointed to good behaviour in the presence of resin of these matrices, obtaining k values similar to the reference matrix, without volume changes (swelling).
- The alkaline-active formulations with and without the waste experienced greater drying shrinkage than the reference one, but no cracking or loss of material was observed.

Acknowledgements

This research was funded by Ayudas de Atracción de Talento Investigador de la Comunidad Autónoma de Madrid, grant number 2019-T1/AMB-13672.

References

- Ishwarya, G., B. Singh, S. Deshwal, and S. K. Bhattacharyya. 2019. "Effect of Sodium Carbonate/Sodium Silicate Activator on the Rheology, Geopolymerization and Strength of Fly Ash/Slag Geopolymer Pastes." *Cement and Concrete Composites* 97 (December 2018): 226–38. <https://doi.org/10.1016/j.cemconcomp.2018.12.007>.
- Kryvenko, P, H Cao, O Petropavlovskiy, L Weng, and O Kovalchuk. 2016. "Applicability of Alkali-Activated Cement for Immobilization of Low-Level Radioactive Waste in Ion-Exchange Resins." *Восточно-Европейский Журнал Передовых Технологий* 6: 40–45. <https://doi.org/10.15587/1729-4061.2016.59489>.
- Lafond, E, C Cau Dit Coumes, S Gauffinet, D Chartier, P Le Bescop, L Stefan, and A Nonat. 2013. "Effect of Blastfurnace Slag Addition to Portland Cement for Cationic Exchange Resins Encapsulation." *EPJ Web of Conferences. EDP Sciences* 56: 02003.
- Winnefeld, F, A Leemann, M Lucuk, P Svoboda, and M Neuroth. 2010. "Assessment of Phase Formation in Alkali Activated Low and High Calcium Fly Ashes in Building Materials." *Construction and Building Materials* 24 (6): 1086–93. <https://doi.org/10.1016/j.conbuildmat.2009.11.007>.

Evaluation of environmental technologies for cement production considering multiple environmental categories

Y. Kirino^{1*}, S. Uchida², T. Shinmi³ and K. Kawai⁴

¹ *Taiheiyo cement corporation, Chiba, Japan*

Email: Yusuke_Kirino@taiheiyo-cement.co.jp

² *Taiheiyo cement corporation, Chiba, Japan*

Email: Shunichiro_Uchida@taiheiyo-cement.co.jp

³ *Tokuyama Corporation, Yamaguchi, Japan*

Email: t.shinmi.1m@tokuyamagr.com

⁴ *Hiroshima University, Hiroshima, Japan*

Email: kkawai@hiroshima-u.ac.jp

ABSTRACT

The environmental impact of cement and concrete is often evaluated by CO₂ emission during clinker burning. However, if only a specific environmental category, such as global warming, is considered, the environmental impact from other categories might increase, and then the overall environmental impact might increase unintentionally. In this study, LIME3 was used to evaluate various environmental technologies for cement production through an integrated indicator that considers multiple environmental categories and local environmental conditions. The results showed that "increased use of alternative fuels" was the most effective environmental technology under typical environmental conditions, followed by "increased use of alternative raw materials" and "increased use of mineral admixture". On the other hand, the effect of "increased use of alternative raw materials" was the largest in the evaluation assuming countries with large environmental impact factors, suggesting that the technology avoiding landfill of wastes should be applied preferentially. Therefore, it was revealed that CO₂ emissions are not a good indicator of overall environmental impact and might generate trade-offs in countries with large environmental impact factors.

KEYWORDS: *Cement production, Life cycle assessment, LIME, Carbon dioxide, Waste use*

1. Introduction

Toward the sustainable development of the world, the cement industry is promoting various initiatives, including environmental impact reduction. Although the cement industry considers various environmental categories to reduce environmental impact, CO₂ emissions are often presented as the only quantitative indicator (Habert et al. (2020); Global Cement and Concrete Association (2021)). However, if only a specific environmental category, such as global warming, is considered, the environmental impact from other categories might increase, and then the overall environmental impact might increase unintentionally.

Detailed assessments of specific environmental technologies in the cement industry include the use of mineral admixtures or recycled aggregates (e.g., Pradhan et al. (2022); Xing et al. (2022)), optimization of concrete mixes (e.g., Damineli et al. (2010)), and others, often based on inventory analysis or characterization of environmental impacts. On the other hand, there are few cases in which several environmental technologies are assessed comprehensively by integration (or weighting) of environmental impact to consider synergies and trade-offs. In addition, there are no examples of assessments that take into account differences in environmental conditions, though the environmental impact depends on the environmental conditions of a country or region (Itsubo and Inaba (2018)). Therefore, the purpose of this study is to assess the representative environmental technologies in the cement industry under multiple

environmental conditions to demonstrate the potential of the technologies from a comprehensive perspective.

2. Assessment Methods

2.1 Inventory data collection

The potential of environmental technologies was evaluated based on the difference between a global average manufacturing process and a hypothetical improved manufacturing process using a specific environmental technology. The functional unit was one ton of cement, and the system boundary covered the process from the mining of natural raw materials to the cement manufacturing process (that is, cradle-to-gate). The contribution of waste use in clinker production to the reduction of CO₂ emissions and landfill volume was also evaluated (Fig.1). However, mineral admixtures for cement, which are not generally treated as wastes, were treated as by-products (or co-products defined in ISO14044), and the contribution to the reduction of landfill volume was not counted.

The inventory data of the Global Cement and Concrete Association (GCCA) in 2016 were mainly used as the average cement manufacturing data. Data not available to the public were estimated using values from the sustainability report published by the core members of the WBCSD CSI in 2016. The potential of several representative environmental technologies was determined by comparing the values of average cement with the highest values of the country or company that introduced each environmental technology.

2.2 Environmental impact assessment method

The environmental impact of cement was assessed using LIME3 (Itsubo and Inaba (2018)), a life cycle impact assessment method that takes into account environmental conditions in various countries around the world. For the environmental impact assessment, the environmental burden was calculated as a negative value and the contribution to the reduction of environmental burden as a positive value. The integrated result, which was expressed by equation (1), was obtained as an economic indicator based on G20 weighting.

$$\text{Environmental impact} = \sum \sum (\text{Inv}(X) \times IF^{\text{Impact}}(X)) \quad (1)$$

Where, $\text{Inv}(X)$ is the emissions of inventory item X and $IF^{\text{Impact}}(X)$ is the integration factor of inventory item X for the impact category Impact . For the integration factor, the median (50th percentile) and 75th percentile values for the entire world were used to consider environmental conditions in several countries. The 75th percentile value corresponds to countries with relatively large impacts on the same inventory data, and some countries in Europe and the Middle East mainly have integration coefficients above the 75th percentile value.

3. Results and discussions

3.1 Assessment results of environmental technologies in typical condition

Assessment results of cement produced by the average method and that with environmental technology, using the median value of LIME3, are shown in Fig.2. The cement produced by the average method had the largest environmental impact due to global warming, the second largest impact due to natural resource consumption, and the smallest impact due to air pollution. The environmental contribution of waste use was comparable to the environmental impact of air pollution. In terms of natural resource consumption, coal consumption had the largest impact and limestone consumption had a relatively small impact because coal has a higher resource value than limestone. In terms of air pollution, NO_x had the largest impact because of its relatively high emissions.

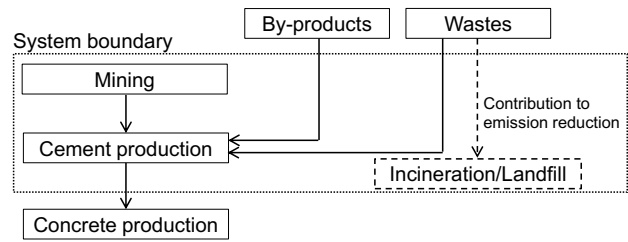


Fig.1 System boundary in this study (dotted line)

Among several environmental technologies, "increased use of alternative fuels (AF)" was rated the most effective because of the large difference between the AF rate in Germany (66%), which makes the most use of AF, and the global average (17%). The technology also creates a synergy between the reduction of CO₂ emissions and the reduction of fossil resource consumption, and the contribution of both effects is almost the same. The second largest effective technology was found for the "increased use of alternative raw materials (ARM)" because the difference between the average ARM rate (3.6%) and the highest rate in Japan (17.8%) was large. The third largest effective technology was obtained by "increased use of mineral admixture". Although this technology can reduce global warming, resource consumption, and air pollution, the difference between the average rate (31%) and the highest rate in India (17.8%) was not large. The difference in the results between natural products and by-products was small, because the resource value of natural products for mineral admixture is not high, and the environmental impact of natural resource consumption is relatively small. A trade-off effect was also observed in the case of the "increased use of mineral admixture" because the environmental contribution from the use of ARM in

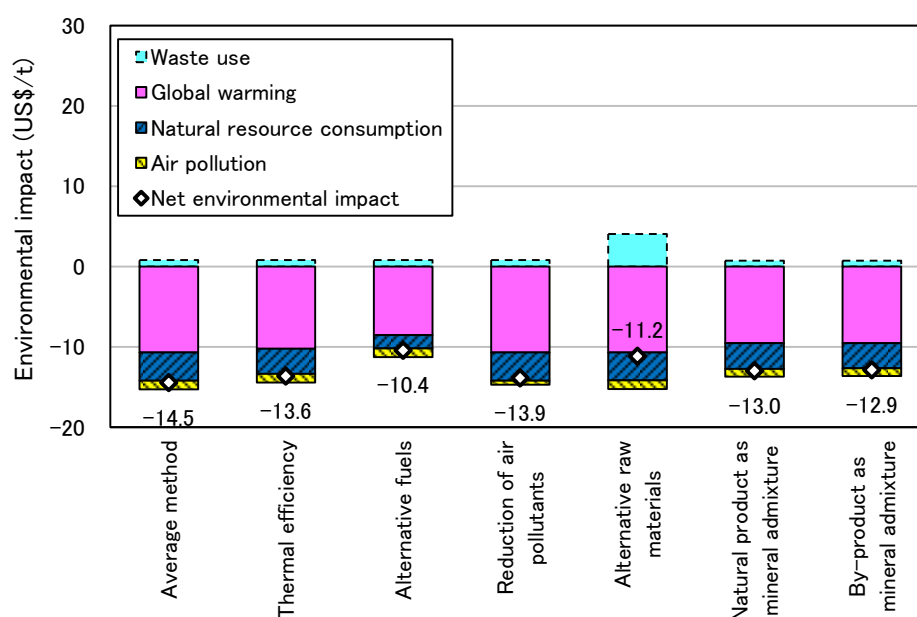


Fig.2 Environmental impact of cement assessed by median value of LIME3

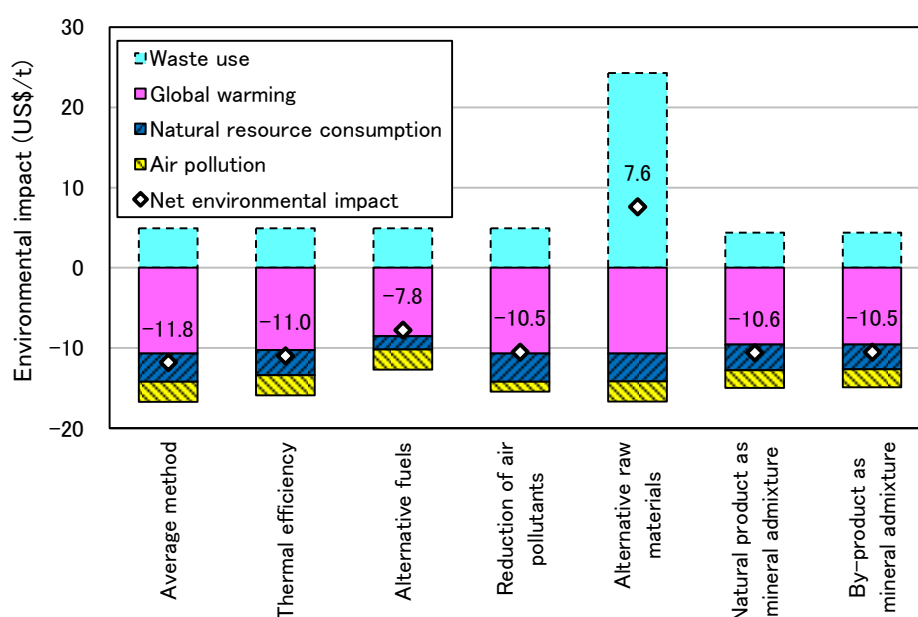


Fig.3 Environmental impact of cement assessed by 75 percentile value of LIME3

clinker production was reduced. The improvement effects of "improved thermal energy efficiency" and "reduced air pollutants" were relatively small.

3.2 Assessment results of environmental technologies in countries with large impact factor

Results using the 75th percentile value of LIME3 are shown in Fig.3 to assess the effect of environmental impact reduction under different environmental conditions. Compared to the results under typical environmental conditions, the impact of categories other than global warming became larger, and the results show that environmental impacts cannot be properly evaluated based on CO₂ emissions alone.

The environmental contribution of "increased use of ARM" is the largest, and the value is larger than the sum of the other environmental impacts, and the total environmental impact is positive. The environmental impact of waste is mainly attributed to the social asset of landfill sites, suggesting that the technology should be prioritized in countries where the impact is significant. The social asset here is an asset when a landfill site is regarded as a depletable resource, and the value is large when the number of candidate sites is small and their economic value is high, as in Japan. However, the results for waste use are considered less reliable than the other results due to the low precision of the estimated impact factors for each country except Japan because the factors were estimated from the Japanese factors. The improvement effect of "reduction of air pollutants" was also relatively large when the 75th percentile value of LIME3 was used. The results suggest that the environmental impact of air pollutants is one of the important issues in countries with a large population living in the diffuse area, because the damage to human health is larger in the countries.

4. Conclusions

Representative environmental technologies in the cement industry were assessed using LIME3, which is a life cycle impact assessment method considering multiple environmental categories and local environmental conditions, and the effectiveness of each technology was presented from a comprehensive perspective. The main conclusions obtained are as follows.

- Under typical environmental conditions, global warming is the most important impact category, and the most effective technology is "increased use of AF" which contributes to the reduction of CO₂ emissions and fossil resources consumption.
- In countries with large environmental impact factors, the effect of "increased use of ARM" was found to be the most effective, and the technology should be introduced as a priority in countries where the social value of landfill sites is high.
- CO₂ emissions are not always appropriate as an indicator of environmental impact, especially in countries with large environmental impact factors.

References

- Damineli, B. L., Kemeid, F. M., Aguiar, P. S. and John, V. M. (2010) "Measuring the eco-efficiency of cement use", *Cement and Concrete Composites*, 32(8): 555-562
- Global Cement and Concrete Association (2021) "Concrete Future – The GCCA 2050 Cement and Concrete Industry Roadmap for Net Zero Concrete", <https://gccassociation.org/concretefuture/>
- Habert, G., Miller, S. A., John, V. M., Provis, J. L., Favier, A., Horvath, A. and Scrivener, K. L. (2020) "Environmental impacts and decarbonization strategies in the cement and concrete industries", *Nature Reviews Earth & Environment*, 1: 559–573
- Itsubo, N. and Inaba, A. (2018) "Development of global scale LCIA method", *The International Journal of Life Cycle Assessment*, 23: 2271–2275
- Pradhan, S., Poh, A. C. B. and Qian, S. (2022) "Impact of service life and system boundaries on life cycle assessment of sustainable concrete mixes", *Journal of Cleaner Production*, 342: 130847
- Xing, W., Tam, V. W. Y., Le, K. N., Butera, A., Hao, J. L. and Wang, J. (2022) "Effects of mix design and functional unit on life cycle assessment of recycled aggregate concrete: Evidence from CO₂ concrete", *Construction and Building Materials*, 348: 128712

Structure and Reactivity of Aqueous Carbonated Blended Cement Pastes

F. M. Maia Neto^{1*}, R. Snellings², and J. Skibsted¹

¹ Aarhus University, Department of Chemistry and Interdisciplinary Nanoscience Center (iNANO),
Langelandsgade 140, DK-8000C Aarhus, Denmark
E-mail: fabio.maia@inano.au.dk; jskib@chem.au.dk

² Earth and Environmental Sciences, KU Leuven, Celestijnenlaan 200e, 3001 Leuven, Belgium
E-mail: ruben.snellings@kuleuven.be

ABSTRACT

Reduction of the clinker content in composite cement compositions is often proposed as a pathway to minimize the CO₂ footprint of the cement industry. In addition, the implementation of Carbon Capture and Utilization (CCU) technologies will likely also be required to achieve future demands of net-zero CO₂ emissions. In this regard, aqueous carbonation of recycled concrete fines is receiving growing attention since it allows CO₂ sequestration from point sources and produces a reactive amorphous aluminosilicate phase that can be used as an SCM in new composite cements. In this study, well-hydrated (+12 years) blended cement pastes based on white Portland cement and the most commonly used SCMs (silica fume, slags, fly ash, and a natural pozzolan) were subjected to aqueous carbonation, and the reaction products were characterized by solid-state ²⁷Al and ²⁹Si NMR and TGA. It is observed that the chemical reactions taking place during the carbonation of the blended pastes are similar to those found in the carbonation of ordinary Portland cement pastes. This shows that equivalent reaction mechanisms dictate the kinetics and phase assemblages for these systems. The phase assemblage of the fully carbonated pastes is dominated by calcite and the amorphous alumina-silica gel, where the proportion of these phases is related to the initial composition of the blended cements. The calcium content, for instance, largely governs the proportion of calcium carbonates formed, and consequently the CO₂-uptake capacity. Moreover, the aluminum content influences the degree of polymerization and the Al/Si ratio of the amorphous alumina-silica gel. Pozzolanic reactivity tests show that the carbonated pastes react fast, and the variation in composition leads to different reactivity performances at early ages. In summary, blended cement pastes can be aqueous carbonated in the same manner as CEM I pastes, which provides a more versatile application of end-of-life concrete for CO₂ sequestration.

KEYWORDS: *Blended cements, carbonation, CO₂ sequestration, pozzolanic reactivity, solid-state NMR*

1. Introduction

Carbonation of end-of-life concrete is attracting increasing interest as a potential pathway to reduce the CO₂ footprint of the lifecycle of cement-based materials. Among the numerous proposed methods, aqueous carbonation stands out due to the high carbonation degree while occurring spontaneously at room temperature (Zajac et al. (2020a)). This method consists of injecting gaseous CO₂ in a reactor containing a solution, where hydrated cement fines are added, triggering a series of overlapping dissolution and precipitation reactions. The final phase assemblage of such systems is composed of calcium carbonates and an amorphous alumina-silica gel, which is proposed as a novel supplementary cementitious material (SCM) (Zajac et al. (2020a), Zajac et al. (2020b)) for new composite cements. On account of a very high surface

area, the alumina-silica gel is found to have a faster pozzolanic reactivity than conventional SCMs such as metakaolin and silica fume, which can favor the application of aqueous carbonated pastes in precast concrete mixtures (Zajac et al. (2020b)).

Previous studies have focused on the resulting phase assemblage, reaction kinetics, performance as an SCM and the effect of solution alkalinity on aqueous carbonation (Zajac et al. (2020a), Zajac et al. (2020b), Zajac et al. (2020c), Zajac et al. (2021)). However, most of these studies have used systems of well-hydrated CEM I and CEM III pastes. Considering the widespread use of SCMs, an understanding of how different cementitious systems will perform under such conditions is lacking. Thus, this work aims to elucidate the effect of chemical composition on the phase assemblage and reactivity of aqueous carbonated cement pastes. Given that the alumina-silica gel is an X-ray amorphous phase, solid-state NMR was chosen as the main technique to probe the structure and composition of such phases.

2. Materials and Methods

Six matured cement pastes, hydrated for 12 to 14 years, were used in this study. The reference paste is made of pure white Portland cement (wPc), while the others are blends of the same cement, partially replaced with different SCM samples. The chemical compositions and replacement levels are summarized in Table 1. The silica fume consists of 99% amorphous silica while the fly ash sample is composition-wise close to a class-F fly ash. The slag 1 sample has a typical composition of blast furnace slags whereas the slag 8 sample has low Ca and high Al content.

Table 1: Chemical composition before hydration of the hydrated cement pastes as determined by XRF.

| Paste | Replacement level (%) | SCM | Chemical Composition (%) | | | | | | | | |
|-------|-----------------------|------------------|--------------------------|------------------|--------------------------------|--------------------------------|-----|-----------------|------------------|-------------------|-----|
| | | | CaO | SiO ₂ | Al ₂ O ₃ | Fe ₂ O ₃ | MgO | SO ₃ | K ₂ O | Na ₂ O | LOI |
| wPc | 0 | - | 68.7 | 24.7 | 2.1 | 0.4 | 0.6 | 1.8 | 0.1 | 0.2 | 1.0 |
| 10MS | 10 | silica fume | 61.8 | 32.0 | 1.9 | 0.4 | 0.5 | 1.6 | 0.1 | 0.2 | 0.9 |
| 30NP | 30 | natural pozzolan | 49.1 | 36.7 | 5.6 | 1.0 | 0.8 | 1.4 | 0.7 | 1.0 | 0.7 |
| 30FA | 30 | fly ash | 48.1 | 38.9 | 8.8 | 0.4 | 0.4 | 1.3 | 0.1 | 0.1 | 0.7 |
| 40S1 | 40 | slag 1 | 57.8 | 29.5 | 6.2 | 0.6 | 3.2 | 1.3 | 0.2 | 0.2 | 0.6 |
| 40S8 | 40 | slag 8 | 54.2 | 28.7 | 9.3 | 0.5 | 4.0 | 1.9 | 0.4 | 0.2 | 0.7 |

The carbonation experiments were carried out in a glass beaker containing 30 mL of a 0.1 M NaOH solution. A flow of gaseous CO₂ and N₂ was continuously introduced to the glass beaker at respective rates of 1 and 9 L/h, which causes a gradual decrease in pH. When the system reaches equilibrium, 1.0 gram of powdered paste (< 64 µm) was added to the solution. A pH meter (Mettler Toledo SevenCompact) coupled with an Inlab Expert Pro-ISM electrode was used to follow the reaction progress. The reaction was stopped after 6 hours by vacuum filtration, and the solid particles were subsequently stored in a desiccator, prior to the solid-state NMR and thermogravimetric (TGA) analyses.

The reactivity tests were conducted following an adaptation of the R³ test (Londono-Zuluaga et al. (2022)). Half a gram of fully carbonated paste was placed in a glass container alongside the same amount of Ca(OH)₂ and 2.7 mL solution of 4 g/L KOH and 20 g/L K₂SO₄. The mixture was manually mixed for 1 to 2 minutes, to ensure homogenization, closed with an airtight screw lid and stored in a ventilated chamber. Considering the high reactivity of the alumina-silica gel, the temperature of the chamber was set to 25 °C. The reaction was interrupted at targeted times by solvent exchange.

The ²⁷Al and ²⁹Si solid-state magic-angle spinning (MAS) NMR spectra were acquired on Varian Direct-Drive 600 (14.1 T) and Varian INOVA-300 (7.05 T) spectrometers, respectively, using home-built CP/MAS probes for 4 and 7 mm zirconia rotors, and employing spinning speeds of 13.0 kHz and 7.0 kHz. ²⁷Al and ²⁹Si chemical shifts are relative to 1.0 M AlCl₃·6H₂O solution and neat TMS.

3. Results and Discussion

3.1 Phase assemblage of carbonated pastes

The phase compositions of the hydrated pastes carbonated for 6 hours are estimated by a multi-technique approach (Figure 1). Calcium carbonates are formed as a result of carbonation of Ca-bearing phases and constitute a significant fraction of the phase assemblage. Calcite is seen as the dominant CaCO_3 polymorph as detected by XRD and ^{13}C MAS NMR (not shown). The TGA quantification reveals that the proportion of calcium carbonates, and consequently the CO_2 -uptake capacity, is largely influenced by the initial bulk Ca content.

As a result of the carbonation of the C-(A)-S-H and calcium aluminate phases, an amorphous alumina-silica gel is formed. Through ^{29}Si and ^{27}Al MAS NMR (not shown), the structure of this phase is seen to change according to the paste's starting composition (Table 1), reflecting the quantity of four-fold coordinated Al incorporated in the gel's silica framework. A model based on the chemical shift of the various $Q^n(\text{mAl})$ sites that form this alumina-silica framework is developed to describe the structure of this phase. Based on that model, the population of $Q^n(\text{mAl})$ sites is determined by means of ^{29}Si NMR spectral deconvolutions, which allow for the calculation of the Al/Si ratio and number of non-bridging oxygens (NBO) per Si tetrahedra using equations 1 and 2, respectively. Figure 1b shows that both the gel's Al/Si ratio and NBO per Si tetrahedra rise with increasing bulk Al content. This indicates that the Al incorporation leads to a more depolymerized silicate framework, which potentially affects the reactivity of the gel. The model is further validated by comparing the Al/Si ratio from ^{29}Si MAS NMR with the ratio from mass-balance calculations.

$$\frac{\text{Al}}{\text{Si}} = \frac{\sum_0^n \sum_0^m \left(\frac{m}{n}\right) Q^n(\text{mAl})}{\sum_0^n Q^n(\text{mAl})} \quad (1)$$

$$\frac{[\text{NBO}]}{[\text{Si}]} = \frac{\sum_0^4 (4 - n) Q^n}{\sum_0^4 Q^n} \quad (2)$$

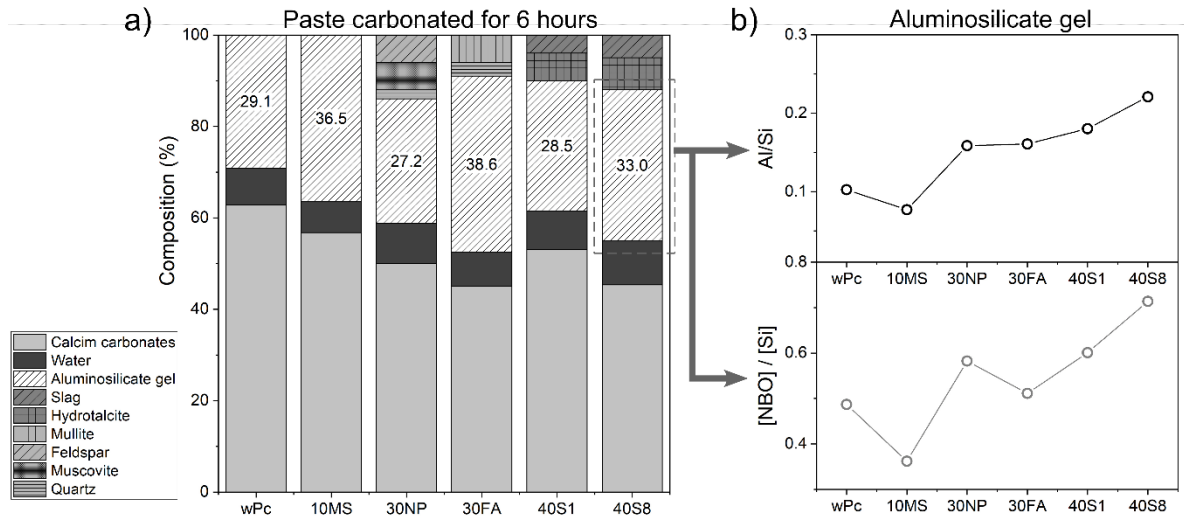


Figure 1: (a) Estimated phase assemblages of pastes carbonated for 6 hours. The carbonate and water contents were determined by TGA whereas the remaining crystalline phases and the slag contents were quantified by Rietveld refinement and ^{29}Si NMR, respectively. (b) The Al/Si ratio and the number of non-bridging oxygens (NBO) per SiO_4 tetrahedra of the aluminosilicate gel, calculated based on the ^{29}Si NMR spectral deconvolutions.

3.2 Reactivity of the aluminosilicate gel

Reactivity tests were conducted to evaluate the effect of different phase assemblages and Al/Si ratios (Figure 1) on the pozzolanic reactions of the alumina-silica gels. The results are illustrated by the ^{29}Si MAS NMR spectra of the carbonated pastes subjected to the reactivity test for 3 h, 8 h, 1 day and 2 days (Figure

2) for four different blends. After 8 hours, a clear difference between the Q^1 and Q^2 intensities observed for the early formed C-(A)-S-H phase indicates that pastes with high Al content (30FA and 40S8) reacted faster than the pastes with low Al content (wPc and 10MS). This is possibly a consequence of the less polymerized alumina-silica network, as observed in Figure 1b. After 2 days, the broad resonance located between -80 and -115 ppm and originating from the alumina-silica gel, completely fades away, indicating the full reaction of this constituent. This emphasizes that all pastes contain a highly reactive alumina-silica gel.

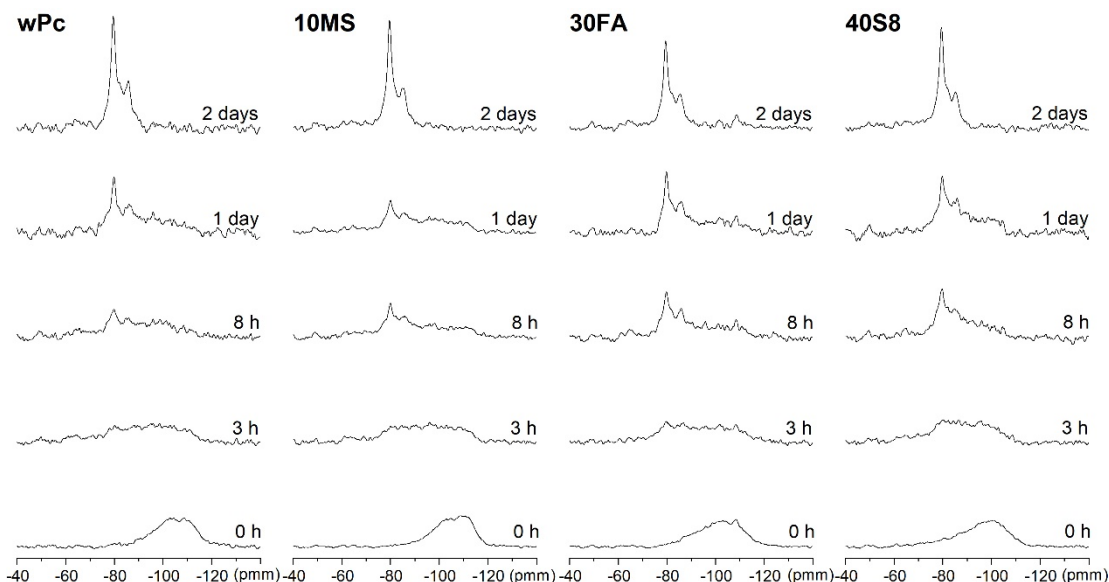


Figure 2: ^{29}Si MAS NMR spectra (7.05 T) of carbonated cement pastes subjected to reactivity tests for up to 2 days.

4. Conclusion

This study investigated the aqueous carbonation of well-hydrated cement pastes incorporating commonly used SCMs. It is observed that cement pastes with different chemical compositions can be aqueous carbonated in the same manner. The chemical composition of the cement pastes is seen to influence the proportion of the main reaction products, calcium carbonates and the amorphous alumino-silicate gel. Also, the alumina-silica gel is not identical for all samples, as its structure is shown to be largely dependent on the Al content of the hydrated cement pastes. Carbonated pastes with high Al content display slightly higher early pozzolanic reactivity compared to carbonated pastes with low Al content, yet all samples show a very high reactivity. In conclusion, the findings support a more versatile utilization of aqueous carbonation as a method for CO_2 sequestration which will contribute to a circular utilization of concrete.

Acknowledgments

The authors wish to thank the Danish Council for Independent Research, Technology and Production for the financial support (Grant No 0136-00355B).

References

- Londono-Zuluaga, D., Gholizadeh-Vayghan, A., Winnefeld, F. *et al.* (2022) "Report of RILEM TC 267-TRM phase 3: validation of the R^3 reactivity test across a wide range of materials" *Materials and Structures*, 55: 142
- Zajac, M., Skibsted J., Durdzinski, P., Skocek, J., Bullerjahn, F. and Haha, M.B. (2020a) "Phase assemblage and microstructure of cement paste subjected to enforced, wet carbonation" *Cement and Concrete Research*, 130: 105990
- Zajac, M., Skocek, J., Durdzinski, P., Bullerjahn, F., Skibsted J. and Haha, M.B. (2020b) "Effect of carbonated cement paste on composite cement hydration and performance" *Cement and Concrete Research*, 134:106090
- Zajac, M., Skibsted J., Durdzinski, P., Bullerjahn, F., Skocek, J. and Haha, M.B. (2020c) "Kinetics of enforced carbonation of cement paste" *Cement and Concrete Research*, 131:106013
- Zajac, M., Skibsted J. and Haha, M.B. (2021) "Effect of alkalis on enforced carbonation of cement paste: Mechanism of reaction" *Journal of the American Ceramic Society*, 104(2): 1076-87

Statistical modelling and optimization of strength in hybrid binders based on volcanic pumice, environmental and cost analysis.

J. López-Salas^{1*}, L.Y. Gomez-Zamorano², J.I. Escalante-García¹

¹ Center for Research and Advanced Studies IPN, Saltillo, México

Email: jesus.lopez.s@cinvestav.edu.mx, ivan.escalante@cinvestav.edu.mx

² Faculty of Mechanical and Electrical Engineering, UANL, San Nicolas de los Garza, México

Email: Lauren.gomezzm@uanl.edu.mx.

ABSTRACT

The surface response method was used to model and optimize the compressive strength of pastes of hybrid binders (HB) of Portland Cement (PC) + Volcanic Pumice (VP), activated with Na₂SO₄ (N⁺) and Ca(OH)₂ (CH). A central composite design was used and the experimental factors were: the composition of precursors contained 0-100%VP (the rest was PC); the activator concentration was 4-12 wt% N⁺ relative to the VP, plus an amount of CH for molar ratios 0.5 < N⁺/CH < 1.5. An analysis of costs, CO₂-emissions and energy demand was also carried out. A linear model indicated optimal formulations with 12% N⁺ and N⁺/CH=1.5 for fixed values of 75 and 50% VP, with predicted 28-day strengths of 23.6±4.5 and 33.2±4.27 MPa, respectively. A quadratic model predicted 90-day strengths with 12% N⁺ and N⁺/CH=0.5 and 75% and 50% VP of 45.6±17.9 MPa and 66.2±15.3 MPa, respectively; experimental corroborations were characterized. The effect of activators on HB was statistically significant after 28 days, which agrees with literature in that dry powdered activators form may have a partially delayed positive effect in the strength; contributions from the VP pozzolanic reaction must also be considered. The dry curing 90-day strength of 66.6 MPa for a paste with 50% VP, 12% N⁺ and N⁺/CH=1, was higher than that of a reference of 100% PC. As the VP precursor is cheap, requires low energy for its grinding and do not require any calcination, these HB are a feasible alternative sustainable option for construction.

KEYWORDS: Hybrid binders, Surface response method, Optimization, sustainability, volcanic pumice.

1. Introduction

Hybrid binders represent an alternative to sustainably replace PC; these have features of blended PC and alkali-activated cements. HB are constituted by a precursor, alkaline activators and PC clinker or PC; the main reactions are the PC hydration, alkaline activation of the precursor, and the pozzolanic activity; the activators can also influence the PC hydration. HB are advantageously in that are safe to prepare, cheap, of low environmental impact, Palomo et al. (2019), and can be prepared using the current PC infrastructure. On the other hand, the response surface methodology is a statistical experimental design tool that allows to model independent variables and analyze response variables, to optimize the response, Montgomery (2005), Myers et al. (2016). Volcanic Pumice (VP) can be a precursor for alkaline cements and HB, with relatively good availability, cheap and safe handling. This research focuses on optimizing the compressive strength of new HB based on volcanic pumice (HB-VP) through a statistical modeling, and compares the CO₂ emissions, energy demand, and their cost for up to 75% of VP with PC.

2. Materials and methods

The starting materials were a VP from a south-central Mexico, a commercial PC (BPC30, 30MPa after 28 days) and industrial grade Na₂SO₄ and Ca(OH)₂. The VP was ball milled to a Blaine surface area of 600 m²/kg. Table 1 shows the formulations as indicated by the RSM using the experimental factors and levels described above; the water binder ratio was w/b=0.38 (0.2% superplasticizer for >50%VP was used).

Pastes were cast in cubic molds of 25 mm per side and vibrated for 10 seconds, covered with a plastic film and cured in isothermal chamber at $20 \pm 3^\circ\text{C}$ for 24 h. Table 1 presents the composition of the 15 paste formulations studied and their 28 and 90-day strengths.

Table 1. Formulations of HB-VP prepared and compressive strength.

| Formulation | HB1 | HB2 | HB3 | HB4 | HB5 | HB6 | HB7 | HB8 | HB9 | HB10 | HB11 | HB12 | HB13 | HB14 | HB15 |
|--|------|------|------|-----|------|------|------|------|------|------|------|------|------|------|------|
| % VP | 0 | 25 | 75 | 100 | 75 | 50 | 50 | 50 | 75 | 25 | 25 | 50 | 25 | 50 | 75 |
| % Na ₂ SO ₄ | 8 | 10 | 10 | 8 | 6 | 8 | 12 | 8 | 10 | 6 | 6 | 4 | 10 | 8 | 6 |
| Na ₂ SO ₄ /Ca(OH) ₂ | 1 | 1.25 | 0.75 | 1 | 1.25 | 1 | 1 | 1.5 | 1.25 | 0.75 | 1.25 | 1 | 0.75 | 0.5 | 0.75 |
| 28-d (MPa) | 48.1 | 43.6 | 18.7 | 2.4 | 23.8 | 38.5 | 38.8 | 30.9 | 22.3 | 36.4 | 31.6 | 32.8 | 35.4 | 35.1 | 21.1 |
| 90-d (MPa) | 48.9 | 47.2 | 26.2 | 2.2 | 24.5 | 47.7 | 66.6 | 40.1 | 25.7 | 51.2 | 44.3 | 42.5 | 53.9 | 53.9 | 24.7 |

Equation **Error! Reference source not found.**) shows the regression model to predict the response surface of the compressive strength. The general mathematical solution to locate the optimal point on the response surface was provided by equation (2) ,Montgomery (2005). The software ‘‘Minitab 20.3’’ was used to analyze the data and plots.

$$Y = \beta_0 + \beta_1 X_1 + \beta_2 X_1^2 + \beta_3 X_2 + \beta_4 X_2^2 \dots + \beta_n X_n^n \quad (1)$$

Where Y is the response variable, $X_1 \dots X_n$ are the independent variables, and $\beta_0 \dots \beta_n$ are coefficients obtained by the regression model.

$$\hat{y} = \hat{\beta}_0 + \mathbf{x}'\mathbf{b} + \mathbf{x}'\mathbf{B}'\mathbf{x} \quad (2)$$

Where 'x' is a vector of variables and 'b' is a vector of regression coefficients, B' is a symmetric matrix (k x k) that contains the quadratic coefficients.

3. Results

3.1 Interpretation of statistical results

Table 2 shows the results of the ANOVA, only the significant terms were incorporated into the model. The only significant factor at 28 days was the %VP, while after 90-day the %NŜ was also significant (quadratic and linear) on the compressive strength. The R^2 values indicated a good correlation between experimental and predicted results; additionally, the difference between R^2_{adj} and $R^2_{\text{predicted}}$ is <0.20 ; which is considered OK to use predictions models.

Equations (1) and (4) present the models to establish the strength response surface for 28 and 90 days.

$$28d \text{ (MPa)} = 30.61 - 9.52 \text{ VP} + 1.2 \text{ NŜ} + 0.0744 \text{ NŜ/CH} \quad (1)$$

$$90d \text{ (MPa)} = 40.81 - 11.81 \text{ VP} + 3.53 \text{ NŜ} - 1.28 \text{ NŜ/CH} + 1.61 \text{ VP} \cdot \text{NŜ/CH} - 4.35 \text{ VP}^2 + 2.9 \text{ NŜ}^2 \quad (2)$$

3.2 Compressive strength optimization based on response surface methodology.

Figure 1 shows contour plots for the 28 and 90-day strength for 50 and 75% VP. Although the only 28-day significant effect was the %VP, the linear contours also showed proportional strength increases for high %NŜ; the highest strength was obtained with $\text{NŜ} > 11$ and $\text{NŜ/CH} > 1$; this was similarly noted for 75%VP, although the higher %VP resulted in lower strengths, as reflected by the negative coefficient in the equation (1). After 90 days the optimum strength (≥ 50 MPa) zone with 50% VP, was for $\text{NŜ} > 8$ and $\text{NŜ/CH} \geq 1$; whereas for 75%VP more than 30 MPa could be obtained with $\text{NŜ} > 10$ and $\text{NŜ/CH} \geq 1$.

The optimization was based on the desirability (D) function restricting the significative independent variable %VP, since equations (1) and (4) it had a negative coefficient; i.e. lower %VP favored the strength. The optimal predicted 28-day strength for 75% VP (Figure 2a), 12% N \hat{S} and 1.5 N \hat{S} /CH was of 24 \pm 4.5 MPa, while for 50% VP was 33 \pm 4.3 MPa for the same amount of activators.

Figure 2 b) shows that the desirability increased with lower %VP.

Table 2. ANOVA for compressive strength for 28 and 90 days of curing.

| Response day | | Terms | Sum of squares | F-value | p-value | Significant |
|--------------|--|--------------------------|----------------|---------|---------------|-------------|
| 28 d | | Model | 1473.67 | 15.25 | <0.0003 | Yes |
| | | VP | 1450.66 | 45.04 | <0.0001 | Yes |
| | | N \hat{S} | 22.92 | 0.71 | 0.4169 | No |
| | | N \hat{S} /CH | 0.09 | 0.002 | 0.9591 | No |
| | R ² = 0.8062, R ² adj = 0.7533, R ² pred = 0.6430 | | | | | |
| 90 d | | Model | 3332.38 | 21.25 | 0.0002 | Yes |
| | | VP | 2230.20 | 85.34 | <0.0001 | Yes |
| | | N \hat{S} | 199.52 | 7.63 | 0.0246 | Yes |
| | | N \hat{S} /CH | 26.27 | 1.01 | 0.3454 | No |
| | | VP*N \hat{S} /CH | 20.80 | 0.80 | 0.3983 | No |
| | | VP ² | 366.21 | 14.01 | 0.0057 | Yes |
| | | N \hat{S} ² | 162.67 | 6.22 | 0.0372 | Yes |
| | R ² = 0.9410, R ² adj = 0.8967, R ² pred = 0.7041 | | | | | |

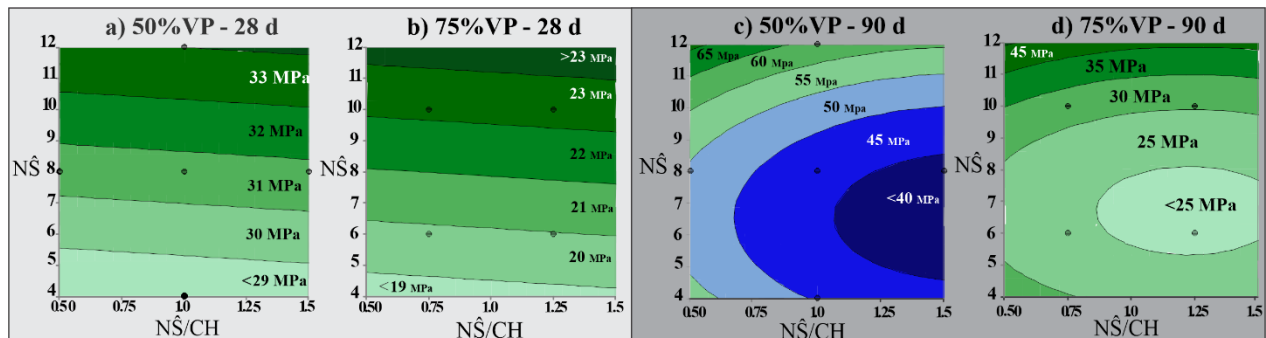


Figure 1. 28 and 90-day compressive strength contour plots for 50 and 75%VP

For the HB with 75% VP the optimum mixture for 90 days of curing showed that the maximum desirability for 12%N \hat{S} and N \hat{S} /CH=0.5, with a predicted strength of 45.6 \pm 17.9 MPa (

Figure 2 c); whereas for 50% VP (

Figure 2 d) the desirability was close to 1, even with same activator amount, and a predicted strength of 66.2 \pm 15.3 MPa. The ANOVA and the optimization showed the %VP was the most significant effect; however, it seems of relatively limited reactivity so PC must be present, which in high amounts increases the environmental impact.

The 28-day experimentally corroborated strengths were 20.2 MPa and 36.6 MPa, for 75%VP and 50%VP, respectively; while the 90-day were 24.5 and 52.6 MPa, for 75%VP and 50%VP, respectively. In general there was fairly good agreement among experimental and predicted strengths, except for 90-day for 75%VP, which was under the lower limit (29.4 MPa), consistent with the 90-day ANOVA results, that indicated the quadratic effect of the %VP had a more significant influence on the strength than the

activators. In general, the HB-VP developed strength over time, similar or higher than the references with no activators (75VP-PC and 50VP-PC,

Figure 2. Strength optimization for %VP a)75 and b)50 for 28-day and c) %VP d)75 and d)50 for 90 days (Figure 3).

3.3 Strength, environmental impact, and cost comparison on optimal HB-VP.

The emissions and energy demand associated with the production of HB-VP and PC were obtained from literature reports, Ouellet-Plamondon and Habert (2015), Cabrera-Luna et al. (2021), Arrigoni et al. (2020) and data bases such as EcoInvent, Althaus et al. (2007), Minera Santa Marta (2021). The costs of raw materials were collected from online suppliers in US dollars.

The HB-VP showed up to 37% and 32% less CO₂ and energy, respectively, relative to PC references (Figure 2. Strength optimization for %VP a)75 and b)50 for 28-day and c) %VP d)75 and d)50 for 90 days (Figure 3), which result as the VP requires low grinding energy and no thermal processing was required. Furthermore, the HB-VP were at least 38% cheaper than PC.

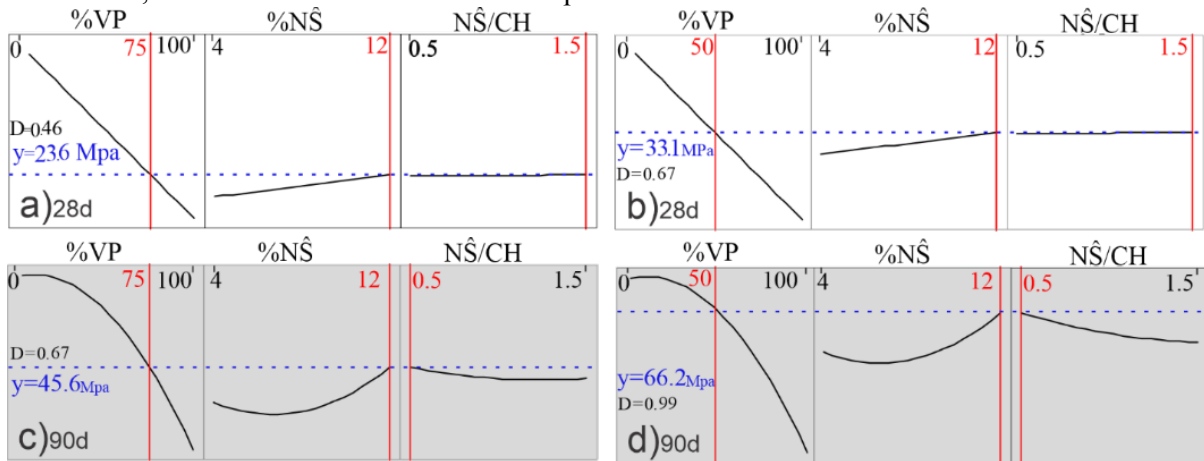


Figure 2. Strength optimization for %VP a)75 and b)50 for 28-day and c) %VP d)75 and d)50 for 90 days

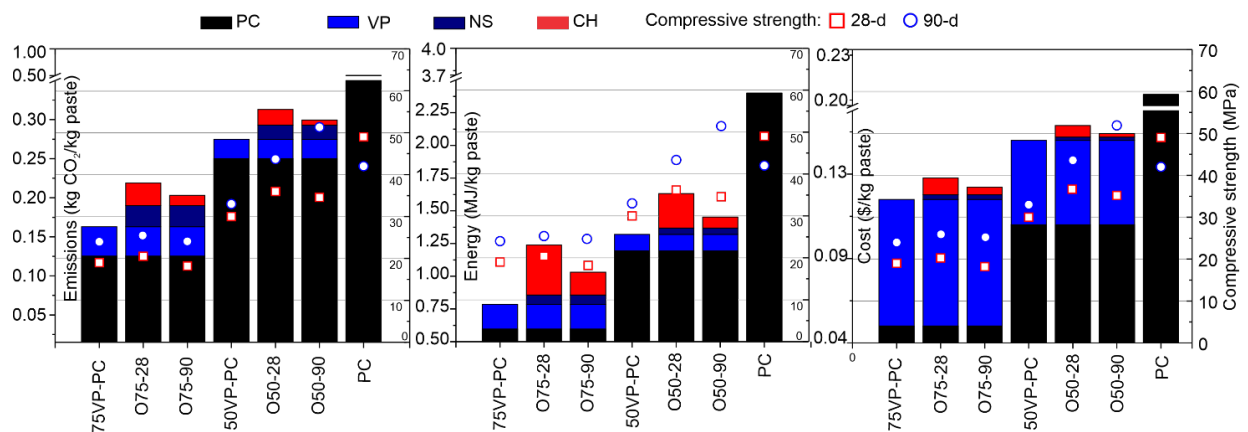


Figure 3. Comparison of environmental impact and cost between HB-VP and PC.

4. Conclusions

The use of powdered activators favored the compressive strength of hybrid binders (HB) with 75% and 50% of volcanic pumice. The statistical analysis indicated that the activators had their main effect on the strength after 28 days, which coincides with the potential VP pozzolanic reaction favoring the strength. Hybrid binders with optimized formulas are promising sustainable alternatives to Portland cement and blended Portland cement.

5. References

- Althaus, H., Hischer, R., Osses, M., Primas, A., Hellweg, S., Jungbluth, N. and Chudacoff, M. (2007) *Life Cycle Inventories of Chemicals*. Dübendorf.
- Arrigoni, A., Panesar, D. K., Duhamel, M., Opher, T., Saxe, S., Posen, I. D. and MacLean, H. L. (2020) "Life cycle greenhouse gas emissions of concrete containing supplementary cementitious materials: cut-off vs. substitution", *Journal of Cleaner Production*, 263: 121465
- Cabrera-Luna, K., Maldonado-Bandala, E., Nieves-Mendoza, D., Castro-Borges, P., Perez-Cortes, P. and Escalante-García, J. (2021) "Supersulfated cements based on pumice with quicklime, anhydrite and hemihydrate: Characterization and environmental impact", *Cement and Concrete Composites*, 124: 104236
- Minera Santa Marta, S. A. (2021) *Climate Declaration For Sodium Sulphate From Minera Santa Marta S.A.* Spain, Minera Santa Marta S.A.
- Montgomery, D. C. (2005) *Diseño y análisis de experimentos*, Limusa Wiley.
- Myers, R. H., Montgomery, D. C. and Anderson-Cook, C. M. (2016) *Response surface methodology: process and product optimization using designed experiments*, John Wiley & Sons, New Jersey.
- Ouellet-Plamondon, C. and Habert, G. (2015) Life cycle assessment (LCA) of alkali-activated cements and concretes. *Handbook of alkali-activated cements, mortars and concretes*. Elsevier, Cambridge.
- Palomo, A., Monteiro, P., Martauz, P., Bílek, V. and Fernandez-Jimenez, A. (2019) "Hybrid binders: A journey from the past to a sustainable future (opus caementicium futurum)", *Cement and Concrete Research*, 124: 105829

CDW waste as retardants of ions harmful to cement

R. Vigil de la Villa¹, V. Rubio², R. García-Giménez^{1*}, M. Frías³, S. Martínez-Ramírez⁴, J. Moreno⁵
and I. Vegas⁵

¹ Facultad de Ciencias. Universidad Autónoma de Madrid. Unidad Asociada UAM-CSIC Madrid, Spain

Email: raquel.vigil@uam.es, rosario.garcia@uam.es

² Facultad de Filosofía y letras. Universidad Autónoma de Madrid. Unidad Asociada UAM-CSIC Madrid, Spain

Email: virginia.rubio@uam.es

³ Instituto Eduardo Torroja. IETcc, CSIC. Madrid, Spain

Email: mfrias@ietcc.csic.es

⁴ Institute for the Structure of Matter (IEM-CSIC), Madrid, Spain

Email: sagrario@iem.cfmac.csic.es

⁵ Tecnia, Basque Research and Technology Alliance (BRTA), Derio, Spain

Email: jaime.moreno@tecnalia.com; inigo.vegas@tecnalia.com

ABSTRACT

Circular Economy promotes the use of industrial materials during various phases of their active life. Construction and demolition waste (CDW) are one of those materials that can be reused several times without losing their properties, even improving them, by participating as substitutions in the Ordinary Portland Cement (OPC). The large volume of CDW wastes makes this substitution one of the most valued in the world of cement at present; it is for this reason that two types of aggregates, siliceous and calcareous, have been selected as potential substitutions in the OPC. In all cases, it is a question of obtaining easily accessible pozzolanic cements, with little contamination and great economy. In this work, binary mixtures of OPC and CDW waste have been prepared, manufacturing mortars that have been studied by means of XRD, XRF, SEM/EDX, and ion diffusion. The results obtained so far indicate that CDW's are suitable for substitution in the OPC in variable proportions that their use improves the slowing down of diffusion for certain ions, so that can link the pore size with the capture of these ions, considering certain pores as traps for the diffusion of polluting ions.

KEYWORDS: CDW waste, diffusion, tomography, pozzolan, porous size.

1. Introduction

Concrete is the most used material in construction. It is characterized by a variable total porosity between 10-30%, depending mainly on the water/cement ratio and the curing conditions. The porous capillary network is the access channel through which aggressive agents degrade the cement matrix. The main aggressive agents are related to the presence of chlorides, sulfates, and CO₂, which have the capacity to react with the anhydrous and hydrated phases of the cement and cause a progressive deterioration of the constructions (Onah et al. (2023)). Therefore, the cement matrices present low resistance to aggressive environmental agents due to the presence of high portlandite contents (24-27% of the total). One of the solutions to increase resistance against aggressive environments is the use of standardized active additions (fly ash, natural pozzolan, silica fume, etc.) and non-standardized (ceramic wastes, CDW wastes, coal mining waste, agro-

industrial residues) (Villar et al. (2008), Snellings et al. (2012), Frias et al. (2018)), which, through the pozzolanic reaction, produce secondary hydrated phases that refine the porous structure, preventing or delaying their entry. Currently, one of the types of waste that is generating special attention from the scientific community and the construction sector is construction and demolition waste (CDW), due to its large annual volume (350 mtms in Europe), generating significant environmental, economic, and social problems when it accumulates in landfills. In this line of research, this paper analyzes, for the first time, the behavior of binary cement mortars made with 7% CDW pozzolan, which were exposed to the environment for 12 months in the city of Madrid (Spain).

2. Materials and methods

2.1. Materials

To carry out this research work, two fine fractions of concrete (<5 mm) from Spanish CDW Treatment Plants have been selected: siliceous concrete (HsT) and limestone concrete (HcG). To obtain the binary cements with a 7% substitution for each of the CDW pozzolans, a commercial cement type CEM I 52.5R was used. The cement mortars were manufactured and cured according to current regulations with a water/binder ratio of 0.5 and the 4x4x16 cm prismatic specimens were previously cured under water for 28 days. Subsequently, the specimens were exposed to outdoor and indoor environments for 12 months (January 2022-December 2022).

2.2. Methods

All samples were studied using X-ray diffraction (XRD) and scanning electron microscopy (SEM), equipped with an energy dispersive X-ray (EDX) analyzer. At the end of the time, a *line scan* was performed on the parts exposed and not exposed to air in the different environments. The data of each element correspond to the average of two analyzes, due to the variability that exists in each measurement field, which is repeated in a variable number, every 491 nanometers, which is the field distance.

3. Results and discussion

The chemical composition by XRF of the fine fractions of the CDW of recycled concrete used as starting materials are collected in Table 1.

Table 1. Chemical composition of starting materials by XRF analyses (HsT = siliceous concrete; HcG = limestone concrete; LOI = loss on ignition).

| (%) | SiO ₂ | Al ₂ O ₃ | CaO | Na ₂ O | K ₂ O | P ₂ O ₅ | Fe ₂ O ₃ | MgO | SO ₃ | TiO ₂ | MnO | LOI |
|------------|------------------|--------------------------------|-------|-------------------|------------------|-------------------------------|--------------------------------|------|-----------------|------------------|------|-------|
| HsT | 49.97 | 8.98 | 18.65 | 0.80 | 3.35 | 0.11 | 2.30 | 1.37 | 2.53 | 0.28 | 0.04 | 11.50 |
| HcG | 9.34 | 2.88 | 50.32 | 0.18 | 0.47 | 0.03 | 1.20 | 1.12 | 0.85 | 0.14 | 0.09 | 33.20 |

The mineralogical quantification of the wastes by the Rietveld method shows that the HsT and HcG concrete wastes are made up of calcite, mica, feldspar, and quartz in different proportions, according to the nature of the primary aggregate (Caneda et al. (2022)). In all samples a sequential analysis from one end of the test piece to the other, an oscillation of the different measured elements is observed. However, and according to the range of variation, three groups can be distinguished: 1) Si and Ca: they are the ones that more varying in ranges that oscillate between 20 and 70%. Both are complementary, that is, an increase in one implies a decrease in the other; 2) ions with concentrations between 9 and 2%. Aluminum, sulphates, iron, and potassium are usually found in this range, the latter only in certain cases (if the concentration is low, it will form part of the so-called group 3). Finally, elements in concentrations lower than 2%, where magnesium, chloride, manganese, sodium, titanium, barium are usually found.

3.1. Mobility within OPC mortar.

The differences between ion diffusion in the laboratory samples present, for sulfate, Fe and Al (all existing in the initial concrete wastes), a behavior similar with three concentration maxima along the profile: an initial moment, another at a medium distance from the specimen and the last one, before covering the total distance. On the other hand, in the environment samples, in the group 2, appears K with three maximum concentrations, which indicates that it absorbs potassium ions from the environment with a change in the behavior of iron and sulfate since it only a maximum concentration appears, stabilizing later. The elements of group 3 are different, thus chlorides are detected on the outside with two moments of diffusion, while Ti appears on the inside at one end, as well as Mg and Na with constant amounts throughout the mobilization.

3.2. Mobility within 7% HcG mortars.

This mortar from a 7% substitution in the OPC by HcG limestone concrete waste, has a different mobility in the elements of group 2 for the sample with natural exposure and the sample exposed in the laboratory; in the latter, Al is the one that is mobilized in three successive moments, while Fe and sulphates remain constant in the profile, except in an area close to the surface where Fe increases its concentration and then decreases and reaches a constant concentration. On the other hand, in the environment sample there is a different behavior for sulfate and Al with two maximums, beginning and middle of line scan. In the elements of group 3, the environment sample presents chlorides, Mn and Na, with three critical moments. It differs from the laboratory sample that offers a variation of Ti in the distal zone (Figure 1).

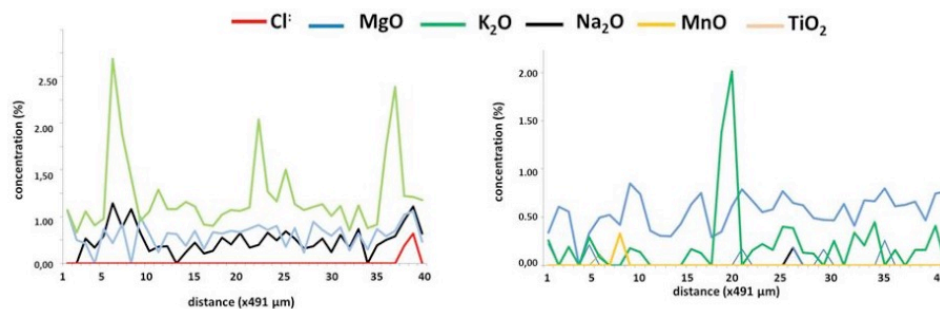


Figure 1. Mobility of ions in HcG mortar samples located in the laboratory room (left) and environment (right).

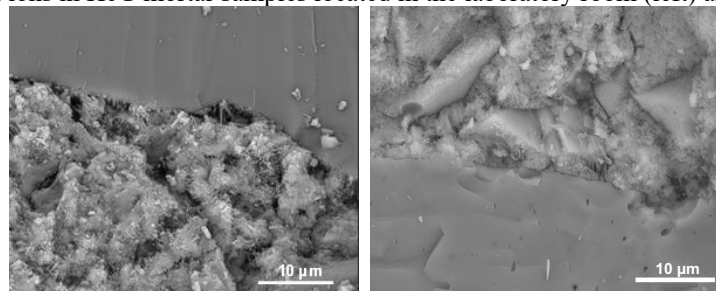


Figure 2. Contact intergrains in HcG mortar. Left) laboratory room. Right) environment.

By SEM the contact between grains of the outer zone indicates less compaction, with spongy and cracked areas that are not detected in the inner zone of the OPC. Phase recrystallizations are identified in the outer zone by an increase in the aggregates size from the contact zone and compaction of the grains (Figure 2).

3.3. Mobility within 7% HsT mortars.

As the same HcG mortar, in the siliceous HsT mortar, the sulfate-iron association was detected in the laboratory sample with two critical points. It is quite different from the behavior of the same ions in the outer sample: sulfate, Fe and Al repeat the diffusion with maximum concentrations at the end of the path. Chloride appears in both exposures and mobility of Pb, Ba and Ti is detected in the laboratory (Figure 3). Studying the contact between grains in the interior zone of the 7% HsT mortar, an intergrowth of laminar

microcrystals, wrinkled lamellae and overlapping fibers is observed, producing cavities, channels and pores, resulting in a slightly larger contact intergrains zone. Spongy and cracked than in the same situation of the HeG mortar. The recrystallizations that occur in the outer zone increase the compaction in the contact between grains (Figure 4).

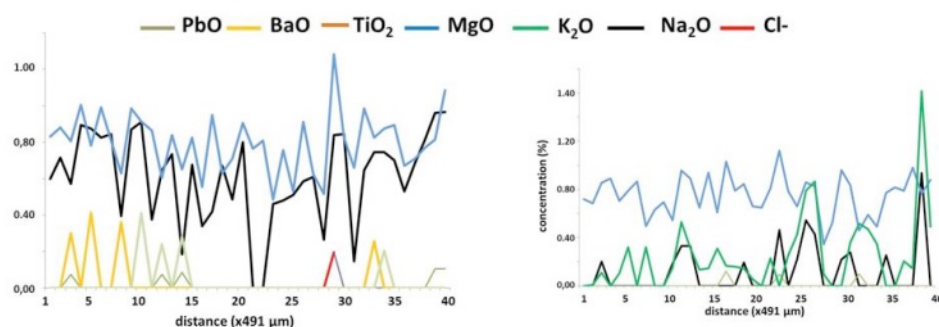


Figure 3. Mobility of ions in HsT mortar samples located in the laboratory room (left) and environment (right).

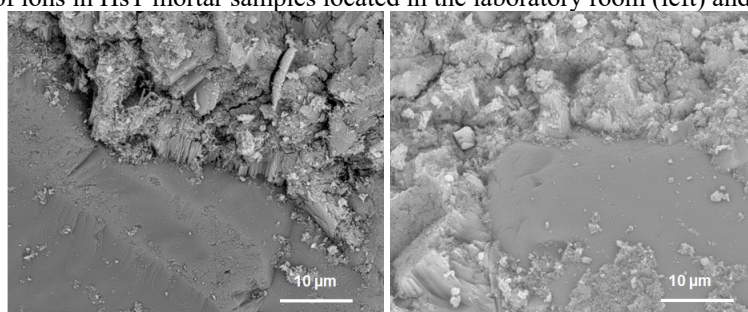


Figure 4. Contact intergrains in HsT mortar. Left) laboratory room. Right) environment.

4. Conclusions

The preparation of mortars with recycled aggregates, limestone or siliceous, facilitates the use of wastes that were once destined for landfills. Mortars made with recycled siliceous concrete are more porous than those related to limestone wastes. Exposure to a polluted environment such as the city of Madrid (Spain), retains or mobilizes polluting elements such as chlorides, Pb, Ba, being more pronounced in limestone mortars manufactured using wastes. Therefore, the fine fractions of recycled concrete may be viable as pozzolanic additions and sinks for polluting elements.

Acknowledgements

This research was funded by Spain's Ministry of Science, Innovation and Universities under National Project RTI2018-097074-B-C21 and C22, the EU's ERDF, AEI, Asociación de RCDs (Spain), Sika (Madrid, Spain) and IECA (Madrid, Spain).

References

- Caneda-Martínez, L., Monasterio, M., Moreno-Juez, J., Martínez-Ramírez, S., García, R. and Frías, M. (2021) "Behaviour and Properties of Eco-Cement Pastes Elaborated with Recycled Concrete Powder from Construction and Demolition Wastes", *Materials*, 14: 1299
- Frías, M., Vigil, R., García, R., Martínez, S. and Fernández, L. (2018) "New developments in low clinker cement paste mineralogy", *Applied Clay Science*, 166: 94-101
- Onah, J., Roland, O. and Black, L. (2023) "Resistance of concretes to external chlorides in the presence and absence of sulphates: A review", *Applied Sciences* 13 (1), 182
- Snellings, R., Mertens, G. and Elsen, J. (2012) "Supplementary cementitious materials", *Reviews in Mineralogy and Geochemistry*, 74: 211-278
- Villar, E., Frías, M., and Valencia, E. (2008) "Sugar cane wastes as pozzolanic materials: Application of mathematical model", *ACI Materials Journal*, 105: 258-264

Production of a hydraulic material from post treated steelmaking slags

K. Schraut^{1*}, B. Adamczyk², C. Adam³, D. Stephan⁴, S. Simon⁵, J. von Werder⁶, and B. Meng⁷

¹ Bundesanstalt für Materialforschung und -prüfung (BAM), Berlin, Germany
Email: katharina.schraut@bam.de

² Bundesanstalt für Materialforschung und -prüfung (BAM), Berlin, Germany
Email: burkart.adamczyk@bam.de

³ Bundesanstalt für Materialforschung und -prüfung (BAM), Berlin, Germany
Email: christian.adam@bam.de

⁴ Technische Universität Berlin, Berlin, Germany
Email: stephan@tu-berlin.de

⁵ Bundesanstalt für Materialforschung und -prüfung (BAM), Berlin, Germany
Email: sebastian.simon82@gmail.com

⁶ Bundesanstalt für Materialforschung und -prüfung (BAM), Berlin, Germany
Email: Julia.von-Werder@bam.de

⁷ Bundesanstalt für Materialforschung und -prüfung (BAM), Berlin, Germany
Email: Birgit.Meng@bam.de

ABSTRACT

Steelmaking slag is a by-product of steel production, of which 4.5 Mt were produced in 2020 in Germany alone. It is mainly used in road construction, earthwork and hydraulic engineering. A smaller part is returned to the metallurgical cycle, used as fertiliser or landfilled.

With this use, iron oxides still contained in steelmaking slag are lost. In addition, the possibility of producing higher-grade products from steelmaking slag is foregone. In recent decades, many researchers have investigated the production of Portland cement clinker and crude iron from basic oxygen furnace slags (BOFS) via a reductive treatment. Carbothermal treatment of liquid BOFS causes a reduction of iron oxides to metallic iron, which separates from the mineral phase due to its higher density. Simultaneously, the chemical composition of the reduced slag is adapted to that of Portland cement clinker.

In this study, German BOFS was reduced in a small-scale electric arc furnace using petrol coke as a reducing agent. The resulting low-iron mineral product has a similar chemical composition to Portland cement clinker and was rich in the tricalcium silicate solid solution alite (Ca₃SiO₅). Based on its chemical and mineralogical composition, similar to that of Portland cement clinker, the reduced BOFS has the potential to react comparably. In our study, the reduced BOFS produced less hydration heat than OPC, and its hydraulic reaction was delayed. However, adding gypsum has shown to accelerate the hydration rate of the reduced BOFS compared to that known from the calcium silicates of Portland cement clinker. Further research to improve the hydraulic properties of the reduced slag is essential. If successful, producing a hydraulic binder and crude iron from BOFS has economic and ecological benefits for both the cement and steel industries.

KEYWORDS: *steelmaking slag, alite, hydraulic reactivity, clinker substitute*

1. Introduction

Basic oxygen furnace slags (BOFS) contain 7–50 wt.% Fe₂O₃, 31–56 wt.% CaO, 10–27 wt.% SiO₂, 1–4.5 wt.% Al₂O₃, 0.3–10 wt.% Mn₂O₃, and 0.8–15 wt.% MgO (Menad et al., 2014). Despite their high basicity (CaO/SiO₂ ratio) and a content of up to 20 wt.% alite (Ca₃SiO₅) and up to 60 wt.% belite (β-Ca₂SiO₄) (Das et al., 2007), BOFS are scarcely used for cement production due to their high iron oxides content, low content of hydraulic phases, and content of up to 15 wt.% free CaO and 5 wt.% MgO, which make BOFS a risk for volume instability (Das et al., 2007, Waligora et al., 2010, Menad et al., 2014).

In the past, several different ways to produce a hydraulic or pozzolanic material from BOFS have been investigated, e.g. (Li et al., 2011, Belhadj et al., 2012, Ludwig and Wulfert, 2012, Li et al., 2013, Neto et al., 2017, Liu et al., 2019). A reductive treatment of BOFS as described in (Kubodera et al., 1979, Piret and Dralants, 1984, Dziarmagowski et al., 1992, Reddy et al., 2006, Ludwig and Wulfert, 2012, Wulfert et al., 2013a, Wulfert et al., 2013b, Liu et al., 2017) is advantageous because it allows both the recovery of iron from the BOFS and the simultaneous production of Portland cement clinker. The properties of the final hydraulic product depend on the composition of the original BOFS, the degree of reduction, and the modifications made during the treatment.

However, it was found that the hydraulic reaction of the Portland cement clinker-like material produced from BOFS was significantly delayed compared to ordinary Portland cement (OPC) (Schraut et al., 2021). Since OPC is a product of finely ground cement clinker mixed with a certain amount of calcium sulfates, such as gypsum ($\text{CaSO}_4 \cdot 2\text{H}_2\text{O}$), the next step was to investigate the hydraulic reactivity of the clinker-like material from BOFS with the addition of gypsum. Besides controlling the tricalcium aluminate reaction, calcium sulfates also accelerate the hydration of calcium silicates (Bentur, 1976, Quennoz and Scrivener, 2013) and increase the dissolution of alite (Menetrier et al., 1980).

To keep the complexity of the system low, the addition of calcium sulfates other than gypsum has been refrained from in this study.

2. Materials and Methods

A BOFS from a German steel plant was used for the thermochemical experiments. The slag was crushed to a maximum grain size of approx. 20 mm and dried at 200 °C before it was molten and reduced in the small technical scale electric arc furnace of the Bundesanstalt für Materialforschung und -prüfung (BAM). The electric arc furnace has a power of 480 kW and is equipped with three graphite electrodes with a diameter of 60 mm. The experiments were conducted in a graphite-lined furnace vessel with a volume of approx. 0.4 m³. 58 g of petrol coke per kg of BOFS was added as a reducing agent. The generated metallic iron was sedimented at the bottom of the furnace and was obtained manually after cooling. Cooling took place in the reactor within ~24 h. For more details, see Schraut et al. (2021).

The chemical composition of the samples was determined by CRB Analyse Service GmbH on fused beads by X-ray fluorescence analysis (XRF). The crystalline phase composition was determined by X-ray diffraction (XRD) with a Bruker D8 Advance X-ray diffraction system at 40 kV and 40 mA over an angular range of 5–85 °2θ with a step size of 0.02 °2θ and a velocity of 2 s/step. The instrument was equipped with a Cu-tube, a LynxEye XE-T detector, and a fixed slit (0.3°). To investigate the crystalline hydrates with XRD, the hydration was stopped after 2, 7, 14, 28, 56, and 90 d using the solvent exchange method with isopropanol.

The hydration heat was measured over two weeks in an isothermal calorimeter TAM Air 8-channel from TA instruments at a temperature of 20 °C. 3 g of the ground sample was externally mixed for 1 min with 1.5 g distilled water resulting in a water-to-binder (W/B)-ratio of 0.5.

As a reference, a commercial CEM I 32.5 R from Schwenk Zement KG was prepared and analysed under the same conditions as the experimental samples. Gypsum (EMSURE® p.A. from Merck KGaA) was added to the sample in a concentration corresponding to 1.0 wt.% SO_3 .

3. Results and Discussion

The reductive treatment resulted in a transformation of the oxide-bound iron in brownmillerite ($\text{Ca}_2(\text{Al,Fe})_2\text{O}_5$), wuestite (FeO) and magnetite (Fe_3O_4) to metallic iron, which separated from the mineral slag. Accordingly, the mass fraction of Fe_2O_3 in the mineral slag (reduced BOFS) decreased from about 29 wt.% to about 6 wt.%, while the mass fractions of CaO and SiO_2 increased proportionally (Table 1). The mineralogical composition of the reduced BOFS changed correspondingly. While the Fe-oxides and Fe-Al-oxides disappeared, alite formed the new main mineral phase in the reduced BOFS. Besides alite, belite, mayenite ($\text{Ca}_{12}\text{Al}_{14}\text{O}_{33}$), tricalcium aluminate ($\text{Ca}_3\text{Al}_2\text{O}_6$), portlandite ($\text{Ca}(\text{OH})_2$) and periclase (MgO) were identified in the reduced BOFS as crystalline phases. Therefore, it can be stated that the mineralogical and chemical composition of the reduced BOFS is close to the mineralogical and chemical composition of Portland cement clinker.

The formation of alite in reduced BOFS was also reported by Kubodera et al. (1979), Wulfert et al. (2013b) and Dziarmagowski et al. (1992) and is likely to depend on the CaO/SiO₂-ratio of the reduced slag. Alite was identified as the main mineral in reduced BOFS with CaO/SiO₂ > 2.9, while belite was the main mineral in reduced BOFS with CaO/SiO₂ < 2.6 (Dziarmagowski et al., 1992, Reddy et al., 2006).

Table 1: Chemical composition of the original BOFS, the reduced BOFS (rBOFS), and a commercial OPC CEM I 32.5 R (CEM I) determined by XRF. All mass fractions are given as wt.% oxides, although this may not always represent the actual oxidation state of each element in the samples. Only element oxides whose mass fractions were > 0.1 wt.% in at least one sample are shown.

| [wt.%] | CaO | SiO ₂ | Fe ₂ O ₃ | MnO | MgO | Al ₂ O ₃ | P ₂ O ₅ | Cr ₂ O ₃ | TiO ₂ | V ₂ O ₅ | SO ₃ | SrO | Na ₂ O | K ₂ O |
|--------|-------|------------------|--------------------------------|-------|------|--------------------------------|-------------------------------|--------------------------------|------------------|-------------------------------|-----------------|-------|-------------------|------------------|
| BOFS | 43.48 | 12.07 | 28.59 | 4.554 | 3.64 | 1.79 | 1.12 | 0.518 | 0.524 | 0.310 | 0.23 | 0.025 | 0.07 | <0.03 |
| rBOFS | 64.00 | 19.54 | 5.64 | 3.151 | 3.15 | 2.53 | 1.20 | 0.419 | 0.730 | 0.399 | 0.05 | 0.035 | <0.06 | <0.03 |
| CEM I | 61.97 | 19.36 | 3.06 | 0.047 | 3.04 | 4.96 | 0.44 | 0.013 | 0.322 | 0.010 | 3.03 | 0.148 | 0.21 | 0.92 |

The main hydration reaction of the reduced BOFS was considerably slower than that of OPC and started only after ~9 d of hydration (Figure 1). The hydration heat maximum was reached after about 14 d of hydration. The cumulative heat of hydration after 14.5 d was ~90 J/g. The first hydrates to form were portlandite (Ca(OH)₂) and brucite (Mg(OH)₂). Additionally, hemicarboaluminate ([Ca₄Al₂(OH)₁₂][OH(CO₃)_{0.5}·4H₂O]) was detected and transformed later to carbonated hemicarboaluminate ([Ca₄Al₂(OH)₁₂][OH_{0.4}(CO₃)_{0.8}·4H₂O]) and monocarboaluminate (Ca₄Al₂(OH)₁₂(CO₃)·5H₂O). The addition of 1 wt.% SO₃ in the form of gypsum accelerated the reaction of the reduced BOFS significantly. The main hydration reaction started after ~1 d of hydration and the cumulative heat of hydration after 14.5 d increased to ~160 J/g. Furthermore, the heat flow curve showed a sharp peak after ~2 d and 5 h that can be interpreted as the reaction peak of the aluminate reaction. Since the aluminate reaction occurred after the silicate reaction, the sample can be considered properly sulfated (Quennoz and Scrivener, 2013). In rBOFS + 1 wt.% SO₃, ettringite formed besides portlandite and brucite. No carboaluminates formed during hydration of rBOFS + 1 wt.% SO₃.

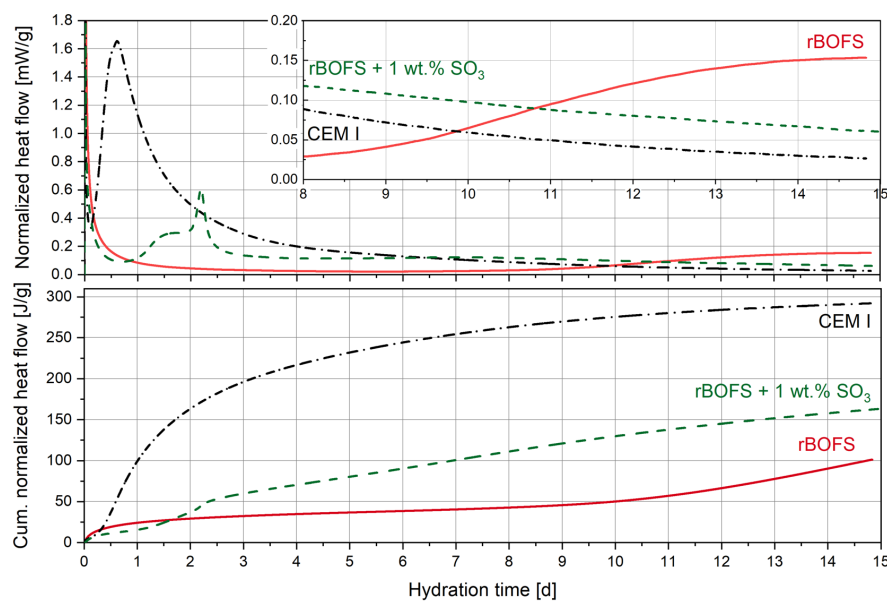


Figure 1: Normalised heat flow and cumulative normalised heat of the reduced BOFS (red, solid line), the reduced BOFS with the addition of an equivalent of 1 wt.% SO₃ as gypsum (green, dashed line) and of a commercial CEM I (black, dash-dotted line) measured for 14.5 d.

Sulfate is known to influence the silicate reaction. An accelerated dissolution of the alite with addition of sulfates was reported by (Bentur, 1976, Menetrier et al., 1980, Zajac et al., 2014, Bergold et al., 2017, Zunino and Scrivener, 2020, Andrade Neto et al., 2022). The reasons for this are still debated. The effect

was proposed to be caused by a promotion of C-S-H growth by ettringite acting as additional nuclei (Bergold et al., 2017, Tan et al., 2019) or by a change in C-S-H morphology (Andrade Neto et al., 2022). Other researchers assumed that a decrease of Ca^{2+} activity due to the formation of CaSO_4^0 species or an increased protonation of the C_3S surface by sulfate ions enhances the alite dissolution (Nicoleau et al., 2014). The binding of Al ions as ettringite is most likely not the causative agent, as acceleration by gypsum was observed in C_3S with and without Al (Andrade Neto et al., 2022).

4. Conclusions

The reductive treatment of BOFS can be used to recover iron from BOFS while simultaneously producing a material similar to Portland cement clinker. The majority of iron was reduced to metallic iron and separated from the mineral melt. The reduced BOFS had a chemical and mineralogical composition close to that of Portland cement clinker and contained alite as the main mineral.

The reduced BOFS reacted considerably more slowly with water than OPC. However, the reaction rate was increased with the addition of gypsum. Further investigations are needed, including using different sulfate carriers and SO_3 contents, to determine the actual mechanisms behind this acceleration. Nevertheless, the reduced BOFS shows potential as a cement component or concrete addition contributing to long-term hardening.

Acknowledgements

We would like to thank I. Feldmann for SEM pictures, D. Al-Sabbagh for XRD measurements and T. Hirsch for calorimetric measurements.

This work was funded by the German ministry of Education and Research (BMBF) under the funding guideline „Resource-efficient circular economy - Building and mineral cycles (ReMin)“ funding number 033R254A.

References

- Menad, N., Kanari, N. and Save, M. (2014) "Recovery of high grade iron compounds from LD slag by enhanced magnetic separation techniques", *International journal of mineral processing*, 126: 1-9
- Das, B., Prakash, S., Reddy, P. and Misra, V. (2007) "An overview of utilization of slag and sludge from steel industries", *Resources, Conservation and Recycling*, 50(1): 40-57
- Waligora, J., Bulteel, D., Degrugilliers, P., Damidot, D., Potdevin, J. and Measson, M. (2010) "Chemical and mineralogical characterizations of LD converter steel slags: A multi-analytical techniques approach", *Materials characterization*, 61(1): 39-48
- Li, J., Yu, Q., Wei, J. and Zhang, T. (2011) "Structural characteristics and hydration kinetics of modified steel slag", *Cement and Concrete Research*, 41(3): 324-329
- Belhadj, E., Diliberto, C. and Lecomte, A. (2012) "Characterization and activation of basic oxygen furnace slag", *Cement and concrete composites*, 34(1): 34-40
- Ludwig, H. and Wulfert, H. (2012) 18. *Int. Baustofftagung ibausil*, pp. 18-25. Weimar
- Li, Z., Zhao, S., Zhao, X. and He, T. (2013) "Cementitious property modification of basic oxygen furnace steel slag", *Construction and Building Materials*, 48: 575-579
- Neto, J.B.F., Fredericci, C., Faria, J.O., Chotoli, F.F., Ribeiro, T.R., Malynowskyj, A., Silva, A.L., Quarcioni, V.A. and Lotto, A.A. (2017) "Modification of Basic Oxygen Furnace Slag for Cement Manufacturing", *Journal of Sustainable Metallurgy*, 3(4): 720-728
- Liu, C., Huang, S., Blanpain, B. and Guo, M. (2019) "Effect of Al_2O_3 Addition on Mineralogical Modification and Crystallization Kinetics of a High Basicity BOF Steel Slag", *Metallurgical and Materials Transactions B*, 50(1): 271-281
- Kubodera, S., Koyama, T., Ando, B. and Kondo, R. (1979) "An approach to the full utilization of LD slag", *Transactions of the Iron and Steel Institute of Japan*, 19(7): 419-427
- Piret, J. and Dralants, A. (1984) "Utilization of LD Process Slag for the Production of Portland Cement Clinker and Pig Iron", *Stahl und Eisen*, 104(16): 774-778
- Dziarmagowski, M., Karbowniczek, M., Pyzalski, M. and Okon, J. (1992) "Reduction of converter slag in electric arc furnace", *Ironmaking & steelmaking*, 19(1): 45-49
- Reddy, A.S., Pradhan, R. and Chandra, S. (2006) "Utilization of basic oxygen furnace (BOF) slag in the production of a hydraulic cement binder", *International journal of mineral processing*, 79(2): 98-105

- Wulfert, H., Keyssner, M., Ludwig, H. and Adamczyk, B. (2013a) "Metal recovery and conversion of steel slag into highly reactive cement components/Metallgewinnung und Umwandlung von LD-Schlacke in hochreaktive Zementkomponenten", *ZKG international*, 9: 34-40
- Wulfert, H., Keyßner, M., Ludwig, H., Adamczyk, B. and Schiffers, A. (2013b) "Hochreaktive Zementkomponenten aus Stahlwerksschlacken verbessern Ökologie und Ökonomie/ Highly reactive cement components from steel slag for optimized ecology and economy", *Stahl und Eisen*, 133(12): 45-50
- Liu, C., Huang, S., Wollants, P., Blanpain, B. and Guo, M. (2017) "Valorization of BOF steel slag by reduction and phase modification: metal recovery and slag valorization", *Metallurgical and Materials Transactions B*, 48(3): 1602-1612
- Schraut, K., Adamczyk, B., Adam, C., Stephan, D., Meng, B., Simon, S. and von Werder, J. (2021) "Synthesis and characterisation of alites from reduced basic oxygen furnace slags", *Cement and Concrete Research*, 147: 106518
- Bentur, A. (1976) "Effect of Gypsum on the Hydration and Strength of C₃S Pastes", *Journal of the American Ceramic Society*, 59(5- 6): 210-213
- Quennoz, A. and Scrivener, K.L. (2013) "Interactions between alite and C₃A-gypsum hydrations in model cements", *Cement and Concrete Research*, 44: 46-54
- Menetrier, D., Jawed, I. and Skalny, J. (1980) "Effect of gypsum on C₃S hydration", *Cement and Concrete Research*, 10(5): 697-701
- Zajac, M., Rossberg, A., Le Saout, G. and Lothenbach, B. (2014) "Influence of limestone and anhydrite on the hydration of Portland cements", *Cement and concrete composites*, 46: 99-108
- Bergold, S., Goetz-Neunhoeffler, F. and Neubauer, J. (2017) "Interaction of silicate and aluminate reaction in a synthetic cement system: Implications for the process of alite hydration", *Cement and Concrete Research*, 93: 32-44
- Zunino, F.A. and Scrivener, K. (2020) "Factors influencing the sulfate balance in pure phase C₃S/C₃A systems", *Cement and Concrete Research*, 133: 106085
- Andrade Neto, J.S., Rodríguez, E.D., Monteiro, P.J., De la Torre, A.G. and Kirchheim, A.P. (2022) "Hydration of C₃S and Al-doped C₃S in the presence of gypsum", *Cement and Concrete Research*, 152: 106686
- Tan, H., Li, M., Ren, J., Deng, X., Zhang, X., Nie, K., Zhang, J. and Yu, Z. (2019) "Effect of aluminum sulfate on the hydration of tricalcium silicate", *Construction and Building Materials*, 205: 414-424
- Nicoleau, L., Schreiner, E. and Nonat, A. (2014) "Ion-specific effects influencing the dissolution of tricalcium silicate", *Cement and Concrete Research*, 59: 118-138

Influence of sisal fiber on mechanical, shrinkage and high temperature performance of UHPC

Xiaojian Gao*, Guosheng Ren

School of Civil Engineering, Harbin Institute of Technology, Harbin, CHINA

Email: gaoxj@hit.edu.cn; 19B333002@stu.hit.edu.cn

ABSTRACT

Ultra-high performance concrete (UHPC) has become one of the most promising building materials due to its ultra-high mechanical properties and excellent durability. However, the characteristics of high content of cementing material, low water to binder ratio, and dense microstructure for UHPC lead to its poor volume stability and high-temperature resistance. Natural sisal fibers have the advantages of being renewable, low-price, low carbon footprint, and easy to access. This study attempts to utilize natural sisal fibers to decrease autogenous shrinkage and eliminate high-temperature spalling of UHPC. The effect of sisal fibers on mechanical properties, autogenous shrinkage, internal relative humidity, and high-temperature behavior of UHPC was investigated. Moreover, a new method of using sol-gel deposition of nanosilica on the sisal fiber surface to strategically improve the interface bonding with UHPC was proposed. The results indicated that the 7-day autogenous shrinkage of UHPC was decreased by 71.4% after adding sisal fibers, owing to the internal curing and reinforcement effect induced by sisal fibers. The spalling phenomenon of UHPC was completely eliminated. This is because sisal fibers shrink at high temperatures, and tangential space is formed between sisal fibers and the matrix for vapor escape. Furthermore, the bond strength (pullout energy) between sisal fiber and UHPC matrix was improved by 28.0% (40.8%) after nanosilica deposition. This study provides a new sight into the utilization of natural sisal fibers to manufacture sustainable UHPC with good volume stability and high-temperature resistance. The long-term durability of UHPC incorporated with sisal fibers should be more **comprehensively studied**.

KEYWORDS: *Sisal fibers, Autogenous shrinkage, High temperatures, Interface bonding, UHPC*

1. Introduction

Compared with ordinary concrete, ultra-high performance concrete (UHPC) has the disadvantages of poor volume stability and high-temperature resistance (Hisseine et al., 2021). At present, the method of reducing the autogenous shrinkage of UHPC is adding shrinkage-reducing agents, expansion agents, and internal curing materials, and the method of improving the high-temperature resistance is adding polymer fibers. However, the addition of the above materials will bring some damage to the mechanical properties and durability of UHPC. In addition, these materials consume natural resources and emit a large amount of greenhouse gases in the production process, which does not meet the strategic requirements of sustainable development.

Sisal fiber is a kind of plant fiber extracted from sisal leaves. It is rich in resources, low in price, renewable and pollution-free, and does not endanger health (Li et al., 2020). Therefore, this paper investigated the potential of adding sisal fibers to UHPC for reducing autogenous shrinkage and preventing high-temperature spalling. In addition, a new technique of sol-gel deposition of nanosilica on the fiber surfaces was proposed to improve the bonding between sisal fiber and UHPC matrix.

2. Experimental program

2.1 Materials

P•O 42.5 ordinary Portland cement and silica fume were used as binder **materials**. Coarse quartz sand (0.21~0.38 mm) and fine quartz sand (0.11~0.21 mm) were used as aggregates. Straight steel fibers with a

length of 13 mm, a diameter of 0.2 mm, and tensile strength of 2850 MPa were used. The polycarboxylate superplasticizer was added to improve the flowability of fresh mixtures. The length and diameter of sisal fiber used in this study were 13 mm and 140~200 μm , respectively. Reagents used for sol-gel method include ethanol (AR, $\geq 99.7\%$), tetraethylorthosilicate (TEOS) (GC, $>99.0\%$) and ammonia (GR, $25.0\%\sim 28.0\%$).

2.2 Sisal fibers modification process

Sisal fiber was soaked in NaOH solution (6.0 wt%) for 4 h at room temperature. Then, washed sisal fibers with distilled water until neutral and dried (60 $^{\circ}\text{C}$) for 6 h. The process of depositing nanosilica on sisal fibers was as follows: 1) 1.5 g pre-treatment sisal fibers were firstly immersed in 30.0 ml ethanol, then 1.0 ml TEOS was slowly dropped and sonification (40 kHz) for 10 min to obtain solution A; 2) the mixed solution of 2.0 ml distilled water and 10.0 ml ethanol was quickly poured into solution A to obtain solution B; 3) the mixed solution of 5.0 ml ethanol and 2.0 ml ammonia was slowly dropped into solution B using a dropper, then sonification for 10 min to obtain solution C; 4) the solution C was continuously stirred (400 rpm) for 11 h at 40 $^{\circ}\text{C}$; 5) washed sisal fibers with distilled water for eliminating precursor, then drying (60 $^{\circ}\text{C}$) for 6 h. Fig. 1 shows the modification process.

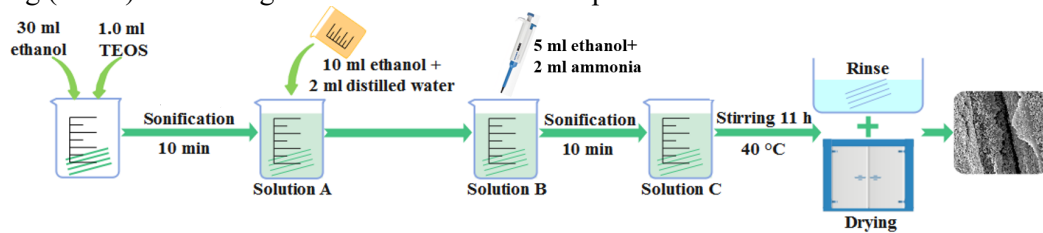


Fig. 1. Procedure of nanosilica deposited on sisal fibers

2.3 Specimen preparation

The w/b of UHPC was 0.21, and the content of cement, silica fume, coarse sand, and fine sand were 920, 258, 690, 340, and 35.3 kg/m^3 respectively according to the previous study (Ren et al., 2021). To investigate the effects of sisal fiber on autogenous shrinkage, internal relative humidity and mechanical properties of UHPC, the content of sisal fiber (SI) was 0/0.5/1.0/1.5 vol%, and the content of steel fiber was 1.0 vol%. The extra water was added to compensate for the water uptake by sisal fibers based on the water absorption of dried sisal fibers (93.24%). To investigate the effects of sisal fiber on the high-temperature spalling resistance of UHPC, 0/0.3/0.6/0.9 vol% sisal fibers were hybrid with 0/1.0/1.5/2.0 vol% steel fibers. The preparation process of UHPC mixtures was as follows: 1) mix cement, silica fume, coarse sand, and fine sand for 4 min; 2) the solution of superplasticizer and water (including extra water) was added by two times in 6 min; 3) the steel fibers and dried sisal fibers were slowly added within 6 min; 4) continue mixing for 4 min to disperse the fiber evenly.

2.4 Methods

The autogenous shrinkage of UHPC was tested by the non-contact autogenous shrinkage test device (bellows method) produced by Beijing Hangjian Huaye Technology Development Co., Ltd., as shown in Fig. 2(a). The setting time of UHPC mixture was used as the starting point of autogenous shrinkage test. The internal relative humidity was measured according to Chen et al (2021), and the schematic diagram of the internal relative humidity test setup is shown in Fig. 2(b).

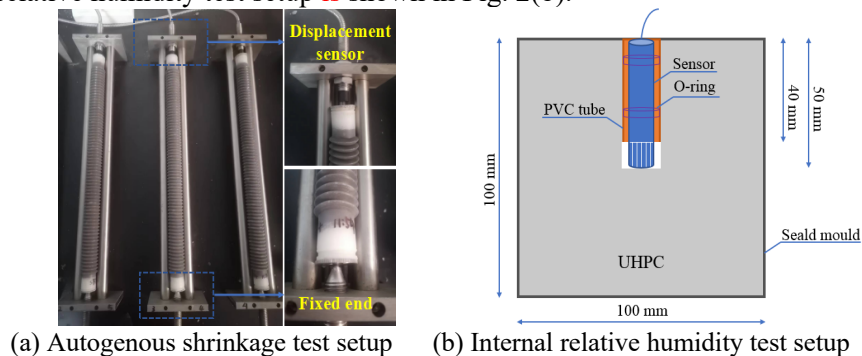


Fig. 2. Test setup of autogenous shrinkage and internal relative humidity

The flexural strength of UHPC was obtained by a three-point bending test, the loading rate and span were 0.4 mm/min and 100 mm respectively. Three specimens (40 mm×40 mm×160 mm) were tested, and the average value was reported. After the bending test, six broken specimens were used to test compressive strength of UHPC with a loading rate of 2.4 kN/s. The 800 °C high temperatures test was heated by a chamber electric furnace. The heating rate was set to 10 °C/min, and the temperature was kept at 800 °C for 2 h. Cylindrical specimens (Ø50 mm×100 mm) were used to observe the spalling degree of UHPC. Finally, it was naturally cooled to room temperature in the furnace. The bond performance between sisal fiber and UHPC matrix was measured by the fiber pullout test. The size of sample was 20 mm×20 mm×12 mm, and the embedded length of sisal fiber was 12 mm. The loading rate was set as 0.4 mm/min.

3. Experimental results

3.1 Autogenous shrinkage and internal relative humidity

The autogenous shrinkage of UHPC is shown in Fig. 3(a). The autogenous shrinkage of specimen SI0.0 developed rapidly, reaching 395 $\mu\epsilon$ at 1 d and 837 $\mu\epsilon$ at 7 d. The sisal fiber significantly reduced the autogenous shrinkage of UHPC, and the autogenous shrinkage decreased with the increase in sisal fiber content. For example, when 0.5, 1.0, and 1.5 vol% sisal fiber is added, the autogenous shrinkage of UHPC at 7 d is reduced by 23.2%, 45.3%, and 71.4% respectively. The internal relative humidity (IRH) of UHPC is shown in Fig. 3(b). It can be seen that the IRH of specimen SI0.0 reduced rapidly due to self-desiccation, and the IRH decreased to 89.9% after 7 d. With the incorporation of sisal fiber, the rate of IRH reduction was effectively reduced. For example, the IRH of specimens SI0.5, SI1.0, and SI1.5 reached 91.8%, 94.1%, and 96.3% at 7 d, indicating that sisal fiber has a good internal curing effect on UHPC.

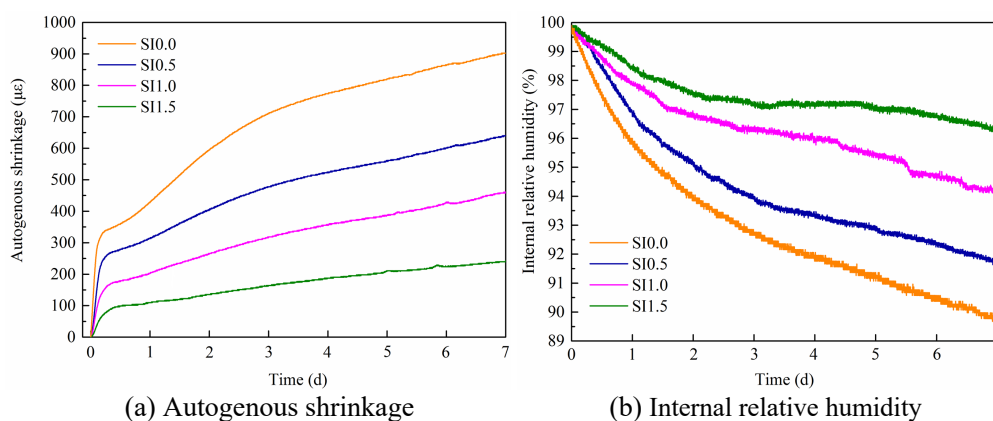


Fig. 3. Autogenous shrinkage and Internal relative humidity of UHPC

3.2 Mechanical properties

The compressive strength and flexural strength of UHPC specimens with different content of sisal fibers are listed in Table 1. The incorporation of sisal fibers reduced the compressive strength of the UHPC, and the 7 d compressive strength of the specimens decreased with the increase of sisal fibers content, but fiber content has no significant impact on the 28 d compressive strength. Moreover, the 7 d (28 d) flexural strength of specimen SI1.5 was 16.8% (18.6%) higher than specimen SI0.0. This is because there are many sisal fibers in the fracture plane, thus increasing the bridging strength of the fibers.

Table 1. Compressive and flexural strength of UHPC specimens

| Specimens | Compressive strength/MPa | | Flexural strength/MPa | |
|-----------|--------------------------|-------|-----------------------|-------|
| | 7 d | 28 d | 7 d | 28 d |
| SI0.0 | 85.8 | 110.6 | 16.93 | 21.06 |
| SI0.5 | 78.5 | 102.1 | 15.71 | 20.39 |
| SI1.0 | 76.2 | 101.5 | 19.66 | 21.49 |
| SI1.5 | 70.6 | 101.8 | 19.77 | 24.98 |

3.3 Spalling resistance

Fig. 4 shows the visual appearance of UHPC specimens after exposure to high temperatures. For specimens reinforced with steel fiber alone, as the amount of steel fiber increases, the degree of spalling was gradually reduced. The spalling occurs even though a steel fiber content of 2.0 vol% is used. The sisal fiber can effectively prevent spalling, and the addition of 0.6 vol% sisal fibers can prevent spalling.

This is **because** sisal fibers shrink at high temperatures, and tangential space was induced between sisal fibers and the matrix for vapor escape (Ren et al., 2022).

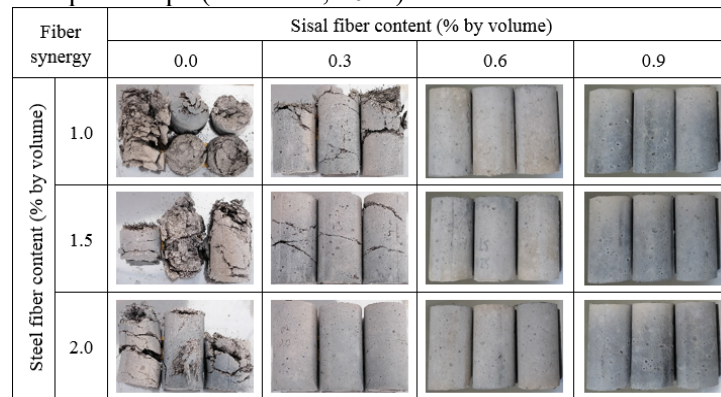


Fig. 4. The visual appearance of fiber reinforced UHPC after exposure to high temperatures

3.4 Bond performance

The bond strength and pullout energy between sisal fiber and UHPC matrix are shown in Fig. 5. The bond strength and pullout energy between sisal fiber and UHPC was effectively enhanced after modification. The bond strength and pullout energy of alkali-treated fiber were 0.85 MPa and 820 J/m², 13.3% and 15.5% higher than the value of 0.75 MPa and 710 J/m² for untreated fiber. For the sisal fiber deposited with nanosilica, the bond strength and pullout energy were 0.96 MPa and 1000 J/m², 28.0% and 40.8% higher than the untreated fiber.

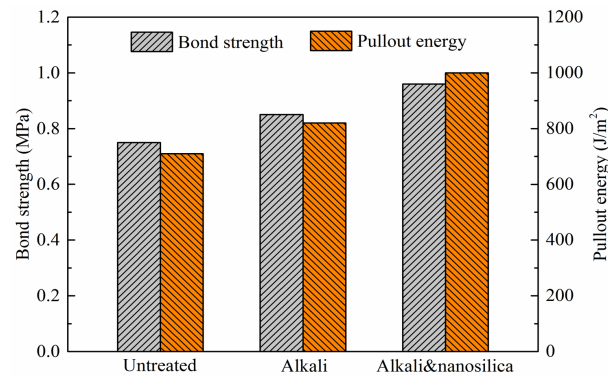


Fig. 5. Bond performance between sisal fiber and UHPC matrix

4. Conclusions

Incorporating sisal fibers can effectively reduce the autogenous shrinkage of UHPC, which is mainly attributed to the internal curing effect of sisal fibers, and sisal fiber has little influence on the 28 d compressive strength of UHPC. The spalling of UHPC at high temperatures was eliminated after the addition of 0.6 vol% sisal fibers, and this effect was more significant when steel fibers hybrid with sisal fibers. The bond strength (pullout energy) between sisal fiber and UHPC matrix was increased by 28.0% (40.8%) by nanosilica deposition compared with untreated sisal fiber.

Acknowledgements

This work was supported by the National Natural Science Foundation of China (No. U2106220), and the Key Project of Natural Science Foundation of Heilongjiang Province (No. ZD2021E007).

References

- Chen W., Li B., Wang J., Thom N. (2021) "Effects of alkali dosage and silicate modulus on autogenous shrinkage of alkali-activated slag cement paste", *Cement and Concrete Research*, 141: 106322.
- Hisseine O.A., Soliman N.A., Tolnai B., Tagnit-Hamou A. (2020) "Nano-engineered ultrahigh performance concrete for controlled autogenous shrinkage using nanocellulose", *Cement and Concrete Research*, 137: 106217.
- Li M., Pu Y., Thomas V.M., Yoo C.G., Ozcan S., Deng Y., Nelson K., Ragauskas A.J. (2020) "Recent advancements of plant-based natural fiber-reinforced composites and their applications", *Composites Part B: Engineering*, 200: 108254.
- Ren G., Yao B., Huang H., Gao X. (2021) "Influence of sisal fibers on the mechanical performance of ultra-high performance concretes", *Construction and building materials*, 286: 122958.

Ren G., Gao X., Zhang H. (2022) “Utilization of hybrid sisal and steel fibers to improve elevated temperature resistance of ultra-high performance concrete”, *Cement and concrete composites*, 130: 104555.

Acid activation of phosphate by-products in geopolymerization technology

S. En-naji^{1*,a}, S. Mabroum^{1,b}, K. Khatib^{1,c}, M. Benzaazoua^{2,d} and R. Hakkou^{1,2,e}

¹: Cadi Ayyad University (UCA), Faculty of Science and Technology, Marrakech, Morocco

²: Mohammed VI Polytechnic University (UM6P), Ben Guerir, Morocco

^a: salma.en-naji@ced.uca.ma

^b: safaa.mabroum@ced.uca.ma

^c: k.khatib@uca.ma

^d: Mostafa.benzaazoua@um6p.ma

^e: r.hakkou@uca.ac.ma

ABSTRACT

In this study, four formulations of geopolymers were elaborated using varying ratios of calcined yellow clay (a phosphate by-product) and metakaolin as aluminosilicate sources. A 5M concentration of phosphoric acid (H₃PO₄) solution was used to activate the precursors. Different analyses such as X-Ray Fluorescence (XRF), X-Ray Diffraction (XRD), Scanning Electron Microscopy (SEM), Mercury Intrusion Porosimetry (MIP), and Thermogravimetric analysis (TGA) were performed to characterize raw clays and geopolymers. In addition, investigations were also conducted into the developed geopolymers' mechanical and physical characteristics. The results indicated that by increasing the amount of calcined yellow clay, the porosity of the geopolymers increased from 25.63% to 45.56%. This increase in porosity allowed for the production of construction materials with good properties, particularly in terms of thermal insulation, as the thermal conductivity reached a value of 0.08 W/mK. The results found in this work constitute a promising approach for the sustainable management of phosphate by-products.

KEYWORDS: *Thermal insulation, waste rock, phosphate, acid activation.*

1. Introduction

Morocco is reputed to have the largest phosphate reserves in the world. Four Moroccan sedimentary basins contain two-thirds of the world's reserves (Hakkou et al., 2016). The extraction of this mineral results in significant amounts of waste, due to the deep location of the phosphate layers. Nowadays, researchers are becoming more interested in recycling these wastes for their use in various fields. The purpose is to reduce the amount of mining waste and concurrently develop eco-friendly and useful products. Studies have indicated that phosphate by-products could be used in construction applications, such as bricks, concrete, roads, and geopolymers (Mabroum et al., 2022). Geopolymers represent a class of inorganic materials synthesized by activating an aluminosilicate source with an alkaline or an acidic solution (Celerier et al., 2018). Their elaboration using phosphoric acid as an activator has facilitated the development of materials with a wide range of characteristics, including porous materials that might be successfully used for thermal insulation. Several studies have investigated the development of geopolymer materials for thermal insulation by incorporating a pore-foaming agent to create porous materials. In this context, (Natali Murri et al., 2017) have used metakaolin and biomass ash as aluminosilicate sources for the synthesis of alkali-activated geopolymers that foam when exposed to H₂O₂ and achieved a thermal conductivity of 0.07 W/mK. Additionally, silica fume and metakaolin activated by an alkaline solution were used and achieved 0.22 W/mK in thermal conductivity (Luna-Galiano et al., 2018), while the use of metakaolin with limestone activated by phosphoric acid achieved a thermal conductivity of 0.133 W/mK (Morsy et al., 2019). The aim of this study is to investigate and evaluate the production of pores in phosphate-based geopolymers, using metakaolin and calcined yellow clay as

precursors, and phosphoric acid as an activator, to develop a porous material suitable for thermal insulation.

2. Raw materials, samples preparation, and analysis methods

Geopolymers were synthesized using yellow clay (phosphate by-product) and kaolin (purchased from LOBA Chemie) as aluminosilicate sources. In table 1, the physical properties and chemical compositions of the precursors are presented. The yellow clay was crushed, ground, sieved, and calcined at 850°C (2h), while the kaolin was similarly calcined for the same duration and temperature. The calcined yellow clay was mixed with metakaolin at different mass ratios (C-YC/MK: GP1 0/100, GP2 25/75, GP3 50/50, and GP4 75/25). After activation with phosphoric acid (5M), the resulting mixtures were poured into cylindrical molds and left 24h at ambient temperature, then cured for 72h at 60°C. Finally, the samples were sealed in plastic films to avoid air contamination.

Thermal analysis (TGA) was employed to define the adequate temperature of calcination. X-Ray Diffraction analysis (XRD) and X-ray fluorescence analysis (XRF) were used to determine the mineralogical and chemical compositions of both precursors using RIKAGU diffractometer with a copper anode and XRF Epsilon 4, respectively. Mercury intrusion porosimetry (MIP) was performed to analyze the porosity of the geopolymers using Auto Pore IV 9500 V1.05. Scanning electron microscopy (SEM) was performed for microstructure examination using ESCAN VEGA3 Emission scanning electron microscope. In addition, the compressive strength and thermal conductivity were measured by using a hydraulic press and the Hot Disk TPS 1500, respectively.

Table 1: Physical properties and chemical compositions of yellow clay and kaolin

| Physical properties | Density (g/cm ³) | | | | D ₉₀ (μm) | | Specific surface (m ² /g) | | |
|-----------------------------|------------------------------|--------------------------------|-------|-------|--------------------------------|-------------------------------|--------------------------------------|------------------|------|
| Yellow clay | 2.64 | | | | 89.12 | | 63.56 | | |
| Kaolin | 2.43 | | | | 54.79 | | 28.16 | | |
| Chemical composition, wt. % | SiO ₂ | Al ₂ O ₃ | CaO | MgO | Fe ₂ O ₃ | P ₂ O ₅ | Na ₂ O | TiO ₂ | LOI |
| Yellow clay | 29.00 | 6.26 | 16.91 | 12.44 | 2.84 | 0.84 | 0.05 | 0.33 | 30.8 |
| Kaolin | 48.56 | 34.99 | 0.3 | 0.17 | 0.28 | 0.31 | 0.12 | 0.15 | 14.2 |

LOI: loss of ignition at 1000°C

3. Results and discussion

Based on thermogravimetric analysis, the calcination temperature was chosen at 850°C. The TGA graph of yellow clay (Figure 1-a) showed three peaks, representing clay dehydration, dehydroxylation of montmorillonite ((Na,Ca)_{0.3}(Al,Mg)₂Si₄O₁₀(OH)₂.n(H₂O)), and decarbonation of dolomite (CaMg(CO₃)₂) (mabroum et al, 2022). During the decarbonation process, calcite (CaCO₃) and periclase (MgO) are first formed, and then the calcite decomposes to produce lime (CaO). The XRD analysis revealed that the decarbonation of dolomite was incomplete, as traces of calcite were detected in addition to periclase and lime. In the case of kaolin, the disappearance of kaolinite (Al₂Si₂O₅(OH)₄) peaks in the XRD analysis (figure 1-e) confirmed the complete dehydroxylation of kaolinite at approximately 790°C as shown in Figure 1-b. SEM images of yellow clay and kaolin before calcination are in accordance with XRD results. The carbonates in yellow clay are presented in the form of rhombic crystals as it is shown in figure 1-c (Mabroum et al., 2022). As well as, the presence of the laminated structure in kaolin characterizing the presence of kaolinite (figure 1-d). Figure 2 illustrates a cross-section of the developed geopolymers at 28 days after the day of activation. Figure 3-a displays the XRD analysis of the four geopolymers. The presence of quartz after geopolymerization reaction has been distinguished in all geopolymers indicating its resistance in an acidic environment. For GP1, which contains 100% metakaolin, the formation of aluminum phosphate (AlPO₄), as well as ALPH (AlH₃P₃O₁₀.2H₂O) was observed. Geopolymers GP2, GP3, and GP4, containing 25%, 50%, and 75% of calcined yellow clay respectively, also exhibited the presence of AlPO₄ phase, along with the formation of other new phases. In GP2, monetite (CaHPO₄) was distinguished as a result of the reaction between CaO and H₃PO₄. Newberyite (Mg(PO₃OH).3H₂O) was formed in GP3 through the reaction between MgO and H₃PO₄ in addition to the formation of monetite, Ca₈P₆O₂₈ and hydroxylwagnerite (Mg₂PO₄OH). In GP4, which contains 75% of calcined yellow clay, a reaction between lime and phosphoric acid led to the brushite formation (CaHPO₄.2(H₂O)), along with the

formation of other phases such as newberyite and monetite. It should be noted that the dissolution of lime and periclase in phosphoric acid, which is an exothermic reaction, may contribute to porosity formation (figure 2). This is in agreement with the study of (Walling and Provis, 2016) which states that highly basic oxides such as CaO and MgO react violently with phosphoric acid, resulting in pore formation. SEM analysis was performed for all the samples and the micrographs are displayed in figure 3-b.

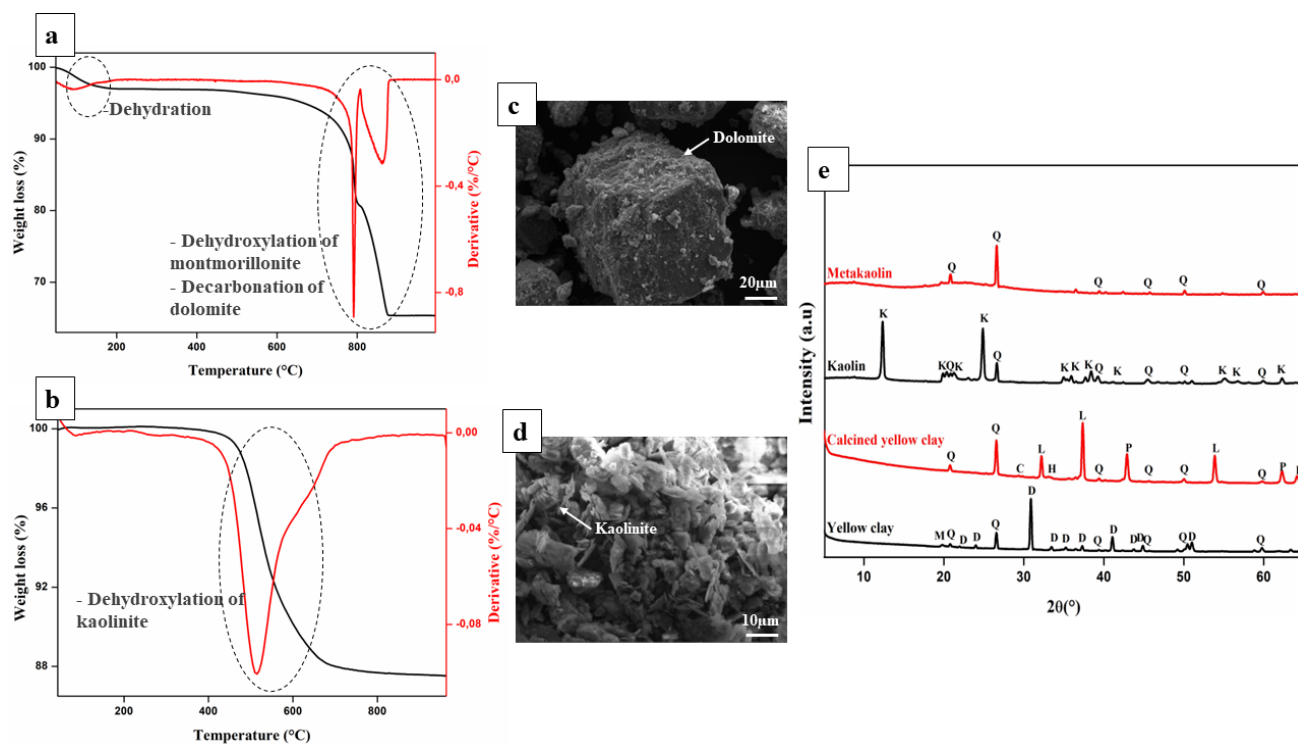


Figure 1: TGA of yellow clay (a) and kaolin (b); SEM analysis of yellow clay (c) and kaolin (d); (e) XRD analysis of yellow clay and kaolin before and after calcination (Q: quartz, K: kaolinite, M: montmorillonite, D: dolomite, H: hematite, L: lime, P: periclase, C: calcite).

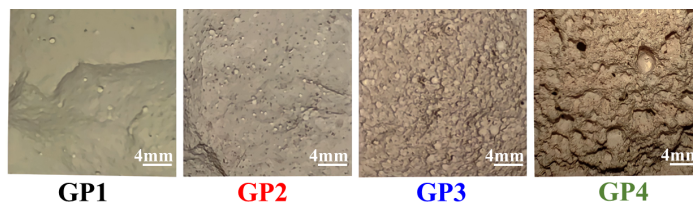


Figure 2: Cross-sectional view of the elaborated geopolymers

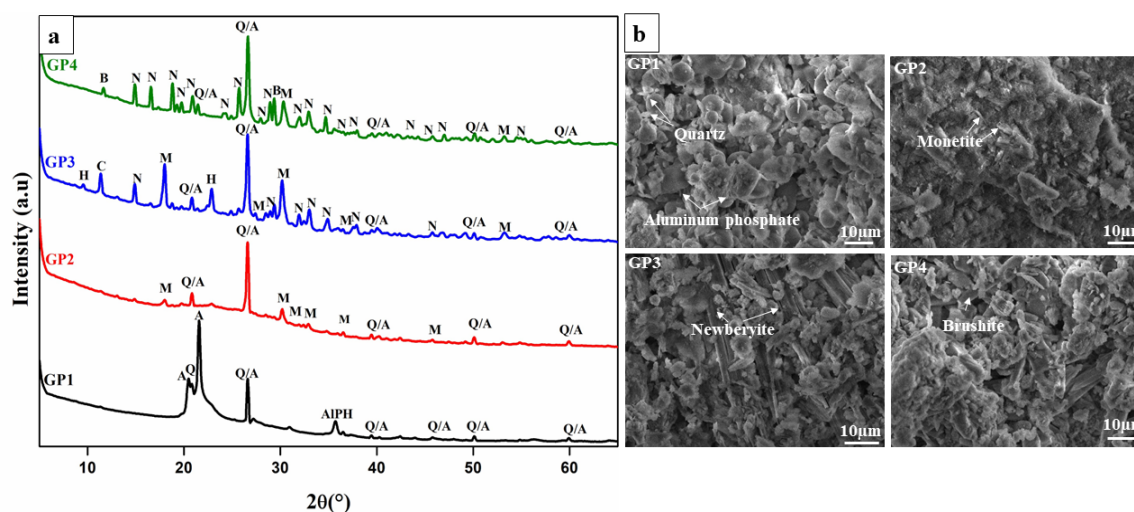


Figure 3: (a) XRD analysis (A: Aluminum phosphate, M: Monetite, H: hydroxylwagnerite, C: Ca₈P₆O₂₈, N: Newberyite, B: Brushite, Q: Quartz, ALPH: AlH₃P₃O₁₀·2H₂O) and (b) SEM analysis of the elaborated geopolymers.

In Table 2, the mechanical strength, porosity, density, and thermal conductivity measurements are presented for GP1, GP2, GP3 and GP4. It is obvious that the addition of calcined yellow clay had a notable effect on geopolymers' properties. Specifically, it resulted in a decrease in density and an increase in porosity. As abovementioned, the carbonates were not completely decomposed. The increase in porosity is due to residual carbonates (CaCO_3), reacting with phosphoric acid to produce bubbles from the generated CO_2 gas, resulting in porous materials. It was also mentioned before that the dissolution of CaO and MgO in phosphoric acid may also contribute to porosity formation. Moreover, there was a significant reduction in compressive strength (UCS) from 7.11 MPa for GP1 to 0.41 MPa for GP4 due to the generated porosity, and the thermal conductivity values also decreased from 0.14 W/mK (GP1) to 0.08 W/mK (GP4). The values obtained for compressive strength align with those found in the literature (Natali Murri et al., 2017). In addition, the thermal conductivity values of the developed geopolymers, whether they contain only metakaolin (GP1) or phosphate waste (GP2, GP3, and GP4), indicate their good thermal insulation performance. Therefore, acid-based geopolymers, based on phosphate by-products, could potentially replace the use of pore foaming agents generally used during the synthesis of alkaline-based geopolymers. This is due to the fact that when the aluminosilicate material is dissolved in a phosphoric acid solution, pores are immediately created, making them promising materials for thermal insulation applications (Natali Murri et al. 2017; Hung et al. 2013; Bai et al. 2017).

Table 2: Physical and mechanical characteristics of geopolymers

| Geopolymers | GP1 | GP2 | GP3 | GP4 |
|------------------------------------|------------|------------|------------|------------|
| Compositions C-YC/MK | 0/100 | 25/75 | 50/50 | 75/25 |
| Density (g/mL) | 1.31 | 1.05 | 0.85 | 0.46 |
| Porosity (%) | 25.63 | 32.77 | 37.22 | 45.56 |
| UCS (MPa) | 7.11 | 4.95 | 2.24 | 0.41 |
| Thermal conductivity (W/mK) | 0.14 | 0.12 | 0.08 | 0.08 |

4. Conclusions

In this study, geopolymers were synthesized by acid activation of metakaolin and calcined yellow clay with varying proportions. The addition of calcined yellow clay significantly increased porosity, resulting in a reduction of thermal conductivity from 0.14 W/mK to 0.08 W/mK, indicating its effectiveness as a foaming agent. Furthermore, even the GP1 sample containing only metakaolin showed promising insulation properties with low thermal conductivity compared to similar materials reported in the literature. In general, these materials have potential for reducing mining waste and producing eco-friendly construction materials.

Acknowledgements

We would like to extend our gratitude to the Moroccan Ministry of Higher Education, Scientific Research, and Innovation, as well as the OCP Foundation, for their funding and support through the APRD research Program (Eco-MAT 21-24 grant). Furthermore, we express our sincere appreciation to the collaborators from the Eduardo Torroja Institute for their valuable contributions to the ICOOP project 2022 (ref COOPA22026).

References

- Celerier, H., Jouin, J., Mathivet, V., Tessier-Doyen, N., Rossignol, S., 2018. Composition and properties of phosphoric acid-based geopolymers. *Journal of Non-Crystalline Solids* 493, 94–98. <https://doi.org/10.1016/j.jnoncrysol.2018.04.044>
- Luna-Galiano, Y., Leiva, C., Arenas, C., Fernández-Pereira, C., 2018. Fly ash based geopolymeric foams using silica fume as pore generation agent. Physical, mechanical and acoustic properties. *Journal of Non-Crystalline Solids* 500, 196–204. <https://doi.org/10.1016/j.jnoncrysol.2018.07.069>
- Mabroum, S., Taha, Y., Benzaazoua, M., Hakkou, R., 2022. Recycling of marls from phosphate by-products to produce alkali-activated geopolymers. *Materials Today: Proceedings, International Conference on Phosphates (ICP): Fundamentals, Processes and Technologies (ICP2020)* 51, 1931–1936. <https://doi.org/10.1016/j.matpr.2021.03.206>

- Morsy, M.S., Rashad, A.M., Shoukry, H., Mokhtar, M.M., 2019. Potential use of limestone in metakaolin-based geopolymer activated with H_3PO_4 for thermal insulation. *Construction and Building Materials* 229, 117088. <https://doi.org/10.1016/j.conbuildmat.2019.117088>
- Natali Murri, A., Medri, V., Papa, E., Laghi, L., Mingazzini, C., Landi, E., 2017. Porous Geopolymer Insulating Core from a Metakaolin/Biomass Ash Composite. *Environments* 4, 86. <https://doi.org/10.3390/environments4040086>
- Walling, S.A., Provis, J.L., 2016. Magnesia-Based Cements: A Journey of 150 Years, and Cements for the Future? *Chem. Rev.* 116, 4170–4204. <https://doi.org/10.1021/acs.chemrev.5b00463>

Sulfate Resistance of Mortar Containing Low-Grade Calcined Clay

Y. Wang¹, and H. Du^{2*}

¹ National University of Singapore, Singapore, Singapore

Email: wangyue.wy@u.nus.edu

² National University of Singapore, Singapore, Singapore

Email: ceedhj@nus.edu.sg

ABSTRACT

Marine clay, a low-grade kaolinitic clay widely existing in coastal areas, can be used to partially replace cement in concrete after calcination to reduce construction waste and embodied carbon in concrete. This paper investigates the sulfate resistance of mortars with 20 wt% marine clay replacement ratios and varying kaolin contents. These mixes are exposed to 50 g/L Na₂SO₄ solution after 28-day curing in saturated lime water. Marine clay from the construction sites is calcinated at 700°C to ensure pozzolanic reactivity during hydration. Thermogravimetric analysis and X-ray diffraction are conducted to calculate the content of kaolinite and components of clay minerals in marine clay, respectively. The progressive deterioration of compressive strength and the relative length change of mortars are evaluated through compressive strength tests and length change apparatus. Results from this study could estimate the effects of marine clay on mortar sulfate resistance and obtain an optimal cement replacement level with no significant strength reduction and length change.

KEYWORDS: *calcined marine clay, sulfate resistance, compressive strength, length change, low-grade kaolinite*

1. Introduction

Since the 1950s, researchers in many countries have begun exploring geotechnical characteristics of marine clay (Bjerrum, L., 1954; Ohtsubo et al., 1995). The study of marine clay in Singapore could be traced back to 1977, and Tan and Lee (1977) investigated the geological nature and distribution of the marine clay in Singapore. Currently, there are two primary methods for using marine clay in concrete production. One is treated marine clay as concrete aggregates, such as lightweight aggregate manufacture (Laursen et al., 2006). Moreover, Tay et al. (2003) examined the potential use of sludge-marine clay mixtures as concrete aggregates. The other is to replace cement with marine clay, such as Du and Pang (2018). 30% cement replaced by marine clay experiments were conducted and the result showed a good activity of strength. Moreover, similar results were demonstrated in their subsequent experiments (Dang et al., 2020).

Sulfate attack poses a significant threat to the long-term performance of concrete structures as it is one of the most aggressive environmental deteriorations because the sulfate attack can cause expansion and cracking (Brown, 1981). Al-Akhras (2006) studied the effect of metakaolin replacing cement on concrete durability against sulfate attack. His results indicated that incorporating metakaolin as a cement replacement could enhance the sulfate resistance of concrete, and the sulfate resistance rose with increased replacement levels which were also drawn by Cordoba et al. (2021). Mehta (1983) established that sulfate attack could form gypsum and ettringite caused by the reaction between sulfate ions and calcium hydroxide as well as calcium aluminate hydrate. The gypsum and ettringite formed due to sulfate attack significantly expanding about 2.2 times than the initial reactants (Hooton, 1993). Furthermore, Hooton (1993) provided evidence that the degradation due to sulfate attack is partially caused by the degradation of calcium compounds, which reduced the stiffness of the C-S-H gel and deteriorated the cement paste. This process leads to loss of C-S-H gel stiffness and overall deterioration of the cement paste. Sulfate resistance of concrete with blended cement containing different calcined pozzolans has been compared recently (Cordoba et al., 2018; Trümer et al., 2019), and many researchers investigated calcined clay as ternary cement with limestone (Shi et al., 2019; Huang et al., 2021) or as based geopolymer (Caselles et al., 2023). Rossetti et al. (2021) estimate the sulfate performance of cement replaced by two different illitic calcined clays. The superior sulfate resistance results from microscale and macroscale proved calcined clay can refine pore structure, increase strength, and reduce available CH.

Although replacing marine clay with cement has developed rapidly in recent years, previous studies mainly focus on the mortar mechanical performance instead of durability, especially in sulfate attacks.

2. Experimental

2.1 Materials

The materials required are mainly to prepare mortar components, including cement, sand, calcined marine clay (MC) treated at 700°C (Du and Pang, 2018), and calcined kaolin clay (MK) treated at 800°C (Al-Akhras, 2006). MC samples were sourced from a local construction site at Ulu Pandan, Singapore. The raw samples were dried in a 105°C oven for 24h and broken into small lumps by jaw crusher. Then samples were ground by ball-mill for 180 min and heated in a furnace from room temperature to 700°C at a rate of 10°C/min with 120 min holding (Dang et al., 2020). Fig. 1 presents the recycling process of marine clay. CEM I 52.5N cement, MK and natural river sand (through 4.75mm sieve) were used. The sulfate corrosion solution was used the concentration of 352 moles of sodium sulfate (Na_2SO_4) per m^3 (50g/L).

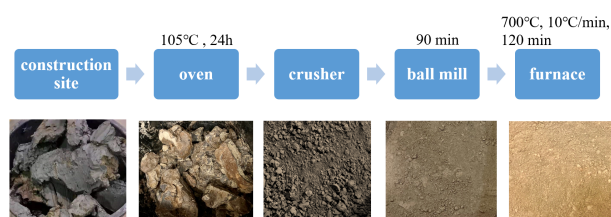


Fig. 1. Recycle process of marine clay

2.2 Characterization methods

Thermogravimetric analysis (TGA) was conducted in N_2 environment with the temperature from 30°C to 950°C at a rate of 10°C/min using Discovery TGA. A Bruker D8 X-ray Diffractometer (XRD) was used to determine the crystal patterns of marine clay and kaolin clay, and quantitative phase analysis (QPA) through internal standard method was used to determine phase contents of cement and clays.

2.3 Pozzolanic reactivity measurement

The water-to-binder (w/b) ratio of 0.50 was used for the paste and mortar. Mix proportion for the mortar was water: binder: sand = 0.5: 1: 2.75. Calcined marine clay replaced cement at 20% level. The compressive strength of mortar was tested on 50mm cubes as per ASTM C109 (ASTM C109, 2021) at 28 days. The length change of bar was measured on 25mm×25mm×285mm as per ASTM C1012 (ASTM C1012, 2019), at 4, 5, 7, 8, 9, 12 and 13 weeks. After 24 hours, demoulding specimens were placed in saturated lime water ($\text{Ca}(\text{OH})_2$) for 28 days. Then half of samples were transferred into Na_2SO_4 solution, and the other half were remained in $\text{Ca}(\text{OH})_2$ solution for reference.

3. Results and discussion

3.1 Material characterization

Refer to research by Fernandez Lopez (2009), the kaolinite content was used tangent method to calculate through TGA curve, and the kaolinite content could be calculated through the equation: $\text{Al}_2\text{SiO}_5(\text{OH})_4 \rightarrow \text{Al}_2\text{Si}_2\text{O}_7 + 2\text{H}_2\text{O}$. TGA curves for marine clay are shown in Fig. 2, and the kaolinite content can be investigated to be about 34.94%. By contrast, there is no significant change for 700°C calcinated marine clay, indicating that the calcination process can be deemed as complete. Similar trends are showed in MK (30°C and 800°C), and the content of kaolinite is estimated about 80.02%.

Fig. 3 illustrates that before calcination (30°C), peaks of kaolinite ($2\theta = 12.44^\circ$ and 24.96°) can be clearly noticed. After calcination (700°C), peaks of kaolinite decrease. However, peaks of illite ($2\theta = 17.97^\circ$ and 19.90°) and quartz ($2\theta = 21.00^\circ$, 26.76° , 36.70° and 39.58°) remain unaltered even when the temperature reaches 700°C. Similar trends are showed in kaolin clay. The amounts of various crystalline phases through Rietveld analysis are also listed in Table 1. Compared with XRD QPA results, kaolinite contents

are overestimated in TGA because the mass loss curve of illite overlaps that of kaolinite and cannot be distinguished.

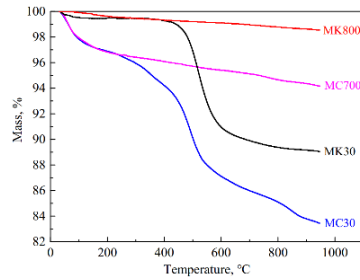


Fig. 2. TGA curves of marine clay and kaolin clay

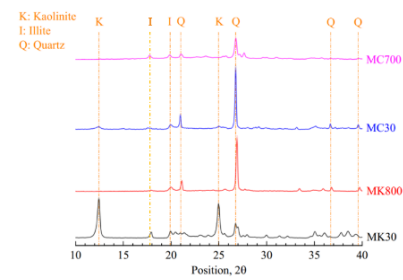


Fig. 3. XRD patterns of marine clay and kaolin clay

Table 1 QPA results of cement and clays

| Phases (wt.%) | C ₃ S | C ₂ S | C ₃ A | C ₄ AF | Kaolinite | Illite | Quartz | Amorphous |
|---------------|------------------|------------------|------------------|-------------------|-----------|--------|--------|-----------|
| Cement | 69.4 | 8.7 | 6.2 | 8.2 | / | / | / | / |
| MC(30°C) | / | / | / | / | 21.8 | 14.5 | 37.9 | 25.8 |
| MC(700°C) | / | / | / | / | 0 | 12.8 | 35.8 | 51.4 |
| MK(30°C) | / | / | / | / | 62.5 | 33.7 | / | 3.9 |
| MK(700°C) | / | / | / | / | 0 | 30.6 | / | 69.4 |

3.3 Compressive strength

Table 2 shows 28-day compressive strengths and strength activity indices (SAI) of 20% replace-level mortar cubes cured in saturated water. The results show that the ordinary Portland cement (OPC) group has highest compressive strength, but the other three groups replaced by clay are lower than OPC.

Table 2 Compressive strength of Mortar at 28 days

| Group | Compressive strength, MPa | Standard deviation, MPa | SAI |
|-------------|---------------------------|-------------------------|------|
| OPC | 49.09 | 1.15 | / |
| 20%MC | 43.40 | 0.62 | 0.88 |
| 20%MK | 44.33 | 0.88 | 0.90 |
| 10%MC+10%MK | 44.49 | 0.93 | 0.91 |

3.4 Length change

Fig. 4 shows the length strains of mortar bars after immersion in Na₂SO₄ solution in different periods. The lengths of bar have no obvious change within eight weeks, but they change obviously from the eighth week. Compared with OPC, replacing with MC or MK both reduce the length micro-strain value, and the higher the kaolin content, the smaller the change in length. This also proves the positive effect of MC on sulfate corrosion resistance of mortar.

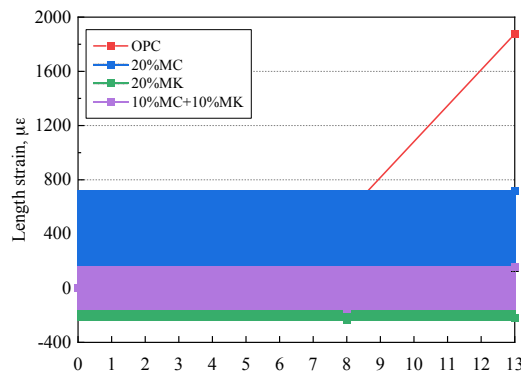


Fig. 4. Length strain during 91 days' immersion period in Na_2SO_4 solution

4. Conclusions

The main conclusions of this study are as follows,

- 1) Compared with OPC, replacing cement with MC decreases the early-age compressive strength of mortar cubes.
- 2) The replacement of MC reduces the volume expansion degrees of mortar bars, decreases the generation of cracks and minimizes the degrees of bending. The performance of sulfate resistance is most obviously improved with 20% MC replacing.

References

- Al-Akhras, N.M., (2006). Durability of metakaolin to sulfate attack. *Cement and Concrete Research* 36 (9), 1727–1734.
- ASTM C1012/C1012M-18a, 2019. Standard Test Method for Length Change of Hydraulic-Cement Mortars Exposed to a Sulfate Solution. ASTM International.
- ASTM C109/C109M-20b, 2021. Standard Test Method for Compressive Strength of Hydraulic Cement Mortars (Using 2-in. Or [50-mm] Cube Specimens). ASTM International.
- Bjerrum, L. (1954). Geotechnical properties of Norwegian marine clays. *Geotechnique*, 4(2), 49-69.
- Brown, P. W. (1981). An evaluation of the sulfate resistance of cements in a controlled environment. *Cement and Concrete Research*, 11(5-6), 719-727.
- Caselles, L. D., Balsamo, B., Benavent, V., Trincal, V., Lahalle, H., Patapy, C., ... & Cyr, M. (2023). Behavior of calcined clay based geopolymers under sulfuric acid attack: Meta-illite and metakaolin. *Construction and Building Materials*, 363, 129889.
- Choa, V., Chu, J., Bawajee, R., Bo, M.W. and Arulrajah, A.(1997) . The strength and consolidation behaviour of Singapore marine clay at Changi. *Proceedings of the 12th Southeast Asian Geotechnical Conference*, Kuala Lumpur, Malaysia. Vol. 1, 81-85.
- Cordoba, G., & Irassar, E. F. (2021). Sulfate performance of calcined illitic shales. *Construction and Building Materials*, 291, 123215.
- Cordoba, G., Rossetti, A., Falcone, D., & Irassar, E. F. (2018). Sulfate and alkali-silica performance of blended cements containing illitic calcined clays. In *Calcined Clays for Sustainable Concrete: Proceedings of the 2nd International Conference on Calcined Clays for Sustainable Concrete* (pp. 117-123). Springer Netherlands.
- Dang, J., Du, H., & Dai Pang, S. (2020). Hydration, strength and microstructure evaluation of eco-friendly mortar containing waste marine clay. *Journal of Cleaner Production*, 272.
- Du, H., & Dai Pang, S. (2018). Value-added utilization of marine clay as cement replacement for sustainable concrete production. *Journal of Cleaner Production*, 198, 867-873.
- Fernandez Lopez, R. (2009). Calcined clayey soils as a potential replacement for cement in developing countries (No. THESIS). EPFL.
- Hooton, R. D. (1993). Influence of silica fume replacement of cement on physical properties and resistance to sulfate attack, freezing and thawing, and alkali-silica reactivity. *Materials Journal*, 90(2), 143-151.
- Huang, H., Li, X., Avet, F., Hanpongpan, W., & Scrivener, K. (2021). Strength-promoting mechanism of alkanolamines on limestone-calcined clay cement and the role of sulfate. *Cement and Concrete Research*, 147, 106527.
- Laursen, K., White, T.J., Cresswell, D.J.F., Wainwright, P.J., Barton, J.R., (2006). Recycling of an industrial sludge and marine clay as light-weight aggregates. *J. Environ. Manag.* 80, 208-213.
- Mehta, P. K. (1983). Mechanism of sulfate attack on portland cement concrete—Another look. *Cement and Concrete Research*, 13(3), 401-406.
- Ohtsubo, M., Egashira, K., & Kashima, K. (1995). Depositional and post-depositional geochemistry, and its correlation with the geotechnical properties of marine clays in Ariake Bay, Japan. *Geotechnique*, 45(3), 509-523.

- Rossetti, A., Ikumi, T., Segura, I., & Irassar, E. F. (2021). Sulfate performance of blended cements (limestone and illite calcined clay) exposed to aggressive environment after casting. *Cement and Concrete Research*, 147, 106495.
- Shi, Z., Ferreiro, S., Lothenbach, B., Geiker, M. R., Kunther, W., Kaufmann, J., ... & Skibsted, J. (2019). Sulfate resistance of calcined clay–Limestone–Portland cements. *Cement and Concrete Research*, 116, 238-251.
- Tan, S. B. and Lee, K. W. (1977). Engineering geology of the marine member of the Kallang Formation in Singapore. *Proceedings of the International Symposium on Soft Clays*, Bangkok.
- Tay, J. H., Hong, S. Y., Show, K. Y., Chien, C. Y., (2003). Manufacturing artificial aggregates from industrial sludge and marine clay with addition of sodium salt. *Water science and technology*, 47(1), 173-178.
- Trümer, A., Ludwig, H. M., Schellhorn, M., & Diedel, R. (2019). Effect of a calcined Westerwald bentonite as supplementary cementitious material on the long-term performance of concrete. *Applied Clay Science*, 168, 36-42.

The role of C₁₂A₇, α_H-C₂S and dehydrated amorphous nesosilicate in rehydration of recycled cement

Lei Xu¹, Junjie Wang^{2*}, Kefei Li³, Zhe Li⁴, and Le Li⁵

Department of Civil Engineering, Tsinghua University, Beijing, 100084, P.R. China

¹ Email: xl21@mails.tsinghua.edu.cn ² Email: junjiawang@tsinghua.edu.cn (corresponding author)

³ Email: likefei@tsinghua.edu.cn ⁴ Email: lizhequt@163.com ⁵ Email: liniannian15@163.com

ABSTRACT

Waste hardened cement paste can be recycled and used as valuable precursor material to produce recycled cement (RC) with low energy consumption and CO₂ emissions through thermal activation. This paper intends to contribute to a better knowledge of the role of C₁₂A₇, α_H-C₂S and dehydrated amorphous nesosilicate in rehydration of RC and investigated the contributions of different dehydration phases on the reactivity of the RC through thermogravimetry, quantitative X-ray diffraction, nitrogen adsorption, isothermal calorimetry and scanning electron microscopy. The results show that C₁₂A₇, as the main dehydrated aluminum phase in the RC, showed very high reactivity at the beginning of the rehydration, generating needle-like AFt, which gradually transformed into layered AFm (mainly hemicarboaluminate and monocarboaluminate due to the presence of carbonates) as the reaction continued. α_H-C₂S, the most important part of the dehydrated phase, played a decisive role in the strength of the RC paste. The dehydrated amorphous nesosilicate, as the main reactant in the accelerated phase of the rehydration process, mainly affected the early age strength of reclaimed cement paste.

KEYWORDS: *rehydration, recycled cement, dehydrated amorphous nesosilicate, α_H-C₂S, C₁₂A₇*

1. Introduction

Recycled cement (RC) is an alternative binder with a low CO₂ footprint, which can be produced from waste cement paste through thermal treatment. When waste cement paste undergoes thermal activation, with the increase of temperature, it mainly involves dehydration reactions of gypsum, AFt, AFm, C-S-H, dehydroxylation reaction of calcium hydroxide and decarburization reaction of calcium carbonate (Xu et al (2023b)). The thermal-activated RC also has a very complex chemical composition, including partially dehydrated phases, residual hydration products, and unhydrated clinker. Compared with OPC, thermal-activated RC usually contains a higher amount of CaO and many polycrystalline C₂S, while lacks C₃S (Xu et al (2023b)). In the process of thermal activation, the composition and quantity of the dehydrated phases of the corresponding RC precursor are intrinsically related to the thermal activation temperature, which further determines the phase compositions of the rehydrated thermal-activated RC paste. In addition, RC usually has a high water demand (Bogas et al (2020)), short setting time, and high heat release (Wang et al (2018), Xu et al (2023a)), but the total heat release of rehydration is generally lower than that of OPC. However, as a low-CO₂ binder and an effective recycling material, its behaviour is difficult to predict due to the complex compositions. The reactions involved and the explanation of the exothermic rate are still controversial. This uncertainty seems to indicate that different thermal activation conditions might lead to different reactions between RC particles and water. This paper intends to contribute to a better knowledge of the role and contributions of C₁₂A₇, α_H-C₂S and dehydrated amorphous nesosilicate in rehydration mechanisms and the reactivity of RC.

2. Materials, compositions, test methods and characterization techniques

Waste cement paste with an age of over 120 days was first prepared, to be used as precursor throughout all further experiments. OPC complying with GB/T 175-2007 was used, and the water-binder ratio is 0.45.

The specific chemical properties and preparation process were based on our previous work (Xu et al (2023b)). The precursor was grounded into particles $< 150 \mu\text{m}$ and subsequently heated in a furnace at target temperatures of 450, 550, 650, 750 and 850 $^{\circ}\text{C}$ with a heating rate of 10 $^{\circ}\text{C}/\text{min}$ and a duration at target temperature of 3 hours, followed by cooling inside the oven until room temperature was reached. The obtained thermal-activated RC was used to produce RC paste with a same w/b ratio 0.65, labelled from RC450-850.

A set of characterization techniques containing isothermal calorimetry, scanning electron microscopy (SEM), thermogravimetry (TG), quantitative X-ray diffraction (QXRD) and mechanical tests was used to investigate the dehydration of the RC precursor and rehydration of RC systematically. In addition, N_2 adsorption test was carried out using an automated surface area analyser TriStarII 3020 instrument (Micromeritics, U.S.A), and the SSA was determined based on the amount of adsorbed N_2 according to the BET methods (Lowell et al (2005), Mantellato et al (2015)).

3. Results and discussions

3.1 Characterization of RC

The results of PSD and BET surface areas of RC450-RC850 are presented in Fig. 1. Thermal activation significantly increased the SSA of RC450-RC850, while it could be found that the SSA gradually decreased above 650 $^{\circ}\text{C}$, reflecting that the adhesion between particles could promote possible bonding and crystallization during the calcination process. Since SSA is highly sensitive to the morphology of the dehydrated C-S-H phases, it suggests that during thermal activation between 450 and 850 $^{\circ}\text{C}$, C-S-H phases were gradually undergoing substantial changes.

QXRD results in Fig. 1 show that C-S-H did not decompose to C_2S at 450 $^{\circ}\text{C}$, and C_2S polycrystalline crystal appeared at 550 $^{\circ}\text{C}$, while the amount of C_2S was small and there were many amorphous substances. The content of dehydrated amorphous C-S-H and amorphous nesosilicate in RC550 was higher than that in RC650-850. When the temperature rose to 650 $^{\circ}\text{C}$, C_{12}A_7 began to appear. The content of CaO was increasing over 650 $^{\circ}\text{C}$, especially up to 850 $^{\circ}\text{C}$ with a content exceeding 10%. The existence of $\text{Ca}(\text{OH})_2$ is due to that CaO reabsorbed water during furnace cooling and storage. $\text{Ca}(\text{OH})_2$ from the precursor was decomposed incompletely below 550 $^{\circ}\text{C}$ but completely over 650 $^{\circ}\text{C}$, and the amount of $\text{Ca}(\text{OH})_2$ in RC650-850 is significantly reduced. The amount of calcium carbonate was significantly decreased from 750 $^{\circ}\text{C}$ to 850 $^{\circ}\text{C}$, but there remained a little in RC850, which might be caused by the carbonization of CaO and $\text{Ca}(\text{OH})_2$ during cooling and storage. It is noteworthy that the content of α' - C_2S increased first and then decreased, and the peak content was obtained at RC750. The amount of amorphous continued to decrease with the increase of treating temperature.

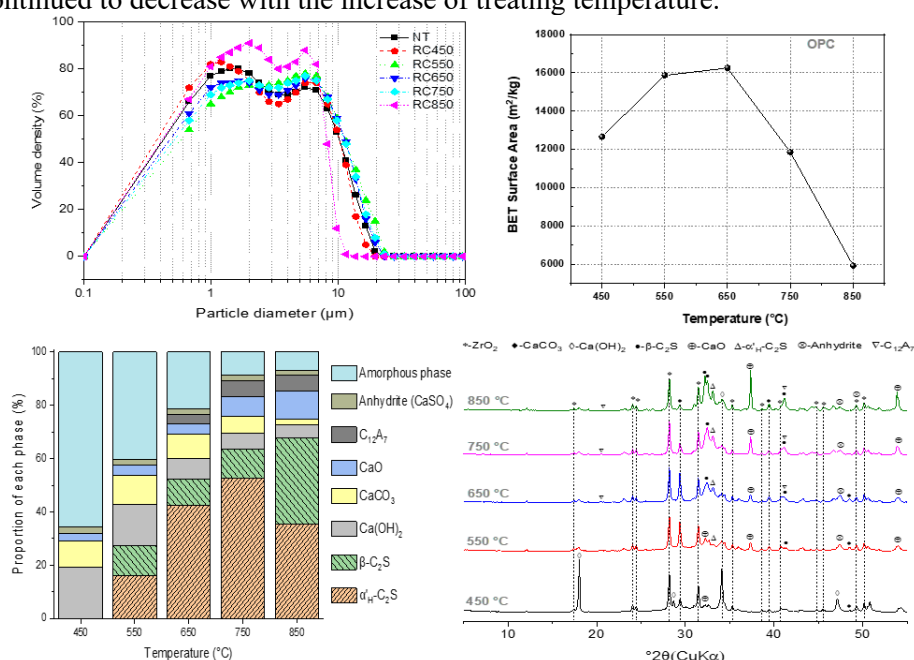


Fig. 1. PSD, BET S. A. and QXRD results of RC.

3.2 Rehydration of RC pastes

The results of the compressive strength (3d, 7d, 28d and 90d) of the precursor and RC pastes are shown in Fig. 3a. The results of mechanical properties are consistent with the rehydration kinetics of dehydrated phases. Because precursor was only partially dehydrated and not entirely depolymerized at 450 °C, relatively poor mechanical strength was obtained. Rehydration of RC450 produced mostly internal hydration products, but with no effective connections between these internal hydration products (Fig. 4), which affected the development of overall cohesion, thus affecting the mechanical strength of RC paste. The temperature over 550 °C led to a progressive depolymerization of the C-S-H, which was expected to display a fast rehydration capacity. The compressive strength of RC pastes varied with different treatment temperatures, but it could be concluded that the compressive strength was positively correlated with the content of $\alpha'_H\text{-C}_2\text{S}$ from the QXRD results, that was, the more $\alpha'_H\text{-C}_2\text{S}$, the higher the compressive strength of RC pastes, indicating that $\alpha'_H\text{-C}_2\text{S}$, the most important part of the dehydrated phase, played a decisive role in the strength development of the RC paste.

The results of rehydration heat rate and total heat of the OPC and RC obtained from different target temperatures are shown in Figs. 3b-3c. It has been found that at the initial stage of hydrolysis, the heat flow of RC was over 10 times that of the original precursor. The high specific surface areas of the RC particles, which were roughly 10 times higher than those of the OPC, and the high content of calcium aluminates (mostly C_{12}A_7) and CaO in the RC, were all associated with the high heat flow peak. C_{12}A_7 , as the main dehydrated aluminum phase in the RC, showed a very high reactivity at the beginning of the rehydration, generating needle-like AFt, which gradually transformed into layered AFm (mainly hemicarboaluminate and monocarboaluminate due to the presence of carbonates) as the reaction continued (Xu et al (2023a), Xu et al (2023b)). Besides, Juilland et al. attributed the heat flow peak to the crystallographic defects of the silicates (mainly $\alpha'_H\text{-C}_2\text{S}$ and $\beta\text{-C}_2\text{S}$) which increased the dissolution rate (Juilland et al (2010)). They inferred that rehydration occurred through a simple wetting mechanism: the adsorption of water in dehydrated phases and the reformation of original phases. However, in this study, in addition to the initial wetting heat peak, there is an additional heat flow peak from rehydration after about 8 hours, similar to the induction and acceleration periods of OPC hydration, which can be considered that the rehydration mechanism of RC is not only due to the wetting mechanism but also to the dissolution-precipitation mechanisms. However, different from OPC, the reactants causing this heat flow peak was not the polycrystalline C_2S , but the dehydrated amorphous nesosilicates. With the increase of target temperature from 550 °C to 750 °C, the content of the dehydrated amorphous phase decreased, the content of polymorphic C_2S increased, and the peak of this heat flow was consistent with the content of amorphous phases.

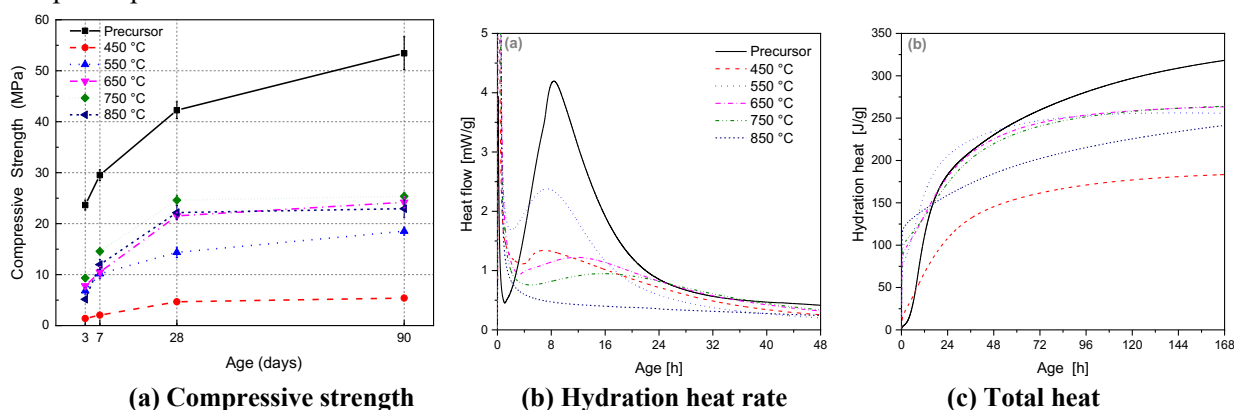


Fig. 2. Hydration heat rate, total heat and compressive strength of OPC and RC.

The micromorphology images of RC pastes at 28 days are shown in Fig. 3. All RC pastes presented clear evidence of rehydration, displaying common hydration products that include needles-like ettringite, plate-like AFm, C-S-H gel and CH hexagonal platelets. Among them, AFt and AFm were obtained by rehydration of C_{12}A_7 , and $\alpha'_H\text{-C}_2\text{S}$ had relatively high activity, and was rehydrated to form C-S-H gel and $\text{Ca}(\text{OH})_2$. The rehydration of dehydrated amorphous C-S-H gel in the RC450 was associated with the regeneration of internal hydration products, but the clusters of gel were not continuous, lapping butt by AFt and AFm (external hydration products), which resulted in a loose structure with a high porosity and

poor consolidation. The weak connections between the layers may also be the source of microcracks when the RC paste was subjected to stresses. Unlike normal C-S-H gel, it was obvious that this dispersed C-S-H gel could not contribute significantly to its strength, which is consistent with the low mechanical strength of RC 450 paste. RC650-RC850 pastes were denser than RC 450-550 pastes and the regenerated C-S-H in these pastes had a variety of morphologies. The CH crystals same as in OPC paste were also regenerated and this should come from the initial hydration of CaO and active $\alpha'_H\text{-C}_2\text{S}$.

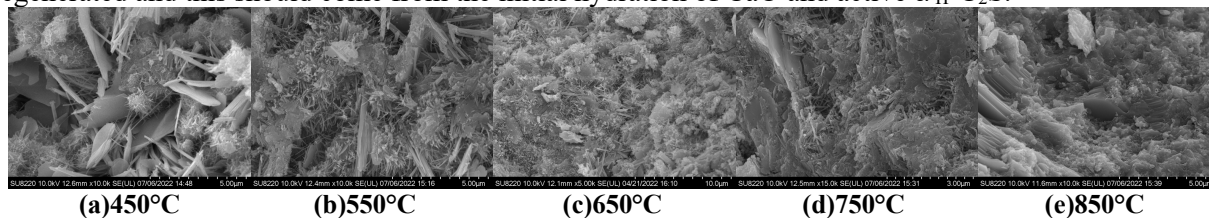


Fig. 3. SEM images of RC pastes at 28 days.

4. Conclusions

The roles of C_{12}A_7 , $\alpha'_H\text{-C}_2\text{S}$ and dehydrated amorphous nesosilicate in rehydration of recycled cement have been investigated. Phase changes during dehydration and rehydration were determined using QXRD, TG, isothermal calorimetry and SEM. Compressive strengths of RC pastes were tested. In particular it has been concluded that:

- (1) Waste cement paste would produce different dehydration products through thermal activation under different temperatures. Most of chemically bound water from C-S-H and other hydrated compounds were decomposed at 550 °C. After dehydration, most $\text{Ca}(\text{OH})_2$ changed into calcite. RC pastes presented clear evidence of rehydration, displaying common hydration products that include needles-like Aft, plate-like AFm, C-S-H gel and $\text{Ca}(\text{OH})_2$.
- (2) C_{12}A_7 showed very high reactivity at the beginning of the rehydration, generating Aft, which gradually transforms into layered AFms (mainly hemicarboaluminate and monocarboaluminate due to the presence of carbonates) as the reaction continued. $\alpha'_H\text{-C}_2\text{S}$ also had high reactivity and played a decisive role in the strength development at all stages of the RC paste. The dehydrated amorphous nesosilicate, as the main reactant in the accelerating phase of the early rehydration process, contributed to the early strength of RC paste.

Acknowledgements

The authors wish to acknowledge the financial support provided by the National Natural Science Foundation of China (Nos. 52008232, 52038004).

References

- Bogas, J., Carriço, A. and Tenza-Abril, A. (2020) "Microstructure of thermoactivated recycled cement pastes", *Cement and Concrete Research*, 138: 106226.
- Juilland, P., Gallucci, E., Flatt, R. and Scrivener, K. (2010) "Dissolution theory applied to the induction period in alite hydration", *Cement and Concrete Research*, 40: 831-844.
- Lowell, M., Shields, S., Thomas, J. and Thommes, M. (2005) "Characterization of Porous Solids and Powders: Surface Area, Pore Size, and Density", *Kluwer Academic Publishers*.
- Mantellato, S., Palacios, M. and Flatt, R. (2015) "Reliable specific surface area measurements on anhydrous cements", *Cement and Concrete Research*, 67: 286-291.
- Wang, J., Mu, M. and Liu, Y. (2018) "Recycled cement", *Construction and Building Materials*, 190: 1124-1132.
- Xu, L., Wang, J., Li, K., Hao, T., Li, Z., Li, L., Ran, B. and Du, H. (2023a) "New insights on dehydration at elevated temperature and rehydration of GGBS blended cement", *Cement and Concrete Composites*, 139: 105068.
- Xu, L., Wang, J., Li, K., Li, M., Lin, S., Hao, T., Wang, T., Guo, Y. and Ling Z. (2023b) "Investigations on the rehydration of recycled blended SCMs cement", *Cement and Concrete Research*, 163: 107036.
- Xu, L., Wang, J., Li, K., Lin, S., Li, M., Hao, T., Ling, Z., Xiang, D. and Wang, T. (2022) "A systematic review of factors affecting properties of thermal-activated recycled cement", *Resources Conservation and Recycling*, 185: 106432.

Carbonation and hydration kinetics of CO₂ injected ready-mixed concrete

Suhui Zhang^{1,2}, Qiang Yuan^{1,2*}, Jun Ni³, Caijun Shi⁴

¹ School of Civil Engineering, Central South University, Changsha, 410075, China

Email: zsh_0910@csu.edu.cn

yuanqiang@csu.edu.cn

² National Engineering Research Center of High-speed Railway Construction Technology, Changsha, 410075, China

³ Jiangsu Shuanglong Group Co., LTD. Nanjing, 211112 China

Email: nijun228@163.com

⁴ College of Civil Engineering, Hunan University, Changsha, 410082, China.

Email: cshi@hnu.edu.cn

ABSTRACT

Carbonation ready-mixed concrete (CRC), defined as ready-mixed concrete mixed with CO₂ injection, is a promising technique for low/negative carbon cement and concrete industry. In this study, we investigated the influence of CO₂ injection on the carbonation and hydration kinetics of ready-mixed concrete. Adiabatic temperature rise, X-ray diffraction, thermal gravimetric analysis, and scanning electron micrograph are performed to explore the corresponding changes in carbonation and hydration, microstructure, and CO₂ sequestration capacity. It was found that CO₂ injection is beneficial for hydration reaction by the significant adiabatic temperature rise of cement paste, which accelerates the formation of hydration products. The large amounts of Ca²⁺ consumption by CO₃²⁻ has a competitive relationship to the formation of calcium hydroxide (Ca(OH)₂) and calcium silicate hydrate (C-S-H). However, enhanced dissolution of clinker by the unsaturated Ca²⁺ and crystallization agglomeration of hydration product by the nucleation effect of CaCO₃ lead to more hydration products, denser microstructure, and a higher hydration degree at the same mixing time. Meanwhile, the formation of CaCO₃ was analyzed to evaluate the CO₂ sequestration capacity of ready-mixed concrete by CO₂ uptake calculated.

KEYWORDS: Ready-mixed concrete, CO₂ injection, Carbonation, Hydration, CO₂ uptake

1. Introduction

Ready-mixed concrete mixed with CO₂ gas injected, is described as carbonation ready-mixed concrete (CRC). In previous literature, the feasibility of the technology of CCUS in ready-mixed concrete has been confirmed (Monkman and MacDonald (2017), Black and Purnell (2016)). And there were two main methods to implement the sequestration of CO₂ in CRC, CO₂ treatment of mixing water (Qian et al. (2018)) and CO₂ injection of mixing process (He, Li, and Shao (2017)). CO₃²⁻ formed by the dissolution of CO₂ in mixing water can react with Ca²⁺ mainly obtained from calcium silicate, C-S-H, and CH in cement paste to form CaCO₃ (Zhang, Ghoulah, and Shao (2017), Ashraf and Olek (2016), Huijgen, Witkamp, and Comans (2006), Guan et al. (2016), Haselbach (2009)). For the reasons given above, the microstructure could be changed which mainly refers to the research reports of accelerated carbonation curing. The nucleation effect caused by the formation of nano-CaCO₃ particles promotes the hydration of cement clinker. Then, due to the nano-CaCO₃ formed in the pores, the pore structure was refined especially gel pores and capillary pores. Also, the more active hydration reaction and denser microstructure could provide higher strength. However, the carbonation reaction in fresh concrete when CO₂ is injected is different from it in hardened concrete of accelerated carbonation curing. CO₂ play an important role in the microstructural build-up at the beginning of the hydration reaction. Moreover, the nano-CaCO₃ not only can be formed in pores but also can attach on the surface of cement clinker.

Therefore, the effect of carbonation reaction in ready-mixed concrete can not simply follow the mechanism of accelerate carbonation curing. The carbonation and hydration kinetics of CO₂ injected ready-mixed concrete remain to be discussed.

For a full understanding of the carbonation and hydration kinetics of CO₂ injected ready-mixed concrete, we focus on the evolution of the carbonation and hydration process of fresh cement paste. Based on the analysis of solid phase assemblage and ionic composition of interstitial solution, the factors contributing to the changes of carbonation and hydration kinetics are indicated and further the morphology of carbonation and hydration products are observed.

2. Experimental part

2.1 Materials

A commercial reference cement (PC) was used in this study with a density of 3020 kg/m³ and a Blaine-specific surface area of 346 m²/kg. Deionized water was used for preparing the cement paste. Deionized water was obtained from a Barnstead Nanopure filtration system with a minimum resistivity of 18.2 MΩ·cm. Purified liquid CO₂ with a concentration of 99.5% was used in this study.

2.2 Test methods

The samples were designed as cement paste mixed normally (Nor-Mix) and cement paste mixed with CO₂ injected (CO₂-Mix). All pastes were prepared at a constant water-to-cement (w/c) ratio of 0.5. Following the standards ASTM C94 and GB/T 14902, the mixing time in mixing plant should be lower than 120 s and the transport time in mixer truck should be lower than 90 mins. Deionized water was added to the closed chamber at 25 °C. Also, after the liquid CO₂ is released as gas CO₂ and heated to 25 °C, it can be injected into the mixing chamber. The adiabatic temperature rise was measured at 25 °C using customized equipment, which has three main functional components: a closed adiabatic mixing chamber, a temperature-measuring instrument, and a servo gas supply unit. The inner diameter and depth of the chamber were 100 mm and 200 mm, respectively. The stirring rate was controlled to be in the range of 100-1800 rpm. The measuring span of the temperature-measuring instrument was 0-260 °C with an accuracy of 0.1 °C. The servo gas supply unit ensured that the temperature of CO₂ gas was the same as that in the closed adiabatic mixing chamber to avoid the use of external heat sources. The interstitial solutions of all pastes were extracted by a centrifuge at 5120 × g for 4 min. And the different hydration times (0.5, 1, 1.5, 2, 10, 30, 60, and 90 min) were selected. Afterward, the obtained solutions were immediately filtered using 0.45 μm nylon filters. To prevent the precipitation of the solid phase, HNO₃ (3.6% by volume) was used to acidize the residual filtered solutions. The concentrations of K, Na, Ca, Al, S, and Si in the interstitial solutions were measured by an ICP-OES (Spectro Blue, Analytical Instruments GmbH) to present the ions of K⁺, Na⁺, Ca²⁺, Al(OH)₄⁻, SO₄²⁻, and H₃SiO₄⁻, respectively (Huang et al. (2022), Huang et al. (2021)). The samples for the solid phases analysis were acquired after hydration arrested at different hydration times (0.5, 1, 1.5, 2, 10, 30, 60, and 90 min). About 10 ml cement paste was taken out and immediately immersed into 300 ml isopropanol. The suspension was stirred for 5 min using a glass rod and then was filtrated by a 2.5 μm filter. Afterward, following the above processes, the residual powders were washed twice. Then, the powders were stored in a vacuum drying oven at the temperature of 35 °C for 7 days. Finally, the obtained powders samples can be used for TGA, XRD, and SEM. In the TGA, the mass loss at a temperature range of 500-950 °C was used to calculate the content of CaCO₃, which further calculate the content of CO₂ uptake.

3. Results and discussion

3.1 Adiabatic temperature rise

Fig. 1 shows the adiabatic temperature rise and heat flow of the cement pastes of Nor-Mix and CO₂-Mix within 10 h. The temperature curves can be divided into five stages within 10 h, including the initial period with logarithmic growth (stage I), the induction period with linear growth (stage II), the acceleration period with exponential growth (stage III), the deceleration period with a slowing decrease (stage IV), and the diffusion controlling period with a stable period (stage V). As seen in **Fig. 1**, although the paste mixed with the CO₂ injection consists of a similar temperature curve as the paste mixed normally, the developments of temperature rise in each stage are quite different. With CO₂ injected into cement paste, CO₂-Mix seems to have a minor impact on the duration of stage I. However, it is most

important that with the CO₂ injection, the induction period of CO₂-Mix is prolonged, compared with Nor-Mix. The end of the induction period is prolonged from 125 min for Nor-Mix to 144 min for CO₂-Mix. It means that the duration of induction period is prolonged from 110 min to 129 min. The duration of stage III is severely shortened from 265 min to 211 min based on the end of acceleration period at 390 min for Nor-Mix and 355 min for CO₂-Mix. For stage IV, the temperature rise of CO₂-Mix shows a similar trend to that of Nor-Mix based on the heat flow. Yet, the duration of deceleration period of CO₂-Mix is prolonged, compared with Nor-Mix (prolonged from 170 min to 225 min). The ends of deceleration period are at 560 min for Nor-Mix and 580 min for CO₂-Mix respectively.

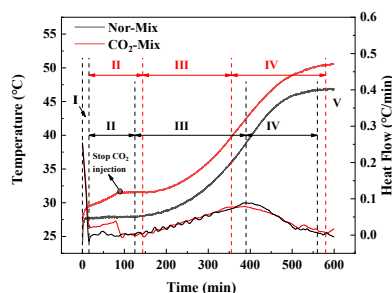


Fig. 1 Adiabatic temperature rise of Nor-Mix and CO₂-Mix

3.2 Evolution of solid phase and liquid phase

Following the mixing process of Nor-Mix and CO₂-Mix within 90 min, the evolution of solid phase and liquid phase are presented in **Fig. 2**. **Fig. 2(a)** presents the evolution of CO₂ uptake and bond water. It is found that CO₂ injection in CO₂-Mix has a great impact on environmental benefits. During the mixing process for 90 min, CO₂ uptake in cement paste can reach 2.89% of the weight of cement. The content of bond water in the samples is calculated, which in CO₂-Mix is higher than that in Nor-Mix during the whole mixing process of cement paste. Therefore, CO₂ injection can promote the hydration reaction. To ensure the conservation of mass during calculating the solid phases, the obtained powders samples should be normalized based on the consideration of extra chemical bonding of water and CO₂. As seen in **Fig. 2(b)**, the CO₂ injection in cement paste has a significant effect on the Ca(OH)₂ content. When the cement paste is mixed for 60 min, the Ca(OH)₂ content of Nor-Mix is fourth times to that of CO₂-Mix (2.41% for Nor-Mix and 0.61% for CO₂-Mix). Though after cement paste mixed for 60 min, the Ca(OH)₂ in CO₂-Mix has a minor growth, the Ca(OH)₂ content of Nor-Mix is nearly triple to that of CO₂-Mix (2.4% for Nor-Mix and 0.86% for CO₂-Mix). Moreover, CaCO₃ has an opposite trend to Ca(OH)₂. With the CO₂ injection, CaCO₃ shows a growth within the mixing process for 90 min. Only after the cement paste is mixed for 60 min, the growth of CaCO₃ is slowed down. At 90 min, the contents of CaCO₃ are 2.08% for Nor-Mix and 9.12% for CO₂-Mix, respectively.

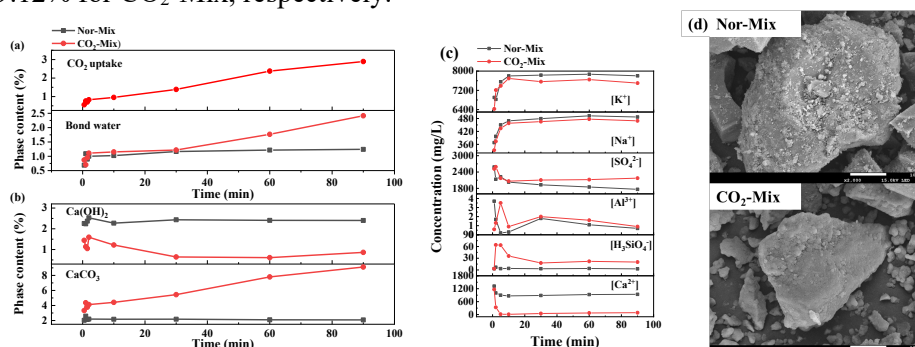


Fig. 2 The evolution of solid phase and liquid phase: (a) CO₂ uptake and bond water; (b) Ca(OH)₂ and CaCO₃ content; (c) Liquid phase (K⁺, Na⁺, Ca²⁺, Al(OH)₄⁻, SO₄²⁻, and H₃SiO₄⁻); (d) Morphology of hydration and carbonation products at 90 min.

Fig. 2(c) shows the changes in ionic concentration of the interstitial solution in Nor-Mix and CO₂-Mix over time during the mixing process. Due to the CO₂ injected into the cement paste, CO₃²⁻ is formed by the dissolution of CO₂ in mixing water. The concentration of K⁺ and Na⁺ have a minor reduction inferred from the increase of pH value caused by the formation of CO₃²⁻ (Qian et al. (2018)). Moreover, CO₃²⁻ has the highest priority in the carbonation and hydration reaction which consumes a great deal of Ca²⁺

dissolved from cement clinker and gypsum. Thus, the concentration of SO_4^{2-} in CO_2 -Mix is slightly higher than that of Nor-Mix, also the concentration of Al^{3+} has the same trend. Furthermore, the concentration of H_3SiO_4^- also is reduced which is resulted from the reduction of Ca^{2+} in the interstitial solution caused by the consumption of CO_3^{2-} . Therefore, it is important that the formation of CaCO_3 has a competition with the C-S-H and $\text{Ca}(\text{OH})_2$.

Fig. 2(d) presents the morphology of hydration and carbonation products on the surface of cement particles at 90 min. It can be seen that there are lots of fragmentary products on the surface of cement particles of Nor-Mix. Yet, for CO_2 -Mix, the more hydration products (more C-S-H and other crystals) are agglomerates and completely cover the surface of cement particles. That also indicated that CO_2 injection can promote the hydration reaction and also can prolong the induction period due to the denser microstructure which is defined as the protective membrane layer.

4. Conclusions

The study investigated the carbonation and hydration kinetics of fresh cement paste to indicate the effect of CO_2 injection on ready-mixed concrete. Following a series of scientific tests and analyses, the following conclusions can be drawn:

- (1) CO_2 injection for CO_2 -Mix, compared with Nor-Mix, can increase the temperature rise of cement paste and further prolong the induction period, shorten the acceleration period, and enter diffusion controlling period slightly ahead of schedule.
- (2) CO_2 injected into cement paste has a CO_2 uptake of 2.89% to the weight of cement, which proves that the application of CO_2 injection in ready-mixed concrete has a huge environmental benefit.
- (3) The formation of CaCO_3 has a competition with the C-S-H and $\text{Ca}(\text{OH})_2$, which is indicated by the more products (lower C-S-H and $\text{Ca}(\text{OH})_2$), lower H_3SiO_4^- and denser microstructure for CO_2 -Mix, compared with Nor-Mix.

Acknowledgements

Financial supports by Key Technologies R&D Program of CNBM (2021HX0506) and National Natural Science Foundation of China (contract No. 51922109) are greatly appreciated.

References

- Ashraf, Warda, and Jan Olek. (2016). "Carbonation behavior of hydraulic and non-hydraulic calcium silicates: potential of utilizing low-lime calcium silicates in cement-based materials." *Journal of Materials Science* 51 (13):6173-6191.
- Black, Leon, and Phil Purnell. (2016). "Is carbon dioxide pricing a driver in concrete mix design?" *Magazine of Concrete Research* 68 (11):561-567.
- Guan, Xuemao, Songhui Liu, Chunhua Feng, and Man Qiu. (2016). "The hardening behavior of γ -C2S binder using accelerated carbonation." *Construction and Building Materials* 114:204-207.
- Haselbach, Liv. (2009). "Potential for Carbon Dioxide Absorption in Concrete." *Journal of Environmental Engineering* 135 (6):465-472.
- He, Zhen, Zhen Li, and Yixin Shao. (2017). "Effect of Carbonation Mixing on CO_2 Uptake and Strength Gain in Concrete." *Journal of Materials in Civil Engineering* 29 (10).
- Huang, Tingjie, Qiang Yuan, Shenghao Zuo, Baiyun Li, Qihong Wu, and Youjun Xie. (2021). "Evaluation of microstructural changes in fresh cement paste using AC impedance spectroscopy vs. oscillation rheology and ^1H NMR relaxometry." *Cement and Concrete Research* 149.
- Huang, Tingjie, Qiang Yuan, Shenghao Zuo, Youjun Xie, and Caijun Shi. (2022). "New insights into the effect of gypsum on hydration and elasticity development of C3S paste during setting." *Cement and Concrete Research* 159:106860.
- Huijgen, Wouter J. J., Geert-Jan Witkamp, and Rob N. J. Comans. (2006). "Mechanisms of aqueous wollastonite carbonation as a possible CO_2 sequestration process." *Chemical Engineering Science* 61 (13):4242-4251.
- Monkman, Sean, and Mark MacDonald. (2017). "On carbon dioxide utilization as a means to improve the sustainability of ready-mixed concrete." *Journal of Cleaner Production* 167:365-375.
- Qian, Xin, Jialai Wang, Yi Fang, and Liang Wang. (2018). "Carbon dioxide as an admixture for better performance of OPC-based concrete." *Journal of CO_2 Utilization* 25:31-38.
- Zhang, Duo, Zaid Ghoulleh, and Yixin Shao. (2017). "Review on carbonation curing of cement-based materials." *Journal of CO_2 Utilization* 21:119-131.

Assessment of the Microstructure and Mass Transfer in Strontium-Loaded Geopolymer Cement Wasteforms

Charlotte Nevin¹, Daniel A. Geddes^{1,2}, John L. Provis², and Brant Walkley¹

¹Department of Chemical and Biological Engineering, University of Sheffield, Sheffield, United Kingdom
Email: cnevin1@sheffield.ac.uk, d.geddes@sheffield.ac.uk, b.walkley@sheffield.ac.uk

² Department of Materials Science and Engineering, University of Sheffield, Sheffield, United Kingdom
Email: d.geddes@sheffield.ac.uk, j.provis@sheffield.ac.uk

ABSTRACT

Fission products generated in the running of nuclear power reactors, such as strontium-90, are often conditioned before disposal through cementation, specifically in Portland cement-blast furnace slag blends. Due to their enhanced physical and chemical properties, geopolymers are being investigated as potential alternatives for the cementation of certain radioactive waste streams. This study shows that the microstructure of geopolymers, made up predominantly of a largely X-ray amorphous, three-dimensional, aluminosilicate gel (K-A-S-H), remains unchanged with the introduction of Sr(OH)₂ into the gel. Furthermore, a 28-day leach test in synthetic granitic groundwater induces no observable differences in the microstructure. This work suggests that potassium-activated geopolymer gels are excellent candidates for the disposal of ⁹⁰Sr-containing waste. The findings are important for understanding the effect of incorporating certain radionuclides into the structure of candidate wasteforms, and subsequently the effect of long-term storage within a geological disposal facility, where the wasteforms will be subject to the flow of groundwater over hundreds of years.

KEYWORDS: *Geopolymers, Radioactive Waste, Leaching, Microstructure.*

1. Introduction

Nuclear power reactors can provide low carbon, reliable electricity generation with a low environmental impact [1], but conditioning of the radioactive waste associated with fission reactor operation and decommissioning is essential to ensure long-term safety and viability of this form of power generation. Strontium-90 is a fission product with high solubility in water. As such, it is often present in reactor cooling water and, as a radionuclide with high radiotoxicity (5217 Bq/g). ⁹⁰Sr is often harmful as its biological function is analogous to calcium [2]. Immobilisation of radionuclides such as ⁹⁰Sr is often achieved through cementation, traditionally in Portland cement (PC)-blast furnace slag (BFS) blends [3], due to its simplicity, low cost, and relatively high throughput [4].

Geopolymer cements have been highlighted as a potential alternative to PC for the cementation of radioactive waste due to their enhanced physical and chemical properties, their capability to immobilise cations, their stability under chemical attack, their potentially low leaching rates compared to PC [3], and the CO₂ savings during production. Geopolymers comprise a largely X-ray amorphous, three-dimensional aluminosilicate binder that is are highly cross-linked and structurally disordered. The binding phase is almost exclusively an alkali aluminosilicate gel, referred to as (N,K)-A-S-H, where N and K are sodium and potassium; common alkalis used in their production [4]. These alkali metal cations balance the tetrahedral Al(III) sites [5] and are directly associated with the negatively charged oxygen ions, rendering them exchangeable in ion exchange processes. It is this mechanism which the disposal of strontium cations takes advantage of during disposal in geopolymer cement wasteforms.

Previous work highlighted minimal variation in the local environments within the (N,K)-A-S-H gel upon the addition of Sr²⁺ to geopolymers [4], suggesting that incorporation of these ions does not significantly alter the gel structure as the Sr²⁺ ion displaces the alkali cation. This increases structural

stability of the geopolymer gel. Additionally, previous work has shown very effective immobilisation of Cs and Sr into AAMs [6], and that geopolymers act like zeolites when retaining certain cations [3].

This study investigates the chemical and microstructural changes during leaching of potassium-based geopolymer cement containing Strontium as a non-radioactive analogue for ^{90}Sr . A 28-day leach test was conducted in synthetic groundwater, representing granitic regions of the UK.

2. Experimental Methodology

The geopolymer gels were produced from the reaction between metakaolin powder (MetaMax, BASF) and potassium silicate solution, prepared by dissolving potassium hydroxide powder (Sigma Aldrich, AnalaR, 99wt.%) in distilled water and subsequently mixing with potassium silicate (PQ-KS, 51.6 wt.%, with a solution modulus of $\text{SiO}_2/\text{K}_2\text{O} = 2.2$, with the balance water). This yielded an activating solution modulus (defined on a molar basis) of $\text{SiO}_2/\text{K}_2\text{O} = 1$.

Samples containing strontium were prepared by dissolving $\text{Sr}(\text{OH})_2$ (Sigma Aldrich, 95%) in the activating solution, before the addition of metakaolin powder. To ensure homogeneity, the samples were mixed with a high-shear mixer at 1800 rpm for 10 minutes, cast in sealed containers, and cured at 20 °C for 28 days. The samples contained 0wt.%, 1 wt.%, and 3 wt.% $\text{Sr}(\text{OH})_2$, and had $\text{H}_2\text{O}/\text{K}_2\text{O} = 13.0$.

After the 28 days of curing, the geopolymer samples were formed into cylinders (14 mm in diameter and 24.5 mm in length), with the ends sealed in epoxy resin to prevent axial mass transfer. A modified ANSI/ANS 16.1 leach test was performed to determine the effect of the groundwater on the wasteforms. The cylindrical sample, in triplicate, was submerged into the leachate (synthetic groundwater representative of granitic regions of the UK). Each leaching vessel contained 157.6 mL of leachate, giving a surface area/volume ratio of 10 m^{-1} . At given time intervals (1 hour, 8 hours, 24 hours, 72 hours, 7 days, 14 days, and 28 days) the leachate was fully replaced to simulate slow moving groundwater. After the last time point, the monoliths were removed from the leachate and submerged in isopropanol to remove any bound water through ion exchange. This ensures no further reaction without altering the geopolymer gel structure. The samples were then prepared for characterisation.

3. Results and Discussion

3.1. Fourier Transform Infrared Spectroscopy

The FTIR spectra for the pre-leach and post-leach samples are shown in Figure 1, and the evolution of pH during the leach tests in Figure 2. The bonds identified are shown in Table 2, and are characteristic of formation of a fully polymerised K-A-S-H gel in each sample.

Table 2 - FTIR bands identified.

| Wavenumber (cm^{-1}) | Assignment |
|---------------------------------|--|
| 870 (shoulder) | Asymmetric stretching of Al-O-Si bonds linking AlO_4 and SiO_4 groups. |
| 900-1200 | Asymmetric stretching of Si-O-Si and Al-O-Si bonds in K-A-S-H gel. |
| 1380 - 1420 | Vibrations of the CO_3^{2-} anion in potassium and/or strontium carbonate. |
| 1660 and 3250 - 3750 | O-H bonds in chemically bound and free water. |
| 2300 – 2370 | C=O bonds in CO_2 . |

Further to those identified in Table 2, the fingerprint region at $500\text{-}850 \text{ cm}^{-1}$ is characteristic of aluminosilicate frameworks and includes contributions such as those from symmetric stretching of Al-O-Si (560 cm^{-1}), vibrations within 6-membered single rings and 6-membered double rings of SiO_4 or AlO_4 units (585 cm^{-1}), the symmetrical stretching of Si-O-Si (620 cm^{-1}), and pseudo-lattice vibrations of small aluminosilicate rings (720 cm^{-1}).

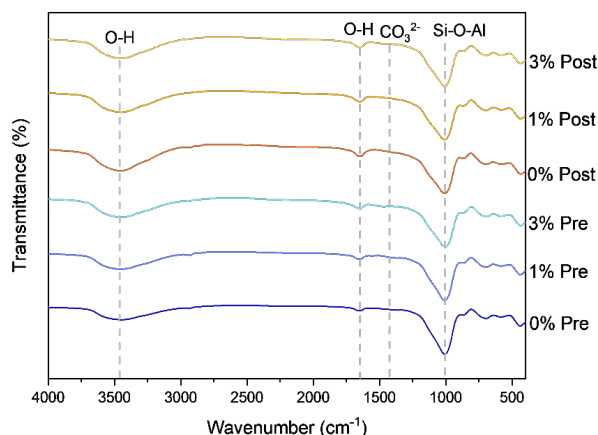


Figure 1 - FTIR Spectra of samples pre-and post-leaching

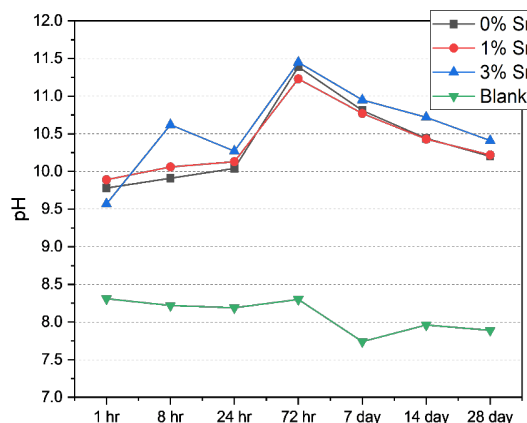


Figure 2 - pH measured during leach testing

Overall, the spectra in Figure 1 show minimal variation between the pre- and post-leach samples, indicating the structure is not significantly altered upon contact with groundwater as no additional bonds are being formed, or any existing bonds broken. Therefore, the strontium may have been incorporated into the aluminosilicate gel in place of the potassium, the charge balancing ion. The presence of the OH⁻ and CO₃²⁻ vibrational/stretching modes show that complete conversion of the Sr²⁺ into the gel structure has not occurred and refinement of the geopolymer gel could help to increase the waste loading. Additionally, XRD analysis, data not shown, indicates no formation of new crystalline phases during geopolymerisation reactions or leaching.

3.2. pH Data

Figure 2 shows the pH of the leachate at each time point during the leach test. An increase in alkalinity generally indicates a higher rate of mass transfer between the alkaline pore solution in the geopolymer samples and the leaching medium. At 72-hour s the concentration of alkali cations in solution reaches a maximum, before reducing with each time point after. This is most likely due to the high rate of surface wash-off often observed in the first 3 days. This is mainly the leaching of non- or loosely-bound ions present in the pore solution at, or close to, the surface of the sample [8]. After this time point, the leaching was much slower, likely due to diffusion-controlled migration of ions, through a complex structure, from deeper within the structure, or due to dissolution of the sample (dissolving of the sample into the solution). Furthermore, the measured pH increases with increasing strontium content. This indicates that the addition of the strontium has led to the release of more alkali cations (be that Sr²⁺ or K⁺) and therefore it may be inferred that the composition of the aluminosilicate matrix may change will increasing Sr²⁺ content. It is not yet clear whether strontium is also leaching out with the pore water, and thus inductively coupled plasma optical emission spectroscopy (ICP-OES) will be used to confirm this.

3.3. Scanning Electron Microscopy

SEM images comparing pre- and post-leached samples reveal a relatively dense, highly porous, homogeneous surface showing the presence of some unreacted metakaolin and pores or deposits of other material, potentially such as potassium carbonate. The high porosity can lead to a higher rate of mass transfer throughout the matrix [7] and is likely caused by entrained air introduced during the mixing stage. Furthermore, the samples contain micro-cracks, especially in the post-leach samples, which could potentially lead to a higher leach rate. Overall, the pre- and post-leach micrographs appear very similar, which suggests these geopolymers may be very durable in groundwater conditions for extended periods of time. Furthermore, SEM images comparing the 0% and the 3% strontium samples reveal similar findings.

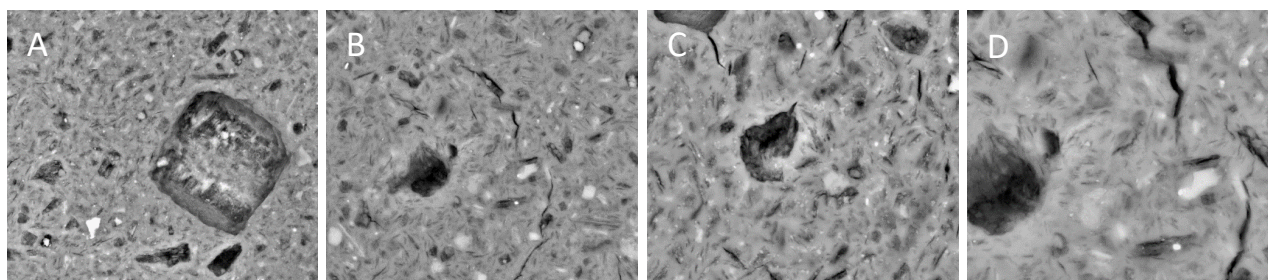


Figure 3 - SEM micrographs of 0% Sr samples at (A) pre-leach, 5000x magnification, (B) post-leach, 5000x magnification, (C) pre-leach, 10000x magnification, and (D) post-leach, 10000x magnification.

4. Conclusions

A modified ANSI/ANS 16.1 leach test was conducted for 28 days to highlight the microstructural changes resulting from the addition of strontium to the cement alongside the effects of leaching in synthetic granitic groundwater. The introduction of strontium to the system does not induce any significant observable differences to the gel structure, highlighting that the Sr^{2+} was possibly incorporated into the aluminosilicate gel structure in place of the potassium ion, which provides a charge balancing role, or as strontium salts. This suggests that the properties influenced by the gel structure are unlikely to be altered significantly by the introduction of strontium-containing radioactive waste. Overall, this work has revealed that potassium-activated geopolymer cement wasteforms could be a suitable candidate wasteform for the disposal of radioactive waste containing alkaline earth metals. However, the pH data reveal a degree of mass transfer between the pore solution in the waste matrix and the groundwater leachate. It is not clear if the strontium is leaching out with the pore water, but this will be studied in greater detail going forward.

Acknowledgements

The authors would like to express appreciation for the financial support of Sellafield Ltd., EPSRC and GREEN CDT, and the help of Jess McWilliams and Ella Cliff with laboratory work. The authors would like to thank both PQ-Silicates for the potassium silicate and BASF/Lawrence for the metakaolin used in this work.

References

- [1] A. Horvath and E. Rachlew, "Nuclear power in the 21st century: Challenges and possibilities," *Ambio*, vol. 45, pp. 38-49, 2016.
- [2] A. M. James, S. Harding, T. Robshaw, N. Bramall, M. D. Ogden and R. Dawson, "Selective environmental remediation of strontium and cesium using sulfonated hyper-cross-linked polymers (SHCPs)," *ACS Applied Materials and Interfaces*, vol. 11, no. 25, pp. 22464-22473, 2019.
- [3] C. Shi and A. Fernandez-Jimenez, "Stabilization/solidification of hazardous and radioactive wastes with alkali-activated cements," *Journal of Hazardous Materials*, vol. 137, no. 3, pp. 1656-1663, 2006.
- [4] B. Walkley, X. Ke, O. H. Hussein, S. A. Bernal and J. L. Provis, "Incorporation of strontium and calcium in geopolymer gels," *Journal of Hazardous Materials*, vol. 382, #121015, 2020.
- [5] J. L. Provis and J. S. J. van Deventer (eds.), "Alkali Activated Materials," Springer, RILEM, 2014.
- [6] N. Vandevenne, R. I. Iacobescu, R. Carleer, P. Samyn, J. D'Haen, Y. Pontikes, S. Schreurs and W. Schroyers, "Alkali-activated materials for radionuclide immobilisation and the effect of precursor composition on Cs/Sr retention," *Journal of Nuclear Materials*, vol. 510, pp. 575-584, 2018.
- [7] A. Hajimohammadi, J. L. Provis and J. S. J. van Deventer, "The effect of silica availability on the mechanism of geopolymerisation," *Cement and Concrete Research*, vol. 41, pp. 210-216, 2011.
- [8] M. Komljenović, G. Tanasijević, N. Džunuzović and J. L. Provis, "Immobilization of cesium with alkali-activated blast furnace slag," *Journal of Hazardous Materials*, vol. 388, #121765, 2020.

Pretreatments processes of alkaline recycled concrete aggregates to maximize CO₂ capture in accelerated carbonation processes.

J. Moreno-Juez^{1*}, I. Vegas-Ramiro¹, M. Frías², S. Martínez-Ramírez³, R. García-Giménez⁴

¹ TECNALIA, Basque Research and Technology Alliance (BRTA), Astondo Bidea, Edificio 700, Parque Tecnológico de Bizkaia, 48160 Derio, Spain

Email: jaine.moreno@tecnalia.com; inigo.vegas@tecnalia.com

² Eduardo Torroja Institute for Construction Sciences (IETcc-CSIC), 28033 Madrid, Spain

Email: mfrias@ietcc.csic.es

³ Institute for the Structure of Matter (IEM-CSIC), 28006 Madrid, Spain

Email: sagrario@iem.cfmac.csic.es

⁴ Facultad de Ciencias. Universidad Autónoma de Madrid. Unidad Asociada UAM-CSIC Madrid, Spain

Email: rosario.garcia@uam.es

ABSTRACT

One of the most promising strategies of Carbon Capture and Utilization (CCU) implemented by the cement sector consists of the accelerated carbonation (AC) of alkaline waste mainly from industry, urban waste and construction and demolition waste (CDW). The optimization of the AC process entails improving the combination of both the process conditions (time, pressure, CO₂ concentration, temperature, etc.) and the conditions of the waste to be carbonated (particle size distribution, mineralogical and chemical composition, humidity, etc.). Due to the high heterogeneity of the CDW, one of the main problems in optimizing the process is related to the variable composition of the CDW and the presence of minerals that are not susceptible to AC.

This study focused on the preparation stage of fine recycled concrete aggregates from CDW to maximize the concentration of carbonatable minerals (cement paste) and maximize CO₂ capture during the AC process. Different pretreatment technologies were used to maximize the concentration of cement paste: i) Densimetric technologies allowed concentrations of cement paste greater than 97%, free of impurities (light and gypsum); ii) Abrasion technologies allowed to increase the amount and the concentration of cement paste in the ultrafine fractions (<0.063 mm) from clean recycled concrete aggregates and, at the same time, the improvement of water absorption in the coarse fractions to enhance its use in concrete.

Fine fractions (<4 mm) of recycled concrete aggregates are then obtained with high quality and high concentration in cement paste to improve the carbonation process, as well as coarse fractions (4-20 mm) free of impurities with improved density and water absorption (<5% WA).

KEYWORDS: accelerated carbonation; improvement of recycled concrete aggregates; pretreatment processes; enrichment of cement paste.

1. Introduction

The Construction Sector seeks cost-effective pathways to cut its global direct CO₂ emissions by 2050. There are different strategies to cut emissions; one of the most promising is Carbon Capture and Utilization (CCU) consisting of the accelerated carbonation (AC) of alkaline waste mainly from industry, urban waste, and construction and demolition waste (CDW) and the use of alternative recycled aggregates in the construction sector. Accelerated Carbonation Technologies (ACT) applied to alkaline CDW have been widely researched, showing that they are an effective way to capture CO₂, while improving their properties and thus improving the performance of recycled aggregates [1-3]. In addition to optimizing the technology and operating parameters, it is key to adequately condition the materials that are going to be carbonated to maximize yield and CO₂ capture. For this, it is essential to increase the content of CaO and MgO.

There are different strategies for preparing materials prior to carbonation that are mainly focused on adapting particle sizes to maximize the specific surface area and enriching the wastes in carbonatable elements (CaO, MgO, Ca(OH)₂ and C₂S). This work deals with two pretreatment processes that, in addition, are aimed at improving the quality of recycled aggregates from CDW.

Densimetric tables are used for the effective separation of dry materials due to density. Separation is achieved by vibrating movement on an inclined treatment surface [4]. Air flows cross this surface from below and cause two kinds of effects for the material to be treated: products with a lower density are entrained without touching the floor and slide down the floor surface in the direction of the air stream. Higher density products touch the ground and are transported to the top of the ground surface as result of vibration. This technology is designed to treat mixed recycled aggregates and remove impurities (gypsum, ceramic, and light organic particles), thus enriching the clean fraction in recycled aggregates and aggregates rich in cement paste (CaO).

Abrasion techniques are used to remove, on the surface, the cement paste adhered to the original particles [5,6] and, therefore, enrich the finer fractions (<1 mm) with cement paste and reduce the water absorption of the thicker fractions, all of this in an economically viable way. The easiest way is to turn the material over and apply abrasion, due to the collision effect between particles.

The treated materials were characterized to study the effect of the techniques on different parameters, among which was the content of carbonate elements.

2. Materials and methods

To carry out this research work, two types of siliceous recycled aggregates from CDW were employed from a local CDW Treatment Plant: (1) Recycled Mixed Aggregate (RMA) for the densimetric treatment and (2) Recycled Concrete Aggregate (RCA) for the abrasion treatment (Figure 1). Both types of aggregates were treated and characterized independently in each of the technologies studied:

Densimetric process : the treatment of RMA using densimetric tables was carried out at the ALLGAIER facilities in Madrid (Spain), where they have a pilot plant with a 6 t/h treatment capacity. Prior to the treatment, a classification was carried out in order to generate different granulometric fractions for individual treatments: 1-2 mm; 2-4 mm; 4-8 mm and 8-16 mm. The process allows obtaining two differentiated samples: one called Heavy Fraction (recovered quality material concentrated in stony fraction) and another called Light Fraction (rejects that are discarded and rich in light particles, such as ceramic and gypsum). The applied process aims to maximize the quality of the Heavy fraction by eliminating as many impurities as possible. After the process, the obtained materials were characterized (components, density and absorption, XRF).

Abrasion process: the treatment of the RCA by mechanical abrasion was carried out at the IETcc facilities. From the original fraction (0-40 mm), optimization of the material is performed to obtain fine recycled aggregates (0-4 mm) concentrated in cement paste. To carry out optimization, following processes are implemented: i) drying of the sample; ii) abrasion process in a concrete mixer of the 0-40 mm fraction for 15 min; iii) characterization (density and absorption, XRF).



Figure 1. (Left) Densimetric table – ALLGAIERMogensen; (Right) Abrasion in concrete mixer - IETcc.

The following table summarizes the samples obtained:

Table 1 Samples obtained from both treatment processes.

| Densimetric treatment | | | Abrasion treatment | |
|-----------------------|------------------|-----------|--------------------|------------------|
| Input material | Treated material | | Input material | Treated material |
| | Heavy | Light | | |
| 1-2 mm | H 1-2 mm | L 1-2 mm | 0-1 mm | A 0-1 mm |
| 2-4 mm | H 2-4 mm | L 2-4 mm | 0-4 mm | A 0-4 mm |
| 4-8 mm | H 4-8 mm | L 4-8 mm | 4-20 mm | A 4-20 mm |
| 8-16 mm | H 8-16 mm | L 8-16 mm | 0-40 mm | A 0-40 mm |

3. Results and discussion

3.1. Densimetric technologies.

The treatment by densimetric tables allows the removal of unwanted impurities (gypsum, ceramic, and light) from the stone fractions rich in natural aggregates and mortar/concrete aggregates and therefore more interesting for carbonatation. The following Table 2 and Figure 2 show the results of components, water absorption, CaO, and sulfate content (%SO₃) of the treated and untreated RMA (only the results of the finest fractions are shown, 2-4 mm and 4-8 mm).

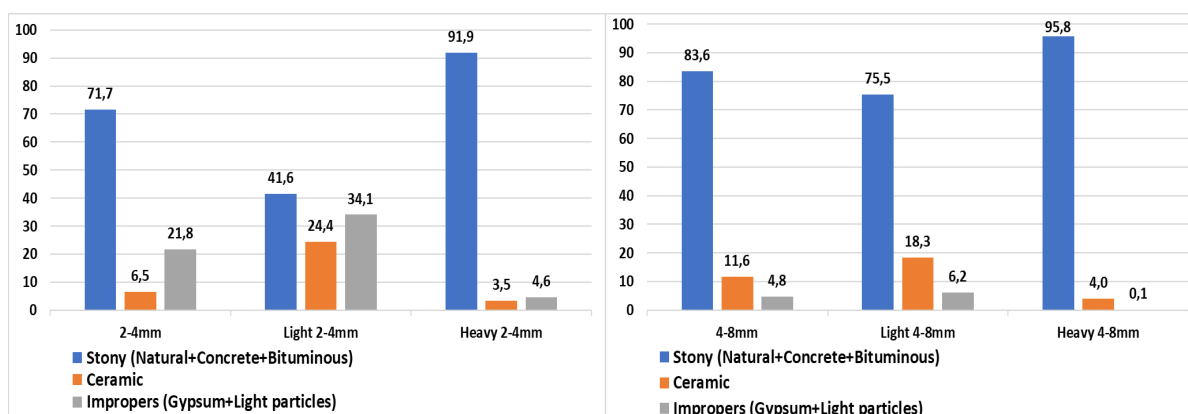


Figure 2. Components of the fine fractions (1-2 mm and 2-4 mm) of the RMA treated using a densimetric table.

Table 2 Water absorption, %CaO and % SO₃ after the densimetric treatment.

| | Input 1-2 mm | Treated H 1-2 mm | Treated L 1-2 mm | Input 2-4 mm | Treated H 2-4 mm | Treated L 2-4 mm |
|----------------------|-----------------|---------------------|---------------------|-----------------|---------------------|---------------------|
| Water absorption (%) | 17,11 | 13,66 | 35,78 | 12,93 | 8,75 | 21,82 |
| Difference (%) | | -20,16 % | +109% | | -32,3% | +68,8% |
| % CaO | 29,007 | 32,199 | 27,586 | 29,420 | 32,316 | 26,541 |
| Difference (%) | | +11% | -4,9% | | +9,8% | -9,8% |
| % SO ₃ | 3,118 | 2,585 | 8,127 | 2,032 | 0,782 | 3,038 |
| Difference (%) | | -17,1% | +160,7% | | -61,5% | +49,5% |

Different effects can be observed in the processed materials:

- The content of improper (gypsum + light) is considerably reduced in the fine fractions, reaching an elimination of almost 98%.
- Ceramic removal is less efficient than gypsum removal but still reaches final values of less than 3,5% (65,5% of removal).
- The CaO content increases by 11% and the sulphate content is reduced by more than 61% (<0,782%), thus enriching the aggregate in carbonatable particles and achieving sufficient quality for the use of fine fractions in applications with high added value.

3.2. Abrasion technologies.

The following table shows the values of water absorption and CaO content of the fine (0-4 mm) and coarse (4-20 mm) fractions of RCA treated by mechanical abrasion for 15 minutes in a traditional concrete mixer.

Table 3 Water absorption and %CaO after the abrasion treatment.

| | Input 0-4 mm | Treated A 0-4 mm | Input 4-20mm | Treated A 4-20 mm |
|----------------------|-----------------|---------------------|-----------------|----------------------|
| Water absorption (%) | 5,43 | 4,30 | 8,03 | 5,63 |
| Difference (%) | | - 20,8% | | - 29,9% |
| % CaO | 26,246 | 32,930 | 29,326 | 20,47 |
| Difference (%) | | + 25,5 % | | - 30,2% |

Different effects can be observed in the processed materials derived from the removal of the cement paste adhered to the natural aggregate in the coarse fractions and the concentration of this cement paste in the fine fractions:

- The water absorption of the treated fractions is reduced by up to 30%, reaching values below 5%.
- The CaO content, coming from the cement paste, increases in the fine fraction (0-4 mm) by 26% while it is reduced in the coarse fraction (30%) due to the elimination of the cement paste adhered to the original natural aggregate.

4. Conclusions

The quality of the recycled aggregates is improved by applying both processing techniques to enable their use in high added value applications (achieving compliance with aggregate standards for cement/mortar/concrete), and the CaO content in the fine fractions is increased to improve the performance of the accelerated carbonation processes and thus increase the CO₂ capture potential.

- Densimetric technologies allow the removal of up to 98% of gypsum and light impurities in the fine fractions of RMA (<4 mm) and increase the content of carbonatable CaO by 11%.
- Abrasion techniques allow us to reduce the absorption of fine and coarse RCA below 4,3% and 5,6% respectively. In addition, an increment of +25,5% of CaO is generated from the removal of cement paste adhered to the original natural sand.

Both technologies are designed to simplify the process and not add an additional cost to the recycled aggregates that prevents its economic viability. Each one of the processes, separately, guarantees a cost of treatment of the recycled aggregate of less than €2/t.

Acknowledgements

This research was developed under VALREC project, funded by the Community of Madrid, through the program "Innovation Hubs - 2020" together. Special thanks to the research project CIDEAR funded by Spain's Ministry of Science and Innovation, AEI and eRDF funds under National Project PID2021-122390OB-C21.

This work was supported by Spain's Ministry of Science and Innovation, AEI, and eRDF (CIDEAR-PID2021-122390OB-C21

Special thanks to ALLGAIER MOGENSEN Spain for supporting this research activity.

References

- [1] Pan, S. Y., Chang, E. E., & Chiang, P. C. (2012). "CO₂ capture by accelerated carbonation of alkaline wastes: a review on its principles and applications". *Aerosol and Air Quality Research*, 12(5), 770-791.
- [2] Skocek, J., Zajac, M., & Ben Haha, M. (2020). "Carbon Capture and Utilization by mineralization of cement pastes derived from recycled concrete". *Scientific Reports*, 10(1), 1-12.
- [3] Schoon, J, et al. (2015) "Fines extracted from recycled concrete as alternative raw material for Portland cement clinker production." *Cement & Concrete Composites*, 2015, Vol. 58.
- [4] Bogdan, C., Carlos, H. S., Gerson, M., Carlos, P., Lauredan, L. G., Régis, P., Florian, H., Ana Paula, K., (2014) "The potential of using air jigging to sort recycled aggregates", *Journal of Cleaner Production*, Volume 66, 2014, Pages 46-53.
- [5] A. Akbarnezhad et al. (2013) "Separation processes to improve the quality of recycled concrete aggregates (RCA)" *Woodhead Publishing Series in Civil and Structural Engineering*. Pages 246-269.
- [6] Takenama Corporation (1999). "High-quality Recycled Aggregates «Cyclite» Acquires FirstApproval of Innovative Technologies from Building Center of Japan".

Effect of Manganese Sulfate Replacing Gypsum on Properties and Reducing Cr(VI) of Cement Paste

Y. Wang¹, Z. Wang^{2*}

Chongqing university, Chongqing, China

¹Email: wangyuan9558@163.com

²Email: cquwangzhi@126.com

ABSTRACT

The amount of water-soluble Cr(VI) is increasing in cement as a result of raw materials and production technologies. Cr(VI) reducing agent manganese sulfate has high chromium reducing efficiency, however, Cr(VI) reduction efficiency will be reduced when it is dissolved in water or applied in liquid form. This paper uses manganese sulfate to replace part of gypsum in cement in order to improve the Cr(VI) reducing ability of manganese sulfate in cement slurry. The setting time and compressive strength were used to analyze the macroscopic characteristics of cement slurry when the manganese sulfate replace gypsum. The hydration process and hydration products of cement slurry were determined by X-ray diffraction (XRD) and thermogravimetry(TG). The reduction and dissolution of hexavalent chromium were studied by the generalized acid neutralization test. The results confirmed that manganese sulfate can adjust setting time, increase compressive strength and promote the early hydration of cement when the replacement amount of manganese sulfate is 25% and 50%. The reduction efficiency of chromium(VI) were 7.4%, 30.9%, 49.6%, 65.2%, 72.6% respectively when the amount of manganese sulfate replacing gypsum is 0%, 25%, 50%, 75% and 100%. So, replacing gypsum with manganese sulfate can improve the Cr(VI) reduction efficiency of cement without affecting the properties of cement.

KEYWORDS: *Manganese sulfate, Portland cement, Chromium(VI), Reduction*

1. Introduction

In the process of cement production, Cr(III) in raw materials changes into Cr(VI) under the condition of high temperature and high alkalinity, which leads to the increase of water-soluble Cr(VI) concentration in cement. Water-soluble Cr(VI) is a heavy metal element with high toxicity and is not easy to be decomposed, and it can cause harm to human body through skin contact, respiratory inhalation, environment contact and other ways. According to GB31893-2015, the content of water-soluble Cr(VI) in cement is not more than 10mg/kg, so the reduction of Cr(VI) in cement is very important. The commonly used Cr(VI) reducing agents in cement are ferrous salt, stannous salt, manganous salt, sulphide, aldehydes, slag and so on. Manganese sulfate has strong reducibility and stable chemical properties, and does not have adverse effects on cement properties (e.g., Nocuń-Wczelik, Golonka and Malata (2014)). However, in practical applications, studies have found that manganese sulfate can reduce the Cr(VI) reduction performance when it is dissolved in water or applied in liquid form. In order to improve the Cr(VI) reducing ability of manganese sulfate in cement slurry, while increasing the amount of manganese sulfate without increasing the content of SO₃ in cement, this paper uses manganese sulfate to replace part of gypsum in cement. The cement properties and reducing water-soluble Cr(VI) of cement paste was studied by setting time, compressive strength, X-ray diffraction (XRD), TG and dissolution of water-soluble Cr(VI).

2. Materials and Methods

2.1 Materials

The Portland cement clinker was ground and passed through a 200-mesh screen. Its chemical composition is shown in Table 1. Potassium dichromate ($K_2Cr_2O_7$), manganese sulfate ($MnSO_4 \cdot H_2O$), gypsum ($CaSO_4 \cdot 2H_2O$) were analytically pure; Manganese sulfate and potassium dichromate were finely ground over 100 mesh. The mix ratio of paste is designed by replacing the same molar amount of gypsum with manganese sulfate under the condition that the mass percentage of SO_3 in cement is 3.6%, and the water-binder ratio is 0.3.

Table 1 Chemical composition of clinker

| CaO | SiO ₂ | Al ₂ O ₃ | Fe ₂ O ₃ | MgO | SO ₃ | K ₂ O | Na ₂ O | LOI |
|-------|------------------|--------------------------------|--------------------------------|------|-----------------|------------------|-------------------|------|
| 70.17 | 15.02 | 3.48 | 4.03 | 2.92 | 1.24 | 1.45 | 0.34 | 1.24 |

2.2 Test methods

The setting time was tested by using Vicat apparatus according to the standard GB/T1346-2001; The compressive strength was tested according to GB/T17671-1999; The crushed test block is used for hexavalent chromium leaching test and microscopic test. The broken test block was soaked in alcohol to terminate hydration and then removed and placed in a 40°C oven to dry for use. The dried samples were grinded to 75μm for XRD test with a step of 0.02° and a test time of 5min.

The effect of pH on dissolution of hexavalent chromium was tested by generalized acid neutralization test, specimen cured for 28 days were broken and passed through a 200-mesh screen, the acetic acid solution of 2N was used to prepare different pH solutions, so that the acetic acid amount used per kilogram of solid was 0, 4, 6, 8, 10, 12, 14, 16, 18 and 20 equivalents, the samples are added to different solutions, the liquid-solid ratio was 20, after soaking for 30 days, filter out the liquid with a 0.45μm filter membrane, the concentration of water soluble Cr(VI) in liquid was measured by Model TU-1901 double beam ultraviolet visible spectrophotometer.

3. Results and Discussion

3.1 Setting time

The effect of replacing gypsum with manganese sulfate on the setting time of cement is shown in Figure 1. The setting time of cement increase first and then decrease with the increase of the amount of manganese sulfate. The mass fraction of SO_3 in cement is kept constant, thus the change of setting time of cement is mainly related to the solubility of manganese sulfate and the performance of manganese ion. The data show that the solubility of manganese sulfate is 10g at 20°C, nearly 40 times that of gypsum(0.255g), therefore, the concentration of SO_4^{2-} will be increased in cement paste when the manganese sulfate was added to cement. The formation of ettringite will be promote when the concentration of SO_4^{2-} was increased in liquid phase, which will delay cement hydration and prolong the setting time. In cement, alkali metal ions of alkali metal sulfate tend to accelerate cement hydration, while sulfate ions tend to delay cement hydration(e.g., Samet, and Sarkar (1997)). In this experiment, sulfate ions in manganese sulfate slow coagulation, and manganese ions promote cement hydration, which cause the setting time increasing first and then decreasing with the increase of the amount of manganese sulfate. Therefore, it can be concluded that manganese sulfate can replace gypsum to adjust the setting time of cement, and has a stronger ability to adjust the setting time in a certain range.

3.2 Compressive strength

The compressive strength of cement is shown in Figure.2 when the gypsum was replaced manganese sulfate in cement. The compressive strength increased when the gypsum was added to cement clinker. Gypsum in cement not only plays a role in regulating setting time, but also plays a positive role in the development of compressive strength(e.g., Cui, Gu, Wang, Lan and Jia (2005)). Secondly, the compressive strength increased first and then decrease with the increase of the amount of manganese sulfate. The compressive strength of manganese sulfate increased at 25%, the compressive strength was basically the same at 50%, and the compressive strength decreased at 75% and 100% compared with pure gypsum cement paste. It is because the concentration of SO_4^{2-} will be increased in the liquid phase of cement paste with the increase of manganese sulfate replacement, which promoted the formation of

ettringite. The volume will expand when the ettringite content exceeds the threshold, which will reduce the compressive strength of the cement. Therefore, a certain amount of manganese sulfate will promote cement hydration and increase the strength of cement when it was replaced gypsum.

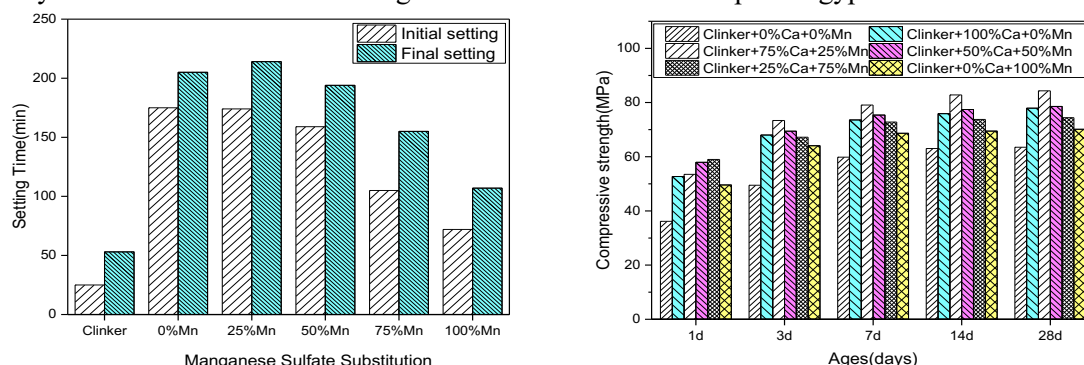


Figure 1 Setting time (left), Figure 2 Compressive strength (right)

3.3 XRD

The XRD patterns of cement paste at 1d and 28d are shown in Figure 3. The most prominent peaks in the hydrated cement were those of unhydrated minerals and hydration products. The peaks of unhydrated minerals were those of tricalcium silicate and dicalcium silicate, the peak of tricalcium aluminate was not found, because it was already reacted. The peaks of hydration products were those of portlandite in the cement hydration process. The peaks of calcium hydroxide in the XRD patterns were changed when the manganese sulfate was added to cement. It can be seen that the law of calcium hydroxide peaks in the XRD patterns at 1 and 28 days is the same as that of the corresponding compressive strength. Secondly, it can be seen from the figure that the peaks of tricalcium silicate and dicalcium silicate were reduced when the gypsum was added to cement, the peaks of tricalcium silicate and dicalcium silicate first decrease and then increase with the increase of the replacement amount of manganese sulfate, which indicated that a certain amount of manganese sulfate will promote the hydration of tricalcium silicate and dicalcium silicate. Cement particles are coated with ettringite formed in the early stage with the increase of manganese sulfate replacement amount, which prevents cement hydration. These results indicate that a small amount of manganese sulfate can promote cement hydration, and more than a certain amount will have an inhibitory effect.

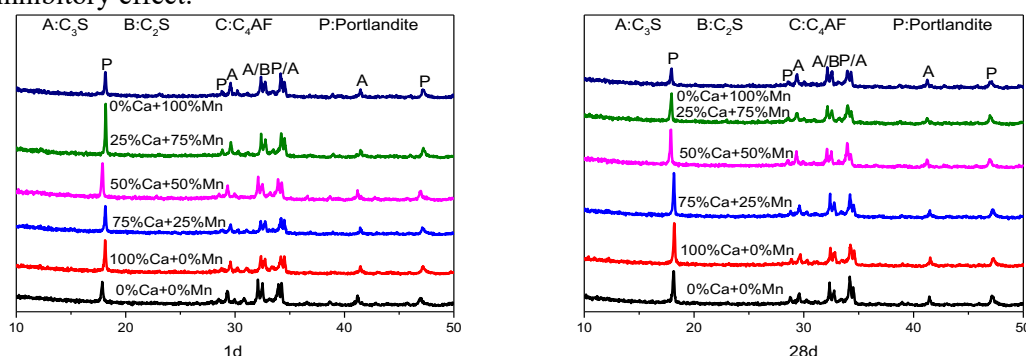


Figure 3 XRD patterns of hydrated cement pastes at 1d and 28d.

3.4 TGA

The TGA curves of cement paste at 28d are shown in Figure 4. There are three main endothermic peaks at room temperature to 1000°C. The weight loss 40°C at 40-180°C was caused by dehydration of the gel phase, such as Aft, C-S-H, etc. The weight loss at 410-450°C and 500-680°C was caused by the dehydration of Ca(OH)₂ and the decomposition of CaCO₃ (e.g., Meng, Ouyang, Fu, Niu and Ma (2021), Liu, Tan and He (2019)). The CH content calculated according to literature (e.g., Zhang, Ma, Wu, Jin and Wang (2022)) is given in Figure 5. The CH content is 17.90%, 17.08%, 16.38%, 15.63% and 14.96% respectively when the replacement amount of manganese sulfate is 0%, 25%, 50%, 75% and 100%, which can be seen that the content of CH decreased.

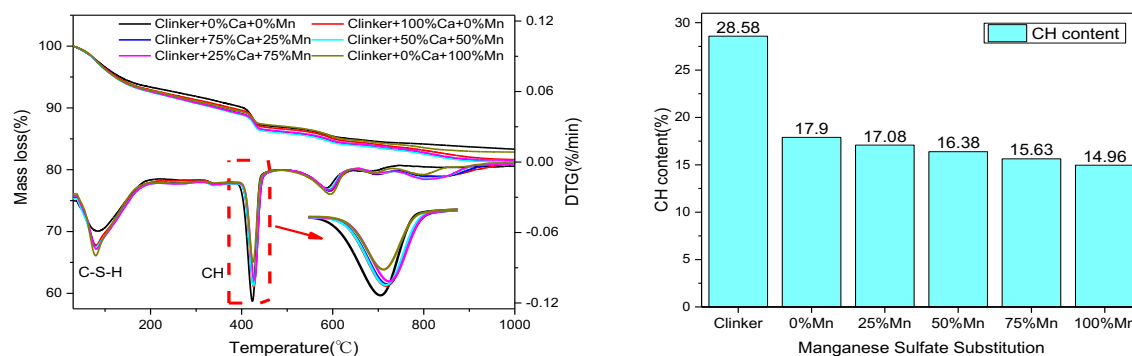


Figure 4 TGA of cement paste samples at 28d(left), Figure 5 CH content of cement paste(right)

3.5 Effect of pH on Cr^{6+} Leaching

The dissolution of Cr(VI) at 28d under different acetic acid contents is shown in Figure 6. The dissolution curves of chromium(VI) are similar and the dissolution of chromium(VI) was decreased with the increase of the replacement amount of manganese sulfate, these indicate that the chromium(VI) had been reduced by manganese ion in the process of cement hydration. Thus, this is very effective to replace gypsum with manganese sulfate to reduce the content of chromium(VI) in cement. According to the remaining hexavalent chromium in the cement slurry, the reduction rate of manganese sulfate to hexavalent chromium in the cement slurry is calculated. The total dissolution amount of chromium(VI) is 1404, 1048, 764, 528 and 416 mg/kg respectively when the amount of manganese sulfate replacing gypsum is 0%, 25%, 50%, 75% and 100%, while the total dissolution amount of clinker is 1516 mg/kg. The reduction efficiency of chromium(VI) were 7.4%, 30.9%, 49.6%, 65.2%, 72.6% respectively in Figure 7.

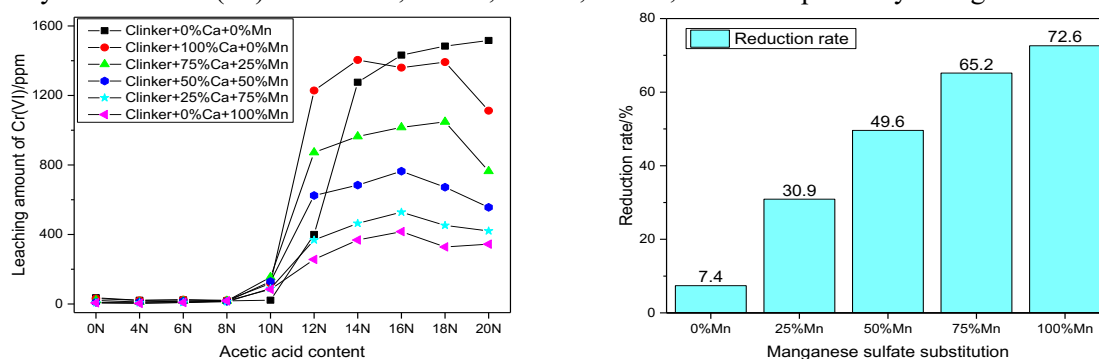


Figure 6 Release of Cr(VI) against the pH(left), Figure 7 Reduction rate(right)

4. Conclusions

Manganese sulfate can reduce its Cr(VI) reduction efficiency in water. It is used to replace gypsum in cement to increase its Cr(VI) reduction efficiency. It is found that manganese sulfate can adjust setting time, increase strength and increase its Cr(VI) reduction efficiency after replacing gypsum, which provides a theoretical basis for better Cr(VI) reduction of manganese sulfate.

References

- Nocuń-Wczelik, W., Golonka, P., and Malata, G. (2014) "The studies of the effect of sulfates added as chromium (VI) reducers in portland cement", *Journal of Thermal Analysis and Calorimetry*, 118, 59-66
- Samet, B., and Sarkar, S. L. (1997) "The influence of calcium sulfate form on the initial hydration of clinkers containing different alkali combinations", *Cement and concrete research*, 27(3), 369-380
- Cui S P, Gu X C, Wang Z M, Lan M Z, and Jia B S. (2005) "Effects of Different Kinds of Gypsum on Properties of Portland Cement", *Cement Technology*, 02:29-32
- Meng, S., Ouyang, X., Fu, J., Niu, Y., and Ma, Y. (2021) "The role of graphene/graphene oxide in cement hydration", *Nanotechnology Reviews*, 10(1), 768-778
- Liu, M., Tan, H., and He, X. (2019) "Effects of nano- SiO_2 on early strength and microstructure of steam-cured high volume fly ash cement system", *Construction and Building Materials*, 194, 350-359
- Zhang, T., Ma, B., Wu, S., Jin, Z., and Wang, J. (2022) "Mechanical properties and hydration process of steel slag-cement binder containing nano- SiO_2 ", *Construction and Building Materials*, 314, 125660

Study on MSWI fly ash solidifiers based on product composition design

Qing Wang¹, Qiang Zhang^{2*}, Xinrui Wang³ and Zhaoyang Ding⁴

¹ School of Materials Science and Engineering, Shenyang Jianzhu University, Shenyang, China

Email: wangqingmxy@126.com

² School of Materials Science and Engineering, Shenyang Jianzhu University, Shenyang, China

Email: 863261770@qq.com

³ School of Materials Science and Engineering, Shenyang Jianzhu University, Shenyang, China

Email: 994987029@qq.com

⁴ School of Materials Science and Engineering, Shenyang Jianzhu University, Shenyang, China

Email: smallnew69@126.com

ABSTRACT

Municipal solid waste incineration (MSWI) fly ash contains toxic heavy metals. In this study, solidifiers based on MSWI fly ash were prepared by alkali excitation (hereinafter referred to as solidified matrices), focusing on the effects of $n(\text{SiO}_2)/n(\text{Al}_2\text{O}_3)$ and $n(\text{CaO})/n(\text{SiO}_2+\text{Al}_2\text{O}_3)$ ratio on the product composition, compressive strength and heavy metal ions (Pb^{2+} and Cd^{2+}) leaching performance. Experimental results shows that 20% and 35% of CaO content is the characteristic content of strength zone. when $n(\text{CaO})/n(\text{SiO}_2+\text{Al}_2\text{O}_3)$ is less than 0.25, the compressive strength will less than 10MPa, and the strength will rise with the increase of $n(\text{SiO}_2)/n(\text{Al}_2\text{O}_3)$. When $n(\text{CaO})/n(\text{SiO}_2+\text{Al}_2\text{O}_3)$ is 0.4, the strength is mainly affected by $n(\text{CaO})/n(\text{SiO}_2+\text{Al}_2\text{O}_3)$ and compressive strength will exceed 20MPa. XRD and FTIR shows that when $n(\text{CaO})/n(\text{SiO}_2+\text{Al}_2\text{O}_3)$ is less than 0.25, heavy metal ions are mainly cured by forming Friedel's salt, and gels in the solidified matrices was closer to the frame silicate structure. When $n(\text{CaO})/n(\text{SiO}_2+\text{Al}_2\text{O}_3)$ is larger than 0.4, heavy metal ions are mainly solidified by C-(A)-S-H. The larger $n(\text{CaO})/n(\text{SiO}_2+\text{Al}_2\text{O}_3)$ is, the less Friedel's salt is formed. And gels in this system is mostly chain-like and phyllosilicates. The curing efficiency of solidified matrices on Cd^{2+} is better than Pb^{2+} . When $n(\text{CaO})/n(\text{SiO}_2+\text{Al}_2\text{O}_3)$ exceeds 0.4, the curing efficiency of Cd^{2+} is stable reached 99.9%.

KEYWORDS: MSWI fly ash, Solidifier, Compressive strength, Heavy metal leaching

1. Introduction

In recent years, rapid urbanization and industrialization have resulted in an increasing amount of municipal solid waste and caused serious environmental problems. Statistics show that the domestic waste removal volume of Chinese cities in 2021 reached 320 million tons (Zhang et al., 2010). At present, composting, landfill and incineration are three commonly used methods to deal with municipal solid waste (Cheng et al., 2012). Incineration is the main way to deal with municipal solid waste, because it has advantages in volume and quality to reduce municipal solid waste (Krausova et al., 2016). The incineration of municipal solid waste will produce a large amount of toxic waste, and MSWI fly ash is one of the most important products. MSWI fly ash contains large amounts of heavy metals, chlorides, acids and other pollutants. In many countries, it is considered hazardous waste.

Compared with traditional curing methods such as cement curing (Shi, et al., 2009), chemical curing (Zhao, et al., 2002; Quina, M.J., Bordado, et al., 2010), extraction and separation of heavy metals curing, geopolymer curing is an excellent treatment method. Geopolymers were first proposed by Davidovits (Davidovits, 2011) in 1978. Geopolymers have the advantages of high early strength, corrosion resistance, good long-term stability, good impermeability and low heavy metal leaching concentration (Tang et al., 2015; Phair, et al. 2002).

In this study, MSWI fly ash was used as the main raw material, and different proportions of mineral regulators were added to adjust the oxide composition to control the performance of solidified matrices. And the curing efficiency of heavy metal was discussed.

2. Materials and methods

2.1 Raw materials

Solidified matrices was fabricated by mixing MSWI fly ash (Shenyang, Liaoning, China), Blast furnace slag powder (Lingshou, Hebei, China), Metakaolin (Lingshou, Hebei, China) and an alkaline activator solution, which was a mixture of sodium silicate and NaOH. Table 1 illustrates the chemical compositions of raw materials. It needs to be stated that the MSWI fly ash comes from Shenyang,China.

Table 1 The main chemical composition of raw materials(%)

| Raw materials | CaO | SiO ₂ | Al ₂ O ₃ | Na ₂ O | K ₂ O | Fe ₂ O ₃ | MgO | Cl | Others |
|---------------|-------|------------------|--------------------------------|-------------------|------------------|--------------------------------|------|-------|--------|
| MSWI fly ash | 38.31 | 3.33 | 1.00 | 6.10 | 7.40 | 0.73 | 2.10 | 29.26 | 11.77 |
| Metakaolin | 1.43 | 57.61 | 34.41 | 2.20 | 1.63 | 0.67 | 0.80 | 0.06 | 1.19 |
| Slag | 36.99 | 31.53 | 16.45 | 0.80 | 0.71 | 1.04 | 7.80 | 0.07 | 4.61 |

2.2 Experimental methods

The experiment on the leaching of heavy metal ions was performed in accordance with the national standard HJ/T300. The leaching concentration of heavy metal ions was in accordance with the national standard GB/T15555.2. Solidified matrices was tested for compressive strength according to DL/T5126.A Powder X-ray diffraction (XRD) experiment was performed on an XRD-7000 X-ray diffractometer operated at 36 kV and 20 mA by using the Cu Ka radiation ($\lambda = 0.15406$ nm). The Fourier transform infrared spectroscopy (FT-IR) of the sample was measured via an FTS 2000.

2.3 Preparation of solidified matrices

NaOH and solid instant Na₂SiO₃ were mixed according to a ratio to prepare an alkali activator. Mixing the silico-alumina raw materials and alkali activator with continue stirring until the slurry has a certain fluidity and viscosity. Then pour the slurry into the mortar mould (40mm×40mm×160mm). The mold was removed after curing for 24 hours. Solidified matrices cured to age in a standard curing room.

2.4 Calculation curing efficiency

The curing efficiency(φ) of heavy metal ions in the solidified matrices is calculated by formula (1).

$$\varphi = \frac{A_0 - A_1}{A_0} \times 100\% \quad (1)$$

A_0 —Leaching concentration of heavy metal ions of raw material before solidified, mg/L; A_1 —Leaching concentration of heavy metal ions of solidified matrices, mg/L。

3. Results and discussion

3.1 Compressive strength of Solidified matrices

The modulus of alkali activator was set as 1.2, the dosage of alkali activator was set as 15% of powder, the minimum dosage of fly ash was set as 50%. The compressive strength is shown in Fig.1.

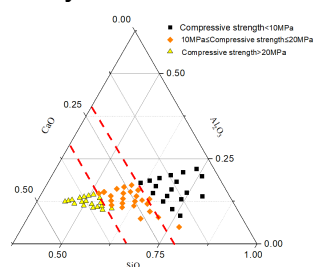


Fig.1 Compressive strength in ternary oxide system

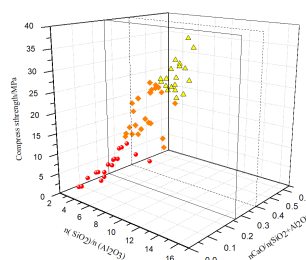


Fig.2 Compressive strength of solidified matrices

As can be seen from Fig.1, When the strength of the solidified matrices is greater than 20MPa, composition of CaO is 35%~45%, SiO₂ is 40%~60%, and Al₂O₃ is 10%~15%. While the strength is between 10MPa and 20MPa, CaO is from 20% to 35%, SiO₂ is 50%~70%, and Al₂O₃ is between 5%~20%. Once the strength of the solidified matrix is less than 10MPa, the CaO composition is less than 20%. Strength distribution of solidified matrices in the ternary system significantly with the change of CaO content. 20% and 35% is the characteristic content of strength zone. Fig.2 shows the relationship between strength and molar ratio of oxides. Compressive strength less than 10MPa, while $n(\text{CaO})/n(\text{SiO}_2 + \text{Al}_2\text{O}_3)$ is less than 0.25. If it is more than 0.4, compressive strength will exceed 20MPa.

The data points in Fig. 2 were fitted with a surface through origin, and the fitted surface was projected on the bottom surface of the three-dimensional figure to get Fig.3. Fig.3 shows the plot of compressive strength fitting for solidified matrices. The compressive strength of area below line a-1 ($n(\text{CaO})/n(\text{SiO}_2+\text{Al}_2\text{O}_3) < 0.15$, $n(\text{SiO}_2)/n(\text{Al}_2\text{O}_3) < 5.0$) is less than 5MPa. With the increase of $n(\text{SiO}_2)/n(\text{Al}_2\text{O}_3)$, the strength increased, but not more than 10MPa. Because the products were mainly N-A-S-H gels, and its strength developed slowly. With the increase of $n(\text{CaO})/n(\text{SiO}_2+\text{Al}_2\text{O}_3)$, the compressive strength of area between A-1 and A-2 basically remained close to each other with the increase of $n(\text{SiO}_2)/n(\text{Al}_2\text{O}_3)$. The main reason was that a little of C-A-S-H gels began to form in the product, and the strength was improved, but the overall N-A-S-H gels was still dominant. When $n(\text{CaO})/n(\text{SiO}_2+\text{Al}_2\text{O}_3)$ increases to 0.25 (line b), the strength increases with the change of $n(\text{SiO}_2)/n(\text{Al}_2\text{O}_3)$, which is mainly due to the increase of CaO content. Active SiO_2 is more conducive to the formation of more C-(A)-S-H gels, so the strength increases significantly. However, when $n(\text{CaO})/n(\text{SiO}_2+\text{Al}_2\text{O}_3)$ increases to exceed 0.25 (such as line c), the strength growth is mainly influenced by $n(\text{CaO})/n(\text{SiO}_2+\text{Al}_2\text{O}_3)$, and the influence of $n(\text{SiO}_2)/n(\text{Al}_2\text{O}_3)$ on the strength has no obvious rule, because the products are mainly C-(A)-S-H gels.

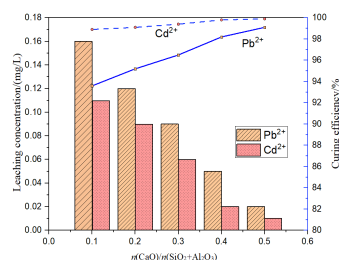
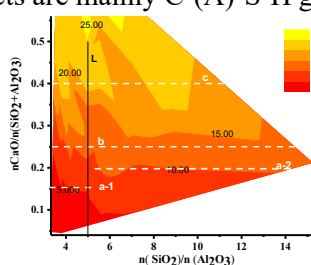


Fig.3 Plot of intensity fitting for solidified matrices Fig. 4 Leaching concentration of heavy metal ions

3.2 Heavy metal leaching of Solidified matrices

5 points were selected on line L ($n(\text{SiO}_2)/n(\text{Al}_2\text{O}_3)$ is 5.0) in Fig.3 to study the effect of $n(\text{CaO})/n(\text{SiO}_2+\text{Al}_2\text{O}_3)$ ratio on heavy metal leaching concentration. It can be seen from Fig.4 that the leaching concentration of heavy metals in solidified matrices gradually decreased with the increase of $n(\text{CaO})/n(\text{SiO}_2+\text{Al}_2\text{O}_3)$. When $n(\text{CaO})/n(\text{SiO}_2+\text{Al}_2\text{O}_3)$ is 0.5, the leaching concentration of heavy metals is the lowest. The leaching concentrations of Pb^{2+} and Cd^{2+} are 0.02mg/L and 0.01mg/L respectively. The curing efficiency of solidified matrices on Cd^{2+} is better than Pb^{2+} . When $n(\text{CaO})/n(\text{SiO}_2+\text{Al}_2\text{O}_3)$ exceeds 0.4, the curing efficiency of Cd^{2+} is stable. The main reason is that there is a large amount of C-(A)-S-H gels in the product. This gels coat the unreacted raw material particles so the solidified matrices is denser. As a result the heavy metal leaching concentration reduced. The curing efficiency of Pb^{2+} and Cd^{2+} can reach more than 93.6% after curing by geopolymers.

3.3 Characteristics of solidified matrices

The XRD patterns of solidified matrices were exhibited in Fig.5. The main substances in solidified matrices were calcite (CaCO_3), Halite (NaCl), and Friedel's salt. In the XRD pattern there is a broad scattering peak appearing at about $20^\circ \sim 40^\circ$. The widened peak area increases with the increase of $n(\text{CaO})/n(\text{SiO}_2+\text{Al}_2\text{O}_3)$, indicating that C-(A)-S-H of solidified matrices has increased. The characteristic peaks of Friedel's salt in XRD patterns for 2θ from 10° to 12° (Jiang et al.,2022). As $n(\text{CaO})/n(\text{SiO}_2+\text{Al}_2\text{O}_3)$ increases, the characteristic peaks of Friedel's salt shifted to low angles and gradually disappeared. Interlayer anion exchange between Cl^- and heavy metal gradually decreased. Heavy metal ions are solidified mainly by forming Friedel's salt when $n(\text{CaO})/n(\text{SiO}_2+\text{Al}_2\text{O}_3)$ is less than 0.25. When $n(\text{CaO})/n(\text{SiO}_2+\text{Al}_2\text{O}_3)$ is larger than 0.4, heavy metal ions are mainly coated by C-(A)-S-H gels. The larger $n(\text{CaO})/n(\text{SiO}_2+\text{Al}_2\text{O}_3)$ is, the less Friedel's salt is formed.

The chemical bonds of the solidified matrices were analyzed using FTIR. The main characteristic peak of each spectral line (the asymmetric stretching peak of Si-O-Si) appears in the area of $1112\text{ cm}^{-1} \sim 1091\text{ cm}^{-1}$ (band d). With the increase of $n(\text{CaO})/n(\text{SiO}_2+\text{Al}_2\text{O}_3)$, band d moves to the high wave number, and the increase of peak area indicates that Si-O-Si of the system increases (Zhao et al.,2006). Figure 7 shows the deconvolution analysis of infrared characteristic peaks around 1100 cm^{-1} . Absorption band of SiQ^4 is near 1170 cm^{-1} , and absorption band in the range of $1109 \sim 1046\text{ cm}^{-1}$ and $962 \sim 943\text{ cm}^{-1}$ corresponds to SiQ^3 and

SiQ², respectively. SiQ⁰ absorption band appears around 850cm⁻¹. With the increase of $n(\text{CaO})/n(\text{SiO}_2+\text{Al}_2\text{O}_3)$, the absorption band of SiQ³ becomes wider, indicating that gels is mostly chain-like and phyllosilicates. With the decrease of CaO content, the specific gravity of SiQ⁰ absorption band decreased, indicating that gels in the solidified matrices was closer to the frame silicate structure.

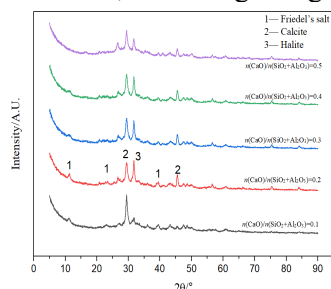


Fig.5 XRD patterns

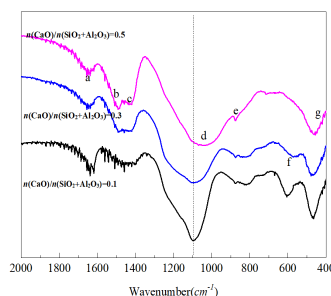


Fig.6 FTIR spectra

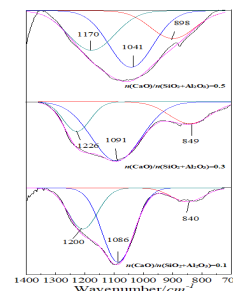


Fig.7 Deconvoluted bands spectra

4. Conclusions

The relations between oxide composition, compressive strength and leaching behaviour of MSWI fly ash solidified matrices were investigated. The design system of MSWI fly ash solidified matrices was established by product composition and strength distribution.

20% and 35% CaO content is the characteristic content for solidified matrices. When $n(\text{CaO})/n(\text{SiO}_2+\text{Al}_2\text{O}_3)$ is less than 0.25, the compressive strength will less than 10 MPa, and strength will rise with the increase of $n(\text{SiO}_2)/n(\text{Al}_2\text{O}_3)$. With the increase of $n(\text{CaO})/n(\text{SiO}_2+\text{Al}_2\text{O}_3)$, the change of strength is mainly affected by $n(\text{CaO})/n(\text{SiO}_2+\text{Al}_2\text{O}_3)$, and the influence of $n(\text{SiO}_2)/n(\text{Al}_2\text{O}_3)$ on the strength has no obvious rule.

Solidified matrices for heavy metal ions are solidified mainly by forming Friedel's salt when $n(\text{CaO})/n(\text{SiO}_2+\text{Al}_2\text{O}_3)$ is less than 0.25, When $n(\text{CaO})/n(\text{SiO}_2+\text{Al}_2\text{O}_3)$ is larger than 0.4, heavy metal ions are mainly coated by C-(A)-S-H coating. With the increase of $n(\text{CaO})/n(\text{SiO}_2+\text{Al}_2\text{O}_3)$, gels in solidified matrices closer to the chain-like and phyllosilicates silicate structure.

Acknowledgements

The authors acknowledge the financial support provided by the Applied Basic Research Program of Liaoning Province (2022JH2/101300118), Research and Development Projects of the Ministry of Housing and Urban-Rural Development (2022-K-087).

References

- Li, Y. (2022) "Practice of the Green, Low-Carbon and Circular Concept --Optimizing the Treatment of Municipal Solid Waste", *Administration Reform*, 2022(11):62-70
- Cheng H., Hu Y. (2012) "Mercury in Municipal Solid Waste in China and Its Control: A Review", *Environmental Science & Technology*, 46(2):593-605.
- Krausova, K., et al. (2016) "Glass ceramics and mineral materials for the immobilization of lead and cadmium. " *Ceramics International* 42.7:8779-8788.
- Shi, H.S., Kan, L.L. (2009) "Leaching behavior of heavy metals from municipal solid wastes incineration (MSWI) fly ash used in concrete", *Journal of Hazardous Materials*, 164(2-3):750-754.
- Zhao, Y., Song, L., Li, G. (2002) "Chemical stabilization of MSW incinerator fly ashes", *Journal of Hazardous Materials*, 95(1-2):47-63.
- Quina, M.J., Bordado, J C M, Quinta-Ferreira R M. (2010) "Chemical stabilization of air pollution control residues from municipal solid waste incineration", *Journal of Hazardous Materials*, 179(1-3):382-392.
- Davidovits, J. . (2011). *Geopolymer Chemistry and Applications*.
- Tang, L. , Huang, Q. , Wang, Q. , Zhang, H. , & Shi, X. . (2015). "Research on corrosion resistance and relevant mechanism of geopolymer concrete and ordinary concrete in the same sulfate solution". *Materials Review*.
- J., W., Phair, et al. (2002). "Characterization of fly-ash-based geopolymeric binders activated with sodium aluminate". *Industrial & Engineering Chemistry Research*, 41(17), 4242-4251.
- Jiang, G. , Min, X. , Ke, Y. , Liang, Y. , Yan, X. , & Xu, W. , et al. (2022). "Solidification/stabilization of highly toxic arsenic-alkali residue by mswi fly ash-based cementitious material containing friedel's salt: efficiency and mechanism". *Journal of hazardous materials*(Mar.5), 425.
- Zhao, W. , Zhang, Q. , & Peng, C. . (2006). "Ftir spectra for molecular structure of wollastonite". *Journal of the Chinese Ceramic Society*.

An Experimental Study of Sulfur and Chlorine Stripping from Cement Hot Meal

A.J. Damoe^{1*}, X. Wang¹, G. Cafaggi¹, T.E. Nielsen^{1,2}, M.N. Pedersen², F.J. Frandsen¹, P.A. Jensen¹
and H. Wu¹

¹ Technical University of Denmark, Kongens Lyngby, Denmark
Email: ajp@kt.dtu.dk, xiwang@kt.dtu.dk, giovanni.cafaggi@gmail.com, ff@kt.dtu.dk, paj@kt.dtu.dk,
haw@kt.dtu.dk

² FLSmidth A/S, Valby, Denmark
Email: Tobias.EchbergNielsen@FLSmidth.com, MNPE@FLSMIDTH.COM

ABSTRACT

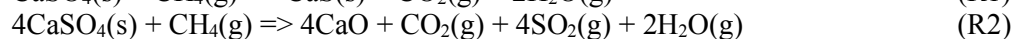
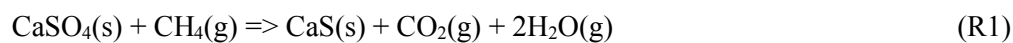
This work explores the feasibility of developing a new process, as an alternative to the current bypass system, for stripping S, Cl and K from cement hot meal. Laboratory scale stripping experiments have been conducted in a horizontal tube reactor. The effect of the process conditions (gaseous atmosphere, temperature, time) on the removal of S, Cl and K from a cement hot meal collected from a full-scale plant has been investigated. It was hypothesized that sulfur removal can be enhanced in reducing conditions, by converting CaSO₄(s) to SO₂(g), while Cl (and K) removal is mainly due to evaporation of KCl. Experiments were carried out in the temperature range of 800 – 1100 °C and at residence times 10 – 60 minutes. The gaseous atmosphere used was either air, or 1 – 1.8% CH₄ (with N₂ for balance). During the experiments, a gas analyzer was used to monitor the release of SO₂ during the sample conversion. After the experiments, the solid residues were collected and analyzed by, e.g., ICP-OES / IC for elemental composition, and XRD for determination of crystal phases. The experimental results revealed that a reducing atmosphere promotes the release of S from the hot meal. Substantial release of S (~40%), Cl (~40%) and K (~20%) from the hot meal was obtained at 900 °C, 30 minutes and 1% CH₄ conditions. At higher temperatures, deviation of S release calculated from integration of SO₂ and ICP-OES, respectively, indicated that other forms of sulfur (e.g. SO₃ or H₂S) released. Increasing the CH₄ concentration from 1% to 1.8% slightly decreased S release from the hot meal at 900-1100 °C, probably due to over-reduction forming solid phase CaS(s).

KEYWORDS: *Cement Hot Meal, Sulfur, Chlorine, Stripping*

1. Introduction

Cement production is a highly energy intensive process which has seen a growing interest in a shift to the use of alternative fuels, leading to reduced fuel expenses and CO₂ emissions. One of the issues connected with the use of alternative fuels, such as Solid Recovered Fuel (SRF), is an increased input of sulfur and chlorine into the pyro process. The circulation and accumulation of S and Cl bearing compounds between rotary kiln and preheating system result in deposit formation, corrosion and has an impact on the cement quality. One of the current solutions to address this issue is using a bypass to remove a fraction of the Cl from the system (Cortada Mut et al., 2015), but this solution has a significant impact on the efficiency of the process, leading to an increased fuel consumption, and the effect on S removal is limited. The present work explores the feasibility of developing a new process, as a replacement of the current by-pass system, to remove sulfur, chlorine and alkali from cement hot meal. In the hot meal, sulfur is mainly present as CaSO₄(s). A fraction of the sulfur can potentially be stripped by reductive decomposition of CaSO₄. The reductive decomposition of CaSO₄ has been widely studied in relation to chemical-looping combustion. CaSO₄ can be reduced to CaO and CaS, which occur with a reducing atmosphere containing CO, H₂, and/or CH₄ (Cortada Mut et al., 2015; Song et al., 2008). The reductive decomposition of CaSO₄ with

CH₄ may occur according to the reactions R1 and R2 below. The objectives of the current work are to examine the potential of sulfur, chlorine and potassium stripping from cement hot meal by mean of laboratory scale thermal stripping experiments using reducing conditions and temperature range 800 – 1100 °C.



2. Methodology

A new concept for stripping a fraction of hot meal for its content of S and Cl, thereby decreasing the total amount of S and Cl in the cement plant, is proposed. The concept is based on the idea that a fraction of the hot meal can be extracted from the last preheater cyclone, before reaching the rotary kiln. The hot meal coming with a temperature of 850-900 °C will then meet a reducing gas, and the reducing gas will strip the S and Cl from the extracted hot meal, before the extracted hot meal enters the rotary kiln. There is an optimization aspect, since the aim is to find the best operational point with respect to stripping gas composition and mass of stripping gas/kg hot meal. Preliminary laboratory scale experiments have revealed that a reducing atmosphere promotes the release of S from hot meal (as compared to air), and a stripping gas composed of around 1%CH₄ (balanced with N₂) has proved promising for stripping of both S and Cl, with a maximum release of S around 900 °C. Cl (and K) release is independent of the applied atmosphere and mainly due to evaporation of KCl. The present experimental work focuses on evaluating further the effects of the process conditions (CH₄ concentration, temperature, time) on stripping of S, Cl and K from a cement hot meal. Laboratory scale thermal stripping experiments are conducted using CH₄ as a reducing agent at 800-1100 °C. Mixtures of model compounds (CaSO₄, SiO₂, K₂CO₃) are also subjected to stripping experiments, and subsequent XRD analysis, in order to better understand the release mechanisms.

2.1 Materials

The solid material used for the experiments is C5 hot meal (C5HM, coming from the 5th stage preheater cyclone in an industrial cement plant)). Mixtures of pure model compounds (CaSO₄, SiO₂, and K₂CO₃) are also used in the study. The inorganic composition of the C5HM is provided in Table 1.

Table 1: XRF analysis (dry basis) and LOI of C5 hot meal, wt% (dry basis)

| SiO ₂ | Al ₂ O ₃ | Fe ₂ O ₃ | CaO | MgO | Mn ₂ O ₃ | TiO ₂ | P ₂ O ₅ | K ₂ O | Na ₂ O | SrO | SO ₃ | Cl | LOI, 975C |
|------------------|--------------------------------|--------------------------------|-------|------|--------------------------------|------------------|-------------------------------|------------------|-------------------|------|-----------------|------|-----------|
| 19.44 | 4.77 | 2.70 | 61.11 | 1.73 | 0.06 | 0.29 | 0.10 | 1.91 | 0.24 | 0.04 | 1.05 | 0.98 | 6.56 |

2.2 The horizontal tube reactor

The experimental setup consists of a gas supply system, an electrically heated horizontal tube reactor, and a flue gas sampling and treatment system. The maximum set temperature is 1200 °C. The oven is 95 cm in length and the ceramic reactor tube inside the oven has a diameter of 5 cm. At the inlet of the oven, a water cooled chamber is attached, and at the outlet a pressure gauge is placed. A PI-diagram of the experimental setup used is provided in Figure 1.

2.3 Experimental procedure

Experiments are carried out in the temperature range of 800 – 1100 °C and at residence times 10 – 60 minutes. The gaseous atmosphere used is either air, or 1 – 1.8% CH₄ (with N₂ for balance). During the experiments, gas analyzers (CO, CO₂, O₂, SO₂, NO) are used to monitor the sample conversion, including the release of SO₂. The principles of the experimental methodology are the same for the series of experiments conducted. The oven is heated to the desired temperatures. A ceramic crucible containing the solid sample of interest (typically 10g of hot meal, or 1g of model compounds) is placed in the water-cooled chamber and the reactor tube is sealed. The gas is then switched on and adjusted to the desired

composition and flowrate. When the system is stabilised, the crucible is quickly pushed into the oven by a rod attached to the end of the crucible. After a desired residence time, the gas is switched to nitrogen and the crucible is quickly pulled out of the oven to the water cooled chamber. The crucible is left in the water-cooled chamber for 10 min with nitrogen flow, in order to cool it down to ambient temperature before it is taken out, weighed and the residual sample collected for chemical analysis (ICP-OES / IC for elemental composition, and XRD for crystal phases). The release of S/Cl/K can be calculated based on ICP-OES analysis of solid material, or based on integration of SO₂ gas analysis, respectively.

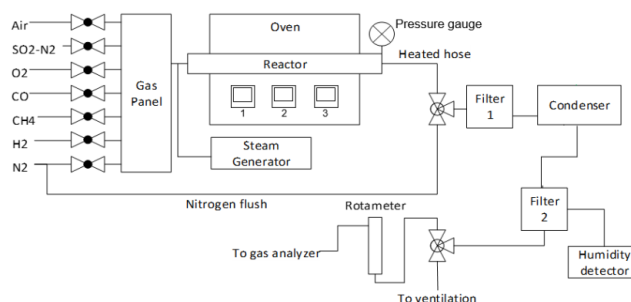


Figure 1: PI-diagram of the experimental set-up.

3. Results and discussion

3.1 Effect of temperature, residence time and CH₄ concentration on S/Cl/K release of C5HM

Figure 2 shows the release of S, Cl, K and Ca from C5HM in 1% CH₄ atmosphere as a function of temperature and residence time, respectively.

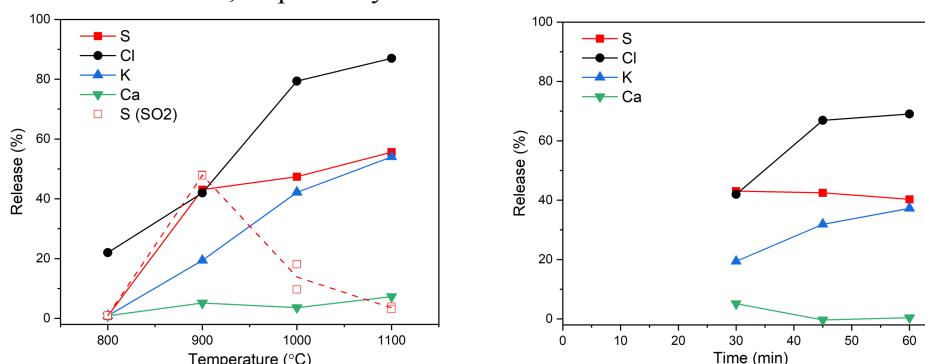


Figure 2: Release of S, Cl, K and Ca from C5HM. Conditions: 5Nl/min gas flow, 10g C5HM, 1% CH₄ in N₂. Solid lines: The quantification of release is based on ICP-OES / IC analysis of solid residue (one experiment at each temperature or residence time, indicated by the filled data points). Dotted line (S (SO₂) mean) and unfilled data points: The S release is calculated from SO₂ integration (based on one or two experiments at each temperature). Left figure: Fixed residence time (30 minutes). Right figure: Fixed temperature (900 °C).

It can be seen from Figure 2 (left) that there is a substantial release of ~40% S, ~40% Cl and ~20% K at 900 °C, and there is a significant deviation of S release calculated by ICP-OES and SO₂ integration at 1000 °C and 1100 °C. The latter may indicate that the sulfur escapes the reaction system in other forms than SO₂, such as H₂S or SO₃, at higher temperatures. It can be seen from Figure 2 (right) that increasing residence time from 30 minutes to 60 minutes increases the release of Cl and K, but not S. Increasing CH₄ concentration from 1% to 1.8% slightly lowers the SO₂ release (results not shown). This may suggest the possibility of over-reduction according to Reaction R1.

3.2 Investigation of CaSO₄ decomposition

Figure 3 shows the XRD patterns of mixtures of model compounds (CaSO₄, SiO₂, K₂CO₃) subjected to release experiments in 1% CH₄. The normalized mass loss (%) of the compounds after release

experiments in 1%CH₄ or N₂ is also shown. It can be seen that there is no decomposition of pure CaSO₄ in 1%CH₄ at 1000 °C (no other species are detected); while the presence of CaS at sample '50% CaSO₄+50% SiO₂' at 1100C, suggests the possibility of over-reduction. The addition of K₂CO₃ to some extent hinders the stripping of S by forming K₂SO₄, while K₂CO₃ has disappeared due to decomposition.

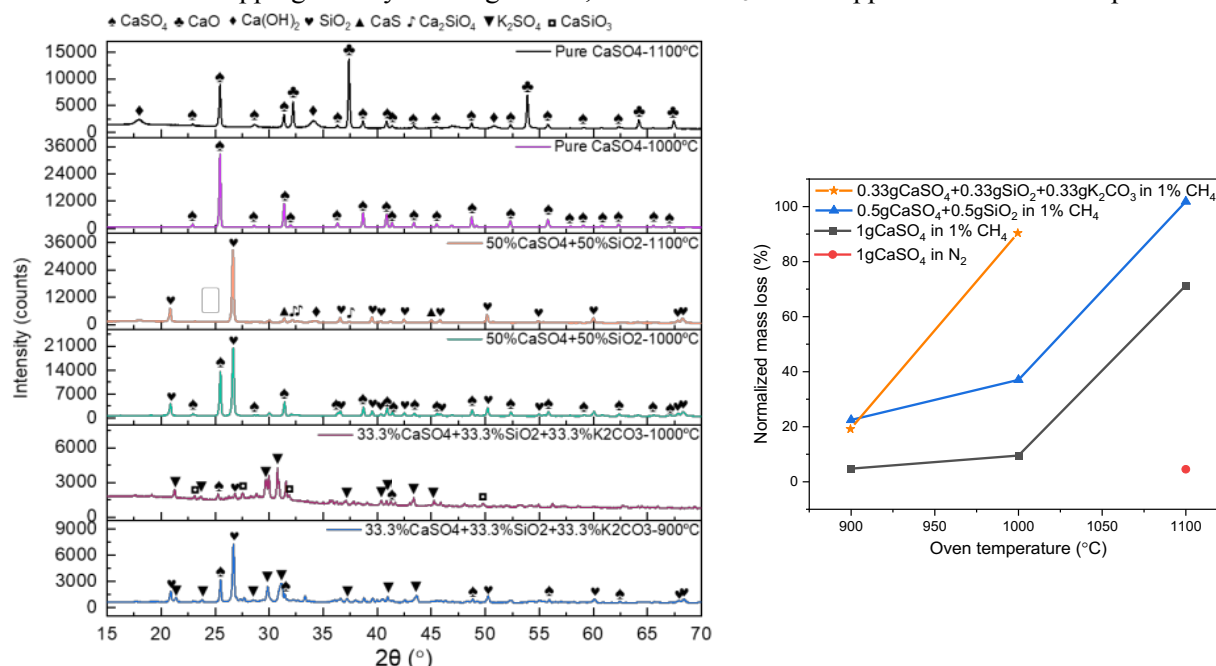


Figure 3: Left: XRD pattern of mixtures of model compounds (CaSO₄, SiO₂, K₂CO₃) subjected to release experiments in 1% CH₄. Right: Normalized mass loss (% of theoretical mass loss due to decomposition of CaSO₄ and K₂CO₃) of mixed model compounds after release experiments in 1%CH₄ or N₂. Release conditions: 5Nl/min gas flow, 1g material, temperature 900-1100 °C

4. Conclusions

Laboratory scale thermal stripping experiments have been conducted to examine the S, Cl and K stripping from C5 hot meal and model compounds (CaSO₄, CaSO₄, K₂CO₃). S removal from hot meal takes place by converting CaSO₄(s) to SO₂(g) at ~900 °C in a reducing atmosphere, and other species in hot meal promotes the decomposition of CaSO₄ (there is no decomposition of pure CaSO₄ at 1000 °C). Cl removal takes place by vaporization of KCl. ~40% S, ~40% Cl and ~20% K was released from C5 hot meal at 900 °C, 30 minutes and 1% CH₄ conditions. At higher temperatures, probably other forms of sulfur (e.g. SO₃ or H₂S) released. Increasing the CH₄ concentration from 1% to 1.8% slightly decreased S release from C5 hot meal at 900-1100 °C, probably due to over-reduction forming solid phase CaS(s). Increasing residence time from 30 minutes to 60 minutes increased Cl and K release but not S release at 900 °C. The addition of K₂CO₃ to model compounds hindered the stripping of S by forming K₂SO₄.

Acknowledgements

This work is part of the ProBu – Process technology for sustainable Building materials production – project (grant number: 8055-00014B), funded by Innovation Fund Denmark, FLSmidth A/S, ROCKWOOL International A/S and the Technical University of Denmark.

References

- Cortada Mut, M. D. M., Nørskov, L. K., Jappe Frandsen, F., Glarborg, P. and Dam-Johansen, K. (2015) "Review: Circulation of Inorganic Elements in Combustion of Alternative Fuels in Cement Plants", *Energy and Fuels*, 29(7): 4076-4099.
- Song, Q., Xiao, R., Deng, Z., Zhang, H., Shen, L., Xiao, J. and Zhang, M. (2008) "Chemical looping combustion of methane with CaSO₄ oxygen carrier in a fixed bed reactor", *Energy Conversion and Management*, 49(11): 3178-3187.

Effect of copper tailing powder on the hydration and mechanical properties of concrete under low atmospheric pressures

Y.B. Du¹, Z.G. Wu^{2*}, and Y. Ge³

¹ *Central Research Institute of Building and Construction Co., Ltd., MCC Group, Beijing, China*
Email: 915439482@qq.com

² *School of Civil Engineering, Tianjin University, Tianjin, China*
Email: 388560@qq.com

³ *School of Transportation Science and Engineering, Harbin Institute of Technology, Harbin, China*
Email: geyong@hit.edu.cn

ABSTRACT

Copper tailing in the plateau area brings serious pollution and ecological damage to the local area. In this laboratory study, the effects of copper tailing powder as a mineral admixture on the early hydration, compressive strength, chloride resistance, frost resistance and microstructure of concrete were investigated. The results indicated that the low atmospheric pressure had little effect on the early hydration heat and hydration heat evolution rate of cement paste. The addition of copper tailing powder decreased hydration heat of cement paste, but it had no significant effect on the induction period of cement paste. The compressive strength, chloride and frost resistance of concrete cured in low atmospheric pressure environments decreased. Moreover, the existence of copper tailing powder could make the microstructure of concrete loose, and finally decreased the compressive strength, chloride and frost resistance of concrete. The decrement increased with the content of copper tailing powder. This research provides the reference for application of copper tailing to produce green concrete in the plateau area.

KEYWORDS: *concrete, copper tailing powder, hydration, microstructure, frost resistance*

1. Introduction

Tibet Plateau is endowed with rich copper resources. The identified copper resources in Tibet are around 53 Mt (Tang et al., 2021). With the development of copper resources in the Tibet, a large amount of tailings has been produced. Up to now, the copper tailings in Tibet has reached about 6 Mt. In fact, only small part of copper tailings is utilized, and most of the copper tailings is piled in tailings pond (Huang et al., 2012). The tailings pond occupies a lot of arable land. On the other hand, the copper tailings contain large number of heavy metals, such as Fe, Pb, Cd, Zn and Cu, posing a potential threat to the surrounding environment. Thus, it is urgent to utilize the copper tailings in Tibet. Copper tailing can be used as admixtures in concrete (Ghazi et al., 2022). This paper studied the influence of copper tailing powder on the hydration, compressive strength, chloride resistance, frost resistance and microstructure of concrete in the normal atmospheric pressure area (NAPA) and low atmospheric pressure area (LAPA).

2. Experiments

2.1 Materials

Ordinary Portland cement (P·O 42.5) supplied by the Jidong Cement Co., Ltd (Tangshan, China) was used in this study. Copper tailing powder (CTP) was produced by Huatailong Mining Development Co., Ltd (Tibet, China). Fine aggregate is river sand with a fineness modulus of 3.0. Coarse aggregate is crushed limestone with a maximum size of 20 mm (continuous grading).

2.2 Specimens preparation and Test methods

In order to study the influence of air pressure on the hydration and mechanical properties of concrete with CTP, concrete specimens were prepared in Beijing (China, 31.2 meters above the sea level, atmospheric pressures is 99.86 kPa) and Tibet (China, 3658 meters above the sea level, atmospheric pressures is 65.23

kPa). For all specimens in this study, the water to cement (W/C) ratio was 0.41, the cementing agent content, including the cement and CTP, was 430 kg/m^3 , sand content was 765 kg/m^3 , Coarse aggregate content was 1010 kg/m^3 . The contents of CTP in cementing agent were 0%, 10%, 20% and 30%. The raw materials were mixed according to Chinese standard GB/T 50080-2016. After that fresh concrete was cast in steel molds, cured at room temperature and humidity ambient for 24 h. Then these samples were demolded and placed into a curing room ($20 \pm 1 \text{ }^\circ\text{C}$, $\text{RH} \geq 98\%$) for 7 days. Finally, they were removed and kept in an outdoor natural environment until the test age. The compressive strength, rapid chloride permeability test (RCPT) and freeze-thaw cycle test (FTCT) were performed according to Chinese standard GB/T50082-2009. The hydration process and microstructure of cement paste (W/C=0.41) were tested by a TAM Air 8 and EVO-MA10, respectively.

3. Results and Discussions

3.1 Heat release during early hydration reactions

Fig. 1 shows the hydration heat flow and cumulative hydration heat of cement paste with CTP. As show in Fig. 1 (a) and (b), in NAPA (Beijing), the exothermic curve of cement paste with CTP is similar to that of cement paste without CTP. There are two main exothermic peaks: The first exothermic peak can be assigned to the hydration reaction of tricalcium aluminate and gypsum to produce ettringite. The second exothermic peak can be assigned to the hydration reaction of tricalcium silicate. From Fig. 1 (a), It can be observed that the value of the second exothermic peak decreases with the increase of CTP content. This may due to the low reactivity of CTP and the reduction of cement in compound cementitious system. In addition, it also can be found from Fig. 1 (a) that the position of the second exothermic peak of the cement paste with or without CTP is basically unchanged. This indicates that the use of CTP cannot significantly change the induction period of cement paste.

It can be seen from Fig. 1 (b) that the cumulative hydration heat of the cement paste decreases with the increase of CTP content. This means that adding CTP to cement paste can reduce the risk of thermal cracking caused by the cement hydration. As show in Fig. 1 (c) and (d), in LAPA (Tibet), the use of CTP reduces the cumulative hydration heat and the height of the second exothermic peak, but not significantly changes the position of the second exothermic peak. From Fig. 1, it can be clearly seen that the hydration heat flow and cumulative hydration heat of cement paste in NAPA and LAPA are basically consistent. This indicates that the low air pressure has little effect on the early hydration of cement paste.

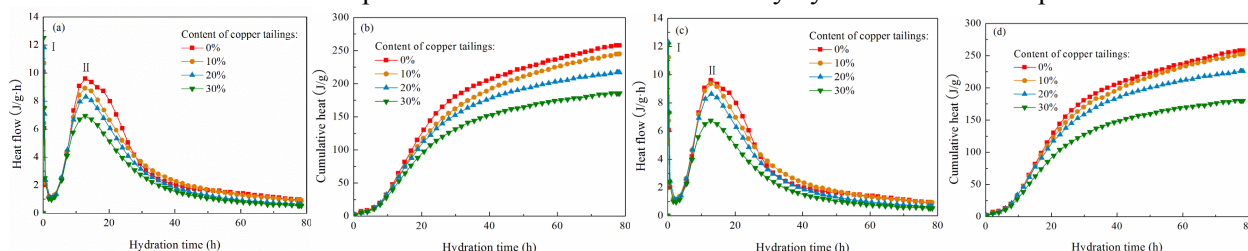


Fig. 1 Hydration of cement paste (a) heat flow in NAPA; (b) cumulative heat in NAPA; (c) heat flow in LAPA (d) cumulative heat in LAPA

3.2 Compressive strength

As show in Fig. 2 (a) and (b), both in NAPA and the LAPA, the compressive strength of concrete increased with the curing age. This increase in the strength can be attributed to the hydration of cement. Furthermore, it is worth noting that if CTP was used as partial cement replacement in concrete, the compressive strength decreased with the increase of the CTP content. This may be related to the fact that the CTP has lower activity than cement. The replacement of cement with CTP reduces cement content in concrete, so as to decrease the hydration products in specimens, and finally reduces the compressive strength of concrete. From Fig. 2 (a) and (b), it can be seen that for the same CTP content and curing age, the compressive strength of concrete in LAPA is lower than that in NAPA. In LAPA, the internal moisture of concrete is easy to evaporated to the environment, resulting in the decreasing of cement hydration degree, and thus the compressive strength of concrete decrease.

3.3 Permeability of concrete

As show in Fig. 2 (c), for concrete in NAPA, the charge passed of concrete increased from 2284 C to 2913 C with the CTP content increase from 0 % to 30%. In the LAPA, the charge passed increased from

2520 C, for the concrete containing 0 % CTP, to 3363 C for the concrete containing 30% CTP. These results imply that CTP can effectively increase the charge passed of concrete. CTP has low pozzolanic activity, thus the addition of CTP in concrete decreases the hydration products in specimens, increases the porosity and connected capillary channels, so as to increase the charge passed of concrete. From Fig. 2 (c), it can be seen that for the same CTP content, the charge passed of concrete in NAPA is lower than that in LAPA. This is mainly because the low atmospheric pressure is able to enhance the evaporation rate of water in specimens, so as to decrease the cement hydration degree, and increase the porosity and charge passed of concrete. Based on the fitting of obtained results, it is noted that the relationship between charge passed and CTP content is approximately linear. The slope of fitting equation for concrete in LAPA is sharper than that in NAPA. This implies that CTP can significantly increase the charge passed of concrete in LAPA.

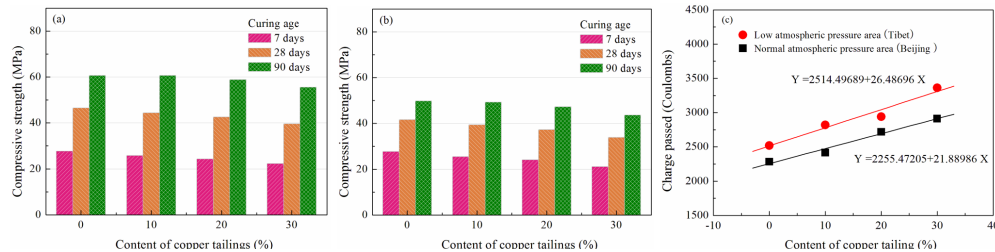


Fig. 2 Compressive strength and charge passed of concrete: (a) compressive strength in LAPA; (b) compressive strength in NAPA; (c) charge passed

3.4 Freeze-thaw resistance of concrete

From Fig. 3 (a), it can be seen that in NAPA, the mass change of concrete in the first 50 freeze-thaw cycles showed positive values, indicating that the mass of concrete increased with the extension of the freeze-thaw cycles. This can be attributed to two separate effects. Firstly, during the first 50 freeze-thaw cycles, the further hydration of unhydrated cement in concrete can produce more hydration products, resulting in the increasing of the specimen mass. Secondly, the freeze-thaw cycles can lead the water in the environment penetrate into the specimens, so the mass of the specimen increases. With the further increase of freeze-thaw cycles, the mass loss of the specimens was negative, indicating that the mass of the specimens decreased. This is mainly due to the peeling phenomenon of concrete during the freeze-thaw cycles. During the freeze-thaw cycles, the water in concrete forms ice crystals in low temperature, and the resulting frost heaving force destroys the concrete, causing the cracking, peeling off and mass loss of specimens.

As show in Fig. 3 (a), for the same freeze-thaw cycles, the mass loss of concrete containing CTP was larger than that of concrete without CTP. which is mainly due to the fact that the concrete containing CTP has a low compressive strength, so the resistance of concrete to the frost heave force is weak, resulting in a larger mass loss of specimen during the freeze-thaw cycles. As shown in Fig. 3 (b), the relative dynamic elastic modulus of concrete decreased with the extension of the freeze-thaw cycles. After the 200 freeze thaw cycles, the relative dynamic elastic modulus of concrete content 0%, 10%, 20% and 30% of CTP decreased by 28.7%, 32.1%, 36.0% and 41.6%, respectively. This indicated that CTP lowers the freeze-thaw resistance of concrete remarkably.

Through observation of Fig. 3 (c) and (d), it was found that the mass change and the trend in relative dynamic elastic modulus of concrete in the LAPA was consistent basically with the change of concrete in the NAPA, that is, with the increase of the freeze-thaw cycles, the mass loss of concrete first increased and then decreased, the relative dynamic elastic modulus of concrete decreases. From Fig. 3, it was found that for the same freeze-thaw cycles and CTP content, the mass loss of concrete in the LAPA was higher than that in the NAPA, and the relative dynamic elastic modulus of concrete in LAPA was smaller than that in the NAPA. This means that compared with concrete in NAPA, the freeze-thaw damage of concrete in LAPA is more serious. This may be related to the fact that in LAPA, the moisture in concrete evaporates rapidly to the external environment, and thus reduces the water used for cement hydration, so as to increase the porosity, decrease the compressive strength of concrete, and finally low the freeze-thaw resistance of concrete in LAPA.

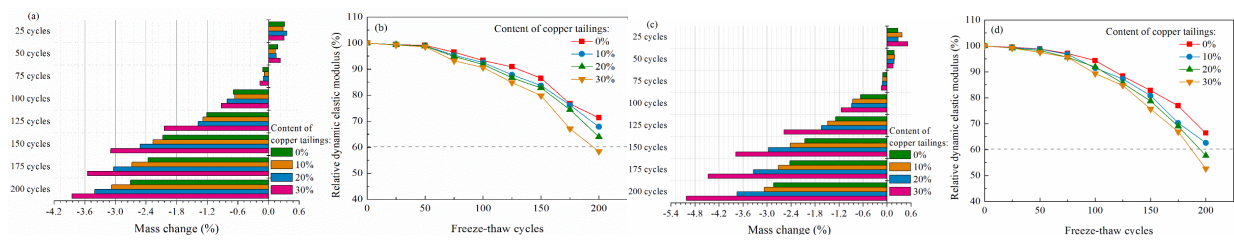


Fig. 3 Freeze-thaw resistance of concrete: (a) mass change in NAPA; (b) relative dynamic elastic modulus in NAPA; (c) mass change in LAPA; (d) relative dynamic elastic modulus in LAPA

3.5 SEM analysis

From the SEM image of the concrete without CTP in NAPA (Fig. 4 (a)), C-S-H gel, plate-like $\text{Ca}(\text{OH})_2$ and needle-like AFT crystals were observed. Those hydration products lapped each other to form a dense structure. Compared to the concrete without CTP, the concrete with 30% CTP contained more pore and exhibited a looser microstructure (Fig. 4 (b)). This could cause a decrease in compressive strength and frost resistance of concrete. As show in Fig. 4 (c) and (d), the use of CTP could also make the microstructure of concrete in LAPA loose. From Fig. 4, it was found that for the same CTP content, the microstructure of concrete in LAPA is looser than that in NAPA. These SEM results are consistent with the mechanical properties, RCPT and FTCT results, explaining the compressive strength, frost resistance and frost resistance of concrete containing CTP.

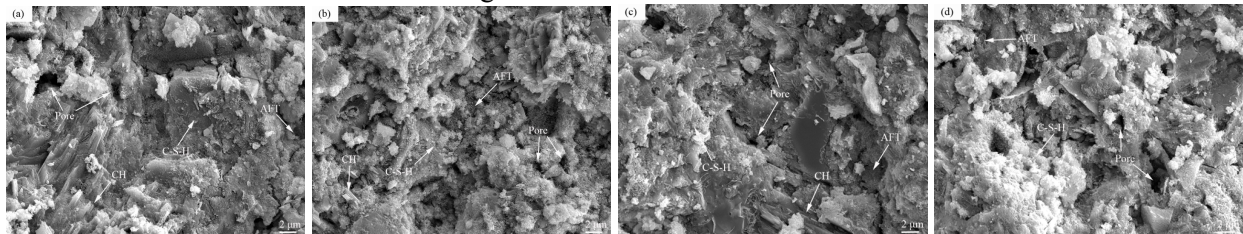


Fig. 4 SEM images of concrete: (a) concrete with 0% CTP in NAPA; (b) concrete with 30% CTP in NAPA; (c) concrete with 0% CTP in LAPA; (d) concrete with 30% CTP in LAPA

4. Conclusions

The effects of CTP on the hydration, compressive strength, permeability, freeze-thaw resistance of concrete in NAPA (Beijing) and LAPA (Tibet) were studied. Based on the results of this study, the following conclusions can be drawn:

1. With the increasing of CTP content, the hydration heat of cement paste decreased, the second exothermic peak value decreased, and the position of the second exothermic peaks remained basically unchanged. Moreover, the low atmospheric pressure has little effect on the early hydration heat and hydration heat evolution rate of cement paste.
2. By increasing the amount of CTP from 0 to 30%, the 28-days and 90-days compressive strength of concrete in NAPA decreased by 14.8% and 8.4% respectively, the 28-days and 90-days compressive strength of concrete in the LAPA decreased by 18.8% and 12.4% respectively.
3. The addition of CTP could significantly increase the charge passed of concrete. The relationship between charge passed and CTP content is approximately linear. The slope of fitting equation for concrete in the LAPA is sharper than that in the NAPA.
4. When partial cement was replaced with CTP, the freeze-thaw resistance of concrete decreased. For the same freeze-thaw cycles and CTP content, the freeze-thaw damage of concrete in NAPA was less than that in LAPA. The use of CTP could make the microstructure of concrete loose.

References

- Tang J, Yang H, Song Y, et al. The copper polymetallic deposits and resource potential in the Tibet Plateau[J]. China Geology, 2021, 4(1): 1-16.
- Huang X, Ni W, Cui W, et al. Preparation of autoclaved aerated concrete using copper tailings and blast furnace slag[J]. Construction and Building Materials, 2012, 27(1): 1-5.
- Ghazi A B, Jamshidi-Zanjani A, Nejati H. Clinkerisation of copper tailings to replace Portland cement in concrete construction[J]. Journal of Building Engineering, 2022, 51: 104275.

Mineralogical Characterization of Waste to Energy (WTE) Ashes - Insights from Raman Imaging

H. Samouh, V. Kumar, and N. Garg*

Department of Civil and Environmental Engineering, University of Illinois Urbana-Champaign, Urbana, United States

Emails: hsamouh@illinois.edu, vikramk3@illinois.edu, nishantg@illinois.edu

ABSTRACT

As coal production declines in Europe and USA, traditional coal fly ashes become scarcer. Waste-to-Energy (WTE) ashes produced post-combustion of solid waste can be a potential solution to this shortage of fly ashes. However, WTE ashes have complex mineralogy and contain chloride and sulfate phases that may affect cement hydration. Hence, the characterization of WTE ashes' mineralogy is the first step to recycling them as SCMs. This study aims to investigate the added value of Raman imaging in determining the complex mineralogy of WTE bottom ash in addition to the classic X-Ray Diffraction (XRD). This paper presents a new pellet-based procedure, wherein a ~3 h scan, 104 spectra were collected and analyzed. Three unique phases were only detected with XRD (hydrocalumite, quartz, and akermanite), in addition to 3 that were also detected by Raman imaging (calcite, anhydrite, and hydroxyapatite). 7 distinct phases were only detected with Raman imaging (carbon, rutile, aphtitalite, gypsum, cotunnite, baryte, and zincite). For example, carbon is a common phase always present in these ashes, which is undetectable via XRD but easily identified via Raman. The XRD insensitivity to these minerals can be due to their low content or amorphous nature. The toxic elements barium and lead are found in baryte and cotunnite, only detectable by Raman imaging. Thus, Raman imaging, in addition to XRD, could eventually help safely divert WTE ashes from landfills to beneficial applications.

KEYWORDS: *Waste to Energy (WTE) ashes, Raman imaging, phase identification*

1. Introduction

Waste production is estimated at 2.24 billion tons and is expected to rise by 73% by 2050 (The World Bank (2022)). Outside of composting and recycling, incineration is preferred to manage the municipal solid waste (MSW) (Al-Ghouti et al. (2021)). MSW thermal treatment aims to reduce mass and volume, destroy organic contaminants, recover metals, and generate energy (Weibel et al. (2017)). In Waste-to-Energy (WTE) facilities, the waste is incinerated, thereby generating byproducts. Iron is recovered through magnetic fields, and aluminum through eddy currents before landfilling WTE bottom ashes (Lancellotti et al. (2015)). The decreasing supply of coal fly ash and the growing demand for supplementary cementitious materials (SCM) make WTE ashes an excellent alternative if their composition is understood. Indeed, the waste stream inconsistency is transmitted to the WTE ashes (Wolffers et al., 2021). Since the composition of WTE ashes is unknown, their recycling is hindered by their uncontrolled impact on concrete properties (Kumar & Garg, 2022). Raman imaging has been successfully applied to characterize the mineralogy of the construction materials (Garg et al., 2013; Polavaram & Garg, 2021; Srivastava & Garg, 2022). However, to the authors' knowledge, it has not yet been used to characterize WTE ashes. This paper explores the application of this technique to WTE ashes. Raman imaging was used to identify phases, and the results were compared to X-Ray Diffraction (XRD) results.

2. Experimental procedure

One WTE bottom ash was selected, ground, and sieved (45 μm). The oxide composition of the powder was determined through X-Ray Fluorescence (XRF), and the mineral composition through XRD. A Shimadzu EDX-7000 was used for XRF, and a Bruker D8 Advance for XRD. The obtained oxide composition is shown in Table 1. Raman imaging was collected on a pellet of 7 mm in diameter. The obtained surface was very smooth, and no slope or cracks were observed with the microscope. A WITec Alpha 300 RA Raman-AFM-SNOM was used for Raman imaging. A 532 nm laser source with 20 mW laser power and 50x objective was selected. Spectra were collected on a 1 x 1 mm² surface. On 100 lines with 100 points each, 10⁴ spectra were obtained. 1s was spent by spectrum, so the measurement took less than 3 hours.

Table 1. Oxide composition obtained by XRF of the bottom ash. Traces oxides are not shown.

| Oxides | CaO | SiO ₂ | SO ₃ | Al ₂ O ₃ | Fe ₂ O ₃ | ZnO | Cl | P ₂ O ₅ | TiO ₂ | MgO | K ₂ O | CuO | PbO ₂ |
|--------|-------|------------------|-----------------|--------------------------------|--------------------------------|------|------|-------------------------------|------------------|------|------------------|------|------------------|
| Wt (%) | 39.76 | 18.26 | 11.31 | 10.22 | 5.89 | 3.30 | 2.61 | 1.90 | 1.77 | 1.40 | 1.38 | 0.85 | 0.69 |

2. Results and discussion

Based on XRD/Rietveld analysis, 40% of the bottom ash was crystalline (6 phases), and 60% was amorphous. Amorphous content is associated with the cooling process. Five of the six crystalline phases had a percentage below 6%. The dominant phase was calcite, at ~22 %. With Raman imaging, 10 minerals were detected (Fig. 1). Seven spectra corresponded to pure phases, while three of them were composed of two (calcite + gypsum and cotunnite + rutile) or three minerals (hydroxyapatite + apththitalite + calcite). XRD and Raman imaging detected calcite, anhydrite, and hydroxyapatite. The remaining minor phases (hydrocalumite, quartz, and akermanite) were undetected via Raman imaging. The following 7 phases were exclusively revealed through Raman imaging: rutile, carbon, apththitalite, gypsum, cotunnite, baryte, and zincite. For instance, carbon is undetectable with XRD, but its content should be under ~10 %. In some cases, like apththitalite, baryte, and hydroxyapatite, the low concentration of these phases prevents their detection by XRD. The maps in Fig. 2 show that these minerals were mixed with others.

It is also possible that some minerals are XRD-amorphous. Indeed, cotunnite and rutile showed broad Raman peaks (Fig. 1), usually indicating lower crystallinity. Lead can be found in different phases, but chlorination is the most common. The zinc in zincite comes from industrial uses like brass, steel galvanization, paper production, filler materials, pigments, and plastic catalysts. In WTE ashes, sulfurous phases are generally found since the sulfur comes from organic materials, paper, paperboard, plastics, and fines. Only Raman imaging detected cotunnite and baryte containing toxic elements lead and barium. This complementary information is critical to safely recycling WTE ashes. Finally, the 10 detected minerals by Raman imaging were observed on a small area of 1 mm². Increasing this area in the future will enable the detection of additional phases and provide more insights regarding the variability of the WTE ashes' mineralogy.

3. Conclusions

This study presents a new procedure for performing Raman imaging directly on a pellet of WTE bottom ash. The phase identification results are very encouraging compared to the well-established XRD analysis. In total, 10 spectra have been detected and assigned to different phases. Many XRD-undetectable phases, such as carbon, have only been observed with this technique. Phases containing toxic elements such as baryte and cotunnite were observed by Raman imaging and were not identified by XRD. The low content or the amorphous nature can explain this non-detection. This result proves the importance of such characterization of WTE ashes for safely recycling them. In the future, a larger surface analysis will better characterize this material and allow the quantification of the phases.

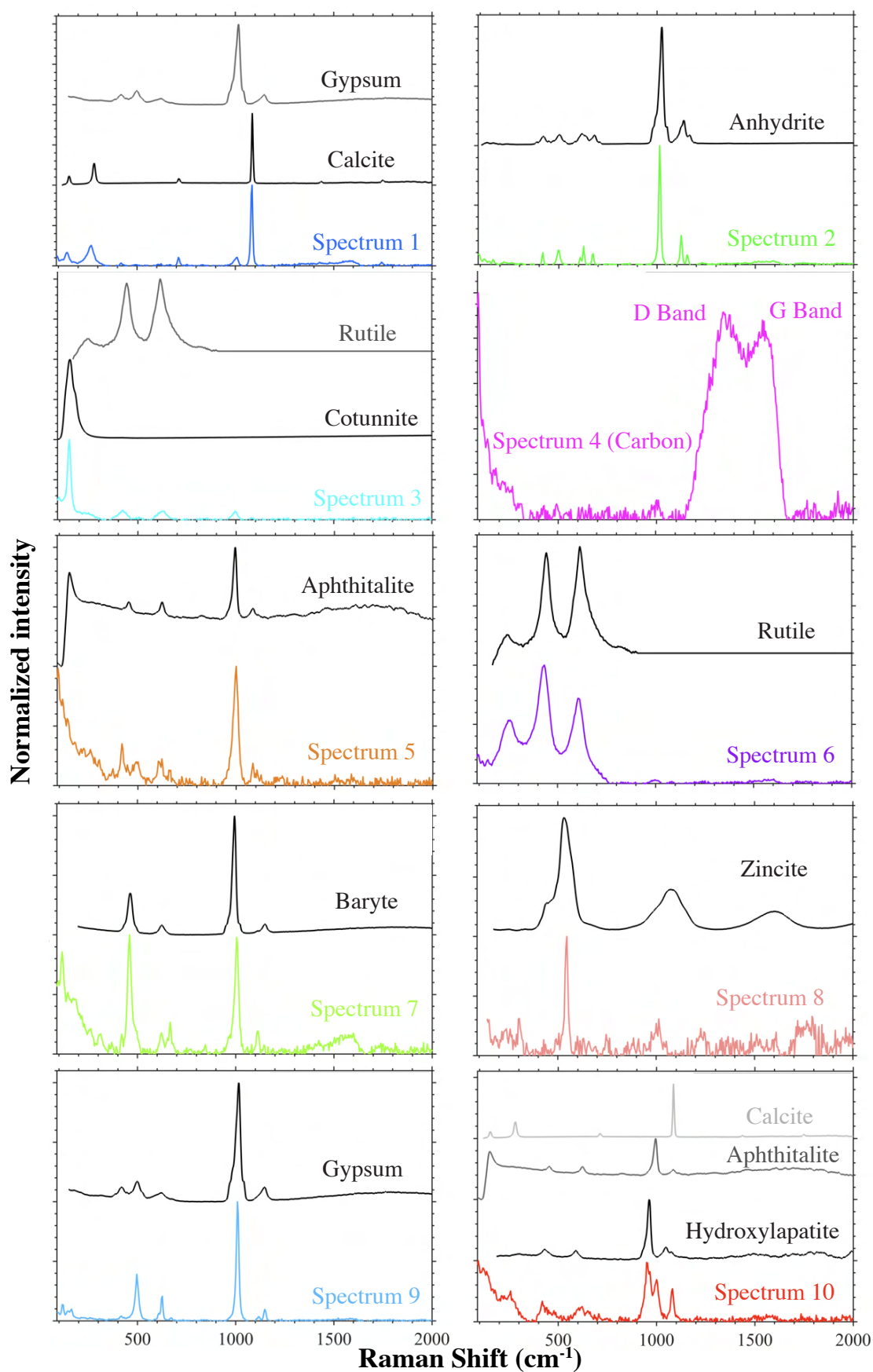


Fig. 1. The Raman spectra for different phases detected by the confocal Raman imaging in the WTE ashes (the bottom curve in each plot). The assignment was performed based on the Ruff database (the upper curves in each plot).

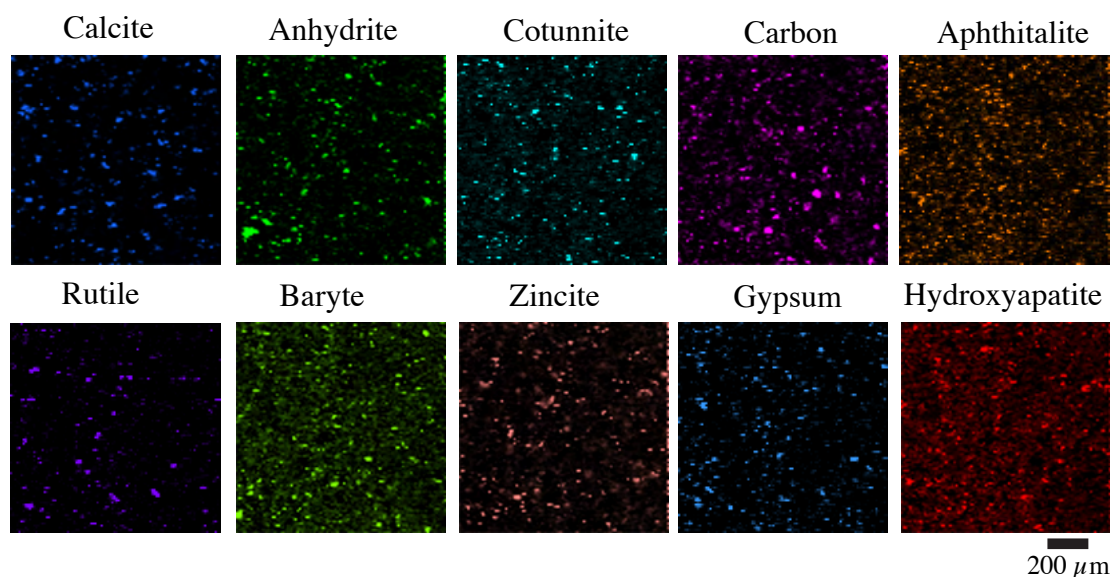


Fig. 2. Ten Raman images of the observed phases on the WTE bottom ash (resolution: 10 $\mu\text{m}/\text{pixel}$).

Acknowledgments

The information, data, or work presented herein was funded by the Advanced Research Projects Agency-Energy (ARPA-E), U.S. Department of Energy, under Award Number DE-AR0001401. The views and opinions of authors expressed herein do not necessarily state or reflect those of the United States Government or any agency thereof. The authors would like to acknowledge that a part of this research was carried out at the Materials Research Laboratory Central Research (MRL) and the Institute for Genomic Biology (IGB) facilities at the University of Illinois at Urbana-Champaign.

References

- Al-Ghouti, M. A., Khan, M., Nasser, M. S., Al-Saad, K., & Heng, O. E. (2021). Recent advances and applications of municipal solid wastes bottom and fly ashes: Insights into sustainable management and conservation of resources. *Environmental Technology and Innovation*, 21, 101267. <https://doi.org/10.1016/j.eti.2020.101267>
- Garg, N., Wang, K., & Martin, S. W. (2013). A Raman spectroscopic study of the evolution of sulfates and hydroxides in cement-fly ash pastes. *Cement and Concrete Research*, 53, 91–103. <https://doi.org/10.1016/j.cemconres.2013.06.009>
- Kumar, V., & Garg, N. (2022). The chemical and physical origin of incineration ash reactivity in cementitious systems. *Resources, Conservation and Recycling*, 177(June 2021), 106009. <https://doi.org/10.1016/j.resconrec.2021.106009>
- Lancellotti, I., Cannio, M., Bollino, F., Catauro, M., Barbieri, L., & Leonelli, C. (2015). Geopolymers: An option for the valorization of incinerator bottom ash derived “end of waste.” *Ceramics International*, 41(2), 2116–2123. <https://doi.org/10.1016/j.ceramint.2014.10.008>
- Polavaram, K. C., & Garg, N. (2021). Enabling phase quantification of anhydrous cements via Raman imaging. *Cement and Concrete Research*, 150(April), 106592. <https://doi.org/10.1016/j.cemconres.2021.106592>
- Srivastava, S., & Garg, N. (2022). Tracking spatiotemporal evolution of cementitious carbonation via Raman imaging. *Journal of Raman Spectroscopy*. <https://doi.org/10.1002/jrs.6483>
- The World Bank. (2022). *Solid Waste Management*. <https://www.worldbank.org/en/topic/urbandevelopment/brief/solid-waste-management>
- Weibel, G., Eggenberger, U., Schlumberger, S., & Mäder, U. K. (2017). Chemical associations and mobilization of heavy metals in fly ash from municipal solid waste incineration. *Waste Management*, 62, 147–159. <https://doi.org/10.1016/j.wasman.2016.12.004>
- Wolffers, M., Eggenberger, U., Schlumberger, S., & Churakov, S. V. (2021). Characterization of MSWI fly ashes along the flue gas cooling path and implications on heavy metal recovery through acid leaching. *Waste Management*, 134(August), 231–240. <https://doi.org/10.1016/j.wasman.2021.08.022>

Recycling of phosphate waste rocks to produce alkali-activated mortars

A. El Machi^{1*}, H. Beniddar¹, S. Mabroum², Y. Taha², M. Benzaazoua² and R. Hakkou¹

¹ Cadi Ayyad University (UCA), Faculty of science and technology, IMED-Lab, BP549 Av. A. El Khattabi, Marrakech 40000, Morocco.

² Mohammed VI Polytechnic University (UM6P), Geology & Sustainable Mining Institute (GSMI) program, Lot 660, Hay Moulay Rachid, Benguerir 43150, Morocco.

Email: aiman.elmachi@ced.uca.ma

ABSTRACT

The extraction, processing and beneficiation of phosphates generate important amounts of waste rocks. The accumulation of those materials causes flagrant environmental issues. On the other hand, the construction industry is a big consumer of raw materials (sand and aggregates) which requires finding new alternatives to tackle the depletion of natural resources. Nevertheless, the commonly used binder in the concrete industry is OPC, while important CO₂ amounts are emitted during its production. This paper sheds the light on a new route towards an effective solution for those issues, by finding a compromise between waste rocks materials and the concrete industry in a context of circular economy. The current study is investigating the feasibility of using flint from phosphate waste rocks as fine and coarse aggregate replacement, with clays based AAM as a replacement for OPC. The results showed that the replacement of OPC by the alkali-activated binder and natural sand by flint present good mechanical strength due to the formation of N-A-S-H and C-A-S-H gels.

KEYWORDS: *Phosphate waste rocks, mortar, alkali-activated binder, circular economy.*

1. Introduction

Alkali-activated materials are produced by mixing an aluminosilicate precursor rich in calcium with an alkaline activator solution (Kou et al., 2020). A calcium aluminosilicate hydrate (C-A-S-H) gel is the primary binder phase in AAMs when the precursor is rich in calcium. Recently, much attention has been paid to mine wastes or tailings usage as an alternative way to produce cementitious materials as an alternative to conventional construction materials (Tian et al., 2020). The mineral industry remains one of the world's biggest producers of tailings and waste rocks. Recently, researchers have considered these wastes as precursors to produce alkali-activated materials presenting different ranges of strength. The activation of sulphidic mine tailings using NaOH-15 M produced hardened materials with compressive strength of up to 3.5 MPa (Kiventerä et al., 2016). While gold mine tailings activated using NaOH and lime sludge presented a compressive strength of about 5.48 MPa (Aseniero et al., 2019). However, the mixture of tungsten mine waste mud with 40% of waste glass activated by a solution of sodium hydroxide and sodium silicate solution cured at 80 °C showed compressive strength reached 22 MPa at 28 days (Kastiukas et al., 2017). The present work aims to study the feasibility of using waste rocks, flint as sand, and yellow clays as precursors, to produce alkali-activated mortars.

2. Experimental procedure

2.1. Raw materials

The waste clay and flint used in this study were collected from the interlayers of the Ben Guerir phosphate mine. The yellow clay was employed as precursor in the alkali-activation, while flint was used as sand for the preparation of the mortar. Yellow clay was crushed, ground to 100 µm, then calcined at 900 °C-2h. Meanwhile, the flint was crushed and sieved through 4 mm sieve. The granulometry curves of both used clay and sand can be found in [Figure 1](#).

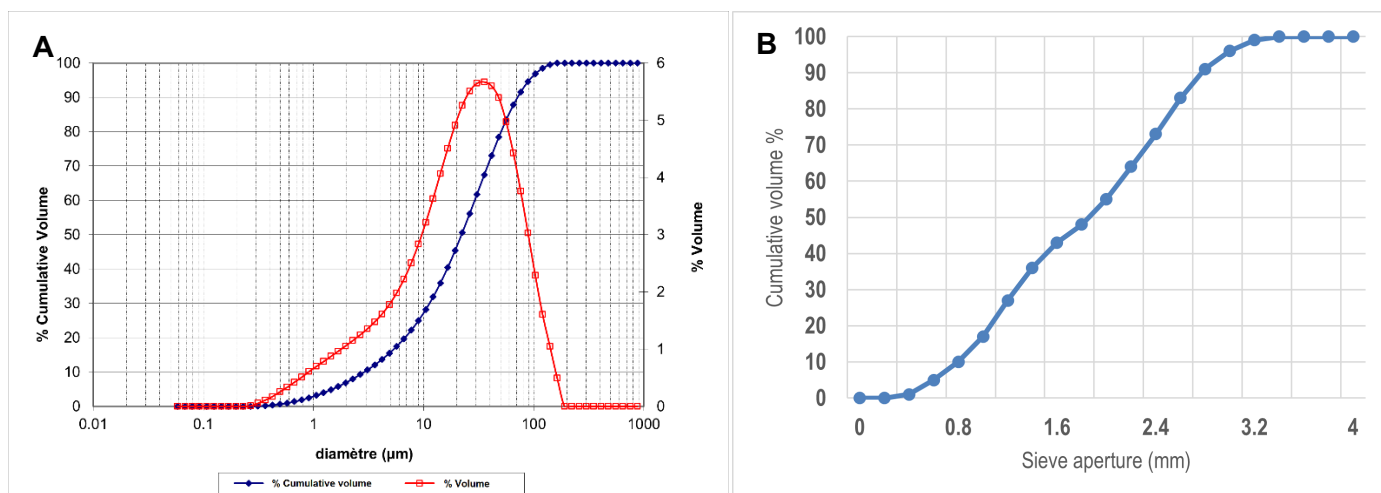


Figure 1. Granulometry curves of A) Yellow clay and B) flint sand used in this study.

2.2. Characterization of raw material

The chemical composition data are shown in Table , silica and aluminum are present in major amounts in the yellow clay. On the other hand, silica is the main component of flint, while the other elements are present in trace amounts.

Table 1. Chemical compositions of YC and flint. LOI: Loss of ignition, YC: yellow clay

| Oxides | SiO ₂ | Al ₂ O ₃ | Fe ₂ O ₃ | MgO | CaO | P ₂ O ₅ | Na ₂ O | TiO ₂ | MnO | K ₂ O | LOI |
|------------------|------------------|--------------------------------|--------------------------------|------|-------|-------------------------------|-------------------|------------------|------|------------------|-------|
| YC (%) | 29.79 | 10.83 | 4.72 | 9.07 | 15.28 | 0.69 | 0.21 | 0.75 | 0.02 | 0.56 | 28.12 |
| Flint (%) | 92.00 | 0.22 | 0.10 | 2.1 | 1.85 | 0.82 | <0.01 | 0.05 | 0.06 | 0.10 | 1.88 |

Error! Reference source not found.. A shows the XRD pattern of the flint waste used in this study. The spectrum shows the presence of quartz as the main phase, which is consistent with the dominance of SiO₂ in the chemical composition of flint. In addition to quartz, traces of dolomite and fluorapatite were detected in the sample confirmed by the presence of MgO, CaO, and P₂O₅ in XRF results. The XRD diffractogram of raw and calcined yellow clay are present in **Error! Reference source not found..** YC contains montmorillonite as the major clay phase which is present at $2\theta = 5.9^\circ$. When the YC is calcined at 900 °C, the montmorillonite and dolomite peaks disappear completely due to the total dihydroxylation of clay and decomposition of carbonates. In addition, the heating treatment does not affect quartz, fluorapatite and hematite phases. However, the heating process leads to the generation of lime (CaO) and periclase (MgO) resulting from the decarbonation of dolomite (Bahhou et al., 2020). Furthermore, the decomposition of montmorillonite and dolomite leads to the formation of gehlenite and diopside.

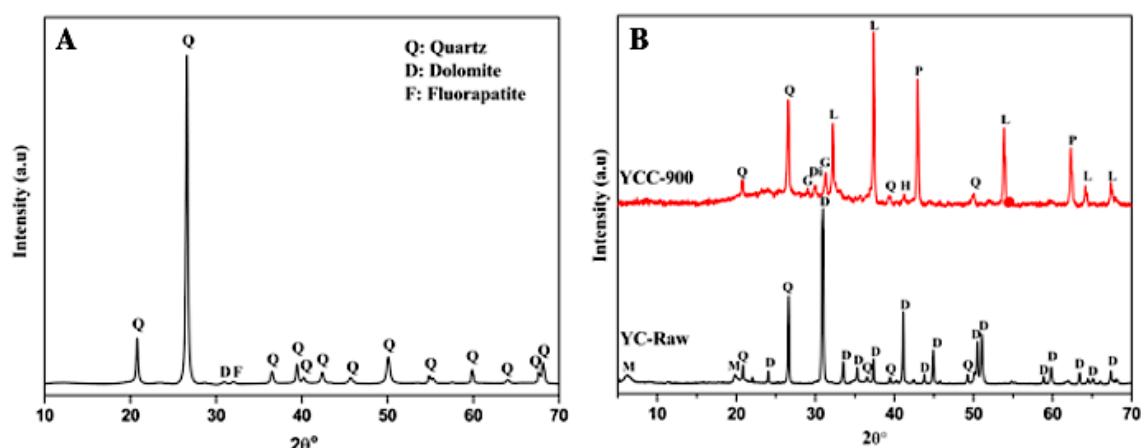


Figure 2. XRD patterns of raw materials A: flint and B: Raw and calcined clays; D: dolomite, Q: quartz, M: montmorillonite, H: hematite, G: gehlenite, P: periclase, Di: diopside.

TGA-DTG curves are shown in Figure 3. The first loss at 150°C corresponds to the remove of interlayer water in montmorillonite. The calcination of this clay leads to the loss of the hydroxyl water in the range

between 600°C and 700°C, confirmed by the second loss around 680°C (Fernandez et al., 2011). The pic around 800°C is attributed to the decomposition of dolomite (Trindade et al., 2009) which agrees with the XRD results. The last loss at 870°C is attributed to the dihydroxylation of montmorillonite clays (Garg & Skibsted, 2014).

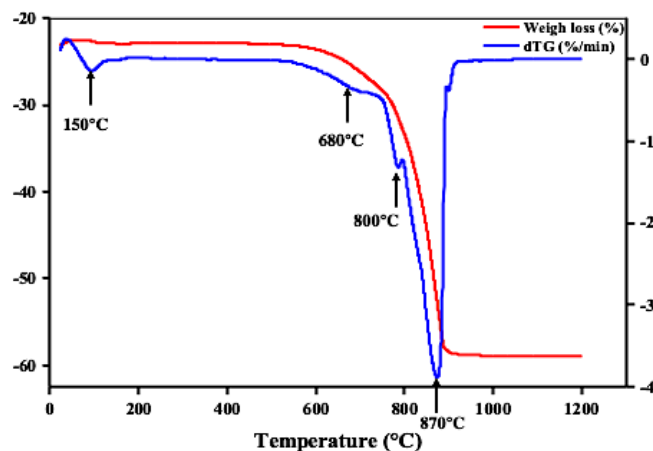


Figure 3. TGA-DTG of raw yellow clay

2.3. Formulation of Alkali-activated mortars

The yellow clay powder calcined at 900 °C was activated using alkaline solution based on mixing sodium hydroxide NaOH (NH) solution-10 M and sodium silicate Na₂SiO₃ (NS) solution with a ratio of 2, which was determined by a previous series of experiments. The L/S ratio was kept at 0.48 to ensure adequate workability of mortars. A clay/sand ratio was set to 0.5 to ensure a good packing density. Calcined clay powder was mixed firstly with the solution, then the sand was added. Fresh paste was introduced in molds (4x4x16 cm) with pricking to remove the air bubbles. The molds were covered with plastics to deny humidity loss and placed into furnace at 60°C for 3 days then demolded and kept at ambient temperature until testing the mechanical strength (7, 14 and 28 days). The hardened mortars were characterized using diverse technics after 28 days.

3. Results and discussion

3.1. Mechanical properties of Alkali-activated mortars

The compressive and flexural strength results of the AAM at different curing times (7, 14, and 28 days) of specimens are presented in Figure 4 (A and B). It is evident that compressive and flexural strength increase with time. The compressive strength of the AAM increased from 12.6 at 7 days to 14.2 at 14 days and further to 17.6 at 28 days. Similarly, the flexural strength showed an improvement from 2.9 at 7 days to 3.3 at 14 days and finally to 3.5 at 28 days. The strength was not as high as expected, possibly due to the addition of extra water to enhance the workability of the mixture, which diluted the alkaline solution and made it hard to dissolve the active clayey phases (Dabbebi et al., 2018). In addition, loss of water during heat treatment in the furnace or lower moisture content during curing time at ambient temperature may have contributed to the lower strength (Fahim Huseien et al., 2017).

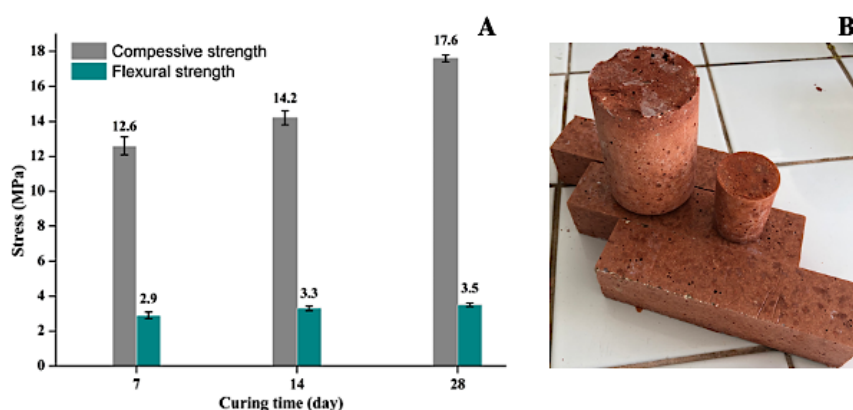


Figure 4. A: Compressive and flexural strength of AAM at 28 days and B: AAM specimens before mechanical tests.

3.2. Characterization of Alkali-activated mortars

XRD diffractograms of the elaborated Alkali-activated mortars (AAM) after 28 days of curing are shown in Figure (A and B), in which the crystalline and amorphous phases are present. It's noted that the quartz peaks are still appearing after the activation as this phase is not affected by alkaline medium. In addition, the peaks related to the quartz appear more important in AAM as the flint particles used as sand. The patterns show that the alkaline solution used to elaborate AAM did not significantly affect the detected phases as quartz, fluorapatite, gehlenite and periclase (Dabbebi et al., 2018; Xing et al., 2019). Furthermore, traces of natron were detected at 28 days, possibly due to the excess of Na^+ and the presence of CO_2 . Additionally, a trace of portlandite was detected in AAM-28d, possibly due to lime's hydration reaction (CaO). Furthermore, the broad hump detected between 20° and 35° corresponds to the formation of amorphous content from the reaction between lime-portlandite and Si-Al from both sodium silicate and dehydroxilated clays that could be probably CASH gel respecting the chemical composition of YC or a mixture of both NASH and CASH. This can explain the resulting compressive strength of the elaborated materials (Dathe et al., 2021). The SEM images show a dense and homogenous structure with the presence of micro-cracks near the interfacial zone between the sand and the binder that could affect negatively the strength. While the EDX analysis (Figure (1 and 2)) shows the presence of the particle of sand and confirms the formation of a mixture of gels (NASH and CASH).

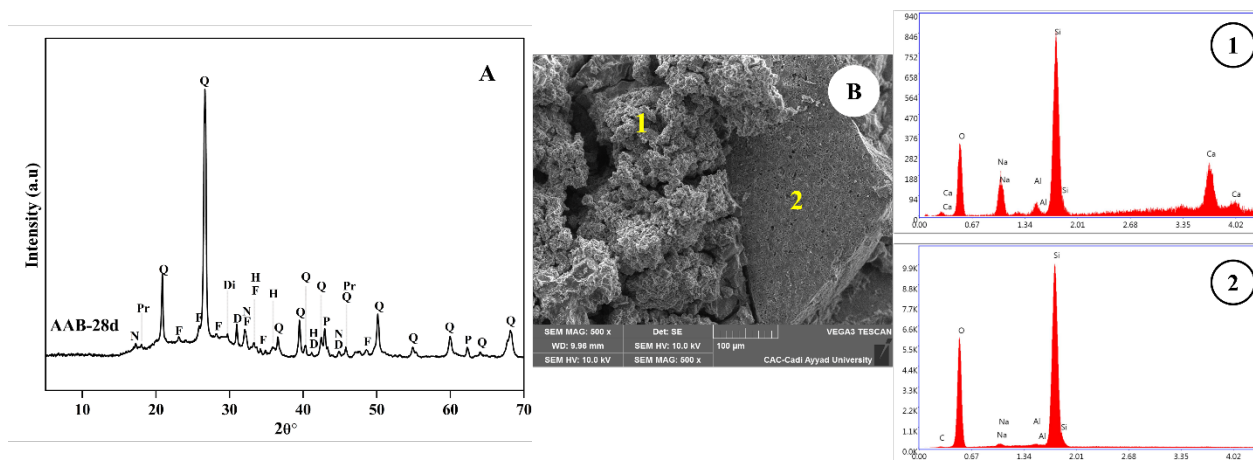


Figure 5. XRD patterns of AAB at 28-days Q: quartz D: dolomite, F: fluorapatite, H: hematite, P: periclase, Di: diopside, Pr: portlandite, N: natron, B: SEM image of AAM, 1 and 2 EDX analysis

4. Conclusions

The main objective of the paper was to evaluate the effectiveness of geopolymer mortars made from waste materials extracted from Moroccan phosphate mines, including flint as fine aggregates and yellow clay-based AAM as a binder. The study involved the chemical and mineralogical characterization of raw materials used, and it was found that the flint was composed mainly of quartz with traces of dolomite and fluorapatite, which was confirmed by high content of SiO_2 , while the yellow clay contained montmorillonite as a clayey component, as well as dolomite and quartz, supporting by high amount of SiO_2 , Al_2O_3 , Fe_2O_3 , CaO and MgO . The study successfully prepared geopolymer mortars from the phosphate waste materials, and the results were very promising. However, further investigation is needed to optimize the mixture formulation and control the curing conditions to achieve higher properties.

Acknowledgments

The authors would like to thank the Moroccan Ministry of Higher Education. Scientific Research and Innovation and the OCP Foundation who funded this work through the APRD Research Program.

References

- Aseniero, J. P. J., Opiso, E. M., Banda, M. H. T., & Tabelin, C. B. (2019). Potential utilization of artisanal gold-mine tailings as geopolymeric source material: preliminary investigation. *SN Applied Sciences*, 1(1), 1–9. <https://doi.org/10.1007/S42452-018-0045-4/TABLES/4>
- Bahhou, A., Taha, Y., el Khessaimi, Y., Idrissi, H., Hakkou, R., Amalik, J., & Benzaazoua, M. (2020). Use of phosphate mine by-products as supplementary cementitious materials. *Materials Today: Proceedings*, 37, 3781–3788. <https://doi.org/10.1016/j.matpr.2020.07.619>

- Dabbebi, R., Barroso de Aguiar, J. L., Camões, A., Samet, B., & Baklouti, S. (2018). Effect of the calcinations temperatures of phosphate washing waste on the structural and mechanical properties of geopolymeric mortar. *Construction and Building Materials*, 185, 489–498. <https://doi.org/10.1016/j.conbuildmat.2018.07.045>
- Dathe, F., Strelnikova, V., Werling, N., Emmerich, K., & Dehn, F. (2021). Influence of lime, calcium silicate and portlandite on alkali activation of calcined common clays. *Open Ceramics*, 7, 100152. <https://doi.org/https://doi.org/10.1016/j.oceram.2021.100152>
- Fahim Huseien, G., Mirza, J., Ismail, M., Ghoshal, S. K., & Abdulameer Hussein, A. (2017). Geopolymer mortars as sustainable repair material: A comprehensive review. *Renewable and Sustainable Energy Reviews*, 80, 54–74. <https://doi.org/10.1016/j.rser.2017.05.076>
- Fernandez, R., Martirena, F., & Scrivener, K. L. (2011). The origin of the pozzolanic activity of calcined clay minerals: A comparison between kaolinite, illite and montmorillonite. *Cement and Concrete Research*, 41(1), 113–122. <https://doi.org/10.1016/j.cemconres.2010.09.013>
- Garg, N., & Skibsted, J. (2014). Thermal Activation of a Pure Montmorillonite Clay and Its Reactivity in Cementitious Systems. *The Journal of Physical Chemistry C*, 118(21), 11464–11477. <https://doi.org/10.1021/jp502529d>
- Kastiukas, G., Zhou, X., Asce, M., & Castro-Gomes, J. (2017). Preparation Conditions for the Synthesis of Alkali-Activated Binders Using Tungsten Mining Waste. *Journal of Materials in Civil Engineering*, 29(10), 04017181. [https://doi.org/10.1061/\(ASCE\)MT.1943-5533.0002029](https://doi.org/10.1061/(ASCE)MT.1943-5533.0002029)
- Kiventerä, J., Golek, L., Yliniemi, J., Ferreira, V., Deja, J., & Illikainen, M. (2016). Utilization of sulphidic tailings from gold mine as a raw material in geopolymerization. *International Journal of Mineral Processing*, 149, 104–110.
- Kou, Y., Jiang, H., Ren, L., Yilmaz, E., & Li, Y. (2020). Rheological Properties of Cemented Paste Backfill with Alkali-Activated Slag. *Minerals* 2020, Vol. 10, Page 288, 10(3), 288. <https://doi.org/10.3390/MIN10030288>
- Tian, X., Xu, W., Song, S., Rao, F., & Xia, L. (2020). Effects of curing temperature on the compressive strength and microstructure of copper tailing-based geopolymers. *Chemosphere*, 253, 126754. <https://doi.org/10.1016/J.CHEMOSPHERE.2020.126754>
- Trindade, M., Dias, M., Coroado, J., & Rocha, F. (2009). Mineralogical transformations of calcareous rich clays with firing: A comparative study between calcite and dolomite rich clays from Algarve, Portugal. *Applied Clay Science*, 42(3–4), 345–355. <https://doi.org/10.1016/j.clay.2008.02.008>
- Xing, J., Zhao, Y., Qiu, J., & Sun, X. (2019). Microstructural and Mechanical Properties of Alkali Activated Materials from Two Types of Blast Furnace Slags. *Materials* 2019, Vol. 12, Page 2089, 12(13), 2089. <https://doi.org/10.3390/MA12132089>

Effect of strontium salts on the kinetics and mechanisms of geopolymer cement formation

K. O'Donoghue^{1*}, D. A. Geddes^{1,2}, J.L. Provis², B. Walkley¹

¹ Department of Chemical and Biological Engineering, University of Sheffield, Sheffield, UK
Email: ktodonoghue1@sheffield.ac.uk, d.geddes@sheffield.ac.uk, b.walkley@sheffield.ac.uk

² Department of Materials Science and Engineering, The University of Sheffield, Sheffield, UK
Email: d.geddes@sheffield.ac.uk, j.provis@sheffield.ac.uk

ABSTRACT

Geopolymers have received significant interest as an alternative to Portland cement for solidification of radioactive waste due to their technical advantages, ability to encapsulate more problematic wastes, and their reduced carbon footprint. ⁹⁰Sr is of interest due to its presence as a fission product, and relatively short half-life. Reaction, setting and hardening of geopolymers is controlled in part by the chemistry of the aqueous and solid phases, and fluid-particle interactions, in fresh cement paste. Little is known about the effect of different Sr salts (OH⁻, NO₃⁻, SO₄²⁻, CO₃²⁻) on the mechanisms and kinetics of dissolution and reaction of solid aluminosilicate raw materials, the gel nanostructure of the resultant geopolymer cement, and the mechanisms that are responsible for incorporation of Sr radionuclides. Here we use isothermal calorimetry and Fourier transform infrared spectroscopy to show that precursor dissolution, reaction and alkali aluminosilicate gel formation, and Sr incorporation are directly dependent on the anion within the salt compound. The information gained is essential to develop robust cements that are capable of encapsulating, and/or immobilising, complex waste streams containing Sr salts.

KEYWORDS: *Geopolymers, Reaction kinetics, Reaction mechanisms, Strontium*

1. Introduction

The generation of radioactive waste from nuclear power facilities poses health and environmental risks. Therefore, the design of a suitable wasteform is imperative to ensure its safe storage until it is no longer deemed harmful. Strontium-90 (⁹⁰Sr), a radioactive isotope of strontium with a half-life of 28.82 years (Hirose et al., 1987), is a problematic waste. ⁹⁰Sr can be found in spent nuclear fuel as a direct fission product of uranium-235, but is also present in treated radioactive waste, nuclear reactor cooling water and, more importantly, in the environment surrounding the sites of nuclear disasters (Whicker et al., 1990). The high solubility of Sr in common Sr salts (OH⁻, NO₃⁻, SO₄²⁻, CO₃²⁻) leads to increased mobility of the radionuclide in water.

Cementation of intermediate level waste (ILW) has been in practice for decades due to the low cost, low temperature, and uncomplicated processing routes of the material among other advantageous properties (Dezerald et al., 2015; Ojovan et al., 2019). Portland cement blended with blast furnace slag (PC-BFS), is commonly used and is not compatible with all of the waste streams generated by the post-reactor processing of spent nuclear fuel. In order to successfully store all forms of waste safely, a ‘toolbox’ approach using specifically engineered wasteforms must be employed (Milestone, 2006).

A novel cementitious material that has attracted interest for this purpose is geopolymer cements. Geopolymers are an alkali-activated material that is formed via the reaction of a raw material, commonly metakaolin or fly ash, with an alkali activator such as sodium or potassium silicate or hydroxide (Provis, 2018). The resulting binder has a chemical composition that is high in aluminium, silicon and alkali but low in calcium content, which leads to the formation of a highly cross-linked and structurally disordered gel (Walkley et al., 2020).

Geopolymers have attracted interest for the storage of radioactive waste due to their chemical resistance, mechanical properties, and, most notably, their cation binding sites. Traditionally, the primary objective for cementation has been physical encapsulation of the waste, but more recently, interest in the chemical immobilisation of radionuclides such as ⁹⁰Sr has arisen (Tits et al., 2006; Wieland et al., 2008); the cation binding sites within the geopolymer offers significant potential for this (Walkley et al., 2020).

This work utilises isothermal conduction calorimetry (ICC) and Fourier transform infrared (FTIR) spectroscopy to show that precursor dissolution and reaction and alkali aluminosilicate gel formation are directly dependent on the strontium compound used within the reaction.

2. Experimental Methods

2.1 Sample Preparation

The geopolymer gels were produced by reacting metakaolin (MK) (Metamax, BASF) powder with potassium silicate solution. The alkalinity of this system, expressed as the $\text{SiO}_2/\text{K}_2\text{O}$ molar ratio of the activating solution, was adjusted by blending the stock solution of potassium silicate (PQ-KS, 51.6 wt.% potassium silicate, with a solution modulus of $\text{SiO}_2/\text{M}_2\text{O} = 2.2$, with the balance water, PQ UK) with analytical reagent grade KOH (99 wt. %, Fisher Chemical) to form the desired formulation ($\text{SiO}_2/\text{K}_2\text{O} = 1$, $\text{H}_2\text{O}/\text{K}_2\text{O} = 11$, $\text{M}_2\text{O}/\text{Al}_2\text{O}_3 = 1$). Strontium, in the form of either strontium hydroxide octahydrate, strontium nitrate, strontium carbonate, or strontium sulphate was added to the MK before the addition of the activating solution. The addition of the strontium salts was such that four distinct Sr/Al ratios remained constant across the set of samples independent of the anion investigated, shown in Table 1.

Table 1: The samples used in this work and their corresponding Sr/Al ratio.

| <i>Sample</i> | <i>Anion</i> | <i>Sr/Al Ratio</i> |
|------------------|--------------------|--------------------|
| KGP | - | - |
| OH_1 | OH^- | 0.025 |
| OH_2 | OH^- | 0.050 |
| OH_3 | OH^- | 0.075 |
| OH_5 | OH^- | 0.125 |
| NO_3 _1 | NO_3^- | 0.025 |
| NO_3 _2 | NO_3^- | 0.050 |
| NO_3 _3 | NO_3^- | 0.075 |
| NO_3 _5 | NO_3^- | 0.125 |
| CO_3 _1 | CO_3^{2-} | 0.025 |
| CO_3 _2 | CO_3^{2-} | 0.050 |
| CO_3 _3 | CO_3^{2-} | 0.075 |
| CO_3 _5 | CO_3^{2-} | 0.125 |
| SO_4 _1 | SO_4^{2-} | 0.025 |
| SO_4 _2 | SO_4^{2-} | 0.050 |
| SO_4 _3 | SO_4^{2-} | 0.075 |
| SO_4 _5 | SO_4^{2-} | 0.125 |

To produce the geopolymer, raw metakaolin powder was added to the required amount of activating solution and mixed slowly until a homogenous paste was formed. This paste was then sheared using a Heidolph RZR2020 overhead stirrer for 10 minutes before being transferred to a sealed tube and stored at 20°C.

The samples were removed from storage after 1, 3, 7, and 28 days of curing; at this point, they were cut, ground and solvent exchanged in isopropanol to halt the alkali-activation reaction without significantly altering the structure.

2.2 Isothermal Conduction Calorimetry (ICC)

ICC allows for the early stage heat evolution to be studied, providing valuable insights into the early stage reaction between the MK and the activating solution. The 20g of geopolymer pastes were tested using a TAM Air isothermal conduction calorimeter from TA instruments at 20°C for a total of 7 days, with water acting as the reference. The samples were mixed within the glass ampoule using a vortex mixer for two minutes before insertion into the calorimeter.

2.3 Fourier Transform Infrared Spectroscopy (FTIR)

FTIR provides information regarding the bonding environments that are present within the samples, allowing changes in these environments over time to be recorded. A 1:100 mix of sample to KBr was

pressed into a pellet prior to analysis. A Perkin Elmer Frontier Mid FT-IR spectrometer equipped with a deuterated triglycine sulfate (DTGS) detector and KBr beam splitter optical system were used to collect the spectra, scanning for 16 iterations at a resolution of 4 cm^{-1} .

3. Results and Discussion

The pairing of FTIR and ICC allows for the early stage kinetics of gel formation to be linked to changes in the phase assemblage and chemical composition of the geopolymer at each of the given time points. Figure 1 displays the effect of including Sr, in the form of the three salts, into the geopolymer mix in the first 3 days of reaction.

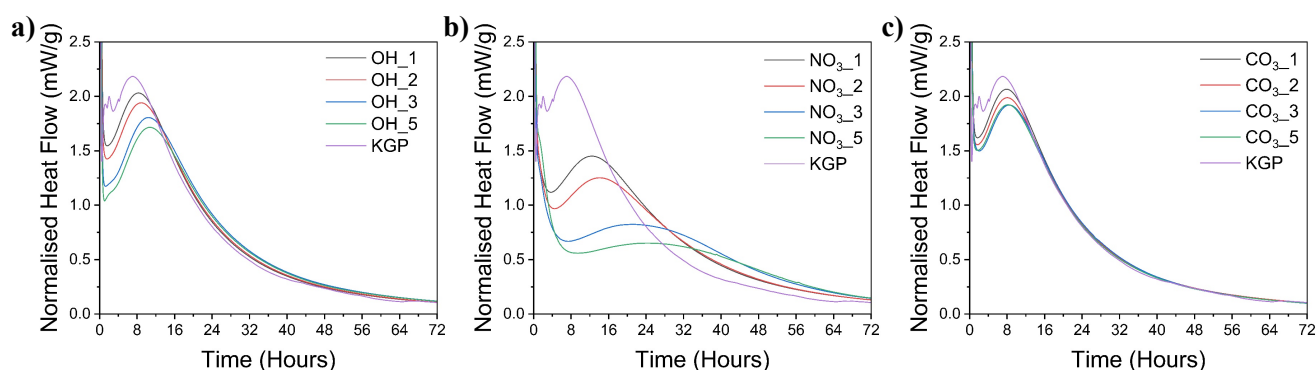


Figure 1: ICC curves generated by the reaction of K-geopolymers loaded with a) strontium hydroxide, b) strontium nitrate and c) strontium carbonate compared with the KGP control over the first 3 days of reaction.

Figure 1 displays 3 phases of reaction: an induction period, an acceleration period, and a deceleration period. The induction period is the dormant period that is observed between the end of the dissolution reaction and the beginning of the polymerisation reaction. This second reaction is indicated by the visible peak in the calorimetry data which starts approximately 2 hours after the initial reaction, known as the acceleration period, which is indicative of the nucleation, growth, and precipitation of the potassium aluminosilicate hydrate (K-A-S-H) phase (Zhang et al., 2012). The data does not include the initial exothermic release associated with the dissolution of the metakaolin in the potassium silicate activating solution due to the mixing of the samples outside of the calorimeter.

The addition of Sr in any form leads to retardation of the polymerisation reaction, represented by the maximum of each visible peak shifting to the right and reducing in intensity, with an increased loading of strontium leading to increased retardation. The samples containing $\text{Sr}(\text{NO}_3)_2$ show the greatest variation from the control sample, with a significant decrease in the maximum values for heat evolution which is further altered by increasing the salt loading. By comparing the samples containing $\text{Sr}(\text{OH})_2$ and the samples containing $\text{Sr}(\text{NO}_3)_2$, it can be suggested that the change in reaction progression between adding ~1-2 wt.% of the Sr salt is not as severe as that witnessed between adding ~2-3 wt.% of the Sr salt. This is not witnessed in the CO_3^{2-} samples, potentially due to the stability of SrCO_3 , which may have led to a lack of dissolution of the salt in the first stages of reaction (Provis et al., 2008).

FTIR spectroscopy techniques were used to identify specific bonding environments present in the sample from their vibrational and/or stretching energies. Figure 2 shows the FTIR spectra for the geopolymer loaded with the 3 salts after the first 3 days of reaction.

The bonding environments identified include symmetric and asymmetric stretching of Si-O-Al and Si-O-Si in a K-A-S-H gel, O-H stretching vibrations due to free and chemically bound water, and vibrations of the CO_3^{2-} anion in potassium and/or strontium carbonate in the CO_3^{2-} samples. Slight carbonation of the hydroxide samples can be seen, which is likely due to exposure to air before analysis was conducted. The NO_3^- containing samples display the peak that is assigned to nitrates. The relative transmission of the peaks assigned to carbonates and nitrates increases with increasing salt loading, suggesting that the Sr salt never dissolved in the first place, which is supported by the results of the ICC of the CO_3^{2-} samples; The difference in normalised heat curves between the samples containing ~3 wt. % and ~5 wt. % of SrCO_3 is not as expected.

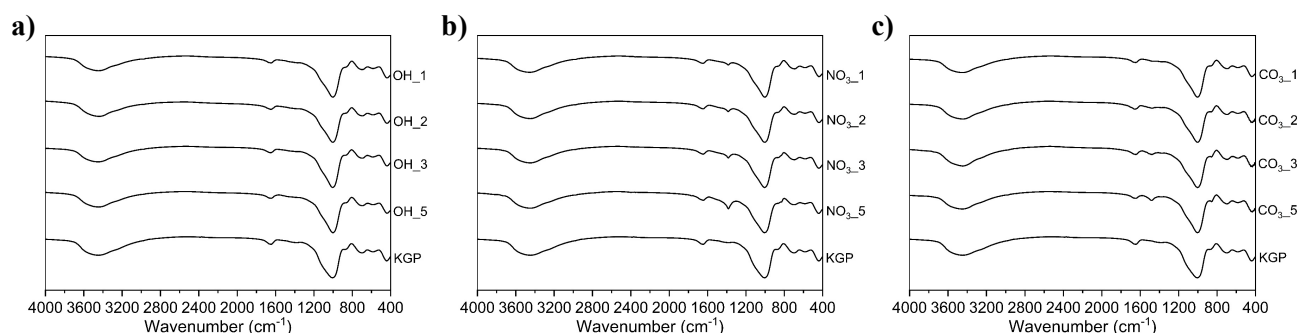


Figure 2: FTIR spectra of Sr-loaded K-geopolymers produced using a) strontium hydroxide, b) strontium nitrate and c) strontium carbonate compared with the KGP control after the first 3 days of reaction.

4. Conclusions

Isothermal conduction calorimetry shows that the anion within the salt compound affects the rate of the polymerisation reaction. The NO_3^- anion causes the greatest degree of retardation of the reaction, severely decreasing the maximum heat evolved during the polymerisation period.

FTIR confirms that the addition of the strontium salts has a negligible effect on the resultant structure of the geopolymer gel indicating minimal nanostructural changes in the K-A-S-H gel, and that the Sr may have been incorporated into the aluminosilicate gel in place of the charge balancing ion.

The conclusions drawn from this work indicate that the kinetics of formation of the geopolymer are directly dependent on the salt of the strontium being incorporated, yet the resultant structure is not detrimentally altered. This suggests that potassium silicate activated, metakaolin-based geopolymers are promising candidates for the production of a wasteform for the disposal of ^{90}Sr salts.

Acknowledgements

This work is funded by the Department of Chemical and Biological Engineering, The University of Sheffield, through a PhD scholarship to K. T. O. We are grateful to the PQ Corporation for the alkali silicate solutions used in this work and to the BASF and Laurence industries for supplying the metakaolin used in this work. We are also grateful to the Grantham Centre for Sustainable Futures for their training and funding.

References

- Dezerald, L., Kohanoff, J. J., Correa, A. A., Caro, A., Pellenq, R. J.-M., Ulm, F. J., & Saúl, A. (2015). Cement as a waste form for nuclear fission products: the case of ^{90}Sr and its daughters. *Environmental science & technology*, 49(22), 13676-13683.
- Hirose, K., Aoyama, M., Katsuragi, Y., & Sugimura, Y. (1987). Annual deposition of Sr-90, Cs-137 and Pu-239, 240 from the 1961-1980 nuclear explosions: A simple model. *Journal of the Meteorological Society of Japan. Ser. II*, 65(2), 259-277.
- Milestone, N. (2006). Reactions in cement encapsulated nuclear wastes: need for toolbox of different cement types. *Advances in Applied Ceramics*, 105(1), 13-20.
- Ojovan, M. I., Lee, W. E., & Kalmykov, S. N. (2019). *An introduction to nuclear waste immobilisation*. Elsevier.
- Provis, J. L. (2018). Alkali-activated materials. *Cement and Concrete Research*, 114, 40-48.
- Provis, J. L., Walls, P. A., & van Deventer, J. S. J. (2008). Geopolymerisation kinetics. 3. Effects of Cs and Sr salts. *Chemical engineering science*, 63(18), 4480-4489.
- Tits, J., Wieland, E., Müller, C. J., Landesman, C., & Bradbury, M. H. (2006). Strontium binding by calcium silicate hydrates. *Journal of Colloid and Interface Science*, 300(1), 78-87.
- Walkley, B., Ke, X., Hussein, O. H., Bernal, S. A., & Provis, J. L. (2020). Incorporation of strontium and calcium in geopolymer gels. *Journal of hazardous materials*, 382, 121015.
- Whicker, F. W., Pinder III, J. E., Bowling, J. W., Alberts, J. J., & Brisbin Jr, I. L. (1990). Distribution of long-lived radionuclides in an abandoned reactor cooling reservoir. *Ecological Monographs*, 60(4), 471-496.
- Wieland, E., Tits, J., Kunz, D., & Dähn, R. (2008). Strontium Uptake by Cementitious Materials. *Environmental science & technology*, 42(2), 403-409.
- Zhang, Z., Wang, H., Provis, J. L., Bullen, F., Reid, A., & Zhu, Y. (2012). Quantitative kinetic and structural analysis of geopolymers. Part 1. The activation of metakaolin with sodium hydroxide. *Thermochimica acta*, 539, 23-33.

Developing Pickering emulsion routes towards oil immobilisation in geopolymers

J. McWilliams^{*1}, B. Walkley², J. L. Provis¹

¹*Department of Materials Science and Engineering, University of Sheffield, United Kingdom
(E-mail jmcwilliams1@sheffield.ac.uk, j.provis@sheffield.ac.uk)*

²*Department of Chemical and Biological Engineering, University of Sheffield, United Kingdom
(Email: b.walkley@sheffield.ac.uk)*

Keywords: Geopolymers, Radioactive waste, Tributyl phosphate (TBP), Dodecane, Nevastane

ABSTRACT

Pickering emulsion with fumed silica has been investigated as a potential immobilisation route for liquid organic oils. The potassium geopolymers developed were based on a>NNL formulation with 1 wt% of fumed silica and 10/20/30/40 wt% of either TBP/Dodecane or Nevastane. The initial observation highlights a clear difference in the immobilisation of the two oils. The Nevastane appeared to be immobilised successfully whilst TBP/Dodecane separated from the geopolymer matrix. This separation was found to get worse with an increasing weight percentage of the TBP/Dodecane.

KEYWORDS: *Geopolymer, Radioactive waste, Immobilisation, Oils*

1. Introduction

Cement has been widely used for nuclear waste immobilisation, particularly for low level and intermediate level wastes, because it is a versatile, cheap, easy process, has high radiation stability, and is fire and impact resistant (Hyatt and Ojovan 2019). However, cementation increases the volume of the waste, and Portland cement may be considered sub-optimal for incorporating organic liquid waste due to its instability; addition of various types of organics at high loadings will result in strong retardation and the cement will not set (Tsang and Wang 2022). Adding an organic liquid that is immiscible with water makes the system more complicated because it has two individual liquid phases and a large quantity of solid particles (Tsang and Wang 2022). Geopolymers have been suggested as a viable alternative as they undergo a polycondensation reaction which is relatively unaffected by the addition of organic liquids, and so are able to set despite incorporation of these wastes at high loadings (Reeb et al. 2021).

The organic liquids which are the focus of this research are Nevastane and TBP (tributyl phosphate); both of which are organic oils. Oils are used as lubricants in fuel processing and manufacturing, and become classified as secondary nuclear waste due to radiological contamination. Nevastane is a generic motor oil and is used as a representation of the oil waste produced by the nuclear industry. TBP is used in the nuclear process during the PUREX process to extract valuable elements from spent nuclear fuel to be reused (Drinks et al. 2018). During the PUREX process, the spent TBP (30%, diluted with 70% kerosene) is irradiated and forms radiolysis products - the majority of which is dibutyl phosphate (DBP), monobutyl phosphate (MBP), organic acids and butanol. Radioactive waste loadings of 300 µg/mL of uranium, thorium, plutonium, and other radionuclides release alpha radioactivity that has been measured at levels as high as 9.67 Bq/mL (Drinks et al. 2018). The liquid nature of the spent TBP/OK from the PUREX process means that it needs to be treated for disposal.

Geopolymers are a subset of the broader class of alkali-activated materials (AAMs), which contain little to no calcium content (Provis and Bernal 2014). They are produced by a reaction of an aluminosilicate precursor (either metakaolin or fly ash) and alkali activator. The aluminosilicate precursor used in this research is metakaolin. Metakaolin is used instead of fly ash here due to its greater reactivity in the geopolymerisation process, which increases the reaction rate of the initial and final set (Jindal 2019).

When organic oils are added to the geopolymer matrix, it will form an unstable emulsion with the potassium-activating solution. The emulsion will be thermodynamically unstable and will result in the separation of the liquid and the oil (de Carvalho-Guimarães et al. 2022). To retain stability, both kinetically

and thermodynamically for an extended period emulsifying agents are required. Emulsifying agents could either be surfactants (such as Span 20 or Tween 80) or solid particles (either inorganic or organic) to create a Pickering emulsion (de Carvalho-Guimarães *et al.* 2022). Surfactants work by minimising the interfacial tension between the two liquids and resulting in the emulsion being more stable (de Carvalho-Guimarães *et al.* 2022). However, the use of surfactants has to be carefully monitored as they can cause damage to the environment if released (Yuan *et al.* 2014), and their interactions with waste radionuclides may be complex and may result in more rapid leaching of immobilised species.

A Pickering emulsion works by creating a layer of solid particles between the liquid and the oil to minimise tension and cause the emulsion to have greater stability (Pickering 1907). The solid particles irreversibly attach to the interface so provide superior stability to the emulsion than a surfactant (Yang *et al.* 2017). This reduces the likelihood of Pickering coalescence occurring. Pickering agents have the advantage of having additional functional properties, for example TiO_2 , which is both conductive and photocatalytic (Yang *et al.* 2017). Pickering emulsions have a wide range of applications including biomedicine, food and fine chemical synthesis (Yang *et al.* 2017).

Silica fume is an amorphous and very finely divided form of silicon dioxide, and is a by-product in the alloy production of silicon and ferrosilicon in electric arc furnaces. Silica fume has been widely used in the construction industry as a pozzolan, increasing the strength and impermeability of concrete (Chu and Kwan 2019). It can also improve the packing density by its ultrafine particles filling in the matrix. Very fine silica powders have both been investigated for their Pickering properties. Levine *et al.* were able to stabilise an O/W emulsion by hydrophilic silica nanoparticles 572 nm in diameter (Levine *et al.* 1989), forming a monolayer at the O/W interface.

Frelichowsha *et al.* (2009) investigated creating Pickering emulsions with various oils at 20 wt.% with 6 wt.% bare silica. The hydrophilic fumed silica was able to form successful emulsions with polar oils such as butanol, ethyl acetate and butyl lactate. The oil droplets were dispersed as a milky emulsion. Their unsuccessful emulsion attempts involved non-polar oils such as mineral oil, silicon oil and diethyl hexyl adipate; these oils very quickly underwent creaming and the oil was found on the top of the creamed emulsion. This work concluded that the favourable oils to form a Pickering emulsion were more polar and short-chained, e.g. mono or diesters (Frelichowska *et al.* 2009).

Katepelli *et al.* (2016) used two types of fumed silica to destabilise Pickering emulsion formed by Triton X-100 (non-ionic surfactant). Aerosil 200 (hydrophilic) and Aerosil R816 (particularly hydrophobic modified with hexadecyl (C16) chains). It was found that the Aerosil R816 was able to undergo coalescence by hydrophobic interactions between the C16 chains and the surfactant tail. This interaction depleted the surfactant from the interface of the oil and water, hence, breaking down the stable Pickering emulsion (Katepalli *et al.* 2016). This work is interesting in understanding the effect different fumed silica can have on a Pickering emulsion, especially the negative effect of hydrophobic fumed silica. It highlights that hydrophilic fumed silica must be used to ensure the stability of the formed Pickering emulsion and not hydrophobic fumed silica, which breaks it down.

Griffith and Daigle (2019) further investigated the effect of hydrophilic and hydrophobic silica fume and its effect on destabilising Pickering emulsions. The work aimed to determine if fumed silica particles with various wettability could be utilised to destabilise the Pickering emulsion. The fumed silica used was A200 (bare, the most hydrophilic), Aerosil R816 (hexadecyl silane modified, intermediate hydrophobicity) and Aerosil R805 (octyl silane modified, most hydrophobic). The authors believed that if the fumed silica was sufficiently hydrophobic, it would cause the particles to create a thin film and, hence, undergo coalescence (Griffith and Daigle 2019). When 0.01 wt.% of Aerosil R805 was added, 60 % of the oil was released (Griffith and Daigle 2019). The oil release was increased to 85 % when 0.05 wt.% Aerosil R805 fumed silica was added, because this type of silica fume would not get wetted by the continuous phase of the emulsion. Instead, the surface of the silica fume would interact with the emulsified oil drops, wetting the silica and producing macroscopic coalescence. When A200 and Aerosil R816 were added at all concentrations, no oil was released and the Pickering emulsion was unable to coalesce. This is because the silica particles were quickly wetted by the continuous phase of the emulsion so stopping any interaction between the emulsified oil drops and the surface of the silica particles. Griffith and Daigle concluded that the ability to coalesce the emulsion is related to the wettability of the silica fume by the continuous phase (Griffith and Daigle 2019).

The work described above has highlighted that if seeking to develop a Pickering emulsion as a pathway for oil immobilisation in a geopolymer, using hydrophobic silica fume would be detrimental to the stability of

the Pickering emulsion as it would destabilize it. Instead, it would be beneficial to use hydrophilic silica fume as it retains the stability of the Pickering emulsion.

2. Experimental

This work investigates the creation of Pickering emulsions with silica fume (1 wt.%) with TBP/dodecane (where dodecane represents the industrially-used kerosene) and Nevastane oil, at 10, 20, 30 and 40 wt.%, in geopolymer formulations that have been developed by the UK National Nuclear Laboratory for the PREDIS European Project, Table 1 (Phung). The geopolymer formulation is defined by the $\text{SiO}_2/\text{K}_2\text{O}$ and $\text{H}_2\text{O}/\text{K}_2\text{O}$ molar ratios of the activating solution, and the bulk $\text{K}_2\text{O}/\text{Al}_2\text{O}_3$ molar ratio of the mix (which thus defines the proportions between the activator and metakaolin constituents). The metakaolin used was Metamax (BASF).

Table 1 – The geopolymer formulation tested in this work

| Metakaolin | Activator $\text{SiO}_2/\text{K}_2\text{O}$ | Activator $\text{H}_2\text{O}/\text{K}_2\text{O}$ | Bulk $\text{K}_2\text{O}/\text{Al}_2\text{O}_3$ |
|------------|---|---|---|
| Metamax | 1.2 | 13 | 1.2 |

3. Results and Discussion

Samples of Metamax-potassium silicate geopolymers of the formulation 1.2/13/1.2 defined in Table 1 were prepared. The Metamax, activating solution, fumed silica and the organic oil were mixed together for ten minutes under 1,200 rpm. From the initial observation of the preparation process, at 10 wt.% TBP/dodecane there was a layer of liquid above the cement. It is likely that a quantity of oil was not incorporated in the geopolymer matrix and separated due to the unfavourability of the O/W emulsion. When the weight fraction of TBP/Dodecane was increased from 10 wt% to 40 wt%, there is a clear separation of the liquids with a significant quantity of the oil sitting above the cement, Figure 1. This suggests that the silica fume was not successful in aiding the immobilisation of the TBP/dodecane by Pickering emulsion.

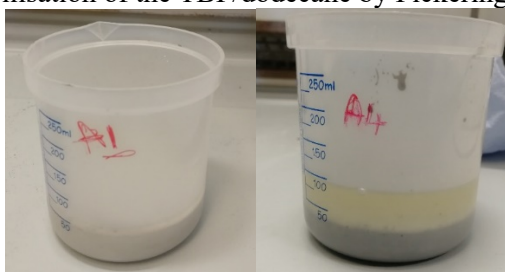


Figure 1 – Samples A1 and A4, 10 and 40 wt%, respectively, of TBP/dodecane potassium geopolymer with a layer of liquid above the cement sample.

For Nevastane, when the weight percentage was increased from 10 to 30 wt%, there was an increase in the viscosity of the sample; 30 wt% Nevastane was the most viscous of all the samples made and was difficult to pour, Figure 2.



Figure 2 – Sample B3, 30 wt% of Nevastane potassium geopolymer.

For 10, 20 and 30 wt% Nevastane there was no formation of a liquid layer on top of the cement sample which suggests that there was immobilisation of the oil. At 40 wt% Nevastane, there was a decrease in viscosity and was easier to pour than at 30 wt% Nevastane. It also had a ‘shiny’ surface, which suggests that not all of the oil was immobilised; Figure 3.



Figure 3 – Sample B4, 40 wt% of Nevastane potassium geopolymer with a ‘shiny’ layer on the surface of the cement.

4. Conclusions

This work has shown that there is a clear difference between the immobilisation of Nevastane and TBP/dodecane within the potassium geopolymer using a Pickering emulsion strategy to attempt to disperse and stabilise the oil. Nevastane looks to be incorporated with the geopolymer matrix, while the TBP/dodecane has separated from the matrix, and is worse as the oil loading increases. Further characterisation will be vital to understand the nature of these samples and how they interact with the oil.

Acknowledgements: The authors would like to express appreciation for the financial support of PREDIS (the PREDIS project has received funding from the Euratom research and training programme 2019-2020 under grant agreement No 945098) and the EPSRC GREEN CDT, and the constant support of the Cements@Sheffield team. We are also grateful to the PREDIS WP5 partners, particularly Martin Hayes of NNL, for discussions and ongoing collaboration related to geopolymer mix design development and validation in the context of radioactive waste immobilisation.

References:

- Chu, S. and Kwan, A. (2019). "Co-addition of metakaolin and silica fume in mortar: Effects and advantages." *Construction and Building Materials* **197**: 716-724.
- de Carvalho-Guimarães, F.B., Correa, K.L., de Souza, T.P., Rodríguez Amado, J.R., Ribeiro-Costa, R.M. and Silva-Júnior, J.O.C. (2022). "A Review of Pickering Emulsions: Perspectives and Applications." *Pharmaceuticals* **15**(11): 1413.
- Drinks, E., Lepeytre, C., Lorentz, C., Dunand, M., Mangematin, S., Dappozze, F. and Guillard, C. (2018). "UV-a photocatalytic degradation of the radionuclide complexants tributylphosphate and dibutylphosphate." *Chemical Engineering Journal* **352**: 143-150.
- Frelichowska, J., Bolzinger, M.-A. and Chevalier, Y. (2009). "Pickering emulsions with bare silica." *Colloids and Surfaces A: Physicochemical and Engineering Aspects* **343**(1-3): 70-74.
- Griffith, C. and Daigle, H. (2019). "Destabilizing Pickering emulsions using fumed silica particles with different wettabilities." *Journal of colloid and interface science* **547**: 117-126.
- Hyatt, N.C. and Ojovan, M.I. (2019). *Materials for nuclear waste immobilization, Multidisciplinary Digital Publishing Institute*. **12**: 3611.
- Jindal, B.B. (2019). "Investigations on the properties of geopolymer mortar and concrete with mineral admixtures: A review." *Construction and building materials* **227**: 116644.
- Katepalli, H., Bose, A., Hatton, T.A. and Blankschtein, D. (2016). "Destabilization of oil-in-water emulsions stabilized by non-ionic surfactants: effect of particle hydrophilicity." *Langmuir* **32**(41): 10694-10698.
- Levine, S., Bowen, B.D. and Partridge, S.J. (1989). "Stabilization of emulsions by fine particles I. Partitioning of particles between continuous phase and oil/water interface." *Colloids and surfaces* **38**(2): 325-343.
- Phung, Q.T. "Proceedings PREDIS May Workshop 2021 WP5-Progress on experimental protocols, formulation of conditioning materials and performance assessment for the direct conditioning of RLOW."
- Pickering, S.U. (1907). "Cxcvi.—emulsions." *Journal of the Chemical Society, Transactions* **91**: 2001-2021.
- Provis, J.L. and Bernal, S.A. (2014). "Geopolymers and Related Alkali-Activated Materials." *Annual Review of Materials Research* **44**(1): 299-327.
- Reeb, C., Pierlot, C., Davy, C. and Lambertin, D. (2021). "Incorporation of organic liquids into geopolymer materials-A review of processing, properties and applications." *Ceramics International* **47**(6): 7369-7385.
- Tsang, D. and Wang, L. (2022). *Low Carbon Stabilization and Solidification of Hazardous Wastes*, Elsevier.
- Yang, Y., Fang, Z., Chen, X., Zhang, W., Xie, Y., Chen, Y., Liu, Z. and Yuan, W. (2017). "An overview of Pickering emulsions: solid-particle materials, classification, morphology, and applications." *Frontiers in pharmacology* **8**: 287.
- Yuan, C., Xu, Z., Fan, M., Liu, H., Xie, Y. and Zhu, T. (2014). "Study on characteristics and harm of surfactants." *Journal of chemical and pharmaceutical research* **6**(7): 2233-2237.

Developing circular concrete through acid leaching of waste fines

T. Ding¹, H.S. Wong², M.H.N. Yio³, X. Qiao⁴ and C.R. Cheeseman^{5*}

¹ Imperial College London, London, UK

Email: tiejun.ding18@imperial.ac.uk

² Imperial College London, London, UK

Email: hong.wong@imperial.ac.uk

³ Imperial College London, London, UK

Email: marcus.yio@imperial.ac.uk

⁴ East China University of Science and Technology, Shanghai, China

Email: xiuchenqiao@ecust.edu.cn

⁵ Imperial College London, London, UK

Email: c.cheeseman@imperial.ac.uk

ABSTRACT

Acetic acid solutions have been used to leach hydrated Portland cement paste. The optimal acid concentration, liquid/solid ratio and effect of temperature on Ca²⁺ leaching is reported. The chemical composition and pozzolanic reactivity of the silica-rich solid residue from leaching waste concrete fines and hydrated cement paste are assessed, and the pozzolanic reactivity compared to commercially available supplementary cementitious materials such as fly ash, silica fume and ground limestone. The results show the pozzolanic reactivity of the silica-rich solid residue is comparable with fly ash, while that extracted from hydrated cement paste shows higher reactivity. The leachate formed contains high levels of Ca²⁺ ions that can react with carbonate ions under controlled conditions to form vaterite, a spherical polymorph of CaCO₃. The precipitated vaterite has hardening reactivity at high temperatures, making it a promising candidate for carbon negative construction materials. Hydrated cement paste is an important component in waste concrete and this work demonstrates how this can be beneficially used to generate new supplementary cementitious material, sequester CO₂ and form construction products.

KEYWORDS: *Waste concrete; acid treatment; SCM; circular concrete; carbon sequestration; vaterite*

1. Introduction

Concrete recycling primarily focusses on the reclamation of aggregates from construction and demolition waste through crushing and screening. This leaves adhered cement paste in the recycled concrete aggregates leading to reduced properties. Additionally, the recycling process generates a fine powder (< 0.15 mm) where most old cement paste accumulates. This adversely affect the performance of concrete and is unsuitable for reuse (Fang et al., 2021).

Using supplementary cementitious materials (SCMs) to replace some cement is effective in reducing the carbon emission in construction. Commonly used SCMs, such as fly ash, silica fume and blast furnace slag, are produced through highly energy-intensive and carbon positive processes. These materials are anticipated to be less available because these industrial processes are moving to more sustainable practices (Zhou et al., 2017). To meet the high demand for low-carbon construction materials, developing new SCMs with large availability and high quality has become an important research focus.

Indirect carbonation has been shown to improve the value of waste concrete fines. This method includes dissolving the hydrated cement paste using acid and sequestering CO₂ using the resulting Ca²⁺-rich

solution. Acetic acid (CH_3COOH) has been widely used because its safety and lack of Cl^- and SO_4^{2-} which have adverse effects on concrete durability. After acid leaching, the properties of the recycled aggregates are improved, making them suitable for reusing in new concrete. CO_2 sequestration using the Ca^{2+} -rich solution reduces the carbon footprint of the concrete and generates precipitated calcium carbonate (PCC) which can also be reused in concrete (Chen et al., 2017). This process has significant potential to achieve circular concrete. However, few studies have examined the silica-rich solid residue generated from this process. In our previous research, acetic acid solutions were used to remove the adhered cement paste from waste concrete fine aggregates. The properties of recovered sand were the same as new sand. Furthermore, the silica-rich solid residue formed during acid leaching is found to be pozzolanic (Ding et al., 2022). However, more detailed evaluations are required to understand its characterisation, reactivity and impact on mortar strength. Also, it is necessary to assess the applicability of this technology to waste concrete fine powder to make all components of concrete circular. Waste concrete fine powder from actual recycling facilities has a complex mineral composition because of contamination, so finely ground hydrated cement paste is used as the synthetic waste powder. The objectives of this work are to optimise process variables to maximise Ca^{2+} extraction, to compare the silica-rich residue generated from actual waste concrete fines and hydrated cement paste, to assess the potential for these materials to be used as an SCM by investigating their effect on the strength of cement mortars and to investigate the production of PCC through carbonation of the Ca^{2+} -rich solution.

2. Methods

Ground 28-day hydrated cement paste using CEM I 52.5 N at a water/cement ratio of 0.5 is used to simulate the concrete fine powder. Acetic acid leaching experiments are carried out at different acetic acid concentration (1, 2, 2.25, 2.5 mol/L), L/S ratio (7.5, 10, 12.5, 15, 20 mL/g) and temperature (20, 40, 60, 80, 100 °C). Ca^{2+} concentrations were measured at 15, 30, 60, 120, 240 and 480 minutes to determine the optimal leaching conditions.

The silica-rich solid residue from waste concrete fines (SR1) is prepared according to the optimised process in our previous work (Ding et al., 2022). The solid residue from hydrated cement paste (SR2) is produced under the optimal leaching conditions found in this work. In the pozzolanic reactivity testing, SR1, SR2 together with commercially available SCMs including fly ash (FA), silica fume (SF) and ground limestone (GL) are used. Ground quartz sand (QZ) is used as a non-reactive reference. The pozzolanic reactivity test follows the R^3 method specified in ASTM 1897-20. Potassium solution is made by dissolving 4 g of potassium hydroxide (KOH) and 20 g of potassium sulfate (K_2SO_4) in 1 L of deionized water. 10 g of test pozzolans, 30 g of $\text{Ca}(\text{OH})_2$, 5 g of CaCO_3 and 54 g potassium solution are thoroughly mixed. Then, 15 g of the paste is extracted, placed in the isothermal calorimeter and measured at 40 °C for 7 days. The cumulative heat released by every test pozzolan is recorded after the measurement. The compressive strength test follows British Standard BS 3892-1-1997. Superplasticiser is added to adjust the flow of mortar mixes to ensure it is same as the control flow with 100 % CEM I. The mortars are casted into 50×50×50 mm cubes, demoulded after 24 hours and cured in saturated lime water at 25 °C for 3, 7 and 28 days. At each time, the compressive strengths of each mortar mix are tested as an average of three samples.

The pH of the Ca^{2+} rich leachate is adjusted to 10.5 by adding concentrated ammonia solution ($\text{NH}_3 \cdot \text{H}_2\text{O}$). The impurities are removed by vacuum filtration. Pure CO_2 gas is then bubbled into this solution at ambient temperature (25 °C) with 600 rpm magnetic stirring until the pH drops to around 8. The precipitates formed are then separated by vacuum filtration, washed with deionised water and isopropanol and dried at 60 °C overnight.

3. Results and discussions

The variation in Ca^{2+} extraction with different process parameters is shown in Figure 1. Increasing acid concentration, L/S ratio can improve both the reaction rate and Ca extraction ratio. However, this effect has a boundary, beyond which there will be large amount of excess acid. Increasing temperature can improve the Ca extraction ratio probably by accelerating the dissolution of unhydrated C2S. However, the

energy cost will be significant if very high temperature is applied. Based on these, the optimal leaching conditions use 2 mol/L CH_3COOH , an L/S ratio of 12.5 mL/g, a temperature of 60 °C and 1 hour. The resulting pH is around 5.0. This enables almost all the calcium in the hydrated cement paste to be extracted and minimises the excess acid. The silica-rich residue (SR2) produced under these conditions are used in the subsequent experiments.

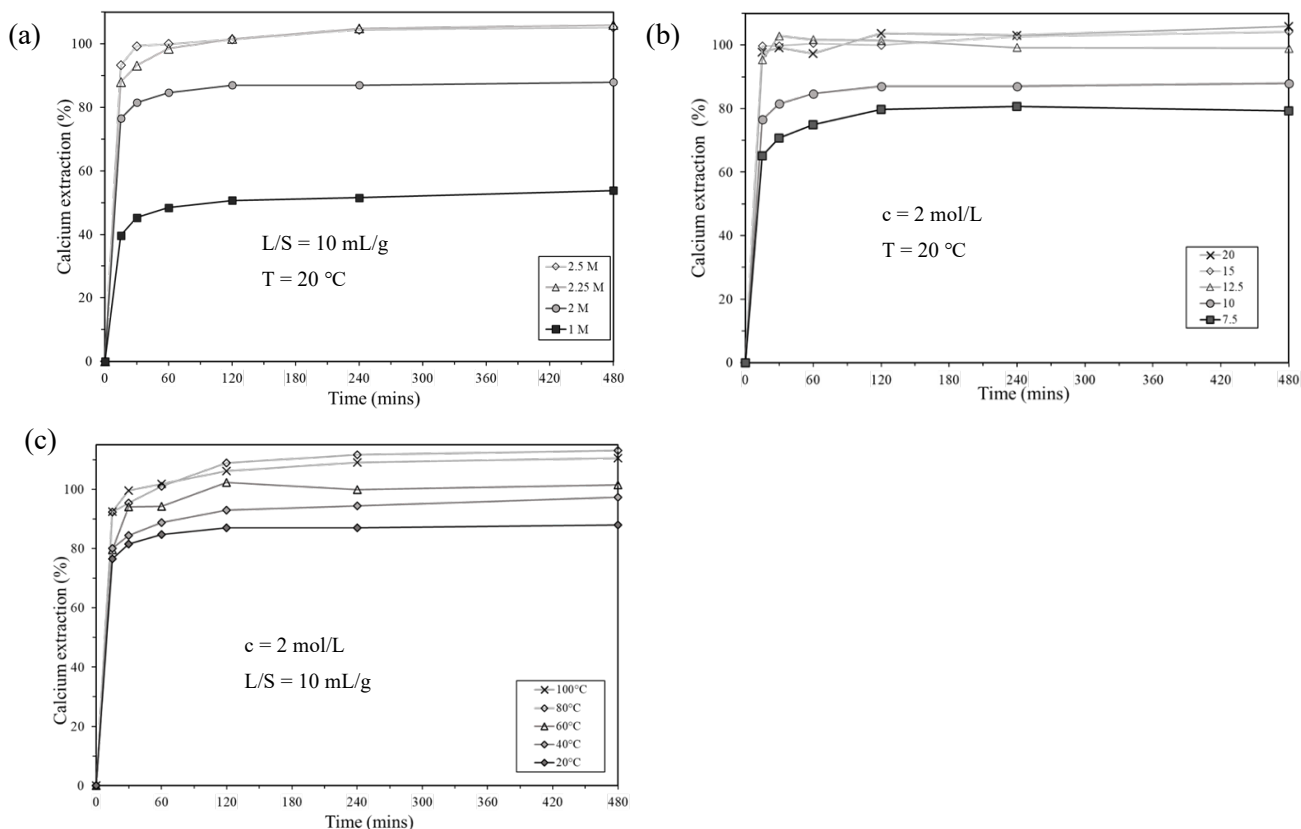


Figure 1. Effect of (a) acetic acid concentration (b) L/S ratio and (c) temperature on percentage of calcium extraction.

The chemical compositions of SR1 and SR2 are shown in Table 1. Both are mainly aluminosilicate materials. SR1 has a higher $\text{SiO}_2/\text{Al}_2\text{O}_3$ ratio together with higher magnesium and potassium contents compared to SR2. These are due to the contamination of quartz and crushed coarse aggregates, respectively. SR2 has a higher LOI value (24.3 %) than SR1 (9.2 %), because SR2 contains more aluminosilicate gel, which loses water through the condensation of silanol groups upon heating (Farias and Airoidi, 1998).

Table 1. Chemical composition of the silica-rich solid residues

| Material | Percentage (%) | | | | | | | | | |
|----------|----------------|------------------|--------------------------------|--------------------------------|-----------------|-----|------------------|-------------------|-------------------------------|------|
| | CaO | SiO ₂ | Al ₂ O ₃ | Fe ₂ O ₃ | SO ₃ | MgO | K ₂ O | Na ₂ O | P ₂ O ₅ | LOI |
| SR1 | 2.9 | 59.7 | 16.4 | 5.0 | 0.2 | 1.8 | 2.4 | 0.9 | 0.2 | 9.2 |
| SR2 | 5.1 | 47.7 | 10.5 | 4.1 | 0.3 | 0.1 | 0.2 | N/A | 0.1 | 24.3 |

The R^3 method tests the heat release of paste mixtures of test pozzolan, portlandite, calcite and alkali sulfate solution. This is a simpler system compared to cement pastes which helps to distinguish the chemical reaction of SCM from that of cement clinker. The isothermal calorimetry results are presented in Figure 2. At 7 days, silica fume is the most reactive, releasing 363.1 J/g of heat. This is followed by SR2 releasing 265.1 J/g of heat. The reactivity of SR1 and fly ash are similar, being lower than that of silica fume and SR2. Fly ash shows a slow reaction rate but continues to increase at later stage. The heat release of quartz sand and ground limestone are near zero, indicating that these are inert materials without

consumption of portlandite. The heat release rate for SR1 and SR2 are higher than other test pozzolans during the first 24 hours, probably because their smaller particle size and larger specific surface area, offering more nucleation sites for C-S-H gel formation.

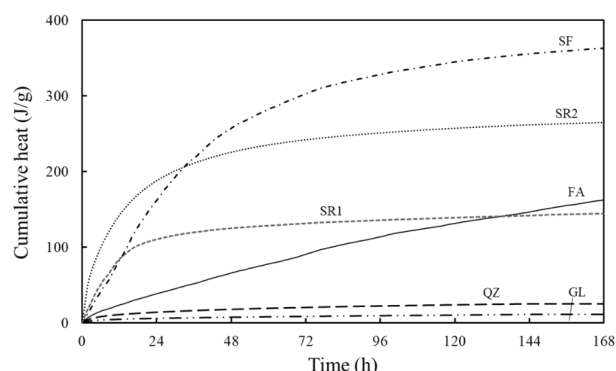


Figure 2. Cumulative heat flow of the test pozzolans at 40 °C for 7 days.

Figure 3 shows the compressive strength of the test mortars. The average compressive strengths of 20 % SR1 and SR2 mortars are 28.6, 32.9, 42.3 MPa and 26.8, 35.7, 47.3 MPa at 3, 7 and 28 days, respectively. The compressive strength of mortars containing SR2 is comparable to those containing same mass of silica fume. SR1 contributes less to the compressive strength of mortar but is still comparable to fly ash. The results prove the applicability of the silica-rich residue as a novel SCM.

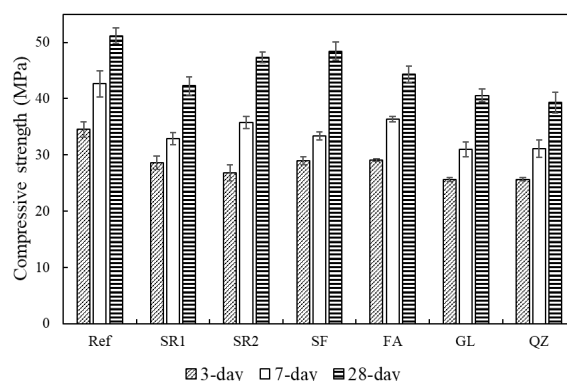


Figure 3. Compressive strength of the test mortars.

In the carbonation experiments, 100 % CO₂ is bubbled until the pH of the solution decreases to around 8, after which HCO₃⁻ ions starts to dominate over CO₃²⁻, resulting in the dissolution of PCC. This process takes approximately 30 minutes. The purity of PCC is 99.1 %. The XRD pattern (Figure 4a) only shows diffraction peaks of vaterite. This is further justified by the SEM image (Figure 4b), where the particle shape of PCC is predominantly spherical. The results illustrate that vaterite CaCO₃ with a very high purity can form through indirect carbonation of hydrated cement paste.

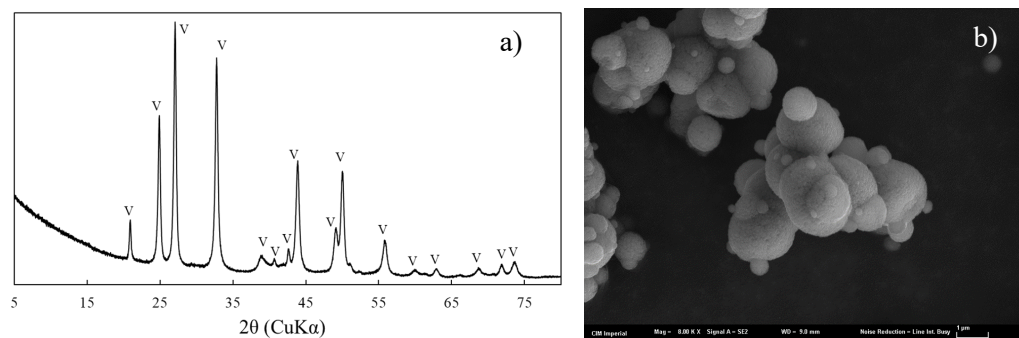


Figure 4. XRD pattern (a) and SEM image (b) of PCC. v – vaterite.

Vaterite is a reactive calcium carbonate phase and can be used as construction material under controlled curing conditions (Hargis et al., 2021). The next phase of our research will focus on converting the vaterite to applicable carbon-negative aggregates, enabling the production of carbon-negative concrete.

4. Conclusions

This study has proposed a novel aluminosilicate SCM from acetic acid recycling process for waste concrete fines to produce sustainable circular concrete and reduce emissions from concrete production processes. The optimal leaching conditions for hydrated cement paste are an acid concentration, L/S ratio and temperature of 2 mol/L, 12.5 mL/g, and 60 °C, respectively. The aluminosilicate SCM has significant pozzolanic reactivity, comparable to silica fume and fly ash. The reactivity of SR1 is lower than SR2 but is sufficient for compressive strength contributions. High-purity vaterite can be produced through CO₂ sequestration using the Ca-rich leachate.

References

- Chen P., Wang J., Wang L., Xu Y., Qian X. and Ma H. (2017) "Producing vaterite by CO₂ sequestration in the waste solution of chemical treatment of recycled concrete aggregates", *Journal of Cleaner Production*, 149: 735-742
- Ding T., Wong H., Qiao X. and Cheeseman C. (2022) "Developing circular concrete: Acid treatment of waste concrete fines", *Journal of Cleaner Production*, 365: 132615
- Fang X., Xuan D., Shen P. and Poon C. (2021) "Fast enhancement of recycled fine aggregates properties by wet carbonation", *Journal of Cleaner Production*, 313: 127867
- Hargis C., Chen I., Devenney M., Fernandez M., Gilliam R. and Thatcher R. (2021) "Calcium Carbonate Cement: A Carbon Capture, Utilization, and Storage (CCUS) Technique", *Materials*, 14(2709): 1-12
- Zhou D., Wang R., Tyrer M., Wong H. and Cheeseman C. (2017) "Sustainable infrastructure development through use of calcined excavated waste clay as a supplementary cementitious material", *Journal of Cleaner Production*, 168: 1180-1192

Application of Recycled Cementitious Material from Concrete Waste for UK Nuclear Waste Encapsulation

D.G. Scammell¹, H. Kinoshita^{*1}

¹ Department of Materials Science & Engineering, University of Sheffield, Sheffield, S1 3JD, United Kingdom

Email: dscammell1@sheffield.ac.uk¹, h.kinoshita@sheffield.ac.uk^{*1}

ABSTRACT

The study investigates the effects of using three-size fractions of recycled cement to replace Sellafield specification Portland cement by 80 wt.% for the development of new cementing grouts for nuclear waste encapsulation. Larger size fractions were not suitable for a cementitious grout due to their tendency to segregate, likely because of the high replacement level. The grout with the smaller size fraction was the most promising and could be a starting point for future development.

KEYWORDS: *Encapsulation, Recycling, Cementation, Nuclear waste, Concrete waste*

1. Introduction

Currently, 2.4 million m³ of concrete are expected to be consigned to landfill from the decommissioning of 25 nuclear facilities in the UK, UKRWI (2020); most of this concrete is expected to be ‘out of scope’, but strict legislation prevents this material from being used outside of the nuclear industry. One solution to reduce the amount of such concrete wastes, is to use them in the cementation of nuclear wastes, either replacing supplementary cementitious materials i.e., blast furnace slag (BFS) and pulverised fuel ash (PFA), or Portland cement (PC). This is significant due to the supply of BFS and PFA becoming more unpredictable as the UK transitions to net-zero. There are grout specifications set out by the UK nuclear industry, any cementing grout formulation must conform to these. The following criteria, the ‘plant acceptance tests’, are set out by the UK nuclear industry and must be met before a material can be considered for an encapsulation wasteform, Bart et al (2012):

- The flowability of the mix after 150 minutes of mixing, must be > 200 mm (Colflow test)
- The mix should have a bleed of less than 2 vol. % at 24 hours after mixing
- The initial setting time should be greater than 4 hours with the final set not occurring later than 48 hours (ideally 24 hours, NDA (2016))
- The compressive strength should exceed 7 MPa at 90 days

The heat of hydration must be kept ≤ 180 kJ/kg after 24 hours at 35 °C, Kearney et al (2021), as a high thermal gradient can lead to cracks within the wasteform, decreasing their durability, Sharp et al (2003). In the present study, simulant of recycled cementitious material (RCM) was prepared and blended with the Sellafield specification Portland cement at 80 wt.% to understand the effects of their size fractions to develop new cementing grouts for nuclear waste encapsulation. The investigation was conducted in comparison with the neat Portland cement paste, against the criteria.

2. Methods

The RCM simulants were prepared using CEM I 52,5 N (produced by Breedon) and distilled water, mixed at a water-to-cement (w/c) ratio of 0.35 in a Kenwood mixer for 10 minutes. After 14 weeks of hydration, the RCM simulant was reduced to a suitable feed size ($< \sim 40$ mm), and at 17 weeks, further crushed using a Retsch jawcrusher, to separate into three size fractions using a sieve shaker. At 18 weeks

of hydration, the prepared RCM simulants were used to produce the grouts with the formulations shown in *Table 1*. The notations S, M, and L in the grout name refer to small, medium, and large-size fractions.

Table 1: The grout formulations used in the experiment. Values are normalised to be (RCM + PC) = 100 g

| Grout | RCM simulant | PC | Distilled water | RCM size fraction |
|-----------|--------------|-------|-----------------|-------------------|
| Reference | - | 100 g | 35 g | - |
| S-grout | 80 g | 20 g | 35 g | < 0.5 mm |
| M-grout | 80 g | 20 g | 35 g | 0.5 mm - 1.18 mm |
| L-grout | 80 g | 20 g | 35 g | 1.18 mm - 2.36 mm |

The RCM simulants were blended with anhydrous Portland cement (Sellafield specification CEM I produced by Hanson) powder for over 20 minutes in a Kenwood mixer. The blends (RCM + PC) were then mixed with distilled water for 15 minutes. The grouts were placed in 15 ml centrifuge tubes, vibrated for 30 seconds, and then sealed for curing. A part of the grouts were cast in 50 mm steel cube moulds for 24 hours in a sealed bag with 100 % RH, then demoulded and kept in the bag for curing. The M-grout had to be remade at 20 weeks of RCM hydration due to demoulding issues in the initial samples.

After 14 or 28 days of curing, samples were removed from the centrifuge tubes and sliced into ~2 mm disks with a slow-speed saw. The samples were then immersed in isopropanol for 24 hours, air-dried for 24 hours, and then stored in sealed containers. This material was further broken into pieces or powdered (< 63 μ m) and analysed using mercury intrusion porosimetry (MIP) (Micromeritics autopore V) and X-ray diffraction (XRD) (Bruker D2 phaser). The 50 mm cube samples were used to measure the compressive strength after 91 days of curing (Controls compressive testing machine for the reference sample, Zwick/Roell z050 50 kN testing machine for the other grouts).

Using 19-week-old RCM, 600 g of grout were produced for each formulation for bleed and mini-slump measurements: sealed 100 ml measuring cylinders were utilised at the 100 ml mark, with the measurement taken at 24 hours; 3 mini-slump tests were performed per grout. With 23-week-old RCM, 675 g of grout were produced for each formulation for calorimetry and VICAT measurements. The heat generation was recorded relative to 15 g of distilled water using a TAM Air isothermal calorimeter. The VICAT measurements were collected using a Matest vicatronic using a 1.13 mm penetration head. The sample preparation time of ~10 minutes have been accounted for in the results. The reference and S-grout utilised a penetration step time of 10 minutes, which was increased to 20 minutes for the M- and L-grouts.

3. Results and Discussion

The obtained fresh state properties i.e., slump area, bleed, setting time, and heat generation are summarised in *Table 2*, together with the compressive strength data of the corresponding formulations after 91 days of curing.

Table 2: Mini slump, Bleed, VICAT, calorimetry, and strength results for the reference and three grouts

| Grout | Slump area (cm ²) | Bleed (%) | Initial setting time (min) | Final setting time (min) | Heat [24 hrs] (J/g) | Strength [91 days] (Mpa) |
|-----------|-------------------------------|-----------|----------------------------|--------------------------|---------------------|--------------------------|
| Reference | 38.79 \pm 3.15 | 0% | 230 | 410 | 112.52 | 92.31 \pm 4.88 |
| S grout | - | < 1 | 470 | 880 | 51.43 | 12.01 \pm 0.20 |
| M grout | - | ~3 | 180 | 560 | 41.69* | 6.27 \pm 0.07 |
| L grout | - | ~5 | 140 | 1,280 | 35.55* | 6.19 \pm 0.49 |

*Due to the inhomogeneous nature, the more flowable cement/water mixture may have been preferentially collected in the sample holder, and thus the data may not be accurate

In the mini-slump test, the reference grout proved satisfactory; an average slump area of 38.79 \pm 3.15 cm² was obtained. A homogenous mixture was produced for the S-grout, but its viscosity was very high and did not produce a satisfactory slump result that could be measured. It has been reported, that upon the addition of fine recycled concrete aggregate, a mixture can become less workable, Rao et al (2018), Deju et al (2015). For the other two grouts, the separation of the RCM fraction and the cement/water mixture was observed, and they were deemed unsatisfactory in the slump test and thus workability.

A small amount of bleed was observed in the formulation containing the smaller size fraction of RCM, which increased in the grouts with larger RCM size fractions. There was a decrease in the initial setting time with the larger RCM size fractions, while no obvious trend was identified for the final setting time. The S-grout satisfied the setting time requirement, NDA (2016).

A general decreasing trend was observed in the heat generation (24 hours at 25 °C) with an increase in the RCM size fraction, with their values less than half of that in the reference formulation, likely due to the small fraction (20 wt.%) of anhydrous PC used in the fresh pastes. Due to the inhomogeneous nature of the M- and L-grouts, the more flowable cement/water mixture may have been preferentially collected in the sample holder for the measurement, and thus the data may not be accurate, although this was not the case for the reference and the S-grout.

The compressive strength was much smaller in the formulations with RCM fractions compared to the reference, but a smaller RCM size fraction appears to be better than the larger ones. The S-grout met the required value of 7 Mpa.

Figure 1 shows MIP data for the grouts at 14 and 28 days. In the earlier stage of 14 days, the larger RCM size fractions resulted in lower porosity. This implies that the smaller RCM size fractions introduced more microstructural imperfections into the system. The larger surface area of the RCM may also result in an increased interfacial transition zone. The difference in porosity between the RCM-containing grouts decreased at 28 days, owing to the increased hydration in the system with smaller RCM sizes.

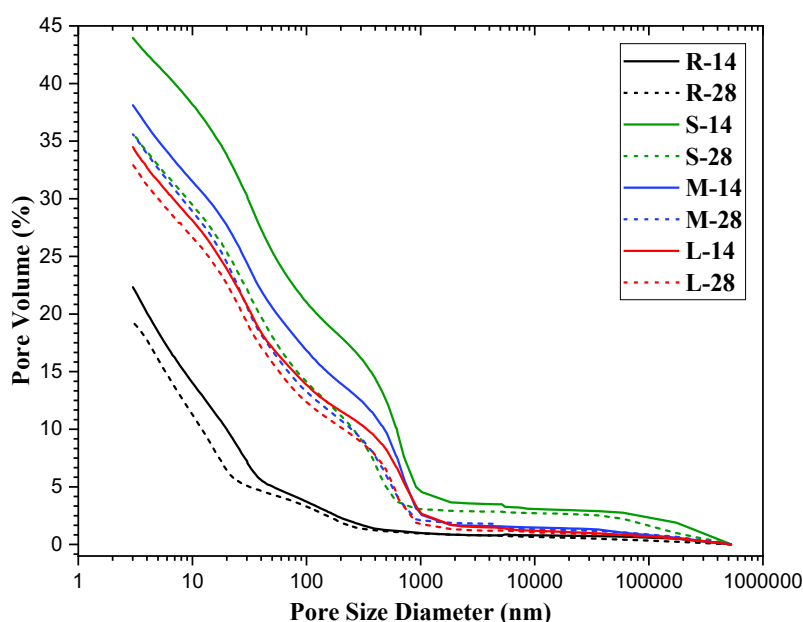


Figure 1: Pore volume vs Pore size diameter of the reference and 3 grouts at 14 and 28 days of hydration

The XRD data can be viewed in Figure 2. The reflection peaks for portlandite are observed in all samples. In regards to clinker phases, as shown in Figures 2 (a) and 2 (c), alite was more prevalent in the reference at 14 days of hydration, due to the presence of more unreacted alite in this formulation. All alite and belite peaks decreased in their intensity for all samples from 14 to 28 days. Ferrite peaks are detectable at 28 days only in the M-grout and reference. Aluminate peaks are detectable in all samples, decreasing with time as expected. Focusing on hydrates, as shown in Figures 2 (a) and 2 (b), ettringite peaks are observed for all grouts. The S-grout appears to have a defining phase of monocarbonate while the M-grout appears to have both hemicarbonates and monocarbonate in addition to monosulphate. The L-grout also has hemicarbonates and monocarbonate, but less prominent in the monosulphate peaks.

4. Conclusion

This paper examined the effects of replacing Sellafield specification CEM I with RCM simulant with 3 different size fractions. The reference and the S-grout met the required specification for bleed with only the S-grout meeting the required specifications for setting times. The S-grout also met the required specifications for strength. The heat production was less in the RCM grouts. XRD showed different phase

constitutions: S-grout (Mc), M-grout (Hc, Mc, & Ms), and L-grout (Hc & Mc). Although the RCM grouts did not fulfill all the requirements, the S-grout was the most promising and could form the base for further development.

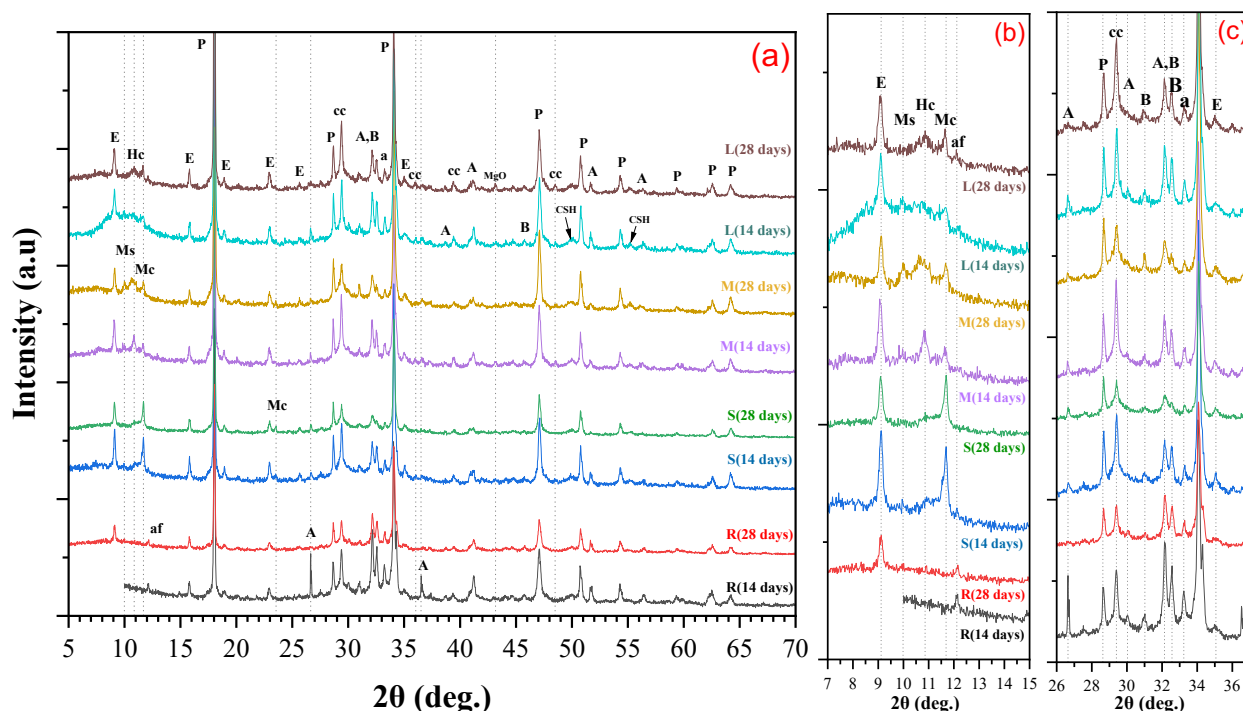


Figure 2: XRD data for the reference and grouts for the range (a) 5-70 ° 2θ, (b) 7-15 ° 2θ, and (c) 26 - 37 ° 2θ. Phases: E-ettringite, Ms-monosulphate, Hc-hemicarbonate, Mc-monocarbonate, af-ferrite, P-portlandite, cc-calcite, A-alite, B-belite, a-aluminate, CSH-calcium silicate hydrate.

Acknowledgements

The authors would like to express appreciation to Breendon's Hope cement works for aid in material processing, and for the financial support of the project from EPSRC under grant EP/T517835/1.

References

- Bart, F., Cau-Di-Coumes, C., Frizon, F. and Lorente, S. (2012) *Cement-based materials for nuclear waste storage*, New York, Springer.
- Deju, R., Dragusin, M., Mazilu, C. & Tuca, C. (2015) "Tests regarding filling performance of the mortars obtained by radioactive recycled sand", *Rom Rep Phys*, 67(3): 1159-1175
- Kearney, S. et al. (2021) "Cement-based stabilisation/solidification of radioactive waste", *Low Carbonation Stabilisation and Solidification of Hazardous Wastes*, Elsevier, Chapter 25.
- NDA. (2016) *RWM HAW Innovation and Delivery: A Review of Cement Powders Security of Supply, Specification and Disposability Issues*.
- Rao, M. C., Bhattacharyya, S. K. & Barai, S. V. (2018) *Systematic Approach of Characterisation and Behaviour of Recycled Aggregate Concrete*, Springer Singapore Pte. Limited.
- Sharp, J. H., Hill, J., Milestone, N. B. & Miller, E. W. (2003) "Cementitious systems for encapsulation of intermediate level waste", *Proceedings of the International Conference on Radioactive Waste Management and Environmental Remediation*, ICEM, vol.3: 1425-1433.
- UKRWI. (2020) *UKRWI 2019 Site data*. [Online] Available at: <https://ukinventory.nda.gov.uk/the2022inventory/2022-site-data/> [Accessed Nov 2020].

Investigation on the effect of recycled powders from demolished concrete on the rheological properties of cement paste

J.Z. Li¹, B.G. Zhan^{1,2*}, L. Hu¹, P. Gao^{1,2}, Q.J. Yu^{1,2}

¹ Hefei University of Technology, Anhui Province, 230009, China;

² Engineering Research Center of Low-carbon Technology and Equipment for Cement-based Materials, Ministry of Education, Hefei University of Technology, Anhui Province, 230009, China.

Email: ljz0512@mail.hfut.edu.cn; bgzhan@hfut.edu.cn; 2020170676@mail.hfut.edu.cn; gaop@hfut.edu.cn; concyuyq@hfut.edu.cn.

ABSTRACT

Recently, recycled powder from demolished concrete has been gradually applied to replace binders in preparing cementitious materials with the aim of environmental protection and carbon reduction, whereas the workability of fresh paste mixed with recycled concrete powders (RCPs) was obviously decreased and became a serious problem in application. The paper aims to explore the rheological properties of cement paste mixed with various types of RCPs. Firstly, the basic properties of various RCPs (e.g., specific surface area, mineral/chemical composition, etc.), were studied. Following this, the zeta potential and rheological properties of cement paste having different substitute contents of RCPs were examined. Results showed that the zeta potentials of cement pastes decreased with the substitute contents of RCPs increasing due to the large negative zeta potential values of main mineral compositions in RCPs (e.g., quartz, dolomite, albite, etc.). The yield stress and plastic viscosity of composite paste increased with the substitute contents of RCPs increasing. Compared with the cement paste mixed with RCPB, the cement paste mixed with RCPA has the higher yield stress and plastic viscosity at 11 min, which can be attributed to the smaller zeta potentials, the smaller density and the larger specific surface area.

KEYWORDS: *Recycled powder, Rheological property, Zeta potential, Yield stress, Plastic viscosity.*

1. Introduction

The recycled concrete powder (RCP) with size of < 75 μm , approximately accounting for 10% - 20% of the waste concrete (Kwon et al (2015)) is ineffective utilized due to its disadvantages such as high-water absorption, low activity, complex and variable components. Previous studies indicated that in terms of the durability and mechanical properties, RCPs have the potential to be used as a supplementary cementitious material (Liu et al. (2020), Ma et al. (2019)). Unfortunately, due to the large water absorption, the incorporation of RCPs significantly affected the fluidity of fresh cement-based materials (Li et al (2020) and Moon et al. (2008)). For instance, Kim et al. (2012) found that with the replacement rate of cement by RCPs increasing, both the plastic viscosity and yield stress of the composite paste gradually decreased due to the increase in the amount of water not related to hydration reaction, whereas the opposite conclusion was observed by Duan et al. (2020). This can be attributed to the variation in the properties of RCPs in the various literatures. According to the existing literatures, in order to reveal the influence mechanism of basic properties of RCPs on the rheological properties of cement paste, there are still a great deal of work needed to be done. Hence, this paper collected two types of RCPs in China and aims to investigate the effect of the basic properties of RCPs on the rheological properties of the cement paste mixed with different incorporation rates of various RCPs. The results are expected to provide a guidance for the efficient utilization of RCPs in cement-based materials.

2. Experiments

2.1 Raw materials

The P-I 42.5 Portland cement and two types of demolition waste concretes (named respectively as RCPA and RCPB) were used. Their chemical compositions were shown in Table. 1. And Their particle size distributions were showed in Fig. 1, where their micromorphologies were also given. As can be seen, the RCPs possess more fine particles with a size of $< 10\mu\text{m}$ than cement, and the surface of cement particles is relatively smooth, whereas there are much loose hydration product on the surface of RCP particles. The BET specific surface area of cement, RCPA and RCPB were respectively measured as 1188, 11040 and 4482 m^2/kg , which consist of their internal and external through-hole areas. The measured densities of cement, RCPA and RCPB materials were 3.07, 2.50 and 2.56 g/cm^3 , respectively. The mineral compositions of two RCPs were respectively shown in Fig. 2. As can be seen, the primary mineral compositions in various RCPs are quartz, calcite and dolomite.

Table 1 The chemical compositions of cement and RCPs (wt.%)

| Material | Chemical composition (%) | | | | | | | | | | LOI |
|----------|--------------------------|------------------|--------------------------------|-----------------|--------------------------------|------------------|------|------------------|-------------------|--------|-------|
| | CaO | SiO ₂ | Fe ₂ O ₃ | SO ₃ | Al ₂ O ₃ | K ₂ O | MgO | TiO ₂ | Na ₂ O | Others | |
| Cement | 76.34 | 10.36 | 4.58 | 2.80 | 2.28 | 1.20 | 0.55 | 0.33 | 0.21 | 1.35 | 3.25 |
| RCPA | 52.16 | 20.72 | 7.53 | 1.28 | 6.13 | 2.09 | 1.66 | 2.96 | 0.14 | 5.33 | 22.61 |
| RCPB | 55.81 | 18.89 | 6.88 | 1.13 | 4.91 | 2.27 | 1.74 | 3.38 | 0.14 | 4.85 | 22.30 |

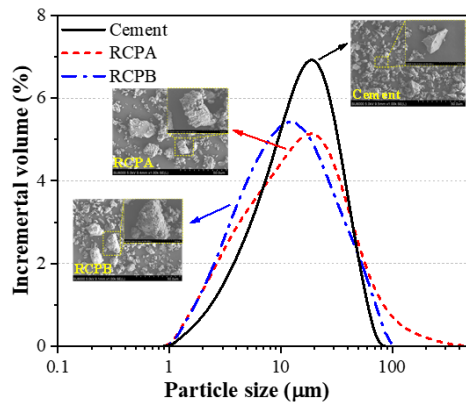


Fig. 1 Particle size distributions of various RCPs and cement

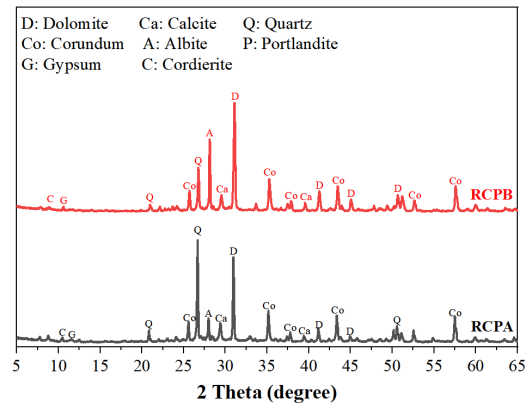


Fig. 2 The mineral compositions of various types of RCPs

2.2 Mixture preparation

The detailed mixture proportions of fresh paste used to test the rheological properties are listed in Table 2. The water/binder ratio (w/c) is adopted as 0.45. The replacement levels of each RCPs are 0, 10%, 20% and 30% by mass.

Table 2 The chemical compositions of cement and RCPs (wt.%)

| Names | Cement/g | RCPA/g | RCPB/g | Water/g | w/c |
|----------|----------|--------|--------|---------|-------|
| Cement | 300 | - | - | 135 | 0.45 |
| C/RCPA10 | 270 | 30 | - | 135 | |
| C/RCPA20 | 240 | 60 | - | 135 | |
| C/RCPA30 | 210 | 90 | - | 135 | |
| C/RCPB10 | 270 | - | 30 | 135 | |
| C/RCPB20 | 240 | - | 60 | 135 | |
| C/RCPB30 | 210 | - | 90 | 135 | |

2.3 Testing methods

The zeta potential was measured by the Malvern ZS90. During the test, 1 g of each blend was added into 100ml deionized water and magnetically stirred for 5 min to obtain the suspension. The zeta potential of each blends was tested after the blends contact with water for 11 min, where each test was obtained from the mean value of 5 measurements.

The rheological properties of fresh composite paste were measured using a rotational rheometer (Anton-Paar MCR302). The fresh composite paste started to be tested at the time of 7 min of contact between powders and water. The rheological test program was shown in Fig. 3.

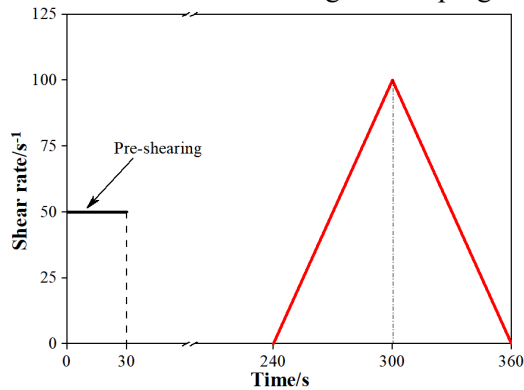


Fig. 3 The shearing program of the rheological measurements

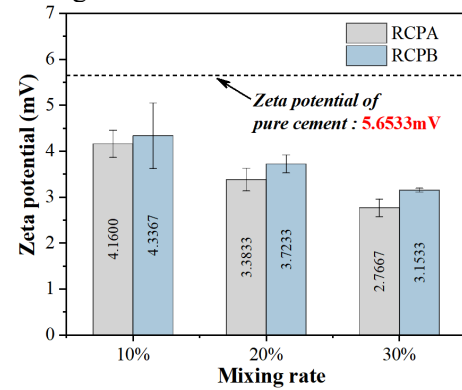


Fig. 4 Effect of various types of RCPs incorporation on the zeta potential

3. Results and discussion

3.1 Surface charge analysis

Fig. 4 showed the zeta potentials of the water-cement-RCPs (if any) system at 11min. As can be seen, the zeta potential values generally decreased with increasing the RCPs content. This is attributed to the mineral compositions of RCPs, the quartz, dolomite, albite in RCPs possess large negative zeta potential values when the pH in system is > 7 (Wang et al. (2020), Sun et al. (2018)). Compared with the cement paste containing with RCPB, the suspension solution of cement paste mixed with RCPA has a lower zeta potential value at 11 min. This may be attributed to their difference of hydration rate, the paste containing RCPB has a higher alkali-content and fineness than the paste containing RCPA, thus could products more hydration products produced by C_3A hydration possess large positive zeta potentials at the 11 min.

3.2 Shear stress-shear rate behaviour of cement paste with RCPs

Fig. 5 showed the shear stress-shear rate curves at 11 min for cement pastes mixed with two RCPs. Considering the reliability of the data of down curves, this paper adopted the down curves to fit and obtain the rheological parameters. The Bingham model (Zhou et al. (2022)) was adopted to model the rheological parameters.

Fig. 6 summarized the yield stresses and the plastic viscosity of composite pastes mixed with different types of RCPs. As can be seen, the incorporation of RCPs increases the yield stress of cement paste, and the yield stress increases with the RCPs content increasing. The similar trend was observed in the plastic viscosity. This can be explained using the thickness of the water film theory (Guo et al. (2021)). Both RCPs are finer than cement, their filling effects can increase the filling density and release interstitial water. In contrast, the large specific surface area of RCP requires a large amount of water for wetting the particle surface, which occupies the dominant factor, thus the water film thickness of composite paste reduced with the RCP content increasing, resulting the increase of the dynamic shear stress and plastic viscosity. Compared with the paste containing the RCPB, the paste containing the same dose of RCPA possesses a higher shear stress and plastic viscosity, which is because that the RCPA has a higher specific surface area than RCPB, and the paste mixed with RCPA has a lower zeta potential at 11 min.

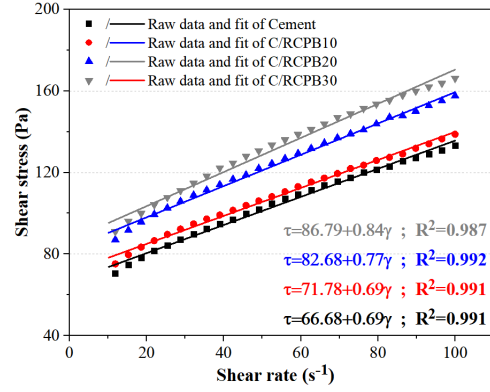
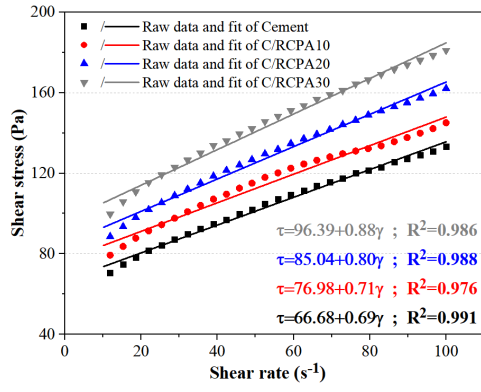


Fig. 5 Rheological behaviour of cement pastes mixed with various types of RCPs

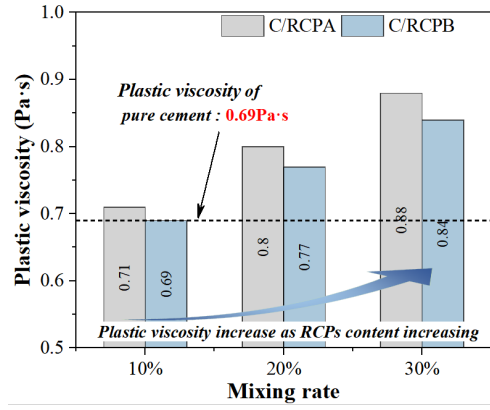
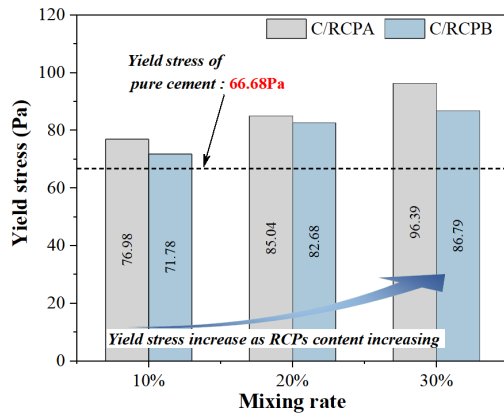


Fig. 6 The rheological parameters of composite paste containing various types of RCPs

4. Conclusions

Based on the data herein, some main conclusions can be concluded as follows:

- (1) The surface of RCPs is encapsulated with much hydrated C-S-H gels, resulting in its rougher surface and a larger specific surface area, and all RCPs have more fine particles than cement.
- (2) The zeta potentials of cement pastes were generally reduced after incorporated with RCPs.
- (3) The yield stress and plastic viscosity of the cement paste obviously increased with the RCPs content increasing. Compared with the paste containing RCPB, the cement paste mixed with RCPA possesses larger yield stress and plastic viscosity due to its the lower zeta potential and the large specific surface.

Acknowledgements

The authors sincerely appreciate the support of the National Key Research and Development Program (2020YFC1909902), the National Natural Science Foundation of China (Grant No. 52002129).

References

- Kwon E., Ahn J., Cho B., et al. (2015) "A Study on Development of Recycled Cement Made from Waste Cementitious Powder". *Construction and Building Materials*, 83: 174-180.
- Liu Q., Li B., Xiao J.Z., Singh A. (2020) "Utilization Potential of Aerated Concrete Block Powder and Clay Brick Powder from C&D Waste". *Constr. Build. Mater.*, 238: 117721.
- Ma Z.M., Li W., Wu H.X., et al. (2019) "Chloride Permeability of Concrete Mixed with Activity Recycled Powder Obtained from C&D Waste". *Construction and Building Materials*, 199: 652-663.
- Li S., Gao J., Li Q., et al. (2020) "Investigation of Using Recycled Powder from the Preparation of Recycled Aggregate as A Supplementary Cementitious Material". *Construction and Building Materials*, 267 (4): 120976.
- Moon D.J., Kim Y.B., Ryou J.S. (2008) "An Approach for The Recycling of Waste Concrete Powder as Cementitious Materials". *Journal of Ceramic Processing research*, 9 (3): 278-281.

- Kim Y.J., Yun W.C. "Utilization of Waste Concrete Powder as A Substitution Material for Cement". *Construction and Building Materials*, 30: 500-504.
- Duan Z.H., Hou S.D., Xiao J.Z., et al. (2020) "Study on the essential properties of recycled powders from construction and demolition waste". *Journal of Cleaner Production*, 253: 119865.
- Wang L.Q. (2020) "The Effect and Mechanism of Construction Solid Waste Powder on the Properties of Cement-Based Materials at the Micro-Nano Scale". *Guangzhou University*.
- Sun L., Chen P., Jiang X.Q., et al. (2018) "Adsorption Characteristics of Lead from Dolomite from Different Areas". *Non-Metallic Mines*, 41 (05) :89-91.
- Zhou Y., Pu S.C., Han F.H., et al. (2022) "Effect of Ultrafine Slag on Hydration Heat and Rheology Properties of Portland Cement Paste". *Powder Technology*, 405: 117549.
- Guo Z.B., Qiu J.P., Jiang H.Q., et al. (2021) "Flowability of ultrafine-tailings cemented paste backfill incorporating superplasticizer: insight from water film thickness theory". *Powder Technology*, 381: 509-517.

Evaluating the potential of Steel slags as alternative raw materials for Portland cement clinker production

D. Makhija ^{1*}, M. Rustagi ², J. Kole ³, J. Suresh ⁴, P. Patra ⁵, V. Reddy ⁶

1 - JSW Cement Ltd, Bellary, India, dilip.makhija@jsw.in

2 - JSW Cement Ltd, Mumbai, India, manoj.rustagi@jsw.in

3 - JSW Cement Ltd, Mumbai, India, jagabandhu.kole@jsw.in

4 - JSW Cement Ltd, Bellary, India, j.suresh1@jsw.in

5 - JSW Cement Ltd, Bellary, India, priyapratim.patra@jsw.in

6 - JSW Cement Ltd, Mumbai, India, kvamsi.reddy@jsw.in

ABSTRACT

The Steelmaking process generates different slag types during the refining and alloying stages. Some of these slags especially the LD slag (Linz-Donawitz Slag) and the Al-killed LF slag (AKLF) contain minerals that can be effectively recycled through clinkerization process in Portland cement production.

Research work was carried out to investigate the possibility of using above type of steel slags in the raw meal for the production of cement clinker. The objective was to find the threshold limit of utilizing both these type of slags without affecting the clinker and portland cement properties. The baseline raw meal was prepared as a reference for comparison (BL) while a set of 4 raw meals were prepared in which the proportion of LD slag and the AKLF slags were varied (S1 to S4). The LD slag was varied between 1.5 - 15 wt%, while the AKLF slag was varied between 1.5 - 6.0 wt%.

All the five sets of raw meals were sintered individually in a muffle furnace at a temperature of 1450 °C for 45 minutes. The sintered samples were separately evaluated for chemical and mineralogical properties and physical properties to understand the effect of slag addition on the above properties. The results of physical, chemical and mineralogical examination showed that the addition of steel slags (LD and AKLF) improved the clinker quality up to a maximum of 7 % LD slag and 6% AKLF slag when compared with baseline clinker. The compressive strengths at 1, 3, 7 and 28 days observed for clinkers (S1 to S3) were all exceeding the corresponding values of baseline clinker sample (BL). It was concluded from the above research work that LD slag and AKLF slag together can be used up to 13% as an alternative material without affecting the portland cement quality produced from such clinker.

Keywords: LD slag, Al Killed Slag, Alternative material, Clinker, Burnability

1. Introduction

Industry by-products recycling and reuse such as that of steel slags offer a unique advantage that not only it lowers the specific raw material consumption but it also helps in lowering the overall disposal costs and other environmental hazards that are associated with the waste disposal. Steel industry generates various types of by-products such as granulated blast furnace slag, steel slag of various types depending on their chemistry, flue dust and sludge (Tsakiridis et.al,2008). Efficient utilization of such by-products within the steel plant and in other manufacturing industries such as cement industry helps in resource conservation. The part replacement of clinker with ground granulated blast furnace slag to produce Portland Slag cement is the best example where the by-product utilization has achieved the most efficient use not only resulting in cost optimization but also improving the cement product quality with regards to its chemical attack properties (Malhotra, 1987).

Most of the metallurgical slags in view of their quality are used as aggregates for different applications such as in concrete replacing the river sand, as coarse aggregates in concrete roads and pavements, paver blocks etc. However, all these innovations coupled together have solved only about 50% of the problem (Motz and Geiseler, 2001). Today, about 50% of Steel slag is still unutilized and disposed of at safer places to avoid land and water pollution.

The literature published so far has research gaps with respect to usage of steel slags such as high alumina Ladle furnace (LF) slag, LD slag as a raw material for raw meal in clinker production. The clinker production utilizes various corrective minerals such as iron ore and aluminum laterite. These can be substituted by LD slag and Al killed LF slags (AKLF) since these two types of slags contain good proportion of alumina and iron minerals. In this Research work the objective was to find the threshold limit of utilizing both these types of slags without affecting the clinker and portland cement properties. The baseline raw meal was prepared as a reference for comparison (BL) while a set of 4 raw meals were prepared in which the proportion of LD slag and the AKLF slags were varied (S1 to S4). The LD slag was varied between 1.5 - 15 wt%, while the AKLF slag was varied between 1.5 - 6.0 wt%. The lab produced clinkers were analyzed chemically, physically and mineralogically. The individual clinkers were tested for setting time, soundness and compressive strength at 1, 3, 7 and 28 days.

2. Experimental

The steel slags i.e. LD and AKLF slags were sourced from the SMS unit of JSW Steel, Vijayanagar.

The raw mix incorporating the limestone, LD slag, AKLF slag and AOD (Argon Oxygen Decarburization) slag was designed such that the final modulus values of lime saturation factor (LSF), silica modulus (SM) and alumina modulus (AM) values were close to the modulus values of baseline raw mix which did not contain any of these slags.

Based on the chemistry of the raw materials and predefined set of moduli values, the raw mixes were designed for one baseline and for four other sets where the proportion of LD slag and AKLF were varied within a range to meet the moduli values criteria. The raw mix designs are presented in Table 1.

Table 1: Raw mix designs for assessing the effect of LD and AKLF slags.

| S.No | Raw Mix Design | Limestone | High grade Limestone | LD slag | AKLF slag | AOD slag | Flue dust | Al laterite | Red Mud | BF slag |
|------|----------------|-----------|----------------------|---------|-----------|----------|-----------|-------------|---------|---------|
| 1 | BL | 83.7 | 8.9 | 0.0 | 2.0 | 0.0 | 0.3 | 4.6 | 0.5 | 0.0 |
| 2 | S1 | 75.0 | 8.6 | 6.8 | 6.0 | 3.8 | 0.0 | 0.0 | 0.0 | 0.0 |
| 3 | S2 | 78.0 | 8.5 | 7.0 | 1.5 | 0.0 | 0.0 | 0.0 | 0.0 | 5.0 |
| 4 | S3 | 83.0 | 8.5 | 1.5 | 1.5 | 0.0 | 2.5 | 0.0 | 0.0 | 3.0 |
| 5 | S4 | 57.0 | 20.0 | 15.0 | 2.0 | 0.0 | 0.0 | 0.0 | 0.0 | 6.0 |

For carrying out the sintering of raw meal, the individual raw mixes were initially ground to a size of -100 μm followed by formation of green balls through addition of moisture. The green balls were then dried in an air oven at 110°C for about 1.5 hours which was followed by stage wise sintering of dried balls to a temperature of 500°C for 1 hour followed by stepwise increase of temperature to 1450°C. The dried balls were then soaked at this temperature for 45 minutes after which the sintered clinker balls were quickly cooled to room temperature through forced air cooling (Kolovos et.al, 2005). This was done to avoid the formation of γ -C₂S (belite) which is a low reactive allotrope of C₂S. A faster cooling ensures the formation and retention of β -C₂S phase. The clinkers produced were analyzed through chemical analysis and X-ray diffraction. For evaluation of physical and mechanical properties, the clinker samples were ground to a fine powder such that the specific surface area measured as Blaine value was about 3500 cm²/g. The ground material of individual

clinkers S1 to S4 and BL were all individually blended with 5% powdered mineral gypsum (calcium sulphate set retarder) to produce ordinary portland cement (OPC) which was then subjected to various tests such as consistency, setting time, mortar compressive strength, soundness etc.

3. Results and Discussions

3.1 Chemical composition and mineralogy of Clinkers

The chemistry and mineralogical composition (Bogue's calculation) is given in Table 2 and physical properties of clinkers are given in Table 3

Table 2: Chemical composition and Mineralogy of Clinkers

| Clmk | Value % | | | | | | | | Bogue Value % | | | LSF |
|------|---------|------------------|--------------------------------|--------------------------------|-------|------|-----------------|----------|------------------|------------------|-----------------------------------|------|
| | LOI | SiO ₂ | Al ₂ O ₃ | Fe ₂ O ₃ | CaO | MgO | SO ₃ | Free CaO | C ₃ S | C ₃ A | C ₃ S+C ₂ S | |
| BL | 0.30 | 20.92 | 5.56 | 3.95 | 64.19 | 1.22 | 1.43 | 0.90 | 52.80 | 8.05 | 72.82 | 0.94 |
| S1 | 0.11 | 20.64 | 5.94 | 4.46 | 64.49 | 2.52 | 0.65 | 0.63 | 55.06 | 8.20 | 72.55 | 0.95 |
| S2 | 0.46 | 21.00 | 5.85 | 3.89 | 65.19 | 2.53 | 0.54 | 1.30 | 54.18 | 8.93 | 73.37 | 0.95 |
| S3 | 0.10 | 21.90 | 5.13 | 4.37 | 64.84 | 2.53 | 0.64 | 0.90 | 51.41 | 6.21 | 75.26 | 0.92 |
| S4 | 0.25 | 19.78 | 5.27 | 6.81 | 62.06 | 2.57 | 1.07 | 0.65 | 52.27 | 2.45 | 69.42 | 0.95 |

The mortars of clinker samples under investigation were tested for compressive strength for 1,3,7 and 28 days. As shown in Figure 1, the cement mortars of S1 to S3 all showed better results when compared with 28 days' strength of BL (Baseline) mortar. However, all the clinker samples containing slags showed relatively a lower 1-day strength. From the test results, it was inferred that the raw mix S1 was the optimum design to produce clinker utilizing various slags. This raw mix design had the proportion of LD slag 6.8%, AKLF slag 6.0% and AOD slag 3.8% with balance material being limestone.

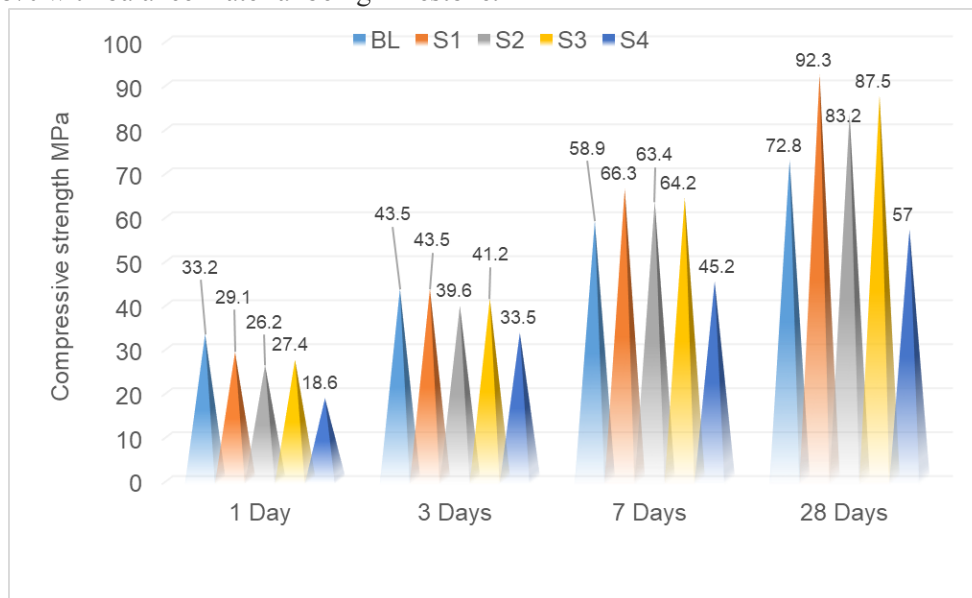


Figure 1: Compressive strengths of OPC mortar of BL and S1 to SL4 clinkers

Table 3: Physical properties of clinkers

| Parameter | BL | S1 | S2 | S3 | S4 | IS-12353 |
|--|------|------|------|------|------|----------|
| Residue on 45 μm | 13.5 | 13.6 | 13.9 | 14.1 | 13.8 | - |
| Blaine value cm^2/g | 352 | 348 | 350 | 352 | 354 | - |
| Normal Consistency % | 28.7 | 28.6 | 28.8 | 28.7 | 28.7 | - |
| Initial setting time in minutes(minimum) | 95 | 98 | 100 | 102 | 101 | 30.0 |
| Final Setting time in minutes (maximum) | 148 | 150 | 146 | 148 | 150 | 600.0 |
| Le-Chatelier Expansion in mm (max) | 0.1 | 0.1 | 0.1 | 0.0 | 0.1 | 10.0 |

4. Conclusions

The addition of 6.8% LD slag, 6.0% AKLF slag and 3.8% AOD slag in raw meal did not affect the mineralogical and chemical properties of the clinker produced. The presence of various phases such as Alite, Belite and C_3A (tricalcium aluminate) and C_4AF (tetra calcium aluminoferrite) were similar in proportion in comparison to the baseline clinker which was produced without slags in raw meal. Following conclusions were drawn from the laboratory findings.

1. The clinker chemistry and the free CaO content were all matching the baseline clinker without slag input in raw meal.
2. The Alite, Belite, C_3A and C_4AF phases were all detected in the XRD analysis.
3. The 28 days' compressive strengths of the clinker sample containing upto 6.8% LD slag and 6.0% AKLF slag was better than the baseline clinker sample. The 1-day strength was marginally lower.
4. The clinker sample containing 15% LD slag was found to be inferior to the baseline clinker both in terms of proportion of cementitious phases Alite and Belite and also the compressive strength of the mortar.

References

- Kolovos.K, Tsivilis.S, Kakali.G, "SEM examination of clinkers containing foreign elements", *Cement Concrete Composites*, 27(2),2005, 163-170
- Malhotra.V.M, "Properties of fresh and hardened concrete incorporating ground granulated blast furnace slag", in *V.M.Malhotra (Ed), Supplementary cementing properties for concrete*, Ministry of Supply and Services, Canada, 1987, pp 291-336
- Motz.H and Geiseler.J, "Products of steel slag- an opportunity to save natural resources", *Waste Management*, 21(3), (2001), 285-293
- Tsakiridis.P. E, Papadimitriou.G. D, Tsivilis.S, Koroneous.C, "Utilization of steel slag for portland cement production", *Journal of Hazardous Materials*, 152(2008), 805-811

UPCYCLING OF BIO-WASTE ASHES INTO ADDITIVE FOR CONCRETE

Mateusz Wyrzykowski^{1*}, Sadegh Ghourchian^{1,2}, Nikolajs Toropovs¹, Sakprayut Sinthupinyo³,
Kritsada Sisomphon³ and Pietro Lura^{1,4}

¹ Empa, Swiss Federal Laboratories for Materials Science and Technology, Duebendorf, Switzerland

Email: mateusz.wyrzykowski@empa.ch

² Concrefy B.V., The Netherlands

Email: sadegh.ghourchian@concrefy.com

³ Siam Research and Innovation, SCG Cement Building Materials, Saraburi, Thailand

Email: sakprays@scg.com

⁴ Institute for Building Materials, ETH Zurich, Zurich, Switzerland

Email: pietro.lura@empa.ch

ABSTRACT

Ashes from different industrial processes are a significant burden to the environment. One promising alternative to landfilling is upcycling the ashes into a valuable resource for concrete. This paper focuses on the use of waste ashes as fine fraction of lightweight aggregates. Thanks to their open porosity and high water absorption, the ashes can retain water during mixing and release it to concrete in the process referred to as "internal curing". We tested two types of ashes: bottom ashes and rice husk ashes. The performance of concretes with the preselected ashes was assessed, focusing on the mechanical properties, creep, autogenous and drying shrinkage. The ashes can replace part of the mineral aggregates (fine fractions of sand) in concrete, which saves resources and enhances the properties of the concrete, primarily thanks to internal curing. This can be of special benefit for concretes hardening in harsh climates in lack of appropriate curing. The study shows that the porous ashes can significantly reduce the autogenous shrinkage and improve the strength of concrete.

KEYWORDS: *Internal curing, Ashes, Lightweight aggregates, Concrete, Upcycling*

1. Introduction

Proper management of ashes poses a significant strain on the incineration industry. Incorporation of ashes in concrete could provide a high-capacity sink. Ashes that improve certain properties of concrete, rather than acting just as a filler, are most relevant. A prominent example are siliceous ashes with pozzolanic activity, most often fly ashes from coal combustion, but also e.g. rice husk ashes (Agarwal 2006). In this work, we focus on other functionalities, stemming from the high water absorption potential of certain types of ashes. Thanks to the latter property, porous ashes can deliver water to the hardening concrete in a process referred to as "internal curing" (Bentur et al. 2001). Our previous studies have shown that this is a feasible strategy towards upcycling of waste and improving concrete performance at the same time (Wyrzykowski et al. 2016). The action of porous ashes relies on the same principle as that of the lightweight aggregates, LWA (synthetic or natural porous aggregates). Namely, the ashes are expected to absorb water (either in a presaturation step or during concrete mixing) and release it to concrete to compensate for the water lost due to evaporation from fresh concrete or due to consumption by cement. Internal curing can be especially beneficial for concretes hardening in harsh drying conditions, i.e. at elevated temperature and in dry climate and where traditional, external water curing cannot be applied.

We studied two different types of ashes: bottom ash (BTA) and rice husk ash (RHA). They were selected based on their high open porosity (see Fig. 1) and high water absorption and desorption potential. The ashes were employed as partial sand replacement in concrete. We tested the influence of ashes on mechanical properties (compressive strength), creep and shrinkage.

2. Materials and methods

We tested three different concrete mixes: a reference mix (REF), and mixes with BTA and RHA. BTA originated from coal boilers of paper industry. BTA was sieved from an original stock and the fraction 300-600 μm was used. RHA was used directly as obtained from the burning process. The grains had sizes up to about 300 μm (see Fig. 1).

The amount of the ashes in concrete mix was calculated following their internal curing potential according to the approach proposed in (Bentz et al. 2005). The water absorption potential of the ashes was estimated as 10% and 20% for the BTA and the RHA, respectively. The w/b was increased from 0.51 to 0.56 for the concretes with ashes. The ashes replaced aggregates in an amount corresponding to 12% or 7% of volume for BTA or RHA, respectively. The mix compositions are presented in Table 1.

Table 1. Mix composition of concretes (in kg/m^3 of concrete)

| Material/Concrete mix | REF | BTA | RHA |
|----------------------------------|-------|-------|-------|
| Sand 0-4 mm | 909 | 691 | 787 |
| Gravel 4-16 mm | 910 | 908 | 908 |
| Porous ash (BTA or RHA) | 0 | 174 | 87 |
| Cement CEM I 42.5N | 235 | 235 | 235 |
| Fly Ash (pozzolanic) | 113 | 113 | 113 |
| Superplasticizer (mass-% cement) | 0.12% | 0.52% | 1.57% |
| Water | 177 | 177 | 177 |
| Add. water | 0 | 18 | 18 |
| w/b | 0.51 | 0.56 | 0.56 |

2.1 Shrinkage and creep

Shrinkage and creep were measured on prismatic samples $120 \times 120 \times 360 \text{ mm}^3$. The prisms were demolded at 1 d and the steel markers were glued on two faces of each specimen (gauge length 250 mm). The length change measurements were carried out between the steel markers using manual dilatometer. The strains were referenced to the length at 1 d. After the first length measurement, the specimens were placed in climate room at $70 \pm 3 \text{ \%RH}$ and $20 \pm 0.3 \text{ }^\circ\text{C}$. Two groups of specimens were used: sealed with aluminum foil (used for autogenous shrinkage and basic creep) and with open surfaces (used for total shrinkage and drying creep). In creep measurements, specimens were loaded at 2 d in hydraulic loading cells to a stress corresponding to 33% of the compressive strength at 2 d (see Section 2.2) and the load was updated at 28 d to 33% of the compressive strength at that age.

2.2 Strength

Compressive strength was measured on 150-mm cubes according to EN 12390-3:2009 at different ages (2-91 d). The cubes were demolded at the age of 1 d and kept underwater at $20 \pm 2 \text{ }^\circ\text{C}$ or exposed to drying at $57 \pm 3 \text{ \%RH}$ and $20 \pm 0.3 \text{ }^\circ\text{C}$. Duplicate specimens were measured per mix and age. Standard deviation was 0.5 MPa on average and 2 MPa at most.

2.3. SEM-BSE

The porous ashes were dried in an oven at $50 \text{ }^\circ\text{C}$, impregnated under vacuum with modified bisphenol-A epoxy resin and polished with polycrystalline diamond suspensions. After carbon coating, the samples

were imaged with an environmental scanning electron microscope (ESEM-FEG XL30) in the backscattered electron mode (SEM-BSE).

3. Results

The Mercury Intrusion Porosimetry (MIP) measurements (not presented here in detail, carried out according to the same procedure as in (Wyrzykowski et al. 2016)) revealed relatively large dominant pore sizes, $0.4\ \mu\text{m}$ for the BTA and $0.8\ \mu\text{m}$ for the RHA. According to the criteria established in our previous works (Ghourchian et al. 2013, Wyrzykowski et al. 2016), these results allow to identify the porous ashes as promising internal curing agents in concrete.

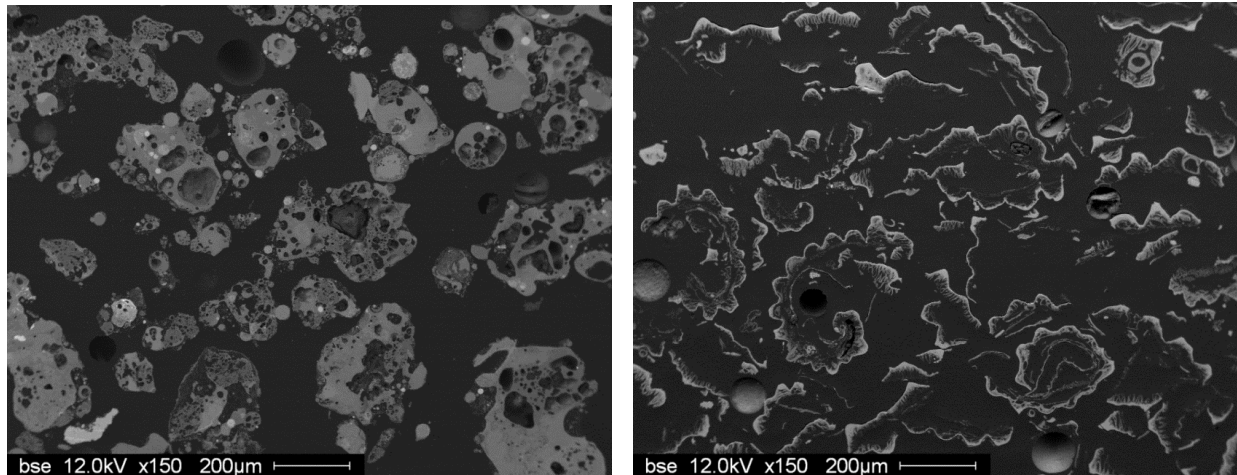


Figure 1. SEM-BSE images of the polished particles of BTA (left) and RHA (right). Large pores (from micrometres to several tenths of micrometres) that are opened to the surface can serve as water reservoirs for internal curing.

In Fig. 2 the results of the compressive strength tests are presented. The first feature visible on the graphs is that the curing under drying conditions leads to a significant reduction of strength. On the other hand, the addition of porous ashes led to improvement of strength. In fact, the presence of both types of ashes allowed a partial compensation of the effect of poor curing – the concretes with ashes exposed to drying from early age could reach similar strength at 28 d (BTA) and at 91 d (RHA) as the reference concrete cured underwater. The particularly positive effect of the RHA on strength in both curing regimes was likely due to the reactivity of the RHA. According to EDX analysis (not presented here), the RHA are composed in major part of Si. Thus, high pozzolanic activity can be expected, especially considering the high fineness of the RHA (see Fig. 1, right) (Agarwal 2006).

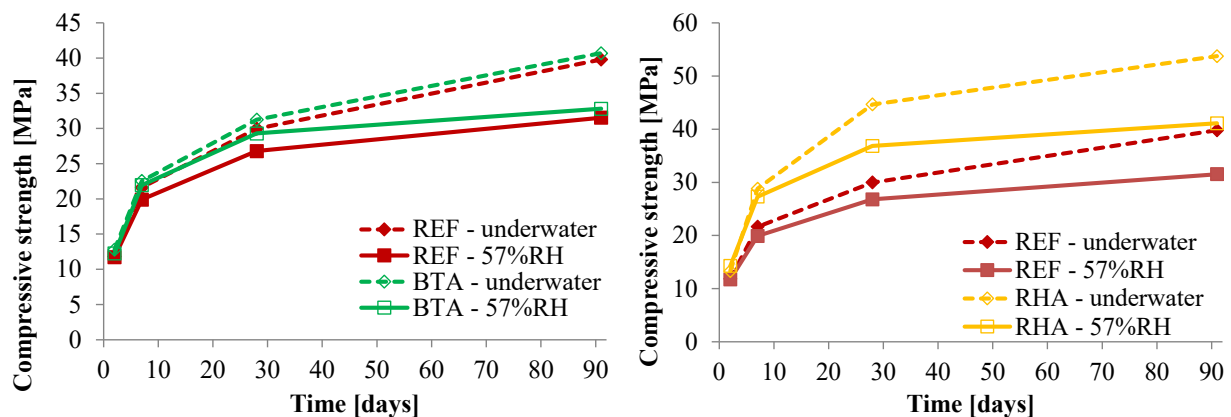


Figure 2. Compressive strength results of the reference concrete and concrete with BTA (left) and concrete with RHA (right). Two curing regimes were applied: underwater curing and drying at 57%RH.

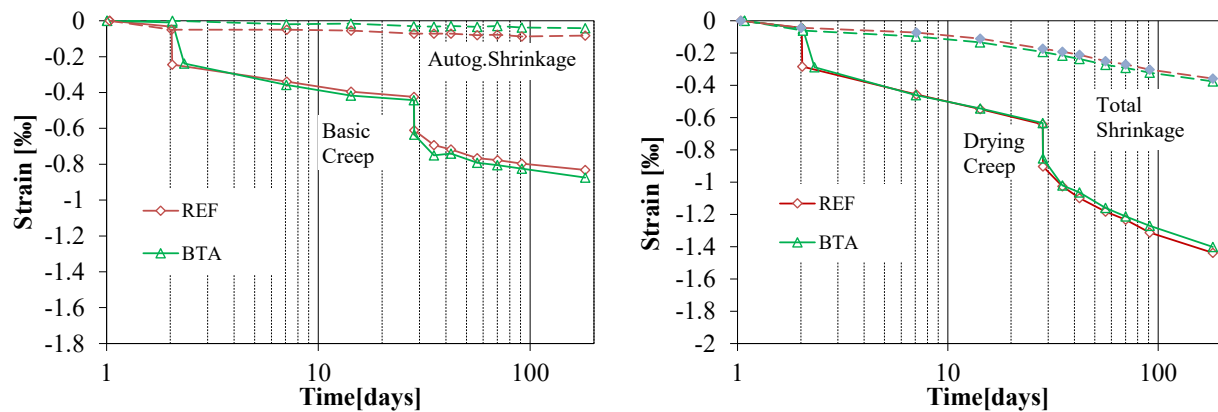


Figure 3. Shrinkage and creep measurements of REF concrete and concrete with BTA: sealed samples (autogenous shrinkage and basic creep, left) and drying at 70%RH (total shrinkage and drying creep, right).

The results of creep measurements in Fig. 3 show that BTA has no negative effect on creep deformations or total shrinkage during drying. A clear positive effect was observed regarding autogenous shrinkage (Fig. 3 left) – autogenous shrinkage at 180 d was reduced from 83 $\mu\text{m}/\text{m}$ for the REF concrete down to 41 $\mu\text{m}/\text{m}$ for the BTA concrete. This reduction can be attributed to the internal curing.

4. Conclusions

The porous ashes: bottom ash and rice husk ash (BTA and RHA) tested here can act as efficient internal curing agents and hence compensate for poor curing of concretes exposed to drying from early age. In addition to the benefit of better curing, it is most likely that the porous additives have themselves a positive effect on strength. In fact, the compressive strength at 28 d was similar or higher for concretes with porous ashes exposed to drying than the reference concrete cured underwater. A significant improvement also at later ages, both in drying regime and in underwater curing, was obtained for concrete with RHA. The latter was most likely due to the pozzolanic activity of the RHA. Autogenous shrinkage was reduced in concrete with BTA compared to the reference concrete, while no negative effect on creep could be found.

The results presented here show that upcycling of ashes as functional additive for internal curing of concrete is a feasible way for improving the sustainability of concrete and reducing the environmental burden stemming from the incineration of waste.

Acknowledgements

The study reported in this paper was co-funded by Siam Research and Innovation, SCG and by Empa.

References

- Agarwal, S. (2006). "Pozzolanic activity of various siliceous materials." *Cement and Concrete Research* 36(9): 1735-1739.
- Bentur, A., S.-i. Igarashi and K. Kovler (2001). "Prevention of autogenous shrinkage in high-strength concrete by internal curing using wet lightweight aggregates." *Cement and Concrete Research* 31(11): 1587-1591.
- Bentz, D. P., P. Lura and J. W. Roberts (2005). "Mixture proportioning for internal curing." *Concrete International* 27(2): 35-40.
- Ghourchian, S., M. Wyrzykowski, P. Lura, M. Shekarchi and B. Ahmadi (2013). "An investigation on the use of zeolite aggregates for internal curing of concrete." *Construction and Building Materials* 40: 135-144.
- Wyrzykowski, M., S. Ghourchian, S. Sinthupinyo, N. Chitvoranund, T. Chintana and P. Lura (2016). "Internal curing of high performance mortars with bottom ash." *Cement and Concrete Composites* 71: 1-9.

Decarbonizing UAE Cement Industry with Limestone Calcined Clay Cement (LC³)

F. Shahbaz¹, R. Hay², and K. Celik^{3*}

¹ Division of Engineering, New York University Abu Dhabi, Abu Dhabi, P.O. Box 129188, United Arab Emirates
Email: fs1399@nyu.edu

² Division of Engineering, New York University Abu Dhabi, Abu Dhabi, P.O. Box 129188, United Arab Emirates
Email: rh137@nyu.edu

³ Division of Engineering, New York University Abu Dhabi, Abu Dhabi, P.O. Box 129188, United Arab Emirates
Email: kemal.celik@nyu.edu

ABSTRACT

Limestone calcined clay cement (LC³) has been mainly investigated as a low-carbon cement alternative in Latin America and India. With a potential clay source suitable for LC³ mixes found in the Gulf region, this life cycle assessment (LCA) study investigates the environmental performance of introducing LC³ in the United Arab Emirates (UAE). This LCA study adopted the cradle-to-gate approach to compare the carbon dioxide (CO₂) equivalent (eq.) emissions of LC³ mortar to that of ordinary Portland cement (OPC) using Global Warming Potential (GWP-100). The life cycle analysis was performed using SimaPro 9.1. The results indicated that LC³ mortar with a 50% OPC replacement level could reduce 34% of the CO₂ eq. emissions once compared with 100% OPC mortar. When normalizing the CO₂ eq. emissions with the compressive strength, LC³ mortar still reduced 27 – 32% of CO₂ eq. emissions for testing days ranging from 1 to 90 days. This LCA study provides useful insights for implementing LC³ as a decarbonization strategy for the cement industry in the UAE.

KEYWORDS: CO₂ emissions, LC³, OPC decarbonization, GWP, strength normalization

1. Introduction

Ordinary Portland cement (OPC) significantly contributes to 7% of global anthropogenic carbon dioxide (CO₂) emissions (Olivieier and Peters (2017)). The calcination of limestone is the major source of CO₂ emissions during cement production and is responsible for roughly 60% of the CO₂ emissions (Celik et al (2015)). To lower the carbon footprint of cement production, industry and research community promote using supplementary cementitious materials (SCMs) to replace OPC. However, typical SCMs, such as fly ash and slag, are limited in supply and cannot satisfy the cement demand (Scrivener et al (2018)). Calcined clay and limestone are promising widely available alternatives and could potentially replace 50% of OPC in limestone calcined clay cement (LC³) (Scrivener et al (2018)).

The CO₂ emissions of LC³ compared with OPC were extensively investigated in India (Gettu et al (2019)), Cuba (Berriete et al (2016)), and Brazil (Malacarne et al (2021)). LC³ production was reported to reduce CO₂ emissions by 30 – 40% compared to OPC production (Gettu et al (2019)). With the United Arab Emirates (UAE) hosting UN Framework Convention on Climate Change (COP 28) in 2023, there is a need to investigate the environmental performance of introducing LC³ in the UAE to decarbonize the cement industry. Kaolinitic clay was the most effective type for formulating LC³ (Fernandez et al (2011)). The reactivity of calcined clay, the main ingredient in LC³ mixes, is mainly affected by the kaolinitic clay content (Ramadji et al (2022)). LC³ mixes require adequate kaolinitic clay content to achieve similar compressive strength to OPC (Sharma et al (2021)). Clay supplied from Oman with medium reactivity has been identified as a potential source for LC³ production in the UAE.

Since no previous investigations have been conducted for the prospect LC³ production in the UAE, this study performed a life cycle assessment (LCA) analysis to compare the CO₂ equivalent (eq.) emissions for LC³ mortar produced from Oman clay compared with that of OPC mortar using the Global Warming Potential (GWP-100). The OPC production inventory was collected from 2 cement plants located in the

UAE to determine the average GWP of OPC production in the UAE. The GWP of OPC was compared to LC³ with a 50% OPC replacement level in terms of 1 m³ of mortar. The GWP values were further normalized by the compressive strength values of each mortar type to determine if LC³ mixes can potentially reach similar strength values to OPC. The results of this LCA study provide useful insights for implementing LC³ as a decarbonization strategy for the UAE cement industry.

2. Methodology

2.1 Materials

OPC Type I blended with limestone at ~ 5 wt.%, supplied by Binani Cement, was used as the main binder for OPC and LC³ samples. The OPC chemical composition analyzed by X-ray fluoresce is summarized in Table 1. Medium-reactivity calcined clay, limestone powder supplied by Gulf Lime Company LLC, and ACS-grade gypsum were used as the remaining constituents of LC³. The calcined clay was produced from kaolinitic clay sourced from Ibra, Oman. Thermal gravimetric analysis revealed that the clay has a kaolinitic content of 29.3%, which was determined based on an assumed dehydroxylation temperature between 400 – 600 °C (Ipavec et al (2011)). The clay was calcined to 800 °C in a furnace at 10 °C/ min. A holding time of 60 min at the maximum temperature and subsequent natural cooling in the furnace were implemented. The calcined clay was ground using a ball mill set at 300 rpm for 1 hour and with a feed of 1/3 of the total ball weight.

2.2 Sample preparation

Cement pastes were prepared for OPC and LC³ with a water-to-binder ratio of 0.485. OPC samples were produced using 100% OPC as the main binder. LC³ mixes were formulated at an OPC replacement of 50 wt.%, which consists of 32 wt.% of calcined clay, 16 wt.% of limestone, and 2 wt.% of gypsum. The mortar samples for OPC and LC³ were prepared using a sand-to-binder ratio of 2.75, as recommended by ASTM C109 (ASTM 2016). Table 2 summarizes the mix proportions of OPC and LC³ samples in kg/m³.

Table 1. Oxide compositions of OPC (%)

| | SiO ₂ | Al ₂ O ₃ | Fe ₂ O ₃ | CaO | MgO |
|---------------|------------------|--------------------------------|--------------------------------|------------------|-------------------------------|
| OPC | 19.58 | 3.61 | 3.02 | 68.06 | 1.67 |
| Type I | SO ₃ | Na ₂ O | K ₂ O | TiO ₂ | P ₂ O ₅ |
| | 2.74 | 0.25 | 0.74 | 0.20 | 0.14 |

Table 2. Mix proportions of OPC and LC³ block samples (kg/m³)

| | OPC | LC ³ |
|----------------------|--------|-----------------|
| Water | 263.6 | 260.4 |
| OPC | 543.4 | 268.5 |
| Calcined Clay | 0.0 | 171.8 |
| Limestone | 0.0 | 85.9 |
| Gypsum | 0.0 | 10.7 |
| Sand | 1494.4 | 1447.1 |

2.3 Compressive strength testing

The mechanical properties of the composites were assessed with Ø25 mm x 25 mm cylindrical mortar samples using an MTS universal testing machine with a load capacity of 100 kN. A loading rate of 1.2 mm/ min, as recommended by ASTM C469 (ASTM 2014), was implemented. The testing was performed 28 days after moist curing and 1, 28, and 90 days under carbonation.

2.4 Life cycle assessment (LCA)

The LCA study was conducted to compare CO₂ eq. emissions of OPC mortar produced in the UAE to potential LC³ mortar produced in the UAE using clay sources from Oman. LCA analysis was performed using SimaPro 9.1 software and the ecoinvent v3.8 database. A ‘cradle-to-gate’ approach was adopted to define the system boundaries for 1 m³ of OPC and LC³ mortar.

The OPC and LC³ mortar inventories were based on the mix proportions in Table 2. The emissions inventories of water, calcined clay, limestone, gypsum, and sand were retrieved from the ecoinvent database. The calcined clay eco-invent process included emissions from grinding and calcination processes. OPC inventory was collected based on 2 integrated cement plants in the UAE because no

inventory exists for UAE cement production. To maintain the plants' confidentiality, their emissions were not reported in this study. The transportation emissions of clay from Ibra, Oman, to Abu Dhabi, UAE, were included in the LC³ mix for an average road distance of 604.1 km. The ecoinvent process for calcined clay assumes 1.3 kg of clay is needed to produce 1 kg of calcined clay. The transportation emissions were measured at 134.9 tonnes.km of clay for 1 m³ of LC³ mortar.

The CO₂ eq. emissions were calculated using the GWP IPCC 2007 indicator for 100 years. The CO₂ eq. emissions for OPC production in the UAE were averaged by the mass production of each plant; 53.5% of emissions were allocated to the first plant and 46.5% to the second plant. The GWP for the OPC production in the UAE was compared to the GWP for the OPC production in other major regions, including the United States (US), Europe without Switzerland, and Switzerland, whose inventories were obtained from the ecoinvent database. The CO₂ eq. emissions for OPC and LC³ mortar were reported for 1 m³ of mortar. To incorporate the strength of mortar in the environmental performance, the CO₂ eq. emissions for 1 m³ of OPC and LC³ mortar were further normalized by the compressive strength developed on days 1, 28, and 90. GWP contribution analysis was also performed for LC³ mortar to determine the contributions of all processes involved in LC³ production.

3. Results and discussion

3.1 GWP for the average OPC production in the UAE

Table 3 provides the GWP for the average OPC production in the UAE based on the inventories collected from 2 integrated cement plants. The CO₂ eq. emissions for OPC production in the UAE is 13% higher than that of Switzerland, similar to Europe without Switzerland, and 4% lower than that of the US. The GWP estimate for UAE was suitable for the LCA analysis in sections 3.2 and 3.3 since the GWP for OPC production in the UAE is within a close range of GWP values in other regions.

3.2 GWP comparison between OPC and LC³ mortar

Figure 1 shows the GWP comparison between OPC and LC³ mortar, given that both are produced in the UAE. The results indicate that LC₃ mortar with a 50% OPC replacement significantly reduces CO₂ eq. emissions by 34% compared with 100% OPC mortar. A previous study similarly investigated OPC mortar and LC₃ mortar with a 50% replacement in India. The CO₂ eq. emissions for OPC and LC₃ mortar were 375 and 270 kg CO₂ eq./ m³ of mortar, respectively, which gave rise to 28% CO₂ reductions when LC₃ mortar is used in India (Gettu et al (2019)). The CO₂ eq. reductions for using LC₃ mortar obtained in this study is higher than that reported in the previous study, possibly due to the different mix designs and the different sources of raw materials. The results in Figure 1 demonstrate the improved environmental performance of LC₃ mortar compared with OPC mortar in the UAE.

Table 4 reports the compressive strength developed by OPC and LC³ mortar on days 1, 28, and 90. The results show that LC³ mortar using Oman clay can achieve similar strength for days 1, 28, and 90. The compressive strength values are used to normalize the GWP results for OPC and LC³ mortar in Figure 2. Figure 2 shows that the normalized GWP for LC³ mortar is lower than that of OPC for all tested days. The percentage reductions in normalized CO₂ eq. emissions between OPC and LC³ mortar for days 1, 28, and 90 are approximately 27%, 29%, and 32%, respectively. The normalized GWP shows that LC³ mortar produced in the UAE using Oman clay could significantly reduce CO₂ eq. emissions while maintaining compressive strength similar to OPC.

Table 3. GWP for OPC production in the UAE compared to other regions (kg CO₂ eq./ kg cement)

| | UAE | US | Europe without Switzerland | Switzerland |
|------------|-------|-------|----------------------------|-------------|
| GWP | 0.855 | 0.888 | 0.857 | 0.743 |

Table 4. Compressive strength developed on days 1, 28, and 90 for OPC and LC³ mortar (MPa)

| Day | OPC | LC ³ |
|-----------|------|-----------------|
| 1 | 4.9 | 4.4 |
| 28 | 24.8 | 23.0 |
| 90 | 29.0 | 28.0 |

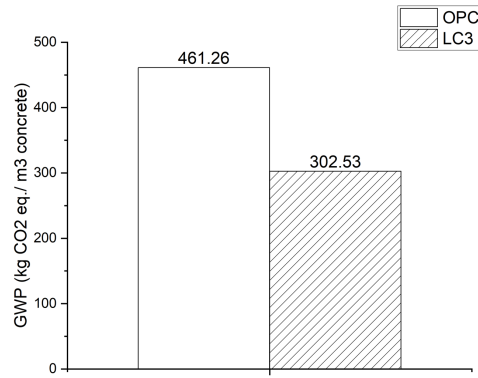


Figure 1. GWP comparison between OPC and LC³ mortar (kg CO₂ eq./ m³ of mortar)

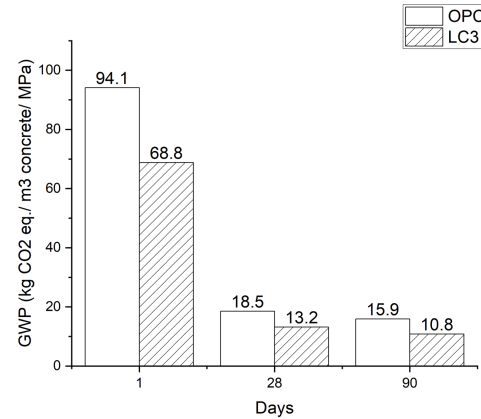


Figure 2. GWP comparison between OPC and LC³ mortar normalized by the compressive strength developed at days 1, 28, and 90 (kg CO₂ eq./ m³ of mortar/ MPa)

3.3 Contribution analysis of the GWP for LC³ mortar

Contribution analysis of the GWP indicator for LC³ mortar produced in the UAE using Oman clay was performed to investigate the contributions of all processes, including OPC cement, calcined clay, and clay transportation. The contributions of limestone and gypsum are not shown in Figure 3 because their combined contribution is not as significant as the other processes (< 0.1%). The major GWP contributor of LC³ mortar is OPC cement, contributing around 75.5% of the total CO₂ eq. emissions. Calcined clay, which includes the emissions generated from raw material acquisition and clay calcination, contributes 14.5%. The results also show that clay transportation emissions significantly contribute around 9.9%. The CO₂ eq. emissions could be reduced by determining local clay sources with higher kaolinitic clay content. The contributions of adding superplasticizers to LC³ mortars to achieve a similar slump to OPC mortars need to be considered in a more comprehensive LCA study.

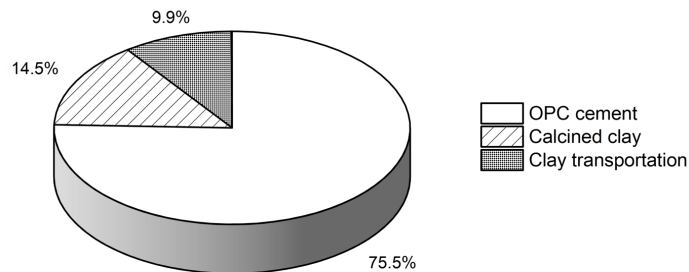


Figure 3. GWP contribution analysis for LC³ mortar (limestone and gypsum contributions are not shown)

4. Conclusions

This study investigates the life cycle assessment of introducing LC³ in the UAE compared to OPC. The environmental impact of OPC and LC³ mortar is evaluated in terms of CO₂ eq. emissions using Global Warming Potential (GWP-100). The results indicate that LC³ mortar produced using Oman clay is a potential decarbonization strategy for the UAE cement industry. The main results are summarized below.

- (1) Based on 1 m³ mortar, LC³ can potentially reduce CO₂ eq. emissions by 34% compared with OPC.
- (2) LC³ mortar achieves similar compressive strengths to OPC mortar for days 1, 28, and 90.
- (3) CO₂ eq. emissions of LC³ mortar normalized by the compressive strength values is 27 – 32% lower than that of OPC mortar for testing days between 1 to 90 days, which indicates that LC³ mortar is a sustainable alternative for OPC mortar given that it achieves similar strength.
- (4) The emissions from clay transportation significantly contribute (by 9.9%) to the total CO₂ eq. LC³ mortar emissions could be reduced by adopting local clay sources.

Acknowledgments

This work was supported by HSBC Bank Middle East Limited under grant number ADHPG-S4456.

References

- American Society for Testing and Materials (ASTM). (2014) *ASTM C469/469M-10: Standard test method for static modulus of elasticity and Poisson's ratio of concrete in compression*, ASTM International Standards.
- American Society for Testing and Materials (ASTM). (2016) *ASTM C109/C109M-16a: Standard Test Method for Compressive Strength of Hydraulic Cement Mortar*, ASTM International Standards.
- Berriel, S. S., Favier, A., Domínguez, E. R., Machado, I. S., Heierli, U., Scrivener, K., ... & Habert, G. (2016) "Assessing the environmental and economic potential of Limestone Calcined Clay Cement in Cuba," *Journal of Cleaner Production*, 124, 361-369.
- Celik, K., Meral, C., Gursel, A. P., Mehta, P. K., Horvath, A., & Monteiro, P. J. (2015) "Mechanical properties, durability, and life-cycle assessment of self-consolidating concrete mixtures made with blended portland cements containing fly ash and limestone powder," *Cement and Concrete Composites*, 56, 59-72.
- Fernandez, R., Martirena, F., & Scrivener, K. L. (2011) "The origin of the pozzolanic activity of calcined clay minerals: A comparison between kaolinite, illite and montmorillonite," *Cement and concrete research*, 41(1), 113-122.
- Gettu, R., Patel, A., Rathi, V., Prakasan, S., Basavaraj, A. S., Palaniappan, S., & Maity, S. (2019) "Influence of supplementary cementitious materials on the sustainability parameters of cements and concretes in the Indian context," *Materials and Structures*, 52, 1-11.
- Ipavec, A., Gabrovšek, R., Vuk, T., Kaučič, V., Maček, J., & Meden, A. (2011) "Carboaluminate phases formation during the hydration of calcite-containing Portland cement," *Journal of the American Ceramic Society*, 94(4), 1238-1242.
- Malacarne, C. S., da Silva, M. R. C., Danieli, S., Maciel, V. G., & Kirchheim, A. P. (2021) "Environmental and technical assessment to support sustainable strategies for limestone calcined clay cement production in Brazil" *Construction and Building Materials*, 310, 125261.
- Olivier, J. G., Schure, K. M., & Peters, J. A. H. W. (2017) *Trends in global CO2 and total greenhouse gas emissions*, PBL Netherlands Environmental Assessment Agency, 5, 1-11.
- Ramadji, C., Messan, A., Sore, S. O., Prud'homme, E., & Nshimiyimana, P. (2022) "Microstructural Analysis of the Reactivity Parameters of Calcined Clays," *Sustainability*, 14(4), 2308.
- Scrivener, K., Martirena, F., Bishnoi, S., & Maity, S. (2018) "Calcined clay limestone cements (LC3)," *Cement and Concrete Research*, 114, 49-56.
- Sharma, M., Bishnoi, S., Martirena, F., & Scrivener, K. (2021) "Limestone calcined clay cement and concrete: A state-of-the-art review," *Cement and Concrete Research*, 149, 106564.

Development of a CO₂ mineralization technology for concrete wash water upcycling

S. Monkman^{1*}, Y. Sargam¹, A. Hanmore¹

¹ CarbonCure Technologies, Halifax, Canada
Email: smonkman@carboncure.com

ABSTRACT

A CO₂-based beneficiation technology for recycling concrete wash slurry has been developed in the lab, validated internationally, and deployed in the field. Lab work demonstrated that a novel carbon dioxide treatment could mineralize CO₂ into the suspended cementitious phases present within high solids (specific gravity 1.10) wash water slurry, at 28% by mass of the treated solids. Using the slurry as a complete replacement of mix water improved the compressive strength relative to both the reference and the concrete produced with untreated wash water. The suspended solids containing mineralized CO₂ were shown to be a viable cement replacement. The technology was installed as a retrofit to a reclaimer at a concrete producer in Victoria, Canada. The CO₂ utilization approach was integrated into the plant operations. Waste concrete slurry from ready mix operations has been treated with CO₂ whereby the carbon is permanently mineralized and removed. The slurry is then recycled back into fresh concrete as a portion of the mix water while the treated solids allow for a reduction in the virgin cement content. A durability study confirmed that the recycled water did not have a negative effect on the concrete performance. Across eighteen months of field operations, the technology has mineralized more than 65 tonnes of CO₂ and saved more than 360 tonnes of cement.

KEYWORDS: *CO₂ Utilization, concrete wash water, concrete waste slurry, recycling, industrialization*

1. Introduction

The production of ready mixed concrete involves the periodic washing of trucks and mixers. They may be washed after the concrete has been discharged to prepare them for a new load of concrete. A slurry is produced comprising a blend of water, very fine sand, and cementitious materials. The handling and disposal of this waste stream is an operational, regulatory, and logistical challenge for the concrete producer. Ideally, the wash water can be recycled as part of the mix water in concrete, but increased water demand and undesirable set acceleration can result (Lobo and Mullings 2003). In practice, the solution is often to dilute slurry with fresh water to have a blended mix water with a solids content less than 50,000-ppm, a specific gravity of approximately 1.03 (ASTM C1602M–18 2018).

The present work concerns the CO₂ treatment of high solids concrete wash water for reuse as mix water. Carbon dioxide is readily mineralized into calcium carbonate upon reaction with tricalcium or dicalcium silicate or calcium hydroxide. A lab proof of concept study used a high solids content CO₂-treated slurry as mix water without dilution (maximum uptake, maximum mix water replacement). Subsequently, a durability study was completed to pair with the first industrial user of a retrofit CO₂ beneficiation system for a concrete reclaimer. Tests showed that the virgin cement was reduced in proportion to the carbonated slurry solids that were incorporated. The durability and sustainability of the process has been studied and industrial operations have verified that it is a scalable circular recycling approach for concrete producers.

2. Technology Development

A simulated concrete wash water slurry (cement and water) was produced at a specific gravity of 1.10. After 24 hours of gentle agitation, the slurry was placed in a barrel reactor with a recirculating pump. CO₂

gas was injected into the slurry recycling loop until neutralization of the slurry (the added CO₂ had started to acidify the solution rather than mineralizing). The carbon uptake and bound water of the cement slurry solids were determined through thermogravimetric analysis. A series of concrete mixes were produced comparing potable water against untreated slurry and CO₂ treated slurry (Monkman and Meyer 2022). Batches were created using untreated slurry and CO₂-treated slurry as 100% replacement of the mix water. The slurry batches included the use of a retarder as a dispersant to improve slump. Adjustments were made to the binder loadings of batches containing wash water to compensate for the additional solids present in the wash water slurry. The total powder content (binder + wash water solids) was maintained at 330 kg/m³. The concrete was measured in terms of slump and compressive strength at 7 and 28 days. A durability study was completed (Monkman et al. 2022) in preparation for the installation of a retrofit CO₂ system on the reclaimer of an industrial user. A simulated reclaimed water with a specific gravity of 1.10 was used as a partial (44%) replacement for mix water in concrete production. The mix designs (different from those used in lab study) incorporated a reduction to the virgin binder in proportion to the added reclaimed water solids. A comparison was made between reference concrete, batches made with untreated reclaimed water, and reclaimed water treated with CO₂ to either a low or high CO₂ uptake. A suite of testing (including RCPT, bulk resistivity, bulk diffusion, abrasion, freeze/thaw, salt scaling, drying shrinkage, carbonation, and corrosion) was completed. Finally, the technology was installed at a concrete plant, featuring a retrofit CO₂ injection system integrated into a concrete reclaimer. Operating for over a year, the system successfully recycled CO₂ treated slurry into concrete mixes and supported reductions of virgin cement.

3. Results

3.1 Lab Study

The lab study took a prepared slurry (7.7 kg cement and 18 kg water) and injected gaseous CO₂ into the reactor over 150 minutes. Thermal analysis of the treated solids afterwards confirmed that they contained CO₂ at 42% by mass of the original cement. The slump, compressive strength and carbon intensity data is shown in Figure 1. The reference mix design had a w/b of 0.55 and a binder content of 330 kg/m³ comprised of 81% cement and 19% limestone. The untreated (UT) and CO₂ treated (C) slurry batches reduced the limestone in proportion to the solids incorporated. The CO₂ treated with extra superplasticizer reduced both the cement and limestone in proportion to the slurry solids.

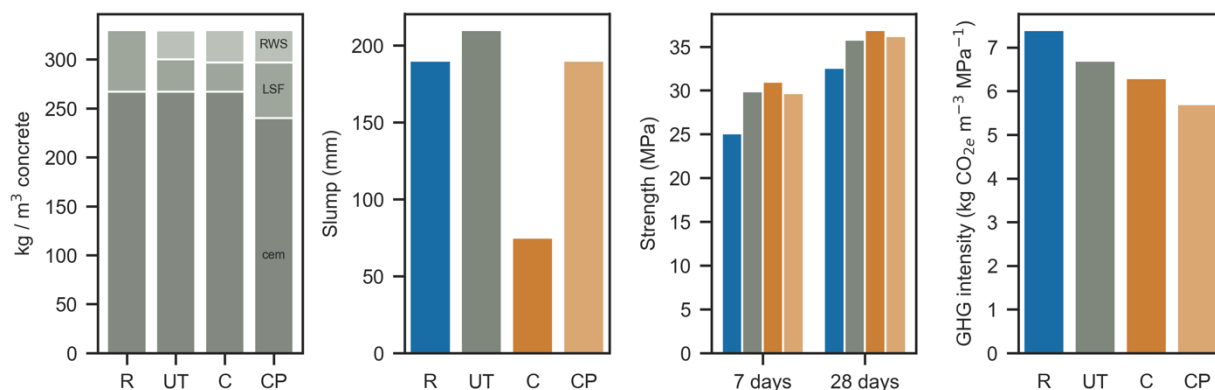


Figure 1: Binder (cement, limestone filler, wash water solids), slump, compressive strength development and GHG impact of concrete produced with potable water (R), untreated slurry (UT), CO₂ treated slurry (C), and CO₂ treated slurry with an adjustment to the PCE based superplasticizer (CP)

The control (R), untreated (UT) and CO₂ treated (C) slurry concrete included a PCE at 0.34% by weight of binder; the UT concrete additionally included 0.68% retarder. The slump of the untreated was slightly higher than the control (210 mm to 190 mm). The concrete with the CO₂ slurry included more retarder (0.74%) but the slump was reduced to 75 mm. In turn, an increase of the PCE to 0.77% on the next case (CP) resulted in the desired slump.

The use of the slurry increased the compressive strength of the concrete 18 to 24% at 7 days and 10 to 13% at 28 days. The environmental impact was assessed based upon the GHG impacts of the binder blends and the mineralized CO₂. The carbon impacts of the cement and limestone were 0.898 and 0.008 kg/kg, respectively. The treated slurry solids were 28% by mass mineralized CO₂ (uptake 40% by weight of the

cement). The control and UT concretes each had an embodied CO₂ of 240 kg CO₂/m³ concrete. The CO₂ concrete was 231 (4% lower) while the CO₂ + PCE concrete was 207 (14% lower). In terms of the carbon index (kg CO_{2e} m⁻³ MPa⁻¹) the control was 7.4, the untreated was 9% lower, the CO₂ batch was 15% lower and the CO₂ + PCE batch was 22% lower.

3.2 Durability study

A CO₂-treated s.g. 1.10 slurry was produced with CO₂ mineralized at 5 and 20% by weight of the cement in the reclaimed water solids. The compressive strength was improved with the use of both untreated and treated wash water. A suite of testing (including RCPT, bulk resistivity, bulk diffusion, abrasion, freeze/thaw, salt scaling, drying shrinkage, carbonation, and corrosion) demonstrated that the durability was not affected by the incorporation of the treated reclaimed water (Monkman et al. 2022). Examples of the strength, bulk resistivity, abrasion, and corrosion testing are summarized in Figure 2. The concrete made with the CO₂ treated wash water slurry showed a 10 to 14% improvement in the carbon index.

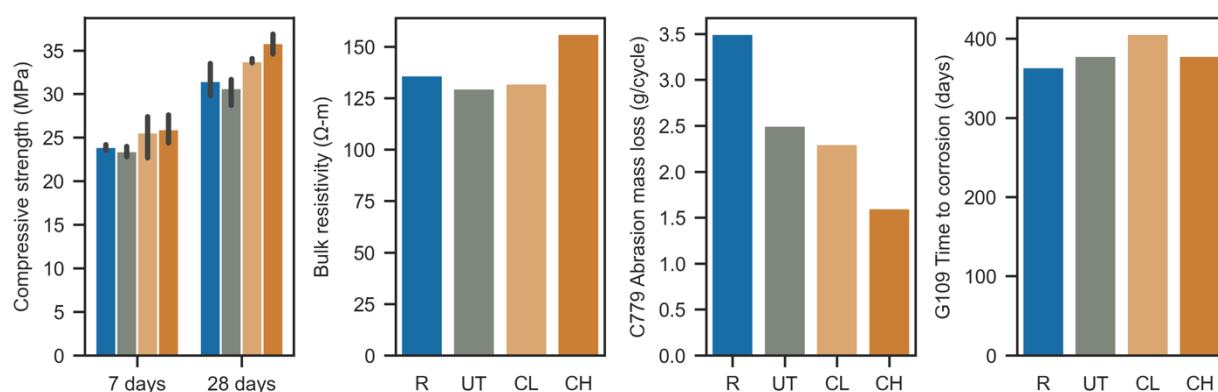


Figure 2: Compressive strength, bulk resistivity, ASTM C779 abrasion mass loss, and ASTM G109 time to corrosion for concrete produced with potable water (R), untreated wash water slurry (UT), CO₂ treated wash water slurry to 5% uptake (CL), and CO₂ treated wash water slurry to 20% uptake (CH). The wash water batches had the same total powder content but 3% less virgin binder than the reference.

3.3 Industrial Implementation

An industrial implementation of the CO₂ beneficiation process has been in operation for over 18 months (see Figure 3). The retrofit CO₂ injection system comprises a pump, a slurry recirculation conduit, a CO₂ supply, and a control system. The system injects CO₂ into the slurry as it passes through the conduit and is directed back into the tank. The control system contains both specific gravity and water level measurements which are input into a process control model to determine the estimated CO₂ and cement contents, respectively. The process targets a CO₂ uptake of 10-15% CO₂ by mass of the cementitious material in the slurry; the target balances process efficiency and material performance.

The amount of slurry and the solids content of the slurry varies but the mix batching logic replaces the cement at a rate of 0.7 units of cement removed per unit of treated slurry solids incorporated. The average slurry usage allows a 2 to 4% reduction in virgin cement. Across the first year of operation the technology has utilized 65 tonnes of CO₂ mineralized at 90% efficiency and supported savings of 363 tonnes of cement. The cumulative environmental impact is 400 tonnes of CO₂. The observation assured that the technology could be incorporated into the reclaimer operations seamlessly. The producer uses treated reclaimed water in over 75% of their mixes.

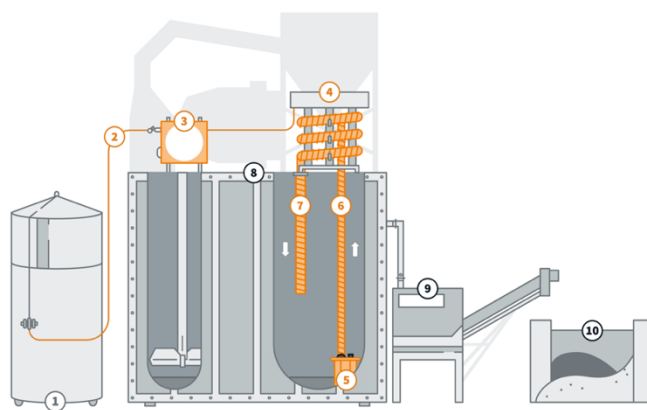


Figure 3: Schematic overview of industrial implementation of the idea. 1 CO₂ tank, 2 gas transfer line, 3 gas valve assembly, 4 treatment system, 5 slurry pump, 6 slurry infeed conduit, 7 treated slurry return, 8 reclaimer slurry tank, 9 aggregate reclaimer, 10 reclaimed aggregate.

3.4 Mechanistic Understanding

The current understanding dictates that the CO₂ treated wash water slurry improves compressive strength and carbon index through various mechanisms: (1) residual chemical reactivity of treated solids contributing to strength development; (2) formation of carboaluminates due to the reaction of CaCO₃ (formed due to CO₂ treatment) with reactive alumina present in cement; (3) enhanced packing density due to the formation of particles finer than cement; and (4) effective reduction of water-to-binder ratio as the solids/gel phases of the treated slurry may contain bound water that may not be available lubricate the mix and chemically.

4. Conclusions

A CO₂ mineralization technology was developed for recycling concrete wash slurry. A lab study demonstrated that the slurry could uptake CO₂ up to 40% by mass of the cement and replace 100% of the mix water. The concrete workability was reduced but the issue was solved by adjusting the chemical admixtures. The slurry solids proved to be a viable replacement for virgin cement, improving the environmental performance of the concrete by 22%. A durability study confirmed that using CO₂ treated slurry with a reduced proportion of virgin binder maintained concrete performance. Treatments of 5 and 20% CO₂ uptake and replacing 44% of the mix water achieved a 10 - 14% improvement in the environmental performance. The lab work supported a first-of-a-kind industrial implementation with a retrofit to a concrete reclaimer. Over one year of operation, the treated slurry was used in varying amounts in concrete and supported a 2 to 4% replacement of virgin cement. Environmental benefits were realized from both the mineralization of the CO₂ and the cement savings.

Acknowledgements

The technology development received the support of Sustainable Technology Development Canada (SDTC), and the National Research Council of Canada Industrial Research Assistance Program (NRC IRAP). Technical support was received from Larry Sutter and the late Mike Thomas.

References

- ASTM C1602M-18 (2018). *Standard Specification for Mixing Water Used in the Production of Hydraulic Cement Concrete*.
- Lobo C and Mullings G (2003). *Recycled Water in Ready Mixed Concrete Operations*. Concrete In Focus, Volume 2, pp 17-26.
- Monkman S, Hanmore A and Thomas M (2022). *Sustainability and durability of concrete produced with CO₂ beneficiated reclaimed water*. Materials and Structures, Volume 55, pp 170.
- Monkman S and Meyer V (2022). *Sustainable Concrete Production with Recycled Concrete Wash Water Beneficiated with CO₂*. Acta Polytechnica CTU Proceedings, Volume 33, pp 377-382.

Properties of a Magnesium-Silicate-Hydrate Cement Paste Prepared Using Magnesium Hydroxide

M. Baxter Chinery^{1*}, H.S. Wong², and C.R. Cheeseman³, L.J. Vandeperre¹

¹ *Department of Materials, Imperial College London, South Kensington, United Kingdom, SW7 2AZ*
Email: mcb119@ic.ac.uk

² *Department of Civil and Environmental Engineering, Imperial College London, London, United Kingdom, SW7 2AZ*

Email: hong.wong@imperial.ac.uk

³ *Department of Civil and Environmental Engineering, Imperial College London, London, United Kingdom, SW7 2AZ*

Email: c.cheeseman@imperial.ac.uk

ABSTRACT

The cladding from decommissioned UK MAGNOX nuclear reactors produced a magnesium-based alloy waste. This waste has changed over time to become a magnesium hydroxide rich sludge, which needs to be encapsulated for storage in a geological disposal facility. Reacting magnesium oxide with silica and water produces a magnesium silicate hydrate (M-S-H) cementitious matrix. This work aims to determine if the magnesium hydroxide rich sludge could be used as a cementitious material to substantially reduce the volume of waste. M-S-H cement, utilising magnesium hydroxide and optimised for waste use, has been studied to understand the development of properties and ensure that the requirements for encapsulation are continuously met. Compressive strength, porosity, and phase assemblage of the hardened M-S-H cement paste have been characterised for up to 1 year. The results show that peak strength above that required for storage is achieved by 90 days, with the porosity decreasing as M-S-H formation occurs. These demonstrate that the use of magnesium hydroxide as a raw material is a potential solution for waste encapsulation.

KEYWORDS: *M-S-H, magnesium-silicate-hydrate cement, magnesium hydroxide, waste management*

1. Introduction

The first civil nuclear reactor in the UK used natural uranium, clad in a “magnesium non-oxidising” alloy (MAGNOX) (MacKerron 2012, Kuenzel, Neville et al. 2014, Walling, Kinoshita et al. 2015, Wheeler 2016). Once the fuel had been depleted, the fuel rods and cladding were removed and stored in fuel ponds for some time, before removing the cladding and placing it in wet storage silos (Zhang 2012, Walling, Kinoshita et al. 2015). The cladding, along with phosphates, metal ions and the aluminium present in the alloy make up the legacy waste stream, which has evolved over the past ~70 years to become a magnesium hydroxide rich sludge (MacKerron 2012, Kuenzel, Neville et al. 2014, Walling, Kinoshita et al. 2015, Wheeler 2016).

This waste needs containing as a solid to be stored below ground in a geological disposal facility for a long time due to uranium being present (Zhang 2012, Wheeler 2016). These wastes are solidified within cement, the current system uses a mixture of Portland cement and a supplementary cementitious material (SCM), most commonly granulated blast furnace slag (GBFS) or pulverised fuel ash (PFA) (Zhang 2012, Kinoshita, Swift et al. 2013, Walling, Kinoshita et al. 2015). However, the supply of the SCMs are becoming scarce due to the steel and coal power industries diminishing within the UK (Zhang 2012). The composite cement also has a pH between 12 and 13, which would cause aluminium corrosion, producing expansive products and hydrogen gas (Zhang 2012, Kuenzel, Neville et al. 2014).

Magnesium-silicate-hydrate (M-S-H) cements show promise as an alternative encapsulation cement. M-S-H is formed by hydrating a magnesium source with a silica source. Magnesium oxide-based M-S-H cements have been studied most widely. As M-S-H formation begins, the pH decreases to around 9, within the desired range for encapsulating the magnesium hydroxide sludge (Zhang 2012). The cement achieves

strengths over 30MPa in 28 days, as well as reducing the corrosion of encapsulated aluminium and magnesium metal (Zhang 2012). M-S-H cements have also been shown to immobilise caesium and heavy metals as well as absorb alkali and sodium ions and incorporate aluminium ions into its structure (Bernard, Lothenbach et al. 2019, Zhang, Li et al. 2019, Bernard, Lothenbach et al. 2020, Wang and Fan 2020). The aim of this work is to determine if magnesium hydroxide could be used in the place of magnesium oxide to form an M-S-H cement which meets the encapsulation criteria, as this could substantially reduce the volume of the waste sludge. The encapsulation matrix needs to contribute towards the mechanical performance, minimise the volume of voids, whilst also being sufficiently permeable to allow gases generated to be released (Zhang 2012).

2. Materials and Methods

2.1 Materials

The magnesium sources used were magnesium hydroxide ($\text{Mg}(\text{OH})_2$) (Magshield 10, MAF Magnesite, Netherlands) and magnesium oxide (MgO) (Magchem 30, MAF Magnesite, Netherlands). $\text{Mg}(\text{OH})_2$ was used to simulate waste sludge and MgO was used to improve the early age reactivity. Elkem Microsilica 920 EN D was used as a silica source (SiO_2). Silica sand (RH110 Silica Sand, average diameter of 120 μm , Minerals Marketing Ltd.) was used as a filler and sodium hexametaphosphate (NaHMP) (extra pure, SLR, powder, mainly $(\text{NaPO}_3)_6$, Fisher Chemical) was added to improve fluidity. The mix proportions used were 23.4 wt% $\text{Mg}(\text{OH})_2$, 9.1 wt% MgO , 27.5 wt% SiO_2 and 40 wt% silica sand, with a water/solid ratio of 0.35 and an addition of 1 wt% NaHMP.

2.2 Methods

Samples were mixed using a CONTROLS tabletop mixer. NaHMP was added to the water and mixed for 10 minutes. Microsilica and the magnesium sources were mixed and then incrementally added, before adding silica sand in small proportions. Once all the silica sand was added, mixing was continued until a smooth consistency had been achieved and no increase in fluidity was observed. This was then poured into 50x50x50 mm cube moulds. These were stored at room temperature (20°C) with a relative humidity (RH) of $98 \pm 2\%$ and were then tested at various ages for up to 1 year.

For the compressive strength tests, the dimensions of the cube faces were measured using callipers (accuracy of 0.01 mm) and the area calculated. The cubes were tested in a AUTOMAX 5 CONTROLS compression tester using 2500 mm² area insert plates at a load speed of 300 kPa s⁻¹. The compressive strength was calculated by dividing the maximum applied to the cube by the exposed surface area.

Fragments of the tested cubes were dried in an oven at 80°C for one hour, then crushed using a pestle and mortar and passed through a 600 μm sieve. The powder collected was compressed into a specimen holder and placed in the Rigaku MiniFlex 600 X-ray diffractometer. The samples were tested using Cu radiation at angles from 3° to 90°, with a voltage of 40 kV and current of 15 mA without rotation.

To determine the porosity, cubes were dried in an oven at 40°C until the mass did not change in an hour (measured hourly after 24 hours on a balance with an accuracy of 0.01 g). The cubes were then completely submerged in water until they were fully saturated (no mass change observed over an hour, using the same balance). The final mass was then recorded, and the porosity found by dividing the change in mass by the dry mass, expressed as a percentage. For each test, three replicate cubes were used.

3. Results

Figure 1 shows the evolution of the strength and porosity of the M-S-H over a year. Figure 1(a) shows that a peak strength of 17.8 MPa is achieved by 90 days, plateauing after this time. The greatest strength increase occurred between 7 and 14 days (1.94 MPa in 7 days), followed by an average of 1.73 MPa every 7 days between 28 and 60 days. Figure 1(b) shows the porosity of the mortar at 7 days was 19.5 %, this declined slowly within the first 60 days (18 %), before sharply dropping by 90 days (12.4 %). This minimum porosity was observed over the next 120 days, before increasing and plateauing at 16 % by 270 days.

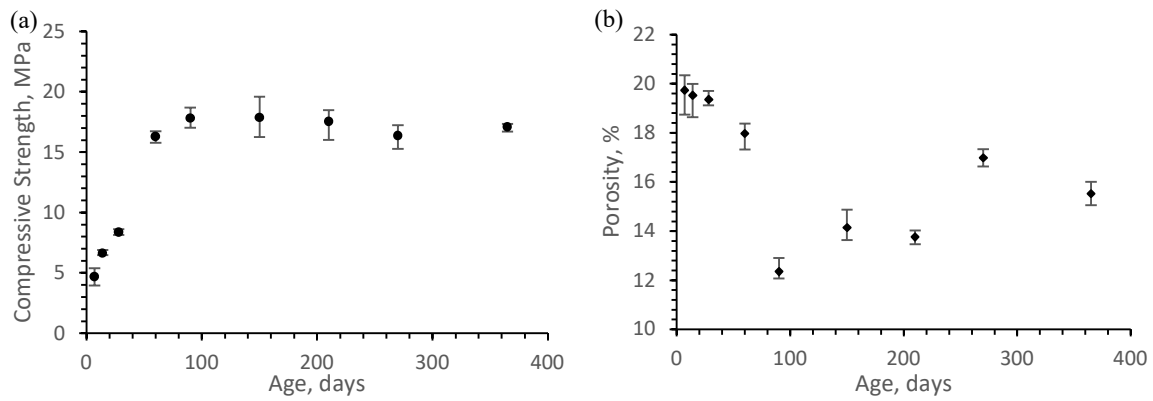


Figure 1: The evolution of the M-S-H cement mortar properties over the course of a year (a) compressive strength vs age (b) porosity vs age.

Figure 2 shows the XRD patterns for the samples at ages from 7 days to 1 year. The magnesium hydroxide peaks at 21° , 27° and 50° decrease in intensity by about 40 % over the year, however, are still present. This is due to an excess of magnesium hydroxide in the initial mix, which would also cause slight variability in the peak intensity (lower intensities at 90 and 28 days). Broad M-S-H peaks at $34-36^\circ$ can be observed from around 60 days, becoming more distinguished by 90 days.

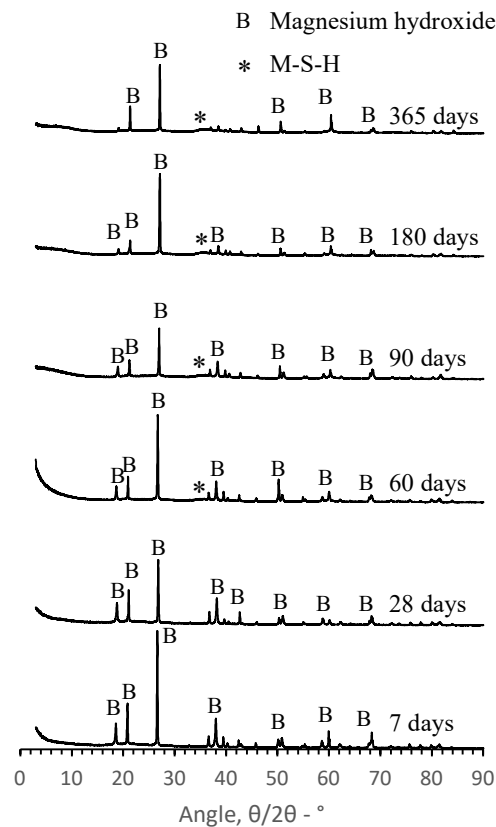


Figure 2: XRD patterns of M-S-H cement mortar from 7 days to 1 year in age.

4. Discussion

The greatest improvement in M-S-H intensity, strength and porosity occurs between the ages of 60 and 90 days. This shows that M-S-H formation is directly linked to increases in densification and strength, as M-S-H gel replaces the unbound particles. Formation of the denser matrix would cause microstructural changes, including pore refinement. The compressive strength plateaus after 90 days, suggesting an equilibrium has been reached, where enhancements due to the continued M-S-H formation are offset by shrinkage and cavities caused by the gel formation, which led to microcracking. The presence of microcracks is supported by the increase in the porosity values. The large increase suggests the magnesium hydroxide powder added is not effective as a filler material.

A compressive strength of 17.8 MPa is sufficient to successfully contribute to the overall mechanical performance of the container. The porosity values, between 20 % and 12.4 % of the overall cement volume would allow for sufficient dispersion of gases over the life of the container, without having a deleterious effect on strength. Further research is ongoing to verify the presence of microcracks, and the influence that the filler proportions have on these, and the diffusivity, permeability and sorptivity of the mortar.

5. Conclusions

M-S-H cement formed from magnesium hydroxide has the potential to be used as an encapsulating cement, with a peak strength (17.8 MPa) above that required for an encapsulation matrix, and a porosity (peak at 12.4 %, final plateau at 16%) which would potentially satisfy the voidage and permeability requirements. This would help reduce the volume of containers requiring long term storage. M-S-H peaks were observed after 60 days and this contributed to densification and the strength improvement of the waste form.

References

- Bernard, E., B. Lothenbach, C. Cau-Dit-Coumes, I. Pochard and D. Rentsch (2020). "Aluminum incorporation into magnesium silicate hydrate (M-S-H)." *Cement and Concrete Research* **128**.
- Bernard, E., B. Lothenbach, I. Pochard and C. Cau-Dit-Coumes (2019). "Alkali binding by magnesium silicate hydrates." *Journal of the American Ceramic Society* **102**(10): 6322-6336.
- Kinoshita, H., P. Swift, C. Utton, B. Carro-Mateo, G. Marchand, N. Collier and N. Milestone (2013). "Corrosion of aluminium metal in OPC- and CAC-based cement matrices." *Cement and Concrete Research* **50**: 11-18.
- Kuenzel, C., T. P. Neville, T. Omakowski, L. Vandeperre, A. R. Boccaccini, J. Bensted, S. J. R. Simons and C. R. Cheeseman (2014). "Encapsulation of aluminium in geopolymers produced from metakaolin." *Journal of Nuclear Materials* **447**(1-3): 208-214.
- MacKerron, G. (2012). Evaluation of nuclear decommissioning and waste management, University of Sussex.
- Walling, S. A., H. Kinoshita, S. A. Bernal, N. C. Collier and J. L. Provis (2015). "Structure and properties of binder gels formed in the system Mg(OH)₂-SiO₂-H₂O for immobilisation of Magnox sludge." *Dalton Trans* **44**(17): 8126-8137.
- Wang, B. and C. Fan (2020). "Hydration behavior and immobilization mechanism of MgO-SiO₂-H₂O cementitious system blended with MSWI fly ash." *Chemosphere* **250**: 126269.
- Wheeler, P. y. E. a. A. F. (2016). Radioactive Wastes in the UK: A Summary of the 2016 Inventory. E. a. I. S. Department for Business and N. D. Authority.
- Zhang, T. (2012). *Development of Novel low pH Magnesium Silicate Hydrate (M-S-H) Cement Systems for Encapsulation of Problematic Nuclear Wastes*. PhD, Imperial College London.
- Zhang, T., T. Li, J. Zou, Y. Li, S. Zhi, Y. Jia and C. R. Cheeseman (2019). "Immobilization of Radionuclide (133)Cs by Magnesium Silicate Hydrate Cement." *Materials (Basel)* **13**(1).

Influence of Rice Husk on the Thermal Activation and Pozzolanic Activity of Tropical Soils

F.D. Cabrera-Poloché^{1*}, A.A. Hoyos-Montilla¹, J.I. Tobón¹, A.C. Díaz-García¹, M. Echeverri-Aguirre¹, D. González Betancur¹

¹Grupo del Cemento y Materiales de Construcción -CEMATCO, Facultad de Minas, Facultad de Arquitectura, Universidad Nacional de Colombia, Medellín-Colombia. Email: fdcabrerap@unal.edu.co^{1*}

ABSTRACT: Alternative cementitious materials with lower carbon footprints have been deeply studied in recent years. Supplementary Cementitious Materials (SCMs) as calcined clays are highlighted since they are more abundant, widely distributed, and require lower temperatures to get activated. Furthermore, disposal of rice husk (RH) by the cement industry respond to circular economy strategies. Consequently, the influence of RH on thermal activation of clay minerals in low-grade kaolinitic soils has been addressed in this paper. RH and soils were co-fired (S-RH). Pozzolanic activity as SCM was evaluated in S-RH pastes replaced with 20wt.% of Ca(OH)₂ through lime fixing (L.F.) by means of TG/DTG at 7 and 28 days. Also, the influence of RH on soil calcination was assessed through dehydroxylation degree (D.D.) and TG/DTG. Despite the fact that those soils had a low kaolinitic content (3.6% weight loss between 340-700 °C in the more clayey soil S2) they presented 41% L.F. at 7 days when co-fired with 12.5% RH-700 °C-2.5 h; with a higher D.D. (95.5%) compared to the calcined soil without RH (91.3%) under the same conditions. This suggests a potential use of S-RH as SCM, while RH improved the pozzolanic activity by increasing D.D. in clay minerals. **KEYWORDS:** *Thermal activation, dehydroxylation degree, pozzolanic activity, low-grade kaolinitic soil*

1. Introduction

Cement is widely used for the manufacturing of concrete. This has made the global cement production grow at a 10%/yearly rate (Restrepo et al (2020)). However, this entails problems as an accelerated consumption of raw materials, an increased energy consumption and atmospheric pollution caused by CO₂ anthropogenic emissions (cement industry contributes with 7%) (Palanisamy and Kumar (2018)). For these reasons, SCMs have been studied, specifically those based on calcined clays (Restrepo et al (2020)). In addition, rice crops are large generators of agro-industrial waste (0.23 t RH / 1 t rice produced) (Chandrasekhar et al (2003)). The world's rice production for 2014 was 741.48 Mt, being it mostly produced in Asia (> 90%) (Zou and Yang (2019)). Thus, the use of RH as rice husk ash (RHA) has been intensively studied due to its amorphous silica content > 80%, its specific surface area and chemical reactivity (Arcos et al (2007)). In cement industry, RHA has been used as a material that replaces or mixes with silica fume, fly ash or blast furnace slag for the manufacturing of alkaline-activated cements or hybrid cements (Zou and Yang (2019)); however, its influence on clay calcination has not been deeply studied; there are some studies on the manufacturing of light bricks (Phonphuak et al (2019)) and SCM with kaolinitic clays (Bediako et al (2020)). Therefore, the influence of RH on the thermal activation of tropical soils was reviewed taking advantage of the energy-producing capacity of biomass and enriching the soil with reactive silica. The RH and the soils were co-fired (S-RH) with varying temperatures (650, 700, 750 °C), dwell time (2, 2.5, 3 h) and substitution of soil by RH (5, 12.5, 20%). Pozzolanic activity was evaluated by L.F. and, the RH influence on soil activation through D.D.

2. Materials and methods

2.1 Materials

For the physical characterization, the Unified Soil Classification System (USCS–ASTM D2487-11) was used, and the particle size distribution was determined by laser diffraction. For the soil classification, the Atterberg Limits were found (ASTM D4318-17). X-ray fluorescence (XRF) was performed to determine the chemical composition with loss on ignition (LOI). For the mineralogical identification, an X-ray diffraction (XRD) was carried out. As a complement and to establish the burning temperature in thermal

activation, a thermogravimetric analysis (TG) and its derivative (DTG) were performed. The test conditions included an oxidizing atmosphere (75 mL/min), from 25 to 1000 °C and 10 °C/min heating rate.

2.2 Methods

An analysis of the activation temperature was carried out using the method by Seiffarth et al (2013), where D.D. (eq 1) was calculated from the weight loss of uncalcined and calcined samples in the temperature range of clay minerals' dehydroxylation. For the L.F. through TG/DTG, cementitious pastes of 80% S-RH + 20% Ca(OH)₂ at 0.5 w/c ratio were prepared. The calculation method by Gaviria et al (2017) and Tobón and Mendoza (2009) was used, in which by knowing the molecular weight (PM) of Ca(OH)₂ and H₂O and the OH⁻ weight loss percentage of Ca(OH)₂ on TG/DTG (denoted H%), the Ca(OH)₂ in the cement paste at different curing ages can be calculated (eq 2). For each age and cement paste, H% was determined by calculating the area under the curve associated to Ca(OH)₂ dehydroxylation on DTG (Ca(OH)₂ generally peaks at 450 °C). Then, knowing the initial content of Ca(OH)₂ in the paste's % (Ca(OH)₂ initial), and the percentage of Ca(OH)₂ at a certain curing age (Ca(OH)₂ curing age), the % L.F. due to the pozzolanic reaction can be calculated (eq 3).

$$D.D. (\%) = 100 - 100 \left(\frac{\text{mass loss of calcined sample}}{\text{mass loss of uncalcined sample}} \right) \quad (1)$$

$$\% Ca(OH)_2 = \frac{H\%}{PM_{H_2O}} * PM_{Ca(OH)_2} \quad (2)$$

$$\% Ca(OH)_2 \text{ fixed} = \frac{\% Ca(OH)_2 \text{ initial} - \% Ca(OH)_2 \text{ curing age}}{\% Ca(OH)_2 \text{ initial}} * 100 \quad (3)$$

3. Results and discussion

3.1 Materials characterization

The samples correspond to low-plasticity soils where the presence of fine-granular materials predominates (Table 1) with a greater amount of clayey and silty material in S2. According to the USCS, soils were classified as low-plasticity silt (S1) and clay (S2) with presence of fine sand, indicating a clear difference between soils of the same nature but containing different quantities of clay size particles.

Table 1. Particle size of soils and geotechnical properties of soils.

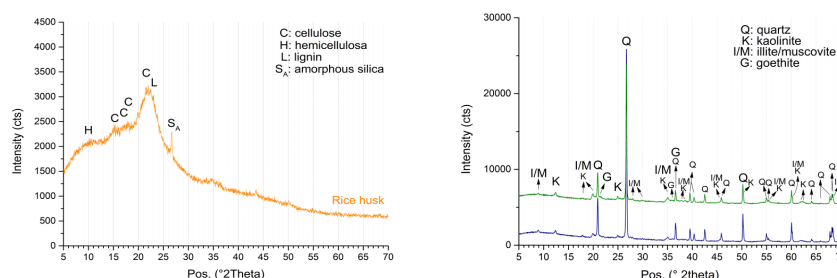
| Size particle (mm) | Particle type | Soil type | | Geotechnical properties | Soil type | |
|--------------------|---------------|-----------|--------|-------------------------|---------------|-------|
| | | S1 | S2 | | S1 | S2 |
| 2.000-63.000 | Gravel | 0.00 | 0.00 | Atterberg Limits | LL (%) | 18 22 |
| 0.063-2.000 | Sand | 56.87 | 26.95 | | PL (%) | 16 14 |
| 0.002-0.063 | Silt | 40.28 | 66.33 | | PI (%) | 2 8 |
| ≤ 0.002 | Clay | 2.85 | 6.72 | USCS | | |
| Total | | 100.00 | 100.00 | | ML | CL |

LL, PL, IP: liquid, plastic limit, plasticity index. ML, CL: Low-plasticity sandy silt, Low-plasticity clay with sand.

The chemical composition and mineralogical identification showed the presence of minerals associated to clayey soils, with clay minerals as illite, kaolinite and other minerals as quartz, muscovite (mica) and goethite (hydrated iron oxide). According to Table 2 and Fig. 1, S2 had greater clay minerals content due to the higher content of Al, K, Na, Fe oxides; it also showed more defined mineralogical phases in XRD patterns; in addition, S1 showed a higher degree of crystallinity due to its more slender and higher intensity peaks (quartz and mica with high intensity), moreover, S2 showed greater amorphicity (kaolinite and illite with wide peaks). Thus, the difference between soils was clear. On the other hand, rice husk (RH) showed a high degree of amorphicity (Fig. 1, left), with mineralogical phases mainly composed of silica.

Table 2. Chemical analysis of tropical soils (wt.%) by X-ray fluorescence (XRF).

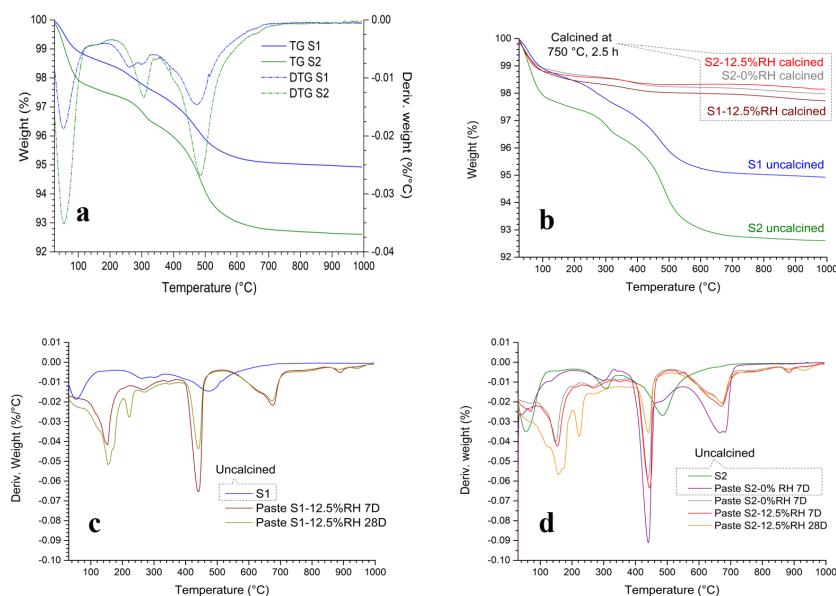
| Oxide | LOI | SiO ₂ | Al ₂ O ₃ | Fe ₂ O ₃ | MgO | K ₂ O | P ₂ O ₅ | TiO ₂ | Na ₂ O | CaO | Others |
|-------|------|------------------|--------------------------------|--------------------------------|------|------------------|-------------------------------|------------------|-------------------|------|--------|
| S1 | 4.82 | 80.06 | 7.40 | 5.34 | 0.21 | 0.89 | 0.27 | 0.53 | 0.27 | 0.07 | 0.14 |
| S2 | 6.48 | 74.86 | 11.58 | 3.88 | 0.44 | 1.24 | 0.05 | 0.66 | 0.48 | 0.14 | 0.19 |

**Figure 1.** X-ray diffraction (XRD) of raw materials: Rice husk (left) and tropical soils S1, S2 (right).

TG/DTG showed characteristics of low-grade kaolinitic soils (Fig. 2a) due to the dehydroxylation peaks at 350°C associated to goethite and the main dehydroxylation peak at 500°C associated to clay minerals 1:1 as kaolinite (usually between 340-700°C (Yanguatin et al (2017))). In general, S2 showed a greater presence of clay minerals and hydrated iron oxides minerals (a greater area under the curve in the DTG for each dehydroxylation phenomenon), however, the total weight loss between room temperature - 1000 °C was max. 7%, similar to that was found in the FRX results (Table 2).

3.2. Dehydroxylation degree (D.D.) and pozzolanic activity

According to TG/DTG of raw materials (Fig. 2a) and co-fired S-RH (Fig. 2b), D.D. was higher for S2-RH (95.5%) than for S1-RH (88.6%) at 750°C/2.5h. This was because S2 presented higher clay minerals content, with 3.6% weight loss of dehydroxylation of clay minerals (340-700°C), compared to 2.4% in S1. Moreover, the influence of RH on the D.D. was evidenced too, since at same activation conditions the D.D. was higher for samples with 12.5%RH (95.5%) compared to those without RH (91.3%). Thus, the D.D. increased with the clay minerals and RH content; consequently, tropical soils were successfully activated.

**Figure 2.** Uncalcined tropical soils (a), influence of RH and temperature on the D.D. (b), influence of RH on mineralogy of pastes S1-RH (c), S2-RH (d) at 750°C, 2.5 h dwell time by TG analysis.

Regarding the pozzolanic activity by DTG in pastes of 80%S-RH + 20% Ca(OH)₂ (Fig. 2c-d), regardless of soil type, the main hydration products at 7 curing days were C-S-H (75-225°C) and C-A-S-H at 28 curing days (200-250°C). C-S-H were also evidenced at 28 curing days with greater area under the curve

compared to the same peaks at 7 curing days. Moreover, the generation of hydration gels was evidenced when TG/DTG of calcined S-RH pastes were compared with uncalcined S-RH pastes (S2-0%RH 7D) and raw materials (S1, S2); where there was no presence of these gels, similar as to what was found by Uchima et al (2016), where an increase in the pozzolanic activity was due to gels formation from calcium hydration.

The generation of C-S-H and C-A-S-H gels at 28 curing days was higher in S2-RH pastes (5.24% and 1.27% respectively) than in S1-RH pastes (4.24% and 0.94% respectively), at 750°C/2.5h/2.5%RH. This was related to the higher Al₂O₃ (11.58 wt.%), clay minerals (3.6% weight loss) and D.D. (95.5%) found in S2, similar to reactivity of low plasticity soils that had a higher amount of clay minerals showed by Lemaire et al (2013). Comparing calcined pastes (750°C/2.5h) at 7 curing days in S2, a higher C-S-H content was found at 12.5% RH (3.62% weight loss C-S-H dehydroxylation) compared to the pastes without RH (3.25% weight loss C-S-H dehydroxylation); the above may be related to RHA reactive silica, as well as to the higher D.D. obtained in paste with 12.5% RH (95.5% vs 91.3%). These can be seen on the L.F. of S-RH pastes (Fig. 2-3). L.F. of uncalcined S-0%RH pastes was zero, i.e., the Ca(OH)₂ calculated corresponded to the initial value. So, thermal activation of soil is necessary before preparing the pastes. According to L.F. at 7 and 28 curing days (Fig. 3), pozzolanic reactions in both soils were late, i.e., in tropical soils with low kaolinitic content the reaction progresses slowly, similar to kaolinitic clays commonly studied. A direct relation was found between RH and L.F., since the higher RH, the higher D.D.

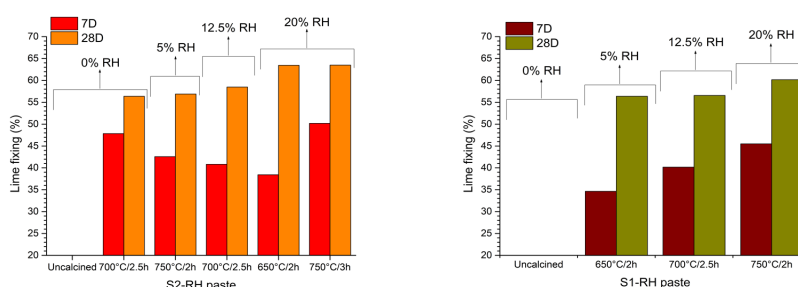


Figure 3. Influence of RH, temperature and dwell time on lime fixing of pastes S2-RH (left) and S1-RH (right).

4. Conclusions

Two different soils were well thermally activated. Soils with a higher content of clay minerals (CL) were more susceptible to be used as SCM than those with a higher content of quartz (ML). Hence, this susceptibility can be determined with D.D., which showed a direct relation with the clay minerals and RH content. The contribution of RH to D.D. was related to the utilization of the heat capacity of RH, which was evidenced indirectly by its effect through TG/DTG. Furthermore, both soils presented pozzolanic activity due to the consumption of lime at 28 curing days (55-64%), being higher in soils with higher clay minerals and RH content, which was confirmed by the presence of C-S-H and C-A-S-H hydration gels in S-RH pastes. This was directly related to D.D. since the best thermally activated soil (S2) was the one that performed best as SCM. In addition, reactive silica of RH when it is burned may also influence the results obtained from lime fixing, however, this should be confirmed in future research.

Acknowledgements: This work is derived from the project “BPIN 2020000100407”.

References

- Arcos, C., Macías, D. and Rodríguez, J. (2007) “La cascarilla de arroz como fuente de SiO₂”, *Revista Facultad de Ingeniería Universidad de Antioquia*, 41: 7–20
- Bediako, M., Adjaottor, A.A., Gawu, S.K.Y. and Amankwah, E.O. (2020) “Compressive strength and durability properties of pozzolan obtained from co-fired clay and rice husk”, *Cogent Engineering*, 7(1): 1811453, DOI: 10.1080/23311916.2020.1811453

- Chandrasekhar, S., Satyanarayana, K., Pramada, P. and Raghavan, P. (2003) “Review Processing, properties and applications of reactive silica from rice husk—an overview”, *Journal of Materials Science*, 38: 3159–3168, DOI: 10.1023/A:1025157114800
- Gaviria, X., Borrachero, M., Payá, J., Monzó, J. and Tobón, J. (2017) “Mineralogical evolution of cement pastes at early ages based on thermogravimetric analysis (TG)”, *Journal of Thermal Analysis and Calorimetry*, DOI: 10.1007/s10973-017-6905-0
- Lemaire, K., Deneele, D., Bonnet, S. and Legret, M. (2013) “Effects of lime and cement treatment on the physicochemical, microstructural and mechanical characteristics of a plastic silt”, *Engineering Geology*, 166: 255–261, DOI: 10.1016/j.enggeo.2013.09.012
- Palanisamy, P. and Kumar, P. S. (2018) “Effect of molarity in geo polymer earth brick reinforced with fibrous coir wastes using sandy soil and quarry dust as fine aggregate. (Case study)”, *Case Studies in Construction Materials*, 8: 347–358, DOI: 10.1016/j.cscm.2018.01.009
- Phonphuak, N., Saengthong, C. and Srisuwan, A. (2019) “Physical and mechanical properties of fired clay bricks with rice husk waste addition as construction materials”, *Materials Today: Proceedings*, 17: 1668–1674, DOI: 10.1016/j.matpr.2019.06.197
- Restrepo, O., Cabrera, F., Tobón, J., Escudero, S. and Álvarez, S. (2020) “Valorization of waste from sand wash muds of an aggregates plant: Evaluation as a supplementary cementitious material”, *International Journal of Applied Ceramic Technology*, 17(6): 2669–2680, DOI: 10.1111/ijac.13597
- Seiffarth, T., Hohmann, M., Posern, K. and Kaos, C. (2013) “Effect of thermal pre-treatment conditions of common clays on the performance of clay-based geopolymeric binders”, *Applied Clay Science*, 73: 35–41, DOI: 10.1016/j.clay.2012.09.010
- Tobón, J. and Mendoza, O. (2009) “Estudio comparativo de la actividad puzolánica de la nanosílice y el humo de sílice en pastas de cal”, *V Encuentro Nacional De Materiales 2009 - Módulo Materiales Cerámicos*
- Uchima, J., Restrepo, O. and Tobon, J. (2016) “Mineralogical evolution of Portland cement blended with metakaolin obtained in simultaneous calcination of kaolinitic clay and rice husk”, *Construction and Building Materials*, 118: 286–293, DOI: 10.1016/j.conbuildmat.2016.05.063
- Yanguatin, H., Tobón, J. and Ramírez, J. (2017) “Reactividad puzolánica de arcillas caoliníticas: una revisión”, *Revista Ingeniería de Construcción*, 32(2): 13–24. DOI: 10.4067/s0718-50732017000200002
- Zou, Y. and Yang, T. (2019) “Chapter 9 - Rice husk, rice husk ash and their applications”, In *Rice Bran and Rice Bran Oil - Chemistry, Processing and Utilization*, AOCS Press, 207–246, DOI: 10.1016/B978-0-12-812828-2.00009-3

Effect of Mix Proportion as W/C and Amount of GGBS Contents on CO₂ Adsorption

R. Yahiro^{1*}, M. Kojima², and T. Iyoda³

¹ Shibaura Institute of Technology, Tokyo, Japan
Email: mh22020@shibaura-it.ac.jp

² Takenaka Corp., Chiba, Japan
Email: kojima.masarou@takenaka.co.jp

³ Shibaura Institute of Technology, Tokyo, Japan
Email: iyoda@shibaura-it.ac.jp

ABSTRACT

In recent years, there has been a growing movement in the world toward the realization of a carbon neutral society as a measure against global warming. There are also a number of efforts in the construction industry. Types of cement with a high percentage of admixture replacement are becoming widely used to reduce CO₂ emissions during cement production. In addition, technology that uses the carbonation reaction of concrete to adsorb CO₂ into concrete is attracting attention. At higher W/C, CO₂ penetrates deeper into the concrete because of the larger pores, resulting in a greater depth of carbonation. In this study, we examined the effect of different mix proportions on the amount of CO₂ adsorption. Cement pastes with different W/C and blast furnace slag fine powder substitution rates were carbonated in a high concentration CO₂ chamber and measured the amount of adsorption, considering the ease of CO₂ penetration. As a result, a tendency was observed that the CO₂ penetrates more deeply, and the amount of CO₂ adsorption is higher in mix proportion with high blast furnace slag fine powder content or high W/C. Also, it shows a trend that the potential to adsorb CO₂ is greater as the CaO percentage that the sample has is increased.

KEYWORDS: CO₂ adsorption, ground granulated blast furnace slag, carbonation reaction, CO₂ penetration

1. Introduction

In recent years, rising seas, droughts, floods, and extreme weather conditions caused by global warming have occurred in the world. Therefore, as a measure against global warming, there is a growing movement toward the realization of a carbon-neutral society, in which the sum of emissions and absorption of the greenhouse gases that cause the problem is substantially zero. There are also a number of initiatives being undertaken in the construction industry. It is a problem of CO₂ emissions during cement production. In an effort to reduce CO₂ emissions from the cement production process, cement with high replacement of admixtures such as ground granulated blast furnace slag or fly ash is being used. In addition, there has been a growing interest in technologies that use the carbonation reaction of concrete in order to absorb CO₂ into the concrete. Considering the carbonation reaction, even if the concrete is carbonated in the same period of time and in the same environmental place, the ease of CO₂ penetration is different depending on the types of cement and W/C. Therefore, the carbonation depth is different. CO₂ absorption cannot be determined by only the carbonation depth because different types of W/C and cement absorb different amounts of CO₂ when carbonated.

In this study, we prepared specimens of cement paste with different types of cement and W/C. Accelerated carbonation was applied. The sample was divided, and the CO₂ absorption was calculated for each part of the sample. This allowed us to study the quantification of CO₂ absorption considering the ease of CO₂ penetration and the CO₂ absorption potential of different types of cement.

2. Materials and outline of experiments

2.1 Materials and mix proportions

In this study, cement paste samples were used to eliminate the influence of aggregate as a fundamental study. The mix proportion is shown in Table 1. The experiment was conducted with four mix proportions, different types of cement and different W/C. As cement, Ordinary Portland Cement (OPC) and Blast Furnace Cement, which is made by replacing ground granulated blast-furnace slag (GGBS) with OPC, were used in the test. The blast furnace slag cement was set as BB with 50% replacement of GGBS and BC with 70% replacement of GGBS. Table 2 also shows the chemical composition of OPC and GGBS. The amount of CaO in the cement was changed by changing the percentage of GGBS.

Table 1 Mix proportion of cement paste

| No. | Type of cement | W/C (%) | Unit weight (kg/m ³) | | |
|------|----------------|---------|----------------------------------|------|------|
| | | | W | OPC | GGBS |
| N30 | OPC | 30 | 487 | 1622 | - |
| N50 | OPC | 50 | 612 | 1225 | - |
| BB50 | BB | 50 | 602 | 602 | 602 |
| BC70 | BC | 70 | 675 | 289 | 675 |

Table 2 Chemical Compositions of OPC and GGBS

| | Chemical composition (%) | | | | | | | | | | | |
|------|--------------------------|--------------------------------|------|--------------------------------|-------|------|------------------|------|-----------------|-------------------|------------------|-------------------------------|
| | SiO ₂ | Al ₂ O ₃ | FeO | Fe ₂ O ₃ | CaO | MgO | TiO ₂ | MnO | SO ₃ | Na ₂ O | K ₂ O | P ₂ O ₅ |
| OPC | 20.19 | 5.18 | - | 2.78 | 65.01 | 1.18 | 0.25 | 0.15 | 2.10 | 0.31 | 0.36 | 0.16 |
| GGBS | 33.27 | 13.94 | 0.31 | - | 40.00 | 5.47 | 0.57 | 0.15 | 1.99 | 0.26 | 0.26 | 0.02 |

2.2 Calculation of CO₂ absorption

Figure 1 shows the outline of the experiment. Rectangular specimens of 40×40×160mm were casted, demolded the day after placing, and sealing cured for 7 days. After curing was completed, the sides were sealed with aluminium tape and one 40×40mm surface was released. The specimens were placed in an accelerated carbonation chamber (20°C, 60% RH, 5% CO₂ concentration) for 28 days of accelerated carbonation. After carbonation, they were sliced at 10 mm intervals from the release surface and treated with acetone to stop the hydration reaction. The measurement of TG-DTA was performed under N₂ flow environment with a temperature increase rate of 20°C/min from room temperature to 1000°C. The CaCO₃ content ratio was calculated by using the inflection point of the peak in the DTA curve to estimate the amount of decarbonation. Amount of CO₂ absorption was calculated using difference in CaCO₃ content ratio between carbonated and uncarbonated. In addition, specimens made under the same conditions were saturated with water under vacuum conditions, and the saturated mass and mass in water were measured. After that, the specimens were placed at 40°C, 30% RH until the mass loss became constant, and then the dry mass was measured. Porosity was calculated by Archimedes' method using saturated mass, mass in water, and dry mass.

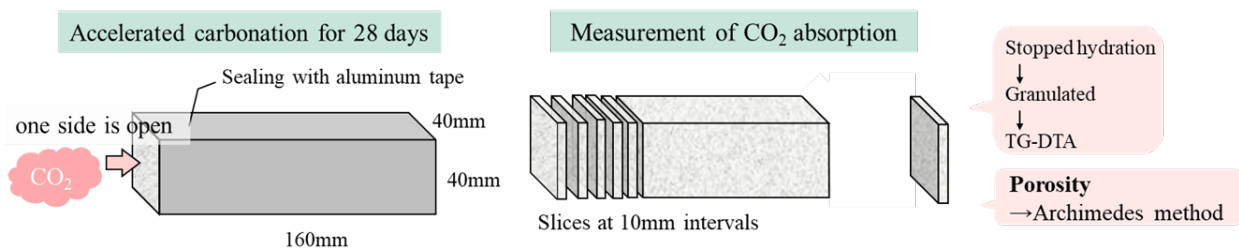


Figure 1 Outline of the experiment

The amount of CO₂ absorption per sliced 40 × 40 × 10mm sample which volume is 16 cm³, with porosity taken into account, was calculated using Equation (1).

$$\text{CO}_2 \text{ absorption [g]} = \text{density [g/cm}^3] \times \text{Volume (16cm}^3) \times (1 - \text{Porosity}) \times A[\%] \times \frac{44}{100} \quad (1)$$

where, A: difference in CaCO₃ content ratio between carbonated and uncarbonated

3. Results and discussion

3.1 CO₂ absorption as hardened cement

Figure 2 shows the amount of CO₂ absorption in each mix proportion for each sliced sample. The horizontal shows the distance from the surface in contact with the CO₂. N30 and N50 were not completely carbonated even at 10 mm from the surface. On the other hand, carbonation reached 20 mm in BB50 and 40 mm in BC70. It is clear that the depth of CO₂ absorption is different depending on the types of cement and W/C as well as the carbonation depth. It was found that in the order of BC70, BB50, N50, and N30, CO₂ was absorbed more deeply into the specimen. In BC70, CO₂ absorption from 0~10 mm, 10~20 mm, and 20~30 mm was about the same in each layer.

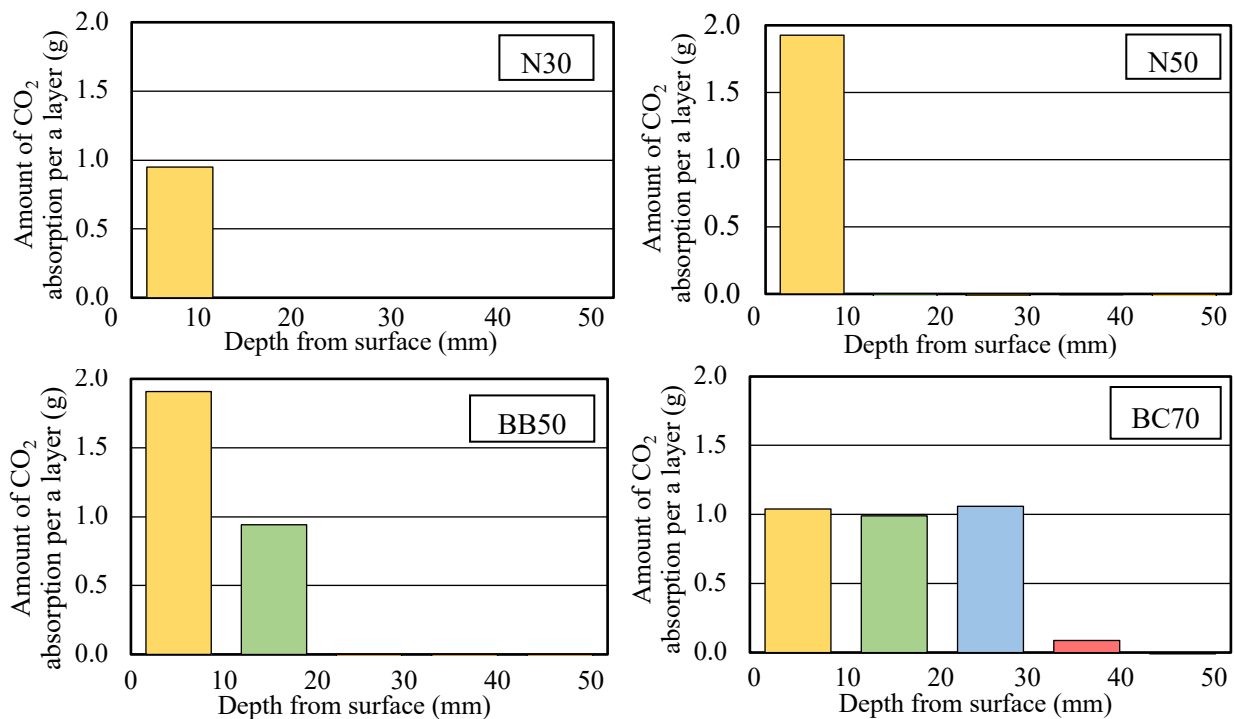


Figure 2 The amount of CO₂ absorption

Figure 3 shows the amount of CO₂ absorption by the total of 40×40×160mm specimen. CO₂ absorption was high in the order of BC70, BB50, N50, and N30. It was found that CO₂ absorption is greater in total as it absorbs CO₂ to a more internal level by carbonating at 5% CO₂ concentration for 28 days.

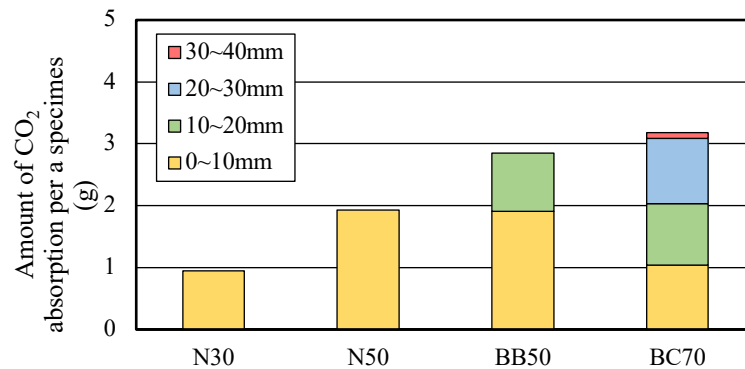


Figure 3 Amount of CO₂ absorption by the total of 40×40×160mm specimen

3.2 CO₂ absorption potential of each mix proportion

We focused on the amount of CO₂ absorbed per layer shown in Figure 3. It can be seen that the amount of CO₂ absorption in one layer is different depending on the mix proportion. Though the largest total absorption was BC70, amount of CO₂ absorption of the first layer was smaller in BC70 than in BB50. In addition, the CO₂ absorption of N30 and N50 did not reach the second layer, and the first layer is not considered to be fully carbonated either, but the CO₂ absorption of the first layer was equal to or higher than that of B70. Therefore, we considered there was potential for the amount of CO₂ that could be absorbed by each mix proportion.

CO₂ absorption was measured using powder samples in which the effect of porosity was eliminated so that carbonation proceeds in the same regardless of mix proportion. Samples of 48×40×2 mm were made and sealing cured for 7 days. And hydration was stopped and the specimens were granulated. Based on previous studies, accelerated carbonation was performed for 7 days after adding 70% water to the sample mass to eliminate the effect of sample drying. After carbonation, CO₂ absorption was measured by TG-DTA.

The results of the CO₂ absorption per 1m³ of cement paste are shown in Figure 4. Amount of CO₂ absorption was high in the order of N30, N50, BB50, and BC70 and smaller for higher GGBS content. Figure 5 shows the relationship between the amount of CaO content per 1m³ of cement and the amount of CO₂ absorption. The larger the CaO content, the greater the CO₂ absorption potential. BC70, which has a smaller CO₂ absorption potential, has a smaller CaO content, indicating that the potential for CO₂ absorption is affected by the CaO content. It is thought that this difference in potential affected the amount of CO₂ absorption in each layer.

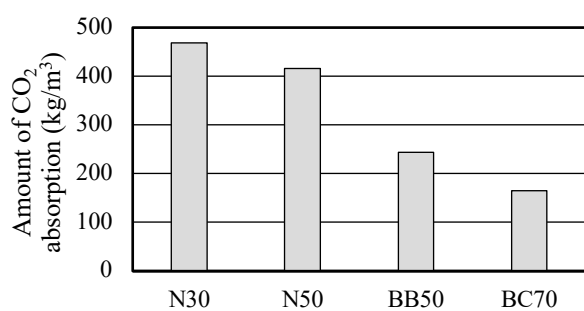


Figure 4 Amount of CO₂ absorption

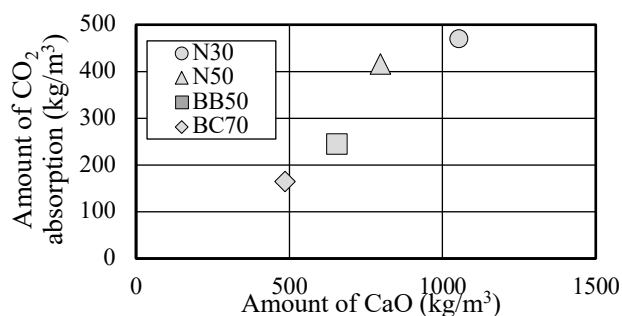


Figure 5 Relationship between the amount of CaO

4. Conclusions

- 1) By carbonating the hardened cement pastes and measuring the amount of CO₂ absorbed by separating it at each distance from the surface, it was found that the deeper the CO₂ absorption, the more CO₂ was absorbed.
- 2) Carbonation with powder samples without considering the ease of CO₂ absorption, such as porosity, is thought to provide the potential for CO₂ absorption of cement paste, and the higher the amount of CaO in the mix proportion, the greater the potential for CO₂ absorption.

Acknowledgements

This paper is based on results of “Development of Materials, Manufacturing Methods and Quality Control System on Innovative Carbon Negative Concrete”, JPNP21014, commissioned by the New Energy and Industrial Technology Development Organization (NEDO).

References

- Iyoda, T., Ishikawa, E. and Ikeo, Y. (2023) “Experimental study on quantification of carbon dioxide adsorption by different cement types and mix proportions”, *Eighth International Symposium on Life-Cycle Civil Engineering (IALCCE 2023)* (Printing)
- Kuroda, Y. and Kikuchi, T. (2009) “Uptake of Carbon Dioxide in the Demolished and Crushed Concrete”, *Concrete Research and Technology*, Vol.20, No.1, :15-22

Use of concrete slurry waste as an accelerator - Effect on early-age strength development and hydration of steam-cured specimen

M. Kobayashi^{1*}

¹ Mitsubishi UBE Cement Corporation, Ube, Japan
Email: mari.kobayashi@mu-cc.com

ABSTRACT

The concrete slurry waste (CSW) is produced as the leftover of ready-mixed concrete mills and through washing process of leftover concrete. Most of the sludge is dehydrated to dewatered cake and disposed in landfills as industrial waste. The transportation of CSW emits CO₂ and the cost of disposal is also quite expensive. Thus, the effective use of CSW is really required. The addition of wet-milled CSW to concrete can improve initial strength development. If this can be applied to precast products, i.e., steam-cured products, it will contribute to improvement of production efficiency, resulting in energy savings. This study investigated the possibility of using CSW as an accelerator of cement hydration, especially for secondary products that are steam cured. Firstly, concrete sludge was wet-milled for 24 hours using a ball mill at 20% solids content. The CSW after wet milling was added to the mortar in the form of replacement of 3-5% of the cement volume. The specimens were then steam cured at 65°C for 3 hours. After curing, compressive strength was measured, and the addition of ground concrete sludge resulted in 1.5 to 1.9 times higher compressive strength than that of the specimens without the addition. This technology is expected to contribute to a sustainable society. This method is expected to contribute labor savings.

KEYWORDS: *Recycling, Concrete slurry waste, Concrete secondary product, Accelerator*

1. Introduction

Concrete slurry waste (CSW) is generated from the production process of concrete. Waste fresh concrete and the sewage from the cleaning of agitator truck and mixer are collected in sedimentation ponds. Then through concrete sandstone separator and filter press, clarified water is recycled and CSW is obtained. The disposal of CSW is generally landfilled, which is expensive to disposal and transport. The transportation of CSW also emits CO₂, which is harmful to environment. Therefore, CSWs must be utilized effectively.

The CSW is mainly comprise hydrated/carbonated cement particles, such as C–S–H gel, portlandite, calcite, calcium aluminate hydrates, and unclaimed fine aggregates (Tang et al., 2020). Various effective utilization of CSW have been investigated, including use as soil stabilizer (Zhang and Fujiwara (2007)), replacement of limestone fillers (Audo et al (2016)), and use as concrete sludge-based geopolymer (Yang (2009)). However, the presence of many relatively coarse or inert particles in CSW can result in a significant decrease in the strength of concrete (Correia et al (2009)). Therefore, the current utilisation of CSW in manufacturing recycled cement and concrete, particularly with a large replacement ratio, has been limited owing to the low activity of CSW, which requires further treatment. He et al (2020) conducted to utilise wet-milling to refine CSW to partially replace the use of cement, and compressive strength showed a positive effect when the wet-milling CSW dosage was lower than 15%. Based on these results, CSW could be used as an accelerator, and demand for accelerators is predicted to arise in the future. Binders that reduced the use of clinker in cement, which are being studied to reduce CO₂ emissions, are still not being actively used because they have problems with initial strength development.

In this study, the potential use of wet-milling CSW as a hydration accelerator especially for precast concrete cured by heat was investigated. The hydration characteristics of the cement paste were analysed using heat evolution and X-ray diffraction (XRD), and compressive strength was also measured.

2. Experimental

2.1 Materials

The CSW was provided by Kanto UBE Concrete corporate. The CSW was dried at 105°C until constant volume. Mineralogical analysis of CSW was characterised by X-ray diffractometry (XRD), and the result is shown in Fig. 1. The crystalline phase consists mainly of calcium hydroxide, with some calcite formed by carbonation, while unhydrated clinker phase was not detected. A small amount of quartz derived from fine aggregate was detected. The chemical composition measured by X-ray Fluorescence (XRF) of CSW is given in Table 1.

2.2 Wet-milling

The wet-milling process was carried out using a pot mill with a volume of 500 ml, in which 100 zirconia balls of $\phi 100$ mm were put. Dried CSW 30 g and distilled water 120 g were put in the pot (solid content concentration is 20%), and wet milled for 24 hours. Particle size distribution were then measured to characterize the physical properties of wet-milled CSW. A laser scattering particle size distribution analyzer (LA-950V2, HORIBA) was used to measure particle size distribution. Ethanol was used as a dispersion medium. Also, the wet-milled CSW was suction filtered, and the composition of the filtrate was determined by inductively coupled plasma optical emission spectrometer (ICP-OES).

2.3 Mixture preparation and method

Mortar specimens with size $\phi 50$ mm \times 100 mm were prepared using Portland cement (PC). The weight replacement ratios of wet milled CSW were fixed at 2%, 3% and 5%. The water content in wet milled CSW was calculated as water, and the water to binder ratio (W/B) was always constant at 0.44. The mixing procedure of the mortar followed JSCE-G505. For curing, treatment temperature was chosen to be 65 °C, and heat treatment cycle has a total duration of 3h; the preheating duration is 20 minutes, the heat duration is 40 minutes, the treatment duration is 2 hours. After curing, compressive strength of the mortar specimens were determined according to the JSCE-G505. The Isothermal conduction calorimetry of cement pastes was performed at 20 °C using a heat flow monitor (CHC-OM6, Tokyo Riko Co.). The weight replacement ratios of wet milled CSW were fixed at 2% and 4%.

3. Result and discussion

3. 1 Characteristics of wet-milled CSW

The particle size of wet-milled CSW was shown in Fig. 2. The minimum and maximum particle size are 0.2 and 19.9 μ m. Particles of PC are generally in the range of 1–50 μ m, and the particle size of wet-milled

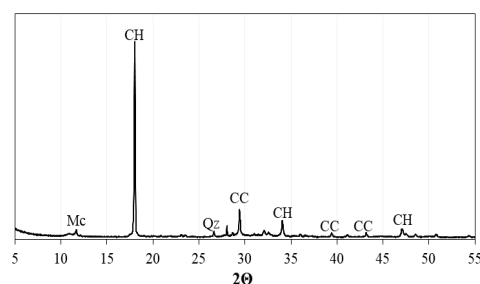


Figure. 1 X-ray diffraction (XRD) patterns of CSW after dried. Mc: monocarboaluminate, CH: calcium hydroxide, Qz: quartz, CC: calcite.

Table 1 Composition of the CSW determined XRF (wt%).

| SiO ₂ | Al ₂ O ₃ | Fe ₂ O ₃ | CaO | MgO | SO ₃ | K ₂ O | Na ₂ O |
|------------------|--------------------------------|--------------------------------|------|-----|-----------------|------------------|-------------------|
| 17.1 | 4.9 | 2.4 | 50.4 | 1.2 | 1.5 | 0.2 | 0.2 |

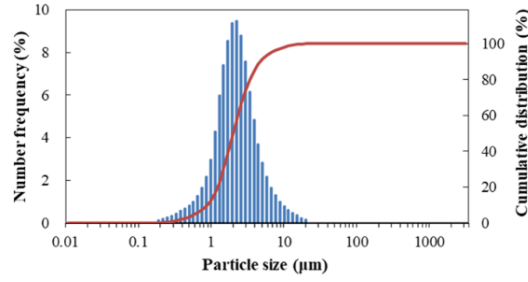


Figure. 2 The particle distribution of CSW after wet-milling.

Table 2 The composition of the filtrate CSW after wet milling (mg/l).

| Na | K | SO ₄ | Ca | Mg | Fe | Al | Si |
|-----|-----|-----------------|-----|--------|------|------|-----|
| 256 | 231 | 16.3 | 598 | < 0.01 | n.d. | n.d. | 0.3 |

CSW is smaller than PC. Table 2 shows the composition of the filtrate of CSW after wet milling. During the wet milling process of CSW, much calcium is dissolved into the water.

3. 2 Characteristics of CSW addition

The compressive strengths of the mortars cured for 3 hours are shown in Fig. 3. Compared with control, substitution with CSW significantly increased the compressive strength at all specimens. As the amount of CSW substitution increased, the compressive strength increased.

The curves of hydration heat liberation of pastes are given in Fig. 4. The substitution of CSW accelerates the hydration process of pastes. The higher amount of CSW substitution makes the hydration process accelerate more, and this result agrees with the results of the compressive strength of the mortar.

CSW after wet milling acts as a hydration accelerator, and enhances early strength development, which is consistent with the results reported in He (2020) and Ren (2022). From the result of particle size distribution, the particles of CSW after wet-milling were several microns to several tens of microns in size, and it is unlikely that the hydration was physically accelerated by heterogeneous nucleation sites provided by addition of nanoparticles. After ball milling, lattice defects could be generated on the surface of CSW

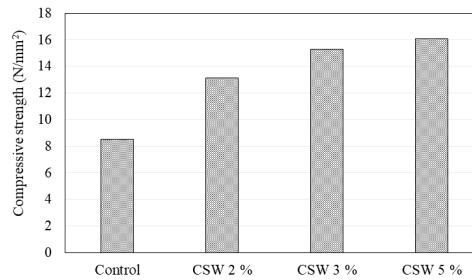


Figure. 3 Effect of CSW substitution ratio on compressive strength of the mortar specimens.

particles (Huang et al, 1995), which can be conducive to the hydration process of PC and generate more hydration products. In addition, focusing on the aqueous component of CSW after wet milling,

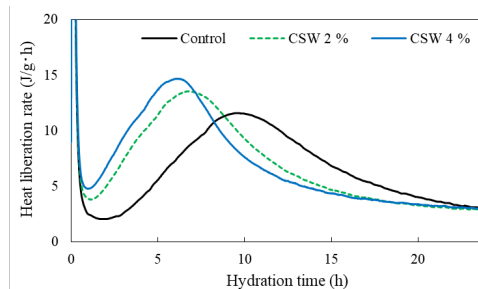


Figure. 4 Hydration heat liberation curve of cement pastes at 20°C.

concentration of calcium ions in the liquid phase is quite high, followed by sodium and potassium ion concentrations. These ions were derived from cement hydrates during wet milling, and pH value of this liquid phase is also expected to be so high (pH = ca.13). When adding CSW with a solid content of 20% after wet milling, the liquid phase is calculated as “water” so that the w/c of the mortar is always 0.44. However, the liquid phase of the CSW after wet milling is not just water, but highly alkaline water. Accordingly, the mortar with a large amount of wet-milled CSW added was mixed with alkaline solution. The addition of this calcium-containing alkaline solution to the mortar leads a fast supersaturation of solution with respect to Ca^{2+} and that resulting crystallization of portlandite might trigger an early onset of fast C_3S hydration (Justnes et al, 1995). Thus, the addition of CSW after wet milling is expected to be used as an accelerator of cement hydration, and it will be more environmentally friendly than other accelerators. Since CSW replaced a part of the binder in this study, however, further increase in the amount of CSW added may have the effect of promoting hydration, but it is also predicted to cause a decrease in the compressive strength of the specimen, and further study is needed.

4. Conclusion

In this study, CSW wet milled and added to mortar, and its initial strength development was investigated under steam curing conditions in order to make effective use of CSW. The results showed that the addition of CSW after wet-milling accelerate cement hydration, resulting in a maximum 1.9 times increase in compressive strength compared to the mortar without wet-milled CSW. This effect could be due to the dormation of lattice defects by wet milling, and/or the high Ca^{2+} concentration and alkaline environment in the liquid phase after wet milling could lead a fast supersaturation of solution with respect to Ca^{2+} and that resulting crystallization of portlandite might trigger an early onset of fast C_3S hydration. The addition of CSW after wet milling could improve the production efficiency of secondary concrete products and is expected to contribute labor-savings significantly.

Acknowledgements

I sincerely thank Mr. Takayasu Ito, Mr. Tetsuhiro Sakai and Masaaki Nagai for their technical assistance with the experiments and discussion.

References

- Audo, M., Mahieux, P.Y. and Turcry, P. (2016) “Utilization of sludge from ready-mixed concrete plants as a substitute for limestone fillers”, *Construction and Building Materials*, 112: 790-799
- Correia, S.L., Souza, F.L., Dienstmann, G. and Segadães, A.M. (2009) “Assessment of the recycling potential of fresh concrete waste using a factorial design of experiments”, *Waste Management*, 29 (11): 2886-2891
- He, X., Zheng, Z., Yang, J., Su, Y., Wang, T. and Strnadel, B. (2020) “Feasibility of incorporating autoclaved aerated concrete waste for cement replacement in sustainable building materials”, *Journal of Cleaner Production*, 250: 119455
- Huang, J.Y., Wu, Y.K. and Ye, H.Q. (1995) “Ball milling of ductile metals”, *Materials Science and Engineering A*, 199 (2): 165-172
- Justnes H., Nygaard E.C. (1995) “Technical calcium nitrate as set accelerator for cement at low temperatures”, *Cement and Concrete Research*, 25: 1766-1774
- Ren, J., Xue, Y., Zhang, J., Liu, B., Luo, S., Xu, S., Xing, F. and Liu, M. (2022) “Pre-treatment of reclaimed concrete slurry waste for substituting cementitious materials: Effect of treatment approach and substitution content”, *Journal of Cleaner Production*, 380: 134987
- Tang, P., Xuan, D., Cheng, H.W., Poon, C.S. and Tsang, D.C.W. (2020) “Use of CO_2 curing to enhance the properties of cold bonded lightweight aggregates (CBLAs) produced with concrete slurry waste (CSW) and fine incineration bottom ash (IBA)”, *Journal of Hazardous Materials*, 381: 120951
- Yang, Z.X., Ha, N.R., Jang, M.S., Hwang, K.H., Jun, B.S. and Lee, J.K. (2010) “The Performance of Geopolymer Based on Recycled Concrete Sludge”, *Ceramic Materials and Components for Energy and Environmental Applications*, pp. 221–224.
- Zhang, J. and Fujiwara, T. (2007) “Concrete sludge powder for soil stabilization” *Transport Research Record*, 2026 (1), 54–59.

A Study on Mortar Properties Focusing on Water Absorption Ratio of Carbonated Recycled Fine Aggregate

Y. INOUE^{1*}, Y. IKEO², and T. IYODA³

¹ Shibaura Institute of Technology, Tokyo, Japan

Email: mh22001@shibaura-it.ac.jp

² Takenaka Corporation, Chiba, Japan

Email: ikeo.yousaku@takenaka.co.jp

³ Shibaura Institute of Technology, Tokyo, Japan

Email: iyoda@shibaura-it.ac.jp

ABSTRACT

In Japan, concrete waste has been reused as roadbed material. In the future, the amount of concrete waste generated is expected to increase due to the increase in demolition of concrete structures. Therefore, the amount of concrete waste generated is expected to exceed the demand for roadbed material. Also, new road construction is expected to decline. This means that, concrete waste should be reused as recycled aggregate for concrete. Recycled aggregates are classified as class H, M, and L in order of aggregate quality in Japan. Recycled aggregate class L can be produced with less energy and cost. Meanwhile, concrete made with Recycled aggregate class L has low strength and large drying shrinkage. To promote the use of recycled aggregate concrete, technology for modifying Recycled aggregate class L at low cost is required. We have proposed a method of carbonating recycled aggregate using CO₂ gas. This method improves the water absorption ratio and density of the aggregate by carbonating the attached mortar. It is reported that the higher the density and lower the water absorption ratio of the recycled aggregate, the higher the concrete's property. The density and the water absorption ratio of the recycled aggregate depend on amount of attached mortar, type of raw aggregate, and carbonation. In this study, the water absorption ratio of recycled fine aggregate was improved by focusing on carbonation period and carbonation method of the aggregate. Regardless of the method, the mortar's property was found to improve along with the improvement in water absorption ratio by carbonation. It is estimated that the water absorption ratio of the aggregate can be used to determine the mortar's property. Improvement of the recycled fine aggregate and mortar property was significant when the aggregate was soaked in calcium hydroxide and carbonated for 7 days.

KEYWORDS: *recycled fine aggregate, carbonation, water absorption ratio, carbonation period, mortar properties*

1. Introduction

In order to achieve a sustainable society, efforts to reduce the impact on the environment and to create a recycling-oriented society are required in the construction field as well. In Japan, 90% concrete waste generated when concrete structures are demolished has been reused as roadbed and backfill materials. However, a decrease in new road construction is expected in the future. On the other hand, the amount of concrete waste is expected to increase with the demolition of many concrete structures constructed during the period of rapid economic growth. Therefore, the amount of concrete waste generated is expected to exceed the demand for roadbed material. Thus, concrete waste should be reused as recycled aggregate for concrete. And it is hoped that the use of concrete with recycled aggregate will be promoted. However, recycled aggregate is rarely used in Japan.

In Japan, recycled aggregate is classified into three types using aggregate quality. They are called class H, M, and L, in descending order of quality. Recycled aggregate class L can be produced with less energy and cost than recycled aggregate class H and class M. And it generates less by-product fine powder. On the other hand, concrete made with low-quality recycled aggregate has problems when compared to concrete

made with normal aggregate. It has lower strength and higher drying shrinkage. If recycled aggregate concrete is to become widely used, there is a need for a technology to modify low-quality recycled aggregate that does not require special manufacturing equipment. We have previously proposed a method of carbonation of recycled aggregate using CO_2 gas as a modification technology for low-quality recycled aggregate.

Among them, recycled fine aggregate is noted to have a significant improvement effect due to forced carbonation. Figure 1 shows an image of the mechanism of carbonation of recycled aggregate. Carbonation converts calcium hydroxide in the aggregate to calcium carbonate. When calcium carbonate with a large volume is produced, the voids in the aggregate are filled, water absorption ratio is reduced, and absolute dry density is increased. It is reported that, in general, the higher the density of the recycled aggregate and the lower the water absorption ratio, the higher the physical properties of the recycled aggregate. They are highly dependent on the amount of attached mortar, the type of original aggregate, and the presence or absence of carbonation.

In this study, we focused on the number of days of aggregate carbonation and carbonation methods to improve the water absorption ratio of recycled fine aggregate. The same low-quality recycled fine aggregate was modified by several methods. We examined the effect of water absorption ratio of those aggregates on the strength and durability of the mortar.

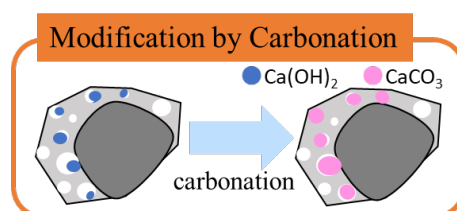


Figure 1 Modification by carbonation

2. Modification of Recycled Fine Aggregate by Carbonation

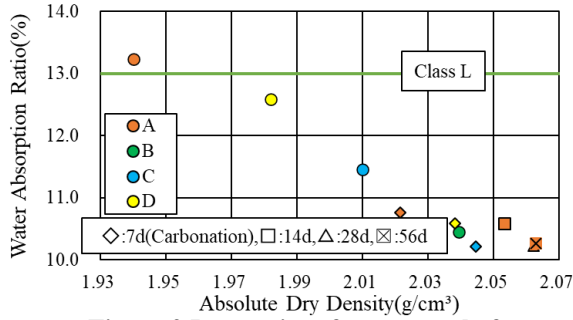
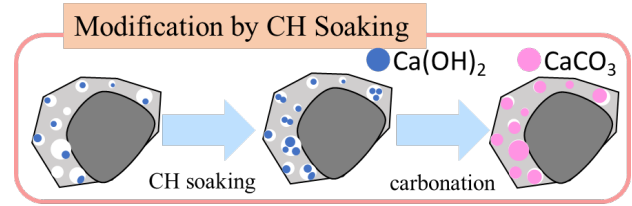
Table 1 shows the physical properties of the recycled fine aggregate used in this study, and Figure 2 shows the relationship between the absolute dry density and water absorption ratio of the aggregate before and after modification. In this study, the recycled fine aggregate of lower quality than Class L was used as recycled fine aggregate before modification (A). The following studies were conducted to confirm the effects of different carbonation periods and modification methods. These modifications brought all the recycled fine aggregate within the class L. First, we extended the carbonation period. Carbonation of aggregate was performed using an accelerated carbonation system at 20°C , 60% relative humidity, and 5% CO_2 concentration. The extended periods were 7, 14, 28, and 56 days (A-7d, 14d, 28d, 56d). 7 days carbonation resulted in the same improvement as in the previous studies. The improvement effect has varied in previous studies, but this time the improvement effect was different from previous studies. Focusing on the carbonation period, the physical properties of the aggregate are more improved by extending the period compared to the 7 days carbonation. However, the physical property data for 28 days and 56 days are almost the same. Also, aggregates were prepared to confirm whether the improvement in water absorption ratio by carbonation was significant. (B). It has the same water absorption ratio together with A-7d.

Next, the fine particles were pre-cut and carbonated in water using carbonated water (C). The same improvement was observed in carbonation in water (CC).

In a different carbonation method, the aggregate was soaked with calcium hydroxide water solution (hereafter referred to as CH) (D). A saturated water solution of calcium hydroxide was used. Then, after soaking, carbonation was performed for 7 days (DC). When the aggregate was impregnated with CH, the physical properties were within the class L as well as others. Furthermore, the aggregate with 7 days carbonation showed improved physical properties compared to the aggregate with only 7 days carbonation. The improvement effect of CH soaking is as follows. Figure 3 shows an image of modification by CH soaking. CH soaking of the recycled fine aggregate initially allows CH to penetrate the voids in the attached paste of the aggregate. When this recycled fine aggregate is carbonated, the CH originally present in the attached paste of the aggregate is carbonated, as well as the CH that has been soaked in the paste. We consider that the effect of improvement will be greater. In this study, the water absorption ratio confirmed here was used as an indicator of the aggregate, and the mortar property using these modified aggregates were compared.

Table 1 Physical properties of the recycled fine aggregate

| Sample name | Modification Method | Surface Dry Density (g/cm ³) | Absolute Dry Density (g/cm ³) | Water Absorption ratio (%) |
|-------------|--------------------------|--|---|----------------------------|
| A | No Modification | 2.20 | 1.94 | 13.24 |
| A-7d | Carbonation Period | 7days | 2.24 | 10.75 |
| A-14d | | 14days | 2.27 | 10.59 |
| A-28d | | 28days | 2.27 | 10.22 |
| A-56d | | 56days | 2.27 | 10.26 |
| B | Water Absorption Ratio | 2.25 | 2.04 | 10.45 |
| C | Fine particle cut | 2.24 | 2.01 | 11.46 |
| CC | carbonation in water | 2.25 | 2.04 | 10.20 |
| D | CH Soaking | 2.23 | 1.98 | 12.59 |
| DC | CH Soaking & Carbonation | 2.25 | 2.04 | 10.58 |

**Figure 2 Properties of aggregate before and after modification aggregate****Figure 3 Modification by CH soaking**

3. Mortar using Modified Aggregate

3.1 Materials and Mix Proportion

The mortar was formulated with a water cement ratio 50% and fine aggregate to cement ratio 3.0. The cement used was Ordinary Portland Cement. The recycled fine aggregate shown in Table 1 was used as the fine aggregate. Recycled aggregate has a high water absorption ratio, and slump loss is a concern if used as is. The fine aggregate was prewetted for 24 hours before mixing and used as a surface dry condition.

3.2 Testing Methods

(1) Compressive strength test

Mortar bars of $40 \times 40 \times 160$ mm were used, and the test was conducted in accordance with JIS R 5201 after water curing for 28 days.

(2) Air permeability test

A cylindrical specimen of $\phi 100 \times 25$ mm cured in water for 28 days was placed in a drying oven at 40°C until its mass became constant, and the test was conducted. Air was allowed to permeate through the material at a pressure of 0.1 MPa in an air permeability testing chamber. The amount of air permeation was measured by the water displacement method using a measuring cylinder, and the permeability coefficient was calculated from the following equation (1).

$$K = \frac{2LP_1}{(P_1^2 - P_2^2)} \cdot \frac{Q}{A} \quad (1)$$

K: Air permeability coefficient ($\text{cm}^4/\text{N} \cdot \text{s}$), L: Specimen thickness (cm), P_1 : Loading pressure (N/mm^2), P_2 : Outflow side pressure (N/cm^2), Q: Amount of air permeability (cm^3/s), A: permeable area (cm^2)

3.3 Results and Discussion

Figure 4 shows the relationship between compressive strength and water absorption ratio of aggregate, and Figure 5 shows the relationship between air permeability and water absorption ratio of aggregate. For all modification methods, we observed a tendency for the physical properties of the mortar to improve as water absorption ratio improves. Comparing A-7d and B, mortar properties are better A-7d. It can be said that the improvement of water absorption ratio by carbonation is significant. When carbonated, there is a correlation

between the water absorption ratio of the aggregate and the mortar's property. Focusing on the carbonation period, the improvement effect of A-28d is significant, as are the physical properties of the aggregate. We had previously assumed 7days as a carbonation technique. However, the extended period, 28days carbonation, is found to be more effective. Similarly, carbonation in water showed almost the same improvement as A-28d. Yet, carbonation in water cuts off the fine particles that have a large amount of attached paste as a pre-processing step. It is thought that this is because of cutting off the fine particles. It should be examined whether there is a difference in the improvement effect of carbonation in water with fine particles left in the water.

Focusing on the different modification methods, first, the air permeability was improved when CH was soaked. Furthermore, when CH was soaked and 7days carbonation was performed, both strength and air permeability were greatly improved. The results were like those of A-28d. From the above, it is considered that the physical properties of mortar are greatly affected by the improvement of water absorption ratio due to carbonation. In the future, it is necessary to confirm whether the improvement in water absorption ratio and mortar properties due to CH soaking is greater when the carbonation period is extended.

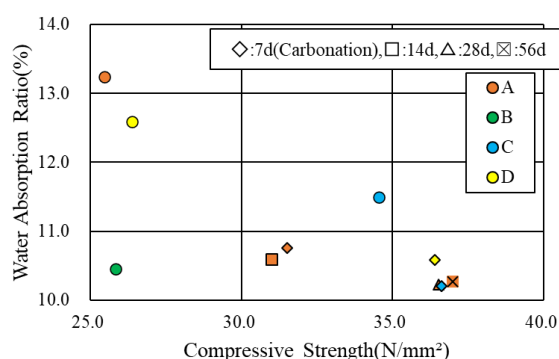


Figure 4 Compressive Strength

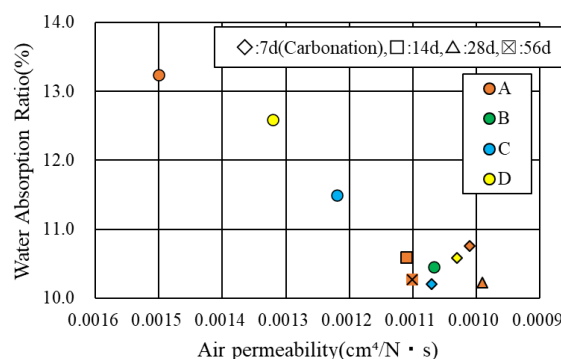


Figure 5 Air Permeability

4. Conclusions

- (1) Carbonation of recycled fine aggregate modified water absorption ratio, and properties of mortar using modified recycled fine aggregates improved. As well, it is significant that carbonation improves water absorption ratio. Furthermore, there was a correlation between water absorption ratio of recycled fine aggregate modified by carbonation and physical properties of mortar using the aggregate. It is also evident that the improvement is greater when the carbonation period is extended. It may be possible to assume some improvement effect of the mortar from the improvement of water absorption ratio.
- (2) Carbonation of recycled fine aggregate after impregnation with CH has a greater improvement effect than carbonation alone. This is thought to be due to the fact that CH soaking increases the amount of calcium hydroxide water solution that can be carbonated.

Acknowledgements

This paper is based on results of “Development of Materials, Manufacturing Methods and Quality Control System on Innovative Carbon Negative Concrete”, JPNP21014, commissioned by the New Energy and Industrial Technology Development Organization (NEDO).

References

- Takahiro, K., Nobuhiro, M and Takeshi, I. (2010) “METHOD FOR IMPROVING THE QUALITY OF LOW-GRADE RECYCLED AGGREGATE”, *The 6th International Conference of Asia Concrete Federation*, pp1137-1141
- Nobuhiro, M., Takahiro, K., Mina, M and Takeshi, I. (2014) “Study of Low-Energy Type Recycled Aggregate Production Method by Forced Adsorption of CO₂ Gas”, *Concrete Annual Journal of Engineering*, vol.36, No.1, pp.1732-1737
- Nobuhiro, M and Takeshi, I. (2019) “Proposal of Technology for Modification of Low-Quality Recycled Aggregate by Carbonation and Effect of Modified Recycled Aggregate on Concrete”, *Concrete Engineering Journal*, vol.30, pp.65-76

Effect of Conditions on Pore structure of silica gel in Wet Carbonated Recycled Cement Paste Powder

Yuguang Mao ^{1,2,3}, Pingping He ^{1,2,3}, Sarra Drissi ⁴, Xiang Hu ^{1,2,3}, Caijun Shi ^{1,2,3,5} *

1. Key Laboratory for Green & Advanced Civil Engineering Materials and Application Technology of Hunan Province, College of Civil Engineering, Hunan University, Changsha 410082, P. R. China
2. International Science Innovation Collaboration Base for Green & Advanced Civil Engineering Materials of Hunan Province, Hunan University, Changsha 410082, P. R. China
3. Key Laboratory of Building Safety and Energy Efficiency of the Ministry of Education, Hunan University, Changsha 410082, China
4. Department of Civil Engineering and Energy Technology, Faculty of Technology, Art and Design, Oslo Metropolitan University, PO box 4 St. Olavs plass, Oslo, NO-0130, Norway
5. Department of Civil Engineering, The University of British Columbia, Vancouver, BC V6T 1Z4, Canada

ABSTRACT

Wet carbonation is deemed a successful approach to recycling waste concrete powder. Controlling the properties of products in the recycled cement paste powder (CPP) is highly dependent on the wet carbonation conditions. This study aims to examine the effect of carbonation conditions on the pore structure of silica gel in CPP. The present study investigated the effect of CO₂ flow rates, temperatures, and carbonation times on the pore structure of silica gel in CPP using ¹H NMR. CO₂ flow rate was the key factor affecting the pore structure of silica gel. Capillary pores were mainly formed at a flow rate of 3L/min, while gel pores were mainly formed at a CO₂ flow rate of 5 L/min. The effect of carbonation temperature was insignificant. The findings of this study contribute to a better understanding of the best experimental parameters for achieving a more efficient and effective waste concrete recycling process.

KEYWORDS: *Recycled cement paste powder; Wet carbonation; Carbonation condition; Silica gel*

1. Introduction

The quality of the recycled aggregates (RA) is usually affected by the adhered mortar left from the original concrete adhered to the RA surface (Ouyang et al., 2020; Shi et al., 2016). To overcome this issue, it is often necessary to remove this attached mortar. Mechanical grinding is currently the most common method for removing adhered mortar due to the simplicity of the process (Ouyang et al., 2020; Shi et al., 2016). However, it can produce a large amount of cement paste powder (CPP) with particle size less than 0.15 mm (Lu et al., 2018). Carbonation has been proven to be a feasible method for treating recycled CPP and reusing them as supplementary cementitious material to replace cement (Chen et al., 2022; Liu et al., 2022; Lu et al., 2018). CO₂ can react with hydration products (e.g., Ca(OH)₂ and C-S-H gels) to produce CaCO₃ and silica gel, improving thus the microstructure of recycled CPP and decreasing its porosity and water absorption. Despite the importance of temperature and CO₂ flow rate, their effect on the products in recycled CPP during wet carbonation has not been thoroughly investigated. This results in the inability to control well the amount and properties of the carbonation product, including pore structure of silica gel, by adjusting the carbonation condition to make it a valuable recycled product. To gain insight into how these parameters affect the products precipitated in recycled CPP following wet carbonation, a systematic investigation was conducted using various analytical techniques. Silica gel in wet carbonated CPP was extracted by acid solution, and its properties were further examined by solid-state Nuclear Magnetic Resonance (¹H NMR).

2. Materials and test methods

2.1. Materials

To have better control over the composition of the studied samples and to accurately analyze the properties of carbonation products, the recycled CPP was replicated using a hydrated CPP. First, cement paste specimens, made using Portland cement (P.I 42.5) and a w/c of 0.4, were cured in a steam curing chamber at 60°C until their hydration degree reached close to 90%, as determined by XRD analysis. Then, the hydrated samples were crushed and ground to pass through a 150 μm sieve. The resulting powder was then stored in a vacuum-drying oven at 20°C.

2.2. Carbonation of CPP

The carbonation of CPP was carried out on a heating magnetic stirrer, as illustrated in **Fig. 1 (a)**. The carbonation conditions were varied to study the effect of temperature (25°C and 80°C), time (30 and 60 min), and CO₂ flow rate (3 L/min and 5 L/min) on the carbonation products. The wet carbonation process involved heating 500 mL of deionized water. Once the desired temperature was reached, 50 g of CPP was added to the water. Meanwhile, pure CO₂, with a purity greater than 99.9%, was injected at the selected rate and time. The flow rate was controlled using a flow meter. During the experiment, the solution was stirred at 400 rpm. The carbonated CPP samples were collected from the solution through centrifugation using a benchtop high-speed centrifuge. Uncarbonated CPP (UC) and dry carbonated CPP specimens (D-360 and D-1080) were used as reference samples. The specimens, D-360 and D-1080, were dry carbonated in a pressured chamber using a CO₂ pressure of 0.2 MPa, as shown in **Fig. 1(b)**.

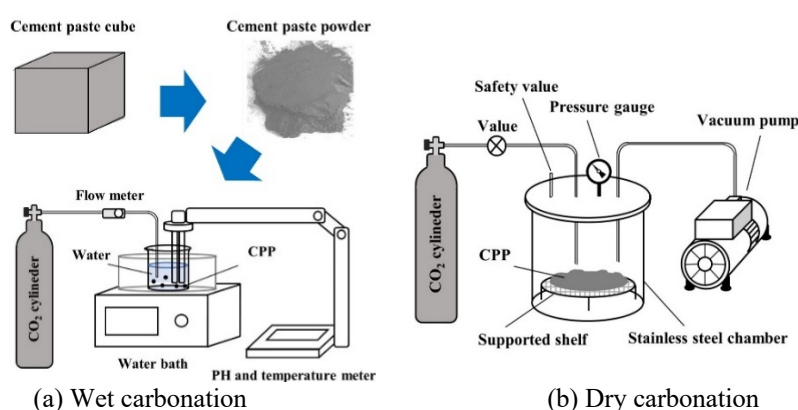


Fig. 1. Schematic of carbonation setup and process.

2.3. Extraction of silica gel

Fig. 2 shows the extraction process of silica gel (SG) from carbonated CPP. 4g carbonated CPP sample was placed in 1000 ml HCl solution (0.5 mol/L) and stirred for 2h using a magnetic stirrer. The solution was then vacuum filtered using a 0.2 μm microporous filter membrane. The collected solid samples were placed in a vacuum-drying oven at 20°C.

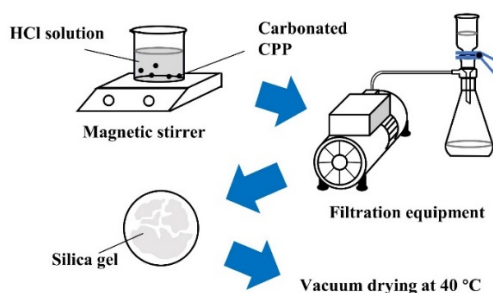


Fig. 2. Schematic of the process of silica gel extraction.

2.4. Test methods

2.4.1. ^1H Nuclear magnetic resonance (^1H NMR)

The silica gel samples were placed in a standard curing box for 3 d before testing. PM-1030 MAG-MED ^1H NMR spectroscopy at 10MHz was used to determine the water content and consequently the variation of pore size in silica gel. The Carr-Purcell-Meiboom-Gill (CPMG) of samples was measured using a 10 mm probe to determine the T_2 relaxation time. The spin relaxation was 121 recycle times, and the recycle delay was 7s. The transverse relaxation rate $1/T_2$ was transferred into pore size distribution.

3. Results and discussion

The pore size distributions of the samples were determined from the water state measured by ^1H NMR. **Fig. 4** shows the ^1H NMR spectra of silica gel samples, from which the content and distribution of gel water and capillary water in each sample were obtained (with 100 nm serving as the threshold for different types of water). **Table 1** lists the percentage of different types of water in each silica gel specimen. Notably, the silica gel samples extracted from dry carbonated CPP had a high percentage of gel water, which was comparable to that observed in samples extracted from CPP carbonated from 60min at a CO_2 flow rate of 5 L/min.

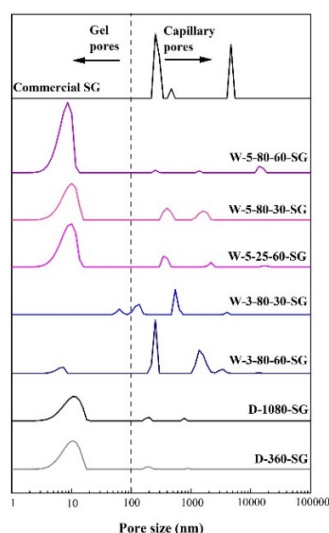


Table 1 Water content of carbonated CPP samples under different carbonation conditions.

| | Water sate | |
|---------------|---------------------|---------------|
| | Capillary water (%) | Gel water (%) |
| W-3-80-30-SG | 88.9 | 11.1 |
| W-3-80-60-SG | 89.4 | 10.6 |
| W-5-25-60-SG | 14.1 | 85.9 |
| W-5-80-30-SG | 23.4 | 76.6 |
| W-5-80-60-SG | 6.5 | 93.5 |
| D-360-SG | 3.8 | 96.2 |
| D-1080-SG | 5.8 | 94.2 |
| Commercial SG | 100 | 0 |

Fig. 4. ^1H NMR spectra of carbonated CPP samples under different carbonation conditions and commercial silica gel.

Regarding the effect of CO_2 flow rate, silica gel extracted from CPP carbonated with a CO_2 flow rate of 3 L/min contained mainly capillary water. Samples W-3-80-30-SG and W-3-80-60-SG had 88.9 and 89.4 % capillary water, respectively, similar to the commercial silica gel desiccant. This finding confirms that sample W-3-80-60-SG has similar water absorption and desorption properties to commercial silica gel. In contrast, the silica gel samples extracted from CPP carbonated with CO_2 flow rate of 5 L/min had higher gel water, indicating that increasing the CO_2 flow rate from 3L/min to 5L/min promotes the shifts from capillary to gel pores. A CO_2 flow rate of 5L/min accelerates the dissolution of CO_2 in water and promotes CO_3^{2-} to move more in water, allowing for a greater reaction with the silica-rich particle that has diffused out of the coating (**Fig. 5(a)**). This results in the concentration of newly generated silica gel on the inner side of the gap between the coating (closer to C-S-H) (**Fig. 5(b)**), leading to mostly gel pores in silica gel **Fig. 5(c)**. This process of CO_3^{2-} diffusion into the interior of the coating is similar to the internal diffusion of CO_2 gas in dry carbonation. This explains why silica gel obtained by dry carbonation mostly consists of gel pores. In contrast, a CO_2 flow rate of 3L/min results in slower CO_2 gas dissolution in water and less extensive CO_3^{2-} movement (**Fig. 5(d)**). The silica-rich particle is then freed from the coating layer and decalcified, resulting in the formation of silica gel outside the coating layer (**Fig. 5(e)**). This eventually

leads to a high percentage of capillary pores in silica gel (**Fig. 5(f)**). With regards to temperature, sample W-5-80-60-SG had higher gel water than samples W-5-25-60-SG by 7.6%. This result suggests that the rise in temperature also induced a shift from capillary pores to gel pores. The mechanism involved is similar to that of the CO₂ flow rate, although the impact of temperature is less pronounced than that of the CO₂ flow rate.

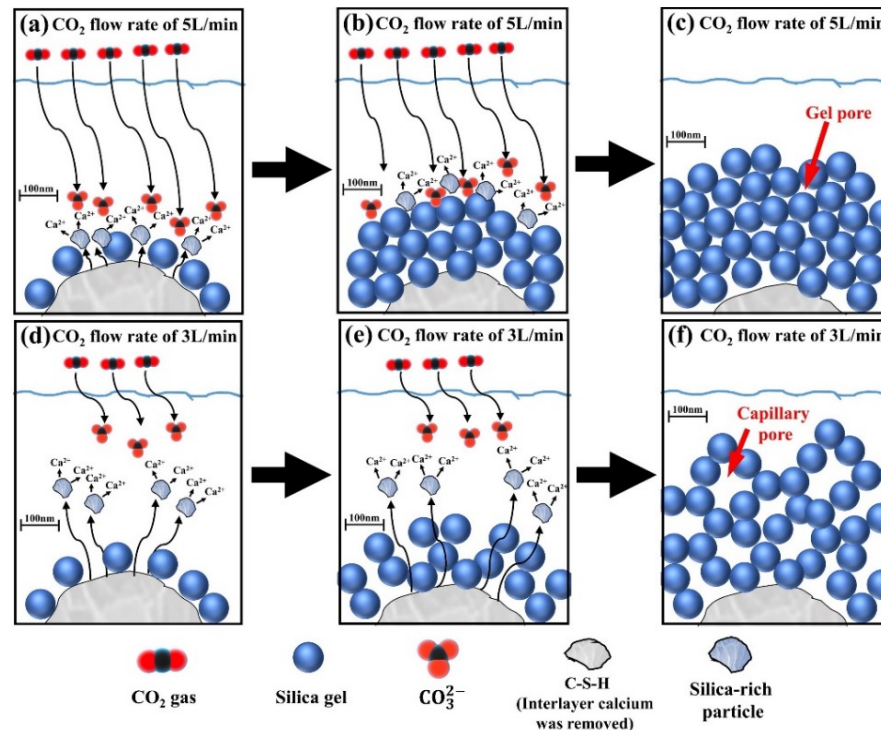


Fig. 5. Effect of conditions on the pore structure of CPP during wet carbonation.

3. Conclusions

CO₂ flow rate was the key factor affecting the composition and pore structure of silica gel. Capillary pores were mainly formed at a flow rate of 3L/min, while gel pores were mainly formed at a CO₂ flow rate of 5 L/min. In addition, The effect of carbonation temperature was insignificant.

Acknowledgements

The authors would like to acknowledge the financial support from National Natural Science Foundation of China grant numbers 52050410333 and 52078204, and Innovandi core project 10 of Global Cement and Concrete Association (GCCA).

References

- Chen, X., Li, Y., Zhu, Z., Ma, L. (2022). Evaluation of waste concrete recycled powder (WCRP) on the preparation of low-exothermic cement. *Journal of Building Engineering*, 53, 104511.
- Liu, X., Liu, L., Lyu, K., Li, T., Zhao, P., Liu, R., Zuo, J., Fu, F., Shah, S.P., 2022. Enhanced early hydration and mechanical properties of cement-based materials with recycled concrete powder modified by nano-silica. *Journal of Building Engineering*, 50, 104175.
- Lu, B., Shi, C., Zhang, J., Wang, J. (2018). Effects of carbonated hardened cement paste powder on hydration and microstructure of Portland cement. *Construction and Building Materials*, 186, 699-708.
- Ouyang, K., Shi, C., Chu, H., Guo, H., Song, B., Ding, Y., Guan, X., Zhu, J., Zhang, H., Wang, Y., Zheng, J. (2020). An overview on the efficiency of different pretreatment techniques for recycled concrete aggregate. *Journal of Cleaner Production*, 263, 121264.
- Shi, C., Li, Y., Zhang, J., Li, W., Chong, L., Xie, Z. (2016). Performance enhancement of recycled concrete aggregate – A review. *Journal of Cleaner Production*, 112, 466-472.

Aqueous Carbonation of Recycled Concrete Fines: Towards Higher Efficiency

Yi Jiang¹, Zihan Ma², Peiliang Shen³, and Chi Sun Poon^{4*}

Department of Civil and Environmental Engineering & Research Centre for Resources Engineering towards Carbon Neutrality, The Hong Kong Polytechnic University, Hong Kong, China

¹ Email: yi289.jiang@connect.polyu.hk

² Email: zihan.ma@connect.polyu.hk

³ Email: peiliang.shen@polyu.edu.hk

⁴ Email: cecspoon@polyu.edu.hk

ABSTRACT

Recycled concrete fines (0.3-2.36 mm) are the fine fractions of crushed waste concrete. Accelerated carbonation has been widely reported as an effective technique in improving the qualities of RCFs. However, the carbonation rate is generally slow due to the limitation in the gaseous diffusion of CO₂. In this study, an improved aqueous carbonation method, by using alkali for the preparation of the initial carbonation solution, was adopted for carbonating RCFs. It aims to enhance carbonation efficiency for improving industrial productivity. The rate and amount of calcium carbonate (Cc) precipitations, the morphology of Cc, the advance of the carbonation front, and the evolution of physical properties of the carbonated RCFs were investigated. The results indicated that carbonation efficiency was significantly improved by increasing the rate and total amount of Cc precipitation by up to 100%, and the carbonation depth by two times. After carbonation, the physical properties of these RCFs were enhanced and could facilitate their recycling and application.

KEYWORDS: *Aqueous carbonation, recycled concrete fines, water absorption, density*

1. Introduction

Recycled concrete fines (RCFs) are the fine fractions generated during waste concrete recycling. They have smaller particle sizes, higher amounts of residual cement pastes and thus more defects (**including pores and microcracks**) than both the recycled coarse aggregates (RCAs) and natural fine aggregates. These defects would particularly worsen the workability, drying shrinkage, and transport properties of concrete (Pedro et al. 2017, Xiao et al. 2018).

Accelerated carbonation has been reckoned as an effective and sustainable method to improve the qualities of RCFs. Carbonated RCFs/RCAs generally have refined pore structure and higher reactivity than uncarbonated counterparts (Shi et al. 2018) **due to the reactions between CO₂ and hydration products in the residual cement paste that precipitates calcium carbonate (Cc) filling the pores and amorphous gel providing pozzolanic reactivity**. Investigations have consistently revealed that carbonated RCFs could not only act as a stronger physical framework in new concrete to resist external load (Li et al. 2019) but also interact more intimately with surroundings to establish vigorous interfacial transition zones (Zhan et al. 2020). However, the slow carbonation kinetics has been a major concern. The excess moisture that existed in the pore system reduces the continuity of pores that is accessible to CO₂ gas, thus impeding the gaseous diffusion of CO₂ and inhibiting the carbonation reaction (Phung et al. 2015). Nevertheless, aqueous carbonation employs a bulk liquid environment to create a full saturation of pore system, thereby proceeding with the carbonation by transforming the gaseous diffusion into aqueous diffusion, in a way of dissolving CO₂ into aqueous carbonate species before carbonation (Jiang et al. 2022). Previous studies (Zajac et al. 2020, Ren et al. 2022) have indicated that aqueous carbonation proceeds faster than gas-solid carbonation.

More importantly, the aqueous carbonation method allows the manipulation of the concentration of reactants e.g., by buffering the CO₂ in alkali solutions. As such, the concentration of carbonate species is expected to increase by several magnitudes. According to Fick's law, the diffusion of carbonate species could thus be remarkably accelerated. Zajac et al. (2021) used sodium hydroxide solutions as the initial solution for carbonating ground cement paste. It was found that even though the ultimate phase assemblage was similar, the rate of Cc precipitation at the early age increased by up to 5 times. Similarly, Eikeland et al. (2015) reported that a significant increase in carbonation yield from 5% to 100% was attained by increasing the NaHCO₃ concentration from 0 to 0.5M during the carbonation of magnesium silicate minerals.

Therefore, this study aims at enhancing the efficiency of aqueous carbonation on RCFs using alkali (sodium hydroxide) as the initial solution. The rate and amount of Cc precipitation, and the evolution of microstructural and physical properties were determined and discussed.

2. Materials and methods

2.1 Materials

The RCFs used in this study was shown in Fig. 1 which included real RCFs and simulated RCFs. The real RCFs were obtained by crushing the waste concrete collected from a local demolition site in Hong Kong, while the simulated RCFs were obtained by crushing a cement paste that was hydrated for 1.5 years. After crushing, they were sieved to get the fractions with the particle sizes between 0.3mm and 2.36mm. The main chemical compositions of the two RCFs are given in Table 1.



Fig. 1. The RCFs used in this study (a) real RCFs and (b) simulated RCFs

Table 1. The chemical compositions of the RCFs used in this study.

| | CaO ^a | SiO ₂ | Al ₂ O ₃ | Fe ₂ O ₃ | MgO | Na ₂ O+K ₂ O | Others | CO ₂ ^b | LOI ^b |
|-----------|------------------|------------------|--------------------------------|--------------------------------|-----|------------------------------------|--------|------------------------------|------------------|
| Real | 27.5 | 51.1 | 9.5 | 2.1 | 0.9 | 5.7 | 4.9 | 2.5 | 25.9 |
| Simulated | 65.7 | 19.9 | 4.4 | 3.4 | 1.5 | 0.7 | 4.4 | 3.3 | 8.9 |

Note: a. The oxide composition was determined using X-ray fluorescence.

b. The CO₂ content and LOI were determined using thermogravimetric analysis.

2.2 Methods

The RCFs were carbonated using the aqueous carbonation method as described in our previous study (Jiang et al. 2022). Deionized water and 0.5M sodium hydroxide were used as the initial solution. CO₂ (approximately 20 vol%) was injected into the initial solutions until pH stabilized and then RCFs were added into the solutions (at a solid-to-solution ratio of 10g:100mL) which marked the start of carbonation. During the carbonation process, CO₂ was constantly injected at 0.1L/min/10g RCFs, and carbonation was stopped at 6h. The RCFs carbonated in a deionized-water-based solution and sodium-hydroxide-based solution were named cRCFs-1 and cRCFs-2 respectively.

Simulated RCFs were used for mineralogical analysis to exclude the contaminations from natural aggregate, while the real RCFs were used for examining physical and microstructural properties. Thermogravimetric analysis (TGA) and X-ray diffraction (XRD) were performed on simulated RCFs after solvent exchange and vacuum drying to characterize the amount and polymorphs of Cc (Jiang et al. 2022). Scanning electron microscopy (SEM) was performed directly on dried and gold-coated samples to observe the surface morphologies with secondary electron (SE) mode and on polished epoxy-impregnated samples to observe the carbonation depth with backscattered electron (BSE) mode and energy-dispersive

X-ray spectroscopy following the same procedures in Ref. (Jiang et al. 2022). The density and water absorption of the RCFs were determined basically as per ASTM C128.

3. Results and discussions

3.1 The rate and amount of Cc precipitations

The amount of Cc precipitated in RCFs was determined by TGA and plotted in Fig. 2a. It was found that the raw RCFs contained 6.9 % Cc possibly due to the natural carbonation, while cRCF-1 had 11.6 %, 12.6 % and 13.8 % Cc after carbonation for 10 min, 30 min and 60 min respectively and then reached the peak value of 15.6 % at 3h. As a comparison, using 0.5M sodium hydroxide solution to prepare 0.5M carbonate species prior to carbonation significantly improved the reaction rate. The cRCFs-2 obtained 16.5 % Cc at 10 min and 31.1 % Cc at 3 h, corresponding to respective increases of 42% and 100%. Besides, it was noted that the cRCFs-2 carbonated at 10 min obtained even higher amount of Cc than cRCFs-1 that was carbonated for 3 h, indicating the significance of elevating the initial carbonate species for enhancing carbonation. The morphologies of Cc on the surface of cRCFs-1 and cRCFs-2 were shown in Fig. 2b and c respectively. As seen, the Cc precipitated on the cRCFs-1 was predominantly the cubic calcite, while some elongated spear-like calcite and spheroidal vaterite was found to the primary polymorphs of Cc in cRCFs-2 based on the XRD patterns shown in Fig. 2d.

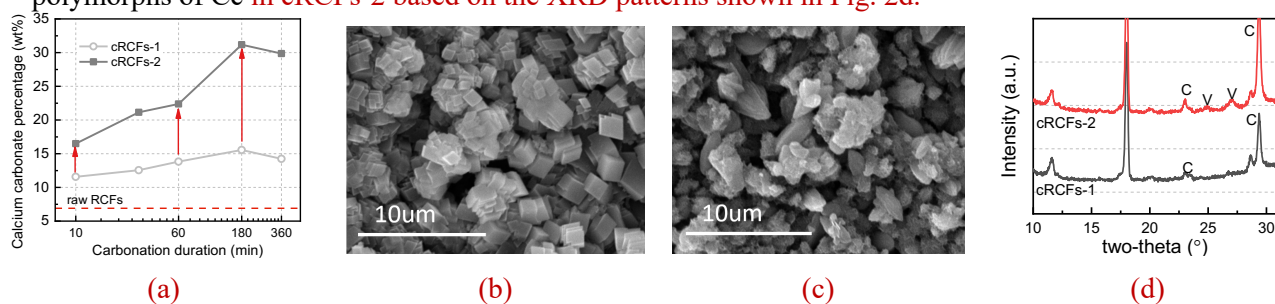


Fig. 2. (a) The evolution of Cc amount in different RCFs, and the surface morphologies of (b) cRCFs-1, (c) cRCFs-2, and (d) the XRD patterns of RCFs.

3.2 Carbonation depth

The backscattered electron (BSE) images of cRCFs-1 and cRCFs-2 and the mapping information are presented in Fig. 3a and b respectively. Given that the yellow pixels in the images represent calcium, the outer layer was thus confirmed as the carbonated zone where extensive Cc were precipitated. The measurement of the thickness of the carbonated zone (carbonation depth) was carried out, and average carbonation depth and their distributions were given in Fig. 3c. Based on the results, cRCFs-1 had a mean carbonation depth of 0.027 mm. This value was averaged from around 2000 measurements that were widely distributed between 0 and 0.1 mm. By contrast, the cRCFs-2 that were carbonated in a 0.5M sodium-hydroxide-based solution had a mean carbonation depth of 0.067 mm, which was 148% thicker than the cRCFs-1. Generally, during the carbonation process, the passivation effect related to the formation of the carbonated layer became gradually dominant, thus limiting the advance of carbonation front. Nevertheless, increasing the initial carbonate species was found to alleviate part of the passivation effect and thus the carbonation font moved further inward.

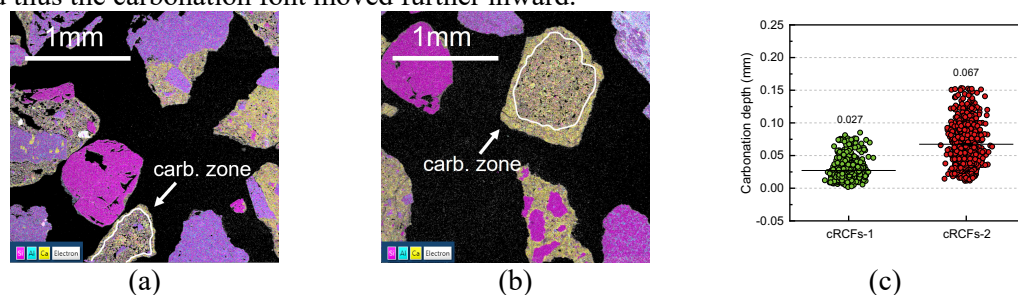


Fig. 3. Backscattered electron images of (a) cRCFs-1 and (b) cRCFs-2, and the corresponding carbonation depth.

3.3 Physical properties

The raw RCFs had the water absorption of around 11.3 % and the density of 2493 kg/m³. After carbonation, the cRCFs-1 had the water absorption of 10.5 % and density of 2509 kg/m³. Nevertheless, with the recorded higher carbonation degree and thicker carbonation depth, the corresponding water absorption was further reduced to 9.2%, and the density was increased to 2538 kg/m³.

Table 2. The water absorption and density of the RCFs.

| | Water absorption (%) | Density (kg/m ³) |
|----------|----------------------|------------------------------|
| Raw RCFs | 11.3% | 2493 |
| cRCFs-1 | 10.5% | 2509 |
| cRCFs-2 | 9.2% | 2538 |

4. Conclusions

In this study, a 0.5M sodium bicarbonate solution was prepared by injecting CO₂ into a sodium hydroxide solution of equivalent concentration. The sodium bicarbonate solution was then used as the starting solution for carbonating RCFs through an aqueous route. In this way, the initial carbonate concentration was improved by several magnitudes and thus could promote carbonation. Based on the results, the following conclusions could be drawn:

(a) The amount of Cc precipitations was doubled due to the use of this improved aqueous carbonation method. The total Cc amount reached over 30 wt.%, as compared with 15.6 % of the reference RCFs carbonated with CO₂-saturated water, and the morphologies of Cc transformed from the cubic shape into elongated and spheroidal morphologies.

(b) The carbonation depth was increased from 0.027 mm to 0.67 mm, indicating the reactive carbonation front was further moved inwards.

(c) The water absorption was decreased from 11.3% to 9.2%, while the density was increased from 2493 to 2538 kg/m³, suggesting the improved quality of RCFs.

Overall, the improved aqueous carbonation method could accelerate carbonation and enhance carbonation efficiency.

References

- Eikeland, E., A. B. Blichfeld, C. Tyrsted, A. Jensen and B. B. Iversen (2015). "Optimized carbonation of magnesium silicate mineral for CO₂ storage." *ACS Appl Mater Interfaces* 7(9): 5258-5264.
- Jiang, Y., L. Li, J.-x. Lu, P. Shen, T.-C. Ling and C. S. Poon (2022). "Mechanism of carbonating recycled concrete fines in aqueous environment: The particle size effect." *Cement and Concrete Composites* 133: 104655.
- Li, Y., S. Zhang, R. Wang, Y. Zhao and C. Men (2019). "Effects of carbonation treatment on the crushing characteristics of recycled coarse aggregates." *Construction and Building Materials* 201: 408-420.
- Pedro, D., J. de Brito and L. Evangelista (2017). "Structural concrete with simultaneous incorporation of fine and coarse recycled concrete aggregates: Mechanical, durability and long-term properties." *Construction and Building Materials* 154: 294-309.
- Phung, Q. T., N. Maes, D. Jacques, E. Bruneel, I. Van Driessche, G. Ye and G. De Schutter (2015). "Effect of limestone fillers on microstructure and permeability due to carbonation of cement pastes under controlled CO₂ pressure conditions." *Construction and Building Materials* 82: 376-390.
- Ren, P., T.-C. Ling and K. H. Mo (2022). "CO₂ pretreatment of municipal solid waste incineration fly ash and its feasible use as supplementary cementitious material." *Journal of Hazardous Materials* 424: 127457.
- Shi, C., Z. Wu, Z. Cao, T. C. Ling and J. Zheng (2018). "Performance of mortar prepared with recycled concrete aggregate enhanced by CO₂ and pozzolan slurry." *Cement and Concrete Composites* 86: 130-138.
- Xiao, J., C. Wang, T. Ding and A. Akbarnezhad (2018). "A recycled aggregate concrete high-rise building: Structural performance and embodied carbon footprint." *Journal of Cleaner Production* 199: 868-881.
- Zajac, M., J. Skibsted, P. Durdzinski and M. Ben Haha (2021). "Effect of alkalis on products of enforced carbonation of cement paste." *Construction and Building Materials* 291: 123203.
- Zajac, M., J. Skibsted, P. Durdzinski, F. Bullerjahn, J. Skocek and M. Ben Haha (2020). "Kinetics of enforced carbonation of cement paste." *Cement and Concrete Research* 131: 106013.
- Zhan, B. J., D. X. Xuan, C. S. Poon and K. L. Scrivener (2020). "Characterization of interfacial transition zone in concrete prepared with carbonated modeled recycled concrete aggregates." *Cement and Concrete Research* 136: 106175.

Study on the Use of Recycled Aggregates for the Production of Cementless Pervious Concrete

W.T. Lin^{1*}, L. Fiala², M. Záleská³ and A. Cheng⁴

¹ *Department of Civil Engineering, National ILan University, Yilan, Taiwan*
Email: wtlin@niu.edu.tw

² *Department of Materials Engineering and Chemistry, Faculty of Civil Engineering, Czech Technical University, Prague, Czech Republic*
Email: fialal@fsv.cvut.cz

³ *Department of Materials Engineering and Chemistry, Faculty of Civil Engineering, Czech Technical University, Prague, Czech Republic*
Email: martina.zaleska@fsv.cvut.cz

⁴ *Department of Civil Engineering, National ILan University, Yilan, Taiwan*
Email: ancheng@niu.edu.tw

ABSTRACT

This study focuses on cementless composite materials in pervious concrete. The main objective was to create cementless ternary pastes using ground granulated blast furnace slag (GGBS), co-fired fly ash (CFA), and desulphurization gypsum (DG). These pastes were combined with recycled coarse aggregates or circulating fluidized bed bottom ash (BA) to produce cementless recycled pervious concrete, which can be applied for sustainable and high-quality industrial waste applications in a circular economy. The study used 70% GGBS, 25% CFA, and 5% DG to replace cement in the concrete mixture. This proportion met the initial and final setting time of cement as per ASTM C150. The mixture of cementless binders had the best compressive strength, combined with recycled coarse aggregates to produce cementless recycled pervious concrete, supplemented by BA to improve hardening properties. The results showed that cementless recycled pervious concrete performed worse than cemented pervious concrete in terms of vertical flow rate, unit weight, compressive strength, splitting strength, resistance to sulfate attack, and physical abrasion. However, it had better porosity, permeability, and saturated water absorption. Increasing the weight percentage of recycled coarse aggregates replaced by BA effectively improved compressive strength, splitting strength, sulfate attack resistance, and physical abrasion resistance. The permeability coefficient met the requirement of greater than 0.01cm/s at 10% of BA content.

KEYWORDS: *cementless binders, ternary green materials, high quality recycling, permeability coefficient*

1. Introduction

The cement industry is a high-carbon emission industry that requires a large amount of fuel and natural raw materials for its manufacturing process. It has a substantial negative impact on global climate change, natural resource consumption, and environmental pollution. Therefore, developing green materials to replace cement has become essential for achieving net-zero carbon emissions (Amran et al. (2022) and Tan et al. (2022)). Fly ash, ground granulated blast-furnace slag (GGBS), co-fired fly ash (CFA), and other materials are widely used to replace cement. These materials are industrial by-products with lower carbon emissions and energy consumption in making cement-based materials and have significant reusability. Using cement substitutes has also improved the performance and quality of construction materials, reduced environmental pollution, and reduced waste generation (Golewski (2021) and Lei and Pavia (2023)). Pervious concrete is a building material with permeable properties, and its application in engineering has become increasingly widespread. Compared with traditional concrete materials, pervious concrete reduced the burden on urban drainage systems, improving the efficiency of urban water recycling. It also reduced

the damage and impact of flooding and surface runoff on cities (Khankhaje et al. (2023)). The permeability of pervious concrete was usually achieved by controlling the porosity and pore size. In the process of proportioning design, the permeability of concrete was controlled by adding specific aggregates and altering the concrete mix proportions (Elnaz et al. (2022)). It was also possible to achieve net-zero carbon emissions using a mixture of different industrial by-products as a complete cement replacement for cementless pervious concrete (Lin et al. (2022)). In this study, GGBS, CFA, and flue gas desulfurization gypsum (DG) were mixed as cementless binders for pervious concrete based on the research results of Lin et al. (2022). The cementless binders, recycled aggregates, and circulating fluidized bed bottom ash (BA) produced cementless recycled pervious concrete in this study. The study intended to investigate the effect of recycled coarse aggregates and BA on manufacturing cementless recycled pervious concrete. It was also designed to evaluate whether it meets the relevant specifications of existing pervious pavement in Taiwan.

2. Experimental details

2.1 Materials and mix design

As a benchmark for the mentioned study by Lin et al (2022), the present study produced cementless blended materials (70% ggbs, 25% CFA and 5% DG). CFA referred to fly ash generated from circulating fluidized bed boilers, while DG was a by-product of coal-fired power plants. The engineering properties were verified by fully replacing the natural aggregates with recycled aggregates to produce recycled pervious concrete and replacing the recycled aggregates with BA (2.5, 5.0, 7.5 and 10% by weight). The properties of GGBS, CFA and DG were described in detail in the previous study by Lin et al (2022). The BA used in this study was provided by a paper manufacturer in Taiwan. The manufacturer used coal, pulp sludge and waste rubber as raw materials to burn in a circulating fluidized bed boiler from 850°C to 920°C to produce residual bottom ashes. According to the chemical composition of BA, it consisted mainly of SiO₂, Al₂O₃, CaO, and SO₃ for a percentage of 8.30%, 4.00%, 61.37%, and 18.08%, respectively. The specific gravity of BA was 2.83, the water absorption was 9.82, and the fineness modulus was 1.89. The recycled coarse aggregates were used for the demolition of buildings with a maximum diameter of 19mm, a specific gravity of 2.34 and water absorption of 8.76%. The nominal size range for recycled coarse aggregates was 19.0mm~4.75mm. The mix design is shown in Table 1 and the proportioning of pervious concrete was done regarding the ACI 211 specification and present study by Lin et al (2022).

Table 1: Mix design (kg/m³)

| Mix no. | water | CFA | GGBS | DG | Superplasticizer | Recycled coarse aggregates | BA |
|---------|-------|-----|------|----|------------------|----------------------------|-----|
| N2A | 149 | 108 | 303 | 22 | 3 | 1525 | 0 |
| N2B | 149 | 108 | 303 | 22 | 3 | 1487 | 38 |
| N2C | 149 | 108 | 303 | 22 | 3 | 1449 | 76 |
| N2D | 149 | 108 | 303 | 22 | 3 | 1411 | 114 |
| N2E | 149 | 108 | 303 | 22 | 3 | 1373 | 153 |

2.2 Test methods

The experimental items are shown in Table 2. The average value was taken after the test of three specimens for each mixture. All tests were controlled to within 5% of the standard deviation.

Table 2: Experimental items

| Experimental name | Experimental specification | Testing age (days) | Size of specimen |
|--------------------------|----------------------------|--------------------|------------------|
| Unit weight | ASTM C29 | - | φ100×200mm |
| Vertical flow | As described below* | - | - |
| Slump | ASTM C143 | - | - |
| Compressive strength | ASTM C39 | 7, 14, 28, 56 | φ100×200mm |
| Abrasion | ASTM C779 | 28, 56 | 300×300×100mm |
| Permeability coefficient | As described below** | 28 | φ100×200mm |

* Ministry of Economic Affairs, Water Resources Department Construction Regulations

** Japanese Road Association specifications

3. Results and discussion

3.1 Fresh properties of pervious concrete

To maintain the permeability of pervious concrete, the slump of pervious concrete should be close to zero slump by the ACI proportioning design. The test results indicated that the five sets of proportions met the requirements of a zero slump. According to the construction specification of the Water Resources Administration in Taiwan, the vertical flow of pervious concrete should be less than 2%. Vertical flow in specimens from N2A, N2B, N2C, N2D, and N2E was 0.48%, 0.30%, 0.27%, 0.17%, and 0.08%, respectively. The BA particles were finer than the recycled coarse aggregates, which allowed free water to be absorbed faster, improving consistency and decreasing vertical flow. The results showed that they all met the less than 2% requirement. The test results for unit weight are shown in Figure 1. BA has a lighter unit weight and smaller particle size than recycled coarse aggregates, thus filling the pores and increasing the unit weight of the specimen.

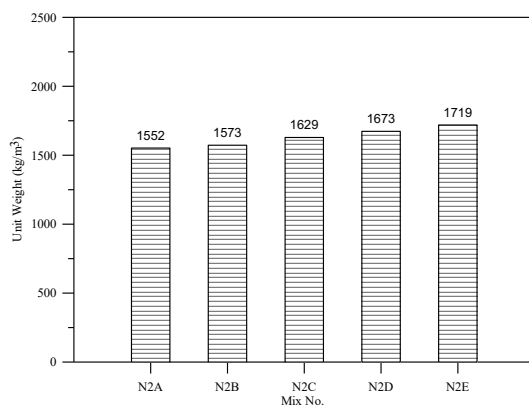


Fig. 1: Histograms of unit weight

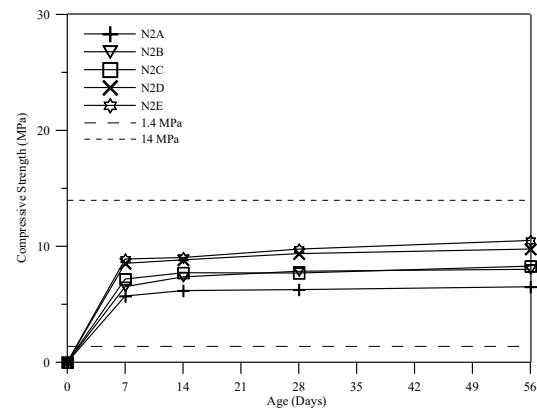


Fig. 2: Development curves of compressive strength

3.2 Compressive strength and abrasion resistance

The results of applying BA to the compressive strength of recycled pervious concrete are shown in Figure 2. The addition of BA increased the amount of paste filling between the aggregates of the pervious concrete. It led to a tendency to increase the unit weight of pervious concrete. Such results indicated that raising the amount of BA content contributed to improving compressive strength. Each 1% increase in BA enhanced the compressive strength of recycled pervious concrete by 4.6% to 10.1% at each curing age. The maximum compressive strength exceeded 10 MPa in 56 days. The abrasion test results are shown in Fig. 3, and the test results revealed that the weight loss of the specimen decreased with the increase in age and the amount of BA addition. The addition of recycled coarse aggregates and cementless materials reduced the abrasion resistance of the material. However, using these recycled resources kept the abrasion loss to 3.3%, which was still suitable for general artificial pavements.

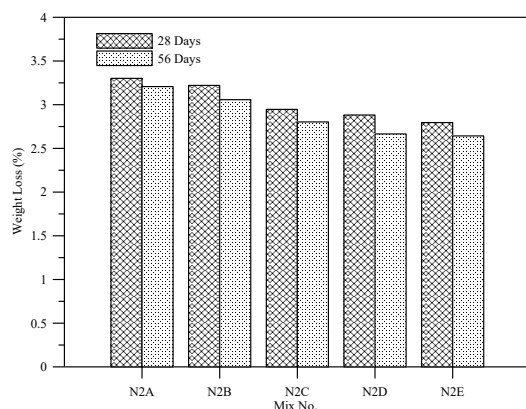


Fig. 3: Histograms of weight loss

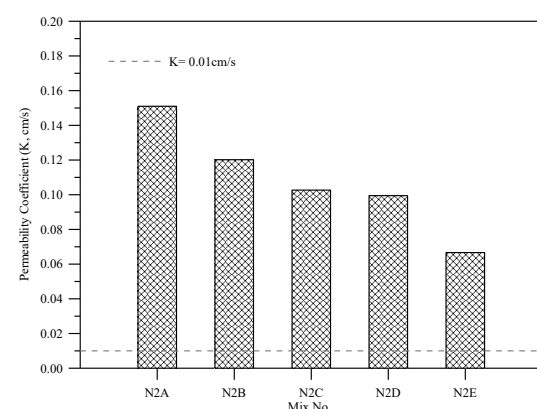


Fig. 4: Histograms of permeability coefficient

3.3 Permeability

The permeability test is a critical indicator for evaluating the suitability of pervious concrete. The higher the permeability coefficient, the better the permeability of the pavement surface, which minimizes the chance of flooding. At 10% BA replacement, the permeability coefficient of the specimens decreased from 0.151 cm/s to 0.067 cm/s (compared to the N2A specimens) as shown in Figure 4. BA replaced the recycled aggregates by filling the gaps between the aggregates, thus improving the compressive strength but significantly reducing the permeability coefficient. Under the requirements for construction performance, the N2E specimen (10% BA substitution) had the most impressive compressive strength, and its permeability coefficient met Taiwan's specification (higher than 0.01cm/s).

4. Conclusions

Compared to recycled coarse aggregates, BA had a higher water absorption rate. The study discovered that BA had smaller particle sizes than recycled aggregates when utilized as a partial substitute. This yielded increased compressive strength, better consistency, and lessened vertical flow. The permeability coefficient of specimens containing 10% BA met the Taiwanese standard (greater than 0.01 cm/s). Including BA in specimens increased mortar content and the thickness of the coarse-grained surface coating, improving the hardening properties of pervious concrete. The N2E specimen had the highest compressive strength of 10.5 MPa, which also met the requirements of pervious pavement in Taiwan. It was found that each 1% of BA increased the compressive strength of the cementless recycled pervious concrete by 4.6% to 10.1%. Green pervious concrete can be used for pedestrian pavement and other specific applications.

Acknowledgements

This research was supported by the National Science and Technology Council (NSTC) in Taiwan under project: NSTC 111-2221-E-197-009-MY3 and the Czech Science Foundation under project: GAČR 22-00987J, for which funding is gratefully acknowledged.

References

- Amran, M., Makul, N., Fediuk, R., Lee, Y.H., Vatin, N.I., Lee, Y.Y. and Mohammed, K. (2022) "Global Carbon Recoverability Experiences from the Cement Industry", *Case Studies in Construction Materials*, 17: e01439.
- Tan, C., Yu, X. and Guan, Y. (2022) "A Technology-driven Pathway to Net-zero Carbon Emissions for China's Cement Industry", *Applied Energy*, 325: 119804.
- Lei, Z. and Pavia, S. (2023) "Reactivity of Raw, Pyroprocessed and GGBS-blended Alum Sludge (AS) Waste for Sustainable Cement Production", *Journal of Building Engineering*, 65: 105787.
- Golewski, G.L. (2021) "Green Concrete based on Quaternary Binders with Significant Reduced of CO₂ Emissions", *Energies*, 14(15): 4558.
- Khankhaje, E., Kim, T., Jang, H., Kim, C.S., Kim, J. and Rafieizonooz, M. (2023) "Properties of Pervious Concrete Incorporating Fly Ash as Partial Replacement of Cement: A Review", *Developments in the Built Environment*, 14: 100130.
- Elnaz, K., Mahdi, R. and Jahangir, M. (2022) "Characteristics of Pervious Concrete Incorporating Cockleshell as Coarse Aggregate for Pavements", *Journal of Transportation Engineering, Part B: Pavements*, 148(2): 4022026.
- Lin, K.L., Lin, W.T., Korniejenco, K. and Hsu, H.M. (2022) "Application of Ternary Cementless Hybrid Binders for Pervious Concrete", *Construction and Building Materials*, 346:128497.

Eco-toxicity assessment of cement. Bioassays on luminescent bacteria and sea urchin embryogenesis

A. Andrés^{1*}, J. Santos, A. Fernandez-Jimenez², O. Maltseva², E. Cifrian and A. Palomo²

¹ Green Engineering and Resources Group, Department of Chemistry and Process & Resource Engineering, ETSIT, University of Cantabria, Santander, Spain

² Materials Department. Eduardo Torroja Institute (CSIC). Madrid, Spain

ABSTRACT

In most of research works, Portland cement is analysed regarding its interaction with the environment (environmental processes affecting its durability). In this research, however, attention has been focused to the opposite analysis; it means to understand how the environment is being affected by cement. In this work, the ecotoxicity of cement mortars on marine biological life has been evaluated. For this purpose, the UNE-EN 12457-4 leaching test as well as two different toxicity bioassays (luminosity reduction with marine bacteria *Vibrio fischeri* UNE-EN 11348-3 and the success of embryo-larval development of sea urchin *Paracentrotus lividus*) were conducted. From the leaching perspective, it should be noted that the mobility of all trace elements were considered to meet the inert landfill limits. No effects were observed on the bioluminescent bacteria within the concentration range indicated by the standard (45%). But the use of the sea urchin embryogenesis bioassay has allowed authors to accurately assess the ecotoxicity of cement in marine ecosystem. This biological test has a great robustness given its enormous sensitivity to potential effects in the environment since it is incorporating a big number of toxicity levels (endpoints). In summary, the results obtained from both bioassays show consistency with the leaching behaviour: the cement mortars present very low mobility of trace chemical elements.

KEYWORDS: *Toxicity, Bioassay, Leaching, Microtox, Sea Urchin embryogenesis.*

1. Introduction

The scientific community from different perspectives is facing cement sustainability challenge. The aim of this work is to include the “ecotoxical view” in the research context, aspect of sustainability not yet enough connected to cement industry. Ecotoxic characteristics will allow estimating the potential environmental impacts of construction materials on the environment by using chemical and biological methods. In particular, the proposed bioecotoxic tests (based on a set of biological selected species having the advantage of integrating all pollutants with their synergistic, antagonistic and additive effects as well as their bioavailability) are really novel (Gartiser et al., 2017). Bioassays, might help to detect the joint effects of ingredients through the impact in living organisms (Santos et al., 2023). For these reasons, a set of tests for the ecotoxicological characterization of eluates from construction products for European regulatory purposes has been elaborated. In this work, the ecotoxicity of cement mortars on marine ecosystem using two different toxicity bioassays (luminosity reduction with marine bacteria *Vibrio fischeri* and the success of embryo-larval development of sea urchin *P. lividus*) were conducted.

2. Material and Methods

2.1. Material

The cementitious material used was a Spanish CEM I 52.5R (62.94% CaO, 19.29%SiO₂, 5.28% Al₂O₃). Mortar specimens (4x4x16 cm) were prepared with a sand/cement ratio of 3/1 and water/cement ratio=0.5. After 28 days of curing in a climatic chamber (21 °C and relative humidity > 95%), mortar were broken to obtained a granular material (5mm> mortars < 10mm) according to the recommendations of EN-12457.

2.2. Leaching test

The compliance leaching test EN 12457-2:2003 was used to determine the release of trace elements from the cement mortars in equilibrium conditions. The test was conducted at a liquid/solid ratio (L/S) of 10L:kg⁻¹ of dry matter (< 10 mm) into a rotating equipment (10 rpm) for 24 h at room temperature using as leaching agent, deionized water or seawater, depending on subsequent bioassay. The obtained leachates were filtered (0.45µm) and analysed using Inductive Coupled Plasma Atomic Emission Spectrometry (ICP-AES) (Agilent, 7700) according to ISO quality control standards. The results were obtained in triplicate and the mean values are shown.

2.3. Bioluminescence test

The bioluminescence test has been carried out according to the international standard ISO 11348-3:2007 using MICROTOX LX model bioluminescence toxicity analyser. Four sample dilutions of each deionized water leachate and a blank were used: 45, 22.5, 11.25, 5.6 and 0%. The pH values were adjusted (6.5–7.5) by adding different aliquots of NaOH or HCl (0.1 N) and the osmotic adjustment (20 g/L of NaCl). The luminescence emitted by the bacteria was measured before and 30 min after the bacteria have been come into contact with the leachate dilutions (in triplicate). The ecotoxicity parameter obtained is the reduction in luminosity between both measurements.

2.4. Sea Urchin Embryogenesis bioassay

The embryogenesis assay was performed using the procedure described in Fig. 1.

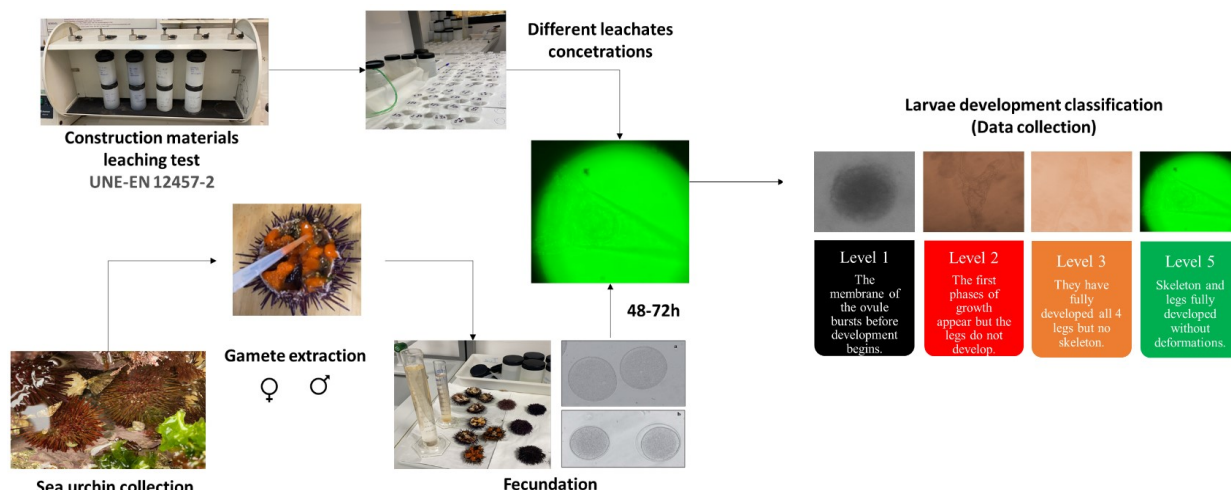


Figure 1. Embryogenesis assay adapting the procedure described by Garmendia et al., (2009)

Briefly, vials (20 mL) were filled with the different selected dilutions (5 replicates per dilution) of each leachate and approximately 500 fertilized eggs were placed in each vial. The fertilized eggs were incubated for 48 hours at 20 °C under dark conditions. After the incubation period, the larvae were observed under inverted microscope and the percentage of the pluteus larvae developed according to the different endpoints, per 100 organisms were recorded in each replicate (Khosrovyan et al., 2013). The control treatment was used to ensure the acceptability of the tests (> 90% normal larval development).

3. Results

3.1. Leaching behaviour

The concentration of contaminants in the leachates is shown in Table 1, using as leaching agent deionized water (DW) and seawater (SW). The conductivity and pH values are also displayed.

Table 1. Leaching concentration values ($\mu\text{g.L}^{-1}$) of Portland cement according to Compliance leaching test EN 12457-2 using as leaching agent, deionized water (DW) and seawater (SW).

| Elements ($\mu\text{g.L}^{-1}$) | DW leachate | Inert Limits * | SW Leachate | SW** | Elements ($\mu\text{g.L}^{-1}$) | DW leachate | Inert Limits * | SW Leachate | SW** |
|--------------------------------------|----------------|-------------------|----------------|-------|--------------------------------------|----------------|-------------------|----------------|--------------------|
| As | 0.159 | 50 | 1.258 | 2.146 | Se | 1.406 | 10 | 0.990 | 0.364 |
| Ba | 1371.8 | 2000 | 705.55 | 6.364 | V | 4.167 | - | 3.716 | 1.912 |
| Cd | 0.036 | 4 | 0.040 | 0.259 | Zn | 7.949 | 400 | 1.537 | 4.099 [^] |
| Cr | 4.608 | 50 | 121.18 | 0.496 | Cl ⁻ | 646.5 | 80000 | n.d. | n.d. |
| Cu | 0.911 | 200 | 0.745 | 0.362 | F ⁻ | 110.5 | 1000 | n.d. | n.d. |
| Mo | 3.253 | 50 | 12.635 | 12.26 | SO ₄ ²⁻ | 2584.5 | 100000 | n.d. | n.d. |
| Ni | 0.736 | 40 | 1.008 | 0.766 | pH | 12.38 | - | 9.27 | 7.98 |
| Pb | 0.482 | 50 | 0.282 | 0.689 | Cond. | 7.540 | - | 51.1 | 49.9 |
| Sb | 0.044 | 6 | 2.750 | 1.309 | (mS/cm) | | | | |

* Limit values according to EU Landfill Waste Acceptance Criteria 2003/33/EC; ** Control: clean seawater used as reference leachate; [^] Contaminated sample.

The values obtained for each of the elements in DW are very low, all of them below the values taken as reference for inert residues. In the case of leaching with seawater, the values of Ba and Cr stand out, well above the value of seawater. In the case of Zn, there is external contamination, since the reference value (clean seawater) is higher than the leachate sample.

3.1 Bioluminescence test

The bioluminescence reduction test has been applied to two replicates of cement leachate (CEM-Ii and CEM-Iii), as well as a blank (Control) (Figure 2).

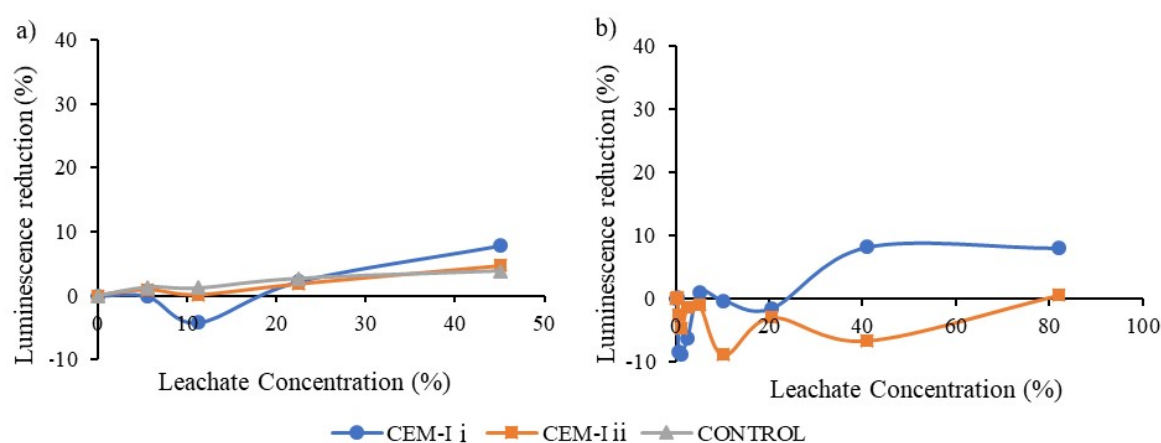


Figure 2. Bioluminescence test results expressed as percentage of luminescence emission reduction of bacteria *Vibrio fischeri* after 30 min exposure as a function of leachate concentration: a) according to the international standard ISO 11348-3:2007; B) and retested as higher leachate concentrations.

The samples do not present toxicity, obtaining results of luminescence reduction much lower than 20%, threshold concentration test proposed by framework of construction products (CEN/TR 17105:2017) and even close to the control sample (Fig 2a). The bioassay at higher leachate concentrations performed, never exceeding a 10% reduction in luminescence (Fig 2b).

3.1 Sea Urchin embryogenesis bioassay

The results of the sea urchin embryogenesis bioassay (Figure 3) show significant effects from 10% concentration of leachate. For level 3, corresponding to the most used endpoint in this bioassay, the development of the four legs of the embryo, shows a significant effect from 25% leachate concentration. It is noteworthy that no embryo appears with a level 1 effect, the most destructive.

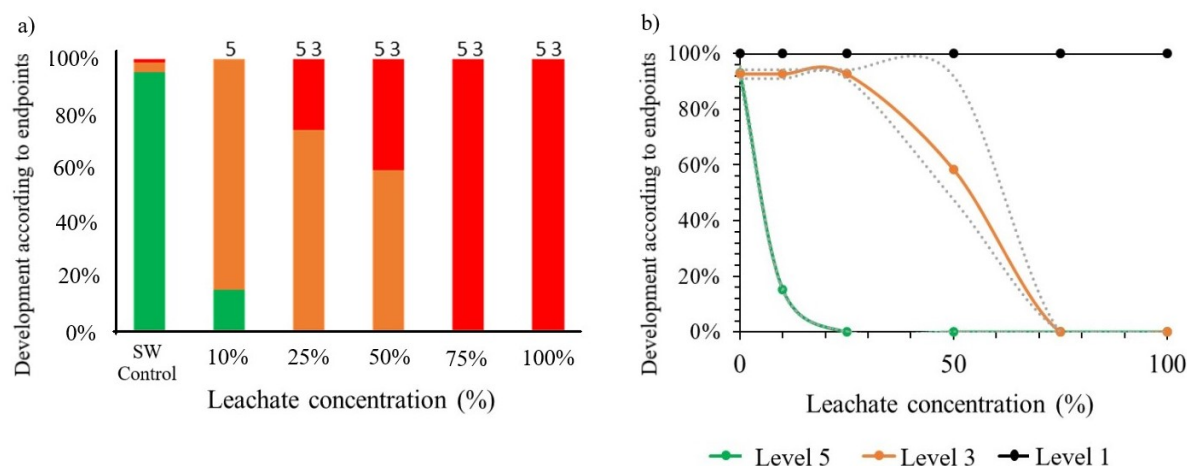


Figure 3. Sea urchin embryogenesis bioassay results: a) Percentage of *P. lividus* normal embryos incubated according to the endpoints classification on the different leachates. 5, 3, 1 number above bars refers to significant differences in toxicity level percentage to the control treatment ($p < 0.05^*$) for the toxicity level represented; b) Early development dose-response curves exposed to the leachates of CEM-I for different toxicity levels.

4. Conclusions

Eco-toxicity of cement through leaching and toxicity using two aquatic bioassay performed. The mobility of all chemical elements studied when using deionized water as leaching agent is below the limits for inert materials and the bioluminescence results below the limit value proposed in the construction products framework. While the mobility of Ba and Cr when using seawater as leaching agent could show a certain influence on the embryogenesis results. However, if the level 3 endpoint is considered, the most used in this bioassay, which corresponds to the development of all the legs of the embryos, show significant differences with the control, and 50% leachate concentration affects a very small number of embryos. These results represent an advance in the understanding of the environmental risk associated with cement in a marine ecosystem.

Acknowledgements

Authors wish to thank the Spanish Ministry of Science and Innovation, the Spanish State Agency for Research (AEI), and the FEDER funds for the award of the research project "Synthesis of low-temperature glassy supplementary cementitious materials (GlassyMat)" (PID2019-11464RB-I00).

References

- Garmendia, J.M. Menchaca, I. Belzunce, M.J. Revilla, M. (2009) "Induction to Maturation of the Sea Urchin *Paracentrotus lividus* (Lamarck, 1816) under Laboratory Conditions" *Environ Technol*, 30(13):1441-6
- Gartiser, S. Heisterkamp, I. Schoknecht, U. Bandow, N. Burkhardt, N.M. Ratte, M. Ilvonen, O. (2017). "Recommendation for a test battery for the ecotoxicological evaluation of the environmental safety of construction products". *Chemosphere* 171: 580–587.
- Khosrovyan, A. Rodríguez-romero, A. Salamanca, M.J. Valls, T.A. Riba, I. Serrano, F. (2013). "Comparative performances of eggs and embryos of sea urchin (*Paracentrotus lividus*) in toxicity bioassays used for assessment of marine sediment quality". *Mar. Pollut. Bull.* 70: 204–209.
- Santos, J., Cifrian, E., Rodríguez-Romero, A., Yoris-Nobile, A.I., Blanco-Fernandez, E., Castro-Fresno, D., Andres, A. (2023) "Assessment of the environmental acceptability of potential artificial reef materials using two ecotoxicity tests: luminescent bacteria and sea urchin embryogenesis". *Chemosphere* 310, 136773.

Influence of low carbon cement and recycled aggregates on mortar fresh state and early hydration

L. Ferrari^{1*}, V. Bortolotti¹, N. Mikanovic², M. Ben-Haha² and E. Franzoni¹

¹ University of Bologna, DICAM Department, via Terracini 28, 40131 Bologna, Italy

² Global R&D, Heidelberg Materials AG, Oberklamweg 2-4, 69181 Leimen, Germany

*Email: lucia.ferrari9@unibo.it,

villiam.bortolotti@unibo.it

Nikola.Mikanovic@heidelbergmaterials.com

mohsen.ben.haha@heidelbergmaterials.com

Elisa.franzoni@unibo.it

ABSTRACT

Calcined clay and limestone are promising clinker substitutes for production of new low carbon cements. Limestone calcined clay cement (or LC³) can reduce carbon dioxide emissions by up to 40% and are made of raw materials which are abundant and globally available. Many studies have already examined the hydration behavior of calcined clay-based cements and linked it to early- and late-age strength development. However, very few works were dedicated to the analysis of mortars prepared with this type of binder and recycled sand. The introduction of construction and demolition waste as aggregate in combination with low-carbon cement would further decrease the environmental impact of building materials.

In this paper, the fresh state of mortar containing recycled sand and calcined clay in variable amounts was analyzed by means of flow table test. The pore size distribution of fresh mortar was identified using ¹H Time Domain Nuclear Magnetic Resonance (TD-NMR), that is a low field TD-NMR approach. The compressive strength of samples was also measured. Results show that mortar containing calcined clay immediately consumes part of the available capillary water with drastic consequences on its rheological behavior. Moreover, the recycled sand influences fresh properties and mechanical compressive strength. However, proper mix designs obtained by substituting the natural sand with recycled sand according to the occupied volume proved that mortar composed by low-carbon cement and recycled aggregate is still suitable for many applications contributing to the sustainability of construction materials.

KEYWORDS: *calcined clay, limestone, recycled sand, rheology, ¹H TD-NMR.*

1. Introduction

Concrete is the most widely used building material for infrastructures and habitations. Cement, concrete's key ingredient, has a dramatic carbon footprint as clinker production is responsible of about 7% of the global CO₂ emissions (WBCSD, 2009). For this reason, European Standard EN 197-5:2021 was published in May 2021 to allow formulation of cement of class CEM II/C-M containing from 50% to 64% of clinker, while previous version CEM II/B required minimum 65% of clinker. The properties of calcined clay limestone cement have been studied over last years in terms of chemistry and hydration, showing that this material has promising properties concerning cement reactivity and sustainability (K. L. Scrivener et al., 2018). However, workability studies on calcined clay cements showed that higher amount of admixture is required to provide rheological properties comparable to Ordinary Portland Cement (OPC) (Dhandapani et al., 2022). Another strategy to reduce concrete environmental impact is the use of recycled aggregates, i.e., obtained from construction and demolition waste. This has been extensively studied, highlighting that the high porosity of recycled aggregate makes them absorb more water than natural aggregates, making difficult the right estimation of the required effective water (Manzi et al., 2013). Indeed, recycled aggregates may be highly porous and sorptive, thus affecting some properties of concrete mixes like workability and

mechanical strength (Théréne et al., 2020). Therefore, the combination of these aggregates with calcined clay-based binders, that provides a further step in improving concrete sustainability (Xing et al., 2023), arises important technical challenges as both components, the binder and the aggregate, significantly affect concrete workability and compressive strength. In this work, mortar containing calcined clay-based cement and recycled sand was studied to analyse rheological behaviour and mechanical strength properties. The amount of consumed water and the pore size distribution of mortar was quantified using the ^1H Time Domain Nuclear Magnetic Resonance (TD-NMR). The aim of this work is to show which technical adjustments are necessary to obtain a usable mortar composed of low carbon cement and recycled sand.

2. Materials

The materials to blend low carbon cements and aggregates were supplied by Heidelberg Materials AG, Germany. The binders and powders used in this study were: CEM I 52.5 R (CEM I), CEM II/A-LL containing 12% of limestone (CEM II), calcined clay from France (CC), and limestone (LS). The polycarboxylate ether-based superplasticizers (SP) was kindly provided by CHRYSO SAINT-GOBAIN R&D laboratory in Sermaises (France) and contains 22% of solid.

The Natural Sand (NS) was provided by Italcementi in Bergamo, Italy, while the Recycled Sand (RS) was provided by Heidelberg Materials and comes from construction and demolition waste. Characteristics of natural sand and recycled sand, measured according to EN 1097-6 standard, are reported in Table 1. Water absorption refers to the mass of the saturated and surface-dried aggregate in the air.

Table 1 – Characteristics of sands according to EN 1097-6 standard.

| | Oven dried particle density (kg/m^3) | Water Absorption (%) |
|---------------|--|-------------------------|
| Natural Sand | 2660 ± 20 | 0.44 ± 0.02 |
| Recycled Sand | 2274 ± 20 | 4.66 ± 0.23 |

Particle size distribution of sands was measured by quarting and sieving. The max diameter of NS is 4 mm while for RS is 2 mm.

3. Formulation

3.1 Binder

The two commercial cements, CEM I and CEM II, were used as reference binders. Other three binders were formulated according to the following proportions by mass: LC³-50 2:1 with 50% of clinker, CC:LS=2:1, LC³-50 1:1 with 50% of clinker, CC:LS=1:1 and LC³-70 2:1 with 70% of clinker, CC:LS=2:1

3.2 Mortar

The mortar mixing and preparation were conducted in a Hobart mixer, according to standard EN 196-1:2016. The composition for mortars prepared with 100% NS was: (450 ± 2) g of binder, (1350 ± 5) g of NS, (225 ± 1) g of water. The composition for mortars prepared with 50% of NS and 50% of the same volume of RS was: (450 ± 2) g of binder, (675 ± 2) g of NS and (584 ± 2) g of RS (in oven dried condition), (252 ± 1) g of water. The amount of water was calculated by adding the effective water (225 g) and the water necessary to bring the RS to saturated surface dry conditions 27 g). The superplasticizer dosage was adjusted to provide target flowability.

4. Methods

4.1 Mortar test

The mortar flow was measured immediately after mixing by flow table test according to EN 1015-3 standard specification. A mortar spread diameter between 20 and 22 cm was targeted by using an appropriate superplasticizer dosage to obtain a mortar which is neither too sticky, nor too liquid, in order to allow a good flow and avoid segregation. The mechanical compressive strength was measured at 2d according to the EN 196-1 standard.

4.2 Water detection by ^1H TD-NMR

The objective of ^1H TD-NMR measurements was to detect the amount of the capillary, interhydrate and interlayer water in mortar. NMR equipment allows the detection of the transverse (T_2) relaxation curves and the computed values of T_2 provide information about water confinement in cement matrix and porous media in general. The instrumental setup is composed of a permanent magnet (ESAOTE, Genova, Italy) with a magnetic field $B_0 \approx 0.2$ T (corresponding to ^1H Larmor frequency ≈ 8 MHz), a 25 mm probe, and an NMR console (Stelar s.r.l., Mede, Italy). Relaxation T_2 curves were detected using the Carr–Purcell–Mei–boom–Gill (CPMG) sequence with 512–2048 number of echoes, depending on the mobility of water in the sample microstructure, with an echo time of 60 μs and 100–500 scans. Data acquisitions were conducted at 1 hour of hydration and two repeated measurements were performed on each sample or around 20 g. The T_2 quasi-continuous distribution was computed by the software UpenWin (Borgia et al., 2000), developed by the group at the University of Bologna, to verify the presence of specific peaks, while for multi-exponential non-linear fitting a script in Psi-Plot was implemented (*Poly Software International, USA*, n.d.). For tri-exponential fitting, the T_2 , the corresponding assignment and pore size are as follow, according to previous studies carried out on white cement (K. Scrivener et al., n.d.):

- Capillary water pore size ≈ 1000 nm T_2 8–10 ms
- Interhydrate water pore size 10–20 nm T_2 1–2 ms
- Interlayer water pore size 3–5 nm T_2 0.1–0.2 ms

5. Results

The superplasticizer dosage to obtain target workability and the water distribution in the different pore classes of the mortar at 1 hour hydration are shown in Table 2.

Table 2 – Summary of results obtained with mortar flow test and TD-NMR.

| Sand | Binder | Average mortar spread diameter (cm) | SP dosage for target workability (g SP/g binder) | Capillary water – 1 μm pores (%) | Interhydrate water – 10–20 nm pores (%) |
|------|-------------------------|-------------------------------------|--|---|---|
| NS | CEM I | 21.3 | 0.6% | 68 | 32 |
| | CEM II | 21.0 | 0.6% | 54 | 46 |
| | LC ³ -50 2:1 | 20.7 | 1.3% | 27 | 73 |
| | LC ³ -50 1:1 | 21.4 | 1.1% | 36 | 64 |
| | LC ³ -70 2:1 | 21.8 | 1.0% | 42 | 58 |
| RS | CEM I | 21.8 | 0.5% | 69 | 31 |
| | CEM II | 20.9 | 0.5% | 50 | 50 |
| | LC ³ -50 2:1 | 20.8 | 1.2% | 29 | 71 |
| | LC ³ -50 1:1 | 20.4 | 1.0% | 29 | 71 |
| | LC ³ -70 2:1 | 20.7 | 0.9% | 35 | 65 |

It has to be noticed that SP dosage increases linearly with the amount of calcined clay in the binder. The results also show that, if the sand substitution is carried out by volume (i.e., not altering the binder to aggregate ratio in the material) and the water absorption by the recycled sand is properly compensated, the amount of SP additive necessary to obtain a sufficiently fluid mortar is basically the same when using natural and recycled sand, or even slightly lower SP for the mortars containing RS. This result is not controversial if it is considered that in literature studies the aggregate substitution is usually calculated by mass (Faleschini et al., 2014). The TD-NMR results highlight that a significant amount of capillary water, i.e. pores of nearly 1 μm size, is consumed by cement containing calcined clay after only 1 hour of hydration, generating voids of 10–20 nm assigned to interhydrate water, as showed by (Ferrari et al., 2023). This highlights a specific consumption of water by calcined clay that directly affect workability. Unexpectedly, no significant difference in porosity between mortars containing NS and RS is detectable in these preliminary experimental conditions. This new approach is still under investigation to possibly highlight differences between natural sand and recycled aggregates.

Compressive strength measured at 2 days of curing is reported in Table 3.

| Table 3 – Compressive strength values at 2 days (MPa). | | | | | |
|--|-------|--------|-------------------------|-------------------------|-------------------------|
| Sand | CEM I | CEM II | LC ³ -50 2:1 | LC ³ -50 1:1 | LC ³ -70 2:1 |
| NS | 50 | 38 | 33 | 29 | 42 |
| RS | 36 | 30 | 19 | 19 | 32 |

Recycled Sand has a strong impact on mechanical strength development, although the values obtained with the LC³-50 cements and RS can be considered still acceptable, as they are above the minimum value of 18 MPa prescribed by EN 197-1 standard for 42.5R or 52.5N cements.

6. Conclusions

This paper demonstrates that the combination of low carbon cement and recycled sand may lead to mortars with good rheological properties as well as acceptable early compressive strengths. The approach proposed showed that a substitution of 50 % of sand particles according to their volume, instead of their mass, is a successful strategy to limit the impact of recycled aggregate on mortar rheology. Moreover, the consideration of effective water, related to water absorption of recycled material, helps to adjust superplasticizer dosage with almost no change in comparison to the standard mortar.

Further investigations by TD-NMR highlighted that calcined clay consumes high amount of water directly impacting mortar workability and consequent superplasticizer dosage. However, the interaction between water and recycled aggregates still needs to be more investigated.

Acknowledgements

The authors would like to acknowledge Heidelberg Materials AG for the financial support. Paolo Carta from University of Bologna is warmly thanked for his support during laboratory tests.

References

- Borgia, G. C., Brown, R. J. S., & Fantazzini, P. (2000). Uniform-Penalty Inversion of Multiexponential Decay Data II. Data Spacing, T 2 Data, Systematic Data Errors, and Diagnostics. In *Journal of Magnetic Resonance* (Vol. 147). <https://doi.org/DOI: 10.1006/jmre.2000.2197>
- Dhandapani, Y., Joseph, S., Geddes, D. A., Zhao, Z., Boustingorry, P., Bishnoi, S., Vieira, M., Martirena, F., Castel, A., Kanavaris, F., & Riding, K. A. (2022). Fresh properties of concrete containing calcined clays: a review by RILEM TC-282 CCL. *Materials and Structures/Materiaux et Constructions*, 55(6). <https://doi.org/10.1617/s11527-022-01971-3>
- Faleschini, F., Jiménez, C., Barra, M., Aponte, D., Vázquez, E., & Pellegrino, C. (2014). Rheology of fresh concretes with recycled aggregates. *Construction and Building Materials*, 73, 407–416. <https://doi.org/10.1016/j.conbuildmat.2014.09.068>
- Ferrari, L., Bortolotti, V., Mikanovic, N., Ben-Haha, M., & Franzoni, E. (2023). *Influence of calcined clay on workability of mortars with low-carbon cement*. Nanoworld journal, article in press.
- Manzi, S., Mazzotti, C., & Bignozzi, M. C. (2013). Short and long-term behavior of structural concrete with recycled concrete aggregate. *Cement and Concrete Composites*, 37(1), 312–318. <https://doi.org/10.1016/j.cemconcomp.2013.01.003>
- Poly Software International, USA. (n.d.). Retrieved March 13, 2023, from www.polysoftware.com
- Scrivener, K. L., John, V. M., & Gartner, E. M. (2018). Eco-efficient cements: Potential economically viable solutions for a low-CO₂ cement-based materials industry. *Cement and Concrete Research*, 114, 2–26. <https://doi.org/10.1016/j.cemconres.2018.03.015>
- Scrivener, K., Snellings, R., & Lothenbach, B. (n.d.). *A practical guide to microstructural analysis of cementitious materials* (CRC Press). 2016 by Taylor & Francis Group, LLC.
- Théréné, F., Keita, E., Naël-Redolfi, J., Boustingorry, P., Bonafous, L., & Roussel, N. (2020). Water absorption of recycled aggregates: Measurements, influence of temperature and practical consequences. *Cement and Concrete Research*, 137. <https://doi.org/10.1016/j.cemconres.2020.106196>
- WBCSD, I.-I. E. A. (2009). *Technology Roadmap - Low-Carbon Transition in the Cement Industry*. www.wbcsdcement.org.
- Xing, W., Tam, V. W., Le, K. N., Hao, J. L., & Wang, J. (2023). Life cycle assessment of sustainable concrete with recycled aggregate and supplementary cementitious materials. *Resources, Conservation and Recycling*, 193. <https://doi.org/10.1016/j.resconrec.2023.106947>.

Rehydration of ettringite: microstructure and mechanical properties

A.A. Lima Pacheco^{1*}, N.C. Nascimento Faria², A.C. Vieira Coelho³, and S.C. Angulo⁴

¹ Department of Construction Engineering, Escola Politécnica, University of São Paulo, São Paulo, Brazil
Email: alanapacheco@usp.br

² Department of Construction Engineering, Escola Politécnica, University of São Paulo, São Paulo, Brazil
Email: natacha.faria@lme.pcc.usp.br

³ Department of Construction Engineering, Escola Politécnica, University of São Paulo, São Paulo, Brazil
Email: acvcoelh@usp.br

⁴ Department of Construction Engineering, Escola Politécnica, University of São Paulo, São Paulo, Brazil
Email: sergio.angulo@lme.pcc.usp.br

ABSTRACT

Ettringite is the main compound in calcium sulfoaluminate-based cements. Literature shows that the dehydration of ettringite at 100–200 °C could be reversible depending on the decomposition conditions. Still, fewer studies investigated the reformation of ettringite after calcination at mild temperatures, generally used for the thermal activation of waste materials. Thus, the present work explores the rehydration of ettringite pastes calcined at 400 °C and investigates the microstructural composition and mechanical properties over time. Ettringite was synthesized by mechanochemical method. Rehydrated pastes cured for 6 h showed well-defined ettringite reformation by XRD, attaining 90% of reformed ettringite compared to the synthesized compound. A reduced-size sample test was used to measure the tensile strength of rehydrated pastes from 6 h to 28 d. The higher tensile strength of 1.91 MPa occurred after 3 d of curing, coinciding with higher content of ettringite and lower porosity. The results showed the prompt recovery of ettringite after calcination at 400 °C and the rapid binding capacity of rehydrated ettringite.

KEYWORDS: *ettringite, calcination, rehydration, alternative binder.*

1. Introduction

Ettringite is formed in the initial hours of Portland cement (PC) hydration, and it is partially responsible for the setting, also contributing to the early strength development of the pastes (Taylor (1997)). When studying the recycling of Portland cement compounds, ettringite can be found in cementitious waste materials and in the rehydration of cement fines after thermal activation (Bogas et al (2020), Baldusco et al (2019)).

In calcium sulfoaluminate (CSA)-based cements (including belite/alite sulfoaluminate cements), ettringite is one of the main hydration compounds and its rapid formation yields exclusive characteristics for these types of cement, such as early strength development and expansive behaviour (Winnefeld and Lothenbach (2010)). Although few references provide data on world CSA-based cements production, it is well known that they are used in large scales for special applications in China (Aranda and De La Torre (2013), with an estimated production of 1 million tons per year (Péra and Ambroise (2007), Liao et al. (2020)). Also, these types of cements are receiving more attention over the years due to the reduced CO₂ emissions during its production when compared to PC (Afroughsabet et al. (2021), Nie et al. (2022), Tao et al. (2023)). Therefore, with the increasing use of CSA-based types of cement and blended CSA-PC compounds, it is expected that ettringite should be more present in cementitious waste materials with time.

According to studies up to ~200 °C (Skoblinskaya et al (1975), Zhou and Glasser (2001), Baquerizo (2016)), the decomposition and reformation of ettringite can be reversible, depending on the temperature and relative humidity. However, even though ettringite decomposes completely at 120 °C, this compound is formed in complex cement systems containing other hydrated phases such as C-S-H and Ca-Al LDHs. Thus, when thinking about recycling strategies, the chosen temperature for thermal activation of cement wastes should take into consideration the dehydration of other phases that may occur up to 400 °C, while avoiding the release of CO₂ through decarbonation.

This study investigates the behaviour of ettringite upon calcination at 400 °C and the following rehydration behaviour, including the use for construction applications. The study of its rehydration may help understand the behaviour of ettringite when thermoactivated (a recycling strategy) and its potential use as an alternative binder or SCM (i.e., partial substitution for Portland cement). Also, this work shows how ettringite can be obtained by a simple mechanochemical method and opens the possibility of using waste sources instead of reagents for obtaining ettringite through mechanosynthesis.

2. Experimental program

In this work, ettringite was synthesized, thermoactivated at 400 °C, and its rehydration was investigated regarding the phase reformation and mechanical properties. Calcined ettringite was rehydrated with water/solid ratio (w/s, g/g) of 0.5. The materials were mixed by hand for 30 s and for 1 min at 10,000 rpm in a Makita RT0700C mixer to acquire a dispersed (homogeneous) suspension rapidly. The quantity of water was not sufficient to ensure a plastic consistency resulting in a “wet agglomerated powder”. Therefore, the mixtures were moulded by pressure. The paste was placed in a cylindrical mould (11 mm diameter) and pressed into tablets until 1 kN, resulting in a reduced-size specimen with thickness of 10 ± 1 mm. The cylindrical specimens were cured in a moisture chamber (100% RH, 25 °C) until the test time.

2.1 Synthesis and dehydration of ettringite

Ettringite was synthesized mechanically by milling a wet mixture of approximately 50 g of Ca(OH)_2 , Al(OH)_3 and $\text{CaSO}_4 \cdot 2\text{H}_2\text{O}$ (all P.A. reagents from Sigma-Aldrich) in a proportion of 3:2:3 mol, respectively. Deionized water was added, corresponding to twice the amount of the total reagent powder by weight. A planetary ball mill (Pulverisette 6 Mono-Mill, Fritsch) was used with stainless steel jar with 500 ml capacity and 35, 8 and 5 unities of stainless-steel balls having diameters of 5, 10, and 20 mm, respectively. The milling was conducted at room temperature, maintaining a constant speed of 600 rpm for 3 h, pausing for 10 min every 20 min of milling to avoid overheating. After that, the paste was dried in an oven at 50 °C for 48 h to remove free water. Then, the material was ground into powder, passed through a 0.15 mm sieve, and stored in a vacuum desiccator. XRD analysis with Rietveld quantification (refinement parameters: Rwp 9.7, GOF 3.1) confirmed ettringite as the main phase (84 wt.%) in the mechanosynthesis product, with gypsum, calcite, bassanite and portlandite as secondary phases. The thermoactivation of synthesized ettringite was conducted in an oven at 400 °C for 2 h (heating rate 10 °C/min). The material was cooled at room temperature and stored in a vacuum desiccator until its use.

2.2 Characterization methods

XRD powder analyses were performed on a Panalytical Empyrean diffractometer, at room temperature, with $\text{CuK}\alpha$ radiation ($\lambda = 1.54 \text{ \AA}$), at 40 kV and 40 mA and $0.02^\circ 2\theta - 600$ s steps. For calcined ettringite, an internal standard (LiF) was used to quantify amorphous phases. Due to high crystallinity, the phase quantifications of the other samples were not performed with internal standard. The analyses were conducted using HighScore Plus software with Crystallography Open Database (COD) files.

Thermogravimetric analysis (TGA) was conducted in equipment Netzsch (TG 209 F1 Libra) with a thermobalance and analysed by Proteus software. The samples were placed in an alumina crucible and heated from 25 to 1000 °C at a constant heat rate of $10^\circ\text{C min}^{-1}$ in an inert N_2 atmosphere.

The mechanical properties (tensile strength, σ_t and elastic modulus, E) of hardened cement pastes were determined using a new method, which used Point Load Test (ASTM D5731-16 (2017)), to determine tensile strength of cement pastes, and Hertz Contact Theory (Hertz (1882)), to determine elastic modulus; the method was named PLT-LVDT (Silva (2019), Oliveira (2021)). The compression load was applied in quasi-static condition, load speed of 0.2 mm/min, in two parallel faces of the samples, in a universal Instron machine (Model 5569) with a 50 kN load cell. The mechanical properties of the pastes of rehydrated ettringite (w/s 0.5) were evaluated from 6 h to 28 d of curing, 12 samples for each curing time.

Some fractured pieces from the samples tested for tensile strength after hydration stoppage were analysed by mercury intrusion porosimetry (AutoPore III 9410, Micromeritics), under pressure range of 0 – 412 MPa, detection range from 0.003 to 308 μm . Data were obtained from one sample of each curing time.

3. Results

3.1 Dehydration

The XRD analysis (Rwp 9.6, GOF 3.9) of the calcined product showed 68 wt.% of amorphous material, and calcite and anhydrite as secondary phases. By laser diffraction particle-size analyser (Mastersizer 3000, Malvern Instruments) the median particle size of the powder product was of 19.1 μm , and a surface area of 11.1 m^2/g by use of BET method using N_2 sorption at 77 K data (Belsorp Max equipment).

3.2 Phase reformation over time

The microstructure of the rehydrated pastes was investigated by XRD analyses and the phases were quantified by Rietveld refinement (Rwp 9.5-10.5, GOF 4.7-5.2). Ettringite was successfully rehydrated even after 6 h of curing, attaining approximately 90% of reformation when compared to synthesized ettringite. The rehydrated product of all samples contained mostly ettringite, gypsum and carbonates (calcite and aragonite), with the presence of portlandite, bassanite and anhydrite as minor phases.

Figure 1 shows the quantity of the main phases over time, considering the total porosity found by MIP. It was observed two different periods in the rehydration of ettringite. Until 3 d of curing, ettringite attained maximum values as well as the porosity presented the lowest values. After 3 d of curing, the amount of ettringite decreased slightly with time until 14 d (showing stability at 28 d) whereas the gypsum and carbonates contents increased, as well as the porosity. A possible explanation for this behaviour is firstly the formation of ettringite and secondly the carbonation reaction. Carbonation became the predominant mechanism after 3 d, slightly decomposing ettringite into gypsum and carbonate phases. Nevertheless, this explanation is rather initial and further analyses need to be conducted to confirm the mechanism.

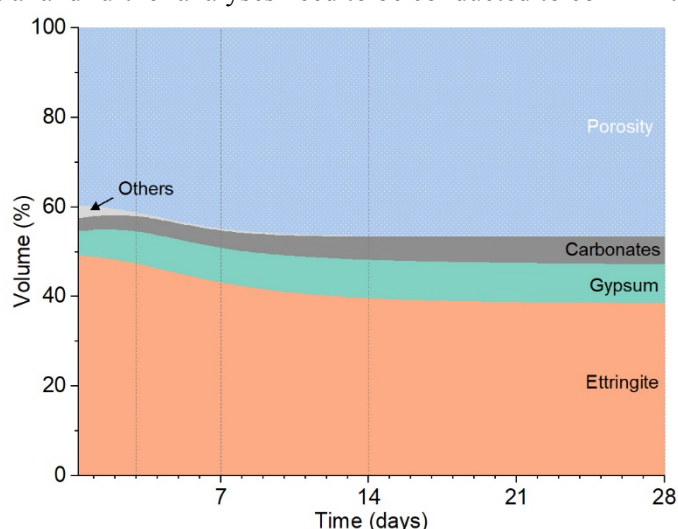


Figure 1. Volume of phases (estimated by quantitative XRD) and porosity (MIP results) over time.

3.3 Physical and mechanical properties of rehydrated ettringite pastes

The tensile strength and elastic modulus of the rehydrated ettringite pastes over time are exhibited in Figure 2a. The main tensile strength gain occurred from 6 h to 3 d (~74%-increase). Subsequently, the sample reached maximum values at 3 days (difference of means between 3 and 7 days was not significant), after 7 days the strength steadily decreased, reaching a value of 1.37 MPa at 28 d. The elastic modulus of the rehydrated pastes started at 6 h and 3 d of curing with the maximum values of approximately 1.38 GPa. After this time, the elastic modulus decreased until 0.71 GPa which corresponds to 48.5% of reduction. In both cases, there is a tendency for values to stabilize. The scale of observation of PLT-LVDT was close to the macroscale and because of that elastic modulus results can be underestimated (Oliveira (2021)).

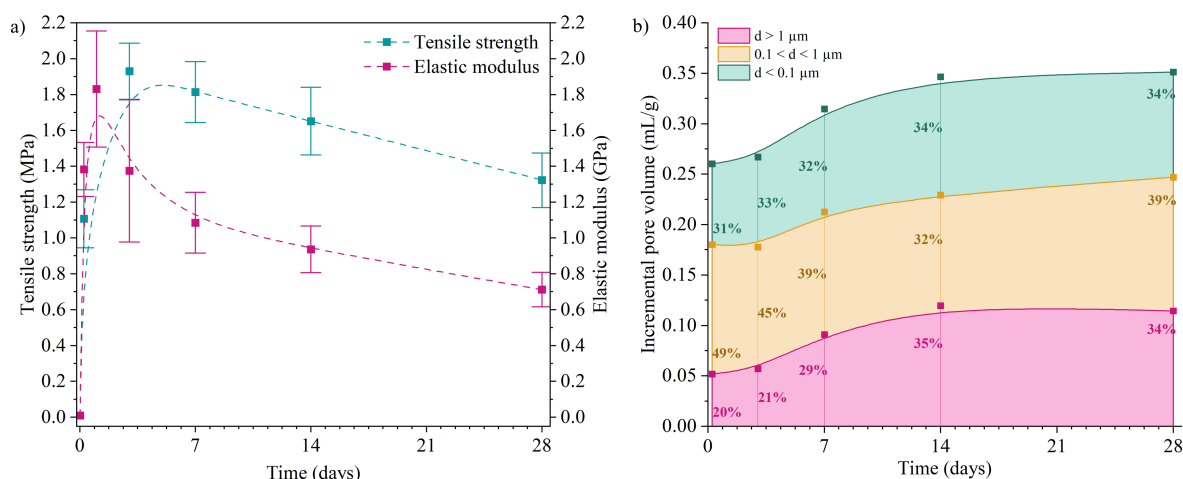


Figure 2. Mechanical properties of rehydrated ettringite pastes (a) and incremental pore volume discriminated by pore size diameter (b) in function of time.

To better understand the behaviour of the mechanical properties, the pore structures of the rehydrated pastes were investigated, as showed in Figure 2b. In the first times (6 h and 3 d) it was observed lower quantity of pores with more than $1 \mu\text{m}$ (20%) and higher proportion of pores between 0.1 and $1 \mu\text{m}$ (49%). After that, the quantity of pores with diameter greater than $1 \mu\text{m}$ increases and the quantity of pores between 0.1 and $1 \mu\text{m}$ decreases, until they attained similar proportions (34 – 39%) after 28 d of curing.

It was observed a good relation between the mechanical properties of the rehydrated pastes and their pore structure. The higher elastic modulus occurred when the pastes presented the lower value of total porosity. Similarly, the pastes showed higher tensile strength at 3 d, when the pore structure presented one of the lowest value of pores bigger than $0.1 \mu\text{m}$ (66%), that could have favoured the strength at this curing time. The results of rehydrated ettringite pastes agreed with the findings of Kendall et al. (1983) about cement-based materials, in which the elastic modulus is mostly influenced by the total porosity of the material and the tensile strength is more affected by the presence of larger pores.

4. Conclusions

The phase assemblage and the microstructure of the rehydrated ettringite products affected the pore structure of the pastes with time, which, in turn, affected the mechanical properties. In the first times, the rehydrated pastes had the major formation of ettringite and presented a fine pore structure, with lower quantity of larger pores. Consequently, in these times it was observed the maximum values of tensile strength and elastic modulus. At later ages, the decomposition of ettringite resulted in larger pores, since the products formed (gypsum and carbonates) present higher densities and then occupy less volume. Thus, both tensile strength and elastic modulus decreased. By analyzing the results from a technological perspective, the rehydration reformed ettringite rapidly and presented considerable mechanical strength. Therefore, there is potential of applying calcined ettringite as an alternative binder, but the low consistency of the pastes can limit its application. Also, additional care should be taken with the later decomposition of ettringite and carbonation of the rehydrated pastes.

Acknowledgements

The authors acknowledge CNPq (process 423072/2018-8 and grant 140054/2020-0), FAPESP (process 2019/27284-5) and Innovandi GCCRN (CP10). This work was supported by the INCT “Advanced Eco-Efficient Cement-Based Technologies” (process 2014/50948-3).

References

Aranda, M.A.G., De La Torre, A.G. (2013) “Sulfoaluminate cement”, *Eco-Efficient Concrete*, Woodhead Publishing.

- Afroughsabet, V., Biolzi, L., Monteiro, P.J.M., Gastaldi, M.M. (2021) "Investigation of the mechanical and durability properties of sustainable high performance concrete based on calcium sulfoaluminate cement", *Journal of Building Engineering*, 43: 102656.
- Baldusco, R., et al. (2019) "Dehydration and rehydration of blast furnace slag cement", *Journal of Materials in Civil Engineering*, 31(8) 04019132-2.
- Baquerizo, L.G., Matschei, T., Scrivener, K.L. (2016) "Impact of water activity on the stability of ettringite", *Cement and Concrete Research*, 79: 31-44.
- Bogas, J.A., Carriço, A., Tenza-Abril, A.J. (2020) "Microstructure of thermoactivated recycled cement pastes", *Cement and Concrete Research*, 138: 106-226.
- Kendall, K. et al. (1983) "The relation between porosity, microstructure and strength, and the approach to advanced cement-based materials", *Philosophical Transactions of the Royal Society of London, Mathematical and Physical Sciences*, 310 (1511): 139-153.
- Liao, Y., Jiang, G., Wang, K., Qunaynah, S.A., Yuan, W. (2020) "Effect of steel slag on the hydration and strength development of calcium sulfoaluminate cement", *Construction and Building Materials*, 265: 120301.
- Nie, S., Zhou, J., Yang, F., Lan, M., Li, J., Zhang, Z., Chen, Z., Xu, M., Li, H., Sanjayan, J.G. (2022) "Analysis of theoretical carbon dioxide emissions from cement production: Methodology and application", *Journal of Cleaner Production*, 334: 30270.
- Oliveira, F.C., et al. (2021) "Probabilistic functions of mechanical properties of plain cement pastes determined by a reduced-size test", *Construction and Building Materials*, 286: 122907.
- Péra, J., Ambroise, J. (2007) "Thermal behaviour of materials based on calcium sulfo-aluminate cement", *Proceedings of the 12th International Congress on the Chemistry of Cement (ICCC)*.
- Silva, N.V., et al. (2019) "Improved method to measure the strength and elastic modulus of single aggregate particles", *Materials and Structures*, 52(4): 77.
- Skoblinskaya, N.N., et al. (1975) "Changes in crystal structure of ettringite on dehydration. 1", *Cement and Concrete Research*, 5(5): 419-431.
- Taylor, H.F.W. (1997) "Hydrated aluminate, ferrite and sulfate phases", In: *Cement Chemistry*, Thomas Telford.
- Tao, Y., Rahul, A.V., Mohan, M.K., De Schutter, G., Tittelboom, K.V. (2023) "Recent progress and technical challenges in using calcium sulfoaluminate (CSA) cement", *Cement and Concrete Composites*, 137: 104908.
- Winnefeld, F., Lothenbach, B. (2010) "Hydration of calcium sulfoaluminate cements—Experimental findings and thermodynamic modelling", *Cement and Concrete Research*, 40: 1239-1247.
- Zhou, Q., Glasser, F.P. (2001) "Thermal stability and decomposition mechanisms of ettringite at < 120 °C", *Cement and Concrete Research*, 31(9): 1333-1339.

Physical Properties of Biochar Enhance the Rheological Behavior of Cement-Based Materials

L. Zembereski^{1*}, D. Woo², and E. Pinheiro³, S.D. Nair⁴, and K.C. Hover⁵

¹ Cornell University, Ithaca, N.Y.

Email: lz549@cornell.edu

² Cornell University, Ithaca, N.Y.

Email: dw498@cornell.edu

³ Cornell University, Ithaca, N.Y.

Email: erp79@cornell.edu

⁴ Cornell University, Ithaca, N.Y.

Email: sn599@cornell.edu

⁵ Cornell University, Ithaca, N.Y.

Email: kch7@cornell.edu

ABSTRACT

Biochar pyrolyzed from wood chips has found uses in many applications including heat and power production, soil amendment, and construction with its unique physical and chemical properties. Biochar has a high potential for carbon sequestration, making it a suitable candidate as a carbon offset. A cementitious mortar mix incorporating biochar as a partial fine aggregate replacement can lower the carbon footprint of ordinary Portland cement-based materials. Such mortars, mixed using a benchtop mixer, transition from extremely unworkable to essentially flowing at about 15 minutes after the beginning of mixing, as measured by the ASTM Mortar Flow Test (C1437-20). The work reported here studies the rheological aspect of this transition using a paste rheometer with a cup and bob geometry.

Herein, we assess the effect that biochar has on the fluidity and rheological behavior of cement paste in the presence of 1–6.25% of biochar relative to the intended mass of the sand. We observed that up to 4000 rpm, the speed of the paste mixer is correlated with the flowability of the paste with time. More energetic mixing may break the friable, highly porous biochar particles, changing particle size distribution, perhaps accompanied by the release of absorbed water. This study identified variable rheological behaviors of cement pastes containing biochar as influenced by mixing speeds and biochar content. Further studies are underway to evaluate the proposed hypotheses.

KEYWORDS: *biochar, carbon neutral, rheology, sequestration, slump flow*

1. Introduction

Prior studies have focused on producing a carbon-neutral, portland cement-based mortar mixture incorporating biochar, primarily for low-strength applications. The selected biochar had been pyrolyzed from timber and contained 80% carbon by mass with negligible cementitious properties. Biochar was therefore used to partially replace sand to produce a cement, sand, water, and biochar mortar that sequestered carbon in the same amount as carbon (in the form of CO₂), released in the manufacture of the cement. However, it was difficult to produce a biochar mortar with sufficient initial workability in 3 to 5 minutes of mixing, necessitating added water that resulted in a significant reduction in the strength of the hardened product (Cheng et al., 2019). In a follow-on project focused on enhancing workability, it was observed that continued mixing for up to about 15 minutes resulted in increased or extended workability of biochar mortar, in contrast to the continuous decrease

in workability over time typically observed with cement-based mortars not incorporating biochar. The study reported here focuses on this time-dependent rheological behavior and the effects of the mixing operation itself, via control and biochar pastes in a cup and bob geometry in a paste rheometer.

2. Materials and Methods

Type I/II ASTM C150 cement from manufacturer “Quikrete” was used in this research along with tap water. Normal weight, natural concrete sand meeting ASTM C33 requirements was used for all mortar mixes. Sand was observed to meet ASTM C33 requirements via ASTM C136-06. Biochar was purchased from company BiocharNow in their “small” size and was subsequently sieved to pass through the ASTM E11 #25 sieve and be retained on the ASTM E11 #50 sieve to limit the variability of biochar particle size.

Both natural sand and biochar were oven dried upon receipt, sieved to meet a desired particle size, or check compliance with ASTM standards, and then “preconditioned”, or corrected by its observed absorption rate with water to saturated surface dry (SSD) conditions, the day prior to mixing. The lower bounds of the absorption rates used throughout the experiments were 2.5% for sand and 80% for biochar used per ASTM test C128-15. This method was used to help monitor the water content of each mix.

2.1 Experimental Methods

Mortar samples were prepared according to ASTM C305-20 and flow tests were conducted according to ASTM C1437-20 and a modified flow test previously developed for highly flowable mortar by counting the number of drops to reach a flow of 100% (Xu et al., 2021). The mixture proportions of the mortar samples are shown in Table 1.

Cement paste samples were also prepared with and without any biochar as shown in Table 1. Mix ID BP-6.25% represents a biochar paste containing approximately 6.25% of the dry biochar weight relative to a supposed sand weight (if sand were to be added to create a mortar), and 6.25% was selected as the upper limit to ensure mixability. Cement pastes were mixed using a blender that complies with ASTM C1738-19, but at lower speeds varying between 2000 – 4000 rpm. During mixing, water was first placed into the mixer, followed by addition of cement and biochar. Upon addition of the powders, a timer was started to establish a recorded time for $t = 0$ minutes. After 1 minute of mixing, the timer and the variable speed mixer were stopped for approximately 30 seconds, sides were scrapped and mixing was resumed. Samples were collected at 4 and 15 minutes time stamps. Rheological tests were conducted using an Anton Paar MCR302 rheometer with a cup and bob geometry. Samples were pre-sheared at 100 s^{-1} for 30 seconds, rested for 30 seconds followed by shearing for 10 seconds to reach equilibrium. The flow tests were conducted at shear rates of 5, 10, 50, 100, 170, 325, 511 s^{-1} and ramped down at the same shear rates.

Table 1: Mixture Proportions of Mortar and Paste

| | Mix ID | Water to SSD ⁺ (g) | Mixing Water (g) | Portland Cement (g) | Oven Dry Biochar (g) | Oven Dry Sand (g) | w/c ratio |
|-----------------------------------|----------|----------------------------------|---------------------|------------------------|-------------------------|----------------------|-----------|
| Mortar | M1 | 36.5 | 345 | 530.7 | - | 1461 | 0.65 |
| Biochar Mortar[‡] | BM-12.5% | 176.4 | 345 | 530.7 | 180.5 | 1279 | 0.65 |
| Cement Paste | P1 | - | 181.6 | 279.4 | - | - | 0.65 |
| | P2 | - | 135.5 | 279.4 | - | - | 0.485 |
| Biochar Paste[*] | BP-1% | 6.17 | 181.6 | 279.4 | 7.71 | - | 0.65 |
| | BP-2% | 12.3 | 181.6 | 279.4 | 15.4 | - | 0.65 |
| | BP-3% | 18.5 | 181.6 | 279.4 | 23.1 | - | 0.65 |
| | BP-5% | 30.9 | 181.6 | 279.4 | 38.6 | - | 0.65 |
| | BP-6.25% | 38.5 | 181.6 | 279.4 | 48.1 | - | 0.65 |

[‡]Required water to bring aggregates to SSD at absorption of 80% for biochar and 2.5% for sand.

◊In a mortar, all biochar passes through the #25 sieve and is retained on the #50 sieve.

*In a paste, all biochar passes through the #200 sieve.

3. Results & Discussion

In conducting a flow table test according to ASTM C1437-20 for mortar mixes M1 and BM-12.5%, data points were collected every 11 minutes, 7 minutes were used to mix the mortar at low speed and 4 minutes were taken to conduct and record the number of drops to 100% flow, and place the mortar back into the bowl. Figure 1 describes the number of drops necessary to reach a flow of a 100%. As shown in insert 3 and 4, M1 produced a flow of 100% at 4 minutes with only 5 drops and, as expected, decreased in flowability over time requiring twice as many drops at 70 minutes. In contrast, the BM-12.5% mixture did not produce a measurable flow, but rather the mixture crumbled at 4 minutes, as pictured in insert 1, thus no drops were recorded. However, upon continuous mixing, 100% flowability was observed starting at 15 minutes as in insert 2, requiring 25 drops. Beyond that, the number of drops systematically increased after approximately 50 minutes imitating the behavior of M1. In summary, the BM-12.5% mixture transitions from being clearly unworkable to a flowable mixture with continuous mixing in a benchtop planetary mixer at medium speed. This behavior could be attributed to the release of water from the highly absorbent biochar and separation of particles (Gupta et al., 2022). During continuous and long mixing, the larger friable biochar particles (0.29–0.45 mm) could be releasing the initially retained water upon breaking. To further characterize this transition, more sophisticated rheological tests were performed.

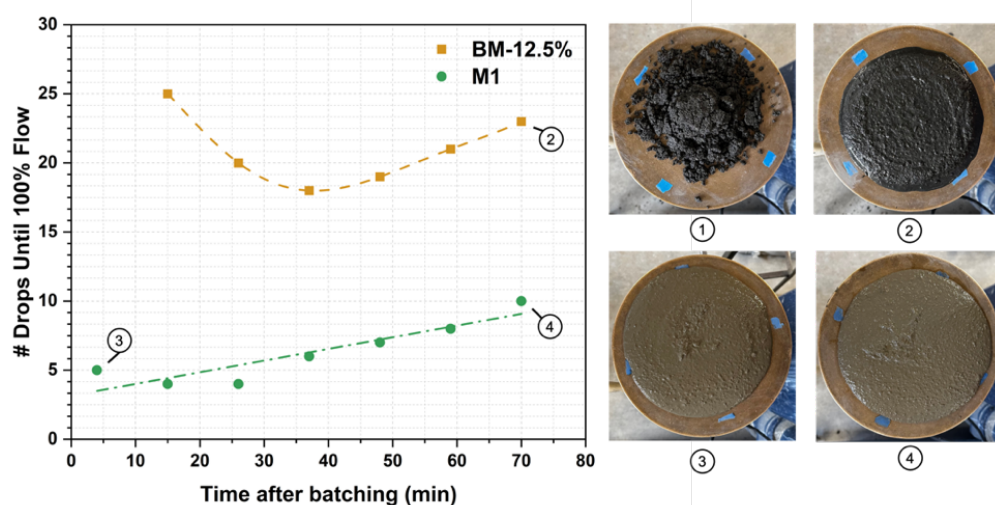


Figure 1: Flow of mortar M1 and BM-12.5 (mortar with 12.5% biochar) measured according to ASTM C1437-20.

(1) BM-12.5% at 4 minutes (2) BM-12.5% at 70 minutes (3) M1 at 4 minutes (4) M1 at 70 minutes

Figure 2 demonstrates the rheological behavior of pastes with varying biochar content from 0 to 6.25%. All pastes in this set were mixed at 4000 rpm. The shear stress increased with increased shear rate as well as with increasing the biochar content. In contrast to the flowability results of the mortar mixtures in Figure 1, the behavior throughout continuous mixing at 4000 rpm was not time dependent as it did not significantly affect the shear stress values for all pastes regardless of the biochar amount between 4 and 15 minutes. This can be attributed to the release of the water early on during the mixing due to the relatively higher speed of the mixer. It is worth mentioning that the ramp up and the ramp down curves are almost identical. Thus, for clarity, the following figures only show shear stress values recorded from the ramp down cycle.

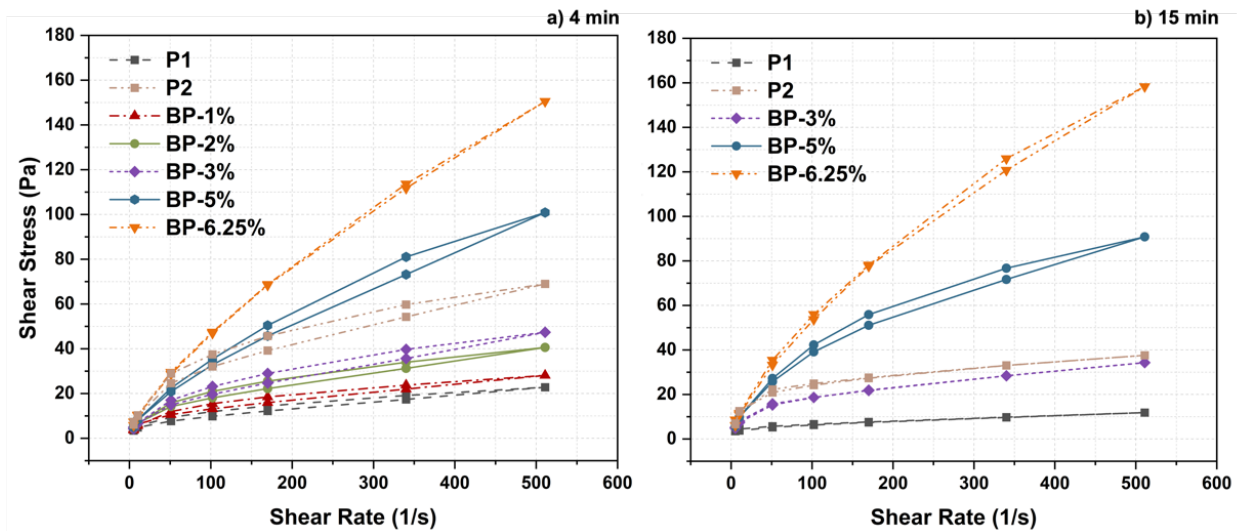


Figure 2: Flow test of pastes with varying amounts of biochar mixed at 4000 rpm at a) 4 min and b) 15 min .

To investigate the influence of the mixing speed on the time dependency of flowability of biochar-containing mixture, flow tests were conducted with varying speeds of 2000–4000 rpm (Figure 3). A mixing speed of 1000 rpm is not shown as the mixture was too viscous. As in both Figure 3 a and b, with increased speed the shear stress increases, possibly due to the large surface area from the breakage of friable small-size biochar (starting size < 0.075 mm). Comparing data shown in Figure 3, a and b, as the speed of the mixing increased from 2000 rpm to 3500 rpm, the change in shear stress increased with time. The percent difference in the shear stress at the highest shear rate, 511 s^{-1} , is approximately 25% for 2500 rpm, 40% for 3000 rpm, and 70% for 3500 rpm. The percentage differences could signify a systematic breakage of particles with longer mixing times. Larger particles disappear at a faster rate with higher mixing speed, thus, increasing the surface area early on. At a mixing speed of 4000 rpm, the percent difference in shear stress is 7%, which is insignificant as discussed in Figure 2.

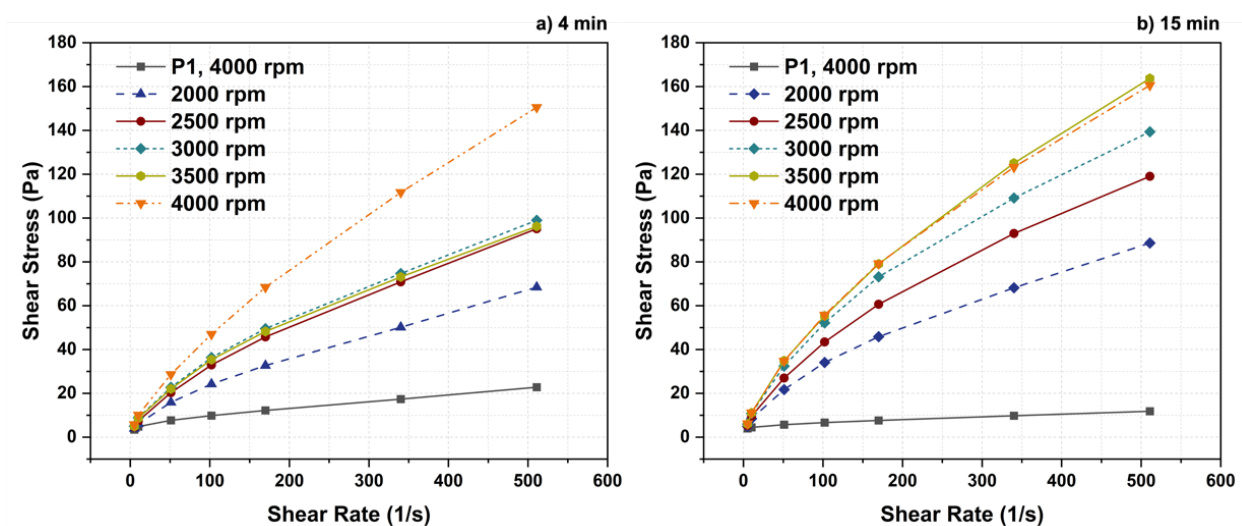


Figure 3: Rheology results of BP-6.25% varying high shear mixing speeds.

4. Conclusions

Although biochar has a high potential for reducing the carbon footprint of concrete, workability challenges might arise. This study demonstrated the influence of biochar content and mixing speed on the rheological behavior of mortars and cement pastes, which could be due to the breakage of friable particles. There is a balancing effect between the release of water and increase of surface area of particles due to this breakage. More studies are required to assess the transition on the micro-scale to further evaluate this physical

behavior of biochar. For using biochar in construction applications care must be taken to adapt modified mixing procedures that consider the dynamic change of state of biochar-containing mortars. The development of a tailored additive to control the water retaining/releasing would be beneficial to enhance the robustness of biochar mixtures.

References

- Cheng, W., Elliott, J.R. and Hover, K.C. (2019). “High-Volume Carbon Sequestration for Controlled Low-Strength Materials:” *ACI Materials Journal*, Vol. 116, No. 4, pp. 235–244.
- Gupta, S., Tulliani, J.-M. and Kua, H.W. (2022). “Carbonaceous admixtures in cementitious building materials: Effect of particle size blending on rheology, packing, early age properties and processing energy demand:” *Science of The Total Environment*, Vol. 807, p. 150884.
- Xu, E., Tejada, K.V., Walker, D., Zivkovic, S. and Hover, K.C. (2021). “Case Study: Measuring Flow and Setting Time for Three-Dimensionally Printed Mortar:” *ACI Materials Journal*, Vol. 118, No. 6.

The reactivity of hydrothermally activated basic oxygen furnace slag

J.C.O. Zepper^{1*}, K. Schollbach², S.R. van der Laan³ and H.J.H. Brouwers⁴

¹ Eindhoven University of Technology, Eindhoven, The Netherlands
Email: j.c.o.zepper@tue.nl

² Eindhoven University of Technology, Eindhoven, The Netherlands
Email: k.schollbach@tue.nl

³ Tata Steel, RDT, IJmuiden, The Netherlands
Email: sieger.van-der-laan@tatasteeleurope.com

⁴ Eindhoven University of Technology, Eindhoven, The Netherlands
Email: jos.brouwers@tue.nl

ABSTRACT

Basic oxygen furnace (BOF) slag is one of the most produced industrial by-products (100 Mt/year worldwide), but largely used in low-end application. Its potential to partially replace Ordinary Portland cement (OPC) is based on the comparable chemical composition with high CaO (> 30 wt%) and moderate SiO₂ (10 – 25 wt%) content and the presence of C₂S as well as C₂(A,F). However, BOF slag itself shows low reactivity during hydration and is known to retard the reactivity of OPC when used as supplementary cementitious material. Therefore, in this study we investigated the combination of hydrothermal treatment followed by mechanochemical activation of BOF slag to develop a possible binder or SCM based on new insights for C-S-H binders. The key findings were that i) after the hydrothermal treatment large amounts of reaction product (i.e. portlandite, hydrogarnet, α -C₂SH, brucite and amorphous) formed (~55 wt%), ii) mechanochemical activation of autoclaved BOF slag causes disruption in long range order in the crystal lattice of hydration products and iii) the followed treatment procedure gives a better synergy with OPC but in itself it lowers reactivity compared to conventional non-activated BOF slag, as shown with isothermal calorimetry.

KEYWORDS: *basic oxygen furnace slag, hydrothermal activation, mechanochemical activation, C-S-H binder, recycling*

1. Introduction

For the past 30 years, researchers have been searching for alternative cementitious materials (ACM) capable of decreasing the CO₂ emissions of ordinary Portland cement (OPC) in the construction industry. For these ACMs to be successful, they need to have comparable performance to OPC, use raw materials that are in abundant supply, and be economically viable to produce.

One of such possible ACMs could be basic oxygen furnace (BOF) slag. BOF slag is an industrial by-product of the steel industry with comparable chemical composition to OPC (Martins et al., 2021; Pöllmann, 2021) and is produced in large amounts (100 Mt/year worldwide). However, while BOF slag contains large amounts of C₂S and C₂(A,F), it has much lower levels of C₃S than OPC and therefore its hydraulic reactivity is low (Murphy et al., 1997). Unlike blast furnace slag, only small amounts of BOF slag are recommended to be used as a supplementary cementitious material (SCM) (10 – 20 wt%) (Ahmed et al., 2023) because it decreases the hydraulic reactivity of OPC. Consequently, researcher have aimed to apply BOF slag as a standalone binder through chemical, mechanical, thermal or hydrothermal activation using different methods with moderate success (Franco Santos et al., 2023; Kaja et al., 2021; Zepper et al., 2023).

Another treatment method for raw materials that has not yet been investigated with BOF slag, but has shown promising results is the production of reactive CSH phases by hydrothermal treatment and subsequent mechanochemical activation (Garbev et al., 2014). This study investigates the phase composition and reactivity of a hydrothermally and mechanochemical activated binder based on BOF slag using quantitative X-ray diffraction analysis (QXRD), thermogravimetric analysis (TGA) and isothermal calorimetry.

2. Methodology

The investigated BOF slag was derived from the Tata Steel plant in IJmuiden, The Netherlands. For the hydrothermal treatment a slurry was prepared at a w/s of 0.3. The slurry was poured in a steel container and underwent hydrothermal treatment in a Scholz saturated steam laboratory autoclave 140 litres in size. The treatment lasted for 8 hours, with the pressure and temperature increasing linearly for 1.5 hours to 13 bar and 195 °C respectively. The hardened hydrothermally treated slurry was dried in an oven for 24 h at 70 °C. A Fritsch planetary ball mill with zirconia milling pots was used for the mechanochemical activation. Small samples were taken after a total milling time of 2 (HMBS2), 36 (HMBS36) and 72 (HMBS72) minutes. The X-ray fluorescence (XRF) analysis of the initial BOF slag was performed on fused beads. The XRF analysis was performed on a PANalytical Axios (Table 1). QXRD analysis was performed on initial BOF slag (IBS) and the hydrothermally and mechanochemical activated BOF slag samples (HMBS) with the Rietveld method. The samples were milled together with 10 wt% internal Si-Standard prior to the XRD measurement. Diffraction powder patterns were obtained by using a Bruker D8 Endeavor equipped with a Co-tube. TGA was performed on the HMBS samples with a TA Instruments TGA Q500 with a heating rate of 10 K/min under N₂-gas. Isothermal calorimetry was performed on HMBS, IBS and CEM I in a pure system at w/p of 0.3 and BOF slag containing samples were mixed with CEM I in a 50:50 mix to test the compatibility with CEM I. The calorimetry test was performed on a TAM Air Thermometric calorimeter. Particle size distribution measurements were performed on Malvern Mastersizer 2000 (Figure 1 A).

Table 1 Results of the XRF analysis for IBS in wt%. Fe₂O₃* means that it is assumed that all Fe has formed Fe₂O₃. GOI means gain on ignition.

| CaO | Fe ₂ O ₃ * | K ₂ O | MgO | MnO | Na ₂ O | P ₂ O ₅ | SiO ₂ | TiO ₂ | V ₂ O ₅ | Cr ₂ O ₃ | GOI |
|------|----------------------------------|------------------|-----|------|-------------------|-------------------------------|------------------|------------------|-------------------------------|--------------------------------|-----|
| 40.5 | 26.5 | 0.01 | 7.6 | 4.52 | 0.10 | 1.61 | 14.5 | 1.64 | 0.93 | 0.30 | 1.4 |

3. Results

3.1 Quantitative X-ray diffraction

Table 2 presents the QXRD results of the IBS, HMBS2, HMBS36 and HMBS7. After the hydrothermal treatment C₂S, C₂(A,F) and RO-Phase decrease significantly to 17, 5.5 and 11.9 wt%, respectively. New phases developed such as portlandite, hydrogarnet, α-C₂SH, and brucite, which are all highest in HMBS2. During the prolonged mechanochemical activation by milling of the hydrothermally treated material, the newly developed secondary phases progressively decrease and the amorphous content increases from 20.3 to 33 wt%, while the original primary slag amounts remain unaffected. Hence, one can conclude that the secondary phases became amorphous during the milling operation as it was concluded for kaolin by Balczár et al. (2016). This implies, that the milling operation induced distortion of the crystal structure, probably also increasing surface energy which should lead to a higher chemical reactivity (Vizcayno et al., 2010).

Table 2 Results of the QXRD analysis in wt%.

| Phase Name | RO-Phase | Ff | C ₂ (A,F) | C ₂ S | C | CH | Cc | C ₃ (A,F)S ₃ - xH ₂ O | C2SH | MH | Others | Amorphous | GOF | Rwp |
|------------|----------|-----|----------------------|------------------|-----|-----|-----|---|------|-----|--------|-----------|-----|-----|
| IBS | 23.0 | 7.8 | 18.5 | 38.1 | 0.5 | 0.2 | 0.3 | 0.0 | 0.0 | 0.0 | 3.0 | 8.6 | 1.2 | 4.3 |
| HMBS2 | 11.9 | 8.4 | 5.5 | 17.0 | 0.2 | 4.0 | 2.0 | 15.3 | 13.1 | 1.8 | 0.4 | 20.3 | 1.2 | 4.7 |
| HMBS36 | 11.1 | 7.9 | 4.8 | 16.8 | 0.2 | 1.3 | 1.6 | 13.1 | 11.2 | 0.9 | 0.7 | 30.2 | 1.2 | 4.4 |
| HMBS72 | 11.6 | 8.0 | 5.2 | 16.9 | 0.2 | 0.8 | 1.5 | 10.5 | 10.5 | 0.4 | 1.2 | 33.3 | 1.1 | 4.4 |

3.2 Thermographic analysis

TGA results show that almost no weight loss is recorded (< 0.6 wt%) between $40 - 180$ °C (Figure 1 B), which would lead to the conclusions that only minor amounts of CSH are present. This has been reported by Wang et al., 2018 and Zepper et al., 2023, previously. The most significant mass loss appears to be in the range of $180 - 410$ °C ($5 - 6$ wt%) for all HMBS samples. This correlates to the bound-water loss of hydrogarnet and portlandite. The difference in bound-water loss between samples is low (10 % relative), while the amount of hydrogarnet decreased by 1/3 with prolonged milling. This leads to the assumption that due to the mechanochemical treatment an amorphization (i.e disruption in long range order in the crystal lattice) is occurring with only small amounts of bound-water loss compared to a calcination process, where all the bound-water is removed for this temperature range (Garbev et al., 2014). The distortion in long-range order causes an increase in surface energy, which should result in higher reactivity.

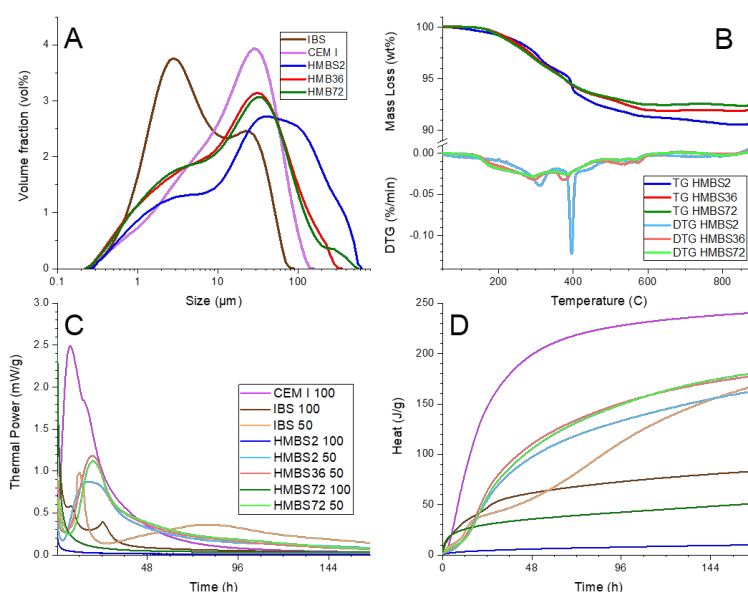


Figure 1 A) Particle size distributions of powder samples. B) TG and DTG curves of HMBS samples. C) and D) Thermal power and cumulative heat curves of the isothermal calorimetry measurements, respectively.

3.3 Isothermal calorimetry

The reactivity of hydrothermally and mechanochemically activated BOF slag was evaluated with isothermal calorimetry (Figure 1 C and D) and eight samples were measured for 7 days. Three of those samples are used as comparison, which included a pure CEM I sample, a pure IBS sample and a 50:50 mix of IBS and CEM I. HMBS samples have been measured pure (e.g. HMBS2 100) or with CEM I in a 50:50 blend by mass (e.g. HMBS22 50). Two questions were addressed: i) what is the effect of mechanochemical activation on the reactivity of HMBS samples and ii) do HMBS samples still delay the hydration of CEM I like regular BOF slag. To answer the first question, HMBS2 100 and HMBS72 100 are compared. HMBS2 100 has a significantly lower total heat release after 7 days (~ 10 J/g) compared to HMBS72 100 (~ 50 J/g). Moreover, the pure HMBS samples have generated less heat than the IBS 100 sample (~ 83 J/g). Hence, autoclaving BOF slag combined with mechanochemical activation does not seem to be a good alternative to create a standalone binder because both HMBS2 100 and HMBS72 100 generate the lowest amount of heat of all samples significant milling causes large amount of agglomeration rather than fine particles than can hydrate. However, blended HMBS-CEM I samples perform significantly better during the first 7 days of the calorimetry measurement compared to IBS with CEM I even at greater particle fineness. The in the literature reported delay of hydration of CEM I by BOF slag is the best visible in the cumulative heat curve of IBS 50. IBS 50 has a lower amount of heat generated compared to all blended HMBS CEM I samples until ~ 6 days after the start of hydration, when

IBS 50 surpasses HMBS2 50 in heat generated. More mechanochemical activation (> 2 min) promotes heat generation in blends with CEM I, but at some point (between 7 and 14 days) it is expected that IBS 50 will surpass HMBS36 50 and HMBS72 50 (see Fig 1 D). The evaluation of strength development still needs to be investigated (EN-197 for 50 wt% substitution of CEM I and EN-450 for 25 wt% substitution of CEM I) to determine the respective activity indices.

4. Conclusions

This study investigated the combination of hydrothermal and mechanochemical treatment in order to develop an ACM or SCM on basis of BOF slag as raw material. BOF slag is known to be reactive under hydrothermal conditions and produces various reaction products such as portlandite, hydrogarnet, brucite, α -C₂SH and amorphous phase. We found that our mechanochemical treatment reduced particle fineness and the amount of all reaction products that have developed during the hydrothermal treatment, but a limited extend. HMBS show less reactivity than conventional BOF slag, however it is more compatible with CEM I compared to conventional BOF slag based on isothermal calorimetry. Moreover, in order to increase the reactivity, longer autoclaving could be considered to increase the amount of reaction product, or, as alternative for mechanochemical activation, calcination might be explored. However, whether such BOF slag treatments create product value is questionable due to the labour intensive preparation, which includes initial milling, and autoclaving followed by another milling operation, but could be a possible option for recycling such future binder products.

Acknowledgements

The authors would like to thank for the financial support of the Nederlandse Organisatie voor Wetenschappelijk Onderzoek (NWO) by funding this research (project no.10023338) and Materials Innovation Institute (M2i) for managing this project. Also, the authors would like to acknowledge the sponsors of this research, which are Tata Steel IJmuiden, ENCI, v. d. Bosch Beton, Blue Phoenix Group and Hess AAC Systems.

References

- Ahmed, M.J., Santos, W.F., Brouwers, H.J.H., 2023. Air granulated basic Oxygen furnace (BOF) slag application as a binder : Effect on strength , volumetric stability , hydration study , and environmental risk. *Constr. Build. Mater.* 367. <https://doi.org/10.1016/j.conbuildmat.2023.130342>
- Balcár, I., Korim, T., Kovács, A., Makó, E., 2016. Mechanochemical and thermal activation of kaolin for manufacturing geopolymer mortars – Comparative study. *Ceram. Int.* 42, 15367–15375. <https://doi.org/10.1016/j.ceramint.2016.06.182>
- Franco Santos, W., Schollbach, K., Melzer, S., Laan, S.R. Van Der, Brouwers, H.J.H., 2023. Quantitative analysis and phase assemblage of basic oxygen furnace slag hydration. *J. Hazard. Mater.* 450. <https://doi.org/10.1016/j.jhazmat.2023.131029>
- Garbev, K., Beuchle, G., Schweike, U., Merz, D., Dregert, O., Stemmermann, P., 2014. Preparation of a novel cementitious material from hydrothermally synthesized C-S-H phases. *J. Am. Ceram. Soc.* 97, 2298–2307. <https://doi.org/10.1111/jace.12920>
- Kaja, A.M., Delsing, A., van der Laan, S.R., Brouwers, H.J.H., Yu, Q., 2021. Effects of carbonation on the retention of heavy metals in chemically activated BOF slag pastes. *Cem. Concr. Res.* 148, 106534. <https://doi.org/10.1016/j.cemconres.2021.106534>
- Martins, A.C.P., Franco de Carvalho, J.M., Costa, L.C.B., Andrade, H.D., de Melo, T.V., Ribeiro, J.C.L., Pedroti, L.G., Peixoto, R.A.F., 2021. Steel slags in cement-based composites: An ultimate review on characterization, applications and performance. *Constr. Build. Mater.* 291, 123265. <https://doi.org/10.1016/j.conbuildmat.2021.123265>
- Murphy, J.N., Meadowcroft, T.R., de Assis Moreira, R., Barr, P. V., 1997. Enhancement of the cementitious properties of steelmaking slag. *Can. Metall. Q.* 36, 315–331. <https://doi.org/10.1179/cm.1997.36.5.315>
- Pöhlmann, H., 2021. *Industrial Waste*, 1st ed. de Gruyter, Berlin, Germany. <https://doi.org/https://doi.org/10.1515/9783110674941>
- Vizcayno, C., de Gutiérrez, R.M., Castello, R., Rodriguez, E., Guerrero, C.E., 2010. Pozzolan obtained by mechanochemical and thermal treatments of kaolin. *Appl. Clay Sci.* 49, 405–413. <https://doi.org/10.1016/j.clay.2009.09.008>

- Wang, S., Wang, C., Wang, Q., Liu, Z., Qian, W., Jin, C.Z., Chen, L., Li, L., 2018. Study on cementitious properties and hydration characteristics of steel slag. *Polish J. Environ. Stud.* 27, 357–364. <https://doi.org/10.15244/pjoes/74133>
- Zepper, J.C.O., van der Laan, S.R., Schollbach, K., Brouwers, H.J.H., 2023. Reactivity of BOF slag under autoclaving conditions. *Constr. Build. Mater.* 364. <https://doi.org/10.1016/j.conbuildmat.2022.129957>

Optimization of low clinker limestone calcined clay cement (LC³) concrete mixes as further carbon footprint reduction strategy

B. Malchiodi^{1*}, H. Hafez², and K. Scrivener³

¹ *Laboratory of Construction Materials, EPFL STI IMX LMC, Station 12, 1015 Lausanne, Switzerland.
beatrice.malchiodi@epfl.ch*

² *School of Civil Engineering, Faculty of Engineering and Physical Sciences, University of Leeds, LS2 9DY Leeds, United Kingdom.
h.hafez@leeds.ac.uk*

³ *Laboratory of Construction Materials, EPFL STI IMX LMC, Station 12, 1015 Lausanne, Switzerland.
karen.scrivener@epfl.ch*

ABSTRACT

The decarbonization of the construction industry can contribute to an 8% reduction of overall CO₂ emissions by 2050 only if effective and rapid actions are adopted. There is a clear consensus that reducing the clinker content in cement along with reducing the cement content in concrete is the principal strategy to achieve this goal. Combining both premises, this study was designed to further reduce the carbon footprint of the most promising and ready-to-use sustainable LC³ binder (Limestone Calcined Clay Cement) and of LC³ structural concrete. The concrete mixes were designed to reduce the LC³ binder content below the 300 kg/m³ prescribed by the construction codes (250 kg/m³) while replacing up to 75% of the clinker content in cement.

The fresh, mechanical and durability properties of the designed concrete mixes were tested and compared to those of the correspondent Ordinary Portland cement (OPC) concrete. The results showed that a lower binder content, given proper rheology maintained, did not involve a loss in performance. Moreover, LC³ concrete mixes with a 40-65% reduction in clinker content showed comparable mechanical and even enhanced durability performance against the control OPC concrete mixes. These performance indicators were then integrated into the functional unit of a cradle-to-gate life cycle assessment to compare the environmental impact of each LC³ concrete mix. The strategies followed showed a potential reduction in the carbon footprint of around 55% compared to the OPC concrete currently prescribed by the construction codes.

KEYWORDS: *Carbon footprint, Limestone calcined clay cement, blended cement concrete, life cycle assessment, performance-based standards.*

1. Introduction

The need for a sustainable built environment is directing construction and building materials research towards exploring effective strategies to produce concrete more sustainably (Colangelo et al., (2018)). Among the identified strategies, reducing the amount of clinker in concrete without compromising its performance is among the most effective (Miller et al., (2018)). A possible solution is to replace clinker with low-energy material such as calcined clay and limestone, as in the newly established Limestone Calcined Clay Cement (LC³) (Sharma et al., (2021)). Previous studies show that LC³ concrete utilizing calcined clays with >40% kaolinitic content exhibits comparable compressive strength to the reference OPC concrete (Du et al., (2020)). Further reduction of clinker in LC³ blends seems promising but has not been explored rigorously yet. Another possible solution to further lower clinker use is reducing the binder content in concrete. Currently, most building codes limit the binder content to a minimum of 300 kg/m³ for exposed structural concrete, although recent studies challenged this limiting factor (Scrivener et al., (2018a)).

The two-fold objective of this study is to investigate the mechanical and durability performance of concrete mixes with very high clinker replacement and a reduced binder content of 250 kg/m³, and then to assess the environmental impact savings potential of the concrete mixes meeting the minimum performance requirements. The outcome is a step towards the establishment of performance-based concrete specifications and an empirical contribution to the concrete performance testing of novel low-carbon concrete.

2. Materials and Methods

2.1. Materials

As shown in Table 1, five concrete mixes were designed: an OPC and four LC³ mixes. The mixes were designed to lower the clinker factor by replacing 40% and 50% clinker with calcined clay and limestone (2:1 ratio) as well as 65% and 75% with calcined clay, limestone and calcium hydroxide (2:1:1 ratio). The water-to-binder ratio was fixed at 0.6 for all mixes, and the total binder content at 250 kg/m³. The OPC used in the study was CEM I 42.5N Normo4 (Holcim, Switzerland), while the clay was sourced from a quarry in Northern Ireland and calcined at the EPFL laboratories. The limestone powder and aggregates (0/4 mm and 4/22.4 mm) were sourced from local quarries, and both fractions of natural aggregates were used in a dry state. A PCE-based superplasticizer (SP), pure commercial gypsum (≥ 98%) and calcium hydroxide (95%) were also used. The concrete mixes were designed based on trial mixes to achieve a minimum slump of 100 mm. The concrete was cast and all specimens were stored under the specified curing conditions as per the standards till the testing day.

Table 1: The OPC and LC³ concrete mix designs and environmental impact inventory data

| Mix ID | CEMI 42.5 | Calcined clay | Limestone | Calcium Hydroxide | Gypsum | SP | Sand 0/4 | Gravel 4/22.4 |
|--|-------------------|-----------------------|-----------|-------------------------|-----------|-----------------------|-----------|---------------|
| | kg/m ³ | | | | | | | |
| OPC | 250 | 0 | 0 | 0 | 0.00 | 0.62 | 819 | 1099 |
| LC ³ -25 | 74 | 87 | 44 | 44 | 0.75 | 3.70 | 801 | 1073 |
| LC ³ -35 | 99 | 75 | 38 | 38 | 1.00 | 3.09 | 803 | 1077 |
| LC ³ -50 | 133 | 75 | 38 | 0 | 5.00 | 1.85 | 811 | 1087 |
| LC ³ -60 | 160 | 57 | 30 | 0 | 2.51 | 1.85 | 812 | 1089 |
| GWP inventory (kg CO ₂ eq/kg) | 0.83 | 0.35 | 0.09 | 0.9 | 0.19 | 1.86 | 0.02 | 0.01 |
| Reference | Ecoinvent | Pillai et al., (2018) | Ecoinvent | Laveglia et al., (2022) | Ecoinvent | Walach et al., (2019) | Ecoinvent | |

2.2. Testing program

The slump cone test was performed according to the EN 12350-2 standard and the mixes with slump <100 mm were rejected, while the SP content was adjusted accordingly. Also, according to EN 12390-3 standard, cylinders with a 110 mm diameter and 220 mm height were tested after 28 days for compressive strength. As per the ASTM C1202-12 standard, cylinders with 100 mm diameter and 50 mm thickness were cored from cured samples and tested after 28 days for chloride resistivity. For each test, the average and standard deviation values of four specimens were recorded.

2.3. LCA study

First, a Cradle-to-Gate scope was defined for the Life Cycle Assessment of the sustainable concrete mixes. This included all the cycle processes from the production of the concrete constituents to the delivery to the concrete batch plant until the concrete production. The unit volume of concrete was selected as the functional unit (FU) for LCA, i.e., the LCA element responsible for quantifying the carbon footprint. In the second stage of the LCA, an inventory database was prepared considering the Ecoinvent database and

recent peer-reviewed articles. The database included the carbon footprint, or upstream impact, of each concrete element constituent (see Table 1). The third and final stage of the LCA estimated the environmental impact of the involved concrete mixes. This was performed by adding up the individual environmental impacts of all the associated processes.

3. Results and Discussions

3.1. Experimental results

As displayed in Table 2, all concrete mixes achieved a characteristic value for 28-day compressive strength higher than 35 MPa, which proved the hypothesis on the possibility of using concrete with a binder content as low as 250 kg/m³. The results also showed that all LC³ concrete mixes performed similarly to OPC except for the 75% clinker replacement mix (LC³-25). The results are consistent with the findings from the literature on the pozzolanic reactivity of binary systems where the calcined clay replaces up to 50% clinker (Maraghechi et al., (2018)). The novelty lies in achieving the same strength by replacing 15% more clinker with calcium hydroxide. Table 3 shows that, similarly to the literature findings (Scrivener et al., (2018b)), the chloride ions penetration capacity was more than halved in all LC³ concrete mixes compared to OPC. According to the ASTM C1202-12, the probability of chloride ions penetration in OPC concrete was “moderate”, while that of LC³ concrete was “very low”.

Table 2: Compressive strength and RCPT results for the OPC and LC³ concrete mixes

| Mix ID | f _{cm} (MPa) | | RCPT (Coulombs) | |
|---------------------|-----------------------|---------|-----------------|---------|
| | mean | st dev. | mean | st dev. |
| OPC | 39.90 | 0.50 | 2478.17 | 103.04 |
| LC ³ -25 | 35.28 | 0.75 | 1160.58 | 131.44 |
| LC ³ -35 | 39.80 | 1.01 | 979.03 | 98.79 |
| LC ³ -50 | 38.80 | 2.09 | 738.55 | 22.16 |
| LC ³ -60 | 39.73 | 0.87 | 705.99 | 37.73 |

3.2. LCA results

The LC³-25 mix was excluded from the LCA comparison limiting it to the concrete mixes that met the minimum compressive strength requirements. As seen in Figure 1, reducing the binder content in OPC to only 250 kg/m³ had a 25% lower environmental impact per unit concrete volume compared to the average of concrete with the same 40 MPa 28-day compressive strength and higher binder contents (Hafez et al., (2020)). Moreover, LC³ concrete achieved a 30% reduction in the carbon footprint per unit volume compared to the optimized OPC concrete and 55% compared to the average. It is worth noting that, although it reduced the clinker by 15% more, the LC³-35 mix had a marginally higher carbon footprint per unit volume than LC³-50. The reason is that the inventory data for calcium hydroxide set a higher GWP than OPC per unit mass, so the addition of 15% of calcium hydroxide in replacement of 15% more clinker is not very effective.

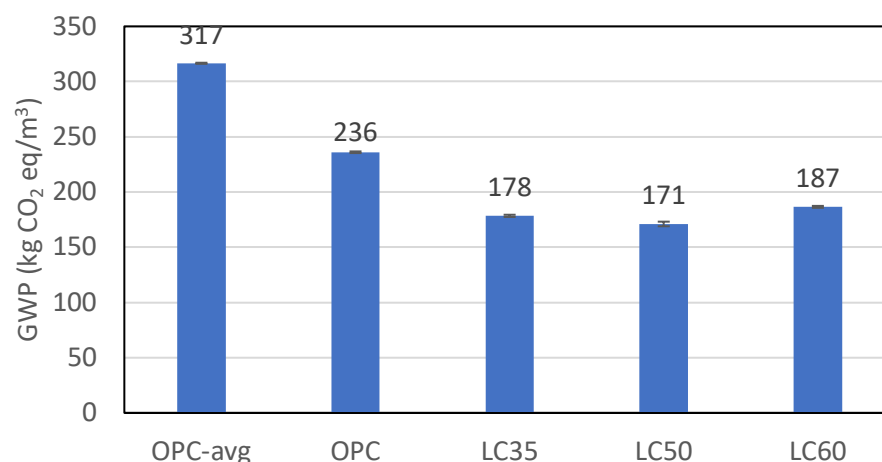


Figure 1: LCA results for the per unit volume carbon footprint of LC³ vs OPC concrete

4. Conclusions

This case study showed the potential of producing structural concrete with adequate mechanical and durability performance with a binder content lower than the 300 kg/m³ prescribed in most building codes. The second part assessed the potential environmental savings in decreasing the clinker content within the 250 kg/m³ of the binder. Replacing 50% clinker with a mixture of limestone and calcined clay showed higher chloride penetration resistance, the same compressive strength and 55% less carbon footprint compared to OPC concrete.

References

- Colangelo, F., Forcina, A., Farina, I. & Petrillo, A. 2018. Life Cycle Assessment (LCA) of different kinds of concrete containing waste for sustainable construction. *Buildings*, 8.
- Du, H. and Dai Pang, S., 2020. High-performance concrete incorporating calcined kaolin clay and limestone as cement substitute. *Construction and Building Materials*, 264, p.120152.
- Hafez, H., Kurda, R., Cheung, W.M. and Nagaratnam, B., 2019. A systematic review of the discrepancies in life cycle assessments of green concrete. *Applied Sciences*, 9(22), p.4803.
- Laveglia, A., Sambataro, L., Ukrainczyk, N., De Belie, N. and Koenders, E., 2022. Hydrated lime life-cycle assessment: Current and future scenarios in four EU countries. *Journal of Cleaner Production*, 369, p.133224.
- Maraghechi, H., Avet, F., Wong, H., Kamyab, H. and Scrivener, K., 2018. Performance of Limestone Calcined Clay Cement (LC3) with various kaolinite contents with respect to chloride transport. *Materials and structures*, 51(5), pp.1-17.
- Miller, S. A. 2018. Supplementary cementitious materials to mitigate greenhouse gas emissions from concrete: can there be too much of a good thing? *Journal of Cleaner Production*, 178, 587-598.
- Pillai, R.G., Gettu, R., Santhanam, M., Rengaraju, S., Dhandapani, Y., Rathnarajan, S. and Basavaraj, A.S., 2019. Service life and life cycle assessment of reinforced concrete systems with limestone calcined clay cement (LC3). *Cement and Concrete Research*, 118, pp.111-119.
- Scrivener, K.L., John, V.M. and Gartner, E.M., 2018a. Eco-efficient cements: Potential economically viable solutions for a low-CO₂ cement-based materials industry. *Cement and Concrete Research*, 114, pp.2-26.
- Scrivener, K., Avet, F., Maraghechi, H., Zunino, F., Ston, J., Hanpongpan, W. and Favier, A., 2018b. Impacting factors and properties of limestone calcined clay cements (LC3). *Green Materials*, 7, pp.3-14.
- Sharma, M., Bishnoi, S., Martirena, F. and Scrivener, K., 2021. Limestone calcined clay cement and concrete: A state-of-the-art review. *Cement and Concrete Research*, 149, p.106564.
- Wałach, D., Dybeł, P., Sagan, J. and Gicala, M., 2019. Environmental performance of ordinary and new generation concrete structures—a comparative analysis. *Environmental Science and Pollution Research*, 26, pp.3980-3990.

RESEARCH ON MULTI-SOLID WASTE CO-EXCITATION OF LEAD SMELTING SLAG TO PREPARE GREEN FILLING MATERIALS FOR MINES AND ITS PERFORMANCE

W.H. Liu¹, R.H. Du², Z.Z. Zhao³, Y.F. Wan⁴, H.Li^{5*}

¹ College of materials science and engineering, Xi'an University of Architecture and Technology, Xi'an, China
Email: xupinjing6100@xauat.edu.cn

² Ecological Cement Engineering Research Center of Ministry of Education, Xi'an, China
Email: lw2204485@163.com

³ College of materials science and engineering, Xi'an University of Architecture and Technology, Xi'an, China
Email: liuwenzian@sina.com

⁴ Shaanxi Ecological Cement & Concrete Engineering Technology Research Center, Xi'an, China
Email: 17570001@qq.com

⁵ College of materials science and engineering, Xi'an University of Architecture and Technology, Xi'an, China
Email: sunshine_lihui@126.com

ABSTRACT

In this paper, the ecological cementitious materials were made using trace amounts of cement clinker (CC), lime ash slag (LAS), slag powder (SP) and bischofite (BF) to promote their activity. To create the unclassified tailings sand (UTS) mine cemented backfill materials (MCBM), the prepared cementitious materials were combined with tailing sand. The results show that the optimal ratio of binder composition by mass is 46% for LSS, 20% for lime ash slag (LAS), 13% for slag powder (SP), 17% for cement clinker (CC), and 4% for bischofite (BF) at which time the compressive strengths of specimens at 3, 7, and 28 days are 11.1 MPa, 16.9 MPa, and 24.2 MPa, respectively. The backfill slurry with a binder-sand ratio of 1:2 and a solid content of 74% has a fluidity of 259 mm and a 28-day compressive strength of 5.48 MPa, which meets the requirements for high-strength grade MCBM for self-weight backfill. The results of MIP show that the larger the cement-sand ratio, the higher the relative proportion of harmless pores and the higher the mechanical properties of the filling. The hydration products will become denser with the increase of cement-sand ratio, and the encapsulation of tailings will be enhanced. The solidification ratio of the MCBM for each heavy metal exceeds 70%, and the leaching of heavy metals conforms to the Chinese Class IV groundwater standard.

KEYWORDS: *Lead smelting slag, Cemented filling material, Mechanical properties, Fluidity, Heavy metal leaching*

1. Introduction

Lead Smelting Slag (LSS) is a hazardous waste slag produced by water quenching and rapid cooling after high-temperature separation of lead from lead ore in metallurgical furnaces (Zhang et al. 2020). The majority of this slag is left untreated and is landfilled or piled up in random places (Han et al. 2017). LSS, is very easy to pollute the surrounding soil and groundwater (Gu et al. 2021). Some researchers extracted Pb and Zn metals from Pb and Zn smelting slag and then used the remaining Pb and Zn slag to produce bricks by sintering (Hu et al. 2014). Others have also removed harmful elements from LSS and utilized it as a recycling fertilizer (Mikula et al. 2022, Song et al. 2019). Buzatu et al (2014). used granulated Pb-Zn slag as aggregate and discovered that granulated Pb smelting slag has superior shear resistance and is an excellent structural material for road construction due to its water resistance and low pore structure. However, when LSS is used as an aggregate, its value is not fully realized (Ma et al. 2022, Penpolcharoen et al. 2005, Zhang, et al. 2005, Albitar et al. 2005). Mine backfill mining is a widespread form of modern mining that includes hydraulic backfill, sand and gravel backfill, and tailings cementation backfill (Xue et al. 2022). However, cement is the main cementing material used for mine backfill at present, and the cost of cement accounts for 75% of mine backfill cost (Qi et al. 2019). Therefore, the use of metallurgical slag to partially or completely replace cement and reduce the cost of mine backfill is the main research

direction at present (Mashifana et al. 2021, Xiao et al. 2021, Lan, et al. 2020, Pan et al. 2005). For the above reasons, this study mainly carried out the feasibility experimental study of preparing ecological cementitious materials and mine backfill materials with LSS as the main raw material, elaborated the properties and hydration products of the prepared ecological cementitious materials and the fluidity performance, mechanical properties, pore structure characteristics and solidification characteristics for heavy metal of ecological mine filling materials were analyzed.

2. Experimental Results and discussion

2.1 Material

The materials used in this paper are LSS, lime ash slag (LAS), bischofite (BF), slag powder (SP), cement clinker (CC), and unclassified tailing sand (UTS).

2.2 Methods

In this study, cementitious materials and MCBM were prepared separately. As shown in Table1, a single-variable stepwise change experimental method was used in this paper to optimize the design of the ratio of LSS-based multi-solid waste cementitious materials.

Table 1 Design table of cementitious material composition.

| | Sample | LSS(%) | LAS(%) | BF(%) | CC(%) | SP(%) |
|-------------------|--------|--------------------------|--------|-------|-------|-------|
| Binary system | A1 | 70 | 30 | -- | -- | |
| | A2 | 75 | 25 | -- | -- | |
| | A3 | 80 | 20 | -- | -- | |
| | A4 | 85 | 15 | -- | -- | |
| | A5 | 90 | 10 | -- | -- | |
| Ternary system | B1 | Optimal ratio of group A | | 3 | -- | |
| | B2 | | | 4 | -- | |
| | B3 | | | 5 | -- | |
| | B4 | | | 6 | -- | |
| | B5 | | | 7 | -- | |
| Quaternary system | C1 | Optimal ratio of group B | | | 10 | |
| | C2 | | | | 15 | |
| | C3 | | | | 20 | |
| | C4 | | | | 25 | |
| | C5 | | | | 30 | |
| Quinary system | D1 | Optimal ratio of group C | | | | 5 |
| | D2 | | | | | 10 |
| | D3 | | | | | 15 |
| | D4 | | | | | 20 |
| | D5 | | | | | 25 |

The TCLP method was used to test the leaching concentration of heavy metals in samples. The fluidity of the MCBM slurry was tested based on the Chinese standard GB/T 2419-2005. Mercury intrusion porosimetry is used to test the pore size distribution of the filling material, and the scanning electron microscope (SEM) is used to examine the microscopic morphology of the hydration products of cement-filled materials.

2.3 Results and discussion

2.3.1 Compressive strength of cementitious materials

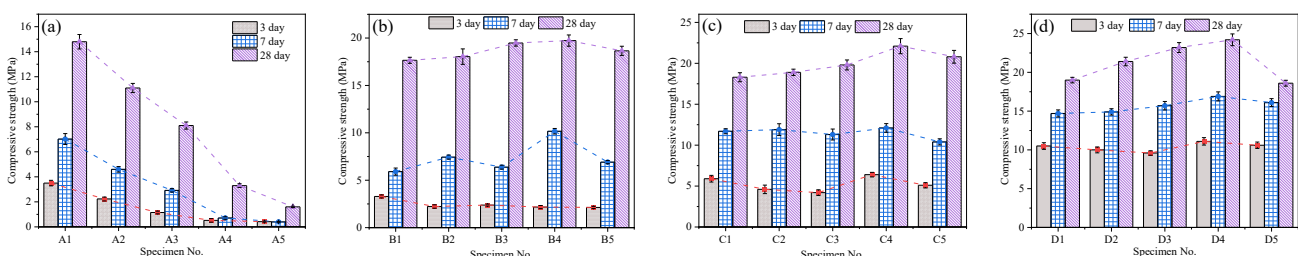


Fig. 1. Compressive strength of cementitious materials at different curing ages.

The compressive strengths of LSS-based multi-solid waste cementitious materials at different ratios and curing ages are shown in Fig. 1. According to Fig. 1, the optimum compressive strength ratio is D4 (46%-LSS+20%-LAS+4%-BF+17%-CC+13%-SP), and the compressive strengths of the cementitious materials are 11.1 MPa, 16.9 MPa, and 24.2 MPa at 3, 7, and 28 days, respectively.

2.3.2 The filling performance of MCBM

According to Fig. 2(a), the fluidity of the MCBM decreases as the slurry concentration increases. When the ratio of binder-sand is 1:2 and the slurry concentration is 74%, the optimal fluidity is 259 mm (> 220 mm), which satisfies the self-weight filling requirement. When the binder-sand ratio is 1:3 and 1:6, the fluidity at various slurry concentrations satisfies self-weight filling requirements (Li et al. 2020). According to Fig. 2(b), the 7 day compressive strengths of the backfill materials are 2.08 MPa, 2.17 MPa, and 2.51 MPa when the ratio of binder-sand is 1:2 and the slurry concentrations are 74%, 75%, and 76%, respectively; and the 28-day compressive strengths are 5.48 MPa, 5.96 MPa, and 7.33 MPa. This satisfies the technical requirements for one-step mining and two-step mining casting layers in the mine. When the ratio of binder-sand is 1:3 and the concentration of slurry is 74%, 75%, and 76%, respectively, the 28-day compressive strengths of backfill materials are 3.15 MPa, 3.47 MPa, and 3.58 MPa.

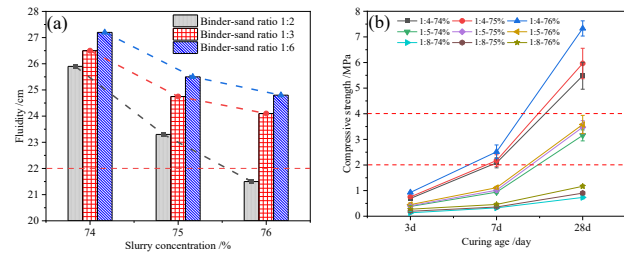


Fig.2. Fluidity of the backfill slurry and compressive strength of the MCBM: (a) fluidity; and (b) compressive strength.

2.3.3 XRD analysis of cementitious materials

After 3, 7, and 28 days of curing, the XRD patterns of the hydration products of the net slurry specimens of cementitious materials are depicted in Fig. 3. The $\text{Ca}(\text{OH})_2$ absorption peaks are visible near 18° and 34° in the XRD patterns at various curing ages, and the peaks significantly diminish as the curing age is increased. This demonstrates that $\text{Ca}(\text{OH})_2$ is involved in the hydration reaction process. CaCO_3 is responsible for the peak at around 29° , which is most likely due to LAS or the carbonation reaction of $\text{Ca}(\text{OH})_2$. Friedel's salt ($\text{Ca}_2\text{Al}(\text{OH})_6\text{Cl}\cdot 2\text{H}_2\text{O}$) is most likely the hydration product near 11° . It can be seen that the peak at this point gets higher as the age of curing increases. This means that the hydration reaction is still going on and that the crystalline shape of the hydration products is getting more complete. Analysis of the XRD patterns revealed the presence of the gypsum mineral phase in the early stage of the hydration reaction, but gypsum was gradually consumed in the later stage. The presence of gypsum provides the conditions for the formation of AFt, which will be converted to AFm after the reduction of gypsum, and the production of Friedel's salt is closely related to AFm.

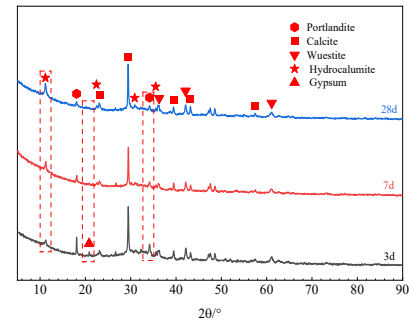


Fig.3. XRD patterns of cementitious materials

2.3.4 Pore size analysis of MCBM

After 28 days of curing, the porosity of the backfill with various binder-sand ratios was analysed using MIP; the results are depicted in Fig. 4.

It can be observed that the backfill with a 1:2 binder-sand ratio contains more pores with pore size < 100 nm, and these pores are regarded as having no effect on the compressive strength of the filler. At a binder-sand ratio of 1:2 and a slurry concentration of 74%, the total porosity was 36.06% and the average pore size was 25.28 nm. As the binder-sand ratio decreased, the total porosity and average pore size increased. For a binder-sand ratio of 1:6, the total porosity rises to 38.54 %, and the average pore size rises to 91.61 nm, which is proportional to the amount of hydration products produced by the cementitious material. The greater the cementitious material content, the more abundant the hydration products and the ensuing decrease in porosity, which leads to an increase in the compressive strength of the filler.

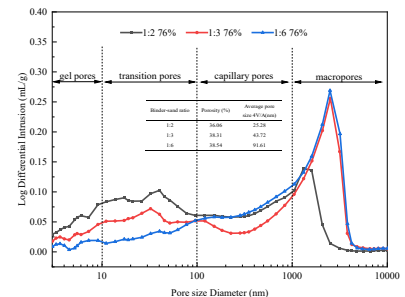


Fig.4. Pore structure analysis of MCBM

2.3.5 SEM analysis of MCBM

From Fig.5, it can be seen that, with a binder-sand ratio of 1:6, the microstructure of the backfill is dispersed and more pore structures are clearly visible. It can be observed that the hydration products in the binder-sand ratio of 1:2 backfill are bundant and dense in structure, while the generation of hydration products gradually decreases and the structure gradually thins out as the binder-sand ratio decreases. In contrast to the backfill with a binder-sand ratio of 1:6, the hydration products with a binder-sand ratio of 1:2 and 1:3 are primarily in the form of lattices when magnified 10,000 times. As the ratio of binder-sand increases, the hydration products become more compact, leading to an increase in compressive strength.

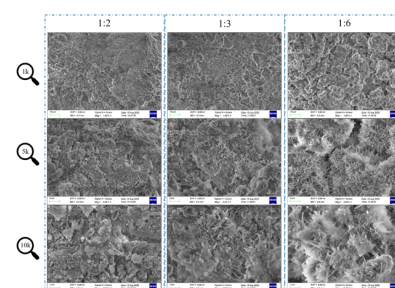


Fig.5. Microscopic morphology of the filler with for curing 28d.

3. Conclusions

The following conclusions can be drawn in light of the findings.

- (1) Under mechanical and chemical excitation of solid wastes, such as LAS and BF, LSS can produce cementitious activity. As the binder-sand ratio increases, the fluidity performance of the backfill slurry degrades. The fluidity of backfill slurry with a binder-sand ratio of 1:2 and a concentration of 74% is 259 mm, which satisfies the requirements for self-weight filling and conveying. After 28 days of natural curing, the compressive strength of backfill with a binder-sand ratio of 1:2 and a concentration of 74% can reach 5.48 MPa.
- (2) The content of the cementitious material affects the leaching of heavy metals from the filler. The larger the binder-sand ratio, the smaller the leaching of Pb, Zn, Ni, Cu, and Cu elements, which is the beneficial effect of cementing material for solidifying heavy metals. The solidification efficiency of the fill materials with different binder-sand ratios on heavy metals in this paper is higher than 70%, and it meets the Chinese standard GB/T14848-2017 for Class IV water quality.

References

- Albitar, M., Mohamed Ali, M. S., Visintin, P., Drechsler, M. (2015) "Effect of granulated lead smelter slag on strength of fly ash-based geopolymer concrete", *Construction and Building Materials*, 83:128-135.
- Buzatu, T., Talpoş, E., Petrescu, M. I., Ghica, V. G., Iacob, G., Buzatu, M. (2014) "Utilization of granulated lead slag as a structural material in roads constructions", *Journal of Material Cycles and Waste Management*, 17(4): 707-717.
- Gu, M., Zhong, Y., Wang, L., Guo, Z. (2021) "Kinetics study of heavy metal removal from the lead smelting slag by carbothermic reduction: Effect of phase transformation", *Journal of Environmental Chemical Engineering*, 9(6): 106516.
- Han, J., Liu, W., Qin, W., Zhang, T., Chang, Z., Xue, K. (2017) "Effects of sodium salts on the sulfidation of lead smelting slag", *Minerals Engineering*, 108:1-11.
- Hu, H., Deng, Q., Li, C., Xie, Y., Dong, Z., Zhang, W. (2014) "The recovery of Zn and Pb and the manufacture of lightweight bricks from zinc smelting slag and clay", *Journal of Hazardous Materials*, 271:220-227.
- Lan, W., Wu, A., Yu, P. (2020) "Development of a new controlled low strength filling material from the activation of copper slag: Influencing factors and mechanism analysis", *Journal of Cleaner Production* 246:119060.
- Li, J., Zhang, S., Wang, Q., Ni, W., Li, K., Fu, P., Hu, W., Li, Z. (2020) "Feasibility of using fly ash-slag-based binder for mine backfilling and its associated leaching risks", *Journal of Hazardous Materials*, 400:123191.
- Ma, H., Niu, X., Feng, J. (2022) "Mechanical and microstructural property evolutions of MgO-slag cementitious materials under high temperatures", *Journal of Building Engineering*, 104756.
- Mashifana, T., Sithole, T. (2021) "Clean production of sustainable backfill material from waste gold tailings and slag", *Journal of Cleaner Production*, 308:127357.
- Mikula, K., Skrzypczak, D., Izydorczyk, G., Basladyńska, S., Szustakiewicz, K., Gorazda, K., Moustakas, K., Chojnacka, K., Witek-Krowiak, A. (2022) "From hazardous waste to fertilizer: Recovery of high-value metals from smelter slag's", *Chemosphere*, 297:134226.
- Pan, D.a., Li, L., Tian, X., Wu, Y., Cheng, N., Yu, H. (2019) "A review on lead slag generation, characteristics, and utilization", *Resources Conservation And Recycling*, 146:140-155.
- Penpolcharoen, M. (2005) "Utilization of secondary lead slag as construction material", *Cement and Concrete Research*, 35(6): 1050-1055.
- Qi, C., Fourie, A. (2019) "Cemented paste backfill for mineral tailings management: Review and future perspectives", *Minerals Engineering*, 144:106025.
- Song, S., Sun, W., Wang, L., Liu, R., Han, H., Hu, Y., Yang, Y. (2019) "Recovery of cobalt and zinc from the leaching solution of zinc smelting slag", *Journal of Environmental Chemical Engineering*, 7(1): 102777.
- Xiao, B., Wen, Z., Miao, S., Gao, Q. (2021) "Utilization of steel slag for cemented tailings backfill: Hydration, strength, pore structure, and cost analysis", *Case Studies in Construction Materials*, 15: e00621.
- Xue, G., Yilmaz, E. (2022) "Strength, acoustic, and fractal behavior of fiber reinforced cemented tailings backfill subjected to triaxial compression loads", *Construction and Building Materials*, 338:127667.
- Zhang, P., Muhammad, F., Yu, L., Xia, M., Lin, H., Huang, X., Jiao, B., Shiao, Y., Li, D. (2020) "Self-cementation solidification of heavy metals in lead-zinc smelting slag through alkali-activated materials", *Construction and Building Materials*, 249:118756.
- Zhang, Q., Cao, X., Sun, S., Yang, W., Fang, L., Ma, R., Lin, C., Li, H. (2022) "Lead zinc slag-based geopolymer: Demonstration of heavy metal solidification mechanism from the new perspectives of electronegativity and ion potential", *Environmental Pollution*, 293:118509.

Effects of phosphate salts on the interfacial bonding between magnesium phosphate cement and steel fiber

X. Wang¹, C. Shi^{1*}, and X. Hu¹

¹ College of Civil Engineering, Hunan University, Changsha, 410082, PR China

Email: wangxin2021@hnu.edu.cn (Xin Wang); cshi@hnu.edu.cn (Caijun Shi); xianghu@hnu.edu.cn (Xiang Hu)

ABSTRACT

The interfacial zone between the fiber and matrix, as the weakest part in the composites, determines whether the advantages of fiber and matrix can exert but poorly understood among the interfacial bonding between MPC and steel fiber research efforts. In this paper, an effective and simple double-side pullout testing method was carried out to characterize the bond properties of steel fiber in MPC. Electrochemical impedance spectroscopy, backscatter scanning electron microscopy, and micro-hardness measurement were applied to evaluate the quality of the interfacial zone. The results indicate that ammonium dihydrogen phosphate and potassium dihydrogen phosphate show significant effects on interfacial bonding. Magnesium ammonium phosphate cement (MAPC) produces ammonia during hydration, which is easy to form pores and voids in the interfacial zone. Besides, the microhardness of MPPC is lower than that of MAPC. The mixed use of ammonium dihydrogen phosphate and potassium dihydrogen phosphate in a 2:1 mass ratio to prepare MPC is conducive to reducing the porosity and increasing the hardness of the interface zone. In addition, phosphating effect which gradually increased with the increase of ammonium dihydrogen phosphate content is found at the interface zone. The microscopic analysis demonstrates the multiple interfacial interactions between steel fiber and MPC: the hydration products around the steel fiber form a highly compact interfacial zone with few defects, leading to mechanical interlock and strong friction effect; etching of the surface of mild steel fiber and penetration of soluble phosphate salts promote the chemical bond at the interface.

KEYWORDS: *Magnesium Phosphate Cement, Interfacial Zone, Steel Fiber, Phosphate Salts*

1. Introduction

Magnesium phosphate cement (MPC) is a new type of cementitious material that forms a chemical bond based on the acid-base reactions between magnesia (MgO) and soluble acid phosphate salts (typically ammonium dihydrogen phosphate (NH₄H₂PO₄, ADP) or potassium dihydrogen phosphate (KH₂PO₄, PDP).

Compared to ordinary Portland cement (OPC), MPC exhibits superior properties such as fast setting, rapid strength development, good volume stability, strong adhesive ability, and good corrosion resistance (Seehra et al., (1993), Fan et al., (2014), Fan et al., (2016)). Reports showed the brittle behavior and low strain hardening properties of MPC, which are mainly due to the high volume of cementitious compounds and crystalline hydration products (Zhang et al., (2021)). The addition of steel fiber can noticeably enhance the compressive strength, flexural strength, toughness, and ductility of MPC because of its high efficiency (Wang et al., (2022) Feng et al., (2018)). The interfacial zone between the fiber and matrix, as the weakest part in the composites, determines whether the advantages of steel fiber and MPC matrix can exert. Therefore, it is of great importance to investigate the interfacial bond between steel fiber and MPC.

Phosphate salt is an indispensable part of MPC, which plays a significant role in the hydration process and hardening properties of MPC. However, there is limited research on the influence of

phosphate salts on the bond properties between MPC and steel fiber. In this regard, the bond behavior of steel fiber and MPC prepared with different phosphate salts is investigated to explore the mechanisms of bond formation.

2. Experimental program

The chemical composition of dead-burnt MgO powder used in this experiment are summarized in Table1. Borax ($\text{Na}_2\text{B}_4\text{O}_7 \cdot 10\text{H}_2\text{O}$) with a purity of 99% and industrial grade PDP and ADP with a purity of 99% were used in this study. The standard sand and tap water were used. Steel fibers used in the study were straight and round, with a diameter of 0.5 mm and length of 30 mm, and a diameter of 1 mm and length of 50 mm. The tensile strength was around 1200 MPa.

Table 1 Chemical composition of MgO.

| Oxide | MgO | Al_2O_3 | SiO_2 | CaO | Fe_2O_3 | Others |
|---------|-------|-------------------------|----------------|------|-------------------------|--------|
| Content | 90.42 | 2.39 | 3.16 | 1.51 | 1.51 | 1.01 |

Table 2 Mixture ratio of MPC.

| No. | ADP content | PDP content | M/P mass ratio | Mass ratio of water to cement | Flow spread (mm) | 7d Compressive strength (MPa) |
|------|-------------|-------------|----------------|-------------------------------|------------------|-------------------------------|
| A1P0 | 100% | 0 | 3 | 0.12 | 204 | 80.6 |
| A2P1 | 66.7% | 33.3% | 3 | 0.125 | 210 | 77.9 |
| A1P1 | 50% | 50% | 3 | 0.13 | 203 | 75.5 |
| A1P2 | 33.3% | 66.7% | 3 | 0.135 | 208 | 70.9 |
| A0P1 | 0 | 100% | 3 | 0.14 | 190 | 69.3 |

Note: The dosage of borax which is used as a retarder set to 6.0% of MgO by mass. The mass ratio of sand to cement is set to 0.9 for MPC mortar.

MPC mortar was prepared according to the designed mixture in Table 2. In order to weaken the influence of the different flow spreads of MPC mortar on the degree of fiber being wrapped, the W/B of the specimen was slightly adjusted with the increase of the amount of PDP to maintain a constant flow spread between 190 to 210 mm. The compressive strength of MPC cured for 7d is shown in Table 2. MPC samples with dog-bone shaped and four steel fibers embedded were prepared to evaluate the pullout behavior according to CECS13-2009. Electrochemical impedance spectroscopy (EIS) tests were carried out by a two-electrode cell system using a CORR TEST 350H workstation. The impedance spectra of the specimens were analyzed using ZsimpWin software. Microstructural characterization of the interfacial zone of the embedded steel fiber and MPC was conducted by BSEM. Image J software was used to perform the successive narrow strip analysis, which can be shown in Fig.1. The micro-indentation was performed by HMAS D1000SM to evaluate the hardness of the interfacial zone. A load of 491 mN was applied to the samples for 10 s.

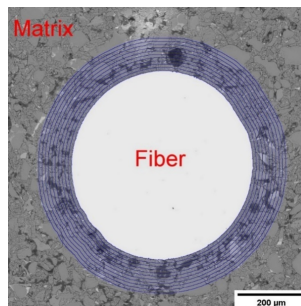


Fig. 1. Binary image representation of concentric rings for A1P0 sample at 7 d.

3. Results and discussion

3.1 Bond properties

The bond strength and pullout energy between steel fiber and MPC are shown in Fig. 2. The bond strength and pullout energy of fibers and MPC cured for 3 d are 56.25%~79.90% and 65.76%~80.60% of those of fiber and MPC cured for 90 d, respectively. It shows that the bond properties of MPC and steel fibers develop rapidly. Moreover, the bond properties of steel fibers in MPC are improved owing to the

combined use of ADP and PDP. The bond properties first increase and then decrease with the ADP content (by mass of phosphates) increasing from 0 to 100%. The pullout energy between steel fiber and A1P0, A2P1, A1P1, and A0P1 after 7d of curing are 79.95%, 95.13%, 93.16%, and 89.22% of that between steel fiber and A0P1.

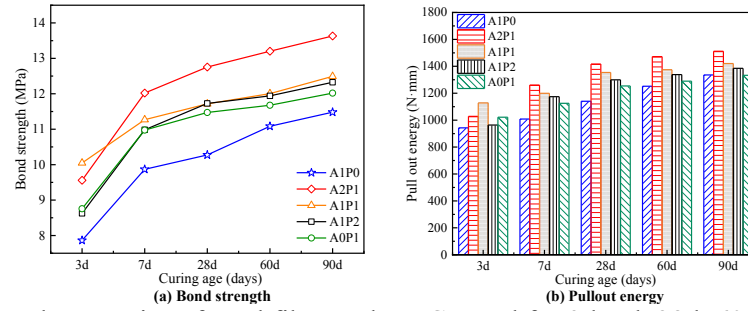
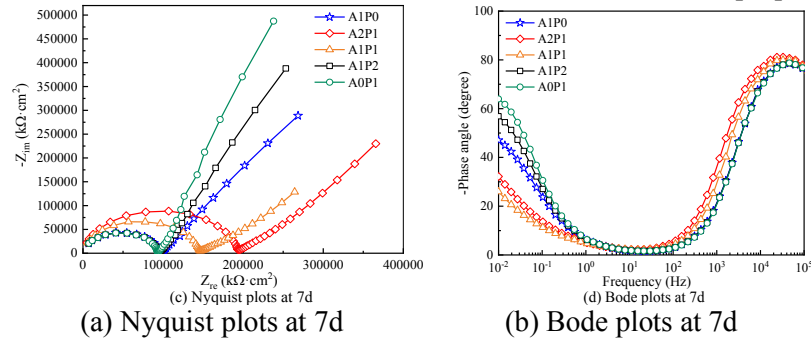


Fig. 2. Bond properties of steel fiber and MPC cured for 3d, 7d, 28d, 60d, and 90d

3.2 EIS

As shown in Fig. 3(a), the diameter of the semicircles of the Nyquist plot of the samples prepared with mixed phosphates is larger than that of the specimens prepared with ADP or PDP alone. In addition, as observed in Fig 3(b), the peak values of the phase angle of A2P1 and A1P1 in the high frequency domain are higher than that of A1P0. It indicates that the impedance value of the interfacial zone of the embedded fiber and MPC with mixed phosphates is larger than that of the A1P0 or A0P1, which means a denser microstructure of the interfacial zone between fiber and MPC with mixed phosphates than that of specimens prepared with ADP or PDP alone. These are consistent with the bond properties results.



(a) Nyquist plots at 7d (b) Bode plots at 7d

Fig. 3. Impedance spectra of steel fibers embedded in MPC

According to the characteristic of the interfacial zone between MPC and steel, **an equivalent circuit model $R(C1R1)(C2R2)$ is proposed to fit the EIS results.** The first time constants ($R1$ and $C1$) are related to the properties of the interfacial zone and the second time constants ($R2$ and $C2$) are related to the properties of the phosphate film. Fig. 4 shows the values of $R1$ and $C1$ obtained according to the equivalent circuit, respectively. As the curing age increases from 3 to 7d, the resistance $R1$ of the interfacial zone increases, and the capacitance $C1$ decreases. It suggests that the structure is gradually densified with the prolongation of curing ages (Koleva et al., (2008a), Koleva et al., (2008b)). In addition, the value of $R1$ in the interfacial zone between A2P1 and A1P1 and the steel fiber is higher. When curing for 7 days, the interface resistance $R1$ of A2P1 is 63.4% and 69.3% larger than that of A1P0 and A0P1, respectively, indicating that the interfacial zone between A2P1 and steel fiber is denser. It can be related to the improved crystallization and strength development of the hydration product of A2P1.

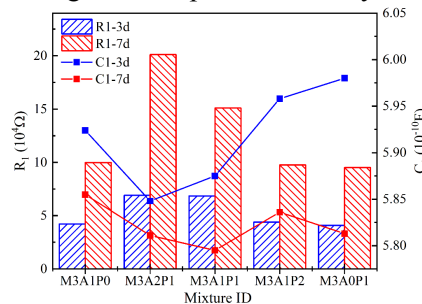


Fig. 4. The fitted electrochemical parameters for impedance spectra of the steel fiber in the MPC.

3.3 Porosity and micro-hardness of the interfacial zone

Fig. 5(a) shows that the porosity of the interfacial zone between MPC and steel fiber decreases with the increase of PDP content. Moreover, the micro-hardness value of the MPC at different distances from the edges of the steel fiber is illustrated in Fig. 5(b). The micro-hardness increases with the increase of distance from the edge of the steel fiber. For instance, the hardness of A2P1 at 10 μm away from the fiber edge is 198.6 HV and increases to 259.1 HV at 50 μm and does not change obviously beyond 50 μm . hardness of the interfacial zone between A2P1 and steel fiber is the highest among the tested samples, which can be due to the dense microstructure, improved crystallization, and strength development of the hydration product in A2P1. This suggests that the combined phosphates can improve the quality of the interfacial zone and increase the interfacial bond.

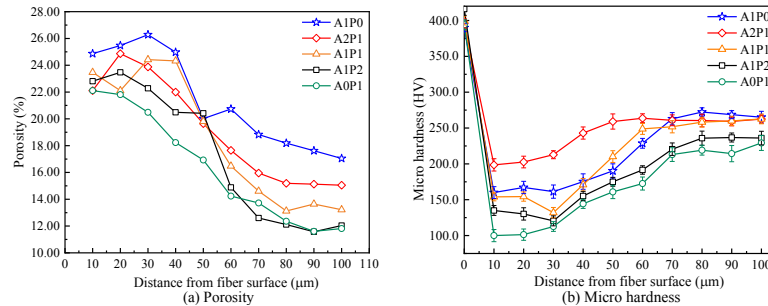


Fig. 5. Variation of porosity and micro-hardness of the interfacial zone between steel fiber and MPC.

4. Conclusions

- (1) The bond strength and pullout energy of MPC and steel fiber increase initially with the increase of ADP content and then decrease.
- (2) ADP has greater potential to promote the hydration and formation of hydration products of MPC. However, the generated ammonia and less solid volume increase than PDP during the hydration of ADP and MgO can result in higher porosity of the interfacial zone between steel fiber and MAPC than that of the interfacial zone between steel fiber and MPPC. Thus, A2P1 shows a denser interfacial zone with higher microhardness and thus greater bond properties with steel fiber.
- (3) EIS can comprehensively reflect the compactness and uniformity of the interfacial zone, which is an effective and non-destructive method for the evaluation of MPC and steel fiber interfacial bonds.

References

- Fan S and Chen B. (2014) "Experimental study of phosphate salts influencing properties of magnesium phosphate cement", *Construction and Building Materials*, 65: 480-6.
- Fan Y, Qin J, Wang H, et al. (2016) "Effect of Phosphates on Bond Performance of Magnesium Phosphate Cement", *Journal of The Chinese Ceramic Society*, 44(02): 218-25.
- Feng H, Sheikh M N, Hadi M N S, et al. (2018) "Interface bond performance of steel fibre embedded in magnesium phosphate cementitious composite", *Construction and Building Materials*, 185: 648-60.
- Koleva. D.A, Breugel. K.V, Wit. J.H.W et al., (2008) "Correlation of microstructure, electrical properties and electrochemical phenomena in reinforced mortar. Breakdown to multi-phase interface structures. Part I: Microstructural observations and electrical properties", *Materials Characterization*, 59(3) 290-300.
- Koleva. D.A, Breugel. K.V, Wit. J.H.W et al., (2008) "Correlation of microstructure, electrical properties and electrochemical phenomena in reinforced mortar. Breakdown to multi-phase interface structures. Part II: Pore network, electrical properties and electrochemical response", *Materials Characterization*, 59(6) 801-815.
- Seehra S S, Gupta S, Kumar S. (1993) "Rapid setting magnesium phosphate cement for quick repair of concrete pavements - characterisation and durability aspects", *Cement and Concrete Research*, 23(2): 254-66.
- Wang X, Hu X, Yang J, et al. (2022) "Research progress on interfacial bonding between magnesium phosphate cement and steel: A review", *Construction and Building Materials*, 342: 127925.
- Zhang G, Li Y, Naderi S, et al. (2021) "Two-scale modelling of fracture of magnesium phosphate cement under bending using X-ray computed tomography characterization", *Cement and Concrete Research*, 121: 104099.

Formation of closed pore structure porous glass-ceramics for thermal insulation

Kefeng. Jiang¹ and Wei. Chen^{2*}

¹ State Key Laboratory of Silicate Materials for Architectures, Wuhan University of Technology, Wuhan, China
Email: jiangkefeng@whut.edu.cn

² State Key Laboratory of Silicate Materials for Architectures, Wuhan University of Technology, Wuhan, China
Email: chen.wei@whut.edu.cn

ABSTRACT

Due to the low density, low thermal conductivity and low water absorption, porous glass-ceramics have demonstrated excellent performance for thermal insulation. Closed pore structure can greatly reduce the thermal conductivity and convection as well as achieve high mechanical strength. Here we use Fe₂O₃, which is the by-product of copper tailings, to optimize the pore structures of the porous glass-ceramics and facilitate the formation of uniform closed pore structure. The porous glass-ceramics were prepared by melting-quenching method, followed by sufficiently foaming through powder sintering route with SiC powders as foaming agent. The micro structure, pore structure and thermal insulation performance were directly observed by X-ray computed tomography and infrared thermal imager. The results show that the addition of Fe₂O₃ modified the depolymerization degree of the glass network and increased the numbers of non-bridged oxygen. The resultant closed pore structure showed a better thermal insulating performance than open pore structure.

KEYWORDS: Porous-glass ceramics; Pore structure control; Closed pores; Fe₂O₃; Foaming process

1. Introduction

Porous glass-ceramic is a kind of porous material, which generally composed by glass phase and crystalline phase with gas inside[1,2]. Due to the unique properties, such as low density, low thermal and acoustic conductivity, low water absorption and excellent chemical resistance[3,4], porous glass-ceramics have been used in thermal insulation, acoustic insulation, catalyst support, water treatment and so on. Pore structure is a key factor to the performance of the porous glass-ceramics. As the air possesses a much lower thermal conductivity ($0.0257 \text{ W}\cdot\text{m}^{-1}\cdot\text{K}^{-1}$ at 20 °C) than Al₂O₃ ceramics ($25 \text{ W}\cdot\text{m}^{-1}\cdot\text{K}^{-1}$) or multicomponent glass ($0.771 \text{ W}\cdot\text{m}^{-1}\cdot\text{K}^{-1}$ to $0.971 \text{ W}\cdot\text{m}^{-1}\cdot\text{K}^{-1}$)[5,6], pores foamed in glass-ceramics can greatly reduce the thermal conductivity of materials. Furthermore, when the pores are disconnected, the closed pores can further reduce the thermal radiation and convection. Therefore, the closed pore structure has the lowest effective thermal conductivity in non-vacuum conditions. In addition, closed pores can also increase mechanical strength and lower water absorption. In this work, the influences of Fe₂O₃ on the foaming process and properties of porous glass ceramics was investigated. We use Fe₂O₃ to optimize the pore structures of porous glass-ceramics and to facilitate the formation of closed pores. We investigated influences of Fe₂O₃ on the glass network in the porous glass-ceramics and analyze the pore structures and thermal insulation performance of the porous glass-ceramics.

2. Materials and methods

The starting materials used in this work are analytical reagents supplied by Sinopharm Chemical Reagent Co. including SiO₂ (≥99.0%), CaO (≥98.0%), Al₂O₃ (≥99.0%), MgO (≥98.5%), Fe₂O₃ (≥99.0%), P₂O₅ (≥98.0%), K₂CO₃ (≥99.0%) and SiC (≥99.9%). SiC is used as foaming agent and grinded below 75 μm. The composition of the designed glass sample is 52SiO₂-15.6CaO-12Al₂O₃-11MgO-3P₂O₅-4K₂O (in wt.%) with additional 0 wt.%, 2.4 wt.%, 4.4 wt.%, 6.4 wt.% and 8.4 wt.% Fe₂O₃ (named as G0, G1, G2, G3, and G4), respectively. The composition of the basic glass is designed by the phase region of diopside

in the phase diagram (Fig. S1) and the normal components of copper tailings and phosphorus tailings. A bunch of 150 g mixed raw material powders were ball-milled in agate ball mills with 20 mm balls for 2h using a rotation speed of 300 rpm and powder/ball ratio of 1:1 before being melted in a corundum crucible at 1450 °C for 2h in a furnace. Then the melt was water quenched and obtained basic glass were dried at 105 °C for 12 h in an oven. The glass was broken into powders in a vibration mill for 3 min and then sieved through 160 screen(97 μ m). The sieved glass powders were mixed with 0.3 wt.% SiC powders in deionized water for 2 h for uniform dispersion. The slurry was dried at 105 °C for 12 h in an oven and then 7 g dried powder was pressed into green bodies with diameter of 2 cm under the pressure of 15 MPa for 1 min. The samples were heated to 1150 °C, respectively, with a heating rate of 10 °C min⁻¹ and kept for 30 min for sufficiently foaming.

3. Results and discussion

As shown in Fig. 1, the broad band of [SiO₄] shifts to smaller wavenumbers with the amount of Fe₂O₃, indicating Si–O tetrahedron linkage becomes relatively loose. The content ratio of the characteristic structural units is related to the area ratio of its characteristic peak. Fig.1 also shows the Gaussian fitting results of Raman spectra and the corresponding Qⁿ in each basic glass. No obvious Q¹ and Q⁴ structural units were observed and the similar phenomenon had also been reported before[7]. The area fraction of Q⁰, Q² and Q³ is summarized in Table. 1. With the increase amount of Fe₂O₃ from 0 to 8.4 wt.%, the relative content of [Si₂O₅]²⁻ structural units decreases from 44 % to 23 %, while the content of [SiO₄]⁴⁻ and [Si₂O₆]⁴⁻ increase. This reveals that addition of Fe₂O₃ destroys the glass network and leads to the overall shift of the broad band. The addition of Fe₂O₃ modifies the depolymerization degree of the glass network and increases the numbers of non-bridged oxygen. As depolymerization degree decreases, the viscosity of the molten glass decreases which helped the pore formation of porous glass ceramics. Therefore, during the preparation of porous glass-ceramics from solid wastes, viscosity of molten glass and pore structures of porous glass ceramics can be controlled by optimizing the amount of solid wastes contain Fe₂O₃.

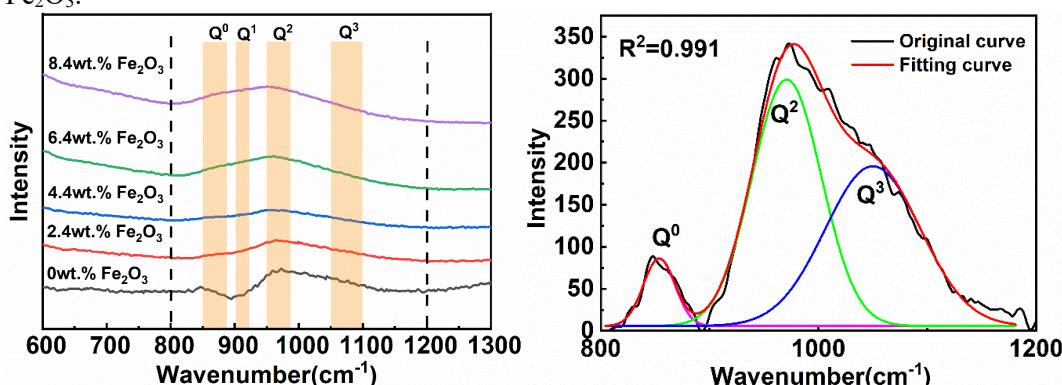


Fig. 1 Raman spectra and peakfit of samples.

Table.1 Area fraction of Qⁿ.

| Content of Fe ₂ O ₃ /wt. % | Q ⁰ /% | Q ² /% | Q ³ /% |
|--|-------------------|-------------------|-------------------|
| 0 | 6 | 50 | 44 |
| 2.4 | 4 | 54 | 42 |
| 4.4 | 8 | 63 | 29 |
| 6.4 | 6 | 65 | 29 |
| 8.4 | 11 | 66 | 23 |

Fig. 2a-c show the 3D and 2D X-CT images of porous glass-ceramics sintered at 1150 °C for 30 min. The images show the pore structures adjusted by different amount of Fe₂O₃. From the 3D images, we found that without the addition of Fe₂O₃, the sample could not form complete and uniform pores. With the increase of Fe₂O₃, the pores of samples became bigger and more uniform. The ratio of the closed porosity to open porosity also changed along with the change of Fe₂O₃ amount. In the 2D X-CT images, red parts

represented the connected pores and blue parts represented the closed pores. It is obvious samples with 2.4 wt.% Fe_2O_3 had the highest closed porosity. It is reasonable to deduce the sample with 2.4 wt.% Fe_2O_3 possessed a totally closed pore structure. As the amount of Fe_2O_3 increased to 4.4 wt.%, all the pores were in red which meant the sample had almost all open pores. When further increasing the amount of Fe_2O_3 , the porosity and pore sizes increased and almost all pores were connected. It can be concluded that appropriate doping amount of Fe_2O_3 and suitable sintering temperature is beneficial to the formation of closed pore structure.

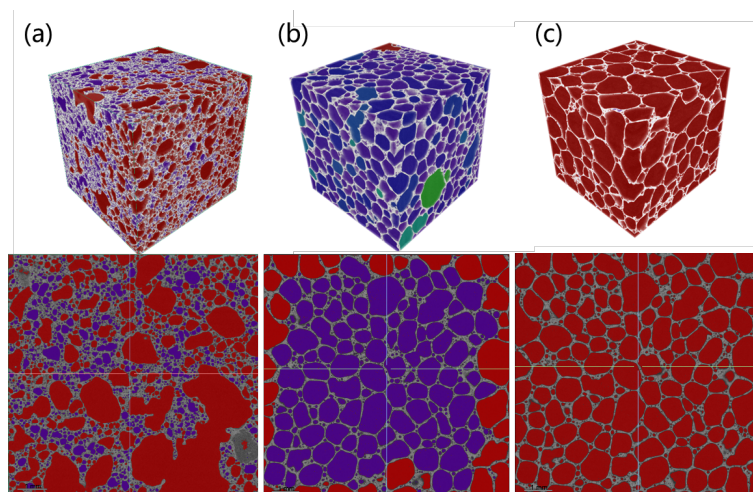


Figure 2 X-CT images of samples with different content of Fe_2O_3 sintered at 1150 °C: (a) G0 sample, (b) G1 sample, (c) G2 sample.

To investigate the thermal insulating performance of the porous glass-ceramics, infrared thermogram of G1 sample (closed pore structure) and G3 sample (open pore structure) heating at 60 °C are recorded, as shown in Fig. 3. The samples were cut into 25 mm×25 mm×15mm. The corresponding maximum temperature, minimum temperature and average temperature were read out along with the heating duration. G1 sample showed more homogeneous temperature distribution than G3 sample because of the uniform closed pore structure, blocking the heat conduction homogeneously. G3 sample exhibited continuous temperature rising and exceeds G1 sample after heating for 10 min, demonstrating the closed pore structure facilitating better insulation effect.

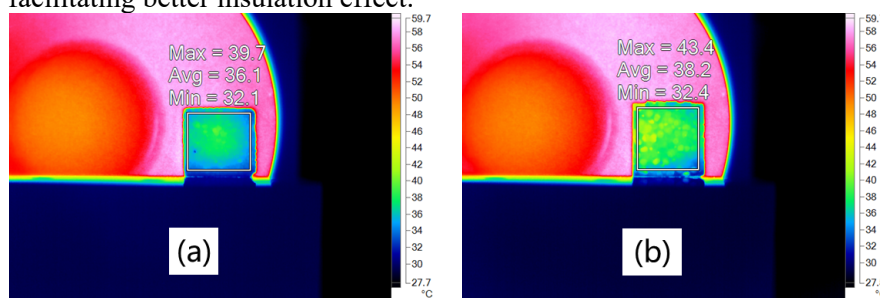


Figure 3 Infrared thermogram of G1 sample and G3 sample heating continuously at 60 °C for 10 min: (a) G1 sample, (b) G3 sample.

4. Conclusions

In summary, we used Fe_2O_3 to optimize the pore structures of the porous glass-ceramics and facilitated the formation of uniform closed pore structure. The effect of Fe_2O_3 on the glass network, pore structure and thermal insulation performances of porous glass-ceramics was studied in details. The addition of Fe_2O_3 modified the depolymerization degree of the glass network and increased the numbers of non-bridged oxygen, decreasing the viscosity and the foaming temperature. 2.4 wt.% Fe_2O_3 doping optimized the pore structure into closed pore structure. The closed pore structure porous glass-ceramics exhibited better thermal insulation performance than open pore structure porous glass-ceramics.

Acknowledgements

This work is financially supported by the National Key Research and Development Program of China (No. 2019YFC1904900).

References

- [1] H. Wang, K. Feng, Q. Sun, Effect of calcium carbonate on the preparation of glass ceramic foams from water-quenched titanium-bearing blast furnace slag and waste glass, *Adv. Appl. Ceram.* 117 (2018) 312–318. <https://doi.org/10.1080/17436753.2017.1412120>.
- [2] Z. Luo, H. Liang, C. Qin, J. Zhang, T. Liu, A. Lu, Sintering behavior, microstructures and mechanical properties of porous CaO-Al₂O₃-SiO₂-Si₃N₄ glass-ceramics, *J. Alloys Compd.* 773 (2019) 71–77. <https://doi.org/10.1016/j.jallcom.2018.09.231>.
- [3] H. Cengizler, M. Koç, O. Şan, Production of ceramic glass foam of low thermal conductivity by a simple method entirely from fly ash, *Ceram. Int.* 47 (2021) 28460–28470. <https://doi.org/10.1016/j.ceramint.2021.06.265>.
- [4] C. Xi, F. Zheng, J. Xu, W. Yang, Y. Peng, Y. Li, P. Li, Q. Zhen, S. Bashir, J.L. Liu, Preparation of glass-ceramic foams using extracted titanium tailing and glass waste as raw materials, *Constr. Build. Mater.* 190 (2018) 896–909. <https://doi.org/10.1016/j.conbuildmat.2018.09.170>.
- [5] S.M. Salman, S. Gharib, Thermal conductivity of some multicomponent silicate glasses, *Thermochim. Acta.* 77 (1984) 227–239. [https://doi.org/10.1016/0040-6031\(84\)87062-8](https://doi.org/10.1016/0040-6031(84)87062-8).
- [6] C. Vakifahmetoglu, T. Semerci, G.D. Soraru, Closed porosity ceramics and glasses, *J. Am. Ceram. Soc.* 103 (2020) 2941–2969. <https://doi.org/10.1111/jace.16934>.
- [7] S. Zhang, Y. Zhang, Z. Qu, Effect of soluble Cr₂O₃ on the silicate network, crystallization kinetics, mineral phase, microstructure of CaO-MgO-SiO₂-(Na₂O) glass ceramics with different CaO/MgO ratio, *Ceram. Int.* 45 (2019) 11216–11225. <https://doi.org/10.1016/j.ceramint.2019.02.106>.

Carbonation effects on mechanical performance and microstructure of LWAs produced with hydrated cement paste powder

Y.J. Tang¹, K. Schollbach², W. Chen^{3*}, and H.J.H. Brouwers⁴

¹ State Key Laboratory of Silicate Materials for Architectures, Wuhan University of Technology, Wuhan 430070, China

Department of the Built Environment, Eindhoven University of Technology, 5612 AP Eindhoven, The Netherlands

Email: y.tang3@tue.nl

² Department of the Built Environment, Eindhoven University of Technology, 5612 AP Eindhoven, The Netherlands

Email: k.schollbach@tue.nl

³ State Key Laboratory of Silicate Materials for Architectures, Wuhan University of Technology, Wuhan 430070, China

Email: chen.wei@whut.edu.cn

⁴ State Key Laboratory of Silicate Materials for Architectures, Wuhan University of Technology, Wuhan 430070, China

Department of the Built Environment, Eindhoven University of Technology, 5612 AP Eindhoven, The Netherlands

Email: jos.brouwers@tue.nl

ABSTRACT

This paper aims to evaluate lightweight aggregates produced with hydrated cement paste powder (HCP) using carbonation. The mechanical properties, reaction products and microstructure were analysed and the results show that the optimal carbonation period for HCP I- and HCP III-type aggregates are different due to different amounts of portlandite. HCP I-type aggregates can gain 3.14 MPa after 7-day carbonation and contain 35.60 wt.% calcium carbonates. The remaining 13.95 wt.% portlandite shows the enormous potential in elevating the strength and CO₂ capture capacity jointly via the optimized carbonation curing method. On the contrary, HCP III-type aggregates gained 2.97 MPa after 1-day carbonation and further carbonation decomposed C-S-H and lead to the formation of calcite and amorphous silica gel with significantly elevated specific surface area (from 10.69 m²/g to 42.96 m²/g) (Tang et al., 2022). This study can provide some understanding in the performance prediction of carbonated LWAs originated from the real demolished cement and concrete materials.

KEYWORDS: carbonation, decomposition, portlandite, C-S-H

1. Introduction

As a newly developed building material, lightweight concrete shows some extraordinary properties such as extremely low density, excellent sound absorption, and thermal insulation (Chandra and Berntsson, 2002). The main ingredients for a lightweight concrete design are cement and lightweight aggregates (LWAs) (Spiesz et al., 2013). Generally, LWAs have a porous structure and low bulk density (less than 1200 kg/m^3) and thus reduce the density of concrete structure effectively. However, the commercial LWAs, for instance, expanded clay, expanded glass and perlite, consume huge amounts of energy, as well as natural resource due to the production at high temperatures (700°C - 1400°C) (Tajra et al., 2019). Consequently, some studies started focusing on the development of a low-carbon footprint and sustainable LWAs.

Cold-bonding technology has been proposed and developed for the purpose of low energy consumption during LWAs manufacture with industrial wastes (Tang et al., 2020). Combined with a pelletizing process, pellets in different sizes with porous structure were produced and then applied as LWAs.

One industrial waste that has attracted much attention in recent years is aged concrete that can be recycled to recover most of the original high-quality fine and coarse aggregates and thus leave 10%-20% of fine concrete waste powder (Lu et al., 2018). The main components in waste powder are hydrated cement paste (HCP) but the exact composition can depend on the crushing and starting composition of the recycled concrete. The waste powder can have a high water demand due to the porous structure and high surface area, along with a very low reactivity when used as supplementary cementitious materials (SCMs) (Shi et al., 2016), causing difficulty in applying to normal concrete production without further treatment or activation (Spiesz et al., 2013).

The HCP contains mainly calcium silicate hydrate (C-S-H) gels, calcium hydroxide, AFt, AFm and some unreacted clinker phases. Gas-solid and aqueous carbonation were reported to be effective to utilize HCP powders as the SCMs. The workability and mechanical property of cement paste blended with carbonated HCP powder can be enhanced via the formation of calcium carbonates which can act as fillers and then optimize the pore structure (Mehdizadeh et al., 2022). Consequently, it is possible to produce HCP powder based cold-bonded LWAs by using carbonation instead of cement and alkali activator addition.

For the purpose of investigating the mechanism of the mechanical and microstructure development of the artificial aggregates under carbonation, this study used the laboratory-made cement paste instead of a real demolished concrete to obtain HCP powder and then produce LWAs, which allows to better control the chemical composition of the waste powder by eliminating the variability of its properties when recovered from demolished materials. Additionally, researchers prefer to investigate the properties of HCP powder from CEM I which contains few SCMs, whereas CEM III is also widely used and deserves more attention in the production of LWAs. Therefore, both CEM I 52.5 R and CEM III/A 52.5 N were chosen as the starting materials. The amount of hydration products from CEM I and CEM III is different, especially the amount of portlandite. A comparative study has been conducted to figure out the effects of portlandite amount in HCP I and HCP III on the aggregates production under carbonation curing. The mechanical properties, reaction products and microstructure were investigated via TGA, Nitrogen physisorption analysis and etc. to figure out the effects of carbonation on LWAs produced with HCP powder.

2. Experiments and methodology

2.1 Raw materials

The HCP powder was produced in the laboratory from the cement paste which was prepared by CEM I 52.5 R and CEM III/A 52.5 N provided by ENCI, the Netherlands. All cement pastes were prepared with a water to cement ratio of 0.5 and then demoulded until 24 hours after mixing, followed by the ambient curing in the resealable bags for at least 3 months.

The HCP was crushed manually and milled with a disc milling (Retsch, RS300XL) for 10 min to obtain the waste cement paste powder for the tests. The milled HCP powder originating from CEM I and CEM III was labelled as HCP I and HCP III, respectively. The chemical composition of HCP I and HCP III was analysed with X-ray fluorescence (XRF, Model Axios Advanced, PANalytical.B. V), as shown in Table 1. The mineral composition of HCP I and HCP III was determined using X-ray diffraction (XRD) analysis, which is shown in Fig. 1 (a) and (b), respectively. The D50 of HCP I and HCP III is $32.3\mu\text{m}$ and

38.3µm, respectively, analysed with a laser particle size analyser (Model Malvern Mastersizer 2000, Malvern PANalytical).

Table 1 The chemical composition of raw materials for preparation of aggregates (milled hydrated cement paste powder I (HCP I) and milled hydrated cement paste powder III (HCP III))

| Materials (wt. %) | CaO | SiO ₂ | Al ₂ O ₃ | Fe ₂ O ₃ | SO ₃ | MgO | MnO | TiO ₂ | Others |
|----------------------|-------|------------------|--------------------------------|--------------------------------|-----------------|------|------|------------------|--------|
| HCP I | 65.96 | 17.42 | 7.57 | 3.51 | 3.08 | 1.43 | 0.08 | 0.44 | 0.51 |
| HCP III | 49.32 | 27.10 | 12.02 | 1.24 | 4.83 | 4.24 | 0.17 | 0.55 | 0.53 |

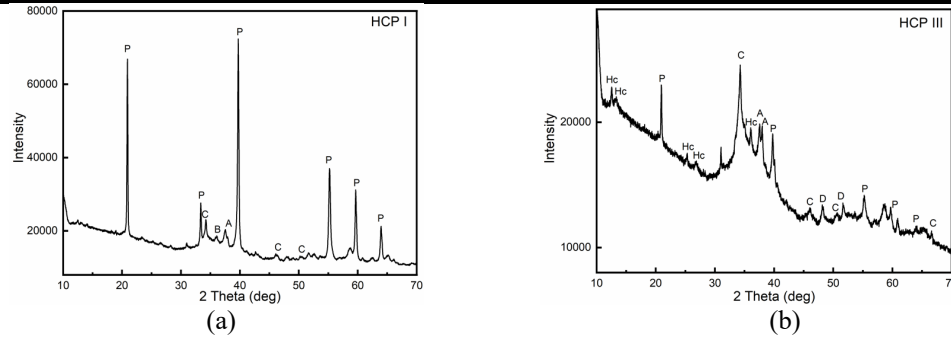


Fig. 1 XRD patterns of HCP I (a) and HCP III (b) (P=portlandite, A=alite, B=belite, C=calcite, Hc=hemihydrate, D=dolomite)

2.2 Pelletizing procedure

The disc pelletizer was used to produce the artificial aggregates. The model was D-7736, Maschinenfabrik Gustav Eirich, Germany. The size of the pelletizer was 40 cm in diameter and 10 cm in collar height. The vertical angle of the pan is 75° and the rotating speed was set as 60 rpm during the production process. 500 grams of HCP were placed on the rotating pan. After about 3 min of rotating, 50 grams of distilled water was sprayed slowly onto the mixed powder in the pan using a spray bottle over 10 min. After the aggregation was observed, the pan continued running for 5 min to form the pellets. The as-prepared aggregates fell out of the pan automatically once they reached sufficient size and were collected. The freshly prepared LWAs were placed in a CO₂ chamber with a CO₂ concentration of 5% and a relative humidity of 75% and carbonated for 1, 3 and 7 days, respectively for carbonation curing. The temperature during curing was constant, around 20 °C. The prepared aggregates, which were originated from HCP I and HCP III, carbonated for 1, 3 and 7 days were labelled as C1A I, C3A I, C7A I, C1A III, C3A III and C7A III, respectively.

2.3 Mechanical property of prepared LWAs

The mechanical properties of the individual pellets with different diameters were tested in an MTS Criterion equipped with a load cell of 100 kN at a speed of 0.6 mm/min until collapse. The maximum compression load was used to calculate the individual crushing strength with Eq. (1). 20 pellets were chosen as representatives for each group of prepared LWAs.

$$\sigma = 2.8P/\pi h^2 \quad (1)$$

Where σ (MPa) is the crushing strength of each pellets tested, P (N) is the maximum compression load each pellet can withstand, h (mm) is the diameter of the round pellet produced.

2.4 Characterization of reaction products and microstructure

The loose bulk density test was carried out according to EN 1097-3. Different artificial aggregates were crushed manually and ground finely to pass a sieve of 68 µm. Afterwards, samples were immersed in isopropanol for 30 min to eliminate hydration according to literature (Scrivener et al., 2018) and then dried in an oven at 40 °C until a constant mass. All samples were stored in desiccators, using a drying agent (CaCl₂ pellets) and sodium hydroxide pellets as a CO₂ trap until further different tests.

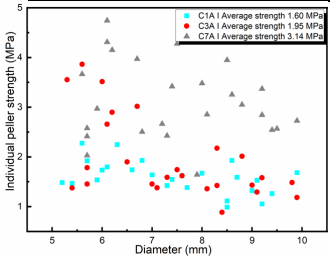
3. Results and discussion

It can be seen that all the samples have a loose bulk density of around 576.0-753.6 kg/m³, which is below 1200 kg/m³ and thus satisfies the density requirement of lightweight aggregates according to EN 13055-1 (2002). The individual strength of the carbonated aggregates originated from HCP I increases from 1.60

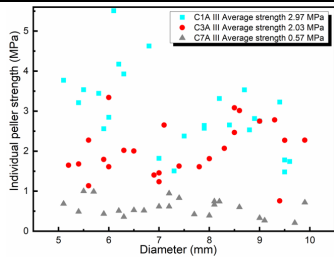
MPa to 3.14 MPa after 7-day carbonation (Fig. 2(a)), in line with the re-cementation effects of carbonation. Without carbonation, the reference aggregates only reach 0.83 MPa (Tang et al., 2022), indicating that carbonation can benefit the strength development. A reduction of porosity is observed most likely because the volume of the carbonates formed is 11–12% greater than the volume of portlandite as reported in (Šavija and Luković, 2016), which can optimize the pore structure and then enhance the mechanical property. However, the HCP III system shows the opposite results, where the individual strength of the carbonated aggregates decreases from 2.97 MPa to 0.57 MPa (Fig. 2(b)).

Table 2 Bulk density of the produced LWAs

| Bulk density (kg/m ³) | C1A I | C3A I | C7A I | C1A III | C3A III | C7A III |
|-----------------------------------|-----------|-----------|-----------|-----------|-----------|-----------|
| | 614.6±2.0 | 668.6±3.0 | 738.4±1.8 | 753.6±4.5 | 715.8±3.6 | 605.3±2.2 |



(a)



(b)

Fig. 2 Individual pellet strength of the produced aggregates

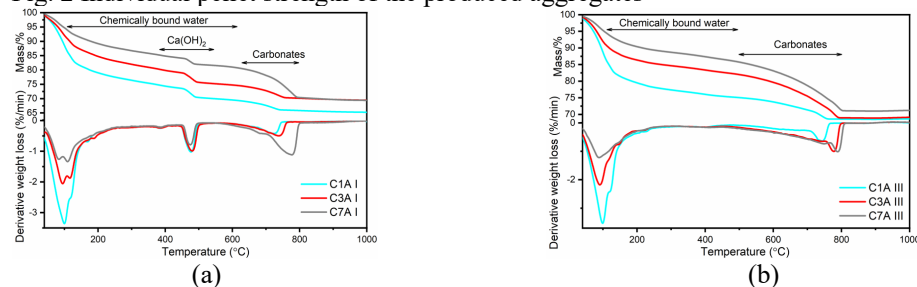


Fig. 3 Weight loss determined with thermogravimetric analysis (TGA) and the first derivative of TGA (DTG) of the produced aggregates

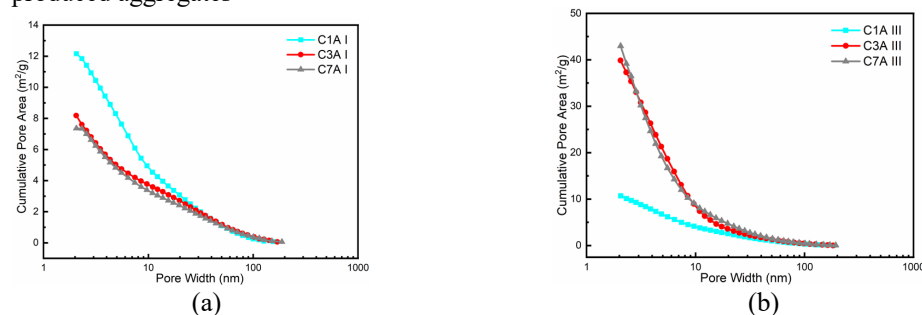


Fig. 4 Cumulative pore area of the produced aggregates

It is suggested that carbonation of C-S-H is accompanied with a decalcification process. The decomposition of C-S-H gel can happen when the Ca/Si ratio is below around 0.66, followed by the severe carbonation shrinkage and cracking. The existence of portlandite can protect the other hydration products from becoming the main carbonated subjects and thus maintain the Ca/Si ratio of C-S-H gel at a high level (Šavija and Luković, 2016). From thermogravimetric analysis (Fig. 3), HCP I shows an initial amount of portlandite of 24.17 wt. % and after 7-day carbonation the amount of portlandite remains 13.95 wt.% while HCP III starts with only 2.55 wt.% portlandite and after 1-day carbonation, portlandite cannot be detected in TGA. XRD and FTIR analysis confirm these results (not shown in this paper). The sufficient portlandite in HCP I system acted like a buffer and prevented the decomposition of other phases like C-S-H gel during the carbonation curing even though C-S-H gel and other phases underwent the carbonation simultaneously (Borges et al., 2010; Šavija and Luković, 2016). The absence of portlandite is detected in HCP III system after 1-day carbonation. Therefore, C-S-H gel, ettringite etc. suffered the strong CO₂ attack, leading to the serious decomposition of C-S-H gel which usually plays a cementitious

role. The peak shift from 958 cm^{-1} to 1026 cm^{-1} in FTIR and the significantly elevated specific surface area from 10.69 m^2/g to 42.96 m^2/g (Fig. 4(b)) after carbonation treatment evidences the decomposition of C-S-H and formation of amorphous silica gel containing abundant evaporation water that can cause dry shrinkage and produce macro pores (Skocek et al., 2020). On all account, the aggregates obtained from HCP III suffered carbonation shrinkage and internal cracking during carbonation process, leading to the reduction of individual strength and increasing water absorption (Borges et al., 2010).

4. Conclusions

The comparative study was conducted to figure out the effects of portlandite amount in HCP I and HCP III on the aggregates production under carbonation curing. Based on the findings from this study, the following conclusions can be drawn.

Carbonation reaction benefits the fast strength development because the formation of calcium carbonates decreases the porosity, optimizing the pore structure and then benefiting the mechanical property. However, carbonation curing is more appropriate for HCP I-type aggregates than HCP III-type aggregates due to the different amount of portlandite. HCP I-type aggregates show the enormous potential in elevating the strength along with CO_2 capture capacity via the extended carbonation curing until the optimal curing period is reached. The optimal curing period for HCP III-type aggregates is short so that the individual strength and CO_2 uptake are undoubtedly limited.

The sufficiently available portlandite acts like a buffer to prevent decomposition in C-S-H and other phases caused by carbonation. The lack of available portlandite makes C-S-H the dominant phase subjected to carbonation, accompanying with the decomposition of C-S-H at the extensive carbonation calcification. Consequently, shrinkage and internal cracking during carbonation can occur, leading to a significant reduction of individual strength.

References

- Borges, P.H.R., Costa, J.O., Milestone, N.B., Lynsdale, C.J., Streatfield, R.E., 2010. Carbonation of CH and C-S-H in composite cement pastes containing high amounts of BFS. *Cem. Concr. Res.* 40, 284–292. <https://doi.org/10.1016/j.cemconres.2009.10.020>
- Chandra, S., Berntsson, L., 2002. Introduction, in: Chandra, S., Berntsson, L.B.T.-L.A.C. (Eds.), *Lightweight Aggregate Concrete*. William Andrew Publishing, Norwich, NY, pp. 1–3. <https://doi.org/https://doi.org/10.1016/B978-081551486-2.50003-1>
- Lu, B., Shi, C., Zhang, J., Wang, J., 2018. Effects of carbonated hardened cement paste powder on hydration and microstructure of Portland cement. *Constr. Build. Mater.* 186, 699–708. <https://doi.org/10.1016/j.conbuildmat.2018.07.159>
- Mehdizadeh, H., Cheng, X., Mo, K.H., Ling, T.C., 2022. Upcycling of waste hydrated cement paste containing high-volume supplementary cementitious materials via CO_2 pre-treatment. *J. Build. Eng.* 52, 104396. <https://doi.org/10.1016/j.jobbe.2022.104396>
- Šavija, B., Luković, M., 2016. Carbonation of cement paste: Understanding, challenges, and opportunities. *Constr. Build. Mater.* 117, 285–301. <https://doi.org/10.1016/j.conbuildmat.2016.04.138>
- Scrivener, K., Snellings, R., Lothenbach, B., Group, F., 2018. *A Practical Guide to Microstructural Analysis of Cementitious Materials*, CRC Press. <https://doi.org/10.1201/b19074>
- Shi, C., Cao, Z., Xie, Z., 2016. Research Progress in the Mechanical Properties of Recycled Aggregate Concrete. *Mater. Rev.* 30, 96–102.
- Skocek, J., Zajac, M., Ben Haha, M., 2020. Carbon Capture and Utilization by mineralization of cement pastes derived from recycled concrete. *Sci. Rep.* 10, 1–12. <https://doi.org/10.1038/s41598-020-62503-z>
- Spiesz, P., Yu, Q.L., Brouwers, H.J.H., 2013. Development of cement-based lightweight composites - Part 2: Durability-related properties. *Cem. Concr. Compos.* 44, 30–40. <https://doi.org/10.1016/j.cemconcomp.2013.03.029>
- Tajra, F., Elrahman, M.A., Stephan, D., 2019. The production and properties of cold-bonded aggregate and its applications in concrete: A review. *Constr. Build. Mater.* 225, 29–43. <https://doi.org/10.1016/j.conbuildmat.2019.07.219>
- Tang, P., Xuan, D., Li, J., Cheng, H.W., Poon, C.S., Tsang, D.C.W., 2020. Investigation of cold bonded lightweight aggregates produced with incineration sewage sludge ash (ISSA) and cementitious waste. *J. Clean. Prod.* 251, 119709. <https://doi.org/10.1016/j.jclepro.2019.119709>
- Tang, Y., Liu, G., Schollbach, K., Chen, Y., Chen, W., Brouwers, H.J.H., 2022. Re-cementation effects by carbonation and the pozzolanic reaction on LWAs produced by hydrated cement paste powder. *J. Clean. Prod.* 377, 134529. <https://doi.org/10.1016/j.jclepro.2022.134529>

Study for New Japanese Industrial Standards; “Volcanic Glass Powder for Use in Concrete”

A. Tomoyose^{1*}, T. Noguchi², and K. Sodeyama³

¹ the University of Tokyo, Tokyo, Japan
Email: tomoyose@bme.arch.t.u-tokyo.ac.jp

² the University of Tokyo, Tokyo, Japan
Email: noguchi@bme.arch.t.u-tokyo.ac.jp

³ Kagoshima Prefectural Institute of Industrial Technology, Kagoshima, Japan
Email: sodeyama@kagoshima-it.go.jp

ABSTRACT

Volcanic deposits, which have pozzolanic reactivity, have long been known to improve the durability of concrete. Nevertheless, it has also been pointed out that the use of a natural pozzolan as a supplementary cementitious material (SCM) can pose problems of low workability and slow strength development. Also, its composition and physical properties have a large variety and variability. The reaction of natural pozzolans is caused by volcanic glass composed of amorphous silicate; however, most of these natural pozzolans contain such inert minerals as quartz and feldspar, along with volcanic glass. Volcanic ejecta also contains pumice, and sometimes weathered clay fraction in their natural conditions. But, by focusing on the differences in physical properties between these components, high-purity volcanic glass can be sorted by dry gravity classification. The previous study demonstrated, by pulverizing this sorted high-purity volcanic glass to powders, high-performance SCM can be manufactured. This paper reports the results of investigations to establish the new Japanese Industrial Standard ‘Volcanic Glass Powder for Use in Concrete’. Mortar tests were performed to check the relationship between BET surface area and activity index, and also to study the appropriate water-binder ratio, replacement ratio, and mixing time for the strength activity index test. The results showed that extending the mixing time is appropriate based on the activity index test method for silica fume and that classifying volcanic glass powder into three classes according to the combination of BET surface area is appropriate considering the manufacturing method.

KEYWORDS: *Natural Pozzolan, Supplementary Cementitious Materials, Japanese Industrial Standards, Volcanic Glass Powder*

1. Introduction

To achieve the United Nations’ Sustainable Development Goals, highly durable low-carbon concrete made with supplementary cementitious materials (SCMs) is required. Volcanic sediments, which have pozzolanic activity, have long been known to improve the durability of concrete, but it has also been noted that using volcanic ash as an SCM can cause problems of low workability and slow strength development. Also, the chemical composition and physical properties of volcanic ash have high variability (Snellings 2016). The reaction of natural pozzolans is due to volcanic glass composed of amorphous silicate, but most natural pozzolans also contain inert minerals such as quartz and feldspar. Furthermore, in their natural state, volcanic ejecta also contains pumice and sometimes weathered clay. However, by focusing on the different densities of these components, high-purity volcanic glass can be sorted by dry gravity classification. This technological development has made it possible to manufacture high-purity volcanic glass powder (VGP) as high-performance SCMs for use in concrete by dry sorting and pulverizing high-purity volcanic glass (Tomoyose 2018). And the possibility of manufacturing VGP as industrial products from volcanic sediments from all over Japan and outside Japan has been noted

(Tomoyose 2020). Considering that VGP is manufactured from volcanic sediments in various locations, standards and test methods for performance evaluation are needed, as are other SCMs of silica fume (SF) and fly ash (FA). Therefore, in order to determine the appropriate activity index test method and classifications, mortar and concrete tests were conducted for different fineness VGPs in this study.

2. Test materials and experimental program

As previously reported (Tomoyose 2018), high-purity volcanic glass was sorted from Ito Shirasu by an air table. After crushing these sorted particles with a roller mill, the VGP was classified by the air classifier and cyclone, and two types of fine VGP and two types of coarse VGP were used. Fig.1 shows the manufacturing process of VGP and Table 1 shows the BET-specific surface areas determined using Nitrogen gas and typical properties of the four VGPs.

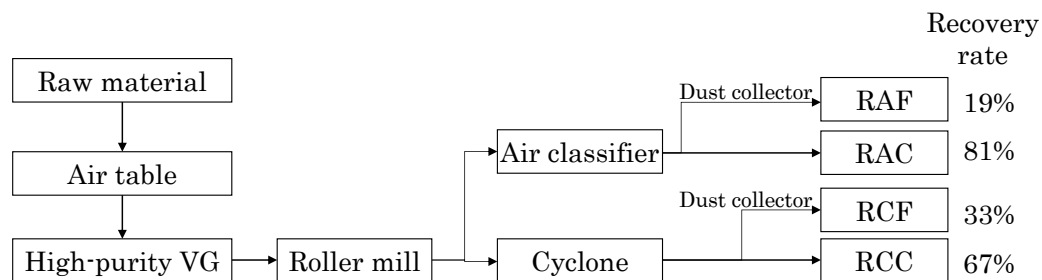


Fig.1 Manufacturing process of four types VGP

Table 1 BET surface area and property of VGP

| Type | Classifier | BET surface area (m ² /g) | Recovery rate (%) | SiO ₂ (%) | Al ₂ O ₃ (%) |
|------|----------------|--------------------------------------|-------------------|----------------------|------------------------------------|
| RAF | Air classifier | 15.2 | 19 | 73.7 | 12.4 |
| RAC | | 5.1 | 81 | | |
| RCF | Cyclone | 12.0 | 33 | | |
| RCC | | 3.6 | 67 | | |

The mortar tests for VGP were divided into two series. In series 1, mortar mixing time was set at two levels: 5 minutes after pouring water, as specified by JIS A 6207; the activity index test method for SF, and 10 minutes after pouring water, which was extended. Referring to JIS A 6207, the water-to-binder ratio was 0.3 and the VGP (RAF and RCF) replacement ratio was 10%. The amount of chemical admixture was set to achieve a mortar flow of 260 mm ± 10 mm and an air content of 2.0% or less in the reference mortar, and the same amount was used in the test mortar. In Series 2, mortar mixing time was set at two levels: 4 minutes after pouring water, as specified by JIS A 6201; the activity index test method for FA, and 7 minutes after pouring water, which was extended. Referring to JIS A 6201, the water-to-binder ratio was 0.5 and the VGP (RAC and RCC) replacement ratio was 10%. Compressive strength tests were conducted at 1 and 4 weeks of curing age for both series.

Concrete tests were also conducted at two levels. A forced twin-shaft mixer was used for mixing, with W/B = 0.2 and 0.5. As in the mortar tests, the replacement ratio was set to 10% for W/B = 0.2 and 25% for W/B = 0.5. SF and FA were also used for comparison. Compressive strength specimens were prepared after adjusting the amount of chemical admixture and fresh testing. Compressive strength tests were performed at 1 and 4 weeks of standard curing material age.

3. Results and discussion

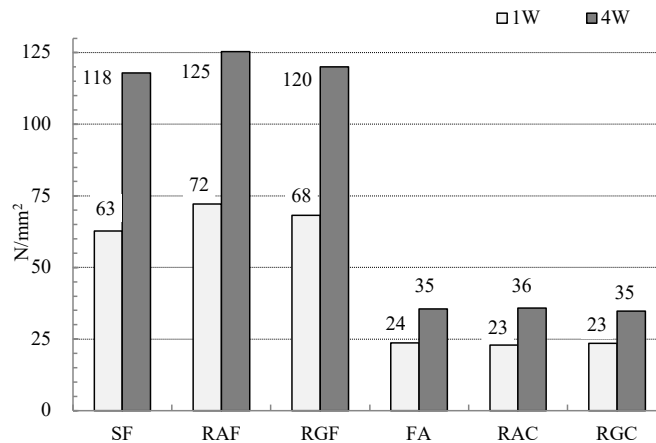
The results of mortar tests are shown in Table 2. When the mixing time of W/B=0.3 was set longer, the mortar flow also became larger, and the activity index at 28 days was confirmed to be about 10% higher. It indicates that the flow increased as the mixing time was extended and the particles of VGP became more dispersed, which may have affected the progress of the pozzolanic reaction by the 28-day age. On the other hand, in all mortars with W/B=0.5, the mortar flow became smaller as the mixing time was extended, and the activity index tended to be a few percent larger in the mortars with VGP. The activity

Table 2 Results of Mortar tests

| Series | mark | Mortar flow (mm) | Activity index (%) | |
|------------------|---------------------|---------------------|--------------------|--------|
| | | | 7days | 28days |
| 1 (W/B = 0.3) | Control | 257.5 | - | - |
| | RAF-5min mixing | 245.5 | 100.6 | 100.8 |
| | RAF-10min mixing | 276.0 | 98.32 | 114.1 |
| | RCF-5min-mixing | 240.0 | 101.7 | 103.1 |
| | RCF-10min mixing | 258.0 | 101.9 | 111.1 |
| 2 (W/B = 0.5) | Control-4min mixing | 156.5 | - | - |
| | Control-7min mixing | 142.0 | 101.6 | 100.6 |
| | RAF-4min mixing | 125.0 | 68.6 | 78.7 |
| | RAF-7min mixing | 122.5 | 72.5 | 83.5 |
| | RCF-4min mixing | 133.0 | 65.4 | 72.6 |
| | RCF-7min mixing | 126.5 | 67.8 | 75.9 |

index of both control mortars was similar, indicating that mixing for more than 4 minutes had little effect on the strength of the control mortars.

The results of compressive strength tests of concrete are shown in Fig. 2. At W/B=0.2, the two types of VGP concrete showed strength equal to or greater than that of SF concrete. And at W/B=0.5, the two types of coarse VGP showed strength equal to that of FA. In addition, the target fresh properties were met at all levels with the same amount of chemical admixture and mixing time, indicating that VGP can be produced under the same mixing conditions as SF and FA in the concrete mixing process.

**Fig. 2 Compressive strength of concrete**

The ratio of the activity index of the VGP obtained in the experiment to that of the comparative SCM was calculated as the activity index ratio, the compressive strength ratio (VGP/SF or FA) obtained in the experiment as the concrete strength ratio, and their mortar/concrete strength ratio (Mor/Con), and the results at 28 days are shown in Table 2. The activity index of SF and FA was taken from the manufacturer's test values.

Table 2 Relation between the results of mortar tests and concrete tests

| mark | Activity index ratio | Concrete strength ratio | Mor/Con |
|------------------|----------------------|-------------------------|---------|
| | VGP/SF | VGP/SF | |
| RAF-5min mixing | 93.3 | 105.9 | 88.1 |
| RAF-10min mixing | 105.7 | | 99.8 |
| RCF-5min mixing | 95.4 | 101.6 | 89.8 |
| RCF-10min mixing | 102.9 | | 98.5 |
| | VGP/FA | VGP/FA | |
| RAC-4min mixing | 95.9 | 101.2 | 94.8 |
| RAC-7min mixing | 101.7 | | 100.5 |
| RCC-4min mixing | 88.5 | 98.0 | 90.3 |
| RCC-7min mixing | 92.5 | | 94.4 |

For both W/B, the longer mortar mixing time resulted in a mortar/concrete strength ratio of around 100%. And for W/B=0.2, the mixing time of 5 minutes resulted in a mortar/concrete strength ratio of about 90%. The results of this experiment indicate that the mixing time required for the mortar test for VGP is not the same as that for silica fume or fly ash, and that a longer mixing time for the same water-to-binder ratio is better for evaluating strength development in the concrete. For mortar, a longer time is required to achieve the same level of VGP dispersion as concrete due to the shear effect of coarse aggregate and the mixer format, and this mixing time may depend on the SCM characteristics such as particle size distribution. Therefore, the results suggest that the mixing time in the activity index test, which evaluates the strength development performance of powders, should be considered for each powder. Based on the present results, the relationship between the 28-day activity index, which was performed with W/B = 0.3 and the mixing time extended to 10 min, and BET specific surface area of VGP is shown in Fig. 3. It shows that the classified coarse VGP and fine VGP and the VGP before classification are classified into three types in terms of BET specific surface area and activity index. Based on these results, it is considered appropriate to evaluate JIS A 6209 Volcanic Glass Powder for Concrete by a mortar test with W/B = 0.3, in which the mixing time is extended to 10 minutes.

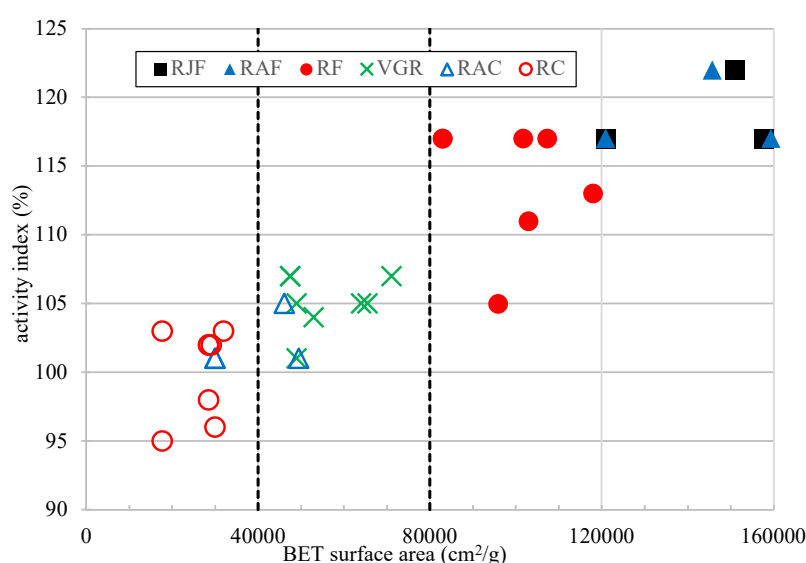


Fig. 3 Relation between BET surface area and activity index of 28days

4. Conclusion

Experiments were conducted at several mixing time and with several W/B in the activity index test with mortar using VGP, with results indicating that mixing time may have an effect on the evaluation of strength development in concrete. And, the result of the evaluation using the extended test method, classifying VGP into three classes according to the combination of BET surface area is appropriate considering the manufacturing method.

Acknowledgements

This study was supported by JSPS KAKENHI Grant Number 22K14357.

References

- Snellings, R. (2016). "Assessing, Understanding and Unlocking Supplementary Cementitious Materials." RILEM Technical Letters 1: 50-55
- Tomoyose, A., Noguchi T., Sodeyama K., and Higashi K. (2018) "Utilization of Volcanic Ejecta as a High-Performance Supplementary Cementitious Material by Gravity Classification and Pulverization." RILEM Technical Letters 3: 66-74
- Tomoyose, A., Noguchi T., Sodeyama K., and Higashi K. (2020) "Concrete with high-purity volcanic glass fine powder manufactured from pyroclastic deposit" SN Appl. Sci 3, 851

Cement types and seawater exposure in Europe – implications for infrastructure and its integration into marine habitats

S.N. Lørup^{1,2}, W.B. Feldthus¹, N.R. Padró¹, L.M Ottosen^{1,4}, W. Kunther^{1,3,*}

¹ Technical University of Denmark, 2800 Kgs.Lyngby, Denmark

²E-mail: sinl@dtu.dk

³E-mail: wolku@dtu.dk

⁴E-mail: limo@dtu.dk

ABSTRACT

In addition to the carbon footprint of construction materials, infrastructure in marine exposure has an environmental impact from construction processes and hardened waterfronts (ocean sprawl), which may amplify the biodiversity crisis. For artificial reef structures, different design approaches have been used and may also improve the integration of infrastructure into marine habitats to breathe life into ecosystems that are heavily influenced by human activity. Downsides of human activity are e.g., contaminants, noise, geometry, and textures that may be suboptimal for biogenic colonization and balanced ecosystems. One of the most reported materials for artificial reef structures is concrete due to its durability, the possibility to control its chemistry, and flexible use when it comes to geometry and surface textures. Hence, different cement types have been used and may yield somewhat different biological results, given equal biological conditions. At the same time, the regulations for the use of cement types for concrete in these exposure conditions differ between European countries, as concrete standard EN 206 is not harmonized. This article reviews the different cement types allowed in European standards for use in seawater exposure in selected European countries together with concrete design strategies of artificial reefs to highlight possibilities and limitations for the integration of infrastructure projects into existing habitats.

KEYWORDS: *Seawater, cement, standardization, EN 206, artificial reefs*

1. Introduction

Even though the distance between the different countries in Europe is relatively short, a significant national variation in concrete standards can be observed. These standards conform with the harmonized standard, EN 197-1 (European Commission (2011)), which defines cement types, but differ in their national application of EN 206 (European Commission, (2021)) which defines the use of concrete in each country as this standard is not harmonized. The intention of standardization was to facilitate trade through product specifications. The differences in national concrete standards, based on the same overall cement standard for Europe have been partially explained by differences in climate, building traditions, products, and market structure (Müller (2012)). Analyzing the differences between national standards and putting them in the context of marine structures that connect many of the chosen countries together with publications on ecosystem rehabilitation, provides insight into the potential of infrastructure projects to support ecosystems. Ultimately, the high environmental impact associated with cement production and infrastructure projects might be offset somewhat by implementing restoration efforts into the projects, while still maintaining the structural and durability requirements for the concrete/structure in question. Possible benefits include resource optimization, decreasing the environmental impact, enhancing biodiversity, and reducing potential damages to the concrete caused by marine exposure (Huang et al. (2016)). The environment of concrete is considered in the design (Eurocode 2) and its severity is defined by their exposure classes. Relevant for the integration of infrastructure into marine habitats are XS2 and 3, and XA3. Here we focus on XS2 and XA3, which is defined as the threat of reinforcement corrosion caused by chloride ions in permanently submerged conditions and an aggressive environment for the cement past in concrete with a special focus on sulfate attack, respectively.

Currently, no systematic studies have been found that link commonly used cement types in European countries in marine environments with infrastructure and ecosystems purposes (e.g., artificial reef), hence we started with a comparison of standards for engineering purposes as these should at least ensure the durability of the materials for 50 years; the design age in many national annexes (NA) to EN 206.

2. Method

A literature study was conducted on different concrete standards in European countries and concrete as a substrate in artificial reefs to potentially enhance biodiversity and maritime ecosystems. The state of technology for cement types used in marine constructions was analyzed by comparison of several NA of the EN 206 concrete standard, which typically refers to the harmonized standard EN 197-1 concerning cement types. During the analysis, we came across DS/CEN/TR 15868:2018 which has been used as a starting point for comparison of the permitted cement types in exposure class XS2 and XA3. The focus here is on permanently submerged structures.

The main results for XS2 and XA3 are based on 14 and 18 countries respectively and 27 cement types in compliance with EN 197-1. The data obtained in DS/CEN/TR 15868:2018 has been compared with 6 individual national standards (Denmark, Norway, Germany, Spain, Sweden, and France) as the reported data of DS/CEN/TR 15868:2018 differed in several aspects from the cited NA for Denmark. Hence it is possible that the listed cements might deviate from other countries as well as we could not get access to all NA. Please contact the authors if you want to share some of these details for other countries than the six listed above.

3. Results and discussion

Tables 1 and 2 summarize the allowed cement types regarding exposure class XS2 and XA3, respectively, for the selected 6 countries. Note that the overall trends for these countries are the same when including the remaining 8 and 12 countries, respectively for XS2 and XA3.

We focus on the cement types first as this parameter is typically provided in biological articles that focus on biofouling, not all desired material parameters such as cement quantity, strength requirement, w/b ratio or aggregate types etc. are included in biology-oriented articles. Nevertheless, the cement type provides an insight into basic design considerations that are applied in the standardization committees and restoration efforts of ecosystems as the minimal denominator.

3.1 Exposure class XS2 – Permanently submerged in seawater.

The cement types permitted for exposure class XS2 in the selected 6 European countries are stated in Table 1, for which some types are permitted under conditional constraints.

CEM I and CEM II/A-V are the only types that are permitted in all selected countries. However, when summarizing the cement types across countries, slag cements (CEM II/S, CEM II/M, CEM III) are permitted significantly more than fly ash cement (CEM II/V, CEM II/W, CEM II/M) with 28 against 16 counts respectively (76 against 56 respectively when all 14 countries are included). Please note that not all footnotes/nuances were implemented in this overview for the sake of clarity and space.

Tabel 1. Permitted cement types for exposure class XS2 for selected relevant countries. Summarized values are stated for cement types permitted in each country, and amount of cement types in each country. Cells marked with √ indicate permitted cement types. Cells marked with (√) indicate conditional use and blank cells indicate no guidance provided in the national standards.

| Country | CEMI | CEM II | | | | | | | | | | | | | | | | CEM III | | | CEM IV | | CEM V | | SUM | | | | |
|----------|------|--------|-----|-----|-----|-----|---|---|---|-----|---|---|---|---|---|-----|----|---------|---|-----|--------|-----|-------|---|-----|---|---|---|----|
| | | S | | D | P | | Q | | V | | W | | T | | L | | LL | | | | | | | | | M | | | |
| | | A | B | A | A | B | A | B | A | B | A | B | A | B | A | B | A | B | A | B | A | B | C | A | | B | A | B | |
| EN 206-1 | √ | | | | | | | | | | | | | | | | | | | | | | | | | | | | 1 |
| Denmark | DK | √ | | | | | | | | √ | | | | | | | | | | | | | | | | | | | 2 |
| France | FR | (√) | (√) | (√) | (√) | (√) | | | | (√) | | | | | | (√) | | (√) | | (√) | (√) | (√) | √ | √ | | | √ | √ | 15 |
| Germany | DE | √ | √ | √ | √ | √ | √ | √ | √ | √ | √ | | | √ | √ | √ | | √ | | | √ | √ | √ | | | | | | 17 |
| Norway | NO | (√) | (√) | √ | | | | | | (√) | √ | | | | | (√) | | (√) | | (√) | (√) | √ | √ | | | | | | 11 |
| Sweden | SE | √ | √ | √ | √ | | | | | √ | √ | | | | | | √ | | √ | √ | √ | √ | | | | | | | 10 |
| Spain | ES | √ | √ | √ | √ | √ | √ | | | √ | √ | | | | | | | | | √ | √ | √ | √ | √ | √ | √ | √ | √ | 14 |
| SUM | - | 6 | 5 | 5 | 4 | 3 | 2 | 1 | 1 | 6 | 4 | 0 | 0 | 1 | 1 | 3 | 0 | 4 | 0 | 3 | 3 | 5 | 4 | 3 | 1 | 1 | 2 | 1 | - |

None of the 6 countries permits calcareous fly ash cement while the different slag cement types (CEM II/S and CEM III/B) have similar counts, except for CEM III/C.

France and Germany are the countries that permit the most with 15 and 17 respectively. However, countries such as Belgium, Greece, and Italy permit more than 23 cement types (Danish Standard Association (2019)). Denmark permits 2 types, and as such is the most restrictive country included.

2.2 Exposure class XA3 – Highly aggressive chemical environment

From the summarized values of XA3 for each cement type across the countries (Table 2), CEM I and CEMII/A-V are observed to be the most permitted types, closely followed by CEM II/S and CEM III/A and B. As with XS2 slag cement dominates the overall permitted type with 28 cases compared to 15 for fly ash. CEM III is again the decisive factor for slag cement to be the most permitted type. None of the 6 countries permits CEM II/W, CEM II/B-L or CEM II/B-LL.

A trend that does not appear in table 2, is the high amount of cement types that require additional conditions ((√)) for XA3. In table 2, 29% are conditional, while for the 18 countries it is 79%, which might be explained by the cultural, climatic and market structure described in Müller (2012).

Denmark is again the country permitting the fewest cement types with only 2 which both additional requirements. The specific additional requirements vary depending on the country, especially Germany specify multiple conditions for XA3 which are described in Danish Standard Association (2019) and NABau (2022).

Tabel 2. Permitted cement types for exposure class XA3 for selected relevant countries. Summarized values are stated for cement types permitted in each country, and amount of cement types in each country. Cells marked with √ indicate permitted cement types. Cells marked with (√) indicate conditional use and blank cells indicate no guidance provided in the national standards.

| Country | | CEM I | CEM II | | | | | | | | | | | | | | | | CEM III | | | CEM IV | | CEM V | | SUM | | |
|----------|----|-------|--------|-----|---|-----|---|---|---|-----|-----|---|---|---|---|-----|---|-----|---------|-----|-----|--------|-----|-------|---|-----|---|---|
| | | | | | | | | | | | | | | | | | | | | | | | | | | | | |
| | | | S | | D | P | | Q | | V | | W | | T | | L | | LL | | M | | | | | | | | |
| A | B | A | A | B | A | B | A | B | A | B | A | B | A | B | A | B | A | B | A | B | A | B | A | B | | | | |
| EN 206-1 | | (v) | | | | | | | | | | | | | | | | | | | | | | | 1 | | | |
| Denmark | DK | √ | | | | | | | | √ | | | | | | | | | | | | | | | 2 | | | |
| France | FR | (v) | (v) | (v) | | (v) | | | | (v) | | | | | | | | | (v) | | (v) | √ | √ | | √ | 11 | | |
| Germany | DE | (v) | √ | √ | √ | √ | √ | √ | √ | √ | √ | | | √ | √ | √ | | √ | | | √ | √ | √ | | | 17 | | |
| Norway | NO | (v) | (v) | (v) | √ | | | | | (v) | (v) | | | | | (v) | | (v) | | (v) | (v) | (v) | (v) | | | 12 | | |
| Sweden | SE | √ | √ | √ | √ | | | | | √ | √ | | | | | | √ | | √ | √ | √ | √ | | | | 11 | | |
| Spain | ES | √ | √ | √ | √ | √ | √ | | | √ | √ | | | | | | | | | | √ | √ | √ | √ | √ | 14 | | |
| SUM | - | 6 | 5 | 5 | 4 | 3 | 2 | 1 | 1 | 6 | 4 | 0 | 0 | 1 | 1 | 2 | 0 | 3 | 0 | 3 | 2 | 5 | 5 | 3 | 1 | 1 | 2 | 1 |

3. Ecosystems restauration

Slag cement is the most permitted standard across the two analyzed exposure classes. It also happens that slag-based cement types are amongst the most utilized cement types in the context of artificial reefs and ecosystems restauration (Padró (2023)), which is maybe somewhat surprising as it is an industrial by-product. Slag cement has shown to outperform fly ash cement and Portland cement on additional parameters such as biodiversity, ecological performance, and durability (Hayek et al. (2021), Perkol-Finkel et al. (2018)), which has been suggested to depend on the pH of the material (Ido and Perkol-Finkel (2015)). Thus, slag cements appear to enhance biological colonization, making it more suitable for ecosystem restoration (Padró (2023)). Furthermore, biofouling depends on the region, for which physical parameters such as pH, salinity and chemical composition are variables, all influencing biomass and colonization (Boukhelf et al. (2022)). On the engineering side, investigations have shown that CEM III/B can display beneficial mechanical properties, particularly for marine environments due to a denser microstructure and resistance towards sulfate attack after hydration (Boukhelf et al. (2022), Ly et al. (2021)).

This insight might provide initiatives toward more balanced standardization in which eco-efficiency and durability are achievable through appropriate monitoring and relevant tests. Implementation of more binder types increases the flexibility to adapt to the increasing CO₂ emissions and the circularity agenda of the future.

4. Conclusions

Even though the cement standard in Europe, EN 197-1, is harmonized, the national standards for concrete create a wide range of possible options. This may lead to significantly different material choices even for countries that share common bodies of water. The reasoning is not necessarily transparent and may lay in traditions, market structure and experiences with different climatic conditions.

Related to constructions in marine environments, slag cements appear to provide biological, physical, and ecological advantages over e.g., Portland cements. The cement type used in marine constructions influences at least the early biological succession and thereby ecological restoration and should thus be considered for marine infrastructures. However, not all cement types which are beneficial for habitat creation/restoration are permitted in marine environments for all national standards. There might be potentials for ecological restoration and the green transition that are therefore not utilized (Scrivener et al. (2018), Sella and Perkol Finkel (2015)).

Acknowledgements

This project has received funding from European Union's Horizon 2020 research and innovation programme under grant agreement No GA 970972 and VELUX FONDEN through the project "Køge Bugt Marine Park".

References

- Boukhelf, F., Sebaibi, N., Boutouil, M., Yoris-Nobile, A. I., Blanco-Fernandez, E., Castro-Fresno, D., Real-Gutierrez, C., Herbert, R. J. H., Greenhill, S., Reis, B., Franco, J. N., Borges, M. T., Sousa-Pinto, I., van der Linden, P., Gómez, O. B., Meyer, H. S., Almada, E., Stafford, R., Danet, V., ... E. Hall, A. (2022). On the Properties Evolution of Eco-Material Dedicated to Manufacturing Artificial Reef via 3D Printing: Long-Term Interactions of Cementitious Materials in the Marine Environment. *Sustainability (Switzerland)*, 14(15). <https://doi.org/10.3390/su14159353>
- Danish Standard Association. (2019). DS/CEN/TR 15868:2018 Survey on provisions valid in the place of use used in conjunction with the European concrete standard and developing practice. Em *Dansk Standard*. www.ds.dk
- European Commission. (2021). EN 206:2013+A2:2021 Concrete-Specification, performance, production and conformity.
- European Commission (2011). EN 197-1:2011 Cement - Part 1: Composition, specifications and conformity criteria for common cements.
- Hayek, M., Salgues, M., Souche, J. C., Cunge, E., Giraudel, C., & Paireau, O. (2021). Influence of the intrinsic characteristics of cementitious materials on biofouling in the marine environment. *Sustainability (Switzerland)*, 13(5), 1–24. <https://doi.org/10.3390/su13052625>
- Huang, X., Wang, Z., Liu, Y., Hu, W., & Ni, W. (2016). On the use of blast furnace slag and steel slag in the preparation of green artificial reef concrete. *Construction and Building Materials*, 112, 241–246. <https://doi.org/10.1016/j.conbuildmat.2016.02.088>
- Ly, O., Yoris-Nobile, A. I., Sebaibi, N., Blanco-Fernandez, E., Boutouil, M., Castro-Fresno, D., Hall, A. E., Herbert, R. J. H., Deboucha, W., Reis, B., Franco, J. N., Teresa Borges, M., Sousa-Pinto, I., van der Linden, P., & Stafford, R. (2021). Optimisation of 3D printed concrete for artificial reefs: Biofouling and mechanical analysis. *Construction and Building Materials*, 272. <https://doi.org/10.1016/j.conbuildmat.2020.121649>
- Müller, C. (2012a). Use of cement in concrete according to European standard EN 206-1. *HBRC Journal*, 8(1), 1–7. <https://doi.org/10.1016/j.hbrj.2012.08.001>
- Müller, C. (2012b). Use of cement in concrete according to European standard EN 206-1. *HBRC Journal*, 8(1), 1–7. <https://doi.org/10.1016/j.hbrj.2012.08.001>
- NABau. (2022). *DIN 1045-2 Tragwerke aus Beton, Stahlbeton und Spannbeton - Teil 2: Beton*.
- Padró, N. R. (2023). *DESIGN OF CONCRETE REEF UNITS FOR DANISH MARINE HABITATS*. www.sustain.dtu.dk/english
- Perkol-Finkel, S., Hadary, T., Rella, A., Shirazi, R., & Sella, I. (2018). Seascape architecture – incorporating ecological considerations in design of coastal and marine infrastructure. *Ecological Engineering*, 120, 645–654. <https://doi.org/10.1016/j.ecoleng.2017.06.051>
- Scrivener, K. L., John, V. M., & Gartner, E. M. (2018). Eco-efficient cements: Potential economically viable solutions for a low-CO2 cement-based materials industry. *Cement and Concrete Research*, 114, 2–26. <https://doi.org/10.1016/j.cemconres.2018.03.015>
- Sella, I., & Perkol Finkel, S. (2015). Blue is the new green - Ecological enhancement of concrete based coastal and marine infrastructure. *Ecological Engineering*, 84, 260–272. <https://doi.org/10.1016/j.ecoleng.2015.09.016>

Effect of water content on fluorescence intensities of cement-based materials

Jusung Yang¹, Juhyuk Moon,^{1, 2*}

¹ Department of Civil and Environmental Engineering, Seoul National University, Seoul 08826, Republic of Korea

² Institute of Construction and Environmental Engineering, Seoul 08826, Republic of Korea

Email: juhyukmoon@snu.ac.kr

ABSTRACT

Water-cement ratio(w/c) is generally the most important design parameter for determining various material properties of construction materials. This study is performed to track the initially designed w/c in hardened concrete using visualization of capillary porosity. The difference of fluorescence intensity according to the fluorescent dyed epoxy resin infiltrated capillary pores of concrete allows to track the original w/c of concrete. The process of infiltrating the epoxy resin into concrete has been determined by making thin section of concrete for the petrography analysis. Prepared thin section samples are each six samples (cement paste, mortar) with w/c ratios ranging from 0.2 to 0.7 and five concrete samples with w/c ratios ranging from 0.35 to 0.55. It was observed that fluorescence intensity of each concrete thin section with different w/c ratios shows proportional relationship with the initial w/c ratios. However, further image processing for removing lump of fluorescent dyed epoxy resin in air voids is required for more accurate analysis.

KEYWORDS: *petrography analysis; water-to-cement ratio; cement paste; mortar; concrete*

1. Introduction

Water-cement(w/c) ratio is crucial indicator of checking safety of structure made of concrete. In order to notice the precursor of using poor concrete at the government level, standard specification amendment has been proposed. These days, the new standard specification inspecting quality of concrete mix by checking water content per unit volume of concrete was introduced in some countries.

Although figuring out the water content can explain exact amount value of w/c ratio in the concrete mix sample, it is difficult to determine the water cement ratio of the overall concrete mix. However, utilizing petrographic analysis on concrete can be the solution to trace the water cement ratio of hardened concrete. Capillary porosity plays a key role at tracking w/c ratio in cement-based materials.

According to previous research, assessing capillary porosity through fluorescence microscopy petrographic analysis is known as an effective method of figuring out w/c ratio. Understanding the influence of fluorescence dye and comparing the fluorescence intensity with cement paste, mortar, concrete will help increasing the accuracy of assessing capillary porosity.

The purpose of this study is to check and examine the accuracy of petrographic analysis on cement paste, mortar, concrete. This study, which has not been attempted so far, is expected to propose criteria for image analysis of the capillary porosity. This novel attempt is expected to suggest useful criteria for image analysis of the capillary porosity of hardened concrete.

2. Materials and experimental methods

The samples used in the study were prepared according to the ratios described in the following tables 1 and 2. The study was conducted by producing six samples of cement paste, six samples of mortar, and five concrete samples that differed in their w/c ratio, as described in the mix proportion table. The coarse aggregate was crushed stone, and the fine aggregate was silica sand. The water and cement contents were varied to achieve the target w/c ratio. Water was added to bring the oven-dried aggregates to a saturated and surface-dry state.

Fluorescence microscope was used to observe the fluorescence intensity. Collected fluorescent images are converted to grayscale images during analysis. Grayscale images of thin section samples were segmented and thresholded by a quantitative and a visual method. In case of quantitative method, the utilized thresholding approaches were the Otsu, triangular and mean selection algorithms. If the shape of a target histogram fit a suitable form for applying the algorithm, the optimum threshold value was determined.

A standard visual method was also applied, based on how much of the aggregate and pores could be filtered. The human eye is sufficiently sensitive to distinguish features present at the mid-range values of intensities; therefore, visual observation is adequate for discriminating the cement phase from the other phases.

Table 1. Mixture proportions of the cement paste and mortar samples

| Mix ID | W/C | Water (g) | OPC (g) | Fine aggregate(g) |
|----------------|-----|-----------|---------|-------------------|
| CP_0.2 | 0.2 | 200 | 1000 | 0 |
| CP_0.3 / M_0.3 | 0.3 | 300 | 1000 | 0 / 2000 |
| CP_0.4 / M_0.4 | 0.4 | 400 | 1000 | 0 / 2000 |
| CP_0.5 / M_0.5 | 0.5 | 500 | 1000 | 0 / 2000 |
| CP_0.6 / M_0.6 | 0.6 | 600 | 1000- | 0 / 2000 |
| CP_0.7 / M_0.7 | 0.7 | 700 | 1000 | 0 / 2000 |

Table 2. Mixture proportions of the concrete sample

| Mix ID | W/C | Water (g) | OPC (g) | Fine aggregate(g) | Coarse aggregate(g) |
|--------|------|-----------|---------|-------------------|---------------------|
| C_1 | 0.35 | 350 | 1000 | 2000 | 2000 |
| C_2 | 0.4 | 400 | 1000 | 2000 | 2000 |
| C_3 | 0.45 | 450 | 1000 | 2000 | 2000 |
| C_4 | 0.5 | 500 | 1000 | 2000 | 2000 |
| C_5 | 0.55 | 550 | 1000 | 2000 | 2000 |

3. Result

The obtained fluorescent images and binarized images of the concrete thin section samples are shown in Fig. 1 and Fig. 2. In the case of cement paste and mortar, samples were cured according to the above-mentioned mixture proportions, and observed in the same manner as concrete thin section was observed. Since each cement paste, mortar, and concrete has different properties such as existence of aggregates or coarse aggregates, shape of histogram differs according to each characteristic of samples. In case of Fig. 3, unimodal shape of histogram suits mean method, the method was also found to be suitable for quantitative analysis of concrete samples as a consequence. Considering that the quantitative methods (Otsu, mean, triangular method) have different suitability depending on the shape of the histogram, the difference of calculated correlation between each method was observed for each sample as shown in Fig. 4. As a result, it is confirmed that otsu method fits in mortar sample, mean method fits concrete sample, and triangular method fits cement paste sample due to its shape of histogram.

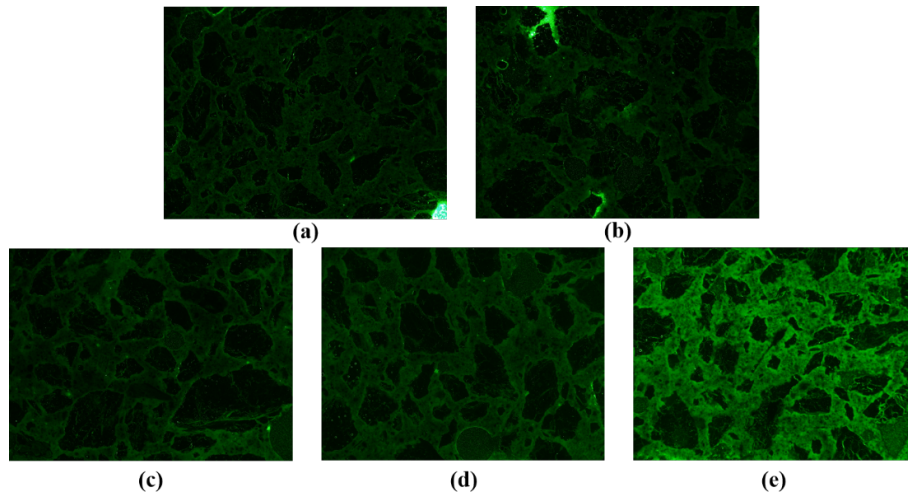


Figure 1. Fluorescent images of the concrete thin section sample.
(a) w/c ratio 0.35 (b) 0.4 (c) 0.45 (d) 0.5 (e) 0.55

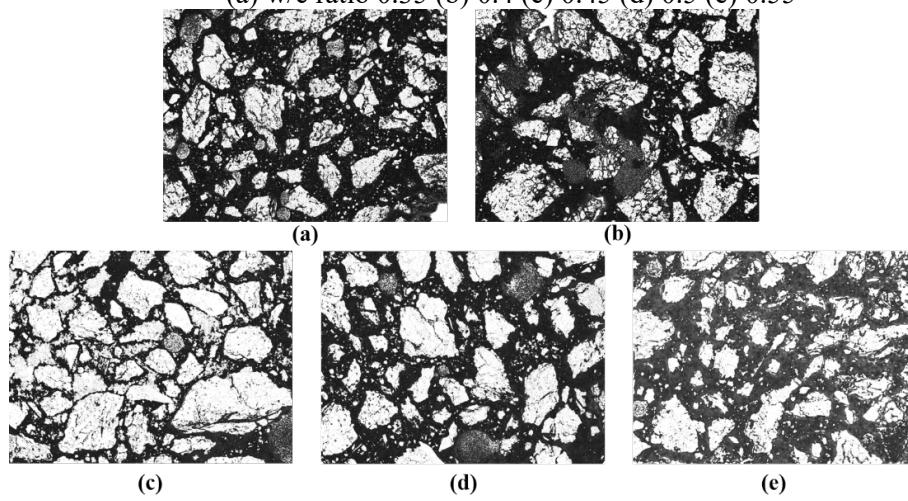


Figure 2. Binarized images of the concrete thin section sample.
(a) w/c ratio 0.35 (b) 0.4 (c) 0.45 (d) 0.5 (e) 0.55

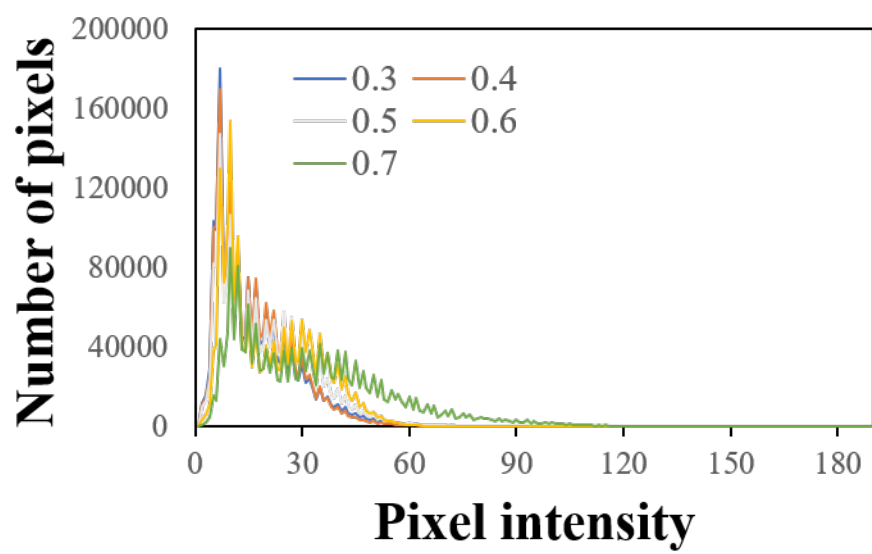


Figure 3. Calculated histogram of concrete thin section sample.

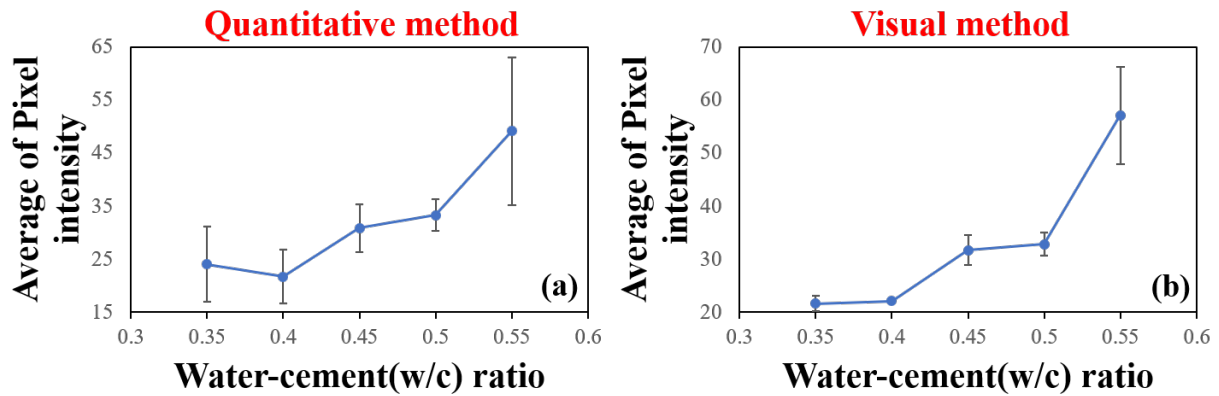


Figure 4. Calculated positive correlation between fluorescent intensity and w/c ratio of concrete thin section sample. correlation calculated by (a) quantitative method, (b) visual method

4. Conclusions

This study provides insight into improving the accuracy of tracking the w/c ratio of hardened concrete. By applying various thresholding methods to fluorescent images, we identified appropriate analysis methods according to the type of concrete.

The lower the water-cement ratio, the smaller the capillary voids, so it can be seen that the less the epoxy resin mixed with the fluorescent dye penetrates, and the lower the water-cement ratio, the lower the fluorescence intensity. By comparing the results of visual analysis of the images with those of quantitative methods, we were able to identify quantitative methods suitable for the shape of the histogram. Moreover, the accuracy and reliability of the analysis method were improved by comparing the correlation between fluorescence intensity and water cement ratio calculated by visual method and quantitative method.

However, unless the complete elimination of fluorescence clumping and brightness anomalies caused by voids is achieved, the accuracy of petrographic image analysis cannot be clearly improved. If sufficient proficiency and fluorescence intensity observation data of the flake production are further achieved in subsequent studies, it is expected that the fluorescence petrographic analysis method can play a key role in observing the water cement ratio of hardened concrete.

Acknowledgements

This work is supported by the Basic Science Research Program through the National Research Foundation of Korea (NRF) funded by the Ministry of Education, Republic of Korea (NRF-2021R1A2C4001944).

References

- Sibbick, R.G., C. LaFleur, and S. Garrity. (2016) "Using Fluorescent Microscopy as a Tool in the Determination of Water to Cementitious Binder Ratios in Hardened Concrete Samples", *Advances in Cement Analysis and Concrete Petrography*, p. 126-141.
- Otsu, N. (1979) "A threshold selection method from gray-level histograms", *IEEE transactions on systems, man, and cybernetics*, 9(1): p. 62-66.
- Gopinathan, S. and P. Deepa. (2015) "Enhancement of image segmentation using automatic histogram thresholding", *International Journal on Recent and Innovation Trends in Computing and Communication*, 3(4): p. 1863-1872.
- O. I. Singh, T. Sinam, O. James and T. R. Singh. (2012) "Local contrast and mean thresholding in image binarization", *International Journal of Computer Applications*, 51(6).
- S. Arora, J. Acharya, A. Verma and P. K. Panigrahi. (2008) "Multilevel thresholding for image segmentation through a fast statistical recursive algorithm", *Pattern Recognition Letters*, 29(2): p. 119-125.

A micromechanical modelling approach to study the effect of shape of hydrates on creep properties of cement pastes

Amit Kumar^{1*}, Shashank Bishnoi¹

¹ Indian Institute of Technology, New Delhi, India

Email: iitd.amitkr@gmail.com, Bishnoi@iitd.ac.in

ABSTRACT

Creep has been one of the major causes of the long-term deterioration of concrete structures. Despite extensive research in this area, it is still not predictable accurately. The most fundamental reason for the same is that the origin of this phenomenon is at the micro-level of cement paste. If the microstructure and its response to an applied load are understood, a better prediction of creep is possible. With recent advancements in the field of characterization techniques, the microstructure of cement pastes is now better understood. Models that can precisely simulate the microstructures and their constitutive behavior are promising techniques to estimate creep at the macro level. Analytical methods based on physics are popular amongst such techniques for simulating this micro-level phenomenon. Besides modeling their interactions fairly, they can account for various shapes of the cement hydrates and their pore structures at micro and nano levels. This work uses a MATLAB model with Eshelby's theory and the homogenization approaches of continuum micromechanics to account for hydrates' shapes and volume fractions and their mutual interaction. The model predicts that with the increase in aspect ratios of the shape of hydrates, the macroscopic creep of cement paste reduces.

KEYWORDS: *Cement, creep, multiscale modeling, continuum micromechanics*

1. Introduction

Creep in concrete is one of the major concerns when it comes to long-term performance of concrete. The reason is that it cannot be precisely predicted and hence its effects cannot be accounted a priori. However, it is known that creep in concrete is mainly in cement paste, as the aggregates are almost elastic when compared to cement paste. Further, the macrostructural behavior of creep of cement paste and hence concrete has its roots at the micro/nano level of cement paste. Therefore, the microstructure of cement paste and the physics of the interaction of the microstructural hydrates (hydration products of cement) of cement becomes essential to be understood and appropriately incorporated while developing the methods of estimation of creep in any structure. Models accounting for the microstructural behaviour of cement paste are therefore powerful techniques for predicting its macrostructure behaviour like creep.

The method of using microstructural creep models of concrete have three stages. Firstly, the microstructure of cement paste (sizes of hydrates and their spatial arrangement), secondly, their individual constitutive property and lastly physics of interaction between them.

This paper will first discuss a brief summary about first two stages and then a detailed discussion of the third stage which involves micromechanical modelling of the intrinsic properties and their upscaling.

2. Cement Paste Microstructure

Knowing the exact shapes, sizes, orientation and spatial arrangement of hydrates is very difficult. It keeps changing with time due to ongoing hydration. Therefore, a cement paste can be classified into an ageing one (whose microstructure is still developing, due to ongoing hydration) and a non-ageing one (whose hydration can be assumed to be almost complete and hence microstructure is stable).

Experimental techniques like Scanning Electron Microscopy (SEM), Transmission electron microscopy (TEM), X-ray diffraction (XRD), Nuclear Magnetic Resonance (NMR), etc. are very much sensitive to the

sample and many of such experiments are required to statistically represent the cement paste. Moreover, the microstructure of even a completely hydrated paste cannot be idealized and used for another hydrated paste, because, it depends upon several factors like, composition of the cement, water-cement ratio, quality of water, curing conditions like temperature and relative humidity, etc.

Microstructural models have the advantage of modelling only the aspects required such as porosity, permeability or say other mechanical properties. They are relatively easy and faster to have a quick and precise representation of the microstructure. One of the most widely used model is the two-phase model: the solid phase consisting of hydrated cement particles and other mineral phases and the other is the pore phase. Other models include multi-phase model, which considers additional phases such as unhydrated clinker too. A detailed review of microstructural models' importance, utility, and current limitations may be found in Bishnoi and Bullard (2022).

3. Intrinsic properties of hydrates

Constitutive properties of hydrates of cement as well as unhydrated clinker particles may be taken as intrinsic in nature. It is the variation in the volume of these constituents, which changes the overall response in different cement pastes. Several works in this area may be found in literature which either used nano/micro indentation tests or have downscaled a macroscopic response of cement paste. A summary of intrinsic properties of different constituents of a cement paste is shown in **Error! Reference source not found.1**.

Table 1 Intrinsic elastic properties of constituents of a cement paste

| Phase | Young's modulus [GPa] | Poisson's ratio | References |
|-------------------|--------------------------|-----------------|--|
| C ₃ S | 128-142,142-152 | 0.3 | Acker (2004),Velez et al. (2001) |
| C ₂ S | 130-150,110-150 | 0.3 | Acker (2004), Velez et al. (2001) |
| C ₃ A | 150-170,135-155 | 0.3 | Acker (2004), Velez et al. (2001) |
| C ₄ AF | 100-150 | - | Velez et al. (2001) |
| Portlandite | 33-39,33-43, 39.77-44.22 | 0.305-0.325 | Acker (2004),Constantinides and Ulm (2004),Monteiro and Chang (1995) |
| LD C-S-H | 18-22,19.5-23.9 | 0.24 | Acker (2004), Constantinides and Ulm (2004) |
| HD C-S-H | 27-35,27.0-31.8 | 0.24 | Acker (2004), Constantinides and Ulm (2004) |

3. Multiscale Models of creep

Multiscale analytical models involve the concept of viewing concrete as a multiscale composite. A concrete which appears homogenous at a macroscale can be viewed as a heterogenous material composed of aggregates and a homogenous cement paste at an observation scale of say millimetres. Similarly, the "homogenous" cement paste at a millimetre scale is a heterogenous material composed of hydrates and pores at few micrometres. Similarly various multiscale thought models have been used for modelling cement pastes Constantinides and Ulm (2004); Honorio, Bary, and Benboudjema (2016).

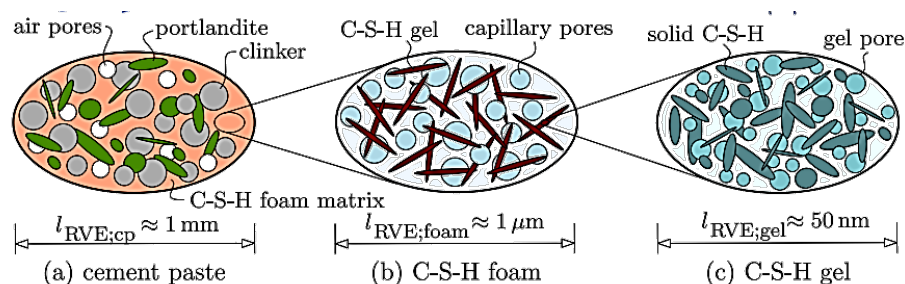


Figure 1 A sample Multiscale micromechanical model

For accounting the response of an individual constituents to an applied stress/strain on the boundary of the RVE, the approach of stress and strain concentration tensors are used which are based upon the Eshelby theory, Eshelby (1957). It gave solution for strain distribution due to an ellipsoidal inclusion inside an infinite homogenous medium (Figure 2).

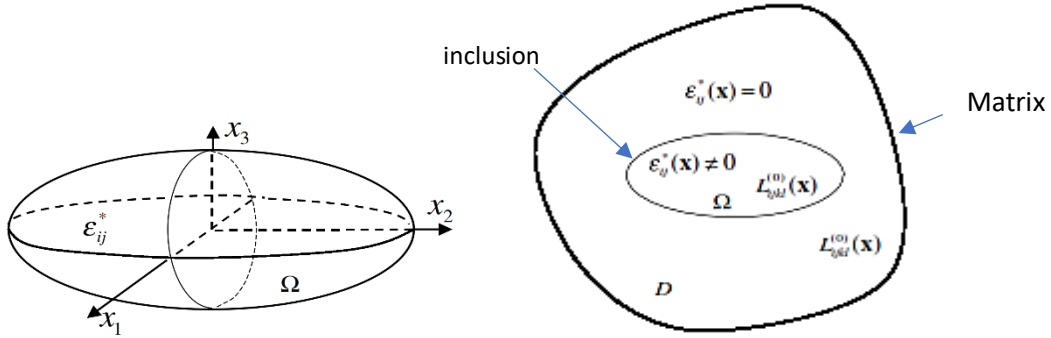


Figure 2 an Ellipsoidal inclusion inside a homogenous matrix

Total strain inside the inclusion $\varepsilon(\mathbf{x})$ due an eigen strain ε^* inside it is given as

$$\varepsilon_{ij}(\mathbf{x}) = S_{ijkl} \varepsilon_{kl}^* \quad (1)$$

Where \mathbf{S} is called the Eshelby's concentration tensor and is independent of the eigen strain and size of the inclusion. It only depends on shape of the inclusion and the stiffness of the matrix. Hydrates of cement paste can be modelled as idealized shapes like spheres, ellipsoids, prolates, oblates, etc. Combining Eshelby's theory with the average stress theorem, various homogenization techniques, for example, the Mori and Tanaka (1973), the Self-Consistent scheme Hill (1965), can be applied to get equivalent properties of the material at a particular scale by accounting the interaction of the constituents of that level. Thereafter, the equivalent stiffness of the heterogeneous RVE can be found from expression like

$$\bar{\mathbf{L}} = \mathbf{L}_0 + \sum_{r=1}^N c_r (\mathbf{L}_r - \mathbf{L}_0) \mathbf{A}_r \quad (2)$$

Where c_r is the volume fraction of r^{th} inhomogeneity. The strain concentration tensor \mathbf{A}_r is then

$$\mathbf{A}_r = [\mathbf{I} + \mathbf{S}_r \mathbf{L}_0^{-1} (\mathbf{L}_r - \mathbf{L}_0)]^{-1} \quad (3)$$

Though exact equations for calculating Eshelby's tensors exist, but they are complex and involve a lot of calculative efforts. Therefore, for modelling, equations by Mura (1987) are used. A relationship between the Eshelby's concentration tensor and aspect ratio of a prolate shaped hydrate is shown by the output of the model in MATLAB in Figure 3 below. The inverse relation between the Eshelby's tensor and stiffness tensor from equation (2) and (3) means a direct relation with the creep compliance. The homogenization techniques mentioned were developed for elastic behavior and can be applied to obtain the equivalent strain response of a heterogeneous viscoelastic material using the correspondence principle.

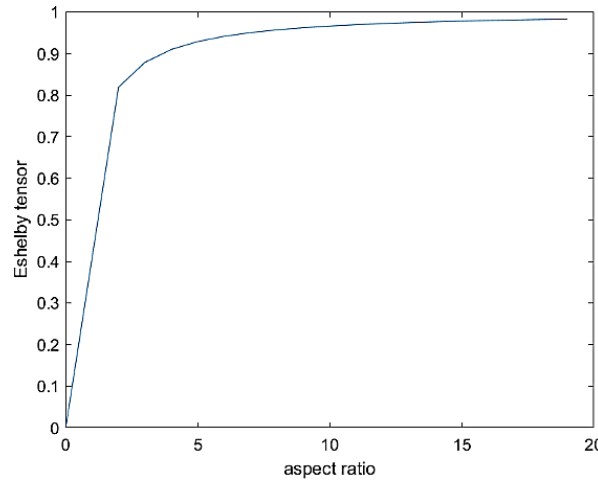


Figure 3 Dependence of strain concentration tensor on aspect ratio

3. Methodology

For the aging case, the material parameters change which change the compliance function $J(t, \tau)$ over time. It means that J is a function of both the time “ τ ” at which the sample was loaded and “ t ” the sample age. Whereas for non-aging cases, the compliance function is not modified with time, only its value increases. Therefore, it only depends upon the time elapsed since loading and can be represented as $J(t-\tau)$. Expression for strain (Figure-2) becomes a convolution integral in this case and Laplace Carson (LC) transformation of the integral gives an expression like elastic material in LC domain. Homogenization techniques can then be employed in the Laplace-Carson (LC) domain using the correspondence principle. After homogenization, the final compliance is converted back to the time domain to get the overall compliance of the material. Figure-2 illustrates the same.

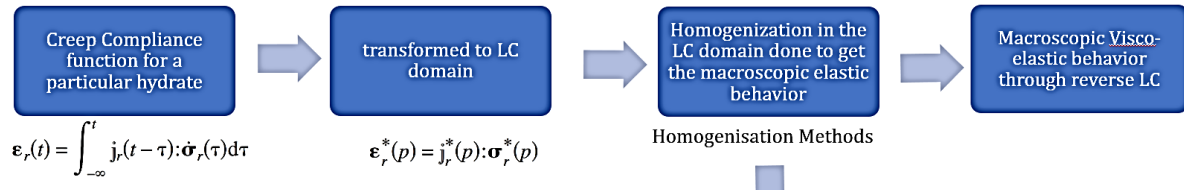


Figure 4 Flowchart for micromechanical analytical models of creep: non-Aging case

The third step in Figure 4 above involves finding an equivalent material for a heterogeneous RVE and homogenisation techniques as listed above are used for it.

4. Conclusions

Eshelby Tensor and hence creep modulus of cement paste is found to increase with the aspect ratio of assumed prolate shape of the hydrates of cement pastes. This may be explained due to the possible mechanism of a more direct interaction between the isotropically arranged hydrates due to their longer shape.

References

- Acker, P. (2004). “Swelling, Shrinkage and Creep: A Mechanical Approach to Cement Hydration.” *Materials and Structures* 37:7.
- Bishnoi, Shashank, and Jeffrey W. Bullard. (2022). “Microstructure Models of Cement: Their Importance, Utility, and Current Limitations.” *RILEM Technical Letters* 6:188–95. doi: 10.21809/rilemtechlett.2021.135.
- Constantinides, Georgios, and Franz-Josef Ulm. (2004). “The Effect of Two Types of C-S-H on the Elasticity of Cement-Based Materials: Results from Nanoindentation and Micromechanical Modeling.” *Cement and Concrete Research* 34(1):67–80. doi: 10.1016/S0008-8846(03)00230-8.
- Eshelby, J. D. (1957). “The Determination of the Elastic Field of an Ellipsoidal Inclusion, and Related Problems.” *Royal Society*.

- Hill, R. (1965). "A Self-Consistent Mechanics of Composite Materials." *Journal of the Mechanics and Physics of Solids* 13(4):213–22. doi: 10.1016/0022-5096(65)90010-4.
- Honorio, Tulio, Benoit Bary, and Farid Benboudjema. (2016) "Multiscale Estimation of Ageing Viscoelastic Properties of Cement-Based Materials: A Combined Analytical and Numerical Approach to Estimate the Behaviour at Early Age." *Cement and Concrete Research* 85:137–55. doi: 10.1016/j.cemconres.2016.03.010.
- Königsberger, Markus, Bernhard Pichler, and Christian Hellmich. (2020). "Multiscale Poro-Elasticity of Densifying Calcium-Silicate Hydrates in Cement Paste: An Experimentally Validated Continuum Micromechanics Approach." *International Journal of Engineering Science* 147:103196. doi: 10.1016/j.ijengsci.2019.103196.
- Monteiro, Paulo J. M., and C. T. Chang. (1995). "The Elastic Moduli of Calcium Hydroxide." *Cement and Concrete Research* 25(8):1605–9. doi: 10.1016/0008-8846(95)00154-9.
- Mori, T., and K. Tanaka. (1973). "Average Stress in Matrix and Average Elastic Energy of Materials with Misfitting Inclusions." *Acta Metallurgica* 21(5):571–74. doi: 10.1016/0001-6160(73)90064-3.
- Mura, Toshio. (1987). *Micromechanics of Defects in Solids*. 2nd, rev. ed ed. Dordrecht, Netherlands ; Boston : Hingham, MA, USA: M. Nijhoff ; Distributors for the U.S. and Canada, Kluwer Academic Publishers.
- Velez, Karine, Sandrine Maximilien, Denis Damidot, Gilbert Fantozzi, and Francois Sorrentino. (2001). "Determination by Nanoindentation of Elastic Modulus and Hardness of Pure Constituents of Portland Cement Clinker." *Cement and Concrete Research* 31(4):555–61. doi: 10.1016/S0008-8846(00)00505-6.